Fundamentals of Acoustical Oceanography

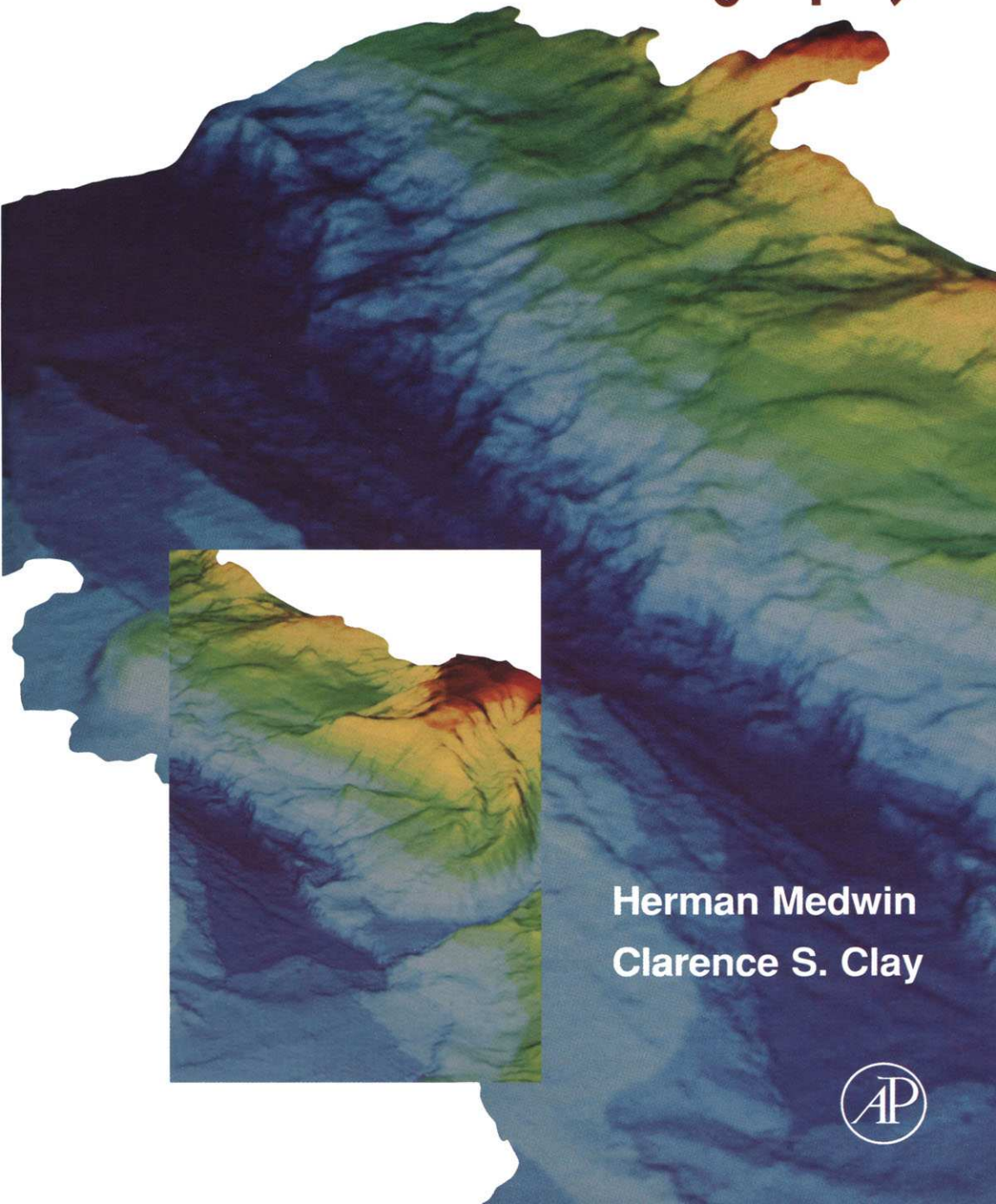

Herman Medwin
Clarence S. Clay

Fundamentals of Acoustical Oceanography

This is a volume in
APPLICATIONS OF MODERN ACOUSTICS

Series Editors:
Richard Stern
Applied Research Laboratory
Pennsylvania State University
State College, Pennsylvania

Moises Levy
Department of Physics
University of Wisconsin at Milwaukee
Milwaukee, Wisconsin

Fundamentals of Acoustical Oceanography

Herman Medwin
Department of Physics
Naval Postgraduate School
Monterey, California

Clarence S. Clay
Department of Geology & Geophysics
University of Wisconsin at Madison
Madison, Wisconsin

ACADEMIC PRESS
Boston San Diego New York
London Sydney Tokyo Toronto

This book is printed on acid-free paper. ∞

ACADEMIC PRESS
525 B Street, Suite 1900, San Diego, CA 92101-4495, USA
1300 Boylston Street, Chestnut Hill, MA 02167, USA
http://www.apnet.com

United Kingdom Edition published by
ACADEMIC PRESS LIMITED
24–28 Oval Road, London NW1 7DX
http://www.hbuk.co.uk/ap/

Library of Congress Cataloging-in-Publication Data
Medwin, Herman
Fundamentals of acoustical oceanography/ Herman Medwin, Clarence S. Clay.
p. cm.
Includes bibliographical references and index.
ISBN 0-12-487570-X (alk. paper)
1. Underwater acoustics. 2. Seawater—Acoustic properties. 3. Oceanography. I. Clay, Clarence S. (Clarence Samuel). II. Title.
OC242.2.M43 1997
551.46'001'53423—DC21 97–35785
CIP

Printed in the United States of America
97 98 99 00 01 IP 9 8 7 6 5 4 3 2 1

Table of Contents

Series Preface xvii
Author Preface xviii
Acknowledgments xx

Chapter 1 The Realm of Acoustical Oceanography: Theory and Applications of Ocean Acoustics 1

1.1 Introduction 1
1.1.1 Definition 1
1.2 Physical and Biological Characteristics of the Sea 2
1.3 Ocean Stratification, Sound Speed, and Ray Refraction 2
1.4 A Few Examples of Acoustical Oceanography 6
1.4.1 Pulse Timing of Transmissions 8
1.4.2 Remote Sensing by Scatter 10
1.4.3 Passive Acoustics 15

Chapter 2 Sound Propagation 17

2.1 Wave Propagation 17
2.1.1 Intensity of a Diverging Wave 18
2.2 Huygens' Principle for Impulse Waves 19
2.2.1 Plane Wave Reflection at a Plane Surface: Law of Reflection 22
2.2.2 Plane Wave Refraction at a Plane Interface: Snell's Law 22
2.2.3 Diffraction at the Edge of a Plane Interface: Scattering of a Spherical Wave 23

2.3 CW Sinusoidal Signals: Spherical Waves 24
2.3.1 Variations in Time and Space 24
2.3.2 Traveling Spherical Waves 27
2.4 CW Interference and Phase Effects 27
2.4.1 Approximations 28
2.4.2 Sum of Sounds from Two Sources 32
2.4.3 Interference Near an Interface: Plane Standing Waves 33
2.4.4 Point Source Near a Plane Reflector: Lloyd's Mirror Interference 34
2.5 The Wave Equation 35
2.5.1 Conservation Laws and the Equation of State for Linear Acoustics 36
2.5.2 The One-Dimensional Wave Equation and Other Relations 38
2.5.3 Acoustic Intensity 40
2.6 Reflection and Transmission at Interfaces 41
2.6.1 Plane Wave Reflection and Transmission Coefficients: Critical Angle 41
2.6.2 Plane Wave Reflection at a Sedimentary Bottom 45
2.6.3 Plane Wave Reflection and Transmission at Multiple Thin Layers 46
2.6.4 Ray Reflection beyond Critical Angle 50
2.6.5 Head Waves: Spherical Waves beyond Critical Angle 51
2.6.6 Fresnel Zones: Spherical Wave Reflection at an Interface 55
2.7 Propagation in Three Dimensions 58
2.7.1 The Three-Dimensional Wave Equation 58
2.7.2 Continuous Waves in Rectangular Coordinates 62
2.7.3 Omnidirectional Waves in Spherical Coordinates 64

Chapter 3 Transmissions along Ray Paths 70
3.1 Impulse and CW Propagation in Ocean Acoustics 72
3.1.1 Impulse Sources 72
3.1.2 Pressure, Particle Velocity, and Intensity in a Pulse 74
3.1.3 Pulse Energy Transmission 75
3.1.4 Radiated Power for Continuous Wave Signals 76
3.2 Ray Paths, Ray Tubes, and Path Times 77
3.2.1 Path Amplitude Factor and Path Time 77
3.2.2 Reflections along Ray Paths 78
3.2.3 Multiple Ray Paths 80
3.2.4 Conservation of Energy in Ray Tubes: Nonabsorbing, Nonscattering Iso-Speed Medium 82

3.2.5 Sound Pressures in Ray Tubes: Homogeneous, Nonabsorbing, Nonscattering Medium 83
3.3 Ray Paths in a Lossless, Refracting Medium 84
3.3.1 Sound Speed in the Ocean 84
3.3.2 Refraction at an Interface: The Ray Parameter 85
3.3.3 Rays through Constant-Speed Layers 86
3.3.4 Rays through Continuous Sound-Speed Changes 87
3.3.5 Examples of Ray Paths 89
3.3.6 Sound Intensity and Pressure in a Horizontally Stratified Ocean 92
3.3.7 Wave Fronts and Crossing Ray Paths: Phase Shifts at Caustics 94
3.3.8 Signal Transmissions in a Refracting Medium with Caustics 96
3.3.9 General Comments on Ray Path Methods 102
3.4 Attenuation 103
3.4.1 Exponential Attenuation of Plane Waves 103
3.4.2 Absorption Losses 104
3.4.3 Scattering Losses 110
3.4.4 Amplitude SONAR Equation 111
3.4.5 Sum of Multiple Arrivals: The Transmission Fraction 111
3.4.6 Logarithmic SONAR Equations: Transmission Loss (dB) 113
3.5 Tomography 116
3.5.1 Inverting for a Map of the Speed of Sound 116
3.5.2 Inverting for Ocean Motions 119
3.6 Doppler Frequency Shift 119
3.6.1 Doppler Theory 119
3.6.2 Doppler Measurements of Particle Motion 120
3.6.3 Sea-Surface Motion 122
3.6.4 Doppler Navigation 124

Chapter 4 Sources and Receivers 127
4.1 Transducer Elements 127
4.1.1 The Pulsating Sphere 127
4.1.2 Sources of Sound 128
4.1.3 The Dipole 130
4.1.4 Materials and Mechanisms 131
4.2 Arrays of Discrete Sources 133
4.3 Directivity of a Line Source 135
4.4 Circular Piston Source 138

4.4.1 Far-Field Directivity 138
4.4.2 Near-Field Directivity 142
4.5 Radiation from a Transducer 143
4.5.1 Total Power Radiated 143
4.5.2 Descriptors of Beam Strength 145
4.6 Equivalence of Source/Receiver Directivity 146
4.7 Free-Field Calibration of Transducers 149
4.8 Self-Reciprocity Calibration of Transducers 150

Chapter 5 High Intensities 153
5.1 Harmonic Distortion and Shock-Wave Growth 153
5.2 Cavitation 158
5.3 Parametric Sources and Receivers 162
5.3.1 CW Parametric Sources 162
5.3.2 Parametric Receivers 168
5.3.3 Intense Tone Bursts, Self-Demodulation 170
5.4 Explosive Sources 170
5.4.1 The Shock Wave 170
5.4.2 Shock Front Propagation; the Rankine-Hugoniot Equations 173
5.4.3 The Gas Globe 174
5.4.4 Interaction with the Ocean Surface 176
5.5 Acoustic Radiation Pressure 177
5.6 Acoustic Streaming 178

Chapter 6 Processing of Ocean Sounds 183
6.1 Sampling Rules 184
6.1.1 Spatial Sampling 185
6.1.2 Temporal Sampling 185
6.2 Filter Operations 188
*6.2.1 Finite Fourier Transformations 188
*6.2.2 Fourier Integrals and Series 191
6.2.3 Filter Response Measurements 194
6.2.4 Time Domain View of Bandpass Filtering 195

* Optional background material.

*6.2.5 Convolution Operations 195
6.2.6 Filter Operations in the Frequency Domain 197
6.3 Gated Signals 199
6.3.1 Dependence of Spectrum on Ping Carrier Periodicity 200
6.3.2 Dependence of Spectrum on Ping Duration 200
6.4 Power Spectra of Random Signals 200
6.4.1 Signals Having Random Characteristics 203
*6.4.2 Spectral Density and Correlation Methods 203
6.4.3 Random Signal Simulations: Intensity Spectral Density 204
6.4.4 Spectral Smoothing 206
6.4.5 Traditional Measures of Sound Spectra 208
6.5 Matched Filters and Autocorrelation 209
6.6 Sounds in the Ocean 211
6.6.1 Natural Physical Sounds 212
6.6.2 Natural Biological Sounds 215
6.6.3 Ship Noise: Sample Calculation 219

Chapter 7 Sound Scattered by a Body 234
7.1 Scattering Measurements: Incident Plane-Wave Approximation 235
7.1.1 Scattering Length 237
7.1.2 Differential Scattering Cross Section 237
7.1.3 Total Scattering and Extinction Cross Sections 238
7.1.4 Target Strength 240
7.1.5 Single Transducer Backscattering 240
7.2 Helmholtz-Kirchhoff Methods 241
*7.2.1 Theorems of Gauss and Green 241
7.2.2 The Helmholtz-Kirchhoff Integral 243
7.2.3 Kirchhoff Approximation 244
7.2.4 Fresnel Approximation 246
7.3 Specular Backscatter by the Kirchhoff Method 249
7.3.1 Rectangular Plane Facet 249
7.3.2 Penetrable Cylinder 252
7.3.3 Finite Fluid Cylinder 255
7.3.4 Low-Contrast Finite Fluid Cylinder 256
7.4 Modal Solutions for a Fluid Cylinder 258

* Optional background material.

*7.4.1 Infinite Cylinder 259
7.4.2 Finite Cylinder 262
7.4.3 Comparison of Kirchhoff and Modal Solutions 265
7.4.4 Equivalent Sphere for Small Fluid Bodies 265
7.5 Scattering from a Sphere 267
7.5.1 Geometrical Scatter from a Rigid Sphere ($ka \gg 1$) 268
7.5.2 Rayleigh Scatter from a Small Sphere ($ka \ll 1$) 271
*7.5.3 Axially Symmetric Spherical Mode Solutions 276
7.5.4 Total Scattering Cross Section 280
7.5.5 Rigid Sphere 281
7.5.6 Fluid Sphere 284

Chapter 8 Bubbles 287
8.1 Scattering from a Spherical Gas Bubble: Modal Solution 289
8.1.1 Scattering Directivity 289
8.1.2 Backscattering Length 290
8.2 Single Pulsating Bubbles: $ka \ll 1$ 292
8.2.1 Lumped Constants of Bubble Pulsation 292
8.2.2 Bubble Stiffness 293
8.2.3 Equivalent Bubble Mass 293
8.2.4 Simple Pulsation; Breathing Frequency 294
*8.2.5 Effects of Surface Tension, Shear Viscosity, and Thermal Conductivity 295
8.2.6 Damping Constants 299
8.2.7 Acoustical Cross Sections 302
8.2.8 Insonified Damped Pulsations 304
8.2.9 Decaying Bubble Pulsations 306
8.2.10 Near-Surface and Nonlinear Bubble Pulsations 307
8.2.11 Nonspherical Bubbles 308
8.2.12 Damping Constants of Bubbles in Seawater 310
8.3 Bubbly Water 310
8.3.1 Sound Backscattered by an Ensemble of Bubbles 311
8.3.2 Excess Attenuation 314
8.3.3 Sound Speed Dispersion and Wood's Equation 317
8.4 Active Measurements in Bubbly Water 322
8.4.1 Techniques for Linear Bubble Counting 322

* Optional background material.

8.4.2 Dependence of Bubble Densities on Winds, Place, and Time 327
8.4.3 Gas Void Fraction 331
8.4.4 Sound Phase Fluctuations 332
8.4.5 Collective Oscillations and Low Frequency Noise 333
8.5 Sea Surface Microbubble Production 333
8.5.1 Bubbles from Breaking Waves 333
8.5.2 Bubbles from Rainfall 338
8.6 Bubbles in Sediments 341

Chapter 9 Biomass Echoes, Reverberation, and Scattering Models 348
9.1 Introduction to Bioacoustics 348
9.2 Sound Backscattered by a Fish: Echoes 350
9.3 Sound Backscattered by Many Bodies: Reverberation 353
9.3.1 Randomly Spaced Objects in a Directional Beam 354
9.3.2 Time-Integral-Pressure-Squared Calculations for Many Scatterers 357
9.3.3 Volume Backscattering Coefficient 358
9.3.4 Scattering Layers 361
9.4 Variability of Fish Structure and Sound Backscatter 363
9.4.1 Physical Structures: X-Rays and High-Frequency Sound Scans 363
9.4.2 Echo Statistics: Rician, Rayleigh, and Extremal 364
9.5 Acoustical Models of Fish 372
9.5.1 Anatomical-Acoustical Models 372
9.5.2 HK Acoustical Scattering Models for Swimbladder Fish ($ka > 1$) 373
9.5.3 Comparisons of High-Frequency Acoustical Models and Data 381
9.5.4 Low-Frequency Swimbladder Resonance Models 384
9.6 Sound Backscattered by Zooplankton 391
9.6.1 HK Acoustical Models of Zooplankton 392
9.6.2 Bent-Cylinder Acoustical Models 396
9.6.3 Scattering Amplitudes of Live Shrimp 398
9.7 Bubble-Carrying Plankton 401
9.8 Allometric Expressions for Zooplankton 401

Chapter 10 Sonar Systems: Measurements and Inversions 405
10.1 Types of Sonars 406
10.1.1 Echo Sounder 407
10.1.2 Side-Scanning Sonar 408

	10.1.3	Multibeam Sonar	408
	10.1.4	Doppler Sonar	411
	10.1.5	Passive Acoustical Systems	411
	10.1.6	Steered Array Systems	413
10.2	Sonar Systems: Details		416
	10.2.1	Generic Sonar	416
	10.2.2	Band-Shifting or Heterodyning Operations	418
	10.2.3	Echo Identification Rules	422
	*10.2.4	Using Sonar System Specifications	424
	10.2.5	Sonar Calibration with a Hard Spherical Target	427
10.3	In Situ Scattering-Length Measurements		430
	10.3.1	Empirical Target Strength Formulas for Fish at $L/\lambda > 1$	430
	10.3.2	Echoes from Single Fish and the Critical Fish Densities	431
	10.3.3	Dual-Beam Sonars	432
	10.3.4	Split-Beam Sonars	435
*10.4	Single Transducer Scattering Length Measurements		437
	10.4.1	Probabilities	438
	10.4.2	Transducer Beam Pattern PDF	439
	10.4.3	Combination of Fish Echo PDF and Transducer PDF	441
	10.4.4	Convolution Expression for Echo PDF	443
	10.4.5	Fish Echo Data Reduction	443
	10.4.6	A Forward Iteration Estimate of Fish Density	445
	10.4.7	Deconvolution Method for Fish Density and Echo PDF	445
	10.4.8	Examples of Single Transducer Surveys	447
10.5	Interactions of Sonars and Fish Behavior: Simulations		449
	10.5.1	Ensemble of the Same Species of Fish	450
	10.5.2	The PDF w_F of an Ensemble of Fish	451
	10.5.3	Very Narrow Beam Width and Random Fish Tilts	454
	10.5.4	Wide Beam Width and Horizontal Fish	456
10.6	Quantitative Reverberation Analysis: Zooplankton		458
	10.6.1	Volume Reverberation Equations	460
	*10.6.2	Inverse Solution Using Multiple Frequencies	461
	10.6.3	Acoustic Profiles of Zooplankton	462

Chapter 11 Waveguides: Plane Layers and Wedges 468

11.1 Normal Modes in Plane-Layered Media 469

* Optional background material.

11.1.1 Wave Equation in a Waveguide 469
11.1.2 Depth Dependence in an "Idealized" Waveguide 471
11.1.3 Orthogonality of Modes 473
11.1.4 Sound Pressure and the Sum of Modes 474
11.1.5 Reflections and Transmissions at the Waveguide Boundaries 476
11.1.6 Modal Equations (Characteristic Equations) 477
11.1.7 Numerical Example: Two-Layer Waveguide 480
11.2 Geometrical Dispersion: Phase and Group Velocities 486
11.2.1 Phase Velocity 486
11.2.2 Group Velocity 487
11.2.3 Dispersed Arrival: $p(t)$ 490
11.3 Arrays, Signals, and Noise 493
11.3.1 Arrays of Sources and Receivers in a Waveguide: Mode Filters 493
11.3.2 Noise in Waveguides 496
11.3.3 Signal-to-Noise Ratio and the Optimum Array Filter 497
11.3.4 Matched Array Filter for Source Location 498
11.4 Transmission Functions in Matrix Notation 499
11.4.1 Example for Two Modes 499
11.4.2 Array of Receivers 500
11.5 Source Location 501
11.5.1 Matched Field Processing 502
11.5.2 Optimum Mode Processing 505
11.5.3 Time Domain Source Location 506
11.6 Range-Dependent Waveguide: Wedge 509
11.6.1 "Adiabatic" Approximation 509
11.6.2 Transmission in Wedge Waveguides 510
11.7 Parabolic Equation (PE) Method 514
11.8 Wedge Waveguide in the Time Domain: Biot-Tolstoy Method 516
11.8.1 Normal Coordinate Method 519
11.8.2 Region 2: Arrivals from Images 524
11.8.3 Region 3: Diffraction Arrival 527
11.8.4 Numerical Examples 532
11.8.5 Comparisons of Theory and Experiments 534

Chapter 12 Scattering at Elements of a Rough Surface 541
12.1 The Helmholtz-Kirchhoff Integral for Surface Scatter 542

12.2 Implementation of Biot-Tolstoy Theory of Impulse Scatter from Wedges and Plates 542
12.2.1 Theory for Infinite Wedges 542
12.2.2 Reflection and Diffraction in the Time Domain: Realizations and Verifications 546
12.2.3 Digital Implementation for Finite Wedges 551
12.2.4 Simplifications 554
12.3 Digital Calculations of Biot-Tolstoy Diffraction in the Frequency Domain 555
12.3.1 Comparison of Diffraction Backscatter Predictions of HK and BT Theories 559
12.3.2 Double Diffraction 559
12.3.3 Forward Diffraction at a Seamount 562
12.3.4 The Finite Wedge Approximation to the Infinite Wedge 565
12.3.5 Components of Reverberation from Rough Surfaces 568
12.4 BT Wedge Assemblage Techniques: Rough Surfaces 569
12.4.1 Parallel Wedges: Laboratory Test of a Sinusoidal Long-Crested Water Surface 569
12.4.2 Parallel Wedges: The Ocean as a Low-Frequency Diffraction Grating 570
12.4.3 Synthetic Seismic Profiles 573

Chapter 13 Scattering and Transmission at Statistically Rough Surfaces 577
13.1 Descriptions of Ocean Surfaces 578
13.1.1 The Wind-Blown Surface 578
13.1.2 The Rough Ocean Bottom 589
13.2 Forward Scatter in the Specular (Mirror) Direction: Simple Concepts 593
13.2.1 Mean Coherent Scattered Pressure in the Specular Direction, Acoustical Roughness 594
13.2.2 Inverting for the PDF of Heights 596
13.2.3 Statistics of Scatter in the Specular Direction 597
13.2.4 Intensity of Sound Scattered in the Specular Direction: Scale-Model Results 601
13.2.5 Other Specular Scatter Effects 605
13.3 Surface Scatter of Sound 606
13.3.1 Scatter of Spherical Waves: Helmholtz-Kirchhoff-Fresnel Solution 607
13.3.2 Mean-Squared Scattered Pressure: Surface Scattering Strength 610
13.3.3 Dependence of Specular Scatter on the Parameters of the Experiment: Apparent Reflection Coefficient and Bottom Loss (dB) 613
13.3.4 Scale-Model Proofs of the Dependence of Scatter on Parameters of the Experiment 615

13.3.5 Computer Model of Point-Source Backscatter from an Ocean Surface 618
13.3.6 Scattering from a Two-Dimensional Rough Surface: Tri-wedge Computer Assemblages 623
13.3.7 Effect of Bubbles below the Ocean Surface 625
13.4 Near Grazing Scatter at a Steep-Sloped, Rough Surface 627
13.5 Point-Source Transmission through a Rough Interface 632
13.5.1 Smooth Air-Sea Interface 632
13.5.2 Rough Air-Sea Interface 635

Chapter 14 Mapping the Sea Floor 640
14.1 Bathymetric and Seismic Profiles: Geophysics 640
14.2 Deep-Tow Side-Scan Sonar Mapping of the Sea Floor 641
14.3 Swath Mapping from Surface Vessels 644
14.3.1 Acoustic Survey: Laurentian Fan 646
14.3.2 Swath Mapping System 647
14.3.3 Data Reduction 649
14.3.4 Theoretical Backscattered Sound Pressures 650
14.4 Analytical and Numerical Evaluations of the Scattering Coefficients 653
14.4.1 Cylindrically Symmetric Correlation Function 653
14.5 An Analysis of the Backscattered Data in Two Areas: Spatial Correlations 654
14.5.1 Assumptions 656
14.6 An Analysis of the Backscattered Data in Two Areas: Spatial Spectra 659

References 662
Bibliography 688
Symbols 692
Subject Index 708

This Page Intentionally Left Blank

Series Preface

When C. S. Clay and H. Medwin published their first book, *Acoustical Oceanography*, twenty years ago, who could have predicted that it would have eleven printings and be translated into Russian? Who could have predicted that it would be used both as a text for college-level courses and as a handbook for practicing scientists and engineers throughout the world? However, much can happen in twenty years, and no matter how valuable their first book became to the acoustical oceanography community, books and their content eventually become less useful.

The unqualified success of their first book, the new and exciting material that has evolved over the past twenty years, and the new generation of scientists and engineers demanded that a second book be written. This is Medwin and Clay's response to that demand. Once again they have brought their knowledge, experience, and insight to the acoustical oceanography community. Further, they have provided an extensive bibliography for those researchers who need to reach deeper and broader into the material covered by the authors. In the opinion of the Editors, Medwin and Clay have written another classic.

The Editors and Publisher are very proud that Medwin and Clay brought their second book, *Fundamentals of Acoustical Oceanography*, to Academic Press. It is also the second book published in the series, "Modern Applications of Acoustics."

Richard Stern
Moises Levy

Author Preface

This book has been written to encourage a new generation of scientists, engineers, and entrepreneurs to break the constraints of traditional disciplines and to apply the modern methods of acoustical physics to probe the mysterious sea. In order to assist the reader, we have included a large number of references that are of either historical or immediate importance. The inspired reader will keep up to date in applied ocean acoustics by referring to the most prominent, appropriate technical periodicals such as *The Journal of the Acoustical Society of America* and *The Journal of Geophysical Research: Oceans and Atmospheres*.

We are both applied physicists—one originally a physical acoustician, the other a geophysicist. We use the tools of applied mathematics, physical acoustics, noise control, seismology, signal theory, and wave propagation to learn about the sea. The reader will find on these pages various techniques to solve the direct problem—that is, to predict the propagation of sound from an essential knowledge of the physical and biological characteristics along the ocean propagation path. He or she will also find examples of inverse problem solutions, in which the vagaries of underwater sound propagation are used to measure the physical and biological characteristics of the sea and its boundaries. Our methods include laboratory scale models of ocean-acoustic environments as well as experiments at sea, and solutions based on theoretical analysis and numerical simulations.

When we published our first book (C. S. Clay and H. Medwin, *Acoustical Oceanography*, 1977), the broad application of acoustics to learn about the sea and its boundaries had barely been defined. Now, two decades later, this exciting field is expanding in several directions. A broad range of imaginative

specialists have used the methods of underwater acoustics to open new areas of ocean engineering, oceanography, marine biology, and even, unexpectedly, meteorology.

Following a brief survey of recent successes in acoustical oceanography (Chapter 1), we explain the principles of underwater sound propagation (Chapters 2–6). We then describe how both actively probing sonars and passively listening hydrophones can reveal what the eye cannot see over vast ranges of the turbid ocean. The goal is to use acoustical remote sensing, variations in sound transmission, in-situ acoustical measurements, computer models, or laboratory models to identify the physical and biological parameters and processes in the sea (Chapters 7–14).

For the reader's convenience, we give brief derivations, summaries, and formulas in several sections and subsections that are marked with an asterisk (*). We will use material given there, but readers may wish to skip those entire sections or omit some of the details.

Both of us have contributed to each of the chapters; however, the principal author of Chapters 1, 2, 4, 5, 8, 12, and 13 was H. Medwin, and that of Chapters 3, 6, 7, 9, 10, 11, 14 was C. S. Clay. We invite you to direct comments and questions to the principal authors: Herman Medwin, Physics Department, Naval Postgraduate School, Monterey, California; Clarence S. Clay, Department of Geology and Geophysics, University of Wisconsin, Madison, Wisconsin.

Acknowledgments

Herman Medwin owes the inspiration for this book to his professors in the Physics Department of the University of California, Los Angeles, the eminent pioneers in theoretical and experimental acoustics, Carl Eckart, Vern O. Knudsen, Robert W. Leonard, and, most particulary, his thesis advisor, Isadore Rudnick, and to his students at the U.S. Naval Postgraduate School. Clarence S. Clay remembers Miss Eastman, Lee Irwin, and Edward Price from his high school years at Emporia, Kansas, and A. B. Cardwell at Kansas State University, who taught him that it is fun to play with physics and mathematics, and his major professors, R. H. MacFarland and J. G. Winans, and students at the University of Wisconsin.

Valuable discussions have been held with Jonathan Berkson, Stephen Brandt, Jacques Chamuel, Dezang Chu, Fred Fisher, Robert Frosch, Joshua Gordis, Charles Greenlaw, D. Vance Holliday, John Horne, Michael Jech, Richard Keiffer, Robert Kieser, Wayne Kinney, Mark Latham, James Lynch, Nicholas Makris, Diana McCammon, Saimu Li, John Magnuson, Gerald Morris, Halcyon Morris, Redwood Nero, Wesley Nyborg, Jeffrey Nystuen, Andrea Prosperetti, Lars Rudstam, Er-Chang Shang, Timothy K. Stanton, Kushal Talukdar, Ivan Tolstoy, Robert Tyce, and Yun-Yu Wang.

Encouragements, suggestions, and technical reviews of specific sections of the book have been received from several colleagues, including Aubrey Anderson, Steven Baker, Mohsen Badiey, N. Ross Chapman, Ching-Sang Chiu, William Cummings, David Farmer, Chris Feuillade, Mark Hamilton, John Horne, James H. Miller, Jorge Novarini, Jeffrey Simmen, Eric Thorsos, and O. Bryan Wilson.

The authors are grateful for years of research support by the Office of Naval Research and the National Science Foundation, and we specifically appreciate the assistance of the Office of Naval Research in the undertaking of this textbook.

This book is dedicated to
Eileen and Andre Jane.

Chapter 1 The Realm of Acoustical Oceanography; Theory and Applications of Ocean Acoustics

1.1 Introduction 1
1.1.1 Definition 1
1.2 Physical and Biological Characteristics of the Sea 2
1.3 Ocean Stratification, Sound Speed, and Ray Refraction 4
1.4 A Few Examples of Acoustical Oceanography 6
1.4.1 Pulse Timing of Transmissions 8
1.4.2 Remote Sensing by Scatter 10
1.4.3 Passive Acoustics 15

1.1 Introduction

This chapter is the reader's gateway to a young science. Throughout the book, wherever we can, we perform the trick of Janus, the mythological Roman God, who simultaneously faces in opposite directions. One view, called "the forward problem of ocean acoustics," is in the traditional direction where the knowledge of ocean parameters allows one to predict the propagation of sound. The opposite view, called "the inverse problem," uses the distinctive details of the propagation at a time and place to deduce the parameters and processes of the particular ocean through which the sound has traveled. We call this inverse view "acoustical oceanography." We encourage our readers to look in both directions.

1.1.1 DEFINITION

Acoustical oceanography is the active or passive use of sound to study physical parameters and processes, as well as biological species and behaviors, at sea. In some cases a specifically designed sound source is used to learn about the ocean and its boundaries. In other research, a natural sound in the sea is analyzed to reveal the physical or biological characteristics of the sound source.

Let us now sample some of the successes of acoustical oceanography: studies of global warming by tomography; images of the ocean bottom, a sunken ship and underwater smokers, measurements of bubble clouds, plumes, and circulations; rainfall at sea and gas interchange in breaking waves; and whale

tracking. In the following chapters, we will develop the fundamentals of ocean acoustics that can be applied to explore the undersea world.

1.2 Physical and Biological Characteristics of the Sea

Light, radar, microwaves, and other electromagnetic waves attenuate very rapidly and do not propagate any significant distance through salt water. Because sound suffers very much less attenuation than electromagnetics, it has become the preeminent tool for sensing, identifying, and communicating under the ocean surface. And yet, for decades, inadequate oceanographic information about the extraordinary spatial and temporal variability of this medium has hindered underwater acousticians in their desire to predict sound propagation. It was necessary to learn more about those ocean characteristics that the traditional oceanographic instruments measure rather crudely, with great difficulty, and at great expense.

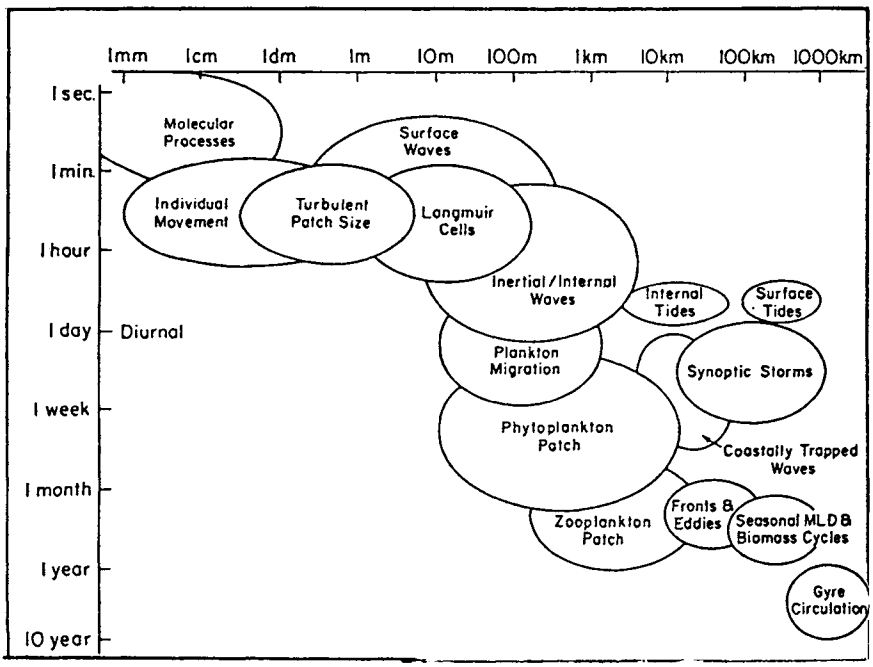

Figure 1.2.1 Spatial and temporal scales of physical and biological parameters and processes in the sea. (T. D. Dickey, "Technology and related developments for interdisciplinary global studies," *Sea Technology*, pp. 47–53, August 1993).

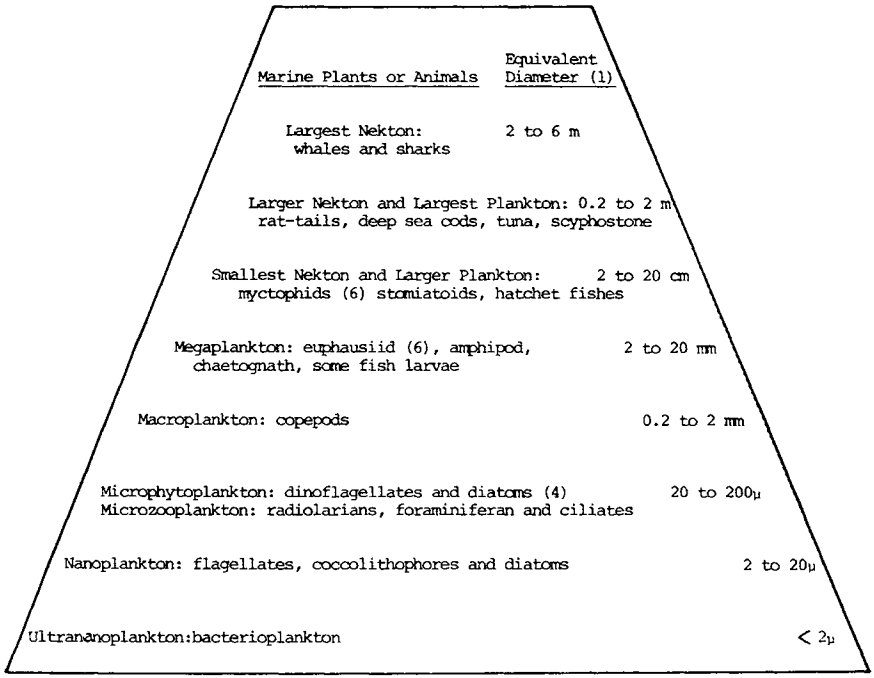

Figure 1.2.2 Marine biological pyramid with diameter (1) of equivalent spherical volume of the plants or animals. (Clay and Medwin, *Acoustical Oceanography,* Wiley; New York [1977].)

Acoustical oceanographers invert the problem; they use the complex nature of sound propagation to learn about the ocean. The many successes of this young science range from the identification and counting of physical and biological inhomogeneities — such as microbubbles, fragile zooplankton, fish, and mammals — to the remote measurement of distant rainfall and sea surface roughness, deep sea mountains, rocks, consolidated and suspended sediments, as well as the shape and strength of internal waves, ocean frontal systems, and immense churning ocean eddies, hundreds of kilometers in extent. Fig. 1.2.1 shows typical sizes and time scales of ocean patches, waves, and other physical and biological features (Dickey 1993). Fig. 1.2.2 is a marine biological pyramid that reveals the immense size range of life at sea. All of these unknowns can be measured by the techniques of acoustical oceanography.

1.3 Ocean Stratification, Sound Speed, and Ray Refraction

In retrospect, acoustical oceanography started in 1912, when the steamship *Titanic* struck an iceberg. The subsequent loss of hundreds of lives triggered man's use of sound to sense scatterers in the sea. Within a month, two patent applications were filed by L. R. Richardson in the United Kingdom for "detecting the presence of large objects under water by means of the echo of compressional waves ... directed in a beam ... by a projector." The basic idea was that a precise knowledge of the speed of sound in water, and the time of travel of the sound, permits the calculation of the distance to the scatterer. By 1935 acoustical sounding was used to determine the ocean depth as well as to hunt for fish schools. Much more recently it has been realized that the physical and spatial character of the scatterers can be inferred from the statistical characteristics of the scattered sound and that high-resolution images can be obtained at large range in optically opaque, turbid water.

Knowing the sound speed in water is critical to many of the applications of acoustical oceanography. The earliest measurement was by Colladon and Sturm (1827) in Lake Geneva, Switzerland. (See Fig. 1.3.1.) A value of 1435 m/s was found, but it was soon realized that the speed in saline water is somewhat greater than this, and that in general the temperature of the water is an even more important parameter.

Numerous laboratory and field measurements have now shown that the sound speed increases in a complicated way with increasing temperature, hydrostatic pressure, and the amount of dissolved salts in the water. A simplified formula for the speed in m/s, accurate to 0.1 m/s but good only to 1 kilometer depth, was given by Medwin (1975):

$$\begin{aligned} c = {} & 1449.2 + 4.6T - 0.055T^2 + 0.00029T^3 \\ & + (1.34 - 0.010T)(S - 35) + 0.016z \end{aligned} \tag{1.3.1}$$

In the above, temperature T is in degrees centigrade, salinity S is parts per thousand of dissolved weight of salts, and the depth z is in meters. A better, but more complicated, empirical expression is in Chapter 3. The best (and most carefully constructed) equations in this vital research area involve a large number of terms with a large number of significant figures in each coefficient. Such formulas can be found in recent articles in *The Journal of the Acoustical Society of America*.

Portable sound "velocimeters" are now available with an accuracy of 0.1 m/s in nonbubbly sea water. The effect of salinity is quite small except near estuaries or in polar regions where fresh water enters the sea. But microbubbles have a very

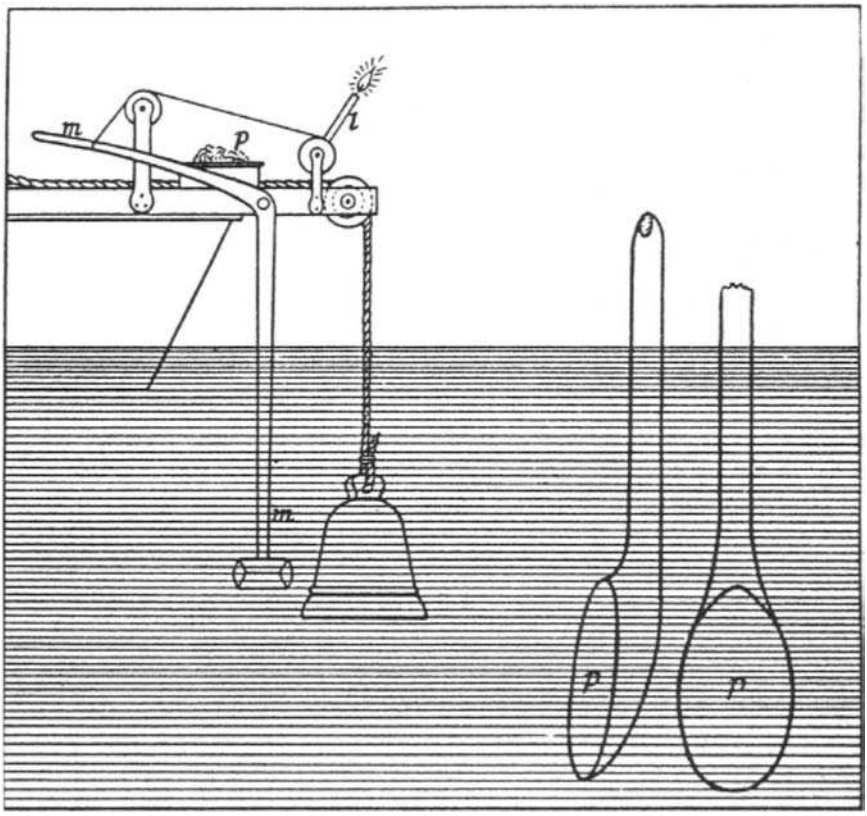

Figure 1.3.1 Colladon and Sturm's apparatus for measuring the speed of sound in water. A bell suspended from a boat was struck under water by means of a lever *m*, which at the same moment caused the candle *l* to ignite powder *p* and set off a flash of light. An observer in a second boat used a listening tube to measure the time elapsed between the flash of light and the sound of the bell. The excellent results were published in both the French and German technical literature. (*Annales de Chimie et de la Physique* **36**, [2], 236 [1827] and Poggendorff's *Annalen der Physik und Chemie* **12**, 171 [1828]).

large effect on the speed of propagation near the ocean surface; frequency-dependent sound speed deviations of tens of meters per second are common in the upper ocean.

An observation that has important acoustical implications is that the water density, temperature, salinity, and the speed of sound are horizontally stratified over most of the world's oceans. A sound speed profile for the Atlantic Ocean is shown in Fig. 1.3.2. As shown, the depth of the minimum varies from near the surface for polar regions, to about 1800 m in mid-latitudes.

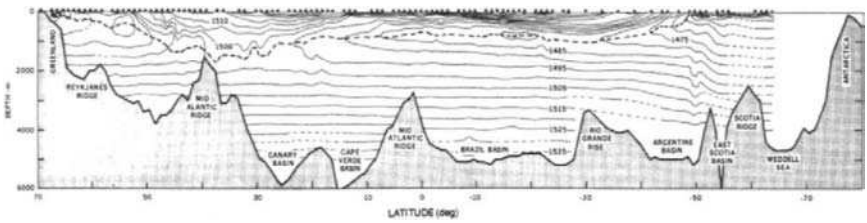

Figure 1.3.2 North-south section of iso-speeds of sound, and the sound channel minimum (speed indicated by dashed line) depths in the North and South Atlantic along the 30.50^0 W meridian. Speeds are in m/sec. Data positions are indicated by dots at the surface. (J. Northrup and J. G. Colborn, "Sofar channel axial sound speed and depth in the Atlantic Ocean," *J. Geophys. Res.* **79,** 5633–41 [1974].)

The significance of this stratification is that if temperature decreases with increasing depth — that is, if there is a "thermocline" — the speed will also tend to decrease. Sound rays in such a speed gradient will bend (refract) downward, just as light passing through a prism. On the other hand, where the temperature is constant, sound rays will bend upward, because the speed increases with increasing depth.

The combination of a thermocline overlying isothermal water and the pressure effect causes sound rays to bend downward, then upward, then downward and so forth, as they pass through the axis of minimum speed as shown in Fig. 1.3.3. Because the sound is constrained to cycle in a pancakelike layer in the deep channel, it diverges cylindrically rather than spherically. It therefore attenuates quite slowly, particularly if it is low-frequency sound (say, 100 Hz). The fact that low-frequency sounds can take advantage of channel propagation to travel thousands of kilometers was probably first demonstrated by Ewing and Worzel (1948), who used 1 kg charges of TNT as their sound source. Fig. 1.3.3 shows one of the first calculations of the sound channeling effect that was used to explain the extraordinary ranges of propagation that were observed. The channel was called the "sofar" (*so*und *f*ixing *a*nd *r*anging) channel because of its originally proposed ability to locate an explosion at sea by triangulation from shore/listening stations.

1.4 A Few Examples of Acoustical Oceanography

In "active" techniques of acoustical oceanography, a specifically designed sound system is used to obtain a precise time of propagation, generally over a long range (section 1.4.1), or scatter is analyzed (section 1.4.2). "Passive" methods, on the

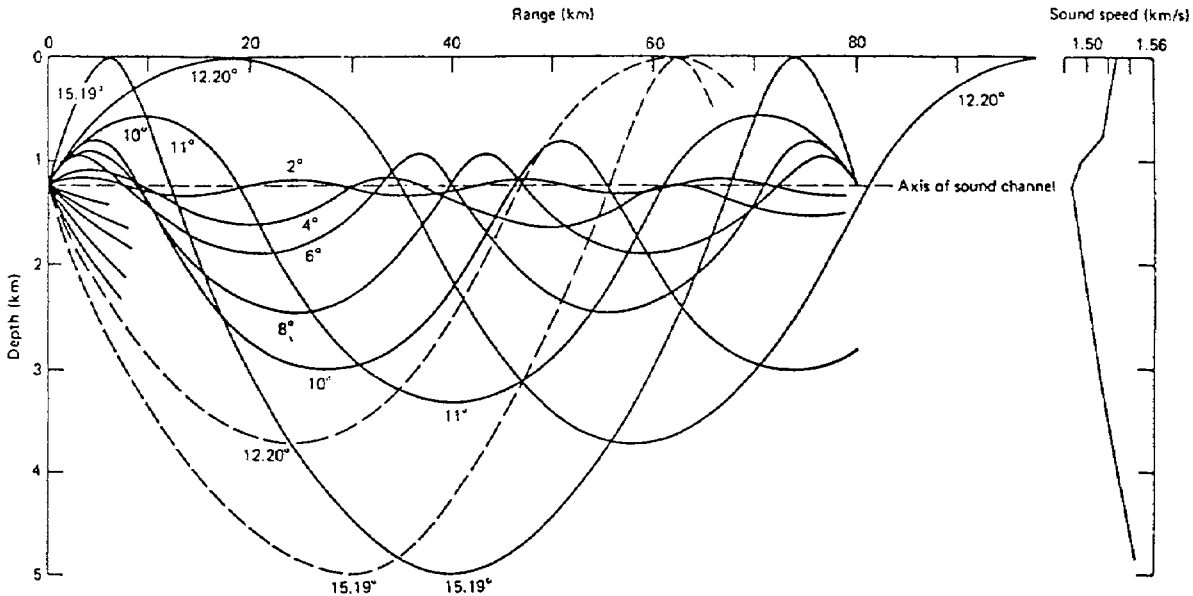

Figure 1.3.3 Ray diagram for an Atlantic Ocean sound channel. Source is on the channel axis at 1.3 km depth. Sound speed profile is at the right. The grazing angles at the axis of the channel are given in degrees. (M. Ewing and J. L. Worzel, "Long range sound transmission," in *Propagation of Sound in the Ocean*, Memoir 237, Geological Society of America: New York [1948].)

other hand, take advantage of the natural sounds of the sea and use a physical understanding of the process to evaluate the ocean parameter that caused the sound (section 1.4.3).

1.4.1 PULSE TIMING OF TRANSMISSIONS

Global Warming

Very-long-range transmission was again demonstrated conclusively in the Heard Island feasibility study in 1989 (Fig. 1.4.1). In this case a programmed electromechanical sound source was lowered to the sound channel axis. The test was the first step in a major international experiment to investigate the heating of the world's oceans by accurately and simultaneously measuring the time required to travel several fixed, submerged acoustical paths. It is expected that over a decade it will become clear whether global warming is taking place, and at what rate.

Acoustical Tomography

Tomography (literally, slice writing) is an imaging technique that inverts propagation measurements through many sections of a volume to determine the physical characteristics of the interior of the volume. Similar inversion techniques are employed in medical tomography (e.g., CAT scans of the brain), optical tomography, geophysical tomography, and acoustical tomography. Ocean acoustic tomographers deduce the temperatures within a slice through the volume by using many accurate measurements of the travel time along several fixed acoustical paths through the volume. The concept of inverting travel time differences to obtain sound speeds and thereby to infer temperatures in a large ocean volume was first suggested by Munk and Wunsch (1979). (See Chapter 3.) It has been used to identify and delineate eddies, and ocean fronts, as illustrated in Plate 1.

Accurate measurements of the sound travel time may be used to determine the water drift velocity by acoustical tomography. The technique is to reverse the sound source and receiver so that the temperature effect can be subtracted and the difference of travel times can be attributed to the three-dimensional motion of the water. When the experiment is carried out over a loop of sound sources and receivers, the circulation can be determined as well.

The technique of acoustical tomography has also provided ocean surface wave determinations when the sound paths of the tomography experiment interact with the ocean surface, ocean bottom slope measurements when the sound path

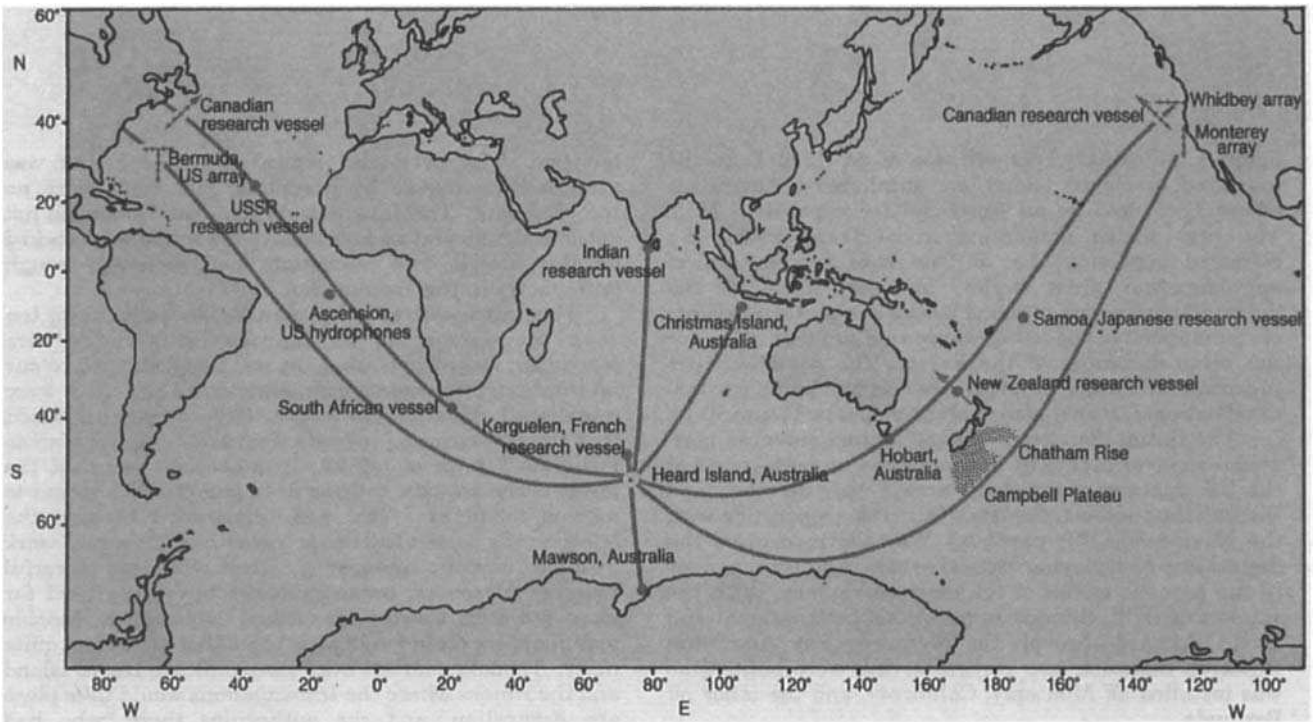

Figure 1.4.1 Paths taken by sound in the Heard Island feasibility test. Black circles indicate receiver sites. Ray paths from source to receivers are along refracted geodesics, which would be great circles but for the Earth's nonspherical shape and the ocean's horizontal sound speed gradients. Signals were received at all sites except the vertical array at Bermuda, which sank, and the Japanese station off Samoa. (Reprinted with permission from A. Baggeroer and W. Munk "The Heard Island feasibility test," *Physics Today*, 22–30, September 1992. Copyright 1992, American Institute of Physics.)

scatters off the ocean bottom, and ocean front and internal wave information within the volume.

1.4.2 REMOTE SENSING BY SCATTER

Fig. 1.4.2 shows a simple remote sensing system. A transmitter sends a sound signal, a receiver picks up the backscatter, and a display gives the travel time and strength of the return. These instruments, called SONARs (SOund NAvigation and Ranging) send out and receive a sound beam, somewhat like a flashlight. The sonar can be pointed, electronically, in any desired direction. Downward-looking sonars, "echo sounders," measure the depth of the sea bottom beneath the ship.

Ocean Bottom Imaging

Multiple-beam sonars are used to measure a strip of depths on each side of a surveying surface ship or submersible. The process is called swath mapping. Digital processing of the multiple-beam echo data gives an image showing the undersea mountains and valleys (Plate 2). The time of arrival of the echo is a

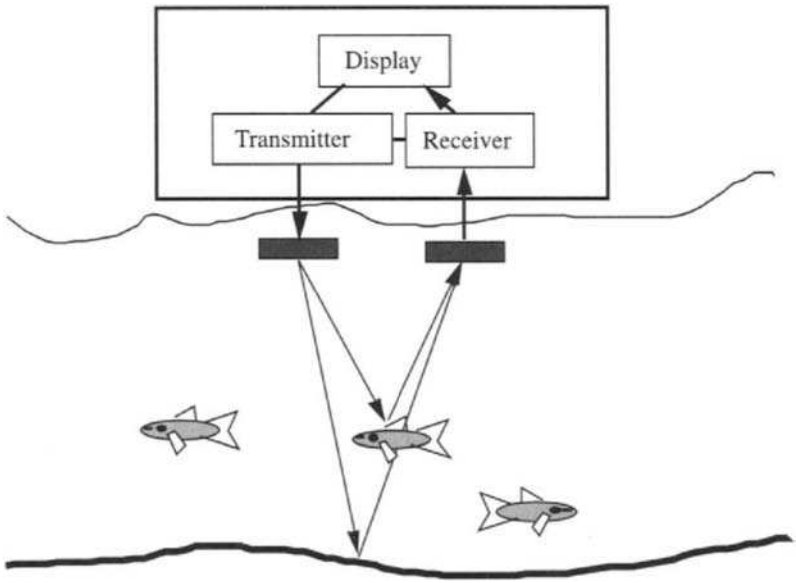

Figure 1.4.2 Backscattering experiment using separate transmitting and receiving transducers. Many echo sounders use the same transducer, which is switched to transmit or receive. The transmission cycle is started by an electronic trigger that can come from the display, the transmitter, or the receiver.

measure of the distance to the bottom feature, and the strength of the echo is interpreted as a measure of the slope or roughness. This technology revolutionized the study of sea-floor morphology in the 1980s. See also Chapters 12, 13, and 14. At higher frequencies and shorter ranges, objects on the sea floor can be revealed in fine detail (Fig. 1.4.3).

Underwater Smokers

An important feature of sea floors is the smoker-type hot spring. Because of the limited field of view and water opacity, photographic information can only show a small section of the smoker at an instant of time. Acoustical imaging, on the other hand, allows one to see the complete character and extent of the smoker as it evolves in time (Rona et al. 1991). Sound frequencies in the hundreds of kilohertz are used to show the activity of the ejected streams of particles. (See Plate 3. See also, Chapter 7.)

Bubble Clouds, Plumes, and Circulations

The massive numbers of bubbles that are created by breaking waves do not lie in stratified layers at the surface. They have been traced by acoustical backscatter to reveal forms described as clouds, plumes (Fig. 1.4.4), and Langmuir circulations. The activity is now known to extend from the surface down sometimes to depths as great as tens of meters. Backscattering from these bubble tracers has indicated the near-surface activity that is responsible for much of the surface heat and gas exchange, as well as the mixing and purging of the ocean surface. (See also Chapter 8.)

Ocean Plankton Biomass

The acoustical oceanographer's knowledge of biological parameters is gained by remote sensing of backscatter from plankton, nekton, sea mammals, and their swimbladders (when they have them). The simplest prototypes that guide us in the identification process for plankton are scatter from a fluid sphere and scatter from a resonating spherical bubble. An instrument developed by D. V. Holliday (1989) uses 21 discrete frequencies, from 100 kHz to 10 MHz for the smaller animals. The biomass of populations of zooplankton of equivalent spherical radius 1 mm to 4 mm is obtained as a function of depth. Many of these plankton would have been destroyed by conventional plankton net sampling; they are unaffected by the acoustic energy. (Plate 4. See also Chapters 9 and 10.)

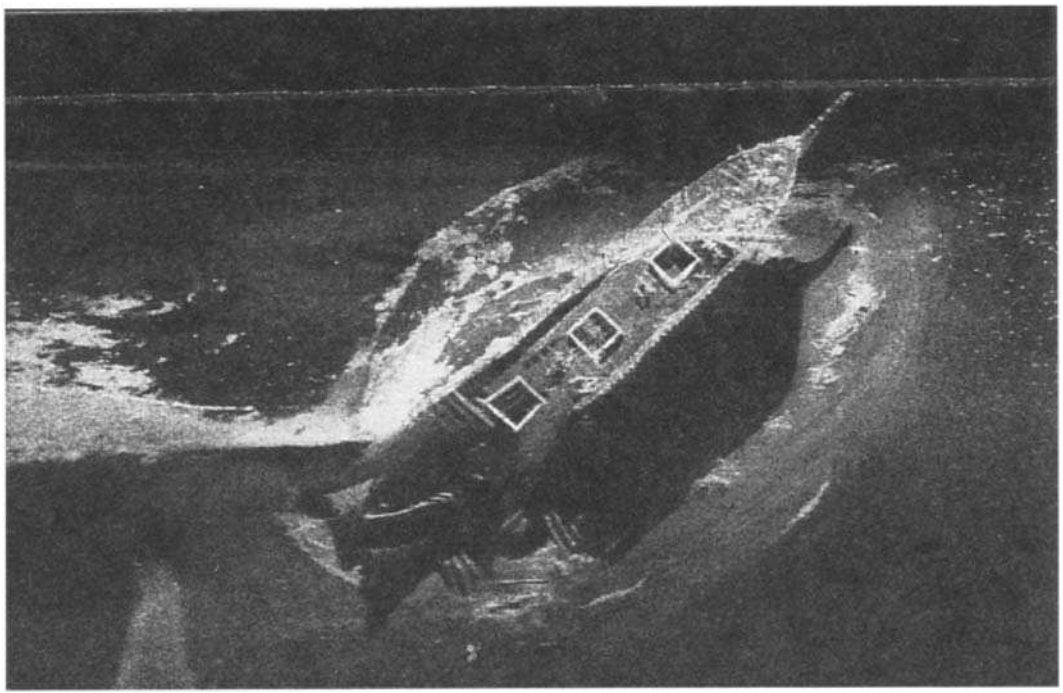

Figure 1.4.3 A 500 kHz sonar side-scan image of the wreck of the four-masted schooner Herbert D. Maxwell. The ship of length 57 m, breadth 12 m, sank in 1910 in water of depth 38 m off Annapolis, Maryland. The socnar "fish" was towed 14 m off the sea floor, when it obtained the image of the wreck at a range 75 m. Note the missing stern section, the three large hatches designed for convenient handling of lumber, and the crater due to sediment erosion. Optical visibility was about 1 m at the time of this test by the equipment designers EDGE TECH, Milford, Massachusetts. (Courtesy of EDGE TECH.)

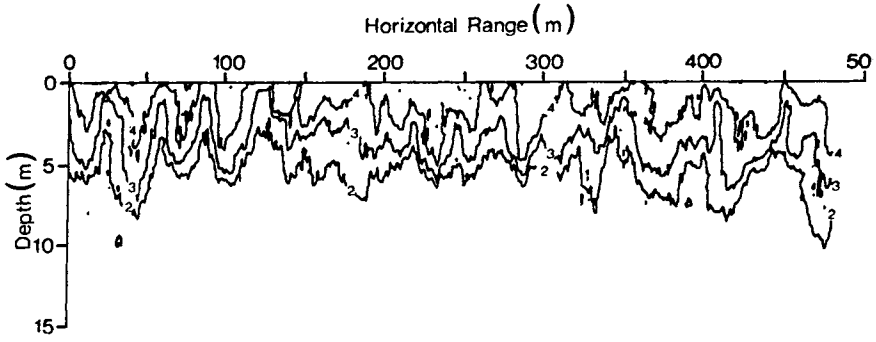

Figure 1.4.4 Lines of constant bubble density observed during 8 m/s winds, calculated from bubble backscatter of 112 kHz sound. Resonant bubble radius approximately 27 microns. The numbers represent the density in powers of 10—that is, 4 represents 10^4 bubbles per cubic meter per micron radius increment. (G. B. Crawford and D. M. Farmer, "On the spatial distribution of ocean bubbles," *J. Geophys. Res.* **92**[C8], 8231–43 [July 1987].)

Ocean Fronts, Convergence, and Divergence

Within a region where ocean masses collide, there are temperature profiles which delineate the front of the water boundary. These may be deduced in an acoustical tomography transmission experiment as shown in Plate 1. But also, since marine animals tend to prefer certain temperatures, they often congregate at temperature gradients in a meandering ocean eddy. Remote acoustical sensing is thereby able to determine the outlines of the water masses by backscatter from the marine animals (Plate 5. See also Chapter 10.)

Daily Fish Migration

During the day many "prey" fish hide on the bottom of shallow coastal water, or below the depth of light penetration in deeper water regions. When darkness approaches, fish will migrate toward the ocean surface to feed. One can study the migration for larger, bottom fish by using a lower sound frequency and for smaller fish by employing a higher frequency. Fig. 1.4.5 shows the migration of fish in a shallow water environment. In less than an hour, the smaller fish move upward by almost 100 meters. (See also Chapters 9 and 10.)

Pollution Monitoring

The waste that is dumped at sea acts as a passive contaminent. It is subject to the temperature and velocity structure at the dumping site and can be detected and

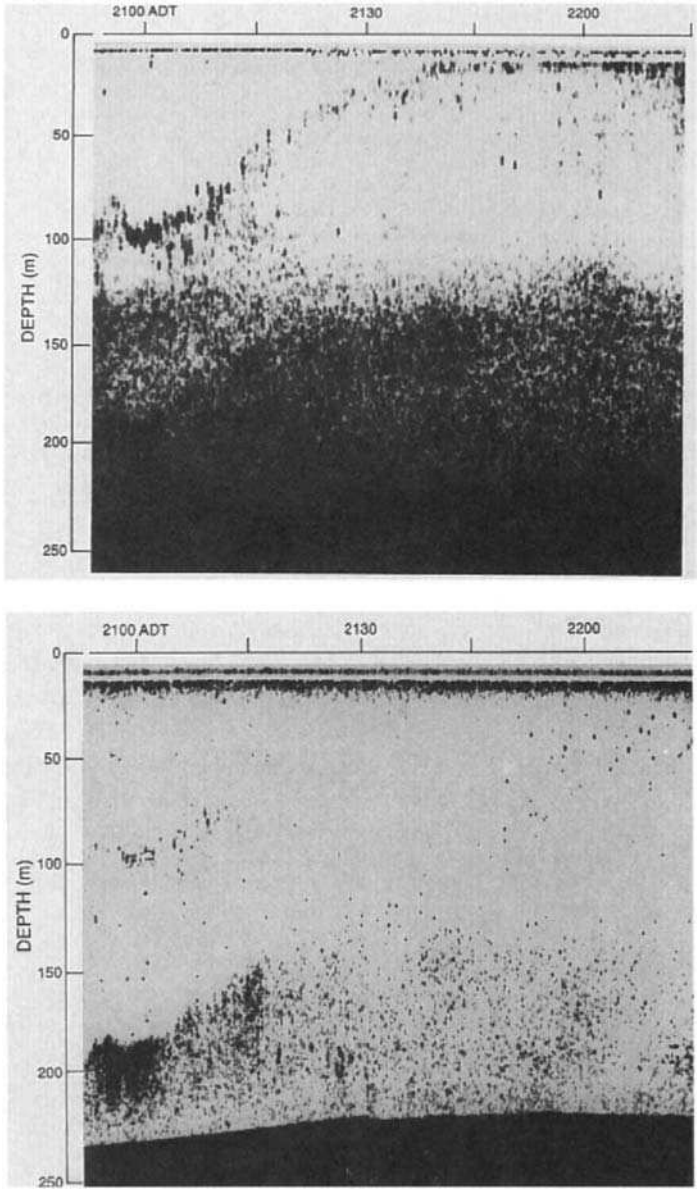

Figure 1.4.5 Migrating fish populations just after sunset (2055 ADT). The use of two different frequencies, 50 kHz (*below*) and 200 kzHz (*above*), permits the tracing of larger and smaller marine organisms, respectively. (N. A. Cochrane et al., "Multiple-frequency acoustic backscattering and zooplankton aggregations in the inner Scotian Shelf basins," *Can. J. Fish. Aquat. Sci.* **48**[3], 340–55 [1991].)

monitored acoustically by backscatter from the particles, bubbles, or temperature differences of the contaminent. Fig. 1.4.6 shows the ability of the dumped waste to delineate internal waves and temperature layers at the site. (See also Chapter 7.)

1.4.3 PASSIVE ACOUSTICS

Rainfall at Sea

When a raindrop strikes the ocean surface, there is an impact sound of duration several microseconds followed in many cases by the definitive sound of a newly created, shock-excited bubble. The sound of the screaming, infant microbubble lasts for many milliseconds and generally radiates much more energy than the impact. Of interest to the oceanographic and meteorological communities is the fact that the frequency of the bubble radiation is correlated to the drop size, and it precisely determines the bubble size. Therefore, passive underwater listening allows one to diagnose the amount of rainfall in terms of its component raindrop diameters. This knowledge also permits a calculation of the number and size of bubbles, per unit ocean surface area, per second, introduced into the water column. The type of cloud from which the rain has fallen can be judged from the shape of the underwater sound spectrum. The gas interchange at the ocean

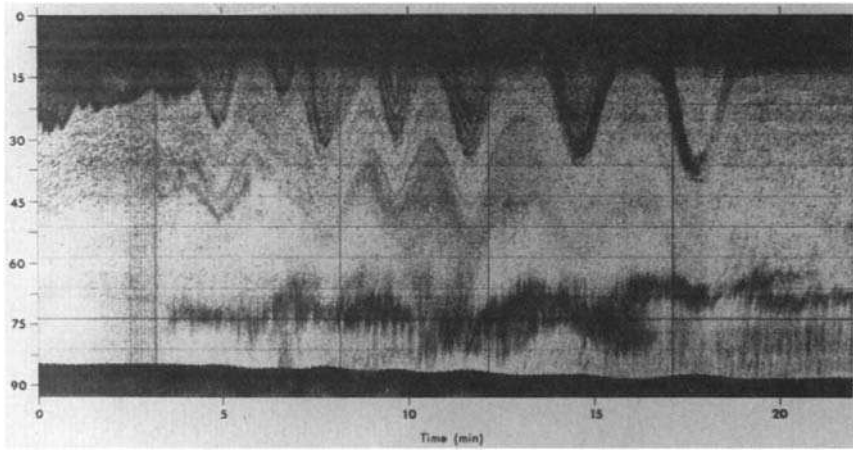

Figure 1.4.6 Acoustical imaging of a nonlinear internal wave packet. Frequency 200 kHz. Note the changing internal wave periodicity of 2 to 3 minutes. At time 9 minutes, the three clearly defined layers between 15 m and 30 m depth have been attributed to temperature structure, while those below have been ascribed to neutrally boyuant marine organisms. (M. Orr, 1989, personal communication.)

surface is strongly dependent on this phenomenon, as is the generation of aerosols from the raindrop splash. (See Chapters 6 and 8.)

Gas Interchange in Breaking Waves

When there is no precipitation, the underwater sound in the frequency range 500 to 20,000 Hz is usually determined by microbubbles generated by breaking waves. The bubbles are shock-excited to large amplitudes of oscillation when they are created. During their short active lives, the bubbles in a small region can be counted by listening to the sound radiation. Their radii and volume are calculated from their resonance frequencies. (See also Chapters 6 and 8.)

Whale Tracking

After the collapse of the Soviet Union, U.S. Navy equipment that had been used to track Soviet submarines was made available to follow singing marine mammals. Using this equipment, a blue whale, which issued distinctive sounds of frequency about 20 Hz, was tracked for 43 days and many hundreds of kilometers as it foraged in the Atlantic Ocean. The use of passive listening devices is providing new insights to the habits of endangered marine mammals (Gagnon and Clark 1993; Clark 1995).

Chapter 2 | Sound Propagation

2.1 Wave Propagation 17
2.1.1 Intensity of a Diverging Wave 18
2.2 Huygens' Principle for Impulse Waves 19
2.2.1 Plane Wave Reflection at a Plane Surface: Law of Reflection 22
2.2.2 Plane Wave Refraction at a Plane Interface: Snell's Law 22
2.2.3 Diffraction at the Edge of a Plane: Scattering of a Spherical Wave 23
2.3 CW Sinusoidal Signals: Spherical Waves 24
2.3.1 Variations in Time and Space 24
2.3.2 Traveling Spherical Waves 27
2.4 CW Interference and Phase Effects 27
2.4.1 Approximations 28
2.4.2 Sum of Sounds from Two Sources 32
2.4.3 Interference near an Interface: Plane Standing Waves 33
2.4.4 Point Source Near a Plane Reflector: Lloyd's Mirror Interference 34
2.5 The Wave Equation 35
2.5.1 Conservation Laws and the Equation of State for Linear Acoustics 36
2.5.2 The One-Dimensional Wave Equation and Other Relations 38
2.5.3 Acoustic Intensity 40
2.6 Reflection and Transmission at Interfaces 41
2.6.1 Plane Wave Reflection and Transmission Coefficients: Critical Angle 41
2.6.2 Plane Wave Reflection at a Sedimentary Bottom 45
2.6.3 Plane Wave Reflection and Transmission at Multiple Thin Fluid Layers 46
2.6.4 Ray Reflection beyond Critical Angle 50
2.6.5 Head Waves: Spherical Waves beyond Critical Angle 51
2.6.6 Fresnel Zones: Spherical Wave Reflection at an Interface 55
2.7 Propagation in Three Dimensions 58
2.7.1 The Wave Equation 58
2.7.2 Continuous Waves in Rectangular Coordinates 62
2.7.3 Omnidirectional Waves in Spherical Coordinates 64

2.1 Wave Propagation

Sound is a mechanical disturbance that travels through a fluid. Generally, the propagating disturbance is identified as an incremental *acoustic pressure* that has a magnitude that is very much smaller than the ambient pressure. But sometimes the sound is described in terms of the incremental density, the incremental temperature, the material displacement from equilibrium, or the transient particle velocity imposed on the medium.

In this chapter we assume that the medium is *homogeneous* (same physical properties at all positions) and *isotropic* (same propagation properties in all directions). And we assume that there is no sound absorption (no sound energy conversion to heat) and no dispersion (no dependence of sound speed on sound frequency), and that the acoustic pressure increment is very small compared with the ambient pressure (no finite amplitude, nonlinear effects). Under these assumptions, in sections 2.2, 2.3, and 2.4 we introduce several wave phenomena that commonly occur in the sea and that were part of the research discussed in Chapter 1. When the sound encounters an obstacle, it bends around it, and *diffraction* takes place; when it is incident on a boundary surface, *reflection* occurs; when it enters a region of different speed, it changes direction, and *refraction* results; when it meets another sound wave, the two pressures can add constructively, destructively, or at any other phase, and *interference* ensues. The plane-wave differential equation that controls such propagation is considered in section 2.5; the effects of smooth boundary interfaces, in 2.6; and three-dimensional propagation, in 2.7.

2.1.1 INTENSITY OF A DIVERGING WAVE

In a medium that is homogeneous and isotropic, a tiny sphere expands suddenly and uniformly and creates an adjacent region of slightly higher density and pressure. The higher-density region is called a *condensation.* Assume that it has a thickness dr. This condensation "impulse" or "pulse" will move outward as a spherical wave shell and will pass a reference point in time δt. It is called a *longitudinal wave* because the displacements in the medium are along the direction of wave propagation. It is also sometimes called a *compressional wave.* As it propagates, the energy of the impulse is spread over new spherical shells of ever larger radii, at ever lower acoustic pressure. By conservation of energy, the energy in the expanding wave front is constant in a lossless medium.

The *acoustic intensity is the energy per unit time that passes through a unit area* . The total energy of the pulse is the integral of the intensity over time and over the spherical surface that it passes through. Fig. 2.1.1 shows the expanding wave front at two radii. Applying the conservation of energy, the energy that passes through the sphere of radius R_0 is the same as the energy passing through the sphere of radius R. For a pulse of duration δt, conservation of energy gives the sound intensity relationship, where i_0 and i_R are the intensities at R_0 and R,

$$4\pi i_R R^2(\delta t) = 4\pi i_0 R_0^2(\delta t) \tag{2.1.1}$$

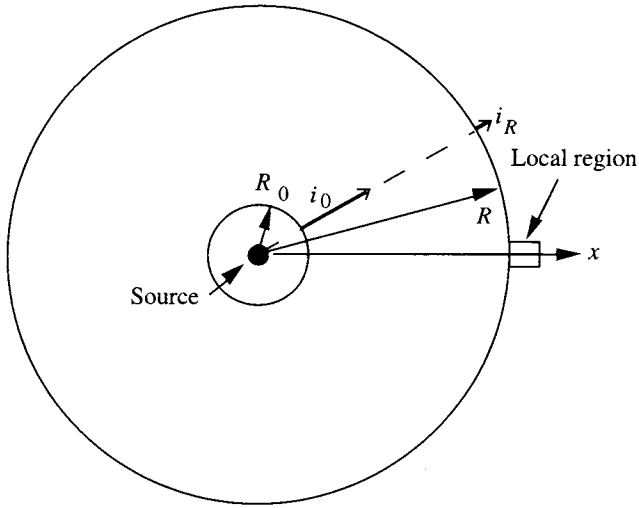

Figure 2.1.1 Spherical spreading of an impulse wave front. The instantaneous intensity is i_0 at the radius R_0 and later is i_R at the radius R.

Solving for the intensity at R, one gets

$$i_R = \frac{i_0 R_0^2}{R^2} \tag{2.1.2}$$

The sound intensity decreases as $1/R^2$, owing to spherical spreading. In section 2.5.3 we will show that the sound intensity is proportional to the square of the sound pressure. Thus, sound pressure decreases as $1/R$ in a spherically diverging wave. We would have got an increase as $1/R$ if the spherical pulse had imploded instead of exploded. A *rarefaction* pulse, a region of density less than the ambient value, can also be created and propagated.

2.2 Huygens' Principle for Impulse Waves

A useful qualitative description of wave propagation was first given by Christian Huygens, Dutch physicist-astronomer (1629–95). Huygens proposed that each point on an advancing wave front can be considered as a source of secondary waves, which move outward as spherical wavelets in a homogeneous, isotropic medium. The outer surface that envelops all these wavelets constitutes the new wave front (Fig. 2.2.1).

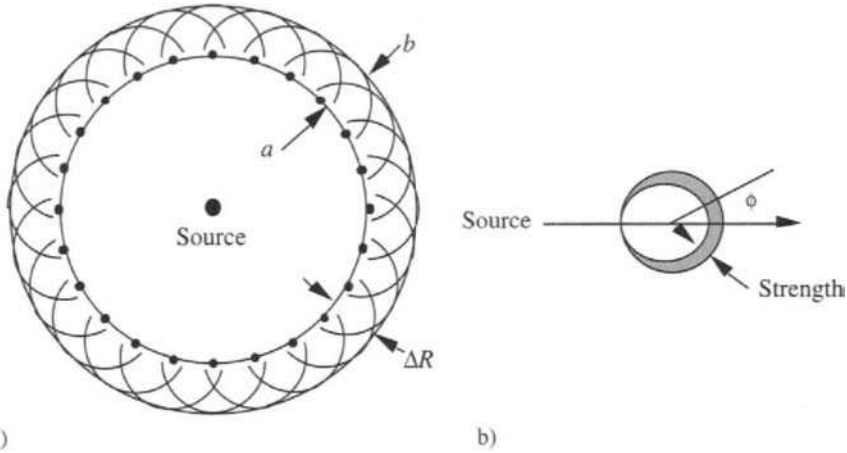

Figure 2.2.1 Huygens wavelet construction for a pulse. a) The wave front moves from *a* to *b*. b) The dependence of wavelet intensity on propagation direction, is called the Stokes obliquity factor.

The sources used in underwater sound measurements are often condensation impulses, somewhat like the shock wave from an explosion. The application of Huygens' Principle to an impulse wave front is particularly simple and physically direct.

Baker and Copson (1939) provided a secure mathematical basis for Huygens' Principle. The methods are extensively used in optics, as well as in acoustics. A good reference book is M. Born and E. Wolf, *Principles of Optics* (1980); in acoustics, see A. L. Pierce (1989).

Stokes (1849) derived an obliquity factor that describes the expanding wavelet with lesser side radiation and no back radiation, which agrees with observation:

$$\text{pressure amplitude} \sim \cos\frac{\varphi}{2} = \sqrt{\frac{1+\cos\varphi}{2}} \qquad \textbf{(2.2.1)}$$

In the short-time Δt, the disturbance from each of the secondary sources on the wave front a travels a distance ΔR (see Fig. 2.2.1). The outward portions of the wavelets coalesce to form the new wave front b. The strength of the wavelet is maximum in the direction away from the source and zero in the backward direction.

The propagation can be demonstrated graphically without the preceding details of the Huygens construction. See Fig. 2.2.2a, where each successive position of the pulse is indicated by 1, 2, 3 and so forth. The time intervals Δt are

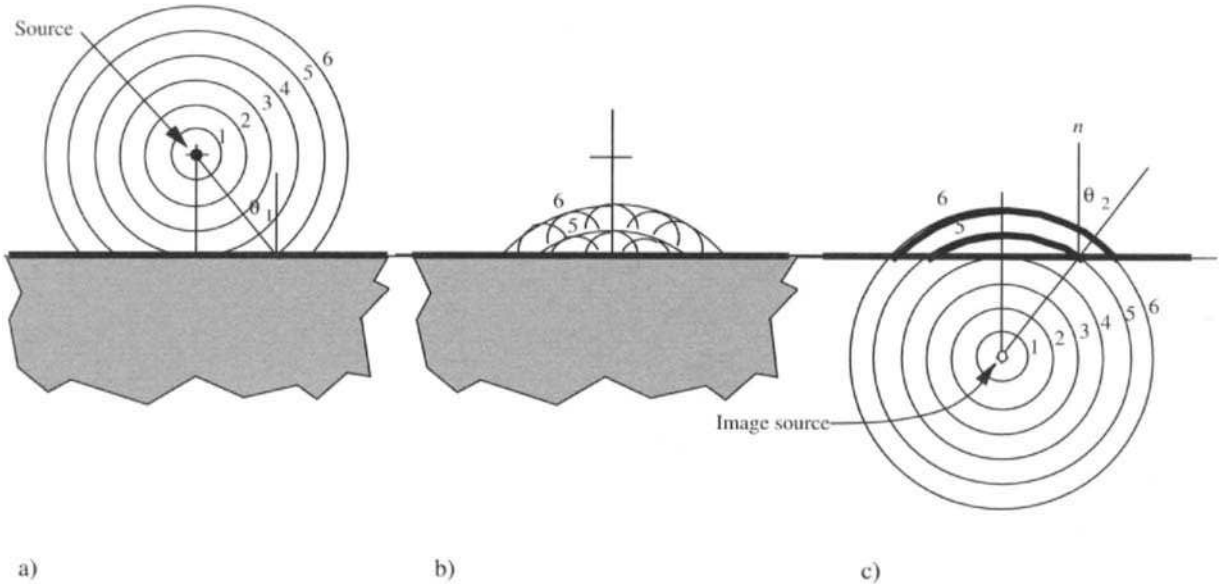

Figure 2.2.2 Hugyens constructions of successive positions of a spherical pulse at a plane reflector. The penetration of the pulse into the lower half-space behind the plane face of the reflector is not shown. a) Point source over a half-space. b) Reflected wave fronts. c) The reflected wave fronts appear to come from an image source in the lower half-space.

equal, and the wave front travels the same distance ΔR during each interval. In the ray direction, normal to the wave front for the isotropic medium, the distance of advance of the wave front is given by

$$\Delta R = c\,\Delta t \tag{2.2.2}$$

where c is the sound speed.

2.2.1 *PLANE WAVE REFLECTION AT A PLANE SURFACE: LAW OF REFLECTION*

The Huygens construction of the interaction of a spherical wave at a plane boundary, Fig. 2.2.2a and b, suggests that the wave front of the reflection is expanding as if it has come from a source beneath the reflecting surface. The apparent source after reflection is called the *image*.

A way to treat the image and the real source is shown in Fig. 2.2.2c. The image wave of the proper strength is initiated at the same time as the source, and when it moves into the real space it becomes the reflected wave. The geometry shows that the angle of reflection θ_2 of the *rays* (perpendicular to the wave front) is equal to the angle of incidence θ_1 and is in the same plane. Both angles are measured to the normal to the surface. This is called the Law of Reflection.

2.2.2 *PLANE WAVE REFRACTION AT A PLANE INTERFACE: SNELL'S LAW*

Now we assume that the impulse wavefront has come from a very distant point source such that the curvature of the spherical wave front is negligible in our region of interest. The wave is incident on the plane boundary between two media

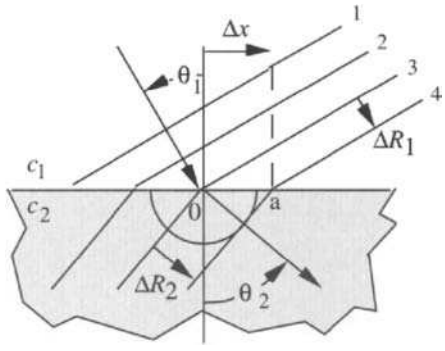

Figure 2.2.3 Huygens construction for Snell's Law of Refraction.

which have sound speeds c_1 and c_2 (see Fig. 2.2.3). The figure is drawn for $c_2 > c_1$ (which is the case for sound going from air to water); the reader can easily sketch the figure for the other case, $c_1 > c_2$. Successive positions of the wave fronts are shown as they move across the interface. To simplify the illustration, the wavelets for wave front position 4 was drawn as originating at a point on the interface. In general, there will also be a reflected wavefront, but it is omitted here for simplicity. In the time Δt the wave front has moved a distance ΔR_1 in medium 1 and ΔR_2 in medium 2. In the same time, the contact of the wavefront at the interface has moved from 0 to a, a distance Δx along the x axis. The angles are measured between the rays and the normal to the interface, or between the wavefront and the interface. The propagation distances in the two media are $\Delta R_1 = \Delta x \sin\theta_1$ and $\Delta R_2 = \Delta x \sin\theta_2$. The speeds are $c_1 = \Delta R_1/\Delta t$ and $c_2 = \Delta R_2/\Delta t$. Therefore,

$$\sin\theta_1/c_1 = \sin\theta_2/c_2 \tag{2.2.3}$$

This is well known as Snell's Law of Refraction. We use Snell's Law throughout Chapter 3.

2.2.3 *DIFFRACTION AT THE EDGE OF A PLANE: SCATTERING OF A SPHERICAL WAVE*

Assume that the source is above a thin, semi-infinite plane that permits part of the impulse wave to be transmitted and part to be reflected. The situation is shown in Fig. 2.2.4, where the plane extends from the boundary edge at B, infinitely to the

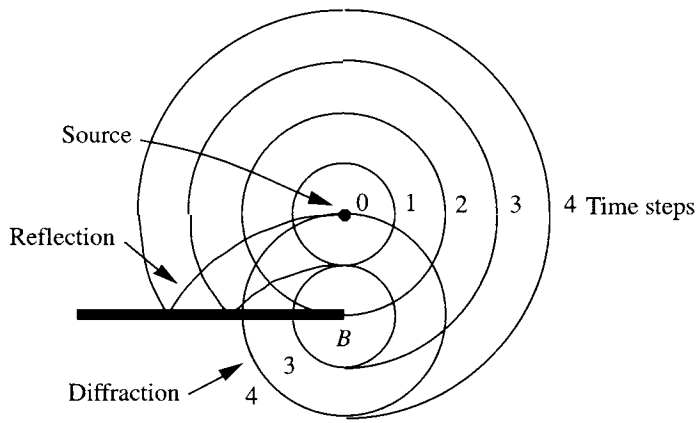

Figure 2.2.4 Huygens construction for diffraction of an impulse at a perfectly reflecting half-plane. The transmitted wave is omitted to simplify the sketch.

left, and infinitely in front and behind the page. The components of the figure are as follows: the wave front spreads from the source and interacts with the plane; the interactions at the plane become sources of Huygens wavelets; the envelopes of the wavelets coming only from the plane become the reflected waves; the outgoing wave beyond the edge of the plane continues, unaffected; the envelope of the Huygens wavelets originating at the edge form a wave front that appears to spread from the edge. That wave is called the *diffracted* wave. The transmitted wave is omitted for simplicity.

The diffracted wave is a separate arrival. It is strongest in the direction of propagation but is more easily detected in any other direction because of its later arrival. The diffracted wave exists because there is a reflecting plane to the left of the edge and none to the right.

In general, "scattering" is a redirection of sound when it interacts with a body. Scattered sound in a fluid is made up of transmitted, reflected, and diffracted waves. Impulse sounds are particularly helpful in analyzing scattering problems because they have distinctive arrival times that depend on their path lengths. Scattering and diffracted waves for various geometries are discussed in quantitative detail in later chapters.

2.3 CW Sinusoidal Signals: Spherical Waves

The abbreviation CW was originally used to designate the "carrier wave" in FM and AM radio. More recently, the same letters have represented a "continuous wave." In either case, for the following simple description of acoustic propagation we will use a particular form of CW, the common sinusoidal wave. The sinusoidal wave is quite simple to apply in theoretical studies, and it is a common output of signal generators.

2.3.1 VARIATIONS IN TIME AND SPACE

A sinusoidally excited source expands and contracts repeatedly and produces a continuous wave, a wave without discontinuities. The resulting condensations (density and pressure above the ambient) and rarefactions (below ambient) in the medium move away from the source at the sound speed c, in the same manner as the disturbance from an impulse source. A representation of the sinusoidal fluctuations at some instant would resemble the cartoon in Fig. 2.3.1a. The distance between adjacent condensations (or adjacent rarefactions) along the direction of travel is the *wavelength,* λ.

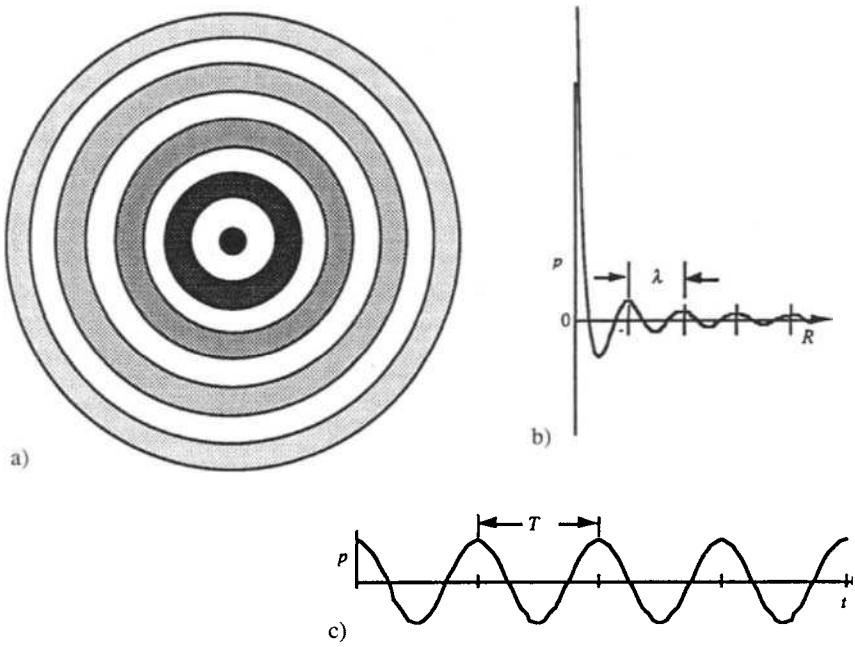

Figure 2.3.1 Radiation from a very small sinusoidal source. a) Pressure field at an instant of time. Dark condensations are lightened to show decreasing acoustic pressure as the range increases. b) Range-dependent pressure at an instant of time. c) Time-dependent pressure signal at a point in space.

The disturbances sketched in Fig. 2.3.1a radiate outward from a point source which is small compared with λ. As a condensation moves outward, the acoustic energy is spread over larger and larger spheres. Correspondingly, the *pressure amplitude* (the acoustic pressure at the peak of the sinusoid) decreases. Later we prove that the pressure amplitude decreases as $1/R$, where R is the distance from the source. The distance between adjacent crests continues to be λ.

The simplest functions that repeat periodically are sine and cosine functions. They repeat themselves for every increment of 2π. For example, $\sin(\theta + 2n\pi) = \sin\theta$, where n is an integer. The spatial dependence of the instantaneous sound pressure at large ranges may be written as, for example,

$$p = \frac{P_0 R_0}{R} \sin\frac{2\pi R}{\lambda} \quad \text{or} \quad p = \frac{P_0 R_0}{R} \cos\frac{2\pi R}{\lambda} \tag{2.3.1}$$

where P_0 is the amplitude of the pressure oscillation at reference range R_0. Equation 2.3.1 includes the decrease of pressure with increasing R. The amplitude at R is $P(R) = P_0 R_0 / R$.

The time between adjacent crests passing any fixed point is the *period*, T (Fig. 2.3.1c). The temporal dependence of the pressure oscillation at R is, for example,

$$p = P(R) \sin 2\pi f t \quad \text{or} \quad p = P(R) \cos 2\pi f t \tag{2.3.2}$$

where f is the *frequency* of the oscillation, measured in cycles per second or hertz (Hz).

For two adjacent crests at t_1 and $t_2 = t_1 + T$, the functions repeat, so that $2\pi f t_2 = 2\pi f t_1 + 2\pi$. Therefore $2\pi f T = 2\pi$, and the period, T, is

$$T = 1 / f \tag{2.3.3}$$

Considering Fig. 2.3.1, in the time T the disturbance has moved the distance λ. Therefore the speed at which it travels, the *sound speed*, is

$$c = \lambda / T = f \lambda \tag{2.3.4}$$

The units of λ are generally meters, so c is in meters per second.

In Equation 2.3.2 the dimensionless product ft is in cycles and $2\pi ft$ is in radians. The latter is sometimes called the *temporal phase*.

It is customary to absorb the 2π into the frequency and to define the *angular frequency*,

$$\omega = 2\pi f = 2\pi / T \quad \text{radians/sec} \tag{2.3.5a}$$

The spatial dependence of pressure change in Equation 2.3.1 is described by $\cos(2\pi R/\lambda)/R$. The dimensionless argument $(2\pi R/\lambda)$ is sometimes called the *spatial phase*.

Comparing with $\cos(2\pi t/T)$, we see that the spatial *wave number*, k,

$$k = 2\pi / \lambda \quad \text{radians/meter} \tag{2.3.5b}$$

is analogous to the temporal *angular frequency*, $\omega = 2\pi/T$. The two quantities are related through the equation for the speed, Equation 2.3.4. The relation is

$$k = \omega / c \tag{2.3.6}$$

2.3.2 *TRAVELING SPHERICAL WAVES*

We have seen that, at a fixed position, the simplest acoustic signal has temporal dependence $\sin(\omega t)$; at a fixed time, the spatial dependence is $(1/R)\sin(kR)$. As shown later, when solutions of spherical wave problems are given, these two concepts combine in a form such as

$$p = (P_0 R_0/R)\sin(\omega t - kR) \tag{2.3.7}$$

or

$$p = (P_0 R_0/R)\sin[\omega(t - R/c)] \tag{2.3.8}$$

or

$$p = (P_0 R_0/R)\sin[2\pi(t/T - R/\lambda)] \tag{2.3.9}$$

and so forth, where P_0 is the pressure amplitude at the reference range $R = R_0$.

It is easy to prove that the foregoing equations represent a radially propagating wave having the speed c. For example, pick an arbitrary phase at time t, position R. At a later time, $t + \Delta t$, the same phase will exist at position $R + \Delta R$. Equating

$$\omega[t + \Delta t - (R + \Delta R)/c] = \omega[t - (R/c)] \tag{2.3.10}$$

Therefore

$$c = \Delta R/\Delta t \tag{2.3.11}$$

To summarize, combinations such as $(t - R/c)$ or $(R/c - t)$ or $(\omega t - kR)$ indicate a wave traveling in the positive, increasing R direction. Others, such as $(t + R/c)$ or $(R/c + t)$ or $(\omega t + kR)$, describe a wave traveling in the negative R direction.

2.4 CW Interference and Phase Effects

Wave interference phenomena are the result of sound pressures from more than one source being present at the same position and at the same time. In "linear acoustics," the resulting sound pressure is the algebraic sum of the contributions. The addition holds, regardless of the directions of travel, time dependencies, and amplitudes of the components. (But see Chapter 5 for very large amplitudes.) In other words, instantaneous acoustic pressures at a point are scalars, and they add algebraically.

2.4.1 APPROXIMATIONS

Approximations have a long and distinguished history in the physical and applied mathematical sciences. They are a guide to understanding, and they permit one to obtain useful solutions to otherwise intractable analytical problems. Approximations continue to be important even in the era of high-speed digital computers because they assist the modeler and the experimentalist in evaluating whether the results of a complex computer calculation are realistic or not. Furthermore, the appropriate implementation of approximations reduces computer processing time.

Local Plane Wave Approximation

The spherical wave is often studied at a large distance from the source. It is then convenient to assume that, within a restricted region of interest, the spherical wave appears to be a plane wave. This local plane wave approximation is extensively used in acoustics, underwater sound, and geophysics. As shown in Fig. 2.4.1, when $\varepsilon \ll R$, the geometry gives

$$R^2 = (R-e)^2 + W^2 / 4 \tag{2.4.1}$$

or

$$\frac{W}{4}^2 = (2R - \varepsilon)(\varepsilon) \approx 2R\varepsilon \tag{2.4.2}$$

A common assumption for the CW plane wave approximation is that, over the restricted region W, the sagitta of the arc $\varepsilon \leq \lambda/8$ is

$$\varepsilon \approx \frac{W^2}{8R} \leq \lambda/8 \tag{2.4.3}$$

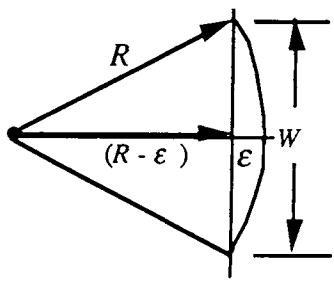

Figure 2.4.1 Geometry for the local plane wave approximation.

Therefore the region for the plane wave approximation has the extent

$$W \leq (\lambda R)^{1/2} \tag{2.4.4}$$

Fresnel and Fraunhofer Approximations for Different Ranges

To add the signals owing to several sinusoidal point sources, we need the distances to the observation point. The geometry is shown in Fig. 2.4.2.

The pressure waves incident at the point Q are spherical and, recalling section 2.1.2, the amplitudes of the pressures depend on the ranges. We suppress the range dependence by letting the *incident sound pressure amplitudes in the local region* have the values P_1, P_2, and so forth. The total sound pressure is

$$p = \sum_n P_n \sin(\omega t - kR_n) \tag{2.4.5}$$

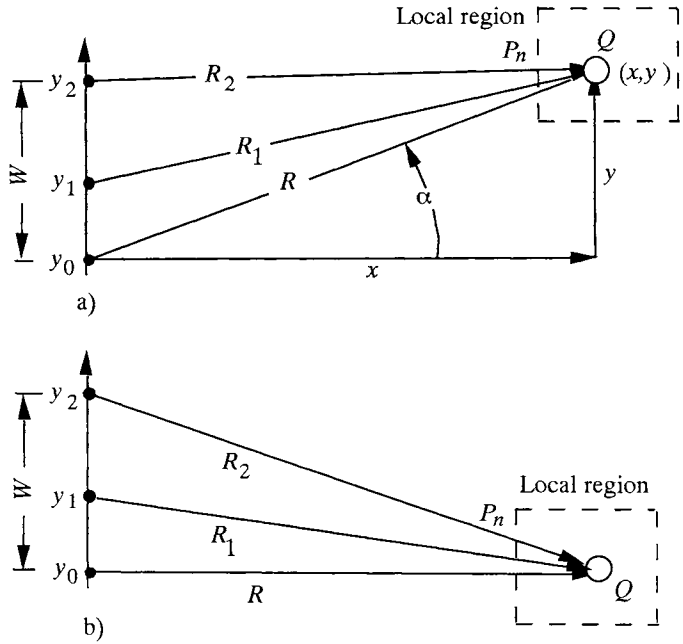

Figure 2.4.2 (a) Geometry for several sources with receiver at Q. The local region for the plane wave approximation is in the dashed-line rectangle. As a plane wave approximation in the region, the incident sound pressures have the amplitudes P_n. The sources are at y_1, y_2, and so forth. The distances from the sources to the listening point Q at R, α are R, R_1, R_2, and so forth. The acoustic pressure at Q is the sum of the pressures contributed by the several sources. b) Redrawing of **a**) to have $\alpha = 0$.

where the P_n are the pressure amplitudes at ranges R_n. The relative phases of the terms are most important because they determine the character of the interference — that is, whether the total instantaneous pressure will be greater or less than the individual pressures. To separate the time dependence from the summation, we expand the sin(...) and get

$$p = \sin(\omega t) \sum_n P_n \cos(kR_n) - \cos(\omega t) \sum_n P_n \sin(kR_n) \tag{2.4.6}$$

There are two terms. The sin (ωt) and cos (ωt) terms have a $\pi/2$ phase difference and are said to be in "phase quadrature."

One can make numerical evaluations of the summations in Equation 2.4.6 by using the following expressions for R and R_n:

$$R^2 = y^2 + x^2 \tag{2.4.7}$$

$$R_n^2 = (y - y_n)^2 + x^2 \tag{2.4.8}$$

$$R_n^2 = (R \sin\alpha - y_n)^2 + R^2 \cos^2(\alpha) \tag{2.4.9}$$

This can be rearranged to

$$R_n = R\left(1 - \frac{2y_n}{R} \sin\alpha + \frac{y_n^2}{R^2}\right)^{1/2} \tag{2.4.10}$$

Simpler forms are possible at very long ranges when $W/R \ll 1$. Then expansion as a binomial gives

$$R_n \approx R\left[1 - \frac{y_n}{R} \sin(\alpha) + \frac{y_n^2}{2R^2}(1 - \sin^2(\alpha)) + \cdots\right] \tag{2.4.11}$$

Depending on how small W/R is, one can neglect most of the higher-order terms. When only the first-order term in y_n/R is kept, we get the Fraunhofer (very long range) approximation to the summation

$$R_n \approx R\left(1 - \frac{y_n}{R} \sin\alpha\right) \tag{2.4.12}$$

On the other hand, when both the first-order term y_n/R and the second-order term $(y_n/R)^2$ are kept, we have the approximation for nearer ranges, which is called the Fresnel Approximation:

$$R_n \approx R\left[1 - \frac{y_n}{R} \sin(\alpha) + \frac{y_n^2}{2R^2}(1 - \sin^2(\alpha))\right] \tag{2.4.13}$$

Near-Field and Far-Field Approximation

Often the terminologies "near field" and "far field" are used to describe different parts of the acoustic field owing to a localized array of sources. The near field is the region where the differential distances to the elements of the source are large enough for the phase differences to cause significant destructive interference. The far field is where the range is greater (usually much greater) than this "critical range" for destructive interference.

To derive the minimum critical range, let $\alpha = 0$ for simplicity in Fig. 2.4.2a, and redraw the geometry as in Fig. 2.4.2b. The critical range R_c is a distance at which it is no longer possible for wavelets traveling the longest path (from y_3, the farthest source away from the axis) to interfere destructively with those traveling the shortest path (from y_0, on the axis). A pressure minimum cannot occur when these two distances differ by less than $\lambda/2$. From the geometry and using the binomial expansion,

$$R_3 = (R^2 + W^2)^{1/2} \approx R\left(1 + \frac{W^2}{2R^2}\right) \tag{2.4.14}$$

The condition in this case is

$$\Delta R = R_3 - R \approx \frac{W^2}{2R} \leq \frac{\lambda}{2} \tag{2.4.15}$$

The critical range, beyond which there can be no minimum, on the axis of the array, is

$$R_c = W^2 / \lambda \tag{2.4.16a}$$

and the far-field range is

$$R > W^2/\lambda \tag{2.4.16b}$$

In practice, if the plane wave approximation is to be used, one usually goes far beyond this critical range to be sure that the simplified calculations and measurements are securely in the far field. Often a range four times the critical range is used to define "far field." The complexity of the acoustic near field and the transition to the far field can only be appreciated by calculating the acoustic pressure for various ranges and frequencies, as suggested in the problems at the end of the chapter.

2.4.2 SUM OF SOUNDS FROM TWO SOURCES

At this point we introduce the powerful complex exponential description which simplifies operations that involve the sums and difference of angles and the products of trigonometric functions. The relations between trigonometric functions and complex exponential functions are

$$\exp(i\Phi) = e^{i\Phi} = \cos\Phi + i\sin\Phi \tag{2.4.17}$$

and

$$\cos\Phi = \frac{e^{i\Phi} + e^{-i\Phi}}{2}, \quad \sin\Phi = \frac{e^{i\Phi} - e^{-i\Phi}}{2i} \tag{2.4.18}$$

In section 2.3.2 we used $\sin(\omega t - kR_n)$ to describe the change of phase of a traveling wave. But notice that the expression $\exp[i(\omega t - kR_n)]$ contains both the sine and cosine components. Using the complex exponential and keeping in mind that the imaginary part is the sine, two pressure oscillations, p_1 and p_2, of the same amplitude P can be expressed as

$$p_1 = P\exp[i(\omega t - kR_1)] \tag{2.4.19}$$

and

$$p_2 = P\exp[i(\omega t - kR_2)] \tag{2.4.20}$$

The exponential description is particularly useful in differentiation and integration, which we will need to do later. For example, differentiation of p with respect to time is equivalent to multiplication by $i\omega$; integration with respect to time is simply division by $i\omega$.

The sum of the pressures is

$$p = p_1 + p_2 = P\{\exp[i(\omega t - kR_1)] + \exp[i(\omega t - kR_2)]\} \tag{2.4.21}$$

or

$$p = P\exp(i\omega t)[\exp(-ikR_1)] + \exp(-ikR_2)] \tag{2.4.22}$$

Now compute the square of the absolute value $|p|^2 = pp^*$, where * denotes the complex conjugate. (The complex conjugate is obtained by changing the sign of the imaginary.) The effect of this operation is to eliminate the time dependence because the product $\exp(i\omega t)\exp(-i\omega t)$ is unity. Then, Equation 2.4.22 becomes

$$\begin{aligned} |p|^2 = P^2[&\exp(-ikR_1) + \exp(-ikR_2)] \\ &\times [\exp(ikR_1) + \exp(ikR_2)] \end{aligned} \tag{2.4.23}$$

and with the aid of Equation 2.4.17 we obtain

$$|p\ |^2 = 2P^2\ \{\ 1 + \cos\ [k\ (R_1 - R_2)]\ \} \tag{2.4.24}$$

The maximum value is $4P^2$ and the minimum value is 0. Therefore, the coexistence of the two pressures, p_1 and p_2, produces interferences with maxima at $k(R_1 - R_2) = 0, 2\pi, 4\pi \ldots$ and minima at $\pi, 3\pi, 5\pi \ldots$.

The phase difference $k(R_1 - R_2)$ causes constructive interference with pressure $2P$ at the maxima, destructive interference with zero pressure at the minima, and any amplitude between 0 and $2P$, depending on the phase difference.

2.4.3 *INTERFERENCE NEAR AN INTERFACE: PLANE STANDING WAVES*

Sound pressures near an interface consist of the incident and reflected components of the signal. The signals may overlap and interfere significantly within a few wavelengths of the surface. The result for a continuous wave is that there are near-surface regions of high acoustic pressure (anti-nodes of pressure) and low pressure (nodes). The warning for experimentalists is that the signal that is received by a near-surface hydrophone depends on both the wavelength and distance from the interface.

To illustrate the effect we first assume that an incident plane wave is traveling vertically downward and that it reflects upward at a perfectly reflecting interface. The sound pressure will be the sum of the two pressures. Let p_i and p_r be the incident and reflected pressures which we assume have the same amplitude, P. Define z as positive upward and write

$$\begin{aligned} p_i &= P\ \exp\ [i\ (\omega t + k\ z\ )] \\ p_r &= P\ \exp\ [i\ (\omega t - k\ z\ )] \end{aligned} \tag{2.4.25}$$

The sum is

$$\begin{aligned} p = p_i + p_r &= P \exp\ (\ i\ \omega\ t\ )[\exp\ (ikz\ ) + \exp\ (-\ ikz\ )] \\ p\ \ &=\ \ 2P \exp\ (\ i\ \omega\ t\ )\ \cos\ (kz\ ) \end{aligned} \tag{2.4.26}$$

The acoustic pressure has an envelope $|2P \cos\ (kz)|$ and a time dependence $\exp\ (i\omega t)$. The *envelope* is stationary in time; therefore the result of the interference is called a "stationary wave" or "standing wave." For example, the nulls at $kz = \pi/2$ are nulls at all times.

Reflection at a *partially* reflecting interface also produces a standing wave. In this case the standing wave consists of the sum of the incident wave and the

reflected fraction of the incident wave. The remainder of the incident wave moves through the minima on the way to the second medium, so the interference minima are not zero.

An obliquely incident plane wave at a perfectly reflecting interface produces a standing wave perpendicular to the interface and a traveling wave parallel to the interface. An obliquely incident wave at a partially reflecting surface creates a standing wave perpendicular to the surface, plus a traveling wave parallel to the surface and a traveling wave perpendicular to the surface.

2.4.4 POINT SOURCE NEAR A PLANE REFLECTOR: LLOYD'S MIRROR INTERFERENCE

During World War II it was discovered that a sinusoidal point source near the ocean surface produced an acoustic field with interferences between the direct sound and the phase-shifted sound which diverged from an above-surface image of the source. In underwater acoustics, the phenomenon is sometimes called "the surface interference effect." The optical effect, Lloyd's Mirror interference, had been discovered in the mid-nineteenth century.

The geometry and some World War II experimental results are shown in Fig. 2.4.3. The direct sound at range R_1 is

$$p_1 = \frac{P_0 R_0}{R_1} e^{i(\omega t - kR_1)} \tag{2.4.27}$$

The surface-reflected sound experiences a 180° phase shift (section 2.6.1), travels a distance R_2 from the image, and is described by

$$p_2 = \frac{P_0 R_0}{R_2} e^{i(\omega t - kR_2)} \tag{2.4.28}$$

It is left as a student problem to show that when the source is at shallow depth $d \ll R$ and the hydrophone is at shallow depth $d \ll R$, the two sounds produce an interference pattern at range R with peaks and troughs given by

$$p(R) = \frac{2iP_0R_0}{R} \sin \frac{khd}{R} e^{i(\omega t - kR)} \tag{2.4.29}$$

The usual amplitude decrease that goes as $1/R$ is modified by a pressure doubling with peaks at

$$khd/R = \pi/2, 3\pi/2, 5\pi/2 \tag{2.4.30}$$

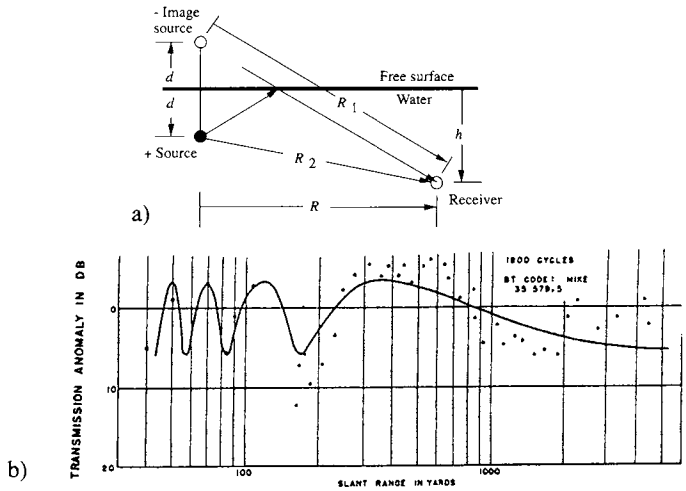

Figure 2.4.3 a) Geometry for Lloyd's Mirror Interference. b) World War II experimental results at sea for frequency 1.8 kHz. Source depth, $d = 14$ ft (4.3 m), receiver at $h = 50$ ft (15.2 m). Ranges are in yards (1 yd = 0.91 m). The curve is a best fit. "Transmission Anomaly" was the name used for the measured loss in decibels corrected for free field spherical divergence (Eckart 1951).

and so forth, and troughs at

$$khd/R = \pi, 2\pi, 3\pi \tag{2.4.31}$$

and so forth.

Beyond the last peak, at $khd \ll R$, the pressure decreases as R^{-2}. This is shown in Fig. 2.4.3, which is a copy of an original WWII experimental result. The ordinate, "Transmission Anomaly, dB," represents pressures compared to the $1/R$ expected. As defined, a negative TA (dB) describes a sound pressure greater than expected. For perfect surface reflection the peaks would have TA $= -6$ dB.

2.5 The Wave Equation

Our discussion in the preceding sections dealt with the phenomena of wave propagation, based on the Huygens description. Now we develop the relations between the properties of the medium and the sound that propagates in the medium. These phenomena are encompassed in the second-order partial differential *wave equation*, which describes the relations in time and space.

2.5.1 *CONSERVATION LAWS AND THE EQUATION OF STATE FOR LINEAR ACOUSTICS*

Assume that a disturbance in the medium is caused by the sudden expansion of a small spherical source. This causes the local density and pressure to increase because the rest of the medium does not instantaneously move to allow space for the expansion. Consider a small region at a very large distance from the source where the plane wave approximation holds (section 2.4.1). In this region the variations of pressure, velocity, and acceleration of a fluid particle are approximately functions of the direction of propagation, which we call x.

Assume that the pressure decreases across our region (Fig. 2.5.1a). The total pressure is

$$p_T = p_A + p \tag{2.5.1a}$$

where p_A is the ambient, static pressure which does not change over our region, and where $p \ll p_A$ is the incremental, acoustic pressure.

Similarly, the total density is

$$\rho_T = \rho_A + \rho \tag{2.5.1b}$$

where the acoustic density ρ is very much less than the the ambient density, $\rho \ll \rho_A$.

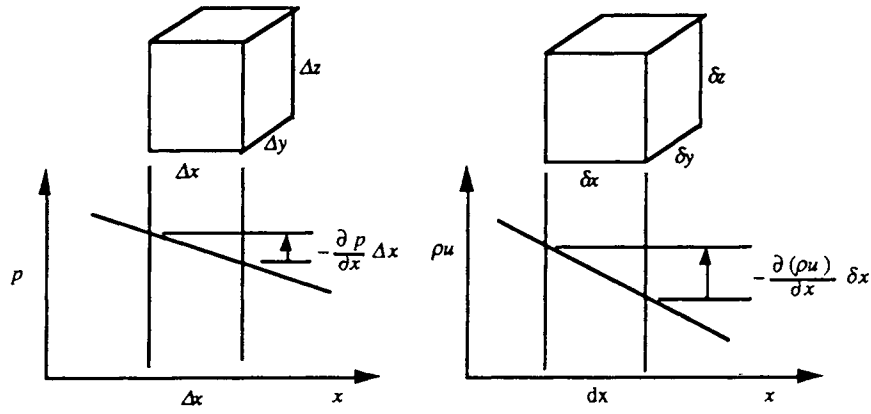

a) b)

Figure 2.5.1 Pressure differential across a small volume. a) The pressure differential causes the mass $\rho_A \Delta x\, \Delta y\, \Delta z$ to move to the right (Lagrangean coordinates). b) Mass flow through the small volume $\delta x\, \delta y\, \delta z$ (Eulerian coordinates); u is the component of velocity of flow along the x-axis; ρ_A is the ambient density.

Newton's Second Law for Acoustics

We consider the moving water particle in a description called the *Lagrangean* (moving) coordinate system as shown in Fig. 2.5.1a. The net pressure in the $+x$ direction, acting on our fluid particle, is

$$\text{net pressure} = -\left(\frac{\partial p}{\partial x}\right)\Delta x \tag{2.5.2a}$$

The net force is $-(\partial p/\partial t)\,\Delta x\,\Delta y\,\Delta z$. The mass of the water particle is $\rho_A\,\Delta x\,\Delta y\,\Delta z$, where ρ_A is the ambient density. We define u as the particle velocity in the $+x$ direction and $\partial u/\partial t$ as the local acceleration. Then Newton's Law, $F = ma$, gives

$$\begin{aligned} -\left(\frac{\partial p}{\partial x}\right)\Delta x\,\Delta y\,\Delta z &= \rho_A \frac{\partial u}{\partial t}\Delta x\,\Delta y\,\Delta z \\ -\frac{\partial p}{\partial x} &= \rho_A \frac{\partial u}{\partial t} \end{aligned} \tag{2.5.2b}$$

We keep in mind that Newton's Law for acoustics, Equation 2.5.2b is a point statement. It applies to the pressure and particle velocity at position x at time t. For the plane wave propagating in the $+x$ direction, $p = p(t - x/c)$ and $u = u(t - x/c)$. For a plane wave propagating in the $-x$ direction, $p = p(t + x/c)$ and $u = u(t + x/c)$. The speed, c, may be a function of position.

Conservation of Mass for Acoustics

The expansion of the source causes an outward flow of mass. Within a small cage that is fixed in space (this is called an *Eulerian*, or fixed, coordinate system), mass flows in one face and out the other. Since the fluid is compressible, more mass may flow in than out, and the density within the cage may increase. The velocity of the fluid flow along the x direction is sketched in Fig. 2.5.1b. The net mass flowing per unit time into the cage is $-[\partial(\rho_T u)/\partial t]\Delta x\,\Delta y\,\Delta z$. This causes a rate of density increase which may be written as $\partial\rho_T/\partial t = \partial\rho/\partial t$ because ρ_A is constant in $\rho_T = \rho_A + \rho$. Equating the two rates of change of mass gives

$$-\left(\frac{\partial(\rho_T u)}{\partial x}\right)\delta x\,\delta y\,\delta z = \left(\frac{\partial \rho}{\partial t}\right)\delta x\,\delta y\,\delta z \tag{2.5.3}$$

Since $\partial(\rho u)/\partial x \ll \rho_A\,\partial u/\partial x$ for acoustic waves, we simplify to the *acoustical equation of conservation of mass,*

$$-\rho_A \frac{\partial u}{\partial x} = \frac{\partial \rho}{\partial t} \tag{2.5.4}$$

Equation of State for Acoustics

Hooke's Law states that, for an elastic body, the stress is proportional to the strain. In the acoustical version of Hooke's Law, the stress (force per unit area) is the acoustic pressure, p, and the strain (relative change of dimension) is the relative change of density, ρ/ρ_A. The proportionality constant is the bulk modulus of elasticity, E. Except for intense sounds (see Chapter 5), Hooke's Law holds for fluids. This relation between acoustic pressure and acoustic density is sometimes called *the acoustical equation of state.*

$$p = \left(\frac{E}{\rho_A}\right)\rho \tag{2.5.5}$$

The above equation also assumes that an instantaneous applied pressure p causes an instantaneous proportional increase of density, ρ. Actually there is generally a time lag in the response of the fluid to applied pressure (molecular relaxation), which causes acoustic energy to be absorbed, as explained in Chapter 3.

2.5.2 *THE ONE-DIMENSIONAL WAVE EQUATION AND OTHER RELATIONS*

The Wave Equation

The one-dimensional wave equation, which incorporates all three laws developed in the previous section, is obtained by taking the $\partial/\partial x$ of Equation 2.5.2b and the $\partial/\partial t$ of (2.5.4) and eliminating the common second derivative $\partial^2 u/\partial x \partial t$. To put it in terms of the acoustic pressure, one uses the pressure density relation, (2.5.5). The result is the one-dimensional linear acoustic wave equation

$$\frac{\partial^2 p}{\partial x^2} = \frac{\rho_A}{E}\frac{\partial^2 p}{\partial t^2} \tag{2.5.6}$$

If we had eliminated p instead of ρ, we would have got an equation identical to Equation 2.5.6, but in terms of ρ. In fact, the wave equation (2.5.6) could also be derived in terms of the particle velocity component u, or the particle displacement ξ, or the incremental temperature ΔT, or any parameter that is characteristic of the acoustic wave. We choose to work with p because virtually all hydrophones that are sensitive to underwater sound are *pressure*-sensitive.

Equations 2.4.19 and 2.4.25 where the directions of propagation were called R or z, are all solutions of the plane wave equation (2.5.6), or are long-range approximations to the plane wave solution. In fact, any linear combination of

solutions is also a solution of Equation 2.5.6, as may be easily proved by substitution.

When we substitute any one of these solutions into the wave equation we obtain

$$c^2 = \frac{E}{\rho_A} \tag{2.5.7}$$

and the one-dimensional wave equation can be written in its more common form

$$\frac{\partial^2 p}{\partial x^2} = \frac{1}{c^2}\frac{\partial^2 p}{\partial t^2} \tag{2.5.8}$$

We have assumed that the elasticity, E, and the speed, c, are not dependent on the direction of propagation. If this were not the case (for example, in solids), we would write E_x and c_x for those quantities.

Impedance of the Medium

There is an important relation between acoustic particle velocity and acoustic pressure in a plane wave. Recall that a wave traveling in the $+x$ direction has particle velocity component $u = u(x - ct)$; therefore

$$\frac{\partial u}{\partial t} = -c\frac{\partial u}{\partial x} \tag{2.5.9}$$

Substitution of Equation 2.5.9 into Equation 2.5.2b gives

$$\frac{\partial p}{\partial x} = \rho_A c \frac{\partial u}{\partial x}$$

Integration yields

$$p = +(\rho_A c)u \tag{2.5.10}$$

where the plus sign is for waves traveling in the positive x direction; a minus sign would result for waves traveling in the negative x direction.

Equation 2.5.10 resembles Ohm's Law, with the acoustic pressure taking the place of voltage, acoustic particle velocity replacing electric current, and $(\rho_A c)$ being the impedance. The analogy is used frequently, and the $(\rho_A c)$, *rho-c*, or *specific acoustic impedance* of the material is a common acoustical characterization of the medium. Often the subscript $_A$ is dropped for simplicity. We retain it to avoid confusion.

Acoustic Particle Velocity/Density Relation: Mach Number of a Sound Wave

The ratio of the acoustic particle velocity to the speed of sound, u/c, may be calculated by starting with Equation 2.5.4. Then, since $u = u(t - x/c)$ and $\partial u/\partial x = -(1/c)(\partial u/\partial t)$, we find

$$\mathcal{M} = u / c = \rho / \rho_A \tag{2.5.11}$$

where $\mathcal{M}$ is called the *acoustical Mach number*. The acoustical Mach number is a measure of the strength of the sound wave, and thereby the linearity of the signal propagation. For intense sounds, when the ratio is large enough, extraordinarily useful nonlinear propagation effects occur as described in Chapter 5.

Acoustic Pressure-Density Relation

Equations 2.5.10 and 2.5.11 allow us to go directly to the valuable relation between the acoustic pressure and the acoustic density,

$$p = \rho c^2 \tag{2.5.12}$$

This equation can be used to calculate the speed of sound if the equation of state, $p = p(\rho)$, is known. For sound in gases, there is a relatively simple equation of state; consequently, the accurate theoretical speed in air has been known for over 200 years. But for liquids, the equation of state is so complicated that the inverse calculation is used. That is, the equation of state for water is calculated from accurate measurements of the speed of sound in water.

2.5.3 ACOUSTIC INTENSITY

As mentioned in section 2.1, the vector intensity of a wave is the power (watts) passing perpendicularly through a unit area; usually the area is 1 m^2. Suppose a plane wave is traveling in the $+x$ direction and the unit area is in the y-z plane. The instantaneous intensity is the product of the instantaneous pressure and the in-phase particle velocity along the x- direction, u_x. The x- component of intensity is

$$i_x = p(t - x/c)\, u_x(t - x/c) \tag{2.5.13}$$

where we show the traveling wave parameter $(t - x/c)$ to emphasize the dependence on position and time. Note, again, that we would need a subscript on c (e.g., c_x) if the speed were a function of direction of propagation.

Since the plane wave is traveling in the $+x$ direction, we apply Equation 2.5.10 so that the intensity can be written in terms of pressure alone.

$$i_x = \frac{[p\ (t - x\ /c\ )]^2}{\rho_A c} \tag{2.5.14}$$

Similarly, using the long-range plane wave approximation to a spherical wave, if the unit area is normal to the direction of R from the source, the intensity along R is

$$i_R = \frac{[p\ (t - R\ /c\ )]^2}{\rho_A c} \tag{2.5.15a}$$

When the wave is a continuous sinusoid $p = P \sin(kx - \omega t)$, the value of i_x is

$$i_x = \frac{P^2}{\rho_A c} \sin^2(kx - \omega t\ ) = P^2 \frac{1 - \cos[2(kx - \omega t\ )]}{2\rho_A c} \tag{2.5.15b}$$

The *instantaneous intensity* i_x oscillates between 0 and $P^2/(\rho_A c)$ and has the frequency 2ω.

For a sinusoidal wave it is useful to calculate the *average intensity* by integrating over time. The time average intensity at x, I_x, is

$$I_x = \langle i_x \rangle = (P^2)/(2\rho_A c) = P_{\text{rms}}^2/(\rho_A c) \tag{2.5.16}$$

where P is the peak pressure and $P_{\text{rms}} = 0.707P$ at x. Again, the analogy of Equation 2.5.16 to power in AC circuits provides a useful mnemonic for electrical engineers and physicists.

2.6 Reflection and Transmission at Interfaces

While the derivations for reflections and transmissions at an interface are given for plane waves, the results are used practically in the context of the local plane wave approximation to a spherical wave, section 2.4.1.

2.6.1 PLANE WAVE REFLECTION AND TRANSMISSION COEFFICIENTS: CRITICAL ANGLE

A very powerful way to do interesting problems uses the satisfaction of physical boundary conditions on each side of an interface between two fluids. The simplest example is the reflection and transmission of plane waves at a fluid interface.

Fig. 2.6.1 shows the ray directions and the components of the incident, reflected and transmitted particle velocities at the interface, u_i, u_r, and u_t

The first condition at the boundary is the equality of pressures on each side of the interface, evaluated at $z = 0$,

$$[p_i(t - z/c_1) + p_r(t + z/c_1)] = p_t(t - z/c_2) \tag{2.6.1}$$

where the letter subscripts designate the incident, reflected, and transmitted sound pressures at time t. The number subscripts indicate the medium.

The second condition at the boundary is the equality of the normal components of particle velocity, evaluated at $z = 0$,

$$[u_{zi}(t - z/c_1) + u_{zr}(t + z/c_1)] = u_{zt}(t - z/c_2) \tag{2.6.2}$$

Suppose a ray is incident at angle θ_1 at the interface. The angle of refraction is θ_2, given by Snell's Law:

$$\theta_2 = \arcsin[(c_2/c_1)(\sin\theta_1)] \quad \text{for} \quad (c_2/c_1)\sin\theta_1 < 1 \tag{2.6.3}$$

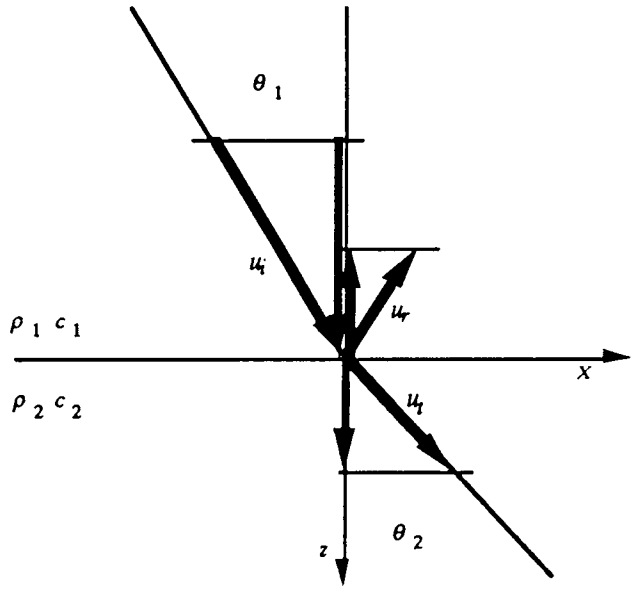

Figure 2.6.1 Reflection and transmission geometry for vector particle velocities (heavy arrows).

The three vertical components of particle velocity at the fluid interface, $z = 0$, are

$$u_{zi}(t) = u_i(t)\cos\theta_1 \tag{2.6.4}$$

$$u_{zr}(t) = u_r(t)\cos\theta_1 \tag{2.6.5}$$

$$u_{zt}(t) = u_t(t)\cos\theta_2 \tag{2.6.6}$$

where u_i, u_r and u_t are in the incident, reflected, and transmitted directions, respectively.

The computation of particle velocities in terms of pressure follows from Equation 2.5.10 where the negative value of ρc is used for propagation in the $(-z)$ direction; subscript A is dropped for simplicity:

$$\begin{aligned} u_{zi}(t) &= \frac{p_i(t)}{\rho_1 c_1}\cos\theta_1 \\ u_{zr}(t) &= -\frac{p_r(t)}{\rho_1 c_1}\cos\theta_1 \\ u_{zt}(t) &= \frac{p_t(t)}{\rho_2 c_2}\cos\theta_2 \end{aligned} \tag{2.6.7}$$

At a simple plane fluid interface, the time dependencies of the incident, reflected, and transmitted waves are the same. The pressure reflection and transmission coefficients for a wave going from medium 1 to medium 2, evaluated at $z = 0$, are defined as

$$\mathcal{R}_{12} \equiv \frac{p_r(t + z/c_1)}{p_i(t - z/c_1)} \quad \text{and} \quad \mathcal{T}_{12} \equiv \frac{p_t(t - z/c_2)}{p_i(t - z/c_1)} \tag{2.6.8}$$

In terms of the coefficients, the pressure condition requires

$$1 + \mathcal{R}_{12} = \mathcal{T}_{12} \tag{2.6.9}$$

and the velocity condition (Equation 2.6.2) leads to

$$(\rho_2 c_2 - \rho_2 c_2 \mathcal{R}_{12})\cos\theta_1 = \rho_1 c_1 \mathcal{T}_{12}\cos\theta_2 \tag{2.6.10}$$

Equations 2.6.9 and 2.6.10 are now solved for the pressure reflection and transmission coefficients,

$$\mathcal{R}_{12} = \frac{\rho_2 c_2 \cos\theta_1 - \rho_1 c_1 \cos\theta_2}{\rho_2 c_2 \cos\theta_1 + \rho_1 c_1 \cos\theta_2} \tag{2.6.11a}$$

and

$$\mathcal{T}_{12} = \frac{2\rho_2 c_2 \cos\theta_1}{\rho_2 c_2 \cos\theta_1 + \rho_1 c_1 \cos\theta_2} \tag{2.6.11b}$$

Snell's Law gives the connection between θ_1 and θ_2:

$$\theta_2 = \arcsin\left(\frac{c_2}{c_1}\sin\theta_1\right) \tag{2.6.12}$$

There are two generic applications for this theory of reflection and transmission between two fluids: the ocean surface and the ocean bottom. Consider the ocean surface under the greatly simplifying assumptions: the surface is a smooth plane between sea water (density 1000 kg/m^3, sound speed 1500 m/s) and air (density 1.03 kg/m^3 and sound speed 330 m/s). Assume underwater sound is normally incident to the interface ($\cos\theta_1 = 1$ and $\cos\theta_2 \cong 1$), since $\rho_1 c_1 \gg \rho_2 c_2$ (Equations 2.6.11a and 2.6.11b) gives $\mathcal{R}_{12} \cong 1$ and $\mathcal{T}_{12} = 4.5 \times 10^{-4}$. Further, from Equation 2.6.1 we find $p_r \cong -p_i$ (i.e., a phase-reversed pressure), which thereby produces a *near-zero total pressure at the surface*. And from Equation 2.6.2 we find $u_r \cong u_i$, so there is a particle velocity *doubling* at the surface. The water/air interface is called a "pressure release" or "soft" surface for underwater sound. But notice that if the direction of propagation had been reversed, sound going from air to the ocean would find a pressure-doubling interface, with essentially zero particle velocity. Viewed from the air, the same surface would be called acoustically "hard."

The above situation is an extreme case of $c_2 < c_1$, which always results in $(c_2/c_1)\sin\theta_1 < 1$ and $\theta_2 < 90°$ for all angles of incidence.

However, for sound going from the ocean to a sediment bottom, when $c_2 > c_1$ there is the possibility of "total reflection." Total reflection occurs at angle of incidence $\theta_1 \geq \theta_c$, where θ_c is the "critical angle" defined by

$$\theta_c = \arcsin(c_1/c_2) \tag{2.6.13}$$

When the angle of incidence is greater than θ_c, Snell's Law can be written as

$$\cos\theta_2 = \left[1 - \left(\frac{c_2}{c_1}\right)^2 \sin^2\theta_1\right]^{1/2} \equiv \pm i g_2 \tag{2.6.14a}$$

where the imaginary value of the cosine is

$$g_2 \equiv \left[\left(\frac{c_2}{c_1}\right)^2 \sin^2\theta_1 - 1\right]^{1/2} \tag{2.6.14b}$$

We choose the solution $(-ig_2)$ because it describes an acoustic pressure that becomes weaker with increasing depth of penetration into the second medium (in the z direction) while it propagates in the x direction. The incorrect choice of the plus sign would have led to the physically absurd description of a wave that had its origin in the first medium and that is stronger at greater distances from the interface in the passive second medium. Using Equation 2.6.11a,

$$\mathcal{R}_{12} = \frac{\rho_2 c_2 \cos\theta_1 + i\rho_1 c_1 g_2}{\rho_2 c_2 \cos\theta_1 - i\rho_1 c_1 g_2} \quad \text{for} \quad \theta > \theta_c \tag{2.6.15}$$

The numerator is the complex conjugate of the denominator. Therefore, the magnitude of the ratio is unity, $|\mathcal{R}_{12}| = 1$.

For angles greater than critical, we write $\mathcal{R}_{12}$ to allow us to calculate the phase shift,

$$\mathcal{R}_{12} = e^{+2i\Phi} \tag{2.6.16}$$

where

$$\Phi \equiv \arctan \frac{\rho_1 c_1 g_2}{\rho_2 c_2 \cos\theta_1} \tag{2.6.17}$$

2.6.2 *PLANE WAVE REFLECTION AT A SEDIMENTARY BOTTOM*

Extensive measurements of the geophysical structure have been made in the shallow water south of Long Island, New York. The sediment parameters are shown in Fig. 2.6.2. The values of the speed and density in the water, and in the uppermost sediment, are known. We assume that the sediment acts as a fluid, and therefore we

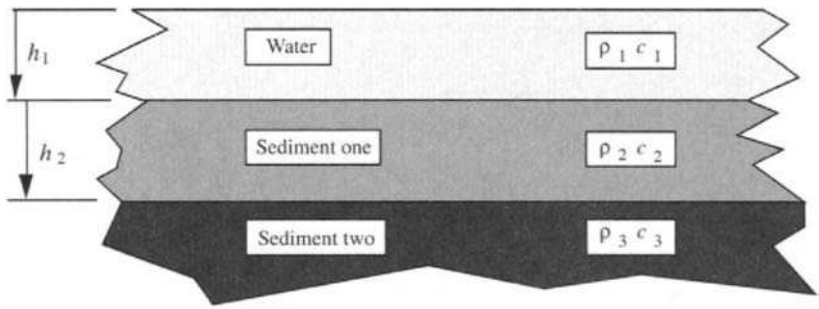

Figure 2.6.2 Water and sediment structure south of Long Island, New York. Parameters are $\rho_1 = 1033\,\text{kg/m}^3$, $c_1 = 1508\,\text{m/s}$, $h_1 = 22.6\,\text{m}$; $\rho_2 = 2\rho_1$, $c_2 = 1.12\,c_1$, $h_2 = 0.9h_1$; $\rho_3 = 2\rho_1$, $c_3 = 1.24c_1$.

use the equations of the previous section to calculate the reflection coefficient and the phase shift, as a function of the angle of incidence. The fractional pressure reflection, $\mathcal{R}_{12}$, is sometimes called the "bottom loss." Quite often bottom loss is expressed in dB as the positive number, $BL = -20\log_{10}\mathcal{R}_{12}$. The values of $\mathcal{R}_{12}$ and the phases plotted in Fig. 2.6.3 should be verified by the student.

2.6.3 *PLANE WAVE REFLECTION AND TRANSMISSION AT MULTIPLE THIN FLUID LAYERS*

The sea floor is usually covered by layers of sediments. The layers are "thin" when the reflection from a sequence of layers can be replaced by the reflection from a composite layer. The local plane wave assumption is used when the thickness of the sequence is very small relative to the distances to the source and receiver. The layers are assumed to act like fluids.

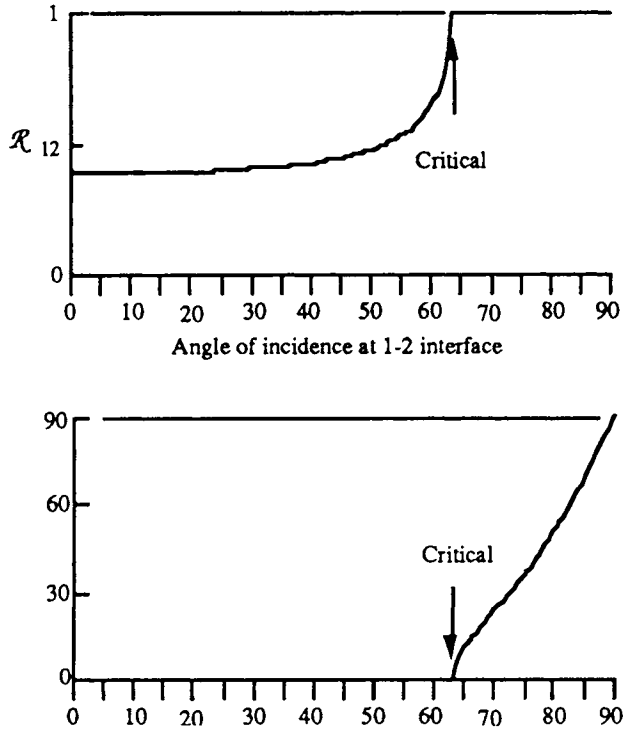

Figure 2.6.3 Amplitude and phase of the reflection at the 1-2 interface shown in Fig. 2.6.2.

Thin layers are also used in the design of sonar windows. The sound passes from the transducer, through a thin protective window, into the water. The transmission coefficient through the window depends on the thickness of the window and the sound speed and ambient density of all three media. The thickness and physical parameters are chosen to maximize the sound transmission through the window.

The geometry and notation for the propagation at a thin fluid layer are in Fig. 2.6.4. The pressure reflection and transmission coefficients for the 1-2 interface were given in Equation 2.6.11a and 2.6.11b. There are similar expressions for the 2-3 interface. From the figure, the total up-traveling signal is the sum of an infinite number of partial transmissions and reflections. Each path within the layer has a phase delay measured by the vertical component of the wave number in the middle layer, $\Phi_2 = k_2 h_2 \cos\theta_2$. The fractional pressure of the total reflection is $\mathcal{R}_{13}$, given by

$$\begin{aligned}\mathcal{R}_{13} = \mathcal{R}_{12} &+ \mathcal{T}_{12}\mathcal{T}_{21}\mathcal{R}_{23}\exp(-i2\Phi_2) \\ &+ \mathcal{T}_{12}\mathcal{T}_{21}\mathcal{R}_{23}^2\mathcal{R}_{12}\exp(-i4\Phi_2) + \cdots\end{aligned}$$

where

$$\Phi_2 = k_2 h_2 \cos\theta_2 \tag{2.6.18}$$

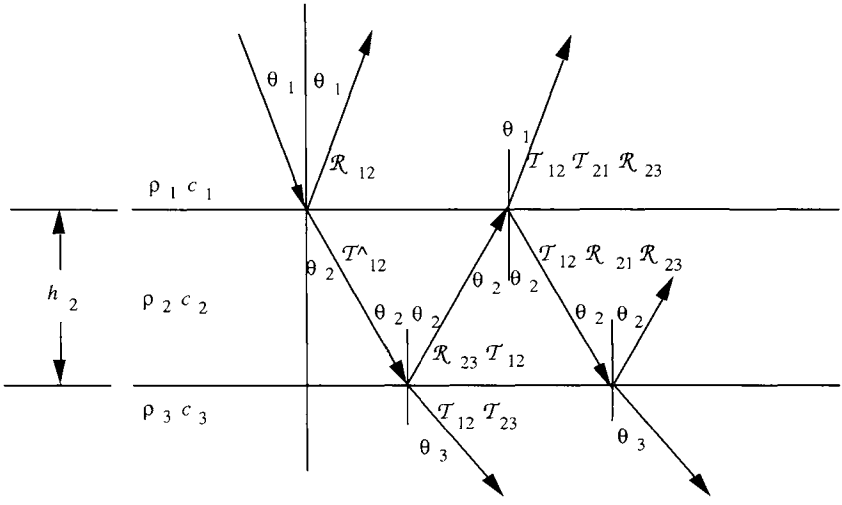

Figure 2.6.4 Reflection and transmission at a thin layer.

Skipping the first reflection term, the rest of Equation 2.6.18 has the form of a geometric series:

$$S = \sum_{0}^{\infty} r^n = \frac{1}{1-r} \quad \text{for} \quad r < 1 \tag{2.6.19}$$

and rearrangement of Equation 2.6.18 gives

$$\mathcal{R}_{13} = \mathcal{R}_{12} + \mathcal{T}_{12}\mathcal{T}_{21}\mathcal{R}_{23}\exp(-i2\Phi_2)\sum_{0}^{\infty}[\mathcal{R}_{23}\mathcal{R}_{12}\exp(-i2\Phi_2)]^n \tag{2.6.20}$$

The pressure reflection and transmission coefficients are related by

$$\mathcal{R}_{12} = -\mathcal{R}_{21} \quad \text{and} \quad \mathcal{T}_{12}\mathcal{T}_{21} = 1 - \mathcal{R}_{12}^2 \tag{2.6.21}$$

Evaluation of the infinite geometric series and some algebraic rearrangement gives

$$\mathcal{R}_{13} = \frac{\mathcal{R}_{12} + \mathcal{R}_{23}\exp(-i2\Phi_2)}{1 + \mathcal{R}_{12}\mathcal{R}_{23}\exp(-i2\Phi_2)} \tag{2.6.22}$$

Using the same construction, the transmission through a thin layer is

$$\mathcal{T}_{13} = \mathcal{T}_{12}\mathcal{T}_{23}\exp(-i\Phi_2) + \mathcal{T}_{12}\mathcal{T}_{23}\mathcal{R}_{23}\mathcal{R}_{21}\exp(-i3\Phi_2) + \ldots \tag{2.6.23}$$

and the sum of the geometric series is

$$\mathcal{T}_{13} = \frac{\mathcal{T}_{12}\mathcal{T}_{23}\exp(-i\Phi_2)}{1 + \mathcal{R}_{12}\mathcal{R}_{23}\exp(-i2\Phi_2)} \tag{2.6.24}$$

The reflection and transmission functions depend on the sound speeds, densities, layer thickness, frequency, and angle of incidence. For very low acoustic contrast, $|R_{12}| \ll 1$, and $|R_{23}| \ll 1$, the denominator is nearly unity, and the coefficients are oscillatory.

Two examples of thin-layer-reflections and transmissions at normal incidence are shown in Fig. 2.6.5. The top shows the reflection from a 1 m thickness of sediment; the reflection is strongly frequency-dependent. The lower example shows the transmission through a well-designed sonar window; the transmission coefficient is nearly unity over the frequency range as desired.

An example of the geophysical use of these relations is given in Fig. 2.6.6, where the bottom layers are identified by use of reflections from different depths. For this "seismic profile," the source and receiver look vertically downward from a "fish" at a depth 3 m below the surface.

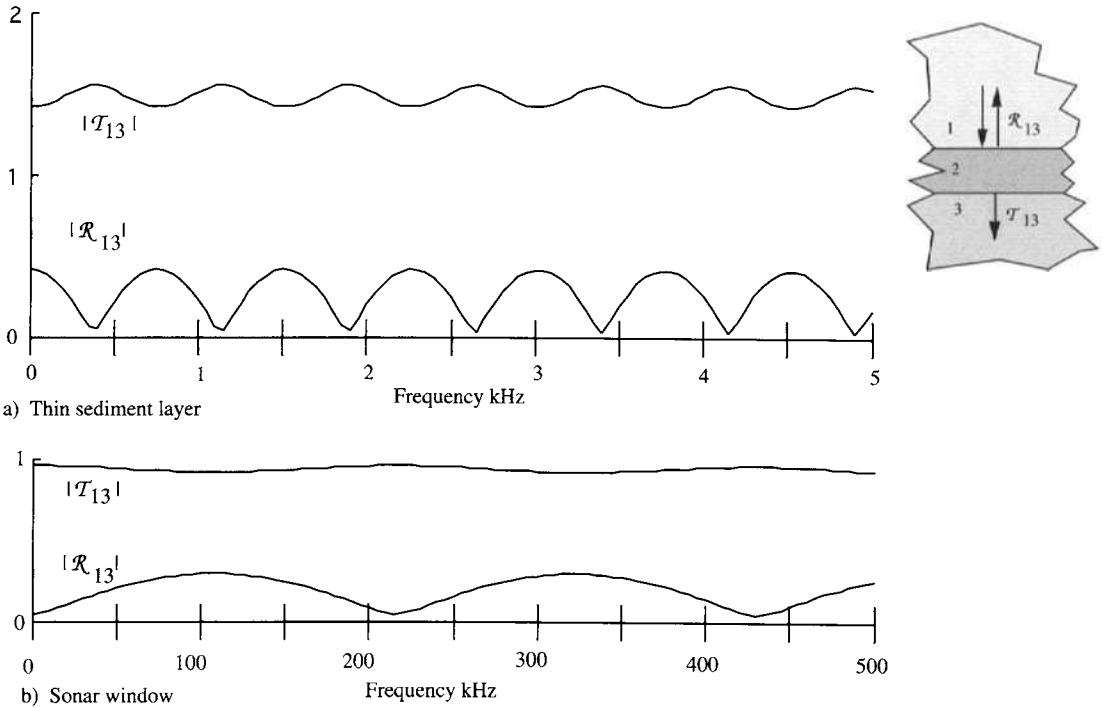

Figure 2.6.5 Transmission and reflection at thin nonabsorbing layers. Normal incident sound. a) Thin sediment layer on the sea floor: $c_1 = 1500\,\text{m/s}$ and $\rho_1 = 1000\,\text{kg/m}^3$; $c_2 = 1509\,\text{m/s}$, $\rho_2 = 1500\,\text{kg/m}^3$ and $h_2 = 1\,\text{m}$; $c_3 = 1800\,\text{m/s}$ and $\rho_3 = 2000\,\text{kg/m}^3$. b) Sonar window: $c_1 = 1500\,\text{m/s}$ and $\rho_1 = 1000\,\text{kg/m}^3$; $c_2 = 1076\,\text{m/s}$, $\rho_2 = 900\,\text{kg/m}^3$ and $h^2 = 0.0025\,\text{m}$; $c_3 = 1350\,\text{m/s}$ and $\rho_3 = 950\,\text{kg/m}^3$.

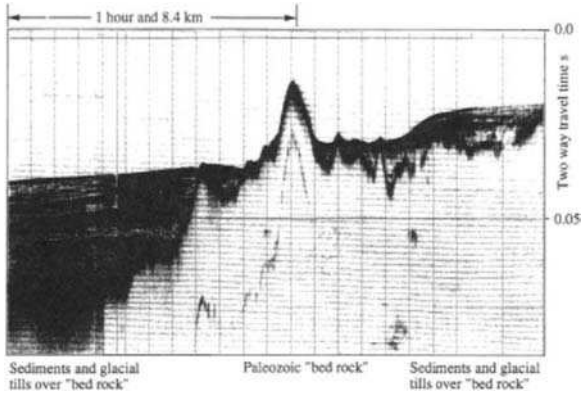

Figure 2.6.6 Subbottom layers in Lake Michigan, identified by seismic reflections. The transmitted signal is 1 cycle of a 7 kHz sinusoidal pulse. (Lineback 1974, p. 18. Courtesy of the Illinois State Geological Survey.)

2.6.4 RAY REFLECTION BEYOND CRITICAL ANGLE

In section 2.6.2 it was demonstrated that for plane wave incidence beyond the critical angle, there is perfect reflection with an accompanying phase shift. Weston (1960) and Buckingham (1985) have shown the usefulness of introducing a virtual, displaced, pressure release surface (i.e., $\mathcal{R} = -1$) to represent the magnitude and the phase shift of a plane wave reflected under that critical condition. Fig. 2.6.7 shows the geometry of the virtual reflector concept.

The two-way travel between the real interface and the virtual reflector produces a phase shift

$$2k_1 \, \Delta z \cos \theta_1 = 2 (\omega / c_1) \, \Delta z \cos \theta_1 \qquad \textbf{(2.6.25)}$$

The phase shift is equated with that in Equation 2.6.16,

$$\mathcal{R}_{12} = e^{i 2\Phi} = -\exp\{i \, [\, 2 (\omega / c_1) \, \Delta z \cos \theta_1 \,]\} \qquad \textbf{(2.6.26)}$$

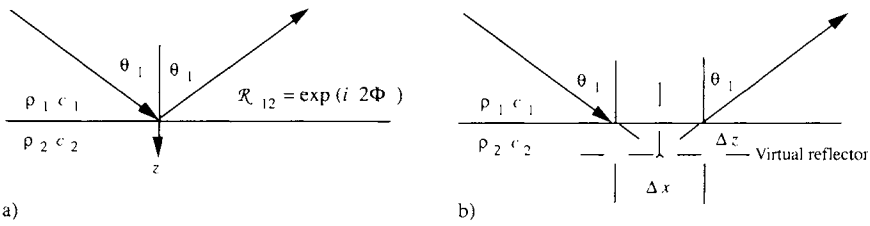

Figure 2.6.7 Reflection beyond critical angle. a) Reflection and phase shift. b) Reflection at a virtual reflector at Δz depth.

and the (−) sign is interpreted as a phase shift of π to give

$$\Phi = (\omega / c_1)\ \Delta z\ \cos\theta_1 + \pi / 2 \tag{2.6.27}$$

Therefore, for a given frequency, the distance of the virtual pressure release reflector below the real interface is

$$\Delta z = \frac{c_1(\Phi - \frac{\pi}{2})}{\omega \cos\theta_1} \tag{2.6.28}$$

and the ray displacement, caused by reflection beyond the critical angle, is

$$\Delta x = 2\Delta z \tan\theta_1 \tag{2.6.29}$$

2.6.5 *HEAD WAVES: SPHERICAL WAVES BEYOND CRITICAL ANGLE*

When there is a higher speed medium adjacent to the source medium, and the incident spherical wave front meets the interface at the critical angle, a *head wave* is produced. The head wave moves at the higher speed c_2 along the interface and radiates into the source medium, c_1. Because it travels at a higher speed, at sufficient ranges the head wave arrives significantly ahead of the spherically diverging direct wave. The energy appears to be continually shed into the lower-speed source medium at the critical angle $\sin\theta_c = c_1/c_2$, as it propagates along the interface (Fig. 2.6.8a).

Huygens wavelets and wave front constructions can explain the processes that produce a head wave in addition to the well-known reflected and refracted waves at the interface. Assume a homogeneous fluid half-space having a higher sound speed c_2 under a lower sound speed c_1 (e.g., most sediments under water). A sequence of positions of the impulse wave front constructions appears in Fig. 2.6.8b. For this example $c_2 = 2c_1$, and θ_c is 30°.

When the contacts of the spherical wave front and the interface are at angles less than the critical angle, the wave front constructions look like that previously shown for simple reflection (Fig. 2.2.2). To understand what happens at and beyond the critical angle, notice that the sound pressures and displacements are equal on both sides of the interface. The sound pressures and displacements at points such as h_1 in medium 2 cause corresponding sound pressures and displacements and determine the radiation of Huygens wavelets into medium 1. Fig. 2.6.8b illustrates the construction in medium 1 for the sequence of wavelet sources at the interface h_c, h_1, h_2, and h_3. The line labeled "head wave" shows the envelope of the wavelets. For a point source, the head wave is a conical surface. The contact h moves along the interface at speed c_2. The head wave radiates, at the critical angle, into the source medium. Some geophysicists refer to

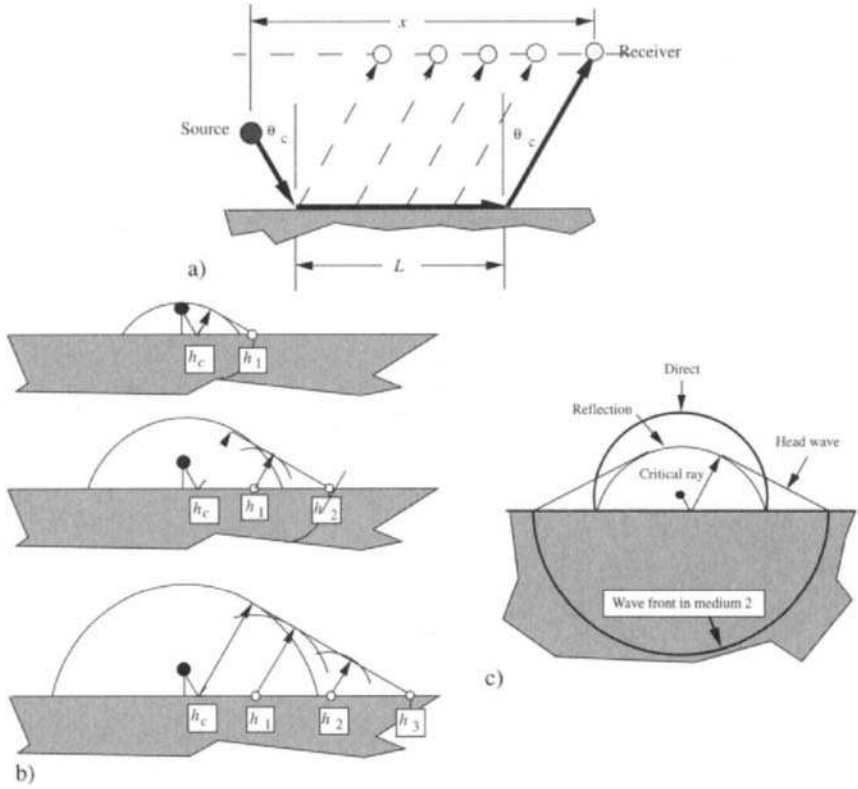

Figure 2.6.8 a) Head wave geometry. b) Huygens head wave construction. The impulse source is in a lower-speed medium over a higher-sound-speed medium, $c_2 = 2c_1$ (e.g., water over most sediments). The Huygens sources move along the interface at speed c_2. The head wave is the wave that connects the refracted wave in the lower medium to the reflected wave front at the critical ray position. The direct and refracted waves are omitted in the construction. c) Snapshot of the direct, reflected, refracted, and head wave fronts at an instant of time.

this as the refracted arrival in medium 1, and the head wave is sometimes called the lateral wave in medium 1. The three field components in the upper region 1 are the direct wave, the reflected wave, and the head wave (Fig. 2.6.8c).

Analytical developments of the head wave are beyond the scope of our text (see Cerveny and Ravinda 1971). One significant conclusion is that, for a point source, the amplitude of the head wave in medium 1 depends on the curvature of the wave front in medium 2 and is given by

$$\text{amplitude of head wave} \quad \sim x^{-1/2} L^{-3/2} k^{-1} \tag{2.6.30}$$

where x and L are defined in Fig. 2.6.8a. Here it is assumed that attenuation is negligible.

Experimental studies of the head wave are most easily accomplished by use of scaled models in the laboratory. The above relation was verified by O'Brien (1955), who used a set of laboratory experiments designed to model typical ocean seismic conditions of water over a high speed bottom. He verified the dependence of amplitudes on range and geometry as in Equation 2.6.30.

The conditions for a head wave also exist for a sound source under Arctic ice even when it is only a fraction of a wavelength in thickness. Arctic "pack ice" often consists of "plates" that are hundreds of meters in extent and 1 or 2 meters thick; the plates are bounded by broken sections called "ridges." A laboratory scale model study of Arctic ice reported by Medwin et al. (1988) verified that the predicted amplitude dependence on range and frequency as given in Equation 2.6.30 for seismic waves exists in this case as well (see Fig. 2.6.9). The physico-acoustical properties of the laboratory synthetic "ice" were in substantial agreement with the arctic ice values as studied by McCammon and McDaniel (1985). The geometry is shown in Fig. 2.6.9.

To model Arctic propagation, it is important to use laboratory materials that have the same physical parameters as the Arctic ice. Then the spatial dimensions of plate thickness, source range, and receiver range are scaled relative to the wavelength. For example, a 3.3 mm acrylic plate floating on water in the laboratory, when insonified at 62.5 kHz, can represent a 1 m thick Arctic plate insonified by 200 Hz sound. In both cases, the point source under the "ice" canopy generates a compressional wave at the critical angle for entry into the ice. As the compressional wave propagates in the plate, it "sheds" a head wave into the water at the critical angle. The hydrophone will receive a reflected wave, and a direct wave (not shown in the sketch) as well. When the range is large enough the head wave precedes the other two arrivals.

In geometrical-acoustical scale modeling, it is also necessary to select the frequency, pulse length, and source and receiver depths in order to isolate and identify the head wave. Since the compressional speed in the laboratory plate and laboratory water were essentially the same as in the Arctic, the critical angle for the compressional wave was approximately the same, $\theta_c = \sin^{-1}(c_1/c_2) \approx \sin^{-1}(1480/2353) = 39°$. A range of frequencies, plate thicknesses, and depths of source and receiver were used for the data of Fig. 2.6.9. For example, the data represented by squares in the figure were acquired with a pulse of 2 cycles of 62.5 kHz energy ($\lambda = 2.37$ cm in water). The plate thickness was 3.3 mm ($\approx 0.14\lambda$ in water and $\approx 0.09\lambda$ of the compressional wave in the plate). The signal used to obtain one square data point is shown in Fig. 2.6.10.

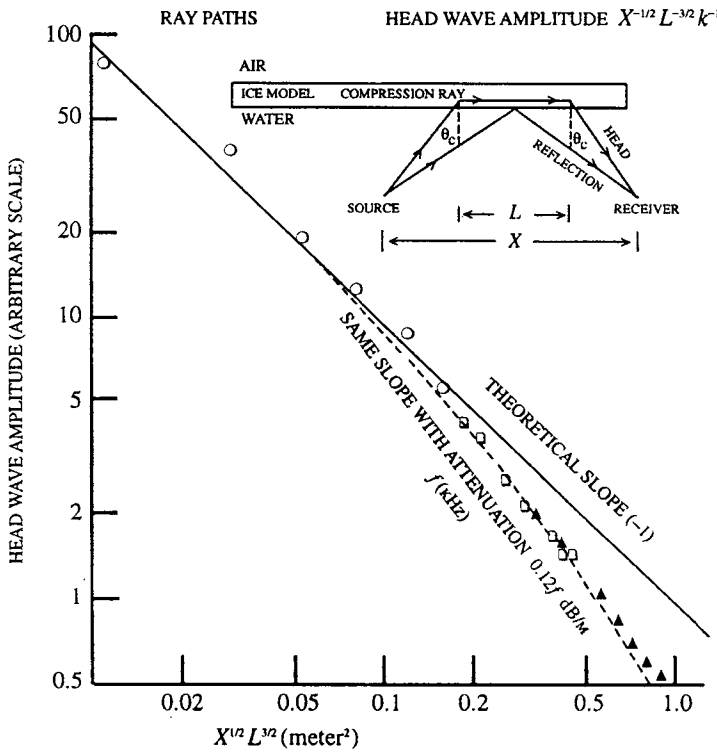

Figure 2.6.9 Dependence of head wave amplitude on path length of a compressional wave in an acrylic plate floating on water. Plate thickness 3.3 mm. Receiver depths were varied from 1 cm to 40 cm. Range X was 70 cm. The three symbols represent data from three experiments. The divergence of the data from the theoretical, nonattenuation behavior was used to determine the attenuation of the compressional wave in the plate. (Medwin, H., K. J. Reitzel, and M. J. Browne, "Elements of Arctic surface scatter: Part III, the head wave," *J. Acoust. Soc. Am.* **82**, (S1), S31 (A) 1987.)

Notice that, although the head wave was isolated as needed for Fig. 2.6.9, there was interference between the later-arriving direct and reflected waves.

Because the thickness of Arctic ice is often a small fraction of a wavelength, early discussions of reflection from the ice cover *incorrectly* assumed that the "thin" ice covered by air was equivalent to a simple water-air pressure-release interface. Model experiments such as that above showed that the problem is far more complex than that. Taking advantage of this complexity, the existence of a head wave in the Arctic provides a technique for measuring the low-frequency compressional wave speed in an ice plate. See also a series of ingenious laboratory experiments by Chamuel — for instance, Chamuel and Brooks (1988).

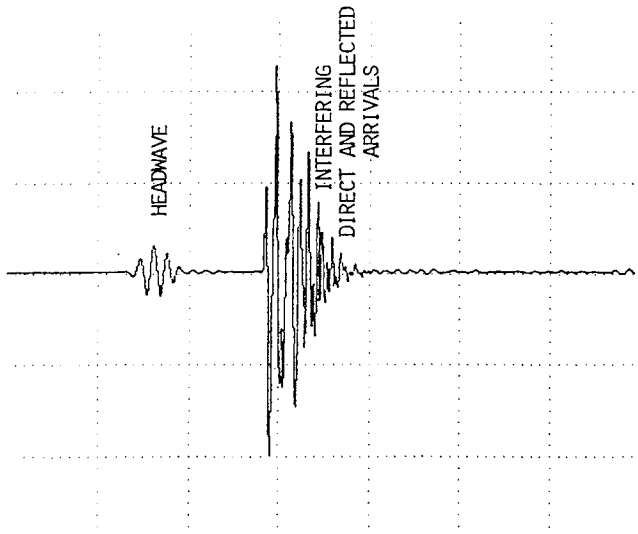

Figure 2.6.10 Impulse response for a shallow point source of sound under a model of the Arctic ice canopy. The source was driven by 2 cycles of 62.5 kHz; $\lambda = 2.37$ cm in water. Source and receiver depths were 0.4 wavelengths in water; source and receiver separation, $X = 27$ wavelengths; path lengh in plate, $L = 26$ wavelengths. (Medwin, H., et al., "Elements of Arctic Surface Scatter; Part III, the head wave," *J. Acoust. Soc. Am.* **82** (S1), S31 (A), 1987.)

2.6.6 FRESNEL ZONES: SPHERICAL WAVE REFLECTION AT AN INTERFACE

Consider the reflection of a spherical wave from a plane surface. An approximate local plane wave solution, which may be used for an *infinite* plane reflector, can be calculated by using an image technique with the reflection coefficient $\mathcal{R}_{12}$.

However, for *finite* reflecting planes, because of interfering phase-shifted components, *the magnitude of the reflection depends on the size of the plane surface as well as the reflection coefficient,* $\mathcal{R}_{12}$. The geometry for a point source and receiver is sketched in Fig. 2.6.11.

Many sonar systems have the source and receiver at the same position. In operation, the source transmits a signal for a short time, then the receiver listens for the returning signal. The source is quiet when the receiver is listening. Assume the point source is at height h above a plane-reflecting circular disk. The calculation of the reflection consists of summing (or integrating) the contributions of all wavelets radiating as point sources from small elements of the reflecting disk.

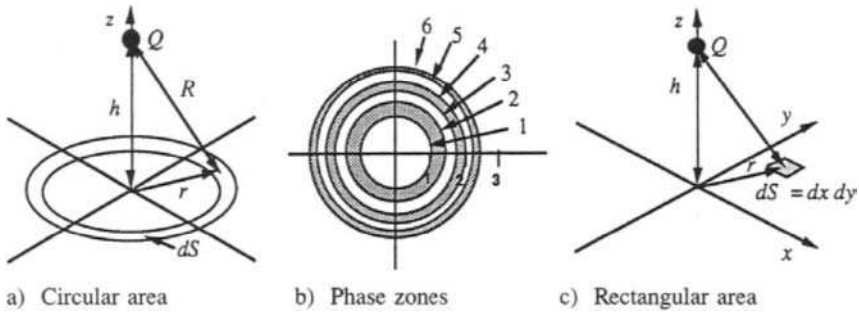

a) Circular area b) Phase zones c) Rectangular area

Figure 2.6.11 Reflection from a finite plane area. The circular geometry is at left, the Fresnel phase zones in the center, and the geometry for a rectangular subangle at right.

We now calculate the dependence of the sum on the radius of the disk. For simplicity, we will not consider the small amount of diffraction at the disk edge. Referring to Fig. 2.6.6, considering the wavefront that travels from the source at Q to the typical scattering area element dS then back to the receiver, a total distance of $2R$, the phase is

$$\Phi = \omega t - 2kR \tag{2.6.31a}$$

where

$$R = (h^2 + r^2)^{1/2} \tag{2.6.31b}$$

In summing the contributions from different elements, as r increases from zero, the quantity of interest is the *phase change*, $2kR$. When we let the smallest value, $2kh$, be the reference phase, the relative phase difference for the element dS is

$$\Delta\Phi = 2\,kR - 2\,kh \tag{2.6.32}$$

Solve for R and then for r as a function of $\Delta\Phi$:

$$R = (r^2 + h^2)^{1/2} = \frac{\lambda\Delta\Phi}{4\pi} + h \tag{2.6.33}$$

$$r^2 = \frac{h\,\lambda\,\Delta\Phi}{2\pi} + \left(\frac{\lambda\Delta\Phi}{4\pi}\right)^2 \tag{2.6.34}$$

We are interested in the situation where the reflector is many wavelengths from the source, $h \gg \lambda$ in which case Equation 2.6.34 can be approximated by the first term only. Then

$$\Delta\Phi \cong \frac{2\pi r^2}{h\lambda} \tag{2.6.35}$$

The contributions are positive for elements at radii such that $\Delta\Phi$ given by Equation 2.6.35 is in the range 0 to π; this is the first-phase zone, the central white circle in Fig. 2.6.11. The contributions are negative when Φ is in the range π to 2π; this is the first shaded ring in the figure.

In general, letting $\Delta\Phi = n\pi$, the phase changes sign at radii given by

$$r_n = \left(\frac{\lambda h}{2}\right)^{1/2} n^{1/2} \tag{2.6.36}$$

Each ring with either phase sign is called a "Fresnel zone" or a "phase zone."

The central circle, with $n = 1$, is the first Fresnel zone. The radius of this important Fresnel zone, in which there is a minimum of destructively interfering phase change, is

$$r_1 = \left(\frac{\lambda h}{2}\right)^{1/2} \tag{2.6.37}$$

A complete calculation shows that a signal reflected at a disk having radius r_1 has a maximum acoustic pressure *almost twice as large as for an infinite plate.* On the other hand, when the radius of the disk is r_2 the first- and second-phase zones both contribute, and the reflected signal is nearly to zero. Other maxima and minima alternate as the radius is increased, and as additional zones contribute.

For a disk of infinite radius an analytical solution gives the reflected signal proportional to

$$\frac{1}{2h} e^{i(\omega t - 2kh)} \tag{2.6.38}$$

The interpretation of Equation 2.6.38 is that the amplitude and phase of the reflected pressure from a very large plate are equivalent to those from a virtual image at distance h behind the reflector. That is, using the image construction, the reflected pressure seems to come from an image below the interface. The factor $1/(2h)$ appears because, for spherical divergence, the acoustic pressure is inversely proportional to the range. If the plate is not perfectly reflecting, the radiation from the image is multiplied by the fractional reflection coefficient at the interface.

The exact solution of the reflection of a spherical wave at an infinite plane interface is a more difficult theoretical problem than we have implied above. The image approximation in this case is acceptable only when the distances R_1 and R_2 are many acoustic wavelengths, and the angle of incidence is not too near the critical angle. The solution is exact when the sound speeds $c_1 = c_2$ and the densities are different. (One can prove this by substitution in boundary

conditions.) A general solution is given by Brekhovski (1960), who finds that for an infinite plane reflector the spherical reflection coefficient is the following modification of the plane wave coefficient:

$$\mathcal{R} = \mathcal{R}_{12} - iN / (kR) \tag{2.6.39}$$

where

$$N = (\mathcal{R}'_{12} + \mathcal{R}'_{12} \cot \theta_1)/2 \tag{2.6.40}$$

The derivatives $\mathcal{R}'_{12}$ and $\mathcal{R}''_{12}$ are taken with respect to θ_1; R is the distance from the image source to the receiver ($2h$ in the case above). The value of N is negligible for θ_1 not too close to the critical angle and for large kR. However, the simple plane wave concept of reflection and transmission will fail near the critical angle. At and beyond the critical angle, part of the energy of the sound wave in the water travels along the interface in the higher-speed medium and sheds energy into the lower-speed water medium as described in section 2.6.5 for head waves.

2.7 Propagation in Three Dimensions

2.7.1 THE WAVE EQUATION

The simple use of an infinite plane wave, or of a point source whose spherical waves at long ranges can be approximated by a local plane wave, have served us well. In a realistic world and for many applications, we use wave fields that are more conveniently described in spherical or cylindrical coordinates. Examples are: 1) sound transmissions in layered waveguides are effectively stated in cylindrical coordinates; 2) computations of the scattering of sound waves by cylinders are simpler if one uses cylindrical coordinates; 3) computations of the scattering of sound waves by spheres use spherical coordinates. An important part of the solution is often accomplished by the expansion of spherical functions in terms of incident plane waves.

To generate the wave equation in three dimensions, we combine the results for each of the coordinate directions. It is easiest to start with rectangular coordinates, and use the unit vectors **i**, **j**, and **k**, Fig. 2.7.1.

Generalization of Equation 2.5.2 gives the three vector equations

$$\begin{aligned} \mathbf{i}\, \partial p / \partial x &= -\mathbf{i}\, \rho_A (du / dt) \\ \mathbf{j}\, \partial p / \partial y &= -\mathbf{j}\, \rho_A (dv / dt) \\ \mathbf{k}\, \partial p / \partial z &= -\mathbf{k}\, \rho_A (dw / dt) \end{aligned} \tag{2.7.1}$$

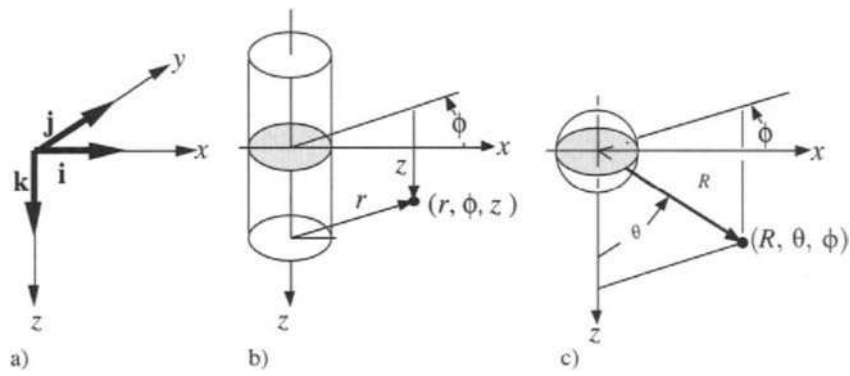

Figure 2.7.1 Three coordinate systems. a) Rectangular. b) Cylindrical. c) Spherical. The z-axis is drawn as positive downward. The (longitude) angles ϕ are measured in planes perpendicular to the z axis. The (latitude) angle θ is measured to the z axis.

where u, v, and w are the components of particle velocity along the x, y, and z directions.

Since u is a function of x and t, the total derivative (du/dt) is found by using implicit differentiation:

$$\frac{du}{dt} = \frac{\partial u}{\partial t} + \frac{\partial u}{\partial x}\frac{\partial x}{\partial t} = \frac{\partial u}{\partial t} + u\frac{\partial u}{\partial x} \tag{2.7.2}$$

with similar expressions for the other components. The first term of the equation on the right is called the local acceleration, the second term is the convective acceleration.

Since $u = u(t - x/c)$, we find $u(\partial u/\partial x) = -(u/c)(\partial u/\partial t)$. For linear acoustics, we require $u/c \ll 1$; therefore, for linear acoustics $(du/dt) = (\partial u/\partial t)$.

Equations 2.7.1 are summed to yield one *three-dimensional acoustic force equation*,

$$\mathbf{i}\frac{\partial p}{\partial x} + \mathbf{j}\frac{\partial p}{\partial y} + \mathbf{k}\frac{\partial p}{\partial z} = -\rho_A\left(\mathbf{i}\frac{\partial u}{\partial t} + \mathbf{j}\frac{\partial v}{\partial t} + \mathbf{k}\frac{\partial w}{\partial t}\right) \tag{2.7.3}$$

or

$$\nabla p = -\rho_A \frac{\partial \mathbf{U}}{\partial t} \tag{2.7.4}$$

where $\boldsymbol{U} = \mathbf{i}u + \mathbf{j}v + \mathbf{k}w$ and the del operator is $\nabla = \mathbf{i}(\partial/\partial x) + \mathbf{j}(\partial/\partial y) + \mathbf{k}(\partial/\partial z)$.

Next, we generalize Equation 2.5.4 to calculate the density change and mass flow for the three-dimensional problem

$$\frac{\partial(\rho_T u)}{\partial x} + \frac{\partial(\rho_T v)}{\partial y} + \frac{\partial(\rho_T w)}{\partial z} = -\frac{\partial \rho}{\partial t} \tag{2.7.5}$$

where $\rho_T = \rho_A + \rho$ is the total density.

Again we use the vector symbols for a concise notation:

$$\nabla\cdot(\rho_T \mathbf{U}) = -\frac{\partial \rho}{\partial t} \tag{2.7.6}$$

where

$$\nabla\cdot(\rho_T \mathbf{U}) = \left(\mathbf{i}\frac{\partial}{\partial x} + \mathbf{j}\frac{\partial}{\partial y} + \mathbf{k}\frac{\partial}{\partial z}\right)\cdot(\mathbf{i}\rho_T u + \mathbf{j}\rho_T v + \mathbf{k}\rho_T w) \tag{2.7.7}$$

is the divergence of $\rho_T \boldsymbol{U}$ and where $\mathbf{i}\cdot\mathbf{i} = 1$, $\mathbf{i}\cdot\mathbf{j} = 0$, and so forth.

Simplification is possible by expansion of the LHS, using $\rho_T = \rho_A + \rho$, because, for linear acoustics, $u/c = \rho/\rho_A \ll 1$.

Therefore the three-dimensional equation for the *acoustic conservation of mass* is

$$\rho_A(\nabla\cdot\mathbf{U}) = -\frac{\partial \rho}{\partial t} \tag{2.7.8}$$

We have derived a pair of equations that depend on $\boldsymbol{U}$. We eliminate $\boldsymbol{U}$ by taking the divergence of Equation 2.7.4 and the $\partial/\partial t$ of Equation 2.7.8. Also, use the acoustical equation of state (2.5.13) to eliminate ρ. The result is the *three-dimensional wave equation* in terms of the acoustic pressure,

$$\nabla^2 p = \frac{1}{c^2}\frac{\partial^2 p}{\partial t^2} \tag{2.7.9}$$

where ∇^2 is the *Laplacian* that takes different forms in the different coordinate systems.

In *rectangular coordinates*,

$$\nabla^2 = \nabla \bullet \nabla = \frac{\partial^2}{\partial x^2} + \frac{\partial^2}{\partial y^2} + \frac{\partial^2}{\partial z^2} \tag{2.7.10}$$

which is the form convenient for plane waves and plane surface interactions.

We use the *spherical coordinate system*, as shown in Fig. 2.7.1c, involving R, θ, and ϕ for spherical waves, or interactions with spherical surfaces. After much manipulation, obtain the gradient operator

$$\nabla = \mathbf{1}_R \frac{\partial}{\partial R} + \mathbf{1}_\phi \frac{1}{R^2 \sin\theta} \frac{\partial}{\partial \phi} + 1_\theta \frac{1}{R} \frac{\partial}{\partial \theta} \tag{2.7.11}$$

where $\mathbf{1}_R$, $\mathbf{1}_\phi$, and $\mathbf{1}_\theta$ are unit vectors along the spherical coordinate directions R, ϕ, and θ.

The vector $\boldsymbol{U}$ in spherical coordinates is

$$\boldsymbol{U} = \mathbf{1}_R U_R + \mathbf{1}_\phi U_\phi + \mathbf{1}_\theta U_\theta \tag{2.7.12}$$

The divergence of $\boldsymbol{U}$ in spherical coordinates is

$$\nabla \cdot \boldsymbol{U} = \frac{\partial(R^2 U_R)}{R^2 \partial R} + \frac{1}{R \sin\theta} \frac{\partial U_\phi}{\partial \phi} + \frac{1}{R \sin\theta} \frac{\partial(U_\theta \sin\theta)}{\partial \theta} \tag{2.7.13}$$

The Laplacian in spherical coordinates is

$$\nabla^2 = \frac{\partial^2}{\partial R^2} + \frac{2}{R} \frac{\partial}{\partial R} + \frac{1}{R^2 \sin^2\theta} \frac{\partial^2}{\partial \phi^2} + \frac{1}{R^2} \left(\frac{\partial^2}{\partial \theta^2} + \cot\theta \frac{\partial}{\partial \theta} \right) \tag{2.7.14}$$

Use *cylindrical coordinates* for cylindrically propagating waves, or waves interacting with cylindrical surfaces. The gradient and Laplacian in coordinates r, z, and ϕ are shown in Fig. 2.7.1b. Note that range in cylindrical coordinates is r, whereas range in spherical coordinates is R. The forms for cylindrical coordinates are

$$\nabla = \mathbf{1}_r \frac{\partial}{\partial r} + \mathbf{1}_\phi \frac{1}{r} \frac{\partial}{\partial \phi} + \mathbf{k} \frac{\partial}{\partial z} \tag{2.7.15}$$

where the unit vectors are $\mathbf{1}_r$, $\mathbf{1}_\phi$, and $\mathbf{k}$ (as in rectangular coordinates).

The vector $\boldsymbol{U}$ in cylindrical coordinates is

$$\boldsymbol{U} = \mathbf{1}_r U_r + \mathbf{1}_\theta U_\theta + k U_z \tag{2.7.16}$$

The divergence operator in cylindrical coordinates is

$$\nabla \cdot = \frac{\partial U_r}{\partial r} + \frac{U_r}{r} + \frac{1}{r} \frac{\partial U_\theta}{\partial \theta} + \frac{\partial U_z}{\partial z} \tag{2.7.17}$$

The Laplacian in cylindrical coordinates is

$$\nabla^2 = \frac{\partial^2}{\partial r^2} + \frac{1}{r} \frac{\partial}{\partial r} + \frac{1}{r^2} \frac{\partial^2}{\partial \phi^2} + \frac{\partial^2}{\partial z^2} \tag{2.7.18}$$

When Equations 2.7.14 and 2.7.18 are used in Equation 2.7.9 we obtain the wave equations in spherical and cylindrical coordinates, respectively. Solutions of the cylindrical and spherical wave equations are considered in Chapter 7. We shall need those solutions in later chapters.

2.7.2 *CONTINUOUS WAVES IN RECTANGULAR COORDINATES*

The solution of the wave equation in rectangular coordinates gives a simple illustration of a very powerful method from classical physics, *the separation of variables*. Rectangular coordinates are simple because all of the functions are sines or cosines or complex exponentials. From above, the wave equation in rectangular coordinates is

$$\nabla^2 p = \frac{\partial^2 p}{\partial x^2} + \frac{\partial^2 p}{\partial y^2} + \frac{\partial^2 p}{\partial z^2} = \frac{1}{c^2}\frac{\partial^2 p}{\partial t^2} \tag{2.7.19}$$

We assume that the waves along the three coordinate directions are independent of one another. Therefore the pressure can be written as a product of functions of the four variables:

$$p = X(x)Y(y)Z(z)T(t) \tag{2.7.20}$$

Substitution into the wave equation in rectangular coordinates gives

$$X''YZT + Y''XZT + Z''XYT = \frac{T''}{c^2}XYZ \tag{2.7.21}$$

where X'' is $\partial^2 X/\partial x^2$ and so on. Now, rearrange to

$$c^2\frac{X''}{X} + c^2\frac{Y''}{Y} + c^2\frac{Z''}{Z} = \frac{T''}{T} \tag{2.7.22}$$

Notice that each term is a function of only one variable. That is, T''/T is only a function of time, and the first term, c^2X''/X is a function of x only, and so on. Therefore, since Equation 2.7.15 is true for all values of x, y, z, and t, *each of the terms must be a constant.*

Assume that the time dependence is harmonic and evaluate the constant. For example, try the solutions:

$$T = A_1 e^{i\omega t} \quad or\ T = A_2 e^{-i\omega t} \quad or\ T = A_1 e^{i\omega t} + A_2 e^{-i\omega t} \tag{2.7.23}$$

where A_1 and A_2 are constants. They all satisfy

$$\frac{T''}{T} = -\omega^2 \tag{2.7.24}$$

For the present illustration, we assume that c is constant. Again we use the logical argument that if Z, Y, and Z are independent of one another, then X''/X, Y''/Y, and Z''/Z must each equal constants. Using X as an example, we try the solution

$$X = B_1 \exp(ik_x x) + B_2 \exp(-ik_x x) \tag{2.7.25}$$

Evaluation of X''/X gives

$$\frac{X''}{X} = -k_x^2 \tag{2.7.26}$$

Similar expressions for Y and Z give

$$\frac{Y''}{Y} = -k_y^2 \tag{2.7.27}$$

and

$$\frac{Z''}{Z} = -k_z^2 \tag{2.7.28}$$

The substitution of these into Equation 2.7.22 yields

$$c^2 (k_x^2 + k_y^2 + k_z^2) = \omega^2 \tag{2.7.29}$$

or

$$k^2 \equiv \frac{\omega^2}{c^2} \tag{2.7.30}$$

where

$$k^2 = k_x^2 + k_y^2 + k_z^2 \tag{2.7.31}$$

Our solution gives us flexibility to describe any set of plane waves propagating in any direction. For example, the equation of a plane wave traveling in the $+x$, $+y$, and $+z$ directions is

$$p = P \exp[i(\omega t - k_x x - k_y y - k_z z)] \tag{2.7.32}$$

The vector wave number $\boldsymbol{k}$, which defines the direction of propagation of the plane wave, can be resolved into its components in the x, y, and z directions by knowing the cosines of the angles with the coordinate axes. Usually it is obvious from the context whether the bold letter $\boldsymbol{k}$ is the vector wave number, as here, or the unit vector $\boldsymbol{k}$ in the z direction, as in Equation 2.7.1 and elsewhere.

2.7.3 *OMNIDIRECTIONAL WAVES IN SPHERICAL COORDINATES*

General solutions to the spherical wave equation are in Abramovitz and Stegun (1964). Here we assume spherical symmetry. The wave equation is thereby greatly simplified, and the solutions are easily comprehended, and useful in many applications.

Omnidirectional Radiation

A very important solution to the wave equation is the pressure wave owing to a pulsating source that radiates the same in all directions in an ideal isotropic, homogeneous medium. Since the wave equation does not depend on θ or ϕ, the last two terms of Equation 2.7.14 are zero. The wave equation in spherical coordinates, with range and time dependence only, reduces to

$$\frac{\partial^2 p}{\partial R^2} + \frac{2}{R}\frac{\partial p}{\partial R} - \frac{1}{c^2}\frac{\partial^2 p}{\partial t^2} = 0 \tag{2.7.33}$$

This can be rearranged to

$$\frac{1}{R}\frac{\partial^2 (Rp)}{\partial R^2} - \frac{1}{c^2}\frac{\partial^2 p}{\partial t^2} = 0 \tag{2.7.34}$$

or

$$\frac{\partial^2 (Rp)}{\partial R^2} - \frac{1}{c^2}\frac{\partial^2 (Rp)}{\partial t^2} = 0 \tag{2.7.35}$$

This equation is identical to the one-dimensional version of the wave equation in rectangular coordinates (2.5.8), but with p replaced by Rp and x replaced by R.

The solutions to Equation 2.7.35 are therefore the same as for plane waves, but with the above replacements. In general,

$$pR = R_0 p_0 (ct \pm R) \quad \text{or} \quad p = \frac{p_0 (ct \pm R) R_0}{R} \tag{2.7.36}$$

where $p_0(ct \pm R)$ describes the acoustic pressure as any function of $(ct \pm R)$. The $\pm$ sign in Equation 2.7.36 indicates that the pressure p may have either or both functional dependences. The choice $(ct - R)]$ designates an outward radiating wave such as the wave from a pulsating sphere. The choice $(ct + R)$ gives an inward radiating wave that might be, for example, an implosion or the inward reflection from a spherical reflector. In many situations, the waves are known to be traveling away from a source, and the inward traveling wave is dropped

on physical grounds. Normally, p_0 is the sound pressure referred to the unit distance R_0.

Acoustic Pressure for Sinusoidal, Omnidirectional Waves

In general, the solution is the product of a radial function and a temporal function

$$p = P\ \Re\ (R)\ T\ (t) \tag{2.7.37}$$

For sinusoidal waves, the time-dependent function is

$$T = e^{i\omega t} \tag{2.7.38}$$

Substitution of Equation 2.7.37 into the omnidirectional spherical wave equation (2.7.33) gives

$$\frac{1}{R}\frac{\partial^2}{\partial R^2}(R\mathcal{R}) + k^2\mathcal{R} = 0 \tag{2.7.39}$$

where $k = \omega/c$.

The radial wave equation has two independent solutions:

$$\Re = \frac{\cos(kR)}{R} \quad \text{and} \quad \Re = \frac{\sin(kR)}{R} \tag{2.7.40}$$

In complex notation, the outward propagating sinusoidal wave is written

$$p = \frac{P_0 R_0}{R} e^{i(\omega t - kR)} \tag{2.7.41}$$

where the amplitude is written in terms of the pressure P_0 at range R_0.

Particle Velocity for Sinusoidal Omnidirectional Waves

Computations of the particle velocity in spherical coordinates start with the acoustic force Equation (2.7.4) and use the gradient (2.7.11) for the case of spherical symmetry

$$\nabla p = -\rho_A \frac{\partial \mathbf{U}}{\partial t} \quad \text{where} \quad \nabla p = \mathbf{1}_R \frac{\partial p}{\partial R} \tag{2.7.42}$$

There is only one component so we write simply:

$$\frac{\partial p}{\partial R} = -\rho_A \frac{\partial u}{\partial t} \tag{2.7.43}$$

When we use u in complex exponential notation, $\partial u/\partial t = i\omega u$, so that Equation 2.7.43 becomes

$$u = -\frac{1}{\rho_A}\frac{\partial p}{\partial R}\left(\frac{1}{i\omega}\right) \tag{2.7.44}$$

Form $\partial p/\partial R$ from Equation 2.7.41, and get

$$\frac{\partial p}{\partial R} = -p\left(\frac{1}{R} + ik\right) \tag{2.7.45}$$

Therefore,

$$u = \frac{p}{\rho_A c}\left(1 - \frac{i}{kR}\right) \tag{2.7.46}$$

Close to the source, small kR, the particle velocity has a "quadrature" component that lags the acoustic pressure by 90°. (A similar conclusion is found for an impulse sound such as an explosion, where there is a great "whooshing" motion as the medium moves outward following the pressure wave.) The nonpropagating energy carried by out-of-phase components such as exist for small kR in Equation 2.7.46 has been discussed by Stanzial et al. (1996).

At large kR, the particle velocity in the spherical wave is proportional to the sound pressure and abides by the same equation as we derived for a plane wave (2.5.10).

Far-Field Intensity for Omnidirectional Waves

In section 2.1 we used the conservation of energy to show that the intensity of sound from an outwardly radiating omnidirection source is proportional to i_0/R^2 (Equation 2.1.2). We now know that for pressure signals that satisfy $kR \gg 1$, the particle velocity along the direction of R is proportional to the pressure. Therefore, for outward propagating waves at large range,

$$u_R \cong \frac{p_0(ct - R)R_0}{\rho_A c R} \quad \text{for} \quad kR \gg 1 \tag{2.7.47}$$

The instantaneous intensity i_R is pu_R and, *when calculated at long ranges*, it is simply the product of Equations 2.7.36 and 2.7.47. Therefore,

$$i_R = p\,u_R = \frac{p_0^2(ct - R)R_0^2}{\rho_A c R^2} \tag{2.7.48}$$

We have come full circle from our assumed solutions in section 2.1. Using our solutions to the wave equation, we have proved that, *in the far field of a point source*, as the range increases both the sound pressure and particle velocity decrease as $1/R$, and the intensity decreases as $1/R^2$.

Problems

Section 2.2

2.2.1 Use a sketch similar to Fig. 2.2.3 to derive the law of reflection for plane waves incident at a plane interface.

2.2.2 Use a sketch similar to Fig. 2.2.2 to derive Snell's Law of refraction for spherical waves from a point source.

Section 2.3

2.3.1 Drop a small object in a shallow pond, or a bathtub, to observe reflection of a circular wave from a small plane reflector, a small concave curved reflector, and a small convex reflector. Sketch what you observe and identify the reflected waves and diffracted waves.

2.3.2 Use your computer, or pencil and paper, to plot $p = P \sin \omega t$ over a range from $\omega t = -2\pi$ to $\omega t = +3\pi$. Do the same for $p = P \cos \omega t$. Compare with $p = P \cos(\omega t + \pi)$. Compare with $p = P \cos(\omega t + \pi/2)$.

2.3.3 Use your computer, or pencil and paper, to add $p = P \sin \omega t$ to $p = P \sin 2\omega t$. Now add $p = P \sin \omega t$ to $p = P \sin 3\omega t$. Comment on the effect of adding harmonics.

2.3.4 Use your computer, or pencil and paper, to add $p = P \sin \omega t$ to $p = P \sin(\omega t + \phi)$ and observe the changing wave form when ϕ takes on values that range from 0° to 180°.

2.3.5 Starting from Equation 2.3.7, derive an expression for the phase speed (the speed of constant phase surfaces) in terms of the wave parameters. Do the same for Equations 2.3.8, and 2.3.9.

Section 2.4

2.4.1 Verify Equations 2.4.25 through 2.4.28.

2.4.2 In section 6.6 we discuss the various sounds in the sea. Consider a 20 Hz sound of pressure amplitude P_0, which radiates omnidirectionally from a whale that is two meters below a smooth (perfectly reflecting) ocean surface. a) What is the total sound pressure as a function of angle at range 1000 m? b) What is it if the whale is 10 m deep? c) If 100 m deep?

2.4.3 Assume that the sound from a complex plane wave is normally incident at a smooth, hard, perfectly reflecting bottom. A hydrophone is fixed on a tripod

two meters above the bottom. The incident sound has equal pressure components of magnitude P at frequencies 1000 Hz, 2000 Hz, and 5000 Hz. What is the total (incident plus reflected) pressure at the hydrophone for each of these frequencies? Comment about the dependence of pressure measurements on the height of the hydrophone. What would be the effect if the bottom were only partially reflecting?

Section 2.5

2.5.1 The speed of sound in gases can be calculated from the equation for adiabatic propagation, $p\rho^{-\gamma} = \text{constant}$, where γ is the ratio of specific heats of the gas. a) Form $dp/d\rho$ and show that the speed of sound in gases is given by $c = (\gamma P_A/\rho_A)^{1/2}$. b) For air $\gamma = 1.4$, calculate the speed of sound in air at sea level, where $P_A = 10^5$ pascals and $\rho_A = 1.29\,\text{kg/m}^3$.

2.5.2 Equation 2.5.11 allows one to compare the particle velocities and acoustic pressures in two different media, such as air and water. The particle velocities at the air-water ocean surface interface are necessarily the same because the air is in contact with the water. a) Compare the pressures in air and water for the same particle velocities. Assume the constants $\rho_A = 1.29\,\text{kg/m}^3$, $c_A = 335\,\text{m/s}$; $\rho_w = 1000\,\text{kg/m}^3$, $c_w = 1500\,\text{m/s}$. b) From the previous answer, comment on the effectiveness of an air sound source when used in water, or an underwater sound source when used in air. Assume that the source transducer maintains a constant velocity at its face, regardless of the medium.

Section 2.6

2.6.1 Plot graphs of magnitude and phase of $\mathcal{R}_{12}$ and $\mathcal{T}_{12}$ versus θ_1 for plane wave propagation fom water to sediment. Use values $\rho_1 = 1000\,\text{kg/m}^3$, $c_1 = 1500\,\text{m/s}$; $\rho_2 = 1400\,\text{kg/m}^3$, $c_2 = 1480\,\text{m/s}$.

2.6.2 Plot graphs of magnitude and phase of $\mathcal{R}_{12}$ and $\mathcal{T}_{12}$ versus θ_1 for plane wave propagation from water to sediment. Use values $\rho_1 = 1000\,\text{kg/m}^3$, $c_1 = 1500\,\text{m/s}$; $\rho_2 = 2000\,\text{kg/m}^3$, $c_2 = 2000\,\text{m/s}$.

2.6.3 Plot graphs of magnitude and phase of $\mathcal{R}_{12}$ and $\mathcal{T}_{12}$ versus θ_1 for plane wave propagation fom water to air. Use values $\rho_1 = 1000\,\text{kg/m}^3$, $c_1 = 1500\,\text{m/s}$; $\rho_2 = 1.3\,\text{kg/m}^3$, $c_2 = 340\,\text{m/s}$.

2.6.4 Plot graphs of magnitude and phase of $\mathcal{R}_{12}$ and $\mathcal{T}_{12}$ versus θ_1 for plane wave propagation fom air to water. Use values $\rho_1 = 1.3\,\text{km/m}^2$, $c_1 = 340\,\text{m/s}$; $\rho_2 = 1000\,\text{kg/m}^3$, $c_2 = 1500\,\text{m/s}$.

2.6.5 Solve for the plane wave reflection and transmission coefficients for particle velocity rather than for pressure. a) Calculate these coefficients as a function of θ_1 for propagation from air to water. b) Calculate these coefficients as a function of θ_1 for propagation from water to air.

2.6.6 Solve for the plane wave reflection and transmission coefficients for sound intensity rather than for pressure.

2.6.7 Solve for the plane wave reflection and transmission coefficients for sound power rather than for pressure. Comment on the difference between the sound intensity coefficients and those for sound power.

Section 2.7

2.7.1 Wave equation 2.7.9 is in terms of the acoustic pressure. Rederive the wave equation. a) in terms of the acoustic density; b) in terms of the particle velocity in the x direction; c) in terms of the particle displacement in the x direction; d) in terms of the excess temperature for a wave propagating in a gas describable by $p_A = \rho_A R_G T_A$, where p_A is the ambient pressure, ρ_A is the ambient density, R_G is a gas constant, and T_A is the ambient temperature in degrees Kelvin.

Chapter 3 | Transmissions Along Ray Paths

3.1 Impulse and CW Propagation in Ocean Acoustics 72
3.1.1 Impulse Sources 72
3.1.2 Pressure, Particle Velocity, and Intensity in a Pulse 74
3.1.3 Pulse Energy Transmission 75
3.1.4 Radiated Power for Continuous Wave Signals 76
3.2 Ray Paths, Ray Tubes, and Path Times 77
3.2.1 Path Amplitude Factor and Path Time 77
3.2.2 Reflections along Ray Paths 78
3.2.3 Multiple Ray Paths 80
3.2.4 Conservation of Energy in Ray Tubes: Nonabsorbing, Nonscattering Iso-speed Medium 82
3.2.5 Sound Pressures in Ray Tubes: Homogeneous, Nonabsorbing, Nonscattering Medium 83
3.3 Ray Paths in a Lossless Refracting Medium 84
3.3.1 Sound Speed in the Ocean 84
3.3.2 Refraction at an Interface: The Ray Parameter 85
3.3.3 Rays through Constant-Speed Layers 86
3.3.4 Rays through Continuous Sound-Speed Changes 87
3.3.5 Examples of Ray Paths 89
3.3.6 Sound Intensity and Pressure in a Horizontally Stratified Ocean 92
3.3.7 Wave Fronts and Crossing Ray Paths: Phase Shifts at Caustics 94
3.3.8 Signal Transmissions in a Refracting Medium with Caustics 96
3.3.9 General Comments on Ray Path Methods 102
3.4 Attenuation 103
3.4.1 Exponential Attenuation of Plane Waves 103
3.4.2 Absorption Losses 104
3.4.3 Scattering Losses 110
3.4.4 Amplitude SONAR Equations 111
3.4.5 Sum of Multiple Arrivals: The Transmission Fraction 111
3.4.6 Logarithmic SONAR Equations: Transmission Loss (dB) 113
3.5 Tomography 116
3.5.1 Inverting for a Map of the Speed of Sound 116
3.5.2 Inverting for Ocean Motions 119
3.6 Doppler Frequency Shift 119
3.6.1 Doppler Theory 119
3.6.2 Doppler Measurements of Particle Motion 120
3.6.3 Sea-Surface Motion 122
3.6.4 Doppler Navigation 124

The concepts based on Huygens's principle, which we used in Chapter 2, have guided the broad field of mechanical wave propagation, diffraction, reflection, refraction and interference for three centuries. When differential wave equations were derived in the nineteenth century, they were, for the most part, used to understand the propagation of *harmonic* waves — that is, waves described in terms of frequency as parameter. Frequency was a natural parameter because of the human perception of musical sounds, in which there is a close connection between pitch, frequency, and the harmonic, sinusoidal components that determine the quality of a musical sound.

Isaac Newton's seventeenth-century concept of corpuscular energy moving along "rays" radiating from a source soon proved to be fruitful in the description of reflection by mirrors and refraction by lenses. Ray-path techniques are popular today not only in optics but also in underwater acoustics and seismology; their great virtue is that they provide insight into propagation in complex environments.

As shown in Fig. 1.2.1, the first effective use of an underwater impulse source (a bell) was the measurement of the speed of sound in 1827. By the 1930s, pulsed ocean sources, "sonars," had been introduced to determine distances, by measuring the time for reflections of the ping off the sea floor or from schools of fish. In those early days, some underwater acousticians still assumed that the sound paths could be described by straight line rays.

Modern ocean acoustics stands on the shoulders of research done in World War II, 1939–45. For example, during the war, Ewing and Worzel extended their experience in geophysics by using explosives as impulse sources and following ray paths (Fig. 1.2.3) to describe long-range propagation at sea (Ewing, Worzel, and Pekeris 1948). They discovered and exploited the deep sound SOFAR (SOund Fixing And Ranging) channel, where the sound from a few kilograms of explosive can be heard at very great ranges across the ocean. In 1960 they dropped 100 kg–depth charges off Perth, Australia, and found that the low-frequency sounds reached hydrophones half-way around the world, off the coast of Bermuda, 3.5 hours later.

Our development of ray methods emphasizes the use of impulse sources because the travel times of multiple arrivals provide information beyond the frequency description. We refer readers to additional analytical details in specialized books and papers. Books with good sections on ray-path methods, and with rich bibliographies, are Cerveny and Ravindra (1971), Cerveny, Molotkov, and Psencik (1977), Aki and Richards (1980), and Hubral and Krey (1980). The papers of Friedlander (1942, 1946), R. Chapman (1976, 1978), Stickler et al. (1981), and Foreman (1989) give valuable discussions of ray theory in acoustics.

Starting in this chapter, we become flexible in describing propagation in terms of frequencies or times, whichever is more suitable. As we shall see in Chapter 6, there is a duality in the two descriptions, and the two parameters are often advantageously interconverted.

3.1 Impulse and CW Propagation in Ocean Acoustics

3.1.1 IMPULSE SOURCES

Chemical explosions, airguns, and sparks are commonly used as short duration "impulse" sources for sound transmissions. The underwater implosion of a collapsing light bulb produces a simple impulse pressure. These sources are small compared with a wavelength, and they initially radiate sound omnidirectionally (see section 5.4). At the instant of the explosion, a pressure wave starts spreading from the source.

As shown in Fig. 3.1.1a, typically the sound pressure is very large at the instant of the explosion and then decays rapidly. Depending on the size of the explosive, the duration of the peak pressure pulse is usually a few milliseconds. For convenience, physicists and engineers sometimes replace the explosive exponential wave form by a simplified impulse source with time dependence given by the ideal *delta function* $\delta(t)$. (One could also appproximate the exponential form by several appropriately timed delta functions, of exponentially decreasing amplitudes, if desired.) A definition of the finite/discrete delta function that can be used in digital calculations is

$$\delta_f(t) = 1/\Delta t \quad \text{for} \quad 0 \leq t \leq \Delta t \tag{3.1.1}$$

and $\delta_f(t) = 0$ for all other t. Also,

$$\int_0^{\Delta t} \frac{dt}{\Delta t} = 1 \tag{3.1.2}$$

Since the integral over time is 1, $\delta_f(t)$ has the units of s^{-1}. Commonly Δt is one time step, the sampling interval. The delay of the impulse by time t_1 is shown in Fig. 3.1.1b. In the limit, one can let $\Delta t \to 0$ and still require that the integral be unity. This limiting form commonly appears in the literature. In its proper usage,

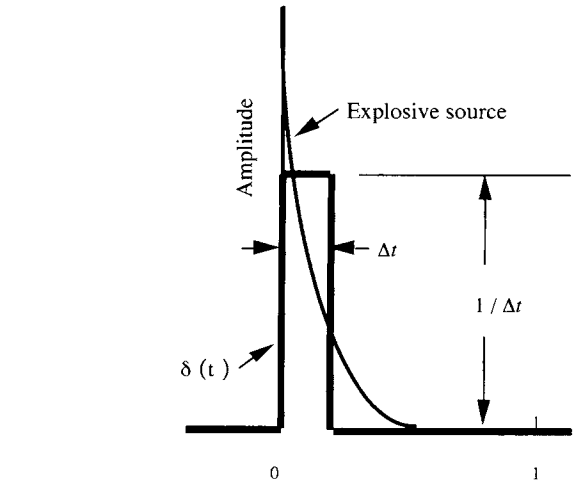

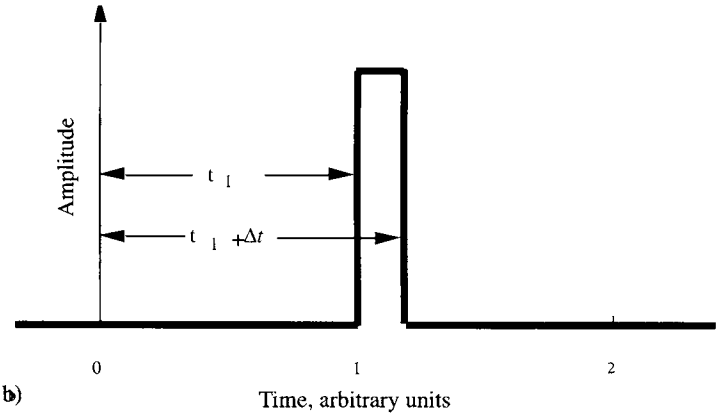

Figure 3.1.1 Impulse pressures. a) Explosive impulse represented by a single discrete delta function $\delta_f(t)$ of duration Δt and amplitude $1/\Delta t$. b) Delta function delayed by the time t_1.

the delta function is defined by an integration operation. An example follows for a function $g(t)$

$$\int_{-\infty}^{\infty} g(t)\,\delta(t - t_1)\,dt = g(t_1) \tag{3.1.3}$$

The delta function integration evaluates $g(t)$ at $t = t_1$. The concept was introduced by the physicist P. A. M. Dirac, and is known as the Dirac delta function.

3.1.2 *PRESSURE, PARTICLE VELOCITY, AND INTENSITY IN A PULSE*

From the discussion of energy conservation in sections 2.1 and 2.7.3, the *far-field* sound pressure, particle velocity, and instantaneous intensity for waves spreading spherically from a point source in a lossless, iso-speed medium are

$$p\ (t\ ) = p_0\ (t\ -R\ /c\ )\ \frac{R_0}{R} \tag{3.1.4}$$

$$u_R \approx \frac{p}{\rho c} = \frac{p_0(t\ -R\ /c\ )}{\rho c}\ \frac{R_0}{R} \tag{3.1.5}$$

$$i_R = p\,u_R = \frac{p_0^{\,2}(t\ -R\ /c\ )}{\rho c}\ \frac{R_0^{\,2}}{R^{\,2}} \tag{3.1.6}$$

where $p_0(t)$ is the source pressure at the range R_0, and $p(t)$ is the outward traveling pressure wave. Although there is a time delay and amplitude change, the waveforms of $p_0(t)$ and $p(t)$ are the same.

A suitable transient signal $p_0(t)$ satisfies two conditions:

$$p_0(t) = 0 \text{ (for } t<0) \tag{3.1.7a}$$

and

$$\int_0^\infty |p_0(t)|dt \quad \text{is finite} \quad (\text{for } t \geq R/c) \tag{3.1.7b}$$

For example, assume for simplicity that the far-field pressure after an explosion (actual details are in section 5.4) is approximated by the exponential decay

$$p(t) = \frac{p_0 R_0}{R} \exp\left[-\frac{1}{\tau_s}\left(t - \frac{R}{c}\right)\right] \tag{3.1.8}$$

where τ_s is the time for the pressure to decay to e^{-1} of its peak value p_0 at 1 m. For $t \geq R/c$,

$$\begin{aligned}\int_{\frac{R}{c}}^{\frac{R}{c}+t_g} \frac{p_0 R_0}{R} \exp\left[-\frac{1}{\tau_s}\left(t - \frac{R}{c}\right)\right] dt \\ = \frac{\tau_s p_0 R_0}{R}\left[1 - \exp\left(\frac{t_g}{\tau_s}\right)\right]\end{aligned} \tag{3.1.9}$$

where t_g is the duration of the integral after the arrival of the pressure signal or the "gate time" for acceptance into the integration operation. As the gate time t_g goes to infinity, the integral tends to $\tau_s p_0 R_0/R$. The integral is within 98 percent of the limit for $t_g > 4\tau_s$.

3.1.3 PULSE ENERGY TRANSMISSION

In the far field, the radial component of particle velocity (units, m/s; Equation 2.7.47) and the instantaneous radial intensity (units, watts/m^2; Equation 2.7.48) are, respectively,

$$u_R = p/(\rho_A c) \quad \text{and} \quad i_R = p u_R \tag{3.1.10}$$

For acoustic propagation, or communication, in a lossless medium, one can define the "message" energy, ΔE_m (units, joules), which passes through an element of surface ΔS at range R in time t_g

$$\Delta E_m = \Delta S \int_{\frac{R}{c}}^{\frac{R}{c}+t_g} p u_R \, dt \approx \frac{R_0^2 \Delta S}{\rho_A c} \int_{\frac{R}{c}}^{\frac{R}{c}+t_g} \frac{[p_0(t - R/c)]^2}{R^2} dt \tag{3.1.11a}$$

where the integration limits are over the effective duration of the transient pressure, t_g.

The element of surface area can be expressed as

$$\Delta S = R^2 \Delta\Omega \tag{3.1.11b}$$

where $\Delta\Omega$ is an element of solid angle.

All energy flows outward through the spherical surface and along R. The radiation from a directional source can be expressed in terms of the solid angle subtended by ΔS. The solid angle viewed from the center of a sphere is 4π. Assuming the source radiation is spherically symmetric, the integral over 4π of solid angle, which gives the total energy, E_m, in the "message," is simply Equation 3.1.11a with $\Delta S = 4\pi R^2$. (Sometimes we drop the subscript m for a general statement of radiated energy and call it simply E.)

Therefore, for isotropic radiation,

$$E_m \approx \frac{4\pi R_0^2}{\rho_A c} \int_{\frac{R}{c}}^{\frac{R}{c}+t_g} [p_0(t - R/c)]^2 \, dt \tag{3.1.12}$$

The total energy transmitted by the source (units, joules, or watt sec) may also be written

$$E_m \approx \frac{4\pi R_0^2}{\rho_A c}[tips] \tag{3.1.13}$$

where $[tips]$, *the time integral of the pressure squared* (units, pascal^2 sec), is

$$[\,tips\,] \equiv \int_{\frac{R}{c}}^{\frac{R}{c}+t_g} [\,p_0(t - R/c)]^2\,dt \tag{3.1.14}$$

The *energy per unit area* (units, joules/m^2), measured at range R, transmitted during the time interval t_g is

$$\varepsilon_R \equiv \int_{\frac{R}{c}}^{\frac{R}{c}+t_g} p\,u_R\,dt \approx \frac{[\,tips]}{R^2}\frac{R_0^2}{\rho_A c} \tag{3.1.15}$$

Equations 3.1.13 and 3.1.15 are energy equations for spherically divergent transmission in an ideal, lossless, homogeneous medium. They give the total sound energy, and the sound energy per unit area, respectively, of a single transient arrival that has the travel time R/c. They are forms of what has been called the *sonar energy equation.*

3.1.4 RADIATED POWER FOR CONTINUOUS WAVE SIGNALS

Assume a point source transmits the continuous wave sinusoid of peak value P_0, written in exponential form as $P_0 e^{i2\pi ft}$. The source power is the average energy transmitted per unit time over the period T of the sinusoidal wave. If there is no loss by scatter or absorption, the total power (units, watts) over all angles at a large range is the same as at the source:

$$\Pi \approx \frac{4\pi R_0^2}{\rho_A c}\frac{P_0^2}{2} \tag{3.1.16a}$$

where

$$P_0^2/2 = \frac{1}{T}\int_0^T |P_0 \sin(2\pi ft)|^2\,dt \tag{3.1.16b}$$

Sometimes $(P_0^2)/2$ is written P_{rms}^2 for a sinusoidal wave.

In addition to sinusoidal source transmissions, Equations 3.1.16a and b are used when *average* power defines the transmitter-transducer output. In that case, the time T is the duration of the transmission.

3.2 Ray Paths, Ray Tubes, and Path Times

The solution of the spherical wave equation in section 2.7 and Equation 2.7.36 is the start of our discussion of ray paths. That solution, using the separation of variables, is the product of a spatial function and a temporal function. We cast our discussion of ray paths in that context. First, the exact solution is taken apart, and each term is identified as either space- or time-dependent.

3.2.1 PATH AMPLITUDE FACTOR AND PATH TIME

In a homogeneous, isotropic, lossless medium, the exact spherical wave solution for the acoustic pressure at R is

$$p\ (t\ ) = p_0(t - R/c\ )\ \frac{R_0}{R} \tag{3.2.1}$$

The sound input to the medium is the temporal function $p_0(t)$. The travel time for the message to arrive, R/c, and the dimensionless ratio, R_0/R, are components of the spatial function. The output temporal function at the receiver is $p(t)$.

To generalize, we identify all spatial components that depend on the *Pressure And Time History* as the function [*path*]. The sound output is

$$p(t) = p_0(t)\ [path] \tag{3.2.2}$$

The [*path*] function has two components, the dimensionless [*path amplitude factor*] or [*paf*], which gives the relative pressure amplitude, and t_{path}, which is the time delay owing to the travel time of the original $p_0(t)$ (Fig. 3.2.1).

The received sound pressure $p(t)$ can be written

$$p(t) = [paf\,]p_0(t - t_{path}) \tag{3.2.3}$$

where, for a point source in a lossless, homogeneous medium, we have

$$[paf\,] = R_0/R \quad \text{and} \quad t_{path} = R/c \tag{3.2.4}$$

For linear acoustics, the factor [*paf*] is independent of the amplitude of the source sound pressures and the source waveform.

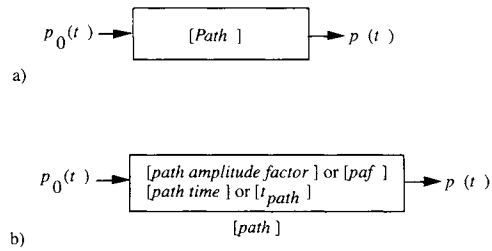

Figure 3.2.1 Temporal input and output functions and the [path] and [*paf*] functions.

3.2.2 REFLECTIONS ALONG RAY PATHS

Ray paths that include reflections are simple examples of the application of the path amplitude factors. The Hugyens construction of a reflected wave was shown in Fig. 2.2.2. In ray-path constructions, the reflected waves appear to come from an "image" source behind the interface, as shown in Fig. 3.2.2a.

We assume that there is a point source, that the medium is homogeneous and lossless, and that the interfaces are smooth. We make the approximation that the ray is reflected locally as if it were a plane wave. Then the plane-wave reflection coefficient is computed for the local angle of incidence using Equation 2.6.11a for simple reflections and Equations 2.6.14 through 2.6.17 for reflections beyond the critical angle. Figure 3.2.2 shows the ray path for a reflection at the bottom and one at the top interface.

The pressure signal for the bottom reflected path, shown in Fig. 3.2.2, is

$$p\ (t\ ) = p_0(t - \frac{R_a + R_b}{c})\ \frac{R_0}{R_a + R_b}\ \mathcal{R}_{12} \tag{3.2.5}$$

or

$$p(t) = p_0(t - t_{path})[paf]\mathcal{R}_{12} \tag{3.2.6}$$

where the path amplitude factor and time delay are

$$[paf] = R_0/(R_a + R_b) \tag{3.2.7}$$

and

$$t_{path} = (R_a + R_b)/c \tag{3.2.8}$$

and $\mathcal{R}_{12}$ is the pressure reflection coefficient at the water/bottom, 1, 2, interface.

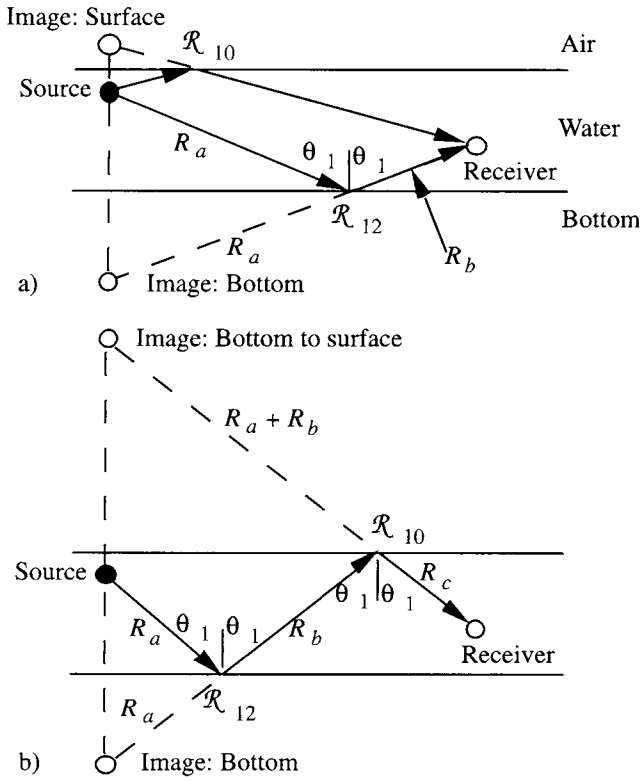

Figure 3.2.2 Image constructions of a) a singly reflected ray, and b) a doubly reflected ray path. The segments of the ray paths are labeled R_a, R_b, and R_c. The direct ray path from the source to the receiver is not shown. It is assumed that the sound speed is the same at all points of the water medium.

It is convenient, at this point, to keep the reflection coefficient out of the amplitude path factor. The pressure signal for the bottom and surface reflected ray path, shown in Fig. 3.2.2, is

$$p(t) = p_0\left(t - \frac{R_a + R_b + R_c}{c}\right) \frac{R_0}{R_a + R_b + R_c} \mathcal{R}_{12}\mathcal{R}_{10} \tag{3.2.9}$$

or

$$p(t) = p_0(t - t_{path})[paf]\mathcal{R}_{12}\mathcal{R}_{10} \tag{3.2.10}$$

The path amplitude factor and time delay are

$$[paf\ ] = R_0/(R_a + R_b + R_c) \tag{3.2.11}$$

and

$$t_{path} = (R_a + R_b + R_c)\ /c \tag{3.2.12}$$

and $\mathcal{R}_{10}$ is the pressure reflection coefficient at the water-air interface.

General methods of constructing [*path*] functions follow from these simple examples.

3.2.3 MULTIPLE RAY PATHS

Transmissions from a source can travel by many paths, and each path has its path amplitude factor [*paf*] and time delay t_{path}. It is very important to recognize that, in acoustic propagation, the signal pressure amplitudes for each path add linearly and may therefore interfere at the receiver. Sketches of four paths are shown in Fig. 3.2.3a. The sound speed is the same at all points in the water.

Ray path R_1 is direct. The other ray paths have reflections at the surface and bottom. Figure 3.2.3b gives a diagram of the individual [*path*] functions and reflection coefficients. Examples of the meaning of [*path*] are shown in Fig. 3.2.3.c. Consider the top trace for a delta function source. Time 0 is the beginning of the transmission. The first arrival [*paf* (1)] is a vertical (delta function) line (1) at the transmission time R_1/c. The height of the vertical line is proportional to R_0/R_1. The second arrival [*paf* (2)] is the negative (owing to surface reflection) vertical line (2) at the transmission time R_2/c. The height of that vertical line is proportional to $(R_0/R_2)\mathcal{R}_{10}$. Similar discussions apply to [*paf* (3)] and [*paf* (4)].

A model source transmission, such as from an explosive, is the exponentially decaying $p_0(t)$ in the middle trace of Fig. 3.2.3c. The bottom trace $p(t)$ is constructed by delaying $p_0(t)$ by the travel time R_1/c and multiplying $p_0(t)$ by the amplitude factor [*paf* (1)]. Similarly, arrival 2 has the time delay R_2/c and a magnitude determined by multiplying $p_0(t)$ by the amplitude factor [*paf* (2)] and $\mathcal{R}_{10}$. Since arrivals 1 and 2 overlap, the signal pressure is the algebraic sum of the pressures. Arrivals 3 and 4 are calculated similarly.

Figure 3.2.3 is an example of sound transmissions to ranges of about three water depths. In perhaps 20 m water depth, straight ray paths are good approximations to the actual ray paths. We will return to multiple arrivals in section 3.3.8, when we model a transmission experiment in the Mediterranean Sea.

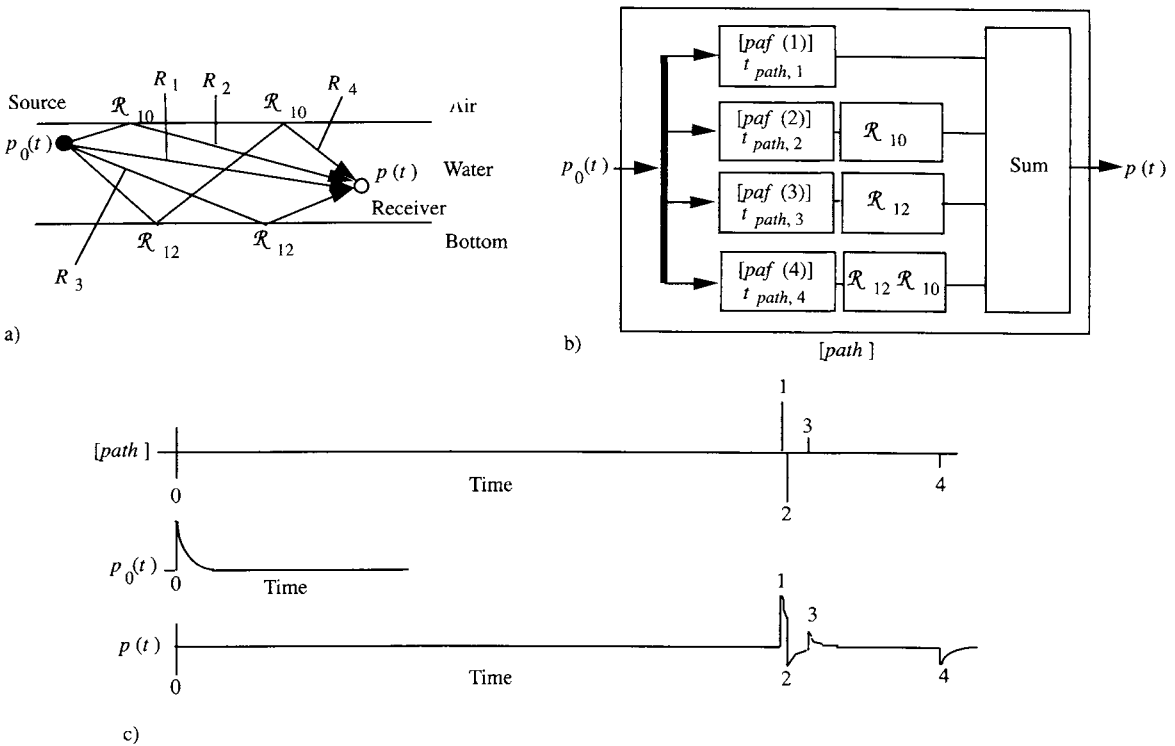

Figure 3.2.3 Four ray paths, path amplitude factors, and a simulation of a transmission from an explosion. a) The ray paths are labeled R_1, R_2, R_3, and R_4. b) The path amplitude factors and time delays for each path are in the four boxes labeled [*path*]. The reflection coefficients are shown explicitly for the appropriate paths. c) The delta function [*path*] is the top trace. The middle trace is the source signal $p_0(t)$. The bottom trace is the pressure signal at the receiver $p(t)$. The reflection coefficients were assumed to be $\mathcal{R}_{12} = 0.3$ and $\mathcal{R}_{10} = -1$, for all angles of incidence.

3.2.4 *CONSERVATION OF ENERGY IN RAY TUBES: NONABSORBING, NONSCATTERING, ISO-SPEED MEDIUM*

Ray tube concepts will be used later in more complicated examples of sound transmission and computations of sound pressures. Ray tubes are constructed by drawing all of the rays from a source to an area of the wavefront; the rays form the surface of the ray tube Fig. 3.2.4. For a constant speed (iso-velocity) medium, the rays are straight lines, the solid angle $\Delta\Omega$ is constant, and the areas of the ends of the ray tube are

$$S_1 = (\Delta\Omega)R_1^2 \tag{3.2.13a}$$

and

$$S_2 = (\Delta\Omega)R_2^2 \tag{3.2.13b}$$

Since ideal rays are normal to wavefronts, no energy passes through the sides of the ray tube. Thus, if there is no sound absorption or scattering, the energy passing through the area S_1 equals the energy passing through S_2.

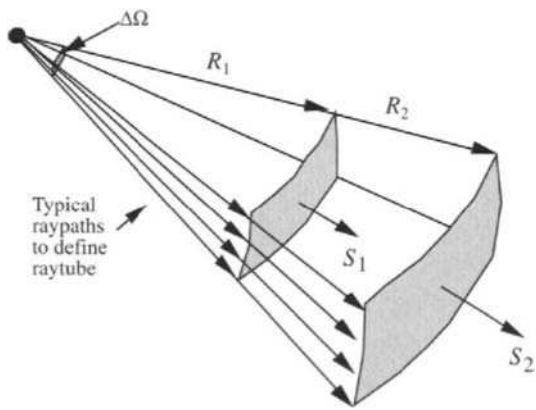

Figure 3.2.4 Ray-tube construction for a homogeneous, nonabsorbing, nonscattering, iso-speed medium. Only a few of the rays that bound the outside surface of the tube are shown for clarity. The vectors representing the surface areas, S_1 and S_2 are along the particular ray path through the center of the tube and at ranges R_1 and R_2.

Now consider the inhomogeneous, lossless (nonabsorbing, nonscattering) medium, in which c and ρ_A depend on position. Put the energy (Equation 3.1.11a) in terms of the local pressures p_1 and p_2, and replace ΔS by S_1 or S_2. The equality of the energy entering and leaving the section of the ray tube gives

$$\frac{S_1}{\rho_{A1}c_1}\int_{\frac{R_1}{c_1}}^{\frac{R_1}{c_1}+t_g}[p_1(t-R_1/c_1)]^2\,dt = \frac{S_2}{\rho_{A2}c_2}\int_{\frac{R_2}{c_2}}^{\frac{R_2}{c_2}+t_g}[p_2(t-R_2/c_2)]^2\,dt \tag{3.2.14}$$

where the subscripts on ρ_{A1}, c_1, ρ_{A2}, and c_2 indicate the local ambient densities and sound speeds. Using the time integral pressure squared notation, conservation of energy within a ray tube is

$$\frac{S_1}{\rho_{A1}c_1}[\,tips_1\,] = \frac{S_2}{\rho_{A2}c_2}[\,tips_2\,] \tag{3.2.15}$$

In a homogeneous medium, the ρ_A and c parameters are constant, and they cancel out, leaving

$$S_1[\,tips_1\,] = S_2[\,tips_2\,] \tag{3.2.16}$$

3.2.5 *SOUND PRESSURES IN RAY TUBES: HOMOGENEOUS, NONABSORBING, NONSCATTERING MEDIUM*

The sound pressures at the surfaces S_1 and S_2 follow the $1/R$ rule of Equation 3.2.1, and of Equation 3.2.5 in a homogeneous, nonscattering, nonabsorbing medium. In such *homogeneous* media, $\rho_{A2}c_1 = \rho_{A2}c_2$, the integral (Equation 3.2.14) is an accurate approximation of the energy propagation, and the wavefronts are nearly spherical. These expressions are the starting place for calculations of the sound pressure in a ray tube. The changes of variable

$$\tau_1 = t - R_1/c \quad \text{and} \quad \tau_2 = t - R_2/c \tag{3.2.17}$$

in the integral (Equation 3.2.14) gives

$$S_1\int_0^{t_g}[p_1(\tau_1)]^2\,d\tau = S_2\int_0^{t_g}[p_2(\tau_2)]^2\,d\tau \tag{3.2.18}$$

The limits of integration t_g can be chosen so that $p_1(\tau_1)$ and $p_2(\tau_2)$ are essentially zero for $\tau > t_g$. Rearrangement of Equation 3.2.18 gives

$$\int_0^{t_g} \{S_1[p_1(\tau_1)]^2 - S_2[p_2(\tau_2)]^2\} d\tau = 0 \tag{3.2.19}$$

When $p_1(\tau_1)$ and $p_2(\tau_2)$ are proportional, one can set the contents of the bracket $\{\ldots\}$ to zero and write

$$p_2(\tau_2) = \pm p_1(\tau_1) \sqrt{\frac{S_1}{S_2}} \tag{3.2.20}$$

The + sign is chosen for the tube sketched in Fig. 3.2.2 because the areas are simple projections on an expanding wavefront.

3.3 Ray Paths in a Lossless, Refracting Medium

Profiles of the sound speed versus depth in oceans, lakes, and rivers are often complicated. Pickard and Emery (1982) give elementary descriptions of the physical structure of oceans and ocean currents, as well as temperature, salinity, and depth, which are the critical parameters of the sound speed. Since water tends to stratify with the density, which increases with depth, the regions of constant salinity and constant temperature and the corresponding sound speed profiles are nearly horizontal in local regions. Currents disrupt horizontal stratifications and cause boundaries, or fronts, between different types of water. Oceanic fronts, such as the boundaries of the Gulf Stream, have very complicated structures.

3.3.1 SOUND SPEED IN THE OCEAN

The sound speed in water does not depend on the direction of the ray. Therefore, the names "sound speed" and "sound velocity" can be used interchangeably. In-situ instruments called *sound velocimeters* operate by timing a megahertz pulse in a small "sing-around" water circuit in the instrument; speed accuracies of 0.1 m/s are claimed (but see Chapter 8, where we find that bubbles can cause deviations of several meters per second).

When the sound speed is to be determined from temperature, salinity, and depth, the best values are obtained by using the empirical formulation of Del Grosso (1974). But that formula has 19 terms, 18 of which have coefficients with 12 significant figures each. The following simplified formula (Medwin 1975) has

less than 0.2 m/s error compared with Del Grosso for $0 < T°C < 32$ and $22 <$ Salinity ppt < 45 for depths under 1000 m:

$$c = 1449.2 + 4.6T - 0.055T^2 + 0.00029T^3 + (1.34 - 0.01T)(S - 35) + 0.016z \tag{3.3.1}$$

where c = sound speed (m/s); T = temperature (°C); S = salinity (‰; i.e., parts per thousand); and z = depth (m).

Mackenzie (1981) gives a longer formula, which claims a standard error of 0.07 m/s and is not restricted to depths less than 1000 m:

$$\begin{aligned} c = {} & 1448.96 + 4.591T - 5.304 \times 10^{-2}T^2 + 2.374 \times 10^{-4}T^3 \\ & + 1.340(S - 35) + 1.630 \times 10^{-2}z + 1.675 \times 10^{-7}z^2 \\ & - 1.025 \times 10^{-2}T(S - 35) - 7.139 \times 10^{-13}Tz^3 \end{aligned} \tag{3.3.2}$$

3.3.2 *REFRACTION AT AN INTERFACE: THE RAY PARAMETER*

Ray paths obey Snell's Law as the waves propagate in water (Fig. 3.3.1):

$$\frac{\sin\theta_0}{c_0} = \frac{\sin\theta_1}{c_1} = \frac{\sin\theta_z}{c_z} = a = \text{constant} \tag{3.3.3}$$

where c_0 is the initial sound speed, θ_0 is the initial incident angle with the vertical, and θ_1 is the refracted angle. The constant a is known as the *ray parameter*. Suppose we start a ray at a depth z_0 and sound speed c_0. By Snell's Law, the incident angle is θ_z at a depth z, where the sound speed is c_z.

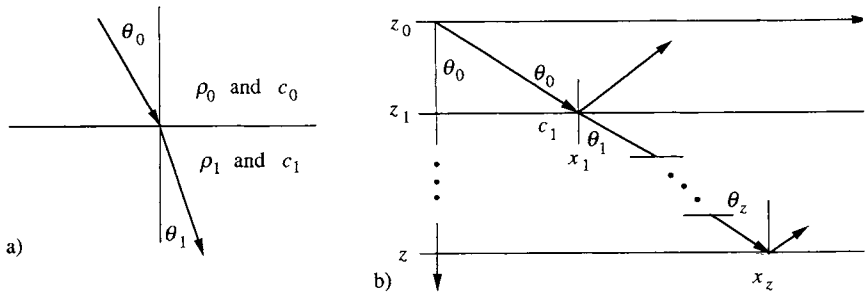

Figure 3.3.1 Snell's Law and ray trace in a multilayered medium. a) Refraction at an interface. b) Refraction in a multilayered medium. The incident, reflected, and transmitted rays are shown.

3.3.3 RAYS THROUGH CONSTANT-SPEED LAYERS

In Chapter 2 we considered reflection and transmission at distinct layers. Here we follow the transmitted ray as it progresses through a continuous medium that is, *for convenience of calculation*, split into several constant speed layers. Since the sound speed in each layer is constant, the ray path within each layer is a straight line. Ray trace calculations use Snell's Law at the interfaces between layers to follow rays through a medium. The calculations are usually done on a computer, because the same algorithm is applied repeatedly.

Let the ray leave the source at an angle θ_0 with the normal. Then the ray parameter is

$$a = \sin\theta_0 / c_0 \tag{3.3.4}$$

At the $(n+1)th$ interface, $\sin\theta_n$ is,

$$\sin\theta_n = a\, c_n \tag{3.3.5}$$

and the other trigonometric functions are

$$\cos\theta_n = \sqrt{1-(ac_n)^2} \quad \text{for} \quad ac_n < 1 \tag{3.3.6}$$

and

$$\tan\theta_n = \frac{a\, c_n}{\sqrt{1-(a\, c_n)^2}} \tag{3.3.7}$$

The ray parameter a is convenient because $\sin\theta_0/c_0$ is computed once, and the rest of the functions are computed using a in Equations 3.3.5 through 3.3.7. Refering to Fig. 3.3.1, we write an expression for computing the horizontal range of the ray trace to its intersection at the Nth interface

$$x_N = \sum_{n=0}^{N-1} (z_{n+1} - z_n) \tan\theta_n \tag{3.3.8}$$

The travel time for the ray to travel to the Nth interface is

$$t_N = \sum_{n=0}^{N-1} \frac{(z_{n+1} - z_n)}{c_n \cos\theta_n} \tag{3.3.9}$$

For ranges less than a few hundred meters, and near vertical angles of incidence, the ray paths are nearly straight lines. We can use the constant sound-speed approximation in most sonar applications where the ranges are less than a few hundred meters.

3.3.4 RAYS THROUGH CONTINUOUS SOUND-SPEED CHANGES

Assume the sound speed profile, $c(z)$, is a continuous function of depth. Along a ray, the differential distance ds and time dt are

$$ds = dz/\cos\theta \quad \text{and} \quad dt = ds/c(z) = dz/[c(z)\cos\theta] \tag{3.3.10}$$

Let the ray be in the x-z plane and measure the horizontal range as distance r. The differential displacement dr is

$$dr = dz\tan\theta \tag{3.3.11}$$

where, using the ray parameter a in Snell's Law, the trigonometric functions are given by Equations 3.3.3 through 3.3.5 and where c_n becomes $c(z)$. The summations become the integrals

$$t_f - t_i = \int_{z_i}^{z_f} dt = \int_{z_i}^{z_f} dz \frac{1}{c(z)\sqrt{1 - a^2 c^2(z)}} \tag{3.3.12}$$

and

$$r_f - r_i = \int_{z_i}^{z_f} dr = \int_{z_i}^{z_f} dz \frac{ac(z)}{\sqrt{1 - a^2 c^2(z)}} \tag{3.3.13}$$

With ingenuity, these integrals can be evaluated in closed form for several sound-speed profiles. See the construction in Fig. 3.3.2.

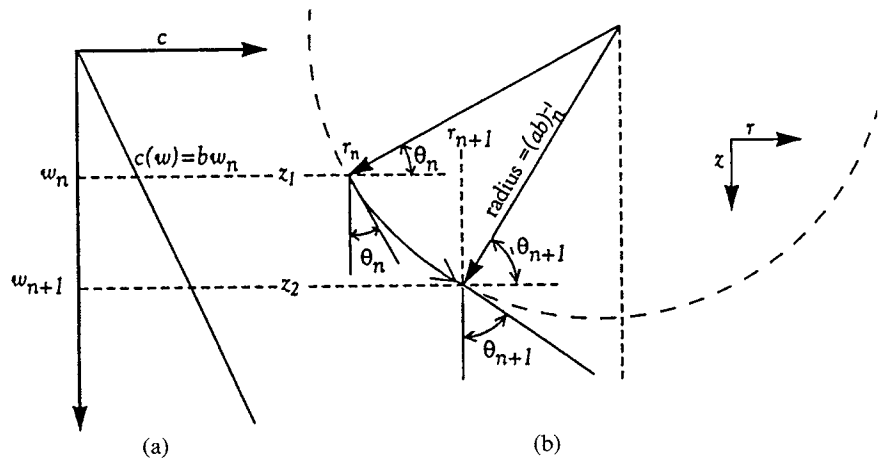

Figure 3.3.2 a) Sound-speed profile in w coordinates. b) Circular ray path for linear dependence of speed on depth between z_n and z_{n+1}. Radius is $(ab_n)^{-1} = w_n/(\sin\theta_n)$, where b_n is the speed in the nth layer.

The sound speed in the nth layer is given by

$$c(z) = c(z_n) + b_n(z - z_n) \quad \text{for} \quad z_n \le z \le z_{n+1} \tag{3.3.14}$$

where the sound speed gradient, with units $[(\text{m/s})/\text{m}] = [\text{s}^{-1}]$, is

$$b_n = \frac{c(z_{n+1}) - c(z_n)}{z_{n+1} - z_n} \tag{3.3.15}$$

The interfaces are at z_n and z_{n+1}. A change of variables from z to w facilitates the integration

$$w_n = z - z_n + \frac{c(z_n)}{b_n} \tag{3.3.16}$$

where

$$dw = dz \quad \text{and} \quad c(w) = b_n w \tag{3.3.17}$$

For downgoing rays (the positive z and w direction), the integrals (Equations 3.3.12 and 3.3.13) are

$$t_{n+1} - t_n = \int_{w_n}^{w_{n+1}} \frac{dw}{b_n w (1 - a^2 b_n^2 w^2)^{1/2}} \tag{3.3.18}$$

$$r_{n+1} - r_n = \int_{w_n}^{w_{n+1}} \frac{a b_n w \, dw}{(1 - a^2 b_n^2 w^2)^{1/2}} \tag{3.3.19}$$

The integrations are in integral tables, which give

$$t_{n+1} - t_n = \left| \frac{1}{b_n} \right| \ln \frac{w_{n+1}[1 + (1 - a^2 b_n^2 w_n^2)^{1/2}]}{w_n[1 + (1 - a^2 b_n^2 w_{n+1}^2)^{1/2}]} \tag{3.3.20}$$

and

$$r_{n+1} - r_n = \left| \frac{1}{a b_n} \right| [(1 - a^2 b_n^2 w_n^2)^{1/2} - (1 - a^2 b_n^2 w_{n+1}^2)^{1/2}] \tag{3.3.21}$$

The travel time and range through a set of layers are

$$t = \sum_{n=0}^{N-1} t_{n+1} - t_n \quad \text{and} \quad r = \sum_{n=0}^{N-1} r_{n+1} - r_n \tag{3.3.22}$$

The ray-path Equations (3.3.20 through 3.3.22) are coded as subroutines in ray-path programs.

If the sound speed increases such that the ray becomes horizontal, and then turns, the turning depth w_t is given by

$$1 - a^2 b_n^2 w_t^2 = 0 \tag{3.3.23}$$

The ray turns and travels upward. If $c(z)$ is not a function of range, the upward trace is the reversal of the downward ray trace.

3.3.5 EXAMPLES OF RAY PATHS

The path of a ray is associated with the sound speed structure of the ocean and the initial conditions at the source. In a horizontally stratified ocean, the sound speed $c(z)$ is the same everywhere at depth z, and this simplification is used in all of our examples. Actual sound speed profiles are time- and space-dependent. Except near ocean currents and fronts, the sound-speed structure is nearly constant for many ocean depths away from the surface. We have chosen typical examples of ocean stratifications to illustrate the range of possibilities and to introduce the nomenclature of ray paths.

Arctic Ocean

The temperature of the water under the sea ice is nearly constant (Pickard and Emery 1982, p. 177). Although below 200 m to 4000 m the temperature ranges from +0.5 to −1.0 °C and the salinity is about 35‰, for a simple example, we choose $T = 0$ and salinity = 35‰ (parts per thousand). Then, from the sound-speed Equation (3.3.2), the sound speed is approximately

$$c(z) \approx 1449 + 1.630 \times 10^{-2} z + 1.675 \times 10^{-7} z^2 \text{ (m/s)} \tag{3.3.24}$$

Since the gradient of the sound speed is constant in our example, one can use the integrated Equations (3.3.20 and 3.3.21) to compute travel times and range for a ray having the incident starting angle θ_0. A set of ray paths for this profile is shown in Fig. 3.3.3.

Each ray becomes horizontal and turns at its *turning depth* w_t, given by Equation 3.3.23. The ray that just grazes the bottom is a limiting ray path. The *shadow zone* is just beyond this ray path, and no direct path can get there. The penetration of sound energy into the shadow region is attenuated exponentially. The steeper paths are reflected at the bottom as shown in Fig. 3.3.4. The reflection paths that can get into the shadow region have at least two bottom reflections. As angles of incidence tend to normal, ray paths tend to straight lines.

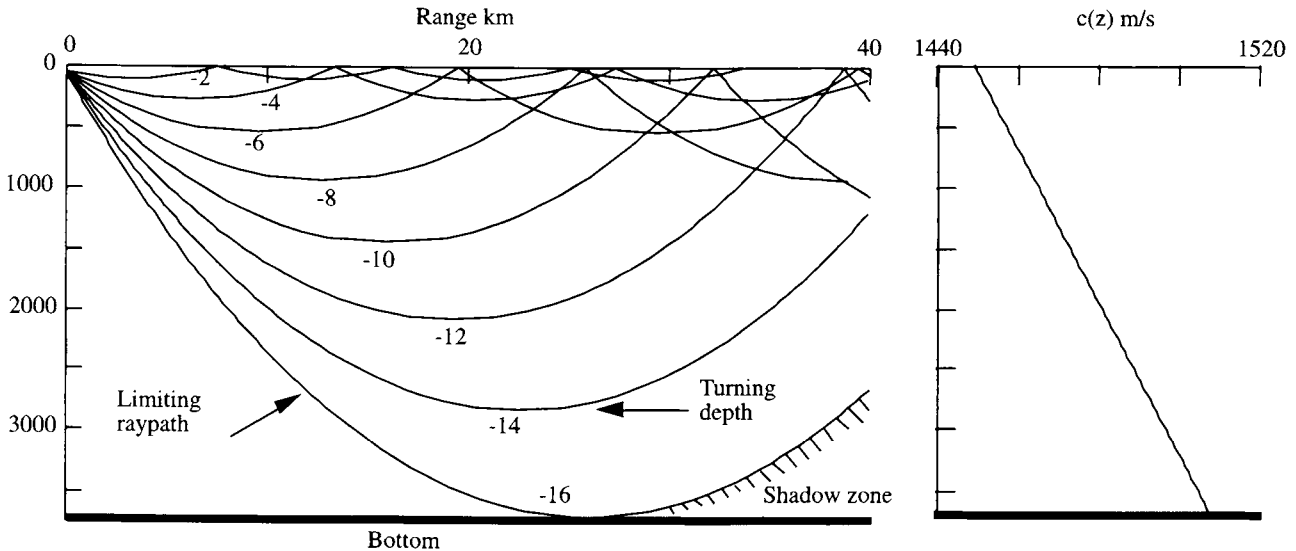

Figure 3.3.3 Refracted and surface-reflected ray paths in an Arctic water structure; sound-speed profile at right. The sound speed increases linearly with depth. Following a common convention for nearly horizontal ray paths, the rays are identified by the initial grazing angle (degrees) with the horizontal, where *grazing angle* $= \theta - 90°$. Each of the rays has a turning depth where the tangent to the ray path is horizontal. Steeper ray paths (omitted here, for simplicity) will reflect from the bottom as shown in Fig. 3.3.4.

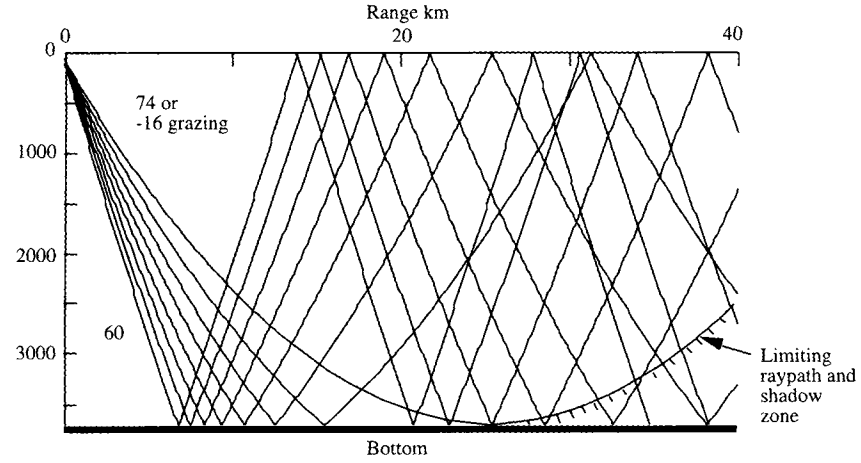

Figure 3.3.4 Reflected ray paths in an Arctic water structure of the profile shown in Fig. 3.3.3. The limiting ray path has an angle of incidence of 74° (16° grazing angle). Angle increments are 2°. These steeper angles are reflected at the bottom and at the surface. The rays at nearer grazing are shown in Fig. 3.3.3.

North Atlantic Profile

The North Atlantic Profile is from the seminal research of Ewing and Worzel (1948). The sound-speed profile has a minimum sound speed, which creates a *sound channel axis* at 1200 m depth. The sound speed is 1524 m/s at the surface and 1527 m/s at 4800 m. As shown in Fig. 3.3.5, the ray paths pass through the axis of the sound channel (dashed line). For illustration, the steepest rays are

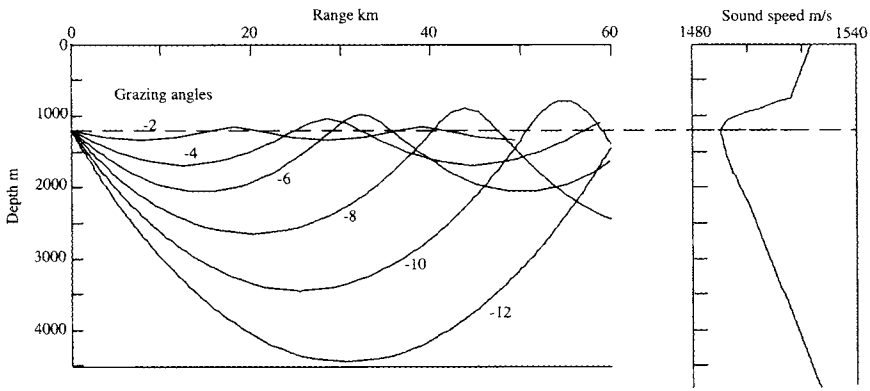

Figure 3.3.5 Ray traces for a source on the sound channel axis (dashed line at 1200 m depth) with a North Atlantic sound-speed profile. Grazing angles given at 2° increments.

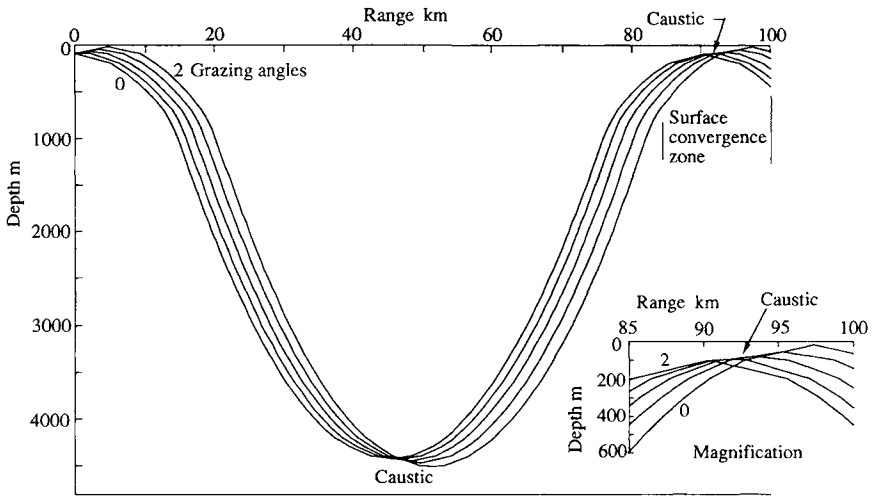

Figure 3.3.6 Convergence-zone ray paths for a source at 50 m. The sound-speed profile is given in Fig. 3.3.5.

$\pm 11°$ grazing angle. If the ray paths do not reflect from the surface or bottom, and are not blocked by features on the ocean floor, sound channel transmissions are very efficient for long-range (thousands of kilometers) communications in the ocean. It is likely that some whales use these paths for communications.

A sound source near the surface excites a different type of phenomenon. Figure 3.3.6 shows a few rays from a shallow source. The ray paths go deep, turn, and return to the surface. At about 90 km range, the ray paths appear to converge in a region named the *convergence zone*. A magnification of the convergence zone is shown in the inset. Because many ray paths converge, the acoustic pressure is large in a convergence zone and smaller elsewhere.

3.3.6 SOUND INTENSITY AND PRESSURE IN A HORIZONTALLY STRATIFIED OCEAN

An example of sound transmission in a stratified ocean is sketched in Fig. 3.3.7. As shown in the inset, the local region around the source is assumed to be homogeneous so that the initial radiation is spherical. As the energy propagates away from the source, the energy trapped in a ray tube follows Snell's Law. The rays that define a ray tube must be very close together over the entire path.

In spherical coordinates, the area of a tube near the source is

$$\Delta S_0 = R_0^2 \sin\theta_0 \, \Delta\theta_0 \, \Delta\phi_0 \tag{3.3.25}$$

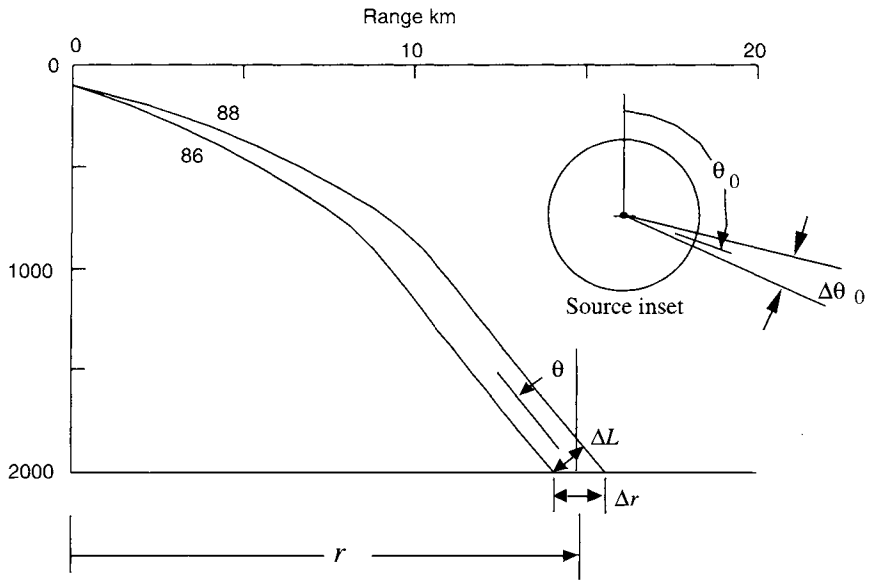

Figure 3.3.7 Construction for conservation of energy in a ray tube showing the separation of the rays ΔL.

To get the area ΔS of the tube (see Fig. 3.3.7) at the horizontal range r and depth h, compute θ, Δr and ΔL and form

$$\Delta S = r \Delta\phi \Delta L \tag{3.3.26}$$

where

$$\Delta L = \Delta r \cos\theta \tag{3.3.27}$$

Conservation of the message energy in the transmission gives

$$\varepsilon_0 \Delta S_0 = \varepsilon_R \Delta S \tag{3.3.28}$$

and

$$\frac{[tips]_0}{\rho_0 c_0} R_0^2 \sin\theta_0 \Delta\theta_0 \Delta\phi_0 = \frac{[tips]}{\rho c} r \Delta\phi \Delta L \tag{3.3.29}$$

where $[tips]$ represents the *time integral of the pressure squared*, and where ρ_0 and c_0 are the density and sound speed at the source, and ρ and c are the values at the receiver. Note that the subscript $_A$ for "ambient" has been dropped to simplify the typography.

If the sound speed is only a function of z (no horizontal refraction), $\Delta\phi = \Delta\phi_0$. Solution for the time integral pressure squared gives

$$\frac{[tips]}{[tips]_0} = \frac{\rho c}{\rho_0 c_0} \frac{R_0^2 \sin\theta_0 \Delta\theta_0}{r\Delta L} \tag{3.3.30a}$$

so that the ratio of the energies per unit area is

$$\frac{\varepsilon_r}{\varepsilon_0} = \frac{R_0^2 \sin\theta_0 \Delta\theta_0}{r\Delta L} \tag{3.3.30b}$$

Using the functional notation for r and θ, the path amplitude factor for this refracting medium is

$$[paf(r,\theta_0)] = \sqrt{\frac{\rho c}{\rho_0 c_0} \frac{R_0^2 \sin\theta_0 \Delta\theta_0}{r\Delta L}} \tag{3.3.31}$$

The energy per unit area at range r is given by

$$\varepsilon_r = \varepsilon_0 [paf\ (r,\theta_0)]^2 \tag{3.3.32}$$

The energy arrives after the path time $[t_{path}]$.

When the sound pressure signal has little distortion in its travel from a source to receiver, the pressures that were integrated to produce Equation 3.3.26 are related by

$$p\ (t\ ) = [paf\ (r,\theta_0)]\, p_0[t - t_{path}(r,\theta_0)] \tag{3.3.33}$$

and $[t_{path}(r,\theta_0)] = t_N$ is the ray path travel time (Equation 3.3.9). The wave form of $p(t)$ is a delayed replica of $p_0(t)$ multiplied by the path amplitude factor.

3.3.7 WAVE FRONTS AND CROSSING RAY PATHS: PHASE SHIFTS AT CAUSTICS

When rays cross we need a special treatment for the refracted signal. We give a heuristic discussion that uses concepts from the seismic literature (Cerveny and Ravindra 1971; Cerveny et al. 1977; Aki and Richards 1980; Hubral and Krey 1980. Figure 3.3.8 shows two situations: a) a pair of noncrossing rays and b) a pair of crossing rays. The tube end areas S_1 and S_2 are drawn the same for illustration.

At a *simultaneous crossing* of ray paths, the ΔL of the wavefront, shown in Fig. 3.3.7, goes to zero as the ray paths go through a focus, as sketched in Fig. 3.3.8b. Correspondingly, the pressure amplitude tends to infinity although

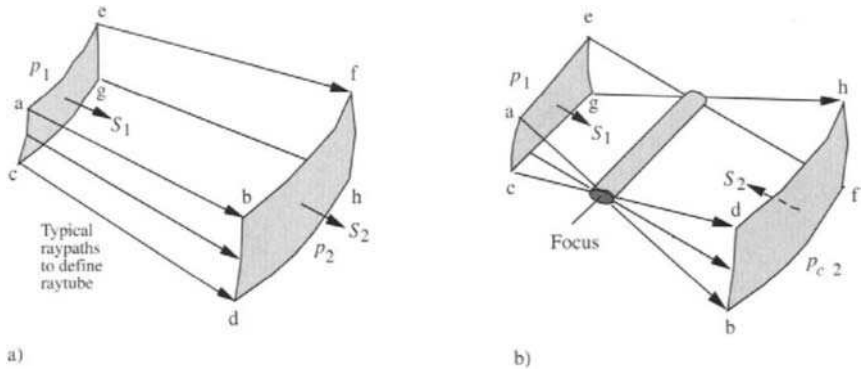

Figure 3.3.8 Construction for crossing ray paths. a) Common expanding wavefront. b) Wavefront that has passed through a focus. The wavefront curvature has been inverted.

fundamental wave-theory computations of the sound pressure in the region of the focus give finite amplitudes. Computations of pressures near the focus are based on using continuous sinusoidal waves and various asymptotic approximations (Pekeris 1946; Kay and Keller 1954; Born and Wolf 1959, 1965; Tolstoy and Clay 1966, 1987; Tolstoy 1968; Clay and Medwin 1977; R. Chapman 1976, 1978; Stickler et al. 1981; L. Brekhovskikh 1980).

Recalling the relations developed from the conservation of energy integral (Equation 3.2.18), for the situation in Fig. 3.3.8a we write

$$S_1 \int_0^{t_g} [p_{\ 1}(\tau)]^2 d\tau = S_2 \int_0^{t_g} [p_{\ 2}(\tau)]^2 d\tau \qquad \textbf{(3.3.34)}$$

The crossing of the ray paths — that is, the situation in Figure 3.3.8b — effectively turns the area S_2 around and introduces a negative sign, because the normal to the area has changed direction and the radius of curvature of the wavefront that is associated with the ray has changed direction (Cerveny and Ravindra 1971, p. 76; Hubral and Krey 1980, p. 52). The energy expression (Equation 3.3.30) then becomes

$$S_1 \int_0^{t_g} [p_{\ 1}(\tau)]^2 d\tau = -S_2 \int_0^{t_g} [p_{\ caus\ 2}(\tau)]^2 d\tau \qquad \textbf{(3.3.35)}$$

where the subscript $_{caus}$ indicates that the rays have crossed or passed through a caustic.

The pressure p_{caus2} is

$$p_{caus\,2} = \pm ip_1\sqrt{\frac{S_1}{S_2}} \tag{3.3.36}$$

The crossing of the rays and turning of the normal to the area S_2 has introduced a factor i, which represents a 90° (quadrature) phase shift.

For sinusoidal pressures, it is fairly easy to show the effect of a 90° phase shift. For example, assume the CW signal has amplitude P, and is described by the real trigonometric form

$$p = P\cos(\omega t + \Phi) = P\cos(\omega t)\cos(\Phi) - P\sin(\omega t)\sin(\Phi) \tag{3.3.37}$$

Notice that when $\Phi = 0$, $p = P\cos\omega t$. When there is a phase shift, $\Phi = \pi/2$, $p = -P\sin\omega t$.

When expressed in the complex exponential form, Equation 3.3.37 becomes

$$p = \text{Real}\{Pe^{i(\omega t+\Phi)}\} \tag{3.3.38}$$

In the complex form, when there is a phase shift $\Phi = \pi/2$, it is equivalent to multiplying the complex signal $e^{i\omega t}$ by i, and then choosing the real part, which is $-P\sin\omega t$. In conclusion, the phase shift $\Phi = \pi/2$, or multiplication by i, gives the *quadrature* component.

The above argument for a sinusoidal signal has its counterpart for an impulse signal, which can also be phase-shifted by 90°. The 90° phase shift operation, which is also known as the Hilbert transformation of the impulse signal, gives the quadrature term.

Examples of a discrete impulse signal and its quadrature transformation are shown in Fig. 3.3.9. The top trace shows the impulse signal. The middle trace is the result of a 90° phase shift. The bottom trace is the result of a quadrature transformation of the middle trace. The application of the second 90° phase shift gives a 180° phase shift, which produces the negative of the original signal. The time delays have been shifted for display. The quadrature component has a precursor. Analytical details of the Hilbert transformations are in Born and Wolf (1965, sec. 10.2), Gabor (1946), and Oppenheim and Schafer (1975, sec. 7.4).

3.3.8 SIGNAL TRANSMISSIONS IN A REFRACTING MEDIUM WITH CAUSTICS

Now we apply methods given in this chapter to interpret signal transmission experiments where there are caustics. The experiments were performed in the Mediterranean Sea (Parkes [1966], Tolstoy and Clay [1966, 1987], and Leroy

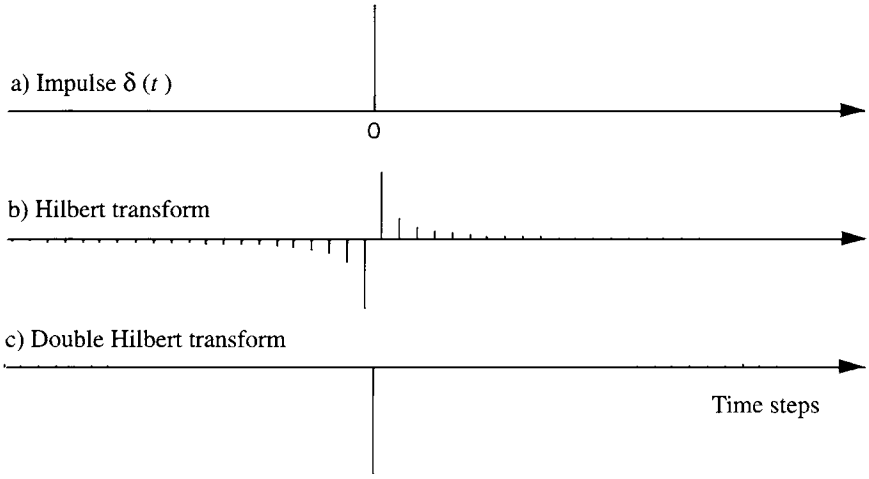

Figure 3.3.9 Impulse signal and quadrature (or Hilbert) transformation operations. The sampled signals are shown as vertical lines. The heights of the vertical lines are proportional to the sampled pressures. a) The original impulse, p_n. b) The quadrature or Hilbert transformation of the impulse. c) The effect of an additional quadrature transformation of b) or double Hilbert transformation of a) gives $-p_n$, the negative of the original signal. The very small vertical lines at large $|n|$ are artifacts.

[1967], where the axis of the sound channel is very shallow (Figs. 3.3.10 and 3.3.11). Some of the upward traveling ray paths are part of a caustic near the 4 km range (Fig. 3.3.11). Other (downward-going) ray paths form a caustic near the surface at approximately 30 km (Fig. 3.3.11). One path (labeled 4) goes through both caustics.

Starting from a source at 100 m depth, it is evident that several ray paths will pass through the same depth and range locations. Since these paths are distinct, each path produces a distinct arrival. Figure 3.3.10 shows the ray paths for the first four arrivals. We will use these arrivals for numerical calculations of the [*path*]s and the received pressure signal waveforms. The received signal is the sum of all [*path*]s. An outline of the numerical computations follows.

Ray-Path Computations: Ranges and Travel Times

The numerical ray path code uses Equations 3.3.20 through 3.3.22 as a subroutine. Downgoing rays are turned upward at a turning point or a reflection at the bottom. Upgoing rays reflect at the surface or are turned downward. The ray path computation starts with an initial θ_0 and proceeds to the range r at depth z_e. The code gives the range as the ray crosses z_e. Picking a value of θ_0 that gives r_e is

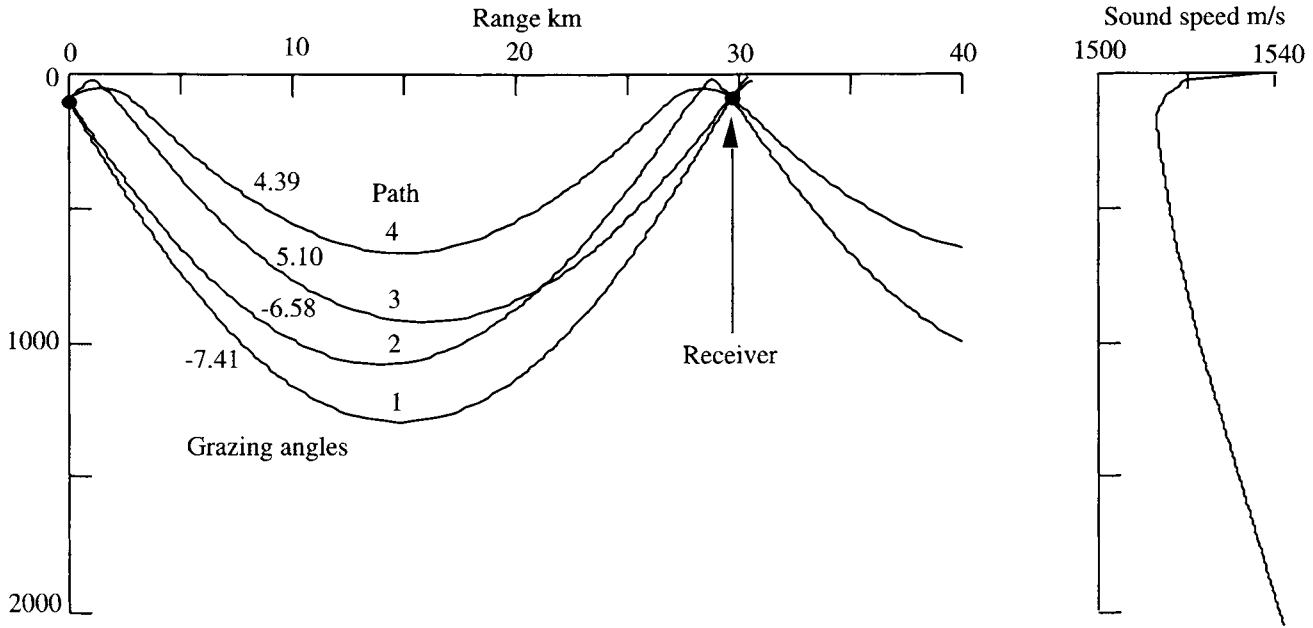

Figure 3.3.10 Four ray paths (*left*) and the Mediterranean Sea sound-speed profile (*right*). The source is at 100 m depth, the receiver is at 90 m depth, the range is 29.7 km. Path 1 goes down and up to the receiver without passing through a caustic. Path 2 goes through a caustic as it turns downard near the sea surface at about 28 km (Fig. 3.3.11a). Path 3 goes through a caustic at about 4 km (Fig. 3.3.10b). Path 4 goes through caustics both near the source and near the receiver. The sound-speed profile was drawn using data from Leroy (1967).

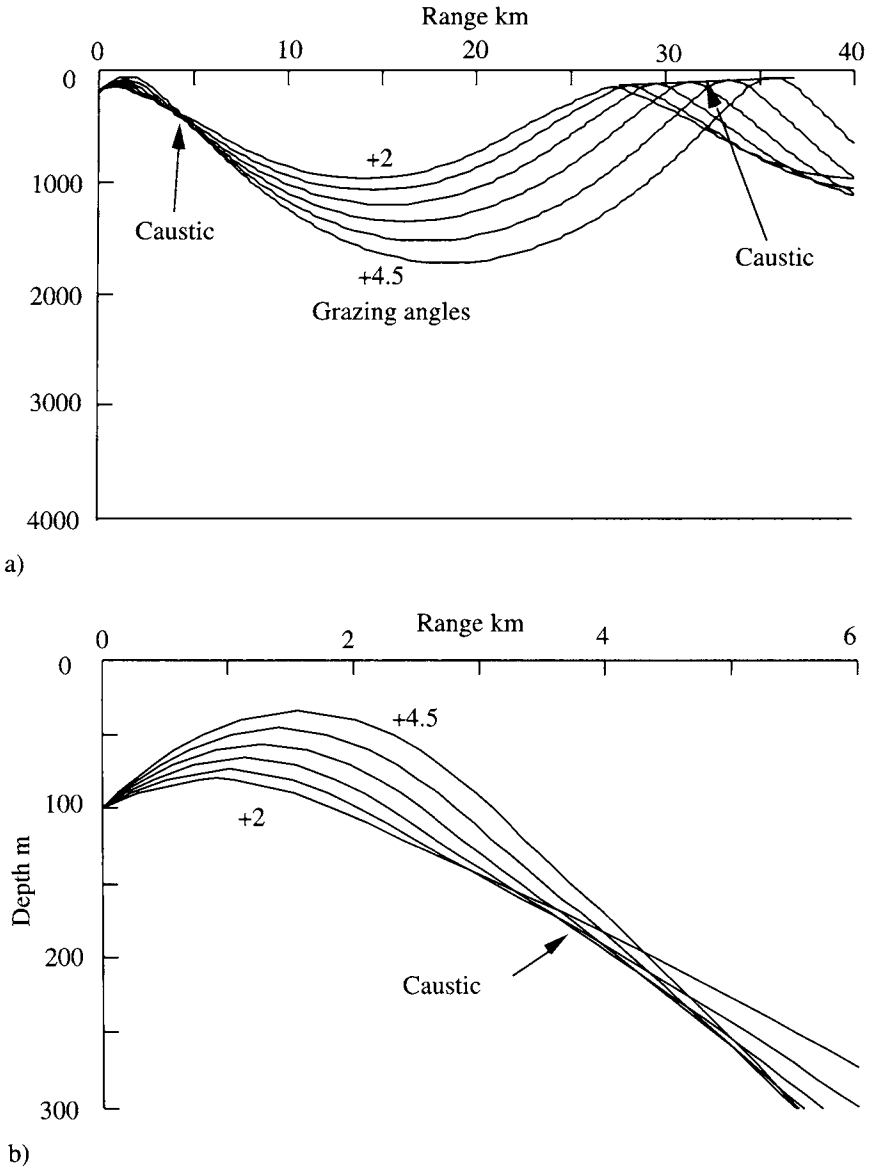

Figure 3.3.11 Upward-starting ray paths for sound-speed profile in Fig. 3.3.10. Caustics are formed by crossing ray paths at range approximately 4 km (see "zoom" below) and in the 27–37 km range (above).

a tedious task. We use Newton's method of iterative calculations. A pair of ray paths at θ_0 and $\theta_0 + \Delta\theta_0$ give $r + \Delta r$ for estimating a new θ_0. The program iterates until r is within 0.5 m of r_e. The angle θ_{final} is the angle that has the ray passing through (r_e, z_e). Its value is the initial angle θ_0 in Equation 3.3.31, which is needed for the next step.

Computations of [*path amplitude factor*] and [*path time*]

Amplitude calculations follow the method of section 3.3.6. A choice $\Delta\theta_0$ of about $0.1°$ gives Δr for the calculation of ΔL in Equation 3.3.31. For notation, let θ_1 be the angle for path 1 and $[paf(r_e, \theta_1)]$ and so on. The calculation also gives the travel time — that is, $[t_{path}(r_e, \theta_1)]$. Calculations of the [*path amplitude factors*] and [*path time*] are performed for each of the four paths.

Source Sound Pressure

The source $p_0(t)$ is chosen to match the apparent source pressure signal of the explosive used in the experiments.

Caustics and Signal Waveforms

Path 1 with no caustics has a factor of unity. Path 2 has one caustic and a phase factor of $[-i]$. Path 3 has one caustic and a phase factor of $[-i]$. (The sign choice in $[-i]$ is arbitrary.) Path 4 has two caustics and a factor of $[-1]$.

The source $p_0(t)$ is numerically convolved with the Hilbert transform (Chapter 6) shown, in Fig. 3.3.9 to give the 90° phase shift. Results of these computations are shown in Fig. 3.3.12.

Summary of the Theoretical Signal Transmissions

Path 1: $p_1(t) = [paf(r_e, \theta_1)]p_0(t - t_{path}(r_e, \theta_1))]$
Path 2: $p_2(t) = [paf(r_e, \theta_2)][-i]p_0(t - t_{path}(r_e, \theta_2))]$
Path 3: $p_3(t) = [paf(r_e, \theta_3)][-i]p_0(t - t_{path}(r_e, \theta_3))]$
Path 4: $p_4(t) = [paf(r_e, \theta_4)][-1]p_0(t - t_{path}(r_e, \theta_4))]$

The sound pressure waveform is the sum of all arrivals. The waveform for the first four arrivals is

$$\textbf{Signal: } p(t) = p_1(t) + p_2(t) + p_3(t) + p_4(t) \qquad \textbf{(3.3.39)}$$

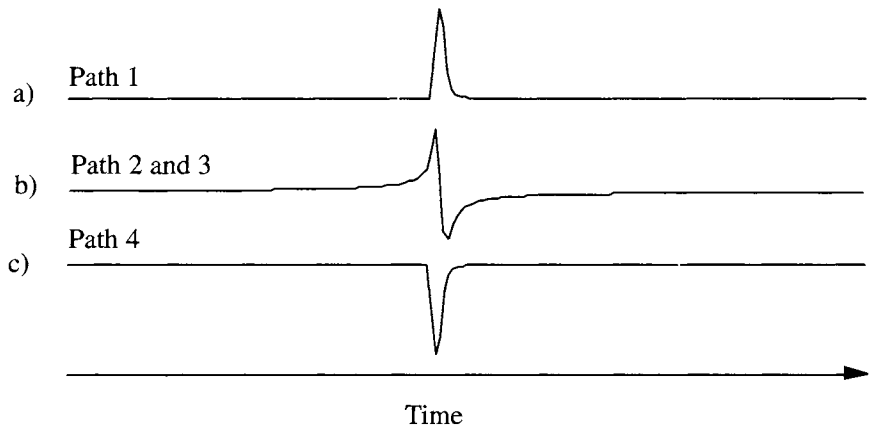

Figure 3.3.12 Sound pressure signal and its Hilbert transforms: a) explosive signal for path 1; b) – 90° phase shift or Hilbert transformation of a) for Paths 2 and 3; c) Double Hilbert transformations for Path 4.

The theoretical signals are shown in Fig. 3.3.13. The experimental data are given in Fig. 3.3.14. The arrivals are aligned on the first arrival. All of the experimental and model arrivals agree within a few milliseconds — that is, two parts in 10^5. The waveforms of the theoretical and experimental signals are similar for all ranges. The ray path, $-90°$ phase shift for a single caustic and 180° for two caustics, properly described the waveforms of the experimental signal transmissions. The [*path amplitude factors*] and [*path times*] analysis gives a good match to the experiments.

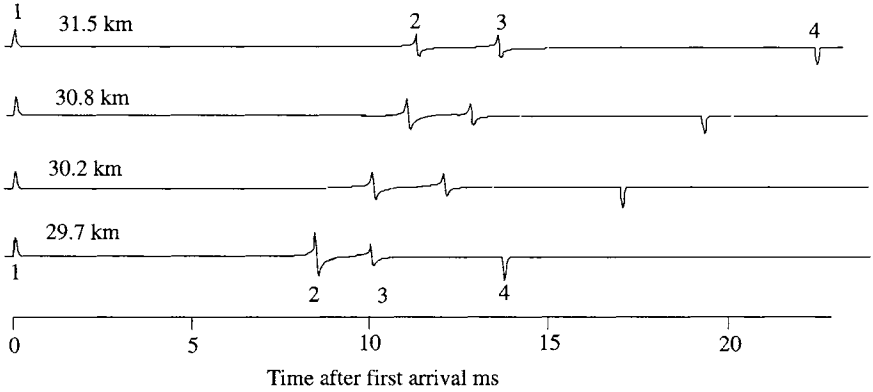

Figure 3.3.13 Theoretical (model) transmissions. We align the first arrivals of the model calculations at all ranges. The model travel time to the 29.7 km range is 19.594 s. The travel time to the 31.5 km range is 20.770 s.

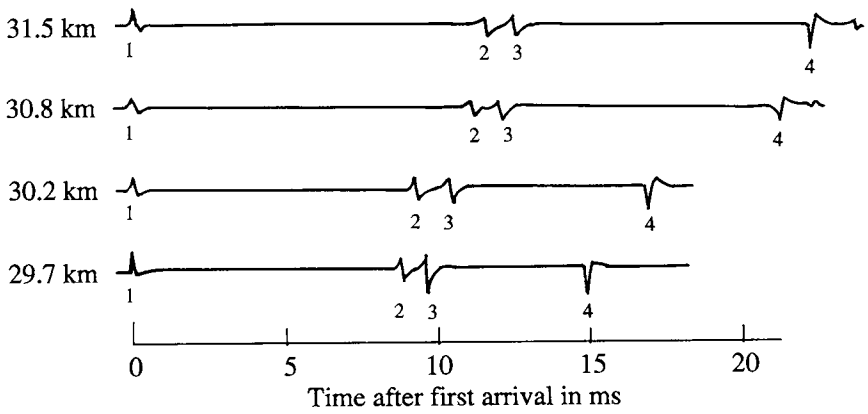

Figure 3.3.14 Experimental transmissions. The first arrivals are aligned. The explosive sources were at 100 m and receivers were at 80–90 m depths. Redrawn for data in Tolstoy (1965). Compare with transmission in Fig. 3.3.13.

3.3.9 GENERAL COMMENTS ON RAY-PATH METHODS

Classical ray-path theory simply uses Snell's Law to determine the ray paths. In a region where several ray paths arrive at a hydrophone, an impulse is received for each of the rays. When there is a longer duration signal, the pressures of the several signals from the several ray paths add coherently at the hydrophone. If ray paths cross *at the same time*, correct interpretation of the interference of the crossing rays requires wavefield calculations.

"Exact ray paths" have been obtained by Foreman (1989) by solving the complete wave equation for certain simple, sound-speed profiles. His exact ray-path solutions do not show crossing rays for situations where the classical ray calculations (incorrectly) do. Foreman suggests that classical ray-path calculations are acceptable for broad frequency bandwidth signals (i.e., impulses).

Some ray-path calculations create artifacts for two main reasons: (1) approximations that are made in going from the wave equation to a ray-path solution can produce errors (e.g., when ray paths cross or go through a focus); and (2) numerical or algebraic approximations that are made to approximate continuously varying sound-speed profiles produce false answers. They can give superfluous arrivals as well as amplitude anomalies (Pedersen 1961; Spiesberger et al. 1994).

Despite these limitations, the ocean acoustics community continues to use ray-trace methods because they give a simple picture and because *careful* computations generally match experimental data.

3.4 Attenuation

3.4.1 EXPONENTIAL ATTENUATION OF PLANE WAVES

The exponential attenuation of propagating plane waves is well known in both electromagnetics and acoustics. The physical basis in acoustics is the fact that, in a homogeneous medium with wave absorption (conversion to heat) or omnidirectional scattering, a plane wave experiences a reduction of acoustic pressure, dp, proportional to the original pressure, p, and proportional to the distance traversed, dx. We call the proportionality constant α_e because the effect leads to an equation,

$$dp = -\alpha_e p\, dx \tag{3.4.1}$$

that, when integrated, gives the natural logarithm to base $e = 2.71828$ — that is,

$$\ln(p/p_0) = -\alpha_e x \tag{3.4.2}$$

or

$$\alpha_e = \left(\frac{1}{x}\right) \ln\left(\frac{p_0}{p}\right) \tag{3.4.3}$$

where we evaluated the constant of integration by letting $p = p_0$ at $x = 0$. The familiar decay law follows by *exponentiating*. Equation 3.4.2 — that is,

$$p = p_0 e^{-\alpha_e t} \tag{3.4.4}$$

The spatial rate of amplitude decay, the amplitude decay coefficient α_e, has SI units of nepers/unit distance. (The unit *neper*, abbreviated Np, was named after John Napier, the inventor of logarithms, which were in everyday use before the advent of digital computers.) The *distance* is usually given in meters or kilometers.

The plane-wave attenuation rate α_e, which depends on the medium, is generally expressed as a function of frequency. Commonly the attenuation per wavelength is very small, that is, $\alpha_e \lambda \ll 1$, which permits attenuation to be included as a factor not only for plane waves but also in the pressure spreading from a point source. For example, including plane-wave attenuation in a lossy medium, the pressure sonar equation (3.1.4) for a spherically diverging wave could be written

$$p\ (t\ ) = p_0\ (\ t - R\ /c\ )\ \frac{R_0}{R}\ e^{-\alpha_e R} \tag{3.4.5}$$

In the 1920s, a new decay coefficient, advocated by the Bell System (Martin 1929) and based on $\log_{10}$ of the *relative power* in lossy communication circuits, came into common usage. The "bel" was named to honor Alexander Graham Bell (1847–1922), and one-tenth bel, the *decibel* (abbreviated dB), became much more popular than the neper in underwater acoustics. To distinguish the attenuation coefficient in decibels per unit distance, we call it simply α. The plane-wave attenuation coefficient is written in terms of the *relative sound intensity* at two points of a plane wave,

$$\alpha = (1/x)[10 \log_{10}(i_1/i_2)] \quad \text{dB/unit distance} \tag{3.4.6}$$

or, since the intensity is proportional to the square of the pressure in a plane wave (or at long range in a spherical wave), one writes

$$\alpha = (1/x)[20 \log_{10}(p_1/p_2)] \quad \text{dB/distance} \tag{3.4.7}$$

Comparing with Equation 3.4.3, we find

$$1 \text{ neper} = 8.68 \text{ dB} \tag{3.4.8a}$$

or

$$8.68\alpha_e = \alpha \tag{3.4.8b}$$

3.4.2 ABSORPTION LOSSES

To understand the attenuation due to absorption, we return to the acoustic force Equation (2.7.4), where, for simplicity, we previously ignored two forces. The complete acoustic force equation includes viscosities and is a simplification of the Navier-Stokes equation found in any good book on fluid dynamics. For acoustics we drop the convective acceleration term compared with the local acceleration, as we did in Equation 2.7.2, and obtain

$$\rho_A \frac{\partial \boldsymbol{U}}{\partial t} = -\nabla p + \left(\frac{4\mu}{3} + \mu_b\right)\nabla\nabla\cdot\boldsymbol{U} - \mu\nabla \times (\nabla \times \boldsymbol{U}) \tag{3.4.9}$$

The two new terms introduce the *dynamic (or absolute) coefficient of shear viscosity*, μ, and the *dynamic bulk viscosity*, μ_b. The shear viscosity, which is generally called simply "the viscosity," is defined as the ratio of the shearing stress to the rate of strain. Each component of the stress is due to a shearing force component F parallel to an area A, caused by a gradient of velocity perpendicular to the area. For example, for velocity components u, v, and w in the x, y, and z directions, the shearing stress in the x direction, F_x, is proportional to

the shearing rate of strain, which is caused by a velocity gradient in the y direction:

$$\frac{F_x}{A} = \mu\left(\frac{\partial u}{\partial y}\right) \tag{3.4.10}$$

The important bulk viscosity appears only when there is a compressible medium (e.g., an acoustic wave in water). It is not found in traditional, incompressible hydrodynamics. Note that it appears only in the divergence term of Equation 3.4.9, which is proportional to the rate of change of density. We will look at the physical origin below.

To calculate the influence of the viscosities on the attenuation of a plane wave, consider the x component of Equation 3.4.9,

$$\rho_A \frac{\partial u}{\partial t} = -\frac{\partial p}{\partial x} + \left(\frac{4\mu}{3} + \mu_b\right)\frac{\partial^2 u}{\partial x^2} \tag{3.4.11}$$

Rederive the plane wave-equation by differentiating Equation 3.4.11 with respect to x, using the conservation of mass, Equation 2.5.4, and the plane-wave relation $p = \rho c^2$, to obtain the wave equation in terms of the acoustic density ρ and the coefficients of viscosity,

$$\frac{\partial^2 \rho}{\partial x^2} + \frac{\left(\frac{4\mu}{3} + \mu_b\right)}{\rho_A c^2}\frac{\partial}{\partial t}\frac{\partial^2 \rho}{\partial x^2} = \frac{1}{c^2}\frac{\partial^2 \rho}{\partial t^2} \tag{3.4.12}$$

Molecular Relaxation

Consider the physical origins of μ and μ_b. It takes a finite time for a fluid to respond to a pressure change, or to relax back to its former state after the pressure has returned to normal. The process is called *relaxation*. Chemical relaxation, which occurs in sea-water, involves ionic dissociation that is alternately activated and deactivated by sound condensations and rarefactions. Surprisingly, magnesium sulfate and boric acid are the two predominant contributors to sound absorption in sea water, even though their contribution to water salinity is very much less than that of common salt (sodium chloride).

To obtain the form of the attenuation due to the molecular relaxation effect, add a time-dependent term to Hooke's Law (Equation 2.5.5),

$$p = c^2 \rho + b\frac{d\rho}{dt} \tag{3.4.13}$$

where b is a constant. To obtain the relaxation time, assume that a pressure is released ($p = 0$) at time $t = 0$, and the density then decays from its initial value, ρ_0. The fractional change in time dt is

$$\frac{d\rho}{\rho} = -\frac{c^2}{b}\,dt \tag{3.4.14}$$

Integrate, and let $\rho = \rho_0$ at $t = 0$, to obtain,

$$\rho = \rho_0 \exp\left(-\frac{t}{\tau_r}\right) \tag{3.4.15}$$

where the *relaxation time* of the process is

$$\tau_r = \frac{b}{c^2} \tag{3.4.16}$$

The value of τ_r depends on the fraction of molecules active in the relaxation process. This depends, in turn, on the temperature and pressure of the liquid. For this reason, as we shall see, the attenuation at sea due to absorption by relaxation processes is sensitive to the temperature and ambient pressure (depth) of the water.

Relaxation in sea water affects the speed of propagation very slightly, but it is the source of a most important factor in the attenuation of sound. To determine these effects, rederive the wave equation (section 2.5.2) with the time-dependent equation of state (3.4.13) instead of Equation 2.5.5. In terms of density one obtains

$$\frac{\partial^2\rho}{\partial x^2} + \tau_r \frac{\partial}{\partial t}\frac{\partial^2\rho}{\partial x^2} = \frac{1}{c^2}\frac{\partial^2\rho}{\partial t^2} \tag{3.4.17}$$

Propose a solution for a plane-wave sinusoid propagating in the $+x$ direction,

$$\rho = \rho_0\, e^{i(\omega t) - (ik_r + \alpha_e)x} \tag{3.4.18}$$

where k_r is the propagation constant in the fluid with molecular relaxation, and α_e is the exponential attenuation rate expected. The values are determined by substitution into Equation 3.4.18, which gives

$$-\left(k_r^2 - \alpha_e^2\right) + \frac{\omega^2}{c^2}\left(1 + \omega^2\tau_r^2\right)^{-1} + i\left[2k_r\alpha_e - \frac{\omega^3\tau_r}{c^2}\left(1 + \omega^2\tau_r^2\right)^{-1}\right] = 0 \tag{3.4.19}$$

Equate the reals and equate the imaginaries to give two equations. Solve simultaneously to get the exponential attenuation rate,

$$\alpha_e = \frac{\omega^2 \tau_r c_r}{2c^2(1 + \omega^2 \tau_r^2)} \tag{3.4.20}$$

and the real propagation constant, the dispersive phase speed.

It turns out that the dispersive speed, c_r, differs from c by only about 1 percent owing to relaxation effects in sea water, so we henceforth assume

$$c \cong c_r \tag{3.4.21}$$

We now define the relaxation frequency

$$f_r = \frac{1}{2\pi \tau_r} \tag{3.4.22}$$

and obtain the characteristic form for the attenuation rate owing to molecular relaxation in a fluid—that is,

$$\alpha_e = \frac{(\pi f_r / c) f^2}{f_r^2 + f^2} \text{ nepers / distance} \tag{3.4.23}$$

For attenuation rate α in decibels/distance, use the conversion one neper $= 20 \log_{10} e = 8.68$ dB, where e is the base of the natural logarithm. The plane-wave attenuation rate for a relaxation process is therefore of the form

$$\alpha = \frac{A f_r f^2}{f_r^2 + f^2} \text{ dB / distance} \tag{3.4.24}$$

where $A = 8.68\pi/c$.

Notice that the attenuation rate in a relaxation process reduces to

$$\begin{aligned} \alpha &= A f_2 = \text{constant} \qquad \text{for} \quad f \gg f_r \\ \alpha &= \frac{A}{f_r} f^2 \sim f^2 \qquad \text{for} \quad f \ll f_r \end{aligned} \tag{3.4.25}$$

These are the behaviors that dominate the attenuation in sea water, as seen in the next section.

A few more words about the physics of the relaxation process may be helpful. When the effect is expressed in terms of attenuation per cycle (α/f), or attenuation per wavelength, one finds that

$$\alpha \lambda = (A\ c\ f_r) \frac{f}{f^2 + f_r^2} \tag{3.4.26}$$

which describes an effect that approaches zero for very high or very low frequencies. This is because, at very high frequencies, the relaxing molecules cannot respond fast enough to be effectively activated. At the other extreme, when the frequency is very low, the molecular relaxation follows in step with the sound wave, and there is no evidence that relaxation is taking place. However, when the frequency is approximately equal to the relaxation frequency, the activated molecules will dump energy from a condensation into a rarefaction, and some of the ordered energy of the sound wave is thereby transformed into random, thermal motion of the medium.

Comparison of the two forms of the wave equation (Equations 3.4.12 and 3.4.17) permits an immediate identification of the macroscopic descriptors of the medium, μ and μ_b, and the molecular behavior in terms of relaxation,

$$\tau_r = \frac{(4/3)\mu + \mu_b}{\rho_A c^2} \tag{3.4.27}$$

Consider fresh water at 14°C. Designating freshwater by the subscript $_F$, the conventional constants are: $\mu_F = 1.17 \times 10^{-3}$ N-s/m^2; $\rho_F = 1000$ kg/m^3; and $c_F = 1480$ m/s. From the experiments in acoustic streaming (section 5.5), it is known that the bulk viscosity for water is 2.8 times the shear viscosity — that is, $\mu_b = 2.8\,\mu_F$. Therefore, Equation 3.4.27 yields

$$\tau_r = 2.1 \times 10^{-12} \text{ (s)} \tag{3.4.28a}$$

Recalling Equation 3.4.25, this very small relaxation time means that the attenuation will be proportional to frequency squared for any useful sound frequencies propagating in fresh water — that is, for

$$f \ll 1/(2\pi \times 2.1 \times 10^{-12} \text{ seconds}) \quad f \ll 10^{11} \text{ Hz} \tag{3.4.28b}$$

This frequency squared component of the total absorption is seen in the straight lines that have slope 2, in the log-log graph plotted in Fig. 3.4.1.

Relaxation in Sea Water

In the 1950s, the mysteriously large attenuation of sound observed at frequencies around 20 kHz during World War II was finally explained by a series of careful laboratory experiments by R. W. Leonard (1949) and his students O. B. Wilson (1954) and D. Bies (1955). The technique used was to drive a water-filled sphere, of diameter approximately 30 cm, into its modes of oscillation, and to determine the damping constants caused by the various sea salts added in proper amounts to the water. The startling realization that the relatively small amounts of

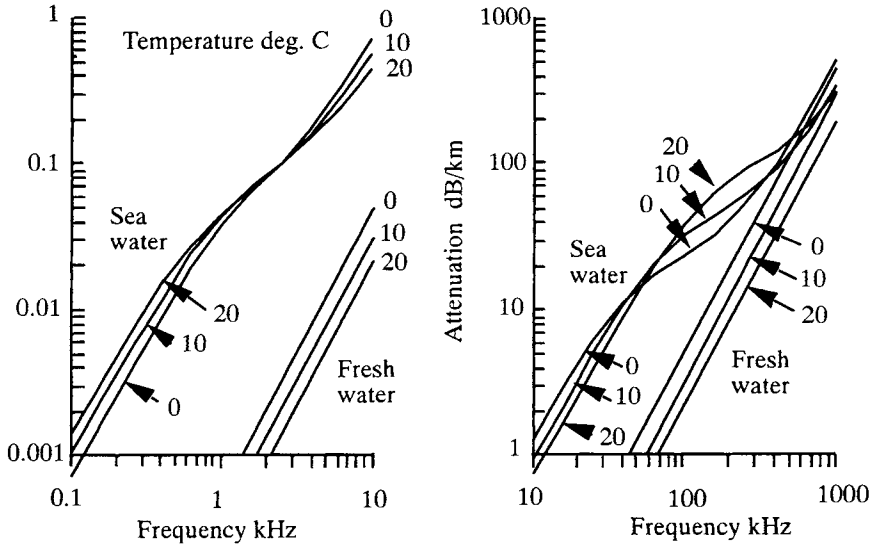

Figure 3.4.1 Sound pressure attenuation rate in dB/km in fresh and sea water at temperatures 0°, 10°, and 20°C. Calculated from François and Garrison (1982). Parameters at pH = 8; S = 35 ppt; and depth, $z = 0$ m.

magnesium sulfate salts were causing a molecular relaxation phenomenon changed, forever, the naïve thought that only viscosity was important.

In the 1970s, similar laboratory experiments by Fisher and Simmons (1977) and experiments by Mellen and Browning (1977) showed that there was another relaxation phenomenon, due to boric acid in sea water, moderated by the pH of the sea water. This causes a strong effect at frequencies around 1 kHz.

The dependence of relaxation effects on temperature, shear viscosity, and bulk viscosity is discussed in somewhat more detail in section A3.2 of Clay and Medwin (1977). The result of much research in the laboratory and at sea have been summarized by François and Garrison (1982). It is their empirical formula that will be used in this text. They give the attenuation in sea water as the sum of the two relaxation terms and the viscosity component:

$$\alpha = \frac{A_1 P_1 f_1 f^2}{f^2 + f_1^2} + \frac{A_2 P_2 f_2 f^2}{f^2 + f_2^2} + A_3 P_3 f^2 \quad \text{dB/km} \tag{3.4.29}$$

where α is the total absorption coefficient in dB/km. The coefficients are expressed in terms of z = depth, (m); T = temperature, (°C); S = salinity (parts/1000); and the relaxation frequencies f_1 for boric acid and f_2 for magnesium sulfate.

Boric Acid Component in Sea Water

$$\begin{aligned} A_1 &= \frac{8.68}{c}\, 10^{(0.78\,\mathrm{pH}-5)} \ \mathrm{dB\ km^{-1}\ kHz^{-1}} \\ P_1 &= 1 \\ f_1 &= 2.8\,(\frac{S}{35})^{0.5}\, 10^{[4-1245/(273+T)]} \ \mathrm{kHz} \\ q &= 1412 + 3.21T + 1.19\,S + 0.0167\,z\ m/s. \end{aligned} \tag{3.4.30}$$

Magnesium Sulfate Component in Sea Water

$$A_2 = 21.44\frac{S}{c}\,(1 + 0.025T) \qquad \mathrm{dB\ km^{-1}\ kHz^{-1}}$$

$$P_2 = 1 - 1.37 \times 10^{-4} z + 6.2 \times 10^{-9} z^2 \tag{3.4.31}$$

$$f_2 = \frac{8.17 \times 10^{[8-1990/(273+T)]}}{1 + 0.0018\,(S-35)} \quad \mathrm{kHz}$$

Pure Water (Viscosities) Component for $T \leq 20°C$

$$\begin{aligned} A_3 = {} & 4.937 \times 10^{-4} - 2.59 \times 10^{-5} T + 9.11 \times 10^{-7} T^2 \\ & - 1.50 \times 10^{-8} T^3 \quad (\mathrm{dB\ km^{-1}\ kHz^{-2}}) \end{aligned} \tag{3.4.32}$$

Pure Water (Viscosities) Component for $T > 20°C$

$$\begin{aligned} A_3 = {} & 3.964 \times 10^{-4} - 1.146 \times 10^{-5} T + 1.45 \times 10^{-7} T^2 \\ & - 6.5 \times 10^{-10} T^3 \quad (\mathrm{dB\ km^{-1}\ kHz^{-2}}) \end{aligned} \tag{3.4.33}$$

$$P_3 = 1 - 3.83 \times 10^{-5} z + 4.9 \times 10^{-10} z^2 \tag{3.4.34}$$

3.4.3 SCATTERING LOSSES

In carrying an acoustical message through a ray tube, any energy that is scattered out of the ray tube causes attenuation, just as effectively as absorption and divergence of sound. In Chapters 7 and 8 we consider the scattering of energy by bodies and bubbles, which is the third source of propagation loss at sea.

3.4.4 AMPLITUDE SONAR EQUATIONS

We now assume that our signal covers a narrow frequency range so that we can include absorption simply, as a factor, in the sound transmission equations. Using Equation 3.4.8 to write Equation 3.4.5 in terms of α, the (linear) pressure sonar equation for a spherically divergent wave in a homogeneous *attenuating* medium is written as, for example,

$$p(t) = p_0(t - R/c)\frac{R_0}{R}10^{-\alpha R/20} \text{ (Pa)} \tag{3.4.35}$$

More generally, including absorption in the *path amplitude factor*, [*paf*], the linear pressure sonar equation can be written

$$p(t) = [paf\,(r, \theta_0, \alpha)]p_0[t - t_{path}(r, \theta_0)] \text{ (Pa)} \tag{3.4.36a}$$

where

$$[paf\,(r, \theta_0, \alpha)] = [paf\,(r, \theta_0)]10^{-\alpha r/20} \tag{3.4.36b}$$

This expression was derived to calculate the sound signal as a theoretical transmission. If the individual arrivals are displayed as in Figs. 3.2.3 or 3.3.14, one can use the source pressure $p_0[t - t_{path}(r, \theta_0)]$ and the received pressure $p(t)$ to compute experimental values of the attenuation for that particular ray path and travel time. Generally all pressures are in pascals.

3.4.5 SUM OF MULTIPLE ARRIVALS: THE TRANSMISSION FRACTION

Multiple arrivals, as shown in Figs. 3.3.13 and 3.3.14, can be expressed as the sum of the individual arrivals. The sum of four arrivals (Equation 3.3.39) can be extended to N arrivals. Each arrival has a path amplitude factor that may include refraction in an inhomogeneous medium (section 3.3), the plane-wave attenuation owing to absorption or scatter (sections 3.4.2 and 3.4.3), coefficients of reflection $\mathcal{R}$ when there are interactions with the bottom or top surfaces, and phase shifts owing to caustics Φ_c (section 3.2.3) when they exist. These are included in the [*paf*] function so that $p(t)$ becomes

$$p\ (t\ ) = \sum_{n\,=\,1}^{N}\ [paf\,(r, \theta_n, \alpha, R, \phi_c)]\ \ p_{\,0}(t\ -t_{\,path\,,\,n}\ ) \tag{3.4.37}$$

In practice, we choose individual arrivals and measure their travel times, amplitudes, and waveforms when the signals are separable in the time domain. If the multiple arrivals are not separable, both the phases and amplitudes of the components determine how they interfere (see, for example, Fig. 2.6.10).

Continuous Source Transmissions

Some sound-transmission measurements in the ocean are made as sketched in Fig. 3.4.2. The ship tows a sinusoidal source away from the receiver, and the receiving system records the pressure signal at the receiver. All of the arrivals are present, and their sound pressures add and interfere at the receiver. The relationship to theory follows by evaluating (Equation 3.4.37) for a continuous, sinusoidal source transmission.

Let the source function $p_0(t)$ be $P_0 e^{i2\pi ft}$, substitute it into Equation 3.4.37, and write

$$p(t) = P_0 e^{i2\pi f t} \sum_{n=1}^{N} [paf(r,\theta_n)]\, e^{-i2\pi f t_{path,n}} \qquad \textbf{(3.4.38)}$$

where the time dependence has been factored from the summation. The $[paf(r, \theta_n)]$ function here must include all of the parameters of Equation 3.4.37; the parameters are omitted here for typographic simplicity. The nth path amplitude factor has the phase $(2\pi f t_{path,n})$. The summation depends on range, travel times or phases of the arrivals, and frequency but not time. The time and space dependencies in Equation 3.4.38 are separable for a continuous wave source transmission.

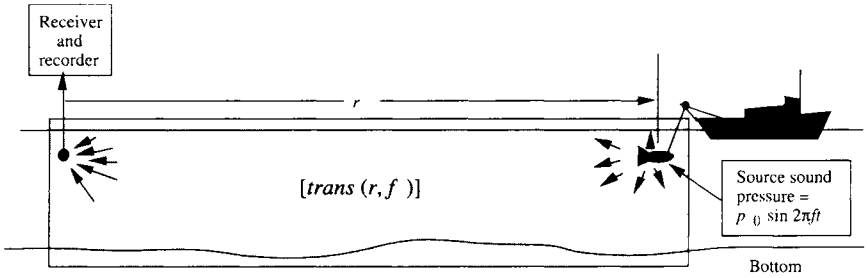

Figure 3.4.2 Transmission from a continuous (e.g., sinusoidal) wave source. The numerous ray paths are not shown. The region within the rectangle contains practically all of the ray paths that contribute to the transmission fraction.

Equation 3.4.38 is a general expression for the sum of many arrivals that travel by many different paths. We use it to define a transmission fraction $[trans(r,f)]$ for N arrivals:

$$[trans(r,f)] \equiv \sum_{n=1}^{N} [paf(r,\theta_n)] e^{-i2\pi f t_{path,n}} \tag{3.4.39}$$

The pressure at a receiver is

$$p(t) = P(r,f)e^{i2\pi ft} = [trans(r,f)]P_0 e^{i2\pi ft} \tag{3.4.40a}$$

and

$$P(r,f) = [trans(r,f)]P_0 \tag{3.4.40b}$$

The *transmission fraction* $[trans(r,f)]$ depends on the summation over all arrivals. Solving Equation 3.4.40 for $[trans(r,f)]$, one gets the transmission fraction in terms of the pressure amplitude of a continuous wave transmission and a measured or calculated sound pressure at the receiver:

$$[trans(r,f)] = P(r,f)/P_0 \tag{3.4.41}$$

3.4.6 *LOGARITHMIC SONAR EQUATIONS: TRANSMISSION LOSS (dB)*

For simplicity in transforming to the log-sonar equations, we consider continuous wave transmissions as just described. In the past, both experimental and theoretical studies have used the amplitudes of the sound pressures and have ignored the phases in the logarithmic operations. Thereby the log-sonar equation is expressed in terms of the logarithm of the absolute value of Equation 3.4.41, after reference pressures have been included to make the argument of *each* logarithmic term dimensionless,

$$20\log|P(r,f)/p_{\text{ref}}| = 20\log(p_0/p_{\text{ref}}) + 20\log|[trans(r,f)]| \quad \text{(dB)} \tag{3.4.42}$$

Reference Pressures

The use of reference sound pressures in acoustics is untidy. The current reference pressure in underwater acoustics is the pascal, 1 Pa = 1 Newton/m^2, or the micropascal, 1 μPa = 10^{-6} pascals. In former years, underwater acousticans used the reference 1 microbar = 0.1 Pa = 10^5 micropascal. Acousticians who work in air use 20 μPa for their reference. The use of different reference pressures in

ocean and air acoustics has caused much confusion. *For this reason, we strongly recommend the use of SI units (pascals or micropascals) to report sound pressure measurements.*

The log-terms in Equation 3.4.42 have been given simple, easy-to-remember names: *sound pressure level SPL*, *source level SL*, and *transmission loss TL*. Their definitions are

$$SL = 20\log_{10}(P_0/p_{\text{ref}}) \qquad (\text{dB referred to } p_{\text{ref}}) \tag{3.4.43}$$

$$SPL = 20\log_{10}(|P(r,f)|/p_{\text{ref}}) \qquad (\text{dB referred to } p_{\text{ref}}) \tag{3.4.44}$$

$$TL = -20\log|[trans(r,f)]| \qquad (\text{dB, dimensionless}) \tag{3.4.45}$$

Using these definitions, the log-sonar equation is

$$SPL = SL - TL \quad (\text{dB}) \tag{3.4.46}$$

and the transmission loss TL is

$$TL = SL - SPL \quad (\text{dB}) \tag{3.4.47}$$

The complexities of underwater acoustics propagation are hidden in the concepts of the transmission fraction $[trans(r, f)]$ and its logarithmic form TL (dB). These quantities depend on the bathymetry, sound-speed profiles, multipath arrivals, range, source frequency, character of the divergence from the source to the receiver, possibility of caustics, and absorption and scattering along the way.

Simple Examples of Transmission Losses in dB

Spherical Spreading. Recalling sections 2.7.3 and 3.4.4, the sound pressure from a point source in a homogeneous medium is (including attenuation)

$$p = P_0(R_0/R)10^{-\alpha R/20} \tag{2.7.41}$$

The logarithmic transformation of the pressure sonar equation (2.7.41) gives

$$20\log|p(R,f)/p_{\text{ref}}| = 20\log(P_0/p_{\text{ref}}) + 20\log(R_0/R) - \alpha R \quad (\text{dB}) \tag{3.4.48}$$

and the transmission loss for spherical spreading is

$$TL_{SPHR} \approx 20\log(R/R_0) + \alpha R \quad (\text{dB}) \tag{3.4.49}$$

The spherical divergence loss is 6 dB for range doubled, if absorption and scattering are negligible.

Cylindrical Spreading. Waveguide propagation will be considered properly in Chapter 11. But notice that in waveguide propagation, such as shown in Fig. 1.3.3, energy is trapped between the top and bottom boundaries of the waveguide. Consequently, at long range, the average energy is expected to spread cylindrically within the waveguide. The intensity would then be inversely proportional to the range and the pressure inversely proportional to the square root of the range, but modified by attenuation,

$$p = \text{const} P_0 (r_0/r)^{1/2} 10^{-\alpha r/20} \tag{3.4.50}$$

where the "const" is a constant of proportionality. The transmission loss for the waveguide is, including the attenuation,

$$TL_{CYL} = \text{Lconst} - 20 \log (r_0/r)^{1/2} + \alpha r \quad \text{(dB)} \tag{3.4.51a}$$

or

$$TL_{CYL} = \text{Lconst} - 10 \log (r_0/r) + \alpha r \quad \text{(dB)} \tag{3.4.51b}$$

where Lconst is a new proportionality constant. When there is no absorption or scattering, doubling the distance increases the TL_{CYL} by 3 dB.

Refraction Spreading. The path amplitude factor $[paf(r, \theta_0)]$ gives the amplitude for a single ray path,

$$[paf(r, \theta_0)] = \sqrt{\frac{\rho c}{\rho_0 c_0} \frac{R_0^2 \sin \theta_0 \Delta\theta_0}{r \Delta L}} \tag{3.4.52}$$

Including attenuation, the transmission loss for a single ray trace path is

$$TL_{[paf]} = -20 \log |[paf(r, \theta_0)]| + \alpha r \quad \text{(dB)} \tag{3.4.53}$$

and

$$TL_{[paf]} = -10 \log \left[\frac{\rho c}{(\rho_0 c_0)} \frac{R_0^2 \sin \theta_0 \Delta\theta_0}{(r \Delta L)} \right] + \alpha r \quad \text{(dB)} \tag{3.4.54}$$

This theoretical transmission loss is useful only when a single arrival is received. If multiple arrivals are received and overlap, one must use the summation in $[trans(r,f)]$ and Equation 3.4.39, because the sound pressures add and interfere at the receiving hydrophone.

3.5 Tomography

Tomography (slice writing) uses the differences in speed, or attenuation, along several paths to deduce the properties of different parts of the region between source and receiver. Its earliest application was in three-dimensional studies of human tissue density variation by the differential attenuation of X-rays along many paths through the human body (CAT scan).

On the other hand, ocean acoustical tomography uses the time difference of arrival to infer the speeds of sound along the ray paths. Experimental and synthetic transmissions show that the pattern of sound pressure arrivals varies systematically as the geometry of the experiment is changed. For this reason, sucessful ocean acoustical tomography requires fixed (or correctable) source and receiver positions, strong signals, and a long time series of transmissions. The Heard Island experiments are described briefly in section 1.4.1. A very detailed 18-paper review of that tomography trial was published in the October 1994 issue of The Journal of the Acoustical Society of America (Volume 96, pp. 2327–2484). See also the excellent monograph *Ocean Acoustic Tomography*, by Munk, Worcester, and Wunsch (1995).

3.5.1 INVERTING FOR A MAP OF THE SPEED OF SOUND

The sound that reaches a distant point in the ocean arrives at its destination after sampling the speeds along the way; its relative time delay is an integrated measure of those speeds. For a point source, issuing a short burst of sound, there are multiple bursts of energy that arrive at different times as shown in sections 3.2.3 and 3.3.8. It is the difference in propagation time along these multipaths that is used in a tomography experiment to determine the speeds of propagation within the vertical slice between source and receiver.

Another example of multiple arrivals is shown in Fig. 3.5.1 for a 300 km path (Howe et al. 1987; Munk 1986). The source and receiver were near the channel axis. The sound-speed gradient and channel depth were similar to that shown in the North Atlantic Profile (Fig. 3.3.5). The arrivals are identified by the number of times the energy crosses the channel axis. The (+) rays started in an upward direction at the source; the (−) rays started downward. The +20 ray traveled closest to the channel axis, where the speed was a minimum, so that it arrived last even though its path length was shorter than that of the other rays.

The beautifully clear, unambiguous, and perfectly understandable arrivals discussed in section 3.3.8 are rare. Fig. 3.5.1 is more typical. To be usable, arrivals such as in Fig. 3.5.1 should be *resolvable* — that is, they should be

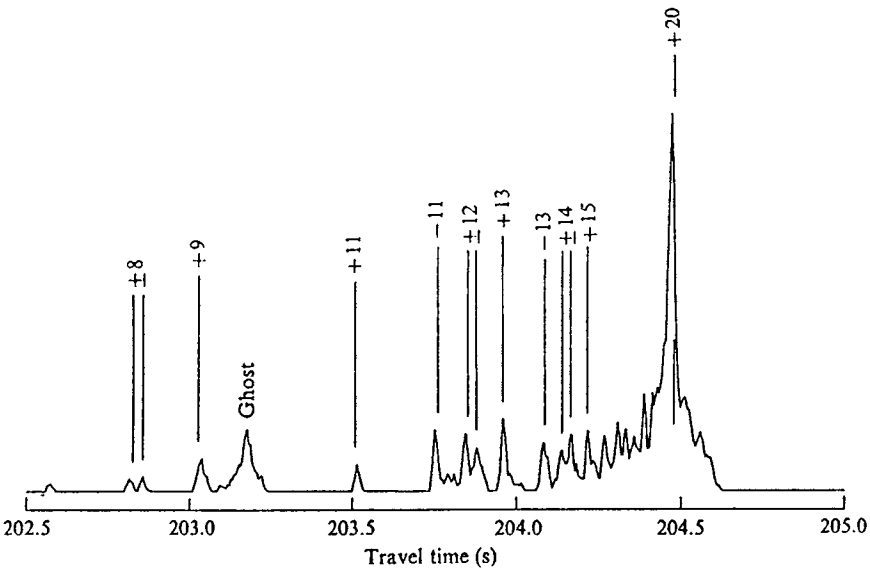

Figure 3.5.1 Measured and computed arrival times of rays at sea. The numbered peaks are identified by the (+) and (−) grazing angle (degrees) at the source. The unidentified peaks were inconsistent and were not used in the analysis. (From Munk, W., "Acoustic monitoring of ocean gyres," *J. Fluid Mech.* **173**, 43–53, 1986.)

sufficiently above the noise and clearly separated in time from other arrivals. The rays that are used in tomography should also be *stable* during times short compared to the duration of the experiment. Finally, the rays should be *identifiable* in terms of the location of the ray path over which they are presumed to have traveled. When these conditions are fulfilled, the time t_i for the ith ray is given by

$$t_i = \Sigma_j R_{ij}/c_j \tag{3.5.1}$$

where c_j is the speed in layer j and R_{ij} is the distance traveled by ray i in layer j.

Equation 3.5.1 is a matrix relation that can be inverted to solve for the "wave slowness," $1/c_j$.

When several transducers are used at different locations, it is possible to observe the medium in three dimensions and to determine movements of ocean eddies or fronts. In the first tomography experiment (1981), four source moorings and five receiver moorings were deployed at 2000 m depth, on the periphery of a 300 km square. This configuration produced evidence of a cold eddy that was first stationary, and then moved out of the monitored volume. Fig. 3.5.2 shows a 30-

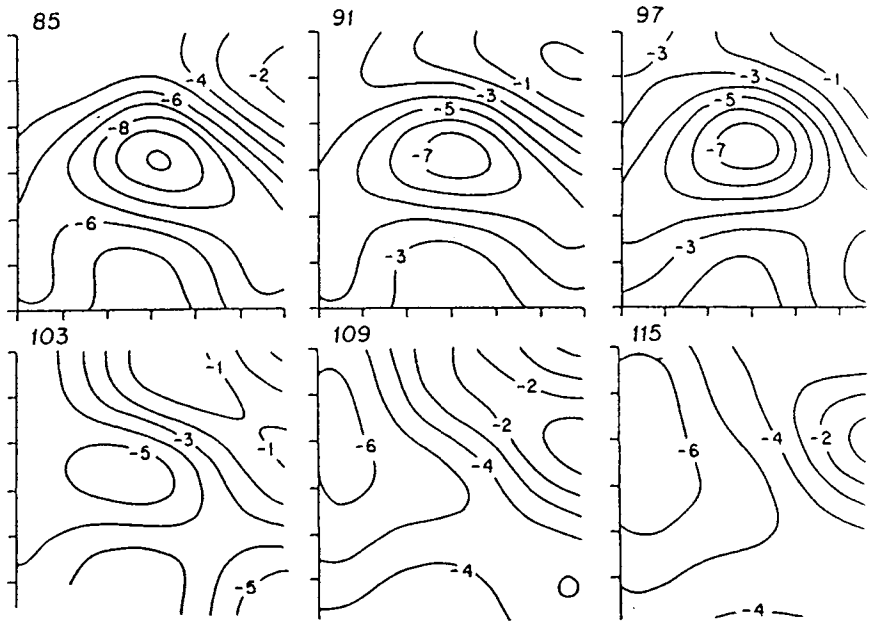

Figure 3.5.2 Movement of a cold eddy, inferred from travel times in the first (1981) tomography experiment. The depth is 700 m; the area is 300 km by 300 km. Constant speed contours (in m/s relative to 1506 m/s) are shown at six-day intervals from Day 85 to Day 115. The cold eddy (low sound speed) is seen to drift to the left. (From Cornuelle, B. D., C. Wunsch, D. Behringer, T. G. Birdsall, M. G. Brown, R. Heinmiller, R. A. Knox, K. Metzger, W. H. Munk, J. L. Spiesberger, R. C. Spindel, D. C. Webb and P. F. Worcester, "Tomographic maps of the ocean mesoscale," *J. Phys. Oceanogr.* **15**, 133–152, 1985.)

day sequence of sound-speed profiles (relative to the reference speed of 1506 m/s) as deduced for 700 m depth. The calculations can be performed for other depths as well.

The precision with which the speeds can be determined depends on the number of rays passing through the unknown region. The effectiveness of the tomographic probe of a slice of the ocean can be improved by using supplementary data such as temperatures or sound speeds as a function of depth, or by utilizing satellite reports of the sea surface temperature (Chiu et al. 1987). Generally, knowledge of the sound-speed profile is sufficient to convert to temperature. However, in polar regions, or near river estuaries, the salinity variations may also be important.

The sound frequency selected for a tomography experiment depends on the scale of the ocean variability that is to be sensed and the range. Lower frequencies, in the hundreds of Hertz, are usable for ranges of hundreds or

thousands of kilometers. Higher frequencies can be employed, consistent with the larger attenuations described in Fig. 3.4.1, for studies over tens of kilometers — for instance, across a bay. However, if the wavelength is comparable to, or smaller than, the ocean inhomogeneities, short-time variability of the microstructure alters the time of arrival.

3.5.2 INVERTING FOR OCEAN MOTIONS

The drift of patches of the ocean between source and receiver may be determined by using a transducer that can be operated to send and receive, or two colocated transducers, at the ends of ray paths. By propagating in opposite directions the sound-speed dependence can be subtracted. The very small differences in travel times for such "reciprocal" sound propagation are then a measure of the ocean currents along the ray path.

When three or more transducers comprise a circuit, reciprocal propagation can be used to calculate the angular momentum (e.g., of an eddy) or the component of vorticity perpendicular to the plane of the transducers. When rays intercept the ocean surface, there are variable time delays, owing to the varying surface heights. These fluctuations can be used to infer characteristics of the surface roughness, as shown by Miller et al. (1989). And by a judicious selection of sets of transducers, and shorter times between pings, it is possible to infer the three-dimensional root-mean-square (rms) displacements and rms currents due to internal waves in a region of the ocean, as demonstrated by Flatte and Stoughton (1986). See also the earlier monograph by Flatte et al. (1979). These and other examples of acoustical oceanography have been attempted, with significant success, in recent years.

3.6 Doppler Frequency Shift

3.6.1 DOPPLER THEORY

Motions of a source, receiver, or scattering object change the frequency of received signals. We assume here that the water is still, and that the propagating signal moves with sound speed c, regardless of the velocities of the source or receiver or scattering objects. A brief review of the Doppler effect follows.

Initially, we consider *source and receiver motions* along the $+x$ axis. The source moving with velocity v_s transmits either a continuous wave or a very long ping of frequency f_s. When the source advances on its own waves, the waves are

shortened, and the apparent wavelength along x is

$$\lambda_a = (c - v_s)/f_s \tag{3.6.1}$$

Also, assume that the receiver has velocity v_r away from the source. In a unit time it detects f_r crests, where

$$f_r = (c - v_r)/\lambda_a \tag{3.6.2}$$

Solve for f_r and obtain

$$f_r = \frac{f_s(c - v_r)}{(c - v_s)} \tag{3.6.3}$$

For both actions, the frequency at the receiver tends to decrease because of the receding receiver (the numerator) and to increase because of the approaching source (denominator). Switching the sense of the movements will change the signs in Equation 3.6.3, of course.

Now consider a *fixed transducer* radiating frequency f_s. A scattering object moving away with velocity v_0 receives a lesser number of crests per second. Therefore, the frequency of sound observed by the receding object is

$$f_0 = f_s(c - v_0)/c \tag{3.6.4}$$

From the point of view of a fixed receiver at the source location, the scattering object becomes a receding source, and the frequency at the transducer is

$$f_r = \frac{f_s(c - v_0)}{(c + v_0)} \tag{3.6.5}$$

In other directions, the velocities in Equation 3.6.5 become the *components* of v_0 along the directions to the source and receiver. For the case in Fig. 3.6.1,

$$f_r = \frac{f_s(c + v_0 \cos\theta_s)}{(c - v_0 \cos\theta_r)} \tag{3.6.6}$$

The Doppler shift may be positive or negative, depending on the geometry and the direction of motion.

3.6.2 DOPPLER MEASUREMENTS OF PARTICLE MOTION

Doppler velocimeters have been used successfully in studies of mixed-layer and upper-ocean dynamics (Pinkel and Smith 1987; Vagle and Farmer 1992), internal waves (Pinkel, Plueddemann, and Williams 1987), and tidal motion (Lhermitte 1983). The platform for the device must either be fixed (e.g., the Floating

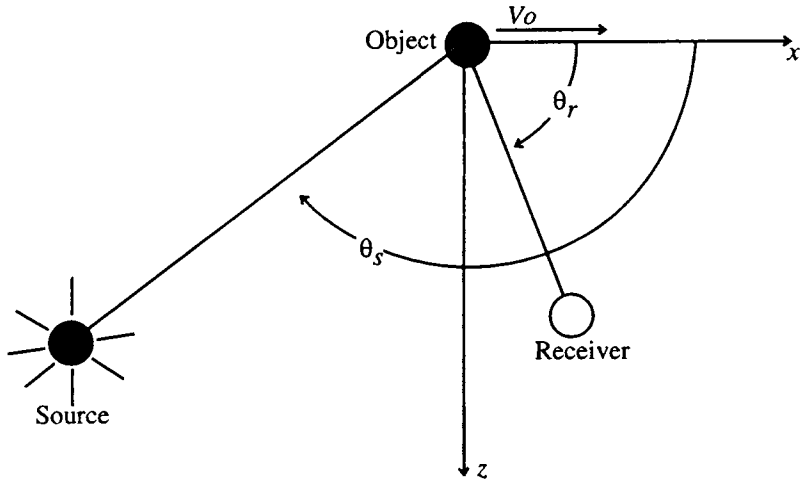

Figure 3.6.1 Doppler effect for an object moving along the x coordinate. Source and receiver at in the x–z plane.

Instrument Platform, FLIP, operated by the Scripps Institution of Oceanography) or have its motion referenced to an inertial frame.

The scatterers that produce the Doppler shift are plankton and detritus, which are found everywhere in the sea. Bubbles are additional Doppler scatterers near the sea surface. These bodies and bubbles, when they are entrained, act as tracers of the moving medium.

Consider the pulse-to-pulse coherent sonar. Two sinusoidal signals are generated at the same frequency but out of phase by 90° (the sin and cos signals). Either one of these is then gated and transmitted. The backscattered Doppler-shifted signal is multiplied by each of these reference signals, and they are then low-pass-filtered. The resulting pair of signals represent the real and imaginary components, which determine the angle of the Doppler phase shift. In the pulse-to-pulse coherent technique, the change of phase from one pulse to the next, at fixed range, is used to calculate the component of the scatterer motion parallel to the beam direction. The great virtue of this technique is that, by pinging millisecond duration pulses many times per second, drift velocities as small as 1 cm/s can be readily measured.

One flaw in the coherent sonar technique is that, if the scatterer were to move by an integral number of wavelengths, the equipment would show no apparent phase shift, and therefore would imply no motion. Also troubling is the

possibility that an echo may have come from a previous pulse, scattered from a larger, more distant body. Signal coding can eliminate that problem.

It is possible to quantify the ambiguity of a pulse-to-pulse *coherent Doppler system*. If the time between pulses is t, the maximum unambiguous range is

$$R_m = c(t/2) \tag{3.6.7}$$

Also, to avoid aliasing, the maximum round-trip distance must change by at most $\lambda/2$ (where λ is the wavelength) between pings. This represents a maximum drift of the medium of $D_m = \lambda/4$. The maximum unambiguous drift velocity for the pulse-to-pulse coherent sonar is then

$$V_m = D_m/t = \lambda/(4t) \tag{3.6.8}$$

The conditions for R_m and V_m are an example of the contradictory uncertainty in their measurements. To decrease the uncertainty in drift velocity, we could increase t, but this would increase the uncertainty in position. In fact, the two conditions can be summarized in the resolution product,

$$V_m R_m = c\lambda/8 \tag{3.6.9}$$

Frequencies of around 100 kHz to 1 MHz are commonly used. The higher frequencies provide smaller values of the resolution product $V_m R_m$. But this improved resolution is achieved at the cost of reduced range, because of the greater attenuation at higher frequencies.

The pulse-to-pulse *incoherent Doppler system* follows the backscatter of a single pulse as its range increases. Doppler shift is estimated from the rate of change of phase with time. The spectrum of the echo is slightly shifted in frequency compared with the outgoing pulse, and the spectrum is rather broad, so that the peak is unclear. Although longer transmitted pulses can be used to improve the narrowness of the spectrum, by the same action the range resolution is deteriorated. In practice, the incoherent Doppler finds its greatest use because of the large ranges possible (kilometers), although the spatial resolution may be as large as many meters (Lhermitte 1983).

3.6.3 SEA-SURFACE MOTION

The sea surface is in constant motion. The water beneath the surface also moves, and the particle velocities are functions of depth. From an elementary oceanography text, the phase velocity for a gravity wave over a bottom at depth d is

$$c_{p,x}^2 = \frac{g}{\kappa_x} \tanh(\kappa_x d) \tag{3.6.10}$$

where g is the gravitational acceleration 9.8 m/s^2. By convention, d is a positive number and coordinate z is positive upward. Depending on $\kappa_x d$, or the ratio of the wave length Λ of the surface wave to the water depth d, water waves are classified as deep-water and shallow-water waves.

Deep-Water Gravity Waves

For the value of $\kappa_x d \gg 1$, the $\tanh(\kappa_x d)$ tends to one, and the phase velocity becomes

$$c_{p,x}^2 \approx \frac{g}{\kappa_x} \tag{3.6.11}$$

and

$$c_{p,x} = \frac{\Omega}{\kappa_x} \tag{3.6.12}$$

The horizontal component of velocity u and the vertical component of velocity w are

$$u = \Omega h \exp(\kappa_x z) \cos(\kappa_x x - \Omega t) \tag{3.6.13}$$

$$w = \Omega h \exp(\kappa_x z) \sin(\kappa_x x - \Omega t) \tag{3.6.14}$$

where κ_x is the horizontal component of the wave number, Ω is the angular frequency, h is the amplitude. The wave particles have circular orbits. In deep water, the magnitudes of the orbits decrease exponentially as depth increases. The group velocity of the deep-water gravity wave is

$$c_{g,x} = c_{p,x} / 2 \tag{3.6.15}$$

The surface tension adds a term as follows:

$$c_{p,x} = \sqrt{\frac{g + \tau \kappa_x^2 / \rho}{\kappa_x}} \tag{3.6.16}$$

where τ is surface tension 0.074 N/m. At short wave lengths, these surface tension waves often appear as ripples following the wave crest.

Shallow Water Gravity Wave

In the limit of small $\kappa_x d$, the expansion of $\tanh(\kappa_x d)$ gives $\kappa_x d$ and Equation 3.6.10 simplifies to

$$c_{p,x}^2 \approx gd \tag{3.6.17}$$

The velocity components of orbital motion are

$$u = \Omega h \cosh[\kappa_x (z + d)] \cos(\kappa_x z - \Omega t) \tag{3.6.18}$$

$$w = \Omega h \sinh[\kappa_x (z + d)] \sin(\kappa_x z - \Omega t) \tag{3.6.19}$$

Doppler Frequency Shifts from the Ocean Surface

Signals scattered at the moving sea surface are shifted in frequency. For a fixed transducer, the amount of the frequency shift is given by Equation 3.6.6. In the back-scatter direction, for $\theta_s = +\theta_r = \theta$ (see Fig. 3.6.1),

$$f_r = \frac{f_s (c + v \cos\theta)}{(c - v \cos\theta)} \tag{3.6.20}$$

Nominally, the Doppler shift from a "smooth" horizontal surface is zero in the specular (mirror) direction. However, when a beam insonifies a real ocean surface, in addition to specular reflection from horizontal facets, some of the scattered components reach the receiver from other parts of the ocean wave system, and these show a Doppler shift. Roderick and Cron (1970) give comparisons of theoretical and experimental Doppler shifts from ocean wave surfaces.

The Doppler shift is a measure of the component of wave velocity along the axis of the sonar system. Usually there are bubbles, zooplankton, and so forth in the water, and these objects scatter sound back to Doppler sonar. The orbital motions of the water carry the objects, which have the velocities given by Equations 3.6.13 and 3.5.14 or 3.6.18 and 3.6.19. Clearly, the results of a Doppler measurement are strongly controled by the location and size of the region being measured. A record of the Doppler shifts versus time will depend on Ω.

3.6.4 DOPPLER NAVIGATION

Doppler navigation systems use the frequency shift of backscattered sound signals to measure the velocity of the ship relative to the bottom, or stationary objects within the water. The algebra is the same as for Equation 3.6.6, and, since $v \ll c$, the frequency shift of the backscattered signal is approximately

$$\Delta f \approx \frac{2 v f_s \cos\theta}{c} \tag{3.6.21}$$

Problems

Section 3.1

3.1.1 From Chapter 5, one learns that there is a maximum acoustic pressure that can be radiated from any source. Near the ocean surface that maximum CW peak source pressure is approximately one atmosphere = 10^5 pascals. Calculate the maximum power output from a point source near (not at) the ocean surface. For simplicity, ignore surface reflection.

3.1.2 From Chapter 5, one learns that the maximum acoustic pressure that can be radiated from any source depends on the *duration* of the signal. Assume that a sinusoidal signal of frequency 7 kHz, duration 100 ms, radiates 6 watts/cm^2 at depth 17 m. Calculate a) the point source pressure (at range 1 m); b) the [*tips*]; c) the energy per unit area at range 10 m.

Section 3.2

3.2.1 Repeat the calculation of Fig. 3.2.3c for a point source radiating a single cycle of a sinusoid of frequency 200 Hz. Assume source depth 5 m, receiver depth 15 m, water depth 20 m, and horizontal range 60 m.

3.2.2 Assume that the source amplitude in the previous problem was 10^4 pascals. Calculate the peak pressure, the [*tips*], and the duration of the interfering signal at the receiver.

Section 3.3

3.3.1 The sound speed profile for a region in the deep sea is approximated by the three linear segments defined by

depth (m)	speed (m/s)
0	1495
500	1495
1000	1485
4000	1520

Compute the paths and travel times of rays leaving the surface at grazing angles 80°, 60°, 30°, 20°, and 10°

3.3.2 Calculate and print out the example in Fig. 3.3.10 on your computer.

Section 3.4

3.4.1 A point source radiates 100 watts of CW acoustic power in homogeneous water. Plot a graph of the rms pressure from 1 m to 1000 m, taking into account attenuation owing to spherical divergence and absorption. Assume that the frequency is a) 1000 Hz, b) 10 kHz, c) 100 kHz, d) Identify the ranges where divergence is the principal source of attenuation for each frequency and the regions where energy absorption is the principal attenuation process.

3.4.2 Near estuaries the salinity varies from zero, in the stream, to close to 35 ppt in the ocean away from the outlet. Plot a curve of the variation of absorption rate with salinity for frequencies 200 Hz, 10 kHz, and 100 kHz.

Section 3.6

3.6.1 A 100 kHz sonar is directed horizontally to insonify a fish. Transmitter and receiver are side by side. The fish is swimming toward the sonar at 12 cm/s. Compute the Doppler shift.

3.6.2 Calculate the frequency shift of a 100 kHz signal aimed at a horizontally swimming fish at 12 cm/s as viewed from the sonar at 10 m below the fish. Assume that the fish is tracked as it approaches, passes overhead, and then receeds from the transducer. Plot a graph of Doppler shift as a function of angle with the vertical.

3.6.3 Derive the Bragg condition for interference scattering of frequency f from a corrugated wave system,

$$(f/c)(\sin\theta_1 - \sin\theta_2) = n/\Lambda$$

where f is the sound frequency; c is the speed of sound; θ_1 and θ_2 are the angles of incidence and scatter; Λ is the surface corrugation wavelength; θ_1 and θ_2 are the angles of incidence and scatter; and n is an integer.

3.6.4 When using a 150 kHz upward-looking sonar at a grazing angle of 30°, a signal with a frequency shift of 1370 Hz is backscattered from a corrugated surface wave. a) What is the velocity of the surface wave along the direction of the sonar?; b) In what directions does one see a maximum of scatter (see previous problem)?

Chapter 4 | Sources and Receivers

4.1 Transducer Elements 127
4.1.1 The Pulsating Sphere 127
4.1.2 Sources of Sound 128
4.1.3 The Dipole 130
4.1.4 Materials and Mechanisms 131
4.2 Arrays of Discrete Sources 133
4.3 Directivity of a Line Source 135
4.4 Circular Piston Source 138
4.4.1 Far-Field Directivity 138
4.4.2 Near-Field 142
4.5 Radiation from a Transducer 143
4.5.1 Total Power Radiated 143
4.5.2 Descriptors of Beam Strength 145
4.6 Equivalence of Source/Receiver Directivity 146
4.7 Free-Field Calibration of Transducers 149
4.8 Self-Reciprocity Calibration of Transducers 150

For theoretical developments, it is often assumed that the source is a pulsating sphere. Typically, it is also assumed that the sound receiver is a device sensitive to acoustic pressure. In fact, sources and receivers, "transducers," have been designed with a wide range of physical, geometrical, acoustical, and electrical characteristics. Proper selection of a transducer element, or an array of elements, can provide increased sensitivity to certain frequencies or to specific directions of propagation. Furthermore, the effectiveness of either a hydrophone or sound source is a function of its physical mounting and the electrical circuit to which it is connected.

4.1 Transducer Elements

4.1.1 THE PULSATING SPHERE

At this point we make the "connection" between a source and the sound field that it radiates. Again, consider the pulsating sphere. The instantaneous radial velocity u_r at the sphere surface, $R = a$ is described by

$$u_r]_{R=a} = U_a e^{i\omega t} \tag{4.1.1}$$

where U_a is the amplitude of the sphere radial velocity.

From section 2.7.3, the isotropic radiated presssure at range R is

$$p = \frac{P_0 R_0 \exp[i(\omega t - kR)]}{R} \tag{4.1.2}$$

In section 2.7.3 we also derived Equation 2.7.46, the radial particle velocity of the acoustic field. At $R = a$, the particle velocity is

$$u_r]_{R=a} = \frac{P_0 R_0 \exp[i(\omega t - ka)]}{a\rho_A c}\left(1 - \frac{i}{ka}\right) \tag{4.1.3}$$

Equate the two expressions for u_r at $R = a$ and thereby obtain an expression for $P_0 R_0$. Insert that value into Equation 4.1.2 to give the acoustic pressure in the "monopole" field in terms of the source parameters

$$p = \frac{ik(\rho_A c)\dot{V} \exp[i(\omega t - kR + ka)]}{4\pi R(1 + ika)} \tag{4.1.4}$$

where $\dot{V} = 4\pi a^2 U_a$.

One concludes that

(1) for a constant source velocity amplitude, the radiated pressure is proportional to the sound frequency of the CW source;

(2) for a given CW frequency, the radiated acoustic pressure is proportional to the amplitude of the source rate of volume flow $4\pi a^2 U_a$ (m^3/sec);

(3) for the same volume flow and sound frequency, the radiated sound pressure is proportional to the $\rho_A c$ of the medium (e.g. since the $\rho_A c$ of water is about 5000 times the $\rho_A c$ of air, an underwater sound source is a very ineffective source of sound in air).

4.1.2 SOURCES OF SOUND

The pulsating sphere is a prototype of some simple underwater sound sources. In fact, Sims (1963) describes a low frequency, high-power, gas-filled bag that is a realization of the pulsating sphere described in the previous section. In addition, as will be seen in Chapter 8, when bubbles are formed at sea, they act as natural pulsating spheres.

But we need a more general answer to the question "What causes a sound to be radiated?" For an answer, reconsider the derivation of the wave equation in section 2.7 by accepting that at a sound source point of the medium there can be

an injection (or removal) of mass or momentum. This occurs not only in the case of the pulsating sphere but also for a siren, and almost all other sources as well. When there is a source or sink of mass, the acoustic conservation of mass equation becomes

$$\nabla \cdot (\rho \boldsymbol{U}) + \frac{\partial \rho}{\partial t} = \frac{\partial m}{\partial t} \tag{4.1.5}$$

where $\partial m/\partial t$ is the rate of injection of mass per unit volume, m.

Likewise, the acoustic equation of conservation of momentum is modified to accept the fact that momentum can be impressed by the source on the medium. This is the situation when an oscillating source is not baffled, so that during oscillation there is mass ejected at one end of the source at the same time that mass is injected at the other end; the net result is a momentum transfer to the medium. Where this occurs, the acoustic conservation of momentum equation becomes

$$\nabla p + \rho_A \frac{\partial \boldsymbol{U}}{\partial t} = \boldsymbol{f} \tag{4.1.6}$$

where $\boldsymbol{f}$ is the force (i.e., rate of injection of momentum) per unit volume. (The *vector* force per unit volume, $\boldsymbol{f}$, should not be confused with the *scalar* sound frequency, f.)

To obtain the wave equation with source terms, take the divergence of Equation 4.1.6 and the partial derivative with respect to time of Equation 4.1.5, combine with the acoustical equation of state, and

$$\nabla^2 p - \frac{1}{c^2}\frac{\partial^2 p}{\partial t^2} = -\frac{\partial^2 m}{\partial t^2} + \nabla \cdot \boldsymbol{f} - \nabla \cdot [\rho(\boldsymbol{U} \cdot \nabla)\boldsymbol{U} + \boldsymbol{U}(\nabla \cdot \rho \boldsymbol{U})] \tag{4.1.7}$$

The terms on the right are the mechanical sources of the radiated acoustic pressure. They consist of

(1) the acceleration of mass per unit volume;

(2) the spatial rate of change (divergence) of force per unit volume exerted on the medium;

(3) a nonsimple third term, which is the double divergence of what hydrodynamicists designate as the "Reynold's stress tensor." This term is acoustically important only as the source of noise owing to turbulence. It is particularly important in air, where it explains the noise caused by the turbulence of a jet aircraft exhaust.

An extended interpretation of Equation 4.1.7 will be found in Lighthill (1978). The various waves that can be produced by a complicated source are described in

the expansion of the wave equation in spherical coordinates. In this context, the first term on the right of Equation 4.1.7, the injected mass source, is sometimes called a monopole source of sound (e.g. the pulsating sphere). In designing a mounting for a transducer, if radiation from the back of the transducer is prevented from propagating into the medium, either by a baffle, an enclosure, or absorption, only the monopole term remains. In that case the radiated energy is not deteriorated by the back radiation.

The second term on the right-hand side of Equation 4.1.7 is most simply interpreted as a dipole source; its prototype is discussed in the next section.

4.1.3 THE DIPOLE

A dipole is the combination of two equal-amplitude, out-of-phase monopoles with a small separation (*re* λ) between them. The dipole occurs, for example, in the case of an unbaffled oscillating membrane which simultaneously creates a condensation at one face and a rarefaction at the other. When the membrane oscillation reverses, the condensation is replaced by a rarefaction, and the rarefaction by a condensation. When the membrane is in a rather small baffle, $kl \ll 1$, where l is the effective separation between the two sides, a dipole exists. Physically, it can be seen that the two out-of-phase radiations will completely cancel each other along a plane perpendicular to the line joining the two poles; the radiation from the two poles will partially cancel each other everywhere else. The idealized dipole is shown in Fig. 4.1.1.

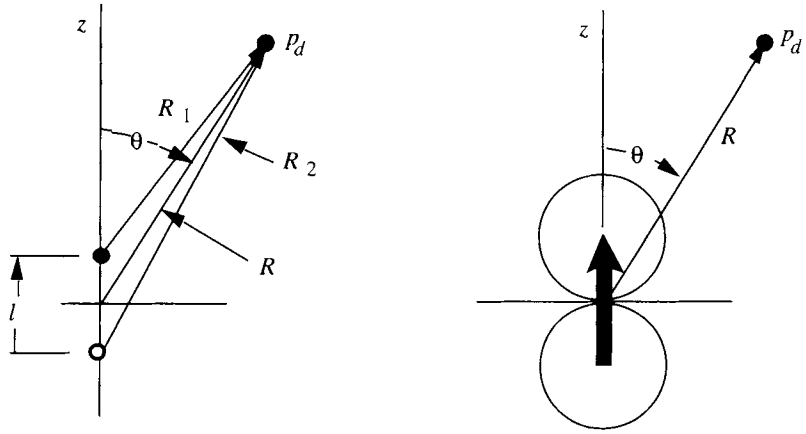

Figure 4.1.1 The idealized dipole source. Two point sources of equal strength but opposite phase are separated by a distance l, much less than a wavelength. The far-field directionality is a figure-eight pattern in polar coordinates.

Call the summation, the dipole pressure $p_d = p_+ + p_-$, and obtain it by using two out-of-phase components of the pressure of a spherical wave from a point source. The addition is

$$p_d = P_0 R_0 \left\{ \frac{exp\,[i\,(\omega t - k R_1)]}{R_1} - \frac{exp\,[i\,(\omega t - k R_2)]}{R_2} \right\} \qquad \textbf{(4.1.8)}$$

For ranges large compared with the separation l, use the Fraunhofer approximation Equation 2.4.12 to write

$$R_1 \simeq R\left(1 - \frac{l}{2R} cos\,(\theta)\right) \; and \; R_2 \simeq R\left(1 + \frac{l}{2R} cos\,(\theta)\right) \qquad \textbf{(4.1.9)}$$

As expected for an interference effect, the small differences between R_1 and R_2 in the denominators of Equation 4.1.8 are not important, and each may be approximated by R. But the terms kR_1 and kR_2 in the exponentials, which determine the phases and the interference, are crucial. After factoring out the common terms, $1/R$ and $\exp[i(\omega t - kR)]$, and expanding the remaining imaginary exponentials for the dipole condition $kl \ll 1$, we obtain

$$p_d = \frac{P_0 R_0}{R} e^{i(\omega t - k R)} \{ i\,k\,l\,cos\,(\theta) \} \qquad \textbf{(4.1.10a)}$$

which is recognized as the monopole pressure multiplied by $\{ikl \cos\theta\}$.

When attenuation is included, this becomes

$$p_d = \frac{P_0 R_0}{R} e^{i(\omega t - k R)} [i\,k\,l\,cos\,(\theta)]\, 10^{-\alpha R / 20} \qquad \textbf{(4.1.10b)}$$

The dipole has produced two significant effects compared with the individual monopole radiations. First, the radiated pressure has been reduced because of the small factor kl. Second, the radiation pattern is no longer isotropic; it now has a directionality given by $\cos\theta$, where θ is the angle with the dipole axis. That is, there is a maximum (but very much reduced) acoustic pressure along the line of the dipole, and there is zero sound pressure in the central plane perpendicular to the dipole line. The directionality is sometimes called a figure-eight pattern because of the way the cosine looks when it is plotted in polar coordinates (Fig. 4.1.1).

4.1.4 MATERIALS AND MECHANISMS

Now a few words about the electro-acoustical materials that are being used for modern transducers. Experimentalists who have specific needs in selecting or designing their transducers should consult a transducer manufacturer or a book on the subject, such as Wilson (1985) or Bobber (1970).

The most common material used for underwater transducers is the polycrystalline, "piezoelectric" material barium titanate ($BaTiO_3$), which was discovered in the 1940s. A piezoelectric material shows a voltage across electodes when subjected to pressure (sound receiver) or changes in dimension when a voltage is appplied (sound source). In the manufacture, the granular material is fused into a ceramic-like block (which looks like the ceramic of a coffee mug). Electrodes are applied to selected surfaces of blocks of any desired shape. The blocks are heated to a temperature (Curie Point, approximately 120° C) at which the minute crystals become cubic. A DC polarizing voltage is applied, and, as the element is cooled, the block becomes an assemblage of tetrahedron crystals with a preferred axis. Depending on the electrode orientation, this causes the material to be piezoelectric for shear or compression. The addition of other chemicals to the barium titanate (e.g., lead zirconate) can lead to specific design advantages as a source or receiver.

Because the electrical polarization properties of the material follow a hysteresis loop (resembling a ferromagnetic material) when an electric field is applied and reversed, the materials are called ferroelectrics. A major advantage of the ferroelectric ceramic is that it can be formed into a large variety of sizes and shapes to fit the particular array design. Transducer manufacturers (e.g., Channel Industries, Santa Barbara, California) have developed elements in various sizes and in the forms of cylinders, rods, tubes, disks, plates, hemispheres, and so forth.

Magnetostrictive transducers depend on the physical phenomenon of certain ferromagnetic materials such as nickel, which expand or contract when a magnetic field is applied. Since the change of dimension (contraction or expansion) is independent of the direction of the current that is creating the magnetic field, there is a frequency doubling when an AC signal is applied. (Note that a noisy 60-cycle power transformer radiates a sound of frequency 120 Hz.) This may be avoided by superimposing the AC signal over a larger DC polarizing field. Magnetostrictive devices have been particularly effective as low-frequency sound sources because at lower frequencies there is less loss caused by hysteresis.

A large variety of piezoelectric plastics (e.g., polyvinylidene fluoride, PVDF) and new electrostrive, ferroelectric, and magnetostrictive materials and composites are now being used as transducer elements. There are unusual configurations such as benders and segmented cylinders, as well as mushroom-shaped (*Tonpilz*) mechanical oscillators for low frequencies. A promising fiber-optic flextensional hydrophone has been patented (Brown 1994). The latest copies of the technical literature must be researched for these rapidly changing developments.

4.2 Arrays of Discrete Sources

The sound pressure produced by an array of discrete sources such as in a multielement sound source is readily adapted to computer summations. For example, assume there are N sources evenly spaced over a distance W in a straight line along the y axis (Fig. 4.2.1). The separation between adjacent elements is

$$b = \frac{W}{N-1} \tag{4.2.1}$$

The pressure p_n of the nth source at distance R and angle θ is

$$p_n = \frac{a_n P_0 R_0}{R_n} \exp\left[i\left(\omega t - kR + \frac{nk W \sin\theta}{N-1}\right)\right] 10^{-\alpha R/20} \tag{4.2.2}$$

where a_n is a dimensionless amplitude factor of the nth source; θ is the angle with the z axis, which is perpendicular to the line array (Fig. 4.2.1); and α is the rate of attenuation in the medium.

In the spirit of the Fraunhofer far-field approximation, let R_n in the denominator become simply R. Also at long range, since $\omega t - kR$ is common to all signals, we factor it out and obtain the pressure in terms of the transducer directional pressure response D_t:

$$p = D_t \frac{P_0 R_0}{R} \exp[i(\omega t - kR)] 10^{-\alpha R/20}, \quad R \gg W \tag{4.2.3}$$

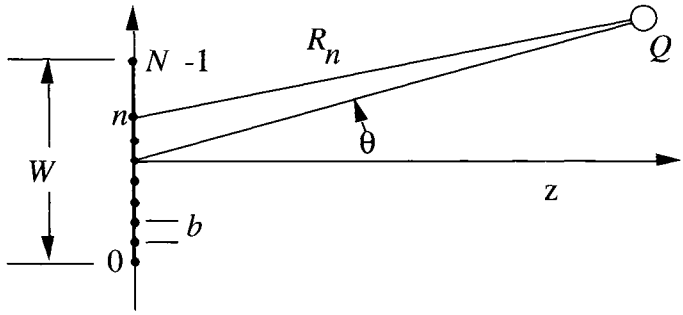

Figure 4.2.1 Geometry for the directivity of a straight line of discrete sources.

where D_t represents the "directional response," the "directivity function," or, simply, the "directivity" of a transducer or an array of transducers:

$$D_t \equiv \sum_{n=0}^{N-1} P_n \exp\left(i \frac{nkW \sin\theta}{N-1}\right) \tag{4.2.4}$$

This can be written in the form $D_t = A + iB$, where

$$A = \sum_{n=0}^{N-1} a_n \cos\left(\frac{nkW \sin\theta}{N-1}\right) \tag{4.2.5}$$

and

$$B = \sum_{n=0}^{N-1} a_n \sin\left(\frac{nkW \sin\theta}{N-1}\right) \tag{4.2.6}$$

Then the magnitude of the array directivity is found from

$$D_t = A + iB \quad \text{and} \quad |D_t| = (A^2 + B^2)^{1/2} \tag{4.2.7}$$

The a_n are relative amplitudes of the transducer elements. It is often convenient to normalize the a_n by setting

$$\sum_{n=0}^{N-1} a_n = 1 \tag{4.2.8}$$

Proper choices of the contributions by elements of the array whose amplitudes are P_n can improve array performance. The simplest equally driven arrays have

$$a_n = 1/N \tag{4.2.9}$$

However, other choices of the contributions by elements of the array can improve array performance. Generally, the improvements desired are either to reduce the side lobes or to narrow the central lobe.

When the functional dependence on θ is included, the directivity of a symmetrical array with an odd number of elements is

$$D_t(\theta) = a_0 + 2 \sum_{n=0}^{N_h} a_n \cos\left(\frac{nkW \sin\theta}{N-1}\right) \tag{4.2.10a}$$

where

$$N_h = \frac{N-1}{2} \tag{4.2.10b}$$

Two common weightings of elements are

$$\text{triangular:} \quad a(n) = a(-n) = (N_h - n)/N_h \tag{4.2.11}$$

$$\text{cosine:} \quad a(n) = a(-n) = (1 + \cos(\pi n/N_h) \tag{4.2.12}$$

where Equations 4.2.11 and 4.2.12 can be normalized by using Equation 4.2.8.

Another weighting choice that is very popular because it often makes theoretical computations more tractable and convergence more rapid, and because it has no side lobes, is the so-called Gaussian directivity:

$$D_{tG}(\theta) = \exp[-(kW_G)^2(\sin^2\theta)/4] \tag{4.2.13}$$

where W_G is the width parameter. One determines the $\theta_{1/2}$ for an array directivity $D(\theta)$ at its "half-power" response, $(1/2^{1/2}) = 0.707$, and solves for W_G in the expression

$$\exp[-(kW_G)^2 \sin^2(\theta_{1/2})/4] = D(\theta_{1/2}) = 0.707 \tag{4.2.14}$$

These types of "weighting" can also be applied to rectangular, circular, and other arrays.

The examples of linear, triangular, cosine, and Gaussian array directivities shown in Fig. 4.2.2 demonstrate the rule that, for the same number of elements, weightings that decrease the side lobes also widen the main beam.

4.3 Directivity of a Line Source

The integration of a continuous distribution of point sources along a straight line yields a line source. As shown in Fig. 4.3.1, let the array be many discrete *sourcelets* at very close spacing over a line of length W. Replace the summation by an integration. The strength of a differential sourcelet is proportional to dy/W. Let p be the resulting sound pressure in the local field region.

In the Fraunhofer plane wave approximation, the path difference from the sourcelet at origin 0 and that at y is $y \sin\theta$. The differential pressure dp owing to a sourcelet at y is

$$dp = (dy/W)P \exp[i(\omega t - kR + ky \sin\theta)] \tag{4.3.1}$$

The pressure is calculated by the integration from $-W/2$ to $W/2$ of

$$p = PD_t \exp[i(\omega t - kR)] \tag{4.3.2}$$

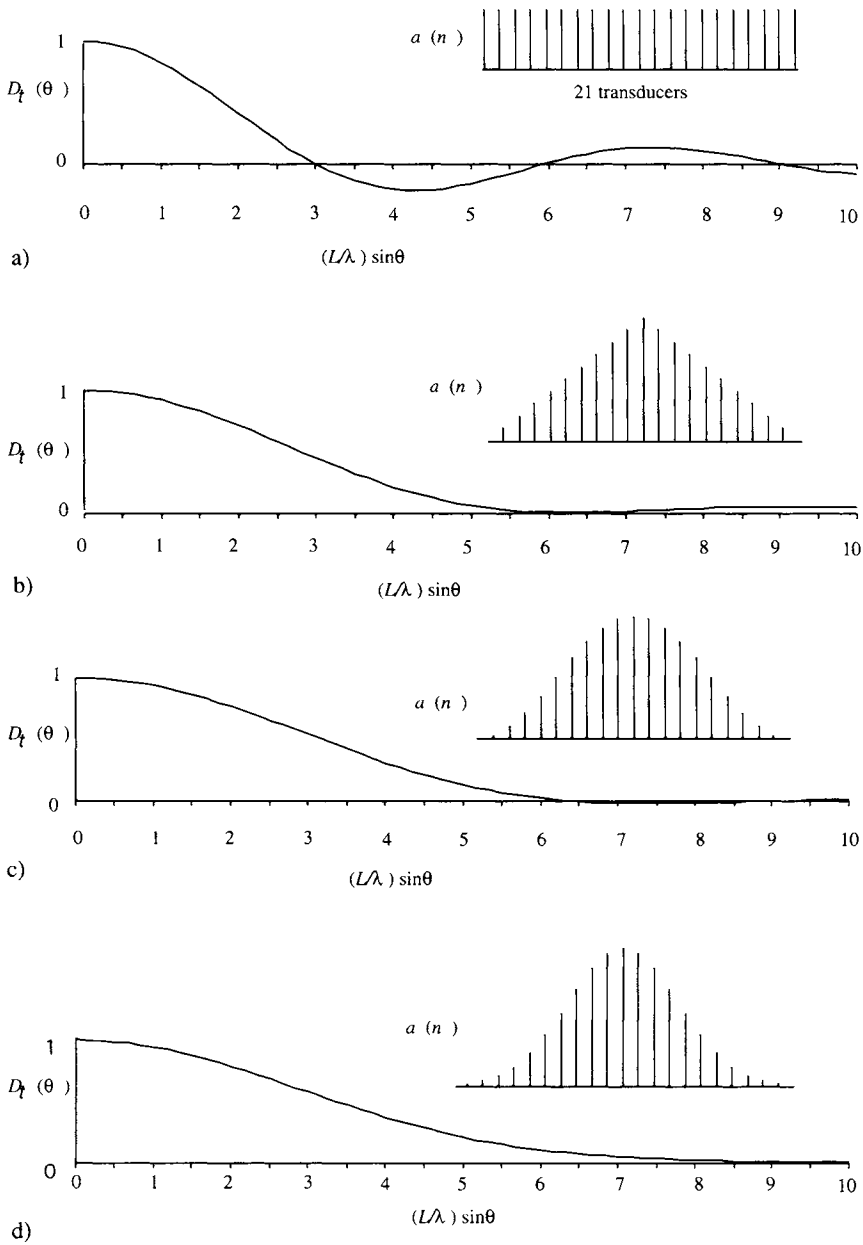

Figure 4.2.2 Examples of array directivities for four common weightings: a) uniform, b) triangular, c) cosine, and d) Gaussian. Angle θ is measured to the normal to the line of elements, the transducer axis z.

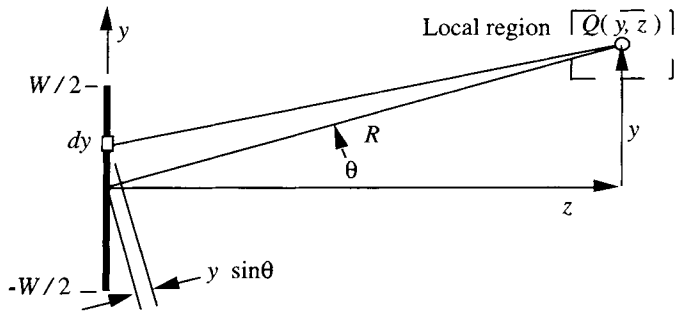

Figure 4.3.1 Construction for a continuously distributed source at large range.

where

$$D_t = \frac{1}{W}\int_{-W/2}^{W/2} \exp\left[i(\omega t - ky\sin\theta)\right] dy \tag{4.3.3}$$

Integration gives

$$D_t = \frac{1}{W}\,\frac{\exp\left(iky\sin\theta\right)}{ik\sin\theta}\,\Bigg|_{-W/2}^{W/2} \tag{4.3.4}$$

Evaluation for the limits of integration gives

$$D_t = \frac{1}{W}\,\frac{\exp\left[(ikW\sin\theta)/2\right] - \exp\left[(-ikW\sin\theta)/2\right]}{ik\sin\theta} \tag{4.3.5}$$

The expression for D_t reduces to

$$D_t = \frac{\sin\left[kW\sin\theta)/2\right]}{(kW\sin\theta)/2} \tag{4.3.6}$$

The preceding expression has the form $(\sin F/F)$, which is sometimes called the *sinc* function. Since the *sinc* is indeterminate as F tends to zero, the directivity D_t at zero is evaluated by forming the derivatives

$$\lim_{F\to 0}\frac{(d/dF)\sin F}{(d/dF)F} = \lim_{F\to 0}\frac{\cos F}{1} = 1 \tag{4.3.7}$$

The *sinc* function is shown in Fig. 4.3.2a in a linear graph, and in Fig. 4.3.2b in polar coordinates for the case $F = (kW\sin\theta)/2$ when the source extent $W = 4\lambda$. In the polar pattern, the length of the radius vector is proportional to the directional response at that angle and, although the source is sketched in, the directivity is applicable only at long ranges from the source. The important sinc function specifies the directional response not only of a line source but of a line receiver as well.

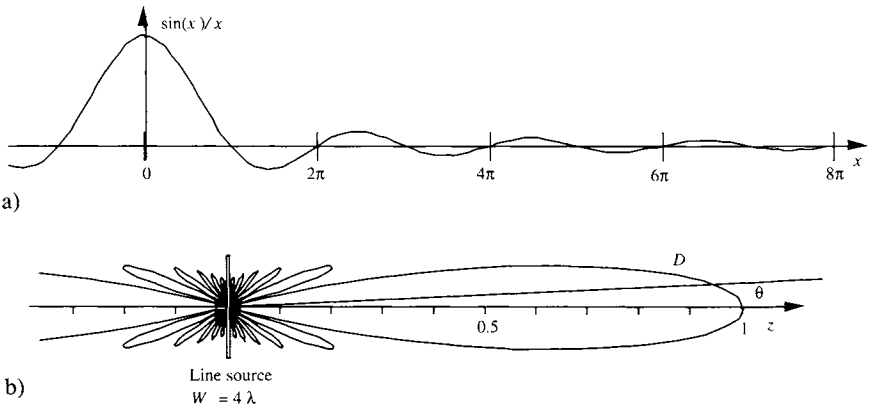

Figure 4.3.2 Far-field radiation from a line source. a) The $(\sin F)/F$ function. b) Directional response, $|D|$ versus angle for a uniform line source, where $F = (kW \sin\theta)/2$ with $W = 4\lambda$. The angle θ is measured from the normal to the line source.

We have given this analysis for point sources aligned in the y direction. We can do the same for sources in the x direction. If each of the dy sources on the y axis were a line of sources along the x axis, a rectangular source would be formed. The resulting directional response would be the product of the directional responses for the x and y directions.

Such a source is called a rectangular "piston source" when the individual elements within the source plane are very close together and have the same amplitude and phase. The function is the same for a receiver. The sinc function comes up again in the scattering of sound from a rectangular plane segment.

4.4 Circular Piston Source

4.4.1 FAR-FIELD DIRECTIVITY

The geometry for a circular piston transducer is given in Fig. 4.4.1. We are interested in the directivity so we suppress the absolute pressure term and the propagation term $\exp[i(\omega t - kR)]$ and consider only the dependence on the "latitude" θ. It is assumed that the piston is in an infinite baffle (or enclosed), so that there is no back radiation, which would produce a dipole term.

The field pressure will depend on an areal integration of the elements $2y\,dx$ in the plane of the source (rather than along the length for the line source in Fig. 4.3.1). In this Fraunhofer far-field approximation, the range to any element is

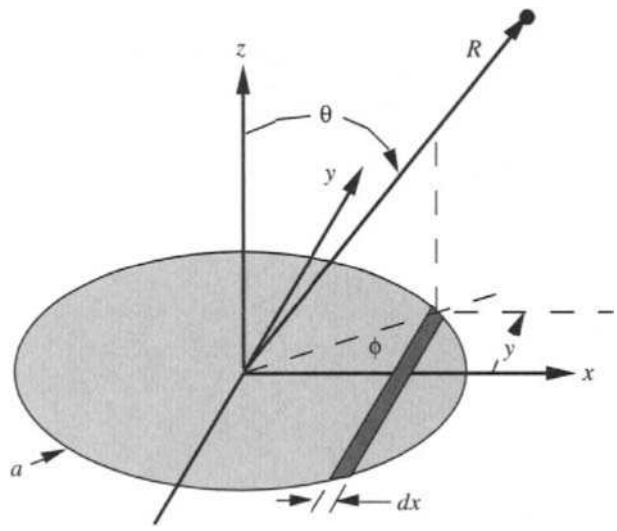

Figure 4.4.1 Geometry for calculation of radiation from a circular piston transducer.

approximately R. When spherical divergence aned medium attenuation are included,

$$p = \frac{P_0 R_0}{R} 10^{-\alpha R/20} \frac{2}{\pi a^2} \int_{-a}^{a} y \cos(kx \sin\theta)\, dx \tag{4.4.1}$$

Define the directional response D_t as

$$D_t \equiv \frac{2}{\pi a^2} \int_{-a}^{a} y \cos(kx \sin\theta)\, dx \tag{4.4.2}$$

Change Equation 4.4.1 to polar coordinates $x = a\cos\phi$ and $y = a\sin\phi$ and obtain

$$D_t = \frac{2}{\pi} \int_0^{\pi} \cos(\zeta \cos\varphi) \sin^2\varphi\, d\varphi \tag{4.4.3}$$

where we use $\zeta = ka\sin\theta$ to agree with the form of the cylindrical Bessel Function in Abramowitz and Stegun (1964), which is written

$$J_1(\zeta) = \frac{\zeta}{\pi} \int_0^{\pi} \cos(\zeta \cos\varphi) \sin^2\varphi\, d\varphi \tag{4.4.4}$$

Using our value of ζ, Equation 4.4.3 and 4.4.4 give the directional response for a circular piston source:

$$D_t = \frac{2J_1(ka\sin\theta)}{ka\sin\theta} \tag{4.4.5}$$

The complete expression for the radiated pressure for a circular piston source has the same form as for a rectangular piston source, but with the different directivity factor as given by Equation 4.4.5. Table 4.1 presents numerical values of the relative pressures and intensities of the circular piston directivity factor.

Table 4.1 **Values of the Circular Piston Pressure Directivity function D_t and Intensity Directivity D_t^2 (in terms of $z = ka\sin\theta$)**

z	$\frac{2J_1(z)}{z}$	$\left[\frac{2J_1(z)}{z}\right]^2$	z	$\frac{2J_1(z)}{z}$	$\left[\frac{2J_1(z)}{z}\right]^2$
0.0	1.0000	1.0000	7.0	−0.0013	0.00000
0.2	0.9950	0.9900	7.016	0	0
0.4	0.9802	0.9608	7.5	+0.0361	0.0013
0.6	0.9557	0.9134	8.0	0.0587	0.0034
0.8	0.9221	0.8503	8.5	0.0643	0.0041
			9.0	0.0545	0.0030
1.0	0.8801	0.7746	9.5	0.0339	0.0011
1.2	0.8305	0.6897			
1.4	0.7743	0.5995	10.0	+0.0087	0.00008
1.6	0.7124	0.5075	10.173	0	0
1.8	0.6461	0.4174	10.5	−0.0150	0.0002
			11.0	−0.0321	0.0010
2.0	0.5767	0.3326	11.5	−0.0397	0.0016
2.2	0.5054	0.2554	12.0	−0.0372	0.0014
2.4	0.4335	0.1879	12.5	−0.0265	0.0007
2.6	0.3622	0.1326			
2.8	0.2927	0.0857	13.0	−0.0108	0.0001
			13.324	0	0
3.0	0.2260	0.0511	13.5	+0.0056	0.00003
3.2	0.1633	0.0267	14.0	0.0191	0.0004
3.4	0.1054	0.0111	14.5	0.0267	0.0007
3.6	0.0530	0.0028	15.0	0.0273	0.0007
3.8	+0.0068	0.00005	15.5	0.0216	0.0005
3.832	0	0			
			16.0	0.0113	0.0001
4.0	−0.0330	0.0011	16.471	0	0
4.5	−0.1027	0.0104	16.5	−0.0007	0.00000
5.0	−0.1310	0.0172			
5.5	−0.1242	0.0154	17.0	−0.0115	0.00013
6.0	−0.0922	0.0085	17.5	−0.01868	0.00035
6.5	−0.0473	0.0022			

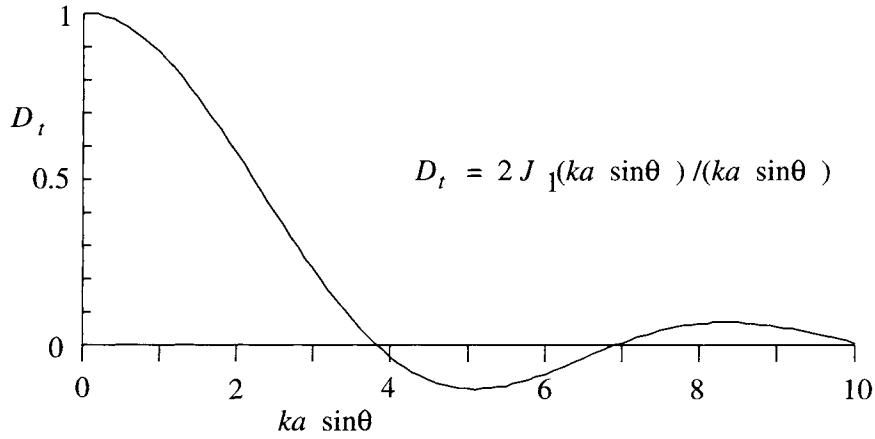

Figure 4.4.2 Directional response of a circular piston transducer.

A linear graph of Equation 4.4.5 is shown in Fig. 4.4.2. The central lobe of the radiation is down to fractional pressure $2^{-1/2} = 0.707$ (i.e. half-intensity) at $ka \sin\theta \cong 1.6$. The central lobe reaches zero at $ka \sin\theta = 3.83$. The first side lobe is 180° out of phase with the central lobe and shows a peak of sound pressure and intensity at $ka \sin\theta \cong 5.0$.

Directivity functions of a circular piston are shown in polar coordinates in Fig. 4.4.3. The pattern begins to resemble a searchlight beam only when ka is quite large.

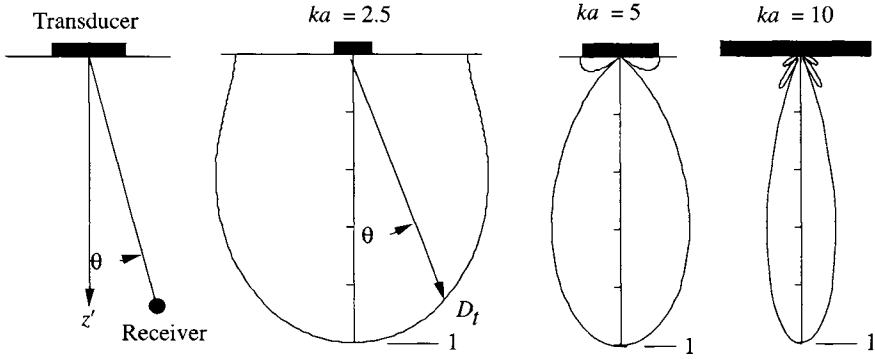

Figure 4.4.3 Polar coordinate graphs of directivity patterns of circular piston transducers for four values of ka.

4.4.2 NEAR-FIELD

The circular piston–radiated pressure field at great distance ($kR \gg 1$), which was derived in the previous section, has been known for a long time. But it was the advent of high-speed computers that permitted the calculation of the very complicated acoustic field closer to the source. Fig. 4.4.4 is an early three-dimensional plot of the pressure field near a circular piston source of size $a/\lambda = 2.5$. There is an inner circle of very high pressure at the face of the transducer and two somewhat lesser-pressure amplitude rings out toward the periphery of the radiating disk. Along the axis of the source the pressure amplitude is an oscillating function of range until it reaches a maximum, which turns out to be at $R \cong a^2/\lambda$. Beyond that range the pressure decreases into the far field. An increase in the ratio a/λ increases the number of pressure maxima and minima over the face of the source and along the axis. The maxima of these pressures on the face of the source can be very much higher than the average, so that destructive cavitation (see section 5.2) may take place at local "hot spots," although the average pressure implies that there is no problem.

The complex "near field" is caused by constructive and destructive interferences of the radiation from different subareas of the transducer face.

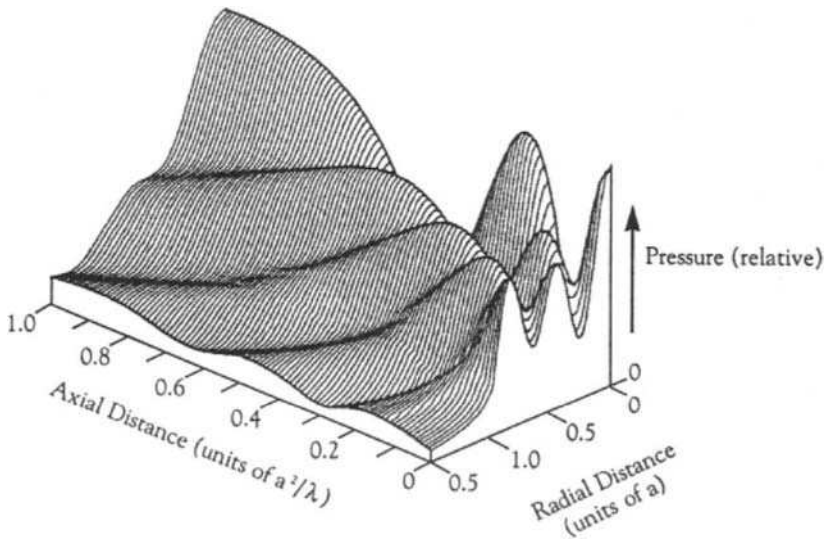

Figure 4.4.4 Three-dimensional plot of relative pressure amplitude in the near field of a circular piston of size $a/\lambda = 2.5$ $ka = 5\pi$. (Lockwood, J. C., and J. G. Willette, "High-speed method for computing the exact solution for the pressure variations in the near field of a baffled piston," *J. Acoust. Soc. Am.* **53**, 735–41, 1973.)

Near the source, these radiating wavelets may differ in travel path by $\lambda/2$ and cause almost complete cancellation of the sound pressure (see section 2.4.1). Along the axis of the transducer, a critical range R_c exists at a range where it is no longer possible for wavelets traveling the longest path (from the rim of the piston) to interfere destructively with those traveling the shortest path (from the center of the piston). It is left as a simple problem for the reader to show that, for a circular piston source, this path difference, beyond which there can be no near-field axial minimum, is

$$R_{\text{rim}} - R_{\text{axis}} \cong a^2/(2R_c) < \lambda/2 \tag{4.4.6a}$$

from which a critical distance is

$$R_c \cong a^2/\lambda \tag{4.4.6b}$$

The range at which the experiment is "safely" in the far field, so that the pressure varies "essentially" as R^{-1}, is somewhat arbitrary. Often the far field for the circular piston is defined as beginning at the greater critical range, $\pi a^2/\lambda$.

4.5 Radiation from a Transducer

4.5.1 TOTAL POWER RADIATED

The total acoustic power output by a CW point source radiating into 4π radians of solid angle is given in section 3.1.4. Computation of the total radiated power when the pressure amplitude directional response is $D_t(\theta, \phi)$ is a simple adaptation of that calculation.

The incremental "message" power passing through an increment of surface ΔS, in terms of the pressures $P(R)$ or $P_{ax}(R)$ at the field range, R, is

$$\Delta \Pi_M = \frac{P^2}{2\rho_A c} \Delta S(R, \theta, \varphi) \tag{4.5.1a}$$

where

$$P(R) = P_{ax}(R) D_t(\theta, \varphi) \tag{4.5.1b}$$

or, in terms of the reference pressure P_0 at axial reference range R_0,

$$\Delta \Pi_M = \frac{P_0^2 R_0^2}{2\rho_A c R^2} D_t^2(\theta, \varphi) 10^{-\alpha R/10} \Delta S(R, \theta, \varphi) \tag{4.5.1c}$$

where the medium attenuation is included.

Using the coordinates sketched in Fig. 4.4.1, the increment of area ΔS can be written as

$$\Delta S = R^2 \sin\theta \, d\theta \, d\phi \tag{4.5.2}$$

An integration over all angles gives the total radiated power Π_M. Typically the transducer is enclosed so that there is no back radiation. Then the θ integration limits are 0 to $\pi/2$,

$$\Pi_M = \frac{P_0^2 R_0^2}{2\rho_A c} 10^{-\alpha R/10} \int_0^{\pi/2} \sin\theta \, d\theta \int_0^{2\pi} D_t^2(\theta, \phi) \, d\varphi \tag{4.5.3}$$

The double integral over the angles appears often. It is called the *integrated beam pattern* ψ_D. For an enclosed transducer ψ_D is defined as

$$\psi_D \equiv \int_0^{\pi/2} \sin\theta \, d\theta \int_0^{2\pi} D_t^2(\theta, \phi) \, d\phi \tag{4.5.4}$$

In general, lacking an analytical expression, the integrated beam pattern is evaluated numerically. The example of the theoretical circular piston transducer is shown in Fig. 4.5.1.

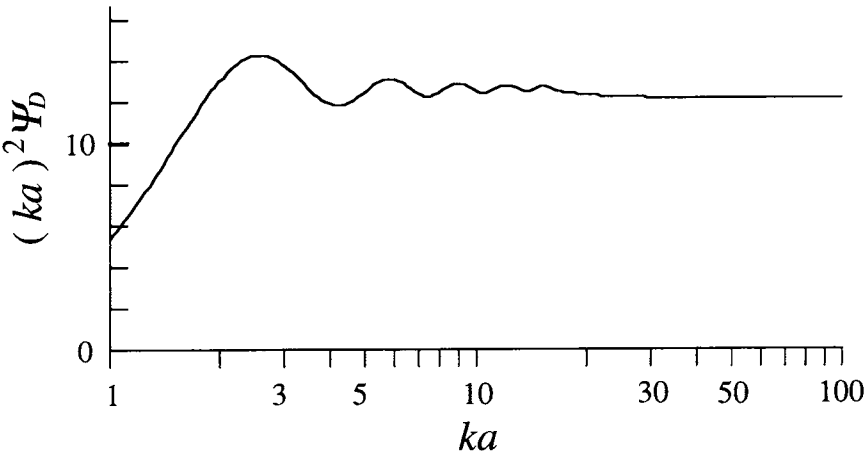

Figure 4.5.1 Integrated beam pattern of the circular piston transducer of radius a as a function of ka. It is customary to plot $(ka)^2\psi_D$ as the ordinate. For $ka > 10$, ψ_D is approximately $4\pi/(ka)^2$.

In terms of the integrated beam pattern Ψ_D, using S.I. units, the total radiated power over all angles is

$$\Pi_M = \left[\frac{P_0^2 R_0^2}{2\rho_A c} 10^{-\alpha R/10}\right]\psi_D = \left[\frac{P_{ax}^2 R^2}{2\rho_A c}\right]\psi_D \quad \text{watts} \tag{4.5.5}$$

For comparison to omnidirectional radiation, recall the expression for total power Equation 3.1.16a. In that case, the point source, $D_t = 1$ and $\Psi_D = 4\pi$. It is strongly recommended that the output of transducers be reported in total watts of radiated power. It is easy, using Equation 4.5.5 to go from peak pressure on the axis of the transducer to total radiated power. However, notice that, because of near-field interferences, P_0 should not be *measured* at one meter from the source. It should be obtained by extrapolation from a measurement at a far-field range.

The total radiated power is proportional to the integrated beam pattern. In order to keep the same sound intensity (proportional to p^2) along the axis of a transducer when there is an increase of beam width, (e.g., from $ka = 10$ to $ka = 5$ in Fig. 4.4.3), the total radiated power must be increased.

If one knows the total radiated power at range R and the integrated beam pattern, one can solve Equation 4.5.5 to obtain the reference peak pressure one meter from the transducer on the radiation axis:

$$P_0^2 = \frac{2\,\Pi_M\,\rho_A\,c}{\psi_D\,R_0^2}\,10^{\alpha R/10} \tag{4.5.6}$$

4.5.2 DESCRIPTORS OF BEAM STRENGTH

The need to comprehend the complicated radiation patterns (and receiving patterns) and to compare transducers, in some simple way, has led to several single-number descriptors.

Directivity Factor

The directivity factor of a transmitter, Q_t, is the ratio of the transducer sound intensity in the axial beam direction ($\theta = 0$) to the intensity, at that same far-field range, that would be caused by a point source radiating the same total power omnidirectionally (over 4π steradians).

$$Q_t = \frac{\text{Beam axial intensity at } R}{\text{Point source intensity at } R} = \frac{P_{ax}^2/(2\rho_A c)}{\Pi_M/(4\pi R_{ax}^2)} \tag{4.5.7}$$

Substitute Π_M from Equation 4.5.5 and obtain the transmitter directivity function

$$Q_t = 4\pi/\Psi_D \tag{4.5.8}$$

Directivity Index

The directivity index is obtained by taking the logarithm to express in dB:

$$DI_t = 10\log_{10} Q_t \tag{4.5.9a}$$

Special cases of the directivity index for piston sources are a rectangle of dimensions,

$$L \cong W: \quad DI_t = 10\log_{10} \frac{k^2 LW}{\pi} \qquad ka \gg 1 \tag{4.5.9b}$$

and a circle of radius a

$$DI_t = 10\log_{10} (k^2 a^2) \qquad ka \gg 1 \tag{4.5.9c}$$

Half-Intensity Beam Width

The *half-intensity beam width* is the angle $\Theta_{\text{beam}} = 2\theta$ measured from $-\theta$, where the acoustic intensity is half the axial value, past the axis, to the angle $+\theta$, where the acoustic intensity is again half the axial value (see Fig. 4.5.2). It is also called the "half-power beam width," an unfortunate misnomer which comes from electric circuit theory.

For example, from Table 4.1, the half-intensity value of the circular piston beam is at $ka \sin\theta = 1.6$. Therefore, for $ka = 20$, the half-intensity angle is $\theta = \sin^{-1} 0.08 = 4.6°$ and the half-intensity beam width is $\Theta_{\text{beam}} = 2\theta = 9.2°$.

4.6 Equivalence of Source/Receiver Directivity

The same analytic expressions that were derived for the pressure field due to an array of sources can be used to describe the directional response of an array of pressure-sensitive receivers. As shown in Fig. 4.6.1, let Q be the location of an omnidirectional source. The electrical source drive is $V_0 e^{i\omega t}$. The source transmits the sound pressure $P_0 e^{i\omega t}$. The pressure/voltage conversion factor for the transmitting transducer is $K_{\text{p/v}}$. The source sound pressure, referred to range R_0, is

$$P_0 = V_0 K_{\text{p/v}} \tag{4.6.1}$$

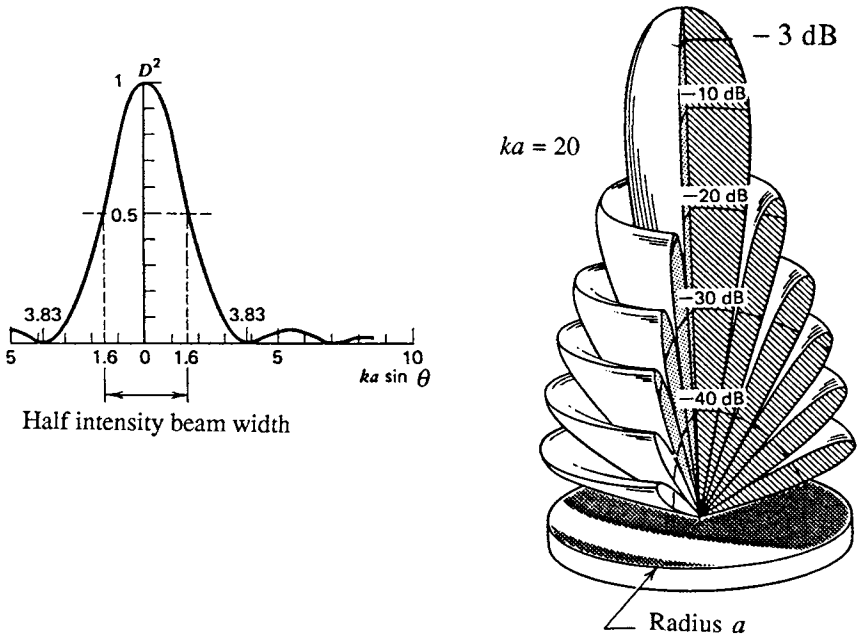

Figure 4.5.2 Directional response of a circular piston transducer of radius a in linear graph as a function of $ka \sin \theta$ (*left*) and in logarithmic, polar plot for $ka = 20$ (*right*). The half-intensity beam-width angle where $D^2 = 0.5$, or -3 dB with respect to the axial value is indicated. (Eckart, C., ed., *Principles and Applications of Underwater Sound*, Department of the Navy, NAVMAT P-9674, Government Printing Office, Washington, D.C., 1968.)

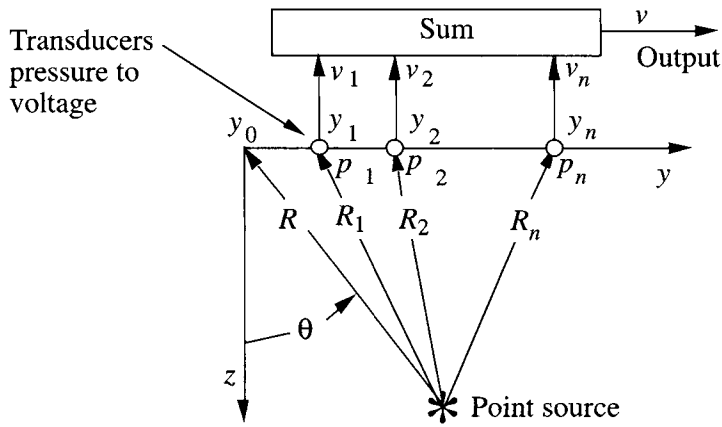

Figure 4.6.1 A point source and an array of receivers.

Pressure-sensitive receiver transducers are at y_1, y_2, and so forth. The sound pressures at these locations are p_1, p_2, and so forth. The sound pressure at y_n is

$$p_n = P_0 R_0 \frac{e^{i(\omega t - kR_n)}}{R_n} \tag{4.6.2}$$

The sound pressure on a transducer causes it to generate an electrical voltage. Common linear transducers give output voltages that are proportional to the sound pressures. The time dependencies are the same. Let $K_{v/p}$, with units volts/μPa be the conversion factor for voltage amplitude to pressure amplitude. For simplicity, the same amplitude factors and conversion factors are used for all receivers. The output voltage of the *nth* transducer is

$$v_n = K_{v/p} P_0 R_0 \frac{e^{i(\omega t - kR_n)}}{R_n} \tag{4.6.3}$$

The simple sum of the voltages from an array is

$$v = \sum_n v_n = P_0 R_0 K_{v/p} \sum_n \frac{e^{i(\omega t - kR_n)}}{R_n} \tag{4.6.4}$$

The substitution of the electrical source drive for P_0 gives

$$v = V_0 R_0 K_{v/p} K_{p/v} \sum_n \frac{e^{i(\omega t - kR_n)}}{R_n} \tag{4.6.5}$$

We next show an important result. Replace all of the receivers shown in Fig. 4.6.1 by source transducers which transmit $P_0 e^{i\omega t}$. A receiver is placed at Q. The voltage/pressure and pressure/voltage factors are numerically the same. Then, calculation of the voltage at Q is the same as before. Therefore, one can interchange sources and receivers and still have the same transmission pattern.

In the Fraunhofer incident plane wave approximation (section 2.4.1), one can write Equation 4.6.4 as follows:

$$v = \sum_n v_n \approx \frac{P_0 R_0}{R} K_{v/p} \sum_n e^{i(\omega t - kR_n)} \tag{4.6.6}$$

where

$$R_n \approx R - \frac{nW \sin\theta}{N-1}$$

In many applications, the same array is used to transmit sound pressures and then to receive sound pressures. These arrays of transducers are reciprocal devices. The directional response of the array as a transmitter is the same as its directional response as a receiver.

4.7 Free-Field Calibration of Transducers

A relatively simple, absolute method for the calibration of transducers is the "free-field" reciprocity technique, which is performed in a region free of scatterers. Needed are two small, "identical," "point" hydrophones, A and B (one of which can be used as a source as well), and a third transducer, C, that acts solely as a source.

Transducers A and B should be "identical" in shape and size to minimize differential sensitivities due solely to different diffraction fields around the transducers. Transducers A and B should be "point" transducers (size $\ll \lambda$) so that pressure is inversely proportional to the separation range R between source and receiver.

The free-field condition can be satisfied by using a ping or an impulse short enough to complete the measurement before extraneous reflections are received at the hydrophone. When an impulse is used, the Fourier transform of the pulse yields a broad spectrum that allows many frequencies to be calibrated simultaneously.

Transducer C is a source of far-field pressures (inversely proportional to the separation) used to determine the relative sensitivities of A and B as hydrophones. The procedure is simple (see Fig. 4.7.1). Transducer A is placed at a position of the sound field produced by C; its open-circuit voltage, V_{AC}, is measured. Then B is placed at the same position and its voltage, V_{BC}, is obtained. This yields the ratio of sensitivies, K_{VPB}/K_{VPA}.

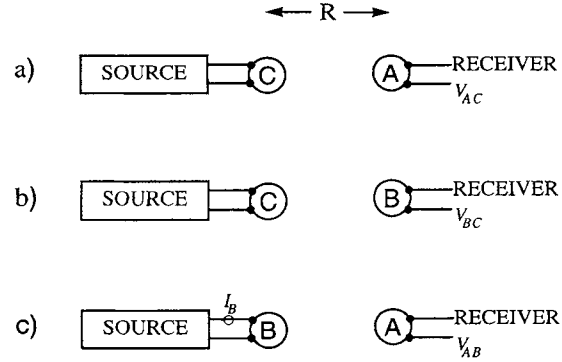

Figure 4.7.1 Scheme for obtaining free-field reciprocity calibrations. In a) C is the source, and the voltage at transducer A is measured to yield V_{AC}. In b) C is the source, and the voltage at B is V_{BC}. In c) B is the source, and the current to B is I_B when the voltage across A is V_{AB}.

The final two measurements are the current I_B, drawn by B when it is used as a source, and the open-circuit voltage V_{AB} across A at the same time. When these voltages, current, and separation are known, the sensitivity of hydrophone A is given by

$$K_{VPA} = \left(\frac{2\, R\, V_{AC}\, V_{AB}}{\rho_A\, c\, V_{BC}\, I_B} \right)^{1/2} \textit{volts / pascal} \tag{4.7.1}$$

where ρ_A = water density and c = speed of sound in water.

The reciprocity technique thereby provides an absolute calibration of the sensitivity of hydrophone A by measurements of electrical quantities and distance alone. Furthermore, the sensitivity of hydrophone A is the key to unlock the sensitivity of B because we know the relative sensitivities, K_{VPB}/K_{VPA}. Finally, by using either hydrophone, we have measured the output of source C or any other transducer that we can specify in terms of pascals produced at the measurement range/source voltage input. A precaution: we have assumed that the transducers are not driven beyond their linear range and that they do not produce nonlinear distortion.

4.8 Self-Reciprocity Calibration of Transducers

A transducer can be calibrated by pointing it toward a large reflecting surface (Carstensen 1947), such as the smooth water-air surface above the transducers in a water tank. Assume that the separation from the mirror is distance d, and the frequency of the short duration CW signal is f.

Define $K_{VP} = V_m/p_m$, the voltage generated by pressure p_m at the transducer, where V_m is the open-circuit voltage after mirror reflection of the signal, and p_m is the pressure after mirror reflection.

Also define $S = p_1/I_s$, the source response, pressure per ampere input, where p_1 is the output pressure at range 1 meter when the source draws a current, I_s amperes.

The ratio of the transducer sensitivity (as a hydrophone) to its response (as a source) is called the reciprocity parameter, J:

$$J = K_{VP} / S = (V_m / p_m) / (p_1 / I_s) \tag{4.8.1}$$

The calibration is performed in a spherically divergent field, so that the pressures are inversely proportional to the distances (in meters):

$$p_m/p_1 = R_0/(2d) \tag{4.8.2}$$

Combining Equations 4.8.1 and 4.8.2, and setting $R_0 = 1\,\text{m}$, we find the transducer sensitivity when used as a hydrophone,

$$K_{VP} = V_m \left(\frac{2\,d}{p_m\, p_1} \right)^{1/2} \tag{4.8.3}$$

and the same transducer output pressure at 1 meter, when used as a source,

$$S = \frac{1}{I_s} (2\,d\,p_m\,p_1)^{1/2} \tag{4.8.4}$$

This simple, nearly magical, calibration of the transducer as a source or receiver is predicated on several conditions: the field is spherically divergent so that the source is effectively a point at the range of the calibration; the reflecting surface is large and smooth (compared with the wavelength); the transducer axial propagation is perpendicular to the reflector; and the source "ping" is long enough to identify the frequency of the CW but short enough to avoid scatter from nearby objects.

Problems

Section 4.1

4.1.1 Use Equation 4.1.4 to set up your own criterion that specifies the range at which the sound pressure from a point source is "essentially" in phase with the radial particle velocity—that is, define "essentially."

4.1.2 Expand the right-hand side of Equation 4.1.7 in vector notation and identify the physical meaning of the component sound source terms in spherical coordinates.

Section 4.2

4.2.1 Calculate the directivity patterns for a 21-element line source (as shown in Fig. 4.2.2) for those four cases: a) uniform (piston) point source weighting; b) triangular weighting; c) cosine weighting; d) Gaussian weighting.

4.2.2 a) Calculate the central lobe beam widths for the four cases in Problem 4.2.1. b) Calculate the relative pressure of the first side lobe peak, compared with the axial value, for the four-beam patterns in Problem 4.2.1.

Section 4.3

4.3.1 State the far-field directivity function for a rectangular piston source of length L in the x direction and width W in the y direction, propagating in the z direction.

4.3.2 Determine the far-field directivity in the xz plane and yz plane of a rectangular piston source of dimensions L and W. Plot the directivity as a function of $0 < \phi < 2\pi$ for the cases in which a) $L = W$; b) $L = 2W$; c) $L = 10W$.

Section 4.4

4.4.1 Use a "reasonable" criterion to derive the critical range for the far-field directivity of a rectangular piston source of dimensions L and W, propagating in the xz plane, or yz plane.

4.4.2 Compare the directivity pattern of a circular piston source of radius a with that of a rectangular source of dimensions $L = W = a$ for the cases $ka = 2.5$ and $ka = 10$.

Section 4.5

4.5.1 Calculate the half-intensity beam widths in the xz and yz planes for a rectangular piston source of $L = 2W$ and $L = 10W$.

4.5.2 Calculate the half-intensity beam widths of the triangular, cosine, and Gaussian line sources in Fig. 4.2.2.

Chapter 5 | High Intensities

5.1 Harmonic Distortion and Shock-Wave Growth 153
5.2 Cavitation 158
5.3 Parametric Sources and Receivers 162
5.3.1 CW Parametric Sources 162
5.3.2 Parametric Receivers 168
5.3.3 Intense Tone Bursts, Self-Demodulation 170
5.4 Explosive Sources 170
5.4.1 The Shock Wave 170
5.4.2 Shock Front Propagation; the Rankine-Hugoniot Equations 173
5.4.3 The Gas Globe 174
5.4.4 Interaction with the Ocean Surface 176
5.5 Acoustic Radiation Pressure 177
5.6 Acoustic Streaming 178

Nonlinear effects, which occur when the sound intensity is sufficiently great, limit the amount of energy that a sound source can radiate into the ocean. The limitations include harmonic distortion and the consequent "saturation" of sound intensity output; cavitation, which limits the pressure swing; and acoustic streaming, which can erode the face of a transducer or nearby object. On the positive side of the ledger, high intensities permit the use of small "parametric" sound sources that have extremely narrow beams and large bandwidths at very low frequency; they allow the determination of source intensity by the measurement of the radiation pressure of the sound.

5.1 Harmonic Distortion and Shock-Wave Growth

The approximations that lead to infinitesimal amplitude acoustics, which is assumed everywhere else in this book, obscure the extraordinary behaviors that occur when sound pressures are large. It is important to understand these effects whenever high-intensity sound sources are used underwater. The first correction that we consider occurs because the sound speed is a function of ambient pressure.

Fig. 5.1.1 sketches the difference between the equations of state of air and water.

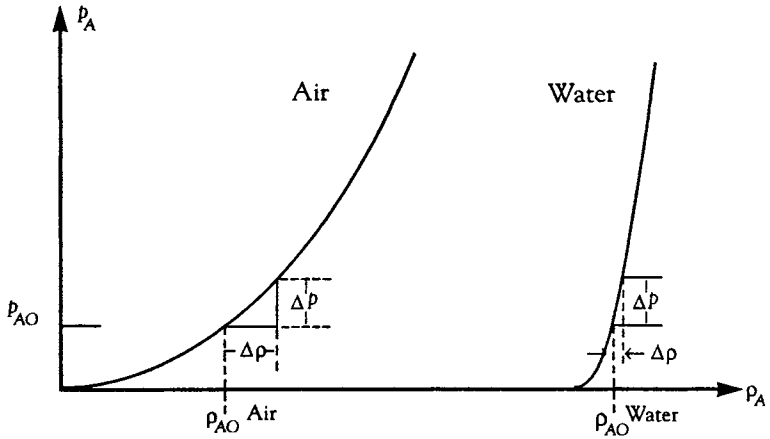

Figure 5.1.1 Schematic sketch of equations of state for air and water, $p_A = p_A(\rho_A)$. The curves are not to scale. The steep slope for water shows its relative incompressibility. The values p_{AO} and ρ_{AO} are the standard conditions (one atmosphere). The correct slopes at standard conditions for water are about 23 times greater than they are for air.

The physical relation between incremental changes of pressure and density determines the speed of sound in the medium as first described in Equation 2.5.7:

$$c^2 = \frac{\Delta p}{\Delta \rho} = \frac{E}{\rho_A} \tag{5.1.1}$$

To calculate the speed, we need an analytic expression for the equation of state of the fluid, $p_A = p_A(\rho_A)$. An appropriate form is the adiabatic relation

$$(p_A \rho_A^{-\Gamma})_S = K \tag{5.1.2}$$

where K is a constant. The subscript s identifies the condition of zero heat exchange in a reversible process (constant entropy). This is generally a good assumption for sound propagation at sea, except in bubbly water.

For gases, Γ (which is usually written as γ in physics texts) is the ratio of the specific heat at constant pressure to the specific heat at constant volume. The adiabatic equation of state for gases is well known. Therefore, the slope is easily calculated and the speed of sound in gases follows. For air, in which $\Gamma = 1.40$, the predicted speed of sound is in excellent agreement with measurements. This has been understood since the works of J. B. Biot and P. S. Laplace at the beginning of the nineteenth century.

However, when Equation 5.1.2 is assumed to describe water, p_A must be interpreted as including not only the external ambient pressure but an internal cohesive pressure of approximately 300 MPa (3000 atmospheres). For water, the

constant Γ is not the ratio of specific heats; it must be determined empirically.

Differentiate Equation 5.1.2 and get the formula for the speed at ambient density ρ_A,

$$c^2{}_A = \left(\frac{\partial p_A}{\partial \rho_A}\right)_s = K\,\Gamma\,\rho_A{}^{\Gamma-1} \tag{5.1.3}$$

For a small excursion in pressure and density, ρ_A becomes

$$\rho_A \rightarrow \rho_A + \Delta\rho = \rho_A\left(1 + \frac{\Delta\rho}{\rho_A}\right) \tag{5.1.4}$$

where, to be explicit, we use Δp and $\Delta\rho$ rather than p and ρ to represent the incremental changes.

Therefore, in that region, the speed is

$$c = [K\Gamma\rho_A^{\Gamma-1}]^{1/2}\left[1 + \frac{\Delta\rho}{\rho_A}\right]^{(\Gamma-1)/2} \tag{5.1.5}$$

The expression in the first bracket is c_A. By the binomial expansion, the second bracket leads to the speed of sound as a function of the incremental density, $\Delta\rho$, and the ambient density, ρ_A:

$$c \approx c_A\left[1 + (\Gamma-1)\frac{(\Delta\rho/\rho_A)}{2}\right] \tag{5.1.6}$$

The sound speed will reduce to c_A at ambient density ρ_A when $\Delta\rho \ll \rho_A$; this infinitesimal amplitude is the realm of acoustic propagation that is assumed elsewhere throughout this book. The second term of Equation 5.1.6 describes the finite amplitude effect that interests us here.

An alternative fitting of the curve of Fig. 5.1.1 is given by the power series expansion

$$\Delta p \approx A(\Delta\rho/\rho_A) + \frac{B(\Delta\rho/\rho_A)^2}{2} \tag{5.1.7}$$

Now form $c^2 = \Delta p/\Delta\rho$ from Equation 5.1.7 and compare with the square of Equation 5.1.6. Define the "parameter of nonlinearity,"

$$B/A = \Gamma - 1 \tag{5.1.8}$$

where $A = \rho_A c_A^2 = \Gamma p_A$ and $B = \Gamma(\Gamma-1)p_A$.

The ratio B/A is a popular descriptor of the nonlinear potentialities of the medium in studies of high-intensity sound. The B/A for water ranges from 5.0 at temperature 20° C to 4.6 at 10° C. In terms of B/A, Equation 5.1.6 becomes

$$c \approx c_A\left[1 + \frac{B}{A}\frac{\Delta\rho/\rho_A}{2}\right] \tag{5.1.9}$$

To calculate the signal speed $u + c$ at a point where the excess density is $\Delta\rho$, use Equation 2.5.11:

$$u = \left(\frac{\Delta\rho}{\rho_A}\right) c_A \tag{5.1.10}$$

Then

$$u + c = c_A\left(1 + \beta\frac{\Delta\rho}{\rho_A}\right) \tag{5.1.11}$$

where $\beta = 1 + B/(2A)$.

Consider the *finite* sinusoidal wave sketched in Fig. 5.1.2a. The wave's crest is at higher pressure than the undisturbed medium; therefore the speed of sound at the crest is $c > c_A$. The particle velocity at the crest is u. The crest advances at speed $c + u$. In a rarefaction, u is negative, $c < c_A$, and the wave trough advances at the lesser speed $c - u$. The net result is that the crests advance relative to the

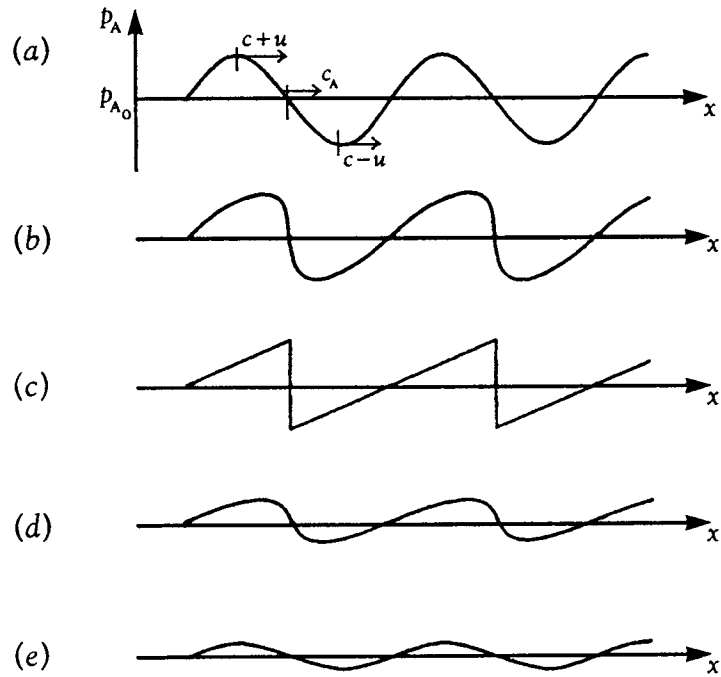

Figure 5.1.2 Stages of a finite-amplitude sinusoidal sound wave. (a) Close to a source with large sinusoidal pressure swings. (b) Nonlinear distortion after propagation away from source. (c) Fully developed repeated shock wave (sawtooth wave) away from source. (d) Aging repeated shock wave after greater loss of higher-frequency components. (e) Infinitesimal amplitude of a former shock wave.

axial positions, and the troughs lag behind the axial positions. As the effect continues, the wave distorts to a form resembling Fig. 5.1.2b. Finally, if the pressure swing is large enough for a sufficient number of wavelengths, the finite amplitude wave becomes a "sawtooth" wave or "repeated shock wave," (Fig. 5.1.2c). The progressive growth construction cannot continue beyond this point; to do so would be to imply double values of pressure at various parts of the wave.

After the shocks are formed, the phenomenon of harmonic distortion proceeds into "old age" as the higher frequencies, which define the corners of the shock-wave fronts, dissipate too rapidly to be compensated by harmonic growth. In that condition the corners of the shock wave erode and become rounded. The shock wave thereby returns toward a sine wave form, but with greatly reduced amplitude (Figs. 5.1.2d and e).

Fourier analysis of the various forms of the sawtooth wave reveals that energy has been taken from the fundamental of frequency f (the original sinusoidal frequency) and redistributed into the second, third, and higher harmonics as the wave distorts. In the ultimate repeated shock, the pressure amplitude of the second harmonic (frequency $2f$) is half that of the fundamental, the third harmonic ($3f$) has one-third the amplitude of the fundamental, and so on. The cascading redistribution of energy from the fundamental to the upper harmonics is accompanied by an increased real loss of acoustic energy because the newly generated higher frequencies dissipate into thermal energy at a much faster rate than the fundamental (Chapter 3).

A simple derivation of the harmonic distortion of an intense, unattenuating plane wave was given by Black (1940) (see Problem 5.1.1). There the amplitude of the second harmonic of such a sawtooth wave is shown to be

$$P_2 = \frac{\beta k X P^2_1}{2 \rho_A c^2_A} \tag{5.1.12}$$

where X is the distance of propagation, and P_1 is the amplitude of the fundamental. The second harmonic amplitude, P_2, is proportional to the fundamental *intensity* and the number of wavelengths progressed, kX.

It is useful to compare nonlinear propagation in air with that in water. Using $B/A = 4.8$ for water and 0.4 for air, β is 3.4 for water and 1.2 for air. But the major difference between the two media comes about because the factor $\rho_A(c_A)^2$ is 1.6×10^4 larger in water than in air. For the same presssure amplitude of the fundamental, the second harmonic will grow to the same magnitude in a distance only 1/5000 as far in air as in water. Even though the sound is diverging from the source, the sensitive listener often hears the popping, crackling sound of mini–shock waves from nearby jet aircraft during takeoff.

The shock wave will have reached its final sawtooth form when the second harmonic amplitiude, P_2 is equal to $P_1/2$. From Equation 5.1.12, the distance required for a plane wave is

$$X_0 = \frac{\rho_A c_A^2}{k P_1 \beta} = (k\mathcal{M}\ \beta)^{-1} \tag{5.1.13}$$

where

$$\mathcal{M} = \text{acoustical Mach number} = \frac{u}{c_A} = \frac{P_1}{\rho_A c_A^2} \tag{5.1.14}$$

A much greater distance is required for a lossless, spherically diverging wave to achieve the sawtooth wave form. Furthermore, the calculation of shock conditions at large ranges *must* take into account energy absorption as well as spherical divergence. This problem has been studied by many investigators and is not repeated here. See Beyer (1974), Novikov et. al. (1987), Naugol'nykh et al. (1997), or the proceedings of the triennial *International Symposium on Nonlinear Acoustics*.

The effect that we have described limits the energy that can be put into a sound beam by a source. As the input power increases, more and more power goes into the higher harmonics which, with their larger attenuation rate, act to dissipate the new power. Consequently an intensity is reached where additional input of energy at the source does *not* produce increased sound pressures in the field. The limit is called "saturation."

The saturation effect for a spherically divergent beam in water is illustrated in Fig. 5.1.3. Where the response is linear, the 45° line shows that field pressure is proportional to source pressure. The ultimate saturation effect is increasingly evident at the larger ranges. For the four greatest ranges, the saturation pressure is indicated by the horizontal lines to the right.

A simultaneous effect of nonlinear harmonic distortion is the modification of the beam radiation pattern. Since the axial part of the beam has the greatest intensity, it suffers more than the off-axis field. As a result, the lesser attenuation at greater angles off-axis causes a broadening of the beam. This also causes the side lobe intensities to be closer to the intensity of the strong central part of the beam.

5.2 Cavitation

Near sea level, minute bubbles of micron or submicron size are always present in the ocean. When the rarefaction tension phase of an acoustic wave is great enough, the medium ruptures or "cavitates." For sound sources near the sea

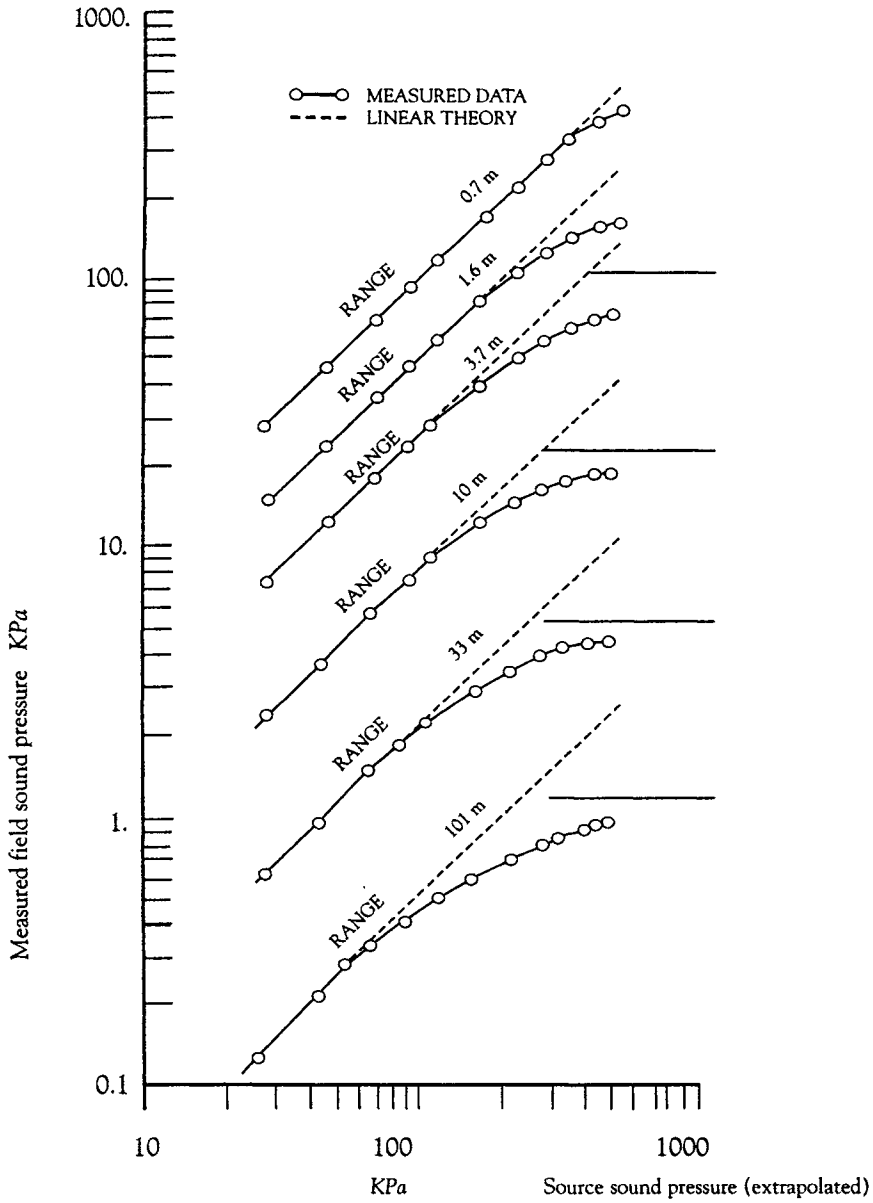

Figure 5.1.3 Amplitude response curves showing the reduced field pressures due to extra losses caused by nonlinear propagation at increased source pressures for six ranges. Piston source diameter = 7.6 cm, f = 454 kHz. The horizontal lines at the right are the asymptotic saturation pressures. (Data from Shooter, J. A., et al., Acoustic saturation of spherical waves in water, *J. Acoust. Soc. Am.* **55**, 54–62, 1974.)

surface, the ever-present cavitation nuclei permit rupture to occur at pressure swings of the order of 1 atm (0.1 MPa), depending on the frequency, duration, and repetition rate of the sound pulse. Cavitation bubbles may also be produced by Bernoulli pressure drops associated with the tips of high-speed underwater propellers. Natural cavitation is created by photosynthesis.

Several extraordinary physical phenomena are associated with acoustic cavitation. Chemical reactions can be initiated or increased in activity; living cells and macromolecules can be ruptured; violently oscillating bubbles close to a solid surface can erode the toughest of metals or plastics; light may be produced by cavitation (sonoluminescence). The high pressures and high temperatures (calculated to be 30,000° Kelvin) at the inteior during the collapsing phase of cavitating single bubbles can cause emission of a reproducible pulse of light of duration less than 50 picoseconds.

Of direct importance to the use of sound sources at sea is the fact that, as the sound pressure amplitude increases, ambient bubbles begin to oscillate nonlinearly, and harmonics are generated. At sea level, the amplitude of the second harmonic is less than 1 percent of the fundamental as long as the pressure amplitude of the fundamental of a CW wave is less than about 0.01 atm rms (1 kPa) (Rusby 1970). This increases to about 5 percent harmonic distortion when the signal is about 10 kPa.

When the peak pressure amplitude is somewhat greater than 1 atm, the absolute pressure for a sound source at sea level will be less than zero during the rarefaction part of the cycle. In using CW below 10 kHz, this negative pressure, or tension, is the trigger for a sharply increased level of harmonic distortion and the issuance of broadband noise. Any attempt to increase the sound pressure amplitude appreciably beyond the ambient pressure will cause not only total distortion but also the generation of a large cloud of bubbles which will actually *decrease* the far-field acoustic pressure.

The detailed bubble activities during cavitation have been studied in several laboratories. Acousticians have identified gaseous cavitation resulting in streamers of hissing bubbles that jet away from regions of high acoustic pressure swings, and vaporous cavitation, which radiates shock waves of broadband noise.

The nuclei for cavitation often are bubbles caught in crevices of solid particles. If the acoustic pressure swing is great enough, the bubbles grow by a process called "rectified diffusion." During a cycle of this action, more gas diffuses inward from the liquid to the bubble during the expansion part of the cycle than moves outward during the contraction part of the cycle, when the bubble surface is smaller. After growth to a critical radius, the bubble will expand explosively.

The acoustic pressure threshold for cavitation depends on the criterion selected to define its existence. In the laboratory it is possible to use visual observation. More commonly, the broadband noise of the cavitating bubbles is evidence of the onset. Additionally, the nonlinear generation of subharmonics of half-frequency is one criterion that defines the onset of cavitation.

The sound field of an oceangoing transducer consists of regions close to the source and on the face of the source where the sound pressure is either greater than, or less than, the calculated pressure at the one meter reference range (see Fig. 4.4.4). Furthermore, both acoustic radiation pressure and streaming (see section 5.5) move cavitating bubbles to new positions where they experience different growth rates. Therefore there are "hot spots" where cavitation activity is significantly greater than the prediction from the average reference pressure. The sound intensities that can be radiated deep below the surface are higher than those that can be radiated at the surface, because there are fewer cavitation nuclei, the radii of these nucleii are smaller, and the ambient pressure is greater.

The dependence of cavitation onset and harmonic distortion on pulse duration is shown in Fig. 5.2.1. For pulse durations less than 100 ms, the average acoustic intensity required for 10 percent distortion is much greater than for CW.

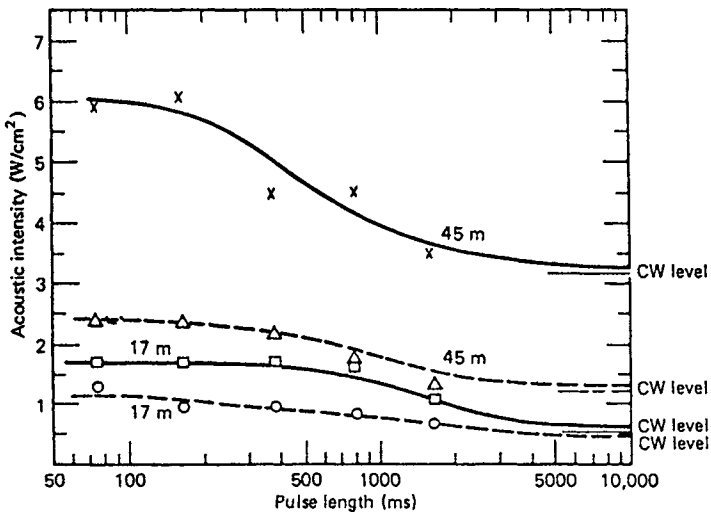

Figure 5.2.1 Pulse-length dependence of the onset of cavitation (solid lines) and of 10 percent harmonic distortion (dashed lines) in seawater for 7 kHz sound at depths of 17 m and 45 m. (Rusby, J. S. M. "The onset of sound wave distortion and cavitation in seawater," *J. Sound Vib.* **13**, 257–67, 1970.)

When the sound is alternately on and off, the allowable acoustic intensity, before distortion or cavitation, increases with decreasing percentage of on-time, $\Delta t/T$, from CW (100 percent) to lower values as shown in Fig. 5.2.2. An asymptotic value is reached that is higher with shorter pulse duration.

5.3 Parametric Sources and Receivers

5.3.1 CW PARAMETRIC SOURCES

Section 5.1 described the harmonic distortion that characterizes a single, intense sound beam. In 1963 Westervelt pointed out that if two intense sound beams are coaxial, the nonlinearity of the medium also creates entirely new propagating frequencies; these are sum and difference frequencies of the original "primary" sound frequencies. For example, when two primary beams of frequencies 500 kHz and 600 kHz are superimposed, a secondary beam of 100 kHz and

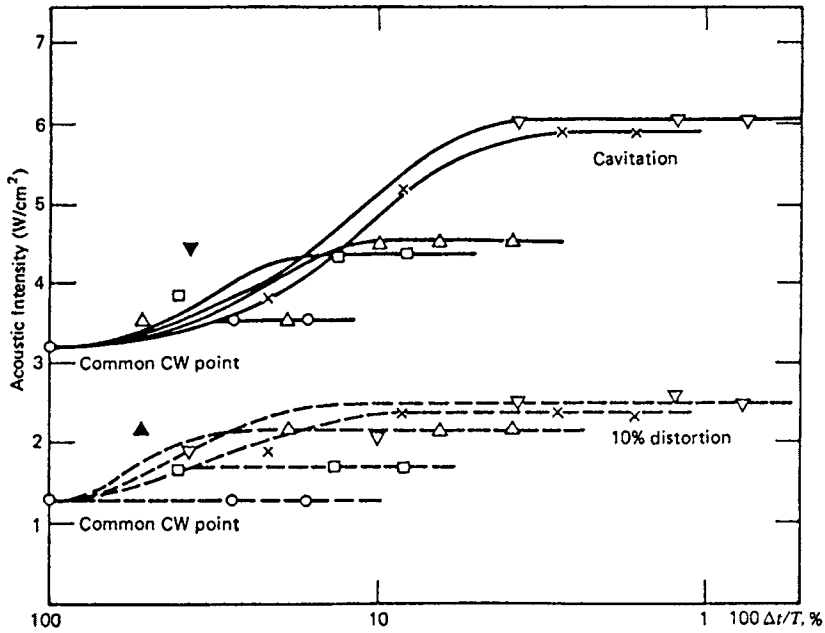

Figure 5.2.2 Duty-cycle dependence of onset of cavitation and 10 percent harmonic distortion at 45 m depth in seawater for different pulse lengths of 7 kHz sound. Pulse durations are: 74 ms, V; 165 ms, ×; 380 ms, Δ; 800 ms, □; 1650 ms, o. (Rusby, J. S. M., "The onset of sound wave distortion and cavitation in seawater, *J. Sound Vib.* **13**, 257–67, 1970.)

another of 1100 kHz will be generated. So-called parametric or virtual sources will be distributed all along the intense part of the interacting primary beams.

The difference frequency is particularly attractive for technical applications because it has an extremely narrow beam at relatively low frequency. In the example given, the difference frequency of 100 kHz will have approximately the narrow beam width of a 550 kHz source radiating from the same transducer. The volume-distributed parametric source acts as if it were a highly directional end-fire array, so it is sometimes called a "virtual-end fire array." Furthermore, the bandwidth of the difference frequency of the parametric source is very much greater than it is for a linear transducer.

For a simple description of the nonlinear action, consider how sum and difference frequencies can be generated at a point traversed by CW sounds of two different frequencies. Assume plane waves carrying the primary frequencies ω_1 and ω_2 described by

$$p_1(t) = P_1 \cos(\omega_1 t) \tag{5.3.1}$$

and

$$p_2(t) = P_2 \cos(\omega_2 t) \tag{5.3.2}$$

Assume that these two primary waves are traveling in the same direction and that they are both very intense. Each beam will be modulated by the other. For example, the amplitude of the p_1 wave will be modulated by the presence of p_2 and will become $P_1(1 + m\cos(\omega_2 t))$, where $m = P_2/P_1$ is the modulation amplitude. When the modulated p_1 is added to Equation 5.3.2, we obtain the sum

$$p(t) = P_1 \cos(\omega_1 t) + P_2 \cos(\omega_2 t) + P_1 m \cos(\omega_1 t)\cos(\omega_2 t) \tag{5.3.3}$$

The third term is the nonlinear interaction and $m(P_1, P_2)$ is a measure of its strength. To recognize that sum and difference frequencies have been generated, rearrange the product of the cosines by using the trigonometric relation

$$2\cos x \cos y = \cos(x + y) + \cos(x - y) \tag{5.3.4}$$

and p becomes

$$p(t) = P_1 \cos(\omega_1 t) + P_2 \cos(\omega_2 t) + \frac{P_1 m}{2}[\cos(\omega_\Sigma t) + \cos(\omega_\Delta t)] \tag{5.3.5}$$

The third term is a function of the sum and difference frequencies;

$$\begin{aligned} \omega_\Sigma &= \omega_1 + \omega_2 \\ \omega_\Delta &= \omega_1 - \omega_2 \end{aligned} \tag{5.3.6}$$

Sum and difference frequencies such as these would be generated at all points of intense interaction along the beams and would constitute a volume distribution of "virtual" secondary sources. For a sound beam they become equivalent to a properly phased array of simple real sources in an end-fire configuration.

To describe and evaluate the distributed secondary sources, we go to the inhomogeneous wave equation derived first by Westervelt. It is a wave equation in which the squared primary pressures act as sources of the secondary or "scattered" waves. In one dimension, this is written

$$\frac{\partial^2 p_s}{\partial x^2} - \frac{1}{c^2}\frac{\partial^2 p_s}{\partial t^2} = -\frac{\beta}{\rho_A c^4}\left[\frac{\partial^2 (p_1 + p_2)^2}{\partial t^2}\right] \tag{5.3.7}$$

where the nonlinear parameter β was defined in Equation 5.1.11.

When we insert the expression for the two primary pressures with their attenuations α_1 and α_2 into the RHS of Equation 5.3.7,

$$\begin{aligned} p_1 + p_2 = {} & P_1 \cos(\omega_1 t - k_1 x)\exp(-\alpha_1 x) \\ & + P_2 \cos(\omega_2 t - k_2 x)\exp(-\alpha_2 x) \end{aligned} \tag{5.3.8}$$

we obtain the terms that describe the source of the scattered pressure:

$$\begin{aligned} \frac{\partial^2 (p_1 + p_2)^2}{\partial t^2} = {} & -2\omega_1^2 P_1^2 \cos[2(\omega_1 t - k_1 x)]\exp(-2\alpha_1 x) \\ & - 2\omega_2^2 P_2^2 \cos[2(\omega_2 t - k_2 x)]\exp(-2\alpha_2 x) \\ & - 2\omega_\Sigma^2 P_1 P_2 \cos(\omega_\Sigma t - k_\Sigma x)\exp[-(\alpha_1 + \alpha_2)x] \\ & - 2\omega_\Delta^2 P_1 P_2 \cos(\omega_\Delta t - k_\Delta x)\exp[-(\alpha_1 + \alpha_2)x] \end{aligned} \tag{5.3.9}$$

The second harmonic terms (first two terms on the RHS) were present in our discussion of shock-wave generation (section 5.1.1). In addition to those shown, there are others that would come from further harmonic distortion. The third and fourth terms on the RHS of Equation 5.3.9 describe the sum and difference frequencies.

The difference frequency can be exploited. To show this, we use a Huygens type of calculation for a distribution of sources to determine the directional dependence of the difference tone component, ω_Δ. Refer to Fig. 5.3.1.

Assume that the cross-sectional diameter of the volume is small compared with the wave length of the difference tone. The element of volume is $S_0\, dx$, where S_0 is the cross-sectional area of the high-frequency primary beams. The secondary wavelets diverge spherically with the relatively low sound-pressure

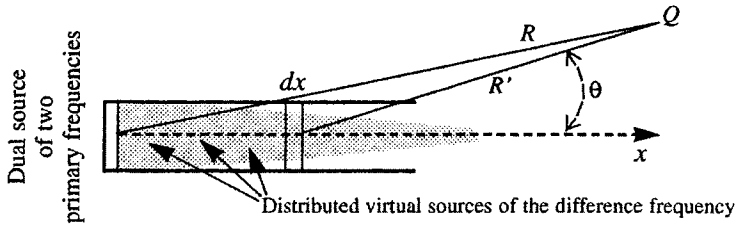

Figure 5.3.1 Geometry for the generation of a difference frequency from two intense coaxial high-frequency beams. The new frequency arises as a continuous distribution of virtual sources throughout the beam. It is observed at Q.

attenuation rate of α_Δ (nepers/m). The sound pressure at Q is proportional to the integral over all sources,

$$p_\Delta(R,\theta) \sim \frac{\omega_\Delta^2 \beta P_1 P_2 S_0}{2\rho_A c^4} \times \int_0^\infty \frac{\exp\left[-\alpha_\Delta R' - (\alpha_1+\alpha_2)x + i(\omega_\Delta t - k_\Delta x - k_\Delta R')\right]}{R'} + \text{C.C.} \tag{5.3.10}$$

where

$$R' = (R^2 - 2xR\cos\theta + x^2)^{1/2} \simeq R - x\cos\theta \tag{5.3.11}$$

and C.C. means the complex conjugate. The limit is given as infinite for convenience; actually, the length of the volume is small compared with R, because $\exp[-(\alpha_1+\alpha_2)x]$ tends rapidly to zero as x increases. Substitution of the approximation for R' and $1-\cos\theta = 2\sin^2(\theta/2)$ permits a simple integration result for the secondary pressure at the field position, R, θ,

$$p_\Delta(R,\theta) \sim \left\{\frac{\omega_\Delta^2 \beta P_1 P_2 S_0 \exp\left[-\alpha_\Delta R + i(\omega_\Delta t - k_\Delta R)\right]}{4R\rho_A c^4[\langle\alpha\rangle + ik_\Delta^2 \sin^2(\theta/2)]}\right\} + \text{C.C.} \tag{5.3.12}$$

where $\langle\alpha\rangle = (\alpha_1+\alpha_2)/2$ is the average attenuation of the primary-source frequencies.

Determination of the amplitude factor requires the solution of the three-dimensional form of Equation 5.3.8. The reader is referred to Westerfelt (1963) for the following quantitative solution:

$$p_\Delta(R,\theta) = \left\{\frac{\omega_\Delta^2 \beta P_1 P_2 S_0 \exp(-\alpha_\Delta R)\cos(\omega_\Delta t - k_\Delta R - \varepsilon)}{8\pi R\langle\alpha\rangle\rho_A c^4\left[1 + \dfrac{k_\Delta^2}{\langle\alpha\rangle^2}\sin^4(\theta/2)\right]^{1/2}}\right\} \tag{5.3.13}$$

where $\varepsilon = \arctan[k_\Delta/\langle\alpha\rangle\sin^2(\theta/2)]$.

The quantity multiplying the cosine term is the peak pressure of the difference tone, P_Δ. This equation shows that P_Δ is proportional to the product of the primary acoustic pressures. Since the primaries are attenuating relatively rapidly, the region of the beams close to the transducer is most important in generating the difference frequency. Once the difference tone is generated, it propagates with its relatively small low-frequency attenuation, α_Δ, far beyond the region of the primaries that created it.

The difference tone diverges spherically, so that the pressure goes as $1/R$. However, its beam pattern is very narrow. The pressure directional response depends on

$$D_\Delta(\theta) = \left[1 + \frac{k_\Delta^2}{\langle\alpha\rangle^2} \sin^4(\theta/2)\right]^{-1/2} \tag{5.3.14}$$

The sound will be down to half-intensity (−3 dB) at the angle given by

$$1 + \frac{k_\Delta^2}{\langle\alpha\rangle^2} \sin^4(\theta_\Delta/2) = 2 \tag{5.3.15}$$

For difference tone generation, the ratio is $\langle\alpha\rangle/k_\Delta \ll 1$, so that $\sin(\theta_\Delta/2) \cong (\theta_\Delta/2)$ and

$$\textit{beam width} = (2\,\theta_\Delta) \cong 4\,[\langle\alpha\rangle/k_\Delta]^{1/2} \tag{5.3.16}$$

Not only is the beam width much narrower than would be expected from a piston of the size used or the primaries, but Equation 5.3.14 predicts that there will be virtually no side lobes in the radiation pattern of the difference frequency. In addition, one notes that, under the assumptions of the development, the beam width of the difference tone does not depend on the size of the primary sources. A further advantage of the parametric source is that its beam width is relatively insensitive to the value of the difference frequency.

Fig. 5.3.2 shows the beam patterns of two primary waves — one at 418 kHz and the other at 482 kHz, and the difference tone produced at 64 kHz. Not only does the difference tone have a central beam width like those of the high-frequency primaries, but its side lobes appear to be down by about 40 dB compared with the axial value. The absence of side lobes is striking.

Another advantage of the parametric array is the increase in bandwidth. The bandwidth of a primary source is normally some percentage of the central frequency, say ±5 percent. When the primaries are operated within this percentage bandwidth, the difference frequency will range over this same

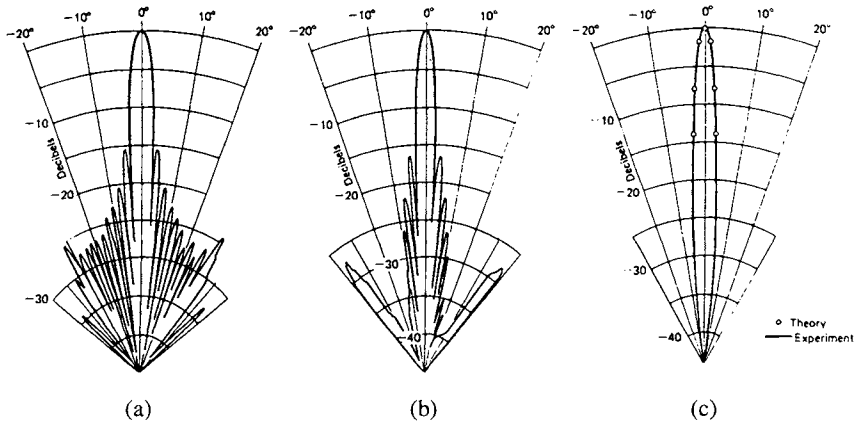

Figure 5.3.2 Directivity patterns of a parametric source. (a) Primary 418 kHz. (b) Primary 482 kHz. (c) Beam pattern of difference frequency, 64 kHz. The solid lines are experimental; values obtained by a few theoretical calculations are shown by open circles. (From Muir, T. G., "Non-linear acoustics and its role in the sedimentary geophysics of the sea," pp. 241–287, in L. L. Hampton, ed., *Physics of Sound in Marine Sediments*, Plenum Press, New York, 1974.)

absolute bandwidth, centered on its lower frequency. For example, if the primaries are 500 ± 5 percent (i.e., 475 to 525 kHz) and 600 ± 5 percent (i.e., 570 to 630 kHz), the difference frequency will have the relatively wide bandwidth of 100 ± 25 kHz.

The great virtues of the parametric source are bought at the cost of very low power efficiency. To calculate the appproximate efficiency of the nonlinear source, assume that the two primary sources radiate the same power, $W_1 = W_2$, that the primary field pressures are equal, $P_1 = P_2$; that they are measured close to the source and have not yet attenuated, and that the attenuation of the difference tone is negligible. The powers radiated through the primary beam area S_0 are

$$\Pi_1 = \Pi_2 = \frac{S_0 P^2_1}{2\rho_A c} \tag{5.3.17}$$

In terms of the total primary power, $\Pi_0 = \Pi_1 + \Pi_2$, from Equation 5.3.13, the axial peak pressure of the CW difference tone is

$$P_\Delta = \frac{\beta\, \omega_\Delta^2\, \Pi_0}{8\pi R \langle\alpha\rangle c^3} \tag{5.3.18}$$

or, in terms of the half–beam width from Equation 5.3.16,

$$P_{\Delta} = \frac{\beta f_{\Delta} \Pi_0}{R c^2 \theta_{\Delta}^2} \tag{5.3.19}$$

where we have used $f_{\Delta} = \omega_{\Delta}/2\pi$.

The power radiated by the difference tone is the product of the average intensity, $P_{\Delta}^2/(2\rho_A c)$, and the beam area, $\pi(R\theta_{\Delta})^2$;

$$\Pi_{\Delta} = \frac{\pi \beta^2 f_{\Delta}^2 \Pi_0^2}{2 \rho_A c^5 \theta_{\Delta}^2} \tag{5.3.20}$$

The percentage efficiency is

$$\frac{100 \Pi_{\Delta}}{\Pi_0} = 100 \frac{\pi \beta^2 f_{\Delta}^2 \Pi_0}{2 \rho_A c^5 \theta_{\Delta}^2} \tag{5.3.21}$$

The efficiency is generally a fraction of one percent. There are three apparent ways to increase the efficiency: improve the difference frequency, improve the primary power, decrease the primary beam width. Only increased power offers direct promise for increased efficiency without sacrificing the advantage of the parametric source. However, that avenue is restricted by saturation effects and beam broadening, as well as cavitation at high intensities.

When gas bubbles are present in an intense sound beam, they may be driven into large-amplitude, nonlinear oscillations at or near their resonance frequencies. This effect can substantially increase the power of the difference frequency, but with some loss in the radiation directionality.

Even though the efficiencies are very low, parametric sources are in active use. They are one solution to the need for transducers which have a narrow beamwidth and a uniform response over a wide range of low frequencies. Because their low frequency permits them to penetrate several layers of sediment, they are particularly desirable as seismic transducers for profiling lower layers of the ocean bottom.

5.3.2 PARAMETRIC RECEIVERS

In his original papers in the 1960s, Westervelt pointed out that it should be possible to develop a parametric *receiver* that would detect very low frequency sound and reveal its direction of propagation. A series of experimental papers has since verified that expectation.

The general scheme for parametric reception is shown in Fig. 5.3.3. A high-intensity "pump" frequency, f_p, radiates a narrow beam toward a receiver. Any incoming low-frequency signal, $f_s \ll f_p$, will interact nonlinearly with the pump sound to produce sum and difference frequencies. The new frequencies will have the directivity, $D(\theta)$ given by

$$D(\theta) = \frac{\sin\left[k_s L \sin^2(\theta/2)\right]}{k_s L \sin^2(\theta/2)} \tag{5.3.22}$$

where θ = angle between signal direction and pump signal direction; k_s = wave number of incoming signal $= 2\pi/\lambda_s$; and L = path length from pump source to receiver. Half-intensity points for this directionality are at

$$D^2(\theta) = \frac{\sin^2(x)}{x^2} = 1/2 \tag{5.3.23}$$

where $x = kL\sin^2(\theta/2)$—that is, at $\theta_{1/2} = 0.94\sqrt{\lambda_s/L}$.

The directionality improves with larger path lengths, L, over which the pump frequency can be maintained at high intensity. Several ideas for accomplishing this have been published. A good review of progress in the development and use of the parametric receiver, as well as other effects of nonlinear propagation, has been written by Hamilton (1986).

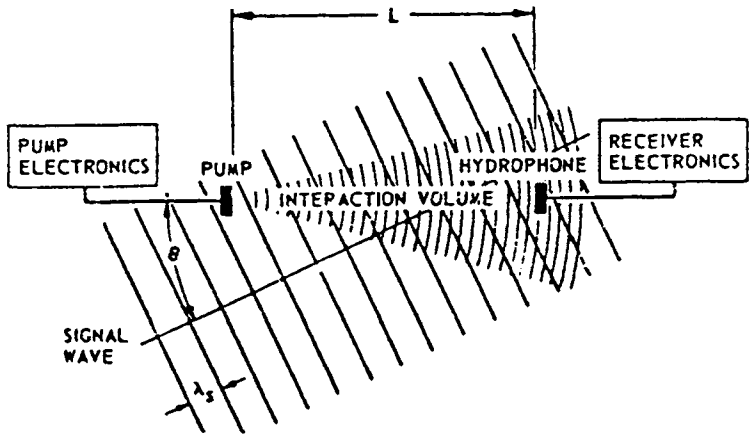

Figure 5.3.3 Schematic diagram of a parametric receiver. (From Rhode, D. F., T. G. Goldsberry, W. S. Olsen, and C. R. Reeves, "Band elimination processor for an experimental parametric receiving array," *J. Acoust. Soc. Am.* **66**, 484–487, 1979.)

5.3.3 INTENSE TONE BURSTS, SELF-DEMODULATION

Not long after the discovery of parametric effects, it was shown by Berktay (1965) that an intense, high-frequency tone burst will be demodulated as it progresses. After propagating a certain range, R, the carrier frequency will have attenuated, and only a low frequency component will remain. The new wave form is determined by the duration of the tone burst and the character of the transient start and stop parts of the burst signal. If one assumes a carrier of frequency ω modulated by the envelope function $f(t)$, Berktay showed that the peak, axial secondary pressure will be given by Equation 5.3.24.

$$P = \left(\frac{\beta P_1^2 S}{16\pi\rho_A c^4 \alpha R}\right) \frac{\partial^2}{\partial t^2}\left[f^2\left(t - \frac{R}{c}\right)\right] \qquad \textbf{(5.3.24)}$$

$$\text{where } R \gg \alpha^{-1} \quad \text{and} \quad R \gg S/\lambda$$

where α is the attenuation of the carrier frequency, λ is its wavelength, and S is the source area. The nonlinear parameter β was defined in section 5.1.

The prediction was confirmed by experiments such as shown in Fig. 5.3.4.

5.4 Explosive Sources

5.4.1 THE SHOCK WAVE

An underwater chemical explosion (e.g., TNT, Pentolite, Tetryl) is an effective source of sound for experiments at sea. The energy available from the explosion is approximately 4.4×10^3 joules/gm (TNT). The explosion starts with a very rapid chemical reaction which creates product gases at temperatures of the order 3,000°C and pressures of about 50,000 atms. The pressure at the gas-water interface is relieved by the rapid outward motion of the water, and a discontinuous shock-wave front is formed for the reasons described in section 5.1. There are then two sources of sound in the water surrounding a deep-water explosion: the shock wave, which carries about half of the energy of the explosion and which propagates spherically at speeds greater than the conventional 1500 m/s; and the huge oscillating gas bubble.

First consider the shock wave. An approximate description is that the shock shows an instantaneous rise in pressure to a maximum value, p_m. The pressure then decays exponentially (Fig. 5.4.1). Studies during and since World War II have shown that both the peak pressure and the time constant of the decay can be scaled according to a universal parameter, $(W^{1/3}/R)$, where W is the weight of the

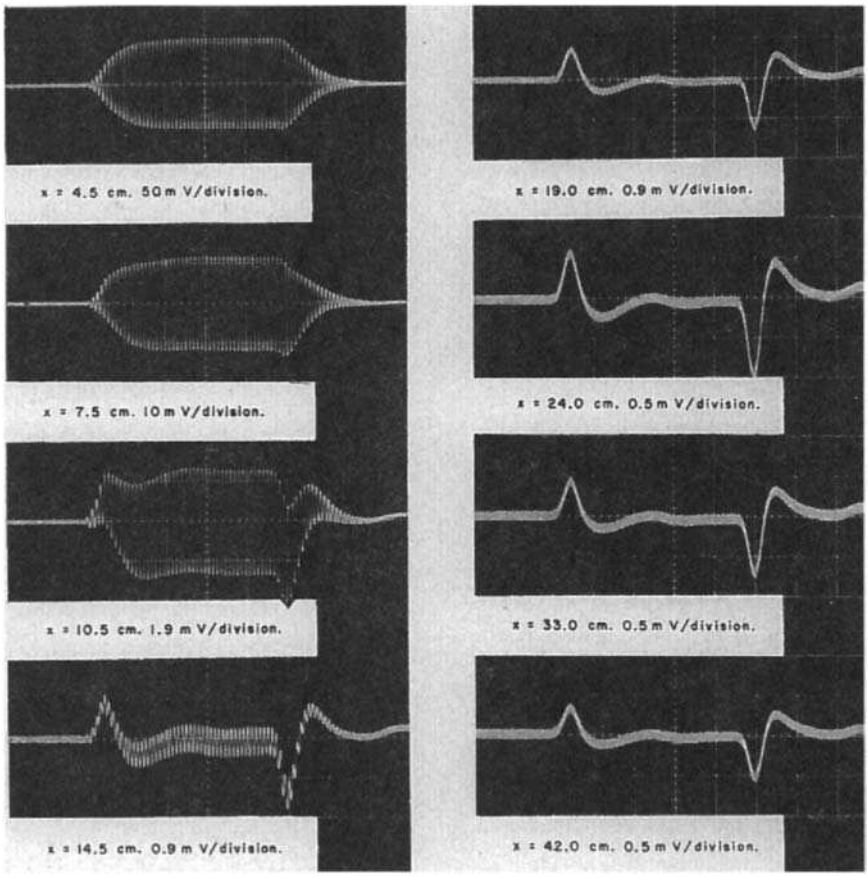

Figure 5.3.4 Self-demodulation of a tone burst. The burst amplitude was 1.9 atms at 10 MHz. The on-off transients caused low-frequency components of fundamental about 100 kHz at an amplitude approximately 3×10^{-3} atms as predicted by Equation 5.3.24. Propagation was as $1/x$, where x is the range. (Moffett, M. B., et al., "Large-amplitude pulse propagation — a transient effect," *J. Acoust. Soc. Am.* **47**, 1473–74, 1970.)

explosive and R is the range to the measurement position. See R. H. Cole, "Underwater Explosions" (1948), for a discussion of theory and early experiments. More recently, Rogers (1977) has used weak shock theory to derive accurate expressions for the peak pressure and decay time constant as a function of the charge-range parameter.

The most common explosives in current experiments at sea are 0.82 kg SUS (Signal, Underwater Sound) charges that are comprised principally of TNT. A

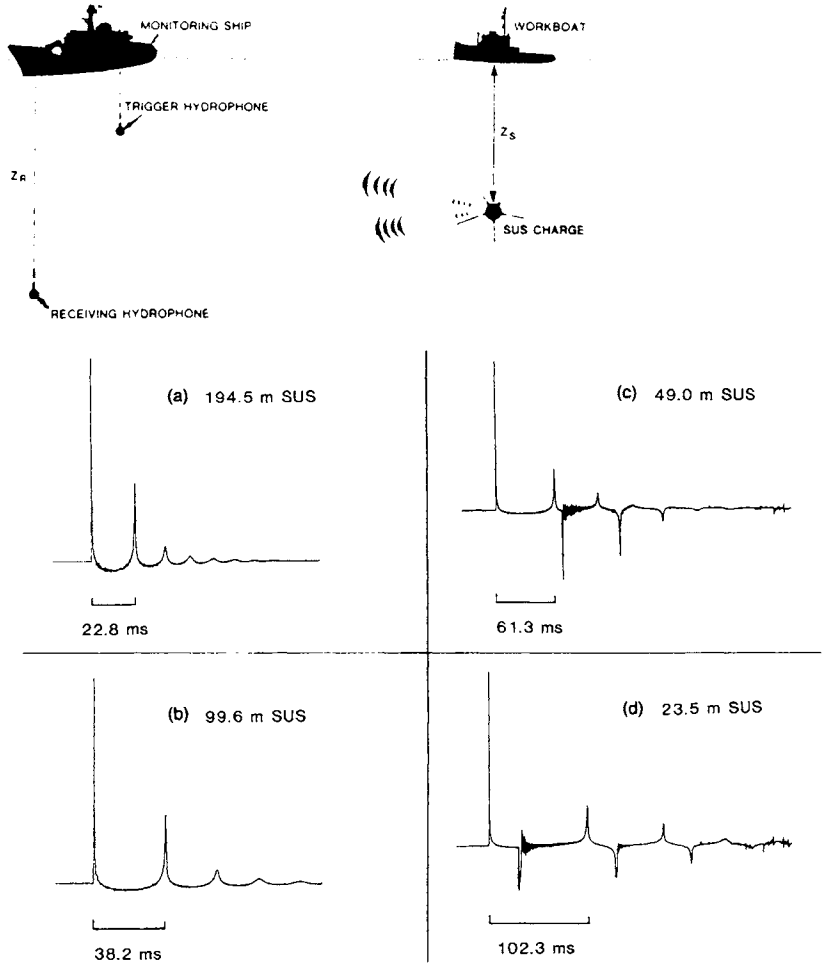

Figure 5.4.1 Sound pressures from an explosive at various depths and ranges at sea. The geometry is at the left. The first sound impulse is the shock wave (note the steep rise in pressure, and exponential decay), which is observed at all depths. At 194.5 m depth, the shock is followed by several oscillations of the bubble pulse. The pressure graph is similar at 99.6 m depth, but there is a greater time between the shock and the first bubble pulse, owing to the depth dependence of the bubble period Equation (5.4.10). At explosive depths 49.0 m and 23.5 m, one can identify the shock wave and the several bubble pulses and their phase-reversed reflections from the ocean surface. (From Chapman, N. R., "Measurement of the waveform parameters of shallow explosive charges," *J. Acoust. Soc. Am.* **78**, 672–81, 1985.)

great deal of effort has been expended to determine the source strength and decay time constant of SUS charges. The best empirical equations appear to be those of Chapman (1985), who conducted extensive trials at sea and verified a

relation originally by Slifko (1967) for the peak shock-wave pressure of the 0.82 kg SUS charge,

$$p_m = 50.94(w^{1/3}/R)^{1.13} \quad \text{MPa} \tag{5.4.1}$$

where p_m is given in megapascals when the charge weight w is in kilograms and the propagation range R is in meters. The range dependence is $R^{-1.13}$ rather than R^{-1}, because of excess attenuation at the shock front.

The early exponential decay immediately after shock passage is given by

$$p = p_m \exp(-t/\tau_s) \tag{5.4.2}$$

where τ_s is in seconds.

Chapman's redetermined expression for the decay time constant for the shock from a 0.82 kg SUS charge is

$$\tau_S = 8.12 \times 10^{-5} w^{1/3}(w^{1/3}/R)^{-0.14} \text{ seconds} \tag{5.4.3}$$

5.4.2 *SHOCK FRONT PROPAGATION; THE RANKINE-HUGONIOT EQUATIONS*

The propagation equations that were derived for infinitesimal (acoustic) waves in Chapter 2 are not valid for shock waves. However, the equations of conservation of mass, momentum, and energy at a shock front, the "Rankine-Hugoniot equations," are easily derived (Fig. 5.4.2).

Conservation of Mass

Let an observer move with the front. The mass per unit area per unit time entering from the right is $M = \rho_A U$. The mass per unit area per unit time leaving the front must be the same, $M = \rho_m(U - u_m)$. Equating, we get the Rankine-Hugoniot

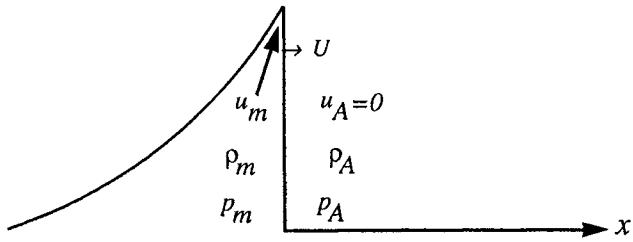

Figure 5.4.2 Conditions at a plane shock front that moves with velocity, U. In front of the shock, the particle velocity is zero, pressure is p_A, and density is ρ_A. At the shock front the pressure, density, and particle velocity are p_m, ρ_m and u_m, respectively.

equations for conservation of mass;

$$M = \rho_A U = \rho_m (U - u_m)$$
$$u_m = \left(\frac{\rho_m - \rho_A}{\rho_m}\right) U \tag{5.4.4}$$

Conservation of Momentum

For conservation of momentum, notice that the net momentum per unit area per unit time delivered to the entering fluid is $\rho_A U^2 - \rho_m (U - u_m)^2$. The net pressure acting toward the right is $p_m - p_A$. Equating the two gives the conservation of momentum equations

$$p_m - p_A = \rho_A U^2 - \rho_m (U - u_m)^2 \tag{5.4.5}$$

or, more simply, using Equation 5.4.4,

$$p_m - p_A = \rho_A u_m U \tag{5.4.6}$$

from which we obtain the shock front propagation speed, U:

$$U = \sqrt{\frac{(p_m - p_A)\rho_m}{(\rho_m - \rho_A)\rho_A}} \tag{5.4.7}$$

Since water is only slightly compressible, $\rho_A/\rho_m \cong 1$. Therefore, the shock speed U depends on the *average* slope $(p_m - p_A)/(\rho_m - \rho_A)$ in the $p\rho$ graph, Fig. 5.1.1. On the other hand, the speed of sound at the peak, c_m, depends on the *local incremental* slope, $(\Delta p/\Delta \rho)_{p_m, \rho_m}$, which is clearly larger than the average slope. Therefore $c_m > U > c_A$.

To obtain the densities in order to calculate u_m and U from Equation 5.4.7, one needs the equation of state for seawater and the conservation of energy equation at the shock front. See section 2.6 of Cole (1948). The result is plotted in Fig. 5.4.3, from which one observes that the speed of the shock front can be significantly greater than the conventional speed of sound in seawater, 1500 m/s.

5.4.3 THE GAS GLOBE

The huge gas globe which encloses the products of the chemical components of the explosion, as well as vaporized water, contains about half the total energy of the explosion. Sound is radiated during acceleration of the bubble radius. After the initial acceleration, the great bubble decelerates, expands past the point where

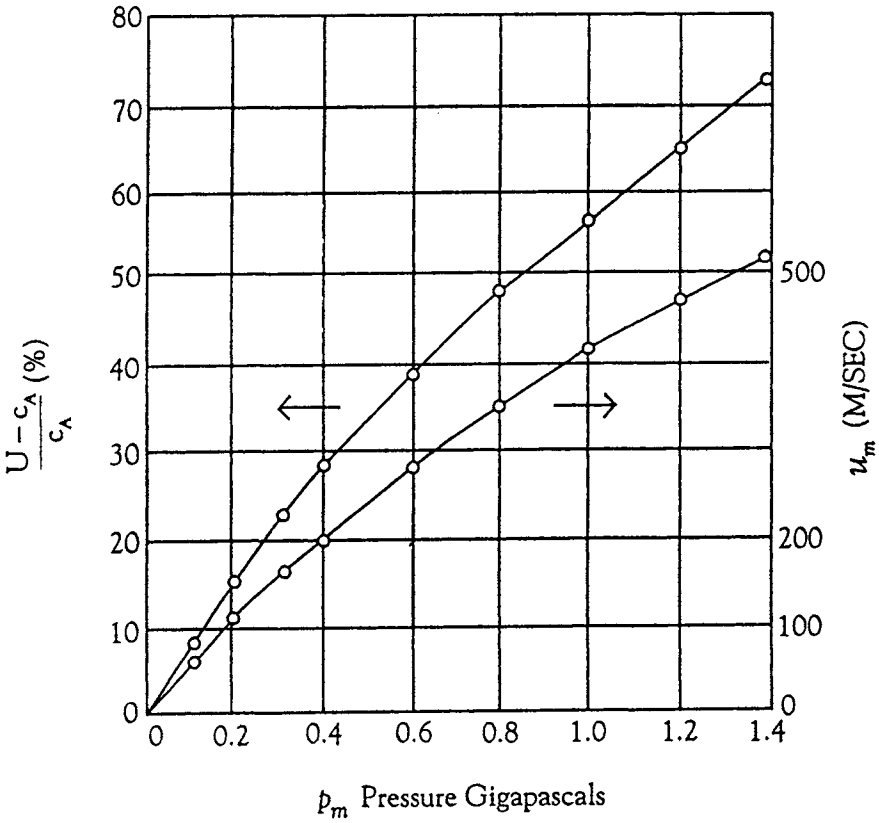

Figure 5.4.3 Particle velocity at shock front u_m and relative speed of shock front in seawater as a function of the peak pressure at the shock front p_m. (From Cole, Robert H., *Underwater Explosions*, Princeton University Press: Princeton, N.J., 1948.)

the internal bubble pressure equals the ambient pressure, slows, and reaches a maximum radius. At maximum radius, the internal gas pressure is less than the ambient pressure, and the bubble contracts. The oscillating gas bubble is responsible for the bubble pulses, following the shock wave in Fig. 5.4.1.

The period of the gas bubble oscillation is a function of the energy available to it after the shock has been formed, and the ambient density and pressure of the water that surround it. To calculate the approximate period, assume that the bubble is spherical and determine the partition of nonshock energy, Y.

At the maximum radius, a_m, the kinetic energy is zero, and the internal energy is much less than the potential energy. Therefore we can assume that the

nonshock energy, which contains about half of the total explosion yield, is all potential energy:

$$Y = (4/3)\,\pi\, a_m{}^3\, P_A \tag{5.4.8a}$$

or

$$a_m = \sqrt[3]{\frac{3Y}{4\pi P_a}} \tag{5.4.8b}$$

To calculate the approximate period of the motion, assume that the bubble oscillates spherically as an ideal bubble (see Chapter 8) at its depth, where the ambient conditions are p_A, ρ_A. The period of oscillation of a spherical bubble Equation 8.2.13 is given by

$$T = 2\pi a_m \sqrt{\frac{\rho_A}{3\gamma P_A}} \tag{5.4.9}$$

Substitute a_m from Equation 5.4.8a to obtain the approximate period,

$$T = K\, Y^{1/3} \rho_A^{1/2} P_A^{-5/6} \tag{5.4.10}$$

where dimensionless $K \cong 2$ depends on our assumptions. The S.I. for Y are joules.

This equation has been derived by others in many ways; it is called the Willis equation. It is important for our purposes because it specifies the approximate dependence of bubble period on depth (recall Fig. 5.4.1) and explosive yield. The reality is that, because of the large differential pressure from its top to bottom, large explosive bubbles are not spherical but are flattened or dimpled at the bottom. Furthermore, the gas globe often splits into two because of that dimpling. Also, the nonharmonic pulsation does not generate a sinusoid, and the effective period changes as the bubble rises owing to buoyancy. Nevertheless, Equation 5.4.10 is a useful initial predictor.

5.4.4 INTERACTION WITH THE OCEAN SURFACE

When the explosive is close to the ocean surface, phase-reversed signals (caused by reflection from the water-air interface) will be received after the direct received signals. Fig 5.4.1, with the source at depth 49.0 m, shows the reflected shock wave just after the first bubble pulse.

Note the "noise" that follows the reflected shock in Fig. 5.4.1. When the positive shock pressure is reflected, it is phase-shifted, and it becomes a tension. This negative pressure can have a greater absolute value than the ambient

pressure. As a result, the water cavitates (section 5.2). The newly created microbubbles near the surface will reradiate damped oscillations at many frequencies (see section 8.2.9). This will give the appearance of random noise radiated from the surface. The reflected shock loses significant energy as it ploughs through the water and causes cavitation. Note, however, that the reflected first *bubble pulse* in this same figure does not appear to have a large enough tension to give evidence of cavitation. The signal shown for explosive depth 23.5 m should now be easy for the reader to explain.

In experiments at sea, it is often the case that the cacophony of multiple sources of sound that comes from an underwater explosive is not desirable. To avoid the bubble pulses and its sea surface reflections, experimenters can set off the explosive close enough to the surface to cause the bubble gases to vent before an oscillation can take place. The isolated shock wave is easier to deal with.

5.5 Acoustic Radiation Pressure

A sound beam transports acoustic energy and acoustic momentum. The average acoustic momentum carried through unit area in unit time causes an *acoustic radiation pressure*. The *Langevin* radiation pressure P_{RL} is the time average of the product of the momentum per unit volume, $\rho_A u$, by the particle velocity, u:

$$P_{RL} = \frac{\text{momentum transfer}}{\text{area time}} = \langle \rho_A u^2 \rangle \tag{5.5.1}$$

The Langevin radiation pressure is the difference between the pressure in the beam perpendicular to the wall and the static pressure in the fluid behind the wall. For additional explanations, see, for example Beyer (1978).

The quantity in Equation 5.5.1 is also the average acoustic energy per unit volume, $\langle \varepsilon \rangle$, at the point. It is equal to the average acoustic intensity divided by the speed of sound,

$$P_{RL} = \langle \rho_A u^2 \rangle = \langle \varepsilon \rangle = \frac{\langle I \rangle}{c_A} \tag{5.5.2}$$

Therefore, if one determines the Langevin radiation pressure, the energy density is obtained, and the intensity of the beam is readily calculated. The technique is frequently used in ultrasonic measurements where the insertion of a hydrophone would disturb the acoustic field that is being measured. It can also be used in calibration of a high-frequency underwater source. To use the technique, a

diaphragm is inserted perpendicular to the beam, and the radiation force is measured as in Figs. 5.5.1 and 5.6.1.

Strictly speaking, radiation pressure is not solely a high intensity effect; it exists for infinitesimal sound amplitudes, as well. However, because the radiation pressure depends on the *square* of the acoustic pressure it is much easier to measure at high intensities than at low intensities.

5.6 Acoustic Streaming

In addition to harmonic distortion, intense sound waves cause a unidirectional flow call "streaming." Acoustic streaming is characterized by an outward jetting of the medium in front of any transducer that propagates high-intensity sounds. In the early days the phenomenon was called the "quartz wind" because quartz crystals were used as underwater sound sources. In air, the effect is experienced most easily by turning up the gain of an audio system and placing one's hand in front of the loudspeaker to feel the breeze.

In the case of a piston transducer propagating a sound beam in the open sea, the acoustic streams are strongest *away* from the source end on the sound axis. This is because the axial stream velocity increases somewhat beyond the source where the higher attenuation of the newly generated frequencies (due to harmonic distortion) increases the momentum transfer from the sound wave to the bulk medium (see, for example, Starritt et al. 1989). At much greater ranges, the stream velocity decreases owing to the weaker acoustic field and fluid mixing. Nevertheless, the streams jet out for distances of the order of meters as they

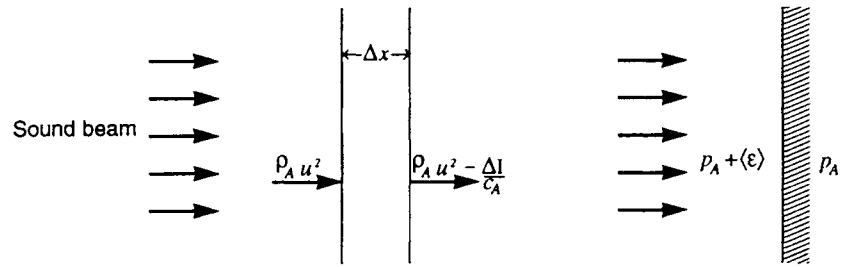

Figure 5.5.1 Acoustic radiation pressure and acoustic streaming in a beam. Left, sound attenuation through the path Δx causes a decreased acoustic momentum along the path $\Delta I / c_A$; this is taken up by a streaming momentum of the bulk medium. Right, Langevin radiation pressure of a sound beam measured at a wall is the average energy density in the beam.

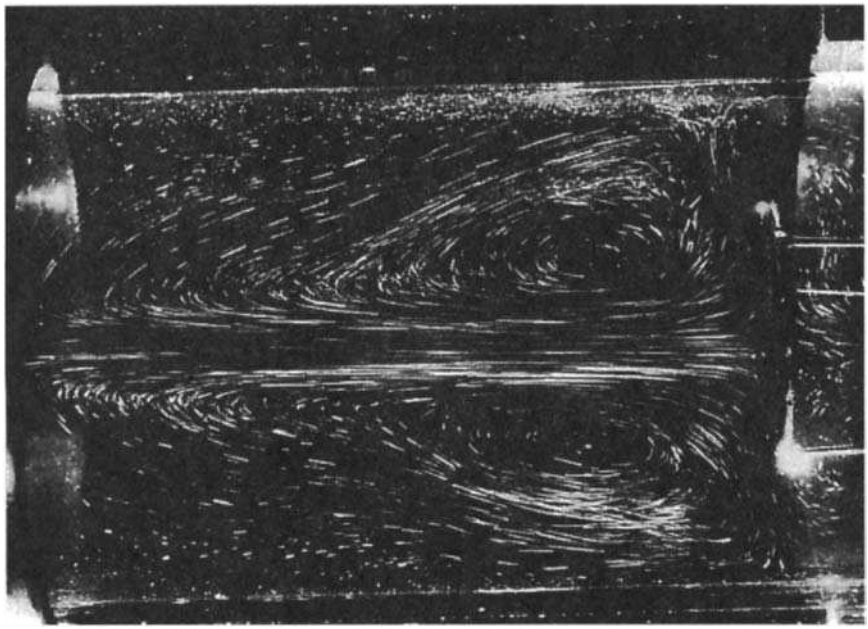

Figure 5.6.1 Acoustic streaming in front of a source in water. The quartz piston sound source is at the left. At the right, a diaphragm, which was used to measure radiation pressure, caused the axial stream to diverge into a tight vortex. The flow was made visible by suspended particles of aluminum. (From Liebermann, L. N., "Second viscosity of fluids, *Phys. Rev.* **75**, 1415–22, 1949.)

gradually circulate back to the side of the transducer (Fig. 5.6.1). The acoustic streams start to flow in tenths of seconds.

The many different acoustic streaming patterns that occur in intense sound fields depend on the geometry of the region and the form of the acoustic field. The basic reason for the flow can be easily understood as momentum transfer from the attenuating sound wave to the bulk medium. Following an argument of Fox and Herzfield (1950), consider a section of a plane wave beam (Fig. 5.5.1) carrying sound in the $+x$ direction.

For an attenuating medium such as water, the spatial change of intensity is given by

$$\Delta\langle I \rangle = -2\alpha_e \langle I \rangle \Delta x \tag{5.6.1}$$

where α_e is the rate of attenuation of acoustic pressure, nepers per unit distance (section 3.4).

The spatial decrease of energy density due to the absorption of energy in distance Δx is

$$\Delta\langle\varepsilon\rangle = \frac{\Delta\langle I\rangle}{c_A} = \frac{-2\alpha_e\langle I\rangle\Delta x}{c_A} \tag{5.6.2}$$

The spatial rate of decrease of acoustic momentum per unit area per unit time is compensated by the change of static pressure:

$$\Delta p_A = \frac{2\alpha_e\langle I\rangle\Delta x}{c_A} \tag{5.6.3}$$

If that pressure is unsupported, it will cause the fluid to drift. Otherwise stated, the loss of momentum from the acoustic beam is taken up by a gain of momentum of the fluid mass; thus conservation of momentum is fulfilled.

A more general study of the streaming phenomenon (Medwin 1953) shows that the streaming *vorticity* (*vorticity* = $\nabla x u_2$ where u_2 is the streaming velocity) is generated at all points where there is sound absorption. If the acoustic field is completely away from boundaries, the volume absorption rate, α_e, determines the vorticity. When the sound field is adjacent to a boundary, the absorption in the *acoustic boundary layer* is the source that drives streams in the medium. The acoustic boundary is the viscous layer within which a grazing plane-wave particle velocity decreases exponentially from the plane-wave value to zero at a rigid wall. It was originally calculated by Lord Rayleigh; (1877); see also Pierce (1981). The thickness to e^{-1} is given as

$$l = \left(\frac{2\mu}{\omega\rho_A}\right)^{1/2} \tag{5.6.4}$$

The detailed flow patterns in specific situations depend on the local absorption of energy, the geometry of the region in which flow is driven by these distributed acoustical sources, and the sound intensity. For example, very strong eddies form around a bubble attached to a wall — say, at a sound transducer (Elder 1959). Potentially destructive streaming velocities thousands of times greater than the acoustic particle velocity have been observed.

The first specific example of streaming in free space was solved by Eckart (1948), who considered a nondivergent beam of radius a within a tube of larger radius a_0. Equation 5.6.5 has been used in this manner to determine the bulk viscosity when the axial streaming velocity is measured and the shear viscosity of the medium is known:

$$u_2 = \frac{2\pi^2 f^2 a^2 G I b}{c^4{}_A \rho_A} \tag{5.6.5}$$

where $G = [(a^2/a_0^2 - 1)/2] - \log(a/a_0)$; $I = P^2/(2\rho_A c)$; $b = 4/3 + \mu_b/\mu$; μ_b = dynamic bulk viscosity; and μ = dynamic shear viscosity .

This equation was used by Liebermann (1949) to calculate the seawater bulk viscosity, μ_b, a quantity whose numerical value was unknown at the time (see section 3.4.3). By this calculation he showed that the great difference between the theoretical and experimental values of the attenuation of sound in seawater that existed prior to the 1950s was due to the lack of knowledge of the macroscopic quantity, bulk viscosity (or the microscopic descriptions, the molecular relaxation or the structural relaxation).

The streaming pattern is sensitive to the form of the primary acoustic field. When the correct divergent beam pattern is used and the physical constants of the medium are known, predictions of the streaming velocity can be within 2 percent of the measured values (Medwin 1954). The streaming technique is a practical means to determine the bulk viscosity of fluids from simple acoustical and drift measurements. An excellent early summary of acoustic streaming was written by Nyborg (1965). Continuing research on the subject can be found in the triennial *Proceedings of the International Symposium on Nonlinear Acoustics.*

Problems

Section 5.1

5.1.1 Calculate the second harmonic generated in an intense unattenuating sinusoidal plane wave as shown in Fig. 5.1.2b by following a scheme first used by Black (1940). First show that in time Δt the advance of a crest is $\Delta x = \beta(\Delta\rho/\rho_A)c_A\Delta t$. Then assume the the distorted wave is simply the sum of a fundamental plus second harmonic, $p = P_1 \cos kx + P_2 \sin 2kx$, and show that the zero-slope peak $(dP/dx) = 0$ results in $P_2 \cong P_1 k\Delta x/2 = \beta(\Delta\rho/\rho_A)kxP_1/2$.

5.1.2 Use Fig. 5.1.3 to determine the rate of attenuation of the 454 kHz nonlinear wave propagating to range 101 m if the source pressure is 100 kPa, 200 kPa, and 300 kPa. Compare with the attenuation rate α in Chapter 3.

Section 5.2

5.2.1 Based on Fig. 5.2.2 and assuming that the density of cavitation nuclei remains constant with depth, plot a graph of onset of cavitation dependence on duty cycle for pulse duration 74 ms at transducer depth 5 m.

5.2.2 Fig. 4.4.4 shows how the near-field pressure varies across the face of a piston transducer. Replot those pressures on a two-dimensional graph and compare the hot-spot pressures where cavitation will most likely occur with the average acoustic pressure over the face of the transducer.

Section 5.3

5.3.1 Given a parametric source device with two primary coaxial beams of frequencies, 418 kHz and 482 kHz, a) calculate the 3 dB beam width of the difference tone and b) calculate the size of the simple piston source that would have been needed to produce the same beam width.

5.3.2 A parametric source is advertised as having a mean primary frequency of 200 kHz, a difference frequency of 12 kHz, and source input powers of $W_1 = W_1 = 200$ watts. Using the value $\beta = 3.5$ and the attenuation rate from Chapter 3 for seawater, calculate the efficiency of the parametric source.

Section 5.4

5.4.1 Plot a graph of peak explosive shock pressure versus range for a deep explosion from a 0.82 kg SUS charge.

5.4.2 Sketch the shock pressure p versus t for the first 200 ms after the detonation of a 0.82 kg SUS charge at depths 10 m, 100 m, and 500 m.

Chapter 6 | Processing of Ocean Sounds

6.1 Sampling Rules 184
6.1.1 Spatial Sampling 185
6.1.2 Temporal Sampling 185
6.2 Filter Operations 188
*6.2.1 Finite Fourier Transformations (Optional) 188
*6.2.2 Fourier Integrals and Series (Optional) 191
6.2.3 Filter Response Measurements 194
6.2.4 Time Domain View of Bandpass Filtering 195
*6.2.5 Convolution Operations (Optional) 195
6.2.6 Filter Operations in the Frequency Domain 197
6.3 Gated Signals 199
6.3.1 Dependence of Spectrum on Ping Carrier Periodicity 200
6.3.2 Dependence of Spectrum on Ping Duration 200
6.4 Power Spectra of Random Signals 200
6.4.1 Signals Having Random Characteristics 203
*6.4.2 Spectral Density and Correlation Methods (Optional) 203
6.4.3 Random Signal Simulations: Intensity Spectral Density 204
6.4.4 Spectral Smoothing 206
6.4.5 Traditional Measures of Sound Spectra 208
6.5 Matched Filters and Autocorrelation 209
6.6 Sounds in the Ocean 211
6.6.1 Natural Physical Sounds 212
6.6.2 Natural Biological Sounds 215
6.3.3 Ship Noise: Sample Calculation 219

Signals are the messages that we want to receive at our hydrophone. Noises are everything that we don't want to receive. The types of signal messages include impulses and CW tones of short or long duration and constant or varying frequency; they also include complicated coded messages and random sequences. The form of noise can run the gamut.

We all know the popular saying "Beauty (or ugliness) is in the eye of the beholder." One can propose a comparable acoustical maxim: "Signals (or noise) are in the ear of the listener." There are many examples: the sonar operator searching for the "signal" of a submarine will call the sounds of whales and dolphins "noise." Needless to say, the marine mammal seeking to communicate or locate food would characterize man-made sounds as "noise." Some sounds that were called "noise" for may years are now recognized as bearing

* Background material.

information that qualifies them as "signals"; for example, the sound of rainfall at sea is now used to measure the size and number of raindrops per square meter per second.

Flow noise at a transducer, electrical circuit noises, and the 60 or 50 Hz electrical interferences from power lines are generally regarded as noise by everybody.

Traditionally, underwater ambient noise has been specified in terms of the sound measured at a convenient hydrophone, some distance from the sources. The origins of the sound are often a mystery. We initiate a different approach. In section 6.5 we will survey the acoustic power, source pressure, directionality, and intermittency of physical, biological, and man-made ocean sounds *at their source*. When this information is known, one's knowledge of propagation in the ocean (e.g., Chapter 3) allows us to calculate the ambient sound at any location.

In addition to our survey of many of the more common sound sources at sea, we need operations that allow the listener to sort out the signal from the noise. The communication literature has many very thick books and lengthy discussions of each signal processing topic that we mention here — for instance, Churchhill and Brown (1987), Kanasewich (1981), Oppenheim and Shafer (1975), and Clay (1990). A comprehensive linear systems theory approach to underwater acoustics is given by Ziomek (1995). The necessary proofs and derivations of signal processing procedures are in these books.

6.1 Sampling Rules

Practically all underwater sound signals and noise are recorded digitally, and the results of analysis are displayed on computer terminals. The acoustician uses signal acquisition and digitizing equipment, signal processing algorithms, and graphic display software to make this happen.

The noisy signal that comes from our hydrophone is an electrical voltage that is a continuous function of time. It is called an analog signal. Hydrophone signals must be sampled to convert them from analog to digital format in order to enter a digital computer.

We must sample signals properly or we get garbage. The sampling rules are general. They apply to either temporal or spatial sampling of the oceanic environment. When the rules are obeyed, the original signal can be recovered from the sampled signal with the aid of an interpolation procedure. If the rules are not obeyed, and sampling is too sparse, the original signal cannot be recovered.

The Nyquist sampling rules are

(1) *Space Domain Rule. The spatial sampling interval must be less than half of the shortest wavelength of the spatial variation.* Spatial sampling is sometimes described in terms of the spatial wave number, $k_s = (2\pi)/\lambda_s$, where λ_s is the distance between samples.

(2) *Time Domain Rule. The time interval between samples must be less than half of the shortest period in the signal.* Sampling is defined in terms of the sampling frequency $f_s = 1/t_0$, where t_0 is the time between samples Otherwise stated, *the sampling frequency must be greater than twice the highest frequency component in the signal.*

6.1.1 SPATIAL SAMPLING

In traditional marine biology, samples are taken by towing a net through the water. A net is lowered to the depth, opened, and towed for a specified distance. Net sampling takes a lot of work. The following example of spatial sampling uses a two-dimensional map (or depth profile) of a marine biological survey in which the results of sparse *net* sampling and detailed *acoustical* sampling are compared. The details of the data acquisition are not important here.

Fig. 6.1.1 shows a simulation of sampling of the density of organisms or "particles" in the ocean, using nets. In this simulation, the length of the tow is 1.5 km. Simulated sampling stations were occupied at approximately 5 km spacings, and samples were simulated at 50 m depth intervals. The inadequately sampled data do not show much structure or pattern.

For comparison with Fig. 6.1.1, almost continuous acoustical sampling of the biomass is shown in Fig. 6.1.2. This figure shows strong features both in having regions with many scatterers, indicating large biomass (black spots), and regions with few or no scatterers (white). The heavy concentrations of biomass show much structure in the ocean biomass.

6.1.2 TEMPORAL SAMPLING

The electrical signal $x(t)$ is sampled by an analog-to-digital converter to create a sequence of numbers, (Fig. 6.1.3). The clock, (Fig. 6.1.3a), gives the sampling instruction. The sample is the instantaneous value of the signal voltage at the clock time. No information is recorded about the signal voltage between samples where straight lines are drawn.

Examples of data taken at two different sampling intervals are shown. In Fig. 6.1.3c there are for four samples in a half-period. In Fig. 6.1.3d the sampling interval is larger than the half-period. Reconstruction of the inadequately sampled

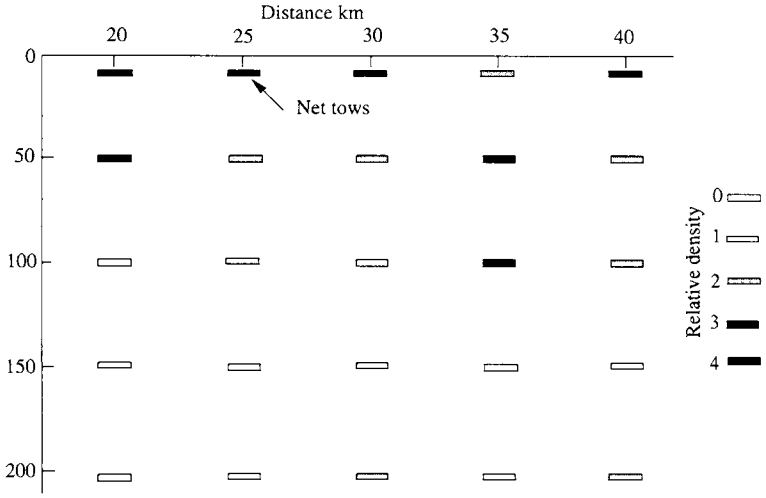

Figure 6.1.1 Simulation of net sampling of marine organisms. The net is towed at a set of stations at different ranges and depths. Each net tow is over a 1.5 km distance. The relative densities of organisms captured in the net tows are indicated by shaded rectangles using the relative density code at the right, 0, 1, 2, 3, and 4.

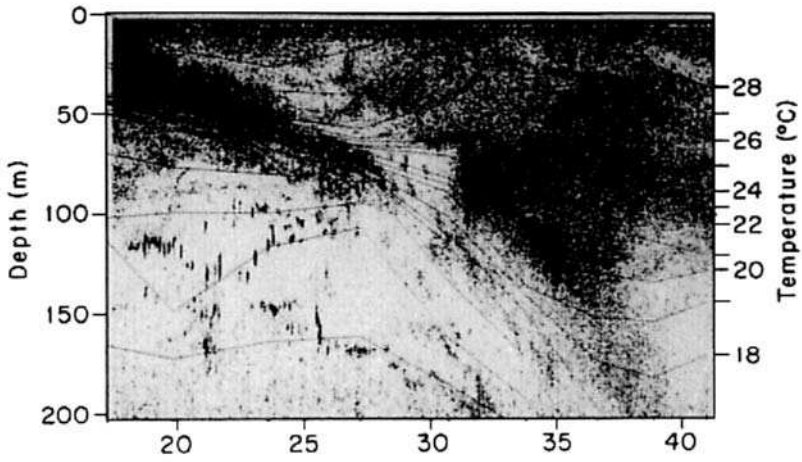

Figure 6.1.2 Acoustical profile of biomass. The profile was made by recording the output of a downward-looking sonar as the ship traveled. The simulation of net samples shown in Fig. 6.1.1 was made from this profile. (From Nero, R. W.; J. J. Magnuson; S. B. Brandt; T. K. Stanton; and J. M. Jech, "Finescale biological patchness of 70 kHz acoustic scattering at the edge of the Gulf Stream–EchoFront 85," *Deep-Sea Res.* **37**, 999–1016, 1990.)

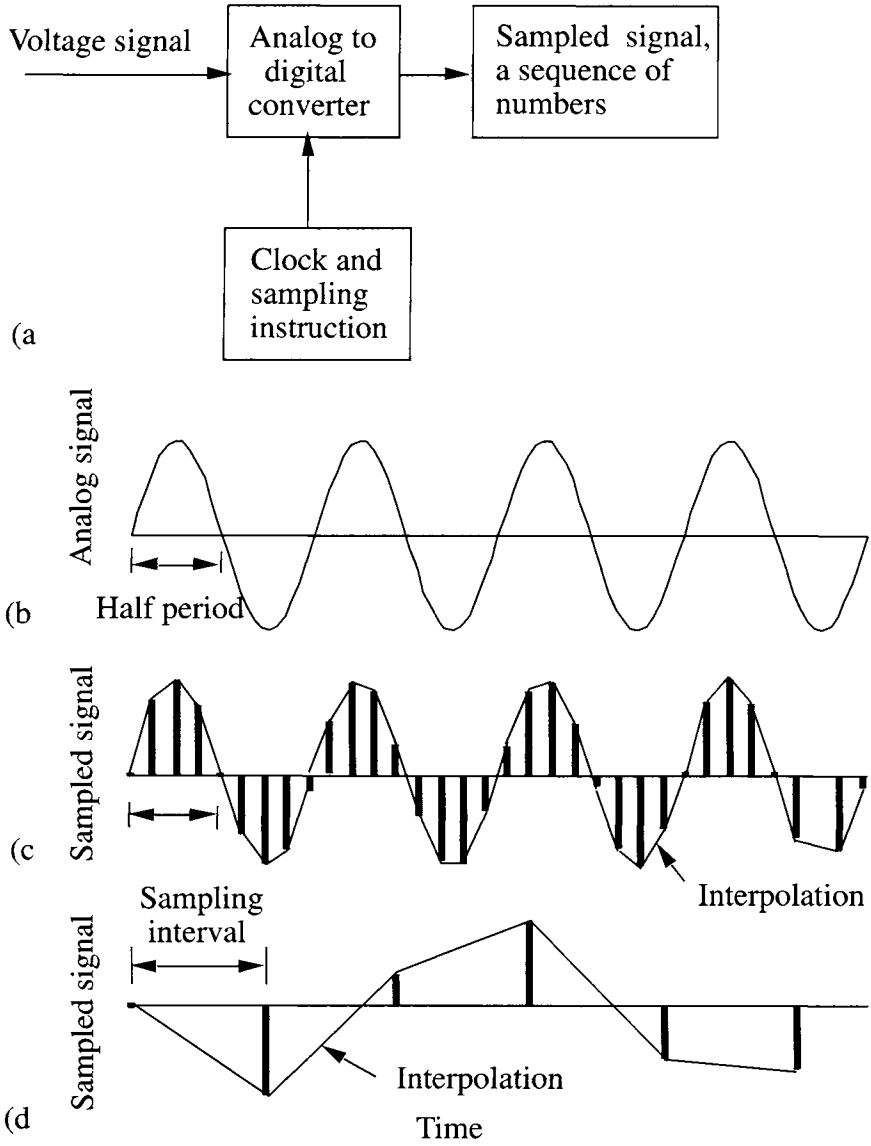

Figure 6.1.3 Temporal sampling of a simple signal. a) Sampling system to change an analog voltage into a sequence of numbers. b) Input analog sinusoidal voltage. c) The result of sampling four times during each half-period. The vertical lines represent the magnitudes of the sampled voltages. The straight lines between the ends of the vertical lines are interpolations. d) The result of sampling at times greater than the half-period. Compare the interpolated waveforms of c) and d) to the analog signal of b).

signal, Fig. 6.1.3d, does not resemble the original signal, whereas Fig. 6.1.3c does.

A practical rule of thumb is to sample at intervals less than the period/3 for approximate reconstruction of the original signal. Communication textbooks give more elaborate methods to get excellent reconstructions based on the Nyquist theorem.

6.2 Filter Operations

Electrical filters were originally introduced into electronic systems by radio and telephone engineers to separate the signals they wanted from those that they didn't. Instrumentation manufactures built analog filters or "black boxes" for research laboratories. These filters had switches on the front to make frequency bandpass choices. We use the filters that are built into our radio or television set when we select a channel that tunes in our desired station and rejects others. Audio amplifiers have filters (equalizers, bass, and treble controls) to modify the amplitudes of the input frequencies and to enhance the quality of the sound coming from the speakers.

Digital communication engineers have developed the digital equivalent of the black box analog filter. The incoming analog electrical signal is digitized by an analog-to-digital converter, and the filter operations are done by a computer. In many systems, the filtered digital sequence of numbers is converted back to an analog signal for listening and display.

For simplicity in our discussion of operations on signals and noise, we use the neutral symbols x, h, and y to represent source, filters, and filter outputs, respectively. Notation, while generally consistent, varies in the literature; for example, x_n and $x(n)$ usually mean the same thing — the series of voltages that have been sampled from the analog input signal.

*6.2.1 *FINITE FOURIER TRANSFORMATIONS (OPTIONAL)*

Digital computers, digitized data, and efficient algorithms have made the numerical computations of Fourier transformations practical. Applications are in MATLAB™, Mathematica™, and Theorist™. Examples and source codes are given in Clay (1990).

* Background material.

The Fourier transformation of a finite number of data points is called the finite Fourier transformation (fft), or discrete Fourier transformation (dft). The time intervals between all digitally sampled data points are t_0. For N data points, the Fourier transformation pairs are

$$X_{fft}(m) = \sum_{n=0}^{N-1} x(n)\, e^{-i\,2\pi mn/N} \tag{6.2.1}$$

$$x(n) = \frac{1}{N} \sum_{m=0}^{N-1} X_{fft}(m)\, e^{i\,2\pi mn/N} \tag{6.2.2}$$

where x_n is the nth digital input signal amplitudes, and $X_{fft}(m)$ is the mth spectral component. Equation 6.2.1 changes a time-dependent series of terms into a frequency spectrum. The companion Equation 6.2.2, or *inverse finite Fourier transformation* or (*ifft*), changes a spectrum into a time-dependent expression. Real $x(n)$ transforms to complex $X_{fft}(m)$ and vice versa.

A simple example demonstrates the periodic properties. Let $N = 64$ and suppose that the original digitized signal is real and exists between $n = 0$ and $n = 63$ as shown in Fig. 6.2.1a. The digitized signal is assumed to be an isolated event, (Fig. 6.2.1a). The *fft* method assumes that the signal has the period $N = 64$, as shown in Fig. 6.2.1b. Evaluations of the *fft* give real and imaginary components of $X_{fft}(m)$. Inspection of Fig. 6.2.1.c shows that the real components are symmetric about 0, $N/2$, and N. In Fig. 6.2.1d the imaginary components are antisymmetric about 0, $N/2$, and N. The modulus $|X_{fft}(m)|$, Fig. 6.2.1e, is

$$|X_{fft}(m)| = [(real\, X_{fft}(m))^2 + (imag\, X_{fft}(m))^2]^{1/2} \tag{6.2.3}$$

which is symmetric about 0, $N/2$, and N. If we had started with *real* $X_{fft}(m)$ and *imag*$X_{fft}(m)$, we would have got the periodic $x(n)$. This figure shows most of the important properties of the finite Fourier transformation.

Symmetry and Periodic Relations

$$real\, X_{fft}(m) = real\, X_{fft}(-m) \tag{6.2.4}$$

$$imag\, X_{fft}(m) = -imag\, X_{fft}(-m) \tag{6.2.5}$$

$$x(n+kN) = x(n) \tag{6.2.6}$$

$$X_{fft}(m+kN) = X_{fft}(m) \tag{6.2.7}$$

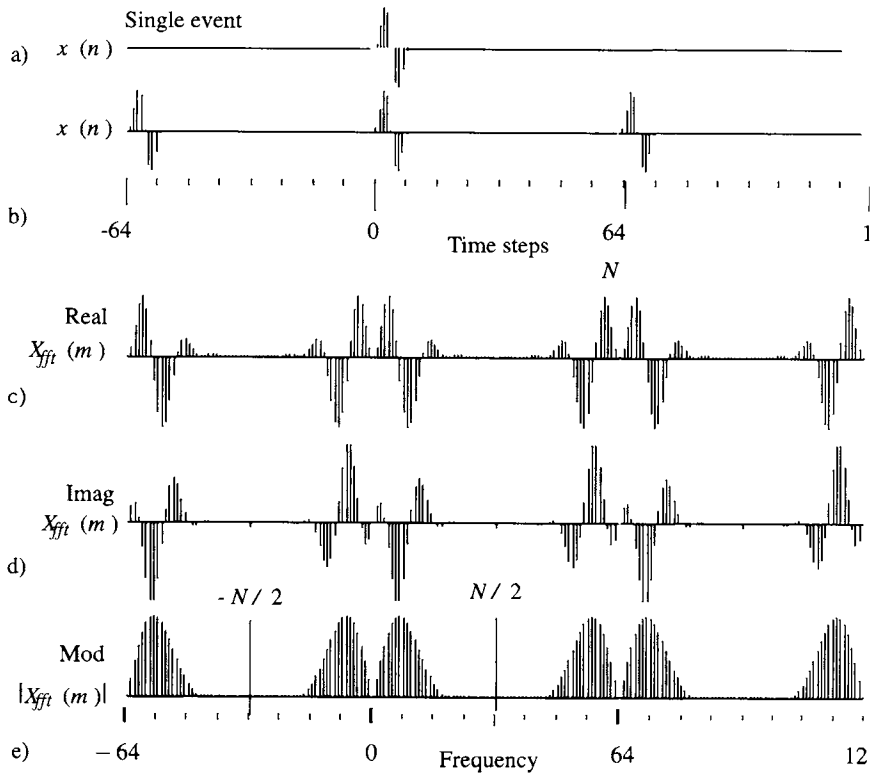

Figure 6.2.1 Signal, periodic Fourier series and its spectrum. Even if the original signal is not periodic, expansion in the Fourier series creates a new signal that is periodic. In applications, many zeros are appended to the signal to move the next cycle out of the way. a) Original signal. b) Periodic signal. c) Real component of $X_{fft}(m)$. d) Imaginary component of $X_{fft}(m)$. e) Modulus of $X_{fft}(m)$, $|X_{fft}(m)|$.

where k is an integer. The symmetry relations and Fig. 6.2.1 show that the summation limits in Equations 6.2.1 and 6.2.2 can be shifted to

$$X_{fft}(m) = \sum_{n=N/2}^{N/2-1} x(n)\, e^{-i\,2\pi mn/N} \tag{6.2.8}$$

and

$$x(n) = \frac{1}{N} \sum_{m=-N/2}^{N/2-1} X_{fft}(m)\, e^{i\,2\pi mn/N} \tag{6.2.9}$$

Time and Frequency Parameters

The time of a sample of the digitized signal is t_n, and its duration is T_1. These are defined by

$$t_n = nt_0 \tag{6.2.10}$$

and

$$T_1 = Nt_0 \tag{6.2.11}$$

The fundamental frequency is f_1, and the mth harmonic is f_m, given by

$$f_1 = 1/T_1 \tag{6.2.12}$$

and

$$f_m = m/T_1 \tag{6.2.13}$$

Substitutions in $2\pi mn/N$ give

$$2\pi mn/N = 2\pi f_m t_0 \tag{6.2.14}$$

Warning: In some applications, the *fft* algorithms use the parameter range 1 to N. These algorithms put sample 0 into $x(1)$ and frequency 0 into $X_{fft}(1)$. Our $x(n)$ goes to $x(n+1)$, and our $X_{fft}(m)$ goes to $X_{fft}(m+1)$. The summations become 1 to N.

*6.2.2 FOURIER INTEGRALS AND SERIES (OPTIONAL)

Fourier Integrals

Our first task is to relate the $X_{fft}(m)$ from the *fft* to the spectral density. Substitute $2\pi f_m t_n$ for the *fft* (Equation 6.2.1) and multiply both sides by t_0. The result is

$$X_{fft}(m)t_0 = \sum_{n=0}^{N-1} x(n) e^{-i2\pi mn/N} t_0 \tag{6.2.15}$$

Write Equation 6.2.15 as follows:

$$X(f_m) = \sum_{n=0}^{N-1} x(n) e^{-i2\pi f_m t_n} t_0 \tag{6.2.16}$$

* Background material.

where

$$X\ (f_m) = X_{fft}\ (m)\ t_0 \tag{6.2.17}$$

The *amplitude spectral density* is $X(f_m)$.

To get the integral, let t_0 become dt, f_m become f, and t_n become t. The summation becomes the infinite integral

$$X\ (f) = \int_0^{\infty} x\ (t)\ e^{-i\ 2\pi f t} dt \tag{6.2.18}$$

The condition for the existence of Equation 6.2.18 is that the integral of the absolute value $|x(t)|$ is finite. The limits can range from finite to doubly infinite $(-, +)$.

The same substitutions or changes of variables give the inverse Fourier integral. Start with the *ifft* (Equation 6.2.9), replace $X_{fft}(m)$ with the amplitude spectral density, and replace Nt_0 with T_1 . The new *ifft* is

$$x\ (n) = \sum_{m\ =-N/2+1}^{N/2} X\ (f_m)\, e^{i\ 2\pi f_m t_n}\ \frac{1}{T_1} \tag{6.2.19}$$

The last step is to let $1/T_1$ become df and replace the summation by the infinite integral,

$$x\ (t) = \int_{-\infty}^{\infty} X\ (f)\, e^{i\ 2\pi f t}\ df \tag{6.2.20}$$

where the negative frequencies are needed to give a real $x(t)$.

Infinite Fourier Series

The classical infinite Fourier series, the one in most texts, assumes that $x(t)$ is continuous and periodic with the period T_1.

$$x\ (t + T_1) = x\ (t) \tag{6.2.21}$$

In the infinite series, the spectral component is the average of the $X_{fft}(m)$ and Equation 6.2.1:

$$X_{avg}\ (m) = X_{fft}\ (m)\ / N \tag{6.2.22}$$

where the subscript *avg* means average. Divide the *fft* (Equation 6.2.1) by N and multiply and divide by t_0 to get

$$X_{avg}(m) = \frac{X_{fft}(m)}{N} = \frac{1}{N t_0} \sum_{n=0}^{N-1} x(n) e^{-i 2\pi m f_1 t} t_0 \qquad \textbf{(6.2.23)}$$

where the fundamental frequency is

$$f_1 = 1/T_1 = 1/(Nt_0) \qquad \textbf{(6.2.24)}$$

Let t_0 become dt and Nt_0 become T_1, and integrate over a full period:

$$X_{avg}(m) = \frac{1}{T_1} \int_0^{T_1} x(t) e^{-i2\pi m f_1 t} dt \qquad \textbf{(6.2.25)}$$

Since the averaging factor $(1/N)$ was moved to Equations 6.2.23 and 6.2.25, the $(1/N)$ is removed from the *ifft* (Equation 6.2.2), and the changes of variables give

$$x(t) = \sum_{m=-\infty}^{\infty} X_{avg}(m) e^{i 2\pi m f_1 t} \qquad \textbf{(6.2.26)}$$

The conversions of the spectral components $X_{avg}(m)$ and $X_{fft}(m)$ to the amplitude spectral density are

$$X(f_m) = X_{avg}(m) T_1 = X_{fft}(m) t_0 \qquad \textbf{(6.2.27)}$$

There are others. *To get a standard result of Fourier analysis, we suggest converting the results of spectral analysis to the amplitude spectral densities* $X(f_m)$ (see Table 6.1), so that $X(f_m) = X_{avg}(m) T_1 = X_{fft}(m) t_0$.

Table 6.1 **Summary of Symbols for Operations on Signals**

Time Domain	***Continuous (analog) t***	***Sampled Digital***
Source signal	$x(t)$	$x(n)$
Filter	$h(t)$	$h(n)$
Filter output	$y(t)$	$y(n)$
Frequency Domain	***Continuous (Analog) f***	***Sampled Digital***
Source signal	$X(f)$	$X_{fft}(m)$
Filter	$H(f)$	$H_{fft}(m)$
Filter output	$Y(f)$	$Y_{fft}(m)$

The analog signal amplitudes (e.g., voltages) are designated (t) before being filtered and $y(t)$ after being filtered by $h(t)$. The amplitude spectral densities, $X(f)$ and $Y(f)$, come from Fourier integral transformations. Fourier series uses $X_{avg}(m)$. The sampling interval is t_0; the period is T_1; and the fundamental frequency is f_1.

6.2.3 *FILTER RESPONSE MEASUREMENTS*

As shown in Fig. 6.2.2, the frequency response of a filter is the ratio of the output/input voltages for a (long-duration) sinusoidal input signal (the oscillator). Two measurements are sketched in Fig. 6.2.2. To record signals digitally, we need a low-pass filter to prepare the signal for the digitizing operation. The filter shown in Fig. 6.2.2b is a "low pass," "anti-aliasing filter." It is adjusted to pass frequencies that are less than half the sampling frequency of the analog-to-digital converter and to reject higher frequencies. It thereby can prevent higher-frequency components from appearing as *alias* signals. The action of a bandpass filter is sketched in Fig. 6.2.2c. It is used to pass a signal and to reject unwanted signals and noise within the designed frequency range.

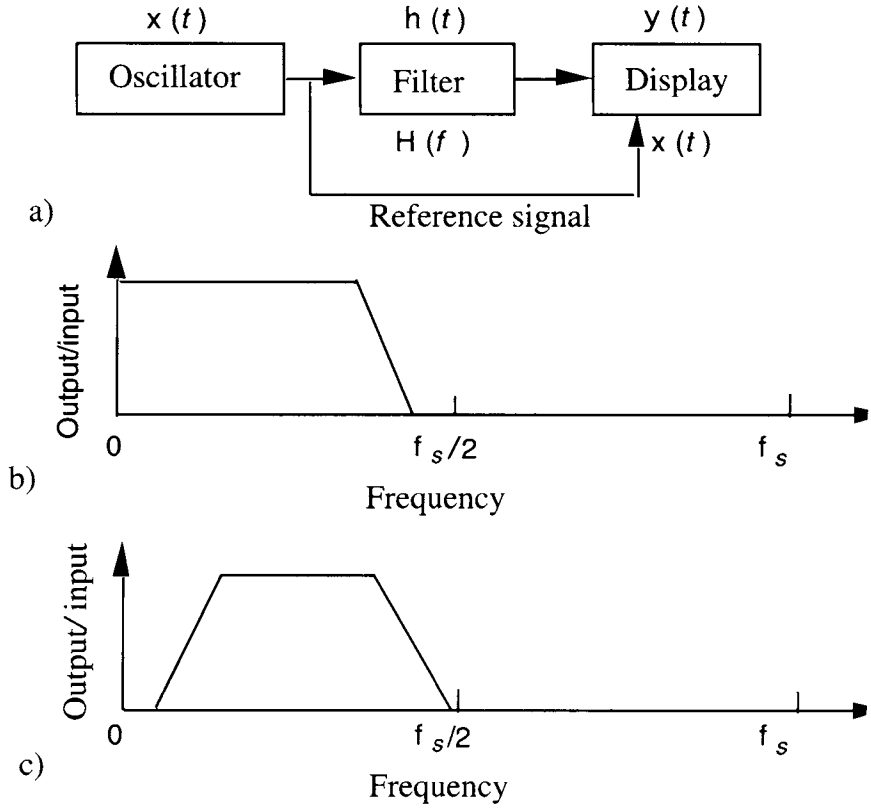

Figure 6.2.2 Filters and their responses. a) Block diagram for a typical filter response measurement . b) Response of an anti-aliasing, low-pass filter that is used ahead of analog-to-digital conversions at sampling frequency f_s. c) Response of a bandpass filter.

6.2.4 TIME DOMAIN VIEW OF BANDPASS FILTERING

Fig. 6.2.3a shows a short-duration signal, $x_1(t)$, which then passes through an appropriate bandpass filter to give the output $y_1(t)$ in Fig. 6.2.3b. The high- and low-pass settings on the filter were chosen to pass the signal with an acceptable amount of distortion of waveform.

A longer-duration, low-frequency whale song $x_2(t)$, is emitted during this same time so that the sum of the two signals at the input (Fig. 6.2.3c) is

$$x(t) = x_1(t) + x_2(t) \tag{6.2.28}$$

The output of the bandpass filter $y(t)$ is shown in Fig. 6.2.3d. The bandpass filter effectively removes the interfering whale song and reveals the short-duration 150 Hz ping.

*6.2.5 CONVOLUTION OPERATIONS (OPTIONAL)

Filter operations on a signal are convolutions of the signal and the filter response. Convolutions are usually evaluated numerically as follows:

$$y(j) = \sum_{m=0}^{m_1} x(m)\, h(j - m) \tag{6.2.29}$$

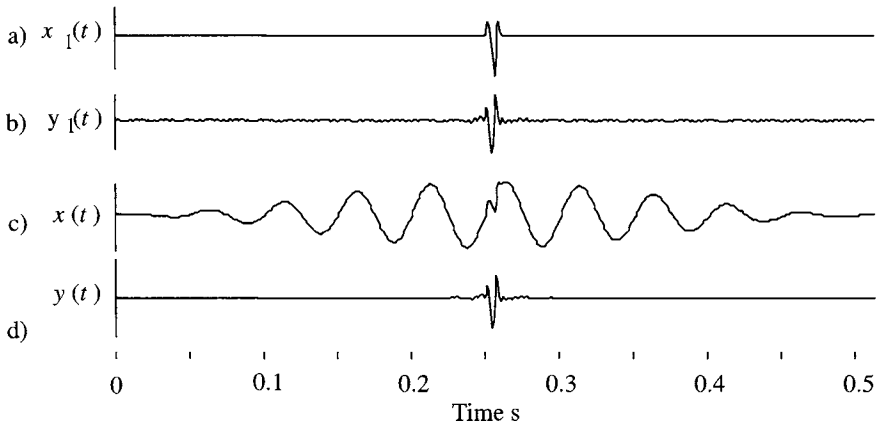

Figure 6.2.3 Filter operation shown in the time domain. a) Signal input is a 150 Hz ping having a duration of 0.01 s. b) Signal out of a 50–150 Hz bandpass filter. c) Input 150 Hz ping and a 20 Hz whale song. d) Filtered signal output using the 50–150 Hz bandpass filter.

* Background material.

For the convolution integral, change the summation to an integration on dt, the subscript m to the time parameter t, and the subscript j to the variable $t = jt_0$. To keep the dimensions right, multiply and divide the summation by t_0 and get

$$y(j) = \sum_{m=0}^{m_1} x(m) \frac{h(j-m)}{t_0} t_0 \tag{6.2.30}$$

Next, define the *temporal density function*, $h_{tdf}(t)$,

$$h_{tdf}(t) = h_j / t_0 \tag{6.2.31}$$

and let t_0 become dt. The integral expression follows:

$$y(t) = \int_{-\infty}^{\infty} x(\tau) h_{tdf}(t-\tau) d\tau \tag{6.2.32}$$

The limits are usually infinite. The dependence of $h_{tdf}(t-\tau)$ on τ is in the negative time direction; therefore, $h_{tdf}(t-\tau)$ has been turned around. The convolution integral is often hard to evaluate analytically.

Frequency Domain Convolution

Using the finite Fourier transformation (Equation 6.2.1),

$$Y_{fft}(m) = H_{fft}(m) X_{fft}(m) \tag{6.2.33}$$

the Fourier transformation is

$$y(n) = \frac{1}{N} \sum_{m=0}^{N-1} Y_{fft}(m) e^{i 2\pi mn/N} \tag{6.2.34}$$

The corresponding convolution integral, using $Y(f) = H(f)X(f)$ and Equation 6.2.20, is

$$y(t) = \int_{-\infty}^{\infty} Y(f) e^{i 2\pi f t} df \tag{6.2.35}$$

In many theoretical computations, the frequency domain is used for computations, and the results are transformed to the time domain.

6.2.6 *FILTER OPERATIONS IN THE FREQUENCY DOMAIN*

Operations in the frequency domain are intuitively simple. The frequency-dependent functions, $X(f)$ and $Y(f)$, are the amplitude spectral densities of the input and output signals, and $H(f)$ is the filter frequency response.

Using the symbols in Table 6.1, the input-output expressions for analog signals are

$$Y(f) = H(f)\,X(f) \tag{6.2.36}$$

and

$$Y_{fft}(m) = H_{fft}(m)\,X_{fft}(m) \tag{6.2.37}$$

The output signals $Y(f)$ or $Y_{fft}(m)$ have the frequency components that are passed by the filters. Our discussion uses the amplitude spectral densities for brevity.

Fig. 6.2.4a represents a spectrum analyzer that was constructed of many bandpass filters. The complex signal is an input to each of the filters. The spectral output of the jth filter is

$$Y_j(f) = H_j(f)\,X(f) \tag{6.2.38}$$

Parseval's theorem gives the equivalence between the integral squares of signals in the time and frequency domains:

$$\int_{-\infty}^{\infty} y^2(t)\,dt = \int_{-\infty}^{\infty} |Y(f)|^2\,df = 2\int_{0}^{\infty} |Y(f)|^2\,df \tag{6.2.39}$$

where the time integral of $y^2(t)$ is finite, and the absolute squares of $|Y(f)|$ and $|Y(-f)|$ are equal. For signals that start at 0 time, the limits of the doubly infinite integral become 0 to ∞. Using the filter input and output (Equation 6.2.38) and Parseval's theorem, the integral square output of the jth filter is

$$\int_{0}^{\infty} y_j^2(t)\,dt = 2\int_{0}^{\infty} |Y_j(f)|^2\,df \tag{6.2.40}$$

The substitution of Equation 6.2.38 into Equation 6.2.40 gives the filter output:

$$\int_{0}^{\infty} y_j^2(t)\,dt = 2\int_{0}^{\infty} |X(f)\,H_j(f)|^2\,df \tag{6.2.41}$$

For an approximation, let $H_j(f)$ be a "boxcar" filter defined by

$$H_j(f) = 1 \quad for\ (f_j - \Delta f/2) \le f \le (f_j + \Delta f/2) \tag{6.2.42a}$$

and

$$H_j(f) = 0 \quad \text{otherwise} \tag{6.2.42b}$$

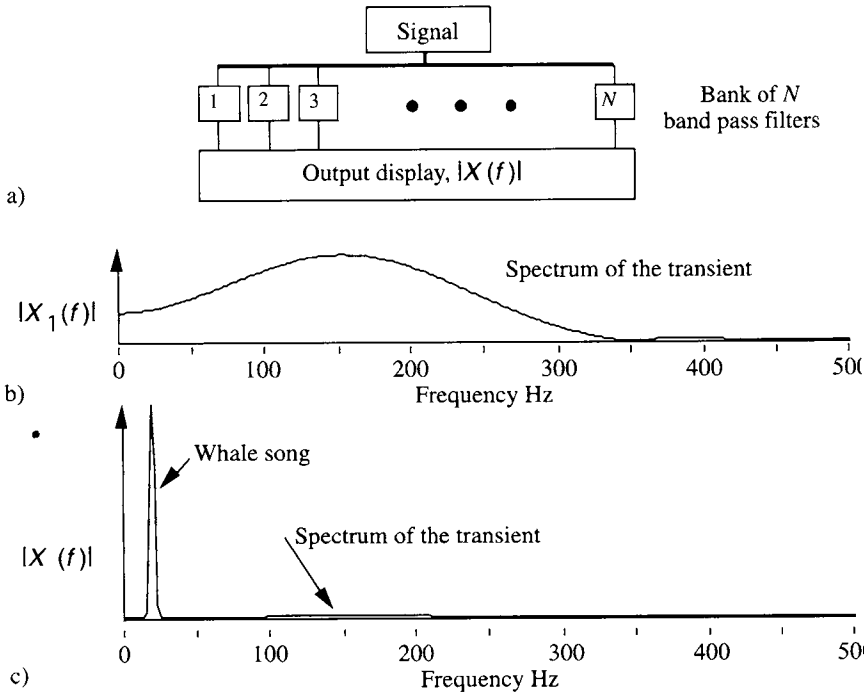

Figure 6.2.4 Spectral analysis of the signals of Fig. 6.2.3 using a digital spectral analysis. The bandwidths of the equivalent bandpass filters are 2 Hz. a) An analog spectrum analyzer that uses a bank of bandpass filters. b) The digitally calculated spectrum of the 150 Hz ping in Fig. 6.2.3a. c) The digitally calculated spectrum of the ping and whale song in Fig. 6.2.3c. The spectral amplitude factor of the ping is 1/40 that of the whale song. The ping doesn't show the detail of 6.2.4c because of the change of scale.

If $X(f)$ is approximately constant in the pass band (Equation 6.2.42), then the time integral square (Equation 6.2.41) is approximately

$$\int_0^\infty y_j^2(t)\,dt \approx 2\,|X(f_j)|^2\,\Delta f \tag{6.2.43}$$

This is the raw output of the boxcar spectrum analyzer.

The spectral density in a 1 Hz bandwidth is obtained by dividing both sides of Equation 6.2.43 by Δf

$$\frac{1}{\Delta f}\int_0^\infty y_j^2(t)\,dt \approx 2\,|X(f_j)|^2 \tag{6.2.44}$$

The quantity in Equation 6.2.44 is sometimes called an "energy spectral density," $E_{xx}(f_j)$, when the signal amplitude is a voltage, because the "integral

quare'' over time is *proportional* to the energy of the electrical signal during that me:

$$E_{xx}(f_j) = \frac{1}{\Delta f}\int_0^\infty y_j^2(t)\,dt \approx 2\,|X(f_j)|^2 \qquad \textbf{(6.2.45)}$$

he subscript $_{xx}$ indicates that $x(t)$ is the function being analyzed.

If $x(t)$ and $y(t)$ have units of Pa, the units of $E_{xx}(f_j)$ are Pa^2 s/Hz. Although the uantity $E_{xx}(f)$ is often called an ''energy spectral density,'' it is actually *oportional* to the energy spectral density of the wave. As shown in the scussion of intensity in section 2.5.3, true expressions for energy spectral nsity ((joules/m^2)/Hz) require that Pa^2 s/Hz be divided by $\rho_A c$.

Most spectrum analyzers are digital and use computers to do the spectral alysis. The digital spectrum analyzers often can have the equivalent of more an 1000 very narrow band-pass filters. Examples of spectrum analysis are own in Fig. 6.2.4b and c. The spectrum of the 150 Hz ping (Fig. 6.2.4b) and the ectrum of the short-duration ping and longer-duration whale song are shown in g. 6.2.4c.

.3 Gated Signals

ne spectrum of a signal depends on its time-domain waveform. Consider some ngs and their spectra. These comparisons display the relation of periodicity and ration, in the time domain, to the peak frequency and bandwidth of the ectrum.

For these examples, the ping has a slow turn-on and turn-off. The signal $x(t)$ is

$$x(t) = 0.5[1 - \cos(2\pi t/t_p)]\sin(2\pi f_c t), \quad \text{for } 0 < t < t_p \qquad \textbf{(6.3.1)}$$

nd

$$x(t) = 0 \quad \text{otherwise} \qquad \textbf{(6.3.2)}$$

here t_p is the total (non-zero) ping duration, and f_c is the (carrier) frequency. The nplitude factor in the [...] gives a spectrum with very small side lobes. This gnal is similar to the sound-pressure signal radiated by many sonar transducers nd some marine animals. The envelope of the sine wave is tapered from zero to a aximum and then back to zero.

6.3.1 DEPENDENCE OF SPECTRUM ON PING CARRIER PERIODICITY

Fig. 6.3.1 shows the dependence of the peak of the spectrum on the carrier frequency of the pings. The durations of the pings were chosen to be long so that the widths of spectral peaks are narrow. The 50 Hz signal has a spectral peak at approximately 50 Hz. The other signals have their spectral peaks at 100 and 150 Hz. The period of the signal can be measured to estimate the peak or central frequency of the spectrum. This is the first rule of thumb.

6.3.2 DEPENDENCE OF SPECTRUM ON PING DURATION

Fig. 6.3.2 shows the dependence of the widths of the spectral peaks on the durations of the pings. The effective durations of the signals t_d are a little less than the t_p in Equation 6.3.1 because the turn-ons and turn-offs are very gradual. The same frequency, 100 Hz, was used for all examples. To define the bandwidth Δf, we use the half-power width, given by the two frequencies where the amplitude is 0.707 of the peak amplitude. The spectra shown in Fig. 6.3.2b are the moduli, the absolute amplitudes. The widths of the spectra decrease as the signal duration increases and are approximately the reciprocals of the durations of the signals. The comparisons are

t_p, sec	t_d, sec	$1/t_d$, Hz	Δf, Hz
0.01	0.0085	118.0	120
0.02	0.017	58.8	60
0.04	0.034	29.4	30
0.10	0.080	12.5	13

(6.3.3)

These comparisons give a second rule of thumb:

$$(\Delta f)\,(t_d) \geq 1 \tag{6.3.4}$$

We use the $\geq$ sign for $(\Delta f)\,(t_d)$ because many signals have durations greater than $1/\Delta f$. The time t_d gives the minimum duration of a signal for a sonar system to have a bandwidth Δf.

6.4 Power Spectra of Random Signals

Sound pressures that have random characteristics are often called noise, whether they are cleverly created as such or are the result of random and uncontrolled processes in the ocean. The spectral analysis of both are the same. As inputs to a

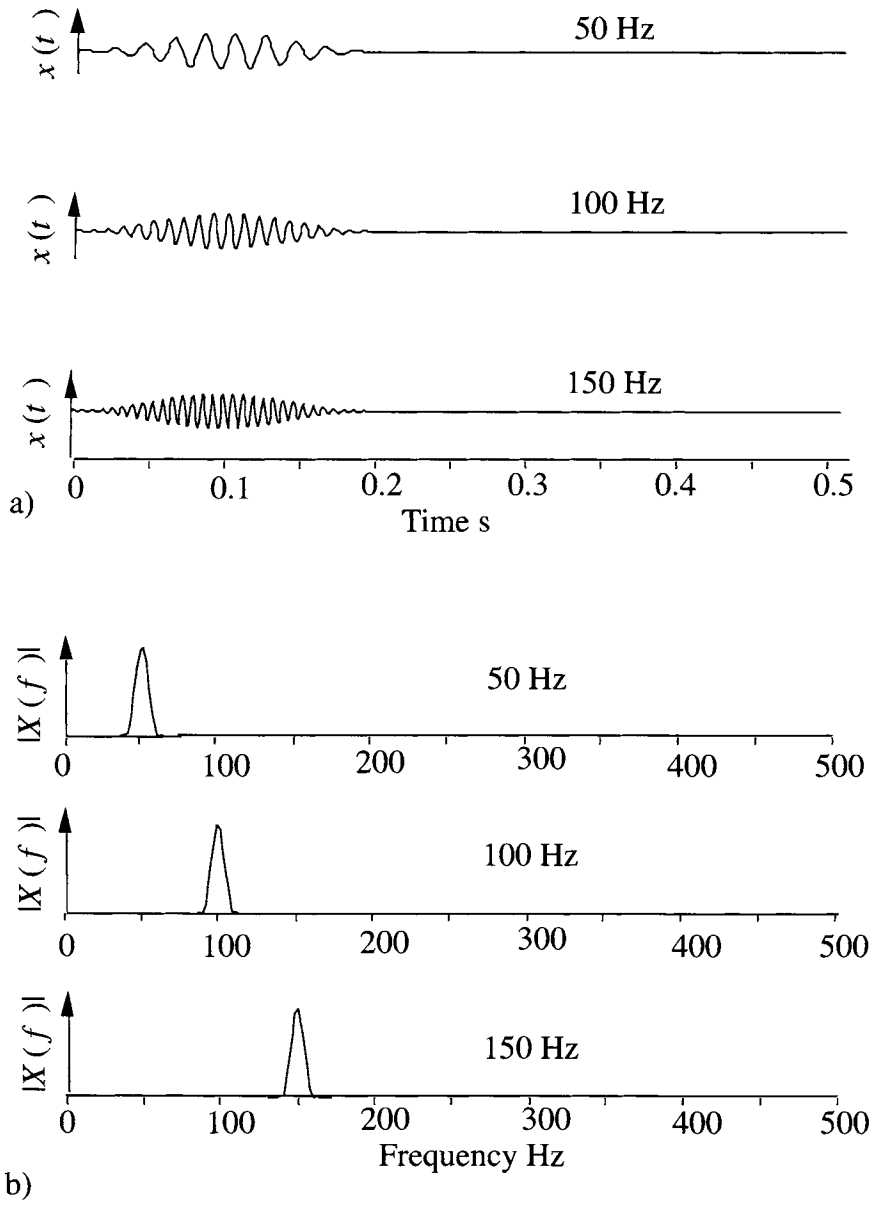

Figure 6.3.1 Signals and their spectra. All of the pings have the same duration. a) Time domain presentation of pings $x(t)$ with carrier frequencies of 50, 100, and 150 Hz. b) Modulus of the spectral amplitudes $|X(f)|$. The moduli of the spectra were computed using digital algorithms.

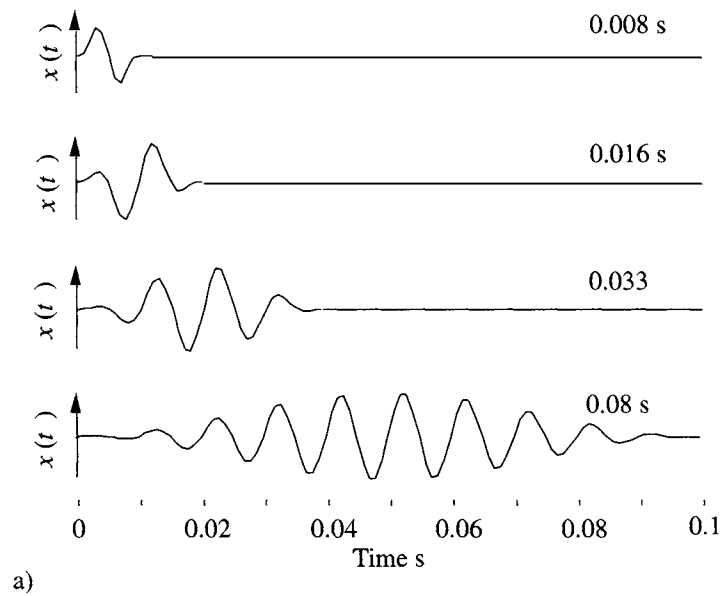

a)

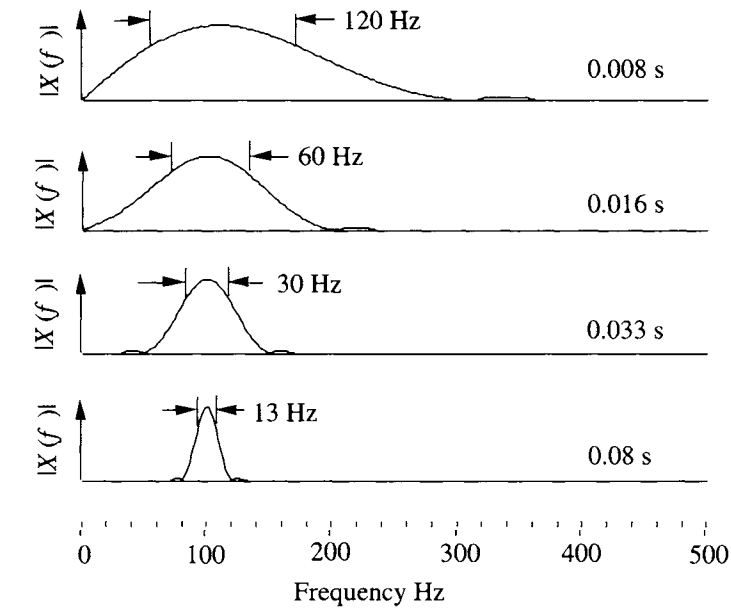

b)

Figure 6.3.2 Signals having the same carrier frequency and different durations. a) Signals in the time domain. b) Moduli of spectral amplitudes in the frequency domain. The bandwidths were measured at the half-power points (i.e., at 0.707 of the peak amplitudes).

spectrum analyzer, they are signals, and their spectral descriptions are to be determined. For a short name, these are called *random signals.*

6.4.1 SIGNALS HAVING RANDOM CHARACTERISTICS

In their simplest form, signals that have random characteristics are the result of some process that is not predictable. In honest games, the toss of a coin and the roll of a die give sequences of random events. In the earth, processes that range from the occurrence and location of earthquakes to rainfall at sea are generators of random signals. For simulations and laboratory tests, we use computers and function generators to make sequences or sets of random numbers. Many of the algorithms generate sequences that repeat, and these algorithms are known as *pseudorandom number generators.* The numerical recipe books give random number–generating algorithms. Programming languages usually include a function call such as rnd( ) in the library of functions.

*6.4.2 SPECTRAL DENSITY AND CORRELATION METHODS (OPTIONAL)

The correlation or covariance method of analyzing random signals is discussed in detail by Blackman and Tukey in their monograph *The Measurement of Power Spectra* (1958). The random signal is the sequence of numbers $x(n)$, and the sequence has $N + k_{\max}$ numbers. The covariance of the random signal is the summation

$$c(k) = \frac{1}{N} \sum_{n=0}^{N-1} x(n)\, x(n+k) \qquad \textbf{(6.4.1a)}$$

and

$$c_{xx}(k) = 0 \quad \text{otherwise} \qquad \textbf{(6.4.1b)}$$

The covariance $c_{xx}(k)$ is symmetric, and $c_{xx}(k) = c_{xx}(-k)$. The Fourier transformation of $c_{xx}(k)$ is, using Equation 6.2.1,

$$C_{xx,fft}(m) = \sum_{k=0}^{N-1} c_{xx}(k)\, e^{-i\,2\pi k m/N} \qquad \textbf{(6.4.2)}$$

* Background material.

The substitution of Equation 6.4.1 in Equation 6.4.2 gives

$$C_{fft}(m) = \frac{1}{N} \sum_{k=0}^{N-1} \sum_{n=0}^{N-1} x(n) x(n+k) e^{-i 2\pi m k / N} \tag{6.4.3}$$

Change variables by letting $j = n + k$, and Equation 6.4.3 becomes

$$C_{fft}(m) = \frac{1}{N} \sum_{n=0}^{N-1} x(n) e^{i2\pi mn/N} \sum_{n=0}^{N-1} x(j) e^{-i2\pi mj/N} \tag{6.4.4}$$

The first summation is the complex conjugate $X^*_{fft}(m)$ and the second summation is $X_{fft}(m)$. The spectrum is

$$C_{xx,\,fft}(m) = X_{fft}^*(m) X_{fft}(m) / N \tag{6.4.5}$$

and, using Equation 6.2.27, the spectral density is

$$C_{xx}(m) = C_{xx,\,fft}(m)\, t_0 \tag{6.4.6}$$

Frequency domain expressions for the autocovariance are

$$c_{xx}(\tau) = \int_{-\infty}^{\infty} C_{xx}(f) e^{i2\pi f \tau} df \tag{6.4.7}$$

and

$$C_{xx}(f) = \int_{-\infty}^{\infty} c_{xx}(\tau) e^{-i 2\pi f \tau} d\tau \tag{6.4.8}$$

where $C_{xx}(f)$ has positive and negative frequencies, and $C_{xx}(f) = C_{xx}(-f)$, or

$$c_{xx}(\tau) = 2 \int_{0}^{\infty} C_{xx}(f) \cos(2\pi f \tau) df \tag{6.4.9}$$

This pair of transformations, Equations 6.4.8 and 6.4.9, are known as the Wiener-Khinchine theorem.

The *power spectral density* of $x(t)$ is the sum of the positive and negative frequency components:

$$\Pi_{xx}(f) = 2C_{xx}(f) \tag{6.4.10}$$

6.4.3 *RANDOM SIGNAL SIMULATIONS: INTENSITY SPECTRAL DENSITY*

In the simulation of a random signal, the random function generator gives a sequence of random numbers: $x(0)$, $x(1)$, and so on. Fig. 6.4.1a shows a sequence where the numbers have been connected by interpolation lines. The result of

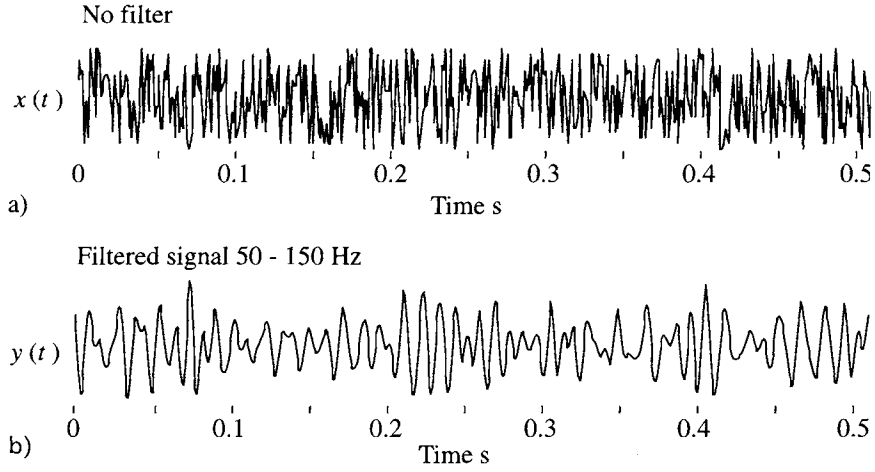

Figure 6.4.1 a) Random signal created by using a random number generator. The sampling interval was 1 ms. b) Result of bandpass filtering the signal in a) through a 50–150 Hz bandpass filter. The duration of the signal is t_d.

bandpass filtering the input random signal gives a new random signal, the output $y(n)$ in Fig. 6.4.1b.

The operations of bandpass filtering, squaring the signal, and summing or integrating the squared signal are indicated in Fig. 6.4.2. The effective number of independent trials is

$$N_{it} = t_d \ \Delta f_m \tag{6.4.11}$$

where t_d is the duration of the signal, and Δf_m is the filter bandwidth:

$$\Pi_{xx}(f_m) = \frac{1}{N \Delta f_m} \sum_{n=0}^{N-1} [y_m(n)]^2 \tag{6.4.12}$$

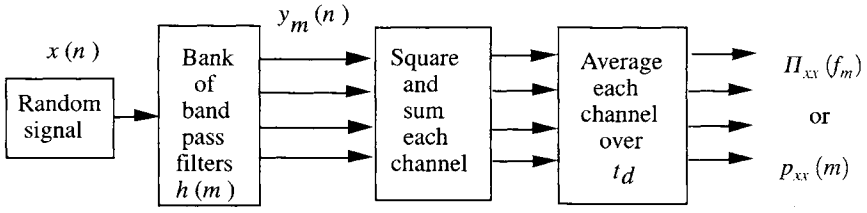

Figure 6.4.2 Block diagram of spectral analysis of a random signal in a computer or a single dedicated instrument. The set of filters $h(m)$ have center frequencies f_m and filter widths Δf_m. The duration of the random signal is t_d.

The filtered signal is $y_m(n)$, where the subscript is added to indicate the filtering by the mth filter. The signal is squared, summed, and averaged over t_d to give the power. Since the mean square output (e.g., volt^2) is proportional to the filter bandwidth and the duration of the signal, it is customary to define the "power" spectral density,

$$\Pi_{xx}(f_m) = \frac{1}{N\,\Delta f_m} \sum_{n=0}^{N-1} [y_m(n)]^2 \tag{6.4.13}$$

where N is the number of samples. The first step in deriving an equivalent integral expression for continuous functions of time uses the multiplication and division by t_0:

$$\Pi_{xx}(f_m) = \frac{1}{N t_0 \Delta f_m} \sum_{n=0}^{N-1} [y_m(n)]^2 t_0 \tag{6.4.14}$$

Let Nt_0 become t_d, the duration of the signal, and t_0 become dt. The summation becomes the integral:

$$\Pi_{xx}(f_m) = \frac{1}{t_d \Delta f_m} \int_0^{t_d} [y_m(n)]^2\, dt \tag{6.4.15}$$

If $x(n)$ has the units of volts, the so-called power spectral density has units of (volts)^2/Hz. True power spectral density would require division by a load resistance in an electrical circuit to give watts/Hz. Since a hydrophone output in volts is proportional to the acoustic pressure, $x(n)$ has the units of Pa, the spectral density has units of (Pa)^2/Hz, and the true *intensity spectral density* requires division by $\rho_A c$, to give $(\text{Pa}^2/\rho Ac)/\text{Hz} = (\text{watts/m}^2)/\text{Hz}$.

Acoustic spectra are often reported in dB relative to one $(\mu\text{Pa})^2$/Hz, so that the Intensity Spectrum Level

$$ISL = 10 \log_{10} \{[\Pi_{xx}(f_m)]/[(\mu\text{Pa})^2/\text{Hz}]\} \tag{6.4.16}$$

The spectrum levels depend on the reference sound pressure, which is sometimes unclear. It is better to use SI units such as (Pa)^2/Hz or (watts/m^2)/Hz.

6.4.4 SPECTRAL SMOOTHING

Consider the following example of spectrum analysis. A random signal is constructed of 512 magnitudes at separation $t_0 = 0.001$ s and duration 0.512 s. Fig. 6.4.3 shows the results of processing the signal by the equivalents of very-narrow, wide, and very-wide bandpass filters.

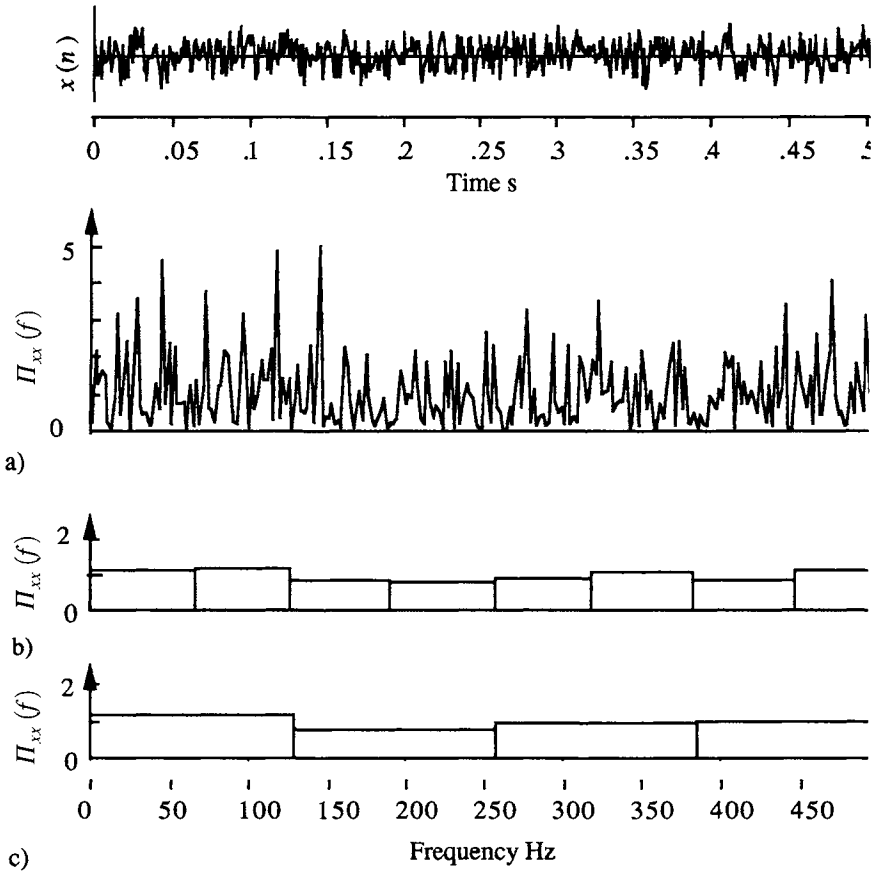

Figure 6.4.3 Smoothing of power spectra by filtering. The top trace is a random signal $x(n)$ or $x(t)$. Filter bandwidths are a) Δf=2 Hz, b) $\Delta f = 64$ Hz, and c) $\Delta f = 128$ Hz.

The output of the narrow 2 Hz filter, Fig. 6.4.3a, is extremely rough. The number of independent samples (see Equation 6.4.1) in the 2 Hz bandpass filter is 1. Fig. 6.4.3b shows the result of using a wider filter, $\Delta f = 64$ Hz. Here the number of independent samples is 32. The spectrum is much smoother and has less detail. An increase of the filter width to $\Delta f = 128$ Hz and the number of independent samples to 64 is shown in Fig. 6.4.3c. Another random signal would have a different spectrum. *These examples show the basic trade-off between resolution and reduction of roughness or variance of the estimate of the spectral density.*

The importance of smoothing power spectra and the trade-off between the reduction of frequency resolution and the reduction of fluctuations is given in detail by Blackman and Tukey (1958).

6.4.5 TRADITIONAL MEASURES OF SOUND SPECTRA

The measurement of underwater sounds has inherited the instrumentation and the vocabulary that were developed for measurements of sounds heard by humans in air. The principal areas of interest to humans have been accoustic pressure threshold for hearing; acoustic threshold of damage to hearing; threshold for speech communication in the presence of noise; and community response to annoying sounds.

The vast amount of data required to evaluate human responses, and then to communicate the recommendations to laymen, forced psychoacousticians and noise control engineers to adopt simple instrumentation and a simple vocabulary that would provide simple numbers for complex problems. Originally this was appropriate to the analog instrumentation. But even now digital measurements are reported according to former constraints. For example, the "octave band," which is named for the eight notes of musical notation that corresponds to the 2 : 1 ratio of the top of the frequency band to the bottom, remains common in noise-control work. For finer analysis, one-third octave band instruments are used; they have an upper- to lower-band frequency ratio of $2^{1/3}$, so that three bands span one octave.

The use in water of instruments and references that were designed for air has caused great confusion. The air reference for acoustic pressure level in dB was logically set at the threshold of hearing (approximately 20 μPa at 1000 Hz) for the average adult human. This is certainly not appropriate for underwater measurements, where the chosen reference is 1 μPa or 1 Pa.

Furthermore, plane-wave intensity (of CW) is calculated from Equation 2.5.16, where Intensity $= P_{rms}^2/(\rho_A c)$ (where P_{rms}^2 is the mean squared pressure; ρ_A = water density; and c = speed of sound in water). Therefore, the dB reference for sound intensity in water is clearly different from that in air because the specific acoustic impedance $\rho_A c$ is about 420 kg/m^{2}s for air compared with 1.5×10^6 for water. This ratio corresponds to about 36 dB, if one insists on using the decibel as a reference.

The potential for confusion in describing the effects of sounds on marine animals is aggravated when physical scientists use the decibel notation in talking to biological scientists. Confusion will be minimized if psychoacoustical characteristics of marine mammals—such as thresholds of pain, hearing,

communication perception and for so forth — are described by the use of SI units, (i.e., pascals; acoustic pressure at a receiver), watts/m^2 (acoustic intensity for CW at a receiver), and joules/m^2 (impulse energy/area at a receiver). Likewise, only SI units should be used for sources — that is watts (power output of a continuous source) and joules (energy output of a transient impulse source). The directivity of the source should always be part of its specification. All of these quantities are functions of sound frequency and may be expressed as *spectral* densities (i.e., per 1 Hz frequency band).

6.5 Matched Filters and Autocorrelation

The coded signal and its matched filter and associated concepts have become very important in the applications to sound transmission in the ocean. The simple elegance of the original paper of Van Vleck and Middleton (1946) is well worth a trip the the library. The generality of their concepts was far ahead of the then-existing signal-processing methods.

Digital signal processing facilitates the design of many types of filters for processing sonar signals (Oppenheim and Schafer 1975). Each definition of an optimum condition also defines a class of optimum filter. We limit our discussion to the simplest of the optimum filters, the *matched filter* (Van Vleck and Middleton 1946). An example is shown in Fig. 6.5.1.

An example of a coded signal $x(n)$ is shown in Fig. 6.5.1b. Recalling the convolution summation (Equation 6.2.29), the convolution of $h_M(n)$ and $x(n)$ is

$$y_M(j) = \sum_{m=0}^{m_1} x(m)\, h_M(j-m) \tag{6.5.1}$$

where the subscript $_M$ means the matched filter. The matched filter uses the criterion that the square of the peak output value $y_M(0)$ is a maximum. To maximize the square of $y_M(0)$, we use Cauchy's inequality (Abramowitz and Stegun, eq. 3.2.9):

$$[y_M(0)]^2 \leq \sum_{m=0}^{m_1} h_M^2(m) \times \sum_{m=0}^{m_1} x^2(m) \tag{6.5.2}$$

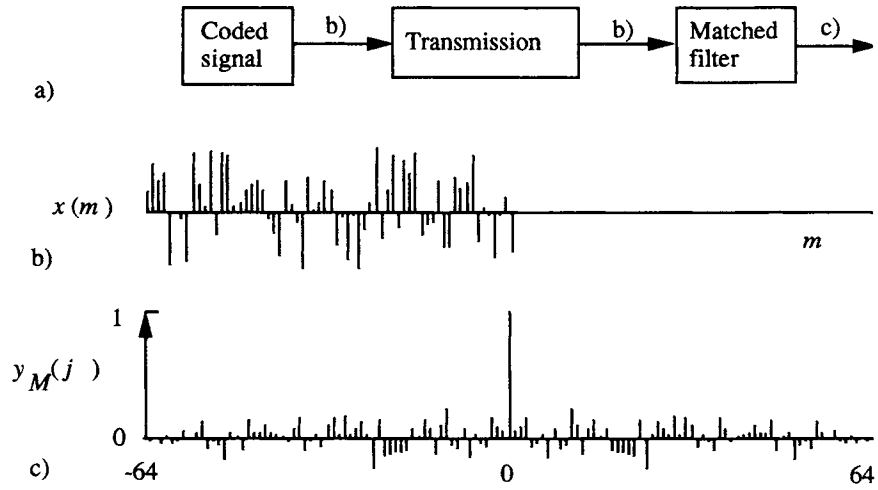

Figure 6.5.1 Coded signal, matched filter, and output. a) Simple matched filter system. b) Coded signal. Here the coded signal is a short sequence from a random-number generator. c) Output of the matched filter.

The filter produces a maximum output (the equal sign in Equation 6.5.2) when $x(m)$ is time-reversed to $x(-m) = x(m)$:

$$h_M(m) = Ax(-m) \quad \text{or} \quad h_M(-m) = Ax(m) \tag{6.5.3}$$

where A is a constant of proportionality. In our examples we use $A = 1/(m_1 + 1)$. The filter defined by Equation 6.5.3 is called the *matched filter*. In computations, it is convenient to shift the indices by m_1 and to shift the time by $m_1 t_0$.

$$h_M(m_1 - m) = h_M(-m) \tag{6.5.4}$$

to give a causal filter. Except for constants and normalization, $y_M(j)$ has the same form as the autocorrelation (Equation 6.4.1)

$$y_M(j) = A \sum_{m=0}^{m_1} x(m)\, x(m + j) \tag{6.5.5}$$

The output of the matched filter is shown in Fig. 6.5.1c. Here the output of the matched filter is the autocorrelation or covariance of $x(n)$.

The signal-to-noise amplitude ratio gain is proportional to the square root of the number of independent samples of the coded signal. While we don't prove it, ignoring noise in our derivation is equivalent to assuming that the noise is an

uncorrelated sequence of random numbers having a mean value of zero. This kind of noise is often called "white noise."

In frequency domain and using Equations 6.2.18 and 6.2.20, the time reversal of $x(m)$ to $h_M(-m)$ is equivalent to taking the complex conjugate of $X_M(m)$ to get $H_M(m)$. Recalling section 6.4.2, *the optimum matched filter operation is equivalent to computing the autocorrelation of the signal.*

In 1962 Parvulescu obtained a classified patent for the use of the *matched equivalent signal*, which he called *MESS*, for measuring the reproducibility of signal transmissions over large ranges in the ocean. In this first use of the matched filter technique in the ocean, the multipath received signals were regarded as a coded signal. An analog tape recorder was employed, with the tape direction reversed to convert the multipath arrivals into a matched filter. See Parvulescu (1995) and Tolstoy and Clay (1987, sec. 7.7).

6.6 Sounds in the Ocean

Ambient sound in the ocean is caused by a large number of physical and biological elements that are indigenous to the sea, as well as by powerful man-made sources. Each contributes to the local sound pressure by an amount that depends on the source characteristics and the attenuation between the source and receiver. Since low-frequency sounds have smaller attenuations, even distant sources of low-frequency sound are important at any measurement position. The sound often reaches the receiver by paths through the bottom, or scatter from the coastal shore, as well as through the water. Where possible, we give an outline of source characteristics such as the acoustic power radiated, the source pressure, directivity pattern, source spectrum, intermittency, and location.

Much of this essential information about sound sources is simply not known at this time, and marine scientists have accepted (by default) any hydrophone measurements they can get. Unfortunately, much published data on sounds at sea do not reveal the conditions of the experiment that affect the quoted numbers — for instance, hydrophone height above the ocean floor, topography at the hydrophone position, nearby scatterers, depth of water, distance from coastal reflectors, source and hydrophone distances from the ocean surface, and roughness of the ocean surface. Sometimes experimenters have buried these details into a single transmission number that is used to "calibrate" the site of the experiment.

When the source is known, algorithms such as the ray-path procedures (Chapter 3) or waveguide propagation (Chapter 11) can be used to predict the sound at any

location. Sections 11.3–11.5 show how arrays of hydrophones can operate as directional or mode filters in the reception of sound in an ocean waveguide.

During World War II, and for 40 years thereafter, the U.S. Defense Department sponsored a huge number of measurements of sound levels in the sea. (Many of these reports have been declassified and may be purchased from the U.S. Department of Commerce, National Technical Information Service, Springfield, VA 22151.) However, most experiments were, for expedience, limited to the frequency range of military interest of the moment, and they are reported in systems of units that are no longer in use.

Historically, several rms reference pressures P_{ref} have been used to calculate SPL $= 20 \log(P/P_{ref})$ dB — for example, P_{ref} may be 0.0002 dyne/cm^2, 1 dyne/cm^2, 1 mb, 1 Pa, 1 μPa. In order to present a simple and consistent system of units, we convert original values in dB to the SI units of pascals, watts, and joules. However, to facilitate reference to the literature, we present both the original values in dB and the converted values in SI units. Converted numbers are rounded to one or two significant figures as seems appropriate.

More recently, the civilian community has recognized that fisheries research vessels must be acoustically designed to minimize the effect on marine life. The International Council for the Exploration of the Sea has given recommendations for the proper acoustical parameters and units that should be measured during such research (Mitson 1995).

6.6.1 NATURAL PHYSICAL SOUNDS

Fig. 6.6.1 is a traditional presentation of spectra of nonbiological sounds sensed by hydrophones at sea. The reader should be aware that these curves are simple, approximate representations that may be incorrect by large factors (many decibels) at specific times or places. The traditional curves have been supplemented by recent measurements of the sound of rain for different wind and cloud conditions. The left ordinate in Fig. 6.6.1 is sometimes incorrectly called *power spectral density* (similarly for the *level* in dB on the right). In fact, the left ordinate is *proportional* to the intensity spectral density [(watts/m^2)/Hz], which can be obtained by dividing Pa^2/Hz by $\rho_A c \cong 1.5{*}10^6$ (kg/m^{-3})(m/s), as described in section 2.5.3.

In general, ocean sound at frequencies from 0.1 Hz to 5 Hz is attributed to the nonlinear interactions of surface waves, "wave-wave interactions," and microseisms, and is dominated by sound propagating through the bottom layers (Kibblewhite and Wu 1991). It is a function of depth as well as the sea surface spectrum of heights.

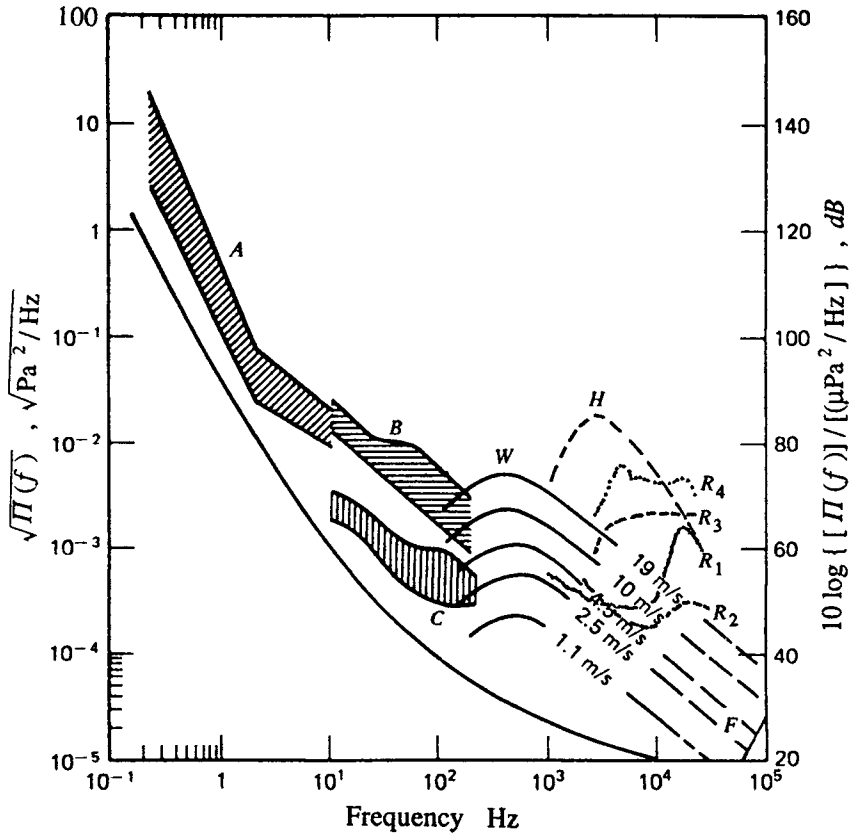

Figure 6.6.1 Published values of "intensity" spectral density levels of physical sounds measured at various locations by many researchers. The heavy solid line at the bottom is the empirical minimum at sea. A, "seismic noise" due to earthquakes and wind; B, ship noise; H, hail; W, sea surface sound at five different wind speeds; R_1, drizzle ($\cong$1 mm/hr) with 0.6 m/s wind over lake; R_2, drizzle with 2.6 m/s wind over lake; R_3, heavy rain (15 mm/hr) at sea; R_4, very heavy rain (100 mm/hr) at sea; T, thermal noise.

From 5 to 20 Hz there is again a strong correlation of noise with wind speed (Nichols 1987). The *natural* sound-producing mechanisms that have been proposed at frequencies between 20 and 500 Hz are wave-turbulence interactions and oscillating bubble clouds (Cary and Bradley 1985; Prosperetti 1988). However, particularly near shipping lanes, the noise in the 10–150 Hz band is due largely to the machinery of distant ships [Ross 1987].)

Ocean sound in the band 500–20,000 Hz has been called "wind noise," "sea state noise," or "Knudsen noise," because, during World War II, Vern O.

Knudsen discovered that it correlated very well with wind speed (Knudsen et al. 1948).

The depth dependence owing to the attenuation of sea surface sound by near-surface bubble layers and bubble plumes cannot be ignored. The sound from radiating surface bubbles is modified by inactive older bubbles below the surface (section 8.4) and by absorption attenuation (Chapter 3). For these reasons, when measured several meters below the surface, the traditional straight lines of the Knudsen spectra in Fig. 6.6.1 actually droop (at about $f > 5$ kHz) to lower levels. Nevertheless, the sound due to breakers has been shown to be sufficiently well correlated with winds at sea to permit estimates of wind speed from ambient sound measurements on the sea floor (Evans et al. 1984). The distribution of these overhead breakers can be determined from the *variation* of the underwater ambient sound (Farmer and Vagle 1989).

Summary of Knudsen Sea State Sound

(For additional details, see section 8.5.1.) Frequency range: greater than 500 Hz, probably to 50 kHz. Microsource description: dipoles near ocean surface; peak source pressures 0.1 to 1.0 Pa. The microsources are transient, damped oscillations of microbubbles radiated immediately after their creation by breakers (Medwin and Beaky 1989; Updegraff and Anderson 1991). Local breaking depends on sea swell as well as local winds. The sound level increases with increasing wind speed partly because there are more waves breaking simultaneously at higher wind speeds than at lower wind speeds. Ignoring absorption, the average spectral intensity is independent of depth. There is potential for determining underwater sound from satellite photos of surface foam coverage (Monahan and O'Muircheartaigh 1986).

Rainfall Sound

The intensity spectral density during rainfall at sea (Fig. 6.6.1) is an example of "noise" that has yielded information about the source (see section 8.5.2). For light rainfall, "drizzle" ($\approx$1 mm/hr), at very low wind speeds over "calm" seas, this most prominent peak (curve R1) is due to transient, exponentially decaying oscillations of bubbles created by normal incident raindrops 0.8 mm < diameter < 1.1 mm. At higher wind speeds the peak spectrum level lowers, broadens, and shifts to higher frequencies (curve R2) because these small raindrops enter at *oblique* incidence (Medwin, Kurgan and Nystuen 1990).

During heavy rainfall (>7.6 mm/hr), there are also raindrops of diameter up to several millimeters falling at terminal speeds up to 10 m/s. The larger drop kinetic energy creates larger bubbles which radiate strongly for greater durations at the lower frequencies from 2 to 10 kHz. Each drop diameter has a distinctive energy spectrum. The larger drops produce a broader spectrum (curves R3 and R4) than those shown for light rain (<2.5 mm/h) in Fig. 6.5.1, partly because the larger drops generate splash hydrosols that create bubbles when they fall back into the sea. The type of rainfall (from stratus or cumulus clouds) can be readily deduced from this shape difference of the underwater sound spectrum.

Summary of Rainfall Sound

(For details, see section 8.5.2.) Radiated power and source level: depends on number and distribution of raindrop sizes and local angle of drop incidence (see Fig. 6.6.1). Significant frequency range: 1 to 25 kHz. Individual sources: dipoles perpendicular to surface; "energy" spectral density per raindrop, up to 10^{-7} Pa^2 sec/Hz. Source location: at surface. Sound is comprised of a broadband impulse source and (usually) much more energetic damped bubble oscillations. Knowledge of the rainfall drop size distribution and the ocean surface slope permits calculation of the underwater sound spectrum, which, except for sound absorption, is essentially independent of depth. By matrix inversion, measurement of the underwater sound spectrum permits calculation of the number of drops/m^2/s within raindrop diameter bands (e.g., 100 μm bands), which are summed to give the total rainfall rate.

Free-drifting ocean buoys reporting signals of rainfall sound via satellite can be inverted to yield rainfall description in remote ocean regions (Nystuen 1996).

6.6.2 NATURAL BIOLOGICAL SOUNDS

Fig. 6.6.1 omits biological sounds, not because they are unimportant but because of their great diversity and complexity, and because so little is known about them. Probably the first identification of the noise of marine animals was by Knudsen et al. (1948), who observed that "colonies of certain species of snapping shrimp close their pincers with a loud audible click." In some coastal regions and in the frequency range of 200 to 20,000 Hz, snapping shrimp "intensity" spectral densities range from 1 to 100 Pa^2/Hz (the corresponding spectrum levels range from 60 to 80 dB re 1 μPa^2/Hz).

A remarkable sound radiation specialization is shown by the "Plainfin midshipman" fish, *Porichtys notatus*. The 15 cm long Type I male can activately

resonate its swimbladder to produce a loud, mating-attractive 100 Hz sound for many minutes duration, or transiently "grunt" 50 ms duration impulses at a repetition rate of two per second, for threat display (Brantley and Bass 1994). A "brain "motor volley" of that same frequency drives the surrounding bladder muscles, which act as a pacemaker to maintain the radiation (Bass and Baker 1990).

An extensive review of animal sounds, how animals use sound, and their anatomy for sound production, is in the symposium volume of Busnel and Fish, *Animal Sonar Systems* (1980), and in *The Sonar of Dolphins* (Au 1993). Sound recordings have been made of many species of odontocete (toothed) animals, including dolphins and porpoises, as well as baleen (nontoothed) whales. The vast diversity of mammalian sounds has been described as "clicks," "whistles," "screams," "barks," "moans," "rumbles," "chirps," "growls," "ratchets," "shrieks," "raucous screeches," "horn blasts," "grunts," and "songs," depending on the poet, naturalist or scientist, as well as the animal itself. Some more recent research has been very specific in terms of the sound's source level, directivity pattern, temporal character, frequency spectrum, and intermittency. A dolphin's train of ultrasonic pulses is in Fig. 6.6.2.

Our purpose in this section is simply to give a "flavor" of the radiation from marine mammals. We use the term "apparent" source power because it is calculated by extrapolation from far-field sound pressure measurements. Similarly, peak sound pressure measurements at the hydrophone are extrapolated back to $R_0 = 1$ m to give the peak "apparent" source pressure P_0.

The apparent source power in watts is calculated from the acoustic radiation equation (4.5.5), taking account of the integated beam pattern Ψ_D (Equation 4.5.4, (which depends on the far-field directivity) and the sound transmission loss between the source and the receiver.

$$\Pi_M = \frac{(P_0 R_0)^2}{2\rho_A c} \Psi_D \tag{6.6.1}$$

The frequency range of baleen whales can be as low as tens of Hertz for "moans" to kilohertz for "songs" to tens of kilohertz for "clicks" (see Cummings and Holliday 1987). The sounds have been extrapolated from hydrophone back to imply sound source pressure amplitudes ranging from 3 Pa to 3000 Pa referred to 1 m (or 130 to 190 dB re 1 μPa). We use these sound pressures and Equation 6.6.1 to estimate the acoustic radiation power. Assuming that the whale radiates omnidirectionally and that $\Psi_D = 4\pi$, the acoustic radiations of whales range from 4×10^{-5} to 40 watts. The combination of low frequencies

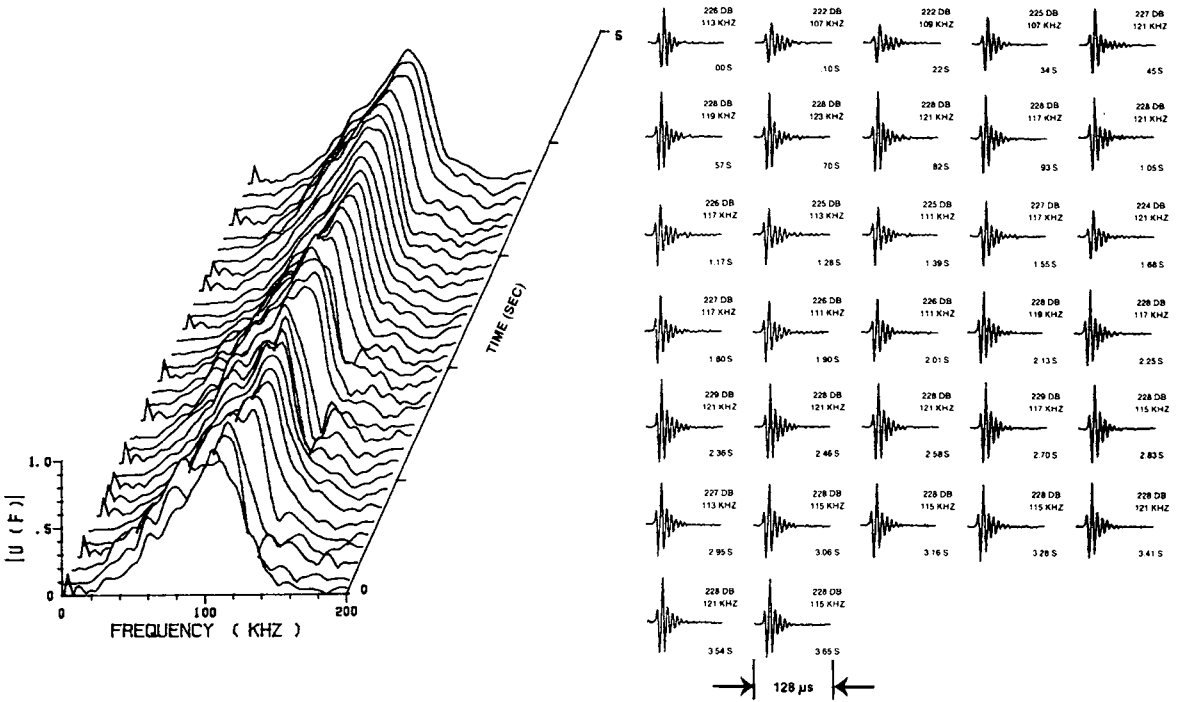

Figure 6.6.2 A typical sonar click train for a *Tursiops truncatus* performing a detection task in the open sea near Hawaii. The spectra of the sequence of clicks are at the left. The ordinates are relative spectral amplitudes. The sound pressure $p(t)$ of individul signal clicks is at the right. The central frequency above each click, and its clock time is below. The (−) peak to (+) peak (at maximum) pressures are indicated in dB re 1 μPa at 1 m. To get the vertical coordinate scale of the signals, these should be converted to sound pressures in Pa. The average time between clicks is about 0.120 ms. (From W. W. L., *The Sonar of Dolphins*, Springer-Verlag, New York, 1993, Fig. 5.2.)

and high source powers implies that these animals can communicate for large ranges across the oceans.

Obviously, different species of dolphins emit different types of sounds. Some dolphin transmissions are frequency-modulated continuous tonals (whistles), from 5 to 30 kHz, which last for several seconds. These appear to be for communication Others, at frequencies near 100 kHz, appear to be for identification of objects. Beam widths (3 dB down) of different species of dolphins have been measured or estimated from 6° to 16°. The monograph by Au (1993) gives results of extensive research on the *Tursiops truncatus* sonar. Au (1993, sec. 6.5.1) that states the radiation is equivalent to that of a circular transducer of radius $a = 5.7$ cm. Note that Au's figures show the (+) peak to (−) peak sound-pressure level in dB re 1 μPa; we convert to pascals in Fig. 6.6.3.

The maximum of the average click, Fig. 6.6.3, has "apparent" peak-to-peak sound pressures of about 200 kPa referred to 1 m (peak-to-peak SPL = 226 dB re 1 μPa). Such a very high-intensity sound would be expected to cause cavitation if it occured continuously at sea level. But the signal is a damped sinusoid of

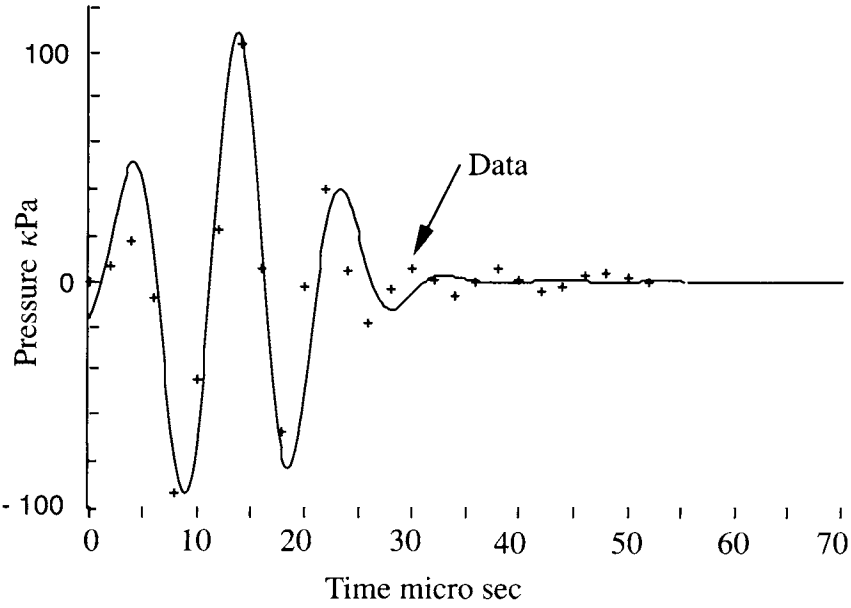

Figure 6.6.3 Dolphin click and an approximate analytical function. The dolphin is a *Tursiops truncatus*. The data points (+) were read from Au (1993, Fig. 5.3), who aligned and averaged (stacked) the 32 clicks shown in Fig. 6.6.2. The smooth curve is Equation 6.6.2, where $P_0 = 110$ kPa: $f_0 = 100$ kHz, $\tau_0 = 13$ ms: $\Delta\tau = 33$ ms, and $\phi = -\pi/4$.

duration only 50 μs, which would not cause cavitation (see section 5.2). An approximate analytical function for the clicks is

$$p(t) = P_0 \sin(2\pi f_0 t + \phi) \exp[-\pi^2 (t - \tau_0)^2 / \Delta\tau^2] \quad (6.6.2)$$

A comparison of Equation 6.6.2 and the data is shown in Fig. 6.6.3.

To compute the acoustic energy radiated by a dolphin, recall the discussion in section 3.1 and the message energy computation, Equation 3.1.12. The message energy is

$$E_m = \frac{\Psi_D R_0^2}{\rho_A c} \int_{R/c}^{R/c + t_g} dt \left[p_0 \left(t - \frac{R}{c}\right)^2\right] \quad (6.6.3)$$

where the 4π is replaced by the integrated beam pattern, Ψ_D, defined in Equation 4.5.5, and t_g is the duration of the click. For $a = 5.7$ cm and $f_0 = 100$ kHz, ka is 11. Using Fig. 4.5.1, the integrated beam pattern, $\Psi_D \approx 12/(ka)^2 = 0.09$. A numerical evaluation of Equation 6.6.3 has been made using the points shown in Fig. 6.6.3. One click has the apparent message energy

$$E_m \approx 2.6 \times 10^{-4} \text{ joules} \quad (6.6.4)$$

The character of repeated "clicks" can be seen in Fig. 6.6.2. The waveforms of the messages are not quite the same.

The dolphin *Tursiops truncatus* appears to alter its sound output according to its environment. The peak sound pressures were about 30 to 300 times higher when measured in the open waters than in tanks, and the output frequencies were near 115 kHz in open waters compared with nearly 50 kHz in tank experiments.

6.6.3 SHIP NOISE: SAMPLE CALCULATION

Intentional sound sources were discussed in Chapter 4. Here we perform a simple calculation of ship noise using World War II raw data.

The principal sources of ship noise are a) radiation of engine noise from the ship hull; b) "blade passage" tones from the propeller; and c) cavitation from propeller blades. The engine noise is common to all rotating machinery. When the engine is not isolated from the ship, its vibration drives the hull; thereupon, sound is radiated according to the modes of vibration of the hull panels. The blade passage tones are caused by the rotating dipole created by the pressure in front of the propeller being positive, while the pressure behind is negative (Gray and Greeley 1980). The frequency of these tones is the product of the number of blades times the shaft rotation frequency. Hydrodynamic cavitation is the

creation of bubbles by the lowered pressures along the edge, particulaly near the tip, of the rotating blades (see also section 5.2 for acoustic cavitation). It is strongly dependent on the propeller tip speed.

The complexity of the multiple sources of ship noise is rendered even more complex by the fact that these noise sources are close to the ocean surface. For a smooth surface, the radiation is a function of the ratio of source depth/sound wavelength, which may cause the lower frequencies to radiate as dipoles, while the higher-frequency sounds act as monopoles (see sections 4.1.2 and 4.1.3,

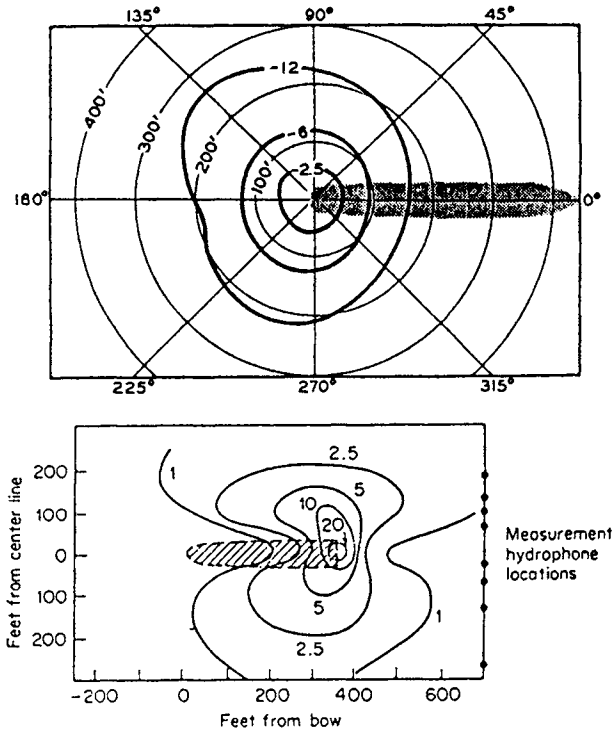

Figure 6.6.4 a) Average noise directivity in 200–400 Hz band for 15 World War II freighters. Contours are sound pressure levels in dB re 1 dyne/cm^2. From Eckart (1946, 1968). b) High-frequency ship noise "butterfly" pattern. (From Urick, R. J., *Principles of Underwater Sound*, 3rd edition, Peninsula Publishing, P.O. Box 867, Los Altos, CA, 1983, Fig. 10.9.) The original caption is "Equal pressure contours on the bottom in 40 ft of water of a freighter at a speed of 8 knots. Contour values are pressures, in dynes per square centimeter in a 1-Hz band, at a point on the bottom, measured in the octave band 2,500 to 5,000 Hz." To translate the U.S. Navy units of the 1940s to SI units, use 1 knot = 1.15 miles/h = 1.85 km/h; 1 ft = 0.3095 m; 1 dyne/cm^2 = 10^5 μPa = 0.1 Pa; intensity spectral density = (watts/m^2)/Hz = (Pa^2/Hz)/$\rho_A c$. The ship outlines are shaded.

which describes multipoles). Finally, when the rms height of the ocean surface is large compared with the sound wavelenght, the sound at the surface is scattered rather than reflected, and the dipoles become relatively strong monopoles.

Radiation at low frequencies of 200 to 400 Hz (Fig. 6.6.4a) looks somewhat omnidirectional. This is not the case at higher frequencies (Fig. 6.6.4b).

Rms pressure contours for the frequency band 2500 to 5000 Hz are shown in Fig. 6.6.4b. They were drawn from the values measured by eight sea floor hydrophones as a freighter steams by. The sources of ship noise are spread along the ship. However, the radiated energy is generally greatest abeam and appears to come principally from the propeller. The propeller noise power radiated astern is reduced by being absorbed and scattered by the bubbly wake. It is reduced forward by diffraction by the ship body. The ocean surface reflection of the dominant dipole source results in radiation not unlike that of convected distributed quadrupole sources in a jet engine exhaust (section 4.1.2). The net effect is that the sea-floor measurement of ship radiation is typically a "butterfly" pattern as shown in Fig. 6.6.4. This figure, here reprinted from Urick (1967), originally came from *U.S. Naval Ordnance Laboratory Report* 7333, by Pomerantz (1943).

The "butterfly" pattern, which is presented as spectral pressures (1 Hz band) in Fig. 6.6.4b, was calculated from the measured squared pressure in the octave band, 2500 to 5000 Hz. This reduction to spectral values is sometimes done by assuming equal intensity in each 1 Hz band and simply dividing by the bandwidth, 2500 Hz. Possibly the stated values were calculated by recognizing that there is an f^{-2} dependence of radiated intensity in the typical ship noise spectrum (see Fig. 6.6.6). We will assume that the spectral values in Fig. 6.6.4b are at the approximate mid-frequency of the band, 4000 Hz.

Directivity Pattern

We first convert the rms pressures to pascals (see caption of Fig. 6.6.4). As the next step in calculating the radiated spectral power, the data in Fig. 6.6.4 are transformed to a directivity pattern (Fig. 6.6.5) in spherical coordinates. This gives us the apparent spectral intensity (Pa^2/Hz) extrapolated back to 1 m as a function of angle. We find that the propeller position is the approximate source of spherical ($1/R$) spreading. Some asymmetry is evident in Fig. 6.6.4b, but, for simplicity, we set the z axis along the ship and assume that there is axial symmetry around the ship (no ϕ dependence). The radiation is at angles θ, with the ship axis into the underwater half space ($0 \leq \theta \leq \pi$).

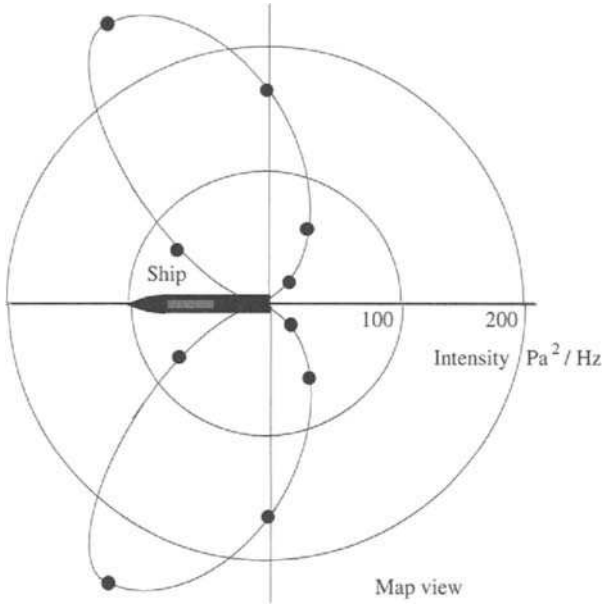

Figure 6.6.5 Directivity pattern for apparent source spectral "intensity" in Pa^2/Hz at 1 m, for the mid-frequency 4000 Hz, calculated from data within octave band 2500 to 5000 Hz for a freighter traveling at speed 8 knots toward the left, as described in Fig. 6.6.4. The data points are plotted as circles. Radiation is in the half-space.

Because we have chosen the convenience of having the coordinate axis along the ship, we are able to calculate the spectral power directly from contributions in incremental areas, rather than by using the integrated beam pattern concept defined for CW in Equation 4.5.4 or numerical integration. The total radiated power spectral density at a given frequency, *PSD* (units, watts/Hz), is calculated by integrating, over the hemisphere, the mean squared pressure in the 1 Hz band at angle θ, $P^2(\theta)$,

$$PSD = \int_{\phi=0}^{\pi} \int_{\theta=0}^{\pi} \frac{P^2(\theta)}{\rho_A c} \, dS \tag{6.6.5a}$$

where

$$dS = R^2 \sin(\theta) \, d\theta \, d\phi \tag{6.6.5b}$$

Assuming axial symmetry, the ϕ integration gives π, the θ integration gives $-P^2(\theta)\cos\theta$, and we are left with the summation over incremental angles,

$$PSD = \frac{-\pi R^2}{\rho_A c} \sum_{\theta=0}^{\pi} P^2(\theta)[\cos(\theta_1) - \cos(\theta_2)] \quad \text{watts/Hz} \tag{6.6.6}$$

Angular Dependence of Power Spectral Density at 4000 Hz

To show the relative contributions at different angles, we divide the 180° of θ into seven incremental regions, between 0 and 15°, 15° and 45°, 45° and 75°, and so on, and determine the following mean values tabulated at the mid-angles:

θ_{mean}	P^2(pascals)^2/Hz	$P^2 \Delta \cos\theta$(pascal)^2/Hz	$(\pi P^2 \Delta \cos\theta)/(\rho_A c)$ Watts/Hz(10^{-6})
7.5	9	000.3	0.6
30.0	64	17	36
60.0	100	45	94
90.0	144	75	158
120.0	256	115	242
150.0	144	37	78
172.0	16	0.5	1
TOTAL		290	610

Total Apparent Power Spectral Density at 4000 Hz

The total apparent power spectral density over all angles is PSD = 610×10^{-6} watts/Hz = 0.61 mW/Hz for the 1 Hz bandwidth at 4000 Hz. Notice that the total is more than twice the peak value, which is found at the angular increment centered at 120°; if one simply looks at the peak transient value and ignores the directivity, as the ship goes by, the observed PSD is about half the correct value.

Power Spectral Density at Other Frequencies

We don't know the freighters' sound radiation directivity except for the octave band from which Fig. 6.6.4 was drawn. Fig. 6.6.6 shows a "typical" peak noise spectral dependence for a naval cruiser. Roughly the dependence f^{-2} appears to be a pretty good assumption for the frequency range from about 20 kHz to about 100 Hz, depending on the ship speed. Spectral values for frequencies less than 20 Hz, which would probably be caused by the blade passage tone and its harmonics, are not available. The low-frequency oscillations below 500 Hz, shown at 8 knot cruiser speed, may be machinery noise. The absence of evidence of machinery noise at higher ship speeds is probably due to the increasing dominance of broadband cavitation noise.

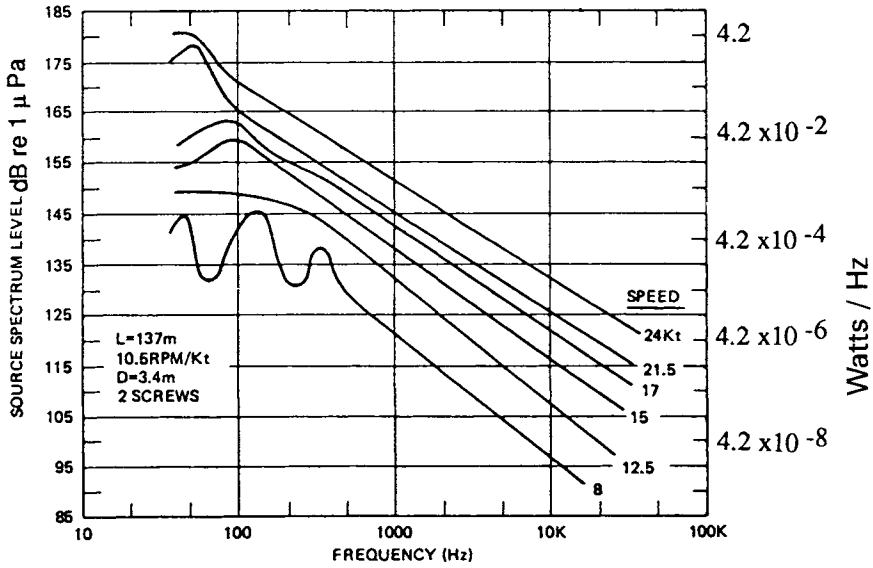

Figure 6.6.6 Radiated spectra of noise maxima referred to 1 m from the British cruiser *Cardiff*, considered as a point source, as measured during World War II. The two ship propeller shafts of diameter 3.4 m rotated at 10.5 RPM/knot. The column on the right is the apparent spectral power, watts/Hz. (Adapted from Ross, D., *Mechanics of Underwater Noise*, Peninsula Publ., Box 867, Los Altos, CA, 1987.)

Total Radiated Power at 8 Knot Speed

To perform an engineering estimate of the overall noise power radiated at a given ship speed, one can, for simplicity again, assume the f^{-2} dependence as described above. To calculate the dominating low-frequency contributions from 100 Hz to 4000 Hz, assuming the same directivity, use the relation

$$\Pi = \int_{50}^{4000} PSD\,(4000\,\text{Hz}) \left(\frac{4000}{f}\right)^2 df \qquad \textbf{(6.6.7)}$$

Accepting these assumptions, this freighter at speed 8 knots radiates a total acoustic power of about about 0.2 watts. But note that Fig. 6.6.6 shows that major power contributors are at $f < 200$ Hz, and our approximation is quite poor in this region; indeed during World War II, when these data were taken, there was *no* interest in $f < 20$ Hz.

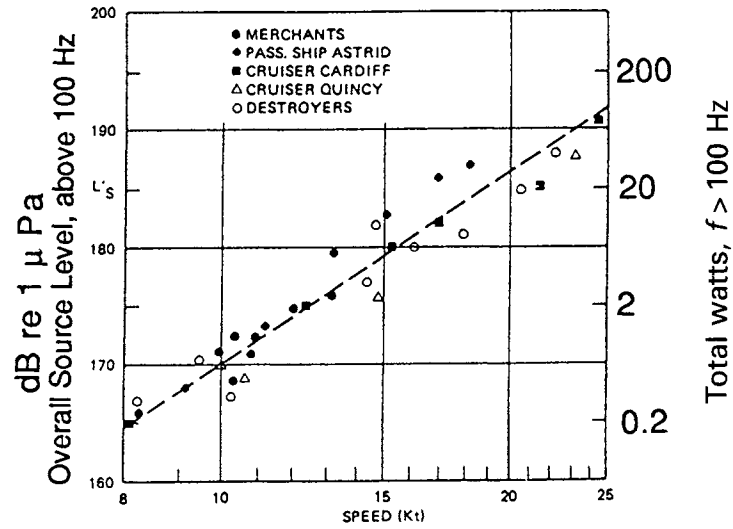

Figure 6.6.7 Dependence of overall noise power in watts, and apparent source level calculated by extrapolation to 1 m from the ship considered as a point source, plotted as a function of ship speed. Data measured for various categories of ship during World War II, and include only frequencies over 100 Hz. (Adapted from Ross, D., *Mechanics of Underwater Noise*, Peninsula Publ., Box 867, Los Altos, CA, 1987.)

Radiated Power at Higher Speeds

The dependence of overall radiated noise on the speed of the ship is presented in Fig. 6.6.7. These data show the freighter noise at about 0.2 watts (frequencies > 100 Hz) in agreement with our computed value of 0.2 watts at 8 knot speed. The agreement is surprising, considering the approximations that we have made in our calculations.

The power rises rapidly for increased speeds. In Fig. 6.6.7 it is up by a factor of 10, to about 10 watts at 13 knot speed, and by another facor of 10 to 100 watts for 19 knot speed.

Problems

Problems in signals and signal processing require numerical computations and displays. Many high-level programming languages are available. MATLAB from the Math Works Inc. does what you need and is reasonably simple to use.

MATLAB comes with a user's guide and reference manuals. Ruda Pratap, *Getting Started with MATLAB* [Harcourt Brace College Pub., Fort Worth (1996)] gives an introduction and examples for scientist and engineers. More examples and applications are in Duane Hanselman and Bruce Littlefield, *Mastering MATLAB* [Prentice-Hall, Upper Saddle River, NJ (1996)]. People who use BASIC and FORTRAN will find sound propagation, ray tracing, and signal processing algorithms in C. S. Clay, *Elementary Exploration Seismology*, the Appendices [Prentice-Hall, Englewood Cliffs (1990)].

We assume that the reader has an elementary knowledge of MATLAB methods; for example, an understanding of the first 5 chapters of Pratap or equivalent.

Section 6.1

6.1 Purpose: To create a simple signal and to sample the signal. Computations at the times t1, t2, etc., are samples of the signal in numerical space at those times. This sampled signal becomes our digital signal and we don't know the values between sampled points.

6.1.1 Create and run a short program or script file to make and display a ping. The graphic output of the program is Fig. P6.1.1

```
%     signal_cos_env; - a MATLAB script file to display a ping.csc 1997
%     The envelope of the ping is 0.5*[1-cos(2*pi*t./tp)]: Eq(6.3.1)
%     The carriers are sin(2*pi*Cf*t) or cos(2*pi*Cf*t)
%     In MATLAB, % is a comment. The ; stops the printing of numbers to
      the screen.
tp = 1;                    % Duration of ping, s
Cf = 10;                   % Carrier frequency, Hz
Sf = 100;                  % Sampling frequency, Hz
Ns = Sf*tp;                % Number of samples in time tp
t = linspace(0,tp,Ns);     % create a time vector t with Ns elements.
x = 0.5*(1-cos(2*pi*t./tp)).*sin(2*pi*Cf.*t);
                           % vector x = term by term multiplication, ''.*''.x
                           has Ns elements.
      % or x = .5*(1-cos(2*pi*t./tp)).*cos(2*pi*Cf.*t);
```

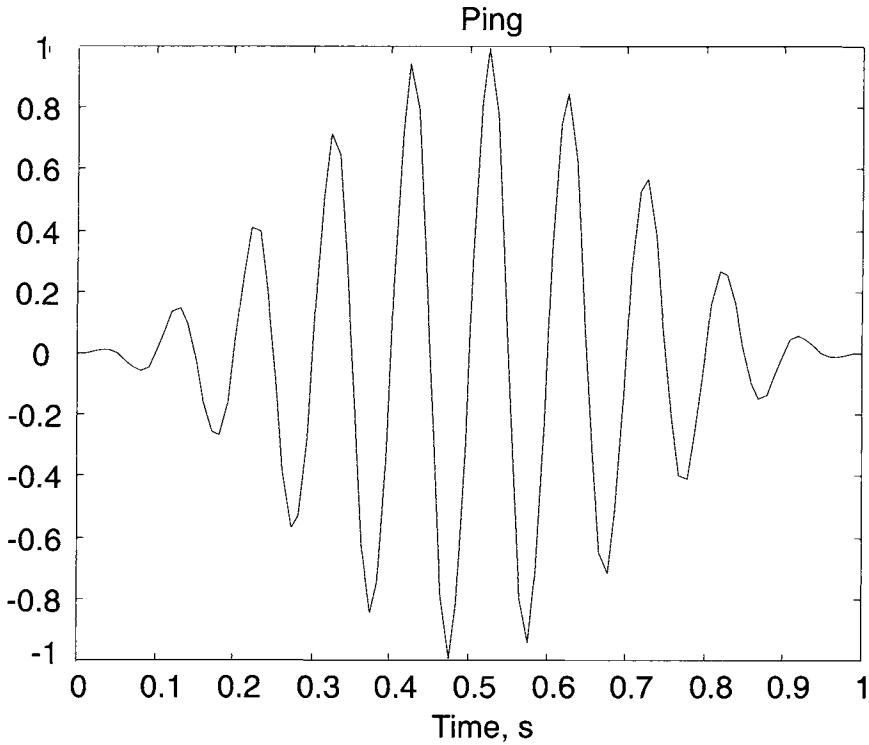

Figure P6.1.1 A ping that has a carrier and envelope. The equation of the signal is (6.3.1). This is the black on white print of the plot(t,x, '−w') instruction. In MATLAB, the monitor shows colors on black.

```
plot(t,x,'-w');          % plot the signal x versus time t. '-w' gives the
                         color white.
xlabel('Time, s');       % label
ylabel('Signal');        % label
title('Ping')            % title
```

"Save" on a Macintosh makes a PICT file that can be read with a graphics application.

6.1.2 Sampling above Nyquist frequency, $2Cf$. Compute and display the signal for the sampling frequencies $1000 > Sf > 20$. ($Cf = 10$ Hz)

6.1.3 Sampling below Nyquist frequency, $2Cf$. Compute and display the signal for $Sf < 20$.

6.1.4 Sampling at carrier frequency. Compute and display the signal for $Sf = f = 10$.
a) The carrier is given by sin(2*pi*Cf.*t).
b) The carrier is given by cos(2*pi*Cf.*t).

Sections 6.2 and 6.3

Fast (Finite) Fourier transformations. The instruction *fft* (...) does the fast Fourier transformation. See Hanselman and Littlefield, Sec. 14.2. These advanced problems use the following MATLAB script.

```
% fft_signal; - a MATLAB script file to do an fft of x.
% Changes some parameters to time domain. The sampling interval is t0 and
% the number of samples Ns=2^n. Let:
t0 = .01;                    % Sampling interval, s
Ns = 128;                    % number of samples, n=6
tp = Ns*t0;                  % Duration of ping, s
Cf = 10;                     % Frequency, Hz
t = linspace(0,tp,Ns);       % create a time vector t with Ns elements
f = linspace(1,1/t0, Ns);
% create a freq vector f with Ns elements
x = 0.5*(1-cos(2*pi*t./tp)).*sin(2*pi*Cf.*t);
                             % Compute x.
plot(t,x)                    % Plot x for inspection.
pause                        % Pause to look at the plot, get P. Press return to
                             continue.
% fft of x.                  This command does the Fourier transformation
                             (Equation 6.2.8).
X = fft(x);
plot(f-1,abs(X),'-w');
xlabel('Frequency, Hz');
ylabel('|Spectrum|');
title('Spectrum of x')
```

6.2.1 Program and run the *fft* script with $Cf = 10$. The *fft* gives peaks at $f = 10$ and 90. Why is the extra peak at 90 Hz? What do the components above 50 Hz mean?

6.2.2 Keeping the same sampling interval $t0$ and Ns, change the carrier Cf. What happens to the sampled signal and the pair of peaks?

6.2.3 What happens to x, $|X|$, and the widths of the spectral peaks when the number of samples = 16, 32, 64, 128, 256, 512? Also try Cf = 10, 20, 30 etc.

6.2.4 Write a convolution program using Equation 6.2.29. The program can be written in MATLAB script, BASIC or FORTRAN. In MATLAB, let the vectors x has mx elements and the vector h has mh elements. An example of a convolution script is

```
%       convl_examp;
%       Given a pair of vectors, x and h compute their convolution.
x=[1 2 3 4];                % mx=4
h=[.7 .3];                  % mh=2
y=conv(x,h)                 % my=mx+mh-1=5
%       y=[.7 1.7 2.7 3.7 1.2]
```

Let $x(1) = 1$, $x(2) = 2$, etc and $h(1) = 0.7$, and $h(2) = 0.3$. Compare the computer result with a hand evaluation of Equation 6.2.29.

6.2.5 Filter operations in the time domain. Let x = 0.5*(1 − cos(2*pi*t./tp)).*sin(2*pi*Cf.*t) and h = 0.5*(1-cos(2*pi*t./tF)).*sin(2*pi*Ft.*t). For the first trial, use the time step, $t0 = 0.01$, $x(t)$: $Cf = 15$ and $tp = 0.4$. $h(t)$: $Ff = 15$ and $tF = 1$. Compute and display the convolution of $x(t)$ and $h(t)$.

6.2.6 Multichannel filter operation. Compute the convolution of $x(t)$ in problem 6.2.5 and a set of filters where the filter frequencies are Ff = 5, 10, 15, 20, 25, 30, 35 Hz. The duration of the filter tF = 1 s for all trials. Observe the wave forms of $y(t)$ and make a graph of the peak amplitudes as a function of the filter frequency Ff.

6.2.7 Construct a signal that is the sum of 2 pings that have different frequencies. Test the multichannel filter on this signal. How much frequency difference do you need to resolve the two pings?

6.2.8 The transmission of a message consists of the message and the transmission paths. Concepts from Section 3.2 on transmission paths and convolution are combined. The message is $p_0(t)$ and the transmission function is [*path*]. Obvious changes of notation were made to create compatible variables in MATLAB. Copy and run the script.

```
%       path_messages;
%       Ray traces give the travel time tpath and message amplitude paf.
%       The impulse response is trPath. trPath can have many arrivals.
%       Here, the travel times and amplitudes of arrivals are assumed.
```

```
%       p(t) = conv( p0(t),path)
%       transmission path, trPath
        tpath1 = 0.5;                   % First arrival travel time
        paf1 = 1.5;                     % Amplitude
        tpath2 = 0.9;                   % Second arrival travel time
        paf2 = -0.8;                    % Amplitude
        t0 = 0.01;                      % Sampling interval
        tmax = 1;                       % Maximum duration of path
        ipath1 = round(tpath1/t0);      % round(.) nearest integer time
                                          step
        ipath2 = round(tpath2/t0);      % Time steps to second arrival
        imax = round(tmax/t0);          % Arbitrary maximum for tpath
        trPath = zeros(1, imax);        % Create array of zeros
        trPath(ipath1) = paf1;          % Put the arrivals into the array
        % Message is p0(t)              Use exp(-st/Ts), where st is
                                          message time.
        Ts = 0.05;                      % Time constant for exponential
                                          p0(t)
        ns = round(4*Ts/t0);            % Time steps for 4 time con-
                                          stants
        st = linspace(0,4*Ts,ns);       % Time vector for message
        p0 = exp(-st/Ts);               % Create a simple exp message
        % convolve the message p0(t) and path(t) to get p(t), the received
          message pressure.
        p = conv(p0,trPath);            % p is the received message
        ntot = ns + imax-1;             % Size of convolved vectors.
        t = linspace(0,ntot*t0,ntot);   % Create the vector t. Size t=size
                                          p.
        plot(t,p);
        xlabel('Time, s');
        ylabel('p(t)');
        title('Convolution of p0(t) and path(t)')
```

Program the convolution computation and test it using the parameters in the script.

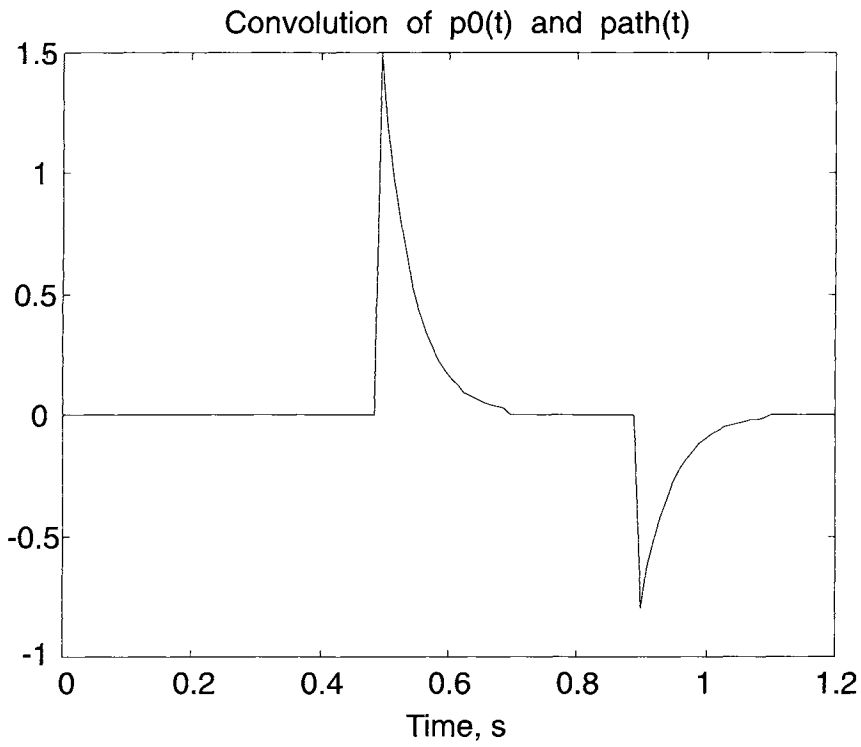

Figure P6.2.2 Example of the transmission of a message $p_0(t)$ along 2 paths. The arrival times are 0.5 an 0.9 s.

6.2.9 Replace the message in problem 6.2.8 with the ping, $p0 = 0.5$*(1-cos(2*pi*t./tp)).*sin(2*pi*Cf.*t). Explore the transmissions of different messages. Try different durations of pings for the same carrier frequency. What is the maximum duration that gives separated arrivals? What happens when the pings are longer? Try different frequencies for these ping durations. What happens if you choose a frequency greater than 50 Hz?

6.2.10 Use the convolution multichannel filter method in problem 6.2.6 to do multichannel filter operations on the pressure p in the script in problem 6.2.8. Here the message is the exponential $p0 = \exp(-st/Ts)$. Try filter durations of 0.4 s and 1 s. What happens if you let $paf1 = 1$ and $paf2 = -1$? What happens as *tpath2* is decreased from 0.9 to 0.5?

6.2.11 Purpose is to display the effect on an *fft* spectrum transformation of how the signal is conditioned prior to the *fft* operation. Let $x(t)$ have $p0(t)$ be a ping

with $tp = 0.1$ s and $Cf = 10$ Hz. To approximate the infinite integral transformation one, add zero to the sampled $p0(t)$. Let the sampling interval $t0 = 0.01$ s. We explore adding different numbers of zero (the number is an art). a) Compute Fourier transformation $P = fft(p0)$ and display the $abs(P)$. What are the frequency increments of the transformed signal? b) Add zeros to make the total duration $td = 2tp$. Compare to a). c) Continue the process for $td = 5tp$, $10tp$, etc., to $td = 50tp$. Do you see an effect on the frequency resolution?

6.2.12 Construct a $p(t)$ using $p0(t)$ and the convolution from problem 6.2.8. Let $Ts = 0.05$ s. Let $tpath1 = 0$ and $paf = 1$. Let $tpath2 = 0.4$ and $paf2 = -1$. The initial total duration is $td1 = tpath1 + tpath2 + 4Ts$. a) Follow the tasks in problem 6.2.11 and add zeros, where $td = 2td1, 5td1$, etc. How large must td be relative to $td1$ for the fft to be insensitive to td?

Section 6.4

MATLAB has a normal distribution, unit variance, and zero mean random number generator, randn(..,..). For a vector, use rand(1, N) for a vector that contains N elements of random numbers. We smoothe adjacent time steps to reduce frequency components above the sampling frequency.

```
% play_w_randn;
N = 1000;
*x = randn(1,N);
for n = 1:N-1;                  % 'DO loop or FOR-NEXT algorithm.
x(n+1) = x(n) + x(n+1);         % Do a running integration to smooth.
end                             % End of operation
x = linspace(0,N-1,N);
plot(x,y,'-w')
```

6.4.1 Simply run this script over and over to get a feel for the properties of a sequence of random numbers. This generator does not have a high-pass filter, so you will see large excursions on some of the runs.

6.4.2 Let the random signal be x in problem 6.2.5. $N = 100$ corresponds to 1 s of signal. Use the convolution multichannel filter method in problem 6.2.6 to do multichannel filter operations on the random signal. Try different filter durations.

6.4.3 Advanced readers can use the methods in section 6.4.4 to do spectral smoothing.

Section 6.5

A matched filter algorithm follows:

```
% matched_filter;
N = 64;
x = randn(1,N);                % x is the signal
h = ip1r(x);                   % Reverse time for filter
zZ = zeros(1,N);               % Create a vector of zeros
x1 = [xzZ];                    % Add a string of zeros to x
y = conv(x1,h);                % Convolve x and its matched filter
t = linspace(0,3*N,3*N-1);     % For plot
plot(t,y,'-w')
```

6.5.1 Run the script several times and notice that the side lobes change for each run. Why?

6.5.2 Why is the peak delayed?

6.5.3 Compare the relative sizes of the side lobes for $N = 16, 32, 64, 128, 256$.

6.5.4 Replace the random signal $x(t)$ with a chirp

$$p_0(t) = \sin[2\pi(f + at)t] \text{ for } 0 \leq t \leq t_p \text{ and } = 0 \text{ otherwise}$$

and try different chirp durations t_p and bandwidths, that is, values of f and a.

Chapter 7 | Sound Scattered by a Body

7.1 Scattering measurements: Incident Plane-Wave Approximation 235
7.1.1 Scattering Length 237
7.1.2 Differential Scattering Cross Sections 237
7.1.3 Total Scattering and Extinction Cross Sections 238
7.1.4 Target Strength 240
7.1.5 Single Transducer Measurements 240
7.2 Helmholtz-Kirchhoff Methods 241
*7.2.1 Theorems of Gauss and Green (Optional) 241
7.2.2 The Helmholtz-Kirchhoff Integral 243
7.2.3 Kirchhoff Approximation 244
7.2.4 Fresnel Approximation 246
7.3 Specular Backscatter by the Kirchhoff Method 249
7.3.1 Rectangular Plane Facet 249
7.3.2 Penetrable Cylinder 252
7.3.3 Finite Fluid Cylinder 255
7.3.4 Low-Contrast Finite Fluid Cylinder 256
7.4 Modal Solutions for a Fluid Cylinder 258
*7.4.1 Infinite Cylinder (Optional) 259
7.4.2 Finite Cylinder 262
7.4.3 Comparison of Kirchhoff and Modal Solutions 265
7.4.4 Equivalent Sphere for Small Fluid Bodies 265
7.5 Scattering from a Sphere 267
7.5.1 Geometrical Scatter from a Rigid Sphere ($ka \gg 1$) 268
7.5.2 Rayleigh Scatter from a Sphere ($ka \ll 1$) 271
*7.5.3 Axially Symmetric Spherical Mode Solutions (Optional) 276
7.5.4 Total Scattering Cross Section 280
7.5.5 Rigid Sphere 281
7.5.6 Fluid Sphere 284

The scattering of sound by bodies has its roots in the classical physics of giants such as Rayleigh, Helmholtz, Kirchhoff, and Born. Their analytical techniques and solutions to problems form the core of the mathematical physics of wave propagation. Where the bodies do not have simple geometries that can be solved analytically, we use numerical techniques based on the classical formulations.

In an underwater acoustics experiment, a pressure-sensitive hydrophone measures the scattered sound pressure, not its square or some other function. The scattered sound pressures are observables. They can be compared with the results

*Background material.

of theoretical and numerical calculations to yield a characterization of the scattering body.

We begin with brief descriptions of experiments and scattering measurements, because they define the meanings of the scattering parameters. These same parameters are used in theoretical calculations.

7.1 Scattering Measurements: Incident Plane-Wave Approximation

An object is *effectively* insonified by plane waves when its dimensions are less than the diameter of the first Fresnel zone, (Fig. 2.6.11). Within the first Fresnel zone, an actual spherical wavefront can be approximated as being a plane wave. The geometry of scattering measurements and theory is sketched in Fig. 7.1.1. The transmission is a gated sinusoid, a "ping." The crests of the ping are sketched as individual wavefronts.

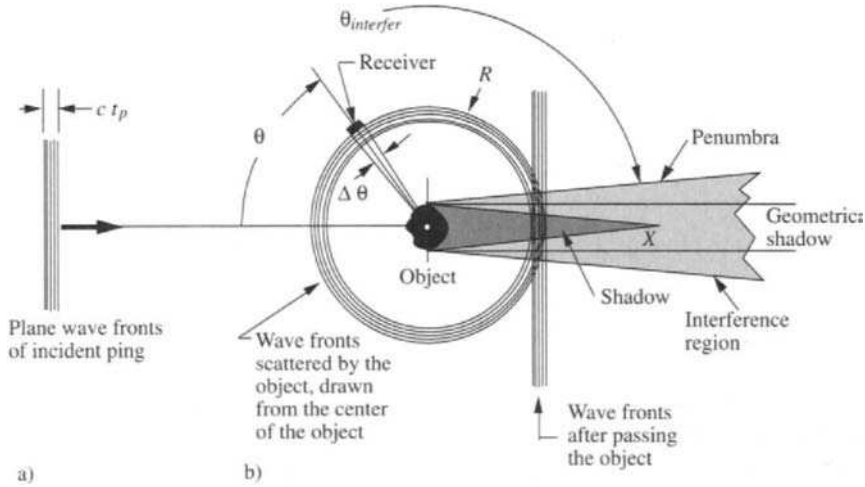

Figure 7.1.1 Sound pressure scattered by a small object. An effective plane wave is incident on the object. The crests of a sinusoidal sound pressure or ping are indicated as a sequence of wavefronts. While there is θ dependence of the incident energy, it is suppressed for simplicity in this sketch. a) The incoming waves. b) The wavefronts after being scattered. For simplicity, the scattered wavefronts are drawn as coming from the center of the object. For a complicated object, such as in the sketch, there would be many interfering wavefronts spreading from the object. The shadow behind the object extends to X. Outside of the shadow, the incident and scattered fields form a penumbra. Beyond the penumbra, where $\theta < \theta_{\text{interfer}}$, the incident and scattered waves can be separated. In some regions, separation can be achieved, also, by use of a pulse.

Oscilloscope traces of the incident and scattered sound pressures are sketched in Fig. 7.1.2. The Incident sound pressure is assumed to be a ping having a high carrier frequency f and the duration t_p.

For very simple and approximate measurements, we use the peak pressures of the pings to measure the incident and scattered sound pressures. The pressure of the incident sound pressure at the object is $p_{\text{inc}}(t)$. It has the peak value P_{inc}. The time dependence is

$$p_{inc}(t) = P_{inc}e^{i2\pi ft} \text{ for } 0 \leq t \leq t_p \text{ and } = 0 \text{ otherwise} \tag{7.1.1}$$

where t_p is the ping duration.

The sign of the exponential was chosen to match that used in most scattering theories.

The scattered sound pressure is $p_{\text{scat}}(t)$. The pressure amplitude is P_{scat}. The time dependence is

$$p_{scat}(t) = P_{scat} \exp\left[i2\pi f(t - R/c)\right]10^{-\alpha R/20} \tag{7.1.2}$$

for $R/c \leq t \leq R/c + t_p$, where t_p is the ping duration, and $p_{\text{scat}}(t) = 0$ otherwise.

Sound attenuation from scatterer to hydrophone is included. Figure 7.1.1 indicates a region of interference and a geometrical shadow behind the object. The theoretical solution shows that the shadow is due to the destructive interference of the scattered sound and the incident sound that arrive at essentially the same time, with the same, but oppositively phased, amplitudes. The gray region of interferences of the incident and scattered sound pressures depends on the relative magnitudes and times of arrival of the two sounds. When the incident wave is a pulse of sufficiently short duration, it is experimentally possible to isolate and measure the scattered sound in this region. The incident and scattered sound pressures are shown as isolated for $\theta < \theta_{\text{interfer}}$.

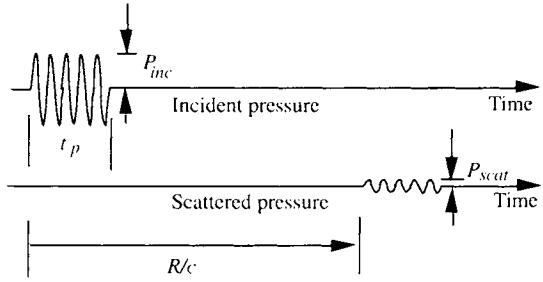

Figure 7.1.2 Sketches of incident and scattered sound pressures. The amplitudes of the envelopes of the incident and scattered sound pressures are P_{inc} and P_{scat}. The travel time for the sound to scatter to the pressure-sensing hydrophone is R/c.

7.1.1 SCATTERING LENGTH

At a large distance from the object, the amplitudes of the scattered waves decrease as $1/R$ by spherical divergence and $10^{-\alpha R/20}$ by energy absorption (and sometimes by scattering in the medium as well). We assume that the scattered energy is separated from the incident. Using the peak amplitudes of the incident and scattered sound pressures of a ping, we define a *complex acoustical scattering length*, $\mathcal{L}(\theta, \phi, f)$, which is determined by the experiment. At this time, we use the absolute value $|\ldots|$ and ignore the phase

$$P_{scat} = P_{inc} |\mathcal{L}(\theta, \phi, f)| (10^{-\alpha R/20})/R \tag{7.1.3}$$

or

$$|\mathcal{L}(\theta, \phi, f)| = P_{scat}[R10^{\alpha R/20}]/P_{inc} \tag{7.1.4}$$

Although the acoustical scattering length has the dimensions of length, it usually turns out to be different from any actual dimension of the body. The scattering expression (Equation 7.1.4) is for a "point" receiver. Actually the receiving transducer in the sketch (Fig. 7.1.1) integrates the sound pressures over its area ΔS. The dimensions of the transducer, which covers angles $\Delta\theta$ and $\Delta\phi$, limit the angular resolution of measurements of the scattering length.

7.1.2 DIFFERENTIAL SCATTERING CROSS SECTIONS

The concept of the differential scattering cross section comes from quantum physics, where it describes the scattering of particles (Shiff 1949, p. 97). In acoustical measurements, the differential scattering cross section at angle θ, ϕ is the absolute square of the scattering length

$$\Delta\sigma_S(\theta, \phi, f) = |\mathcal{L}(\theta, \phi, f)|^2 = \frac{P^2_{scat}(\theta, \varphi, f)R^2}{P^2_{inc}} 10^{\alpha R/10} \tag{7.1.5}$$

where ϕ is the angle out of the plane of Fig. 7.1.1.

The SI dimensions of $\Delta\sigma_s$ are m^2. The functional dependence in Equation 7.1.5 explicitly indicates that, in general, both $\Delta\sigma_s(\theta, \phi, f)$ and $P^2_{\text{scat}}(\theta, \phi, f)$ depend on the geometry of the measurement and the carrier frequency of the ping. This measurement is called *bistatic* scatter when the source and receiver are at different positions. When they are at the same position, it is called backscatter, or *monostatic* scatter.

Specialization to the backscattering direction,

$$\theta = 0 \quad \text{and} \quad \phi = 0 \tag{7.1.6}$$

for backscatter, gives the differential backscattering cross section,

$$\Delta\sigma_S(0,0,f) = \Delta\sigma_{bs}(f) = |\mathcal{L}(0,0,f)|^2 \tag{7.1.7}$$

for backscatter. This very important function has previously been called the *backscattering cross section*, $\sigma_{bs}(f)$ (Clay and Medwin 1977). The Δ notation is used here to emphasize the differential character and to parallel the general case (Equation 7.1.5),

$$\sigma_{bs}(f) \equiv \Delta\sigma_{bs}(f) \tag{7.1.8}$$

The acoustic backscattering length is defined as

$$\mathcal{L}_{bs}(f) = \mathcal{L}(0,0,f) \tag{7.1.9}$$

(Note: For typographical simplicity, we omit functional dependencies when they are obvious.)

7.1.3 TOTAL SCATTERING AND EXTINCTION CROSS SECTIONS

Calculations of the total acoustical cross sections go back to Rayleigh. The theoretical total scattering cross section is the integral of $\Delta\sigma_s(\theta,\phi,f)$, over 4π of solid angle

$$\sigma_s(f) \equiv \int_0^{2\pi} d\phi \int_0^{\pi} \Delta\sigma_s(\theta,\phi,f) \sin\theta \, d\theta \tag{7.1.10}$$

The total scattering cross section can also be defined by

$$\sigma_s = \Pi_{scat} / I_{inc} \tag{7.1.11a}$$

where Π_{scat} is the total power scattered by the body, and I_{inc} is the incident intensity. The two definitions are equivalent, as can be easily proved.

The total power lost from the incident wave owing to absorption by the object, Π_{abs}, determines the absorption cross section

$$\sigma_a = \Pi_{abs}/I_{inc} \tag{7.1.11b}$$

The total power removed from the incident beam, $\Pi_{\text{scat}} + \Pi_{\text{abs}}$, is used to define the *extinction cross section*,

$$\sigma_e = (\Pi_{scat} + \Pi_{abs})I_{inc} \tag{7.1.11c}$$

The sum of the total scattering cross section and the total absorption cross section is the total extinction cross section,

$$\sigma_e = \sigma_s + \sigma_a \tag{7.1.12}$$

If there is no absorption, the total scattering and extinction cross sections are equal,

$$\sigma_e = \sigma_s \qquad \text{(no absorption)} \tag{7.1.13}$$

Experimentally, it is difficult to isolate the integral scattered sound power in regions where there are interferences with the incident sound wave. As an alternative, the differential extinction cross section could be measured (Fig. 7.1.3).

The receiver, which is a distance x behind the scattering object, senses the sum of the scattered and the incident wave pressures. This raw measurement depends on the value of x and $\Delta\sigma_s(\theta, \phi, f)$ within the solid angle $d\Omega$. Appreciable curvature of the wavefront at the receiver can complicate the measurement if the dimensions of the receiver are many wavelengths.

Wave scattering depends on the dimensions of objects a relative to the acoustic wavelength. As we will see later in this chapter, for $a/\lambda \ll 1$, a simple assumption of spherical wave divergence is often a useful approximation; at $a/\lambda \gg 1$, ray-Kirchhoff approximations give accurate results; at intermediate values, $0.5 \ll a/\lambda \ll 20$, solutions require detailed evaluations based on wave theory, particularly if the body can resonate.

Some authors compute a *total acoustic scattering cross section*, σ_s, by multiplying the differential backscattering cross section, $\Delta\sigma_{bs}$ by 4π. This procedure is correct only in special cases where the scattering *is known to be*

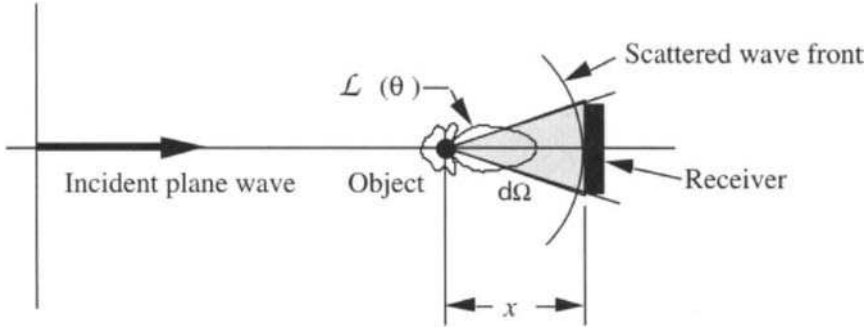

Figure 7.1.3 Measurement of sound extinction in the forward direction. The receiver senses the pressure waves over the subtended solid angle, $d\Omega$, where there are interferences. The sketched scatter directivity $\mathcal{L}(\theta)$ is for a rigid sphere having $ka = 5$.

omnidirectional—for example, scattering from a gas bubble near resonance is known to be isotropic.

7.1.4 TARGET STRENGTH

The target strength is a logarithmic measure (to the base 10) of the differential cross section that depends on the geometry:

$$TS(\theta,\phi,f) = 10\log[\Delta\sigma_s(\theta,\phi,f)/(1\mathrm{m}^2)] \quad (\mathrm{dB}) \tag{7.1.14}$$

where the reference area is/(1 m^2). The most common usage is for backscatter. Then

$$TS(f) = 10\log[\Delta\sigma_{bs}(f)/(1\mathrm{m}^2)] \quad (\mathrm{dB}) \tag{7.1.15}$$

In terms of the general statement of the scattering length, the target strength is

$$TS(\theta,\phi,f) = 20\log[|\mathcal{L}(\theta,\phi,f)/1\mathrm{m}] \quad (\mathrm{dB}) \tag{7.1.16}$$

or, more particularly, in terms of the backscattering length,

$$TS(f) = 20\log[|\mathcal{L}_{bs}(f)|/1\mathrm{m}] \quad (\mathrm{dB}) \tag{7.1.17}$$

The measured scattering lengths are simpler to use and closer to the physical processes than the logarithmic functions. (Note: For most bodies, the backscattering length, backscattering cross section, and target strength are also functions of the angles of entry of the sound at the scatterer.)

7.1.5 SINGLE TRANSDUCER MEASUREMENTS

A typical backscattered sound measurement is sketched in Fig. 7.1.4. Using Fig. 7.1.4, the incident sound pressure at the object is

$$P_{inc}\, e^{i\,2\pi f\,t} = \frac{P_0\, e^{\,i\,[2\pi f\,(t-R\,/c\,)]}\, R_0}{R}\, 10^{-\alpha R\,/20} \tag{7.1.18}$$

where the reference sound pressure for the source P_0 is referred to the reference distance R_0, usually 1 m.

The sound scattered back to the source-receiver, $p_{\mathrm{scat}}(f)$, is

$$P_{scat}e^{i2\pi ft} = \frac{P_0 e^{i[2\pi f(t-2R/c)]} R_0 \mathcal{L}_{bs}(f)}{R^2}\, 10^{-2\alpha R/20} \tag{7.1.19}$$

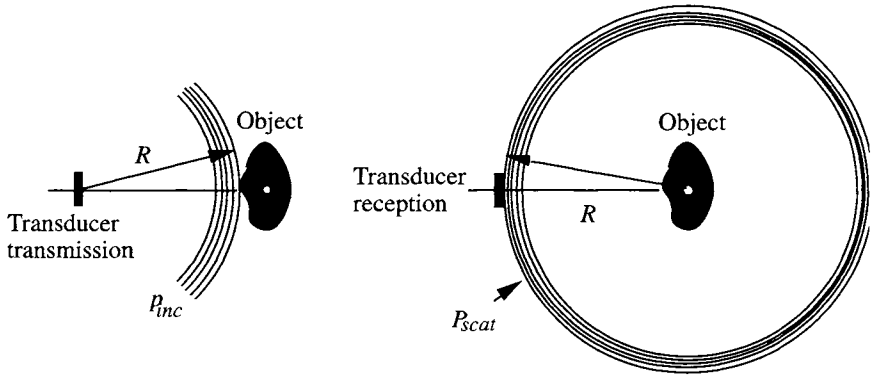

Figure 7.1.4 Sound scattered by a small object. a) Outgoing ping from a transducer. b) Ping scattered back to the transducer. It is assumed that the sound spreads spherically from the transducer and also spreads spherically from the object.

The travel time to go from the source to the scattering object and back to the receiver is $2R/c$.

7.2 Helmholtz-Kirchhoff Methods

The Helmholtz-Kirchhoff integral and the Kirchhoff approximations are analytical statements of the principles discussed in sections 2.2 (Huygens's principle) and 2.6.6 (Fresnel zones). We will use methods from mathematical physics to derive quantitative expressions for the sum of Huygens sourcelets and wavelets. This derivation begins with the Gauss-Green theorem and ends with the Helmholtz-Kirchhoff equation. The fundamental derivations of the Gauss and Green theorems are in the next section, which some readers may wish to skip.

*7.2.1 THEOREMS OF GAUSS AND GREEN (OPTIONAL)

The derivations of these theorems use three-dimensional waves and vectors as introduced in section 2.7. Let the sources within a volume V cause a field $\boldsymbol{F}$, where $\boldsymbol{F}$ is a vector. The surface S encloses the volume V. The outward flux is defined as

$$\text{flux} = \int_S \boldsymbol{F} \cdot d\boldsymbol{S} \tag{7.2.1}$$

*Background material

where $\boldsymbol{dS}$ is the incremental area; its direction is inward, normal to the surface. The dot indicates the scalar or "dot" product, and $\boldsymbol{F}$(dot) $\boldsymbol{dS}$ is proportional to the cosine of the angle between $\boldsymbol{F}$ and $\boldsymbol{dS}$. The divergence operation (Equations 2.7.5 through 2.7.7) is a measure of the flux leaving the source(s) in the volume,

$$\text{flux} = \int_V \nabla \bullet \boldsymbol{F}\ d\boldsymbol{v} \tag{7.2.2}$$

Gauss's theorem states that the net outward flux through the surface S surrounding the volume V is equal to the sum of the divergences from sources within the volume. Analytically, Gauss's theorem is

$$\int_S \boldsymbol{F} \bullet d\boldsymbol{S} = \int_V \nabla \bullet \boldsymbol{F}\ d\boldsymbol{v} \tag{7.2.3}$$

Green's theorem follows by replacing F by a pair of rather carefully chosen vectors and doing manipulations. Recall the force expression (Equation 2.7.4) and that the del operation on a scalar gives a vector. Let U_1 and U_2 be scalar solutions of the wave equation (2.7.9). We create the pair of vectors

$$(U_1 \nabla U_2) \text{ and } (U_2 \nabla U_1) \tag{7.2.4}$$

and insert them into Gauss's theorem:

$$\int_S U_1 (\nabla U_2) \bullet d\boldsymbol{S} = \int_V \nabla \bullet (U_1 \nabla U_2)\ dv \tag{7.2.5}$$

$$\int_S U_2(\nabla U_1) \bullet d\boldsymbol{S} = \int_V \nabla \bullet (U_2 \nabla U_1)\, dv \tag{7.2.6}$$

Expansions of the right-hand sides give

$$\nabla \bullet (U_1 \nabla U_2) = \nabla U_1 \bullet \nabla U_2 + U_1 \nabla^2 U_2 \tag{7.2.7}$$

and

$$\nabla \bullet (U_2 \nabla U_1) = \nabla U_2 \bullet \nabla U_1 + U_2 \nabla^2 U_1 \tag{7.2.8}$$

Insert the expansions into the integrals, take the difference, and get Green's theorem,

$$\int_S (U_1 \nabla U_2 - U_2 \nabla U_1) \bullet d\boldsymbol{S} = \int_V (U_1 \nabla^2 U_2 - U_2 \nabla^2 U_1)\, dv \tag{7.2.9}$$

It is conventional to replace the gradient operations on the left side of Equation 7.2.9 by the normal derivative at the incremental area $\boldsymbol{dS}$. Then the incremental area becomes the scalar dS, and we have

$$\nabla U_1 \bullet d\boldsymbol{S} = -\frac{\partial U_1}{\partial n}\, dS \quad \text{and} \quad \nabla U_2 \bullet d\boldsymbol{S} = -\frac{\partial U_2}{\partial n}\, dS \tag{7.2.10}$$

where the normal is drawn inward. Green's theorem is then written as

$$-\int_S \left(U_1 \frac{\partial U_2}{\partial n} - U_2 \frac{\partial U_1}{\partial n} \right) dS = \int_V (U_1 \nabla^2 U_2 - U_2 \nabla^2 U_1)\, dv \qquad (7.2.11)$$

7.2.2 THE HELMHOLTZ-KIRCHHOFF INTEGRAL

The source at Q emits a continuous wave having the frequency $\omega = kc$. The fields $U_2(x.y, z.t)$ and $U_1(x.y, z.t)$ are solutions of the wave equation, and are functions of position, frequency, and the source sound pressure. The fields have the time dependence $\exp(i\omega t)$. We will find their values by using Green's theorem. Later, we will replace the generic symbol U by the acoustic field pressure p.

The effect of the source singularity, Q, is removed by enclosing it within the surface S'. Since there are then no singularities in the volume between S and S', the right-hand side of Equation 7.2.11 is 0, and we have

$$\int_S \left(U_1 \frac{\partial U_2}{\partial n} - U_2 \frac{\partial U_1}{\partial n} \right) dS + \int_{S'} \left(U_1 \frac{\partial U_2}{\partial n} - U_2 \frac{\partial U_1}{\partial n} \right) dS' = 0 \qquad (7.2.12)$$

We assume that U_2 is the solution of the spherical wave equation

$$U_2 = \frac{e^{-ikR}}{R} \qquad (7.2.13)$$

Let the distance to S be R, the radius of S' be a, and for simplicity drop the subscript on U_1. Then Equation 7.2.12 becomes

$$\int_S \left[U \frac{\partial}{\partial n}\left(\frac{e^{-ikR}}{R} \right) - \frac{e^{-ikR}}{R} \frac{\partial U}{\partial n} \right] dS + \int_{S'} \left[U \frac{\partial}{\partial n}\left(\frac{e^{-ika}}{a} \right) - \frac{e^{-ika}}{a} \frac{\partial U}{\partial n} \right] dS' = 0 \qquad (7.2.14)$$

The normal derivative on S' is $\partial/\partial a$. The differential area is $dS' = a^2 d\Omega$. We evaluate the second term of Equation 7.2.14 at the point Q by letting a tend to zero, and obtain

$$\lim_{a \to 0} \int_{4\pi} \left[U \left(\frac{e^{-ika}}{a} \right)\left(-ik - \frac{1}{a} \right) - \frac{e^{-ika}}{a} \frac{\partial U}{\partial a} \right] a^2\, d\Omega = 4\pi\, U(Q) \qquad (7.2.15)$$

Therefore, Equation 7.2.15 becomes

$$U(Q) = \frac{1}{4\pi} \int_S \left[U \frac{\partial}{\partial n}\left(\frac{e^{-ikR}}{R} \right) - \frac{e^{-ikR}}{R} \frac{\partial U}{\partial n} \right]_S dS \qquad (7.2.16)$$

which is the integral theorem of Helmholtz and Kirchhoff for harmonic sources. In our later calculations, S will be an element of the ocean surface, or an element on the surface of a scatterer in the volume. We use the artifice of transmitting a

ping that is short enough to separate the direct and scattered arrivals and still long enough to permit the application of CW theory. Then the field at Q is determined by the sound that is scattered from the surface elements, alone, because contributions from the source are not present at Q when we observe the scattered signal.

It is possible to use Equation 7.2.16 also to calculate the transmitted sound for a surface element. The geometry is shown in Fig.7.2.1a. The value on the boundary for the outward-traveling wave is

$$U'(Q') = \frac{1}{4\pi}\int_S \left[U' \frac{\partial}{\partial n}\left(\frac{e^{-ik'R'}}{R'}\right) - \frac{e^{-ik'R'}}{R'}\frac{\partial U'}{\partial n}\right]_S dS \qquad (7.2.17)$$

where $k' = \omega/c'$.

The field quantities $U(Q)$ and $U'(Q')$ have the units m^{-1}. When they are multiplied by the source function $P_0 R_0 \exp(i\omega t)$, they become the time-varying sound pressure. As usual, P_0 is the sound pressure amplitude referred to the reference distance R_0 from the source, generally 1 m.

7.2.3 KIRCHHOFF APPROXIMATION

Although the Helmholtz-Kirchhoff integral expresses the wave field $U(Q)$ or $U'(Q')$, the problem is still difficult because we have to evaluate these quantities on the surface S. To do this we make approximations. The first approximation is usually called the *Kirchhoff approximation*. The technique is called the *Kirchhoff method*.

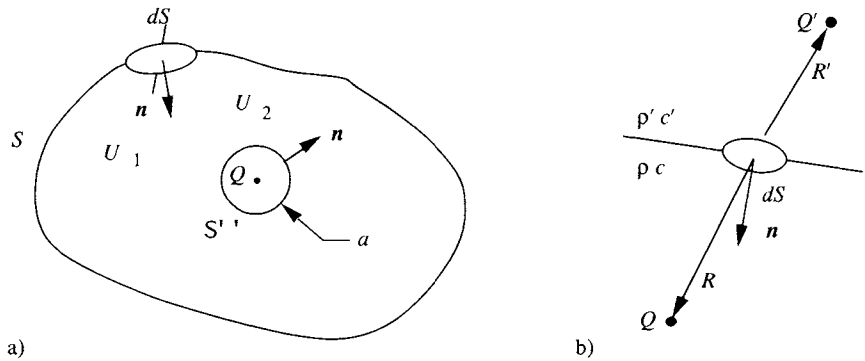

Figure 7.2.1 a) Geometry for calculation of the interior field for scatter from an enclosing surface. b) Geometry for transmission through a surface. The source is a singularity at Q, which is surrounded by a sphere S' of radius a. The normals, $\boldsymbol{n}$, are inward to the volume between S and S'.

The Kirchhoff approximation assumes that the coefficients $\mathcal{R}$ and $\mathcal{T}$ that would be derived for reflection and transmission of an infinite plane wave at an infinite plane interface can be used at every point of a rough surface interface. We use the symbol U_s for the field that would exist at the interface position if the scattering surface were not present; U is the reflected field, and U' is the transmitted field. Both U and U' are evaluated on the surface S. We designate $\mathcal{R}$ as the pressure reflection coefficient and $\mathcal{T}$ as the pressure transmission coefficient, as defined in Chapter 2. Then

$$\begin{aligned} U &= \mathcal{R}\, U_s \\ \frac{\partial U}{\partial n} &= -\mathcal{R}\frac{\partial U_s}{\partial n} \\ U' &= \mathcal{T}\, U_s \\ \frac{\partial U'}{\partial n} &= \mathcal{T}\frac{\partial U_s}{\partial n} \end{aligned} \tag{7.2.18}$$

The substitution of Equation 7.2.18 into Equation 7.2.17 gives the scattered field,

$$U(Q) = \frac{1}{4\pi}\int_S \mathcal{R}\,\frac{\partial}{\partial n}\left(U_S \frac{e^{-ikR}}{R}\right) dS \tag{7.2.19}$$

and the transmitted field,

$$U'(Q') = \frac{1}{4\pi}\int_S \mathcal{T}\left[U_S \frac{\partial}{\partial n}\left(\frac{e^{-ik'R'}}{R'}\right) - \frac{e^{-ik'R'}}{R'}\frac{\partial U_S}{\partial n}\right]_S dS \tag{7.2.20}$$

Even with the Kirchhoff approximation, the integrals are difficult to evaluate because $\mathcal{R}$ and $\mathcal{T}$ are inside the integrals. Four conditions may be considered:

(1) When kR is large and the incident angle θ is not too close to critical, the spherical wave may be approximated as a local plane wave, and the plane wave reflection and transmission coefficients may be used.

(2) When $\mathcal{R}$ and $\mathcal{T}$ are constant, or slowly varying over the surface element, we can use the mean values; this is particularly true near vertical incidence.

(3) When the interface is the water-air interface, the density contrast is so large that $\mathcal{R} = -1$ for virtually any angle of incidence.

(4) When the two sound speeds are nearly the same and the contrast is due to different densities.

Under these conditions, we may move the reflection and transmission coefficients to outside the integral and obtain

$$U(Q) = \frac{\mathcal{R}}{4\pi}\int_S \frac{\partial}{\partial n}\left(U_S \frac{e^{-ikR}}{R}\right) dS \tag{7.2.21}$$

and

$$U'(Q') = \frac{\mathcal{T}}{4\pi}\int_S \left[U_S \frac{\partial}{\partial n}\left(\frac{e^{-ik'R'}}{R'}\right) - \frac{e^{-ik'R'}}{R'}\frac{\partial U_S}{\partial n}\right]_S dS \tag{7.2.22}$$

The Kirchhoff approximation is often called the *geometrical optics approximation* because the ray description is assumed to represent the reflected and transmitted waves at the point where the ray strikes the plane interface.

7.2.4 FRESNEL APPROXIMATION

We now replace the generic symbol U by the scalar acoustic pressure, p. Since the Helmholtz-Kirchhoff integral is for continuous waves, we suppress the time dependence and calculate the pressure $P(f)$ as a function of frequency f. The geometry is shown in Fig. 7.2.2. Assume the attenuation is negligible. Including a source directionality, D, the incident pressure at the surface element dS at distance R_s from the source is

$$U_s = P_{inc} \approx \frac{P_0 R_0 D \exp(-ikR_s)}{R_s} \tag{7.2.23}$$

where k is the wave number $2\pi f/c$, P_0 is the source pressure at range R_0, and $\mathcal{R}_{12}$ is the reflection coefficient at the 1, 2 rough interface. The integral for the scattered field (Equation 7.2.21) becomes

$$P(f) \approx \frac{P_0 R_0 \mathcal{R}_{12}}{4\pi}\int_S D \frac{\partial}{\partial n}\left\{\frac{exp[-ik(R+R_s)]}{RR_s}\right\} dS \tag{7.2.24}$$

The ranges R and R_s are defined in Fig. 7.2.2. The incremental area dS is at the depth $\zeta(x', y')$ relative to the x' and y' plane. The local depth ζ (i.e., the local roughness) is a deviation from the plane interface. The angular displacement of the receiver ψ_3 in the $x' - z'$ plane is not shown. In most applications, ψ_3 is zero. The deviation ζ is small relative to R_s and R. From the geometry, the second-order "Fresnel" approximations of R_s and R are given by

$$R_S^2 = (R_1 \cos\psi_1 + \zeta)^2 + (R_1 \sin\psi_1 + x')^2 + y'^2 \tag{7.2.25a}$$

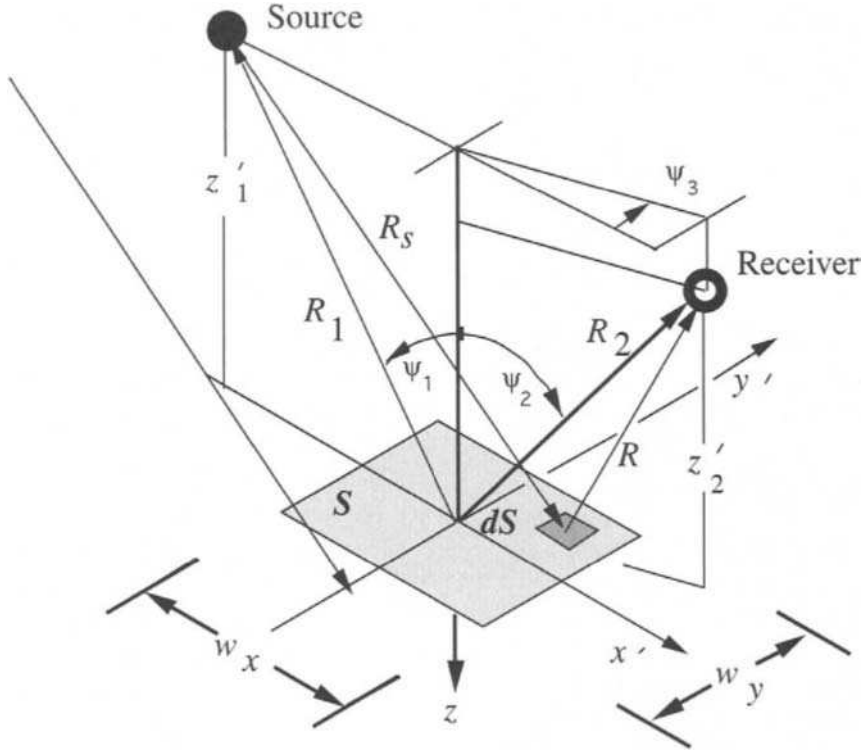

Figure 7.2.2 Geometry for facet scattering calculation. The element of area dS is elevated $-\zeta$ above the $x' - y'$ plane. The receiver can be at the angle ψ_3 relative to the $x' - z'$ plane.

and

$$R^2 = (R_2 \sin\psi_2 \cos\psi_3 - x')^2 + (R_2 \sin\psi_2 \sin\psi_3 - y')^2 + (R_2 \cos\psi_2 - \zeta)^2 \tag{7.2.25b}$$

Using the expansion $(1+a)^{1/2} \approx 1 + a/2 - a^2/8 + \ldots$, the second-order expansion of R_s is

$$R_s \approx R_1 + \frac{x'^2 \cos^2\psi_1}{2R_1} + \frac{y'^2}{2R_1} + x' \sin\psi_1 + \zeta \cos\psi_1 \tag{7.2.26}$$

where ζ^2 was dropped because ζ/R_1 is very small. The expression for R is

$$R = R_2 + \frac{x'^2}{2R_2}(1 - \sin^2\psi_2 \cos^2\psi_3) + \frac{y'^2}{2R_2}(1 - \sin^2\psi_2 \sin^2\psi_3) - x' \sin\psi_2 \cos\psi_3 + \zeta \sin\psi_2 - y' \sin\psi_2 \sin\psi_3 \tag{7.2.27}$$

The approximate sum of $k(R_s + R)$ is

$$\begin{aligned} k(R_S + R) \approx\ & k(R_1 + R_2) + xf^{-2}x'^2 + yf^{-2}y'^2 \\ & + kx'(\sin\psi_1 - \sin\psi_2 \cos\psi_3) \\ & - ky' \sin\psi_2 \sin\psi_3 + k\zeta(\cos\psi_1 + \cos\psi_2) \end{aligned} \tag{7.2.28}$$

where

$$x_f^{-2} \equiv \frac{k}{2}\left(\frac{\cos^2\psi_1}{R_1} + \frac{1 - \sin^2\psi_2 \cos^2\psi_3}{R_2}\right) \tag{7.2.29a}$$

$$y_f^{-2} \equiv \frac{k}{2}\left(\frac{1}{R_1} + \frac{1 - \sin^2\psi_2 \sin^2\psi_3}{R_2}\right) \tag{7.2.29b}$$

To evaluate the normal derivative, we make the *small-slope approximation*

$$\frac{\partial}{\partial n} \approx \frac{\partial}{\partial \zeta} \approx k\ (\cos\psi_1 + \cos\psi_2) \tag{7.2.30}$$

Since the factor (RR_s) varies slowly, it can be replaced by $(R_1 R_2)$ and moved out of the integral. The dependence of D and $\exp[-ik(R + R_s)]$ on x' and y' are important; these terms stay in the integral. With these approximations, the integral (Equation 7.2.24) becomes

$$\begin{aligned} P(f) \approx\ & \frac{iP_0 R_0 \mathcal{R}_{12} k(\cos\psi_1 + \cos\psi_2) e^{-ik(R_1+R_2)}}{4\pi R_1 R_2} \int_{-x_1}^{x_1} dx' \int_{-y_1}^{y_1} \\ & \times D \exp\left\{-i\left[\frac{x'^2}{x_f^2} + \frac{y'^2}{y_f^2} + kx(\sin\psi_1 - \sin\psi_2 \cos\psi_3)\right.\right. \\ & \left.\left. -ky' \sin\psi_2 \sin\psi_3 + k\zeta(\cos\psi_1 + \cos\psi_2)\right]\right\} dy' \end{aligned} \tag{7.2.31}$$

This integral is sometimes called the Helmholtz-Kirchhoff-Fresnel integral, or the HKF integral, because it introduces the Fresnel approximation into the Helmholtz-Kirchhoff integral. The importance of this Fresnel approximation was demonstrated in the acoustic scattering literature by Horton and Melton (1970).

The usefulness and accuracy of the Kirchhoff approximation has been the subject of many theoretical and experimental papers. (Theory: Thorsos 1988; Thorsos and Jackson 1989; Thorsos 1990; Thorsos and Broschat 1995; and references in those papers. Experiments: Neubauer and Dragonette 1967; Jebsen

and Medwin 1982; Kinney, Clay, and Sandness 1983; Neubauer 1986; Thorne and Pace 1984; Clay, Chu, and Li 1993.)

7.3 Specular Backscatter by the Kirchhoff Method

Theory and measurements of the sound scattered by any complicated object often assume that the complex surface may be approximated by plane segments, and that the total scatter is obtained by summing the scatter from each of these facets. We will use the HKF method in this section. However, first we must explore the regions where plane-wave, specular (mirrorlike) backscatter is valid. The scattering of sound waves by a finite plane facet is simple enough that the details are tractable with reasonably simple functions. We will find that the HKF method also "works" quite well for cylinders. It should be noted that the facet reflection solution given by the HKF integral is incomplete because it evaluates the interaction of the sound wave at each increment of the scattering area dS but ignores diffractions at the boundaries of the facet. Usually, in the "specular" (mirror) direction, the "reflection" component from S is much larger than the diffraction component from the boundary, so that the diffractions may be ignored. The method is satisfactory for cylinders but inadequate for spheres. Since the HKF integral is an approximation, we compare HKF calculations to theory, and experimental results to theory, to establish the validity of the approximations.

7.3.1 RECTANGULAR PLANE FACET

Reflection and scattering of sound waves from finite rectangular plane facets is one of the most fundamental applications of the HKF integral. The reflection of a spherical wave at a circular plane interface is described in section 2.6.6. Phase zones (Fresnal zones) were introduced at that time. Finite rectangular facets are drawn on the phase zones in Fig. 7.3.1. If a dimension of a facet extends beyond many phase zones, the contributions average out, and the facet is effectively infinite in that direction. Thus, the facets shown in Fig. 7.3.1a and b are effectively infinite in the y-direction. Then the reflection amplitude is sensitive only to the facet width in the x-direction. The reflection from the wider facet, Fig. 7.3.1a, is expected to be larger than the reflection from the facet in Fig. 7.3.1b. Evaluations of the HKF integral give quantitative measures of these effects, even when we ignore diffractions.

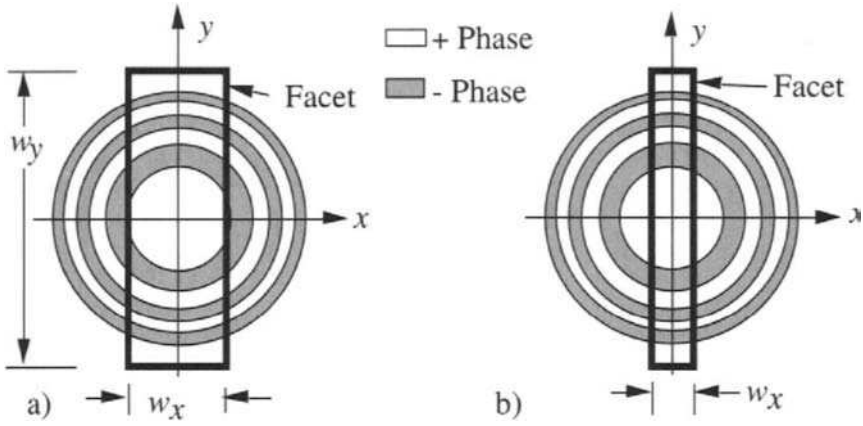

Figure 7.3.1 Phases of Fresnel zones at vertical incidence of a spherical wave at a rectangular facet. The facet lengths W_y as sketched in a) and b) are effectively infinite because they cover many phase zones. (From Clay, C. S.; D. Chu; and C. Li, "Specular reflection of transient pressures from finite width plane facet," *J. Acoust. Soc. Am.* **94**, 2279–86, 1993.)

To describe backscatter amplitudes at normal incidence to the rectangular facet, let

$$D = 1,\ \psi_1 = \psi_2 = 0,\ R_1 = R_2 = R \quad \text{and} \quad \zeta = 0 \tag{7.3.1}$$

The Fresnel parameters x_f^{-2} and y_f^{-2} in Equation 7.2.29 reduce to

$$x_f^{-2} = y_f^{-2} = k/R = 2\pi/(\lambda R) \tag{7.3.2}$$

The HKF integral (Equation 7.2.30) becomes

$$P(f) \approx \frac{iP_0 R_0 \mathcal{R}_{12} k\, e^{-i2kR}}{2\pi R^2} \times \int_{-x_1}^{x_1} dx' \int_{-y_1}^{y_1} \exp\left[-i\frac{k}{R}(x'^2 + y'^2)\right] dy' \tag{7.3.3}$$

where the limits x_1 and y_1 are the half-width and half-length of the rectangular facet. The limits can go to infinity. The expression contains the product of "Fresnel integrals."

Define the following changes of variable to make the length and width dimensionless and to transform Equation 7.3.3 into the "handbook" form of the

Fresnel integrals (Abramowitz and Stegun 1965, sec. 7.3):

$$u = \frac{2}{\sqrt{\lambda R}} x \quad \text{and} \quad v = \frac{2}{\sqrt{\lambda R}} y \tag{7.3.4}$$

$$C(u_1) \equiv \int_0^{u_1} \cos\left(\frac{\pi}{2}u^2\right) du \quad \text{and} \quad S(u_1) \equiv \int_0^{u_1} \sin\left(\frac{\pi}{2}u^2\right) du \tag{7.3.5}$$

The dimensionless limits are

$$u_1 = w_x/\sqrt{\lambda R} \quad \text{and} \quad v_1 = w_y/\sqrt{\lambda R} \tag{7.3.6}$$

The pressure (Equation 7.3.3) is written in terms of the Fresnel integtrals

$$P(w_x, w_y) \approx \frac{iP_0 R_0 \mathcal{R}_{12} e^{-i2kR}}{4R} I(u_1) I(v_1) \tag{7.3.7}$$

where

$$I(u_1) \equiv 2[C(u_1) - i S(u_1)] \tag{7.3.8}$$

The frequency and range dependence are expressed in Equation 7.3.6.

Evaluations of the HKF integral for infinite limits or for an infinite plane interface gives the familiar "image solution" because

$$C(\infty) = 0.5 \quad \text{and} \quad S(\infty) = 0.5 \tag{7.3.9a}$$

and the product $I(u_1)I(v_1)$ is

$$I(u_1)I(v_1) = (1 - i)(1 - i) = -2i \tag{7.3.9b}$$

The substitution of Equation 7.3.9b into Equation 7.3.7 gives

$$P(\infty, \infty) \equiv \frac{P_0 R_0 \mathcal{R}_{12} e^{-i2kR}}{2R} \tag{7.3.10}$$

which is the image solution discussed in section 2.6.6.

The ratio of the reflected pressure from a finite square ($w_x = w_y$) facet to that from an infinite plane $|P(w_x, w_y)|/|P(\infty, \infty)|$ is shown in Fig. 7.3.2. The Fraunhofer (incident plane-wave) region is approximately $w_x/\sqrt{\lambda R} < 0.5$. In this region the relative backscattered pressure is proportional to the area of the facet.

The Fresnel region is characterized by amplitude oscillations above and below unity at approximately $w_x/\sqrt{\lambda R} > 0.5$. The ratio tends to the constant pressure "image" region of unity at large $w_x/\sqrt{\lambda R}$; there the finite facet is large enough to give the same reflected pressure as an infinite plane. Note that we have not calculated the diffraction at the facet edges; Fig. 7.3.2 is solely due to the

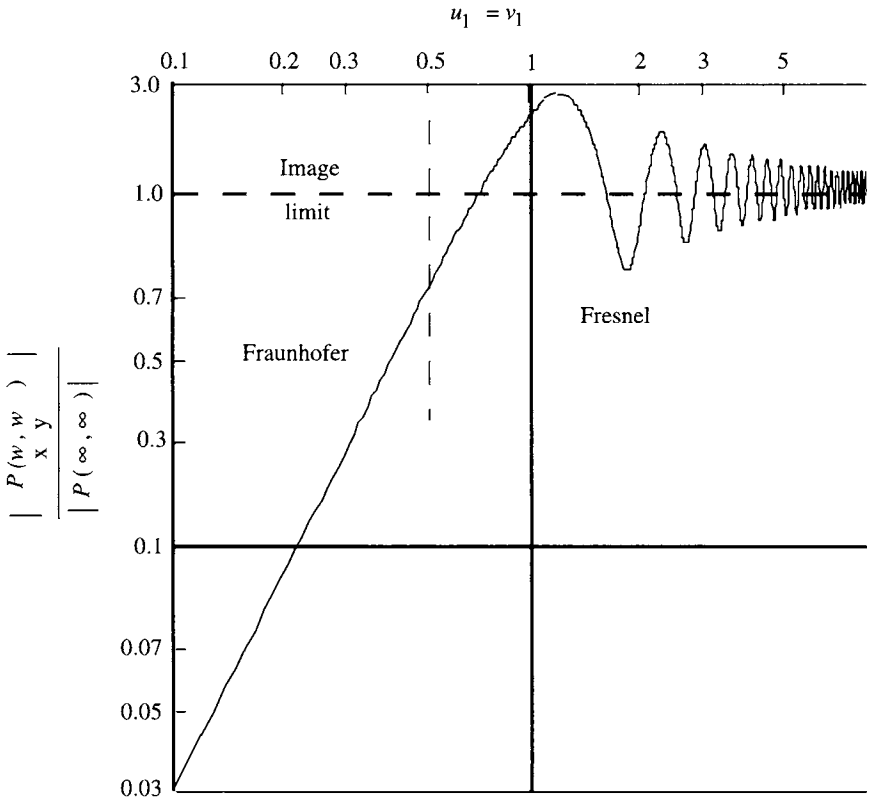

Figure 7.3.2 Presssure of a sinusoidal wave reflected from a square facet ($w_x = w_y$) relative to pressure from an infinite plane. The sound waves are vertically incident. The parameters are $u_1 = w_x/\sqrt{\lambda R}$ and $v_1 = w_y/\sqrt{\lambda R}$. In the Fraunhofer region there is fractional reflection because the dimensions are less than the first Fresnel zone. In the Fresnel region the facet is insonified over several zones, and the reflected pressure oscillates above and below the infinite plane value. (From Clay, C. S.; D. Chu; and C. Li, "Specular reflection of transient pressures from finite width plane facet," *J. Acoust. Soc. Am.* **94**, 2279–86, 1993.)

interference effect when a spherical wave is incident on a square plane facet. These theoretical results have been verified by a set of laboratory experiments (Clay, Chu, and Li 1993).

7.3.2 PENETRABLE CYLINDER

In applying the Kirchhoff method to penetrable cylinders and other three-dimensional objects, it is instructive to sketch the expected wave paths. The

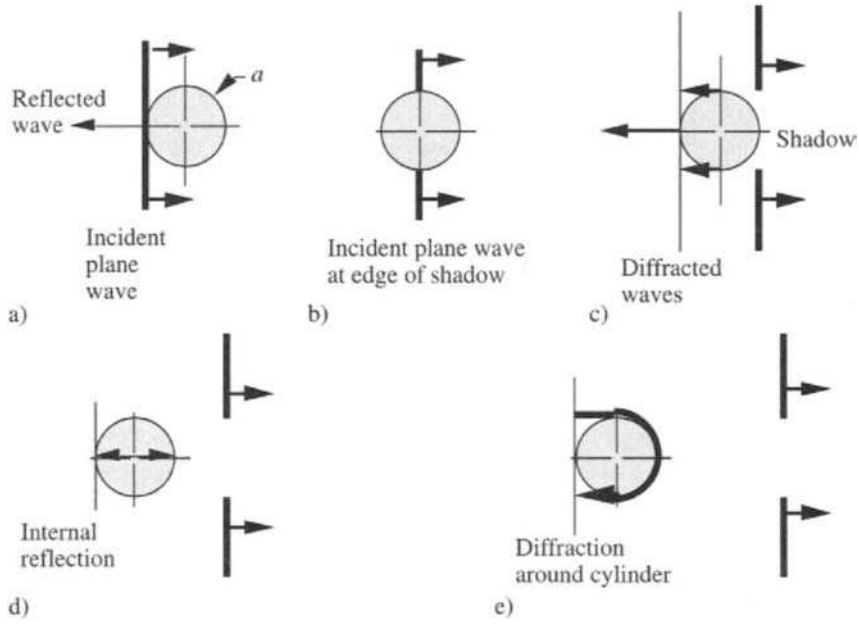

Figure 7.3.3 Sketches of reflection, transmission, and diffraction mechanisms. a) The wave is reflected at the front face of the cylinder. b) The incident wave continues to travel to the right. The wave is shown at the edge of the shadow. c) A diffracted wave travels back from the edge of the shadow with phase shift $2ka$. d) A wave travels through the penetrable cylinder and is reflected at the backside with phase shift $4k_1a$, where k_1 is the wave number in the cylinder. e) A wave, the "Franz wave," is diffracted around the cylinder; its phase shift is $(2 + \pi)ka$ relative to the front face reflection. When the body is rigid, this wave is strong enough to cause observable oscillations in the magnitude of the backscatter as shown in Fig. 7.5.5. (From Clay, C. S., "Low-resolution acoustic scattering models: fluid-filled cylinders and fish with swim bladders," *J. Acoust. Soc. Am.* **89**, 2168–79, 1991.)

sketches, (Fig. 7.3.3) describe a plane sound wave normally incident on a cylinder. The sequence of sketches shows a) the reflection from the front face; b) the transmitted energy outside the shadow; c) a diffracted wave from the shadow edge of the insonified region; d) internal reflections; and e) diffracted waves that travel around the object. The Kirchhoff integral gives the reflected components, (Fig. 7.3.3a and d); it does not give correct values for the diffraction components, (Fig. 7.3.3c and d). One needs exact theoretical solutions, or experiments, to establish the regions of validity and the accuracy of the Kirchhoff integral and the approximations.

We adapt the Helmholtz-Kirchhoff integral (Equation 7.2.21) to the geometry and notation shown in Fig. 7.3.4. For backscatter, both the transmitting and

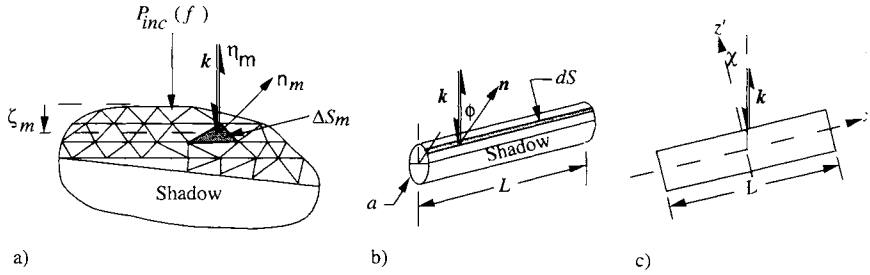

Figure 7.3.4 Geometry for Kirchhoff backscattering calculations for a cylinder. The wave number $\boldsymbol{k}$ indicates the direction of the incident plane wave. Only scattered components that go back to the receiver are considered. The integral is over the insonified area. The shadowed surface is indicated. a) Triangular subareas for numerical evaluations. b) Finite-length cylinder perpendicular to incident rays where the increments of area, dS, have normals at the angle ϕ relative to $\boldsymbol{k}$. c) Tilted cylinder.

receiving transducers are at range R. Replace U_s by the incident pressure $P_{\text{inc}}(f)$, and use the approximation that the amplitude is constant over the body, to write

$$p_{scat}(f) = \frac{1}{R} 10^{-\alpha R/20} \frac{1}{4\pi} \int_S \mathcal{R}_{12} \frac{\partial}{\partial n} (P_{inc}(f) e^{-ik(R+\zeta)})\, dS \tag{7.3.11}$$

After taking the normal derivative and rearranging terms, the backscattered sound pressure is

$$p_{scat}(f) = \frac{D\, p_{inc}(f)\, e^{-ikR}}{R} 10^{-\alpha R/20} \mathcal{L}_{bs} \tag{7.3.12}$$

where

$$\mathcal{L}_{bs} \equiv \frac{1}{4\pi} \int_S \mathcal{R}_{12} \frac{\partial}{\partial n} \left(e^{-2ik\zeta} \right) dS \tag{7.3.13}$$

The ζ is a coordinate at the object (Fig. 7.3.4), and the phase kR is shifted to the incident pressure. The frequency dependence of $\mathcal{L}_{bs}$ is implicit. The normal derivative operation gives

$$\mathcal{L}_{bs} = \frac{-ik}{2\pi} \int_S \mathcal{R}_{12} \left(e^{-2ik\zeta} \right) \cos(n,k)\, dS \tag{7.3.14}$$

where (n, k) is the angle η between vectors $\boldsymbol{n}$ and $\boldsymbol{k}$, as shown in Fig. 7.3.4a. The product $\boldsymbol{k} \cdot \boldsymbol{n} = -k \cos(\eta)$ for the upward-traveling wave.

Numerical evaluations of Equation 7.3.14 replace the integral with the finite summation

$$\mathcal{L}_{bs} \approx \frac{ik}{2\pi} \sum_m \mathcal{R}_{12}(\eta_m) \left(e^{-2ik\zeta_m} \right) \cos(\eta_m)\, \Delta S_m \tag{7.3.15}$$

where the subscripts label the parameters for the mth scattering area ΔS_m. The dependence of the reflection coefficient $\mathcal{R}_{12}(\eta_m)$ on η_m is included for generality, although the reflection coefficient at the surface of a gas-filled swimbladder is approximately -1 everywhere. Foote (1985) used numerical evaluations such as this to calculate the target strengths of the model swimbladder of a fish (Chapter 9).

7.3.3 *FINITE FLUID CYLINDER*

The finite fluid cylinder is shown in Fig. 7.3.4b. For a cylinder of geometrical length L, the equivalent acoustic backscattering length is, using the Helmholtz-Kirchhoff integral,

$$\mathcal{L}_{bs}(ka) \approx \frac{ika\ L\mathcal{R}_{12}}{2\pi} \int_{-\pi/2}^{\pi/2} e^{-2ika(1-\cos\phi)} \cos\phi\ d\phi \qquad \textbf{(7.3.16)}$$

where we assume $\mathcal{R}_{12}$ is a constant, and we explicitly write the dependence on frequency in terms of ka for clarity. The integral is over the illuminated region $-\pi/2$ to $+\pi/2$. This approximation is accurate for gas-filled cylinders and rigid cylinders in water.

Note that when the sound velocities of the body and the water are the same, and the two fluids have a density contrast, the reflection coefficient is constant at all angles of incidence; then the angle of refraction equals the incident angle, and $\mathcal{R}_{12}$ is constant. For example, this is an acceptable approximation for fish flesh in water because the velocity contrasts are small.

An evaluation of the Helmholtz-Kirchhoff integral (Equation 7.3.16) is given in Haines and Langston (1980), Gaunaurd (1985), and Stanton (1988). The integrals are in Gradshteyn and Ryzhik (1980). In the limit of large ka, the acoustic backscattering length of the cylinder is

$$\mathcal{L}_{cyl} = -\frac{i\sqrt{ka}L\mathcal{R}_{12}}{2\sqrt{\pi}} e^{i\pi/4} e^{-i2ka} \quad \text{for} \quad |2ka| \gg 1 \qquad \textbf{(7.3.17)}$$

The magnitude of the backscatter is

$$|\mathcal{L}_{cyl}| \approx \left| \frac{L\mathcal{R}_{12}}{2} \sqrt{\frac{ka}{\pi}} \right| \qquad \textbf{(7.3.18)}$$

where we have dropped the usual backscatter subscript *bs* for simplicity.

An example of the variation of $|\mathcal{L}_{bs}|$ with ka is shown in Fig. 7.3.5. The acoustic scattering length is given relative to the geometrical length, L. Sometimes the ratio $|\mathcal{L}_{bs}|/L$ is called the *reduced scattering length*; we prefer to call it the *relative acoustic backscattering length.*

The figure shows that, for a gas cylinder in water, $ka > 1$, the Helmholtz-Kirchhoff solution agrees with the complete normal-mode wave solution that will be developed in section 7.4.

Tilted Cylinder

The scattering amplitude for a tilted finite cylinder uses the geometry shown in Fig. 7.3.4c. Replace k by $k\cos\chi$ and L by an integral over dx'. The tilt of the cylinder introduces a phase term $2kx' \sin\chi$. Equation 7.3.17 becomes

$$\mathcal{L}_{cyl} \approx \pm \frac{i\sqrt{ka\cos\chi}\,\mathcal{R}_{12}}{2\sqrt{\pi}} e^{i\pi/4} e^{-i2ka\cos\chi} \int_{-L/2}^{L/2} e^{-i2kx'\sin\chi}\, dx' \qquad \textbf{(7.3.19)}$$

Integration over x' gives

$$\mathcal{L}_{cyl} \approx \pm \frac{i\sqrt{ka\cos\chi}\,L\mathcal{R}_{12}}{2\sqrt{\pi}} e^{i\pi/4} \frac{\sin\Delta}{\Delta} e^{-i2ka\cos\chi} \quad \text{for} \quad |2ka\cos\chi| > 2 \qquad \textbf{(7.3.20)}$$
$$\Delta = kL\sin(\chi)$$

7.3.4 *LOW-CONTRAST FINITE FLUID CYLINDER*

A ray-path construction for the penetrable, fluid-filled cylinder is shown in Fig. 7.3.6. In the Kirchhoff approximation, the sound wave is partly reflected from the top of the cylinder; the transmitted wave travels through the cylinder and is

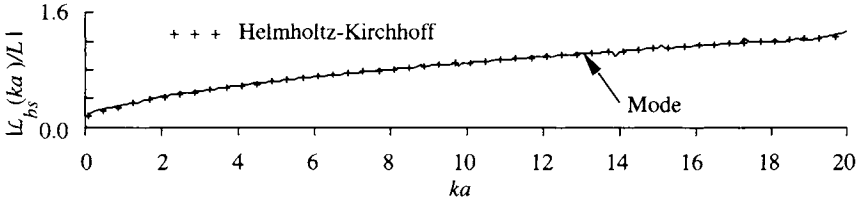

Figure 7.3.5 Relative acoustic backscattering length at normal incidence to a finite gas cylinder in water, solved by HK method and normal mode description (section 7.4). The reflection coefficient for the water-gas interface is $\mathcal{R}_{12} = -0.999$. The mode solution is the finite cylinder approximation of a gas-filled cylinder. (From Clay, C. S., "Composite ray-mode approximations for backscattered sound from gas-filled cylinders and swimbladders," *J. Acoust. Soc. Am.* **92**, 2173–80, 1992.)

reflected from the bottom. It then passes through the top (Fig. 7.3.6). Details are in Stanton, Clay, and Chu (1993) and Clay and Horne (1994).

The Kirchhoff approximation for a low-contrast fluid cylinder is

$$\begin{aligned} \text{fluid } \mathcal{L}_{cyl} \approx -i\,\frac{L}{2\sqrt{\pi}}\left[(ka\,\cos\chi)\right]^{1/2}\frac{\sin\Delta}{\Delta}\,\mathcal{R}_{01} \\ \times\left[e^{-i\,2kz_U} - \mathcal{T}_{01}\mathcal{T}_{10}\,e^{-i\,2kz_U + i\,2k_1(z_U - z_L) + i\,\psi_1}\right] \end{aligned} \tag{7.3.21}$$

where

$$k_1 = \frac{2\pi f}{c_1}\,,\quad \mathcal{R}_{01} = \frac{\rho_1 c_1 - \rho_0 c_0}{\rho_1 c_1 + \rho_0 c_0} \quad \text{and} \quad \mathcal{T}_{01}\,\mathcal{T}_{10} = 1 - \mathcal{R}_{01}^2 \tag{7.3.22}$$

The empirical phase term ψ_1 is

$$\psi_1 = -\frac{\pi k_1 z_U}{2(k_1 z_U + 0.4)} \tag{7.3.23}$$

where z_U and z_L are the upper and lower surfaces of the cylinder. The density and sound speed in water are ρ_0 and c_0, and in the body, ρ_1 and c_1; a is the radius as viewed from the top, and Ψ_1 is an empirical phase correction.

The following parameters are commonly used for relative density and relative speed:

$$g = \rho_1/\rho_0 \quad \text{and} \quad h = c_1/c_0 \tag{7.3.24}$$

For low acoustic contrast and near vertical incidence, refraction is negligible, and the reflection coefficient is approximately

$$\mathcal{R}_{01} \approx (gh-1)/(gh+1) \quad \text{for} \quad |gh-1| \ll 1 \tag{7.3.25}$$

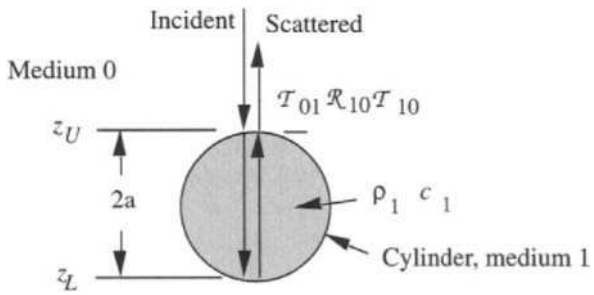

Figure 7.3.6 Construction of rays in the Kirchhoff reflection approximation for a low-contrast, penetrable fluid cylinder.

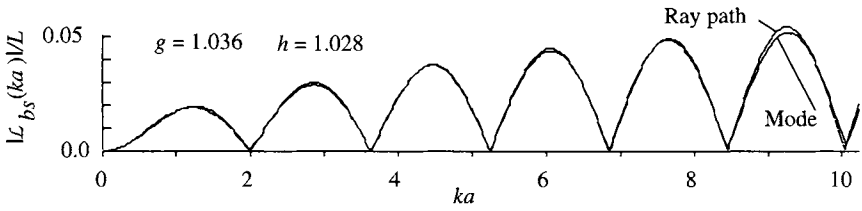

Figure 7.3.7 Comparison of the calculations of the relative acoustic backscattering lengths for a low-contrast fluid cylinder at normal incidence. The ray-path computations were made using Equation 7.3.21. The parameters $g = 1.036$ and $h = 1.028$ approximate fish flesh in water. The mode calculations were made using 14 modes of the normal mode solution for finite-length cylinders, given in section 7.4.2.

The result of a computation of the relative acoustic scattering length for a low-contrast fluid cylinder is shown in Fig. 7.3.7. The parameters are approximately those of fish flesh in water. The sequence of maxima and minima show interferences between the frequency-dependent reflections from the top surface and the bottom surface of the cylinder. These peaks and troughs of scattered pressure are interpreted as changes in the acoustical scattering length.

This Kirchhoff approximation is compared with the normal mode solution (see section 7.4) for the finite cylinder (Stanton et al. 1993). A most remarkable result is that the simple sum of the reflections from the top and bottom surfaces in Fig. 7.3.6 combine to give an excellent approximation to the solution from the detailed modal solution. This simple approximation is accurate for g and h in the range of 1.1 to 0.9. Larger or smaller values give errors that are greater than 10 percent.

7.4 Modal Solutions for a Fluid Cylinder

In section 7.3 we considered the specular reflections, which dominate many scattering situations. To obtain the diffraction contributions to the total scatter, as well as the resonances of penetrable bodies, we turn to normal-mode solutions. The fluid-filled cylinder and fluid-filled sphere are the simplest of the general problems that have been solved by the mode technique, and we will look at the magnitude and the directionality of scattering for these cases. Lord Rayleigh (1877) introduced the modal description. Faran (1951) gives expressions for elastic solid cylinders and spheres. Stanton (1988b) used Faran's expressions for numerical calculations. Scattering computations for prolate spheroids are much more difficult because the spheroidal functions converge slowly and and require

extensive numerical computations (Spence and Granger 1951; Furusawa 1988; Feuillade 1996). The extended boundary condition (EBC) technique, or T-matrix method, can be used to compute the sound scattered by arbitrary objects (Waterman 1965, 1969).

In the beginning of this chapter we introduced several measures of sound scattered by objects: the acoustic scattering length, the differential scattering cross section, and the target strength. There are other parameters of scattering. For example, we have used the concept of reduced or relative acoustical length, (relative to the actual geometrical length) and relative scattering cross section (relative to the geometrical cross section). This was done to make scattering functions nondimensional and easily comprehended.

Anderson (1951) uses the terminology "reflectivity factor" for the relative reflection amplitude for spheres, and Hickling (1962) describes a function, $f_c(ka)$, for cylinders. These types of scattering functions are often called *form functions.*

Unfortunately, the theoretical studies of mode studies use two different sign conventions. For example, the sign convention that is generally used in normal-mode theory has the incident harmonic pressure as $p_{\text{inc}} = P_{\text{inc}} e^{i(kR-2\pi ft)}$ and the scattered pressure

$$p_{scat}(t) = \frac{P_{inc} e^{i(kR-2\pi ft)}}{R} \mathcal{L}_{mode} \quad (\text{here } D = 1) \tag{7.4.1}$$

A comparison of Equations 7.4.1 and 7.1.2 shows that we have changed $2\pi f(t - R/c)$ to $(kR - 2\pi ft)$. Either form describes a wave traveling in the $+R$ direction. The magnitude is the same, of course. However, the result of this sign change is that acoustic scattering lengths in this section will be the *complex conjugates* of the scattering lengths in sections 7.1–7.3. Scattering cross sections are not affected by this sign change.

*7.4.1 *INFINITE CYLINDER (OPTIONAL)*

The normal-mode solutions describe the scattering of CW by matching the incident wave and the scattered wave at the boundary of the body to reveal that only certain "modes" can occur. The mode desciption is similar to the characterization of longitudinal standing waves that exist in organ pipes. We now derive the equations needed to obtain scattering amplitudes or acoustic scattering lengths using the normal mode solutions for the cylinder (Stanton 1988). The geometry of the scattering from a cylinder is shown in Figs. 2.7.1 and 7.3.4b.

*Background material

The normal-mode solutions for the scattering lengths from an infinite-length cylinder of radius a are "exact" over a wide range of ka, where k is the wave number in water. Assume an external medium described by ρ_0 and c_0, and a fluid cylinder of density and sound speed ρ_1 and c_1. The wave number inside the cylinder is $k_c = k_1/h$, where $h = c_1/c_0$. A plane wave, propagating in the $+z$ direction, is incident on the finite cylinder, which is aligned with the x axis (Fig. 2.7.1b). The incident plane wave can be reexpressed as the sum of cylindrical waves (i.e., solutions of the wave equation in cylindrical coordinates) valid at the origin, with radial and azimuthal dependence (Morse 1981, sec. 29):

$$p_{inc}(t,z) = P_{inc}e^{i(kz-2\pi ft)} = P_{inc}e^{-i2\pi ft}\sum_0^\infty \varepsilon_m i^m \cos m\phi J_m(kr) \tag{7.4.2}$$

where ε_m is the Neumann number ($\varepsilon_0 = 1$ and $\varepsilon_m = 2$ for $m = 1, 2, \ldots$). The cylinder interior acoustic pressure is

$$p_{int}(t,r) = P_{inc}e^{-i\,2\pi ft}\sum_0^\infty A_m \cos m\phi J_m(k_c r) \tag{7.4.3}$$

The sound pressure scattered by the infinite cylinder is

$$p_{scat}(t,R) = e^{-i\,2\pi ft}\,P_{inc}\sum_0^\infty b_m (i)^m \cos m\phi H_m^{(1)}(kr) \tag{7.4.4}$$

where the combination $b_m(i)^m$ describes the anticipated unknown amplitude and phase, and where $H_m^{(1)}$ is the Hankel function. Using $\boldsymbol{U}(t,r)$ for the vector radial particle velocity, Newton's law (Equation 2.7.4) is

$$\nabla p(t,r) = -\rho_A \frac{\partial \boldsymbol{U}(t,r)}{\partial t} \tag{7.4.5}$$

For time dependence $e^{-i2\pi ft}$, this is

$$\nabla p(t,r) = i2\pi f\rho_A \boldsymbol{U}(t,r) = ik\rho_A c\boldsymbol{U}(t,r) \tag{7.4.6}$$

The component of particle velocity along r is

$$u_r(t,r) = \frac{-i}{\rho_A ck}\frac{\partial p(t,r)}{\partial r} \tag{7.4.7}$$

The boundary conditions are: the pressures are equal on each side of the interface; the normal components of particle velocities are equal on each side the interface. These give solutions for *the amplitudes of the interior modes*, A_m, and the amplitudes of the scattered modes, b_m, in the equation:

$$p_{scat}(t,r) = e^{-i2\pi ft} P_{inc} \sum_{0}^{\infty} b_m (i)^m H_m^{(1)}(kr) \cos m\phi \qquad \textbf{(7.4.8a)}$$

where

$$H_m^{(1)}(kr) = J_m(kr) + iN_m(kr) \qquad \textbf{(7.4.8b)}$$

and

$$b_m = \frac{-\varepsilon_m}{1 + i C_m} \qquad \textbf{(7.4.9)}$$

$$A_m = \frac{1}{J_m(k_c a)} [\varepsilon_m (i)^m J_m(ka) + B_m H_m^{(1)}(ka)] \qquad \textbf{(7.4.10)}$$

$$C_m \equiv \frac{J'_m(k_c a) N_m(ka) - gh N'_m(ka) J_m(k_c a)}{J'_m(k_c a) J_m(ka) - gh J'_m(ka) J_m(k_c a)} \qquad \textbf{(7.4.11)}$$

The constants A_m, b_m, and C_m result from the solution of the boundary conditions. The functions $J_m(x)$ and $N_m(x)$ are cylindrical Bessel functions, and $J'_m(x)$ and $N'_m(x)$ are their derivatives. Note: Abramowitz and Stegun use the notation $Y_m(x)$ for the Neumann function $N_m(x)$. From Abramowitz and Stegun (1965, Equation 9.2.3), the expansion of the Hankel function for large kr is

$$H_m^{(1)}(kr) \approx \left(\frac{2}{\pi kr}\right)^{1/2} (-i)^m e^{i(kr - \pi/4)} \qquad \textbf{(7.4.12)}$$

The substitution of Equation 7.4.12 into Equation 7.4.8a gives the far-field expression for the pressure scattered by an infinite cylinder:

$$p_{scat}(t,r) \approx P_{inc} e^{i(kr - 2\pi ft)} \sqrt{\frac{2}{\pi kr}} e^{-i\pi/4} \sum_{0}^{\infty} b_m \cos m\phi \qquad \textbf{(7.4.13)}$$

Stanton (1992) gives the solution in terms of the *form function* F for the infinite cylinder (∞):

$$p_{scat}(t,r) \approx P_{inc} e^{i(kr - 2\pi ft)} \sqrt{\frac{a}{2r}} F_{mode}^{(\infty)} \qquad \textbf{(7.4.14)}$$

where

$$F_{mode}^{(\infty)} \equiv \frac{2\,e^{-i\pi/4}}{\sqrt{\pi ka}} \sum_{m=0}^{\infty} b_m \cos m\phi \qquad (7.4.15)$$

The scattering expressions (Equations 7.4.13 and 7.4.14) are equivalent. Sometimes definitions vary and comparisons of expressions such as Equations 7.4.13 through 7.4.15 determine the definition of the form function used by different authors (see Neubauer 1986).

7.4.2 FINITE CYLINDER

Stanton (1988a) used the far-field normal-mode solution (Equation 7.4.13) as the basis of an approximation for finite-length cylinders. As sketched in Fig. 7.4.1a, the finite cylinder has an outward volume flow per unit length of $q_r(\mathrm{m}^3/\mathrm{s})/\mathrm{m}$.

For an incremental length of cylinder, dx, the volume flow is $q_r\,dx$. In Stanton's larger-range approximation, the toroidal increment of volume flow is equivalent to a monopole source on the x-axis. The incremental sound pressure owing to the incremental source of volume flow of a pulsating sphere is discussed in section 4.1.1. For the source flow, $q_r\,dx$, the increment of pressure at range R is

$$dp(t,R) = \frac{-ik\rho_A c}{4\pi} q_r\,dx \frac{e^{i(kR-2\pi ft)}}{R} \qquad (7.4.16)$$

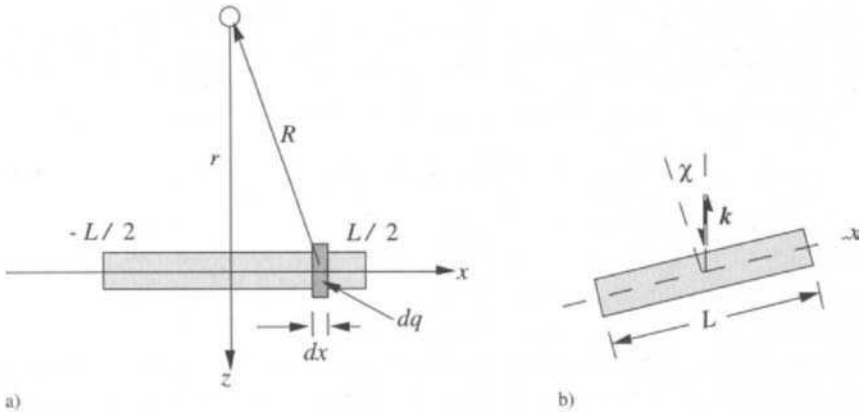

Figure 7.4.1 Geometry for finite cylinder calculation. a) Radiation from an increment of radial volume flow per unit length, q_r, for an annular ring of width dx at the cylinder surface. b) Cylinder tilted at angle χ relative to the normal of the incident wave.

In order to determine the modal constants of Equation 7.4.8a in terms of the flow q_r, we integrate $dp(t, R)$ over infinite x. This gives the sound pressure owing to an infinite cylindrical source at range r normal to the cylinder,

$$p_\infty(t, r) = \frac{-ik\rho_A c}{4\pi} q_r \int_{-\infty}^{\infty} \frac{e^{i(kR(x)-2\pi ft)}}{R(x)}\, dx \tag{7.4.17a}$$

The integral is in Gradshteyn and Ryzhik (1980, equations 3.876.1 and 2),

$$\int_{-\infty}^{\infty} \frac{e^{ikR}}{R} dx = \pi[iJ_0(kr) - N_0(kr)] = i\pi H_0^{(1)}(kr) \tag{7.4.17b}$$

Thus, in terms of q_r, the sound pressure due to a cylindrical source is

$$p_\infty(t, r) = \frac{k\rho_A c}{4} q_r H_0^{(1)}(kr) e^{-i2\pi ft} \tag{7.4.18a}$$

Using the 0th order Hankel function, $H_0^{(1)} = (\sqrt{2/(\pi kr)})\, e^{i(kr-\pi/4)}$,

$$p_{\infty c} \approx \frac{k\rho_A c}{4} q_r \left(\frac{2}{\pi kr}\right)^{1/2} e^{i(kr-\pi/4)} e^{-i2\pi ft} \tag{7.4.18b}$$

At a large range perpendicular to the cylinder, we equate $p_{\text{scat}}(t, r)$ from Equation 7.4.13 and $p_\infty(t, r)$ from Equation 7.4.18b and get

$$P_{inc} \sum_0^\infty b_m \cos m\phi = \frac{k\rho_A c q_r}{4} \tag{7.4.19a}$$

Therefore, the apparent volume flow per unit length, q_r, is given in terms of the amplitudes and phases of modes, m, and the incident pressure amplitude, P_{inc},

$$q_r = \frac{4P_{inc}}{k\rho_A c} \sum_0^\infty b_m \cos m\phi \tag{7.4.19b}$$

Tilted Cylinder

Now consider a finite-length tilted cylinder as sketched in Fig. 7.4.1b. Assume the length L is smaller than the first Fresnel or phase zone and in the Fraunhofer region (Fig. 7.3.2). Then, $R(x)$ in Equation 7.4.17a is

$$R(x) \approx r + 2x \sin\chi \tag{7.4.20a}$$

and the backscattered sound pressure from a cylinder of length L is

$$p_L(t,R) \approx \frac{-ik\rho_A c}{4\pi} q_r \frac{e^{i(kr-2\pi ft)}}{r} \int_{-L/2}^{L/2} e^{i2kx\sin\chi}\, dx \qquad \textbf{(7.4.20b)}$$

There is no flow along the x-axis in this approximation. Sound scattering from the ends is ignored. The pressure is measured at angle χ relative to the normal to the axis of the cylinder, where χ is limited to values near 0^0. Integration gives

$$p_L(t,R) \approx \frac{-ik\rho_A c}{4\pi} q_r \frac{e^{i(kr-2\pi ft)}}{r} \frac{L\sin\Delta}{\Delta}, \qquad \Delta \equiv kL\sin\chi \qquad \textbf{(7.4.21)}$$

The substitution of q_r (Equation 7.4.19b) gives the pressure backscattered by a tilted, finite cylinder,

$$p_L(t\,,R\,) = -\,i\,\frac{LP_{inc}\,e^{\,i\,\,(\,kR\,-\,2\pi ft\,)}}{\pi R}\,\frac{\sin\Delta}{\Delta}\,\sum_{m\,=\,0}^{\infty} b_{\,m}\,\cos\,(m\,\phi\,) \qquad \textbf{(7.4.22)}$$

The factor $-i$ describes the phase of the scattered pressure relative to the phase of the pressure owing to the infinite line of sources (Equation 7.4.17a). A comparison of the scattered pressures in Equations 7.4.13 and 7.4.22 gives the acoustic scattering length in terms of the modal contributions,

$$\mathcal{L}_{\,bs}\;\approx -\,i\,\frac{L}{\pi}\,\frac{\sin\Delta}{\Delta}\,\sum_{m\,=\,0}^{\infty} b_{\,m}\,\cos\,(m\,\phi\,) \qquad \textbf{(7.4.23)}$$

The mode solution, Equation 7.4.23, gives the apparent acoustic length when viewed in a plane essentially perpendicular to the finite cylinder. A perfect cylinder with no losses has been assumed. Realistically there *are* losses, and a so-called cylindrical body may have bumps and deformations that cause destructive wave interferences at its surface. To take account of these possibilities, an empirical mode interference loss factor, $\exp(-\delta_m)$, is sometimes assumed. The mode summation then becomes the finite limit

$$\mathcal{L}_{bs}\;\approx -i\,\frac{L}{\pi}\,\frac{\sin\Delta}{\Delta}\,\sum_{m\,=\,0}^{M\,-\,1} b_{\,m}\,\cos\,(m\,\phi\,)\,e^{\,-\,\delta_{\,m}} \qquad \textbf{(7.4.24)}$$

where M is the number of modes being summed. The mode-loss coefficients can be determined empirically by comparison with experiment. The introduction of mode losses also lowers the resolution of the mode calculation (Clay 1991).

7.4.3 COMPARISON OF KIRCHHOFF AND MODAL SOLUTIONS

Gas filled Cylinder

The gas-filled cylinder is assumed to have the same volume at any depth, and the pressure inside is equal to the pressure outside. This condition describes the swimbladders of some marine animals. By using the gas law, $PV = nRT$, and adding gas to keep the volume constant, the density in the swimbladder ρ_1 is

$$\rho_1 = \frac{\rho_{1,0} P_A}{1.01 \times 10^5} \text{ kg/m}^3 \tag{7.4.25a}$$

and

$$P_A = 1.01 \times 10^5 + 9.8 \rho_w z \tag{7.4.25b}$$

where $\rho_{1,0} = 1.29$ kg/m^3 is the gas density at $z = 0$. The assumed sound speed in the gas cylinder is $c_1 \approx 345$ m/s.

Examples of the dependence of the acoustic scattering lengths on the number of modes are shown in Fig. 7.4.2. As the number of modes is increased, the mode summation tends to the Kirchhoff solution (section 7.3.3 and Fig. 7.3.5). This figure also shows that the number of modes needed depends on the range of ka that is of interest. That number is approximately $ka + 2$. The cylindrical radial breathing modes for a gas envelope in water have expansions and contractions perpendicular to the axis of the cylinder. Fig. 7.4.3 shows the relative backscattering length calculated from Equation 7.4.24 for cylindrical radial pulsation mode, $m = 0$.

7.4.4 EQUIVALENT SPHERE FOR SMALL FLUID BODIES

The scattering of sound by a body that is small relative to the wavelength is somewhat insensitive to the shape because details of the shape are not resolved. Under these conditions, spheroidal models and finite cylindrical models can replace a detailed, complicated body.

Consider various simple body shapes. The volumes of the cylinder, sphere, and prolate spheroid are, respectively,

$$\text{vol}_{\text{cyl}} = \pi a_{ec}^2 L \tag{7.4.26}$$

$$\text{vol}_{\text{sph}} = (4\pi a_{es}^3)/3 \tag{7.4.27}$$

$$\text{vol}_{\text{prl sph}} = (4\pi a_{1ps}^2 a_{2ps})/3 \tag{7.4.28}$$

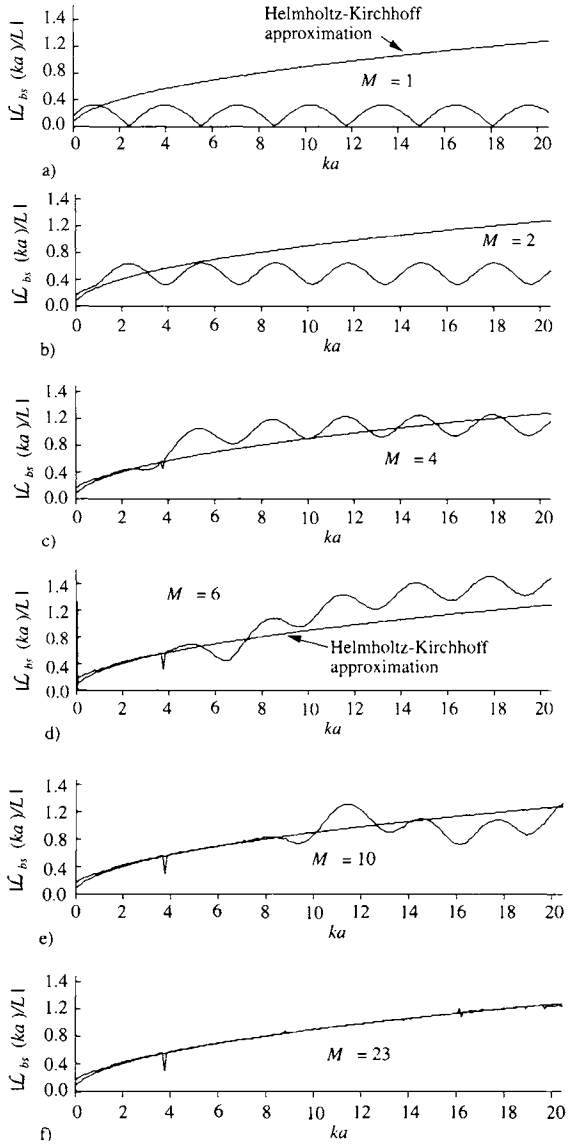

Figure 7.4.2 Comparison of the relative acoustic backscattering lengths $|\mathcal{L}_{bs}/L|$ given by the sum of modal solutions and the HK approximation for a gas cylinder of length L in water. The $M = 1$ curve is the 0th mode. The six graphs show that agreement with HK requires a sufficient number of modes in the sum. (From Clay, C. S., "Low-resolution acoustic scattering models: fluid-filled cylinders and fish with swim bladders," *J. Acoust. Soc. Am.* **89**, 2168–79, 1991.)

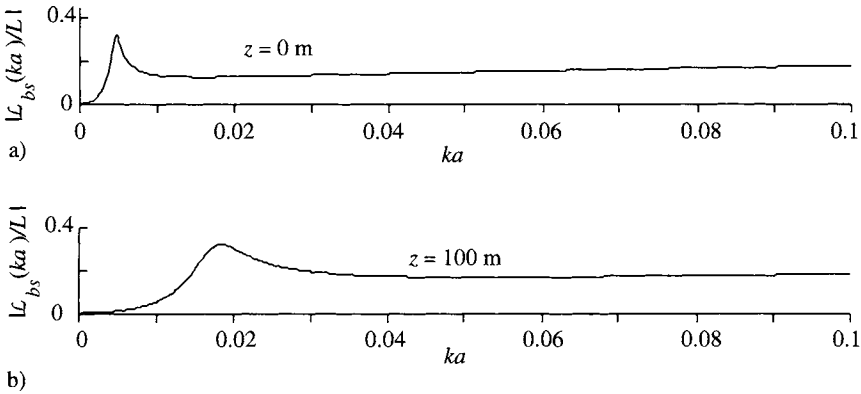

Figure 7.4.3 Relative backscattering length in a plane perpendicular to the axis of a gas-filled cylinder of length L for the lowest frequency cylindrical radial breathing mode. The frequency and breadth of the modal response increase with depth, z, as shown. Viscous and thermal damping have not been included.

where a_{ec} is the radius of the equivalent cylinder; a_{es} is the radius of the equivalent sphere; and a_{1ps} and a_{2ps} are the semi-minor and semi-major axes of the prolate spheroid, respectively. For equal volumes, the radius of the equivalent sphere for the short cylinder is

$$a_{es} = (0.75a_{ec}^2 L)^{1/3} \tag{7.4.29}$$

and for the prolate spheroid it is

$$a_{es} = (a_{1ps}^2 a_{2ps})^{1/3} \tag{7.4.30}$$

These approximations are commonly used to describe scattering of sound by zooplankton.

More accurate modeling must take into account the effects of the animal's curvature.

7.5 Scattering from a Sphere

The marine acoustician is interested in spheres because scattering from these simple models has been well studied, and the results of this research are applicable to many forms of marine life. For example, an acoustically small and compact *nonspherical* body whose dimensions are much less than those of the sound wavelength scatters in about the same way as a sphere of the same volume and same average physical characteristics.

Scattering from a sphere is an ideal vehicle to demonstrate the contributions by the three components of scatter from a fluid body: reflection, diffraction, and transmission. In section 7.5.1 we use the rigid sphere to provide one reference point, the reflection component, which dominates in "geometrical scatter" ($ka \gg 1$). In section 7.5.2 we introduce "Rayleigh scatter" ($ka \ll 1$), in which the wave diffraction around the body dominates. Here the ratio of the backscatter cross section to the geometrical cross section is proportional to the very small quantity $(ka)^4$. We then go on to the complete modal wave solution for scatter from a sphere (section 7.5.3), valid for all values of ka. In this solution all three components of scatter are subsumed in a description that yields the strengths of each mode of an infinite series. In the modal description, the infinite series describes the full range of ka, of which the first two modes are sufficient for the low-frequency range ($ka \ll 1$).

7.5.1 GEOMETRICAL SCATTER FROM A RIGID SPHERE ($ka \gg 1$)

The behavior for $ka \gg 1$ is described as "geometrical," Kirchhoff, or "specular" (mirrorlike) scatter. In the Kirchhoff approximation, a plane wave reflects from an area as if the local, curved surface is a plane. The situation can be understood by using rays as illustrated in Fig 7.5.1. In the ray description, scatter consists of a spray of reflected rays that follow the Kirchhoff reflection approximation. That is, each reflected ray obeys the simple law of reflection, in which each ray is reflected with its angle of reflection equal to its angle of incidence, as if the reflection point is a plane that is tangent to the sphere at that point. Diffraction effects, mainly from the edge of the shadow and behind the sphere, are ignored in this approximation. Those effects will be displayed when we give the normal-mode solution.

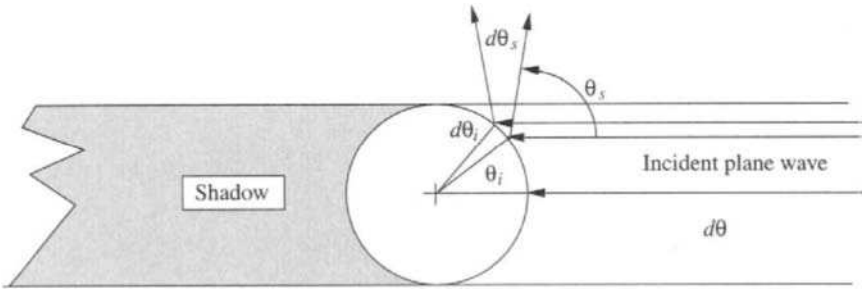

Figure 7.5.1 Ray acoustics for geometrical scatter from a fixed, rigid sphere at high frequencies, $ka \gg 1$.

We now calculate the scattering from a fixed, rigid, perfectly reflecting sphere at very high frequencies, $ka \gg 1$. The incident sound is a plane wave of incident intensity I_{inc}. There is no energy absorption in the medium. No energy penetrates into the sphere.

First, calculate the incoming power at angle θ_i, for ring increments $d\theta_i$, on the sphere surface (Fig. 7.5.1).

The surface area increment is

$$dS_i = 2\pi(a \sin \theta_i) a \, d\theta_i \tag{7.5.1}$$

The component perpendicular to the surface is

$$dS_\perp = dS_i \cos \theta_i \tag{7.5.2}$$

The input power in the ring is

$$d\Pi_{inc} = I_{inc} \, dS_\perp = I_{inc}(2\pi a^2 \sin \theta_i \cos \theta_i \, d\theta_i) \tag{7.5.3a}$$

Therefore

$$d\Pi_{inc} = I_{inc} \pi a^2 \sin(2\theta_i) \, d\theta_i \tag{7.5.3b}$$

Next calculate the scattered power. The rays that are within angular increment $d\theta_i$ at angle θ_i are scattered within increment $d\theta_s = 2d\theta_i$ at angle $\theta_s = 2\theta_i$. The *geometrically scattered* power, measured at range R, is

$$d\Pi_{gs} = I_{gs} \, 2\pi (R \sin \theta_s) R \, d\theta_s \tag{7.5.4a}$$

or

$$d\Pi_{gs} = I_{gs} \, 2\pi R^2 (\sin 2\theta_i)(2d\theta_i) \tag{7.5.4b}$$

Assume that there is no loss of power, $d\Pi_{\text{inc}} = d\Pi_{gs}$. Therefore

$$I_{gs} = I_{inc} \frac{a^2}{4R^2} \quad \text{or} \quad P_{gs} = P_{inc} \frac{a}{2R} \tag{7.5.5a}$$

or, in terms of the scattering length,

$$P_{gs} = P_{inc} \frac{|\mathcal{L}_{gs}|}{R} \quad \text{where} \quad |\mathcal{L}_{gs}| = a/2 \tag{7.5.5b}$$

or

$$|\mathcal{L}_{gs}|/(\pi a^2)^{1/2} = 1/(2\pi^{1/2}) = 0.28 \tag{7.5.5c}$$

(See Fig. 7.5.4.)

In this geometrical scatter approximation, the derivation shows that scattered power is not a function of θ_i. All differential geometrical cross sections, including the backscattering cross section, are equal. A high-frequency acoustical wave gets a "wall-eyed" view of the sphere. From Equation 7.1.5, assuming no attenuation in the medium,

$$\Delta\sigma_{gs} = |\mathcal{L}_{gs}|^2 = (a^2/4) \quad \text{for} \quad ka \gg 1 \tag{7.5.6}$$

and the total geometrical scattering cross section is

$$\sigma_{gs} = 4\pi\Delta\sigma_{gs} = \pi a^2 = A \quad \text{for} \quad ka \gg 1 \tag{7.5.7}$$

where A is the cross-sectional area.

Some of the literature calls σ_{gs} the "total scattering cross section." However, the true total scattering cross section is larger than σ_{gs} because diffractions must be included, even for $ka \gg 1$.

The fact that $\mathcal{L}_{gs}$ and σ_{gs} are approximately independent of frequency for $ka > 10$ has important practical applications. This independence has been exploited by acousticians for many decades in laboratory calibrations of sonars, because the high-frequency backscattered sound pressure is almost a delayed replica of the transmitted signal or message. A detailed analysis of the scatter of an impulse wavefront by a rigid sphere is in Sun, Didier, and Denis (1991).

The ray treatment is deceptively simple. In fact, it is an incomplete description of the problem because it ignores the complicated interferences between direct and scattered sound in the shadow region in the hemisphere behind the object. A complete wave solution (e.g., see section 7.4) shows that the ray solution is accurate for θ in the backscatter direction from zero to 90°. But it does not describe the situation at larger values of θ, where waves are diffracted into the shadow and penumbra, (Fig. 7.1.1).

Brillouin (1949) and Born and Wolf (1965, sec. 13.5.3) give calculations of the *extinction* cross section for electromagnetic waves incident on a nondissipative object in a dielectric. For an object having a cross sectional area A, they find that the extinction cross section is

$$\sigma_e = 2A, ka \gg 1 \tag{7.5.8}$$

Born and Wolf point out that this unexpected, somewhat paradoxical result is due to the nature of the fields at the edge of the shadow. Sinclair (1947) describes optical measurements of the scattering of light waves from spheres ($ka \approx 180$), which verify the extinction cross section (Equation 7.5.8).

Similarly, our numerical calculations using mode descriptions of scattering (Fig. 7.5.7) show that the scattering cross section of a large, acoustically opaque sphere approaches *twice* its geometrical cross section area ($2\pi a^2$) as ka increases. A simple interpretation is that the *geometrically scattered* component of the scattering cross section for a sphere πa^2 (Equation 7.5.7) is supplemented by an effective *diffraction scattering* cross section, also of magnitude πa^2. The electromagnetic description of the high-frequency *extinction* cross section includes the power loss due to interference of the scattered and the incident waves in the region $90° < \theta < 180°$. Therefore, the extinction cross section at large ka tends to $2\pi a^2$.

7.5.2 *RAYLEIGH SCATTER FROM A SPHERE ($ka \ll 1$)*

When the sound wavelength is very much greater than the sphere radius, the scatter is due solely to diffraction. There are two simple conditions that then cause scatter. (1) If the sphere bulk elasticity $E_1 (= compressibility^{-1})$ is less than that of the water, E_0, the incident condensations and rarefactions compress and expand the body, and a spherical wave is reradiated. This monopole reradiation occurs with opposite phase if $E_1 > E_0$. (2) If the sphere density, ρ_1, is much greater than that of the medium, ρ_0, the body's inertia will cause it to lag behind as the plane wave swishes back and forth. The motion is equivalent to the water being at rest and the body being in oscillation. This action generates dipole reradiation (section 4.1.3). When $\rho_1 < \rho_0$, the effect is the same but the phase is reversed. In general, when $\rho_1 \neq \rho_0$, the scattered pressure is proportional to $\cos\theta$, where θ is the angle between the scattered direction and the incident direction.

The simplest sphere model is a small, fixed, incompressible sphere that has no waves in its interior. There will be monopole scatter because the body is incompressible. There will also be dipole scatter because it is fixed. To illustrate this, we use a simple derivation that shows the essential physical concepts. The same result can be derived formally by using the first two terms, which are the largest terms, of the mode solution for $ka \ll 1$.

An incident plane wave moves to the left in the $-z$ direction, Fig. 7.5.2. The fixed, rigid sphere scatters sound to the receiver at range R and angle θ. The sphere is so small relative to λ that, at any instant, its entire surface is exposed to the same incident acoustic pressure at that time. The sound pressure on the sphere $P\,e^{i\omega t}$ is the sum of the incident plane wave pressure of amplitude P_{inc} and the scattered pressure wave of amplitude P_{scat}:

$$Pe^{i\omega t} = P_{inc}e^{i(\omega t+kz)} + P_{scat}e^{i\omega t} \qquad \textbf{(7.5.9a)}$$

where

$$z = R\cos\theta \tag{7.5.9b}$$

The common time dependence $e^{i\omega t}$ is dropped, and Equation 7.5.9a becomes

$$P = P_{inc}e^{ikR\cos\theta} + P_{scat} \tag{7.5.10}$$

The boundary condition on the surface of a rigid sphere is that the normal components of displacement and particle velocity are zero at all times. From Equation 2.7.43, the normal (radial) component of particle velocity is related to the pressure by

$$u_R = -\frac{1}{ik\rho_A c}\left(\frac{\partial P}{\partial R}\right) \tag{7.5.11}$$

We use Equation 7.5.10 to find the velocity relation at $R = a$, where $u_R = 0$,

$$\frac{\partial P}{\partial R}\Big]_{R=a} = ik\,P_{inc}\cos\theta\;e^{ika\cos\theta} + \frac{\partial P_{scat}}{\partial R} = 0 \tag{7.5.12}$$

The gradient of the scattered component is

$$\frac{\partial P_{scat}}{\partial R}\Big]_{R=a} = -ik\,P_{inc}\cos\theta\;e^{ika\cos\theta} \tag{7.5.13}$$

Therefore, from Equation 7.5.11, the radial component of the scattered particle velocity at $R = a$ is

$$U_{scat}]R = a = \frac{P_{inc}}{\rho_A c}\cos\theta\, e^{ika\cos\theta} \tag{7.5.14}$$

Expansion of the exponential for small ka gives

$$u_{scat} = \frac{P_{inc}}{\rho_A c}(\cos\theta + ika\cos^2\theta) \quad \text{at} \quad R = a \tag{7.5.15}$$

Equation 7.5.15 gives the radially scattered particle velocity that is necessary to make the total fluid particle velocity equal to zero on the sphere. We will show that this scattered particle velocity is equivalent to radiation from a source composed of a monopole and a dipole.

Monopole Component

To calculate the equivalent monopole rate of volume flow, $\dot{V}_m$, (m^3/s), we integrate u_{scat} over the surface of the sphere,

$$\dot{V}_m = \int_A u_{scat}\, dA = 2\pi a^2 \int_\pi^0 u_{scat} \sin\theta\, d\theta \tag{7.5.16}$$

The integral over the first term of Equation 7.5.15 is zero. The integral over the second term gives the monopole flow through the surface that surrounds the sphere,

$$\dot{V}_m = \frac{ika}{\rho_A c} \frac{4\pi a^2}{3} P_{inc} \tag{7.5.17}$$

From Equation 4.1.4, the monopole sound pressure at range R is given in terms of its volume flow,

$$P_m = -\frac{ik\rho_A c \dot{V}_m}{4\pi R(1 + ika)} e^{-ik(R-a)} \tag{7.5.18}$$

Using Equation 7.5.17, at large range $kR \gg 1 \gg ka$, the pressure due to the monopole is

$$P_m = \frac{(ka)^2 a}{3} \frac{P_{inc}}{R} e^{-ikR} \tag{7.5.19}$$

Dipole Component

To calculate the acoustic dipole, notice that the first term in Equation 7.5.15 is equivalent to alternating flow in the z direction (because of the time factor that we have suppressed). This dipole flow is obtained by integrating over the sphere:

$$\dot{V}_d = \frac{2\pi P_{inc} a^2}{\rho_A c} \int_{\pi/2}^0 \cos\theta \sin\theta\, d\theta = \frac{\pi P_{inc} a^2}{\rho_A c} \tag{7.5.20}$$

Using Equation 7.5.20 in Equation 4.1.4, the long-range dipole solution (Equation 4.1.10) has the dipole axis $l = 2a$, so that the dipole pressure is

$$P_d = (ka)^2 \frac{a}{2} \cos\theta \frac{P_{inc} e^{-ikR}}{R} \tag{7.5.21}$$

This value of P_d also follows from the exact modal solution that we consider in section 7.5.3, in which case modes 0 and 1 correspond to the monopole and dipole terms, respectively.

Scattered Pressure

The scattered pressure at large R is the sum of the monopole and dipole components of pressure,

$$P_{scat} = P_m + P_d = \left[\frac{2(ka)^2}{3}\left(1 + \frac{3}{2}\cos\theta\right)\frac{a}{2}\right]\frac{P_{inc}e^{-ikR}}{R} \tag{7.5.22}$$

The low-frequency (small-body) polar radiation pattern is shown in Fig. 7.5.2.

The scattering length and differential scattering cross section for the small, fixed, rigid sphere are calculated from $(P_{\text{scat}})^2/(P_{\text{inc}})^2$, as in Equation 7.1.5, and are extrapolated back to $R = 1$ m,

$$|\mathcal{L}| = a\frac{(ka)^2}{3}\left(1 + \frac{3}{2}\cos\theta\right) \tag{7.5.23a}$$

and

$$\Delta\sigma_S(f,\theta) = \frac{(ka)^4}{9}\left(1 + \frac{3}{2}\cos\theta\right)^2 a^2 \tag{7.5.23b}$$

Although the analytical derivation above was for $ka \ll 1$, the mode solution for a large range of ka show that Equations 7.5.23a and 7.5.23b are useful for ka as large as 0.5 (see Fig. 7.5.4). Backscattering is obtained by setting $\theta = 0°$. The results are

$$|\mathcal{L}_{bs}| = a\frac{5(ka)^2}{6} \tag{7.5.24a}$$

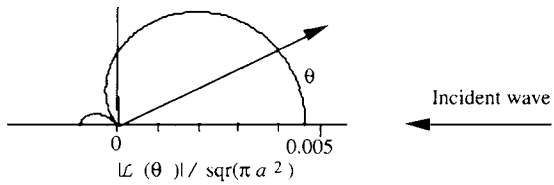

Figure 7.5.2 Polar scattering pattern for a fixed, rigid sphere, at $ka = 0.1$. The reference length is $(\pi a^2)^{1/2}$.

and

$$\sigma_{bs} = a^2 \frac{25(ka)^4}{36} \quad (ka \ll 1) \tag{7.5.24b}$$

The relative scattering cross section, obtained by division by πa^2, is proportional to $(ka)^4$. This dependence characterizes what is widely known in optics and acoustics as "Rayleigh scatter." The Rayleigh region *for scattering lengths* has a $(ka)^2$ dependence. In optics, it is the intensities and cross sections that are directly measured. In acoustics, pressures and scattering lengths are directly measured.

The acoustical scattering cross section in Rayleigh scatter is very much smaller than the geometrical cross section because the sound waves bend around, and are hardly affected by, acoustically small nonresonant bodies. Ocean waves diffract around small rocks, and very-low-frequency/long-wavelength swell waves diffract around small islands, in similar ways.

When the small sphere is an elastic fluid, the Rayleigh scatter region remains. But then the scattering depends also on the relative elasticity and the relative density, compared with the water medium surrounding it. This was first demonstrated by Lord Rayleigh (1896, sec. 335), who found that for a fluid, elastic sphere,

$$\Delta\sigma_S(f,\theta) = (ka)^4 \left[\frac{e-1}{3e} + \frac{g-1}{2g+1}\cos\theta\right]^2 a^2 \quad \text{for} \quad ka \ll 1 \tag{7.5.25a}$$

where

$k = 2\pi/\lambda$ = wave number in the surrounding medium (7.5.25b)

$g = \rho_1/\rho_0$ = ratio of density of sphere to that of the medium (7.5.25c)

$h = c_1/c_0$ = ratio of sound speed in sphere to that in the medium (7.5.25d)

$e = E_1/E_0$ = ratio of elasticity of sphere to that of the medium (7.5.25e)

$c^2 = E/\rho$ (7.5.25f)

$e = gh^2$ (7.5.25g)

θ = angle between incident and scatter directions (7.5.25h)

The backscattering cross section for a small, fluid sphere follows by setting $\theta = 0°$ in Equation 7.5.25a.

The relative magnitude of the monopole component of the polar scattering pattern depends on the first term in the brackets of Equation 7.5.25; the magnitude of the dipole component depends on the second term. Most bodies in

the sea have values of e and g which are close to unity. On the other hand, for a gas bubble, $e \ll 1$ and $g \ll 1$. In that case, the scatter is omnidirectional because the elasticity term dominates.

Highly compressible bodies such as bubbles are capable of resonating in the $ka \ll 1$ region. Resonant bubbles produce scattering cross sections several orders of magnitude greater than for a rigid sphere of the same size. Resonant bubbles are considered in Chapter 8.

The total scattering cross section for the small fluid sphere is obtained by integrating Equation 7.5.25a over all angles θ, as in Equation 7.1.10:

$$\begin{aligned} \sigma_s(f) &= \pi a^2 \int_0^{4\pi} \Delta\sigma_s \, d\Omega \\ &= 4\pi a^2 (ka)^4 \left[\left(\frac{e-1}{3e} \right)^2 + \frac{1}{3} \left(\frac{g-1}{2g+1} \right)^2 \right] \qquad ka \ll 1 \end{aligned} \tag{7.5.26}$$

Light follows essentially the same backscattering laws as sound. One big difference is that the wavelength of visible light is of the order $5*10^{-5}$ cm. Therefore, almost all scattering bodies in the sea, even the everpresent ocean "snow," have optical cross sections equal to their geometrical cross sections. However, the same particles are very much smaller than the wavelength of *sounds* in the sea (almost always 1 cm or more). These bodies are therefore in the Rayleigh region, where they scatter sound very weakly. This is the major reason why the sea is turbid for light but transparent to sound.

*7.5.3 AXIALLY SYMMETRIC SPHERICAL MODE SOLUTIONS (OPTIONAL)

From the previous two sections, valuable approximations are that Rayleigh backscatter operates for $ka \ll 1$, and geometrical backscatter operates for $ka \gg 1$. This means that a body acts as a high-pass backscattering filter with a cutoff at $ka \approx 1$. This simple generalizing concept, proposed by Johnson (1977) and extended by Stanton (1989), is often used to approximate the rigid body backscatter shown in Figs. 7.5.4 and 7.5.5. But these simple behaviors are special cases of the general solution that is given by the modal description for a fluid sphere, which we now consider. We follow Anderson (1950) and use his nomenclature with minor changes.

The external fluid medium has the properties c_0 and ρ_0. The fluid sphere of radius a has the properties c_1 and ρ_1. As shown in Fig. 7.5.3, the incident plane

*Background material

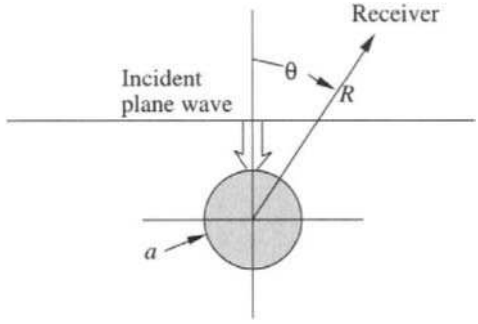

Figure 7.5.3 Scattering geometry for sound incident at a sphere.

wave is traveling in the $-z$ direction and has the amplitude P_{inc}. The wave has the time dependence $e^{-i\omega t}$ and the wave number k. The scattering angle θ is measured from the z-axis. Because of symmetry around the z-axis, there is no dependence on the azimuthal angle ϕ. The amplitude of the pressure at a large distance from the sphere is to be determined by solutions of the spherical wave equation with proper boundary conditions.

The axially symmetric solutions of the spherical wave equation are the axially symmetric spherical harmonics, which are

$$P_m(\mu)[j_m(kR) + in_m(kR)] \tag{7.5.27a}$$

where

$$P_m(\mu) = \text{Legendre function, where } \mu = \cos\theta, \text{ and} \tag{7.5.27b}$$

$$j_m(kR) = \text{spherical Bessel function,} \tag{7.5.27c}$$

$$n_m(kR) = \text{spherical Neumann function,} \tag{7.5.27d}$$

$$h_m(kR) = j_m(kR) + in_m(kR) = \text{spherical Hankel function.} \tag{7.5.28}$$

The notation $y_m(kR)$ is sometimes used for the Neumann function, $n_m(kR)$. The first two r-dependent spherical wave functions are components with no θ dependence,

$$j_0(kR) = \frac{\sin(kr)}{kR} \quad \text{and} \quad n_0(kR) = -\frac{\cos(kR)}{kR} \tag{7.5.29}$$

and the components with simple $\cos\theta$ dependence,

$$j_1(kR) = \frac{\sin(kR)}{(kR)^2} - \frac{\cos(kR)}{kR} \quad \text{and} \quad n_1(kR) = -\frac{\cos(kR)}{(kR)^2} - \frac{\sin(kR)}{kR} \tag{7.5.30}$$

The derivatives at $R = a$ are

$$j_0'(ka) = -j_1(ka) \quad \text{and} \quad n_0'(ka) = -n_1(ka) \tag{7.5.31a}$$

(See Abramowitz and Stegun 1965, Equations 10.1.11 and 10.1.12). The recursion formulas for generating the higher orders are

$$f_{m+1}(ka) = \frac{2m+1}{ka} f_m(ka) - f_{m-1}(ka) \tag{7.5.31b}$$

where $f_m(ka)$ stands for any of the spherical Bessel functions. Abramowitz and Stegun also have graphs and tables of values. The Legendre functions, P_m, are also given (Abramowitz and Stegun 1965, Equation 8.4.1). For example, the first two Legendre polynomials are

$$P_0(\mu) = 1 \tag{7.5.32a}$$

and

$$P_1(\mu) = \mu = \cos\theta \tag{7.5.32b}$$

Other Legendre polynomials can be found by using the recursion formula (Abramowitz and Stegun 1964, Equation 8.5.3),

$$(m+1)\,\mathrm{P}_{m+1}(\mu) = (2m+1)\mu\,\mathrm{P}_m(\mu) - m\,\mathrm{P}_{m-1}(\mu) \tag{7.5.32c}$$

where the superscript ^{0} in Abramowitz and Stegun is not needed here.

The incident plane acoustic wave, expressed as the sum of the spherical harmonics, is in Morse (1974):

$$p_{inc} = P_{inc} \sum_0^\infty (-i)^m (2m+1) P_m(\mu) j_m(kR) e^{-i\omega t} \tag{7.5.33}$$

Inside the sphere, $R \leq a$, the coefficient of the Neumann function in Equation 7.5.27, is set equal to zero to avoid an infinity at $R = 0$. There remains the interior pressure

$$p_{inc} = \sum_0^\infty B_m P_m(\mu) j_m(k_1 R) e^{-i\omega t} \tag{7.5.34}$$

where k_1 is the wave number inside the sphere. The scattered pressure is

$$p_{scat} = \sum_0^\infty A_m \mathrm{P}_m(\mu)\,[\,j_m(kR) + i\,n_m(kR)\,]\,e^{-i\omega t} \tag{7.5.35}$$

The boundary conditions are: pressures are equal on each side of the interface at $R = a$; the normal components of the particle velocities are equal on each side of the interface. The particle velocity for spherical coordinates is

$$u_R = \frac{-i}{\rho c} \frac{\partial p}{\partial (kR)} \tag{7.5.36}$$

Application of the boundary conditions gives two sets of equations — one set for the equality of pressures and one for the equality of the normal components of the particle velocity. Since the modes are orthogonal, individual modes can be equated to give simultaneous equations for the coefficients A_m and B_m. The solution and substitutions give

$$A_m = -P_{inc} (-i)^m \frac{(2m+1)}{1 + i C_m} \tag{7.5.37}$$

where

$$\begin{aligned} C_m &\equiv \frac{j'_m(k_1 a) n_m(ka) - g h j_m(k_1 a) n'_m(ka)}{j'_m(k_1 a) j_m(ka) - g h j_m(k_1 a) j'_m(ka)} \\ g &\equiv \frac{\rho_1}{\rho_0}, \quad h \equiv \frac{c_1}{c_0} \quad \text{and} \quad k_1 = \frac{k}{h} \end{aligned} \tag{7.5.38}$$

Also, $j'_m(kR) = \partial j_m(kR)/\partial(kR)$, where, from Abramowitz and Stegun (1965, Equation 10.1.20),

$$j'_m(kR) = \frac{m}{2m+1} j_{m-1}(kR) - \frac{m+1}{2m+1} j_{m+1}(kR) \tag{7.5.39a}$$

and

$$n'_m(kR) = \frac{m}{2m+1} n_{m-1}(kR) - \frac{m+1}{2m+1} n_{m+1}(kR) \tag{7.5.39b}$$

The general solution for the axially symmetric scattered pressure wave is

$$p_{scat} = -P_{inc} \sum_0^\infty (-i)^m P_m(\mu) \frac{(2m+1)}{1 + iC_m} [j_m(kR) + i n_m(kR)] e^{-i\omega t} \tag{7.5.40}$$

At large kR, the spherical functions can be replaced by simpler expressions (Morse 1981, p. 317):

$$\text{for } kR >> 1, \; j_m(kR) \to \frac{1}{kR} \cos\left[kR - \frac{(m+1)\pi}{2}\right] \tag{7.5.41a}$$

and

$$\text{for } kR >> 1,\ n_m(kR) \rightarrow \frac{1}{kR} \sin\left[kR - \frac{(m+1)\pi}{2}\right] \tag{7.5.41b}$$

The sum of the Bessel function and the Neumann function is called a Hankel function. See Equation 7.5.28. The following Hankel function, combined with the dependence on time $e^{-i\omega t}$, descibes a wave that propagates in the direction of increasing R. To insert into Equation 7.5.40, form

$$(-i)^m[j_m(kR) + in_m(kR)] = \frac{(-i)^m}{kR} e^{i[kR-(m+1)\pi/2]} = \frac{-i(-1)^m}{kR} e^{ikR} \tag{7.5.42}$$

The scattered pressure at large range is

$$p_{scat} = P_{inc} \frac{i}{kR} e^{i(kR - \omega t)} \sum_0^\infty (-1)^m P_m(\mu) \frac{(2m+1)}{1 + i C_m} \tag{7.5.43}$$

This is now expessed in terms of the acoustic scattering length, $\mathcal{L}$,

$$p_{scat} = P_{inc} \frac{1}{R} e^{i(kR - \omega t)} \mathcal{L} \tag{7.5.44}$$

where

$$\mathcal{L} \equiv \frac{i\,a}{ka} \sum_{m=0}^{M-1} (-1)^m P_m(\mu) \frac{(2m+1)}{1 + i C_m} \tag{7.5.45}$$

Here, M is the number of modes needed to obtain acceptable results for the particular problem. Numerical studies have shown that when $M \geq ka + 3$, the sum is effectively the same as for an infinite number of modes.

The backscattering cross section is

$$\Delta\sigma_{bs} = |\mathcal{L}_{bs}|^2 \tag{7.5.46}$$

The backscattering cross section is often displayed as the ratio relative to the actual cross sectional area,

$$\Delta\sigma_{bs}/(\pi a^2) \tag{7.5.47}$$

7.5.4 TOTAL SCATTERING CROSS SECTION

In experimental work, some of the scattered sound may interfere with the incident sound so that a raw measurement must be corrected in order to express the total sound scattered. Theoretical evaluation is more direct; the total sound power

scattered by an object is found from the integral of the absolute pressure squared over the solid angle (Equations 7.1.10 and 7.1.5). The calculation produces the total scattering cross section σ_s (see discussion in section 7.5.1). This integral can be evaluated for nondissipative fluid and rigid spheres. When there is no absorption, total scattering cross section is

$$\sigma_s(ka) = \sigma_e(ka) \equiv \int_0^{2\pi} d\phi \int_0^{\pi} |\mathcal{L}|^2 \sin\theta \, d\theta, \text{ no absorption} \tag{7.5.48}$$

Since the sphere is symmetric, the integral on $d\phi$ becomes 2π, and the subsitution of Equation 7.5.45 gives

$$\sigma_s(ka) \equiv \frac{2\pi a^2}{(ka)^2} \int_0^{\pi} \left[\sum_{m=0}^{M-1} P_m(\mu) \frac{(2m+1)}{1+iC_m} \times \sum_{n=0}^{M-1} P_n(\mu) \frac{(2n+1)}{1-iC_m} \right] \sin\theta \, d\theta \tag{7.5.49}$$

where $\mu = \cos\theta$ and $d\mu = -\sin\theta \, d\theta$. From Morse (1981, p. 315) or Abramowitz and Stegun (1964, Equation 8.14.13), the orthogonality of the Legendre functions is

$$\begin{aligned} \int_{-1}^{1} P_n(\mu) P_m(\mu) \, d\mu &= \frac{2}{2m+1} \quad \text{for} \quad m = n \\ &= 0 \quad \text{for} \quad m \neq n \end{aligned} \tag{7.5.50}$$

The total scattering cross section for a sphere (Anderson 1950) is

$$\sigma_s(ka) = \frac{4\pi a^2}{(ka)^2} \sum_{m=0}^{M-1} \frac{(2m+1)}{1+C_m^2} \tag{7.5.51}$$

7.5.5 *RIGID SPHERE*

The rigid sphere is frequently used to display many of the characteristics of scattering phenomena. One reason is that it gives a fair approximation to a very dense sphere in water, which is often used for calibration in experimental work (see Table 7.1).

The backscattering length is sometimes expressed as a "reflectivity" relative to $a/2$ (Anderson 1950). The literature also uses the name "form function." Using $a/2$ as a reference, the form function for spheres is

$$F_\infty(ka) = |\mathcal{L}_{bs}|/(a/2) \tag{7.5.52}$$

Table 7.1 gives data on the practical realization of backscattering theory, in which a stainless-steel sphere replaces the idealization of a perfectly reflecting rigid sphere, for the range $0.2 < ka < 5$.

Table 7.1 **Relative Acoustic Backscattering Length, or Form Function $F_\infty(ka) = |\mathcal{L}_{bs}|/(a/2)$, for Rigid and Stainless-Steel Spheres**

ka	*Rigid Sphere*	*Stainless-Steel Sphere*	*ka*	*Rigid Sphere*	*Stainless-Steel Sphere*
0	0	0	2.6	1.0025	1.0917
0.2	0.0653	0.0575	2.8	0.8583	0.949
0.4	0.2457	0.2139	3.0	0.7582	0.8477
0.6	0.4972	0.4327	3.2	0.8258	0.9244
0.8	0.7537	0.6468	3.4	0.9771	1.0736
1.0	0.9381	0.7948	3.6	1.0654	1.1792
1.2	0.9886	0.8239	3.8	1.032	1.1458
1.4	0.8924	0.7281	4.0	0.9126	1.0177
1.6	0.7157	0.5898	4.2	0.8233	0.9008
1.8	0.6309	0.5936	4.4	0.8673	0.9186
2.0	0.7617	0.8036	4.6	0.9892	1.0334
2.2	0.9548	1.025	4.8	1.0659	1.1197
2.4	1.0508	1.136	5.0	1.0398	1.098

Stainless steel: Type 302
Density 7900 kg/m^3; compressional wave velocity 5594 m/s; shear wave velocity 3106 m/s.
Computations by T. K. Stanton and R. Eastwood (Personal communication.)

Unlike the solutions for the plane facet and the cylinder, the HK solution for the rigid sphere is not accurate because the diffraction for scatter off from normal incidence is inadequately represented. Therefore, we use the mode solution as developed above.

The relative backscattering length for a rigid sphere is presented in logarithmic scale in Fig. 7.5.4. The figure demonstrates the $(ka)^2$ dependence (slope 2:1) in the Rayleigh scattering region ($ka \ll 1$), the asymptotic constant value of geometrical scatter ($ka > 1$), and the oscillations at $ka > 1$ owing to the diffracted waves described in Fig. 7.3.3e. The relative backscatter length is shown on a linear scale in Fig. 7.5.5. The peaks and troughs of backscatter at $ka > 1$, which are caused by interference between the diffracted wave around the periphery and the wave reflected at the front surface of the sphere, occur with a periodicity due to their path difference, $2a + \pi a = n\lambda$ or $ka = 2\pi n/(2 + \pi) = 1.22n$, where n is an integer.

The directional scattering at various values of ka is shown in Fig. 7.5.6. The sound is not scattered isotropically. However, as ka increases, the sound tends toward isotropic, particularly for $\theta < \pi/2$. The number of diffration side lobes

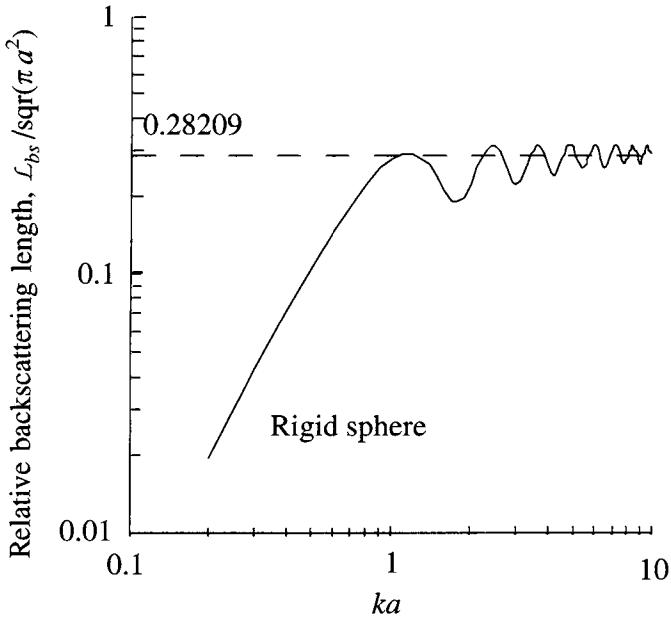

Figure 7.5.4 Relative backscattering lengths for a rigid sphere. The Rayleigh scattering region for relative scattering lengths, which is proportional to $(ka)^2$, is at approximately $ka < 0.5$. The dashed line is the high-frequency asympote, $1/(4\pi)^{1/2}$.

increases as ka increases, and at large ka they oscillate around the ultimate isotropic solution for this component. The increasingly large forward scattered lobe is out of phase with the coexistent incident sound, so that, at high frequencies, the sum gives the shadow.

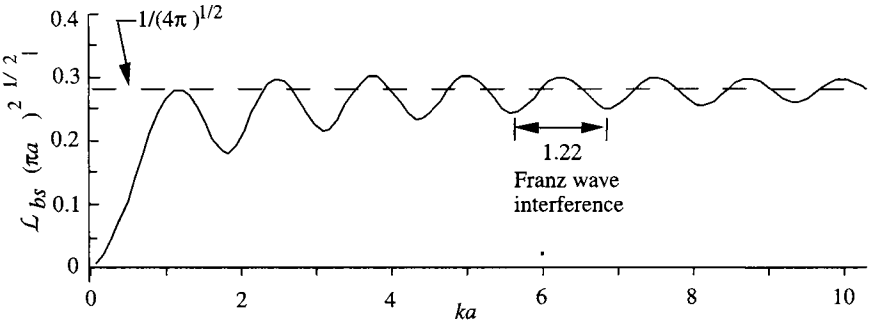

Figure 7.5.5 Linear presentation of the relative backscattering length as a function of ka for a rigid sphere. The periodicity of the peaks and troughs, due to interference between the diffracted wave and the front-face reflection, occurs at intervals of $ka = 1.22$. See also Fig. 7.5.4.

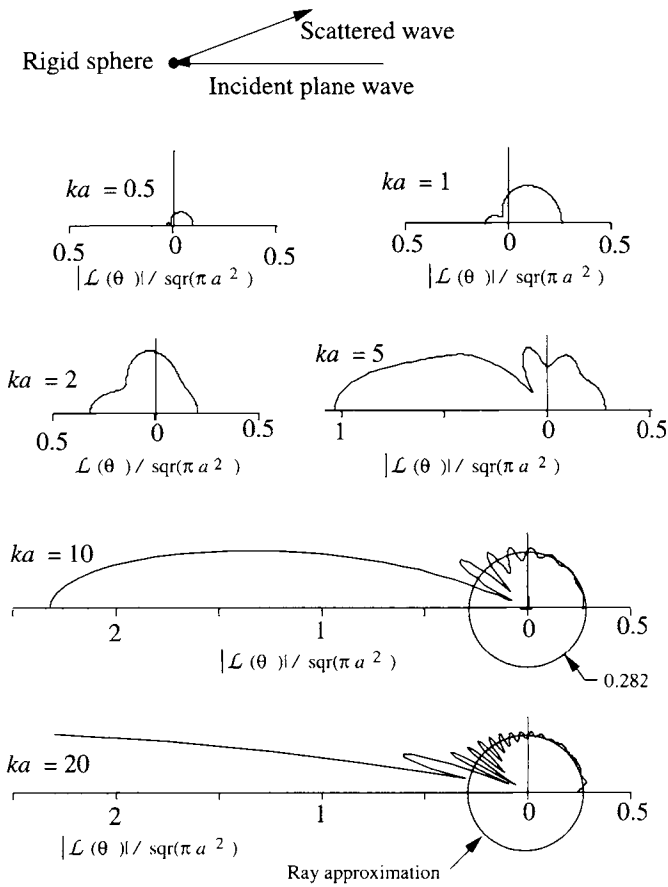

Figure 7.5.6 Directivity of relative acoustic scattering length for a rigid, fixed sphere at a large range. The sound is incident from the right. The circles on $ka = 10$ and $ka = 20$ are the ray approximation described in section 7.5.1.

The total scattering cross section for a rigid sphere is given in Equation 7.5.51, and the value relative to πa^2 is shown in Fig. 7.5.7. The relative total scattering cross section approaches the limiting value of $2\pi a^2$ very slowly as ka increases.

7.5.6 FLUID SPHERE

Fluid spheres are often used to represent small marine animals such as zooplankton, and sometimes even larger animals when the sound frequency is low ($ka \ll 1$). The sound speeds and densities of sea life are nearly those of water. For example, we have calculated the backscatttering magnitude and directivity

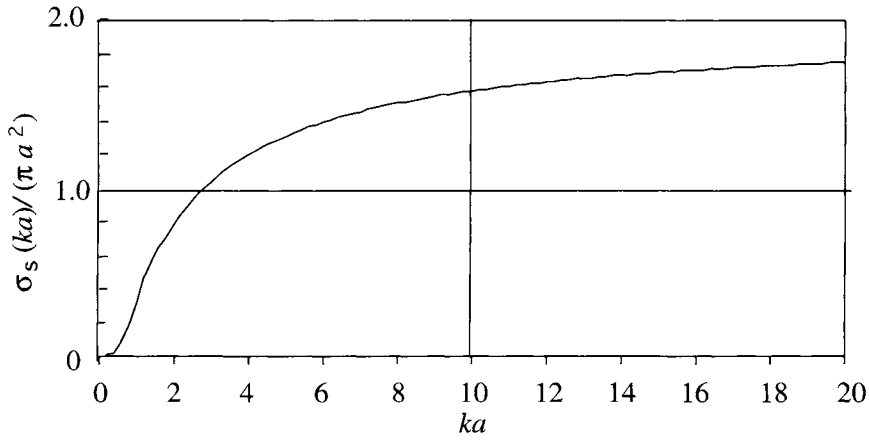

Figure 7.5.7 Relative total scattering cross section for a rigid sphere as a funcion of ka.

patterns for a fluid sphere with characteristics similar to fish flesh, $g = 1.06$ and $h = 1.02$, where

$$g \equiv \frac{\rho_1}{\rho_0}, \qquad h \equiv \frac{c_1}{c_0}, \qquad k_1 = \frac{k}{h} = \frac{\omega}{c_1} \tag{7.5.53}$$

Figure 7.5.8 shows the relative sound backscattering length for a fluid-filled sphere of these constants, as a function of ka. The directional scattering patterns are shown in Fig. 7.5.9. These curves, following Anderson's equations, do not include viscous and thermal losses. The incident plane wave interferes with the scattered wave as described in subsection 7.5.5.

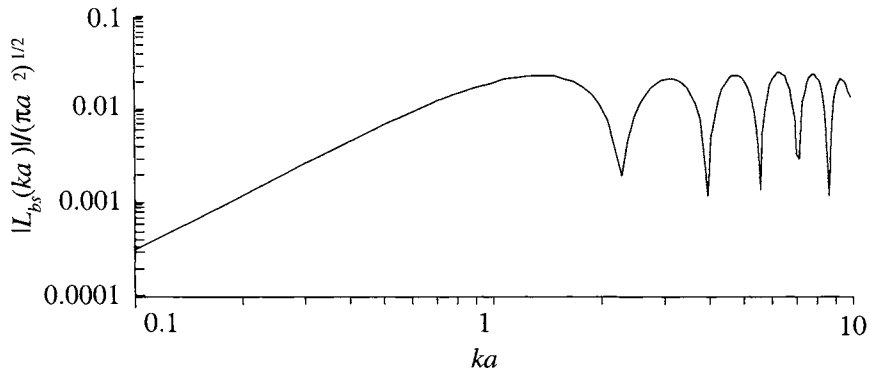

Figure 7.5.8 Relative backscattering length for a fluid-filled sphere, with $g = 1.06$ and $h = 1.02$.

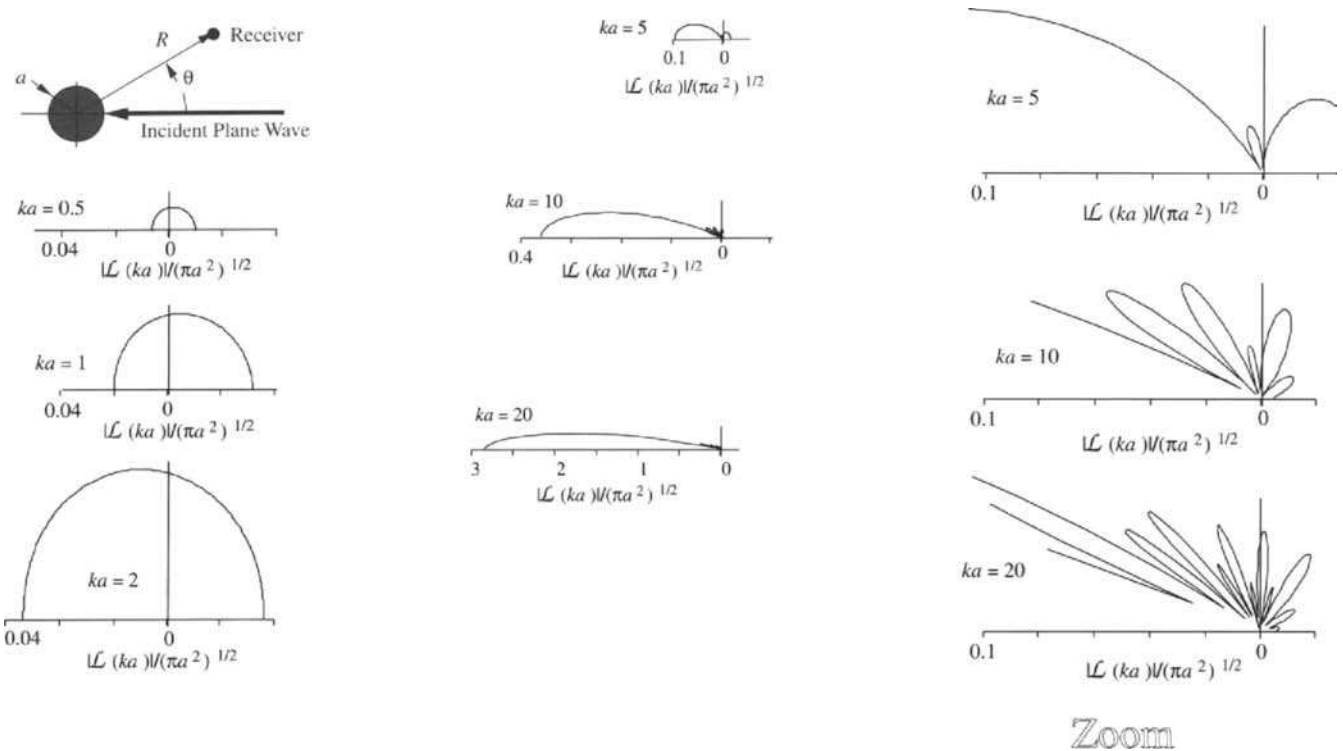

Figure 7.5.9 Directivity of the relative scattering length for a sphere of fluid, with $g = 1.06$ and $h = 1.02$. The scales are chosen to display important features. The Zooms for $ka = 5$, 10, and 20 at the right show that, although the scattering lengths for large ka in the nonforward directions are small relative to the forward direction, they are comparable to the scattering lengths for $ka \cong 1$.

Chapter 8 | Bubbles

8.1 Scattering from a Spherical Gas Bubble: Modal Solution 289
8.1.1 Scattering Directivity 289
8.1.2 Backscattering Length 290
8.2 Single Pulsating Bubbles: $ka \ll 1$ 292
8.2.1 Lumped Constants of Bubble Pulsation 292
8.2.2 Bubble Stiffness 293
8.2.3 Equivalent Bubble Mass 293
8.2.4 Simple Pulsation; Breathing Frequency 294
*8.2.5 Effects of Surface Tension, Shear Viscosity, and Thermal Conductivity (Optional) 295
8.2.6 Damping Constants 299
8.2.7 Acoustical Cross Sections 302
8.2.8 Insonified Damped Pulsations 304
8.2.9 Decaying Bubble Pulsations 306
8.2.10 Near-Surface and Nonlinear Bubble Pulsations 307
8.2.11 Nonspherical Bubbles 308
8.2.12 Damping Constants of Bubbles in Seawater 310
8.3 Scatter, Absorption, and Dispersion in Bubbly Water 310
8.3.1 Sound Backscattered by an Ensemble of Bubbles: Volume Reverberation 311
8.3.2 Excess Attenuation 314
8.3.3 Sound Speed Dispersion and Wood's Equation 317
8.4 Active Measurements in Bubbly Water 322
8.4.1 Techniques for Linear Bubble Counting 322
8.4.2 Dependence of Bubble Densities on Winds, Place, and Time 327
8.4.3 Gas Void Fraction 330
8.4.4 Sound Phase Fluctuations 331
8.4.5 Collective Oscillations and Low-Frequency Noise 331
8.5 Sea Surface Microbubble Production 334
8.5.1 Bubbles from Breaking Waves 334
8.5.2 Bubbles from Rainfall 337
8.6 Bubbles in Sediments 341

In the late 1950s, several studies introduced oceanographers and sonar users to the importance of bubbles at sea. Urick and Hoover (1956) were concerned about the military implications of sound scatter from the rough sea surface; they discovered that much of the scatter came from *below* the surface, presumably fom bubbles created by breaking waves. About the same time, Blanchard and Woodcock (1957) were interested in the airborne salt nuclei, generated from breaking waves, that affect thunderstorm activity at sea and climate throughout the world; they waded out from shore, scooped up a jar of bubbly water in the

surf, and obtained the first measurements of bubbles caused by breaking waves. In the same year, LaFond and Dill (1957) wrote an internal U.S. Navy Laboratory memorandum with the provocative title "Do Invisible Bubbles Exist in the Sea?" Starting from the evidence that sea slicks were formed over turbid surface water convergence zones, or were correlated with internal waves that had brought minute particulate matter to the surface, they concluded that bubbles may indeed be present in some parts of the ocean.

All of this research activity ran counter to laboratory experiments, and intuition. The belief at the time was that any bubbles that may be created would soon disappear either by buoyant action, which would bring them popping to the surface, or by gas diffusion forced by bubble surface tension, which would squeeze the gas out of any small bubble. The flaws in this reasoning are now recognized: (1) bubbles are not clean but may have solid or dissolved material on the surface which would inhibit gas diffusion, or they may exist in crevices; (2) ocean currents will create a friction drag that can overcome buoyant forces; (3) bubble populations are continually replenished by the myriad bubble source mechanisms. Most of the bubbles found near the surface of the open sea appear to be continually generated by spilling or plunging breakers, or during rainfall. Particularly in coastal regions, the sources of ocean bubbles also include those entrained by continental aerosols that drop into the sea, generated by photosynthesis of marine plants, life processes of marine animals, the decomposition of organic material, or released from gas hydrates on or below the ocean floor.

The immense number of microbubbles per unit volume that have been identified in the ocean are a major factor in near-surface sound propagation. They have also proved to be a unique tool in the study of near-surface ocean characteristics.

The statistical size distribution of bubbles caused by breaking waves in a laboratory flume was first measured by Glotov et al. (1962). The first photographic evidence of bubbles in a quiescent sea was that of Barnhouse et al. (1964), and the first measurements in the coastal ocean were by Buxcey et al. (1965), who used acoustical techniques. Research from the latter two master's theses was reported by Medwin (1970). The dependence of ocean bubble densities on depth, season of the year, time of day/night, wind speed, and presence of sea slicks was revealed by using various acoustical techniques (Medwin 1977) and extensive photography (Johnson and Cooke 1979).

The omnipresence of unidentified particles, sometimes called "*detritus*" or "snow," makes it difficult for simple photography to positively identify bubbles of radius less than about 40 microns. It required laser holography (O'Hern et al.

1988) to prove, unequivocally, that there can be as many as 10^5 to 5×10^6 bubbles per cubic meter at radii between 15 and 16 microns near the ocean suface even during calm seas, and that the inverse acoustical determinations of the preceding 20 years had been essentially correct. It is generally assumed that the peak density is somewhere around radius 10 to 15 μm, depending on ocean chemistry.

The principal practical techniques for bubble identification and counting at sea have proved to be inversions of linear acoustical measurements. Determinations of bubble densities have been based on acoustic backscatter, excess attenuation, and differential sound speed (see section 8.4.1), as well as on nonlinear behavior and acoustic doppler shift. The acoustical techniques have also included passive listening at sea to the sound under breaking waves, or during rainfall, to determine the number of newly created bubbles (section 8.5).

The direct consequence of bubbles at sea — for example, during wind speeds of 8 m/s — have been demonstrated to result in near-surface excess attenuations as great as 60 dB/m and speeds of sound that are tens of meters per second less than the approximately 1500 m/s that would be measured by a sound velocimeter, or that would be expected from a calculation based on temperature, salinity, and depth alone.

8.1 Scattering from a Spherical Gas Bubble: Modal Solution

8.1.1 SCATTERING DIRECTIVITY

The modal solution to scatter by a sphere was applied to the rigid sphere and the fluid filled sphere in Chapter 7. The rigid sphere is an extreme limit of the physical properties. Theoretical studies sometimes use the perfect pressure-release vacuum as the other extreme limit. But the acoustic reaction of a spherical vacuum in water is physically unrealistic; the fluid that fills the sphere determines its behavior as a scatterer as well as within the sphere boundaries The realistic gas-filled sphere has a low-frequency, omnidirectional breathing-mode resonance and higher-order, directional resonances. Using the modal solution in Chapter 7, the relative directional scattering lengths of a gas-filled sphere insonified by a plane wave are shown in Fig. 8.1.1. These curves were calculated from Anderson's (1950) equations; they do not include viscous and thermal losses. They show that for small *ka*, the scatter is essentially omnidirectional. For simplicity, the condition for omnidirectional scatter from a bubble is often stated

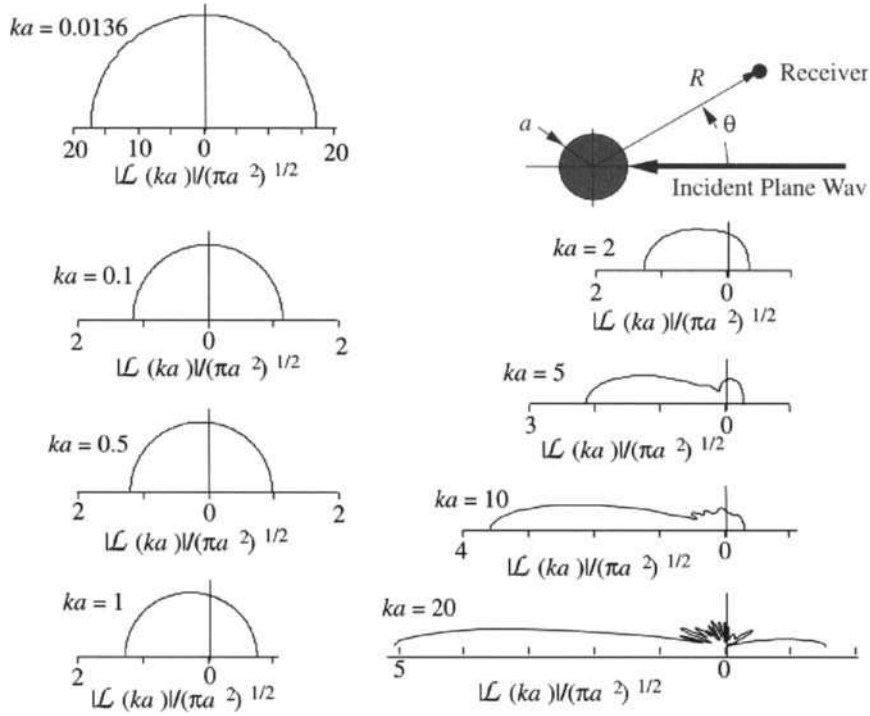

Figure 8.1.1 Directivity of the scattering from an air-filled bubble as a function of ka. Plane wave incidence.

approximately as $ka < 1$. Fig. 8.1.1 shows how the anisotropicity changes for $ka < 1$. (See Problem 8.1.1 for a measure of the anisotropicity.)

8.1.2 BACKSCATTERING LENGTH

The modal solution for backscatter from a sea-level gas bubble, calculated from Equation 7.5.51, is shown in Fig. 8.1.2, where it is compared with the relative backscattering length of the rigid sphere. Fig. 8.1.2 shows that the sea-level bubble has a very large response to a CW plane wave — that is, an $m = 0$ resonance, at $ka = 0.0136$. There are other much weaker resonances for $m = 1$, 2, etc. The calculation does not include the significant bubble damping effects due to viscous and thermal losses. When these are included (in section 8.2), they decrease the height and broaden the resonance curve of backscatter.

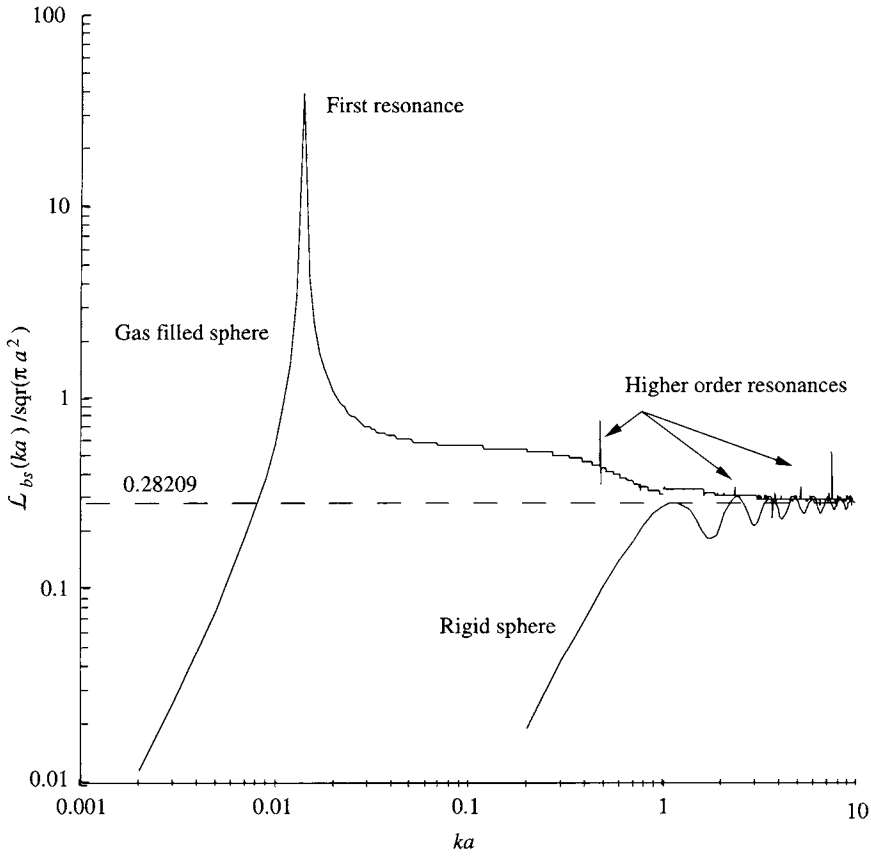

Figure 8.1.2 Relative backscattering length of a spherical air bubble at sea level compared with the rigid sphere solution of section 7.5.5. Inclusion of viscous and thermal damping would lower the bubble peak and broaden the resonance, as shown in section 8.2.

The sea-level resonance peak at $ka = 0.0136$ has been known since the research on the musical sounds of running water (Minnaert 1933). We find the result again if we apply the small ka condition to the mode solution and drop all higher-order terms; this gives the bubble resonance frequency of the scattering expression. Although the starting point, Equation 7.5.51, is complicated, the solution is tractable for the $m = 0$ (omnidirectional) mode, where $ka \ll 1$, and the large resonance response occurs. This approach is left as a student problem.

8.2 Single Pulsating Bubbles: $ka \ll 1$

8.2.1 LUMPED CONSTANTS OF BUBBLE PULSATION

The modal solution of the previous section established that, for $ka \ll 1$, a spherical air bubble in a plane wave oscillates omnidirectionally and has a resonance at $ka = 0.0136$ (at sea level). In the $ka \ll 1$ condition, the bubble is very effectively driven by the virtually uniform acoustic pressure over its surface. Furthermore, a pulsating (breathing) bubble radiates more effectively than in any other mode (section 4.1.1).

When $ka \ll 1$, the acoustical parameters of an oscillating bubble can be "lumped" into an equivalent mass, stiffness, and mechanical resistance, so that the acoustical system resembles the mechanical system of a mass on a spring. This type of analogue is very commonly used by engineering acousticians; see, for instance, Olson (1947). Lighthill (1978) calls these "acoustically compact" regions. The equivalent mass is due to the inertia of the adjacent layer of water that envelops the bubble and that has essentially the same radial displacement as the bubble surface. The compressibility of the bubble volume, plus the surface tension effect for very small bubbles, determines the spring stiffness. The equilibrium bubble radius, a, takes the place of the reference position of the spring at rest, and the radial displacement, $da = \xi$, corresponds to the linear displacement of the spring. The acoustical damping owing to reradiation, viscosity, and thermal conductivity will later be described, in the lumped constant approach, as a mechanical resistance. For the moment, we assume that there is no damping.

The mechanical equation of motion of a mass-stiffness system is

$$m\frac{\partial^2 \xi}{\partial t^2} + s\xi = 0 \tag{8.2.1}$$

The solution is of the form

$$\xi = \xi_0 e^{i\omega_b t} \tag{8.2.2}$$

Substitution into Equation 8.2.1 leads to the system natural frequency,

$$\omega_b = 2\pi f_b = \sqrt{\frac{s}{m}} \tag{8.2.3}$$

We need to determine the equivalent s and m for an oscillating bubble.

8.2.2 BUBBLE STIFFNESS

Consider a spherical gas bubble of volume $V = (4/3)\pi a^3$, surface area $S = 4\pi a^2$, and interior gas pressure $p_{int} \cong p_A$, where p_A is the static ambient pressure at that point in the ocean. Assume the bubble experiences an incremental interior pressure change, $dp_{int} \ll p_A$, and that the gas follows the adiabatic relation, $p_{int}V^{\gamma} = \text{constant}$, where γ is the ratio of specific heats of the bubble gas.

Differentiating yields

$$\frac{dp_{int}}{dV} = \frac{-\gamma p_A}{V} \tag{8.2.4}$$

Use $dV = 4\pi a^2 \xi$, where ξ is the small radial surface displacement. For the present, assume that there is no surface tension force, so that the restoring force is

$$4\pi a^2 \, dp_{int} = -(12\pi\gamma p_A a)\xi \tag{8.2.5}$$

This is a form of Hooke's Law, with stress proportional to strain. The proportionality constant is the stiffness of the bubble,

$$s = 12\pi\gamma p_A a \tag{8.2.6}$$

8.2.3 EQUIVALENT BUBBLE MASS

The inertial force experienced by the radiating bubble is calculated to determine the equivalent mass. It is not the mass of the bubble gas but rather the entrained water next to the bubble that comprises the mass of the pulsating system.

From Fig. 8.1.2, $ka \ll 1$ at the natural pulsation frequency. The pressure radiated omnidirectionally by a pulsating bubble is

$$p = \frac{P_a a}{R} \exp\left[i(\omega_b t - kR)\right] \tag{8.2.7}$$

where P_a is the pressure amplitude at $R = a$.

For radial motion, the acoustic force equation (2.7.43) is

$$\rho_A \frac{\partial^2 \xi}{\partial t^2} = -\frac{\partial p}{\partial R} \tag{8.2.8}$$

where ρ_A is the density of the water.

Use Equation 8.2.7 to obtain

$$\rho_A \frac{\partial^2 \xi}{\partial t^2}\bigg]_{R=a} = \frac{P_a a}{R^2}(1 + ikR) \exp\left[i(\omega_b t - kR)\right]_{R=a} \tag{8.2.9}$$

Since $ka \ll 1$, Equation 8.2.9 simplifies to

$$\rho_A \frac{\partial^2 \xi}{\partial t^2}\Big]_{R=a} = \frac{p}{a}\Big]_{R=a} \tag{8.2.10}$$

The inertial force at the surface is a form of Newton's Second Law,

$$F_m\Big]_{R=a} = -4\pi a^2 p\Big]_{R=a} = -4\pi a^3 \rho_A \frac{\partial^2 \xi}{\partial t^2}\Big]_{R=a} \tag{8.2.11}$$

so we identify the effective mass as

$$m = 4\pi a^3 \rho_A \tag{8.2.12}$$

It is interesting to observe that, in this low-frequency approximation, the effective mass of the pulsating bubble is equivalent to an oscillating shell of water three times the volume of the bubble itself.

8.2.4 SIMPLE PULSATION; BREATHING FREQUENCY

Inserting the mass Equation 8.2.12 and the stiffness Equation 8.2.6 into Equation 8.2.3 gives the simple harmonic breathing frequency of a small bubble ($ka \ll 1$) under the assumptions of this derivation (no surface tension, adiabatic gas oscillations, no energy absorption):

$$f_b = \frac{1}{2\pi}\sqrt{\frac{s}{m}} = \frac{1}{2\pi a}\sqrt{\frac{3\gamma p_A}{\rho_A}} \tag{8.2.13}$$

The ambient pressure can be written in terms of the depth z by expressing

$$p_A = p_{A0} + \rho_A g z \cong 10^5(1.01 + 0.1z) \quad \text{Pascals} \tag{8.2.14}$$

where p_{A0} = sea level atmospheric pressure = 1.01×10^5 pascals; $g = 9.8\,\text{m/s}^2$; $\rho_A \cong 1030\,\text{kg/m}^3$; $\gamma = 1.4$ for an air bubble; z = depth (meters).

For a spherical air bubble in water we get the simplified expression for the breathing frequency:

$$f_b = \frac{3.25\sqrt{(1 + 0.1z)}}{a(\text{meters})} = \frac{3.25 \times 10^6}{a(\text{microns})}\sqrt{(1 + 0.1z)} \tag{8.2.15}$$

At sea level, Equation 8.2.13 may be written $ka = 0.0136$ in agreement with the modal solution in Fig. 8.1.2. Some people use the simple mnemonic that a bubble of radius 60 μm resonates at a frequency of about 60 kHz near the sea surface.

*8.2.5 EFFECTS OF SURFACE TENSION, SHEAR VISCOSITY, AND THERMAL CONDUCTIVITY (OPTIONAL)

We now include concepts of surface tension, shear viscosity, and thermal conductivity to rederive the expressions for the resonance frequency and to determine the damping constant of a spherical bubble that is excited by an incident plane wave.

Effect of Shear Viscosity

Assume that $ka \ll 1$. The incident plane wave is therefore uniform at all points of the bubble,

$$p_{inc} = P_{inc}\, e^{i\omega t}]_{R=a} \tag{8.2.16}$$

where P_{inc} is the incident-plane-wave amplitude.

Since the bubble is small and is not fixed, one obtains a spherically symmetrical scattered pressure

$$p_{scat} = P_{scat} \frac{R_0}{R} \exp\left[i(\omega t - kR)\right] \tag{8.2.17}$$

where R_0 is the reference distance from the scatterer (=1 m) and P_{scat} is the scattered pressure amplitude at $R = R_0$.

To find the pressure ratio p_{scat}/p_{inc}, we use the pressure condition at the bubble boundary:

$$[\text{pressure inside} = \text{pressure outside}]_{R=a} \tag{8.2.18}$$

The excess interior pressure (beyond the ambient p_A), evaluated at the surface, is the sum of the incident acoustic pressure, the scattered pressure, and a shear viscous stress at the surface. The latter is proportional to the product of the dynamic coefficient of shear viscosity for water, μ, and the radial rate of strain, u_r/R, evaluated at the surface,

$$p_{int} = p_{inc} + p_{scat} + C\,\mu\left(\frac{u_r}{R}\right)\Big]_{R=a} \tag{8.2.19}$$

where p_{int} is the interior pressure, and C is a dimensionless proportionality constant. The constant C was evaluated by Devin (1959) as equal to 4.

We have already derived the expression for the radial particle velocity in Equation 4.1.3. For $ka \ll 1$, it reduces to

$$u_r = -i\, P_{scat}\, R_0 \frac{e^{i\omega t}}{\rho_A\, c\, k\, a^2} \tag{8.2.20}$$

*Background material

The expression for the scattered pressure is Equation 8.2.17, in which we now expand the exponential for $ka \ll 1$, and evaluate at $R = a$, to obtain

$$p_{scat} = P_{scat}\left(\frac{R_0}{a}\right)(1 - i\,k\,a)\,e^{i\,\omega\,t} \tag{8.2.21}$$

Therefore, from Equation 8.2.19 we have the *pressure amplitude condition at* $R = a$:

$$P_{int} = P_{inc} + P_{scat}\left(\frac{R_0}{a}\right)(1 - i\,k\,a) - \frac{i\,4\,\mu\,P_{scat}\,R_0}{\rho_A\,c\,k\,a^3} \tag{8.2.22}$$

Effect of Thermal Conductivity

Now consider the particle velocity at $R = a$. If the bubble is large, the reversible adiabatic relation will hold for most of the bubble gas. However, for very small bubbles in water, the action is isothermal at the water temperature, and the effective value of γ approaches unity. Equally important, the bubble pressure and temperature do not instantly follow the volume variation. For example, as the bubble volume is decreasing during a cycle, the temperature will be increasing. But at the minimum volume some heat will still be escaping, which means that the gas temperature and pressure will be decreasing. Therefore we rewrite the adiabatic law and replace γ by the complex expression $\gamma(b + id)$, where b and d are real dimensionless numbers. This allows the magnitude of γ and the phase between pressure and volume to be functions of the driving frequency and the bubble size. We write,

$$p_{int}V^{\gamma(b+id)} = \text{constant} \tag{8.2.23a}$$

where

$$p_{int} = p_A + dp_{int} = \text{total interior pressure} \tag{8.2.23b}$$

Differentiate with respect to time and rearrange to

$$\frac{dV}{dt} = -\frac{i\,\omega\,p_{int}\,V}{\gamma(b + id)p_A} \tag{8.2.24}$$

Use $dV/dt = 4\pi a^2 u_r]_{R=a}$ to obtain the interior radial particle velocity at $R = a$:

$$u_r]_{R=a} = -i\omega a P_{int}\frac{e^{i\omega t}}{[3\gamma(b + id)p_A]} \tag{8.2.25}$$

Equate the two expressions for particle velocity at $R = a$, Equation 8.2.20 and 8.2.25, and obtain the ratio

$$\frac{P_{int}}{P_{scat}} = \frac{3\gamma(b + id)\, p_A R_0}{\rho_A c^2 k^2 a^3} \tag{8.2.26}$$

Frequency Correction

To correct f_b in Equation 8.2.13, define the resonance frequency of the bubble, f_R, in terms of the average interior pressure that depends (through β) on surface tension, $p_{int} = \beta p_A$, and the effective ratio of specific heats that depends (through b) on the thermal conductivity, γb,

$$\begin{aligned} f_R &= \frac{1}{2\pi a}\sqrt{\frac{3\gamma b \beta p_A}{\rho_A}} \\ &= f_b\sqrt{b\beta} \end{aligned} \tag{8.2.27}$$

Equations 8.2.28a, b, c, and d, which permit detailed calculations of the effects of surface tension and thermal conductivity at all frequencies, are developed in Eller (1970) based on work in Devin (1959). See also Prosperetti (1977). (Note, however, that the symbols are defined differently in those references.) In order to extract the resonance frequencies (or damping constants) from these equations, the following order of operations is recommended. After obtaining the physical constants of the gas at the depth and temperature of the bubble, calculate, for a given sound frequency and bubble radius, first X, then d/b, b, and β in that order.

$$X = a\left(\frac{2\,\omega\,\rho_g\, C_{pg}}{K_g}\right)^{1/2} \tag{8.2.28a}$$

$$\frac{d}{b} = 3(\gamma - 1)\left[\frac{X(\sinh X + \sin X) - 2(\cosh X - \cos X)}{X^2(\cosh X - \cos X) + 3(\gamma - 1)X(\sinh X - \sin X)}\right] \tag{8.2.28b}$$

$$b^{-1} = \left[1 + \left(\frac{d}{b}\right)^2\right]\left[1 + \left(\frac{3\gamma - 3}{X}\right)\left(\frac{\sinh X - \sin X}{\cosh X - \cos X}\right)\right] \tag{8.2.28c}$$

$$\beta = \frac{p_{int}}{p_A} = 1 + \frac{2\,\tau}{p_A\, a}\left(1 - \frac{1}{3\,\gamma\, b}\right) \tag{8.2.28d}$$

Most of these constants are traditionally given in cgs units: ρ_g, bubble gas density $= \rho_{gA}[1 + 2\tau/(p_A a)](1 + 0.1\,z)$, where z is depth in meters; p_A, ambient pressure $= 1.013 \times 10^6(1 + 0.1\,z)$ dynes/cm^2; ρ_{gA}, density of free gas at sea level (1.29×10^{-3} g/cm^{-3} for air); C_{pg}, specific heat at constant pressure of

bubble gas ($\cong 0.24$ cal/(g °C) for air); K_g, thermal conductivity of bubble gas ($\cong 5.6 \times 10^{-5}$ cal/(cm) (s) (°C) for air); γ, ratio of specific heats of bubble gas ($= 1.4$ for air); τ, surface tension at the air/water interface ($\cong 75$ dyne/cm). Fig. 8.2.1 shows how b and β affect the resonance frequency. The corrections are significant for small bubbles, but, near resonance, they tend to go in opposite directions. The net effect is that these corrections modify the simple expression for f_b by more than 10 percent only for bubbles smaller than about 5 microns radius (Anderson and Hampton 1980a).

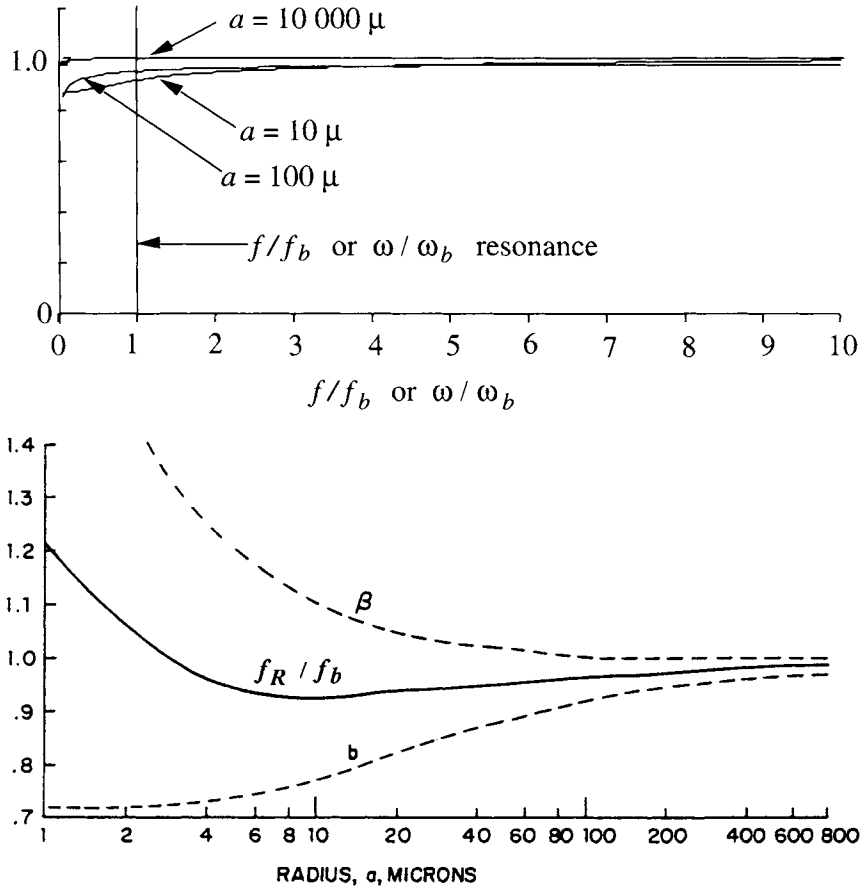

Figure 8.2.1 Corrections for b and β for a resonating clean, free air bubble at sea level. *Above*, dependence of $f_R/f_b = (b\beta)^{1/2}$ on relative frequency for three bubble radii. The corrected resonance frequency, f_R, is defined in Equation 8.2.27. The simple bubble resonance frequency, f_b, is given in Equation 8.2.13. *Below*, the separate variations of b, β, and f_R/f_b at resonance, as a function of bubble radius.

One concludes that the simple Equation 8.2.13 is an acceptable predictor for the resonance frequency of most of the bubbles in the sea. Exceptions are: a) bubbles of radii less than 5 μm (important in cavitation); b) dirty bubbles where b and β are different from our assumed values; c) bubbles in crevices; d) bubbles near surfaces (see section 8.2.10); and e) nonspherical bubbles (see section 8.2.11).

8.2.6 DAMPING CONSTANTS

The inclusion of thermal conductivity and shear viscosity, as described in section 8.2.5, produces significant changes in the bubble damping at resonance. It therefore causes major corrections to resonant bubble scattering, as derived in Chapter 7 and shown in Fig. 8.1.2. To evaluate the effect, use Equations 8.2.22 and 8.2.26 to eliminate p_{int} and form the ratio of the scattered pressure amplitude to the incident plane wave amplitude,

$$\frac{P_{scat}}{P_{inc}} = \frac{-a/R_0}{\left[(f_R/f)^2 - 1\right] + i\left[ka + (d/b)(f_R/f)^2 + 4\mu/(\rho_A \omega a^2)\right]} \tag{8.2.29}$$

The imaginary term in the square brackets is called the *total damping constant*,

$$\delta = \delta_r + \delta_t + \delta_v \tag{8.2.30}$$

which is the sum of the reradiation (scattering) term $\delta_r = ka$; the thermal damping term δ_t, which is a function of d/b; and the viscous damping term δ_v, which is a function of the kinematic coefficient of shear viscosity of the water, μ/ρ_A. Typical curves of the total δ for clean bubbles in fresh water are shown for 1, 10, and 100 kHz, and the three separate components are shown for frequency 10 kHz, in Fig. 8.2.2.

At resonance $f_R = f$, the scattered wave amplitude P_{scat} is limited only by the square-bracket imaginary term in Equation 8.2.29. Now define the *damping constants at resonance* within that term,

$$\delta_R = \delta_{Rr} + \delta_{Rt} + \delta_{Rv} \tag{8.2.31a}$$

where $\delta_{Rr} = k_R a$ = resonance damping constant due to reradiation (scattering); $\delta_{Rt} = (d/b)$ = resonance damping constant due to thermal conductivity; $\delta_{Rv} = 4\mu/(\rho_A \omega_R a^2)$ = resonance damping constant due to shear viscosity.

One can evaluate the damping constants by going to Equations 8.2.27a, b, c, and d for X, d/b, b and β as functions of the frequency, specific heat, bubble depth, gas density, specific heat at constant pressure, and thermal conductivity of the

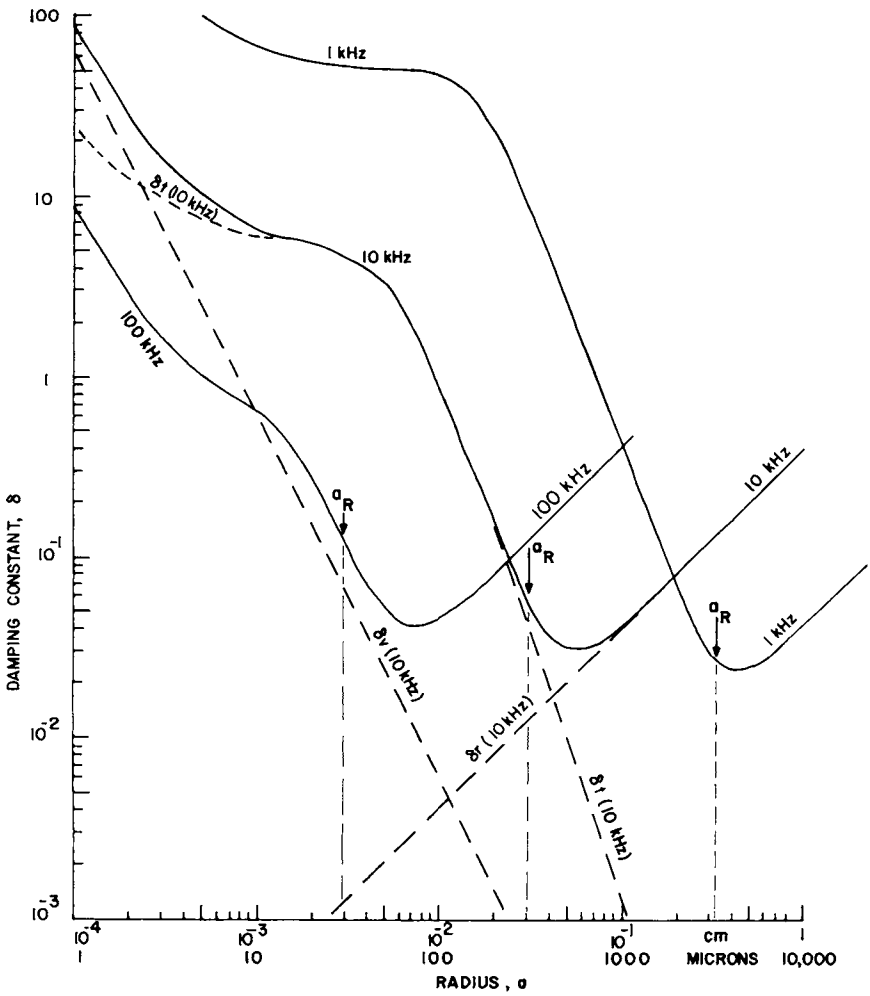

Figure 8.2.2 Damping constants of clean small spherical air bubbles in fresh water at sea level for frequencies 1, 10, and 100 kHz. The three components δ_r, δ_r, and δ_v are shown for frequency 10 kHz. The damping constants at resonance δ_R, δ_{Rt}, δ_{Rv}, and δ_{Rt} are near, but not at, the minimum values of δ.

gas. Fig 8.2.3 shows the damping constants *at resonance* for a small, clean air bubble in fresh water at sea level. One notes that the resonant thermal damping δ_{Rt}, is significant over a very wide range of frequencies; the resonant viscous damping, δ_{Rv}, is important above 1 MHz, and the resonant radiation damping, δ_{Rr} is important below 1 kHz.

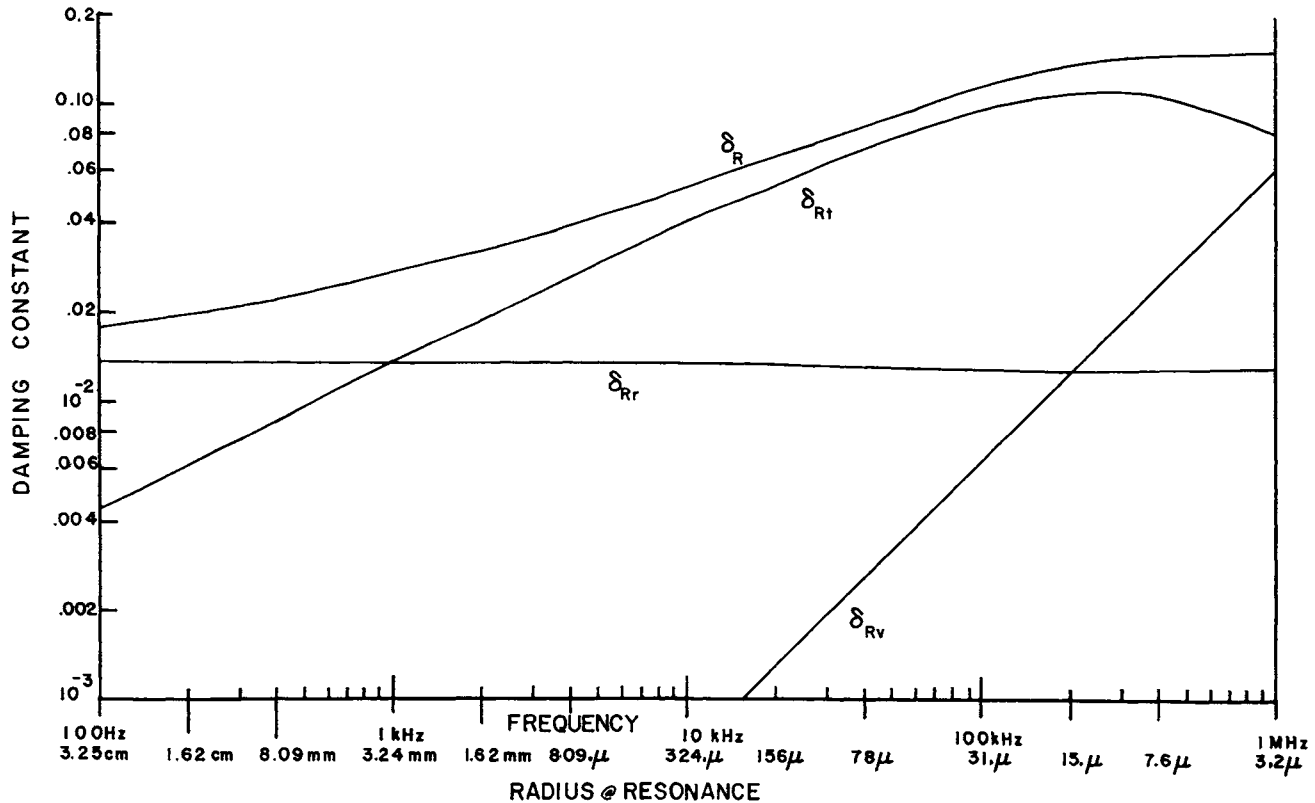

Figure 8.2.3 Resonance damping constants for a small, clean, fresh-water air bubble at sea level. (Adapted from Devin, Charles, Jr., "Survey of thermal, radiation, and viscous damping of pulsating air bubbles in water," *J. Acoust. Soc. Am.* **31**, 1654–67, 1959.)

A simple approximation to the curve from 1 kHz to 100 kHz is

$$\delta_R \cong 0.0025 f^{1/3} \tag{8.2.31b}$$

with f in Hz

8.2.7 ACOUSTICAL CROSS SECTIONS

When the small bubble is insonified by a plane wave, its total *acoustical scattering cross section*, σ_s, is defined as the total scattered power divided by the incident plane-wave intensity:

$$\sigma_s(f) = \Pi_s / I_{inc} = \frac{4\pi R_0^2 (P_{scat}^2/\rho_A c)}{(P_{inc}^2/\rho_A c)} = \frac{4\pi a^2}{[(f_R/f)^2 - 1]^2 + \delta^2(f)} \qquad (ka < 1) \tag{8.2.32a}$$

At resonance, the total scattering cross section is

$$\sigma_s(f_R) = \frac{4\pi a^2}{+\delta_R^2} \quad \text{when} \quad f = f_R \tag{8.2.32b}$$

At resonance, the total scattering cross section becomes $4/\delta_R^2$ greater than the geometrical cross section. For example, from Fig. 8.2.3 we see that a 30 micron radius bubble with resonance frequency of about 100 kHz will have a damping constant of about 0.1, and therefore a total scattering cross section 400 times larger than its geometrical cross section.

Because the scattering is omnidirectional when $ka \ll 0.1$, at resonance the differential scattering cross section in any direction is simply

$$\Delta\sigma_S = \sigma_S/(4\pi) = a^2/\delta_R^2 \tag{8.2.33a}$$

The backscattering length $|\mathcal{L}_{bs}|$ is the square root of $\Delta\sigma_s$, and the relative backscattering length is

$$|\mathcal{L}_{bs}|/(\pi a^2)^{1/2} = (\sigma_S)^{1/2}/(2\pi a) \qquad ka < 1 \tag{8.2.33b}$$

The comparison of the resonant bubble at sea level, where $ka = 0.0136$, with the rigid sphere of the same size reveals the immense selectivity of bubble resonance. This was shown in Fig. 8.1.2 for the oversimplified case, where $\delta_R = ka$ rather than the corrrect value of δ_R in Fig. 8.2.3. The rigid sphere has a relative scattering length that decreases as $(ka)^2$ for frequencies below $ka = 1$ (see Chapter 7). Therefore, at $ka = 0.0136$, the resonating bubble has a relative scattering length of about 10^5 greater than for a rigid sphere of the same size. For this reason, an acoustical scattering experimenter has a very easy task distinguishing a rigid sphere from a resonating bubble of the same size. The

significant corrections for viscous damping and thermal conductivity loss is left as a problem for the student.

The attenuation of a plane wave depends on both the bubble scattering cross section, σ_s, which removes sound from the beam, and the absorption cross section, σ_a, which converts sound energy to heat. The sum of the two is the extinction cross section, σ_e,

$$\sigma_e = \sigma_a + \sigma_s \tag{8.2.34}$$

The extinction coss section is calculated directly from the rate at which the incident pressure does work on the bubble divided by the incident plane-wave intensity,

$$\sigma_e = \frac{\dfrac{4\pi a^2}{T}\displaystyle\int_T \left[p_{inc}\frac{\partial \xi}{\partial t}\right]_{R=a} dt}{I_{inc}} \tag{8.2.35}$$

The integration yields

$$\sigma_e = \frac{4\pi a^2(\delta/\delta_r)}{[(f_R/f)^2 - 1]^2 + \delta^2} \tag{8.2.36}$$

Using Equation 8.2.34, we find the absorption cross section by subtraction of Equation 8.2.32a from Equation 8.2.36. The result is

$$\sigma_a = \frac{4\pi a^2\left(\dfrac{\delta_t + \delta_v}{\delta_r}\right)}{[(f_R/f)^2 - 1]^2 + \delta^2} \tag{8.2.37}$$

Comparing Equations 8.2.32a, 8.2.36, and 8.2.37, we obtain relations between the cross sections in terms of the damping constants,

$$\frac{\sigma_a}{\sigma_s} = \frac{\delta_t + \delta_v}{\delta_r} \tag{8.2.38a}$$

and

$$\frac{\sigma_e}{\sigma_s} = \frac{\delta}{\delta_r} \tag{8.2.38b}$$

Again we see that, at resonance, the acoustical cross sections are much larger than the geometrical cross section. This fact, combined with the simple, direct connection between resonance frequency and bubble radius Equation 8.2.27, is the key to the advantages of acoustical measurements in determining bubble populations at sea. By comparison, when light scatters from a bubble or particle, the optical cross section is at most equal to the geometrical cross section.

Using the concept of specific acoustic impedance (the ratio of the acoustic pressure to the acoustic particle velocity), the bubble at and near resonance is effectively a "hole" of very low impedance compared with the water. This hole distorts the incoming acoustic field over a large volume surrounding the bubble. The distorted field causes a power flow toward the bubble center from a section of the incoming plane wave that is far beyond the bubble cross section. When this is "viewed" acoustically from a great distance, the absorption, scatter, and extinction give the impression of a body that is far larger than its true size.

The left side of Fig. 8.2.4 shows the scattering and extinction cross sections and the right side the absorption cross sections as functions of bubble radius for three frequencies, where $ka < 1$. The very prominent peaks at resonance are clearly seen. For bubbles of radius smaller than the resonance size, the cross sections are approximately proportional to a^6. However, notice that larger bubbles have large extinction and scattering cross sections. Therefore, if there is a mixture of bubble radii, those of radius much greater than the resonance radius may make a significant contribution to the measurement of total scatter or extinction if there are enough of them. An absorption measurement is not contaminated by larger bubbles. See Fig 8.3.1 for an estimate of this effect.

8.2.8 INSONIFIED DAMPED PULSATIONS

We now rewrite the equation of the lumped mechanical motion of a bubble, Equation 8.2.1, to include damping when the bubble is insonified. In addition to the inertial force and the stiffness restoring force, there is a damping force, $R_M(\partial\xi/\partial t)$, which is assumed to be proportional to the radial velocity. The mechanical resistance, R_M, represents energy losses caused by sound reradiation, shear viscosity, and thermal conductivity. The equation describing the radial displacement, ξ, of the insonified bubble is

$$m\frac{\partial^2\xi}{\partial t^2} + R_M\frac{\partial\xi}{\partial t} + s\xi = 4\pi a^2 P_{inc}e^{i\omega t} \qquad \textbf{(8.2.39a)}$$

The solution of Equation 8.2.39a, which may be demonstrated by substitution, is

$$\xi = \frac{-i4\pi a^2(P_{inc}/\omega)e^{i\omega t}}{R_M + i(\omega m - s/\omega)} \qquad \textbf{(8.2.39b)}$$

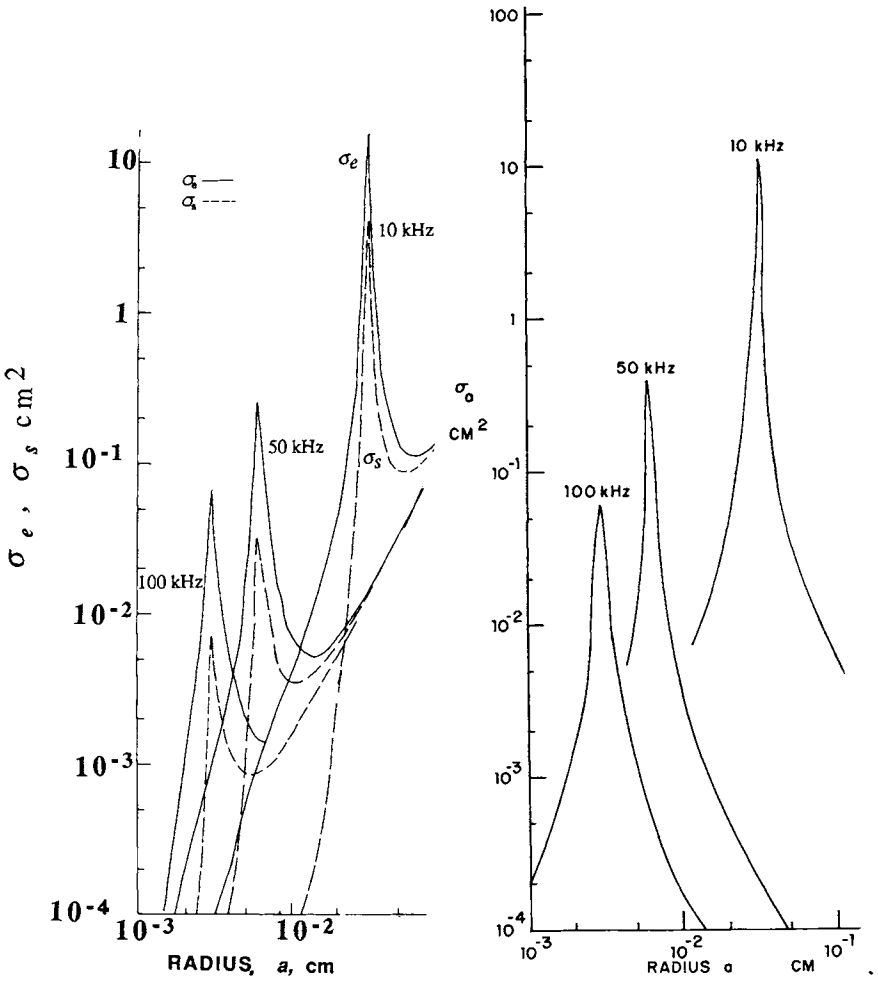

Figure 8.2.4 *Left*, extinction (solid line) and scattering (dashed line) cross sections of small sea-level air bubbles in fresh water, insonified by 10, 50, or 100 kHz plane waves. *Right*, absorption cross sections for the same parameters. (From Medwin, H., "Acoustical determinations of bubble-size spectra," *J. Acoust. Soc. Am.* **62**, 1041–44, 1977b.)

The lumped mechanical resistance, R_M, is simply related to the damping constant, δ. To show this, equate the time derivative of Equation 8.2.39b to the radial velocity from the point of view of the radiating wave Equation 8.2.25. Use Equations 8.2.26 and 8.2.28 to eliminate b and d, and obtain

$$R_M + i\left(\omega m - s/\omega\right) = i\,4\,\pi\,a^3\,\rho_A\,\omega\left\{\left[\left(\frac{f_R}{f}\right)^2 - 1\right] + i\,\delta\right\} \qquad \textbf{(8.2.40)}$$

Equating the reals gives the connection between R_M and δ,

$$R_M = 4\pi a^3 \rho_A \omega \delta = \omega m \delta \tag{8.2.41}$$

where we have used Equation 8.2.12 for the mass m.

8.2.9 *DECAYING BUBBLE PULSATIONS*

After the bubble excitation has ceased and its oscillations are allowed to decay, we use the analytic description of radiation by damped, pulsating bubbles as given by Equation 8.2.39a, with right side equal to zero;

$$m \frac{\partial^2 \xi}{\partial t^2} + R_M \frac{\partial \xi}{\partial t} + s\xi = 0 \tag{8.2.42}$$

Propose the damped sinusoidal solution for the surface displacement with damping rate D_b [sec^{-1}]:

$$\xi = Ae^{-D_b t + i\omega_d t} \tag{8.2.43a}$$

where

$$D_b = \frac{1}{T_e} \ll \omega_d \tag{8.2.43b}$$

The angular frequency of the damped oscillation is ω_d, and the "modulus of decay" is T_e, the time required for the amplitude to decrease to e^{-1} of its former value.

Then Equation 8.2.42 becomes

$$m(i\omega_d - D_b)^2 + R_m(i\omega_d - D_b) + s = 0 \tag{8.2.44}$$

Expand the terms and gather the imaginary and real parts, so that for imaginary terms

$$D_b = R_M/(2m) \tag{8.2.45}$$

and for real terms

$$mD_b^2 - m\omega_d^2 - D_b R_M + s = 0 \tag{8.2.46}$$

The solution of Equation 8.2.46 is

$$\omega_d = \pm\sqrt{\frac{s}{m} - \left(\frac{R_M}{2m}\right)^2}^2 \tag{8.2.47}$$

or

$$\omega_d = \pm\sqrt{\omega_b^2 - D_b^2} \tag{8.2.48}$$

Choosing the cosine of the complex exponential in Equation 8.2.43a, the real displacement is

$$\xi = A\, e^{-D_b t} \cos \omega_d t \tag{8.2.49}$$

Using the damped bubble frequency, $\omega_d = 2\pi f_d$, one can write the damping rate, D_b, in terms of the bubble damping constant at resonance, δ_R:

$$D_b = \pi \delta_R f_d \tag{8.2.50}$$

The time, $T_e = 1/D_b$, for the amplitude to reduce to $(1/e)$ of its original value can be written in a form that permits the determination of δ_R from T_e and f_b,

$$T_e = \frac{1}{\pi \delta_R f_d} \approx \frac{1}{\pi \delta_R f_b} \tag{8.2.51}$$

because $f_d \approx f_b$.

8.2.10 NEAR-SURFACE AND NONLINEAR BUBBLE PULSATIONS

The bubbles created by a breaking wave or by a raindrop are close to the ocean surface—call it depth, z. When a pulsating bubble is close to the "smooth" ocean surface, radiation from the bubble will reflect from the surface as a spherically diverging wave. For a "smooth" ocean surface, the reflected wave will have a virtual source strength that is equal to that of the real pulsating bubble and a phase that is shifted by 180°. The combination of the source and its out-of-phase reflection at a separation $l = 2z$ constitutes a dipole as described in section 4.1.3.

The conditions for a perfect dipole at the sea surface are a) the radiated wavelength, λ, must be very large compared with the distance between the source and its image, $\lambda \gg l = 2z$; and b) the radiated wavelength must be large compared with the rms height of the fine-scale surface roughness (see Chapter 13).

Under these conditions, the pulsating bubble and its image will radiate as a dipole. The dipole axis will be oriented perpendicular to the surface, and the radiation will follow the $\cos\theta$ law of Equation 4.1.10, with the maximum of radiation perpendicular to the local ocean surface. The local ocean surface may be tilted by the low-frequency large-wavelength components of the surface wave spectrum.

Strasberg (1953) has shown that a spherical, pulsating bubble at very close separation z from a free surface will have a resonance frequency higher than that of a more distant bubble. The resonance frequency of a near-surface bubble of radius a is given by

$$f = f_0 F \tag{8.2.52}$$

where

$$F = \left[1 - \left(\frac{a}{2z}\right) - \left(\frac{a}{2z}\right)^4\right]^{-\frac{1}{2}} \tag{8.2.53}$$

Possible evidence of this frequency shift is shown in Fig. 8.5.1 for a bubble produced by a laboratory breaking wave.

Sometimes the pulsations of the bubble are so large that shape oscillations take place, in addition to the radial pulsation. Longuet-Higgins (1992) has proved that under this condition the second harmonic of a shape oscillation can be resonant to the pulsation frequency, and an excess dissipation results. This continues until the oscillation amplitude is lowered to a level where only the omnidirectional pulsation remains, with its predictable theoretical damping.

8.2.11 NONSPHERICAL BUBBLES

Strasberg (1953) showed that an oscillating ellipsoidal bubble of the same volume as a spherical bubble will have weaker radiation and a higher fundamental resonance frequency. The effect may have been observed in laboratory experiments of breaking waves; see caption of Fig. 8.5.1.

The change in volume resonance, when a bubble is nonspheroidal, has been studied also by Weston (1967) and Feuillade and Werby (1994). For the same volume of gas, as the aspect ratio of the prolate ellipsoid, or cylindrical volume with endcaps, increases from that of a spherical bubble, (unity aspect ratio), the resonance frequency increases, the magnitude of the scattered energy decreases, and the breadth of the resonance curve increases (Fig. 8.2.5). Both of these cases are posssible models of swim-bladders of fish.

The complex nonlinear oscillations of bubbles have also been studied optically, most recently by Stroud and Marston (1994) and Asaki and Marston (1995). Because of the difficulty of observing volume fluctuations optically, the work is usually conducted with larger bubbles. It has been found that clean water bubbles of radius greater than 800 microns show damping two to four times larger

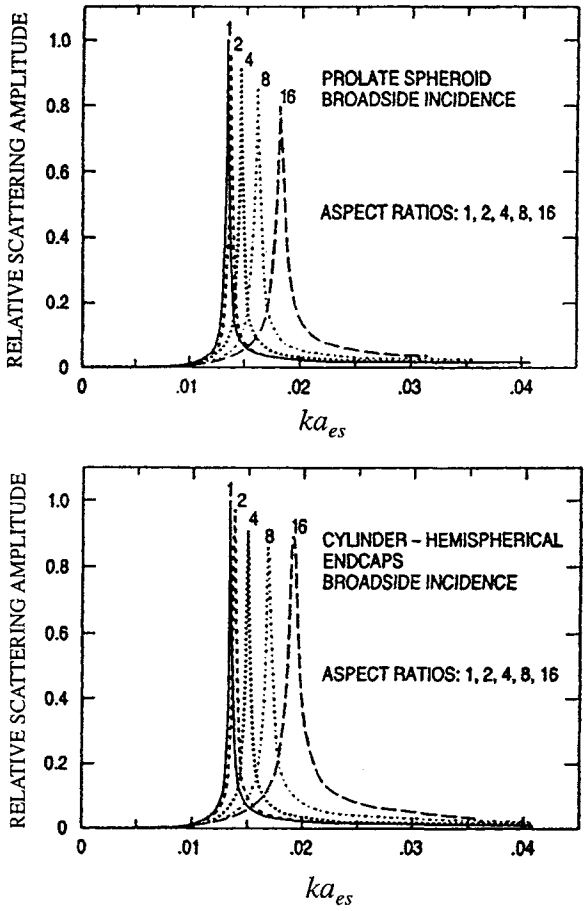

Figure 8.2.5 Change in volume resonance as a function of axial length to cross-sectional diameter for a nonspherical bubble at sea level. *Above*, resonance curves of the prolate spheroid at broadside incidence. *Below*, the same for a cylindrical bubble with hemispherical end caps. Aspect ratios 1, 2, 4, 8, and 16 are the ratio of the major to minor axis of the ellipsoid, or length to cross-section diameter of the cylinder. (From Feuillade, C., and F. Werby, "Resonances of deformed gas bubbles in liquids," *J. Acoust. Soc. Am.* **96**, 3684–92, 1994.)

than predicted by theory, which the authors say is "associated with some nonlinear response of the bubble."

8.2.12 DAMPING CONSTANTS OF BUBBLES IN SEAWATER

Throughout this chapter we have been careful to describe the bubbles as "clean air bubbles in fresh water." The damping constant δ that was derived in section 8.2.6 was based on the assumptions that the surface of the spherical air bubble was uncontaminated and that the bubble was in clean fresh water, not salt water. The potential effects of these assumptions are significant. Different damping constants in the real ocean would cause different expressions for the scattering, absorption and extinction cross sections. These would, in turn, affect the bubble densities obtained by the inversion of those equations.

There is evidence that the bubble damping constant in salt water *is* different from that in fresh water. Scofield (1992) found that the damping constants of rainfall-produced bubbles of radius from 140 to 300 microns ($23 > f_R > 11$ kHz) were about 10 percent greater in 35 ppm salt water than in tap water. Kolaini (personal communication, 1997) has found similar differences for bubbles generated in salt water, compared with fresh water.

8.3 Scatter, Absorption, and Dispersion in Bubbly Water

When widely spaced bubbles are insonified, the acoustical cross sections of the individuals simply add. The classical development assumes that there are no interactions between bubbles. Feuillade (1995a) shows that the scattering cross section of an assemblage of *identical bubbles* depends on the bubble spacing. There is a downward frequency shift and a broadening of the resonance peak when identical bubbles are packed. But truly "identical" bubbles do not exist in the real world. By comparison with attenuation and dispersion experiments in which the air-to- water volume fraction, U, approached 10^{-2}, Feuillade (1995b) has proved that, for realistic ocean distributions of bubble sizes and random spacings, the classical multiple scattering development for attenuation or dispersion of sound in a random-sized bubbly mixture, as used in this chapter, is appropriate.

Clouds of bubbles are produced naturally when large numbers of individual bubbles from breakers are entrained by the turbulence and Langmuir circulations under a breaking wave (Thorpe 1982). These bubble clouds have been offered as an explanation of the significant backscatter of low-frequency sound ($f < 2$ kHz)

from the sea surface (Prosperetti et al. 1993) as well as the ambient low-frequency noise ($f < 500$ Hz) at sea. In the latter case it is postulated that the volume of the bubble cloud has a density and stiffness that allows it to oscillate as a huge "bubble" with low-frequency modes.

When bubbles of random sizes are in a separated, close-packed, random, three-dimensional configuration as in the wake of a ship, there will be significant reflection at the pressure-release face of the bubble cluster.

8.3.1 *SOUND BACKSCATTERED BY AN ENSEMBLE OF BUBBLES: VOLUME REVERBERATION*

Techniques for calculating and measuring the sound scattered by a single object are discussed in section 7.1. The methodology for many objects starts with the scattering by a single object, and includes the distribution of sizes of the objects. We now consider the backscattered sound for a single transducer sonar (monostatic backscatter). Since the same sonar transducer projects a ping into the medium and receives the sum of the scattered sound pressures, we use Equation 7.1.19 as the starting expression. Eventually, the scattering region of N bubbles will be in the range increment ΔR, and this will simplify the calculation. The first bubble of backscattering length $\mathcal{L}_1$ causes the scattered pressure

$$p_1(t) = \frac{P_0 e^{i[2\pi f(t-2R_1/c)]} R_0 \mathcal{L}_1(f)}{R_1^2} 10^{-2\alpha R_1/20} \quad \textbf{(8.3.1)}$$

The sum of the backscattered pressure from the N bubbles of various radii is

$$p_{scat}(t) = P_0 R_0 \sum_{n=1}^{N} \frac{e^{i[2\pi f(t-2R_n/c)]} \mathcal{L}_n}{R_n^2} 10^{-2\alpha R_n/20} \quad \textbf{(8.3.2)}$$

For time-integral-pressure–squared processing of a pulse, one uses the [*tips*] concept of section 3.1.3. Express the absolute square of Equation 8.3.2 and integrate over time, $t_g = 2\Delta R/c$, to obtain the "volume reverberation" due to bubbles (subscript *Reverb*):

$$[tips]_{Reverb} = (P_0 R_0)^2 \int_{R_n/c}^{(R_n/c)+t_g} \sum_{n=1}^{N} \frac{e^{i[2\pi f(t-2R_n/c)]} \mathcal{L}_n}{R_n^2} 10^{-2\alpha R_n/20} \quad \textbf{(8.3.3)}$$

$$\times \sum_{m=1}^{N} \frac{e^{-i[2\pi f(t-2R_m/c)]} \mathcal{L}_m^*}{R_m^2} 10^{-2\alpha R_m/20}\, dt \quad \textbf{(8.3.4)}$$

In our simplified formulation, the sound that is multiply scattered between bubbles is ignored. The product can be wrttten as the sum of a term for $m = n$ and a term for $m \neq n$:

$$[tips]_{Reverb} = (P_0R_0)^2 \int_{R_n/c}^{(R_n/c)+t_g} \sum_{n=1}^{N} \frac{|\mathcal{L}_n|^2}{R_n^4} 10^{-4\alpha R_n/20}\, dt \qquad \textbf{(8.3.5)}$$

$$+(P_0R_0)^2 \int_{R_n/c}^{(R_n/c)+t_g} \sum_{n\neq m}^{N} \sum^{N} e^{i4\pi f(R_m-R_n)/c} \frac{\mathcal{L}_n \mathcal{L}_m^*}{R_n^2 R_m^2} 10^{-2\alpha(R_n+R_m)/20}\, dt \qquad \textbf{(8.3.6)}$$

The first summation Equation 8.3.5 has N terms and is the sum of the absolute squares of the scattering lengths. The double summations Equation 8.3.6 for $n \neq m$ have $N(N-1)$ terms and are the *cross terms*. These cause fluctations in the values of repeated measurements of $[tips]_{Reverb}$. Relative to the first summation Equation 8.3.4, the second summation decreases as $1/N$. If the bubbles keep the same positions and the transducer is fixed, then repeated measurements of $[tips]_{Reverb}$ are the same, including the cross terms. However, in most oceanographic measurements and when the bubbles are well dispersed (all $|R_n - R_m| > \lambda$) and are moving, each repeated measurement of $[tips]_{Reverb}$ has a new and different set of R_n and R_m. Then, the average of many measurements causes the average of the cross terms to tend to zero. Drop the cross terms and use the differential scattering cross section $\Delta\sigma_n$ in place of $|\mathcal{L}_n^2|$, in $[tips]_{Reverb}$, to obtain

$$[tips]_{Reverb} \approx (P_0R_0)^2 \int_{R_n/c}^{(R_n/c)+t_g} \sum_{n=1}^{N} | \frac{\Delta\sigma_n}{R_n^4} 10^{-4\alpha R_n/20}\, dt \qquad \textbf{(8.3.7a)}$$

This expression describes the volume reverberation in which multiple scattering and cross terms are ignored. As a simplification, let $\Delta R \ll R$, $R_n \approx R$. Then

$$[tips]_{Reverb} \approx \frac{(P_0R_0)^2}{R^4} \int_{R_n/c}^{(R/c)+t_g} 10^{-4\alpha R/20} \left[\sum^{N} \Delta\sigma_n\right] dt \qquad \textbf{(8.3.7b)}$$

For omnidirectional scatter, each bubble of radius a_n has its own differential scattering cross section $\Delta\sigma_n = \sigma_s/(4\pi)$, where σ_s is given in Equation 8.2.32a. The volume ΔV contains $N\,\Delta V$ bubbles, and [tips]$_{Reverb}$ could be calculated if the total bubble distribution were known.

In the ocean there is a continuous distribution of sizes, so it is preferable to rewrite the summation as an integration,

$$S_{bs} = \left[\sum^{N} \Delta\sigma_n\right] = \int_a [n(a)\,da][\Delta\sigma_s(a,f)] \qquad \textbf{(8.3.8)}$$

where S_{bs} is the backscattering cross section per unit volume for all bubbles contained in the sampled volume and $n(a)\,da$ = the number of bubbles, of radius between a and $a + da$, per unit volume. Insert the differential cross section for small ($ka < 1$) bubbles, $\Delta\sigma_s(a) = \sigma_s(a)/4\pi$ from Equation 8.2.32a, to get

$$S_{bs} = \left[\sum^{N} \Delta\sigma_n\right] = \int_a [n(a)\,da]\left[\frac{a^2}{[(f_R/f)^2 - 1]^2 + \delta^2(f)}\right] \qquad (ka<1) \quad \textbf{(8.3.9)}$$

When $n(a)\,da$ is known, one can numerically integrate Equation 8.3.9 for a given frequency, f.

A simple analytical integration of this type of equation was first provided by Wildt (1946), who reported on World War II studies of sound scattering and attenuation in ship wakes. In his solution it is assumed that the scatter is dominated by the resonant bubbles, and that neither δ nor $n(a)\,da$ change appreciably over the the important narrow band of radii around the resonance radius. Then $n(a)$ may be factored out of the integration. Also, the substitution is made

$$q = (f_R/f) - 1 = (a/a_R) - 1 \qquad \textbf{(8.3.10)}$$

where q is small number, and $dq = da/a_R$.

For the convenience of using a known definite integral, the integration over q is extended from $-\infty$ to $+\infty$, and we have the backscattering cross section per unit volume, due to bubbles,

$$S_{bs} = (a_R)^2\, n\,(a) \int_{-\infty}^{+\infty} \frac{a_R\,dq}{(2\,q)^2 + \delta_R^2} = \frac{\pi\, a_R^3\, n\,(a)}{2\delta_R} \qquad (ka < 1) \quad \textbf{(8.3.11)}$$

A similar integration is used for the *extinction* cross section (next section). Numerical integrations have been compared with the approximation Equation 8.3.11 by Medwin (1977), Commander and McDonald (1991), and Sarkar and Prosperetti (1994). The accuracy of the approximate integration depends on the assumed ocean variation of bubble density with radius, and the frequency of interest. In the cases studied, the errors are a few percent. Proper calculation of the backscatter for bubbles larger than $ka = 0.1$ would require integration over directional patterns, such as shown in Fig. 8.1.1.

Since most bubbles are close to the ocean surface, another factor that affects the ocean measurement of $[tips]_{Reverb}$, or its inversion to obtain bubble densities by remote backscatter, is the proximity of the bubble to the sea surface and the roughness of the surface. The total picture of backscatter includes consideration of four paths: 1) direct backscatter from the bubble region; 2) bubble scatter that is then backscattered from the sea surface to the source; 3) insonification of the bubble by sound scattered from the sea surface; 4) the path from surface scatter to bubble, back to surface, and finally back to sound source. The answer, which depends on the assumption of the surface roughness effect, has been considered by Clay and Medwin (1964), McDaniel (1987), and Sarkar and Prosperetti (1994).

A further important factor is the dependence of the bubble reverberation on the sonar beam and ping characteristics. Since the bubble density $n(a)$ is known to be strongly dependent on depth (sections 8.4.1 and 8.4.2), the insonified volume must not be large if the backscatter is to be inverted to yield bubble density with good spatial resolution. Sonars that are far from the scatttering region can provide only gross average values of the bubble densities.

8.3.2 EXCESS ATTENUATION

The presence of upper ocean bubbles, each with absorption and scattering cross sections, causes extra attenuation beyond that described in section 3.4.

Bubbles of One Size

Assume that we have water containing N bubbles of radius a per unit volume. Assume, also, that the bubbles are separated enough so that there are no interaction effects. Effectively, this is true when the separation is greater than the square root of σ_e. (Sometimes a stronger criterion is used—separation greater than the wavelength.)

If the incident plane-wave intensity is I_{inc}, the power absorbed and scattered out of the beam by each bubble is $I_{inc}\sigma_e$, where σ_e is calculated from Equation 8.2.36. The spatial rate of change of intensity is

$$\frac{dI}{dx} = -I_{inc}\,\sigma_e\,N \tag{8.3.12}$$

Integrating,

$$I(x) = I_{inc}\exp\left(-\sigma_e N x\right) \tag{8.3.13}$$

After traveling a distance x, the change in intensity level will be

$$\Delta IL(\text{dB}) = 10\log_{10}\left(\frac{I(x)}{I_{inc}}\right) = -10\sigma_e N x \log_{10} e \tag{8.3.14}$$

The spatial attenuation rate due to bubbles is

$$\alpha_b(\text{dB/distance}) = \frac{\Delta IL}{x} = 4.34\sigma_e N \tag{8.3.15}$$

where the units are generally α_b in dB/m, σ_e in m^2, and N in m^{-3}.

Bubbles of Many Sizes

When there are bubbles of several sizes, the number per unit volume must be defined in terms of the number in a radius increment (typically, one micron) as

$$n(a)\,da = \frac{\text{number of bubbles of radius between } a \text{ and } a+da}{\text{volume}} \tag{8.3.16}$$

The extinction cross section per unit volume, S_e, for sound traversing a random mixture of noninteracting bubbles in the range $ka < 1$ is calculated by using Equation 8.2.36 in the integration

$$S_e = \int_0^\infty \sigma_e n(a)\,da = \int_0^\infty \frac{4\pi a^2(\delta/\delta_r)n(a)\,da}{[(f_R/f)^2 - 1]^2 + \delta^2} \tag{8.3.17}$$

This S_e replaces $\sigma_e N$ in Equation 8.3.15 to give the expression for the attenuation rate owing to a mixture of bubbles of $ka < 1$,

$$\alpha_b = 4.34 S_e\ \text{dB/m} \tag{8.3.18}$$

In some bubble determinations at sea, one seeks the bubble density $n(a)\,da$ from the results of an attenuation measurement by inverting Equations 8.3.18 and 8.3.17. The simplest approximation is to assume that the major contribution to the attenuation is near the resonance frequency. As shown in the derivation of Equation 8.3.11, Wildt (1946, p. 470) assumes that only bubbles close to resonance contribute to S_e, and that the bubble density and the damping constant are constant over that interval. Using our notation, the approximate value is

$$S_e = \frac{2\pi^2 a_R^3 n(a_R)}{\delta_R} \tag{8.3.19}$$

Therefore, from Equation 8.3.18 and using Equation 8.3.19, in an extinction experiment an approximate value of the bubble density at the resonance frequency $n(a_R)$ is obtained from

$$\alpha_b = \frac{85.7 a_R^3 n(a_R)}{\delta_R} \tag{8.3.20}$$

Numerical integration will give a better value than this approximate theory. See Sarkar and Prosperetti (1994) for some possibilities.

A graphical solution can also be used to find S_e when one knows the dependence of bubble density on the bubble radius. At sea, it turns out that dependences in the range of a^{-2} to a^{-4} are possible for certain realms of bubble radius (see Figs. 8.4.4 and 8.4.5).

A graphical calculation is shown in Fig. 8.3.1. Assume that the insonification is by a plane wave of frequency 50 kHz. In the graph at the left there is a plot of the single bubble extinction cross section, σ_e, as a function of bubble radius (see the left ordinate). In this same graph, there is a plot of bubble density $n(a)\,da$ that is assumed to vary as a^{-4} (see the right ordinate). In the graph on the right the product of the curves, $\sigma_e n(a)\,da$ is drawn. The total values S_e will be given by the

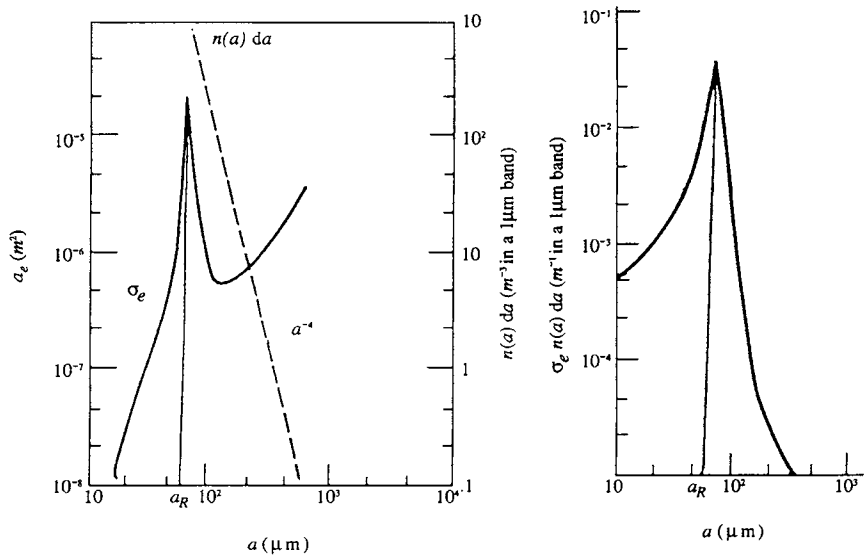

Figure 8.3.1 *Left*, log-log graph of extinction cross sections per bubble, σ_e, for 50 kHz insonification (ordinate at left side) and $n(a)\,da$ bubble density proportional to a^{-4} (ordinate at right side). *Right*, the product of σ_e and $n(a)\,da$ is calculated from the graph on the left. The area under the curve in a linear-linear graph would be S_e.

areas under the curves (when replotted on a linear graph, of course). The strong dominating contribution of $\sigma_e n(a)\, da$ near the resonance radius is quite clear. The dependence on $n(a)\, da$ has been discussed by Commander and McDonald (1991).

8.3.3 SOUND SPEED DISPERSION AND WOOD'S EQUATION

Single Radius Bubbles

From Equation 2.5.7, the speed of longitudinal waves in a fluid medium may be written as

$$c_A^2 = \frac{E_A}{\rho_A} = \frac{1}{\rho_A K_A} \tag{8.3.21}$$

where $K_A = 1/E_A$ is the compressibility of the ambient medium (fractional change of volume per unit applied pressure, Pascals^{-1}) and ρ_A is its density. The presence of a small void fraction of bubbles (e.g., fraction of gas in bubble form to volume of water) $< 10^{-5}$ has a negligible effect on the density, but it has a very significant effect on the compressibility.

In bubbly water the compressibility is made up of a part due to the bubble-free water, K_0, and a part due to the compressibility of the bubbles themselves, K_b:

$$K_A = K_0 + K_b \tag{8.3.22}$$

The compressibility for the bubble-free water is a function of the speed in bubble-free water,

$$K_0 = \frac{1}{\rho_0 c_0^2} \tag{8.3.23}$$

For now, assume all bubbles have the same radius a, and that $ka < 1$. The compressibility of the bubbles is found in terms of the displacement when insonified by an incident plane wave (Equation 8.2.39b),

$$K_b = \frac{(\Delta V/V)}{\Delta P} = \frac{N\Delta v}{\Delta P} = \frac{NS\xi}{P_{inc}\, e^{i\omega t}} = \frac{NS^2}{m\omega^2\left[\left(-1 + \omega_R^2/\omega^2\right) + i R_m/(\omega m)\right]} \tag{8.3.24}$$

where N is the number of bubbles per unit volume, Δv is the change of volume and $S = 4\pi a^2$ is the surface area of each bubble, and ξ is the radial displacement of the bubble surface.

To simplify, we use $\delta = R_M/(\omega m)$ and also define the frequency ratio,

$$Y = \omega_R / \omega \tag{8.3.25}$$

After multiplying numerator and denominator by the complex conjugate, we obtain

$$K_b = \frac{N\,4\,\pi\,a\left(Y^2 - 1 - i\delta\right)}{\rho_A\,\omega^2\left[\left(Y^2-1\right)^2 + \delta^2\right]} = K_0(A - iB) \tag{8.3.26}$$

where

$$A = \frac{(Y^2-1)}{(Y^2-1)^2+\delta^2}\frac{4\pi aNc_0^2}{\omega^2} \quad \text{and} \quad B = \frac{\delta}{(Y^2-1)^2+\delta^2}\frac{4\pi aNc_0^2}{\omega^2} \tag{8.3.27}$$

From Equations 8.3.21 and 8.3.26, the speed in bubbly water is

$$c_A = \left(\frac{1}{\rho_A K_A}\right)^{1/2} = \left(\frac{1}{\rho_A\,(K_0 + K_b)}\right)^{1/2} = \frac{c_0}{(1 + A - iB)^{1/2}} \tag{8.3.28}$$

where we assumed that $\rho_A \cong \rho_0$.

The propagation constant is

$$k_A = \frac{\omega}{c_A} = \frac{\omega\,(1 + A - iB)^{1/2}}{c_0} \tag{8.3.29}$$

Assume that the correction is small compared with unity, so that the first terms of the Taylor expansion may be used to replace the square root,

$$k_A = k_0\left(1 + \frac{A}{2} - i\,\frac{B}{2}\right) \tag{8.3.30}$$

The plane wave propagating through the bubbly medium is

$$p_{inc} = P_{inc}e^{ik_A x} = P_{inc}\exp\left(-k_{im}x\right)\exp\left[i(\omega t - k_{re}x)\right] \tag{8.3.31}$$

where

$$\begin{aligned} k_{im} &= k_0(B/2) \\ k_{re} &= k_0(1 + A/2) \end{aligned} \tag{8.3.32}$$

The imaginary part of the complex propagation constant represents the attenuation of the wave: this was called α_b earlier. The real part is the wave number for the propagation of constant phase surfaces at the dispersive speed ω/k_{re}.

This empirical presentation is a very much simplified form of the Kramers-Kronig relation, which was originally developed to show the connection between dispersion and attenuation of electromagnetic waves. A recent application of the K-K relation to sound propagation in a bubbly medium has been given by Ye (1997). Calculations of α_b and Re $\{c\}$ are given by Farmer et al. (1997) for an assumed bubble density.

From Equation 8.3.32, the speed in bubbly water is a function of frequency:

$$\mathrm{Re}\{c\} = \frac{\omega}{k_{re}} = c_0\left\{1 - \left[\frac{(Y^2-1)}{(Y^2-1)^2+\delta^2}\right]\left[\frac{2\pi a N c_0^2}{\omega^2}\right]\right\} \tag{8.3.33}$$

It is useful to write the speed in fractional terms of volume of gas in bubble form divided by volume of water. This is called the void fraction, U:

$$U = N\left(\frac{4}{3}\pi a^3\right) \tag{8.3.34}$$

$$\mathrm{Re}\{c\} = c_0\left\{1 - \left[\frac{(Y^2-1)}{(Y^2-1)^2+\delta^2}\right]\left[\frac{3UY^2}{2a^2k_R^2}\right]\right\} \qquad (ka<1) \tag{8.3.35}$$

where $k_R = \omega_R/c_0$ is the value of k_0 at resonance.

Graphs of the relative change in sound speed predicted by Equation 8.3.35 are plotted in Fig. 8.3.2 for two different densities of bubbles of the same radius. The dispersion curves show that at incident frequencies below the bubble resonance

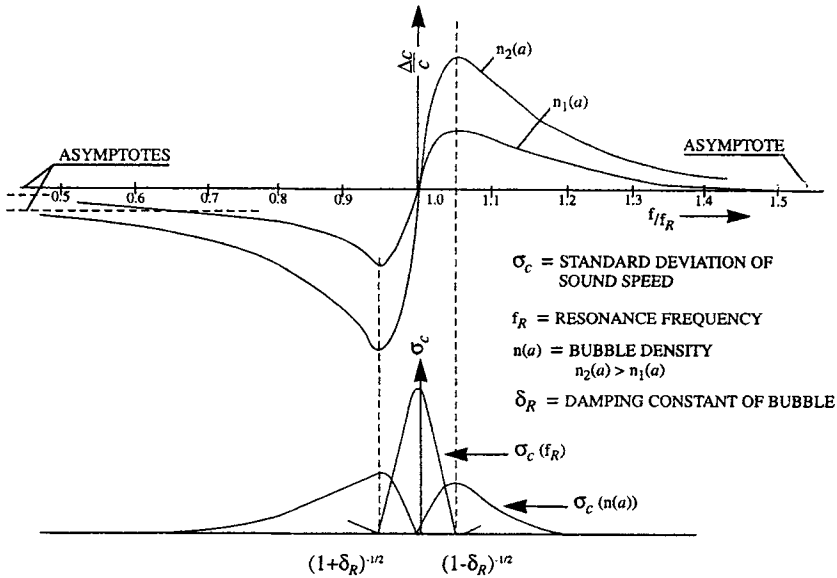

Figure 8.3.2 *Above*, sound speed dependence on frequency for two different bubble densities in a liquid containing only one bubble size. *Below*, standard deviation of the sound speed dispersion as a function of change in bubble density, $\sigma_c[n(a)]$, and as a function of resonance frequency change due to variation of ambient pressure above the bubble population, $\sigma_c(f_R)$. (From Medwin, H., J. Fitzgerald, and G. Rautmann, "Acoustic miniprobing for ocean microstructure and bubbles," *J. Geophys. Res.* **80**, 405–413, 1975b.) See also Wang and Medwin (1975).

frequency, the relative differential sound speeds, $\Delta c/c_0$, are below the value for bubble-free water, and approach a negative asymptote. Incident sounds of frequencies above the bubble resonance frequency reach a peak sound speed and then decrease to approach the speed in bubble-free water as the frequency becomes very large.

The limit of the dispersion curves (Fig. 8.3.2) at high frequencies is

$$c_{hf} = C_0\left[1 + \frac{3UY^2}{2a^2k_R^2(1+\delta^2)}\right] \to c_0;\ f \gg f_R \tag{8.3.36}$$

Therefore, bubbles do not affect the sound phase speed if the frequency is high enough. This explains why commercial *sound velocimeters*, which use megahertz frequency pulses to measure the travel time over a fixed short path, do not recognize the dispersive effect of bubbles. Sound velocimeters provide $c_A = c_0$ even in bubbly water because at 1 MHz, $f \gg f_R$ for all significant bubble fractions in the sea.

The limit at low frequencies is

$$c_{lf} = c_0\left(1 - \frac{3U}{2a^2k_R^2}\right);\ f \ll f_R \tag{8.3.37}$$

Since ak_R is a constant for a given gas at a given depth (for an air bubble at sea level $ak_R = 0.0136$ from section 8.2.4), the low-frequency asymptotic speed depends only on the void fraction, U. The simple approximations above are acceptable for $U < 10^{-5}$ and $ka < 1$.

Multiple Radii Bubbles

Using the same approximations, the generalization to the multiradii bubbles of the ocean medium is accomplished by replacing N by $n(a)\,da$ and U by $u(a)\,da$ in the previous development. Because all contributions to the compressibility are very small quantities, they add linearly, and the speed of sound in the bubbly region can be written in terms of the integral over all radii:

$$\mathrm{Re}\{c\} = c_0\left\{1 - \int_a \frac{(Y^2-1)\dfrac{3Y^2u(a)\,da}{2a^2k_R^2}}{(Y^2-1)^2+\delta^2}\right\} \tag{8.3.38}$$

For values of U greater than 10^{-4}, the approximation of Equation 8.3.30 is inadequate, and consequent predictions of Equations 8.3.35 and 8.3.38 are incorrect. Hall (1989, Appendix 2) and R. Goodman (personal communication, 1997) have proposed alternative expressions that work for $U > 10^{-4}$ provided that $n(a)\,da$ is known over the entire range of the integration. The low-frequency asymptotic value can be obtained by use of Wood's Equation, which is valid for all void fractions and does not require a knowledge of $n(a)\,da$.

Wood's Equation

When $n(a)\,da$ is not known, there is a simple technique to find U for any void fraction because the low-frequency asymptotic value of the speed in Fig. 8.3.2 is dependent only on the fluid "zero frequency" compressibility due to bubbles and the density.

Following Wood (1955), let ρ_b and ρ_w represent the densities of air in bubbles and in water, respectively, and let E_b and E_w be the bulk moduli of elasticity of air and water. Since U is the fraction of air by volume, $(1 - U)$ is the fraction of water by volume. For bubbly water, we first express the average density, ρ_A, and the average elasticity, E_A, which are needed to determine the speed at low frequencies, as follows:

$$\begin{aligned} \rho_A &= U\rho_b + (1-U)\rho_w \\ \frac{1}{E_A} &= \frac{U}{E_b} + \frac{1-U}{E_w} \\ c_{lf} &= \sqrt{\frac{E_A}{\rho_A}} = \sqrt{\frac{E_b E_w}{[UE_w + (1-U)E_b][U\rho_b + (1-U)\rho_w]}} \end{aligned} \tag{8.3.39}$$

For bubble-free water, E_w is calculated from ρ_w and c_w given in section 3.3.1. For the bubble gas, one uses $c^2 = \Delta p/\Delta\rho$ with $p\rho^{-\gamma} =$ constant for adiabatic propagation in a gas to obtain $E_b = \gamma P_A$.

When the low-frequency asymptote of the sound speed is experimentally determined in any mixture of bubbles, U can be calculated from Equation 8.3.39.

The approximate equation (8.3.37) for noninteracting bubbles agrees with Wood's Equation when $U \leq 10^{-5}$. Feuillade (1996) has shown that, although interactions are important if the bubble sizes are identical, there is no significant interaction effect for a mixture of bubble radii, as exists in the sea.

8.4 Active Measurements in Bubbly Water

8.4.1 TECHNIQUES FOR LINEAR BUBBLE COUNTING

Remote Sensing by Backscatter

Determinations of bubble density by backscatter sometimes use an upward-looking source and receiver at the same position on the sea floor and follow an analytical development such as in section 8.3.1. Sometimes the transducers are on a ship, underwater vehicle, or buoy (e.g., Løvik 1980; Vagle and Farmer 1992). Segments of the backscattered sound are received by opening and closing an electronic gate in the receiving system, as described in Chapter 4. The advantage of remote sensing is that the bubbly medium is undisturbed by the intrusion of equipment. A major disadvantage is that the illuminated volume is generally quite large and poorly defined. The axial extent is limited by the windowing procedure; the cross-sectional extent depends on the divergence of the sound beam and the range. Therefore the backscatter comes from a spherical cap which covers more than one depth. Since the bubble populations are sensitive functions of depth, the divergence of the beam produces an undesirable averaging over a range of depths. Another disadvantage is that it is necessary to correct for the attenuation of the signal before and after it acts in the scattering region.

In-situ Sensing

Several techniques, originally used in physical acoustics laboratories to determine the ultrasonic characteristics of liquids or solids, have been brought to sea to measure the acoustical characteristics of bubbly water. "Linear bubble counting" depends on the distinctive dispersive sound speed, attenuation and backscatter in the bubbly parts of the ocean.

The Pulse-Echo Technique. (See Barnhouse et al. 1964; Buxcey et al. 1965; and Medwin 1970), several cycles of a high-frequency sound are emitted from a piston transducer and returned by reflection from a nearby plane-rigid plate, (Fig. 8.4.1, left). After emission the source transducer is switched automatically to receive, and the decreasing amplitude of the series of reflections of the ping is measured (Fig. 8.4.2). The attenuation due to normal absorption and diffraction of the ping is first calibrated in a tank of nonbubbly water. The increased attenuation at sea is attributed to bubble absorption and scatter of sound

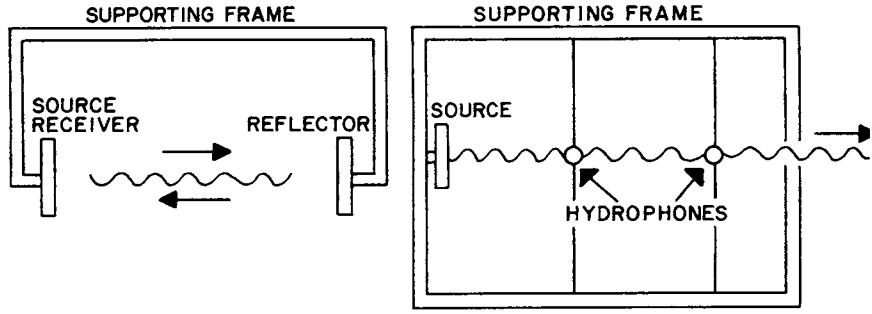

Figure 8.4.1 Experimental schemes for measuring bubble densities and void fractions at sea. The set-up at the left is drawn for a pulse-echo system. When the source and receiver are at separation less than the plate diameters, the device may also be used as a standing wave resonator system. The scheme at the right is for measuring the amplitude and phase changes for propagation past two or more hydrophones. The device is oriented vertically or horizontally. (From Clay and Medwin, 1977.)

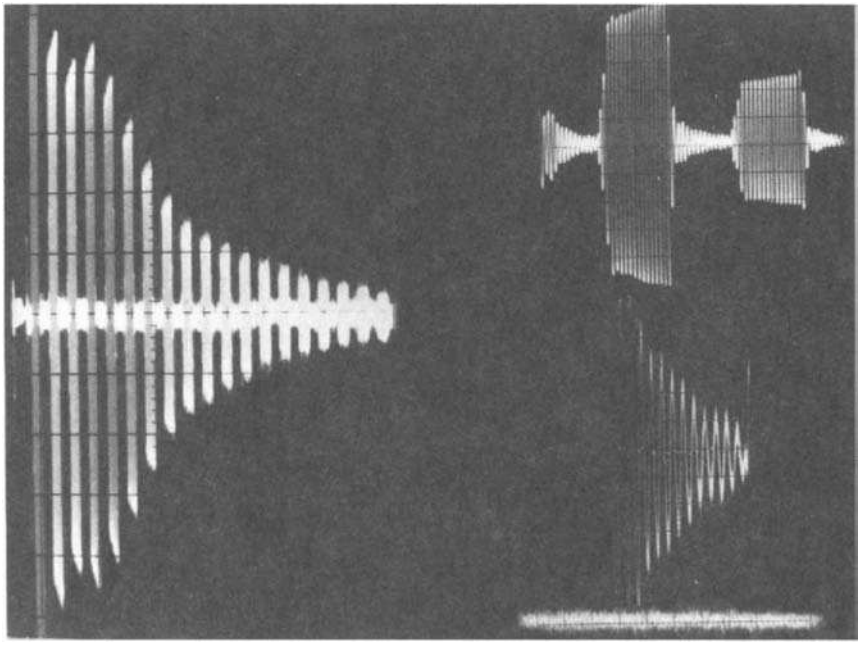

Figure 8.4.2 Oscillograms of pulse-echo signals. The multiple echoes at the left are for sound frequency 200 kHz. The right top shows two ehoes of a 30 kHz signal, with the transient backscatter between them. Right center is the amplified backscatter between echoes. Right bottom is the background noise. (From Clay and Medwin, 1977.)

out of the system (section 8.3.2), and the average bubble density is calculated for the region traversed by the pulse.

An added feature of the pulse echo technique is that backscatter can be detected separately, and measured, between the times of the echoes (Fig. 8.4.2). The backscatter occurs while the ping is traveling away from the transducer. It has the appearance of a tapered signal because the solid angle viewed by the receiver becomes smaller as the ping moves toward the reflector.

A third feature of the pulse-echo system is that the time between pulses can be used to determine the speed of the pulse, provided the phase shifts at the transducer and reflector have been calibrated.

In the pulse-echo system it is necessary to have clean pulses that are replicas of the applied voltage, without the transient growth and decay characteristic of most transducers. The desirable low Q source used in the Buxcey et. al. (1965) experiments was a Mylar electrostatic transducer. This has an output acoustic pressure proportional to the applied voltage and a receiving voltage sensitivity that is inversely proportional to the acoustic pressure at the face over a wide range of frequencies. When used in the send-receive mode, its electro-acoustical transducer performance is therefore independent of frequency to about 200 kHz in this version.

The Resonator Technique. If the source/receiver plate and reflector (Fig. 8.4.1) are close compared with their diameters, and the sound is CW, the source and reflector act as a leaky one-dimensional multifrequency resonator. When a "white noise" CW sound that covers a broad range of frequencies is radiated from the source, a series of standing waves (section 2.4.3) is formed in the resonator. The frequencies of the standing waves are a nearly harmonic series. The amplitudes and breadths of the standing wave responses at these frequencies, measured at the plate pressure antinode, depend on the system attenuation and the bubbly medium absorption between the plates. The resonance Q at sea is compared with the laboratory calibration to obtain the bubble density within the resonator at that frequency (see Fig. 8.4.3). Breitz and Medwin (1989a) describe the equipment and the calculation. Medwin and Breitz (1989b) give experimental results and comparisons with other measurements at sea. In addition to the bubble density determination, it is also possible to calculate the dispersion of the sound speed from the absolute frequency of the harmonics and the corrected separation of the plates.

Cartmill and Su (1993) have used the resonator technique in a very large wave-making facility. They show that the number density of bubbles from 35 to 1200 μm radius produced by breaking waves in salt water is an order of

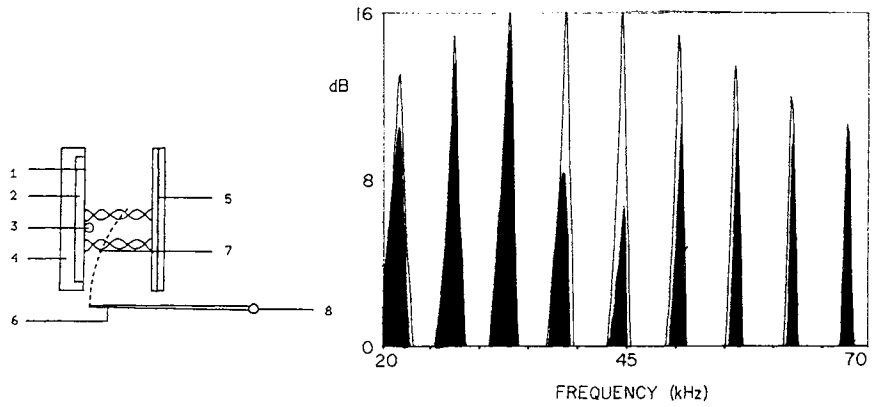

Figure 8.4.3 *Left*, schematic of the standing wave during calibration of the resonator at the fourth "harmonic" as used by Breitz and Medwin, "Instrumentation for *in-situ* acoustical measurements of bubble spectra under breaking waves," *J. Acoust. Soc. Am.* **86**, 739–43 (1989). The source is a solid dielectric flat plane capacitor, 1, backed by an aluminum plate, 2, in a plexiglas base, 4. The receiver is a probe hydrophone, 3. The reflector consists of a constrained damping layer between two aluminum plates, 5. A counted array of bubbles, 7, from a capillary, 6, is swept through the standing waves of the resonator by oscillating the capillary tube. *Right*, 9 resonance peaks from 20 to 70 kHz during calibration with bubbles (blackened) and without bubbles (outlined). The changes of heights and breadths of the peaks are used to determine the sound absorption at these several frequencies; for the calibration, the number of bubbles is calculated and compared with the visually counted bubbles.

magnitude greater than in fresh water for the same wave system. Farmer et al. (1997) have mounted five resonators (depths 0.7, 1.3, 1.9, 3.3, and 5.5 m) on a vertical frame to obtain simultaneous sound speed dispersion and void fractions for radii 20 to 500 μm during 12 m/s winds at sea.

Fig. 8.4.4 is an example of the range of bubble densities that have been measured under breaking waves at sea. Even in quiescent coastal waters, densities as great as 10^3 to 10^5 bubbles within a 1 micron radius (say, between 30 and 31 microns) per cubic meter are not uncommon near the sea surface and in coastal waters. Because bubble density is sensitive to ocean parameters, its measurement can reveal a wealth of information about physical, chemical, and biological processes in the volume and on the sea floor.

The Direct Transmission Technique. The simplest of all techniques uses a source to radiate sound to two or more nearby hydrophones (Fig. 8.4.1, right). The signal received at each hydrophone is analyzed by Fast Fourier Transform to yield the amplitude and phase. The ratio of the amplitudes gives the attenuation;

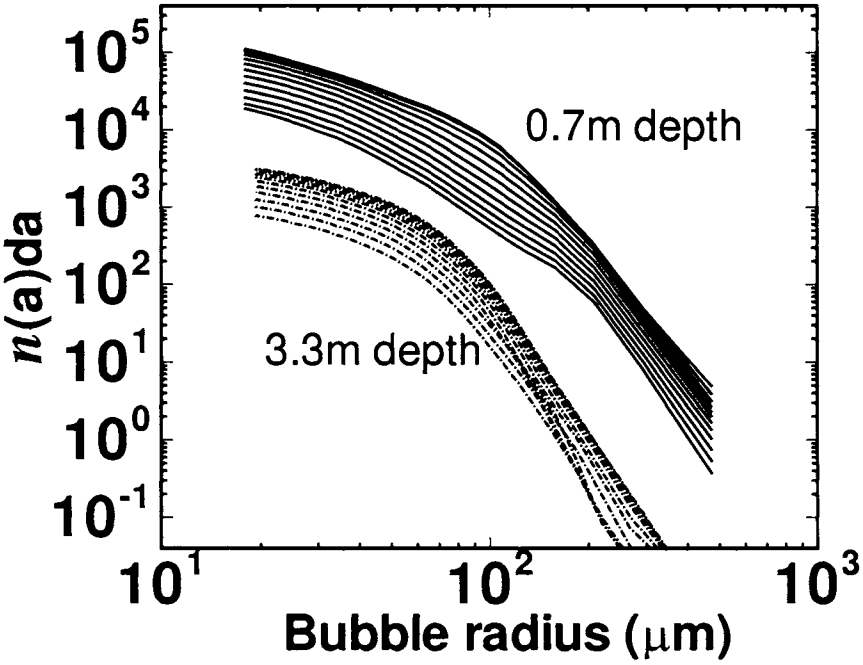

Figure 8.4.4 Resonator determinations of bubble densities at sea during a 12 m/s wind in the Gulf of Mexico. The ordinate is number of bubbles/m^3 in a 1 micron radius increment. Simultaneous measurements were made at 36 frequencies to yield 36 bubble densities for radii from 15 μm to 450 μm every 2 seconds during a 2-minute interval at each of five depths (not all results are shown). Data at the two depths shown are for increasing air fractions due to breaking waves as time progressed. The curves are smoothed between the data points." (D. Farmer, personal communication, 1997.)

the difference of the phases, corrected for the whole number of periods, provides the speed of propagation. When the propagation experiment uses a complex signal such as a sawtooth wave, the bubble densities and dispersion can be evaluated simultaneously for several bubble radii. See Medwin (1977).

Comparison of In Situ Bubble-Counting Techniques

The direct transmission technique involves measurements of both extinction (scatter and absorption) and dispersion. The pulse-echo technique has a lesser dependence on scatter than direct transmission because some of the scattered

energy is retained between the plates. The nearly closed resonator leaks only a small fraction of the scattered energy and is thereby almost a pure bubble absorption device. The resonator largely avoids the "noise" due to scattering from bubbles that are larger than the resonating bubbles (see Fig. 8.2.4, left).

All bubble-counting techniques must be calibrated by use of a known bubble stream, which may be obtained by electrolysis or from a pipette fed with pressurized gas. Results of field measurements are more trustworthy when two of the bubble effects are measured and compared at the same time — for example, scatter and extinction, absorption and dispersion, extinction and dispersion—and the K-K relation shows their compatibility.

8.4.2 DEPENDENCE OF BUBBLE DENSITIES ON WINDS, PLACE, AND TIME

Bubbles are generated by many physical, biological, and chemical actions. A vast range of bubble densities have been measured under different conditions. Measurements, to date, have demonstrated the dependence of bubble densities on water depth, bubble depth, time of day or night, wind speed, rainfall, cloud cover, season of year, presence of sea slicks.

Some results obtained in coastal waters are shown in Fig. 8.4.5; these are a) increased bubbles caused by increased breaking waves at higher wind speeds; b) seasonal dependence of increased biological activity in coastal waters; c) more common smaller bubbles in daylight due to photosynthesis; d) more common larger bubbles at night, possibly due to offshore winds ("sea breeze") dropping continental aerosols, which trap bubbles when they fall into the sea, or biological activity on the sea floor.

Bubbles cause frequency-dependent ray refraction near the sea surface. Because the bubble density increases as rays approach the surface (see Fig. 8.4.5) low frequencies are refracted and reflect at more nearly normal incidence. There is a lesser effect in the opposite direction for higher frequencies. Wave guide modes (Chapter 11) are also distorted by the varying dispersion near the ocean surface. To predict these acoustical behaviors, it is useful to provide some guidelines that take account of the dependence of average bubble densities on bubble radius, experiment depth, and wind speed. Rough empirical formulas that have been published, or can be extracted from published graphs, are in Equations 8.4.1 through 8.4.9.

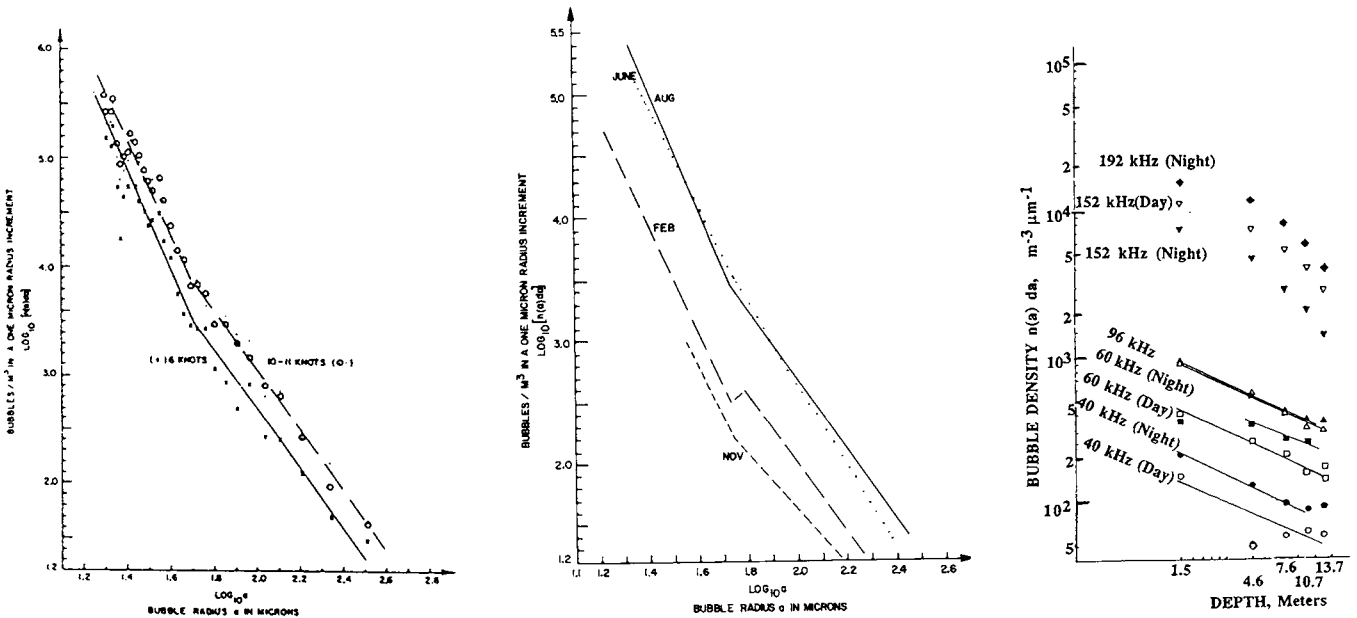

Figure 8.4.5 Wind, season, depth, and diel dependence of bubble densities. *Left*, average at 4 m depth, winds 6 knots (3 m/s) and 10–11 knots (5 to 6 m/s) in water of 40 m depth, Monterey Bay, California. *Center*, daytime average at different seasons; data from two coastal locations (San Diego Mission Bay water depth 20 m, Monterey water depth 40 m) at similar distances below the surface and low wind speeds (1 to 4 m/s). *Right*, diel variations, February off San Diego, as a function of depth and day/night (day, open symbols; night, closed). (From Medwin, H., "*In-situ* acoustic measurements of bubble populations in coastal waters," *J. Geophys. Res.* **75**, 599–611, 1970, and "*In-situ* measurements of microbubbles at sea," *J. Geophys. Res.* **82**, 971–76, 1977a.)

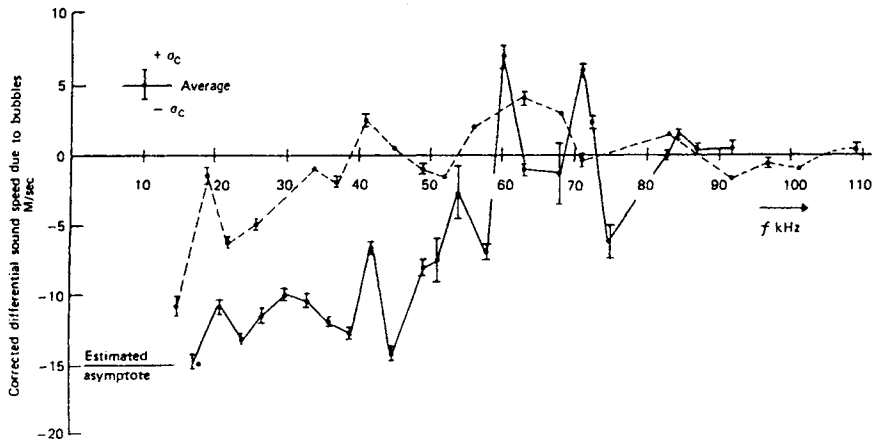

Figure 8.4.6 Early average sound speed dispersions with standard deviations shown by vertical bars. The dashed line data were taken 3.3 m below the surface in water 15 m deep, 1 mile from shore off San Diego, during 6 knot winds. The solid line data were 5 m below the surface, close to an ocean tower in Bass Strait, Australia, during 8 to 10 knot winds. (From Medwin, H., J. Fitzgerald, and G. Rautmann, "Acoustic miniprobing for ocean microstructure and bubbles," *J. Geophys. Res.* **80**, 405–13, 1975b.)

For Biological and Continental Aerosol Sources in Near-Calm, Isothermal Coastal Waters

From Fig. 8.4.5, the slope of bubble density versus radius changes at approximately 40 to 60 microns bubble radius; there is a depth dependence that is different for high frequencies (smaller bubbles) and low frequencies (larger bubbles); the density can be described by

$$n(a)\,da = K_1(a/60)^{-2}(z)^{-1/2} \quad \text{for } 200\,\mu\text{m} > a > 60\ \mu\text{m} \tag{8.4.1}$$

and

$$n(a)\,da = K_2(a/60)^{-4}e^{-z/L} \quad \text{for } 10\,\mu\text{m} < a < 60\ \mu\text{m} \tag{8.4.2}$$

where a = bubble radius in microns; $n(a)\,da$ = number of bubbles in a 1 micron increment, per m^3; L = small bubble folding depth $\cong 7$ m; $z \geq 1.5$ m = depth in meters; K_1 and K_2 are constants that depend on the time of day and season.

To add to the complexity of the coastal situation, there is evidence that bubble densities will be greater under sea slicks and windrows, and are even affected by the presence of fog. Bubble densities in other locations with different flora and

fauna will be very different. (There will also be a wind dependence and a dependence on distance from the surf zone, due to breaking waves.)

For Breaking Wave Sources in Deep Water

See Novarini and Norton (1994), Hall (1989), and Johnson and Cook (1979).

$$n(a)\,da = 1.6 \times 10^4 G(a,z)U(V)D(z,V) \quad (\mu\text{m}^{-1}\ \text{m}^{-3}) \tag{8.4.3}$$

where

$$G(a,z) = (a/a_{\text{ref}})^{-s(z)} \qquad \text{for } a > a_{\text{ref}}$$
$$\text{spectral slope,} \quad s(z) = 4.37 + (z/2.55)^2 \tag{8.4.4}$$

$$G(a,z) = (a/a_{\text{ref}})^{-4} \qquad \text{for } 10\ \mu\text{m} < a < a_{\text{ref}}$$
$$a_{\text{ref}}(\mu\text{m}) = 54.4 + 1.98z \tag{8.4.5}$$

where

$$U(V) = (V/13)^3, \quad \text{wind speed dependence} \tag{8.4.6}$$

where V is the wind speed, m/s, at height 10 m. Also,

$$D(z,V) = \exp[-z/L(V)], \quad \text{depth dependence} \tag{8.4.7}$$

L, the folding depth, is

$$L(V) = 0.4 \quad \text{for} \quad V < 7.5\ \text{m/s} \tag{8.4.8}$$

$$L(V) = 0.4 + 0.115(V - 7.5) \quad \text{for} \quad V > 7.5\ \text{m/s} \tag{8.4.9}$$

8.4.3 GAS VOID FRACTION

The determination of gas void fraction follows from the development of section 8.3.3. The effect of a mixture of bubbles is to superimpose many curves such as in Fig. 8.3.2. Although the details of the average dispersion curves can be quite complicated as shown in Fig. 8.4.6, one can still see that there is a low-frequency asymptote, which can be used in Equation 8.3.37 to determine the gas fraction, U, of the mixture. Also, there is always a high-frequency asymptote, as described for bubbles of one radius, at which there is *no* effect of bubbles on the sound speed.

The sound speed dispersion can be determined, also, by direct time-of-flight measurements over short paths, at several simultaneous frequencies. There is a

large variation with time as patches of bubbles move through the transmission paths as shown in Fig. 8.4.7.

8.4.4 SOUND PHASE FLUCTUATIONS

The temporal variation of bubble densities and bubble radii near the ocean surface causes fluctuations in sound speed. A simple explanation follows from Fig. 8.3.2. When the number of bubbles of a given radius changes, the dispersion curve for that bubble radius moves up and down. Additionally, when the pressure over a bubble changes (e.g., during passage of a wave crest or trough), the bubble resonance frequency changes, and the speed moves from the positive to the negative region of differential speed. The statistics of these changes have been considered by Medwin et al. (1975) and Wang and Medwin (1975). Changing patchiness of bubbles produces sound phase fluctuations that are Gaussian for frequencies less than predominant bubble frequencies. Separately, the variation of ocean pressure over a bubble patch with a predominant bubble radius creates sound phase modulations that are well-correlated with the time variable surface displacement. The phase fluctuation spectrum therefore mimics the ocean wave height spectrum with a slope of F^{-5} over a broad range of ocean spectral frequencies (F is the ocean wave frequency). The spectral density of these sound phase fluctuations decreases with increasing depth and is a measure of decreasing bubble density. See Fig. 8.4.8.

The temporal fluctuation of near-surface sound speed has been measured for several frequencies as shown in Fig. 8.4.7. At frequencies over 25 kHz, the speed is already close to the high-frequency asymptotic value. At lower frequencies, the changing speeds, which are substantially below the bubble-free speed, are evidence of temporal changes in the void fraction.

8.4.5 COLLECTIVE OSCILLATIONS AND LOW-FREQUENCY NOISE

When waves break, particularly in the case of plunging breakers, the cloud or "plume" of bubbles that is produced is a region of much reduced compressibility and slightly reduced density. The bubble cloud is capable of resonating with frequencies that depend on the shape, dimensions, average compressibility, and average density, just as single bubbles can. The theory that ambient noise in the region $f < 500$ Hz (section 6.6.1) may be partly due to collective oscillations of bubble patches (e.g., Prosperetti 1988; Carey et al. 1993) has been supported by several experiments in the laboratory and at sea (e.g., Loewen and Melville 1991).

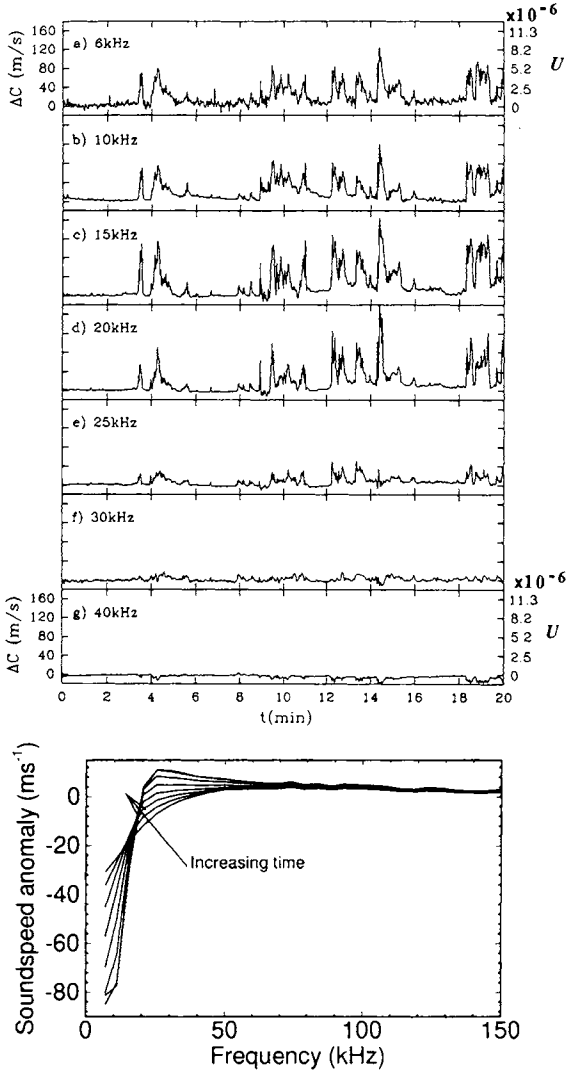

Figure 8.4.7 *Above*, Variation of sound speed with time, obtained by direct measurement at seven frequencies at depth 50 ± 10 cm during 8 m/s wind. (From Lamarre, E. and W. K. Melville, "Sound speed measurements near the sea surface," *J. Acoust. Soc. Am.* **95**, 1317–28, 1994.) For the lower frequencies, 6, 10, 15, 20, and 25 kHz, the asymptotic low speeds were as much as 120 m/s below the value for bubble-free water. The calculated void fraction is at the right. A record low sound speed of 700 m/s and void fraction of 1.6×10^{-4} was observed at 5 kHz at another time. *Below*, seven rapidly changing dispersion curves obtained by resonator technique during 30 seconds at depth 0.7 m with a 12 m/s wind measured by Farmer et al. (1997).

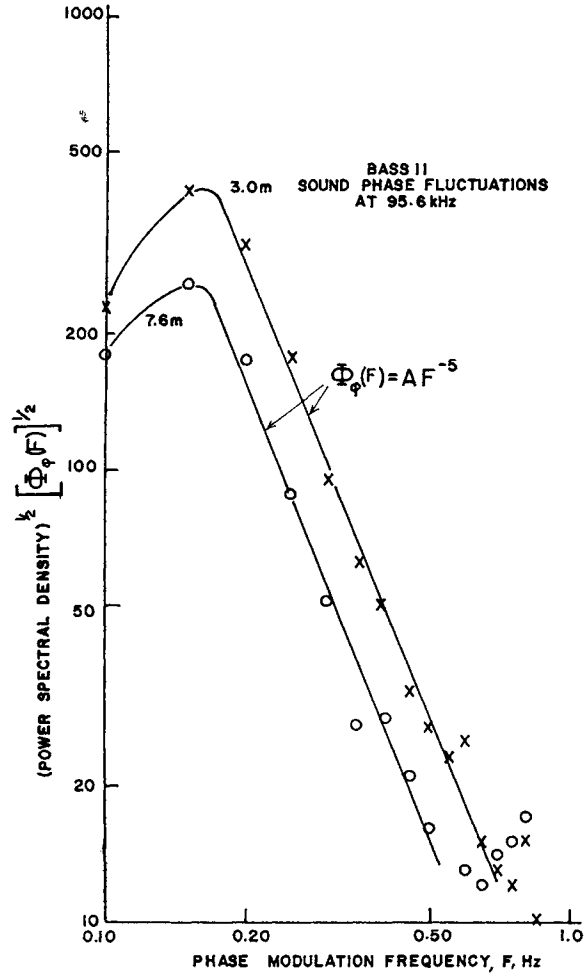

Figure 8.4.8 Frequency spectra of sound phase fluctuations for 95.6 kHz sound at two depths, 3.0 m and 7.6 m, during bubble measurements in Bass Strait, Australia. The log-log plot shows that the sound phase fluctuations with slope F^{-5} compares well with the frequency spectrum of the surface wave displacement for a fully developed sea, which also has the slope F^{-5} (see Fig. 13.1.4). These sound phase fluctuations were highly correlated with the ambient pressure change owing to passing waves, as described by $\sigma_c(f_R)$ in Fig. 8.3.2. This change of the magnitude of the sound phase spectrum with depth could be used to obtain the change of the 95.6 kHz bubble densities with depth. (From Medwin, H., "Acoustic fluctuation due to microbubbles in the near-surface ocean," *J. Acoust. Soc. Am.* **56**, 1100–04, 1974.)

8.5 Sea Surface Microbubble Production

8.5.1 BUBBLES FROM BREAKING WAVES

The ambient underwater sound that has been known since World War II as "Knudsen sea noise" and which, for 40 years, had been attributed to miscellaneous turbulent actions caused by wind at the sea surface is now known to be comprised of the damped radiations from newly formed microbubbles created by spilling breakers (Medwin and Beaky 1989; Loewen and Melville 1991). Fig. 8.5.1 shows two examples of damped pressures due to what have been poetically called "screaming infant microbubbles" created by a laboratory, freshwater-spilling breaker. The bubble radius is determined from the pulsation frequency, which is obtained by reading the zero crossings. The observed damping rate, D_b, when used in Equation 8.2.50, gives an experimental value of δ_R that is generally within 10 percent of the theoretical damping rate for fresh water, calculated from the δ_R in Fig. 8.2.3.

At the moment of their creation, the infant microbubbles are shock-excited by the sudden radial inflow of water and the simultaneous application of surface tension. They then show damped oscillations (Equation 8.2.49) with the damped pulsation frequency given by Equation 8.2.48; these single damping bubbles have been called Type A1. Sometimes there are two damping rates for a bubble; a higher rate of damping due to shape oscillations is followed by the theoretically predicted lower rate (Type A2 in Fig. 8.5.1). These relatively simple oscillations occurred in about 65 percent of the cases observed in the laboratory. Several other types (e.g., Type C in Fig 8.5.1) have been identified, as well as larger bubbles spawning smaller bubbles and bubbles that split into nearly equal parts whose radiation interfered to cause amplitude pulsations called "beats."

By placing a hydrophone close to the breaking wave, an individual oscillation can be isolated, and the bubble radius can be determined from the frequency and the damping constant, Equations 8.2.48 and 8.2.51. This was done during intermittent spilling breakers of a wind-driven laboratory freshwater surface by Medwin and Beaky (1989) and at sea by Updegraff and Anderson (1991). By using two calibrated hydrophones, the differential time of arrival can be employed to deduce the position and orientation of the bubbles, so that their axial source pressures can be calculated (Daniel 1989).

One can duplicate the 5 dB/octave slope of what is sometimes called the Knudsen "wind" noise by listening to sound from spilling breakers generated by a *plunger* with no wind at all; a rather conclusive proof that Knudsen noise is not directly attributable to wind, although it is fairly well correlated to wind speeds! (See Fig. 8.5.2.)

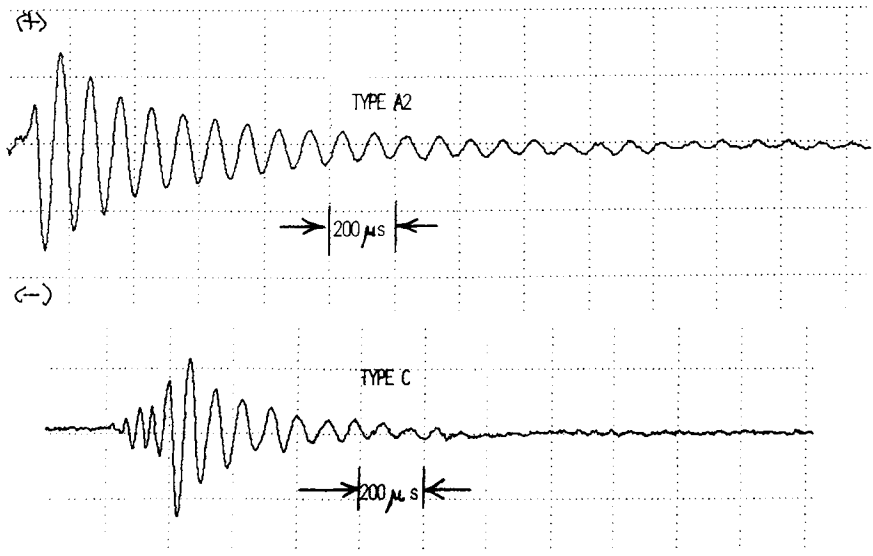

Figure 8.5.1 Damped microbubble oscillations observed in laboratory study of breaking waves. In Type A2 (*above*), the pulsation frequency was 10.4 kHz (radius 312 μm) and there were two decay rates. The fact that the first 4 cycles decayed at a higher than normal rate was explained by Longuet-Higgins (1992) as due to shape oscillations. Initial amplitude was 0.36 Pa, on axis at 1 m. There are two proposed explanations for the early part of Type C (*below*). Possibly it was a bubble that was rapidly moving away from the surface; this would initially make its amplitude increase owing to the dipole axis becoming larger, and its frequency decrease owing to its increasing distance from the surface (see section 8.2.10). Another possibility is that the bubble was initially nonspherical and that, as it became spherical, its radiation became more efficient and its frequency became lower (see section 8.2.11). Initial frequency was 25.6 kHz; final frequency, 11.5 kHz. Peak pressure on axis at 1 m, was 0.33 Pa. (From Medwin, H., and M. M. Beaky, "Bubble sources of the Knudsen sea noise spectra," *J. Acoust. Soc. Am.* **86**, 1124–30, 1989b.)

Because it is easy in the laboratory to identify the individual damped oscillations, one can actually count the bubbles within a 1 micron radius increment, produced per square meter (Medwin and Daniel 1990). (See Fig. 8.5.3.) Supported by similar work at sea, it is now clear that the Knudsen sea-noise spectrum from 500 Hz to probably 50,000 Hz is due to the cumulative sound of damped individual bubble oscillations of a large range of sizes, intermittently created by breaking waves.

In the freshwater study, breaker bubbles of radii 0.050 mm to 7.4 mm were observed with resonance frequencies 65 kHz to 440 Hz respectively (Fig. 8.5.3). Since it is very close to the surface, an oscillating bubble combines with the phase-inverted reflection from the pressure-release surface to radiate as a dipole.

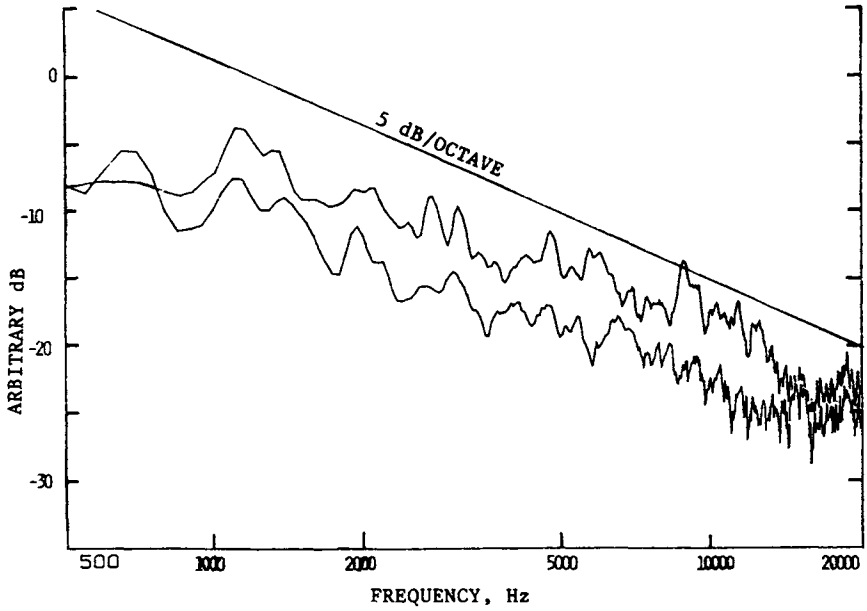

Figure 8.5.2 Laboratory breaking wave spectrum (jagged lines), compared with typical Knudsen sea-noise spectral slope 5 dB/octave. The lower graph was obtained during continuous recording, the upper graph during intermittent recording when breakers were seen over the hydrophones. Breakers were driven by a plunger source with the hydrophone 24 cm below the surface. The height of the comparison Knudsen spectrum is arbitrary. (From Medwin, H., and M. M. Beaky, "Bubble source of the Knudsen sea noise spectra," *J. Acoust. Soc. Am.* **86**, 1124–30, 1989b.)

The peak production was found to be about 6 bubbles per m^2 in a 1 micron radius increment at radius 150 mm for these small "spillers." The total gas encapsulated by the laboratory breaking wave was 23 cm^3/m^2, calculated simply from the number of bubbles and their volumes. This number is of interest to those concerned with the important question of gas exchange at the water surface.

Loewen and Melville (1991) were able to duplicate the surface sound spectrum of Fig. 8.5.2 by combining the bubble production data of Fig. 8.5.3, with the assumption that the relative bubble pulsation amplitudes (ξ/a) were 0.015 and the depth of the bubbles was 1.0 cm (Fig. 8.5.4). Furthermore, they were able to show that, with certain simplifying assumptions, the inverse problem could be solved to yield the number of bubbles in a given radius increment from the spectral sound of the surface. Although this development was for fresh water in a laboratory experiment, it shows promise as an acoustical predictor of ocean bubble production under particular conditions of the ocean surface.

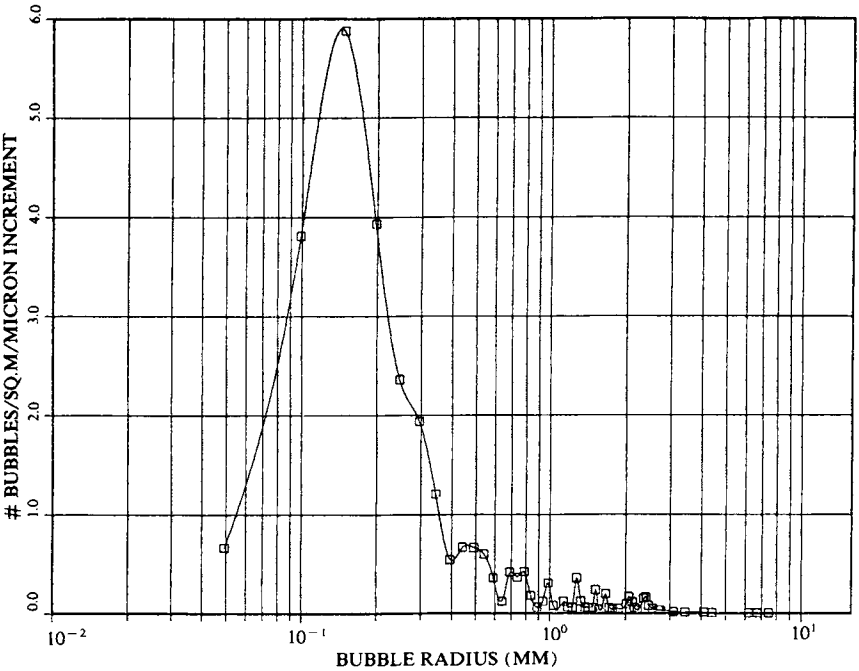

Figure 8.5.3 Bubbles produced by a spilling breaker in fresh water. About 500 bubbles were counted from 10 breakers covering surface areas of an average of 320 cm^2 for this graph. (From Medwin, H., and A. C. Daniel, Jr., "Acoustical measurements of bubble production by spilling breakers," *J. Acoust. Soc. Am.* **88**, 408–12, 1990.)

8.5.2 BUBBLES FROM RAINFALL

Precipitation is an additional source of bubbles near the sea surface. The impact of rain or hail will first create an impulse of radiation (Fig. 8.5.5). More important, this is often followed, after a few milliseconds, by the birth of one or more bubbles, which then radiate sound as described in section 8.2.9, during their damped oscillations. The newly created microbubble is generally the source of *dipole* radiation because its wavelength is generally large compared with its proximity to the ocean surface (section 4.1.3).

Raindrops of diameter 0.8 mm to 1.1 mm, which are common in light rain such as drizzle, are called "small" drops. They *always* create bubbles when they fall at normal incidence to a plane water surface. This has been proved by experiments in the laboratory (Pumphrey et al. 1989), by numerical solution of

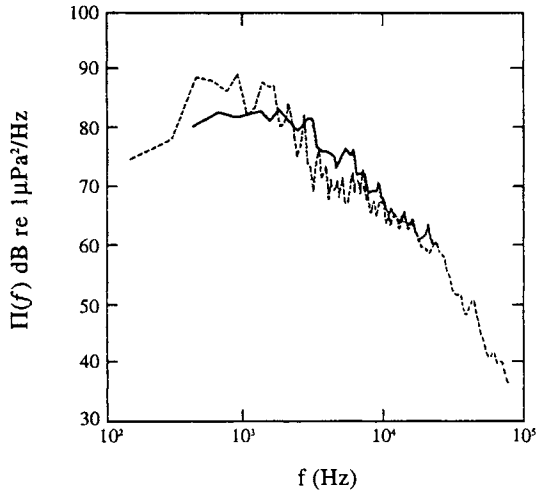

Figure 8.5.4 Comparison of a predicted sound spectrum (thick line), calculated from measurements of bubble production, with the measured laboratory sound spectrum (thin line). The model assumed that the fractional radial displacement to radius of the bubbles, ξ/a, was 0.015 and the depth of the bubbles was 1 cm. (From Loewen, M. R., and W. K. Melville, "A model of the sound generated by breaking waves," *J. Acoust. Soc. Am.* **90**, 2075–80, 1991.)

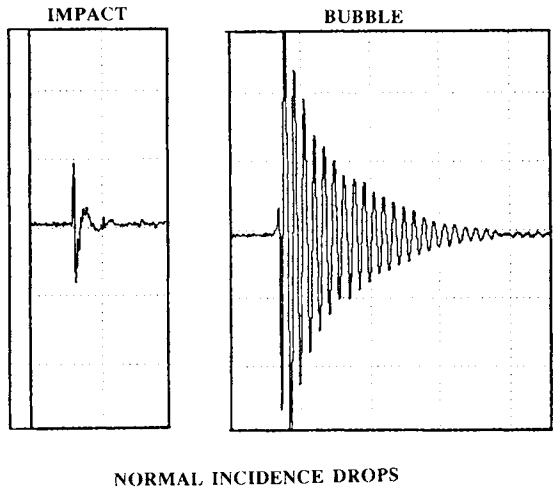

Figure 8.5.5 The pressure signal for the impact sound (*left*) and bubble sound (*right*) caused by a small water drop of diameter 0.83 mm entering the water at normal incidence and terminal velocity. The time between impact peak and bubble peak was 17.7 ms. The spacing of the time grid is 400 μs. (From Medwin, H., J. A. Nystuen, P. W. Jacobus, L. H. Ostwald, and D. E. Snyder, "The anatomy of underwater rain noise," *J. Acoust. Soc. Am.* **92**, 1613–23, 1992.)

the fluid flow (Oguz and Prosperetti 1990), and analytically by Longuet-Higgins (1990). At normal incidence, each of these very special drops creates a shock-excited transient bubble of radius approximately 220 microns, and peak pressure about 0.5 pascals (at 1 m), which rings at about 14.5 kHz for a few milliseconds until its motion is damped to an undetectable level. This is preceded by the impact sound, which has a lower amplitude and a very much lower total energy.

Fig. 8.5.5 shows the relative strengths of the impact and the bubble signals for a normally incident small raindrop. The Fourier transform of the impulse alone gives a broadband spectrum. The damped oscillation, of constant frequency, gives a narrow band spectrum with a band width determined by the bubble damping constant.

But when the angle of incidence moves away from normal, the bubble creation becomes less and less likely and the distinctive spectral peak lowers, broadens, and shifts to higher frequencies (Kurgan 1989; Medwin et al. 1990). This happens when there is a wind, or in the presence of a rough ocean surface. Consideration of the entry angle as a function of wind allows one to predict the underwater sound of rainfall during drizzle (Fig. 8.5.6).

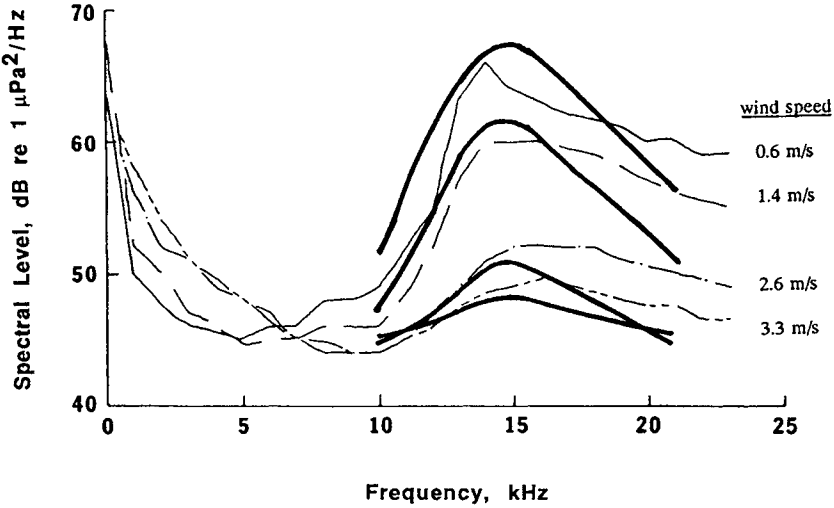

Figure 8.5.6 Light lines are underwater sound levels in a lake during different wind speeds. The heavy lines are predictions based on laboratory results for single small water drops at oblique incidence into fresh water. In the calculation, the angles of incidence were assumed to be the theoretical slopes given by the Cox and Munk relation (Equation 13.1.5) for the wind speed measured at the time of the field experiment. (From Nystuen, J. A., "An explanation of the sound generated by light rain in the presence of wind," in *Natural Physical Sources of Underwater Sound*, ed. B. R. Kerman; Kluwer Press; Dordrecht, Netherlands, pp. 659–69, 1993.) See also Medwin et al. (1992).

Laboratory experiments with single drops of diameters 0.8 mm to 4.6 mm falling at terminal velocities have established that, in all rainfalls at sea, there are potentially three ranges of drop diameters with distinctive acoustical characteristics (Snyder 1990; Jacobus 1991; Medwin et al. 1992). "Small" drops, of diameter 0.8 mm $< D <$ 1.1 mm, will produce the characteristic signal described above. "Mid-size" drops, $1.1 < D < 2.2$ mm, cause only an impact sound, with no bubbles. "Large" drops, $D > 2.2$ mm, create a complex splash that involves not only a crater but also a large, thin, hemispherical canopy of water; an upward moving jet of droplets; and a downward moving jet. Tiny droplets of water, "hydrosols," leave from points of the coronet before the canopy closes and when it shatters. These jets and droplets produce bubbles, which then radiate as dipoles.

Despite the complexity of the splash from a large drop, one can propose a "standard" spectrum of sound for each diameter. The peak of acoustic spectral

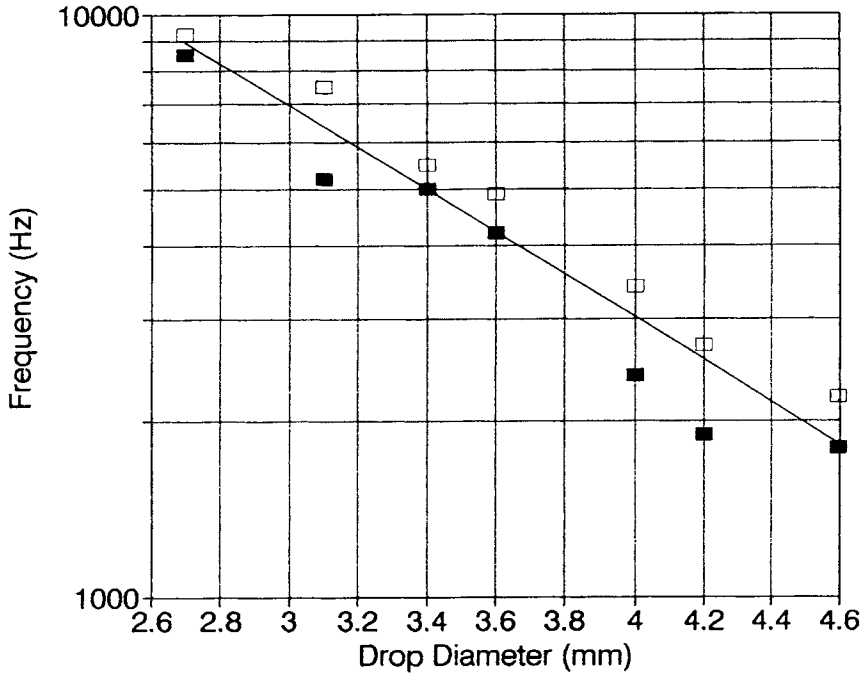

Figure 8.5.7 Frequency dependence of the peak of the underwater sound spectral density for large bubbles created by large water drops falling into fresh water. Closed squares, Snyder (1990); open squares, Jacobus (1991). (From Medwin, H., J. A. Nystuen, P. W. Jacobus, L. H. Ostwald, and D. E. Snyder, "The anatomy of underwater rain noise," *J. Acoust. Soc. Am.* **92**, 1613–23, 1992.)

density is a function of the drop diameter (Fig. 8.5.7). A dependence on salinity, temperature, and water surface slope has been demonstrated by Jacobus (1991) and Miller (1992).

The shape of the underwater sound spectrum provides a characterization of the type of cloud, stratiform or cumuliform, from which the rain came. The meteorological characterization is not really mysterious: stratus are low clouds that produce predominantly small drops of rain, "drizzle." These cause small oscillating bubbles and a narrow spectrum with a predominant peak around 15 kHz. Cumulonimbus clouds have strong vertical air currents that allow raindrops to grow to large diameters before they fall into the sea, where they create larger bubbles and radiate a broad sound spectrum.

One can obtain the drop size distribution (and total rainfall rate) by inversion from the spectrum of the underwater sound (Nystuen 1996).

8.6 Bubbles in Sediments

By the 1950s, seismic exploration geophysicists had extended their activities to offshore and lakes. In some areas, instead of getting the usual reflection records that showed subsurface structure, the records "rang like a bell" (Werth, Liu, and Trorey 1959; Backus 1959; and Levin 1962). Levin's extensive measurements in Lake Maracaibo, Venezuela, showed that there was near-perfect reflection off a pressure-release bubbly layer at the ocean floor. Independently, signal theorists in competing laboratories described the ringing as due to the upward traveling reflection signals being multiply reflected in the water layer (see Backus 1959). Clay (1990) gives an elementary treatment of optimum methods used to sort out the signal. Sonar detection of bubbles rising through the water column (McCartney and Bary 1965) awakened geophysicists and acousticians to the fact that there are significant inclusions of bubbles in ocean and lake sediments. Several thousand gassy areas have now been identified in the sediments of the Gulf of Mexico, Southern California coastal regions, and the Bering Sea (Anderson and Bryant 1989); undoubtedly, many others will be found as geophysical prospecting continues in the oceans of the world.

The acoustical consequences of bubbly sediments are substantial: the sound velocity can be significantly lower than for the water medium, and even more divergent from the expected sediment velocity; the attenuation, principally owing to scattering through the sediment, can be great enough to prevent sound penetration in geophysical oil exploration (Fig. 8.6.1).

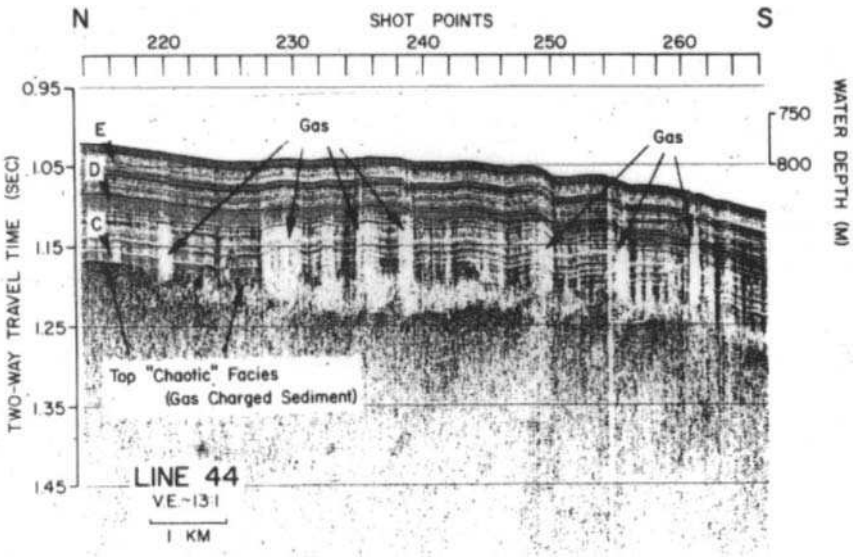

Figure 8.6.1 Minisparker profile of the Texas continental slope. The figure shows regions where the backscatter is "wiped out," as well as reflection terminations and "acoustically turbid" zones, where there is reverberation owing to multiple scatter from bubbles. (From Anderson A. L. and W. R. Bryant, "Gassy sediment occurrence and properties: Northern Gulf of Mexico," *Geo-Marine Letters*, **10**, 209–10, 1990.)

The smaller sediment bubbles (radii less than 1 mm) are expected to be spheroidal. The larger bubbles have been identified by X-ray–computed tomography of enclosed cores brought to the surface without change of original pressure (Orsi et al. 1994). The X-ray–computed tomography technique is sensitive to bulk density and has a length resolution of 1 mm. The larger bubble shapes are described as similar to a "coin on edge" (Fig. 8.6.2), so they are approximated as prolate spheroids in theoretical calculations of the acoustic effect. Gas fractions as great as 4.5×10^{-2} have been measured by this means.

In lake sediments, the predominent gas is methane. At sea, most of the bubbles analyzed appear to be due to anaerobic bacteria acting on organic matter to release predominantly hydrogen sulfide at the shallower depths into the sediment and methane at depths greater than a few decimeters. Another significant source of sea-floor bubbles is the natural "cracking" of organic material buried to great depths (and thereby great temperatures); these travel from great depths to the sediment via sea-floor faults. These "thermogenic" sources of methane are of great interest to the petroleum industry. The acoustical evidence of gas pockets is a function of sound frequency. In accordance with the Rayleigh law of scattering,

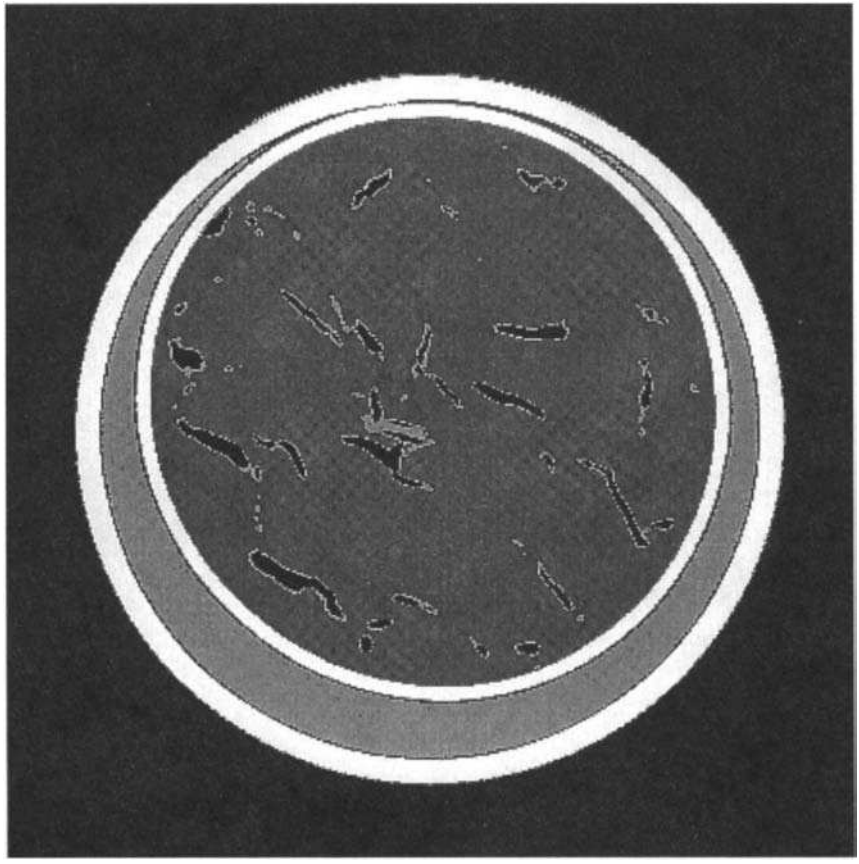

Figure 8.6.2 Horizontal slice through a core from Eckernfoerde Bay, Germany. The bubbles were at depth 38 cm. From Abegg et al. (1994).

lower frequencies do not backscatter from the smaller (λ) bubbles. Penetration to greater depths is achieved because of the lesser attenuation owing to both scatter and absorption.

The definitive papers by Anderson and Hampton (1980a, 1980b) lay out the reason for bubble formation and the effects on sound propagation. For simplicity, one starts with the assumption that the bubble is spherical and the sediment is a slurry of particles in water. Bubble oscillations in water-loaded sediment differ from those in free water by the added visco-elastic forces due to the sediment frame. This produces an increased stiffness term and an added dissipation term, represented by a complex dynamic shear modulus. The real part of the dynamic

shear modulus affects the resonance frequency of the bubble (compared with free water), and the imaginary part enters into the bubble damping constant. (The dynamic shear modulus of an elastic body is the ratio of the shearing stress to the shearing strain; the shear modulus is complex when there is a phase relation between the applied stress and the resulting strain.) The derivation of the equations is in Weston (1967).

The equation for the resonance frequency, (compare with Equation 8.2.27) given by Lyons et al. (1995) may be written

$$f_{Rs} = \frac{1}{2\pi a}\sqrt{\frac{(3\gamma b \beta p_A) + 4G}{\rho_A}} \tag{8.6.1}$$

where f_{Rs} is the resonance frequency for a bubble in sediment and G is the real part of the complex dynamic shear modulus $G^* = G + iG'$.

The other constants were defined in section 8.2, except that ρ_A, the ambient density, is here the density of the sediment.

In general, the sediment shear modulus term ($4G$) in the numerator is greater than the bubble gas elastic restoring term. As a result, the resonance frequency of the bubble in sediment is greater than for the equivalent bubble in water.

Equation 8.6.1 must now be corrected for the eccentricity of the generally ellipsoidal bubble shapes in sediments. A correction scheme that depends on the relative area to volume of the elllipsoid was introduced by Weston (1967) and applied by Lyons et al. (1995) for the type of bubbles identified by X-ray–computed tomography in sediments (e.g., as in Fig. 8.6.2).

The damping constant for a pulsating bubble in a water-filled sediment, δ_s, which is dependent on the imaginary component of the shear modulus, is much larger than the viscous term, δ_v, for a bubble in water (compare with Equation 8.2.29). It thereby causes a wider resonance curve (lower Q) than for the equivalent bubble in water. The damping constant is given as

$$\delta_f = \frac{4G'}{\rho_A \omega^2 a^2} \tag{8.6.2}$$

By using measurements of the density and character of the bubbles observed by X-ray–computed tomography, Lyons et al. (1996) have been able to explain the detailed reverberation and attenuation that is observed in sonar backscatter from a bubbly sediment such as in Fig. 8.6.1.

Problems

8.1.1 Sometimes it is assumed that, when insonified by a plane wave, the bubble scatter directivity at $ka = 1$ is approximately omnidirectional. Compare the scattering cross section for the actual directivity at $ka = 1$ (Fig. 8.1.1) with the omnidirectional scattering cross section to see what the error is in this assumption. Hint: Do the integration numerically, using axially symmetric spherical coordinates.

8.1.2 Calculate the directivity pattern, as in Fig. 8.1.1, for $ka = 15$.

8.1.3 Integrate the directivity patterns of $ka = 2$, 5, 10, and 20 to find the total scattering cross section in each case. Compare with $ka = 1$ and $ka = 0.5$, which are closer to omnidirectional.

8.1.4 Use the lumped constant approach to calculate the $m = 0$ radial, cylindrical pulsation frequency for an air-filled cylinder. Hint: The cylindrically radiated pressure is inversely proportional to $r^{1/2}$, and the derivation is done in terms of the mass per unit length and the stiffness per unit length.

8.1.5 This problem uses Anderson's solution for the fluid sphere in a fluid medium (section 7.5.3). a) From examination of the scattering length for a sphere, show why $C_m = 0$ gives the local maxima of $|\mathcal{L}|$ due to resonances. b) Show why the zeroth mode is spherically symmetric and the others are not. c) For the small ka region and $m = 0$, one can use $|ka| \ll 1$ approximations to develop a relatively simple algebraic expression for calculations of the scattering length. Use small ka expansions of the spherical Bessel functions $j_0(x)$, $n_0(x)$, $j_1(x)$, and $n_1(x)$ to derive small ka expressions for C_0 and $\mathcal{L}$ and obtain

$$C_0 \approx -\frac{1 - 3gh^2/(ka)^2}{ka} \quad \text{and} \quad \omega_b a \equiv \sqrt{3gh^2}$$

and

$$\mathcal{L} \approx \frac{ia}{ka + i\left[\left(\frac{\omega_b}{\omega}\right)^2 - 1\right]} = \frac{a}{\left[\left(\frac{\omega_b}{\omega}\right)^2 - 1\right] - ika} \quad \text{for} \quad ka < 0.1$$

Hints: $k_1 = k/h, j_0' = -j_1$, and $n_0' = -n_1$. d) The adiabatic sound speed in a gas is $c = (\gamma P/\rho)^{1/2}$, where γ is the the ratio of the specific heats. Express ω_b using the adiabatic sound speed. e) What limits the peak value of $\mathcal{L}$? f) Compare a graph of this approximation for $\mathcal{L}$ with the scattering from a gas sphere shown in

Figs. 8.1.1 and 8.1.2. What are the upper limits of ka for the error of $\mathcal{L}$ in backscatter and directional scattered amplitude to be less than 5 percent?

Section 8.2

8.2.1 Assume that surface tension is a significant restoring force, and recalculate the stiffness and the resonance frequency. Plot the effect as a function of bubble radius.

8.2.2 How will a bubble skin of detritus affect the resonance frequency?

8.2.3 Plot the dependence of bubble breathing frequency on depth. Calculate the correction needed for resonance radius, when a constant frequency is used at various depths.

8.2.4 Plot d/b as a function of frequency. Identify the value when $f = f_b$.

8.2.5 Plot β as a function of frequency. Identify the value when $f = f_b$.

8.2.6 Calculate the correction to the relative backscatter length at resonance in Fig. 8.1.2, when the complete damping constant δ_R is used rather than only the reradiation damping δ_{R_l} in the figure.

8.2.7 Plot the dependence of modulus of decay, T_e, on bubble resonance frequency, f_b, for the range 1 kHz to 1 mHz.

8.2.8 Use Equations 8.2.52 and 8.2.53 to plot the dependence of resonance frequency proximity to the ocean surface.

8.2.9 Compare the peak backscattering length at resonance, given in Fig. 8.1.2, with the correct value obtained by considering viscous and thermal damping. Make the comparison for the three sample frequencies 1 kHz, 10 kHz, and 100 kHz.

Section 8.3

8.3.1 Equations 8.3.7 and 8.3.8 give the value of [tips] for a collection of small bubbles. What is the equation for the relative backscattered energy of this "reverberation"?

8.3.2 Fig. 8.3.1 shows a graphical calculation of the effect of an a^{-4} bubble distribution. Complete the calculation by determining S_e for the example given. Warning: Use a linear graph.

8.3.3 Redraw Fig. 8.3.1 for the case of 100 kHz insonification. Comment.

8.3.4 Redraw Fig. 8.3.1 for 50 kHz in an ocean where $n(a)\,da$ varies as a^{-3}. Comment.

8.3.5 Estimate the void fraction implied by Fig. 8.4.6 (left).

8.3.6 Use the low-frequency data in Fig 8.4.8 to estimate the void fractions in the experiment.

Chapter 9 | Biomass Echoes, Reverberation, and Scattering Models

9.1 Introduction to Bioacoustics 348
9.2 Sound Backscattered by a Fish: Echoes 350
9.3 Sound Backscattered by Many Bodies: Reverberation 353
9.3.1 Randomly Spaced Objects in a Directional Beam 354
9.3.2 Time-Integral-Pressure-Squared Calculations for Many Scatterers 357
9.3.3 Volume Backscattering Coefficient 358
9.3.4 Scattering Layers 361
9.4 Variability of Fish Structure and Sound Backscatter 363
9.4.1 Physical Structures: X-Rays and High-Frequency Sound Scans 363
9.4.2 Echo Statistics: Rician, Rayleigh, and Extremal 364
9.5 Acoustical Models of Fish 372
9.5.1 Anatomical-Acoustical Models 372
9.5.2 HK Acoustic-Scattering Models for Swimbladder Fish ($ka > 1$) 373
9.5.3 Comparisons of High-Frequency Acoustical Models and Data 381
9.5.4 Low-Frequency Swimbladder Resonance Models 384
9.6 Sound Backscattered by Zooplankton 391
9.6.1 HK Acoustical Models of Zooplankton 392
9.6.2 Bent-Cylinder Acoustical Models 396
9.6.3 Scattering Amplitudes of Live Shrimp 398
9.7 Bubble-Carrying Plankton 401
9.8 Allometric Expressions for Zooplankton 401

9.1 Introduction to Bioacoustics

Marine biologists study ecological systems, food chains, and the dynamics of marine populations. They attempt to describe the distributions, sizes, and species of the animals and plants, and the interrelationships of these to the ocean environment. The traditional biological pyramid shows a succession of predators and prey; herbivores at the bottom of the food chain eat the phytoplankton and plants; most animals at higher levels are carnivores. The marine *bioacoustical* pyramid, Fig. 9.1.1, is an enhanced version of the traditional marine *biological* pyramid. It includes information about the effective sound frequencies that may be used for detection of the various levels of marine life, based on the backscatter theories developed in Chapters 7 and 8. The right side of the marine bioacoustical pyramid, Fig. 9.1.1, allows us to interpret the distribution of the biomass in terms of the effective frequencies for detection of the impedance mismatch of the body and its swimbladder. The left side of the bioacoustical pyramid lists the critical

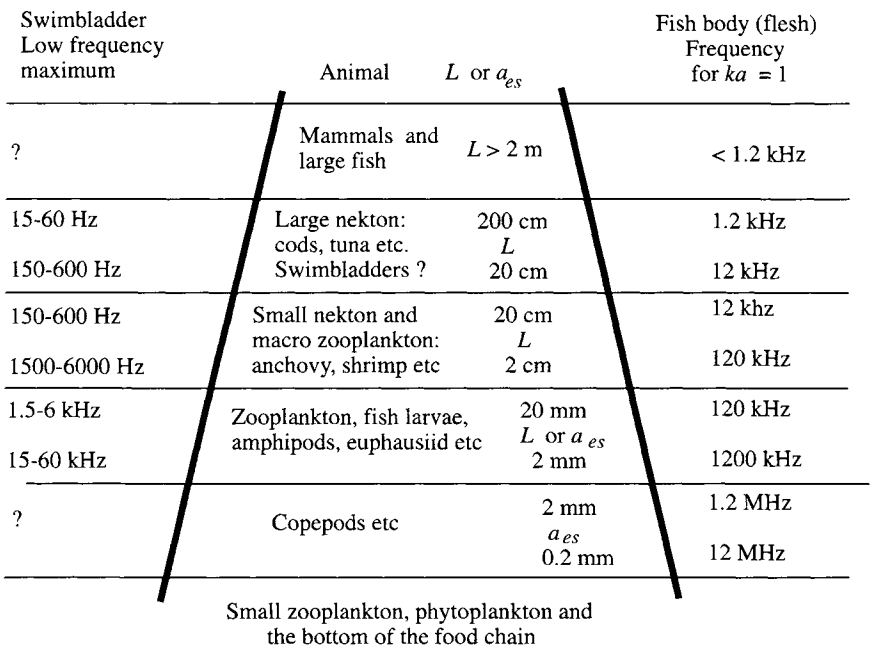

Figure 9.1.1 The marine bioacoustical pyramid, showing the levels of animal lengths or equivalent spherical radius (*esr*) and the effective sound frequencies for their detection. Within each level, two frequency bands are given. The left side shows the radial resonance of an equivalent spherical bubble at the surface; the range of values represents different swimbladder shapes and different fractions of the fish volume. The right side gives the frequencies for $ka = 1$, where a is an equivalent cylindrical radius of the fish body (a_{ec}) or equivalent spherical radius (a_{es}) of small zooplankton. The model fish parameters are calculated as fractions of the actual fish length, L: fish equivalent spherical radius, $a_{es} = 0.1L$, swimbladder equivalent cylindrical radius, $a_{ec} = 0.04L$; swimbladder length $= 0.3L$. Also, swimbladdder volume = 5 percent of fish body volume.

frequencies that may be used for effective detection of resonant bubble-carrying bodies.

Traditionally, marine biologists have used nets to sample fish and plankton. Their purposes have been to determine who is there, and how big or old they are. Nets are biological tools that have become very sophisticated. They may include remote temperature sensing, remote video cameras, and remote control of multiple-opening nets. But there are problems using nets as primary sampling tools. For example, some animals can swim out of the way, and this "net avoidance" biases surveys. Some nets destroy the very plankton that they attempt to recover.

Collaborations between marine biologists and acousticians have had profound effects on the way marine biologists work and visualize their data. These collaborations have changed the bulk of sonar applications from military to civil. There are more sonars on sports and commercial fishing boats than there are on naval vessels.

Traditionally, bioacousticians make sonar transects and measure backscatter. A qualitative interpretation based on the bioacoustical pyramid is that high-frequency sonar transects are sensitive to the distributions of small animals, whereas low-frequency transects show the large animals. But quantitative interpretation of sonar data requires a more detailed knowledge of the scattering of sound waves by animals. Laboratory studies of the scattering of sound by single animals in this chapter are bridges that take us from mere volume scattering measurements to the goal of size and density distributions obtained by inverse methods in Chapter 10. Acoustical oceanography brings new tools to marine biology and limnology and provides challenging problems for acousticians.

Although we use the terms "marine biology" and "oceanography," we mean to include studies in "fresh water" and "limnology." To biologists, the salt water (marine) environment supports life forms that are different from those in freshwater lakes and rivers. To acousticians, the main differences between salty and fresh water are in the physical parameters that affect backscatter: sound absorption, sound speed, and water density.

As physicists and engineers studied the scattering of sound by fish, they created simple acoustical models to "explain" the results of measurements. Their "fish" were constructed of simple elements, spherical and cylindrical bodies and swimbladders, and assemblages of both. A minimum number of elements were used to match a set of data.

9.2 Sound Backscattered by a Fish: Echoes

Sonar transducers can be pointed in any direction and placed at any depth. The fish or animal can have any orientation relative to the sonar beam as sketched in Fig. 9.2.1. The animal can be in any part of the beam. For a consistent geometry, we use vertically downward transducers for most illustrations because almost all bioacoustic surveys use them, and the data analysis is the same for transducers that point in any direction.

The uses of sonars to measure fish echoes are sketched in Fig. 9.2.2. The sonar transmits a ping that has the carrier frequency f_c. The fish is at the range R, angle

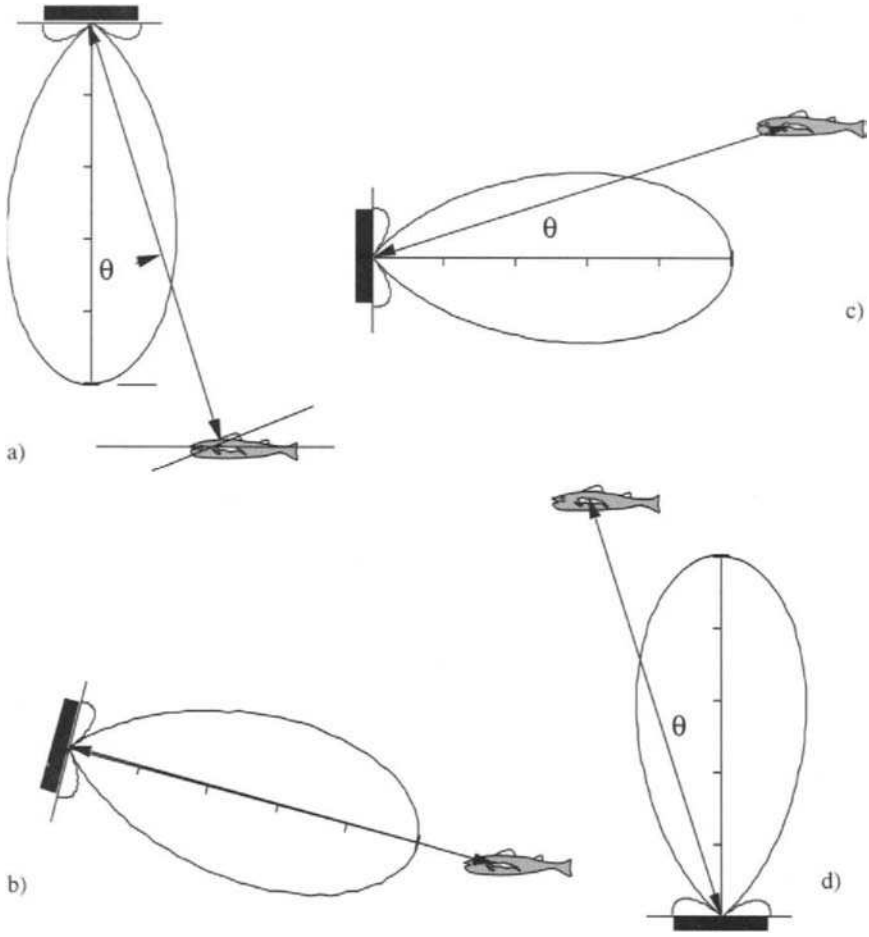

Figure 9.2.1 Sonar transducer orientations. a) Data taken from moving boats generally use downward-looking sonars. The typical frequency range is 10 to 400 kHz. b) Sonar vertical casts are made by lowering a horizontally pointed transducer from a stopped boat. Usually high-frequency instruments (0.1 to 10 MHz) are used. The orientations of fish range from broadside to head and tail aspects. c) Fixed transducers are pointed in various directions to monitor fish swimming in rivers. d) Upward-pointing sonars can monitor fish near the surface.

θ, and directivity D. Assume that the fish of length L is completely within the first Fresnel zone (section 2.6.6):

$$L < r_1 = \sqrt{R\lambda/2} \tag{9.2.1}$$

Then the local wavefront at the fish is effectively a plane wave. From Chapter 4,

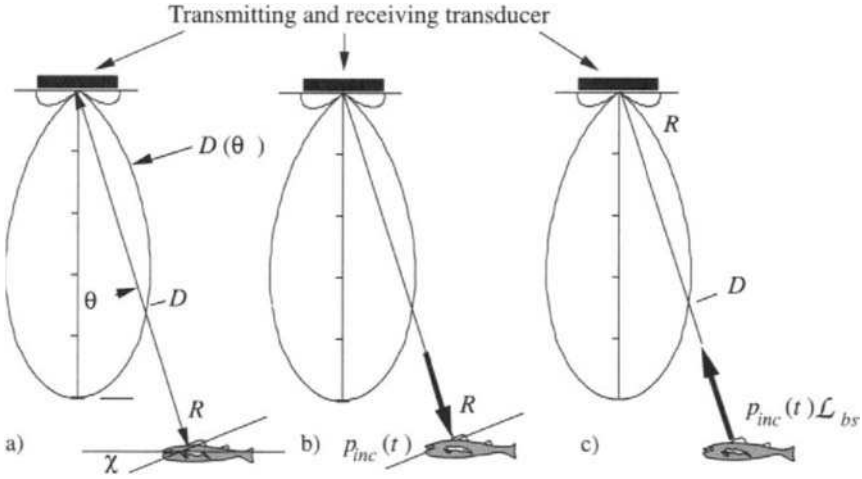

Figure 9.2.2 Scattering of sound by a fish. a) Fish at angle θ, directivity D in a sonar beam. b) Sound pressure incident on a fish. c) Fish as a source of scattered sound pressure. The sourcelet radiates a pressure proportional to $\mathcal{L}_{bs}$ back to the transducer.

the incident sound pressure at the fish is

$$p_{inc}(t) = D \frac{p_0(t - R/c)R_0}{R} 10^{-\alpha R/20} \tag{9.2.2}$$

The scattered sound pressure at the fish, the "echo," is proportional to the incident sound pressure and to the *acoustical backscattering length* of the fish, $\mathcal{L}_{bs}$ (section 7.1.1), which is a function of frequency. The backscattered sound radiates as if the fish is a sound source. Again the fish is at range R and in the beam response D of the receiving transducer. At large ranges the scatterer reradiates spherically, and the backscattered pressure that is received from the fish is

$$p_{scat}(t) = D \frac{p_{inc}(t - R/c)\mathcal{L}_{bs}}{R} 10^{-\alpha R/20} \tag{9.2.3}$$

Use Equation 9.2.2 to replace the incident sound pressure and get

$$p_{scat}(t) = D^2 \frac{p_0(t - 2R/c)\mathcal{L}_{bs} R_0}{R^2} 10^{-\alpha R/10} \tag{9.2.4}$$

Scattering lengths may be measured experimentally or calculated theoretically. Scattering cross sections are described in section 7.1.2. We are interested in the backscattering cross section,

$$\sigma_{bs} = |\mathcal{L}_{bs}|^2 \tag{9.2.5}$$

The backscattering length and backscattering cross section depend on the incident angle at the fish, as well as the sound frequency.

9.3 Sound Backscattered by Many Bodies: Reverberation

The scattering by randomly placed objects in a sonar beam is analyzed in the same way as the scattering by an ensemble of bubbles. In section 8.3.1 we assumed that the relative positions of the bubbles with respect to one another and with respect to the transducers change from ping to ping. The spatial changes are assumed to be large enough to make the relative phases change by several π. In laboratory studies, it is a mistake to place objects at random locations and make repeated echo measurements while not letting the relative positions change enough for the cross terms to tend to zero. Foote (1983) studied the linearity and addition theorems for fisheries acoustics. The ratio (fish length)/λ ranged from 7 to 21. His experiments showed that: 1) the backscattered pressures from fish add linearly; 2) backscattering acoustic cross sections of live free-swimming fish can be determined from measurements on anesthetized samples; and 3) time integral-echo-squared processing is valid for ensembles of "similar" fish. The acoustically estimated and true fish densities are the same. This is important because operations on echoes from simple "objects" that will be developed here will work for the scattering from ensembles of complicated objects such as fish and zooplankton.

Based on laboratory research, and to keep the analysis from being too cumbersome, the following characteristics of the objects are assumed:

(1) Backscatter is essentially the same for the object in any part of the transducer beam.

(2) The backscatter from an object has a broad directional pattern toward the transducer.

(3) The backscattering cross sections of individuals are near the mean of all backscattering cross sections for objects in the ensemble.

(4) For the narrow frequency bandwidth of a sonar ping, the frequency dependence of the backscattering lengths is constant, and the incident ping is scattered back with nearly the same wave form.

(5) Multiple scattering and interactions between objects are ignored.

9.3.1 RANDOMLY SPACED OBJECTS IN A DIRECTIONAL BEAM

The instantaneous acoustic pressure of the backscattering from many objects is the algebraic sum of the time domain pressures from the separate objects. This time-dependent quantity is called "reverberation." Again, the analysis is given for colocated transmitting and receiving transducers. The geometry for a typical sonar measurement of the sound scattered from a volume containing scattering objects is shown in Fig. 9.3.1 for two different transducer directivity patterns. The back radiation from the transducer is assumed to be negligible and all radiation goes into the lower half space. In our usage, the reference omnidirectional "half-space" responses are $D_1 = 1$ and $D_2 = 1$. The location of the ith object in the directional responses of the two transducer beams is indicated by D_{1i} and D_{2i}.

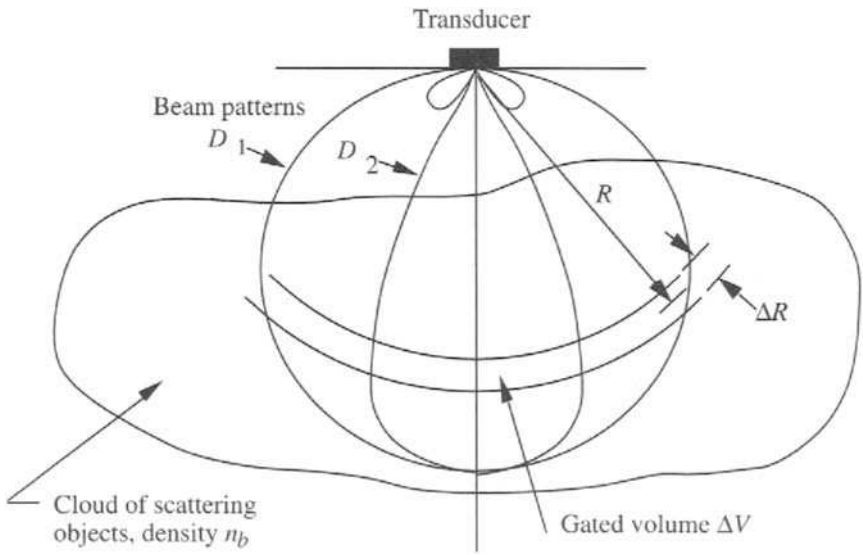

Figure 9.3.1 Scatter from many objects within two beams of different directivity. A time gate in the receiver selects the echoes from the "gated volume." The time-gated volumes are the same for both the senders and receivers. For example, the transmission is in D_1 and the reception is in D_2.

The many-object problem requires summations of the time integral pressure squared [*tips*] described in section 3.1.3. Four simplifying assumptions are used to reduce the expressions to something that can be "explained." First, within a population of scattering objects, the objects are nearly alike and can be replaced by a population of average objects. Second, the objects are uniformly and randomly distributed within layers of the selected volume. Third, the duration of the ping t_d is very small compared with the time gate that selects the shell thickness of the scattering volume, ΔR. And fourth, the attenuation of sonar energy within the ensemble can be ignored because the density of objects is small. Extinction effects *are* observed in dense schools of fish (Foote 1983).

The scattered pressure (Equation 9.2.4) is for a single object. For many objects, we label the scattered pressure of the ith object $p_{i,\mathrm{scat}}(t)$. The ith object is at the range R_i, and the directional responses of the sonar beams are D_{1i} and D_{2i}. The sum is over all objects within the gated volume:

$$p_{\Sigma}(t) = \sum_{i=0}^{N-1} p_{i,scat}(t) \tag{9.3.1}$$

where the subscript Σ means sum of scattered pressures over all objects.

Numerical scattering simulations show the meaning of Equation 9.3.1. Assume many objects are placed at random ranges in a layer and at random map locations in the sonar beam. The properties of the objects are described in the introduction to this section. Fig. 9.3.2a shows the travel times from each randomly spaced scatterer. Each echo is shown as being an impulse for this illustration. The "thickness" of the layer is 1 ms. The map locations of the scatterers are at different angles in the sonar beam. The amplitudes of the echoes are the responses for locations of the objects in the sonar beams. Fig. 9.3.2b shows the echo amplitudes for an omnidirectional source and directional receiver, and Fig. 9.3.2c shows the echo amplitudes for a directional source and directional receiver. The directionality of the transducers increases the relative number of small echoes and decreases the relative number of large echoes. The different combinations of directionality have strong effects on the amplitudes of the echoes from individual objects.

Fig. 9.3.3 is a more realistic example of the simulation of scattered pressures because we use a short ping for the signal. The signals shown are the result of convolving the impulse signals shown in Fig. 9.3.2 with a short ping. Again the echo amplitudes have not been corrected for the different ranges. Echoes from individual objects overlap and usually cannot be identified. (Note, however, the

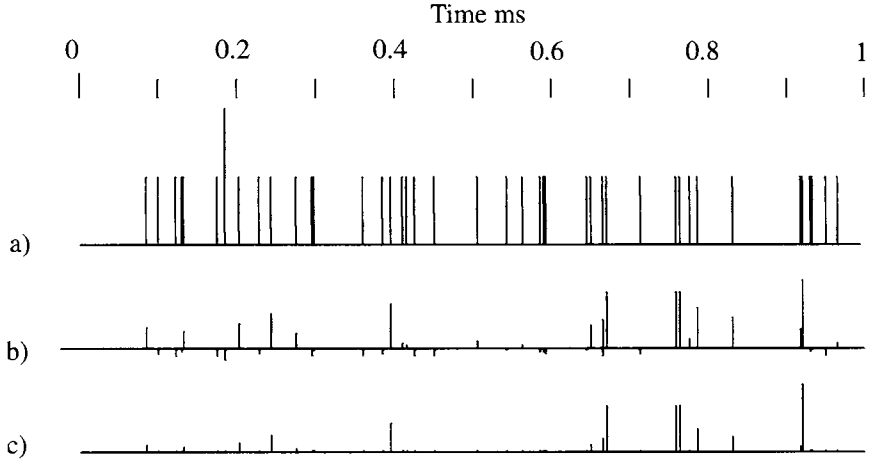

Figure 9.3.2 Scattered delta function impulse signals for different directional responses of source and receiver. The theoretical signals are for 50 objects randomly located in a layer within the source and receiver beams. The gate open duration is 1 ms. The objects are identical. The locations of the objects are the same for each trial. For simplicity, the display amplitudes are the same (although the different ranges would actually produce different amplitudes). The time increment is 0.001 ms. a) Omnidirectional (in half-space) source and receiver. b) Omnidirectional (in half-space) source and directional receiver ($ka = 5$). c) Directional source and directional receiver.

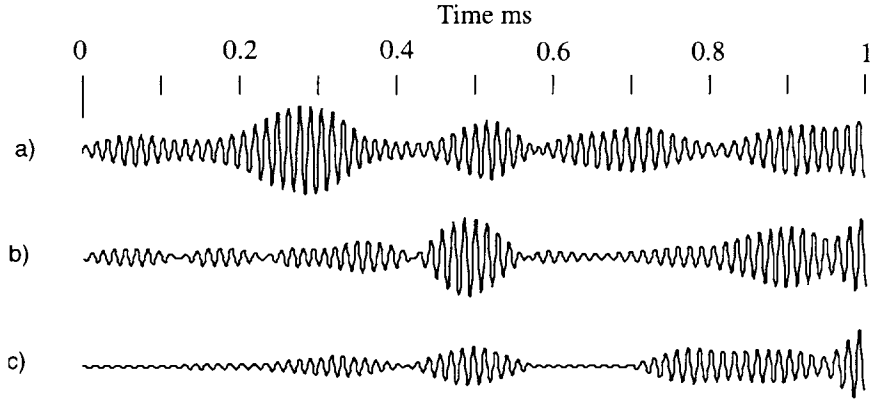

Figure 9.3.3 Scattered ping signals for randomly placed objects for different source and receiver directivities. The impulse responses for this figure are the same as in Fig. 9.3.2. The gate duration is 1 ms. The objects are identical. The ping has frequency 70 kHz and duration 0.2 ms. Note that the arrivals from individual objects overlap. The time increment is 0.001 ms. a) Omnidirectional (in half-space) source and omnidirectional receiver with the presentation reduced by a factor of four. b) Omnidirectional (in half-space) source and directional receiver. c) Directional source and directional receiver.

somewhat isolated pulse at 0.5 ms.) The phase differences, or times of arrival, can no longer be sorted out deterministically, and one must resort to time integral pressure squared calculations [*tips*] to specify the assemblage of scatterers. The development will show that the backscattering cross section $\sigma_{bs} = |\mathcal{L}_{bs}|^2$ is an appropriate descriptor. In fisheries acoustics, [*tips*] processing of an echo is called *echo integration.*

9.3.2 *TIME-INTEGRAL-PRESSURE-SQUARED CALCULATIONS FOR MANY SCATTERERS*

The time integral pressure squared of the gated volume (subscript GV) within opening time $t_2 - t_1$ is a useful measure of the scattering when echoes overlap:

$$[tips]_{GV} = \int_{t_1}^{t_2} |p_\Sigma(t)|^2 \, dt = \sum_{i=0}^{N-1} \int_{t_1}^{t_2} |p_{i,scat}(t)|^2 \, dt + \sum_{i \neq j} \sum \int_{t_1}^{t_2} p_{i,scat}(t) p_{j,scat}(t) \, dt \tag{9.3.2}$$

The left side of Equation 9.3.2 is of the form

$$[tips]_{GV} \equiv \int_{t_1}^{t_2} |p_\Sigma(t)|^2 \, dt = \text{sum of squares} + \text{sum of cross terms} \quad \text{for} \quad t_1 \leq 2R_i/c \leq t_2 \tag{9.3.3}$$

The summations on i and j are for objects within the time-gated volume. The first summation is the sum of the squares of echoes $[p_{i,\text{scat}}(t)]^2$, and all are positive. The double summation for the cross terms contains the products of the pressures $[p_{i,\text{scat}}(t)p_{j,\text{scat}}(t)]$ scattered by a pair of objects at R_i and R_j. These cross products are positive and negative. The first summation is much greater than the contributions of the cross terms. The effect of the cross terms is to cause fluctuations of the $[tips]_{GV}$. In experimental measurements of time integral pressure squared, one averages repeated measurements as the ship moves relative to an ensemble of objects, and this reduces the effects of fluctuations by making the ensemble larger. Although cross terms in the double summation are always present, from now on we ignore them.

9.3.3 VOLUME BACKSCATTERING COEFFICIENT

The $p_{\text{scat}}(t)$ given in Equation 9.2.4 allows one to compute the time integral pressure squared in Equation 9.3.2. Using the simplification that $p(t)_{\text{inc}}$ is a simple incident ping of duration t_d, source pressure p_0 at range R_0, the result is

$$[tips]_{GV} = R_0^2 \sum_{i=0}^{N-1} \frac{D_{1i}^2 D_{2i}^2 10^{-\alpha R_i/5}}{R_i^4} |\mathcal{L}_{bsi}(f)|^2 \int_0^{t_d} |p_0(t)|^2 dt \tag{9.3.4}$$

The time integral pressure squared of the source presssure $p_0(t)$ is *defined* as

$$[tips]_0 \equiv \int_0^{t_d} |p_0(t)|^2 dt \tag{9.3.5}$$

where t_d is the duration of the ping.

Let the $|\mathcal{L}_{bsi}|^2$ be replaced by its average $\langle|\mathcal{L}_{bs}|^2\rangle = \langle\sigma_{bs}\rangle$. Also, let the integral in Equation 9.3.4 be replaced by Equation 9.3.5. Then Equation 9.3.4 becomes

$$[tips]_{GV} \approx R_0^2 \langle\sigma_{bs}\rangle [tips]_0 \sum_{i=0}^{N-1} \frac{D_{1i}^2 D_{2i}^2 10^{-\alpha R_i/5}}{R_i^4} \tag{9.3.6}$$

where $\langle\sigma_{bs}\rangle = \langle|\mathcal{L}_{bs}|^2\rangle$. Now assume that the fish or scattering bodies are uniformly distributed with density n_b in the gated volume,

$$n_b = \text{number of scattering objects/m}^3 \tag{9.3.7}$$

Within the gated volume, Fig. 9.3.1, the R_i can be replaced by their mean range R. For the thin shell, the mean range is

$$R = (R_1 + R_2)/2 \tag{9.3.8}$$

and the shell thickness is

$$\Delta R = (R_2 - R_1) = (t_2 - t_1)c/2, \quad \Delta R << R \tag{9.3.9}$$

where

$$t_1 = 2R_1/c, \; t_2 = 2R_2/c \tag{9.3.10}$$

The summation over the positions of the objects in Equation 9.3.6 counts the number of objects in the insonified shell and weights the amplitudes. The dependence on the beam patterns is gathered into an expression called the *integrated beam pattern* Ψ_D (see also section 4.5 and Equation 4.5.4),

$$\psi_D \equiv \int_\phi d\phi \int_\theta D_1^2(\phi,\theta) D_2^2(\phi,\theta) \sin\theta \, d\theta \tag{9.3.11}$$

Therefore, the summation in Equation 9.3.6 becomes

$$\sum_{i=0}^{N-1} \frac{D_{1i}^2 D_{2i}^2 10^{-\alpha R_i/5}}{R_i^4} \approx \frac{10^{-\alpha R/5}}{R^4} n_b R^2 (\Delta R) \psi_D \tag{9.3.12}$$

Transducer suppliers often give the integrated beam pattern ψ_D as one of the performance parameters. Numerical evaluations of ψ_D are shown for two typical transducer systems in Fig. 9.3.4. Approximate formulas for integrated beam patterns ψ_D for some geometries are given in Table 9.1.

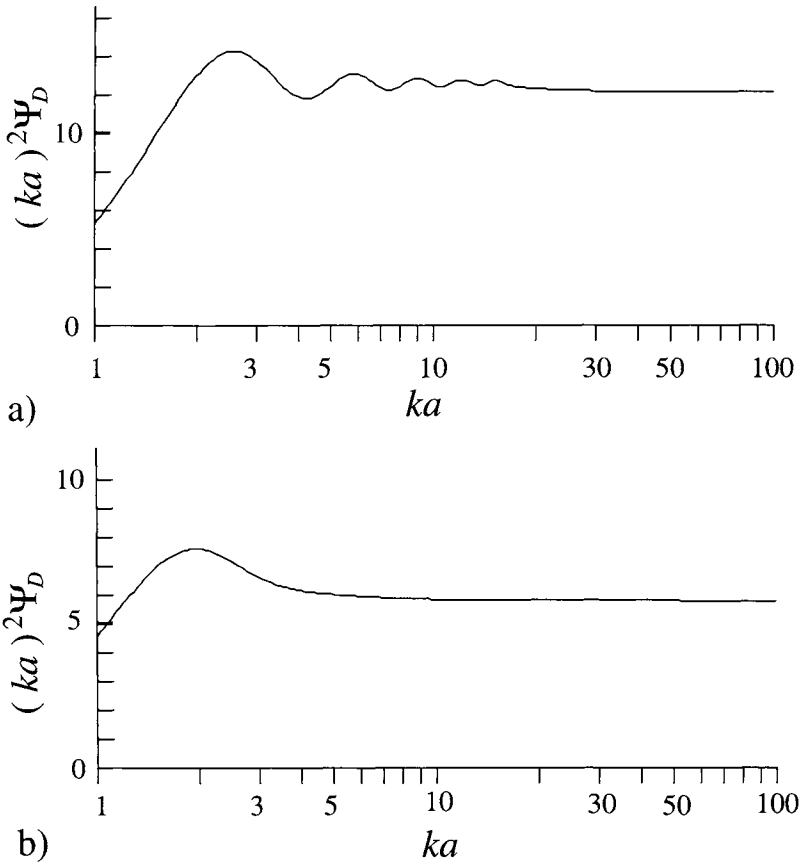

Figure 9.3.4 Numerical evaluations of integrated beam patterns. The high-frequency limits are given in Table 9.1. a) Omnidirectional source and directional receiver. b) Transmission and reception on the same directional transducer. The radius of the circular piston transducer is a, $k = 2\pi/\lambda$.

Table 9.1 **Integrated Beam Pattern Ψ_D**

Source	*Receiver*	Ψ_D	*Condition*
Piston, radius a	Same	$5.78/(ka)^2$	$ka > 10$
Omnidirectional	Piston, radius a	$12/(ka)^2$	$ka > 30$
Rectangular, $L \times W$	Same	$17.4/(k^2LW)$	$kL, kW \gg 1$
Omnidirectional	Rectangular	$\pi^2/(k^2LW)$	$kL, kW \gg 1$
Omnidirectional	Omnidirectional	4π	
Half-space	Half-space	2π	

From Clay and Medwin (1977).

In terms of the integrated beam pattern, an *effective* sampled volume ΔV_e is

$$\Delta V_e = R^2 \Psi_D \Delta R \tag{9.3.13}$$

With these substitutions, the *gated time integral pressure squared of the volume reverberation* (GV) is

$$[tips]_{GV} = \int_{t_1}^{t_2} |p_\Sigma(t)|^2 dt \approx n_b \Delta V_e \frac{R_0^2 10^{-\alpha R/5}}{R^4} \langle \sigma_{bs} \rangle [tips]_0 \tag{9.3.14}$$

Using Ψ_D and the gate times for a colocated source and receiver, the expression is

$$[tips]_{GV} \approx \psi_D (t_2 - t_1) c \frac{R_0^2 10^{-\alpha R/5}}{2R^2} n_b \langle \sigma_{bs} \rangle [tips]_0 \tag{9.3.15}$$

The density of scatterers and the mean square backscattering cross section define the *volume backscattering coefficient*:

$$s_V(f) = n_b \langle \sigma_{bs} \rangle \tag{9.3.16}$$

where both s_V and $\langle \sigma_{bs} \rangle$ depend on frequency.

Scattering measurements give the time integral pressure squared of the gated volume, Equations 9.3.14 and 9.3.15. The *volume scattering coefficient* is

$$s_v(f) \approx 2 \frac{[tips]_{GV} R^2 10^{\alpha R/5}}{\psi_D [tips]_0 (t_2 - t_1) c R_0^2} \tag{9.3.17}$$

The volume scattering coefficient is a measure of the backscattering from particles and inhomogenities in the volume. If the sonar system parameters in Equation 9.3.17 are correct, then measurements of s_v are independent of the sonar

system. If there is only one type of scatterer and its scattering length, $|\mathcal{L}_{bs}|$, is known from theory, laboratory experiment, or *in situ* measurements, the density of animals is obtained from Equation 9.3.16.

If there are different animals, or different sizes of the same species, within the scattering volume, multiple frequencies can be used to sort out the different components. Multiple-frequency sonar surveys require special care because errors in system parameters bias the results of data analysis.

One can adapt the development in Equations 9.3.1 through 9.3.15 to a distribution of different type bodies, or the same type of different sizes. Let the jth kind of object have the density n_{bj} and the squared scattering amplitude $|\mathcal{L}_{bs,\,i}|^2$. If the total number of objects of all types is N_b, the average volume backscattering coefficient is the weighted sum over all objects,

$$\langle s_v \rangle \approx \frac{1}{N_b} \sum_i n_{fi} |\mathcal{L}_{bsi}|^2 \tag{9.3.18}$$

The SI units are n_{fi} in m^{-3} and $|\mathcal{L}_{bs,\,i}|^2$ in m^2.

Some workers prefer the logarithmic sonar equation. Then a reference, $s_{v,\,\mathrm{ref}} = 1\ \mathrm{m}^2/\mathrm{m}^3$, is used, and the *volume backscattering strength* is given as

$$S_v = 10 \log_{10} [(s_v)/(s_{v,ref})]\ \mathrm{dB} \tag{9.3.19}$$

9.3.4 SCATTERING LAYERS

Deep Scattering Layers (DSL)

Many zooplankton and fish respond to light. They move up at dusk and down at daybreak. They tend to concentrate at strong changes of properties in the water column, such as the base of the mixed layer and oceanic fronts. Much of the knowledge of the vertical migrations of plankton has been obtained by echo sounding. Sonars have identified deep scattering layers (DSL) throughout the world's oceans, down to depths of several hundred meters. Although the vertical migration of the DSL is a striking feature on the records, other groups of scatterers seem to remain at almost constant depth, probably because of temperature preferences. Fig. 1.3.6 is a presention of plankton of equivalent spherical radii from 0.1 to 4.0 mm, calculated from volume backscatter of 21 frequencies, in a horizontal backscattering experiment.

Because plankton and nekton are sensitive to the presence of nutrients, food, light, and other physical-chemical characteristics of their environment, they may respond to the change of any of these. Many water properties change at the water mass boundaries, and the boundary is often marked by changes of the volume

scattering strength. Marine animals may concentrate at the interface or behave as if the interface were a barrier. Fig. 1.3.7 illustrates the influence of temperature profiles at an eddy of the Gulf Stream; the biological scatterers act as passive tracers of the temperature structure.

Fig. 1.3.8 uses backscattering to depict the migration of larger marine organisms just after sunset.

The motion of an internal wave of periodicity two or three minutes is illustrated by volume acoustical backscatter in Fig. 1.3.9. In addition to this natural phenomenon, the distribution of man-made garbage is made visible by backscatter in an ocean dumping ground.

Near Surface Scatterers

The near surface region of the ocean plays host to a large number of scatterers, in addition to the transient presence of the DSLs that come up during the night. This is also the region that shows the greatest effects of surface wave action. The full-time residents of the near surface region are both biological and physical in origin.

In one experiment, the biological scatterers in the near surface region were found to be predominantly of the phylum Arthropoda, subclass copepod. The copepods are approximately millimeters in length. To study them required the use of sound frequencies of the order of hundreds of kiloHertz. For example, Barraclough et al. (1969) perfomed net sampling of the upper ocean from the surface to a depth of about 100 m and simultanously measured backscatter with a 200 kHz sonar. The experiment, which was conducted over a great circle route from British Columbia, Canada to Tokyo, showed a coincidence of depth of strong echoes with depth of maximum catches that were 99 percent *Calanus cristatus*, a species of copepod. The peak depth was at about 40 m during the day. There were about 100 copepods per cubic meter, comprising a wet density of about 1.5 gm/m^3.

The near surface ocean is also a nightly host to some anchovies, which ingest a bubble to keep them floating quietly and unobtrusively, while they rest and try to avoid the search by predators. Undoubtedly other behaviors of interest to marine biologists await the concurrent use of sonars.

As discussed in Chapter 8, the upper region of the ocean also contains bubbles that are not part of any zooplankton or fish, and that cause substantial acoustical effects. These bubbles may be the vented gas of zooplankton or fish, the products of photosynthesis, or the result of breaking waves, precipitation, cosmic rays, or decaying matter.

9.4 Variability of Fish Structure and Sound Backscatter

Acoustical models of fish are partly empirical and partly based on the anatomy of a fish. It has been known for a long time that the main contributions of sound scattering by fish come from their swimbladders (Hersey and Backus 1962; Haslett 1962). Early swimbladder models were simple shapes such as gas-filled spheres and prolate spheroids. Laboratory measurements of sound scattering by fish give empirical forumlas such as those of Love (1969) and McCartney and Stubbs (1970). Many papers on biological sound scattering and research are collected in the proceedings, edited by Farquhar (1970).

9.4.1 PHYSICAL STRUCTURES: X-RAYS AND HIGH-FREQUENCY SOUND SCANS

The acoustical response of fish depends on size and physical structure and, most important, on the presence or absence of a swimbladder. The swimbladder is an active organ of the fish that maintains buoyancy and attitude by controlling the bladder volume. For different fish species, the shapes of swimbladders are extremely variable and can be quite complicated (Whitehead and Blaxter 1989). The swimbladder shapes, dimensions, and tilt with respect to the axis of the animal all determine the sound backscattering. Sketches of the wide variety of contours of swimbladders of pollack have been obtained by microslicing after shock-freezing the animal (Fig. 9.4.1). The shape and tilt of swimbladders of Atlantic cod are sketched in Fig. 9.4.2.

High-frequency acoustical scans of two kinds of fish are shown in Fig. 9.4.3. The transducer focused 220 kHz pings at the axis of the fish. The peak amplitudes of the backscattered pressures were measured as the transducer was moved parallel to the axis of the fish. All amplitudes are relative. After the live whole fish was scanned, flesh and body parts were removed to obtain the relative scatter from vertebrae, head, and swimbladder. These four sets of scans are shown for each of two fish with vastly different physical structures. The yellow perch has about 80 percent of its scatter from the pressure release swimbladder and small contributions from flesh and vertebrae. The northern hog sucker has about 22 percent of its scatter from the swimbladder and larger contributions from the flesh, head, and vertebrae. The scans do not show the swimbladder resonance effect, which occurs at very much lower frequencies. Comparative acoustical scans of many small freshwater fish are given in Nash et al. (1987).

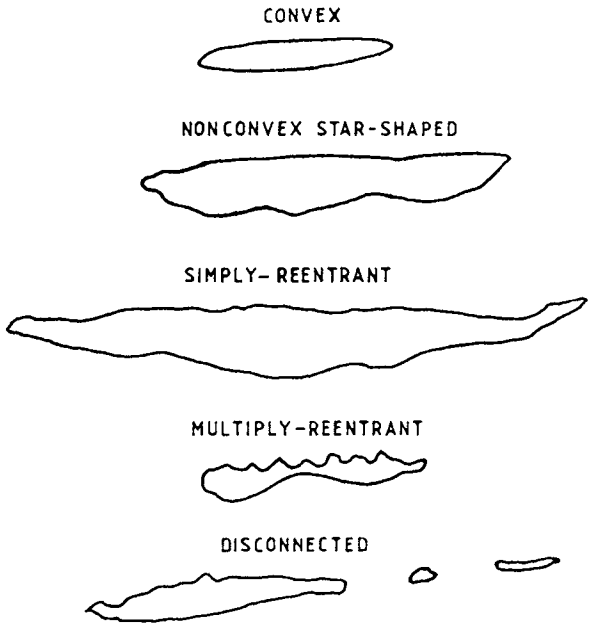

Figure 9.4.1 Sketches of contour types of pollack swimbladders. (From Foote, K. G., "Rather-high-frequency sound scattered by swimbladdered fish," *J. Acoust Soc. Am.* **78**, 688–700, 1985.)

9.4.2 ECHO STATISTICS: RICIAN, RAYLEIGH, AND EXTREMAL

Repeated measurements of echoes always give the same result if the source, receiver, and scattering object *remain constant* and the water *is stationary*. In other words, static measurements are reproducible. However, if a fish changes its tilt in the sonar beam, as shown in Fig. 9.4.4, then the echoes change.

Changes of the echo amplitudes as a target moves in the sonar beam can range from predictable amplitudes for a simple object, such as a sphere, to unpredictable amplitudes for a complicated object, such as a live fish. We are interested in a sequence of measurements in which we use e as the variable that represents the acoustic pressure amplitude of the echo envelope. The statistical variation in the echo amplitude is related to the statistical variation of the acoustical backscattering length $\mathcal{L}_{bs}$. The probability of observing a value of pressure amplitude e between $e_n - \Delta e/2$ and $e_n + \Delta e/2$ is given by

$$w(e_n)\,\Delta e = \mathcal{P}\,[(e_n - \Delta e/2) \le e \le (e_n + \Delta e/2)] \qquad (9.4.1)$$

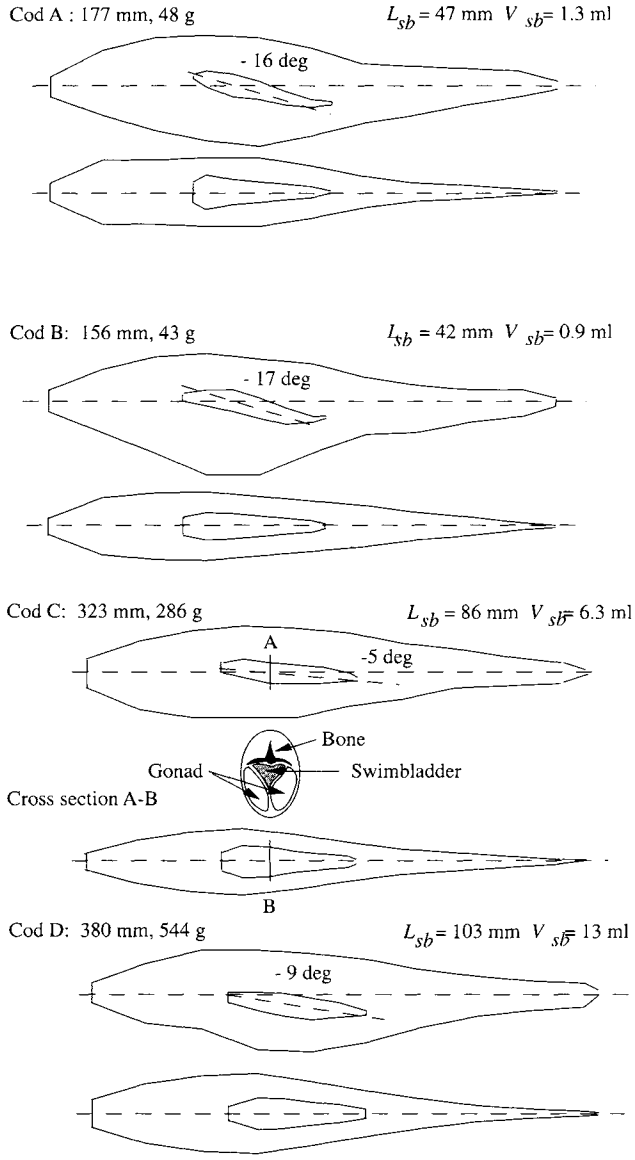

Figure 9.4.2 Sketches and dimensions of four Atlantic cod (*Gadus morhua*). The views are ventral (from above) and lateral (from the side). The swimbladder dimensions were obtained by X-ray. (From Clay, C. S., and J. K. Horne, "Acoustic models of fish: the Atlantic cod (Gadus morhua)," *J. Acoust. Soc. Am.* **96**, 1661–68, 1994.)

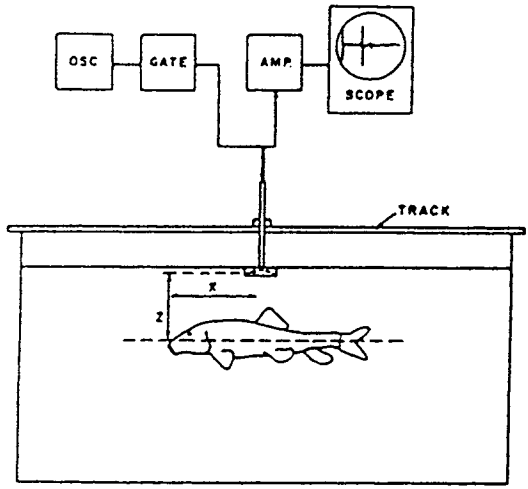

a) Acoustic scanning system.

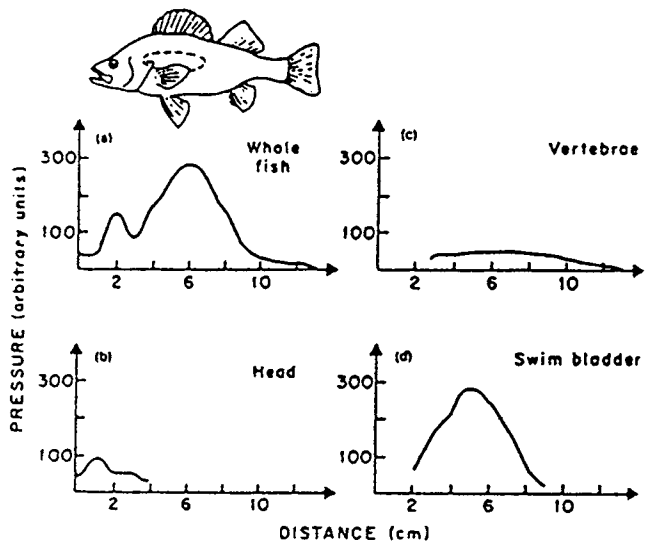

b) Yellow perch

Figure 9.4.3 High-frequency (220 kHz) scans of fish. See text. (From Sun, Y., R. Nash, and C. S. Clay, "Acoustic measurements of the anatomy of fish at 220 kHz," *J. Acoust. Soc. Am.* **78**, 1772–76, 1985.)

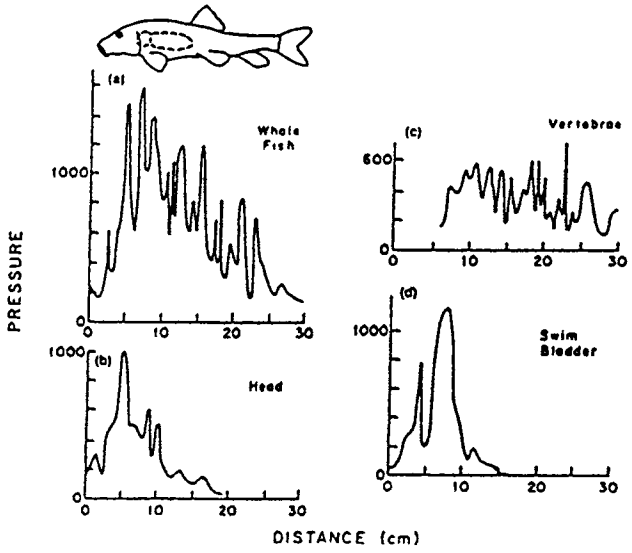

c) Northern hog sucker

Figure 9.4.3 *Continued*

where $\mathcal{P}[\ldots]$ means probability of. The *probability density function* $w(e_n)$ is the limit as Δe goes to 0:

$$w(e_n) = [Limit\ \Delta e \to 0] \frac{\mathcal{P}\left[(e_n - \Delta e/2) \le e \le (e_n + \Delta e/2)\right]}{\Delta e} \quad (9.4.2)$$

The probability distribution function (PDF) of the peaks of the backscattered echoes from a fish depends on the fish behavior. One experiment is described in

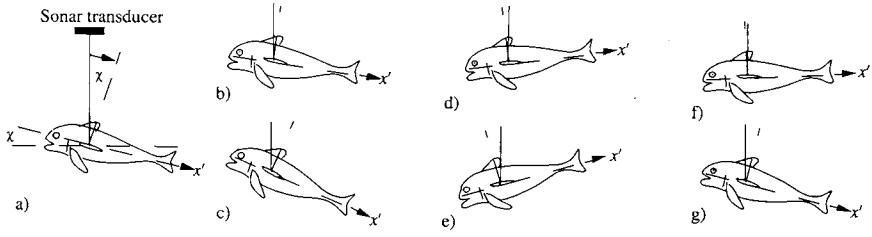

Figure 9.4.4 Repeated "snapshots" of an active fish, showing changes of angle χ in a downward-looking sonar.

Fig. 9.4.5. The 220 kHz sonar was at side aspect relative to the fish (Huang and Clay 1980). (Measurements at top aspect would give different values.) The data labeled "wild" were taken just after the fish had small hooks placed in its tail and lip. Sometimes the fish was very "calm" and nearly stationary. Ripples on the water surface caused the fish to move gently and be "alive." These data reveal the variation of peak echo amplitudes for repeated pings from the sonar. The animal is tethered at a fixed angle in the beam, but small moitions are possible.

The variation of a random variable (e.g., either the echo amplitude or $|\mathcal{L}_{bs}|$) may be defined in terms of the squared quantity that is proportional to the scattered energy. From statistics for a random variable, the "variance" of the scatter amplitude is the mean of the square of the deviation from the mean value,

$$\text{Variance of } |\mathcal{L}_{bs}| = \langle |\mathcal{L}_{bs}| \rangle - \langle |\mathcal{L}_{bs}| \rangle^2 \tag{9.4.3a}$$

or s, expending,

$$\text{Var}\,|\mathcal{L}_{bs}| = \langle |\mathcal{L}_{bs}|^2 \rangle - \langle |\mathcal{L}_{bs}| \rangle^2 \tag{9.4.3b}$$

or

$$\text{Var}\,|\mathcal{L}_{bs}| = \langle \sigma_{bs} \rangle - \langle |\mathcal{L}_{bs}| \rangle^2 \tag{9.4.3c}$$

where $\langle \ldots \rangle$ indicates the mean. Experimental probability density functions of echoes such as in Fig. 9.4.5 have the appearance of amplitude fluctuations about a

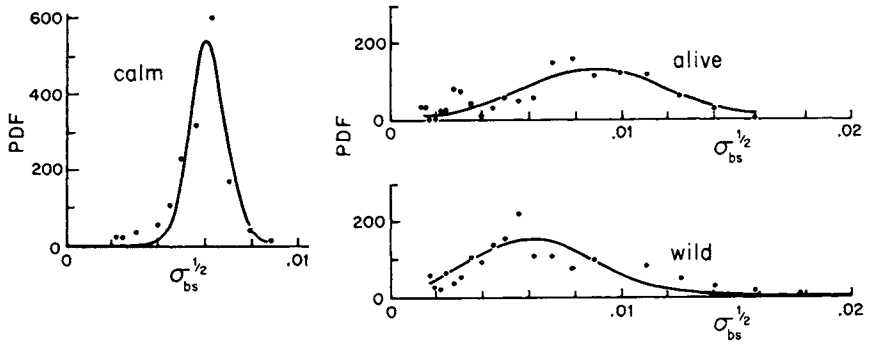

Figure 9.4.5 Probability density functions (PDF) of echo amplitudes from a live fish, beam aspect at 220 kHz. Data are points, and Rician-fitted theory are solid curves. Fish length $L = 12$ cm. Number of echoes is 256. The Rician statistics parameters are a) very calm fish, $\gamma = 33$; b) moving fish, $\gamma = 3.5$; c) wild fish, $\gamma = 1.9$. (From Clay, C. S., and B. G. Heist, "Acoustic scattering by fish acoustic models and a two-parameter fit," *J. Acoust. Soc. Am.* **75**, 1077–83, 1984.) Note that the acoustical length is much less than the actual length, $\mathcal{L}_{bs} = (\sigma_{bs})^{1/2} \ll L$.

mean echo amplitude. The square of the mean amplitude of the acoustical scattering length, $\langle |\mathcal{L}_{bs}| \rangle^2$, is sometimes called the "concentrated" backscattering cross section,

$$\sigma_c = \langle |\mathcal{L}_{bs}| \rangle^2 \tag{9.4.4}$$

The fluctuating component $\mathrm{Var}\,|\mathcal{L}_{bs}|$ is due to animal motions; the notation σ_d represents the scattering cross section of *fluctuations* of echoes from an assemblage of scatterers,

$$\sigma_d = \mathrm{Var}\,|\mathcal{L}_{bs}| \tag{9.4.5}$$

From Equation 9.4.3, the mean backscattering cross section is the sum

$$\langle \sigma_{bs} \rangle = \sigma_c + \sigma_d \tag{9.4.6}$$

Rician PDF

By regarding the scattered component σ_c as "signal" and σ_d as "random noise," the fish scattering problem is analogous to the problem of the complex sum of a sinusoidal signal and narrow band random noise. O. R. Rice (1954) derived a *probability density function* (PDF) for the envelope of this sum and used the two parameters σ_c and σ_d to describe the Rician PDF of the echoes:

$$w_{Rice}(e) = \frac{2e}{\sigma_d} \exp\left(-\frac{e^2 + \sigma_c}{\sigma_d} \right) I_0\left(\frac{2e\,(\sigma_c)^{1/2}}{\sigma_d} \right) \tag{9.4.7}$$

where e is the peak of the echo envelope and $I_0(\,)$ is a modified Bessel function, where $I_0(x) = J_0(ix)$ and $I_0(0) = 1$. Modified Bessel functions are described in Abramowitz and Stegun (1965); their sections 9.6 and 9.8 give polynomial approximations.

In the fish scattering problem, the ratio, σ_c/σ_d, and the average, $\langle \sigma_{bs} \rangle$, are convenient parameters because values of $\langle \sigma_{bs} \rangle$ are measured directly, and the ratio σ_c/σ_d is easy to estimate from data. Following Clay and Heist (1984), we define the ratio by the parameter γ,

$$\gamma \equiv \frac{\sigma_c}{\sigma_d} \tag{9.4.8}$$

and use $\langle \sigma_{bs} \rangle$ and γ to describe the statistics of fish echoes. With these acoustical parameters, $w_{\text{Rice}}(e)$ becomes

$$w_{Rice}(e) = \frac{2e\,[1+\gamma\,]}{<\sigma_{bs}>} \exp\left(-\frac{[1+\gamma\,]e^2+\gamma\,<\sigma_{bs}>}{<\sigma_{bs}>}\right) \times I_0\left(\frac{2e\,\gamma\,[1+\gamma\,]^{1/2}}{<\sigma_{bs}>^{1/2}}\right) \tag{9.4.9}$$

The reduction of the experimental scattering measurements to a two-parameter PDF is a useful description that often approximates the true PDF. Examples of the Rician PDF for echoes are shown in Fig. 9.4.5. The Rician PDF gives a good description of echo amplitudes for single nonoverlapping echoes. Wiebe et al. (1990) also found Rician PDFs in measurements of the statistics of echoes from decapod shrimp.

The Rician PDF is a generalization that encompasses the Gaussian PDF and the Rayleigh PDF. A very large value of γ gives the well-known Gaussian PDF.

Rayleigh PDF

The Rician PDF reduces to the Rayleigh PDF by letting γ go to 0, where there is no concentrated component. Since $I_0(0) = 1$, Equation 9.4.9 reduces to

$$w_{Rayl}\,(e\,) = \frac{2e}{<\sigma_{bs}>} \exp\left(-\frac{e^2}{<\sigma_{bs}>}\right) \tag{9.4.10}$$

Rayleigh derived this PDF to describe the envelope of the sum of many sine waves having the same frequency and random phases.

The probability distribution of echo amplitudes and γ depends on the ratio of the fish length L to λ. At large L/λ, γ is small, and the PDF tends to the Rayleigh. At small L/λ, γ is large, and the Rician PDF becomes the Gaussian with peak near $e = \langle \sigma_{bs}(f) \rangle^{1/2}$. The peak of the PDF in scattering lengths or echo amplitudes is systematically different when the linear PDF is transformed to a PDF of target strengths in dB.

Extremal PDF

When echoes overlap as shown in Fig. 9.3.3, one gets the extremal PDF, Fig. 9.4.6 (Stanton 1985). The extremal PDF gives the density of the maximum value of the echo envelope e_G that is observed within the gate time t_1 to t_2. The extremal

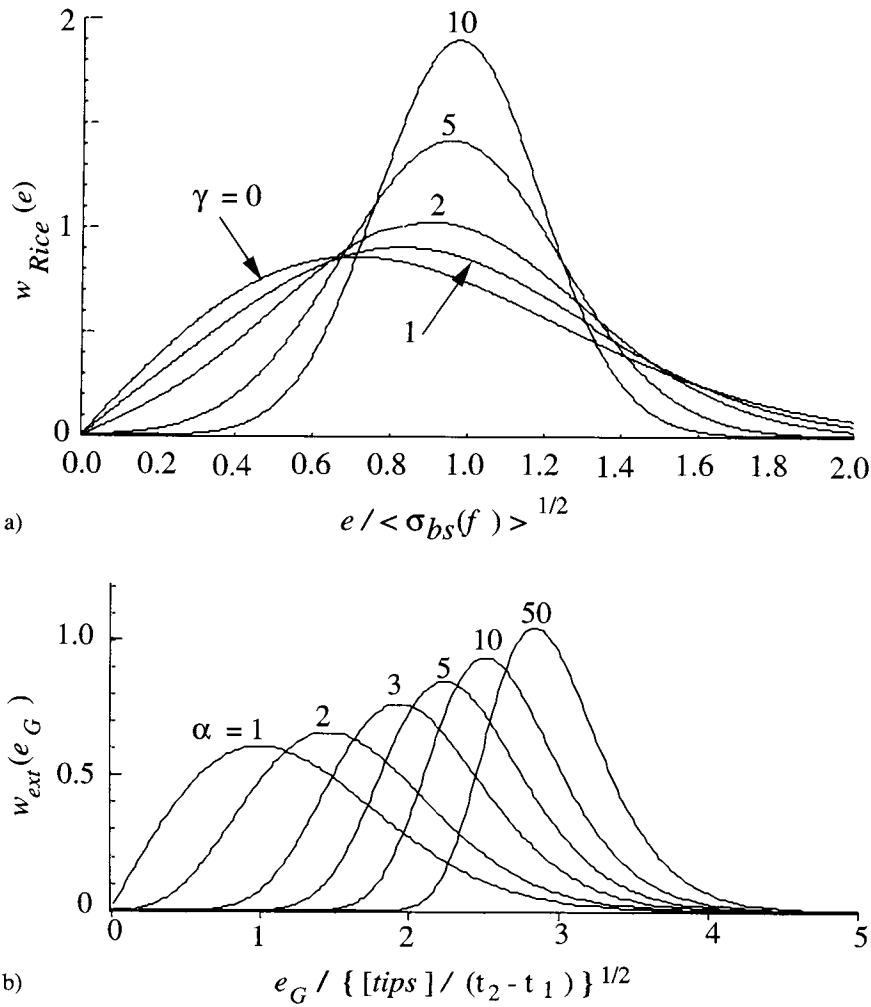

Figure 9.4.6 Rician and extremal PDF in terms of γ and α. a) The Rician PDF describes the statistics of echo peaks when the echoes do not overlap. b) The extremal PDF describes echo peaks when echoes overlap. The maximum value of the echo amplitude observed in the gate time t_1 to t_2 is e_G; the time integral echo pressure squared during the gate open duration t_d is $[tips]$; and $\alpha- = (t_2 - t_1)/t_d$.

calculation depends on the PDF of the nonoverlapping echoes. For a Rayleigh PDF of nonoverlapping echoes, the extremal PDF is

$$w_{ext}(e_G) = \frac{e_G}{[ties]/(t_2 - t_1)} \exp\left(-\frac{e_G^2}{2[ties]/(t_2 - t_1)}\right) \times [1 - \exp\left(-\frac{e_G^2}{2[ties]/(t_2 - t_1)}\right)]^{(\alpha - 1)} \tag{9.4.11}$$

where [*ties*] is the *time integrated echo squared* of echo amplitudes. The e can stand for echo pressure, echo voltage or normalized echo amplitude,

$$[ties] \equiv \int_{t_1}^{t_2} [e(t)]^2 \, dt \tag{9.4.12}$$

The parameter α is the ratio of the gate open time $(t_2 - t_1)$ to the ping duration t_d. It is also the maximum number of independent observations of the echo,

$$\alpha = (t_2 - t_1)/t_d \tag{9.4.13}$$

and [*ties*] is the time integral echo squared for the gate time. The parameter $\alpha = 1$ gives the Rayleigh PDF. When echoes overlap, there is a very low probability of observing very-small-amplitude echoes. For many overlapping echoes, the maximum values of echo amplitudes tend to saturate as the gate open duration increases relative to t_d.

9.5 Acoustical Models of Fish

9.5.1 ANATOMICAL-ACOUSTICAL MODELS

Acoustical models of fish are metaphors for real animals. We use these metaphors in the ways that we think about data. All acoustical models are low-resolution representations of the animals; none has fine details of the shape and anatomy of fish. The simplest models are spheres that are gas-filled to represent the swimbladders or fluid-filled to represent the average flesh of the animal. The progression has been from such simple approximations to more complicated finite cylindrical or prolate spheroidal models that begin to look like the animals. The introduction of multiple-frequency sonars and the acquisition of high-quality data have permitted greater sophistication of the models and correspondingly more accurate identification of unknown animals.

Relationships between actual fish length and high-frequency target strength are important in fisheries research. (We use the terminology "high frequency" when $ka > 1$, although in many cases our developments hold for the larger region $ka > 0.2$.) The radius a is usually subscripted (e.g., a_{ec} is the equivalent cylindrical radius, and a_{es} is the equivalent spherical radius). Acousticians and biologists have used measured target strengths of single fish to construct empirical target strength–fish length formulae (McCartney and Stubbs 1970; Love 1971; and Foote 1988). The earlier measurements used caged fish. More recently, *in situ* target strength measurements have been effectively compared with net captures. When local "calibrations" are used, the empirical formulas work very well.

Validations of acoustical models have several important requirements:

(1) Measurements should be done under reproducible, usually laboratory, conditions.
(2) Fish and zooplankton should be described by simple theories and models, without acoustically-superfluous extensions.
(3) Multiple-frequency scattering measurements of live animals should be made of the same animal and at the same time.
(4) Measurements of the far-field scattering amplitudes or target strengths must be made in the far field of the animal.

When it exists, the gas-filled swimbladder provides a large contrast of acoustic impedance ($\rho_A c$) relative to flesh and skeletal elements and is the major source of high-frequency scattered sound. At very low frequencies ($ka_{es} \ll 1$), the gas-filled organ has a low-frequency resonance. Therefore, over the entire frequency range, most of the scattered sound comes from the swimbladder (Clay and Horne 1994).

9.5.2 *HK ACOUSTIC SCATTERING MODELS FOR SWIMBLADDER FISH ($ka > 1$)*

In the equivalent cylinder description, at high frequencies ($ka_{ec} > 1$, where a_{ec} is the equivalent cylindrical radius) and in the range of $8 < L/\lambda < 36$ (where L is the length of a fish), experiments and theory show that a swimbladder accounts for about 90 percent of the total high-frequency backscatter in the dorsal aspect. Foote (1985) made a precise, postmortem measurement of a fish swimbladder that allowed him to construct a numerical facet model of its three-dimensional surface. He then used a numerical evaluation of the Helmholtz-Kirchhoff (HK) integral to compute the scattered sound from these facets, which he compared

with acoustical measurements. The successful comparison of experimental backscatter with the HK facet reflection calculation (section 7.3) is shown in Fig. 9.5.1.

In Fig. 9.5.1 four frequencies are presented in two different aspects, dorsal and ventral. The correlation coefficient between the experiment and the numerical integration of the HK integral ranges from 0.89 to 0.96 for the dorsal aspect cases, and from 0.58 to 0.80 for the ventral aspects. There is a strong dependence on tilt angle, particularly for the higher frequencies. These detailed figures demonstrate the soundness of combining swimbladder morphology and the HK method.

To demonstrate how the Kirchhoff-ray approximations for the scattering of sound by finite length cylinders can be used for high frequencies, consider the scattering geometry at a fish as sketched in Fig. 9.5.2. In this case the fish is cod D of Fig. 9.4.2. We consider scatter from the swimbladder first, and then from the fish body.

HK Scattering from the Swimbladder

Following the development in Chapter 7, with adjustments, the acoustic scattering length of a gas-filled cylinder in water may be given by

$$\mathcal{L}_{blad}(ka_{ecb}) \approx \frac{L_{ecb}}{2\sqrt{\pi}}[(ka_{ecb} + \psi_a)\cos\chi]^{1/2}\frac{\sin\Delta}{\Delta}\mathcal{R}_{wc} \times e^{-i(2k_b a_{ecb}\cos\chi + \psi_P + \pi/2)} \tag{9.5.1}$$

where ψ_a and ψ_p are empirical amplitude and phase adjustments for small ka_{ecb}; a_{ecb} and L_{ecb} are the radius and length of the equivalent swimbladder as a cylinder. For a swimbladder in a fish body, we include the transmission through the fish body to the swimbladder and back out, $\mathcal{T}_{wb}\mathcal{T}_{bw}$. The revised expression for the scattering length is

$$\mathcal{L}_{blad} \approx \frac{L_{ecb}A_{sb}}{2\sqrt{\pi}}[(k_b a_{ecb} + 1)\cos\chi]^{1/2}\frac{\sin\Delta}{\Delta}\mathcal{T}_{wb}\mathcal{T}_{bw}\mathcal{R}_{bc} \times e^{-i(2k_b a_{ecb}\cos\chi + \psi_P + \pi/2)} \tag{9.5.2}$$

$$\Delta = k_b L_{ecb}\sin\chi, \quad k_b = 2\pi f/c_b$$
$$\mathcal{R}_{bc} = \frac{g'h' - 1}{g'h' + 1} \tag{9.5.3}$$
$$g' = \rho_c/\rho_b \quad \text{and} \quad h' = c_c/c_b$$

$$A_{sb} \approx \frac{ka_s}{ka_{ecb} + 0.083} \quad \text{and} \quad \psi_P \approx \frac{ka_{ecb}}{40 + ka_{ecb}} - 1.05 \tag{9.5.4}$$

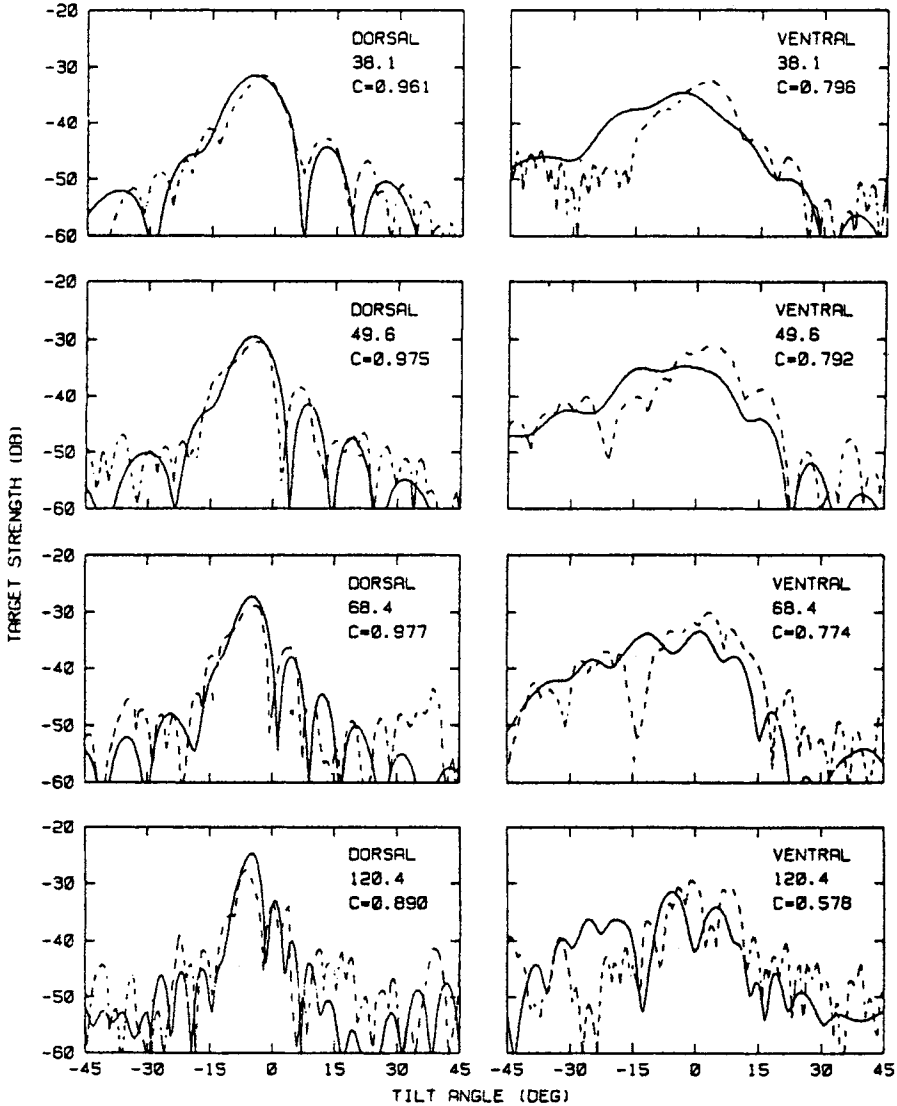

Figure 9.5.1 Target strengths as a function of tilt angle for a 31.5 cm pollack at dorsal (*left*) and ventral (*right*) aspect. The solid line is the experimentally determined value. The dashed line is computed from the fish body and bladder dimensions by means of the HK facet reflection technique. The high correlation coefficients C, calculated for the computed and experimental curves of TS, are a function of frequency. The frequencies (top to bottom) are 38.1, 49.6, 68.4, and 120.4 kHz. There is a strong dependence on tilt angle, particularly at the higher frequencies. (From Foote, K. G., "Rather-high-frequency sound scattered by swimbladdered fish," *J. Acoust. Soc. Am.* **78**, 688–700, 1985.)

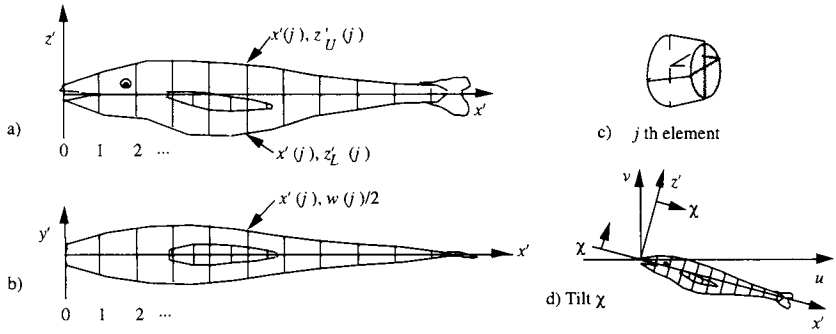

Figure 9.5.2 Geometrical construction of an acoustic fish model. Cod D, previously sketched in Fig. 9.4.2, is used for the example. Outlines of the fish body and swimbladder are digitized at a set of $x'(j)$ along the axis of the fish. The upper and lower coordinates are $x'(j)$, $z_U(j)$, and $z_L(j)$. The width of the body is $w(j)$. The jth volume element is between $x'(j)$ and $x'(j+1)$. The swimbladder is sampled at smaller spacings. The ray path from the source and its normal, the wavefront, define the directions of the u-v coordinate system. Coordinate u is parallel to the incident wavefront, and v is parallel to the incident ray. a) The ray is vertically incident in the x-z plane. b) Top view. c) The swimbladder is omitted from the volume element for clarity. d) Rotation of $x' - z'$ to u-v coordinates. (See Clay, C. S., and J. K. Horne, "Acoustic models of fish: the Atlantic cod (Gadus morhua)," *J. Acoust. Soc. Am.* **96**, 1661–68, 1994.)

where f is frequency; a_{ecb} is the radius of the effective cylinder bladder; L_{ecb} is the length of the effective cylinder bladder; χ is the tilt angle measured from the the horizontal axis to the cylinder (or fish) axis; ρ_b and c_b are the density and sound speed in the fish body; ρ_c and c_c are the density and sound speed in the gas-filled cylinder; $\mathcal{R}_{bc}$ is the reflection coefficient at the fish body–cylinder interface; A_{sb}, $(ka_{ecb} + 1)$ and Ψ_P are empirical amplitude and phase adjustments for small ka_{ecb}; $e^{-i\pi/2} = -i$.

Typical acoustical parameters for water and fish are given in Table 9.2. The reflection coefficients that are calculated for a gas-filled cylinder in the fish body or in water are nearly the same, because $\rho_c/\rho_b \approx \rho_c/\rho_A$ and $c_c/c_b \approx c_c/c_A$. Equation 9.5.2 is accurate for $ka_{ecb} > 0.15$.

Table 9.2 **Acoustical Parameters**

Medium|Subscript	*ρ kg/m³*	*c m/s*	$g = \rho_2/\rho_1$	$h = c_2/c_1$
Ambient Water$\|_A$	1030	1490	—	—
Fish flesh $\|_{bod}$	1070	1570	1.04	1.05
Swimbladder $\|_{blad}$	1.24	345	0.001	0.22

(From Clay, C. S., and J. K. Horne, "Acoustic models of fish: the Atlantic cod (Gadus morhua)," *J. Acoust. Soc. Am.* **96**, 1661–68, 1994.)

Coordinate Rotation

The fish tilt relative to the sonar beam is included by rotating the fish corrdinate system from the x' and z' coordinates to the u and v coordinates:

$$u(j) = x'(j)\cos\chi + z'(j)\sin\chi \tag{9.5.5}$$

$$v(j) = -x'(j)\sin\chi + z'(j)\cos\chi \tag{9.5.6}$$

$$\Delta u_j = [x'(j+1) - x'(j)\cos]\,\chi \tag{9.5.7}$$

$$a_j = \frac{[w(j) + w(j+1)]}{4} \tag{9.5.8}$$

where Δu_j is the projection of $\Delta x'$ along the reference x'-axis on to u. Generally the scattering theory is limited to tilt angles near ζ. Choosing a limit of $\cos\chi > 0.9$ to specify the nearness to 0°, χ can range from −25 to 25°.

The next step uses short sections of modified cylinders as elements of a construction. The transformed coordinates (Equations 9.5.5 through 9.5.8) are used in constructing the summation. The element of scattering length is obtained from Equation 9.5.7 by letting L_{ecb} become Δu_j in the rotated coordinates. The factor $(\sin\Delta)/\Delta$ is approximately 1 because $k_b L_{ecb}\sin\chi$ is small. The sum of the elements is

$$\mathcal{L}_{blad} \approx -i\frac{\mathcal{R}_{bc}(1-R_{wb}^2)}{2\sqrt{\pi}}\sum_{0}^{N_s-1} A_{sb}[(k_b a_j + 1)\cos\chi]^{1/2} e^{-i(2k_b v_j + \psi_P)}\Delta u_j \tag{9.5.9}$$

$$a_j \equiv [\,w_s(j) + w_s(j+1)]\,/\,4 \tag{9.5.10}$$

$$v_j \equiv [\,v_{s\,U}(j) + v_{s\,U}(j+1)]\,/\,2 \tag{9.5.11}$$

and $k_b \approx k$ at low contrast.

As shown in Fig. 9.5.2, the number of terms, $N_s = 8$ for the swimbladder summation and, later, $N_b = 11$ for the fish body summation, is chosen to give an acceptable model of the fish. The model does not give unwarranted details. In the numerical evaluations, we use the coordinates of the middle of each volume element u_j and include a small correction for the tapers of z_U, z_L, and v_j and w_j from one end of the volume element to the other, (Fig. 9.5.2c). If small and large members of a species have the same relative structure, the sizes can be scaled by letting $x'' = (scale\ factor) \times x'$ and $z'' = (scale\ factor) \times z''$.

Scattering from Fish Body

A ray-path construction for the fluid-filled fish body is shown in Fig. 9.5.3a. Somewhat unconventionally, the fish cross section is modeled as a half-cylinder over a straight section over a cylindrical bottom. There is no backscatter from the straight section at vertical incidence.

In the Kirchhoff approximation, the top cylinder gives the scattering of the sound wave from the top, and the bottom surface gives the scattering from the bottom. The sides make no contributions to the HK integral; however, the travel distance adds to the time delay of the reflection from the bottom of the model. The Kirchhoff approximation and construction for low-contrast fluid cylinders are

$$\mathcal{L}_{bod} \approx -i\frac{L_{ecf}}{2\sqrt{\pi}}[(ka_{ecf}\cos\chi)]^{1/2}\frac{\sin\Delta}{\Delta}\mathcal{R}_{wb} \times [e^{-i2kz_U} - \mathcal{T}_{wb}\mathcal{T}_{bw}e^{i2kz_U+i2k_b(z_U-z_L)+i\psi_b}] \tag{9.5.12}$$

where

$$k = \frac{2\pi f}{c_A},\quad \mathcal{R}_{wb} = \frac{\rho_b c_b - \rho_A c_A}{\rho_b c_b + \rho_A c_A} \quad \text{and} \quad \mathcal{T}_{bw} = 1 - \mathcal{R}_{wb}^2$$
$$\psi_b = -\frac{\pi k_b z_U}{2(k_b z_U + 0.4)} \tag{9.5.13}$$

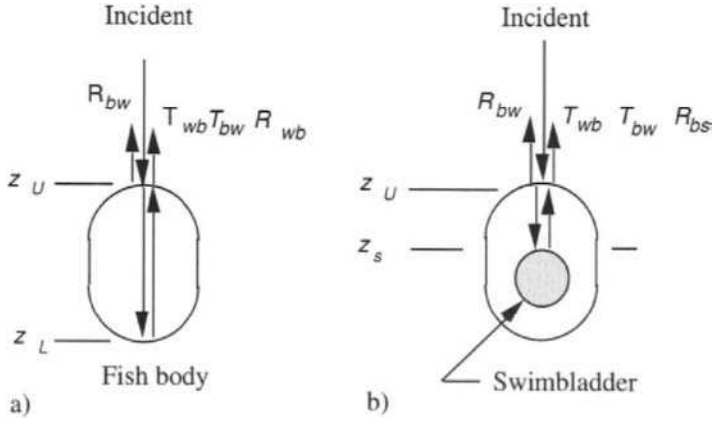

Figure 9.5.3 Ray-path constructions for reflections. a) Fish body. b) Fish body and swimbladder. (From Clay, C. S., and J. K. Horne, "Acoustic models of fish: the Atlantic cod (Gadus morhua)," *J. Acoust. Soc. Am.* **96**, 1661–68, 1994.)

where z_U and z_L are the upper and lower surfaces of the equivalent cylinder; the density and sound speed in ambient water are ρ_A and c_A; a_{ecf} (or $w/2$) is the equivalent cylindrical fish body radius as viewed from the top; Ψ_b is an empirical phase correction.

The sum over the fluid elements of volume follows from Equation 9.5.12:

$$\mathcal{L}_{bod} \approx -i\frac{\mathcal{R}_{wb}}{2\sqrt{\pi}}\sum_{0}^{N_s-1}(ka_j)^{1/2}\Delta u_j \times \left[e^{-i2kv_{Uj}} - \mathcal{T}_{wb}\mathcal{T}_{bw}e^{-i2kv_{Uj}+i2k_b(v_{Uj}-v_{Lj})+i\psi_b}\right] \tag{9.5.14}$$

The number of terms, N_b, is chosen to give an acceptable model of the fish. The transformed coordinates of the fluid body are computed by using expressions similar to Equations 9.5.13 and 9.5.14.

Whole Fish

The ray-path construction for a swimbladder in the fish body is shown in Fig. 9.5.3b. The scattering amplitudes from the fish body and swimbladder are added coherently (i.e., with real and imaginary terms added separately):

$$\mathcal{L}_{bs} = \mathcal{L}_{blad} + \mathcal{L}_{bod} \tag{9.5.15}$$

The acoustical backscattering length $\mathcal{L}_{bs}$ is a function of the relative wavelength (L_{ecf}/λ) and relative equivalent cylindrical radius, ka_{ec}. The *relative (or reduced) scattering length* combines these variables into one expression:

$$\text{relative scattering length} = \mathcal{L}_{bs}(L_{ecf}/\lambda)/L_{ecf} \tag{9.5.16}$$

Simple generalizations may be calculated. For example: changes of fish structure along the body can be included by moving the reflection coefficients inside of Equations 9.5.12 and 9.5.14; the reflection coefficients of the jth element become $\mathcal{R}_{bcj}$ and $\mathcal{R}_{wb}$. When the surface is "bumpy," one can use reflection coefficients that have the form $\mathcal{R}_{wj}\exp[-(k\sigma)^2]$, where σ is the rms roughness of the surface (Stanton 1992; Stanton and Chu 1992).

Results of calculations of the relative scattering length for swimbladder, fish body, and the whole cod D (Fig. 9.4.2) are shown in Fig. 9.5.4 as a function of the length of the animal relative to the wavelength, L/λ. The incident rays are at tilt $\chi = 0$. The swimbladder and body scatter were each computed and then combined by separately adding their real and imaginary components to obtain the value for the whole fish.

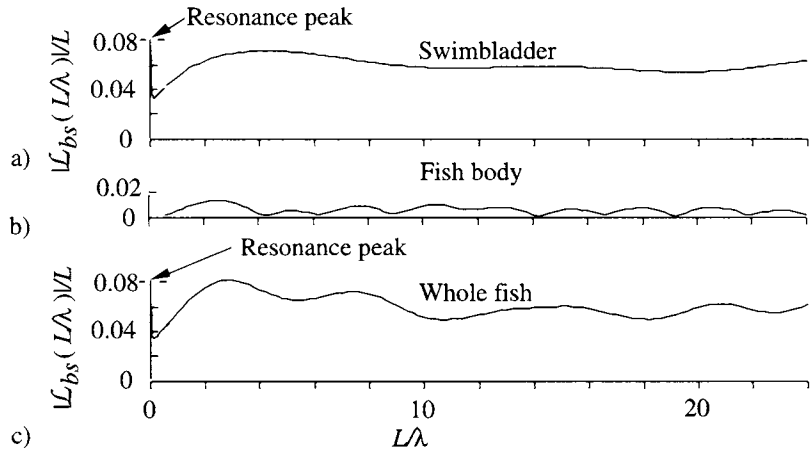

Figure 9.5.4 Theoretical relative high-frequency scattering lengths for a model Atlantic cod (*Gadus morhua*). The acoustical model is cod D ($L = 380$ mm). The low-frequency swimbladder resonance peaks in a) and c) are not shown. a) $|\mathcal{L}_{bs}(L/\lambda)|/L$ for swimbladder. b) Fish body. c) Whole fish. (From Clay, C. S., and J. K. Horne, "Acoustic models of fish: the Atlantic cod (Gadus morhua)," *J. Acoust. Soc. Am.* **96**, 1661–68, 1994.)

The swimbladder backscattering lengths (Fig. 9.5.5a) were computed using Equation 9.5.2. The fish body scattering lengths were computed using Equation 9.5.14. The whole fish is the coherent sum of the scattering from the swimbladder and the fish body (Equation 9.5.15). The oscillatory modulations of $|\mathcal{L}_{bs}(L/\lambda)/L|$ are due to the contributions of the fish body.

Figure 9.5.5 shows the χ dependence for cod C as a function of L/λ for seven frequencies. The higher-frequency scattering lengths have strong dependencies on fish tilt χ. The swimbladder is almost perpendicular to the incident ray at fish body tilt $\chi = -7°$. Recalling the dependence of transducer beam widths on frequency, scattering of sound by fish has a similar dependence. The center lobe is very broad at 12.5 kHz, and the scattering length has a weak dependence on tilt angle. Compare this with the dependence on tilt at 400 kHz. The main lobe is centered at about $-6°$ tilt and has a width of about 5°. Fig. 9.5.5 shows the effect of a progression of beam widths from very broad at 12.5 kHz to narrow at 400 kHz. This dependence can have a profound effect on the measurements of high-frequency backscattered sound with a narrow beam width echo sounder. For example, for a horizontal fish, a vertically incident 5° beam-width transmit-receive transducer system would measure $|\mathcal{L}_{bs}/L| \approx 0.08$ from 12.5 to 25 kHz with small dependence on tilt. Under the same conditions, the relative scattering lengths are about $|\mathcal{L}_{bs}/L| \approx 0.05$ from 100 to 400 kHz, but they are likely to be extremely variable as the fish changes its tilt.

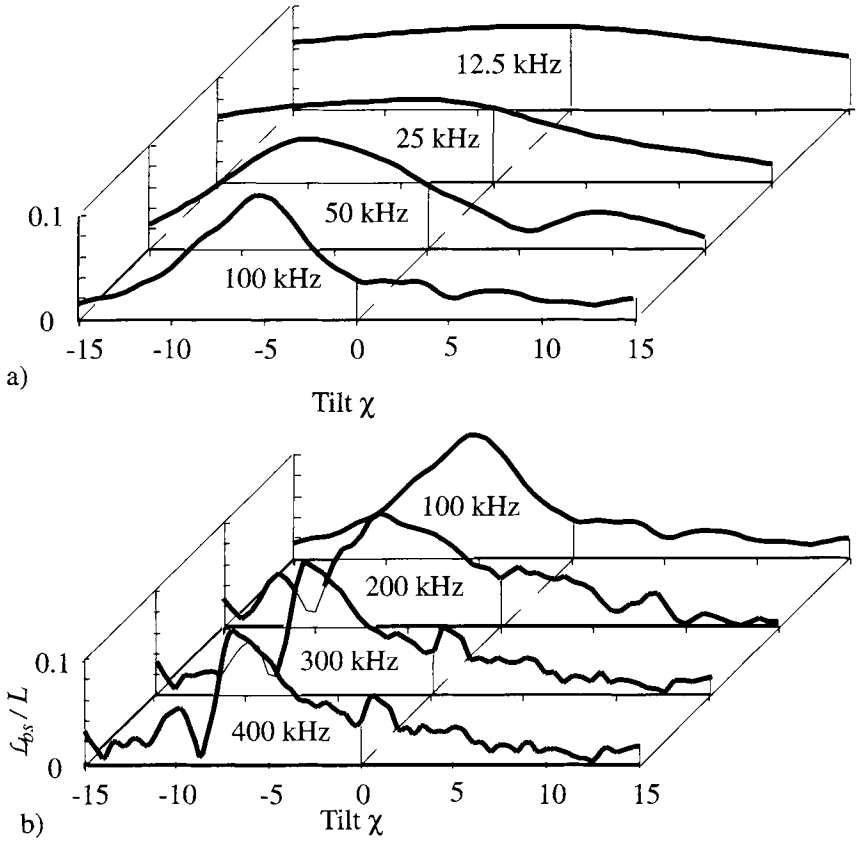

Figure 9.5.5 Relative high-frequency scattering lengths for cod C as a function of tilt angle in degrees. The approximate fish length (cod C) is 300 mm for these calculations. The scattering maxima occur at $\chi \approx -7°$ tilt, at which angle the swimbladder is approximately horizontal and is perpendicular to the sound beam. (From Clay, C. S., and J. K. Horne, "Acoustic models of fish: the Atlantic cod (Gadus morhua)," *J. Acoust. Soc. Am.* **96**, 1661–68, 1994.)

9.5.3 COMPARISONS OF HIGH-FREQUENCY ACOUSTICAL MODELS AND DATA

Laboratory mesurements of scattering use captured fish, identified species, and measured sizes. Ideally, live fish should be used because the swimbladder is an active organ in fish. To control fish orientation, fish are often tethered from a frame. An acoustical model is based on the fish structure, and calculations are made over a wide range of frequencies. Alternatively, assuming that the fish

structures can be scaled over a range on fish lengths, one can use measurements of many lengths of fish at a single frequency.

North Atlantic Cod (*Gadus morhua*)

The extensive 38 kHz scattering data for cod that were taken by Nakken and Olsen (1977) meet all criteria that we have set, except that they used mortally wounded or dead fish. Their Fig. 40 gives the *maximum measured target strength* for any orientation angle as a function of fish length. Fig. 9.5.6 compares the Nakken and Olsen data with the acoustical model calculations.

The acoustical model for cod C ($L = 32.3$ cm) was scaled to a set of lengths by replacing all of the x' and z' shown in Fig. 9.5.3 by $x'' = (scale\ factor) \times x'$ and $z'' = (scale\ factor) \times z'$. A single tilt of $-5°$ was used for fish lengths from 8 to 100 cm. The theoretical calculations and the acoustical models are based on X-rays of cod. Since most of the high-frequency sound scatter comes from the upper surface of the swimbladder, the backscatter calculations are relatively insensitve to the density and sound speed of the fish flesh. The shape of the swimbladder is important in this frequency range because the frequencies are far above the swimbladder resonance.

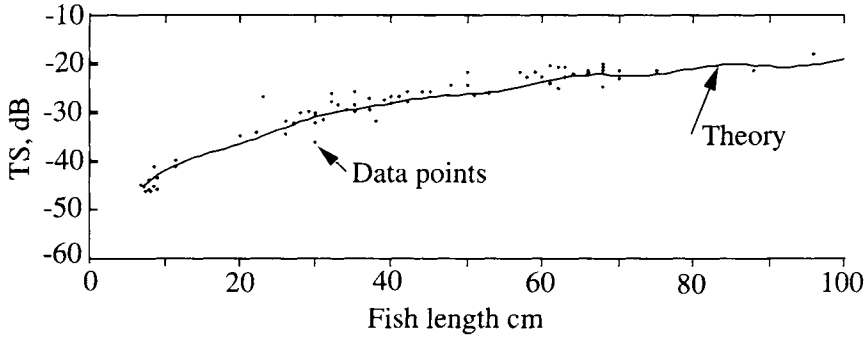

Figure 9.5.6 Atlantic cod (*Gadus morhua*). Comparison of measured data and acoustically modeled, reduced target strengths TS (re 1 m) $= 20 \log_{10} [\mathcal{L}_{bs}/(1\text{ m})]$ at 38 kHz. The data points are maximum target strength measurements of Nakken and Olsen (1977) for Atlantic cod of fish lengths from 8 to 96 cm. The theoretical acoustical model curve for cod C at $-5°$ tilt was scaled for different lengths.

Threadfin Shad (*Dorosoma petenense*)

Dual-beam, high-frequency laboratory measurements of acoustic scattering lengths have been made on live threadfin shad at 120, 200, and 420 kHz (Jech et al. 1995) as a function of the ratio L/λ. Fish lengths ranged from 52 mm to 111 mm. The sonar system accepted measurements only for fish positions that were near the axis of the transducer: specifically, within 7.7° for 120 kHz, 3.9° for 200 kHz, and 5.2° for 420 kHz. The total lengths (L) of the fish were measured from the tip of the snout to the end of the caudal fin. The published paper includes comparisons to the finite bent cylinder model (Stanton 1989) and the low-resolution-mode model (Clay 1991).

One fish was dissected to obtain a photocopy of the swimbladder, which was then digitized. This model was scaled to different fish lengths for theoretical computations of $\mathcal{L}_{bs}(L/\lambda)$. The acoustical model and methods in section 9.5.2 were used for computations. This model is based on the fish anatomy.

The acoustical model, data, and scattering lengths are shown in Fig. 9.5.7. Considering that the swimbladder is tipped about 15° and that the fish were constrained to be near the axis of the high-frequency transducer, small tilt motions of the fish could have had large effects on the echo amplitudes.

The probability density functions of echoes are shown in Fig. 9.5.8. Qualitatively, we expect the Rician PDF to have a large γ and to be Gaussian-like at low frequencies and a smaller γ at high frequencies. The measured PDFs for the same fish had $\gamma = 10$ for 120 kHz and 3.8 at 420 kHz. The small hump at 0.004 to 0.007 may have been caused by tilts of the fish.

Empirical Target Strength Equations

The observation that the high-frequency ($ka > 1$) acoustical scattering lengths are nearly proportional to fish lengths has lead to empirical formulas for $L/\lambda > 2$. Love (1971, 1977), McCartney and Stubbs (1970), and Foote and Traynor (1988) have given target strength formulas, for example:

$$\begin{aligned} &\text{Foote:} \quad TS = 20\log|\mathcal{L}_{wf}/R_0| = m\log(L/R_0) + b \\ &\text{Walleye pollock:} \quad b = -26\,\text{dB} \quad \text{for} \quad R_0 = 1\,\text{m} \\ &\text{or} \quad b = -66\,\text{dB} \quad \text{for} \quad R_0 = 1\,\text{cm} \end{aligned} \tag{9.5.17}$$

$$\begin{aligned} &\text{Love:} \quad TS = 20\log|\mathcal{L}_{wf}/R_0| = 20\log[L/R_0] + b_L + m_L\log[L/\lambda] \\ &m_L = -1.1, \; b_L = -23.8 \quad \text{for} \quad R_0 = 1\,\text{m} \quad \text{or} \quad b_L = -63.8 \quad \text{for} \quad R_0 = 1\,\text{cm} \end{aligned} \tag{9.5.18}$$

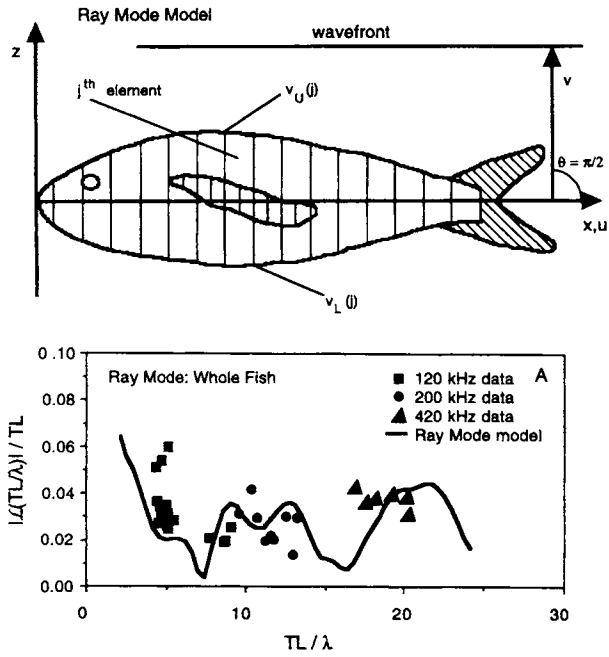

Figure 9.5.7 Relative backscattering lengths $\mathcal{L}_{bs}/L$ of threadfin shad. *Above*, the digitized fish picture. *Below*, experimental data compared with theoretical calculation based on dimensions. The 33 fish were at about 10 m depth and had lengths that ranged from 53 to 111 mm. The solid curve (ray mode model) was computed using the fish acoustical model. (From Jech, J. M., D. M. Schael, and C. S. Clay, "Application of three sound scattering models to threadfin shad (*Dorosoma petenense*)," *J. Acoust. Soc. Am.* **98**, 2262–69, 1995.)

The frequency dependence of $m_L \log(L/\lambda)$ is weak and is often omitted for narrow ranges of frequencies. Since these equations are empirical, bioacousticians usually use data from acoustical surveys and nets to calculate constants for their fish.

9.5.4 LOW-FREQUENCY SWIMBLADDER RESONANCE MODELS

In the low-frequency resonance region, we need a better understanding of the swimbladder and fish structure than is necessary for high-frequency scattering. Simplified sketches of swimbladders are shown in Figs. 9.4.1 and 9.4.2. In Chapter 10 (Fig. 10.5.1), we show X-ray pictures of an ensemble of brook trout. These sketches and the pictures demonstrate that the swimbladder is quite variable and is not a simple prolate spheroid- (cigar-) shaped organ. A physicist or acoustician can learn much by dissecting (gutting) a fresh fish. Starting with a

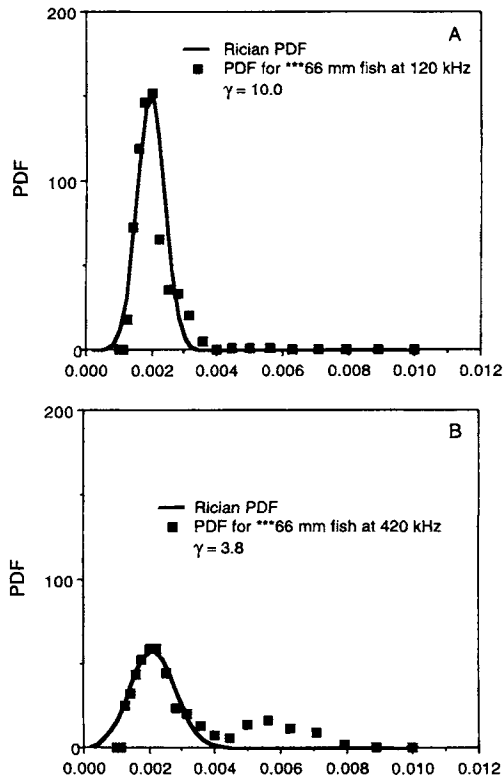

Figure 9.5.8 PDF of scattering from a 66 mm fish. The solid squares are measured echo amplitudes. The solid curves are Rician PDF. (From Jech, J. M., D. M. Schael, and C. S. Clay, "Application of three sound scattering models to threadfin shad (*Dorosoma petenense*)," *J. Acoust. Soc. Am.* **98**, 2262–69, 1995.)

cut along the belly, one finds the liver, intestines, and stomach. The swimbladder is at the top of the cavity, just beneath the spin and ribs. The swimbladder is a gas-filled, elastic-walled sack attached to the ribs. Swimbladder functions include hearing and buoyancy. While the swimbladder can expand and contract downward and sideways as the volume changes, the top keeps the same shape, and the high-frequency back-scattering lengths will be nearly the same at all depths.

Applications of the gas laws to the gas volume and pressure in the swimbladder are complicated because the gas not a free gas bubble (see Chapter 8). In response to external pressure changes, the ability of a fish to adapt to the pressure change by increasing or decreasing gas volume in the swimbladder depends on its physiology. It can take many hours for a fish to adapt to a new depth by adjusting the gas volume and pressure in its swimbladder. The resonance frequency of a full swimbladder

depends on the elastic properties of the membrane and musculature of the fish. A sudden increase of external pressure causes the gas volume to decrease. The swimbladder becomes limp like a sack, causing the resonance frequency to decrease. Sudden decreases of external pressure cause an increase of pressure differential. The gas expands and, correspondingly, the swimbladder membrane expands a little and has a new resonance frequency. Further expansion ruptures the membrane. We strongly recommend the study of the acoustic measurements and their corresponding biological interpretations in Sand and Hawkins (1973) and McCartney and Stubbs (1970). Feuillade and Nero (1997) simulated the Sand and Hawkins experiments. They used a grossly simplified low-frequency resonance model with a gas sphere core, a thin elastic shell around the gas to represent the swimbladder membrane, and a thick viscous shell to represent the fish flesh. The whole fish model is in water. While the high-frequency scattering depends strongly on shape, the low-frequency resonance scattering mainly depends on first behavior, anatomy, physiology, and the physical properties of the swimbladder and the flesh.

Early swimbladder simulations used the classic bubble equation (see Equation 8.2.32). The Qs of the swimbladder resonances were of the order of 1 to 4, much smaller than the Q of a free gas bubble, indicating very large viscous losses. The lumped constant developments in Chapter 8 are for very small viscosity and may be inaccurate for the very large viscosities of fish flesh. Thus, it is prudent to use the traditional wave equation and boundary condition approach.

The spherical wave equation and the boundary conditions are satisfied at each interface between the shells. Elasticity and viscosity greatly increase the complexity of solutions. Analytical solutions have been derived for the gas bubble in an elastic medium (Andreeva, 1964) and for a spherical bubble inside an elastic shell in water (Love, 1978).

In Love's model, the spherical bubble represents the swimbladder and the elastic shell represents the fish flesh. The model is in water. Love chose the shell to be a viscous, heat-conducting Newtonian fluid and derived a total scattering cross-section for $ka_{es} \ll 1$. We give Love's final expressions and follow Love's notation with minor changes. The differential scattering cross-section is $\Delta\sigma$, where $\Delta\sigma = \sigma_{bs} = \sigma/4\pi$.

The scattering expressions are extremely complicated and have many terms. Love made many approximations and dropped terms to reduce the scattering expression to the same form as the classical bubble equation

$$\Delta\sigma = \sigma_{bs} = |\mathcal{L}_{bs}|^2 = \frac{a_{es}^2(\rho_A/\rho_f)^2}{(\omega_0^2/\omega^2 - 1)^2 + \delta^2} \tag{9.5.19}$$

where a_{es} is the radius of the equivalent sphere, δ is the damping constant, ω_0 is the resonance frequency, and ρ_A and ρ_f are the densities of water and fish flesh.

On including the surface tension τ and specific heat ratio $\gamma_a = 1.4$ for the gas, the resonance frequency ω_0 of the spherical bubble is

$$(\omega_0 a_{es})^2 = \frac{3\gamma_a P_A}{\rho_f} + \frac{2\tau}{\rho_f a_{es}(3\gamma_a - 1)} \tag{9.5.20}$$

Surface tension is an approximation for the swimbladder membrane. The distortion of the sphere into a prolate spheroid increases the resonance frequency by a factor that depends on the ratio e of the minor to major axis a_1 and a_2.

$$e = a_1 / a_2 \tag{9.5.21}$$

$$\frac{\omega_{0p}}{\omega_0} = \frac{2^{1/2}(1-e^2)^{1/4}}{e^{1/3}} \left[\ln\left(\frac{1+\sqrt{1-e^2}}{1-\sqrt{1-e^2}} \right) \right]^{-1/2} \tag{9.5.22}$$

where ω_{0p} is the resonance frequency of the prolate spheroid [Strasberg (1953) and Weston (1967)].

The damping constant δ is

$$\delta = \delta_{rad} + \delta_{vis} + \delta_{th,s} \tag{9.5.23}$$

where the damping terms are δ_{rad} for radiation; δ_{vis} for shear viscosity; and $\delta_{th,s}$ for thermal conductivity and surface tension. [In Love, $\omega_0/(\omega H) = \delta$.] The damping terms are

$$\delta_{rad} \equiv \frac{\rho_A \omega a_{es}}{\rho_f c_w}, \quad \delta_{vis} \equiv \frac{2\mu}{\rho_f \omega a_{es}^2} \tag{9.5.24a}$$

$$\delta_{th,s} \equiv \frac{3(\gamma_{air} - 1)}{\omega a_{es}} \left(\frac{\omega \kappa_{air}}{2 \rho_{air} c_{air}} \right)^{1/2} \left(1 + \frac{2\tau}{\rho_f \omega^2 a_{es}^3} \right) \tag{9.5.24b}$$

where μ is shear viscosity, τ is surface tension, κ_{air} is thermal conductivity of air. Love dropped the dependence of the scattering on the dimensions of the spherical shell surrounding the gas bubble. Love's values for the parameters are in Table 9.3.

The distortion of the sphere to a prolate spheroid causes the radiation damping to increase as $1/e$ (Ye, 1996)

$$\text{Spheroid } \delta_{rad} \approx \frac{\rho_A k a_1 \sqrt{1-e^2}}{e \rho_f \ln[(1+\sqrt{1+e^2})/e]} \tag{9.5.25}$$

Table 9.3 **Notation and Swimbladder Parameters**

Parameter and Units	*Air*	*Sea Water*	*Fish Flesh*
a_{es} = radius of equivalent sphere (cm)			
c = sound speed (cm/s)	3.3×10^4	1.5×10^5	1.55×10^5
ρ = density (g/cm^3)	1.3×10^{-3}	1.026	1.05
τ = surface tension (dyne/cm)			10^4 to 6×10^6
γ = ratio of specific heats	1.4	1.01	1.01
C_p = specific heat, constant P (cal/g°C)	0.24	0.93	0.89
κ = thermal conductivity (cal/cm s°C)	5.5×10^{-5}	1.34×10^{-3}	1.32×10^{-3}
μ = dynamic shear viscosity (poise)			1 to 5000
P_A = ambient pressure (dynes/cm^2)			
Surface pressure $= 10^6$ dyne/cm^2			

(From Love, R. H., "Resonant acoustic scattering by swimbladder-bearing fish," *J. Acoust. Soc. Am.* **64**, 571–80, 1978.)

In the limit, as e goes to 1, the spheroid damping becomes the radiation damping constant δ_{rad} in Equation 9.5.24a.

A comparison of the acoustic scatter from a small cod and a computation using Equation 9.5.19b and Cod A (Fig. 9.4.2) is shown in Fig. 9.5.9. A particularly useful set of measurements were made by Sand and Hawkins (1973). They used the technique of McCartney and Stubbs (1970), where fish was placed inside a ring hydrophone in a cylindrical cage. The ring hydrophone measured the monopole component of the scattered sound. The fish and ring hydrophone were insonified by a CW source. The target strength measurements were relative to an arbitrary reference.

At the cod's adapted depth, the maximum of the data is about 1.8 kHz, while the theory has a maximum at 1.2 kHz. One can hypothesize that the connective tissue of the swimbladder causes the frequency increase (Feuillade and Nero, 1997).

In field measurements, one does not have the luxury of having a single length of fish at a single depth. Love (1993) gives real-world results of extensive acoustical surveys in the Norwegian Sea. The scattering data were taken by using small explosive charges and a broad bandwidth directional receiving system. The data processing consisted of selecting a depth range and doing frequency spectral analysis of the pressure signals from a distribution of fish lengths at that depth range. A much simplified set of examples and numerical simulations can

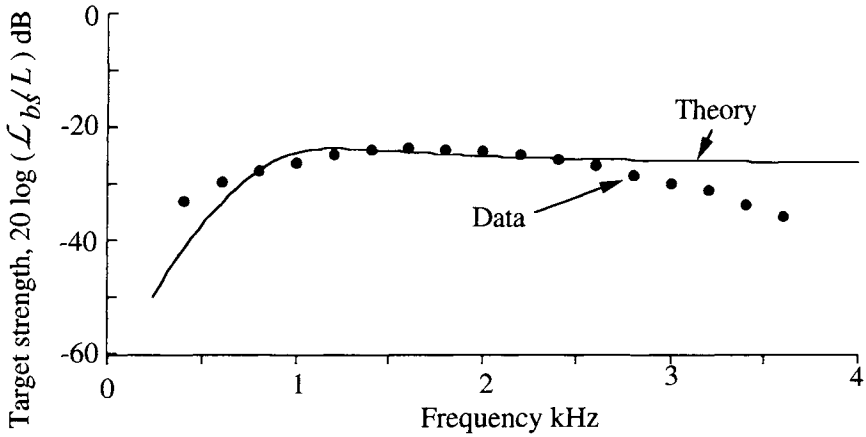

Figure 9.5.9 Comparison of low-frequency range of acoustic scattering from cod A and data from Sand and Hawkins (1973). The fish was a 16 cm cod. The data are for the fish at its adapted depth of 11 m. The numerical calculations used viscosity = 750 poise and cod A for an acoustic model. The swimbladder volume was computed using a triangular cross-section approximation as seen in Fig. 9.4.2. This volume was used to compute an equivalent prolate spheroid. Parameters: fish length $L = 160$ mm, $z = 11$ m, and $\chi = 0$ deg. The data have an arbitrary reference level.

illustrate the separate dependencies on depth and fish length in Love's measurements. To show the effect of the distribution of fish lengths, Equation 9.5.17 was used to calculate target strengths for 25, 28, and 31 cm blue whiting at a fixed depth (375 m); the results are represented in Fig. 9.5.10a. The target strengths for a fixed fish size (28 cm) at different depths (300, 375, and 450 m) are shown in Fig. 9.5.10b.

In Love's surveys, all of the backscattered sounds are from the fish within a depth range. Fig. 9.5.11 shows the data and the theoretical curve for the fish and depths shown in Fig. 9.5.10. The loss of resolution precludes using this kind of field data to test the details of scattering theories.

Fishery surveys usually report fish lengths and species. Fish lengths are measured because it is hard to measure fish weights on a rolling ship. An empirical relation between fish length L and weight W_f is

$$W_f \approx k_{LW} L^3 \tag{9.5.26}$$

where k_{LW} is in gm/cm^3, L is in cm, and W_f is in gm. For blue whiting, the empirical constant k_{LW} may range from 0.0047 to 0.0062 depending on the season, spawning condition, and age of the animal (Love, 1993).

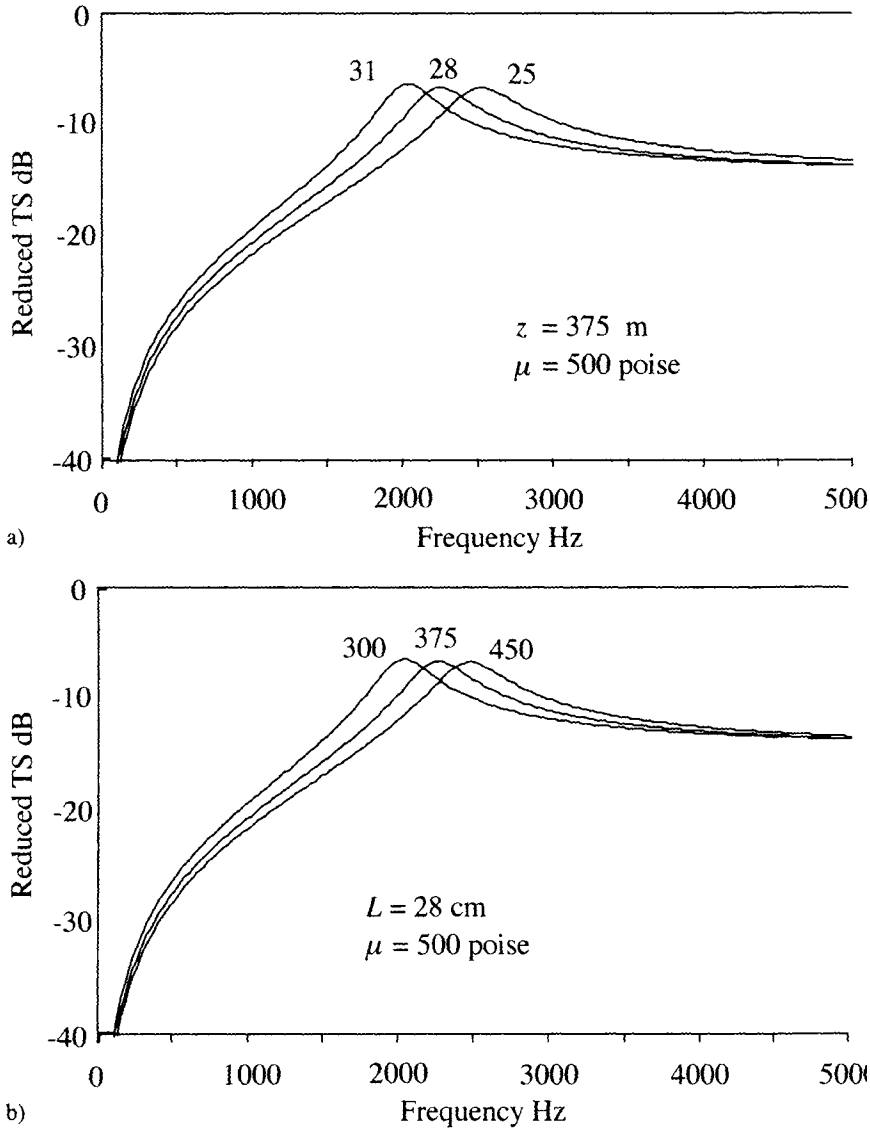

Figure 9.5.10 Reduced target strengths, $TS_{re} = 20 \log[L_{bs}(f)/L)]$ dB, for Love's spheroidal swimbladder model. The parameters were chosen to match blue whiting *Micromesistius poutassou*. See Love (1993). The reference length for the reduced or relative target strength computations is $L = 28$ cm. *Above*, Fixed depth $z = 375$ m for three lengths (cm). *Below*, Fixed fish length $L = 28$ cm at three depths (m).

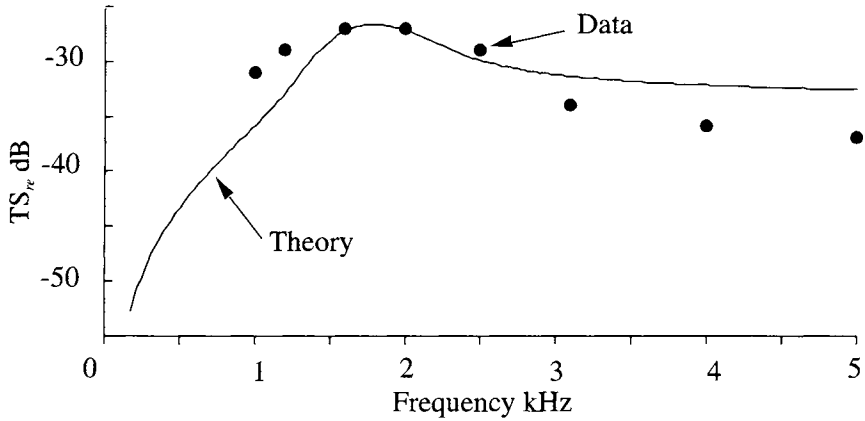

Figure 9.5.11 Comparison of Love's swimbladder model and a survey in the Norwegian Sea. The data are from Love (1993). Target strengths are reduced $TS_{re} = 20 \log[\mathcal{L}_{bs}(f)/L]$ using the reduction length of 28 cm. The depth range is 300 m to 450 m.

9.6 Sound Backscattered by Zooplankton

Acoustical estimates of zooplankton populations can be made if the scattering lengths are known as a function of frequency and zooplankton size. In most acoustical surveys, zooplankton are too close together for echoes from individuals to be resolved. In the laboratory, the echoes from individuals are very small because the animals are small. NcNaught (1968, 1969) and Greenlaw (1979) suggested using multiple-frequency sonars to separate different sizes of zooplankton populations. The methods depend strongly on the frequency dependence of scattered sound as described in Chapter 7.

Zooplankton are often modeled by fluid-filled spheres and cylinders. The fluid sphere model and matrix inversion methods (Chapter 10) have been used by Johnson (1977), Greenlaw (1979), Holliday and Pieper (1980), and Holliday, Peiper, and Kleppel (1989) to interpret scattering from aggregates of small plankton.

Zooplankton have appearances and structures that range from simple to "exotic." Fig. 9.6.1 shows sketches of zooplankton. These animals are examples of the kinds of the structures that we want to model acoustically by using simple elements such as combinations of cylinders and spheres. The physical properties of the animals are needed in order to model them. Physical

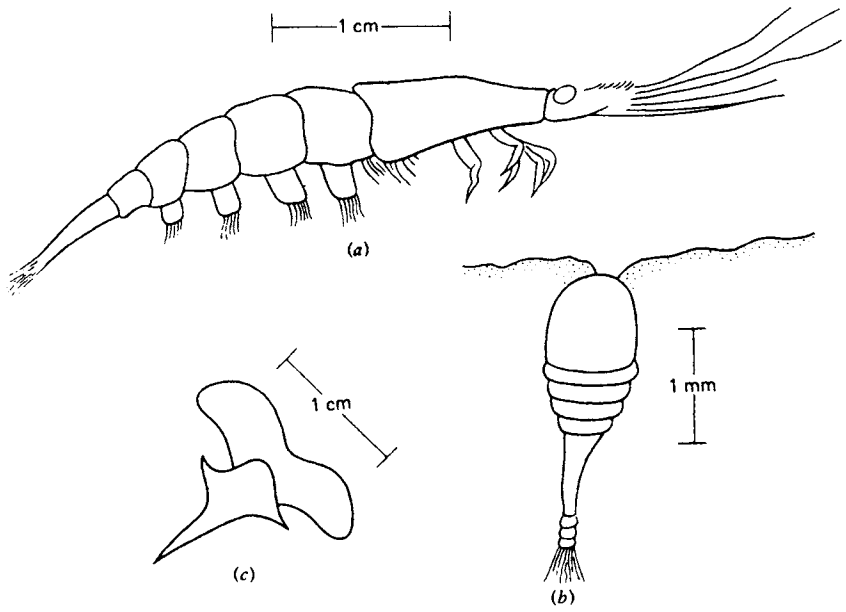

Figure 9.6.1 Zooplankton. a) Euphausid. b) Copepod. c) Pteropod. Based on sketches in M. G. Gross, *Oceanography a view of the earth* (1972), pp. 427–430.

properties of many zooplankton are given in Tables 9.4 and 9.5. The sound velocity and density contrasts of most zooplankton, relative to water, are generally quite small. On the other hand, the finite-length bent fluid cylinder and Kirchhoff models look more like a shrimp and are surprisingly accurate acoustical models of the animal.

Laboratory measurements of sound scattering by zooplankton are difficult to make because the animals are small and the echoes are very small. It is hard to keep the animals alive and in good condition for measurements. Techniques and results are in the papers on preserved zooplankton (Greenlaw 1979), encaged aggregations of krill (Foote 1990a, 1990b), and single zooplankton (Chu, Stanton, and Wiebe 1992).

9.6.1 HK ACOUSTICAL MODELS OF ZOOPLANKTON

The HK expression for sound scattered by zooplankton is the same as for sound scattered by fish bodies (Equations 9.5.12 through 9.5.14). For a straight cylinder

Table 9.4 **Measured Dimensional Properties of Several Zooplankters in Terms of Coefficients of the Allometric Expressions $\Delta V = aL^{\beta}$ and $a_{es} = \gamma L^{\delta}$**

Organism	$a \times 10^6$	β	γ	δ
Euphausiids				
Euphausia sp.	6.03	3.07	0.11	1.02
E. pacifica ($n = 10, r^2 = 0.97$)	20.2	2.80	0.17	0.93
E. superba	3.67	3.16	0.10	1.05
	3.471	3.1761	0.09	1.0587
Meganyctiphanes norvegica	49.0	2.58	0.23	0.86
	43.7	2.59	0.22	0.86
Nematoscelis sp.	1.29	3.50	0.07	1.17
Nematobrachion *sp.*				
Nyctiphanes sp.	9.77	2.79	0.13	0.93
Pseupeuphausia sp.				
Stylocheiron sp.	4.07	3.34	0.10	1.11
Thysanoessa sp.	3.47	3.33	0.09	1.11
Thysanopoda sp.	6.76	3.07	0.12	1.02
All euphausiids	5.75	3.10	0.11	1.03
Decapods				
Sergestes similis ($n = 4, r^2 = 0.96$)	3.74	3.00	0.10	1.00
Copepods				
Acartia tonsa	129.0	3.00	0.31	1.00
Calanus finmarchicus	37.5	3.06	0.21	1.02

Where ΔV is in ml, L is the length in mm and $a_{es} = \gamma L^{\delta}$; where a_{es} is the radius of the equivalent sphere. (From Greenlaw, C. F., and R. K. Johnson, "Physical and acoustical properties of zooplankton," *J. Acoust. Soc. Am.* **72**, 1706–10, 1982.)

having radius a_{ec}, the scattering length is

$$\mathcal{L}_{ec} \approx -i\frac{L_e}{2\sqrt{\pi}}[(ka_{ec}\cos\chi)]^{1/2}\frac{\sin\Delta}{\Delta}\mathcal{R}_{wb} \times e^{-i2ka_{ec}}[1 - \mathcal{T}_{wb}\mathcal{T}_{bw}e^{i4k_b a_{ec}+i\psi_b}] \tag{9.6.1}$$

where the parameters are given in Equations 9.5.12 and 9.5.13. The reader will notice that the bracket [...] in Equation 9.6.1 is the sum of two arrivals: "1" and "$\mathcal{T}_{wb}\mathcal{T}_{bw}\exp(i4k_b a + i\psi_b)$." The term $4k_b a_{ec}$ gives a time delay of $4a_{ec}/c_b$. The phase shift ψ_b, using Equation 9.5.13, tends to

$$\psi_b \approx -\pi/2 \quad \text{for} \quad k_b a \gg 1 \tag{9.6.2}$$

Table 9.5 **Values of Physical Properties for Some Zooplankters**

Organism	*Temp.* °C	ρ *g/ml*	*c* *m/s*	κ 10^{-10} *m-s/kg*	*g*	*h*	*k*
Amphipods							
Cyphocaris sp.	20	1.080–1.100		3.82–3.89	1.055–1.074		0.917–0.933[a]
	25.6						
			1542			1.009	
Gammarus pulex	20				1.066–1.088		
Parathemisto pacifica	20	1.080–1.100	1514	3.96–4.04	1.055–1.074	1.000	0.931–0.948
Sciva sp.	20	1.080–1.100			1.055–1.074		
Cladocerans							
Chirocephalus diaphanus	11.3				1.011		
Daphnia pulex	7				1.017		
Copepods							
Calanus finmarchicus	15.4				1.029–1.033		
	15				1.045–1.049		
					1.0255–1.0265		
					1.043–1.047		
Calanus plumchrus	20	1.070			1.047		
	23.4		1533	4.02		1.006	0.918[a]
	25		1546			1.012	
Eudiaptomus gracilis	8				1.023		
Decapods							
Sergestes similis (preserved)	16.5		1515			1.006	
	24		1522			0.997	
Sergestidae and Oplophoridae							1.075

continued

Organism	*Temp.* °C	*ρ* *g/ml*	*c* *m/s*	*κ* 10^{-10} *m-s/kg*	*g*	*h*	*k*
Euphausiids							
Euphausia pacifica	7.4	1.063			1.037		
	16.2		1513			1.005	
	19		1505			1.000	
	19.2		1504			1.000	0.935[a]
	20	1.060–1.065			1.035–1.040		
	22.4		1555			1.022	
	24.1		1550			1.016	
	25.4		1553			1.015	
E. pacifica (preserved)	9.4	1.043	1502	4.25	1.043	1.038	0.889
	12						0.850
E. superba		1.049–1.068			1.021–1.040		
Meganyctiphanes norvegica		1.035			1.010		
Thysanoessa raschii	12.3	1.055	1511	4.15	1.027	1.010	0.955
	9	1.040–1.045	1532–1555	3.96–4.10	1.013–1.018	1.032–1.046	0.875–0.903
	20	1.070–1.075			1.045–1.050		
Mysids							
Memimysis lamornae	6.4				1.075		

[a] κ, k computed from average values of ρ, c, g, h.

(From Greenlaw, C. F., and R. K. Johnson, "Physical and acoustical properties of zooplankton," *J. Acoust. Soc. Am.* **72**, 1706–10, 1982.)

and the second arrival has a $-90°$ phase shift relative to the first. An example of the frequency domain expression (Equation 9.6.1) and its Fourier transformation are shown in Fig. 9.6.2.

Fig. 9.6.2 might seem to be so idealized that one could not get a corresponding signal from real shrimp. Fig. 9.6.3 shows the corresponding echoes from a shrimp.

9.6.2 *BENT-CYLINDER ACOUSTICAL MODELS*

Finite fluid cylinders are used to model fish bodies (no swimbladder) and zooplankton such as shrimp. Comparisons of the results of models and data show that the fits are improved by bending the cylinders [2,3,8]. The acoustically effective length of a bent cylinder is

$$L_{ebc} = \int_0^L e^{i\,2\,k\,z(x)}\,dx \tag{9.6.3}$$

Using a parabolic displacement function, $z(x)$ is

$$z\ (x\ ) = \beta x^{\,2} \tag{9.6.4}$$

The acoustically equivalent length of a bent cylinder is

$$L_{ebc} = \int_0^L \exp\left(i\,2k\,\beta\,x^{\,2}\right) dx \tag{9.6.5}$$

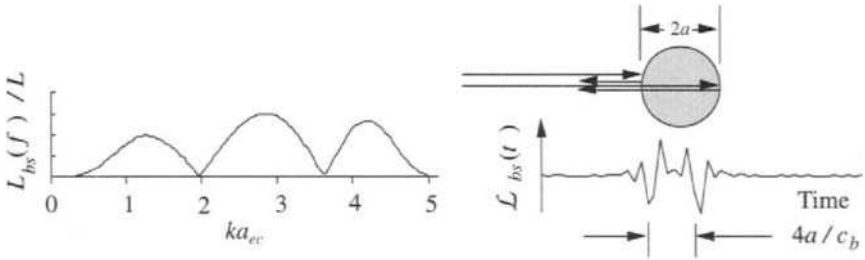

Figure 9.6.2 Frequency and time domain representations of scattering by finite fluid cylinders. Amplitude and time scales are arbitrary. The HK algorithm (Equation 9.6.1) was used to compute the scattering length in the frequency domain and filtered to reduce the amplitudes at low and high frequencies. The finite Fourier transformation was used to compute the time domain signal. a) HK computation for frequency (ka_{ec}) domain. b) Transformation to time domain. Note the reflections from the near and far surfaces of the cylinder. The time delay of the second arrival is the travel time for a round trip through the cylinder.

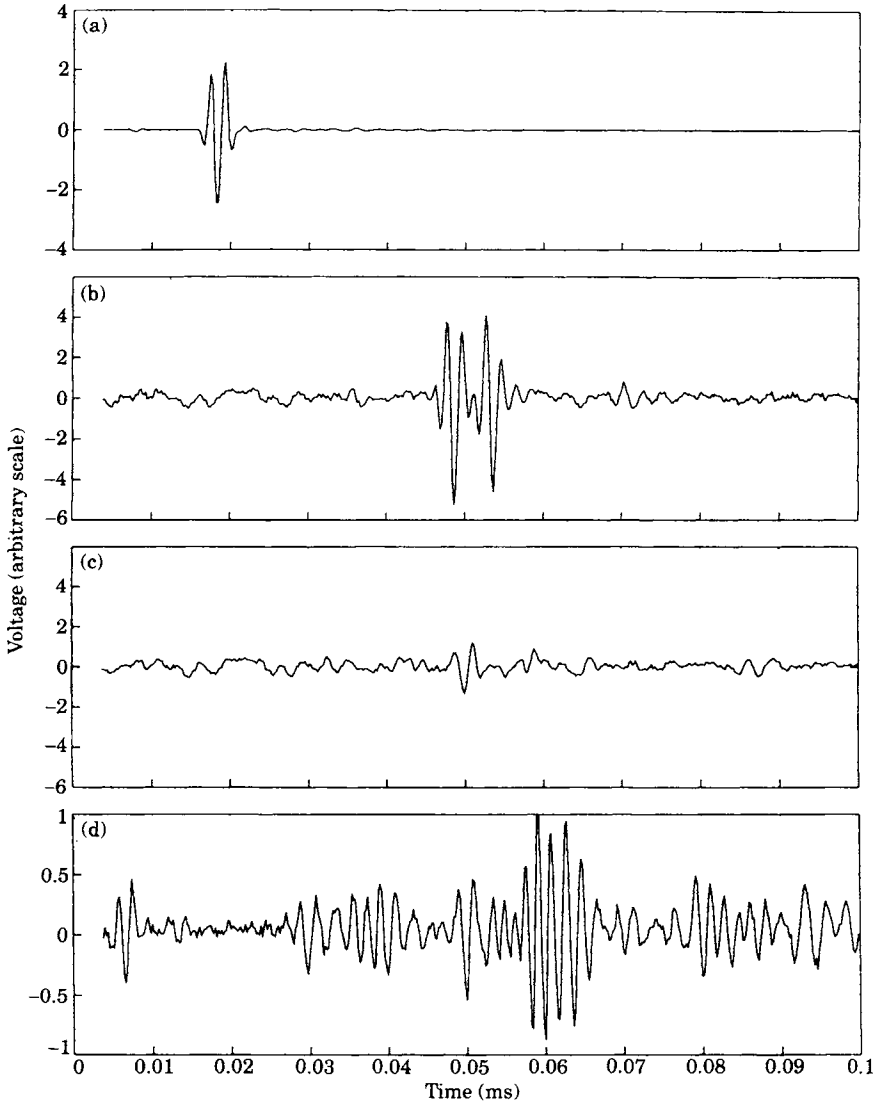

Figure 9.6.3 Scattering of an impulse wave by a live decapod shrimp. a) The incident impulse acoustic signal; b) single echo from a decapod shrimp near broad side incidence; c) single echo from the decapod shrimp near end-on incidence; d) single echo from laboratory generated turbulence. Note the change of scale. (From Stanton, T. K., C. S. Clay, and D. Chu, "Ray representation of sound scattering by weakly scattering deformed fluid cylinders: simple physics and applications to zooplankton," *J. Acoust. Soc. Am.* **94**, 3454–62, 1993.)

where the subscript $_{ebc}$ indicates an equivalent bent cylinder. The integral for L_{ebc} (Equation 9.6.5) has the form of a Fresnel integral. Change the variables to the following parameters

$$\frac{\pi}{2}\xi^{2} \equiv 2k\beta x^{2} \quad \text{and} \quad \xi_1 \equiv 2L\sqrt{k\beta/\pi} \tag{9.6.6}$$

and obtain the standard form of the Fresnel integral (Abramowitz and Stegun 1964, sec. 7.3):

$$C(\xi) = \int_0^{\xi_1} \cos\left(\frac{\pi}{2}\xi^2\right) d\xi \quad \text{and} \quad S(\xi) = \int_0^{\xi_1} \sin\left(\frac{\pi}{2}\xi^2\right) d\xi \tag{9.6.7}$$

The expansion of Equation 9.6.5 gives the sum of the Fresnel integrals:

$$L_{ebc} = \left(\frac{\pi}{4k\beta}\right)^{1/2} [C(\xi_1) + iS(\xi_1)] \tag{9.6.8}$$

where βL^2 is the displacement of the end of the bent cylinder at $x = L$.

Relative (or reduced) scattering amplitudes are computed using L as the reference length. Examples of the effect of bending the fluid-filled cylinder are shown in Fig. 9.6.4. Relative to the straight cylinder ($\beta = 0$), bending causes the scattering amplitudes to decrease at large *ka*.

9.6.3 SCATTERING AMPLITUDES OF LIVE SHRIMP

We have chosen to show the scattering measurements of single shrimp and make comparisons to a rather precise acoustical theory. Once a model is shown to match an individual animal, then one can use the model to compute the scattering amplitudes for a distribution of zooplankton sizes and behaviors.

Laboratory measurements were made of the acoustic scattering by live shrimp *Palaemonetes vulgaris* (Chu, Stanton, and Wiebe 1992), shown in Fig. 9.6.5. Some shrimp may have a short horizontal section that curves down to a tail and others may be straight. Shrimp are different, and depending on the shape, one can use numerical integrations. For model shrimp, it is convenient to use the *arc length* of the shrimp L_a as a primary measure.

Two live shrimp of lengths 13.5 mm and 19.8 mm were used. The shrimp were insonified in dorsal aspect. The acoustical measurements were made by using a wide-band-frequency-modulated "chirp" as the source. The receiver was mounted next to the source. The effective spectrum of the chirp was from 330 to 650 kHz. Echoes from the shrimp were amplified and then were Fourier

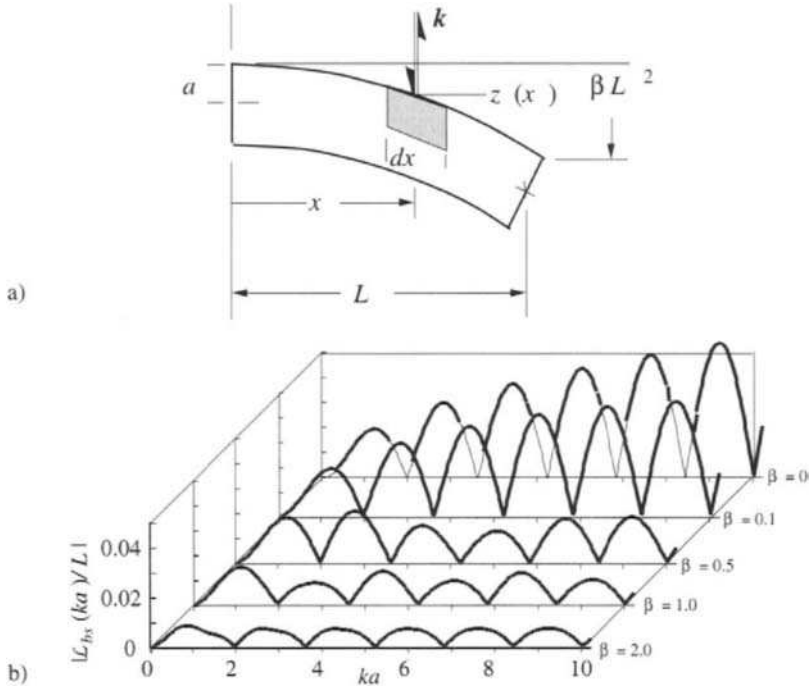

Figure 9.6.4 Bent cylinder and relative scattering amplitude. a) Incident and backscattered component. b) Relative scattering amplitudes for different amounts of deflection of the parabolically bent cylinder, $z(x) = \beta x^2$: $L = 0.1$ m; $a = 0.01$ m; $g = 1.036$; and $h = 1.026$.

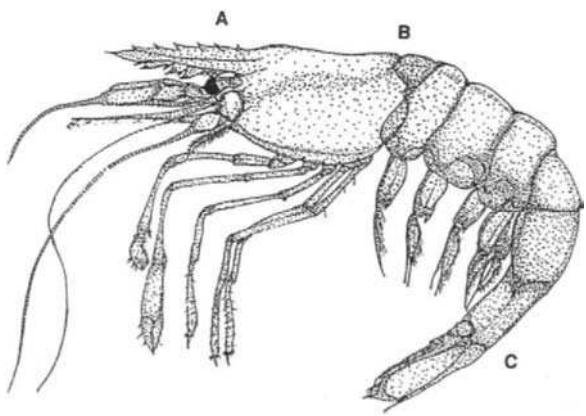

Figure 9.6.5 Lateral view of a typical *Palaemonetes* species. Thorax is from A to B; length L_a is measured from A to C when the body is fully extended. (From Chu, D., T. K. Stanton, and P. H. Wiebe, "Frequency dependence of backscattering from live individual zooplankton," *ICES J. Mar. Sci.* **49**, 97–106, 1992.)

analyzed. Since live shrimp move between pings, single echoes were chosen for analysis. The backscattering cross section and reduced target strengths were computed from the spectral amplitudes:

$$\sigma_{bs} = |\mathcal{L}_{bs}|^2 \quad \text{and} \quad TS_{re} = 10\log(\sigma_{bs}/L_a^2) \tag{9.6.9}$$

where L_a is the shrimp (arc) length, and we introduce the reduced target strength TS_{re}. The frequency dependence is implicit. The reduced/relative target strengths for both shrimp are shown in Fig. 9.6.6. There are deep nulls at $ka \approx 2$, 3.6, and 5. The values and spacings of the nulls are diagnostic of the animal sizes.

The most important results are the agreement of the locations of the experimental and theoretical nulls for cylindrical fluid models. The bent-cylinder theory, Fig. 9.6.4, gives a reduction of the scattering lengths at large ka relative to the straight cylinder. As shown in Fig. 9.6.6, a bent cylinder matches the data better than the straight cylinder. The thorax of the shrimp sketched in Fig. 9.6.5 is

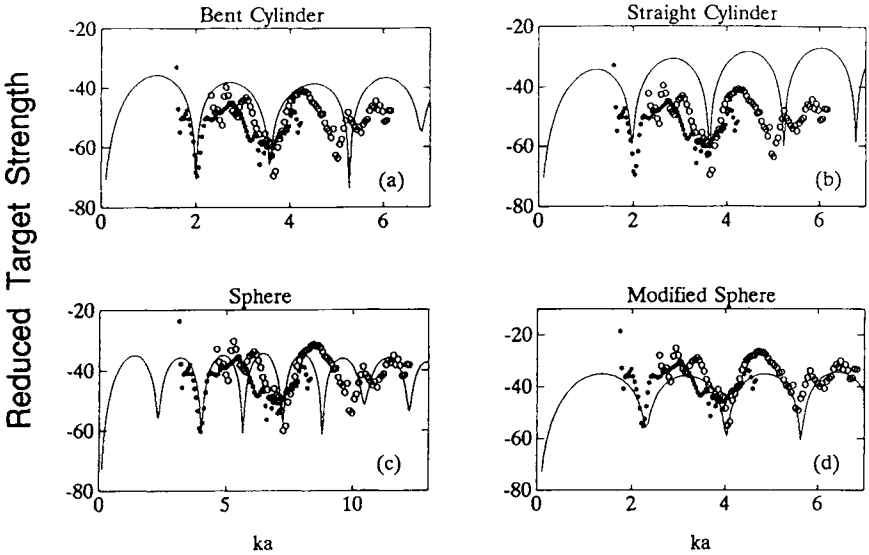

Figure 9.6.6 Comparisons of measured relative target strengths TS_{re} and models: cylinder, bent cylinder, sphere, and modified sphere. The anesthetized shrimp (*Palaemonetes vulgaris*) were tethered by human hairs in an inverted position and insonified in dorsal aspect from below the shrimp. Theoretical reduced target strengths are given relative to the arc length of the shrimp or the area of the sphere. $TS_{rc_c} = 20\log|\mathcal{L}_{cyl}/L_a|$, dB and $TS_{re_s} = 10\log[|\mathcal{L}_{sph}|^2/(\pi a^2)])$], dB. (From Chu, D., T. K. Stanton, and P. H. Wiebe, "Frequency dependence of backscattering from live individual zooplankton," *ICES J. Mar. Sci.* **49**, 97–106, 1992.)

rough. Decreases of g to 1.03 and h to 1.01 would move the theoretical target strength curves down and give a better match to the data.

As mentioned earlier, zooplankton are also modeled as equivalent spheres that have the same volume as the animal. The problems of using this approximation for shrimp are shown in Fig. 9.6.6c and d. The equivalent spherical radius for the shrimp gives nulls at the wrong values of ka. To fit the null spacings, the equivalent radii of the spheres were reduced to $0.56a_{Es}$. These changes gave the curve shown in Fig. 9.6.6d. Reduction of the equivalent radius also reduced the target strengths too much.

The fit of the bent-cylinder model to the scattering amplitudes for a single echo from a shrimp is remarkable. Even though the shrimp looks like a crude and bumpy bent cylinder, the nulls are well defined to $ka \approx 5$. The bent cylinder is an accurate working model for shrimp.

9.7 Bubble-Carrying Plankton

At sea, there are tiny gas-bubble–carrying plankton that, though only millimeters in extent, have a very large scattering effect. One example is *Nanomia bijuga*, a colonial hydrozoan jellyfish (order Siphonophora, suborder Physonectae) that has been identified as a primary cause of some sound scattering layers off San Diego, California. Positive identification was accomplished by simultaneous viewing from a deep-sea submersible while recording the backscattered sound (see Fig. 9.7.1).

Siphonophores consist of many specialized individuals, aligned along an axis that may be as long as 75 cm. One of the major groups of siphonophores, the Physonectae, is identifiable by bubble-carrrying pneumatophores, which operate as flotation elements for the colony. This individual is approximately a prolate spheroid of dimensions about 3 mm × 1 mm and contains from 12.6 mm^3 to 0.25 mm^3 of ejectable, rechargable, carbon monoxide gas ($\gamma = 1.40$). The resonance frequencies, which may be calculated from Equation 8.2.13, adjusted by the ellipticity factor in Fig. 8.2.6, range fom about 7 to 27 kHz at 100 m depth.

9.8 Allometric Expressions for Zooplankton

The overwhelming complexity and vast differences in physical appearance of zooplankton has led acousticians to look for simple generalized dimensional

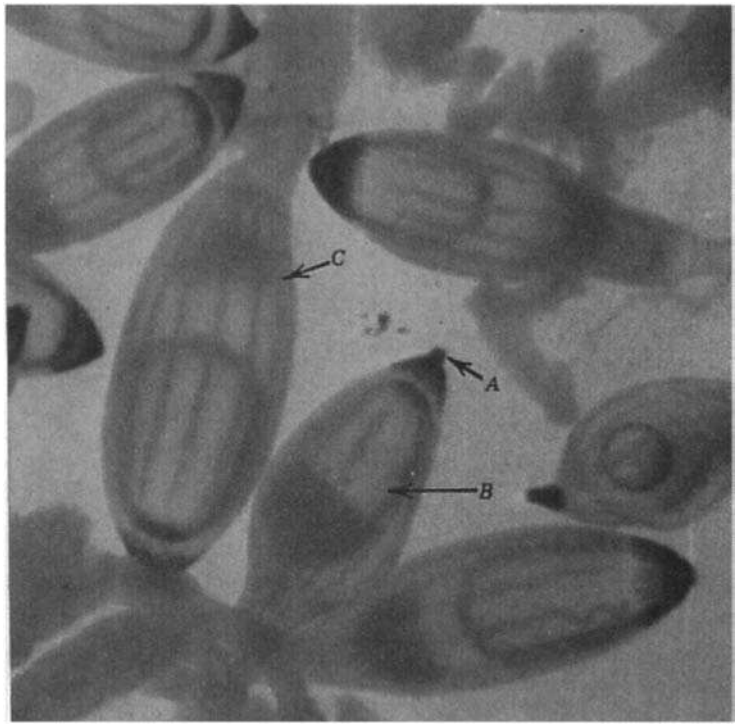

Figure 9.7.1 Photograph of pneumatophores of *Nanomia bijuga* with contained gas bubbles: A, pore; B, gas gland; C, longitudinal muscle band. (From Barham, E. G., "Siphonophores and the deep scattering layer," *Science* **14**, 826–28, 1963.)

"allometric" expressions that are adequate for puposes of scattering calculations. The following expressions are from Greenlaw and Johnson (1982). Where convenient, their notation is used:

$$\Delta V = \alpha L^{\beta} \qquad \Delta V \text{ in ml, } L \text{ in mm} \tag{9.8.1}$$

$$a_{es} = \gamma L^{\delta} \qquad \text{radius of equivalent sphere} \tag{9.8.2}$$

where density ratio is $g =$ (scatterer)/(medium); sound speed ratio is $h =$ (scatterer)/(medium); compressibility ratio is $k =$ (scatterer)/(medium); compressibility is κ.

Problems

Section 9.2

9.2.1 Use Fig. 9.2.2. The sonar frequency is 50 Hz and the circular transducer diameter is 10 cm. The sonar transmits a 1 ms ping. At 1 m from the transducer and on the axis of the transducer, the peak pressure of the ping is 3 Pa. A 2 cm diameter stainless-steel sphere is at 5 m range. a) Calculate the sound pressure incident on the sphere. b) Calculate the sound pressure scattered back to the transducer. c) Plot the peak of the backscattered sound pressure at the transducer as a function of θ.

Section 9.3

9.3.1 The sonar of Problem 9.2.1 insonifies several 5.2 cm diameter stainless-steel spheres at the following ranges: 10, 11, 13, 15, and 19 m. The spheres scatter sound (echoes) back to the transducer. The spheres are on the axis of the transducer. a) Compute and graph the envelopes of the echoes. b) Compute the squared sound pressure and the volume backscattered sound for the volume bounded by 9 and 20 m. c) Compare the values of the cross terms to the squared pressure terms.

9.3.2 Use the same sonar as in Problems 9.3.1 and 9.2.1. The objects are on the axis of the transducer. The ranges are 10, 10.02, 10.93, 11.0, and 11.8 m. Repeat a), b) and c) of Problem 9.3.1. d) Do you obtain interfering arrivals?

9.3.3 Use the sonar of Problem 9.3.1. Choose a random number generator that gives an uniform distribution of random numbers between 0 and 1 (*rnd* is the usual one in computers). Let $R = 10 + 2x$ *random* and select five ranges to do the sonar signal calculations for a) through d) of Problem 9.3.2.

9.3.4 Repeat Problem 9.3.3 for three more sets of random ranges. e) Combine all of the data to compute the mean-squared sound pressures for the set of four random ranges. Compare the average values of the cross terms with the mean-squared pressure.

Section 9.5

9.5.1 Use a gas-filled cylinder to make an oversimplified model of a gas-filled swimbladder in water. Let the length be 10 cm and the diameter be 1 cm. Use the Kirchhoff approximation for backscattering length calculations. a) Calculate and plot $\mathcal{L}_{bs}$ for the range of $0.2 < ka < 10$. b) Plot the same versus frequency.

9.5.2 Use results from Problem 9.5.1 and compute and plot the scattering lengths for $\chi = 0$ to 20° for $ka = 5$.

9.5.3 Use a fluid-filled cylinder to make an oversimplified fluid model of a large zooplankton in water. Let the length be 10 cm, the diameter be 1 cm, $g = 1.036$, and $h = 1.028$. Use the Kirchhoff approximation for backscattering length calculations. a) Calculate and plot $\mathcal{L}_{bs}$ for the range of $0.2 < ka < 10$. b) Plot the $\mathcal{L}_{bs}$ versus frequency.

9.5.4 Use results from Problem 9.5.3. For $ka = 1.7$, 2, and 2.9, compute and plot the scattering lengths for $\chi = 0$ to 20°.

9.5.5 Use a fluid-filled cylinder to make an oversimplified fluid model of a fish body in water. Let the length be 30 cm, the diameter be 3 cm, $g = 1.036$, and $h = 1.028$. Use the Kirchhoff approximation for backscattering length calculations. a) Calculate and plot $\mathcal{L}_{bs}$ for the range of $0.2 < ka < 10$. b) Plot the $\mathcal{L}_{bs}$ versus frequency, 10 to 200 kHz.

9.5.6 Place the gas-filled cylinder, Problem 9.5.1, along the axis of the fish body of Problem 9.5.5. a) Calculate the coherent sum of the scattering lengths and plot the $\mathcal{L}_{bs}$ versus frequency. Let the frequency range be 10 to 200 kHz. b) Tip the axis of the gas-filled cylinder 7° and repeat a).

9.5.7 Use the low-frequency resonance model to calculate the scattering from the simplified fish model of Problem 9.5.6. Calculate $\mathcal{L}_{bs}$ in the frequency range of 50 to 20,000 Hz.

Chapter 10 | Sonar Systems: Measurements and Inversions

10.1 Types of Sonars 406
10.1.1 Echo Sounder 407
10.1.2 Side-Scanning Sonar 408
10.1.3 Multibeam Sonar 408
10.1.4 Doppler Sonar 411
10.1.5 Passive Acoustical Systems 411
10.1.6 Steered Array Systems 413
10.2 Sonar Systems: Details 416
10.2.1 Generic Sonar 416
10.2.2 Band-Shifting or Heterodyning Operations 418
10.2.3 Echo Identification Rules 422
*10.2.4 Using Sonar System Specifications (Optional) 424
10.2.5 Sonar Calibration with a Hard Spherical Target 427
10.3 In Situ Scattering-Length Measurements 430
10.3.1 Empirical Target Strength Formulas for Fish at $L/\lambda > 1$ 430
10.3.2 Echoes from Single Fish and the Critical Fish Density 431
10.3.3 Dual-Beam Sonars 432
10.3.4 Split-Beam Sonars 435
*10.4 Single Transducer: Scattering-Length Measurements (Optional) 437
10.4.1 Probabilities 438
10.4.2 Transducer Beam Pattern PDF 439
10.4.3 Combination of Fish Echo PDF and Transducer PDF 441
10.4.4 Convolution Expression for Echo PDF 443
10.4.5 Fish Echo Data Reduction 443
10.4.6 A Forward Iteration Estimate of Fish Density 445
10.4.7 Deconvolution Method for Fish Density and Echo PDF 445
10.4.8 Examples of Single Transducer Surveys 447
10.5 Interactions of Sonars and Fish Behavior: Simulations 449
10.5.1 Ensemble of the Same Species of Fish 450
10.5.2 The PDF w_F of an Ensemble of Fish 451
10.5.3 Very Narrow Beam Width and Random Fish Tilts 454
10.5.4 Wide Beam Width and Horizontal Fish 456
10.6 Quantitative Reverberation Analysis: Zooplankton 458
10.6.1 Volume Reverberation Equations 460
*10.6.2 Inverse Solution Using Multiple Frequencies (Optional) 461
10.6.3 Acoustic Profiles of Zooplankton 462

*Background material.

Sonar systems are used to remotely sense the interior of the ocean, what is in it, its surface, its bottom, and structure beneath the bottom. Many specialized systems have been developed to do this. Data interpretation methods range from a simple display of "what's there and what's it doing" to statistical analysis of the pressure signals received by a system. In display and analysis there are two signal-processing classes: resolved and unresolved scatterers or reverberation. With *resolved signals*, the sources, scatterers, and so forth are separately displayed or imaged in time and space. Decades of development in sonar systems have improved the time and spatial resolution of the systems. With *unresolved signals*, the pressure signals from the sources, scatterers, and so forth are not separated in time or space and are called "reverberation." Statistical analysis, spectral analysis, and directional scattering are used in the study of unresolved scatterers in the reverberation.

Acoustical studies of animal organs and flesh in medical physics have a striking resemblence to acoustical probing of the ocean. General objectives are to define the shape and structures of organs and to find anomalies within organs. In animals, the frequencies are much higher—from 2 to 50 MHz—and the ranges are measured in mm. Madsen, Insana, and Zagzebski (1984) give a detailed development of the data-reduction methods that are used in medical physics. They compared their data-reduction method to laboratory measurements of the sound scattering by glass beads in agar gel. Another example of a laboratory experiment is the measurements of the scattering of polystyrene beads in agarose (Bridal et al. 1996 and their references).

As our ability to image scatterers has improved, the number and complexity of tasks in the reverberation region are reduced. Even so, for any sonar system, there is always an unresolved region where new kinds of measurements and analysis are needed.

10.1 Types of Sonars

Many sonar systems are almost one-task devices. The introduction of digital recording and data analysis has broadened the range of usefulness of an instrument so that a single instrument may be able to do several related tasks. Digital software has replaced many of the analog operations in sonar systems, and digital signal processing has improved the adaptability of a system to new tasks. Sonar hardware and transducer configurations tend to be specialized to measurement task. Starting with a simple sonar or echo sounder, we describe sonar configurations and their relation to remote sensing tasks. Generally, acoustic pings are used.

10.1.1 ECHO SOUNDER

The most common sonar system is the echo sounder (Fig. 10.1.1). It employs an electrical signal generator and amplifier, called a "transmitter," a transducer to convert an electrical signal to sound; a transducer to convert sound to an electrical signal; an electrical receiving circuit; and display. Many sonar systems use the same transducer for transmission and reception. Systems range in complexity from the "fish finders" that are sold in sporting goods departments to multibeam systems that are used by commercial fishermen and navies. The multibeam systems are basically combinations of many single-beam systems.

A typical echo sounding record is shown in Fig. 10.1.2. This sonar has a time (or depth) varying gain to compensate for the $1/R^2$ dependence of the echo amplitude on range. It is easy to interpret the record *qualitatively*. The small black dots are echoes from single targets, here fish. A school of fish appears as a cloud of returns because the echoes from individual fish overlap. The bottom of the lake is indicated by the black line. Echoes also come from the multiple reflection path, bottom to surface to bottom to the transducer. Those shown appear to come from beneath the bottom. Because of the complexity of the backscatter, quantitative interpretation requires careful analysis.

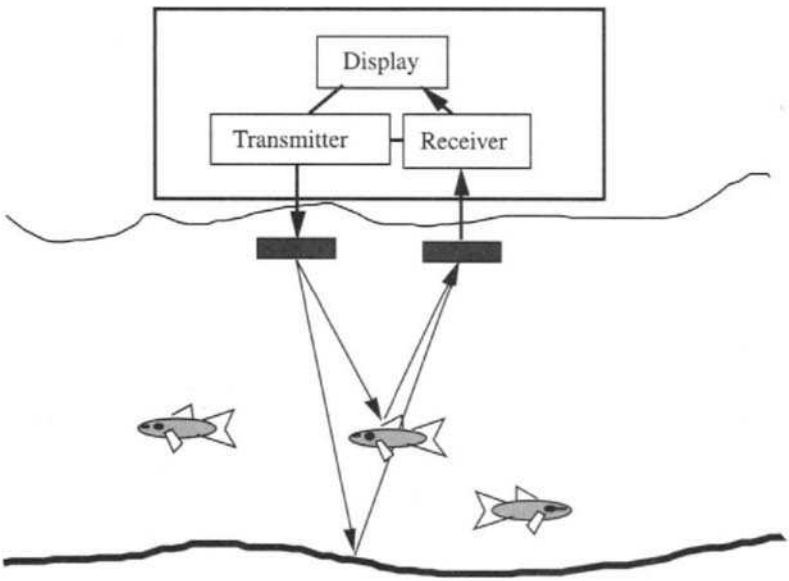

Figure 10.1.1 Echo sounder. Separate transmitting and receiving transducers are shown. Many echo sounders use the same transducer for transmission and reception. The cycle is started by a trigger from the display or transmitter.

Figure 10.1.2 A nighttime 70 kHz echo sounding record taken in Trout Lake, Wisconsin. Some of the bottom echoes saturate the receiver electronics and cause the trace to be white. (From Rudstam, L. G., C. S. Clay, and J. J. Magnuson, "Density estimates and size of cisco, *Coregonus artedii*, using analysis of echo peak PDF from a single transducer sonar," *Can. J. Fish. Aquat. Sci.* **44**, 811–21, 1987.)

10.1.2 SIDE-SCANNING SONAR

The side-scanning sonar is an echo sounder that is pointed sideways (Fig. 10.1.3). However, although the design concepts are the same as the simple echo sounder, the sending transducer produces a fan-shaped beam, and the receiver has a time-variable gain to compensate for range. Side-scanning sonars are used in geological studies to give images of rough features on the sea floor (e.g., Fig. 1.3.5). The instruments are also used to locate objects such as sunken ships on the sea floor. Fig. 10.1.4 shows a side-scanning record.

10.1.3 MULTIBEAM SONAR

Comparisons of mapping and object location operations that use radar in air and sonar in water demonstrate the large differences between the use of electromagnetic waves in air and sound waves in water. Radar (electromagnetic wave velocity $= 3 \times 10^8$ m/s): the radar pulse travel time for a range of 30 km is

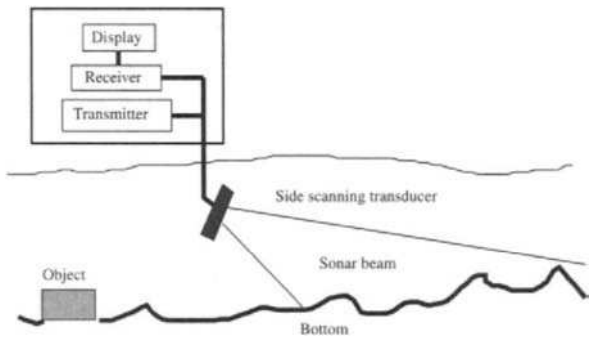

Figure 10.1.3 Side-scanning sonar. The sonar looks to the side of the shp and makes an echo sounding record as the ship moves. The time of return of a pulse is interpreted as the range to the bottom feature that caused the scatter. Display software converts the "raw image" to a map of features on the bottom.

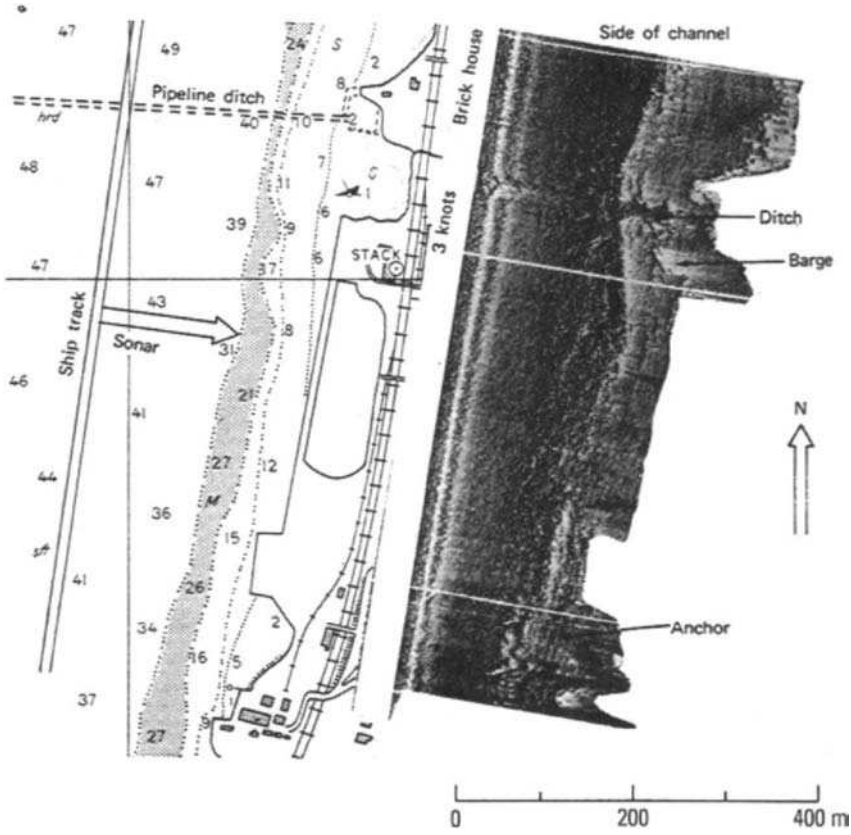

Figure 10.1.4 Sidescan record. (From Clay, C. S., and H. Medwin. *Acoustical Oceanography*; Wiley; New York, 1977.)

2×10^{-4} s, and a simple radar systems can send, receive, and display in a very short time. The time required to make a 360° image at 1° increments can be less than 0.1 s. Thus radar systems can use a single rotating dish to give good images. Consider an airborne radar. In 0.1 s, an aircraft moving at a little less than the speed of sound in air (about 600 miles/hr or 1000 km/hr) moves only about 30 m. The attenuation of electromagnetic waves in sea water is very large, and radar does not have a useful working range in the ocean. However, the attenuation of electromagnetic waves in glacial ice is small enough that radar soundings are used.

Sonar (sound speed = 1500 m/s): the time required for a sonar to range to 30 km is 40 s. In a sequential data acquisition system that takes one echo measurement at a time, several hours at one location would be needed to make

one 360° image. A ship moving at 9 km/hr (2.5 m/s) moves 100 m during the time for a single echo ranging measurement. A technological solution is to acquire sonar data in parallel by transmitting and receiving in many directions at the same time.

Fig. 10.1.5 shows an example of a multibeam sonar for sea-floor mapping. This system is intended to map a swath of depths along the ship track. Since these systems are usually mounted on the hull of the ship, the receiving array points in different directions as the ship pitches and rolls. The data-reduction system must compensate for the ship motions and the direction in which the receiving array is pointing when the echoes arrive.

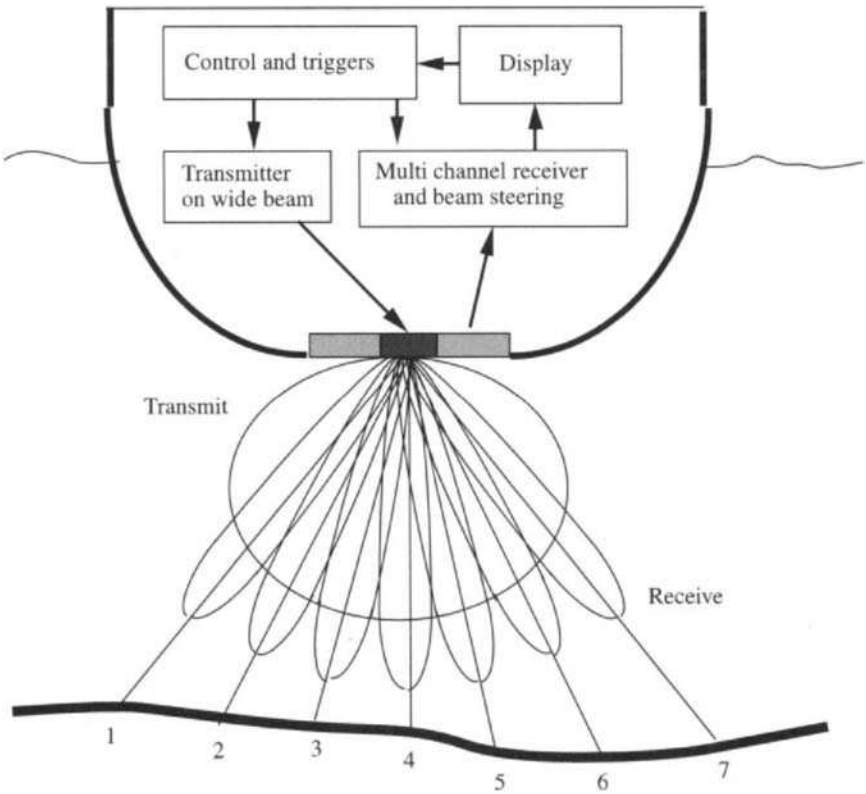

Figure 10.1.5 Multichannel sonar system using preformed beams. A cross section of the ship is shown. The transmission is a broad beam. By adjusting time delays of the receiving elements, the multielement receiving array is preformed to a set of narrow beams that look from port to starboard and measure the depths to various positions such as 1 to 7. As the ship moves, the computer makes a contour plot of the depths. Using color coding, one gets a highly revealing picture such as Fig. 1.3.4.

10.1.4 DOPPLER SONAR

Doppler sonars are used to measure the velocities of ships relative to the water or the sea floor (Fig. 10.1.6). They may also be used to measure the motion of the ocean surface or swimming objects, or internal waves, within the volume. The theory of operation is given in section 3.6.

Another application of the Doppler phenomenon is the oceangoing "portable" Doppler velocimeters, as seen in Figs. 10.1.6 through 10.1.8.

10.1.5 PASSIVE ACOUSTICAL SYSTEMS

Passive acoustical systems listen to sounds in the ocean. A system may range in complexity from a single hydrophone to an elaborate, steered array of hydrophones similar to the multibeam system in Fig. 10.1.5. Examples of noises at sea are described in sections 6.6 and 8.5.

Acoustic Daylight

Buckingham et al. (1992) coined the phrase "acoustic daylight" to describe a very different application of passive acoustics. The basic idea is sketched in Fig. 10.1.9. Physical, biological, and man-made sounds at sea can be used as an acoustic analog of daylight—that is, they illuminate (more correctly, insonify) unknown objects in the sea. Since the ocean water between the surface and the bottom is acoustically transparent, the situation is the acoustic analog of an optically transparent atmosphere. The natural sounds of the sea insonify objects in the water, and the objects scatter these waves. Therefore, if one were to scan with the proper acoustic equipment, one should be able to identify the waves scattered by objects in the ocean, and thereby identify the objects themselves (Buckingham and Potter, 1994).

Using acoustic daylight to sense objects at sea is much more difficult than using our eyes to identify objects on a sunny day. Since the natural sounds are extremely variable in frequency spectrum, amplitude, and phase, some kind of multibeam, acoustic lens-retina or focusing reflector-retina system is needed to compare the relative sounds from many directions at the same time, and to identify the scattering body. One acoustical advantage may be that identifiable sounds in the sea cover a vast frequency range from fractions of a cycle to megaHertz. This is to be compared with the optical frequencies to which the eye is sensitive—frequencies that cover a range (violet to red) of only 2 to 1.

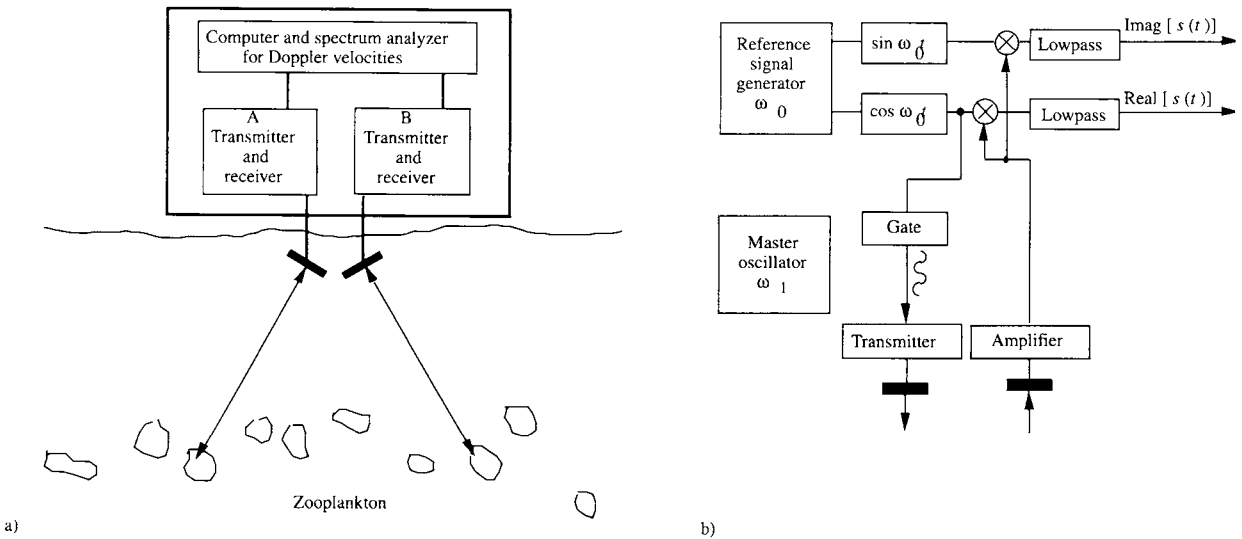

Figure 10.1.6 Doppler sonar system. In a) pings from the transmitter are backscattered from zooplankton. The pings have been Doppler-shifted by the relative velocities of the zooplankton and the sonar transducers. Commonly, Doppler sonars have four channels — two look fore and aft, and two look to starboard and port. In b) we show a block diagram of one channel of a system as described by Pinkel (1986).

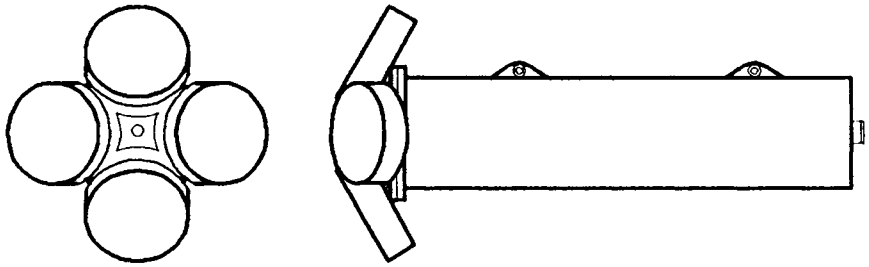

Figure 10.1.7 Physical configuration of an acoustic Doppler current velocimeter. The four transducers here are oriented 30° off the cylinder axis with 90° azimuthal spacing. The instrument body is a cylinder of length 81 cm and diameter 18 cm. When used with 75 kHz transducers, the four transducers span 76 cm measured perpendicular to the instrument axis. At 1200 kHz, with smaller transducers, the span is 22 cm. Courtesy RD Instruments, San Diego, California.

10.1.6 STEERED ARRAY SYSTEMS

Transmitting or receiving arrays of transducers are steered by adding the signals from each transducer with proper time delays. The same analysis applies to send or to receive; we give the analysis for a receiving array.

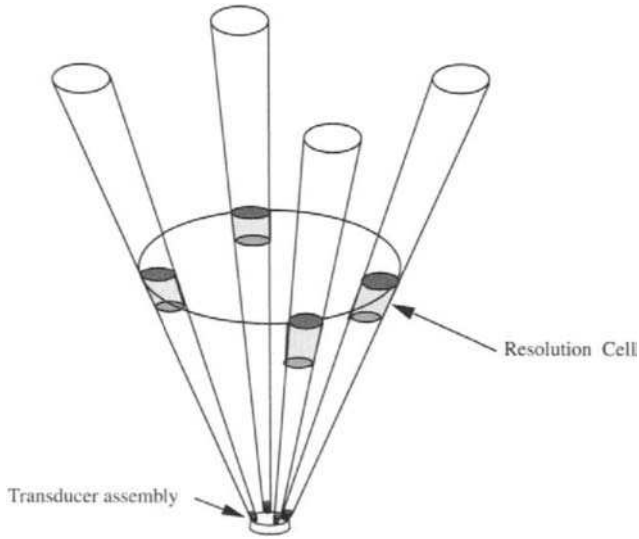

Figure 10.1.8 Beam pattern of the vertically oriented Doppler velocimeter. The velocity measurement region is the space bounded by the four beams. The resolution cell is defined by the transducer beam pattern and the ping duration. Up to 128 cells are available in the instrument shown in Fig. 9.1.7.

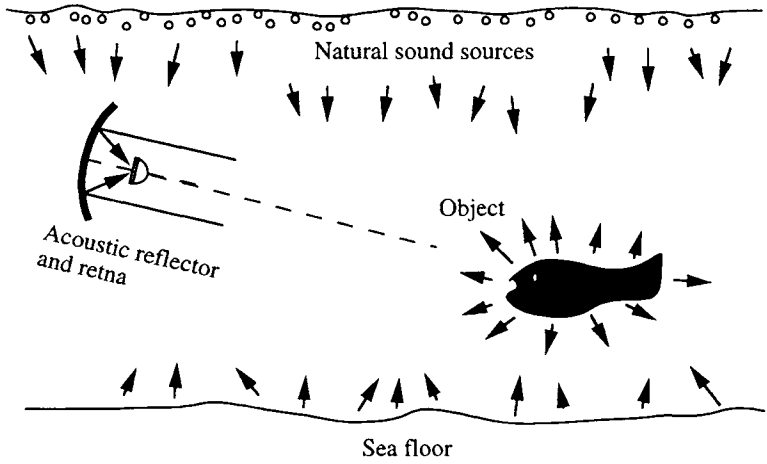

Figure 10.1.9 Object insonified by acoustic daylight. The sketch shows natural sources from near the sea surface and scattered sound from the sea floor, illuminating an object that scatters sound toward a receiver. The directional receiver is sketched as an acoustic reflector that is focused on an acoustic retina.

Consider the array of transducers in a line perpendicular to the direction $\phi = 0$ (Fig. 10.1.10). To electronically/digitally steer the array, we insert appropriate time delays in each y_n-channel.

Let the signal at the 0th hydrophone be $p(t)$ and the channel amplification factor be a_0. From the geometry in Fig. 10.1.10, the plane wavefront arrives at the nth hydrophone at advance Δt_n before reaching the 0th hydrophone, where

$$\Delta t_n = (y_n \sin \phi)/c \tag{10.1.1}$$

The signal at hydrophone n is $p(t - \Delta t_n)$. The A/D conversion and amplification is in the a_n. The time delay τ_n is inserted to give the signal $p(t - \Delta t_n + \tau_n)$.

The sum signal for N channels is

$$A_N p_N(t) = \sum_{n=0}^{N-1} a_n p(t - \Delta t_n + \tau_n) \tag{10.1.2}$$

where A_n is an amplitude factor.

Now, if τ_n is chosen to equal Δt_n, then the signals add in phase for that direction ϕ, and we have

$$A_N p_N(t) = p(t) \sum_{n=0}^{N-1} a_n \quad \text{for } \Delta t_n = \tau_n \tag{10.1.3}$$

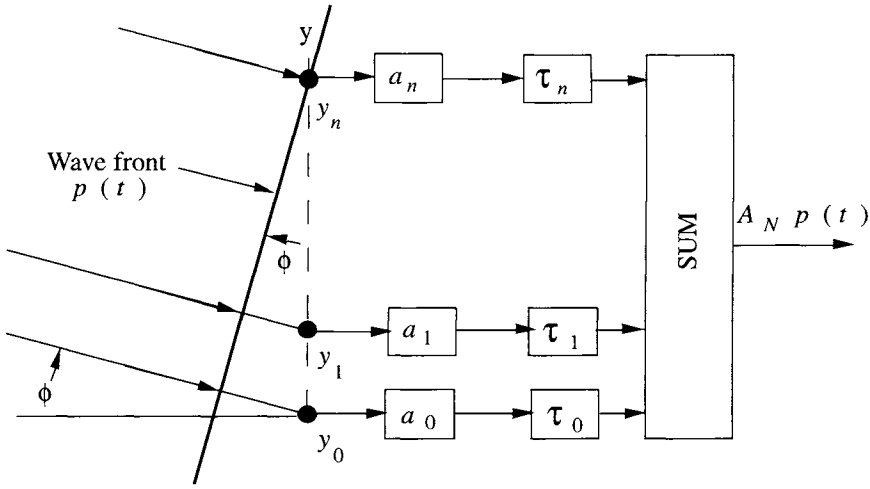

Figure 10.1.10 Electronically/digitally steered array for a plane wave entering the line of transducer array elements at angle ϕ. To steer the array, the elements at positions y_0, y_1, and so forth are given time delays τ_0, τ_1, and so forth that depend on the angle. The combination of the transducer sensitivity, A/D conversion, and amplifiers for the individual elements have the values a_n. The concept works for sources as well as receivers.

This method of array steering is called "delay and sum." The only assumption is that the signals in each channel are the same except for their time delays. Delay and sum processing works for any $p(t)$. The directional response of a steered array in other directions can be computed by choosing an incoming angle ϕ' and letting

$$\tau_n = (y_n \sin \phi')/c \tag{10.1.4}$$

Then

$$\Delta t_n - \tau_n = y_n(\sin \phi - \sin \phi')/c \tag{10.1.5}$$

The directional response of the array as a function of ϕ depends on the value of ϕ'.

We have assumed that the incident sounds are plane waves. This is equivalent to assuming that the curvature of the wavefront is small over the dimensions of the array (e.g., less than $\lambda/8$). The plane-wave assumption is effective for small arrays and distant sources.

Arrays are built in many configurations: cylinders, spheres, and so on. The multibeam sonar described in section 10.1.3 is one example. By using time delays, almost any shape can be steered to receive signals of any curvature from

any direction. However, when the arrays are built around a structure, diffraction effects can cause the performance to be deteriorated.

10.2 Sonar Systems: Details

Quantitative measurements of sound scattered from an object require that we understand the specifications and use of the sonar system as well as the physics of the scattering processes. Sonars are often designed and adapted to the physics of a particular type of measurements. However, the operating characteristics of the sonar and the physics of the reflection and scattering processes (which we described in Chapters 7, 8, and 9) are really independent. We now consider the sonar system.

10.2.1 GENERIC SONAR

A generic sonar, shown in Fig. 10.2.1, is a combination of analog and digital components. Typical displays are paper chart recorders and video display terminals. Sonars that are used for surveys and research usually include control of

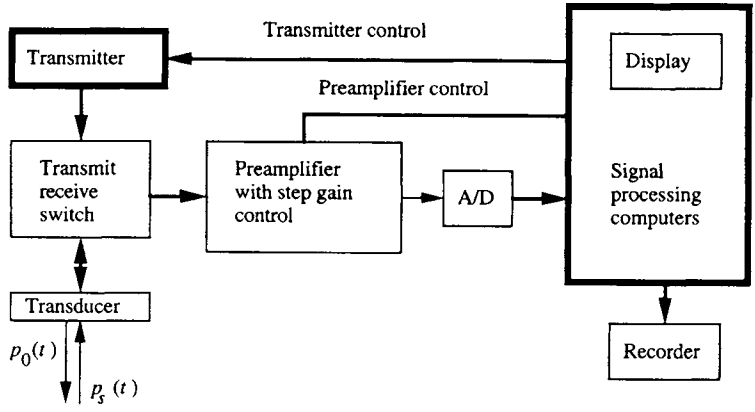

Figure 10.2.1 Block diagram of a generic sonar. The sonar system has an automatic transmit/receive switch. Some systems have separate transducers for sending and receiving. The trigger, from a clock that is internal and/or external, initiates the transmission and reception cycle. The receiver includes the electronic and digital signal processing. The transducers may be mounted on the ship or in a tow body, "the fish." The signals may be recorded on an analog tape, a digital tape, or a compact disc.

ping duration, choice of the time-varying-gain (TVG) function, calibration signals, displays, and analog signal outputs. As shown in Fig. 10.2.2, for each transmission and reception cycle, the TVG starts at low gain and increases as a function of time. All sonar receivers have a minimum output that is related to the

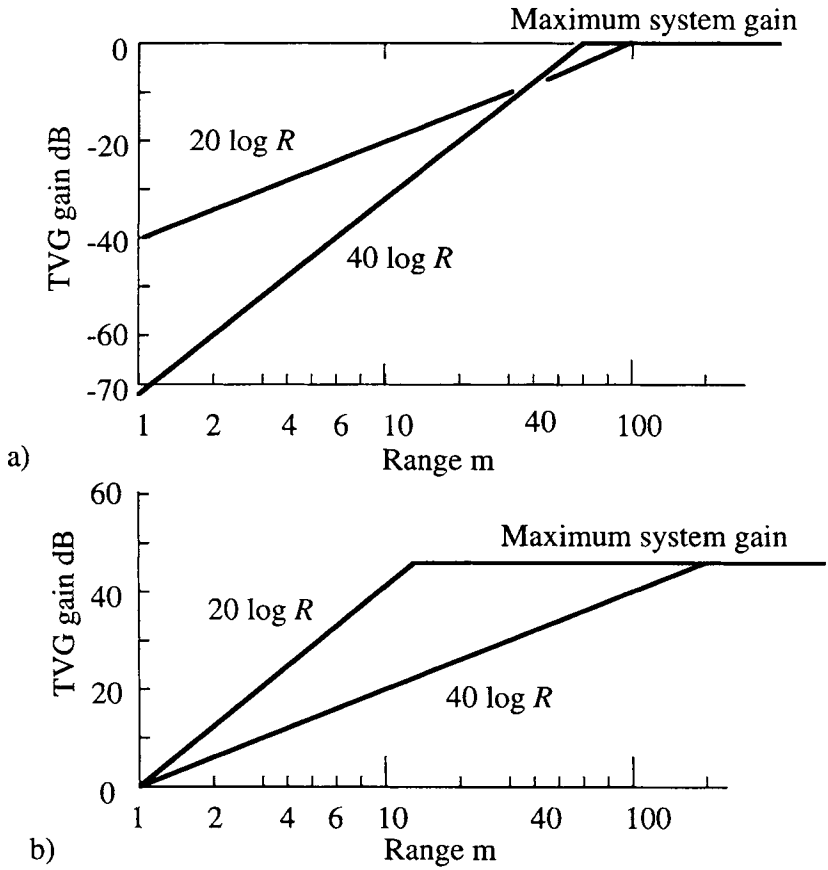

Figure 10.2.2 Time-varying-gain (TVG) as a function of range for two settings for a generic sonar. The operation is used to compensate for range dependence. Unresolved overlapping echoes (volume scatter) have a pressure amplitude proportional to $1/(time)^2$, and the amplitude compensation is proportional to (*time*) and (20 log R). Isolated echoes from individuals have echo amplitudes proportional to $1/(time)^2$ and and compensation is $(time)^2$ or (40 log R). a) The final TVG reference gain is unity (0 dB). b) The initial reference gain is unity (0 dB). The maximum TVG action is limited by the maximum gain of the amplifier.

noise and a maximum output/limit when the amplifier overloads. Digital systems have equivalent minimum and maximum limits. The TVG is chosen to keep the output electrical signal amplitudes approximately the same for near and distant scatterers and to keep the signals above the minimum and less than the maximum limits.

It is preferable to choose a TVG function that keeps the electrical signals in a good recording range rather than trying to match some preconceived notion of what the TVG ought to be. Standard preprogrammed choices are gain proportional to $(time)^2$ or 40 $\log(R)$ and gain proportional to $(time)$ or 20 $\log(R)$. How the TVG operates on voltage signal in an instrument depends on the engineering design. Some designs start with a very low gain and then increase to the amplifiers limit (Fig. 10.2.2a). Others start with an initial gain of unity (0 dB) and increase to the amplifier's limit (Fig. 10.2.2b). If one has individual echoes from many small, isolated targets, then the echo pressure amplitudes (the echoes) decrease as approximately $1/(time)^2$, and a TVG of 40 $\log(R)$ compensates for the spherical divergence.

As discussed later in section 10.4, when the objects are close together, as in a cloud of scatterers, and their echoes overlap, the sum of all of the unresolved echo pressures tends to decrease as $1/(time)$, and a TVG of 20 $\log(R)$ gives compensation. This is characteristic of volume scatter. In acoustical surveys, both clouds of fish and individuals can be present, and neither choice of TVG fits all. It is better to use one TVG choice that keeps the voltage levels in a good range for recording. (Don't twist knobs.) Whatever the TVG choice, an appropriate range dependence can be included in digital signal processing.

Digital-signal-processing technology has enabled the mass manufacture of the small sports-fisherman's sonars. These inexpensive instruments contain preprogrammed computers and are actually very sophisticated. The small portable sonars can identify echoes from individual fish, display relative fish sizes, look sideways and separate echoes of large fish from reverberation, and show water depth.

10.2.2 BAND-SHIFTING OR HETERODYNING OPERATIONS

The ping from a sonar may have a carrier frequency of 100 kHz and a duration of 1 ms. Examples of pings having the same envelope and different carrier frequencies are sketched in Fig. 6.3.1. Since the carrier frequency f_c is known, the ping can be described by sampling the envelope and measuring the relative phase of the carrier frequency. This can simplify the signal processing operations and

greatly reduce memory requirments in sonar systems. The ping is Equation 6.3.1,

$$\begin{aligned} x(t) &= e(t)\sin(2\pi f_c t) \quad \text{for} \quad 0<t<t_p \\ &= 0 \quad \text{otherwise} \end{aligned} \tag{10.2.1}$$

where the envelope of the ping is

$$e(t) = 0.5\,|\,1-\cos(2\pi t/t_p)\,| \tag{10.2.2}$$

The spectrum of $x(t)$ is $X(f)$, which is sketched in Fig. 10.2.3a. The two multiplication operations, shown Fig. 10.2.3b, are the first step:

$$x_H(t) = e(t)\sin(2\pi f_c t)\cos(2\pi f_H t) \tag{10.2.3}$$

and

$$x_Q(t) = e(t)\sin(2\pi f_c t)\sin(2\pi f_H t) \tag{10.2.4}$$

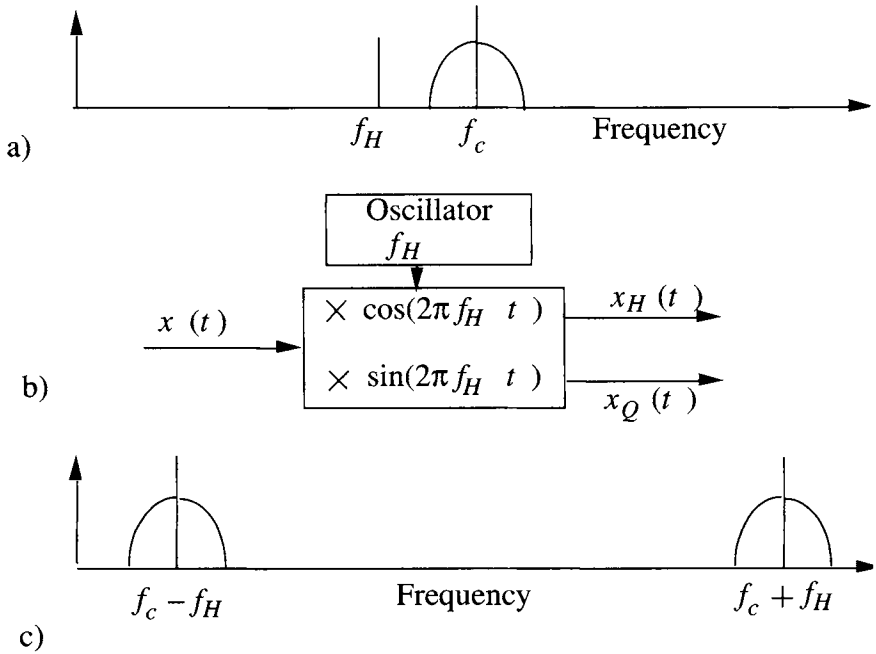

Figure 10.2.3 Band-shift or heterodyne operations. a) Spectrum of the input signal. b) Diagram of the band-shift operation for both cosine (H) and the sine quadrature (Q) multiplications. c) Output spectra.

We make the approximation that the time dependence of the envelope $[1-\cos(2\pi t/t_p)]$ can be ignored because the frequencies are very small compared with f_c. Expansion of the products of the sine and cosine terms gives

$$2\sin(2\pi f_c t)\cos(2\pi f_H t) = \sin[2\pi(f_c - f_H)t] + \sin[2\pi(f_c + f_H)t] \quad \textbf{(10.2.5a)}$$

and

$$2\sin(2\pi f_c t)\sin(2\pi f_H t) = \cos[2\pi(f_c - f_H)t] - \cos[2\pi(f_c + f_H)t] \quad \textbf{(10.2.5b)}$$

and the H and Q components of the band-shifted pings are

$$x_H(t) \approx e(t)\{\sin[2\pi(f_c - f_H)t] + \sin[2\pi(f_c + f_H)t]\}/2 \quad \textbf{(10.2.6a)}$$

and

$$x_Q(t) \approx e(t)\{\cos[2\pi(f_c - f_H)t] - \cos[2\pi(f_c + f_H)t]\}/2 \quad \textbf{(10.2.6b)}$$

The spectra of the band-shifted pings are sketched in Fig. 10.2.3c. Band-shifting operations are also known as *heterodyning*. The final steps are to low-pass-filter the results to select the $(f_c - f_H)$ bands. It is sufficient to sample the heterodyned signal at more than twice the frequency bandwidth of the envelope. For example, let a ping have the duration of 1 ms and a carrier frequency of 100 kHz. The bandwidth of the 1 ms ping is approximately 1 kHz, and thus the minimum sampling frequency is 2 kHz. At 4 kHz, the envelope would be sampled four times.

Phase shifts

The relative phases of heterodyned signals are preserved in the hetrodyning operation. Let the ping (Equation 10.2.1) have a relative phase η,

$$x(t, \eta) = e(t)\sin(2\pi f_c t + \eta) \quad \textbf{(10.2.7)}$$

The shift of the envelope is very small. Repeating the steps that gave Equations 10.2.5 and 10.2.6, the low-pass-heterodyned signals with a phase shift are

$$x_H(t, \eta) \approx e(t)\sin(2\pi f_d t + \eta)/2 \quad \textbf{(10.2.8)}$$

where $f_d = f_c - f_H$, and

$$x_Q(t, \eta) \approx e(t)\cos(2\pi f_d t + \eta)/2 \quad \textbf{(10.2.9)}$$

Cross Correlations for Measuring the Relative Phase

The reference signal is $x(t)$, the phase-shifted signal is $x(t, \eta)$, and we want to measure the relative phase. The cross correlations of the signals are less sensitive to noise than direct comparisons of the phases. Consider the cross correlation of $x_H(t)$ and $x_Q(t, \eta)$,

$$\langle x_H(t) x_Q(t, \eta) \rangle \equiv \frac{1}{Norm} \int_0^{t_p} [e(t)]^2 \sin(2\pi f_d t) \cos(2\pi f_d t + \eta)\, dt \qquad \textbf{(10.2.10)}$$

where

$$Norm \equiv \int_0^{t_p} [e(t)]^2 \sin^2(2\pi f_d t)\, dt \qquad \textbf{(10.2.11)}$$

The expansions of the product of the sines and cosine are

$$\sin(2\pi f_d t) \cos(2\pi f_d t + \eta) = -\frac{1}{2}\sin(\eta) + \frac{1}{2}\sin(4\pi f_d t + \eta) \qquad \textbf{(10.2.12a)}$$

and

$$\sin^2(2\pi f_d t) = \frac{1}{2} - \frac{1}{2}\cos(4\pi f_d t) \qquad \textbf{(10.2.12b)}$$

The substitution of Equation 10.2.12 into Equation 10.2.10 gives the sum of two integrals. The integral that includes the $\sin(4\pi f_d t + \eta)$ term tends to 0. The remaining integral is

$$\langle x_H(t)\, x_Q(t, \eta) \rangle \approx \frac{1}{Norm} \int_0^{t_p} [e(t)]^2 \frac{-\sin(\eta)}{2}\, dt \qquad \textbf{(10.2.13)}$$

The evaluation of *Norm*, using Equation 10.2.12, reduces Equation 10.2.13 to

$$\langle x_H(t)\, x_Q(t, \eta) \rangle \approx -\sin(\eta) \qquad \textbf{(10.2.14)}$$

The other cross correlations are

$$\langle x_Q(t)\, x_H(t, \eta) \rangle \approx \sin(\eta) \qquad \textbf{(10.2.15)}$$

$$\langle x_H(t)\, x_H(t, \eta) \rangle \approx \cos(\eta) \qquad \textbf{(10.2.16)}$$

$$\langle x_Q(t)\, x_Q(t, \eta) \rangle \approx \cos(\eta) \qquad \textbf{(10.2.17)}$$

The following expression gives the $\tan(\eta)$

$$\tan(\eta) \approx -\frac{\langle x_H(t)\, x_Q(t,\eta)\rangle - \langle x_Q(t)\, x_H(t,\eta)\rangle}{\langle x_H(t)\, x_H(t,\eta)\rangle + \langle x_Q(t)\, x_Q(t,\eta)\rangle} \tag{10.2.18}$$

The cross correlation method of measuring the phase difference is useful when two pressure signals (pings) are received on a pair of transducers and their phase difference is used to calculate the direction of the incident pressure signal (Traynor and Ehrenberg 1990).

10.2.3 ECHO IDENTIFICATION RULES

The echo amplitude display from echo sounders shows an interesting phenomenon as the instrument moves slowly over isolated fish. Normally, the TVG compensates for range so that the echo amplitudes are the same for the same sizes of fish at different ranges (Fig. 10.1.2). Since it is difficult to see the details of echo shapes on this figure, we use a simulation, Fig. 10.2.4, to show the details of echoes from one fish in a sonar beam. An echo crescent is formed as the scattering object (fish) moves through the echo sounder's beam pattern. Starting with the object at the left edge of the beam, the echo is weak, and, from the

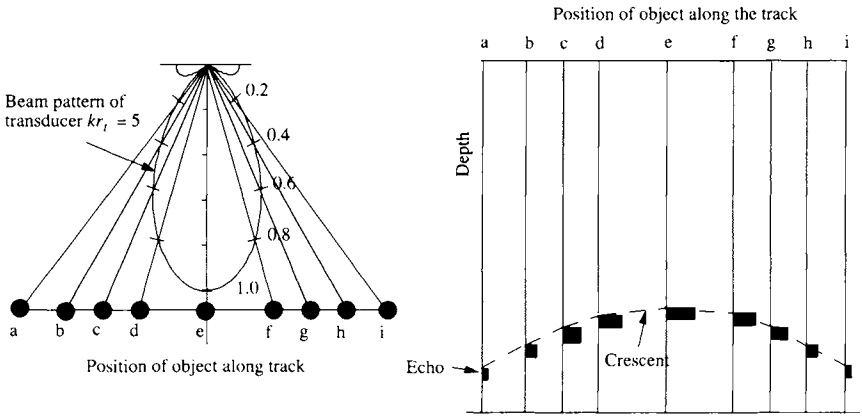

Figure 10.2.4 Simulation of a graphic display of echoes from a single fish. First for simplicity of drawing, the sonar is fixed and the fish swims through the center of the sonar beam. Pings measure the sequence of ranges to the fish at positions a–i. The graphic recorder plots the echoes beneath the time of the ping and the sequence of echoes form a crescent. The echo amplitudes are given by the position of the fish in the transducer response pattern. The graphic record of echoes would be the same if the fish were fixed and the sonar transducer were moved from left to right (a–i) over the fish.

geometry, the range is a little larger than at position e. As the object moves into the center of the beam (e), the echo is larger, and the range is smaller. The width of the crescent and its amplitude depend on depth and whether the object goes through the center of the beam or is off to one side. Craig and Forbes (1969) suggested procedures to use these effects in the analysis of echoes from fish.

The machine identification of an echo requires acceptance rules. The envelopes of a single echo, reverberations, and several echoes are sketched in Fig. 10.2.5.

Single echo identification and acceptance rules are important parts of the signal processing codes that are used in data analysis. Acceptance rules are used in the fish-finding sonars for sportsmen. Latham (1993) is an example of a patent on the "filter" (i.e., the signal processor) that implements the echo acceptance rules. A few of the patents have been tested in court.

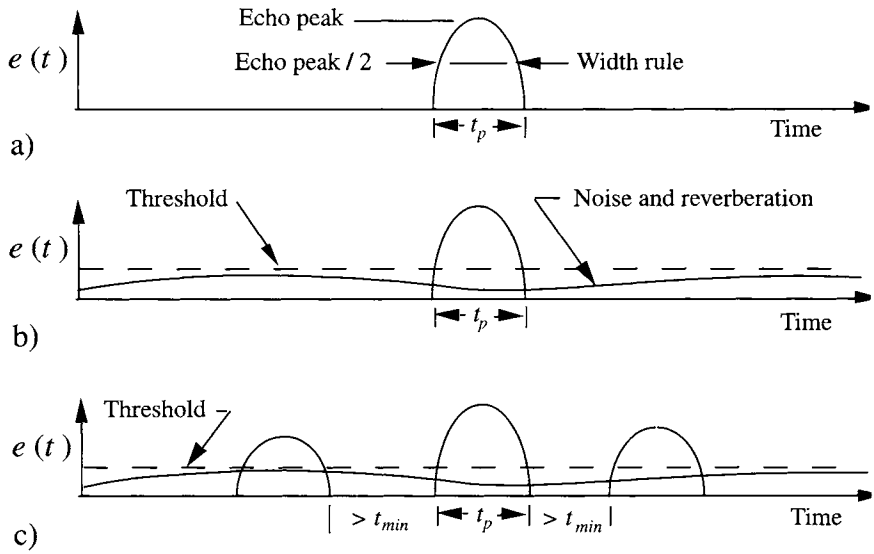

Figure 10.2.5 Identification of echoes. The sonar return has been compensated for spherical spreading. The echo envelope is $e(t)$. A single echo has shape parameters. The ping has a duration of t_p, and ideally the duration of the echo is t_p. A specific example of acceptance rules follows. a) At half-echo amplitude, the width must be less than 1.5 t_p and greater than 0.5 t_p. b) The echo amplitude must be greater than a threshold and the reverberation and noise. c) The echo is less than the threshold before and after the echo. The minimum time t_{min} is greater than the reciprocal frequency bandwidth of the receiver.

*10.2.4 USING SONAR SYSTEM SPECIFICATIONS (OPTIONAL)

An understanding of the system specifications is required to make quantitative measurements of sound scattered by objects.

Example: *The following specifications are from a small sonar. Readers should repeat these calculations, based on the specifications of their own instruments. Manufacturer's pressure specifications in μbar have been changed to μPa, or dB re 1 μPa, using 1 μbar = 10^5 μPa. The two references differ by 100 dB. Manufacturer's specifications are in bold type. Derived quantities and comments are in parentheses.*

Transmitter

Pulse power: 70 watts

Frequency: 70 kHz

Ping duration: 0.6 ms

Transducer

***Circular area* = 85 cm^2** (radius $a = 5.2$ cm) ($ka = 15$)

***Beam width* = 11°** (half-power to half-power)

***10 log*(Ψ_D) = 16.5 dB** (Ψ_D is the integrated beam pattern; see sections 4.5 and 10.4)

***Source Level: SL* = 211.5 dB** (re 1 μPa at 1 m)

(20 log rms pressure measured in the far field on the axis of the transducer and extrapolated back to 1 m).

Receiver

Bandwidth 2.2 kHz

Transducer-receiver voltage response: (TRVR) = −102 dB re 1 volt/μPa

(receiver sensitivity with receiver at full gain and TVG at maximum gain)

Gain control −27 to 0 dB in 3 dB steps

Time-varying-gain (TVG) function (use actual TVG calibration)

TVGs are referenced to gains of unity (i.e., 0 dB) at maximum gain.

*Background material.

$$(\text{TVG}(20) = 20\log(R/R_0) + 2\alpha R - 40 \text{ dB} \pm 1 \text{ dB}, \text{ for } 3 \leq R \leq 100 \text{ m})$$
$$(\text{TVG}(40) = 40\log(R/R_0) + 2\alpha R - 71.9 \text{ dB} \pm 1 \text{ dB}, \text{ for } 3 \leq R \leq 60 \text{ m})$$
$$(\alpha = 2.5 \times 10 - 3 \text{ dB/m}, \; c = 1450 \text{ m/s}, \text{ and } R_0 = 1 \text{ m})$$

Transmission Calculations

Starting at the transmitter, we change the source level in dB to apparent rms source pressure in μPa at 1 m. Also, we need the peak amplitude in our analysis for transient source transmissions and signals. Calculating from SL = 211.5 dB re 1 μPa (rms for a sinusoid), the peak sound pressure referred to 1 m is

$$P_0 = \sqrt{2}(10^{\text{SL}/20})\mu\text{Pa} \qquad \text{(zero to peak)} \tag{10.2.19}$$
$$P_0 = 5.32 \times 10^{10}\,\mu\text{Pa} \qquad \text{(zero to peak)} \tag{10.2.20}$$

A gated sine wave, a ping, starting at $t = 0$ and having a duration t_p, has pressure

$$\begin{aligned} &p_0(t) = P_0 \sin(2\pi f t) \quad \text{for} \quad 0 \leq t \leq t_p \\ &p_0(t) = 0 \quad \text{otherwise} \\ &\text{peak envelope} \quad |p_0(t)| = P_0 \end{aligned} \tag{10.2.21}$$

The symbol $p(t)$ is used for the source transmission at time t. Actual waveforms of $p(t)$ have bell-shaped envelopes. The Pa and μPa pressure units are tiny. This small, 70-watt transmitter gives a peak pressure of 53,200 Pa at 1 m from the transducer.

Receiver Calculation

At maximum gain the transducer-receiver voltage response *TRVR* in dB is given as *TRVR* = -102 dB re 1 volt/μPa. We convert *TRVR* in dB to the gain sensitivity, $K_{v/p}$, in volts/micropascal,

$$\begin{aligned} K_{v/p} &= 10^{TRVR/20} \qquad \text{v}/\mu\text{Pa} \\ K_{v/p} &= 7.9 \times 10^{-6} \qquad \text{v}/\mu\text{Pa} \end{aligned} \tag{10.2.22}$$

where peak echo amplitudes give peak pressure amplitudes. The subscript $_{v/p}$ means volts per pressure unit. The receiver has an amplifier gain control, G, that varies from -27 to 0 dB in three dB steps. The corresponding linear gain g_{rcv} is

$$g_{rcv} = 10^{G/20} \tag{10.2.23}$$

The TVG circuit operates on the signal amplitudes and causes the receiver's gain to be a function of time t. Using the TVG (40) setting for an example, the amplitude TVG function $g_{TVG}(t)$ is

$$g_{TVG}(t) = (R/R_0)^2 \times 10^{(2aR-71.9)/20} \tag{10.2.24}$$

where $R = t/(2c)$. As usual, R_0 is the reference range, 1 m. Combining the gains and calibration, the amplified scattered voltage signal $v_{\text{scat}}(t)$ at the receiver output is

$$v_{scat}(t) = p_{scat}(t) g_{rcv} g_{TVG}(t) K_{v/p}, \quad \text{volts} \tag{10.2.25}$$

where $p_{\text{scat}}(t)$ is the scattered pressure at the hydrophone. For the analysis of echo data Equation 10.2.25 is solved for $p_{\text{scat}}(t)$ in terms of the voltage output and the receiver characteristics at the time of the measurement:

$$p_{scat}(t) = \frac{v_{scat}(t)}{g_{rcv}\, g_{TVG}(t)\, K_{v/p}} \tag{10.2.26}$$

We recommend that readers should correct their sonar data using Equation 10.2.26 prior to signal analysis, so that calculations of scattering are done in acoustic pressure units and scattering lengths rather than voltages, because the scattering lengths are then independent of the sonar. Using the peak values of the pressure envelopes, the scattering length equation (7.1.19) becomes

$$\mathcal{L}_{bs} = \frac{|p_{scat}(t)|\, R^2\, 10^{2\alpha R/20}}{|p_0(t)|\, R_0} \tag{10.2.27}$$

Time Integral Pressure Squared Processing [*tips*]

Presumably the voltages have been converted to pressures. Do the absolute square of Equation 10.2.27 and then let $|p_0(t)|^2$ become [*tips*(*source*)] and $|p_{\text{scat}}(t)|^2$ become [*tips*(*scat*)] as follows. Recalling the time integral pressure squared [*tips*] in Equation 3.1.14, the integrals for the source and scattered pressure squares are

$$[tips\ (source)] = \int_0^{t_p} [p_0(t)]^2\, dt \tag{10.2.28}$$

and for the scattered sound pressure is

$$[tips\ (scat)] = \int_{2R/c}^{2R/c + t_p} [p_{scat}(t)]^2\, dt \tag{10.2.29}$$

where the time gates for the transmitted ping and echo are chosen to be t_p. The absolute square and replacement of the squared envelope peaks by their equivalent [*tips*] gives

$$|\mathcal{L}_{bs}|^2 = \frac{[tips\ (scat\ )]\, R^{\,4}\, 10^{\alpha R/5}}{[tips\ (source\ )]R_0^{\,2}} \tag{10.2.30}$$

10.2.5 SONAR CALIBRATION WITH A HARD SPHERICAL TARGET

Experience with scientific sonars in bioacoustic research has shown that the instruments require calibrations. Calibrations must be done in the far fields of the transducers and must be free of interferences such as reflections from tank sidewalls or the water-air interface. Often a lake or the deep end of a swimming pool can be used as a calibration facility. During the winter, a frozen lake surface is a stable platform for calibrations.

The purposes of the calibration are 1) to measure the directional responses of the transducers; 2) to determine the transmitter-transducer output P_0; and 3) to obtain the receiver sensitivity $K_{v/p}$. In the case of a ping, the center frequency may be used, and the time integral of the square of the transmitted sound pressure, [*tips*], is required. If the same combination of sonar transmitter and receiver is used, P_0 and $K_{v/p}$ can be measured at the same time. In calibration measurements, the scattering length $\mathcal{L}_{bs}$ or backscattering cross section of the target σ_{bs} are known from data or theoretical values such as given in Table 7.1 and Fig. 7.5.6.

Directional Response

The most direct technique to measure the directional response is to use a small "probe" transducer (a calibrated hydrophone) to receive the sound from the sonar (Fig. 10.2.6). The transmission of pings from the same probe transducer, as the sonar is rotated, gives the receiving transducer directional response. In this context, when we say "small" we mean that the probe transducer dimension is small compared with the wavelength and first Fresnel zone. If the same transducer is used for sending and receiving, a known target can be used to measure the directivity.

Measurements of echoes from a calibrated target are a direct way to measure the product $[P_0 K_{v/p}]$. Solid spheres of copper, tungsten-carbide, stainless steel, and so on are used as calibration targets. Stainless-steel ball bearings are inexpensive, and many diameters are available. To demonstrate the method, we used a stainless-steel sphere (ball bearing) to calibrate the 70 kHz (center-

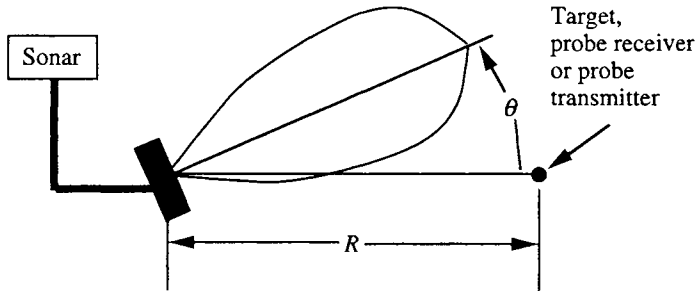

Figure 10.2.6 Setup to measure the directional response of a sonar transducer. If a known omnidirectional target is used, the directional response of the transmitter/receiver may be measured by rotating the sonar. If the transmitter is different from the receiver, a small probe hydrophone may be used as a receiver or source, respectively, rather than the small known target.

frequency) sonar described in the previous section. Recapitulating: the sonar system characteristics are

$$P_0 = 5.32 \times 10^{10}\,\mu\text{Pa} \quad \text{zero to peak (instrument's manual)} \tag{10.2.31}$$

$$K_{v/p} = 7.9 \times 10^{-6}\,\text{v}/\mu\text{Pa} \quad \text{(instrument's manual)} \tag{10.2.32a}$$

$$[P_0 K_{v/p}] = 4.2 \times 10^5\,\text{v} \quad \text{(a calibration target measures the product)} \tag{10.2.32b}$$

$$g_{TVG}(t) = (R/R_0)^2 \times 10^{\alpha R/10 - 71/20}, \quad 40\log(R) \text{ option} \tag{10.2.33}$$

$$p_{scat}(t) = \frac{v_{scat}(t)}{g_{rcv} g_{TVG}(t) K_{v/p}} \tag{10.2.34}$$

In calibrations, one should select a radius of ball bearing that will give ka at one of the peak values of $\mathcal{L}_{bs}$, where the rate of change of $\mathcal{L}_{bs}$ with ka is small (note the oscillations in Table 7.1 and Fig. 7.5.3). The purpose is to measure $[P_0 K_{v/p}]$ and check the manual's value. Using the scattering equation (7.1.19 or 10.2.27), Equation 10.2.26 can be rearranged as

$$[P_0 K_{v/p}] = \frac{|v_{scat}(t)|\, R^2\, 10^{2\alpha R/10}}{g_{rcv}\, g_{TVG}(t)\, \mathcal{L}_{bs}} \tag{10.2.35}$$

Note: the peak envelopes of $|p_0(t)|$ and P_0 are the same.

Target: *a stainless-steel ball bearing of characteristics*

Material: $\rho = 7900\,\text{kg/m}^3$; c_p (compressional speed) $= 5594\,\text{m/s}$; c_s (shear velocity) $= 3106$ m/s

Geometrical Size: $a = 0.9525\,\text{cm}$ (0.375 in); $\pi a^2 = 2.9 \times 10^{-4}\ \text{m}^2$

Acoustical Size: $k = 303\ \text{m}^{-1}$; $c = 1450$ m/s, for freshwater calibration; $ka = 2.89$

Theoretical Acoustical Scattering Length (see Table 7.1): Interpolation for $ka = 2.89$ gives $\mathcal{L}_{bs}/(a/2) \approx 0.89$ and $\mathcal{L}_{bs} \approx 4.24 \times 10^{-3}$ m

Data from Laboratory Calibration Measurements

The actual measurements were made with the target and transducer under lake ice. The transducer was pointed to maximize the target echo.

$$t = 17.8\ \text{ms} \quad \text{(two-way)} \tag{10.2.36}$$

$$R = 12.9\ \text{m} \tag{10.2.37}$$

$$g_{rcv} = 1 \quad \text{gain control setting, } G = 0) \tag{10.2.38a}$$

$$\text{peak}\,|\,v_{scat}(t)\,| = 0.44\,\text{v} \tag{10.2.38b}$$

Computations

Equation 10.2.24 gives $g_{TVG}(t)$ at 17.8 ms:

$$g_{TVG}(t) = 0.042 \tag{10.2.39}$$

The use of Equation 10.2.35, the substitution of these numbers, and, $\mathcal{L}_{bs} \approx 4.24 \times 10^{-3}$ m give

$$[P_0 K_{v/p}] = 4.1 \times 10^5 \quad \text{volts} \tag{10.2.40}$$

From the instrument manual, $[P_0 K_{v/p}] = 4.2 \times 10^5$ v, and the difference is about 2.5 percent. This example is for one radius of ball bearing. One can repeat the measurements for several radii of spheres. The same method can be applied to calibrate the sonar by using time integral pressure squared processing. Use the

absolute square of Equation 10.2.35 and Equations 10.2.28 through 10.2.30, where [*tivs*(*scat*)] replaces $|v_{\text{scat}}(t)|^2$ and [*tips*(*source*)] replaces P_0 or $|p_0(t)|$.

10.3 In Situ Scattering-Length Measurements

In situ measurements of the scattering lengths of freely swimming fish require cooperative fish, care, and good luck. "Cooperative" fish are dispersed so that most of the echoes are from individual fish. In lakes, fish are usually dispersed at night. Fish are in schools or on the bottom during the day. In data processing, one uses the character of the echogram to select data sets for analysis. Lakes, where the populations of fish are relatively simple, are good places to gain experience and test techniques.

10.3.1 EMPIRICAL TARGET STRENGTH FORMULAS FOR FISH AT $L/\lambda > 1$

Fish with swimbladders scatter sound over a very wide range of L/λ (Fig. 9.5.5). The observation that the scattering lengths are approximately proportional to fish lengths has lead to construction of empirical formulas (Love 1971, 1977; McCartney and Stubbs 1970; Rudstam et al. 1987; Foote and Traynor 1988). The frequency dependence of the scattering process is weak and is sometimes ignored. The target strength, as a function of fish length, is the usual form of the expressions

$$TS = 20 \log |\mathcal{L}_{bs}/R_0| = m_{FL} \log (L/R_{fish}) + b_{FL} \quad \text{(dB)} \tag{10.3.1}$$

where $\mathcal{L}_{bs}$ is the backscattering length, L is the fish length and R_{fish} is the unit of length. Fish lengths are usually given in centimeters and millimeters. Our sound-scattering expressions use $\mathcal{L}_{bs}$ in m and $R_0 = 1$ m. The empirical constants are m_{FL} and b_{FL}. Algebraic manipulations give the backscattering length as a function of fish length:

$$|\mathcal{L}_{bs}/R_0| = (L/R_{fish})^{m_{FL}/20} 10^{b_{FL}/20} \tag{10.3.2}$$

$$\text{Fish length, } L \approx 10^{-(b_{FL}+m_{FL})/20} |\mathcal{L}_{bs}/R_0|^{10^{-m_{FL}/20}} R_{fish} \tag{10.3.3}$$

Table 10.1 gives typical values of the parameters.

Table 10.1 **Length-Scattering Length Parameters**

Fish, R_{fish} = 1 cm	*Frequency kHz*	*m_{FL} dB*	*b_{FL} dB*	*Reference*
Gadoids (cod)	38	21.3	−68.3	Foote (1987)
alternate	38	20.0	−66.3	Foote (1987)
Herring	38	21.2	−74.2	Foote (1987)
alternate	38	20.0	−72.5	Foote (1987)
Pollack	38	16.8	−62.5	Foote (1987)
alternate	38	20.0	−67.3	Foote (1987)
Walleye pollock	38	20.0	−66.0	Foote and Traynor (1988)
Cisco	38	21.9	−67.2 dB	Rudstam et al. (1987)

The fish lengths are in centimeters — that is, R_{fish} = 1 cm. Frequency is in kHz.

McCartney and Stubbs (1970) and Love (1971; 1977) give frequency-dependent forms. For simplicity, let L, $\mathcal{L}_{bs}$, and λ be in meters and $R_0 = R_{fish} = 1$ m. Love's equation (1971, 1977) for swimbladdered fish is

$$\mathrm{TS} = 20\log|\mathcal{L}_{bs}/R_0| = 20\log[L/R_0] - 23.8 - 1.1\log[L/\lambda] \qquad \textbf{(10.3.4)}$$

The solution of Equation 10.3.4 for fish length is

$$L \approx 18(\mathcal{L}_{bs})^{1.06}\lambda^{-0.06}\,\mathrm{m} \qquad \textbf{(10.3.5)}$$

Since these equations are empirical, bioacousticians usually use data from acoustic surveys and nets to calculate constants for their fish. Love's equation fits the data for 41 mm and 120 mm fish at frequencies that range from 29 to 198 kHz. Trevorrow (1996) gives interesting results of a study that was made in a Japanese lake.

10.3.2 ECHOES FROM SINGLE FISH AND THE CRITICAL FISH DENSITY

As echoes from individual fish begin to overlap, the echo PDF has the marked changes shown in Fig. 10.3.1. The echogram is a transect across the lake (Stanton 1985). The probability density functions (PDF) of peak echo amplitudes are for 1 m depth intervals at 12, 15, and 18 m. Comparisons of the PDF for 12 and 18 m and the transducer PDF in Fig. 10.3.1 show that these echoes are likely to be from single fish. The PDF for the 15 m depth has the appearance of the extremal PDF, $\alpha = 0$ in Fig. 9.4.6b. Some of the echoes in this depth interval are overlapping.

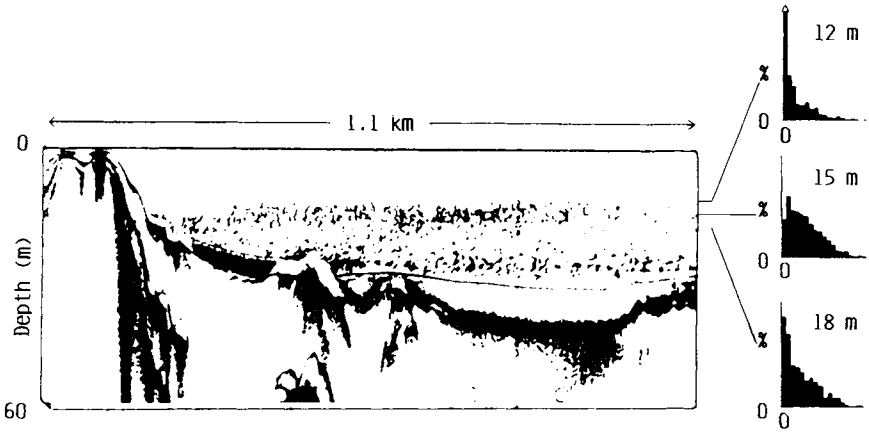

Figure 10.3.1 Echogram and echo peak PDF histograms from a Trout Lake, Wisconsin, survey. The echo sounder was a 70 kHz Simrad EYM. The PDF histogram for the 15 m depth shows the onset of overlapping echoes. (From Stanton, T. K., "Density estimates of biological sound scatters using sonar echo peak PDFs," *J. Acoust. Soc. Amer.* **78**, 1868–1873, 1985b.)

The *critical density of fish* n_{cdf} (number/volume) is the fish density at which the echoes just begin to overlap. The onset of overlapping echoes occurs when the time separations between echoes just tends to zero (Stanton 1985). The resolved thickness of the insonified layers is $(ct_p/2)$, where c is sound speed and t_p is the duration of the ping. Overlapping echoes just begin to occur when adjacent layers have fish. We use the integrated beam pattern Ψ_D (Equation 9.3.11) and Table 9.1 to compute the insonified volume as being equal to

$$(ct_p/2)\psi_D R^2 \tag{10.3.6}$$

and the critical density of fish for an echo in adjacent layers is

$$n_{cdf} \approx 1/[(ct_p/2)\psi_D R^2] \tag{10.3.7}$$

The volume reverberation (Equation 9.3.14), sonar calibration, and critical density (with $n_b = n_{cdf}$) can be combined to estimate the scattering length.

10.3.3 DUAL-BEAM SONARS

The amplitude of an echo from a body depends on its location in the sending and receiving sonar beams. To measure the apparent scattering length or the

backscattering cross section, we must know the object's position in the sonar beams. If the object is uncooperative, like a freely swimming fish, some ingenuity is needed.

In 1974 Ehrenberg suggested the potential effectiveness of the dual-beam sonar system as a means to locate a scatterer. Traynor and Ehrenberg (1979) showed that, in addition to being simple, the method is practical. As shown in Fig. 10.3.2, the system has a wide-beam source transducer and a narrow-beam transducer. The transducers are circular, and their beam patterns are symmetrical about the axis.

Assume spherical divergence from the source and spherical divergence from the scatterer and that there are no refraction effects and no incidental scattering between the source and the scattering object. Transmission can be on either the wide- or narrow-beam transducer. Transmission by the narrow-beam transducer

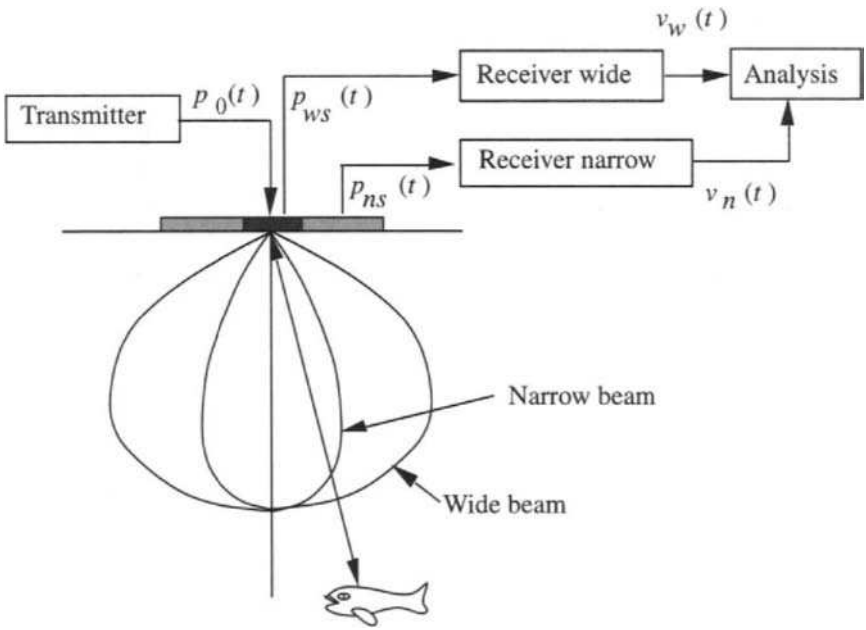

Figure 10.3.2 Dual-beam transducer system. The response of the wide beam is approximately the reciprocal of the response of the narrow beam. The ping is transmitted on the wide beam, and the echo is received on both transducers. The echo amplitudes are compared in the analyzer.

and reception of the backscattered pressures received by the wide and narrow transducers are, using the scattering length $\mathcal{L}_{bs}$,

$$p_{ns}(t) = \frac{R_0}{R^2} p_0(t - 2R/c)\,\mathcal{L}_{bs}\, D_n(\theta) D_n(\theta)\, 10^{-\alpha R/10} \tag{10.3.8}$$

and

$$p_{ws}(t) = \frac{R_0}{R^2} p_0(t - 2R/c)\,\mathcal{L}_{bs}\, D_n(\theta) D_w(\theta)\, 10^{-\alpha R/10} \tag{10.3.9}$$

As a simplification, the scattering length $\mathcal{L}_{bs}$ is assumed to be a constant at the carrier frequency of the ping.

The receivers are calibrated and matched to give the same output signal when the object is on the axis of either transducer. The voltages at the receiver outputs for the wide- and narrow-beam transducers are

$$v_w(t) = p_{ws}(t)\, g_{w\,TVG}(t)\, g_w\, K_{w\,v/p} \tag{10.3.10}$$

and

$$v_n(t) = p_{ns}(t)\, g_{n\,TVG}(t)\, g_n\, K_{n\,v/p} \tag{10.3.11}$$

where p_{ws} and p_{ns} are the equivalent scattered pressures received by the wide- and narrow-beam transducers; subscript $_{TVG}$ is for the time variable gain that is a function of time; g_w and g_n are the gain settings of the wide- and narrow-beam transducers; $K_{w\,v/p}$ and $K_{n\,v/p}$ are the receiver sensitivities in volts per pascal (v/p) for the wide and narrow transducers. On the beam axis, with adjustments to match the receiver gains and TVG, we have

$$g_{w\,TVG}(t)\, g_{w\,A} K_{w\,v/p} = g_{n\,TVG}(t)\, g_{n\,A} K_{n\,v/p} \tag{10.3.12}$$

The acceptance rules, section 10.2.2, identfy an echo at time t and range $R = 2tc$. Then, the processor may "gate" the signal into a time integral pressure (voltage) square [*tips*] processor or measure the peak amplitude of the envelope, or do both. For sonar pings, both methods give equivalent results, and we choose to use the echo peak amplitudes because the algebra is simpler. The ratio of the echo voltage peaks is

$$\frac{|v_n(t)|}{|v_w(t)|} = \frac{D_n(\theta)}{D_w(\theta)} \tag{10.3.13}$$

Many dual-beam systems are designed to make the wide-beam directivity nearly unity for an object in the main lobe of $D_n(\theta)$. Then, Equation 10.3.13 is

approximately

$$\frac{|v_n(t)|}{|v_w(t)|} \approx \frac{D_n(\theta)}{1} \tag{10.3.14}$$

where the functional dependence on θ is included. Therefore, the voltage ratio, when combined with the known polar radiation pattern of the narrow transducer, gives the unknown position of the object in the beam, $D_n(\theta)$ and θ. Since it does not matter whether $D_w(\theta)$ or $D_n(\theta)$ is the transmission beam, the same analysis applies to transmissions on either the wide- or narrow-beam transducers. This value of $D_n(\theta)$ can be substituted into Equation 10.3.11, and, using the echo peak amplitudes, the scattering length is

$$\mathcal{L}_{bs}(f_c, \theta) \approx \frac{R^2 |p_{ns}(t)| 10^{\alpha R/10}}{R_0 |p_0(t)| D_n(\theta)} \tag{10.3.15}$$

The functional dependencies of $\mathcal{L}_{bs}$ on f_c and θ are included because the scattering length depends on both. Recall from Chapter 9 that the scattering lengths of fish are dependent on the angle of incidence of sound waves at a fish. The backscattering cross section is

$$\sigma_{bs}(f_c, \theta) = |\mathcal{L}_{bs}(f_c, \theta)|^2 \tag{10.3.16}$$

Since fish are complicated scattering objects, the averages of many echo measurements are needed to get good estimates of the scattering lengths or backscattering cross sections. Noise in the receiver channels and the rejection of small echoes can bias estimates of the backscattering cross section.

10.3.4 SPLIT-BEAM SONARS

The receiving transducer has four sectors and four receiving channels (Fig. 10.3.3). The first step in the signal processing is to use the echo identification rules, section 10.2.3, to identify an echo in all four receiver channels. The accepted echo is processed to determine its direction. Fig. 10.3.3b and c show the phase comparisons. The receiver amplifiers heterodyne the signals, (section 10.2.2) use the cross correlations (Equations 10.2.14 through 10.2.18) to compute the phase shifts and direction to the fish. The conversion of measured phase shifts to directions requires acoustic calibrations of the system. Commonly, split-beam systems transmit a narrow beam by using all transducers on transmission. Details of the echo processing are in the software.

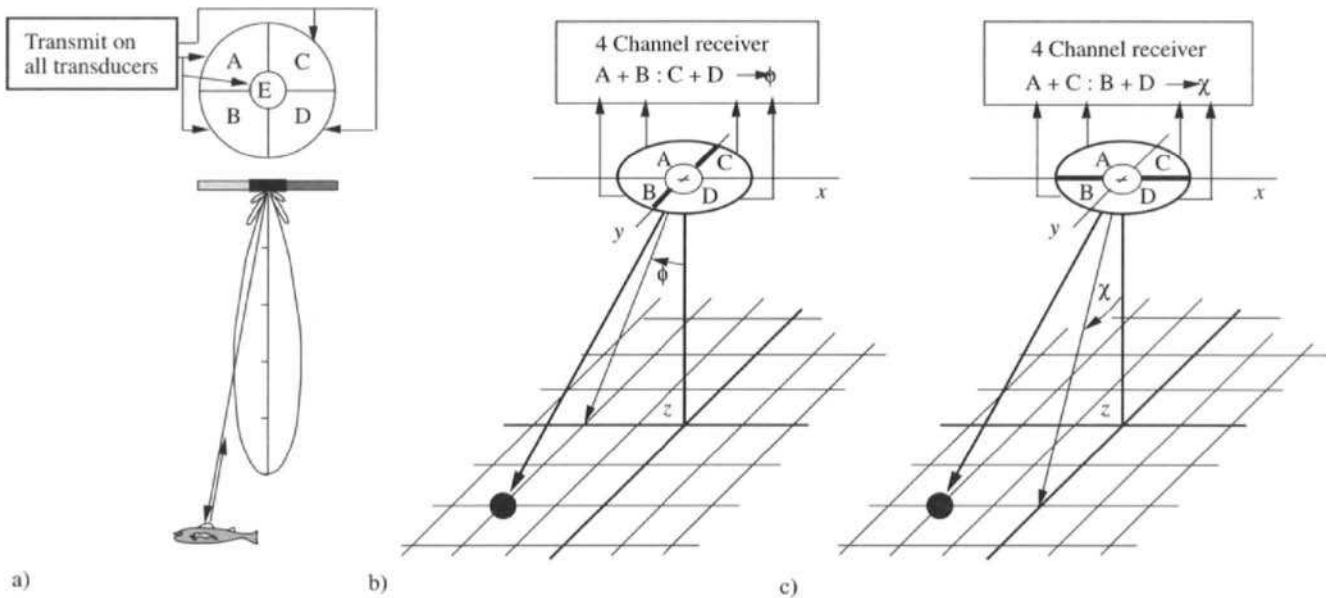

Figure 10.3.3 Split-beam sonar and dual-beam sonar. The sonars transmit a narrow beam by using transducers (A + B + C + D + E) together. For dual-beam echo processing, the output of transducer E gives the wide beam. For split-beam echo processing, the transducers A, B, C, and D are the receivers. a) A fish is in the sonar beam at the range R and angles ϕ and χ. b) The comparison of the phases of $(A + B)$ and $(C + D)$ gives the angle ϕ. c) The comparison of the phases of $(A + B)$ and $(C + D)$ gives the angle χ. (Based on Traynor, J. J., and J. E. Ehrenberg, "Fish and standard-sphere target-strength measurements obtained with a dual-beam and split-beam echo-sounding system," *Rapp. P.-V. Reun. Cons. Int. Explor. Mer.* **189**, 325–335, 1990.)

The sonar system in Fig. 10.3.3 was used for comparisons of the dual-beam and split-beam sonar systems. For the dual-beam sonar, the transducer E was the wide beam (−3 dB to −3 dB is 25°), and all of the transducers were combined to form the narrow beam (−3 dB to −3 dB is 6°). Split-beam echo processing used the system shown in Fig. 10.3.3. Traynor and Ehrenberg (1990) made 460 repeated measurements of the target strengths of the standard spherical target (−42.25 dB). Results of the tests are shown in Fig. 10.3.4. They report that the dual-beam results were more variable than the split-beam results. Since the ratio of the echo amplitudes is used in evaluations of Equations 10.3.14 and 10.3.15, Traynor and Ehrenberg suggest that noise could have made the estimates of $D_n(\theta)$ less accurate.

*10.4 Single Transducer Scattering-Length Measurements (Optional)

Figure 10.3.1 shows how echo amplitudes depend on where a fish is in the sonar beam. Unlike the dual-beam and split-beam sonars, a single transducer system

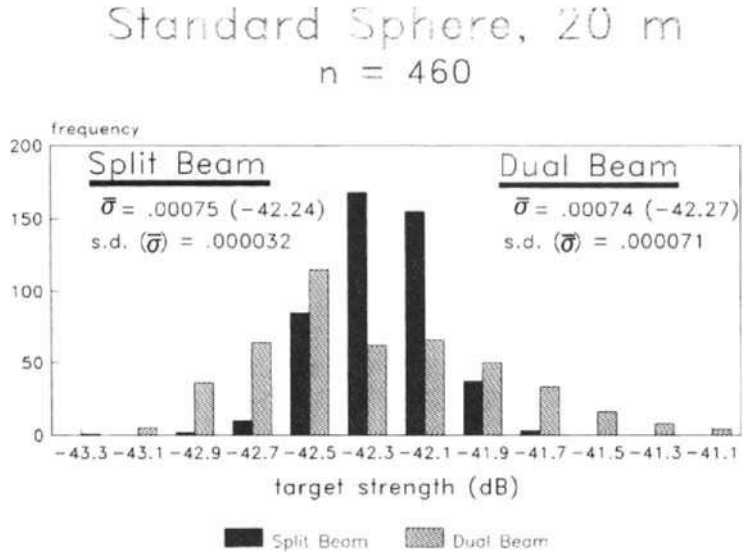

Figure 10.3.4 Comparison of calibrations of dual-beam and split-beam sonars. (From Traynor, J. J., and E. Ehrenberg, "Fish and standard-sphere, target-strength measurements obtained with a dualbeam and split-beam echo-sounding system," *Rapp. P.-V. Reun. Cons. Int. Explor. Mer.* **189**, 325–35, 1990.)

*Background material.

does not give the position of the fish. Again referring to Fig. 10.3.1, it seems that a set of echo amplitudes could be used to estimate the scattering length. This set of echo amplitudes is the result of the scattering at the fish and the positions of the fish in the sonar beam. Our task is to do the inverse problem of using a set of echo amplitudes and the beam pattern to get the scattering length. The basic tools for the inverse problem are an understanding of the forward problem, the probability density functions (PDF) of the echo amplitudes in the sonar beam, and the scattering processes at the fish. Our development is based on concepts from Craig and Forbes (1969), Ehrenberg (1972), Peterson, Clay, and Brandt (1972), Clay and Medwin (1977), Clay (1983), Stanton and Clay (1986) and Furusawa (1991).

Simplifying assumptions: (1) all fish are isolated, and their echoes do not overlap; (2) the fish have Poisson distributions or two-dimensional random positions within a thin horizontal layer; (3) the scattering length is constant; (4) receiver outputs or echoes in volts have been changed to the equivalent sound pressures at the input to the transducer.

10.4.1 PROBABILITIES

Assume the scattering process at a fish and its location in the sonar beam are independent, and each has its own probability of occurrence. As in section 9.4, the envelope of the backscattered sound pressure is e. For a unit scatterer, the directional response of the transmission and receiving transducers is the product

$$\mathcal{D} = D_t D_r = D^2(\theta) \tag{10.4.1}$$

for a single transducer. We use the joint probability to combine the random scattering process at the fish and its random location (θ) in the insonified area of the transducer. The transmit-receive response of the transducer to a scatter at the random location θ is $\mathcal{D}$. The joint probability of the independent events e and $\mathcal{D}$ occurring is the product of the probabilities of e and $\mathcal{D}$—that is,

$$\mathcal{P}(e \text{ and } \mathcal{D}) = \mathcal{P}(e)\mathcal{P}(\mathcal{D}) \tag{10.4.2}$$

For a highly directional scatterer, the angle of incidence of the sound waves at the fish depend on the fish's location in the beam and the orientation of the fish. The inclusion of fish tilt and orientation would put additional probabilities into the joint probability expression.

10.4.2 TRANSDUCER BEAM PATTERN PDF

The computation of the probability density function of the transducer uses the following method of transforming PDF. The transformation of $w_x(x)$ to $w_y(y)$, where $y = g(x)$, uses the equality of the probability of the occurrence of x within dx and the occurrence of y within dy (Lee 1960, pp. 190–93):

$$w_y(y)\,dy = w_x(x)\,dx \tag{10.4.3}$$

$$w_y(y_1) = \frac{w_x(x)}{\left|\frac{dy}{dx}\right|}\Big|_{x=x_1} \quad \text{and} \quad y_1 = g(x_1) \tag{10.4.4}$$

The forward calculation is to compute the frequency distribution of echo amplitudes when an object (fish) is randomly located in a transducer beam. To develop the transducer beam pattern PDF, we assume that the PDF of the echo amplitudes owing to an object's location in the sonar beam is independent of how the object scatters.

The geometry is sketched in Fig. 10.4.1. The object is at the angle θ relative to the axis of the transducer and within the range gate $R - \Delta R/2$ and $R + \Delta R/2$. The

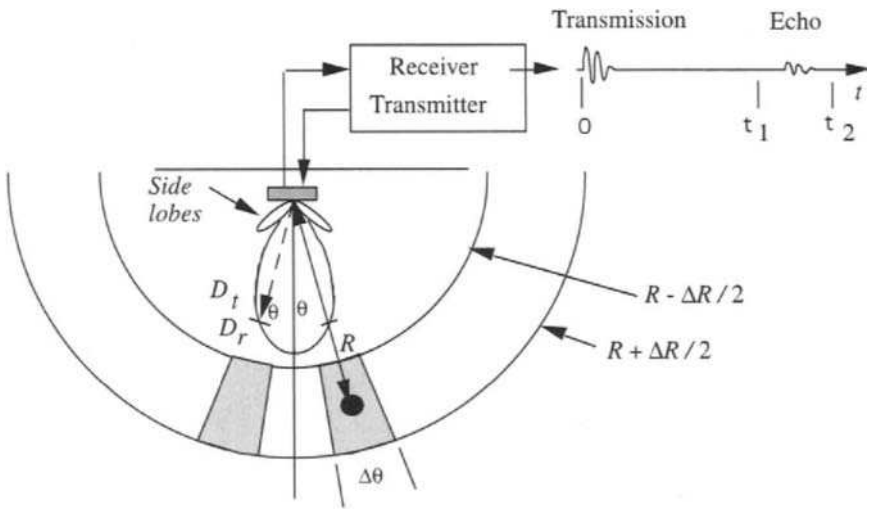

Figure 10.4.1 Geometry and a gated transmission. The probability of the object being on the axis of the transducer is 0, and it increases with $\sin\theta$ to a maximum at $\theta = \pi/2$. At the angle θ, the echo amplitude is proportional to $\mathcal{D}$.

transmission-reception response of the transducer is $\mathcal{D}$. Assuming the back radiation is negligible, the incremental gated volume ΔV_G is

$$\Delta V_G = 2\pi R \sin\theta \, d\theta \, R\Delta R \tag{10.4.5}$$

with cylindrical symmetry about the z axis. The gated volume V_G is

$$V_G = \frac{2\pi}{3}\left[\left(R + \frac{\Delta R}{2}\right)^3 - \left(R - \frac{\Delta R}{2}\right)^3\right] \tag{10.4.6a}$$

$$V_G \approx 2\pi R^2 \Delta R \tag{10.4.6b}$$

$$\Delta R = (R_2 - R_1) = (t_2 - t_1)c/2 \tag{10.4.6c}$$

The probability of an object being within ΔV_G is

$$\mathcal{P}(\Delta V_G) = \frac{\Delta V_G}{V_G} = \sin\theta \, d\theta \tag{10.4.7}$$

The transformation of the probabilities expression (Equation 10.4.4) gives a direct way to write $w_T(\mathcal{D})$:

$$w_T(\mathcal{D})\,\Delta\mathcal{D}\,|_{\theta=\theta_1} = |\sin\theta_1 \Delta\theta| \quad \text{or} \quad w_T(\mathcal{D}) = \frac{|\sin\theta_1|}{\left|\frac{d\mathcal{D}}{d\theta}\right|_{\theta=\theta_1}} \tag{10.4.8}$$

The circular piston transducer has the backscatter amplitude response

$$\mathcal{D} = 4\left[\frac{J_1(z)}{z}\right]^2, \; z \equiv kr_t \sin\theta \tag{10.4.9}$$

where $J_1(z)$ and later $J_0(z)$ are Bessel functions (section 7.4.1). The derivative of $\mathcal{D}$ with respect to θ is

$$\frac{d\mathcal{D}}{d\theta} = \left[\frac{2J_1(z)}{z}\right]\left[J_0(z) - \frac{2J_1(z)}{z}\right]\frac{\cos\theta}{\sin\theta}, \quad \text{for } 0 < \theta < \pi/2 \tag{10.4.10}$$

The substitution of the derivative in Equation 10.4.8 gives the transducer PDF

$$w_T(\mathcal{D}) = \left|\frac{\sin^2\theta}{4\cos\theta\left[\frac{2J_1(z)}{z}\right]\left[J_0(z) - \frac{2J_1(z)}{z}\right]}\right| \tag{10.4.11}$$

Expansion of the Bessel functions as $z \to 0$ gives

$$w_T(\mathcal{D}) \approx \frac{2.00}{(kr_t)^2} \quad \text{as} \quad \theta \to 0 \tag{10.4.12}$$

Ehrenberg (1972) has given an empirical approximation to Equation 10.4.11:

$$w_T(\mathcal{D}) \approx \frac{a_0}{(kr_t)^2}(a_1 + \mathcal{D})^{-a_2} \quad \text{for} \quad 0.005 \leq \mathcal{D} \leq 1, \; w_T(\mathcal{D}) = 0 \quad \text{for} \quad \mathcal{D} > 1$$
$$a_0 = 2.03, \; a_1 = 0.001 \quad \text{and} \quad a_2 = 0.83 \tag{10.4.13}$$

where r_t is the effective radius of the transducer.

A numerical evaluation of Equation 10.4.12 for a circular piston transducer is shown on Fig. 10.4.2. Since numerical evaluations of $(kr_t)^2 w_T(\mathcal{D})$ depend on the derivative of the beam response, directional calibrations should be used when possible.

10.4.3 COMBINATION OF FISH ECHO PDF AND TRANSDUCER PDF

The amplitude of the echo from an object or fish depends on the scattering amplitude of the fish *and* the mth location of the fish in the sonar beam. The joint probability of observing an echo amplitude e_n in the mth trial is

$$\mathcal{P}_E(e_n) = \mathcal{P}_T(\mathcal{D}_m)\mathcal{P}_F(e_n/\mathcal{D}_m) \tag{10.4.14}$$

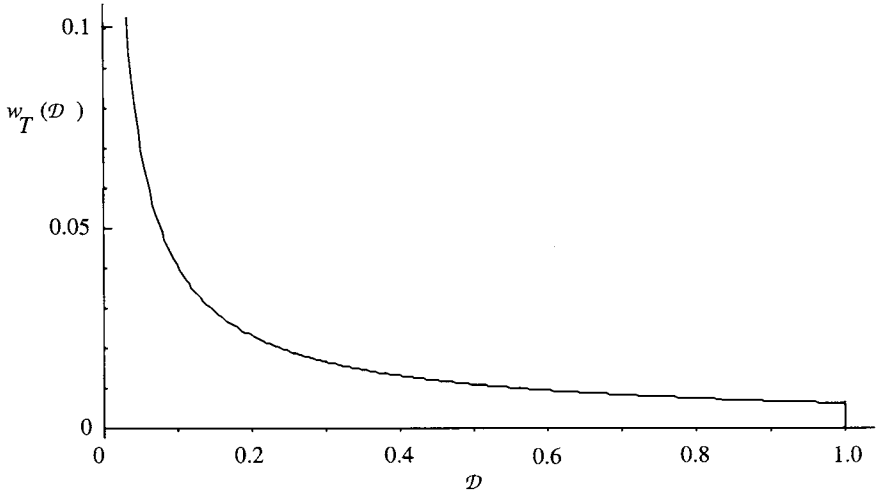

Figure 10.4.2 Transducer PDF, $w_T(\mathcal{D})$ and $kr_t = 18.3$.

where $\mathcal{P}_T(\mathcal{D})$ is the probability of the transducer having the response $\mathcal{D}_m$ at the object, and $\mathcal{P}_F(e_n/\mathcal{D}_m)$ is the probability of the fish having the scattering amplitude $e_n/\mathcal{D}_m$. The total probability is the sum over all trials:

$$\mathcal{P}_E(e_n) = \sum_m \mathcal{P}_T(\mathcal{D}_m)\mathcal{P}_F\left(\frac{e_n}{\mathcal{D}_m}\right) \tag{10.4.15}$$

These probability functions can be replaced by the probability distribution functions (PDF) as follows:

$$\mathcal{P}_E(e_n) = w_E(e_n)\Delta e_n, \quad \mathcal{P}_T(\mathcal{D}_m) = w_T(\mathcal{D}_m)\Delta\mathcal{D}_m \tag{10.4.16}$$

and

$$\mathcal{P}_F\left(\frac{e_n}{\mathcal{D}_n}\right) = w_F\left(\frac{e_n}{\mathcal{D}_m}\right)\frac{\Delta e_n}{\mathcal{D}_m} \tag{10.4.17}$$

The substitution and reduction give

$$w_E(e_n) = \sum_m w_T(\mathcal{D}_m)\, w_F\left(\frac{e_n}{\mathcal{D}_m}\right)\left|\frac{\Delta\mathcal{D}_m}{\mathcal{D}_m}\right| \tag{10.4.18}$$

where the absolute value ensures positive increments of $\Delta\mathcal{D}_m$. Since the total probability of observing all echoes is unity, we write

$$\sum_n \mathcal{P}_E(e_n) = \sum_n w_E(e_n)\,\Delta e_n = 1 \tag{10.4.19}$$

and

$$\Delta e_n = e_0\{\exp[-(n-.5)\,\delta e] - \exp[-(n+.5)\,\delta e]\} \tag{10.4.20}$$

Equation 10.4.18 is a solution because it gives the PDF of echoes in terms of the independent PDF of positions of fish in the sonar beam and the PDF of scattering processes at the fish. Unfortunately, the data or echo frequencies are on the left side of the summation and the unknown scattering by the fish is inside the summation. Direct solution of Equation 10.4.18 is rather difficult. Ehrenberg (1972) and Robinson (1978) developed methods for solving the integral equation that corresponds to Equation 10.4.18. We make nonlinear changes of variables that transform the summation into the much more tractable convolution summation.

10.4.4 CONVOLUTION EXPRESSION FOR ECHO PDF

Changes of the variables e_n and $\mathcal{D}_m$ to the following parametric expressions are the first step in changing Equation 10.4.18 into a convolution summation:

$$\mathcal{D}_m = \exp(-m\delta e) \quad \text{and} \quad e_n = e_0 \exp(-n\delta e) \tag{10.4.21a}$$

$$\delta e = \ln(10)/N_d \tag{10.4.21b}$$

$$\frac{\Delta \mathcal{D}}{\mathcal{D}_m} = \delta e \quad \text{and} \quad e_n = e_0 \exp(n\delta e)\delta e \tag{10.4.21c}$$

Again, the choice of N_d is arbitrary, and $N_d = 10$ gives 2 dB steps. Although the amplitude resolution is small, value of 10 is suitable for a data set of perhaps several hundred. One can use $N_d = 20$ (or 1 dB steps) for data sets having thousands of echoes and improve the amplitude resolution. One can always combine bins to reduce resolution from 20 to 10 steps per decade if desired.

The substitutions of the parametric expressions into Equation 10.4.18 give, making changes of notation,

$$w_E(e_n) \rightarrow w_E[e_0 \exp(-n\delta e)] \rightarrow w_{E,n} \tag{10.4.22a}$$

$$w_T(\mathcal{D}_n) \rightarrow w_T[\exp(-m\delta e)] \rightarrow w_{T,m} \tag{10.4.22b}$$

$$w_F\left(\frac{e_n}{\mathcal{D}_m}\right) \rightarrow w_F\{e_0 \exp[-(n-m)\delta e]\} \rightarrow W_{F,n-m} \tag{10.4.22c}$$

The substitutions of the parametric expressions into Equation 10.4.22 give the convolution summation

$$w_{E,n} = \delta e \sum_m w_{T,m}\ w_{F,n-m} \tag{10.4.23}$$

By using the exponential amplitude steps, the finite summation (Equation 10.4.18) has been transformed into a convolution. The reader will notice that Equation 10.4.23 has the same form as the convolution of the time-dependent functions in section 6.2.5.

10.4.5 FISH ECHO DATA REDUCTION

The first task is to examine the data from a sonar survey and to select data where the echoes appear to be from single fish. For example, Fig. 10.1.1 shows that sonar recordings usually contain several echoes from the same fish, and the trace of the echoes from one fish looks like a cresent. Let us assume that (1) the data

were taken with N_{ping} pings; (2) all of the echoes are from individual fish within the gated volume V_G; (3) the echo amplitudes have been corrected for spherical spreading and absorption losses; and (4) the peak of the envelope of the echo is e.

For digital processing, the echo amplitudes e are counted into amplitude bins as follows. If $e_m \leq e < e_{m+1}$, then add 1 to the number of echoes in bin m, where $e_m = e_m - \Delta e_m/2$; $e_{m+1} = e_m + \Delta e_m/2$; and the number of echoes in mth bin is $N_{E,m}$. To remove the number of pings, let the frequency of echoes $\mathcal{N}_{E,m}$ be the number of echoes per ping in the mth amplitude bin;

$$\mathcal{N}_{E,m} = N_{E,m}/N_{ping} \tag{10.4.24}$$

The echo frequency is proportional to the gated volume V_G, the fish density n_b (i.e., number of bodies), and the size of the echo amplitude bin Δe_m;

$$\mathcal{N}_{E,m} = n_b V_G w_{E,m} \Delta e_m \tag{10.4.25}$$

$$V_G = 2\pi(R_2^3 - R_1^3)/3 \tag{10.4.26}$$

where R_1 and R_2 are the ranges to the near and far ranges of the gated volume. The unknown fish density is n_b. The solution of Equation 10.4.25 for $w_{E,m}$ is

$$w_{E,m} = \frac{\mathcal{N}_{E,m}}{n_b V_G \Delta e_m} \tag{10.4.27}$$

where the knowns are the echo frequencies per ping $\mathcal{N}_{E,m}$, the gated volume, and the echo amplitude bins. Next, define a distribution function $u_{E,m}$ that is proportional to the probability density function (PDF) $w_{E,m}$ and includes the unknown fish density n_b:

$$u_{E,m} \equiv \frac{\mathcal{N}_{E,m}}{V_G \Delta e_m} = n_b w_{E,m} \tag{10.4.28}$$

The PDF of fish echo amplitudes, using Equation 10.4.23, becomes

$$u_{E,n} = n_b \delta e \sum_m w_{T,m} w_{F,n-m} \tag{10.4.29}$$

There are two basic approaches in using Equation 10.4.29 to estimate fish density and the fish echo PDF.

10.4.6 A FORWARD ITERATION ESTIMATE OF FISH DENSITY

Laboratory and in situ measurements of the PDF of fish show that the Ricean PDF is an approximation for the distribution of the echo amplitudes (Equation 9.4.7). The Rician PDF has the parameters γ and $\langle \sigma_{bs} \rangle$. The fish density is unknown. If the fish are of the same species and have the same sizes, then fish have approximately the same Ricean parameters.

Non-overlapping echoes: An iterative method starts with guesses of the parameters γ, $\langle \sigma_{bs} \rangle$, and n_b. The numerical evaluation of Equation 10.4.29 and the data $u_{F,n}$ are compared. The parameters are adjusted for the next iteration.

The result of an iterative analysis is shown in Fig. 10.4.3. The fish PDF was assumed to be Rayleigh ($\gamma = 0$). The transducer PDF and the fish PDF control the shape of $u_{E,m}$, while the amplitude depends on n_b. Thus one can estimate the fish density without knowing the amplitude sensitivity of the sonar. The beam width of the sonar transducer, the gated volume, and the number of pings were used to give the fish density.

10.4.7 DECONVOLUTION METHOD FOR FISH DENSITY AND ECHO PDF

The convolution (Equation 10.4.29) can be solved for the PDF of scattering processes at the fish $w_{F,n}$ by using the *deconvolution* techniques. Deconvolution means undoing a convolution, and it is a linear filter operation. Deconvolution methods are well known in exploration geophysics (Robinson and Treitel 1978; Kanasewich 1981; Oppenheim and Schafer 1975; and Clay 1990). The essence of the method is to change the terms in Equation 10.4.29 into polynomials, the *Laplace generating functions*, or z-transformations. Details are in the references.

The Laplace generating function representations of the PDF are polynomials in powers of z, where each power of z represents an array element. For example, the term $w_{T,m}$ becomes $w_{T,m}z^{-m}$. We use descending powers of z to facilate the use of deconvolution programs in MatLab. The Laplace generating functions for the terms in Equation 10.4.29 are

$$W_T(z) \equiv w_{T,0} + w_{T,1}z^{-1} + w_{T,2}z^{-2} + \ldots \tag{10.4.30}$$

$$U_E(z) \equiv u_E + u_{E,1}z^{-1} + u_{E,2}z^{-2} + \ldots \tag{10.4.31}$$

$$W_E(z) \equiv w_{E,0} + w_{E,1}z^{-1} + w_{E,2}z^{-2} + \ldots \tag{10.4.32}$$

$$W_F(z) \equiv w_{F,0} + w_{F,1}z^{-1} + w_{F,2}z^{-2} + \ldots \tag{10.4.33}$$

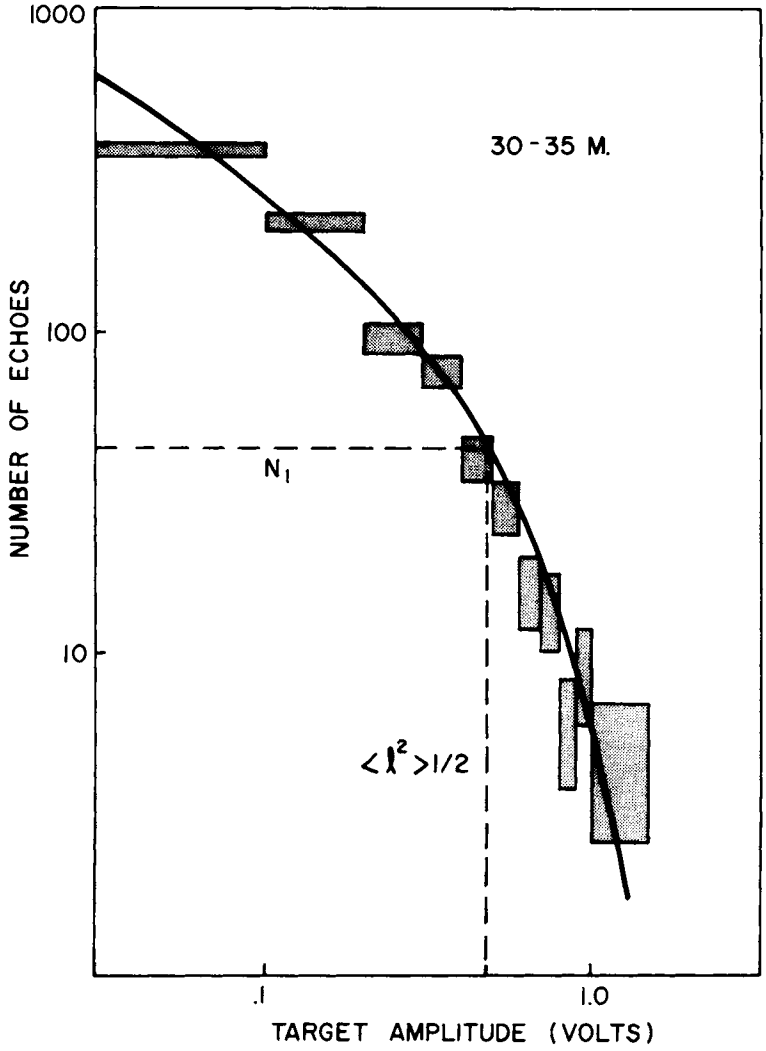

Figure 10.4.3 Amplitude distribution of echoes from individual fish. The sonar was uncalibrated for amplitude measurements, and the peaks of the echo envelopes are in arbitrary units. The data are the shaded areas, where the widths are the amplitude bin and the heights are estimates of the fluctuations (proportional to $1/\sqrt{\mathcal{N}_{E,m}}$). The data were taken in Lake Michigan in the 8–10 m depth range. The fish are believed to be alewives (*Alosa pseudoharengus*). Reduction of the data for the sonar and number of pings gave $n_b \approx 0.0057$ fish/m^3. (From Peterson, M. L., C. S. Clay, and S. B. Brandt, "Acoustic estimates of fish density and scattering functions," *J. Acoust. Soc. Amer.* **60**, 618–622, 1976.)

where Equations 10.4.31 and 10.4.33 are related by fish density, $U_E(z) = n_b W_E(z)$. The convolution (Equation 10.4.29) is the product of the generating functions

$$U_E(z) = n_b \, \delta e \, W_T(z) \, W_F(z) \tag{10.4.34}$$

The convolution (Equation 10.4.34) gives $U_E(z)$ for known $W_T(z)$, $W_F(z)$, and fish density. If fish density is not known, it can determined later. The multiplication of the polynomials (Equations 10.4.30 and 10.4.33) does the convolution computation. When $W_F(z)$ is unknown, Equation 10.4.34 can be solved for $W_F(z)$ as follows:

$$n_b \, W_F(z) = \frac{U_E(z)}{\delta e \, W_T(z)} \tag{10.4.35}$$

Algebraic long division gives $n_b W_F(z)$. The algebraic division undoes the algebraic multiplication and is the deconvolution operation. The algorithms are in Clay (1983), Stanton and Clay (1986), and Clay (1990).

Next we use the properties of PDF to compute fish density. The total probability of all echoes is unity, and this can be used to write

$$\sum_n w_E(e_n) \Delta e_n = \frac{1}{n_b} \sum_n u_E(e_n) \Delta e_n = 1 \tag{10.4.36}$$

and

$$n_b \approx 1 \Big/ \Big[\sum_n u_E(e_n) \Delta e_n \Big] \tag{10.4.37}$$

where e_n is given by Equation 10.4.21 and Δe_n is given by Equation 10.4.20.

The determination of the fish density does not use the sonar calibration. If sonar calibration is used to reduce the echo amplitude data (Equation 10.2.27), then the deconvolved scattering lengths are

$$\mathcal{L}_{bs} \approx W_F(z) \tag{10.4.38}$$

The derivation of the deconvolution method of analyzing fish echo statistics is finished.

10.4.8 EXAMPLES OF SINGLE TRANSDUCER SURVEYS

The results of a survey in Trout Lake, Wisconsin (Jacobson et al. 1990), are shown in Fig. 10.4.4. The echograms, not shown, were similar to the transect shown in Fig. 10.3.1. The inversion or deconvolution method in section 10.4.7

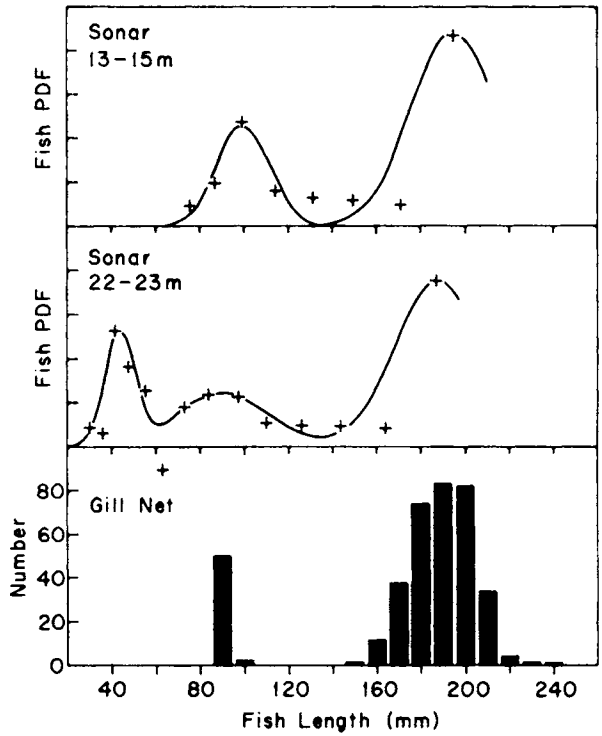

Figure 10.4.4 Fish length distributions from acoustic data and gill nets. a) The data are from Trout Lake Wisconsin, August 1985. The gill net data were corrected for size selectivity. The acoustic data were taken using a 70 kHz Simrad EYM sonar (section 10.2.4). The half-power to half-power beam width was 11°. b) Acoustic estimates of fish lengths and fish lengths from gill net catches for Wisconsin lakes. (From Jacobson, P. T., C. S. Clay, and J. J. Magnuson, "Size distribution and abundance of pelagic fish by deconvolution of single beam acoustic data," *J. Cons. Int. Explor. Mer.* **189**, 404–11, 1990.)

was used to compute the PDF of fish echoes for depth intervals 13–15 m and 22–23 m. The + symbols are the results of deconvolution and PDF of the fish echoes. Ricean PDF's were fitted to the data and are the solid lines. The backscattering lengths were converted to fish length L by using Equation 10.3.5 to estimate L.

The acoustical lengths of the fish were different for the two depth selections. The sonar data are compared with the fish length distributions from gill nets. Note: gill nets are mesh nets that catch the fish that happen to swim into the net. The fish must be larger than the mesh opening to be caught, while the smaller fish swam through the mesh openings. Here the nets were floated up from the bottom. Comparisons of the acoustical data to the gill net sample show that: 1) the 160–220 mm fish were observed elsewhere in the lake at 13–15 m and 22–23 m depths;

2) the population of 90 mm fish was larger in the 13–15 m depth range; 3) the small 40 mm fish were observed in the 22–23 m depth range, and none were caught by the gill net (Jacobson et al. 1990).

Noise and Deconvolution Errors

Noise adds to the echoes, and it carries into the PDF of the echo peaks. Other errors are due to the operation of placing the *peak* amplitudes of echoes into finite width amplitude bins, as in Equations 10.4.19 through 10.4.21. The deconvolution operation passes small errors at large values of the scattering lengths to the small scattering lengths and can cause some of the values of the PDF to be negative. The noise and other errors cause the resulting deconvolution to have alternating positive and negative values that increase for small values of fish length. Considered as an analogy to sampling in the time domain, these alternations occur at the sampling interval and should be low-pass-filtered. Since the deconvolution operation is linear, one can do additional filter operations on the data before or after deconvolution. We ignore this region when alternating values are present.

10.5 Interactions of Sonars and Fish Behavior: Simulations

The sonar system is an acoustic window through which we can watch aquatic organisms. Our preceptions of the images in the window depend on the frequency (color), on the sonar beam width (field of view), and on the echo processing (what is seen). We use numerical simulations to display the interactions of live fish and sonar systems. The simulations are for multi-frequency sonar systems that have narrow-beam or wide-beam transducers.

These simulations will give some guidance in choosing equipment and system specifications. Many details and system considerations are given in Furusawa (1991). There is a strong constraint. The limited resolution of the sonar system does not display the image of a fish in enough detail so that we can see what the fish is doing. Fish behavior appears in the probability density distributions (PDF) of the echoes and repeated measurements.

Sometimes, an *average fish* is used in simulation sonar surveys. In general, it is a mistake to create *one* average fish for simulations because some steps in the echo processing are nonlinear. For example, the average of the tilt dependencies of the sound scattered by a collection of similiar fish is not the same as the tilt dependence of the sound scattered by an average fish.

10.5.1 ENSEMBLE OF THE SAME SPECIES OF FISH

A net was used to scoop 10 small brook trout from a holding tank. The fish were of the same age and species and had the same feeding history. The X-ray images of the fish, Fig. 10.5.1, show the small differences among the 10 fish. The flesh has medium density and shows as gray. The air-filled swimbladder has least density and is almost white. Just above the swimbladder one can see the darker spine. On some of the fish, one can see a dark organ, the stomach, below the swimbladder. The stomach is more visible when it has food in it. Comparisons of the X-rays show that food in the stomach alters the shape of the swimbladder. Here the stomach presses into the swimbladder and decreases the swimbladder volume. The top side of the swimbladder appears to be unaffected by food in the stomach.

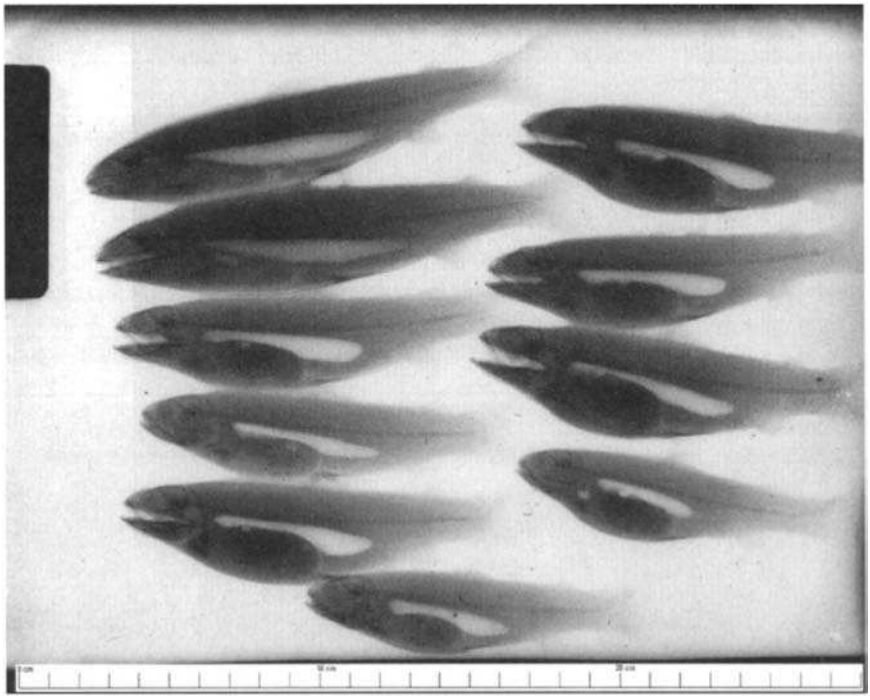

Figure 10.5.1 X-rays of brook trout (*Salvelinus fontinals*). The image is a print (positive) of the X-ray (negative). (From O'Keefe (personal communication) and Clay, C. S., and J. K. Horne, "Analysis of rather high-frequency sound echoes from ensembles of fish," *J. Acoust. Soc. Amer.* **98**, 2881 (A), 1995.)

One can apply these observations to acoustic measurements. The fullness of the stomach will have small affects on the high-frequency sound scattering from the top surface of the swimbladder. The low-frequency volume resonance (section 9.5.4) depends directly on the volume, the swimbladder membrane, the fish flesh, and shape of the swimbladder (Feuillade and Nero 1997). In addition, the resonance frequency depends on activities of the fish (Sand and Hawkins 1973).

The X-rays and the methods of section 9.4 were used to make acoustic models of the fish. Reiterating, the fish were simplified to a gas-filled swimbladder and a simplified fluid-filled body. The acoustic models represent the ensemble of fish for the simulations.

A typical echo sounder survey will be the model for our simulations. During the survey, the recorder will store the nonoverlapping echoes from the ensemble of fish. We don't know which echo comes from which fish. Even if the fish were caught in a net, one could only guess which fish to associate with which echo. If the survey is repeated many times, the fish will have moved about and have different orientations relative to the sonar beam for each survey.

The scattering lengths of the ensemble are shown in Fig. 10.5.2. The dependencies of backscattering lengths on tilt are smallest at the lowest frequency and large at high frequencies. Consider the 25 kHz and $L/\lambda = 2$ simulation. Over the range of tilt 0° to −10°, one can make associations of the backscattering lengths and fish length. Trout 1 and 2 are the largest; trout 6 and 10 are the smallest. At the highest frequency, 200 kHz and $L/\lambda = 16$, the situation is much more complicated. At tilt = 0°, the backscattering lengths are less than the backscattering lengths for 25 kHz. The scattering lengths have large fluctuations between 0° and −15° tilt. The fluctuations and peak amplitudes are largest in the −5° to −15° tilt range. In the −5° to −15° tilt range, the top surface of the swimbladder is approximately normal to the incident ray from the transducer. These dependencies on tilt strongly affect calculations of echo PDF.

10.5.2 THE PDF w_F OF AN ENSEMBLE OF FISH

The analysis and interpretation of acoustic surveys are directly related to fish behavior and their environment. A very simplistic description of fish behavior follows: fish behavior depends on whether a fish is a large predator or the smaller prey. During the day the smaller fish tend to form schools or hide by moving to depths where light penetration is very small. The deep scattering layer is an example. In lakes and streams, the fish may school, move to the bottom, or hide in the shade of trees, piers, and so forth. Fish schools can be dense because they may

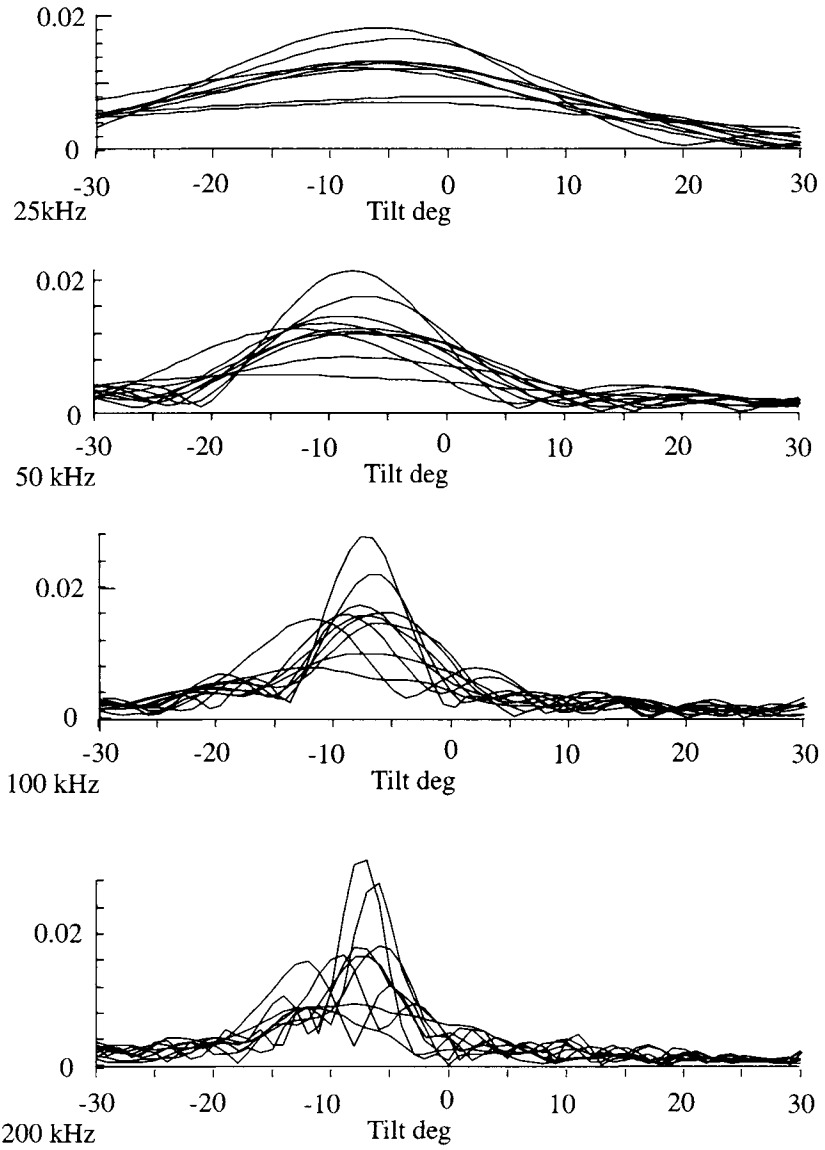

Figure 10.5.2 Scattering lengths as a function of fish tilt and frequency. The fish are the 10 trout shown in Fig. 10.5.1. (From Clay, C. S., and J. K. Horne, "Analysis of rather high-frequency sound echoes from ensembles of fish," *J. Acoust. Soc. Amer.* **98**, 2881, 1995.)

be a fraction of body length apart. At night the schools of fish disperse to random locations where they feed on smaller prey. At dawn the fish schools re-form. It is easier to catch fish in a school, and sonars help fisherpeople to find schools. It is easier to make population estimates when the fish are dispersed. Thus bioacousticians often do their surveys at night.

For economy of illustration, a map of possible random fish locations is shown in Fig. 10.5.3. In the simulation and for any one ping, a fish may be located at any one of the locations, and the sonar receives an echo from this fish. The next ping finds a fish at another location. In our simulations, each echo is from one fish of the ensemble of trout. The angles are the incident and backscattering angles of the ray paths from and to the sonar transducer.

The split-beam processing, dual-beam processing, or transducer PDF deconvolution have been done. The processed echoes from the fish are an ensemble of scattering lengths $\mathcal{L}_{bs}$. The PDF of the scattering lengths is w_F.

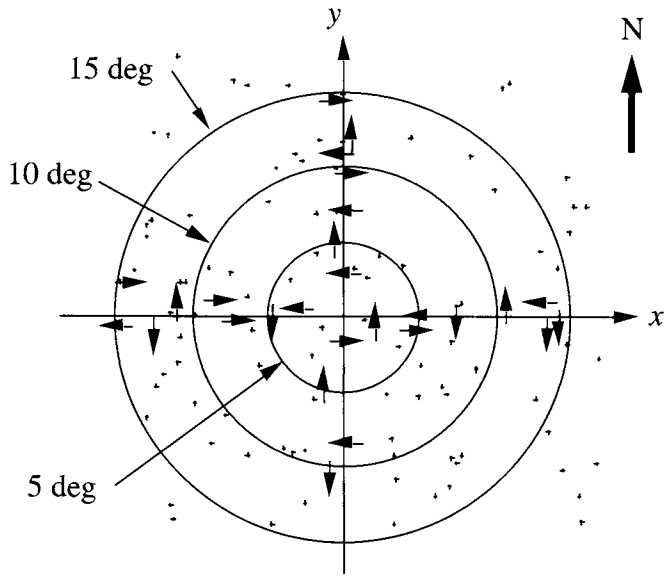

Figure 10.5.3 Map of fish locations and possible directions. The + are the locations that simulate the random locations of fish at night. All locations are assumed to be in the same narrow range of depth. The circles indicate the incident angles of rays from the transducer at the depth of these locations. At each trial (ping) a fish is assumed to be at one of the locations. The fish can point in any direction. For simplicity, we reduce the fish directions to the north, east, south, and west directions. These fish and their directions are indicated by the short arrows. (From Clay, C. S., and J. K. Horne, "Analysis of rather high-frequency sound echoes from ensembles of fish," *J. Acoust. Soc. Amer.* **98**, 2881, 1995.)

Although the echo amplitudes are corrected for the transducer beam pattern $\mathcal{D}$, the width of the beam pattern still limits the field of view because the corrections only apply to echoes within the central beam. Thus a narrow, 5° beam-width transducer measures echoes from the area indicated by the "5 deg" circle shown in Fig. 10.5.3, and the incident angles at a fish are also less than 5°. Wider beam-width transducers measure echoes from larger areas and have a larger range of incident angles.

The echo amplitudes and the backscattering lengths depend on where a fish is in the sonar beam and the direction that it is pointing. Fig. 10.5.4 shows the incident angles for a fish that is under the x-axis on the map and is pointing west. If the fish is east of the transducer (Fig. 10.5.4a), then the incident and fish tilt angle $(\chi + \alpha)$ is large, and the echo amplitude is small. When the fish is west of the transducer (Fig. 10.5.5b), the ray path having the angle $(\chi + \alpha)$ is approximately normal to the top surface of the swimbladder, and the echo amplitude is large. Fish locations north of the transducer (Fig. 10.5.4c) have nearly the same echo amplitudes as if the fish were under the center of the transducer.

10.5.3 VERY NARROW BEAM WIDTH AND RANDOM FISH TILTS

The ensemble of fish have a random distribution of tilts, rms tilt = 15° and mean tilt 1°. The half-power to half-power beam width of the transducer is much less than the rms fish tilts—that is, 5°. The probability density functions (PDF) of the scattering lengths are shown in Fig. 10.5.5. The results are complicated.

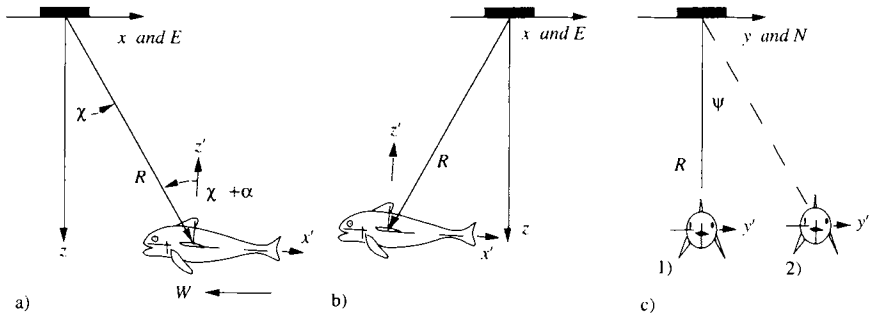

Figure 10.5.4 Positions of a fish in a sonar beam. The fish is pointing west. a) Under the x-axis and east of the transducer. b) Under the x-axis and west of the transducer. c) Under the y-axis. (From Clay, C. S., and J. K. Horne, "Analysis of rather high-frequency sound echoes from ensembles of fish," *J. Acoust. Soc. Amer.* **98**, 2881, 1995.)

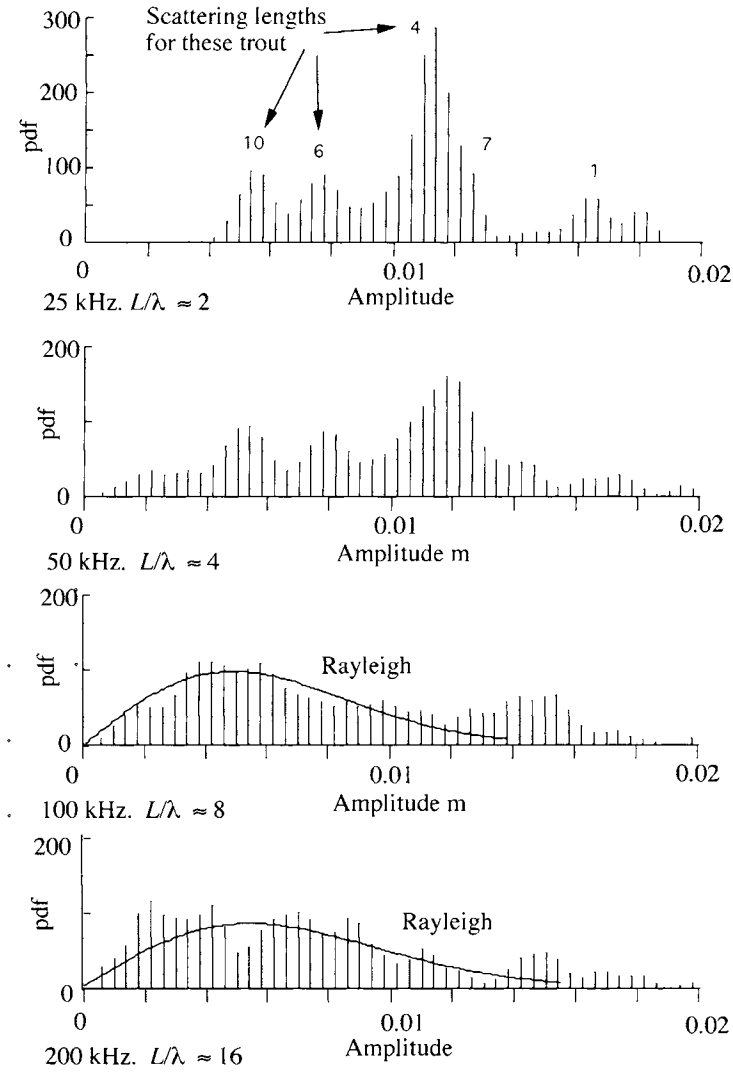

Figure 10.5.5 PDF from a narrow-beam sonar simulation. The ensemble of trout models is used. The root-mean-square (rms) tilt is 15°, and the mean tilt is 1°. The sonar beam is vertically downward and very narrow, $\ll 15°$. The frequencies are given on the examples. (From Clay, C. S., and J. K. Horne, "Analysis of rather high-frequency sound echoes from ensembles of fish," *J. Acoust. Soc. Amer.* **98**, 2881, 1995.)

If one only had the data shown in Fig. 10.5.5, it would be reasonable to interpret each peak as representing fish sizes of 0.0055, 0.008, 0.011, and 0.016 m of scattering lengths. The reader can use one of the empirical formulas (Equations 10.4.2 through 10.4.4) to estimate the fish lengths and compare them with the data shown in Fig. 10.5.2. The simulations at 50 kHz show similar results except that there is evidence of a fish having a scattering length of 0.002 m. At 100 kHz and $L/\lambda = 8$, the PDF is very broad and approximately Rayleigh ($\gamma = 0$). The same is true for 200 kHz.

10.5.4 WIDE BEAM WIDTH AND HORIZONTAL FISH

Except for a wider transducer beam width, this simulation is similiar to the survey described in section 10.4.8. The half-power to half-power beam width of the simlation transducer is approximately 20°. The ensemble of trout are swimming horizontally and are pointing in the directions as shown in Fig. 10.5.3. The average PDF from this simulation are shown in Fig. 10.5.6.

First, the 25 kHz simulation looks as if it can be fitted by the sum of Rician PDFs, one for each fish length. The higher frequencies ($L/\lambda = 4$, 8, and 16) match a single Rician PDF. The peak values of the PDF are at different scattering lengths, and the γ's are different. Superficially at least, the simulated data look like the PDF that were obtained from the analysis of field data (Fig. 10.4.1 and 10.4.2). This suggests that, during these field surveys, the distribution of fish tilts was very narrow. It is clear that the orientation of the swimbladder in the fish body biases the scattering length as the frequency and L/λ increase. And, depending on fish behavior, very narrow transducer beam widths can bias the measurements of backscattering lengths and PDF.

We want robust measurements of fish populations, and it appears that $L/\lambda \approx 2$ may give better measurements than larger L/λ. Furusawa (1991) made a very detailed analysis of the measurements of sound scattered by fish and showed that the sonar frequency corresponding to $L/\lambda = 2$ was least sensitive to the unknown fish tilts. The frequency dependence of the backscattering length on fish tilt may be useful in fish length estimations. Measurements with narrow and wide transducer beam width allow for larger ranges of fish tilts to be observed. Multi-beam sonars could measure the echoes and PDF of echoes over a range of fish tilt angles and fish orientations.

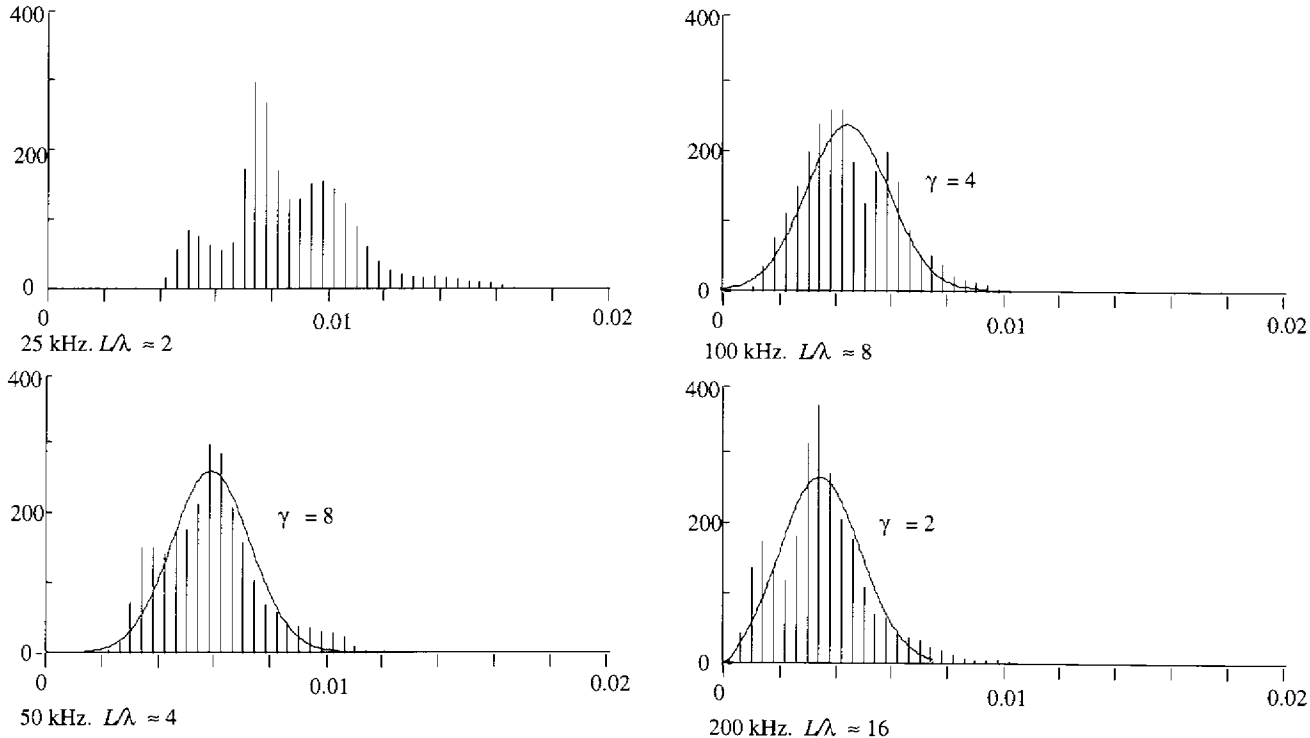

Figure 10.5.6 PDF from the combination of a wide-beam sonar and an ensemble of horizontally swimming trout. The trout are distributed over the polar angle from the beam axis to 15°. The short arrows indicate the trout that were used for the simulation. (From Clay, C. S., and J. K. Horne, "Analysis of rather high-frequency sound echoes from ensembles of fish," *J. Acoust. Soc. Amer.* **98**, 2881, 1995.)

10.6 Quantitative Reverberation Analysis: Zooplankton

Bacteria and nanoplankton are the base of the food chain. Zooplankton eat phytoplankton. As one goes up the food chain, the larger animals eat the smaller animals and transfer energy up the food chain. Some of the energy is lost, and the balance of the energy moves to larger animals as they eat smaller ones (Sheldon et al. 1972; Platt and Denman 1978). In ecological research, the size spectra are important in following the food chain and organism interactions. Acoustic surveys enable us to measure the patches and populations of zooplankton.

Many oceanographers, limnologists, and acousticians have contributed to the developement of acoustic methods for measuring zooplankton. McNaught (1968, 1969) described methods of using multifrequency sonars to estimate biomass in several size ranges. He got interesting results. A combined multifrequency sonar (47, 107, and 197 kHz) and a net biological study of zooplankton were made in the Saanich Inlet, British Columbia (Bary and Pieper 1970). Greenlaw (1979) used a three-frequency sonar in the same inlet. This early research demonstrated the relationship of acoustic volume reverberation and zooplankton populations.

Zooplankton (Fig. 9.6.1) can have all sorts of shapes. In the commom measurement range of ka from 0.2 to 6.0, details of the zooplankton anatomy are not resolved. Laboratory sound-scattering measurements have shown that fluid-filled cylinders and spheres are pretty good acoustic models of zooplankton (Greenlaw 1979; Johnson 1978; Stanton 1988; Wiebe et al. 1990). The laboratory measurements of a shrimp (Fig. 9.6.6), are accurately modeled by a fluid-filled cylinder. While we use shrimp in our examples, the shrimp can stand for any zooplankton, and the fluid cylinder can be replaced by bent cylinders, spheres, and combinations.

An acoustic model of a shrimp and its scattering length is shown in Fig. 10.6.1. The scattering length computations were made using the methods in section

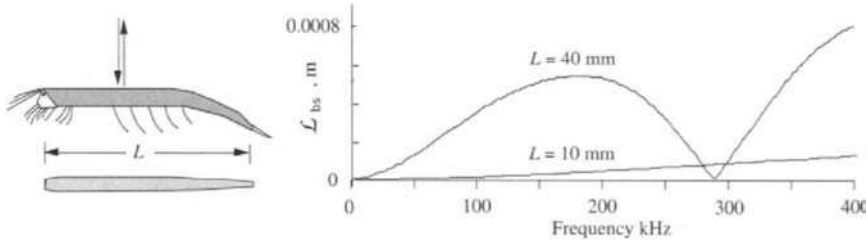

Figure 10.6.1 Backscattering lengths of acoustic models of shrimp. The densities of the shrimp are assumed to be 1.03 times the water density, and their sound speeds are the same as in water. The tilts of the shrimp are $\chi = 0$. The backscattering lengths are in meters.

9.6.1. The backscattering lengths, $\mathcal{L}_{bs}(f)$, are simple functions of frequency. The 40 mm shrimp has a readily identifiable maximum and a null. Using Fig. 10.6.1, a set of scattering measurements at 50, 100, 200, and 300 kHz would define the first maximum of the 40 mm shrimp. Measurements at the same set of frequencies on the 10 mm shrimp would define its slowly increasing scattering length as frequency increases.

A side-looking acoustic plankton sampler is sketched in Fig. 10.6.2.

The beam pattern of the transducers and range (time) gates select a volume sample. Usually the transducers for multifrequency instruments are designed to have the same beam widths and to sample the same volume. The dimensions of the volume sample control the spatial resolution. As an example, three populations of zooplankton (A, B, and C) are in layers. Each of the layers has its own distribution of zooplankton. Layer 1 has mainly types A and B; layer 2 has types B and C; layer 3 has type C. The sketch shows the acoustic plankton sampler in layer 2.

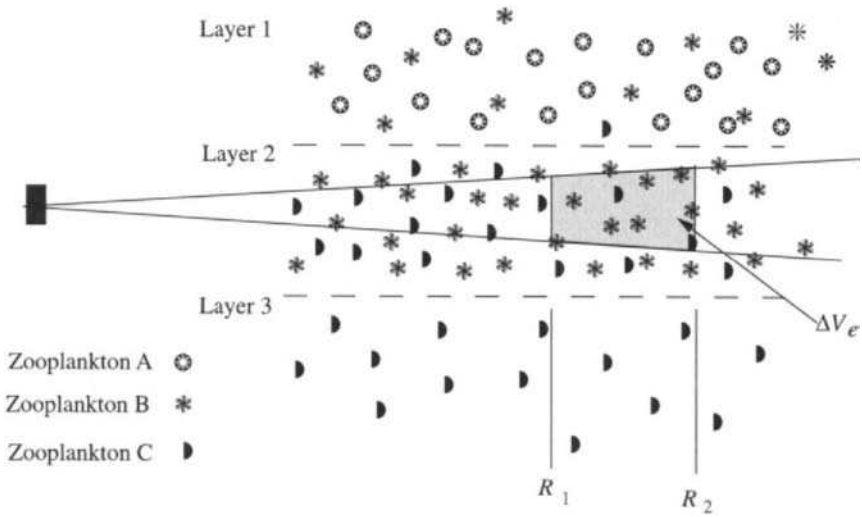

Figure 10.6.2 Zooplankton in layered ocean structure and in an insonified volume. R_1 and R_2 are the ranges that correspond to the time gates t_1 and t_2. The effective sampled volume is ΔV_e. Holliday et al. (1989) use a set of horizontally facing transducers to insonify the volume.

10.6.1 VOLUME REVERBERATION EQUATIONS

We repeat a few formulas from section 9.3. The integrated beam pattern is Ψ_D; the gate times are t_1 and t_2; the effective sampled volume is

$$\Delta Ve = (R_2^3 - R_1^3)\Psi_D \tag{10.6.1a}$$

where

$$t_1 = 2R_1/c,\ t_2 = 2R_2/c \tag{10.6.1b}$$

For a colocated source and receiver, the gated time integral pressure squared [*tips*] of the volume reverberation is

$$[tips]_{GV} \approx \Psi_D(t_2 - t_1)\, c\, \frac{R_0^2\, 10^{-\alpha R/5}}{2R^2}\, n_b <\sigma_{bs}> [tips]_0 \tag{10.6.2a}$$

where

$$R \approx (R_1 + R_2)/2 \tag{10.6.2b}$$

The density of scatterers and the mean backscattering cross section define the *volume scattering coefficient*:

$$s_V(f) = n_b < \sigma_{bs} >, m^{-1} \tag{10.6.3}$$

For a distribution of different type bodies, or the same type of different sizes, the jth kind of object has the density n_{bj}, and the squared scattering amplitude is $|\mathcal{L}_{bs,j}|^2$. The total number of objects of all types is N_b, and the average volume scattering coefficient is the weighted sum over all objects,

$$\langle s_v \rangle \approx \frac{1}{N_b} \sum_j n_{bj} |\mathcal{L}_{bs\,j}|^2 \tag{10.6.4}$$

The SI units are n_{bj} in m^{-3} and $|\mathcal{L}_{bs,j}|^2$ in m^2. Both s_V and $\langle \sigma_{bs} \rangle$ depend on frequency.

In multiple-frequency surveys, it is necessary that scattering measurements be made the same insonified volume, as shown in Fig. 10.6.2. Since the ocean is highly variable, the scattering measurements at different frequencies should be made as near to simultaneous as possible.

*10.6.2 INVERSE SOLUTION USING MULTIPLE FREQUENCIES (OPTIONAL)

Our discussion follows Greenlaw (1979) and Holliday et al. (1989). It uses standard matrix algebra. First, we recall the volume scattering coefficient (Equation 10.6.3),

$$s_V(f_c) = n_b \langle |\mathcal{L}_{bs}(f_c)|^2 \rangle \tag{10.6.5}$$

where f_c is the center frequency of the ping; $\mathcal{L}_{bs}(f_c)$ is the scattering length; n_b is the density or bodies/m^3; and the functional dependence on frequency is included. We compress the notation by defining the set of volume scattering coefficients as the vector **s**:

$$\mathbf{S} \equiv \begin{pmatrix} S_0 \\ S_1 \\ \cdot \\ \cdot \\ \cdot \\ S_M \end{pmatrix} \tag{10.6.6a}$$

where

$$S_i \equiv s_v(f_i) \tag{10.6.6b}$$

where M is the number of frequencies. The densities of the N size classes are in the vector **n**:

$$\mathbf{n} \equiv \begin{pmatrix} n_0 \\ n_1 \\ \cdot \\ \cdot \\ \cdot \\ n_N \end{pmatrix} \tag{10.6.7a}$$

where

$$n_j \equiv n_{b,j} \tag{10.6.7b}$$

*Background material.

and $n_{b,j}$ is the density of the jth size class of N classes. The n_j are also known as the size spectra. The mean square scattering lengths as a function of frequency and size class are $\langle |\mathcal{L}_{bs}$ and $j(f_i)|^2\rangle$, and the scattering matrix $\mathbf{S}$ is

$$\mathbf{S} \equiv \begin{pmatrix} s_{0,0}\ s_{0,1} \cdots s_{0,N} \\ s_{1,0}\ s_{1,1} \cdots s_{1,N} \\ \vdots \\ s_{M,0}\ s_{M,1} \cdots s_{M,N} \end{pmatrix} \tag{10.6.8a}$$

where

$$s_{i,j} \equiv \langle |\mathcal{L}_{bs,j}(f_i)|^2 \rangle \tag{10.6.8b}$$

The vector $\mathbf{s}$ contains the measured volume scattering coefficients. The theoretical scattering amplitudes are contained in the matrix $\mathbf{S}$. We seek the animal densities in the vector $\mathbf{n}$. For more observations M than unknown coefficients N, the error vector,

$$\mathbf{e} = \mathbf{s} - \mathbf{Sn} \tag{10.6.9}$$

is minimized. Least squares minimization is also known as the "L_2 norm." After much algebraic manipulation, the estimated vector for the densities is (Menke 1984, pp. 40–46)

$$\mathbf{n}^{\text{est}} = \frac{\mathbf{S}^{\mathrm{T}}\mathbf{s}}{\mathbf{S}^{\mathrm{T}}\mathbf{S}} \tag{10.6.10}$$

This least squares solution is for the "overdetermined problem"—namely, one makes measurements at more frequencies M than the number of animals N, $M > N$. The literature on generalized inversions includes constraints on solutions and methods when N is larger than M (Menke 1984).

10.6.3 ACOUSTIC PROFILES OF ZOOPLANKTON

From the literature we select an example of an acoustic profile and the relation of the distribution of zooplankton relative to ocean structure. Holliday, Pieper, and Kleppel (1989) used a 21-frequency sonar in different oceanic environments. Figure 10.6.3 shows the zooplankton size spectra in the northern Pacific ocean. The zooplankton are in the size range of 0.1 to 4.0 mm. The hydrographic, biological, and acoustic casts included biological samples, temperature, conductivity, and fluorescence (for chlorophyll). The profiles was taken during

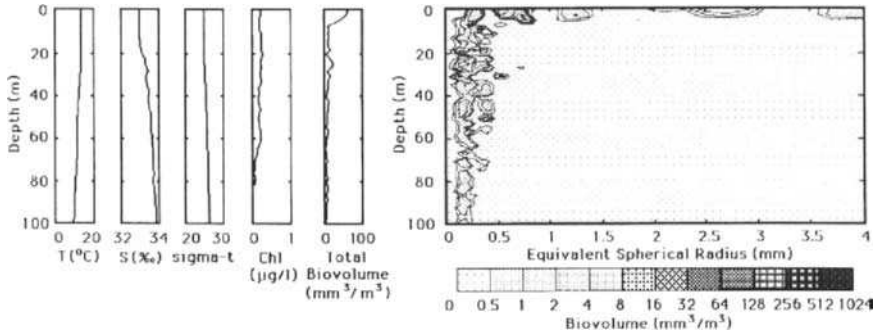

Figure 10.6.3 Acoustic profile from Northern California. Data were taken in a coastal transition (33° 220.82′N, 124° 05.52′ W) at 09:30 local time, 30 June 1985. (From Holliday, D. V., R. E. Pieper, and G. S. Klepple, "Determination of zooplankton size and distribution with multifrequency acoustic technology," *J. Cons. Int. Explor. Mer.* **46**, 52–61, 1989.)

the day to sample the usual inhabitants of the shallow depths. Holliday and Pieper (1995) discuss methods and the approach for doing bioacoustical oceanography at high frequencies. The size spectra are shown as a function of depth and "biovolume," an analog of biomass. The biovolume contours are drawn on the doubling of the biovolumes. The size spectra are also given using the "equivalent spherical radius" (esr) in millimeters.

An acoustic profile and oceanographic data from Southern California are shown in (Plate 4 Holliday, Pieper, and Kleppel 1989), most of the biovolume is in the first 10 m, and the biovolume is very small (below 50 m). Near the surface, the size spectra is large, in the 0.3 mm to 0.6 mm esr, and then skips to 3.2 mm esr and larger. Below 10 m depth, the spectral peaks are at 0.3 and 0.5 mm. Organisms in the 3 mm esr may include fish larvae.

North Wall of the Gulf Stream

The north wall of the Gulf Stream is a major boundary between water masses (Fig. 10.6.4). The warm Gulf Stream water flows over the colder and more dense slope water. The front is very dynamic, with large surface currents of about 8 km/h. The transition zone between the water masses is very sharp and is easily identified on echo sounder profiles (Fig. 10.6.5).

These results are from the multidisciplinary cruise EchoFront 85. Downward-looking echo sounders and the multiple-frequency acoustic profiling system were used (Holliday, Pieper, and Klepple 1989; Nero et al. 1990).

Holliday, Pieper, and Kleppel (1989) measured the oceanographic and biological details in a series of casts along the acoustic transect. One of these

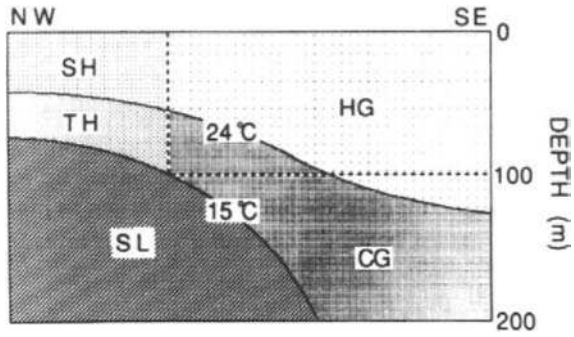

Figure 10.6.4 Representation of the Gulf Stream front with generalized water masses. Slope water (SL) temperature < 15°; thermocline (TH); hot Gulf Stream (HG) temperature >24°; cold Gulf Stream (CG) temperature < 24°. (From Nero, R. W., J. J. Magnuson, S. B. Brandt, T. K. Stanton, and J. M. Jech, "Finescale biological patchness of 70 kHz acoustic scattering at the edge of the Gulf Stream-EchoFront 85," *Deep-Sea Research* **37**, 999–1016, 1990.)

casts is shown in Fig. 10.6.6. The thermocline is at about 60 m depth. The biovolume maximum at 60 m depth coincides with a maximum of the chlorophyll.

In this chapter we have given examples of bioacoustic research in the ocean. Gaps in the data exist, and it is difficult to obey the Nyquist sampling rules in

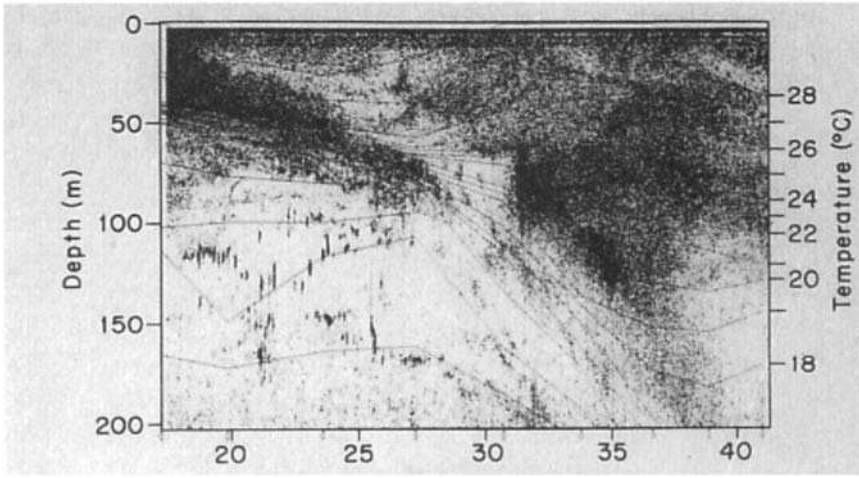

Figure 10.6.5 Acoustic transect (70 kHz) across the Gulf Stream front. The strong sound scattering is in the hot Gulf Stream and slope waters (Fig. 10.6.4). The dynamic range of the volume scatter exceeds the range of a black and white picture. (From Nero, R. W., J. J. Magnuson, S. B. Brandt, T. K. Stanton, and J. M. Jech, "Finescale biological patchness of 70 kHz acoustic scattering at the edge of the Gulf Stream-EchoFront 85," *Deep-Sea Research* **37**, 999–1016, 1990.)

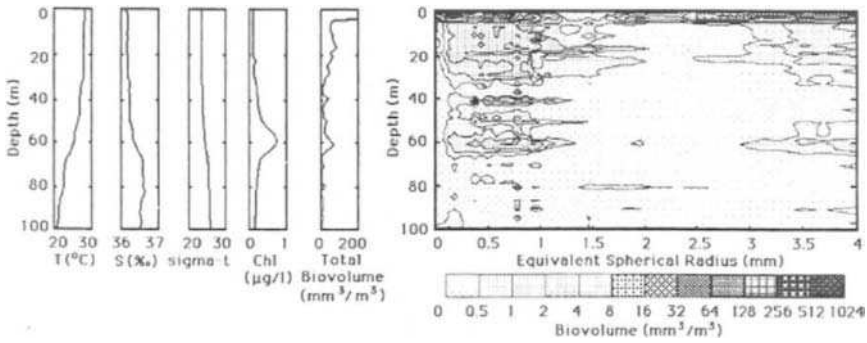

Figure 10.6.6 Acoustic profile at the Gulf Stream front. Data were taken in the Gulf Stream (35° 20N, 74° 35′ W) at 1849:30 local time, 12 August 1985. (From Holliday, D. V., R. E. Pieper, and G. S. Klepple, "Determination of zooplankton size and distribution with multifrequency acoustic technology," *J. Cons. Int. Explor. Mer.* **46**, 52–61, 1989.)

time, frequency, and space. Bioacoustic research is expensive, difficult, and at times very frustrating because storms can destroy equipment, disrupt schedules, and change the ocean. Although the examples are a minuscule sample of the ocean, these measurements and their analysis represent very large efforts.

Problems

Section 10.3

10.3.1 Use the sonar specifications in section 10.2.4 to compute the maximum density of fish (i.e., the critical density) for echoes from single fish. a) 15 to 17 m depth range. b) 99 to 101 m depth range.

10.3.2 The sonar described in section 10.2.4 is used. In a laboratory measurement of sound scattered by a 20 cm fish with swimbladder, replace the stainless-steel sphere with the fish at the same range, 12.9 m. The output peak voltage is 1.1 v. a) Calculate the scattering length of the fish. b) Compare this with the value computed using the empirical target strength formulas.

10.3.3 A dual-beam sonar has the on-axis peak sound pressure $P_0 = 5 \times 10^{10}$ μPa at 1 m. The carrier frequency of the sonar is 200 kHz, and the ping duration is 0.7 ms. The fish echo referred to the sound pressure at the face of the narrow transducer is 3×10^6 μPa. Both the narrow- and wide-beam transducers are circular pistons. The narrow transducer beam width is 5° from half-power to half-power. The wide beam is 30° from half-power to half-power. The peak echo from the narow beam is 0.5 v, and the peak echo from the wide

beam is 0.9 v. The two-way travel time is 0.03 s. a) Compute the angle by which the fish is off the transducer axis. b) Compute the backscattering length of the fish. c) Assuming a swimbladder and estimate the length of the fish.

Section 10.4

(Advanced) For the following problems, the Laplace-transformation expressions are

$$W_T(z) = [2.0 + 2.4z^{-1} + 2.9z^{-2} + 3.5z^{-3} + 4.2z^{-4} + 5.1^{-5} + 6.1z^{-6} + 7.3z^{-7}]/(ka)^2$$

$$U_E(z) = [4.3 + 5.2z^{-1} + 6.5z^{-2} + 7.9z^{-3} + 9.3z^{-4} + 12z^{-5}] \times 10^{-4}$$

$$\delta e = \ln(10)/10 = 0.230 \quad \text{and} \quad e_0 = 1$$

10.4.1 (Advanced) Do algebraic long division (deconvolution) to estimate, to a constant of proportionality, the Laplace-transformation of the fish.

10.4.2 (Advanced) Let $W_F(z) = 4.62 + 0.05z^{-1} + 0.31z^{-2} + 0.06z^{-3}$. Comput the convolution of $W_F(z)$ and $W_T(z)$.

10.4.3 (Advanced) Write an algorithm to do the convolution of $W_F(z)$ and $W_T(z)$ on a computer.

10.4.4 (Advanced) Write an algorithm to do the deconvolution of $U_E(z)$ and $W_T(z)$ on a computer.

10.4.5 (Advanced) Try Problems 10.4.3 and 10.4.4 using MATLAB.

Section 10.5

For the following problems, all of the echoes are from individual fish.

10.5.1 Use the simplified model of a swimbladder (Problem 9.5.1 [L = 10 cm, $a = 0.5cm$)]. Tilt the cylinder 6° relative to the horizontal. Let the incident angle Ψ (Fig. 10.5.4) be from $-10°$ to 10°. Compute and plot the PDF of the peak echo amplitudes for carrier frequencies of 10, 20, 50, 100, and 200 kHz.

10.5.2 An ensemble of fish are represented as swimbladder models with the gas cylinders having the following:

Length (cm)	Radius (cm)	Tilt degrees
10	0.05	6
11	0.05	4
9	0.04	7
12	0.06	5
8	0.04	6

The incident angle range is $-10°$ to $10°$. For carrier frequencies of 10, 20, 50, 100, and 200 kHz, compute the PDF of the individual fish. Assuming that all measurements are independent, compute the PDF of the ensemble.

10.5.3 Use the ensemble of fish in Problem 10.5.2, but here the fish are looking about and their fish axis tilts are 0. The frequencies are the same set. a) What would the PDF of the ensemble be for a sonar that has a beam from $-1°$ to $1°$? b) All fish are looking west as in Fig. 10.5.4. b) Compute the PDF of the ensemble when the sonar beam is from $5°$ to $7°$. c) Compute the PDF of the ensemble when the sonar beam is from $-5°$ to $-7°$. d) Compare the PDF and discuss the possibility of using multibeam sonars to study fish tilts and fish schools.

10.5.4 The fish are looking in "random" directions. The simplified ensemble has four sets of the fish in Problem 10.5.2. The fish in set A look west; those in set B look south; those in set C look east; those in set D look north. The frequencies are the same set. a) What would the PDF of the ensemble of A, B, C, and D be for a sonar that has a beam from $-1°$ to $1°$? b) Compute the PDF of the ensemble when the sonar beam is from $5°$ to $7°$. c) Compute the PDF of the ensemble when the sonar beam is from $-5°$ to $-7°$. d) Compare the PDFs and discuss the possibility of using multibeam sonars to study fish tilts and fish schools.

Section 10.6

10.6.1 The scattering lengths of shrimp are shown in Fig. 10.6.1. Measurements are made at 50, 100, 200, and 300 kHz. All data are reduced to the volume scattering coefficient. Interpret the data in the table to estimate the density of 40 mm shrimp (A) and 10 mm shrimp (B).

Table P10.6.1 $\mathcal{L}_{bs}$ **in m and** $\langle s_v \rangle$ **in** $\mathbf{m}^{-1}$.

	Data Set	*50 kHz*	*100 kHz*	*200 kHz*	*300 kHz*
	(A) $\mathcal{L}_{bs}$	1.3×10^{-4}	3.5×10^{-4}	5.4×10^{-4}	1.0×10^{-4}
	(B) $\mathcal{L}_{bs}$	1.0×10^{-5}	2×10^{-5}	5.0×10^{-5}	9.0×10^{-5}
Set	(1) $\langle s_v \rangle$	8×10^{-7}	0.6×10^{-5}	1.5×10^{-5}	5.0×10^{-7}
	(2) $\langle s_v \rangle$	5×10^{-7}	2×10^{-6}	1.2×10^{-5}	4.0×10^{-5}
	(3) $\langle s_v \rangle$	1.3×10^{-6}	6.2×10^{-6}	2.7×10^{-5}	4.1×10^{-5}

Use a least squares method to estimate the populations of shrimp (A) and (B).

Chapter 11 | Waveguides: Plane Layers and Wedges

11.1 Normal Modes in Plane-Layered Media 469
11.1.1 Wave Equation in a Waveguide 469
11.1.2 Depth Dependence in an Idealized Waveguide 471
11.1.3 Orthogonality of Modes 473
11.1.4 Sound Pressure and the Sum of Modes 474
11.1.5 Reflections and Transmissions at the Waveguide Boundaries 476
11.1.6 Modal Equations (Characteristic Equations) 477
11.1.7 Numerical example: Two-Layer Waveguide 480
11.2 Geometrical Dispersion: Phase and Group Velocities 486
11.2.1 Phase Velocity 486
11.2.2 Group Velocity 487
11.2.3 Dispersed Arrival: $p(t)$ 490
11.3 Arrays, Signals, and Noise 493
11.3.1 Arrays of Sources and Receivers in a Waveguide: Mode Filters 493
11.3.2 Noise in Waveguides 496
11.3.3 Signal-to-Noise Ratio and the Optimum Array Filter 497
11.3.4 Matched Array Filter for Source Location 498
11.4 Transmission Functions in Matrix Notation 499
11.4.1 Example for Two Modes 499
11.4.2 Array of Receivers 500
11.5 Source Location 501
11.5.1 Matched Field Processing for Source Location 502
11.5.2 Optimum Mode Processing for Source Location 505
11.5.3 Time Domain Source Location 506
11.6 Range-Dependent Waveguide: Wedge 509
11.6.1 "Adiabatic" Approximation 509
11.6.2 Transmissions in Wedge Waveguides 510
11.7 Parabolic Equation (PE) Method 514
11.8 Wedge Waveguide in the Time Domain: Biot-Tolstoy Method 516
11.8.1 Normal Coordinate Method 519
11.8.2 Region 2: Arrivals from Images 524
11.8.3 Region 3: Diffraction Arrival 527
11.8.4 Numerical Examples 532
11.8.5 Comparisons of Theory and Experiments 534

We give simple intuitive developments to display the physics of sound transmissions in plane-layered waveguides and wedge waveguides. The long-range sound transmissions are for either trapped rays or modes where the ranges are usually greater than 10 times the depth. The ray-path solutions were derived in the time domain. Normal mode solutions are derived in the frequency domain. Fourier transformations can be used to go from one to the other and compare them. Normal mode computations are reasonably simple using a student version

of MATLAB. Advanced theoretical waveguide solutions are very elegant and have huge, complicated codes.

Since the literature is extremely rich, we will reference only the early contributions. The classic reference is Ewing, Worzel, and Pekeris (1948). Their research was done during World War II, as part of the undersea warfare effort. Ewing and Worzel did a set of sound transmissions in shallow water in 1943. They discovered the frequency-group velocity dispersion relation for sound transmission in a shallow-water waveguide. Pekeris, a theoretician, formulated the normal-mode solution for sound transmission in a shallow-water waveguide in both the frequency and time domains, and compared it with Ewing and Worzel's data. Details of normal-mode theory and extensive references are provided in Tolsoy and Clay (1996, 1987), Tolstoy (1973), and Brekhovskikh and Godin (1990).

The concepts and examples of trapped rays are given in Chapter 3. Rays are trapped when a ray path reflects at the surface, has "total" reflection at the bottom, or turns above the bottom. Examples are given in section 3.3.5. In normal-mode solutions for sound-wave transmissions, the sound energy is trapped between the upper and lower boundaries.

11.1 Normal Modes in Plane-Layered Media

The normal modes are a way of solving the wave equation. In Chapter 7 we used expansions of the normal modes to solve the scattering of sound waves by fluid spheres and cylinders. The spherical Hankel functions were used for the sphere. The cylindrical Hankel functions were used for the cylinder. These choices were based on using the the most convenient coordinates for the problem. In a plane-layered medium, cylindrical Hankel functions are convenient, because the structure of the medium is only a function of depth z, and the source transmission has radial symmetry. As before, the solutions are for a simple harmonic source or continuous wave of angular frequency ω. A basic waveguide is sketched in Fig. 11.1.1.

11.1.1 WAVE EQUATION IN A WAVEGUIDE

The cylindrical scaler wave equation for sound pressure is

$$\frac{\partial^2 p}{\partial r^2} + \frac{1}{r}\frac{\partial p}{\partial r} + \frac{\partial^2 p}{\partial z^2} = \frac{1}{c^2}\frac{\partial^2 p}{\partial t^2} \tag{11.1.1}$$

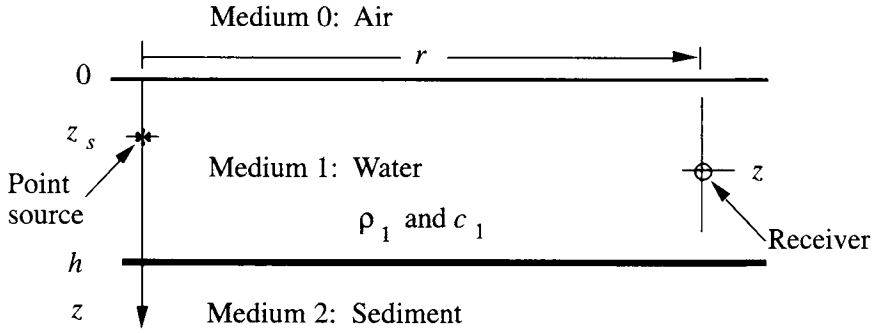

Figure 11.1.1 Source and receiver in a plane-layered waveguide. For simplicity, the upper layer, medium 0, is air. The water layer is medium 1. The sediment, medium 2, may be a single or half-space have many layers.

Letting the pressure be expressed as being proportional to the product,

$$p \sim U(r)Z(z)T(t) \tag{11.1.2}$$

the substitution of Equation 11.1.2 into Equation 11.1.1 and division by p gives

$$\frac{1}{U(r)}\left(\frac{\partial^2 U(r)}{\partial r^2} + \frac{1}{r}\frac{\partial U(r)}{\partial r}\right) + \frac{1}{Z(z)}\frac{\partial^2 Z(z)}{\partial z^2} = \frac{1}{c^2 T(t)}\frac{\partial^2 T(t)}{\partial t^2} \tag{11.2.3}$$

For the harmonic source, $T(t) = \exp(i\omega t)$, the right-hand side reduces to $-\omega^2/c^2$. For all values of r and z, the r-dependent term and the z-dependent term are equal to constants. The separation constants are designated $-\kappa^2$ for the radial term and $-\gamma^2$ for the vertical term. The separated expressions are

$$\frac{\partial^2 U(r)}{\partial r^2} + \frac{1}{r}\frac{\partial U(r)}{\partial r} = -\kappa^2 U(r) \tag{11.1.4}$$

$$\frac{\partial^2 Z(z)}{\partial z^2} = -\gamma^2 Z(z) \tag{11.1.5}$$

$$k^2 = \omega^2/c^2(z) \tag{11.1.6}$$

$$\kappa^2 + \gamma^2 = k^2 \tag{11.1.7}$$

where c depends on z; κ is the horizontal component of the wave number; γ is the vertical component of the wave number. Since $U(r)$ is only a function of r, this implies that κ is constant for all values of z.

For the angle of incidence θ, the horizontal and vertical components of k are

$$\kappa = k \sin\theta \tag{11.1.8a}$$

and

$$\gamma = k \cos\theta \tag{11.1.8b}$$

and this is another way of expressing Snell's Law. The solution of Equation 11.1.7 for γ^2 shows that γ depends on $c(z)$. Correspondingly, the function $Z(z)$ depends on $c(z)$ and ω.

The 0th order solution of the radial equation (11.1.4) for an outgoing wave is the Hankel function, $H_0^{(2)}(\kappa r)$:

$$H_0^{(2)}(\kappa r) = J_0(\kappa r) - i N_0(\kappa r) \tag{11.1.9}$$

At very large range, the Hankel function has the convenient approximation of an outgoing wave:

$$H_0^{(2)}(\kappa r) \approx \sqrt{\frac{2}{\pi \kappa r}} e^{-i(\kappa r - \pi/4)} \quad \text{for} \quad \kappa r \gg 1 \tag{11.1.10}$$

For trapped waves, the upper and lower reflection coefficients both have the absolute value of unity. In real waveguides, there is a minimum range for trapping, because rays must be reflected at angles larger than the critical angles of incidence.

11.1.2 DEPTH DEPENDENCE IN AN IDEALIZED WAVEGUIDE

A simple idealized waveguide consists of a homogeneous fluid (water) that has pressure-release interfaces at the upper and lower boundaries. Recalling section 2.6.4 and Equation 2.6.26, reflections beyond the critical angle can be replaced by a pseudo-pressure release interface at Δz beneath the water sediment interface. Hence, a water layer over a real sediment bottom can be approximated by an idealized waveguide. The boundary conditions require the pressure to vanish at the upper and lower interfaces. Correspondingly, the *eigenfunctions*, $Z(z)$, must satisfy

$$Z(z)|_{z=0} = 0 \quad \text{and} \quad Z(z)|_{z=h} = 0 \tag{11.1.11}$$

Solutions of the $Z(z)$ for the boundary conditions of Equation 11.1.11 are

$$Z(z) = \sin(\gamma z) = 0 \text{ at } z = 0 \text{ and } z = h \tag{11.1.12}$$

where γ is the vertical component of the wave number. A fluid layer between "rigid" interfaces has the other possible solution, $Z(z) = \cos(\gamma z)$.

The requirements of Equation 11.1.12 give the "modal equation" for the idealized waveguide:

$$\gamma_m h = m\pi, \quad \text{or} \quad \gamma_m = m\pi/h \tag{11.1.13}$$

where m is an integer and designates the "mode number." The γ_m are known as the *eigenvalues*. The values of κ_m are given by Equations 11.1.7 and 11.1.13:

$$\kappa_m = (k^2 - \gamma_m^2)^{1/2} \quad \text{and} \quad k^2 \geq \gamma_m^2 \tag{11.1.14}$$

The requirement that κ_m be real gives the mode cut-off condition, because the γ_m increase with mode number.

In an idealized (pressure-release) waveguide, the *eigenfunctions*, $Z_m(z)$, are

$$Z_m(z) = \sin(m\pi z/h), \; m = 1, 2, 3 \tag{11.1.15}$$

Examples of the $Z_m(z)$ are shown in Fig. 11.1.2.

The top and bottom interfaces have pressure-release boundaries. The fluid layer is homogeneous.

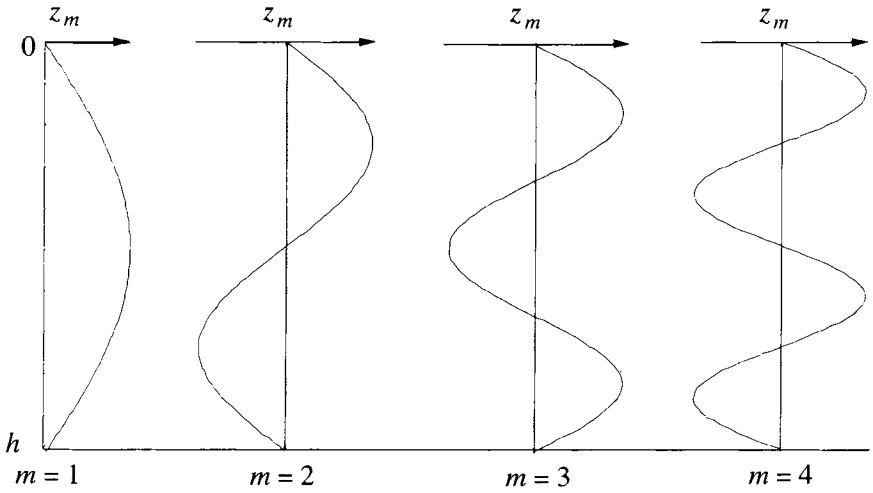

Figure 11.1.2 Eigen functions in an idealized waveguide.

11.1.3 ORTHOGONALITY OF MODES

The eigen functions of the ideal waveguide are sinusoidal, and the eigen functions are 0 for $z > h$ and $z < 0$. Evaluation of the following integral for the mth and nth eigen functions of the ideal waveguide gives

$$\int_0^h \rho \sin\left(\frac{m\pi}{h} z\right) \sin\left(\frac{n\pi}{h} z\right) dz = v_m \delta(m - n) \tag{11.1.16}$$

where

$$v_m = \rho h/2 \tag{11.1.17a}$$

$$\delta(n - m) = 1 \quad \text{for} \quad n = m \text{ and} = 0 \quad \text{for} \quad n \neq m \tag{11.1.17b}$$

Note: In this section, for typographical convenience, we drop the subscript $_A$ and use ρ rather than ρ_A for the ambient density. The symbol $\delta(n - m)$ is the "Kronecker delta," which has value unity when $m = n$ and is otherwise 0. This is a specific example of the orthogonality of the eigen functions. In general, the integral is over the full thickness of the waveguide in which the sound field is not 0. The general orthogonality integral is

$$\int_{-\infty}^{\infty} \rho Z_m(z) Z_n(z)\, dz = v_m \delta(m - n) \tag{11.1.18}$$

where the density depends on depth. Proof of this integral is part of the discussion of the Sturm-Liouville problem in texts on boundary value problems (Churchill and Brown 1987, section 57).

Thus, the orthogonality constant v_m is equal to

$$v_m = \int_{-\infty}^{\infty} \rho Z_m^2(z)\, dz \tag{11.1.19}$$

The orthogonality of the eigen functions enables us to expand the dependence of sound pressure on depth as the sum of eigen functions. The orthogonality integral requires that the integral be taken over the full range of depth for which the $Z_m(z)$ are not 0.

A source function at the depth z_s is proportional to the delta function $\delta(z - z_s)$ and is null for $z \neq z_s$. The delta function for a source at z_s can be expanded as a series sum of eigen functions. Using the analogy of a Fourier series, we write

$$\delta\ (z - z_s\ ) = \sum_m A_m\ Z_m\ (z\ ) \tag{11.1.20}$$

Using the standard procedure to solve for the A_m, we multiply both sides of Equation 11.1.20 by $\rho\, Z_m(z)$, then integrate over the depth of the waveguide:

$$\int_0^\infty \rho Z_m(z)\,\delta(z - z_s)\,dz = \sum_m A_m \int_0^\infty \rho Z_m(z)\,Z_m(z)\,dz \tag{11.1.21}$$

The integral on the right-hand side is Equation 11.1.18, and the values of the A_m are

$$A_m = \rho_1 Z_m(z_s)/v_m \tag{11.1.22}$$

where ρ_1 is the ambient density at the source depth z_s.

11.1.4 SOUND PRESSURE AND THE SUM OF MODES

The sound pressure is the sum of the pressures in each mode. The sound pressure, for source and receiver in medium 1,

$$p(r, z_s, z, t) = A_s e^{i\omega t} \sum_{m=1}^{M} \frac{\rho_1}{v_m (2\pi \kappa_m r)^{1/2}} Z_m(z_s) Z_m(z)\, e^{-(i\kappa_m r - \pi/4)} \tag{11.1.23}$$

where A_s depends on source power. The summation is over the allowed modes M. Starting with a source power Π, computations of the amplitude factor A_s require much analysis (Tolstoy and Clay 1987, p. 81–84). Comparision of pressure amplitude in our Equation 11.1.23 and the pressure amplitude given in Tolstoy and Clay's Equation 3.122 shows that

$$A_s = 2\pi \sqrt{2\pi \rho_1 c_1 \Pi} \tag{11.1.24a}$$

The replacement of A_s in Equation 11.1.23 by Equation 11.1.24 gives

$$p(r, z_s, z, t) = e^{i\omega t}\, 2\pi \sqrt{\rho_1 c_1 \Pi} \sum_{m=1}^{M} \frac{\rho_1}{v_m \sqrt{\kappa_m r}} Z_m(z_s) Z_m(z) e^{-(i\kappa_m r - \pi/4)} \tag{11.1.24b}$$

Next, rearrange the parameters, use a reference power Π_0, and define the *mode excitation*,

$$q_m \equiv 2\pi \sqrt{\rho_1 c_1 \Pi_0}\, \frac{\rho_1}{v_m} \tag{11.1.25}$$

where $\Pi_0 = 1$ watt, and then write the expression for the time-dependent sound pressure:

$$p(r, z_s, z, t) = e^{i\omega t}\sqrt{\Pi/\Pi_0}\sum_{m=1}^{M}\frac{q_m}{\sqrt{\kappa_m r}}Z_m(z_s)Z_m(z)e^{-(i\kappa_m r-\pi/4)} \qquad \textbf{(11.1.26)}$$

The ratio $(\Pi/\Pi_0)^{1/2}$ is proportional to P_0/P_{ref}, where P_0 is the sound pressure referred to 1 m and P_{ref} is a reference pressure—that is, 1 Pa. To show that q_m has the unit of pressure, recall the expression for the source power of a point source (Equation 3.1.16a),

$$\Pi = \frac{2\pi R_0^2 P_0^2}{\rho_1 c_1}$$

and substitute it into Equation 11.1.25.

The pressure amplitude of the trapped wave decreases as $1/\sqrt{r}$, as one would expect for a spreading wave that is trapped in a layer. While the sound pressure has a single frequency, its dependence on range and depth is complicated because the components of sound pressures in each of the modes have different dependencies on range and depth.

In real waveguides, the absorption losses in the bottom and the water layer cause the sound pressures to decrease faster than $1/\sqrt{r}$. All of these kinds of losses are included in the empirical mode attenuation rates δ_m, so that Equation 11.1.26 becomes

$$p(r, z_s, z, t) = e^{i\omega t}\sqrt{\Pi/\Pi_0}\sum_{m=1}^{M}\frac{q_m}{\sqrt{\kappa_m r}}Z_m(z_s)Z_m(z)e^{-(i\kappa_m r-\pi/4)-\delta_m r} \qquad \textbf{(11.1.27)}$$

$$p(r, z_s, z, t) = e^{i\omega t}\sqrt{\Pi/\Pi_0}P(\omega, r, z_s, z) \qquad \textbf{(11.1.28)}$$

$$P(\omega, r, z_s, z) = \sum_{m=1}^{M}\frac{q_m}{\sqrt{\kappa_m r}}Z_m(z_s)Z_m(z)e^{-(i\kappa_m r-\pi/4)-\delta_m r} \qquad \textbf{(11.1.29)}$$

The pressure *transmission function*, $P(\omega, r, z_s, z)$, has frequency dependence in the γ_m, κ_m, ν_m, and q_m. The pressure transmission function is also known as the *Green's function*, with the notation $G(\omega, r, z_s, z)$. We will use the transmission function when we do its Fourier transformation to compute the transmission of a transient sound in a waveguide. These equations will be referred to many times.

11.1.5 REFLECTIONS AND TRANSMISSIONS AT THE WAVEGUIDE BOUNDARIES

When a real waveguide has horizontal stratification and parallel interfaces, theoretical models can be excellent approximations to reality. Many areas of the deep ocean and the shallow water environments have nearly horizontal stratifications. The main changes in going from ideal to real waveguides are to include many layers and finite sound speed and density changes. Later we will give examples that show that the requirement of parallel interfaces can be relaxed.

We repeat a few formulas from section 2.6.1. In an n-layered medium, the wave number in the nth layer is

$$\begin{aligned} \text{wave number} \quad & k_n = \omega/c_n \\ \text{Snell's Law} \quad & k_1 \sin\theta_1 = k_n \sin\theta_n \end{aligned} \tag{11.1.30}$$

Reflection coefficients are

$$\mathcal{R}_{12} = \frac{\rho_2 c_2 \cos\theta_1 - \rho_1 c_1 \cos\theta_2}{\rho_2 c_2 \cos\theta_1 + \rho_1 c_1 \cos\theta_2} \tag{11.1.31}$$

critical angle and $c_2 > c_1$, $\theta_c = \arcsin(c_1/c_2)$; and

$$g_2 \equiv \left[\left(\frac{c_2}{c_1}\right)\sin^2\theta_1 - 1\right]^{1/2} \quad \text{and} \quad \cos\theta_2 = -ig_2 \tag{11.1.32}$$

Beyond critical angle, the reflection coefficient is

$$\mathcal{R}_{12} = \frac{\rho_2 c_2 \cos\theta_1 + i\,\rho_1 c_1 g_2}{\rho_2 c_2 \cos\theta_1 - i\,\rho_1 c_1 g_2} \tag{11.1.33}$$

where

$$\begin{aligned} |\mathcal{R}_{12}| &= 1, \\ \mathcal{R}_{12} &= e^{2i\Phi} \end{aligned} \tag{11.1.34}$$

and

$$\Phi = \arctan \frac{\rho_1 c_1 g_2}{\rho_2 c_2 \cos\theta_1} \tag{11.1.35}$$

Figure 11.1.1 shows the waveguide. In the water layer, the z-dependence of a downward-traveling wave (z + down) is

$$Z(z) \approx e^{-ik_1 z \cos\theta_1} \tag{11.1.36}$$

Below the depth h, as in Fig. 11.1.1, and beyond the critical angle, the downward-traveling wave is

$$Z(z) \approx e^{-k_2 g_2 (z-h)} \quad \text{for} \quad z > h, \ \theta_1 > \theta_c \tag{11.1.37}$$

and the amplitude of the $Z(z)$ decreases exponentially beneath the interface.

Multiple Layers

It is easy to extend the ideal model to waveguides having many layers by letting the upper and lower reflection coefficients in Fig. 11.1.1 represent many layers. Recalling Section 2.6.3, the reflection coefficient at a thin layer is

$$\begin{aligned} \mathcal{R}_{13} &= \frac{\mathcal{R}_{12} + \mathcal{R}_{23} \exp(-i2\Phi_2)}{1 + \mathcal{R}_{12}\mathcal{R}_{23} \exp(-i2\Phi_2)} \\ \Phi_2 &= k_2 h_2 \cos\theta_2 \end{aligned} \tag{11.1.38}$$

It is easy to extend this formula to n layers by replacing the reflection coefficient $\mathcal{R}_{23}$ by the reflection from a layer beneath it and so forth. Usually if the wave (or ray) is critically reflected at an interface, layers beneath that interface can be ignored. The exception is for a very thin layer where the wave field penetrates through the layer. Methods and algorithms for computing the reflection coefficient for a wave reflected by a sequence of thin layers are provided in Tolstoy and Clay (1987, sec. 2.5), Brekhovskikh (1980, sec. 3.6), and Clay (1990, sec. B1.3).

11.1.6 MODAL EQUATIONS (CHARACTERISTIC EQUATIONS)

The waveguide boundaries (Fig. 11.1.3) have upper and lower reflection coefficients. The reflection at the lower boundary has unity amplitude and the phase shift as given in Equation 11.1.34. The reflection at the upper free surface has

$$\begin{aligned} &\mathcal{R}_{upper} = -1; \ \mathcal{R}_{upper} = \exp(i\pi); \ \mathcal{R}_{upper} = \exp(2i\Phi_{upper}) \\ &\Phi_{upper} = \pi/2 \end{aligned} \tag{11.1.39}$$

In trapped wave propagation, the z-dependencies of the upward- and downward-traveling components of the sound pressure combine to form standing waves. Since the time factor $\exp(i\omega t)$ is the same for all sound pressures, it is

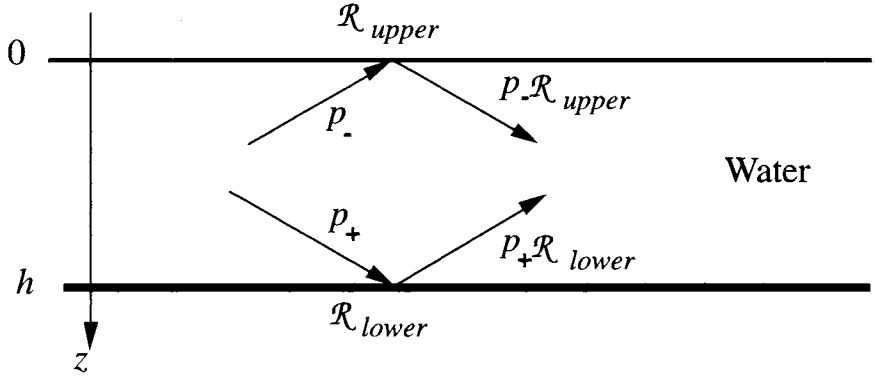

Figure 11.1.3 Reflections of pressure waves at the upper and lower boundaries. The arrows show the directions the waves are traveling. The incident waves are p_+ and p_-.

omitted. The downward $(+z)$ traveling pressure p_+ and the upward $(-z)$ traveling pressure p_- are

$$\begin{aligned} p_+ &= Ae^{-i(\kappa r+\gamma z)} \\ p_- &= Be^{-i(\kappa r-\gamma z)} \end{aligned} \tag{11.1.40}$$

where A and B are constants. The reflection coefficient at the lower interface is

$$\mathcal{R}_{lower} = \frac{p_-}{p_+}\bigg|_{z=h} = \frac{B}{A}e^{i2\gamma z} \tag{11.1.41}$$

and at the upper interface is

$$\mathcal{R}_{upper} = \frac{p_+}{p_-}|_{z=0} = \frac{A}{B} \tag{11.1.42}$$

To obtain the modal equation, we first solve Equation 11.1.42 for B/A, and then substitute it into Equation 11.1.41:

$$\mathcal{R}_{upper}\mathcal{R}_{lower}\, e^{-i2\gamma z} = 1 = e^{i2n\pi} \tag{11.1.43a}$$

where n = integer, and

$$\mathcal{R}_{upper} = \exp(2i\Phi_{upper}),\ \mathcal{R}_{lower} = \exp(2i\Phi_{lower}) \tag{11.1.43b}$$

The phase form of the modal equation comes from equating the phases

$$2(\gamma h) = 2(n\pi + \Phi_{upper} + \Phi_{lower}) \tag{11.1.44}$$

where Equations 11.1.43 and 11.1.44 are satisfied for any n. Since the integer n is arbitrary, we can write the modal equation for the mth mode as follows:

$$\gamma_m h = (m-1)\pi + \Phi_{upper} + \Phi_{lower} \tag{11.1.45}$$

where m is the mode number and where we use the subscript m or γ_m for mode number. The modal equations are also known as the "characteristic equations" in the waveguide literature.

The eigen function for a waveguide that has a free surface is

$$Z_m(z) = \sin(\gamma_m h) \tag{11.1.46a}$$

and

$$\Phi_{upper} = \pi/2 \tag{11.1.46b}$$

and the horizontal component of the wave number is

$$\kappa_m = (k_1^2 - \gamma_m^2)^{1/2} \tag{11.1.47a}$$

and

$$k_1 = \omega/c_1 \tag{11.1.47b}$$

In medium 2, the eigen functions decay exponentially because the incident angles are greater than the critical angle:

$$Z_m(z) = \exp[-k_2 \kappa_{m2} g_{2m}(z-h)] \tag{11.1.48}$$

where $z \geq h$, and

$$k_2 g_{2m} = (k_m^2 - k_2^2)^{1/2} \tag{11.1.49}$$

where $k_2 = \omega/c_2$

The excitation function (Equation 11.1.25) uses the orthogonality integral (Equation 11.1.18). The energy flux function (Equation 11.1.16) that includes the penetration of the pressure field into medium 2 is

$$v_m = \int_0^h \rho_1 \sin^2(\gamma_m z)\, dz + \int_h^\infty \rho_2 e^{-k_2 g_2 (z-h)}\, dz \tag{11.1.50}$$

and

$$v_m = \rho_1 \left[\frac{h}{2} - \frac{\sin(2\gamma_m h)}{4\gamma_m} \right] + \frac{\rho_2}{k_2 g_2} \tag{11.1.51}$$

The numerical solutions for γ_m, κ_m, ν_m, and q_m are the biggest part of evaluating the equations for sound pressures in a waveguide (Equations 11.1.27 through 11.1.29).

11.1.7 NUMERICAL EXAMPLE: TWO-LAYER WAVEGUIDE

The numerical example uses the acoustic model, Table 11.1 to compute a set of graphs of the waveguide acoustical parameters and sound pressures. MATLAB was used to perform the computations. The modal (characteristic) equation (11.1.46) is a transcendental equation, therefore direct numerical solutions for a selected frequency can be difficult. A simpler method uses a set of incident angles θ_1 as inputs to the reflected phase expression (Equation 11.1.33).

The phases Φ_{upper} and Φ_{lower} are substituted into the modal equation (11.1.42), and γ_m is computed. The frequency ω follows directly by using Equation 11.1.47. The interpolation between a pair of evaluations of γ_m gives the values of γ_m, κ_m, and q_m for a chosen frequency. A set of numerical solutions is shown in Fig. 11.1.4.

Cut-off Frequencies

Figure 11.1.4 shows γ_m and κ_m as functions of frequency. In this example, the smallest frequency for γ_1, κ_m, and mode 1 is about 37 Hz. The next modes start at 110 Hz, 182 Hz, and 255 Hz. These are the mode "cut-off" frequencies. The requirement that the sound pressures be trapped requires that all angles of incidence be greater than the critical angle $\theta_c = \arcsin(c_1/c_2)$. At the critical angle of incidence, we use

$$\gamma_m = \frac{2\pi f \cos(\theta)}{c_1} \tag{11.1.52}$$

and the modal equation (11.1.45), and solve for the cut-off frequency:

$$f_c = \frac{c_1}{2\pi \cos(\theta_c)} [(m-1)\pi + \Phi_{upper} + \Phi_{lower}] \quad \text{for} \quad \theta = \theta_c \tag{11.1.53}$$

Table 11.1 **Waveguide Physical Parameters**

Layer n	*Thickness h, m*	$\rho_n kg/m^3$	$c_n, m/s$
1	22.3	1033	1500
2	∞	$2\rho 1$	$1.12c_1$

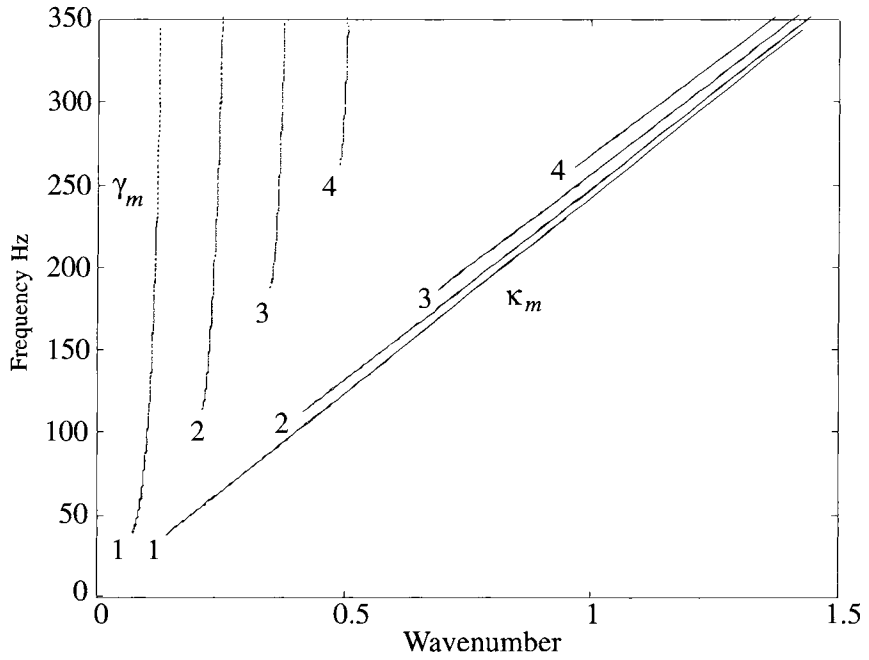

Figure 11.1.4 Numerical solutions of the modal (characteristic) equation. The 2 layer, or "Pekeris" waveguide, has the parameters given above. The vertical component of wave number, γ_m, is shown by the dashed curve; the horizontal component, κ_m, is shown by the solid curve; and the mode number is m.

As shown in Fig. 11.1.4, the cut-off frequency (Equation 11.1.46) increases with mode number. Since the critical angle is the same for all modes, the differences of the cut-off frequencies should be the same. The differences are 72 and 73 Hz and are within graphic errors. The mode excitations, Fig. 11.1.5, also show the cut-off frequency for trapped modes.

We remind the reader that untrapped paths exist, and contributions having frequencies less than the cut-off frequency can be received. Examples are the direct path, image reflections, and the head wave. Generally, the pressure amplitudes of the untrapped arrivals decrease as $1/r$ or faster. Analytical developments for the untrapped arrivals is beyond the level of difficulty of this book. Recalling the normal mode solution (Equation 11.1.27) and ignoring losses, the pressure amplitudes of trapped modes decrease as $1/\sqrt{r}$; these will dominate the received signals at large range.

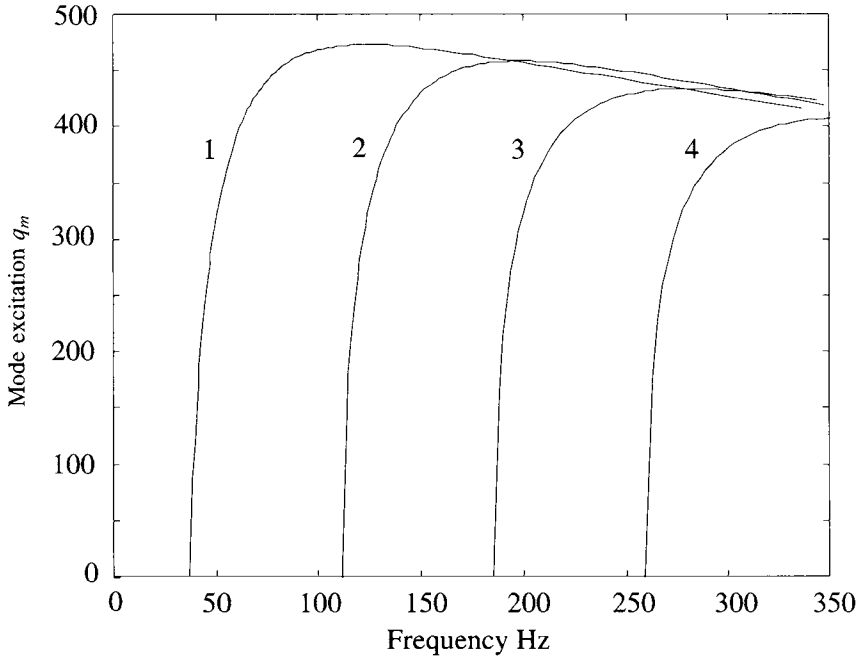

Figure 11.1.5 Mode excitations, q_m. The mode excitations were computed using Fig. 11.1.4 and Equation 11.1.51. The units of the q_m are pressure, Pa. The reference power is 1 watt.

Sound Pressure Due to a Sinusoidal Sound Source

One of the classic sound transmission measurements consists of towing a sound source away from, or toward, a receiver (Tolstoy and Clay 1966, 1987, sec. 4.6). The sound source or "projector" transmits a sinusoidal sound pressure that has a constant frequency. The absolute sound pressure is measured as a function of range. These experiments were designed to match the sound transmission equation (11.1.27). Continuing our numerical example, we choose a frequency of 150 Hz for computations. From Fig. 11.1.4 and Fig. 11.1.5 the eigenvalues are listed in Table 11.2.

The eigenfunctions Z_m for 150 Hz are shown in Fig. 11.1.6. Comparisons of this figure and Fig. 11.1.2 for the ideal waveguide show the effects of including the sediment sound speed on the eigenfunctions.

Table 11.2 **Eigen Values**

m	$\gamma_m, [m^{-1}]$	$\kappa_m, [m^{-1}]$	$k_2 g_{2m} [m]^{-1}$	$q_m, [Pa]$
1	0.110	0.612	0.16	470
2	0.225	0.583	0.24	425

Computations are for the frequency 150 Hz, mode attenuations $\delta_m = 0$, source power 1 watt, the waveguide structure is in Table 11.1.

The source and receiver depths are important. If the depth of the source were chosen to be at the null of Z_2 at 14 m, then mode 2 would not be excited. Only mode 1 would be excited. Putting a single source on the bottom would strongly excite mode 2 and mode 1. The reader can show that placing a pair of equal sources at approximately 7 and 21 m depths will cancel the sound pressures in mode 2. And the same pair of sources would transmit in mode 1. Examples of the sound transmissions for single modes are shown in Fig. 11.1.7.

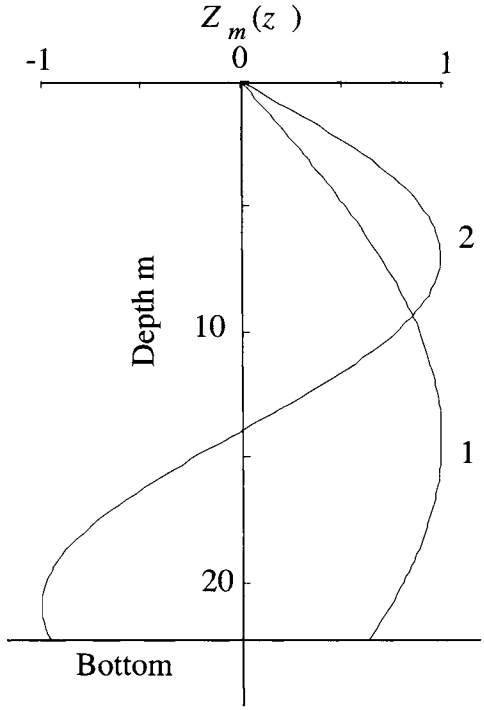

Figure 11.1.6 Eigen functions Z_1 and Z_2. The parameters for the waveguide are given in Table 11.1. The eigen values are in Table 11.2. The frequency is 150 Hz.

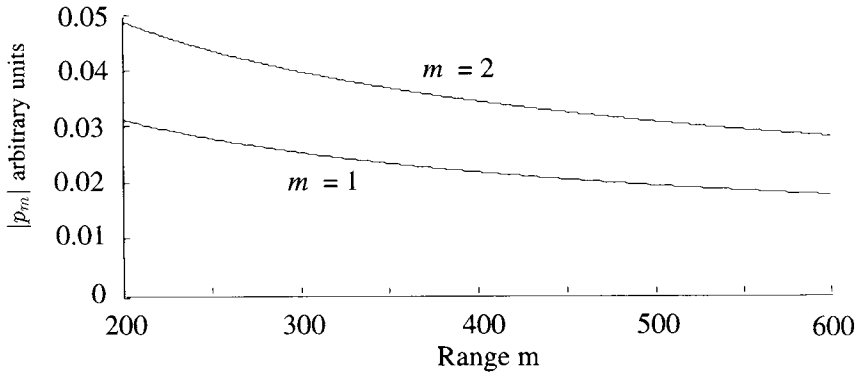

Figure 11.1.7 Sound transmission $|p|$ in modes 1 and 2. The amplitudes are arbitrarily chosen to display the two transmissions. The parameters are given in Tables 11.1 and 11.2. Frequency is 150 Hz. The individual modes decrease with range as $1/\sqrt{r}$. If the attenuations δ_1 and δ_2 were appreciable, the modes would decrease faster.

Commonly in analog receiving systems, either the absolute amplitude or the absolute square of the sound pressure is measured in sound transmissions from a sinusoidal source. The absolute square of the transmission (Equation 11.1.26) is

$$|p(r, z_s, z)|^2 = \Pi/\Pi_0 \left\{ \sum_{m=1}^{M} \frac{q_m^2}{r\kappa_m} Z_m^2(z_s) Z_m^2(z) + 2 \sum_{m>n} \sum \frac{q_m q_n}{r(\kappa_m \kappa_n)^{1/2}} Z_m(z_s) Z_n(z_s) Z_m(z) Z_n(z) \times \cos[(\kappa_m - \kappa_n)r] \right\} \quad (11.1.54)$$

where the double summation for $m > n$ means that the $(m - n)$ and $(n - m)$ terms are combined to give $2\cos[(\kappa_m - \kappa_n)r]$. The first summation gives the mean absolute square. The second summation gives the "mode interferences." The second summation is not (lightly) ignored because mode interferences have been observed over the huge range from Antigua to Newfoundland (2800 km). These low-frequency sound transmissions were at 13.89 Hz (Guthrie et al. 1974).

Simulated Sound Transmission

A simulation of a sound transmission in the shallow-water waveguide is shown in Fig. 11.1.8. The regular sequence of maxima and minima are the result of coherently adding the first two modes and then taking the absolute value of the

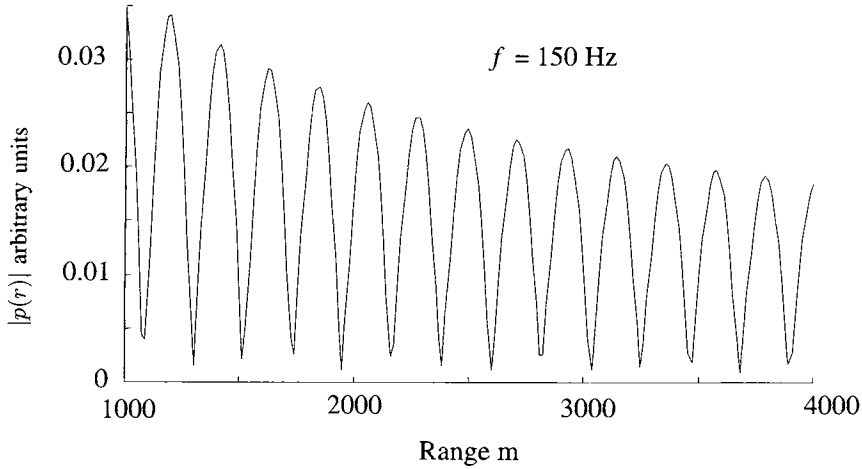

Figure 11.1.8 Simulation of sound transmission at 150 Hz. The pressure is the absolute value of the coherent sum of mode 1 and 2. The waveguide parameters are given in Tables 11.1 and 11.2. The source is at 8 m depth, and the receiver is at 18 m depth.

result. The mode interferences are due to the cosine terms in the second summation (Equation 11.1.54).

If the two-mode simulation shown in Fig. 11.1.8 were an experiment, one could start an interpretation by measuring the "interference wavelength" $\Lambda_{1,2}$ of the sequence of maxima and minima. From this figure we count 14 peaks over a range of 3000 m; the interference wavelength is approximately 214 m. Using the cosine term in Equation 11.1.47, the interference wavelength is

$$\Lambda_{m,n} = |2\pi/(\kappa_m - \kappa_n)| \tag{11.1.55}$$

From Table 11.2, the interference wavelength $\Lambda_{1,2}$ is predicted to be 217 m. The simulation is within 1.5 percent.

Real Sound Transmissions

The results of a shallow-water sound transmission experiment are shown in Fig. 11.1.9. In addition to the experimental waveguide parameters given in Table 11.1, the theoretical calculations were for three-layer model. The agreement is excellent for the smooth sea surface.

The same transmission measurements were repeated a week later, when the rms wave heights were approximately 0.5 m. The maxima and minima of the mode interferences were much smaller. It is apparent that the fluctuating sea

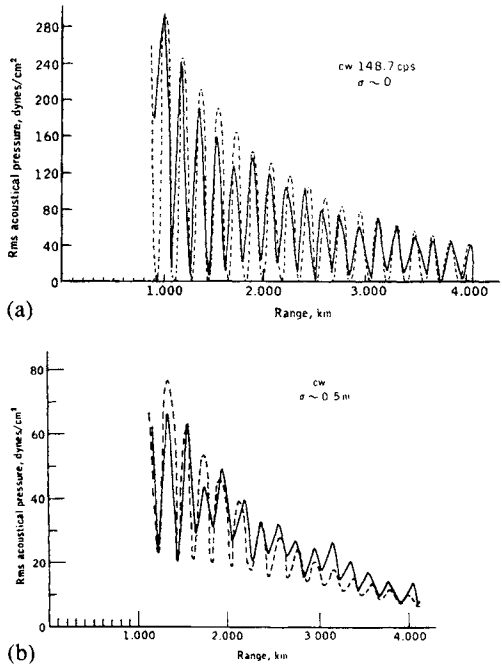

Figure 11.1.9 Comparisons of experimental and theoretical sound transmissions. The experiments were done in the shallow water south of the Fire Islands of New York. Solid line is experiment, and dashed line is theory. Pressure amplitudes are arbitrary. The theory used a three-layer waveguide. The top two layers are those given in Table 11.1. Physical parameters for the third layer are $h_2 = 0.9h_1$; $\rho_3 = 2\rho_1$; and $c_3 = 1.24c_1$. Source was at 10 m depth, and the receiver was at 19.8 m depth. Two transmission runs were made. a) The sea surface was very smooth, and the rms wave height was $\sigma = 0$. b) The experiment was repeated when the wave swell had the rms height $\sigma \approx 0.5$ m. From Tolstoy and Clay (1987, Fig. 6.17).

surface reduced the magnitude of the interference term (Clay 1964 and Tolstoy and Clay 1987).

11.2 Geometrical Dispersion: Phase and Group Velocities

The propagation of pressure signals in a waveguide exhibits a phenomenon called *dispersion*, where different frequency components of the signal travel at different velocities. In a waveguide, the dispersion is due to the geometry and the physical properties of the waveguide, hence it is called *geometric dispersion*. There are two velocities—the *phase velocity* and the *group velocity*.

11.2.1 PHASE VELOCITY

Let us pick a mode and phase of the sound pressure and "ride" it as it moves along the waveguide. The mth mode phase in Equation 11.1.23 is given as the imaginary part of the exponential:

$$\text{Phase of mode } m = (\omega t - \kappa_m r - \pi/4) \tag{11.2.1}$$

For example, a pressure maximum travels with the velocity $r/t = \omega/\kappa_m$, and this defines the phase velocity along the r-coordinate. Using the subscripts r and m for the velocity along r and the mth mode, the phase velocity is

$$v_{r\,m} = \omega / \kappa_m \tag{11.2.2}$$

11.2.2 GROUP VELOCITY

Figure 11.2.1 shows a section of the sound transmission from an explosive source in shallow water. The experimental details are in the figure. The duration of this arrival is approximately 180 ms. From the oscillograph trace, the frequencies at the beginning and ends of this arrival are approximately 500 Hz and 70 Hz. Using a range of 8.42 km and travel times of 5.555 s and 5.73 s for the beginning and end, the velocity of the 500 Hz frequency component is 1516 m/s, and the velocity of the 70 Hz component is 1470 m/s. The data for this waveguide was used to calculate a set of phase and group velocity curves. Since the high-frequency limit was used to calculate the range, we can only calculate the group velocity for the end of the dispersed signal. For the first mode, the group velocity has a minimum of 1475 m/s, and the frequency at the minimum is 70–75 Hz. The agreement with the experiment is excellent.

We can use the Fourier integral, the convolution of a source $S(\omega)$, and the pressure transmission function $P(\omega, r, z)$ (Equation 11.1.29) to compute the transient arrivals. The transient arrival in the mth mode is

$$p_m(t) = \int_{-\infty}^{\infty} S(\omega) P_m(\omega, r, z_s, z) e^{i\omega t} d\omega \tag{11.2.3}$$

where the mth mode pressure transmission function is

$$P_m(\omega, r, z_s, z) \equiv \frac{q_m}{(\kappa_m r)^{1/2}} Z_m(z_s) Z_m(z) e^{-i(\kappa_m r - \pi/4) - \delta_m r} \tag{11.2.4}$$

Numerical evaluations of this integral (Equation 11.2.3) are practical, and analytical evaluations are very difficult.

Consider a very narrow range of frequency $\Delta\omega$ that is centered on ω. Then, the source $S(\omega)$ and the eigenfunctions Z_m and q_m are approximately constant and can be moved out of the integral:

$$p_m(t) \approx \frac{S(\omega)\, q_m}{(\kappa_m r)^{1/2}} Z_m(z_s)\, Z_m(z)\, e^{i\pi/4 - \delta_m r} \int_{\Delta\omega} e^{i(\omega t - \kappa_m r)}\, d\omega \tag{11.2.5}$$

The oscillations of the integrand effectively cancel each other out on integration, except where $(\omega t - \kappa_m r)$ is constant over the range of ω within $\Delta\omega$. These values are known as *stationary phases*. The stationary phase condition requires that the slope of $(\omega t - \kappa_m r)$ be null as a function of κ_m. Differentiating $(\omega t - \kappa_m r)$ with respect to κ_m gives

$$\frac{d}{d\kappa_m}(\omega t - \kappa_m r) = 0 \tag{11.2.6}$$

so that

$$\frac{d\omega}{d\kappa_m} = \frac{r}{t} \tag{11.2.7}$$

where t is the time required for the component of signal having the frequency ω to travel the distance r. The *group velocity* of the mth mode is

$$u_{g\,m} = \frac{d\omega}{d\kappa_m} \tag{11.2.8}$$

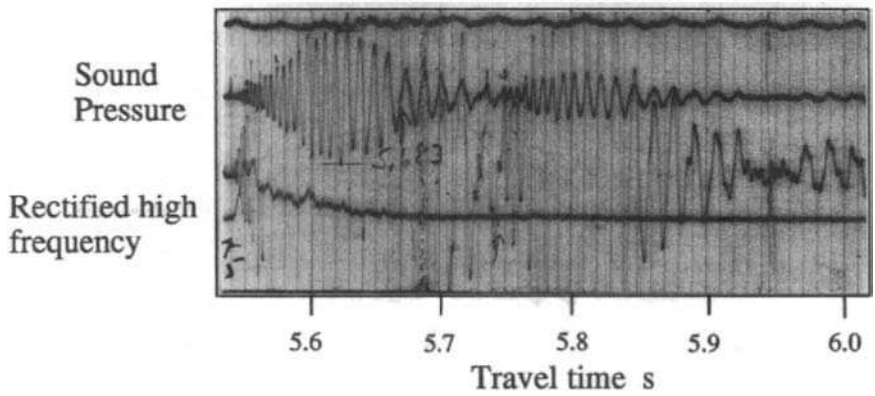

Figure 11.2.1 Dispersion in the shallow-water transmission from an explosive source, Shot #91. Ewing, Worzel, and Pekeris called this pressure signal the "water wave" because the sound wave travels in the water layer. The signal is an oscillograph trace of the wide-band hydrophone output, and the time lines are 10 ms. The water depth was 18 m (60 ft). Both shot and hydrophone were on the bottom. The sound speed in water was 1516 m/s. The travel time was 5.555 s. The travel time and sound speed in water were used to compute the range of 8.42 km. The second layer was approximately 300 m of sand over limestone. Refraction measurements gave the sand speed 1935 m/s. From Ewing, Worzel, and Pekeris (1948). Worzel and Ewing Fig. 12, Pekeris Plate 10.

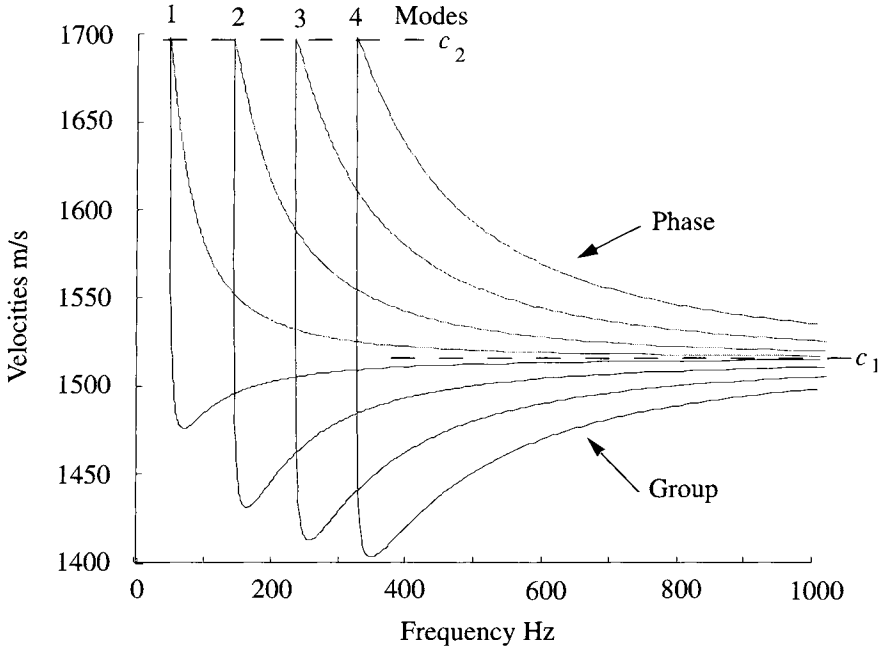

Figure 11.2.2 Phase and group velocities for the Jacksonville, Florida, shoal shallow-water waveguide. The parameters are $c_1 = 1516\,\text{m/s}$; $\rho_1 = 1033\,\text{kg/m}^3$; $c_2 = 1.12c_1$, (1698 m/s), $\rho_2 = 2\rho_1$; $h = 18\,\text{m}$. The first four modes are shown. The maximum velocities are c_2, and the high-frequency limit is c_1. The values are from Ewing, Worzel, and Pekeris (1948, Fig. 9). They also give other values of c_2 that range from 1592 m/s to 1935 m/s.

Numerical examples of the phase and group velocities are shown in Fig. 11.2.2. Obvious observations are (1) the highest velocities are c_2; (2) the mode cut-off moves to higher frequency as the mode number increases (as in Fig. 11.1.4); (3) the group velocities have minima that are much smaller than the sound speed in the water layer, c_1 (these give the last arrivals in a mode); (4) the group velocities decrease as the mode number increases; and (5) at very high frequency, the phase and group velocities tend to c_1.

Before computers (B.C.), data such as shown in Fig. 11.2.1 were analyzed by hand. The times between peaks and the travel times to the peaks were used to compute a group velocity for the short segment of the signal with that period. The experimental group velocities were compared with theoretical group velocities. If the fit was poor, the parameters of the waveguide were adjusted, and new hand calculations of the group velocities were made for the next iteration.

11.2.3 DISPERSED ARRIVAL: p(t)

The time domain expression $p(t)$ is computed by taking the Fourier transformation of the sound transmission function (Equation 11.2.4). Numerical evaluations are a practical method. A few modifications are needed to change the integral into a numerical summation. The first step is to change the infinite integral (Equation 11.2.3) to a numerical finite summation (Equation 6.2.19) as follows: the infinite integral becomes the summation $-N_F$ to N_F; the time and frequency variables are computed using the sampling interval t_0 (for dt) and the frequency step f_1 (for df); thus, t and f are

$$t_n = nt_0 \quad \text{and} \quad f_j = jf_1 \tag{11.2.9}$$

With these changes, the Fourier transformation from frequency to time becomes

$$x(n) = \sum_{j=-N_F}^{N_F} X(j) \exp(i 2\pi f_j t_n) f_1 \tag{11.2.10}$$

and the companion Fourier transformation from time to frequency is

$$X(j) = \sum_{n=-N_T}^{N_T} x(n) \exp(-i 2\pi f_j t_n) t_0 \tag{11.2.11}$$

Assuming that the sound transmissions are real, the spectral terms have a complex conjugate relationship (Equations 6.2.4 and 6.2.5):

$$X(-j) = X^*(j) \tag{11.2.12}$$

where * indicates complex conjugate. Equation 11.2.10 simplifies to a sum, its complex conjugate, and $X(0)$:

$$\begin{aligned} x(n) = &\sum_{j=1}^{N_F} X(j) \exp(i 2\pi f_j t_n) f_1 \\ &+ X(0) f_1 + \sum_{j=1}^{N_F} X^*(j) \exp(-i 2\pi f_j t_n) f_1 \end{aligned} \tag{11.2.13}$$

The choice of the summation limits in Equations 11.2.11 and 11.2.13 can be different.

In numerical computations, we let $X(j) = S(f)P(f, r, z_s, z)$. The sound pressure for the mth mode is, dropping some of the functional dependence in P,

$$p_m(n) = \sum_{j=1}^{N_F} S(j) P_m(j) \exp(i 2\pi f_j t_n) f_1 + S(0) P_m(0) f_1 + \sum_{j=1}^{N_F} [S(j) P_m]^*(j) \exp(-i 2\pi f_j t_n) f_1 \tag{11.2.14}$$

Notice the choice of the summation limits in Equation 11.2.14. The conditions of the transmission simulation control the choices of the parameters t_0, f_1, and N_F. For a specific example, we use a Pekeris model for the Jacksonville shoal and the parameters given in Fig. 11.2.2.

Time

The time to the beginning of the "water wave" is r/c_1. At 8420 m range, the time is 5.55 s. The longest time is approximately r/(group velocity minimum 1475 m/s) and is 5.71 s. The sampling interval should be less than half of the shortest period of interest. From Figure 11.2.2 and the first mode, most of the dispersion occurs between frequencies of 70 to 500 Hz. A sampling interval of 0.001 s will display the dispersed waveform.

Frequency

The frequency range is approximately 70 to 500 Hz. The frequency step f_1 depends on the complexity of $P_m(j)$ and the detail needed to compute $k_m r$ for the largest values of j and r. A sampling interval of 2 Hz is sufficient to describe P_m.

Source, Filter, and Computations: Numerical Details

Evaluation of the Fourier summation (Equation 11.2.12) gives a time domain signal that repeats at $1/f_1$. At a 2 Hz sampling rate, the Fourier summation will give a signal that repeats (or folds) every 0.5 s. Figure 6.2.1 shows examples of folding.

The numerical evaluations of Equation 11.2.14 are very sensitive, and the choices of parameters can require many trials. So, we give the ones that we used. For the range of 8.42 km and the high-frequency group velocity of 1.516 km/s, the simulated sound pressure is expected to start a little after 5.5 s and to have a duration of less than 0.5 s. The bandpass filter $S(f)$ simulates the explosion,

transmission, and electrical system. It was necessary to taper the ends of the bandpass filter. The parameters are

$$
\begin{aligned}
&r = 8.42\,\text{km}\\
&f_1 = 2\,\text{Hz} \quad \text{and} \quad N_F = 270\\
&t_0 = 0.00099\ \text{s}\\
&n_{max} = 505\\
&S(j) = 0 \quad \text{for} \quad 0 \le f < 70\,\text{Hz}\\
&S(j) = (+\,\text{taper}) \quad \text{for} \quad 70 \le f \le 120\,\text{Hz}\\
&S(j) = 1 \quad \text{for} \quad 120 \le f \le 480\,\text{Hz}\\
&S(j) = (-\text{taper}) \quad \text{for} \quad 480 < f < 530\,\text{Hz}\\
&S(j) = 0 \quad \text{for} \quad 530 \le f \le 540\,\text{Hz}
\end{aligned}
\tag{11.2.15}
$$

where

$$
\begin{aligned}
(+\,\text{taper}) &= 0.5\{1 - \cos[\pi(f - 70)/50]\}\\
(-\,\text{taper}) &= 0.5\{1 - \cos[\pi(530 - f)/50]\}
\end{aligned}
$$

With these choices, the dispersed transient appears in a 0 to 0.5 s window. The display starts at 5.5 s and lasts to 6 s. A simulated transmission in the first mode is shown in Fig. 11.2.3.

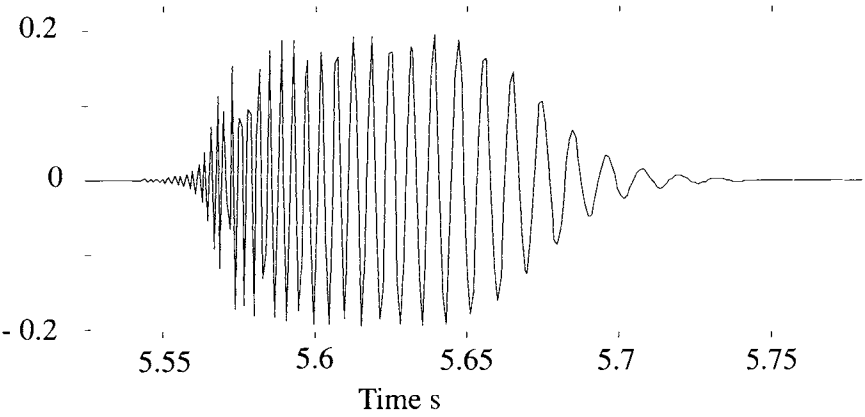

Figure 11.2.3 Simulation of the dispersed mode 1 arrival in a Pekeris waveguide. Physical parameters are given in the caption of Fig. 11.2.2. The source and receiver were on the bottom, 18 m, and the range was 8420 m. The numerical parameters for the Fourier transformation are in Equation 11.2.15.

Starting in the 1950s, the slender volume of Ewing, Worzel, and Pekeris, Memoir 27 of the Geological Society of America (1948), was required reading. It had a profound effect on a generation of underwater acousticians and geophysicists all over the world. While our discussion has focused on the developments in the United States, very important research was done in the Soviet Union (Russia). Brekhovskikh's book, *Waves in Layered Media* (1960, 1980), is a comprehensive and excellent reference. Chinese research is in the monograph of Wang Te-Chao and Shang Er-Chang, *Underwater Acoustics* (1981).

11.3 Arrays, Signals, and Noise

For simplicity, we assume (1) the waveguide is horizontally stratified and time-independent; (2) the transmission is from a sinusoidal (CW) source; and (3) the noise sources are uncorrelated and have stationary statistical properties. An extensive review is provided in Clay (1966) and Tolstoy and Clay (1987, Appendix 6).

11.3.1 ARRAYS OF SOURCES AND RECEIVERS IN A WAVEGUIDE: MODE FILTERS

The source and receiver arrays are shown in Fig. 11.3.1. In general, each transducer in the vertical arrays can, by itself, be a horizontal array.

The sound pressures from each source transducer add at each receiving transducer, and the output signal of the receiving array $s(t)$ is the sum of all

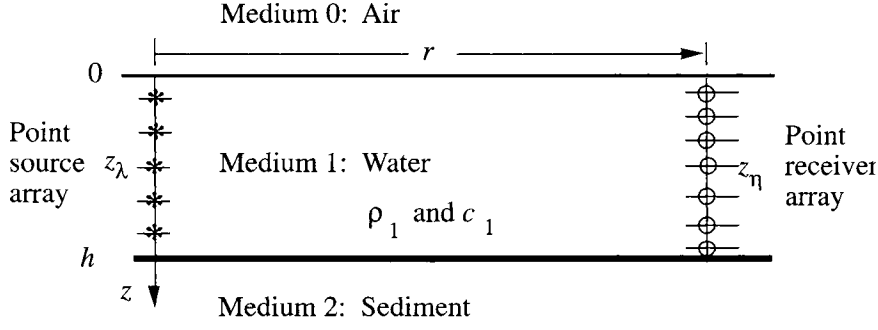

Figure 11.3.1 Vertical arrays of sources and receivers in a waveguide.

pressures. Using Equations 11.1.27 through 11.1.29, we write the sum of sound transmissions from all sources to all receivers as follows:

$$s\ (t\ ) = e^{\ i\omega t} \sqrt{\frac{\Pi}{\Pi_0}} \sum_{m\ =\ 1}^{M} a_{\ m}\ U_{\ m}\ b_{\ m} \tag{11.3.1}$$

where the source array of Λ transducers is

$$a_{\ m} \equiv \sum_{\lambda\ =\ 0}^{\Lambda\ -\ 1} \alpha_{\lambda}\ Z_{\ m}\ (z_{\ \lambda}\ ) \tag{11.3.2}$$

the receiver array of L transducers is

$$b_m \equiv \sum_{\eta=0}^{L-1} \beta_\eta Z_m(z_\eta) \tag{11.3.3}$$

where α_λ is the relative pressure amplitude of the λth source at depth z_λ; β_η is the relative sensitivity of the ηth hydrophone at depth z_η. The density is assumed to be constant over the depth of the arrays. The waveguide function U_m for the mth mode is taken from Equation 11.1.29:

$$U_{\ m} \equiv \frac{q_{\ m}}{(\ \kappa_m r\ )^{\ 1/2}} \exp\left[\ -(i\ \kappa_{\ m}\ r\ -\pi\ /4\ ) - \delta_{\ m}\ r\ \right] \tag{11.3.4}$$

The waveguide function has the units of sound pressure Pa.

The vertical arrays operate as "mode filters" and can be adjusted to transmit and receive in selected modes. The arrays should span most of the depth of the waveguide. For M modes, the number of sources (or receivers) should be more than the number of modes, if $\Lambda > M$. Using the transmitting array as an example, the transmission drives α_λ are chosen to satisfy the following equations:

$$\sum_{\lambda\ =\ 0}^{\Lambda\ -\ 1} \alpha_{\lambda}\ Z_{\ m_0}\ (z_{\ \lambda}\ ) = 1 \tag{11.3.5}$$

for the m_0th mode, and

$$\sum_{\lambda=0}^{\Lambda-1} \alpha_\lambda Z_m(z_\lambda) = 0, m \neq m_0 \tag{11.3.6}$$

for all other modes. When the eigen functions are large in the water layer and negligible below it, letting the transducer drive be proportional to the eigenfunction is a good approximation to Equations 11.3.5 and 11.3.6:

$$\alpha_\lambda \approx Z_{m_0}(z_\lambda) \tag{11.3.7}$$

Results of the laboratory experiments of Gazanhes and Garnier (1981) are shown in Fig. 11.3.2. The model was a thin water layer over a thick sand layer.

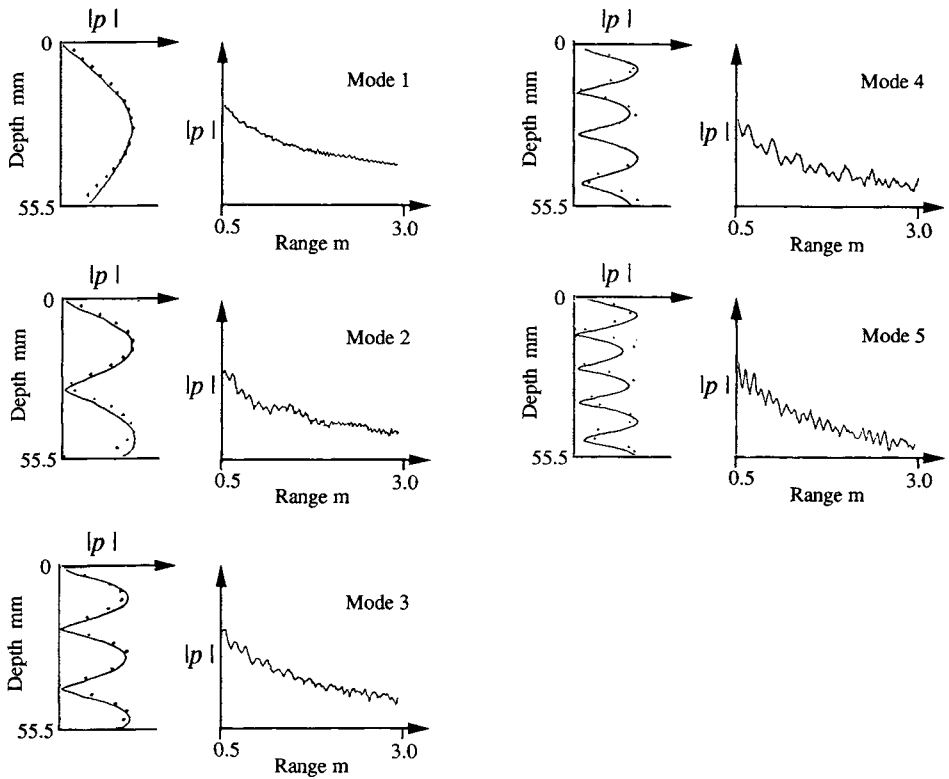

Figure 11.3.2 Array mode filtering in a laboratory waveguide. The 57 mm thick water layer is over a thick bed of sand. The frequency is 124 kHz. Sound pressures as functions of depth (z) and range (r) for modes 1–5. (From Gazanhes, C., and J. L. Garnier, "Experiments on single mode excitation in shallow water propagation," *J. Acoust. Soc. Am.* **69**, 963–69, 1981.)

The transducer drive amplitudes of the 15-element array α_λ were proportional to the eigenfunction of the desired mode (Equation 11.3.7). For transmission in a single mode, one would expect the depth dependence of the sound pressure to be proportional to the eigenfunction. The measurements verify this. The attenuation of sound pressure as a function of range shows that the mode attenuations δ_m are larger for higher modes.

11.3.2 NOISE IN WAVEGUIDES

Following the discussion in Chapter 6, analog measurements of "noises" are made by bandpass filtering the "noise voltage," squaring it, and averaging the square over time to give the mean square noise voltage. We do the same to the outputs of the receiving array. In Figure 11.3.3, an array is shown in an ocean environment, and numerous noise sources are distributed in the ocean.

The noise sources may be breaking waves, rain, seismic activity, ships, animals, and so on. The sound pressures from the "natural noise sources" propagate the same as the sound pressures from man-made noise sources. All of the "noise signals" add at a hydrophone. Array mode filters select the "noise signal" components in the modes. At large range from the noise sources and for finite frequency bandwidth $\Delta\omega$, the noise signals in different modes are incoherent and add as the sums of squares. Measurements of the bandpass-filtered noise pressure squared for each mode give the noise terms N_m^2. The mean-square-filtered noise is the sum over all modes:

$$\langle n_b^2 \rangle = \Delta\omega \sum_{m=1} N_m^2 \, | b_m |^2 \tag{11.3.8}$$

where the subscript b is for the array output, and $\Delta\omega$ is a narrow frequency band. If one were measuring the sound transmission from a distant source, this noise would interfere with the measurement.

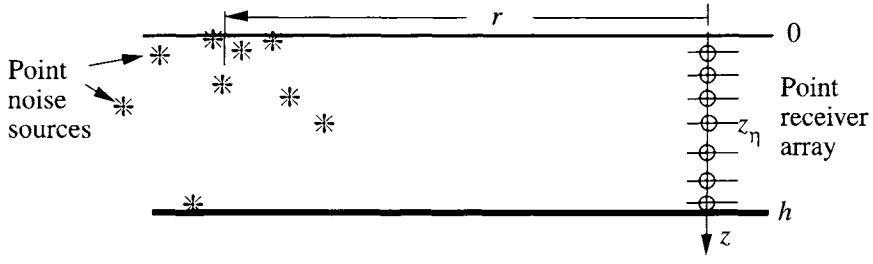

Figure 11.3.3 Noise sources in the ocean. Conventionally, the range to a noise source is measured from the receiving array.

11.3.3 SIGNAL-TO-NOISE RATIO AND THE OPTIMUM ARRAY FILTER

The mean-square signal-to-noise pressure ratio in a waveguide is

$$\frac{|s^2|}{\langle n_b^2 \rangle} = \frac{\Pi}{\Pi_0} \frac{\left| \sum_{m=1} a_m U_m b_m \right|^2}{\Delta\omega \sum_{m=1} N_m^2 b_m^2} \tag{11.3.9}$$

We multiply and divide by N_m to write the numerator of Equation 11.3.9 as follows:

$$\left| \sum_{m=1} a_m U_m b_m \right|^2 = \left| \sum_{m=1} \frac{a_m U_m}{N_m} (b_m N_m) \right|^2 \tag{11.3.10}$$

and then apply Cauchy's inequality (Abramowitz and Stegun 1964, sec. 3.2.9):

$$\left| \sum_{m=1} \frac{a_m U_m}{N_m} (b_m N_m) \right|^2 \leq \sum_{m=1} \left| \frac{a_m U_m}{N_m} \right|^2 \sum_{m=1} |b_m|^2 N_m \tag{11.3.11}$$

The equality holds for the condition

$$\left(\frac{a_m U_m}{N_m} \right)^* \simeq (b_m N_m) \tag{11.3.12}$$

where (...)* means the complex conjugate. Since the U_m depend on range, the b_m must include the range and depth of the source. The ratio of signal to noise simplifies to

$$\frac{|s^2|}{\langle n_b^2 \rangle} = \leq \frac{1}{\Delta\omega} \frac{\Pi}{\Pi_0} \sum_{m=1} \left| \frac{a_m U_m}{N_m} \right|^2 \tag{11.3.13}$$

The signal-to-noise ratio can be improved by making the source power Π larger and $\Delta\omega$ smaller. The maximum signal-to-noise pressure-squared ratio occurs for the phase-matching condition

$$b_m \sim \frac{(a_m U_m)^*}{N_m^2} \tag{11.3.14}$$

Analogous to section 6.5, the array is a "matched array filter" in mode space. The matched filter transmission function (Equation 11.3.1) becomes

$$s(t) \sim e^{i\omega t} \sqrt{\frac{\Pi}{\Pi_0}} \sum_{m=1}^{M} \frac{1}{N_m^2} a_m a_m^* U_m U_m^* \tag{11.3.15}$$

If matching to the source range and depth is impractical, the ratio of the signal-to-noise pressure squared can be improved by using

$$|b_m| \sim \frac{|a_m U_m|}{N_m^2} \tag{11.3.16}$$

These expressions clearly show that (1) the signal-to-noise ratio is improved by selecting the modes that have the smallest noises relative to the signal; (2) the phase-matching condition adjusts the phases in all of the modes so that the components add in phase to maximize $s(t)$; (3) the parameters of the theoretical model must be the same as the actual waveguide; (4) and the maximum occurs when the range and depth for the model calculation are the same as the actual source's range and depth (i.e., giving the source location).

11.3.4 MATCHED ARRAY FILTER FOR SOURCE LOCATION

Suppose a single source is at an unknown range r_{uk} and unknown depth z_{uk}. The signal-to-noise ratio is large enough to measure the source frequency. Then, the product $a_m U_m$ is

$$a_{m,uk} U_{m,uk} = \frac{q_m e^{\pi/4 - \delta_m r_{uk}}}{(\kappa_m r_{uk})^{1/2}} [Z_m(z_{uk}) \exp(-i \kappa_m r_{uk})] \tag{11.3.17}$$

and, keeping only the phase-dependent parameters in the [...], $a_{m,uk}U_{m,uk}$ is approximately proportional to the [...] as follows:

$$a_{m,uk} U_{m,uk} \sim [Z_m(z_{uk}) \exp(-i \kappa_m r_{uk})] \tag{11.3.18}$$

We construct a *trial matched filter* for the trial range and depth r_{tr} and z_{tr},

$$b_{m,tr} \sim \frac{[Z_m(z_{tr}) \exp(-i \kappa_m r_{tr})]^*}{N_m^2} \tag{11.3.19}$$

The substitution of the trial matched filter into Equation 11.3.15 gives a detection algorithm,

$$|s(r_{tr}, z_{tr})| \sim \left| \sum_{m=1}^{M} a_{m,uk} U_{m,uk} b_{m,tr} \right| \tag{11.3.20}$$

One searches in the trial ranges and depths to maximize the output $|s|$. The trial range and depth match the source range and depth (i.e., $r_{tr} = r_{uk}$ and $z_{tr} = z_{uk}$). Hinich (1973) derived the maximum likelihood equations for the vertical array in a waveguide.

11.4 Transmission Functions in Matrix Notation

The signal transmission equation can be expressed as products of vectors and matrices. The results are compact and show clearly the roles of the input, waveguide function, and the output filter. The eigenfunction vector can be written as

$$z_j \equiv \begin{bmatrix} Z_1(z_j) \\ \vdots \\ Z_M(z_j) \end{bmatrix} \tag{11.4.1}$$

where z_j is the depth of a transducer. Similarly, the source array vector is $\boldsymbol{Z}_i$.

The diagonal matrix $\boldsymbol{U}$ is the waveguide function. The matrix elements are the U_{mm}—that is, the U_m in Equation 11.3.4:

$$\boldsymbol{U} \equiv \begin{bmatrix} U_{11} & \cdots & 0 \\ 0 \cdots & U_{22} & \cdots 0 \\ & \cdots & \\ 0 & \cdots & U_{MM} \end{bmatrix} \tag{11.4.2}$$

Let the source be at depth z_i and the receiver be at depth z_j. In matrix notation, the transmission function (Equation 11.1.29) from a source at depth z_i to the hydrophone at depth z_j is

$$P(\omega, r, z_i, z_j) = z_j^T \; U \; z_i \tag{11.4.3}$$

where T indicates the transpose of z_j. The vectors z_j and z_i have M elements, and the matrix U is M by M. The resulting scalar is the product of a source vector, a diagonal transmission matrix, and the receiver vector.

11.4.1 EXAMPLE FOR TWO MODES

The purpose is to demonstrate that matrix expression (Equation 11.4.3) is the same as Equation 11.2.29. The expansion of Equation 11.4.3 is

$$P(\omega, r, z_i, z_j) = [\, Z_1(z_j) \;\; Z_2(z_j) \,] \begin{bmatrix} U_{11} & 0 \\ 0 & U_{22} \end{bmatrix} \begin{bmatrix} Z_1(z_i) \\ Z_2(z_i) \end{bmatrix} \tag{11.4.4}$$

and its expansion gives the sum

$$P(\omega, r, z_i, z_j) = [Z_1(z_j)U_{11}\ Z_1(z_i) + Z_2(z_j)U_{22}\ Z_2(z_i)] \tag{11.4.5}$$

And this is the same as the evaluation of Equation 11.1.29 for two modes.

11.4.2 ARRAY OF RECEIVERS

The source is at range r and depth z_i. The observations are made by the receivers at the depths z_1 to z_L. The transmissions to one receiver can be extended to L receivers by constructing an observation matrix:

$$\boldsymbol{b} = \begin{bmatrix} Z_1(z_1) & \cdots & Z_1(z_L) \\ & \vdots & \\ Z_M(z_1) & \cdots & Z_M(z_L) \end{bmatrix} \tag{11.4.6}$$

The transmission functions to the set of L receivers can be written as the following vector:

$$\boldsymbol{p} = \begin{bmatrix} P(\omega, r, z_1) \\ \vdots \\ P(\omega, r, z_L) \end{bmatrix} \tag{11.4.7}$$

and the transmission function to the set of receivers is

$$\boldsymbol{p} = \boldsymbol{b}^T\ \boldsymbol{U}\ \boldsymbol{z}_i \tag{11.4.8}$$

where $z_i = [Z_1(z_i)| \ldots |Z_M(z_i)]^T$. The array sensitivity parameters are the β_η in Equation 11.3.3. The vector of these parameters is

$$\boldsymbol{\beta} \equiv \begin{bmatrix} \beta_1 \\ \vdots \\ \beta_L \end{bmatrix} \tag{11.4.9}$$

Recalling Equation 11.3.1, array output gives the pressure signal,

$$s(t) = e^{i\omega t}\sqrt{\frac{\Pi}{\Pi_0}}\boldsymbol{\beta}^T\boldsymbol{p} \tag{11.4.10}$$

Expansion of the vector product gives Equation 11.4.3 for the transmission from a single source.

11.5 Source Location

Our ability to locate sources and do ocean tomography is limited by the ocean. Sound transmissions should be reproducible and have small fluctuations. The structure of the ocean is time-dependent, and the time dependence causes transmitted signals to be time-dependent. From the theory of Chernov (1960), the time-dependent fluctuations of the phases and amplitudes of pressure signals were expected to be large.

Measurement of the transmission limits imposed by the ocean is an old problem. Scientists at the Hudson Laboratories (1950–69) made long-range CW sound transmission studies (10 to 30 Hz) over the ranges of 30–2000 km. The phases of the received pressure signals were very stable relative to a local oscillator. The source ship towed the source, and many of the signals were received on bottomed hydrophones. The radial velocity component of the ship's velocity caused the relative phase of the received signal to go through 2π as the range changed by one wavelength, 0.1 km at 15 Hz. This was observed for distances as large as 1000 km. These experiments only gave upper limits of fluctuations attributed to time-dependent changes of the structure of the ocean.

The study of reproducibility of signal transmission required repeated transmission of a transient signal and the comparison of sequence of received pressure signals. This problem was studied by using Parvulescu's *matched-signal* method (1961, and in Parvulescu's review, 1995). The matched signal is created by first transmitting a short transient into a complicated multipath environment. The transmission is recorded as $s(t)$. The time-reversed signal $s(-t)$ is the matched signal. When $s(-t)$ is transmitted by the source, the received signal is the covariance of $s(t)$ at the matched position. The covariance of the matched signal and the transmission decreased rapidly for small changes of the positions of the source and receiver relative to the matched position. At a range of 36 km, transmissions of transients (400 Hz center-frequency) were reproducible. The details are in Tolstoy and Clay (1966, 1987, chaps. 6, 7, and 8) and Parvulescu (1995). Williams and Battestin (1971) used a correlation receiver to extend the research to 250 nm (460 km) and demonstrated a 6 s stability of the ocean response without establishing an upper limit of fluctuation effects.

Acoustic tomography of the oceans has made the transmissions of sound in a fluctuating ocean a central issue. Analytic treatments such as Flatte et. al (1979)

are beyond the level of our discussion. Ocean variability and acoustic propagation are in the workshop proceedings of Potter and Warn-Varnas (1990).

11.5.1 MATCHED FIELD PROCESSING FOR SOURCE LOCATION

To determine the location of a source, Bucker's (1976) *matched field processing* algorithms compare the measured pressure signals at the receivers with the theoretical simulations of transmissions from a source at a set of trial ranges and depths r_{tr} and z_{tr} (Fig. 11.5.1).

The source is at the unknown range r_{uk} and depth z_{uk}. Since the pressure field owing to the source is being received with a large signal-to-noise ratio, the source frequency is known. The sound pressures are observed at a vertical array of receivers, and the sound pressure at the jth hydrophone is p_j. The vector of the sound pressures is

$$\mathbf{p}_{uk} \equiv \begin{bmatrix} p_1 \\ \vdots \\ p_N \end{bmatrix} \tag{11.5.1}$$

The relative phases of the pressures at the receivers depend on the source's range and depth.

Bucker computed the cross covariance of the pressure signals at the jth and kth hydrophones to eliminate the time dependence,

$$c_{jk} = \langle p_j p_k^* \rangle \tag{11.5.2a}$$

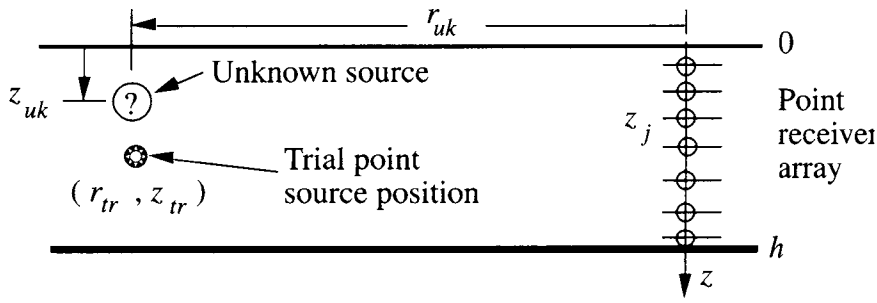

Figure 11.5.1 Transmissions from the source and a trial source to an array of receivers. The unknown range and depth are r_{uk} and z_{uk}. The trial range and depth are r_{tr} and z_{tr}.

where time average is $< \ldots >$, and the c_{jk} depend on the unknown depth and range of the source. The covariances of the sound pressures from all of the N hydrophones are collected as the elements of the *cross spectral matrix*,

$$\boldsymbol{C}_{uk} = \boldsymbol{p}_{uk}\boldsymbol{p}_{uk}^{T} = \begin{bmatrix} c_{11,uk} & \cdots & c_{1N,uk} \\ & \cdots & \\ & \cdots & \\ & \cdots & \\ c_{N1,uk} & \cdots & c_{NN,uk} \end{bmatrix} \tag{11.5.2b}$$

The matrix is also called the *sample covariance matrix*. The diagonal elements c_{jj} are the squares of the sound pressures, and the c_{kj} elements are the complex conjugates of c_{jk}. In his computations, Bucker kept the cross terms of the covariance matrix and dropped the diagonal c_{jj} elements.

The simulation of the transmission from the trial source position gives the trial pressure s_j at the jth hydrophone. It is sufficient to only calculate the relative phases of the trial pressures. The vector of the trial pressures at the set of hydrophones is

$$\boldsymbol{s}_{tr} \equiv \begin{bmatrix} s_1 \\ \vdots \\ s_N \end{bmatrix} \tag{11.5.3}$$

The detection factor is defined as follows:

$$DF \equiv \frac{\boldsymbol{s}_{tr}^{*T}\boldsymbol{C}_{uk}\boldsymbol{s}_{tr}}{Normal} \tag{11.5.4}$$

where T is the complex conjugate transpose and the normalization factor is

$$Normal \equiv \left(\boldsymbol{s}_{tr}^{*T}\boldsymbol{s}_{tr}\right)^{1/2}\left(\boldsymbol{p}_{uk}^{*T}\boldsymbol{p}_{uk}\right)^{1/2} \tag{11.5.5}$$

At match, the detection factor DF is unity. Fizell (1987) shows that keeping the diagonal terms in Equation 11.5.2 improves the detection and defines a detection index DI that includes all terms of the cross spectral matrix. The "ambiguity surface" is the map of DI as a function of r and z.

Figure 11.5.2 shows the shallow-water waveguide that Bucker used for his numerical simulation. A map of the detection factor, essentially the ambiguity surface, is shown in Fig. 11.5.3. The number and heights of the "false" peaks are major problems in using matched field processing to locate sources in the field.

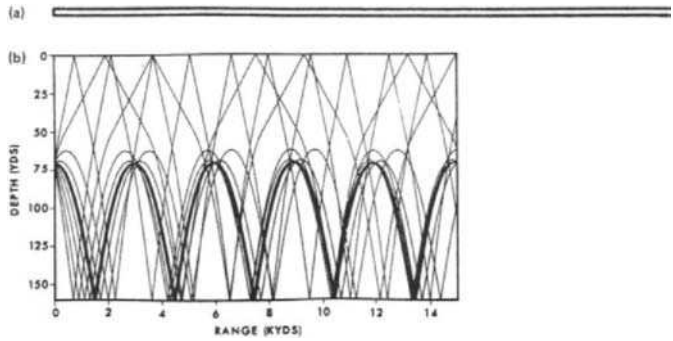

Figure 11.5.2 Waveguide and ray traces. a) Waveguide without vertical exaggeration. b) Waveguide with vertical exaggeration and ray traces. The source is at range 10,000 yd and depth 70 yd. The conversion from English yards to meters is 1 yd = 0.9144 m. (From Bucker, H. P., "Use of calculated sound fields and matched-field detection to locate sound sources in shallow water," *J. Acoust. Soc. Am.* **59**, 368–73, 1976.)

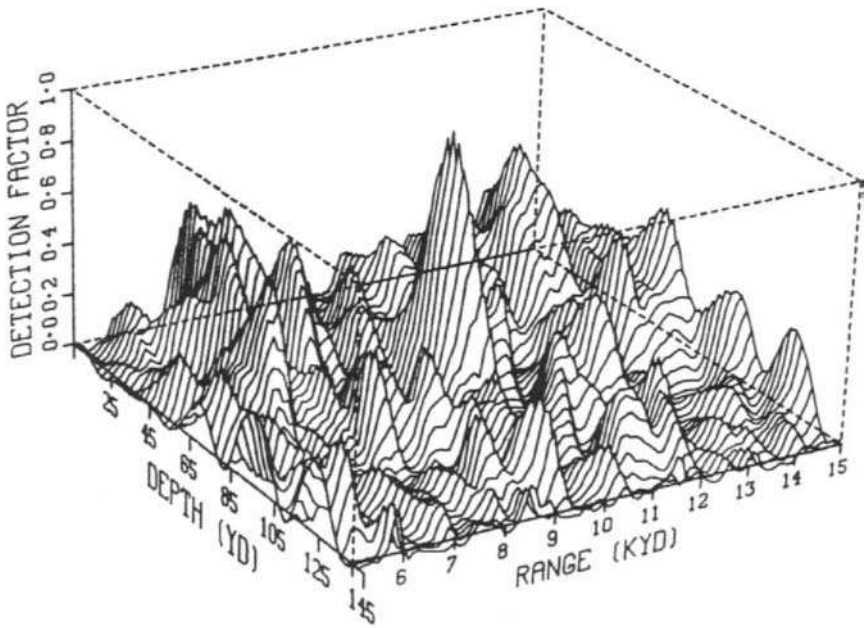

Figure 11.5.3 Map of *DF* for range and depth. The single vertical array has 24 receivers that are equally spaced between 25 and 14 yd. The source frequency is 300 Hz. (From Bucker, H. P., "Use of calculated sound fields and matched-field detection to locate sound sources in shallow water," *J. Acoust. Soc. Am.* **59**, 368–73, 1976.)

11.5.2 OPTIMUM MODE PROCESSING FOR SOURCE LOCATION

The source at the unknown position transmits a signal that is received by the jth receiver. In the transmission equation (11.1.27), the source power, mode excitations, and mode attenuations are the same for transmissions to all receivers in the vertical array. We drop the amplitude terms, suppress the time dependence, and write

$$p_j = A \sum_{m=1}^{M} Z_m(z_{uk}) Z_m(z_j) e^{-i\kappa_m r_{uk}} \tag{11.5.6}$$

where p_j is the sound pressure at the jth receiver, and A is the pressure amplitude factor.

The source power, depth, and range are unknown, so we replace them by the parameter

$$\mu_m = A\, Z_m(z_{uk})\, e^{-i\kappa_m r_{uk}} \tag{11.5.7}$$

and write the summation for each receiver as follows:

$$p_1 = Z_1(z_1)\mu_1 + \ldots + Z_M(z_1)\mu_M \tag{11.5.8a}$$

$$\ldots$$

$$p_N = Z_1(z_N)\mu_1 + \ldots + Z_M(z_N)\mu_M \tag{11.5.8b}$$

This is a set of N linear equations with M unknowns. Methods of solving the linear equations for the μ_m are in texts on linear algebra. Because of the choices of receiver depths, some of the coefficients of $Z_m(z_j)$ may be very small, and having $N > M$ is helpful.

Again, we use the artifice of making a trial transmission from r_{tr} and z_{tr} and write the $\mu_{m,tr}$ as follows:

$$\mu_{m,tr} = Z_m(z_{tr})\, e^{-i\kappa_m r_{tr}} \tag{11.5.9}$$

The modal detection function is, including the modal noise (Equation 11.3.8),

$$MDF \equiv \frac{1}{normal} \left| \sum_{m=1}^{M} \frac{\mu^*_{m,tr}\mu_m}{N_m^2} \right| \tag{11.5.10}$$

where *normal* gives *MDF* equal to unity at match.

Many papers have been published on matched field processing since 1987. Yang (1990) used simulations of sound transmissions in Arctic and Pacific environments to compare matched field and matched mode processing. He got better locations and lower side lobes with matched mode processing. As reviewed

in Baggeroer and Kuperman (1993); Baggeroer, Kuperman, and Mikhalevsky (1993); and Porter (1993), most of the papers are at advanced levels of signal processing. There are many more numerical simulations than location trials that use real data. The results of field tests are in Hamson and Heitmeyer (1989); Frisk, Lynch, and Rajan (1989); Livingston and Diachok (1989); Feuillade, Kinney, and DelBalzo (1990); and Jesus (1993).

11.5.3 TIME DOMAIN SOURCE LOCATION

Sound transmission from an explosion in a shallow-water waveguide gives the dispersed waveform shown in Fig. 11.2.1. The "water wave" begins with very high frequency (more than 300 Hz), and the frequency decreases to about 70 Hz at its end. The duration of the water wave—that is, the time from the highest frequency at the beginning to the lowest at the end—depends on the range, the group velocity minimum, and the high-frequency limiting velocity,

$$\Delta t_{ww} \approx \frac{r}{u_{g,min}} - \frac{r}{u_{g,limit}} \tag{11.5.11}$$

The phase and group velocities are shown in Fig. 11.2.2. The first mode has a group velocity minimum of $u_{g,\min} = 1475$ m/s at approximately 70 Hz, and the high-frequency limit is $u_{g,\lim} = 1516$ m/s. Depending on one's estimate of the end of the "water wave," the duration is 0.15 ± 0.02 s. The solution of Equation 11.5.11 for r gives 8200 ± 1100 m, while the measured distance was 8400 m. In a waveguide, the systematic changes of the waveform of a signal can be used to estimate the range. Yang (1993) gives modal techniques for broadwidth signals.

The correlation (matched filter) receiver technique is a way of doing the waveform recognition and analysis (section 6.5). In source location applications, one knows the structure of the waveguide and has a recording of the received pressure $p_{uk}(t)$. A pair of simulations of sound pressures is shown in Fig. 11.5.4. To create replicas for the correlation receiver, one transmits an impulse from a set of possible source locations $p_{rcp}(t)$ and then correlates these with the sound pressure from the unknown position. Transmissions from the matched position give the maximum correlation peak.

The matched-signal technique is equivalent to a matched-filter receiver (section 6.5). Feuillade and Clay (1992) used a matched-signal approach for source location because it is easy to adapt it to transmissions from an array of receivers. In their simulations, the received sound pressure $p_{uk}(t)$ is time-reversed to give $p_{uk}(-t)$. The time-reversed signal is transmitted from the receiver location, and the sound field in the waveguide is explored with a probe receiver.

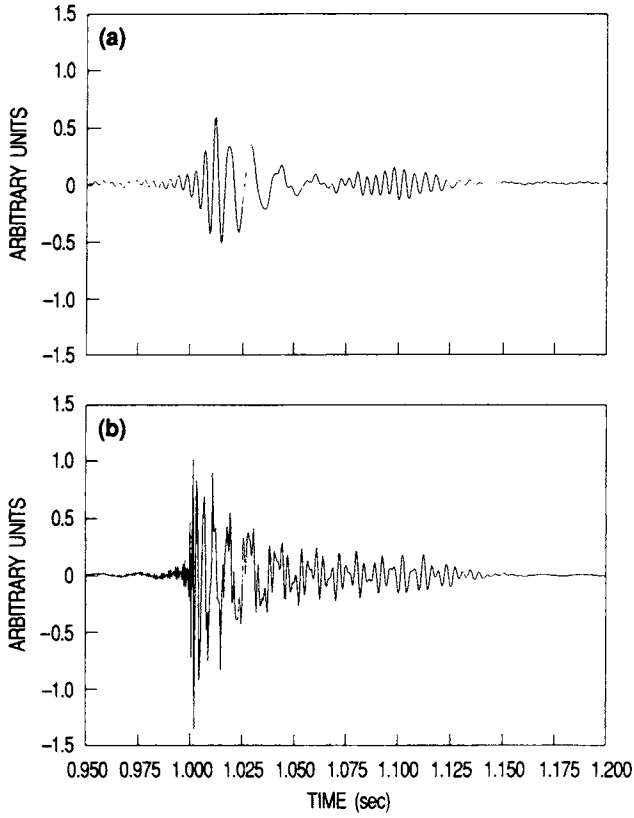

Figure 11.5.4 Simulated transmission from a source to a receiver in a Pekeris waveguide. Parameters are water layer $c_1 = 1500\,\text{m/s}$ and $\rho_1 = 1000\,\text{kg/m}^3$; thickness 20 m; sediment $c_2 = 1800\,\text{m/s}$ and $\rho_2 = 1760\,\text{kg/m}^3$; range 1500 m; source depth 13 m and receiver depth 10 m. a) Bandwidth 192 Hz and 4 modes. b) Bandwidth 825 Hz and 13 modes. (From Feuillade, C., and C. S. Clay, "Source imaging and sidelobe suppression using time-domain techniques in a shallow water waveguide," *J. Acoust. Soc. Am.* **92**, 2165–72, 1992.)

The low-frequency component is transmitted first, and the high-frequency component is transmitted last. All components arrive at the matched position at the same time. Figure 11.5.5 shows examples of receptions at matched and unmatched positions for both signal frequency bandwidths. The process of transmitting time-reversed signals from an array of receivers is a form of holography (Clay 1990, chap. 15). In the underwater sound literature, time-reversed transmissions are called *back-propagation* (Porter 1993).

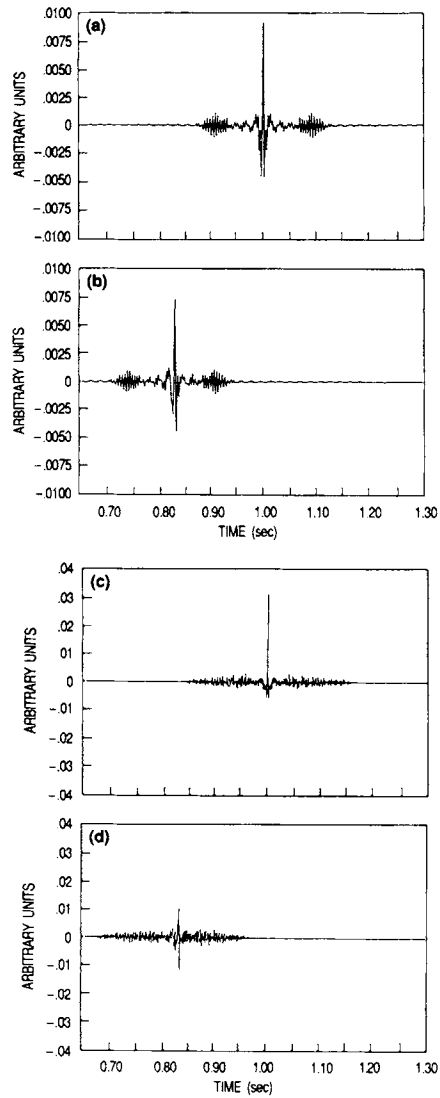

Figure 11.5.5 Reception of time-reversed transmissions at matched and unmatched locations. The pressures are shown in Fig. 11.5.4. In all examples, the probe depth is 13 m, the same as the original source. The matched range is 1500 m, and the unmatched range is 1250 m. a) Matched position: 192 Hz bandwidth and 4 modes. b) Unmatched position: 192 Hz bandwidth and 4 modes. c) Matched position: 825 Hz and 13 modes. d) Unmatched position: 825 Hz and 13 modes. (From Feuillade, C., and C. S. Clay, "Source imaging and sidelobe suppression using time-domain techniques in a shallow water waveguide," *J. Acoust. Soc. Am.* **92**, 2165–72, 1992.)

11.6 Range-Dependent Waveguide: Wedge

Range-dependent waveguides are actually the normal waveguides found most often in nature. Since this is the case, one may ask why the normal-mode solutions of plane-layered waveguides have been so successful in describing sound propagation. Perhaps the theory is much more robust than is superficially apparent.

11.6.1 "ADIABATIC" APPROXIMATION

Early suggestions of the robustness of normal-mode theory came from the Brown University acoustics group and their sound transmission research with a small, two-layered model (Eby et al. 1960). They measured the effects of rough bottoms and a sloping bottom on sound transmissions. Lead shot was put on the bottom to make the randomly rough bottom. With mode 1 excitation, the randomly rough bottoms increased the attenuation and did not cause the transfer of appreciable energy into the second mode. Organized roughness, such as ridges, caused energy transfer into the second mode. Eby and his colleagues measured the attenuation of sound transmissions for both up-slope and down-slope propagation. The local attenuations were those expected for a uniform layer having those depths: "If sound is propagated straight upslope or downslope from a source, the 'adiabatic' assumption (of Williams and Lewis, 1956) permits calculation of the received pressure amplitude as a function of range. We assume that the slope is small (a few degrees at the most), that a single mode is used and that the mode is not cutoff anywhere along the path" (Eby et al. 1960). With no losses and no mode cut-offs, Williams and Lewis postulated that the energy trapped in a mode stays in the mode as the depth and properties of a waveguide vary slowly. Since no energy is lost from the mode, by analogy with thermodynamic processes without heat exchange, it is called the "adiabatic" approximation.

Theoretical treatments of the slowly varying waveguide are given in Pierce (1965), McDaniel (1982), Arnold and Felsen (1984), Desaubies and Dysthe (1995), and references in these papers. The coupled-mode solutions are interesting because the apparent cross-mode coupling may be due to the observation coordinates used for calculations and measurements while the actual transfers of energy between modes may be very small. Desaubies and Dysthe (1995) give a comprehensive discussion of roles of the adiabatic approximation, intrinsic modes, coupled modes, and comparisons to experiments.

11.6.2 TRANSMISSIONS IN WEDGE WAVEGUIDES

Exact theoretical solutions for a range-dependent wedge waveguide are given via the normal-mode solution of Buckingham (1987) and the normal-coordinate solution of Biot and Tolstoy (in Tolstoy and Clay 1987) and later in section 11.8. Numerical solutions for sound transmissions in a wedge can be complicated and need to be tested. For the tests, the Technical Committee on Underwater Acoustics of the Acoustical Society of America designed two "benchmark" wedge problems as a challenge (Felsen 1990). Seven groups responded, and their results were collected into a single issue of the *Journal of the Acoustical Society of America* **87**, 1497–1545 (1990). The groups are Jensen and Ferla; Buckingham and Tolstoy; Thomson; Thomson, Brooke, and DeSanto; Stephen; Collins; and Westwood. While people used different theoretical and numerical techniques, their results were almost the same.

Experiments and Adiabatic Theory

The laboratory waveguide of Tindle, Hobaek, and Muir (1987a, 1987b) is shown in Fig. 11.6.1. The details are in the caption. The source array was constructed of line sources. The excitation was a gated 4-cycle, 80 kHz sine wave that was bandpass-filtered between 60 and 100 kHz. The excitations of the elements of the array were chosen to transmit selectively single modes. The receiver is a probe hydrophone. Signals from the hydrophone were recorded as a function of depth, and the receiving array processing was performed by the computer. The slope of the bottom interface was adjusted for different wedge angles.

In range-dependent waveguides, it is important to use the local coordinates in making sound field measurements and for mode-filtering of the sound pressures. The shallow-water wedge is simple because cylindrical coordinates are its reference. The air-water interface is the upper surface of the wedge and is in the x-y plane. The water sediment interface is the lower plane of the wedge. In cylindrical coordinates, the intersecting planes are the wedge axis and are along the y-direction; r is the radial distance from the line of the intersecting planes; and the angle θ is measured relative to the x-y plane.

According to the adiabatic approximation, the eigen functions $Z_m(z, r)$ should stretch as the water depth increases. Figure 11.6.2 shows the stretching or adjustment of the third mode to fit the bottom depth for bottom slopes of 0°, 1°, 4°, and 9°. If the amplitudes of the sound pressures were plotted instead of the levels in dB, one would see the nulls and changes of phase of $Z_m(z, r)$. The third-mode structure is the same at different ranges for the constant-depth waveguide

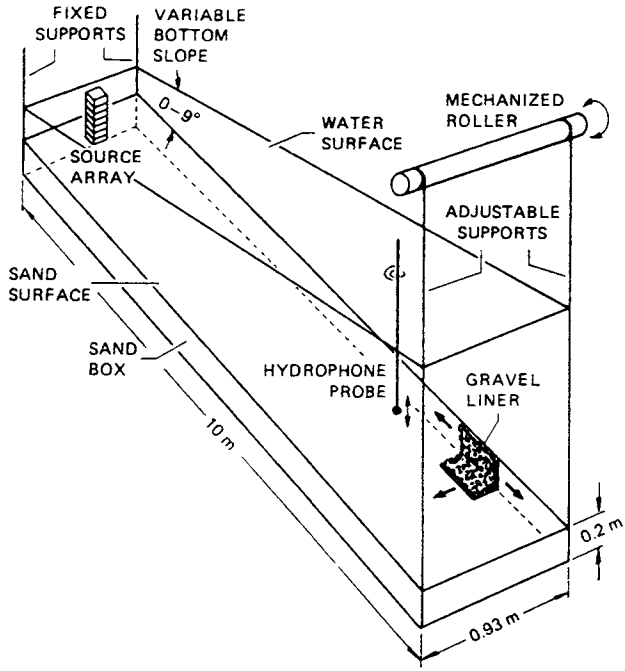

Figure 11.6.1 Shallow-water model of a wedge waveguide: water over sand. Water: $c_1 = 1490\,\text{m/s}$ and $\rho_1 = 1000\,\text{kg/m}^3$. Sand: $c_2 = 1780\,\text{m/s}$ and $\rho_2 = 1.97\rho_1$. The water depth at the source was 10 cm. The measured attenuation in sand was 1 dB per wavelength, and reflections from the bottom of the sand were not detectable. The waveguide attenuation coefficient in the water layer was $0.06f/(\text{m kHz})$. (From Tindle, C. T., H. Hobaek, and T. G. Muir, "Downslope propagation of normal modes in a shallow water wedge," *J. Acoust. Soc. Am.* **81**, 275–86, 1987.)

(slope 0°). The increase of the slopes to 1°, 4°, and 9° show how the modes are stretched as they adjust to the changing depths. The wave numbers γ_m and κ_m are functions of the local depth.

Waveforms of sound transmissions for the Pekeris constant-depth waveguide, and for a set of wedges with 0° and 9° slopes, are shown in Fig. 11.6.3. The laboratory model can be scaled to real-world conditions by letting the frequency be 80 Hz, and then the depth at the source becomes 100 m and the maximum range becomes 8900 m.

The waveforms of the transmission in a uniform layer and the 9° slope are shown in Fig. 11.6.3a and b. The amplitudes and travel times of the waveforms depend on mode number, receiver depth, and slope. First we consider the travel times in the uniform waveguide (Fig. 11.6.3a). The delays of the arrivals depend

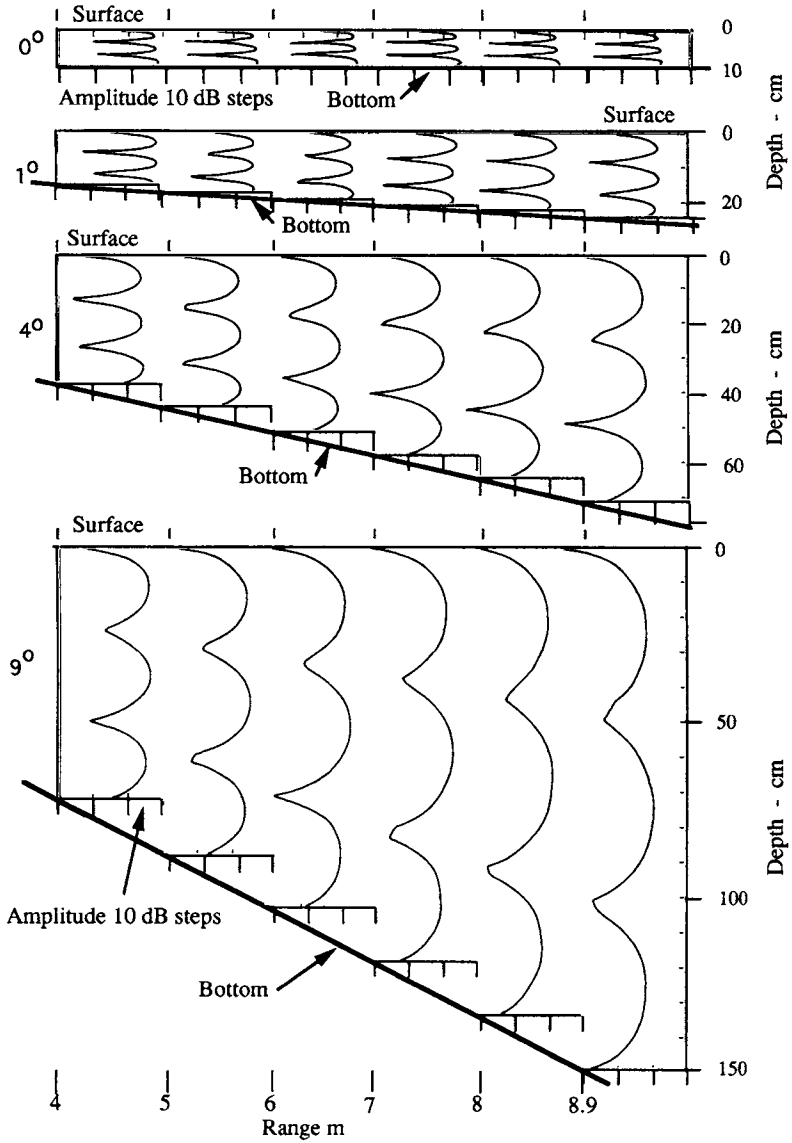

Figure 11.6.2 Amplitude levels of the sound pressure in dB for the third mode. The source array is at 0 range, and the local water depth is 10 cm. The source array was adjusted to excite the third mode at 80 kHz. At each range, the probe hydrophone was run from top to bottom to measure the sound pressures. Converted to dB, the amplitude levels are $20 \log[|Z_3(z, r)|]$ in dB relative to arbitrary levels. The steps are 10 dB. (From Tindle, C. T., H. Hobaek, and T. G. Muir, "Downslope propagation of normal modes in a shallow water wedge," *J. Acoust. Soc. Am.* **81**, 275–86, 1987.)

a)

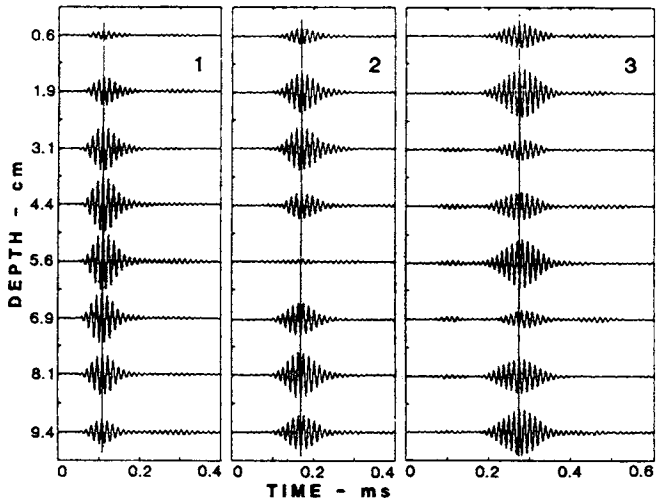

b)

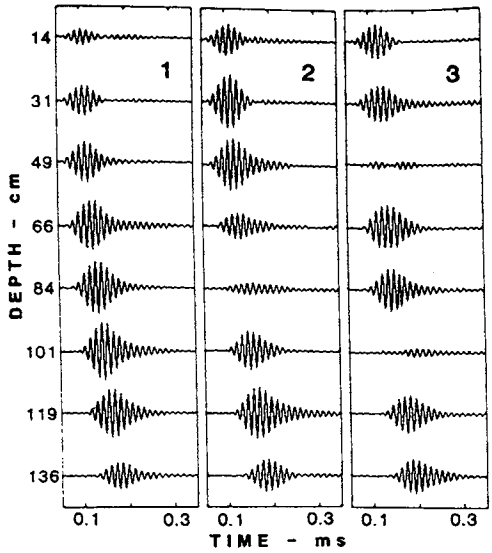

Figure 11.6.3 Single-mode transmissions as functions of depth and slope. For all transmissions, the water depth at the source is 10 cm. The range is 8.9 m. Time is measured relative to a convenient time delay after the transmission, and all traces have the same delay. The figures 1, 2, and 3 indicate the mode numbers. a) Constant depth (0° slope): the source array is vertical. The depth at the receiver is 10 cm. b) Wedge 9° slope: the source array is curved to match the cylindrical coordinates. The probe receiver is moved vertically, and the waveforms arrive later as depths increase. (From Tindle, C. T., H. Hobaek, and T. G. Muir, "Downslope propagation of normal modes in a shallow water wedge," *J. Acoust. Soc. Am.* **81**, 275–86, 1987.)

on the group velocities of the modes. Figure 11.2.2. shows the group velocities for the 18 m water depth. If the laboratory waveguide depth were scaled to 18 m, the frequency would be 440 Hz. As consistent with the group velocities, the travel times increase as the mode numbers increase. The amplitude and phases of the waveforms depend on depth, as in the eigenfunctions (Fig. 11.6.2). Next, the laboratory world changes, and the bottom has the 9° slope. The transmitting array is curved to keep constant range from the axis of the wedge. If the adiabatic approximation works, then the waveforms should be trapped in each mode and be identifiable at the probe hydrophone depths (Fig. 11.6.3b). The arrivals maintain their identities, and the amplitudes and phases correspond to the local eigenfunctions. Waveforms at the deeper receivers have time delays relative to the receiver at 14 cm depth because the receiving hydrophone was moved vertically and the receivers were not at constant radius from the axis. Thus, the deepest receiver is 9 cm farther from the axis than the top receiver. This demonstrates the importance of measuring along the local coordinates—that is, at constant radius for a wedge waveguide. The adiabatic mode theory gives the correct arrival times and amplitude dependence on range for different bottom slopes.

11.7 Parabolic Equation (PE) Method

The parabolic form of the wave equation was introduced into computational acoustics by Tappert and Hardin (1974) to take account of slowly varying range dependence. Our purpose here is to give a derivation of the "standard" parabolic equation—to say what it is and to give a few of the early references.

Ignoring the angular dependence, the wave equation in cylindrical coordinates is (Lee 1984)

$$\frac{\partial^2 p}{\partial r^2} + \frac{1}{r}\frac{\partial p}{\partial r} + \frac{\partial^2 p}{\partial^2 z} + k_0^2 n^2 p = 0 \qquad \textbf{(11.7.1a)}$$

where n is the index of refraction and a function of r and z; k_0 is the reference wave number. To simplify the notation, we let the partial derivatives be indicated by subscripts,

$$\begin{aligned} p_{rr} &\equiv \frac{\partial^2 p}{\partial r^2} \\ p_r &\equiv \frac{\partial p}{\partial r} \\ p_{zz} &\equiv \frac{\partial^2 p}{\partial^2 z} \end{aligned} \qquad \textbf{(11.7.1b)}$$

and so forth for all functions. The field pressure is written as the product of a function that combines range and depth $u(r, z)$ and a function of range $v(r)$:

$$p \sim u(r, z)v(r) \tag{11.7.2}$$

The substitution of Equation 11.7.2 in Equation 11.7.1a gives

$$\left[v_{rr} + \frac{1}{r}v_r\right]u + \left[u_{rr} + \frac{1}{r}u_r + \frac{2}{v}u_r v_r + u_{zz} + k_0^2 n^2 u\right]v = 0 \tag{11.7.3}$$

Add and subtract $k_0^2 uv$ to the brackets, rearrange, and then set the brackets to 0. This gives two equations because the coefficient of u must vanish for the first bracket and the coefficient of v must vanish for the second bracket:

$$v_{rr} + \frac{1}{r}v_r + k_0^2 v = 0 \tag{11.7.4}$$

and

$$u_{rr} + \frac{1}{r}u_r + \frac{2}{v}u_r v_r + u_{zz} + k_0^2(n^2 - 1)u = 0 \tag{11.7.5}$$

The solution of Equation 11.7.4 is the Hankel function of the first kind, $H_0^{(1)}(k_0 r)$. The approximation for large r is

$$v = H_0^{(1)}(k_0 r) \approx \sqrt{\frac{2}{\pi}} \frac{1}{\sqrt{k_0 r}} \exp[i(k_0 r - \frac{\pi}{4})] \tag{11.7.6}$$

The substitutions of v and v_r in Equation 11.7.5 give

$$u_{rr} + i\,2k_0 u_r + u_{zz} + k_0^2(n^2 - 1)u = 0 \tag{11.7.7}$$

The approximation $|u_{rr}| \ll |2k_0 u_r|$, so that u_{rr} can be dropped, gives the standard parabolic equation

$$u_r \approx \frac{i}{2}k_0(n^2 - 1)u + \frac{i}{2k_0}u_{zz} \tag{11.7.8}$$

This is referred to as the "standard" PE (Hardin and Tappert 1973; Tappert and Hardin 1974; Tappert 1977). Other early papers are by Fitzgerald (1975); S. T. McDaniel (1975a, 1975b); Palmer (1976); DeSanto (1977); and DeSanto, Perkins, and Baer (1977). Lee, Sternberg, and Shultz (1988) are the editors of two

volumes on computational acoustics that include PE methods. An integrated treatment is in *Computational Ocean Acoustics* (1994), by Jensen et al.

11.8 Wedge Waveguide in the Time Domain: Biot–Tolstoy Method

A closed-form, time-domain solution for the fluid-filled-wedge was given by Biot and Tolstoy (1957) as an example of normal coordinate applications to problems in wave propagation. The diffraction part of the solution was significantly different from the Kirchhoff boundary wave solution of Born and Wolf (1965, sec. 8.9), Trorey (1970), and Clay and Medwin (1977, Appendix 10). Beginning in 1978, the BT theory was interpreted, and a series of diffraction experiments was conducted in the Ocean Acoustics Laboratory of the Naval Postgraduate School. The experiments by Bremhorst and Medwin (1978) and Jebsen and Medwin (1982) tested crucial parts of the BT and HK theories and made extensions. The BT solution was found to be accurate, and the Kirchhoff boundary wave solution proved to have large errors in certain geometries (section 12.3.1).

The original Biot-Tolstoy solution was for the transmissions from a doublet (two opposing delta functions) impulse point source near a rigid wedge. Later, Kinney, Clay, and Sandness (1983) gave a solution for the wedge with free boundaries. Chu (1989a, 1989b, 1990) derived the exact impulse response of a density-contrast wedge and expressions for a half-space of air over a rigid wedge and a half-space that contains a density-contrast wedge. In the density-contrast wedge, the source and receiver can be in either medium.

The time domain impulse solutions for the wedges have tremendous advantages compared with the harmonic normal-mode solution. In the time domain, all of the reflection arrivals and the diffraction from the intersection of the planes are identifiable and separable. Depending on the practical situation, one can keep, modify, and discard any of the arrivals. Numerical Fourier transformations give frequency domain transmissions of any combination of arrivals.

The coordinates and geometry are shown in Fig. 11.8.1. The line of the intersecting planes is along the y-axis. The line of intersection is called the "wedge apex" in some of the literature. The boundary planes of the wedge are normal to the x-z plane. These choices let us use the z-coordinate for depth and to have the x and y coordinates in the horizontal plane. The source is in the x-z plane

at $y = 0$. The receiver can be displaced at a distance y. The radial distance from the y-axis is r. The wedge angle θ_w can have any value, $0 < \theta_w \leq 2\pi$. The solution is general, and Fig. 11.8.1 also shows other wedge angles, source positions, and wedge constructions. The sound speed is c_1. To simplify notation in the fluid, we use c for the sound speed; ρ for the density in the wedge.

The acoustic wave equation in these cylindrical coordinates is

$$\frac{\partial^2 p}{\partial r^2} + \frac{1}{r}\frac{\partial p}{\partial r} + \frac{1}{r^2}\frac{\partial^2 p}{\partial \theta^2} + \frac{\partial^2 p}{\partial y^2} = \frac{1}{c^2}\frac{\partial^2 p}{\partial t^2} \tag{11.8.1}$$

where p is the sound pressure. The sound pressure is the product of a spatial function $\psi(r, y, \theta)$ and a time-dependent function $T(t)$. We use pressure in the derivation because it is a scalar and the pressure is a measurable quantity.

As in section 11.1, the separation constants are κ and γ and ω. The spatial part of the solution is

$$\psi_n \sim R(r)Y(y)\Theta(\theta) \tag{11.8.2}$$

$$\frac{\omega^2}{c^2} = \kappa^2 + \gamma^2 \tag{11.8.3a}$$

where

$$R(r) = J_{n\upsilon}(\kappa r) \tag{11.8.3b}$$

$$Y(y) = \cos(\gamma y) \tag{11.8.3c}$$

$$\Theta(\theta) = \cos(n\upsilon\theta) \tag{11.8.3d}$$

$$\psi_n = J_{n\upsilon}(\kappa r)\cos(\gamma y)\cos(n\upsilon\theta) \tag{11.8.4}$$

n and v are defined in the boundary conditions, and ψ_n is defined as being dimensionless.

The boundary conditions for a fluid within the rigid wedge walls ($\rho_2 = \infty$) require that the normal displacement along Θ vanish on the walls:

$$\frac{\partial\Theta}{\partial\theta} = 0 \text{ at } \theta = 0 \text{ and } \theta = \theta_w \qquad \Theta = \cos(n\upsilon\theta) \tag{11.8.5}$$

where $v = \pi/\theta_w$ and n is an integer. The wedge angle θ_w can have any value from 0 to 2π. The boundary conditions for a fluid within free wedge walls ($\rho_2 = 0$) are

$$\Theta = 0 \quad \text{at} \quad \theta = 0 \quad \text{and} \quad \theta = \theta_w \qquad \Theta = \sin(nv\theta) \tag{11.8.6}$$

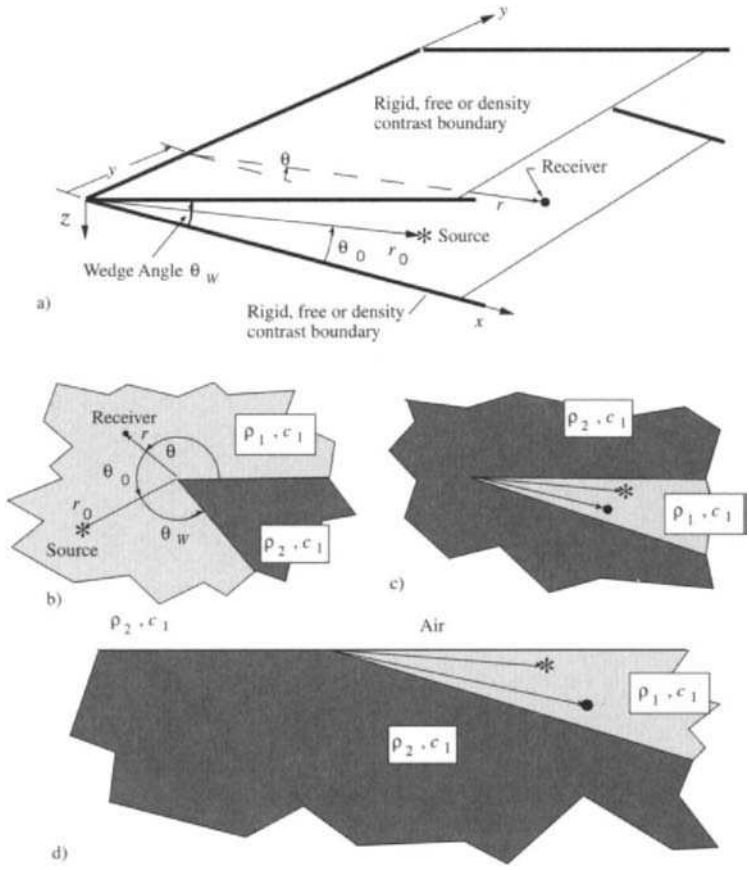

Figure 11.8.1 Coordinate system and wedge constructions. Two planes are the boundaries between the lightly shaded region and the darker shaded region. The line of the intersecting planes is along the y-axis, and all radial distances are measured normal to this line. The lighter shaded region has the density ρ_1 and sound speed c_1. The darker shaded region has the density ρ_2 and sound speed c_1. For the rigid boundaries, the source is in the lightly shaded region, and ρ_2 becomes infinite. For free boundaries, the source is in the lightly shaded region, and ρ_2 becomes 0. The density-contrast model has the same sound speeds and different densities. In the analysis, c is the sound speed, and ρ is the density of the fluid in the wedge. a) Wedge construction and the locations of the source and receiver. b) View along y-direction to show a large wedge angle. c) Same for a small wedge angle. d) A beach model. The density contrast wedge is under a half-space of air (free boundary).

11.8.1 NORMAL COORDINATE METHOD

The normal coordinate—that is, the Lagrangian—method is one of the most powerful tools in physics. Intermediate mechanics textbooks give introductory discussions and examples. Expositions of normal coordinate methods in wave propagation are in Chapter 3 and Appendix 5 of Tolstoy and Clay, *Ocean Acoustics* (1987), and Chapter 8 of Tolstoy, *Wave Propagation* (1973). Chu (1989) gives many of the analytical details. The mathematical manipulations are rather complicated, so we give results of manipulations from the references. The text of v. Ka'rma'n and Biot, *Mathematical Methods in Engineering* (1940), may be particularly helpful.

The normal coordinates q_n have time and space dependence. Each of the coordinates represents a component of energy of the system. In a continuous medium, the normal coordinates become the differentials d^2q_n. The sound pressure is the sum of the integrals of the $d^2q_n\psi_n$,

$$p = \sum_{n=0}^{\infty} \int_0^{\infty} \int_0^{\infty} \psi_n \, d^2 q_n \tag{11.8.7}$$

The q_n are solutions of the differential equation

$$\frac{\partial^2 q_n}{\partial t^2} + \omega^2 q_n = \frac{Q_n}{\mu_n} \tag{11.8.8}$$

where the source is in the generalized force Q_n and the pseudo-normalization is μ_n,

$$\mu_n \equiv \rho \int_{vol.} (\nabla \psi_n)^2 \, dV \tag{11.8.9}$$

An evaluation of μ_n is provided in Tolstoy (1973, Eq. 8-146) and Chu (1989b, Appendix A):

$$\mu_n = \frac{\rho \theta_w}{2} \frac{\omega^2}{c^2} \frac{\pi}{\kappa \, d\kappa \, d\gamma} \tag{11.8.10}$$

where the expression $1/(\kappa \, d\kappa \, d\gamma)$ is symbolic.

Source and the Generalized Force

Many acoustic experiments use explosive sources (i.e., sparks) that give a delta function of pressure. In our discussion we use the finite/discrete $\delta_f(t)$ [s^{-1}] and Equation 3.1.1. The sound pressure has a peak pressure P_0 referred to R_0; the duration of the peak is Δt; and the impulse is $P_0 \Delta t$. The Fourier cosine integral

transformation of the impulse source (unity for time equal to 0 to t and zero otherwise) is

$$\int_0^t \cos(\omega t)\, dt = \frac{\sin(\omega t)}{\omega} \tag{11.8.11}$$

The solution of the differential equation is, using Equation 11.8.11 and the impulse source $P_0 \Delta t R_0$,

$$d^2 q_n = 4\pi P_0 \Delta t R_0 \frac{\rho c^2 \nabla^2 \psi_0}{\mu_n} \frac{\sin(\omega t)}{\omega} \tag{11.8.12}$$

where

$$\nabla^2 \psi_0 = \frac{\omega^2}{c^2} \psi_0 \tag{11.8.13}$$

and ψ_0 is the value of ψ at the source position (r_0, θ_0, and $y = 0$), and the constants are chosen to give pressure for the impulse source. Note, the constants and ψ_0 are not functions of time in the solution of Equation 11.8.8. The substitution of μ_n into Equation 11.8.12 gives

$$d^2 q_n = \frac{8 P_0 \Delta t R_0 c^2}{\theta_w} \cos(n\nu\theta_0) J_{n\nu}(\kappa r_0) \cos(\gamma y) \frac{\sin(\omega t)}{\omega} \kappa\, d\kappa\, d\gamma \tag{11.8.14}$$

The nth term of the summation (Equation 11.8.7) is

$$\begin{aligned} \int_0^\infty \int_0^\infty \psi_n\, d^2 q_n = {} & \frac{8 P_0 \Delta t R_0 c^2}{\theta_w} \cos(n\nu\theta) \cos(n\nu\theta_0) \\ & \times \int_0^\infty \int_0^\infty J_{n\nu}(\kappa r) J_{n\nu}(\kappa r_0) \cos(\gamma y) \frac{\sin(\omega t)}{\omega} \kappa\, d\kappa\, dy \end{aligned} \tag{11.8.15}$$

The integration over $d\gamma$ yields (Gradshteyn and Ryzhik 1980, no. 3.876.1):

$$\begin{aligned} \int_0^\infty \cos(\gamma y) \frac{\sin(\omega t)}{\omega} d\gamma &= \int_0^\infty \cos(\gamma y) \frac{\sin[ct(\gamma^2 + \kappa^2)^{1/2}]}{c(\gamma^2 + \kappa^2)^{1/2}} d\gamma \\ &= \frac{\pi}{2c} J_0[\kappa (c^2 t^2 - y^2)] \end{aligned} \tag{11.8.16}$$

and the expression for integral $d^2 q_n \psi_n$ becomes

$$\int_0^\infty \int_0^\infty \psi_n\, d^2 q_n = 4\pi P_0 \Delta t R_0 c \frac{\cos(n\nu\theta_0) \cos(n\nu\theta)}{\theta_w} I_n \tag{11.8.17}$$

where

$$I_n \equiv \int_0^\infty J_{n\upsilon}(\kappa r) J_{n\upsilon}(\kappa r_0) J_0[\kappa (c^2 t^2 - y^2)^{1/2}] \kappa \, d\kappa \tag{11.8.18}$$

The sound pressure is the infinite summation

$$p(t) = P_0 \Delta t R_0 \frac{4\pi c}{\theta_w} \sum_{n=0}^{\infty} \cos(nv\theta) \cos(nv\theta_0) I_n \quad \text{for} \quad ct \geq y \tag{11.8.19}$$

where the source is at $(r_0, \theta_0, 0)$; the receiver is at (r, θ, y); the wedge angle is θ_w; and $v = \pi/\theta_w$. Each term in the summation represents the component of energy in its normal coordinate. The integral is evaluated in Erde'lye (1954, vol. II, p. 52) and in Gradshteyn and Ryzhik (1980, p. 695 and no. 6.578.8, where $m = 0$). Convenient forms of the Legendre functions are in Abramowitz and Stegun (1964, formulas 8.6.10–8.6.13). Three regions of the solution are defined by the values of t relative to t_{dir} and τ_0:

$$t_{dir} = \frac{1}{c} [(r - r_0)^2 + y^2]^{1/2} \tag{11.8.20}$$

where t_{dir} is the time for a ray to travel from the source to the receiver, and

$$\tau_0 = \frac{1}{c} [(r + r_0)^2 + y^2]^{1/2} \tag{11.8.21}$$

where τ_0 is the time required for a ray to go from the source to the line of the intersecting planes and then to the receiver. The diffraction from the line of intersection begins after τ_0.

Region 1: Before the First Arrival and $t < t_{dir}$

$$p(t) = 0 \quad \text{and} \quad j_{\text{dir}} = \textbf{int}(t_{\text{dir}}/t_0) \tag{11.8.22}$$

where t_0 is the finite time step.

Region 2: Direct Arrival and Images and $t_{\text{dir}} \leq t < \tau_0$

$$I_n = \frac{1}{\pi r_0 r \sin \xi} \cos(nv\xi) \tag{11.8.23}$$

where

$$\xi = \arccos \frac{r^2 + r_0^2 + y^2 - c^2 t^2}{2 r_0 r} \quad \text{for} \quad 0 \le |\xi| \le \pi \tag{11.8.24}$$

The parameter ξ includes time and space as would be expected of a normal coordinate in the Lagrangian. A few manipulations are needed to transform this normal coordinate frequency domain solution into the image solution with $\delta(t)$ time dependence.

Region 3: Diffraction Arrival and $t > \tau_0$

The travel time τ_0 is the beginning of the last arrival:

$$I_n = \frac{1}{\pi r_0 r \sinh \eta} \sin(n\nu\pi)\, e^{-n\nu\eta} \tag{11.8.25}$$

$$\eta = \operatorname{arg\,cosh} U = \log [\, U + (U^2 - 1)^{1/2} \,] \tag{11.8.26}$$

$$U \equiv \frac{c^2 t^2 - (r^2 + r_0^2 + y^2)}{2 r_0 r} \tag{11.8.27}$$

The parameter η is a function of time, and it starts at the beginning of the diffraction arrival τ_0. To display the relationship of η and t, we write,

$$t = \tau_0 + \tau \quad \text{where} \quad \tau/\tau_0 \ll 1 \tag{11.8.28}$$

and the expression for U (Equation 11.8.24) becomes

$$U \approx \frac{c^2\tau_0^2 + \tau^2 c^2 + 2\tau_0 \tau c^2 - (r_0^2 + r^2 + y^2)}{2 r r_0} \tag{11.8.29}$$

and the substitution of Equation 11.8.18 for τ_0 gives, after dropping τ^2,

$$U \approx 1 + \frac{\tau_0 \tau c^2}{r r_0} \tag{11.8.30}$$

Equation 11.8.26 is convenient for computations over a wide range of η. The substitution of the small τ approximation and expansion of the logarithm $[\log(1 + x) \approx x]$ gives

$$\eta \approx c\sqrt{\frac{2\tau_0 \tau}{r r_0}} \ll 1 \tag{11.8.31}$$

where we keep $\sqrt{\tau}$ and drop higher-order terms for very small values of τ. The parameter η includes time and space dependence.

For special values of $\theta_w = \pi/m$, the substitution $v = m$ into Equation 11.8.25 causes the diffraction component I_n to be 0, and the images are the complete solution.

The expressions or solutions for the pressures within the wedge depend on the values of t relative to t_{dir} and τ_0. Figure 11.8.2 shows the regions and a typical time domain solution for sound transmission in a wedge. The arrivals in each of the regions are separated by time from arrivals in the other regions. While the diffraction is the more challenging physics problem, the image part is usually more important because the reflected components are larger. The relative contributions are shown in Fig. 11.8.2 for this wedge.

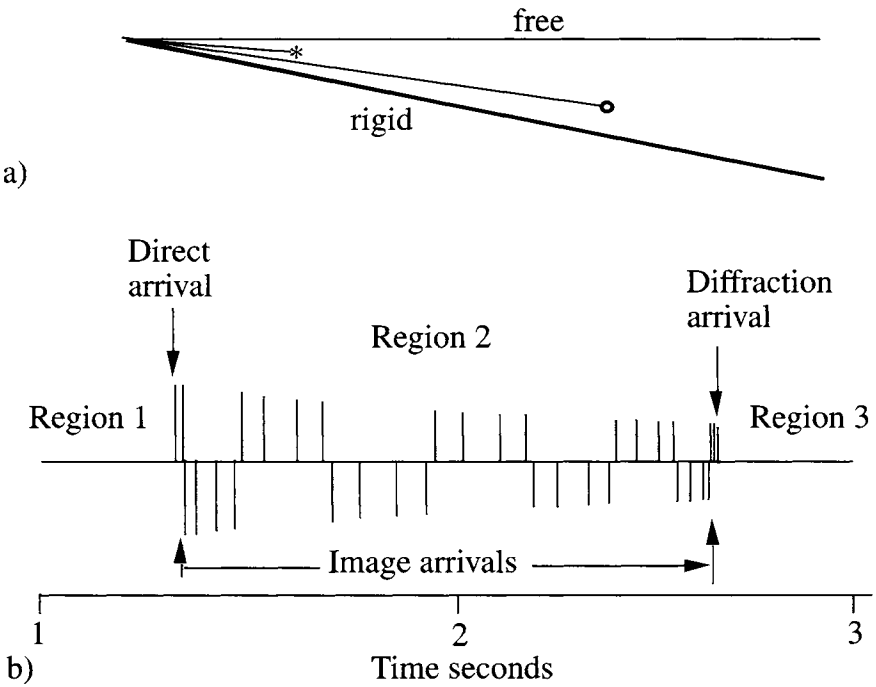

Figure 11.8.2 Time domain arrivals in a wedge. a) Source and receiver in a 11° wedge. The source * is at $r_0 = 1000\,\text{m}$ and $\theta_0 = 4°$. The receiver (circle) is at $r = 3000\,\text{m}$; $\theta = 8°$, and $y = 0$. The sound speed is $c = 1500\,\text{m/s}$. The upper boundary is free, and the lower boundary is rigid. b) Pressure signal due to an impulse source. Region 1 has no arrivals before the direct arrival. Region 2 contains the image arrivals. Region 3 is the diffraction arrival.

11.8.2 REGION 2: ARRIVALS FROM IMAGES

In a wedge waveguide, the amplitudes of the arrivals from the images are usually about the same or larger than the diffraction arrival. The substitution of Equation 11.8.23 in Equation 11.8.19 gives the solution for region 2. Although the image results are expected, much manipulation is needed to demonstrate that the exact solution gives image reflection arrivals;

$$p(t) = \frac{4P_0 \Delta t R_0 c}{\theta_w r r_0 \sin \xi} \sum_{n=0}^{\infty} \cos(n\nu\theta) \cos(n\nu\theta_0) \cos(n\nu\xi) \tag{11.8.32}$$

The transformation of the summation as a function of ξ to one of t requires much manipulation.

Details for Images

The expansion of the product of the cosines in Equation 11.8.32 gives the sum of four terms:

$$\cos(n\nu\theta)\cos(n\nu\theta_0)\cos(n\nu\xi) = \frac{1}{4}[\cos n\nu(\xi + \theta - \theta_0) + \cos n\nu(\xi - \theta + \theta_0) + \cos n\nu(\xi + \theta + \theta_0) + \cos n\nu(\xi - \theta - \theta_0)] \tag{11.8.33}$$

Use the Fourier series, Equations 6.2.25 and 6.2.26, and compute the spectral component of the function $\delta(\xi - \xi_0) + \delta(\xi + \xi_0)$, where ξ_0 represents $\theta \pm \theta_0$ and $2\theta_w$ is the period,

$$\frac{1}{2\theta_w} \int_0^{2\theta_w} [\delta(\xi - \xi_0) + \delta(\xi + \xi_0)] \exp\left(\frac{-in\pi}{\theta_w}\xi\right) d\xi = \frac{1}{\theta_w} \cos\left(\frac{n\pi\xi_0}{\theta_w}\right) \tag{11.8.34}$$

The right side of Equations 11.8.32 and 11.8.33 is the infinite series expansion of $\delta(\xi - \xi_0) + \delta(\xi + \xi_0)$ and the periodic sequence is $\delta(\xi \pm \xi_0 - 2k\theta_w)$. The sound pressure becomes

$$p(t) = P_0 \Delta t R_0 c \sum_k \frac{1}{r r_0 \sin \xi} \delta(\xi \pm \theta \pm \theta_0 - 2k\theta_w) \tag{11.8.35}$$

Next we equate the delta function integrals:

$$\int_{-\infty}^{\infty} \delta(\xi)\, d\xi = \int_{-\infty}^{\infty} \delta(t)\, dt = 1 \quad \text{and} \quad \delta(\xi)\, d\xi = \delta(t)\, dt$$

$$\delta(t) = \delta(\xi)\frac{d\xi}{dt} \tag{11.8.36}$$

and letting $ct = R_k \pm$, where $R_k(\pm)$ is given later,

$$\delta\left[t - \frac{R_k(\pm)}{c}\right] = \delta\left[\xi - (2k\theta_w \pm \theta \pm \theta_0)\right]\frac{d\xi}{dt} \tag{11.8.37}$$

The cosine of ξ is, using Equation 11.8.24,

$$\cos\xi = \frac{r^2 + r_0^2 + y^2 - c^2 t^2}{2 r r_0} = \cos(\pm\theta \pm \theta_0 - 2k\theta_w) \tag{11.8.38}$$

and differentiation with respect to t and solving for $\sin(\xi)$ gives

$$\sin(\xi) = \frac{c^2}{r r_0}\frac{dt}{d\xi} \tag{11.8.39}$$

The change of variable from ξ to t in Equation 11.8.36 gives the sum of delta functions from the image sources.

Again, the finite/discrete delta function is

$$\delta_f(t) \equiv \frac{1}{t_0} \quad \text{for} \quad 0 \le t \le t_0, \quad \text{and} = 0 \quad \text{otherwise} \tag{11.8.40}$$

The sound pressure in region 2, the image region, is

$$p(t) = P_0 \Delta t R_0 \sum_k \frac{\delta_f\left[t - \frac{R_k(\pm)}{c}\right]}{R_k(\pm)} p(t) = P_0 \Delta t R_0 \sum_k \frac{\delta_f\left[t - \frac{R_k(\pm)}{c}\right]}{R_k(\pm)} \tag{11.8.41}$$

where the $R_k(\pm)$ are the combinations that are given by

$$R_k(+-) = [\, r_0^2 + r^2 + y^2 - 2\, r_0 r \cos(2k\theta_w + \theta - \theta_0)\,]^{1/2} \quad \textbf{(11.8.42a)}$$

$$R_k(-+) = [\, r_0^2 + r^2 + y^2 - 2\, r_0 r \cos(2k\theta_w - \theta + \theta_0)\,]^{1/2} \quad \textbf{(11.8.42b)}$$

$$R_k(++) = [\, r_0^2 + r^2 + y^2 - 2\, r_0 r \cos(2k\theta_w + \theta + \theta_0)\,]^{1/2} \quad \textbf{(11.8.42c)}$$

$$R_k(--) = [\, r_0^2 + r^2 + y^2 - 2\, r_0 r \cos(2k\theta_w - \theta - \theta_0)\,]^{1/2} \quad \textbf{(11.8.42d)}$$

$$R_k(\pm) = [\, r_0^2 + r^2 + y^2 - 2\, r_0 r \cos(2k\theta_w \pm \theta \pm \theta_0)\,]^{1/2} \quad \textbf{(11.8.43)}$$

Collectively, the notation $R_k(\pm)$ is used to represent all of the combinations in Equation 11.8.43. Each of the image contributions represents the energy for a normal coordinate. In region 2 there are a discrete number of normal coordinates. The maximum value of k or $k_{\max}$ is given by the condition in Equation 11.8.24, or

$$0 < |2k\theta_w \pm \theta_0 \pm \theta| \leq \pi \quad \textbf{(11.8.44)}$$

This condition gives a finite number of images. The pressure disturbance from the last image arrives before τ_0, the diffraction from the line of intersecting planes. We show the image construction in Fig. 11.8.3. The images are reflections of the source in wedge planes. Possible image locations are on the circle containing the source and at the angles given by $2k\theta_w \pm \theta_0$ and $\theta = 0$. Here k ranges from $-k_{\max}$ to $+k_{\max}$, and the image angles satisfy Equation 11.8.44.

The choice of a receiver angle θ requires that the satisfaction of Equation 11.8.44 be tested to determine if one can receive an arrival from that image. The positive values of k use $(2k\theta_w \pm \theta_0 - \theta)$, and the negative values of k use $(2k\theta_w \pm \theta_0 + \theta)$.

If one lets $k = -k_{\max}, \ldots 0, \ldots k_{\max}$, then $(2k\theta_w + \theta_0 + \theta)$ and $(2k\theta_w - \theta_0 + \theta)$ give all of the combinations.

The travel times are computed at

$$t_k(\pm) = \frac{R_k(\pm)}{c} \quad \textbf{(11.8.45)}$$

In numerical computations and at a sequence of time steps jt_0, the jth time step is

$$j = \text{int}\left(\frac{t_k(\pm)}{t_0}\right) \quad \textbf{(11.8.46)}$$

where the small fluctuation of the arrival time within a time step is acceptable.

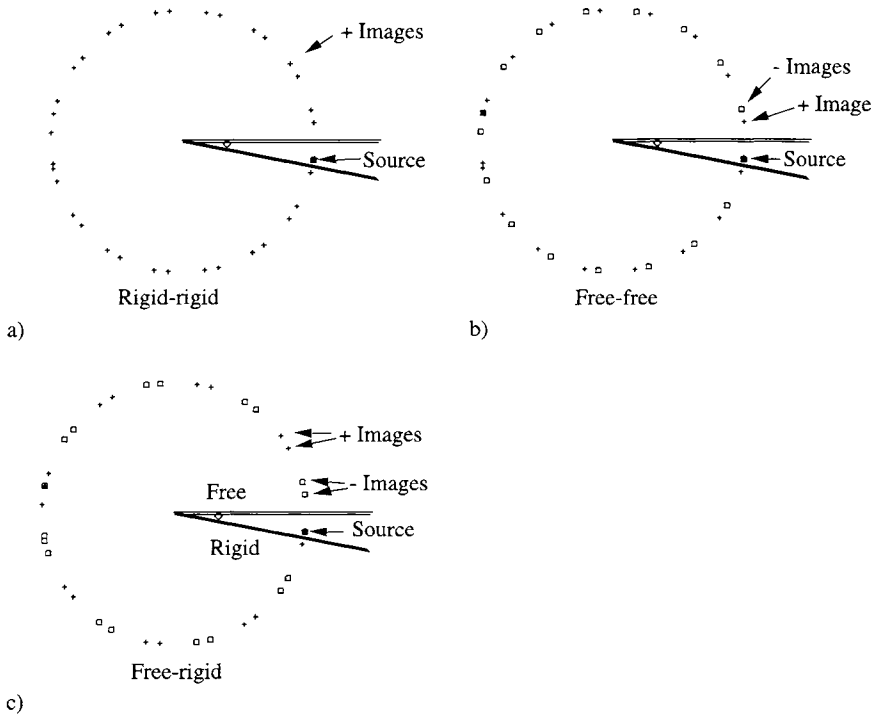

Figure 11.8.3 Examples of image constructions. a) Rigid-rigid boundaries have all positive images. b) Free-free boundaries have pairs of positive and negative images. c) Free-rigid boundaries have positive-image pairs and negative-image pairs.

The ray paths from the images to the receivers in the density-contrast model are straight because the sound speeds are the same in all regions. The reflection coefficients and transmission coefficients are constant for all angles of incidence.

11.8.3 REGION 3: DIFFRACTION ARRIVAL

The diffraction arrival exists for $t > \tau_0$, and, by Equation 11.8.20, τ_0 is the minimum time for a disturbance to go from the source to the line of intersection and to the receiver. The closed form expressions for I_n in region 3 are given by Equations 11.8.25 through 11.8.27. The substitution of Equation 11.8.25 in

Equation 11.8.19 gives

$$p(t) = \frac{-4P_0 \Delta t R_0 c}{r r_0 \theta_w \sinh \eta} \sum_{n=0}^{\infty} \cos(n\nu\theta) \cos(n\nu\theta_0) \sin(n\nu\pi) e^{-n\nu\eta} \quad \text{for} \quad t > \tau_0 \tag{11.8.47}$$

The experiments of Li and Clay (1988) have shown that the diffraction arrival from the line of intersecting planes is extremely sensitive to the perfection of the wedge. Let us assume that τ in Equations 11.8.28 and 11.8.29 can go to zero for perfect intersection of the wedge plane, but can't for an imperfect wedge. Thus, we add an empirical limit δ to form $(\eta + \delta)$ and include a mode attenuation factor $\exp(-n\nu\phi)$ in the summation. It seems reasonable to use $n\nu\delta$ because one would expect the effects of leakage and roughness at the wedge apex to increase with larger mode number and smaller wedge angle. For an imperfect wedge, $p(t)$ in Equation 11.8.39 becomes

$$p(t) = \frac{-4P_0 \Delta t R_0 c}{r r_0 \theta_w \sinh(\eta + \delta)} \sum_{n=0}^{\infty} \cos(n\nu\theta) \cos(n\nu\theta_0) \sin(n\nu\pi) e^{-n\nu(\eta+\delta)} \quad \text{for} \quad t > \tau_0 \tag{11.8.48}$$

In the normal coordinates, the terms in Equations 11.8.47 and 11.8.48 represent components of energy. Each term is time-dependent as a function of η

$$\textit{Time dependence} \sim \frac{1}{\sinh(\eta + \delta)} e^{-n\nu(\eta+\delta)} \quad \text{for} \quad \eta \geq 0 \tag{11.8.49}$$

For large η, the time dependence tends to zero. As η tends to 0, Equation 11.8.49 tends to finite limit that is proportional to $1/\delta$.

In comparisons of the theory to experimental data, $p(t)$ is convolved with the source and system responses, and thus $p(t)$ is band-pass filtered. Effectively, the filter operation makes a running time average of $p(t)$, and this time-averaging operation also reduces the maximum value of $p(t)$ as η tends to zero.

Details for Diffraction

Expand the product of the sine and cosine functions:

$$\cos \nu_n \theta \cos \nu_n \theta_0 \sin \nu_n \pi = \frac{1}{4} [\sin \nu_n(\pi + \theta - \theta_0) + \sin \nu_n(\pi - \theta + \theta_0) + \sin \nu_n(\pi + \theta + \theta_0) + \sin \nu_n(\pi - \theta - \theta_0)] \tag{11.8.50}$$

The sine functions are expanded as exponentials to give the sum of eight infinite geometric series. Evaluations of the sums, and simplification, give the sum of four terms where the ± combinations indicate the terms

$$p(t) = \frac{-P_0 \Delta t R_0 c}{2\theta_w r r_0} [D(\eta,+-) + D(\eta,-+) + D(\eta,++) + D(\eta,--)] \tag{11.8.51}$$

where $D(\eta, \pm)$ is

$$D(\eta,+-) \equiv \frac{\sin v(\pi + \theta - \theta_0)}{\sinh(\eta+\delta)\{\cosh[v(\eta+\delta)] - \cos v(\pi+\theta-\theta_0)\}} \tag{11.8.52a}$$

$$v = \pi/\Theta_0 \tag{11.8.52b}$$

and so forth for the other sign combinations. We abbreviate the sum of the sign combinations in Equation 11.8.52a by writing $D(\eta, \pm)$ and $\theta\pm$, where

$$\theta \pm = v(\pi \pm \theta \pm \theta_0) \tag{11.8.53}$$

This is the exact time domain solution for the diffraction arrival. The values of $D(\eta, +-)$ are very sensitive to the locations of the source and receiver and to the values of $\theta\pm$ in Equation 11.8.3. As $\sin(\theta\pm)$ passes through zero, the sign of $D(\eta, +-)$ changes. Finite values of δ keep $D(\eta, +-)$ finite. If $\delta = 0$, then Equation 11.8.52 becomes infinite and/or indeterminate as η tends to zero. Laboratory acoustic experiments show that $p(t)$ is well behaved as $\sin(\theta\pm)$ passes through zero.

Numerical calculations of $D(\eta, \pm)$ are measured from τ_0 as $\tau = t - \tau_0$. Equations 11.8.25 through 11.8.31 are used in numerical calculations of η. In numerical calculations, the use of the various approximations for $(\eta + \delta) \ll 1$ is not advised.

When times are a little greater than τ_0, expansions or approximations for $(\eta + \delta) \ll 1$ are useful for making analytical approximations and for displaying the properties of Equation 11.8.52. For example, the value of $\sinh(\eta + \delta)$, using the first term of the series expansion $[\sinh x \approx x]$, is

$$\sinh(\eta + \delta) \approx (\eta + \delta) \tag{11.8.54a}$$

$$\text{as } \eta \text{ tends to 0 and } \delta \ll 1 \tag{11.8.54b}$$

To estimate δ for an imperfect line of intersection, first recall Equation 11.8.31, and then write

$$(\eta + \delta) \approx c\sqrt{\frac{2\tau_0\tau}{rr_0}} \rightarrow \delta \rightarrow c\sqrt{\frac{2\tau_0\tau_{imperfect}}{rr_0}} \tag{11.8.55}$$

where $\tau_{\text{imperfect}}$ represents the imperfections—i.e., the leakiness-roughness—at the intersection of the wedge planes. The imperfectness is assumed to be small compared to τ_0.

Numerical Computations

In the time expression $t = \tau_0 + \tau$, the time τ after the beginning of the diffraction arrival τ_0 must be accurately computed. One can compute accurate values of τ by using very small sampling steps and measuring all distances in the sampling steps ct_0. A simpler robust method uses a secondary time reference to compute τ as follows:

$$\tau = t - \tau_0 \tag{11.8.56}$$

Let the integer operation (**INT**, basic) or (*round* in MATLAB) give

$$j_{tau} = \mathbf{INT}\,[(t - \tau_0)/t_0] \tag{11.8.57}$$

the secondary reference is

$$j_{dif} = \mathbf{INT}\,(\tau_0/t_0) \tag{11.8.58}$$

$$n = \mathbf{INT}\,(t/t_0) \tag{11.8.59}$$

$$n = j_{dif} + j_{tau} \tag{11.8.60}$$

The reference array element for τ_0 is j_{dif} and at $\tau = 0$, $j_{\text{tau}} = 0$. The diffraction terms are computed for $n = 0, 1, \ldots, j_{\text{dif}} + 0, +1 \ldots$, the expression for $D(\eta, \pm)$ is

$$D(\eta,+\text{-}) \equiv \frac{\sin[\frac{\pi}{\theta_w}(\pi + \theta - \theta_0)]}{\sinh(\eta + \delta)\{\cosh[\frac{\pi}{\theta_w}(\eta + \delta)] - \cos[\frac{\pi}{\theta_w}(\pi + \theta - \theta_0)]\}} \tag{11.8.61}$$

where the dependence of η on τ is given by Equations 11.8.26 and 11.8.29. In our numerical tests, the computer computations were well behaved for $\delta > 10^{-6}$ and $\eta \geq 0$. Thus, special evaluations and approximations of $p(t)$ for very small η were not needed.

An alternative form of the diffraction expression is used in section 12.2.1,

$$\frac{D(\eta, +-)}{2} = \frac{\beta_+}{\sinh(\eta + \delta)} \exp\left[-\frac{\pi}{\theta_w}(\eta + \delta)\right] \tag{11.8.62}$$

where

$$\beta_+ \equiv \sum \frac{\sin\left[\frac{\pi}{\theta_w}(\pi \pm \theta \pm \theta_0)\right]}{1 - 2\exp\left[-\frac{\pi}{\theta_w}(\eta + \delta)\right]\cos\left[\frac{\pi}{\theta_w}(\pi \pm \theta \pm \theta_w)\right] + \exp\left[-2\frac{\pi}{\theta_w}(\eta + \delta)\right]} \tag{11.8.63}$$

and

$$p(t) = -\frac{P_0\, \Delta t\, R_0\, c}{\theta_w\, r\, r_0} \frac{\beta_+}{\sinh(\eta + \delta)} \exp\left[-\frac{\pi}{\theta_w}(\eta + \delta)\right] \tag{11.8.64}$$

In general, β_+ is sensitive to θ_w, θ_0, and θ. It is also time dependent because η is time dependent.

Diffraction Expressions for Different Boundaries

The conditions give different combinations of the $D(\eta, +-)$ as follows:

Rigid-rigid

$$p(t) = -\frac{P_0\, \Delta t\, R_0\, c}{2\theta_w\, r\, r_0} [D(\eta, +-) + D(\eta, -+) + D(\eta, ++) + D(\eta, --)] \tag{11.8.65}$$

Free-free

$$p(t) = -\frac{P_0\, \Delta t\, R_0\, c}{2\theta_w\, r\, r_0} [D(\eta, +-) + D(\eta, -+) - D(\eta, ++) - D(\eta, --)] \tag{11.8.66}$$

Free-rigid

$$p(t) = -\frac{P_0 R_0 t_0 c}{2\theta_w r r_0}[D_{r/f}(\eta,+-) + D_{r/f}(\eta,-+) + D_{r/f}(\eta,++) + D_{r/f}(\eta,--)] \tag{11.8.67}$$

where

$$D_{r/f}(\eta,+-) \equiv \frac{\sin\frac{\upsilon}{2}(\pi + \theta - \theta_0)\cosh(\frac{\upsilon}{2} + \frac{\delta}{2})}{\sinh(\eta + \delta)\{\cosh[\upsilon(\eta + \delta)] - \cos\upsilon(\pi + \theta - \theta_0)\}} \tag{11.8.68}$$

Density Contrast Wedges

Chu (1989) has shown the following: the wave equation for the density-contrast wedge is seperable when the sound speeds are the same as sketched in Fig. 11.8.1. Since the wedge is penetrable, the source and receiver can be in either region. The direct, reflected, and transmitted arrivals are the same as computed by using ray-path and image methods. Numerical evaluations of the diffracted component show that the diffracted component is not the ideal wedge solution multiplied by an impedance factor.

11.8.4 NUMERICAL EXAMPLES

The first numerical example is the wedge transmission shown in Fig. 11.8.2. This example simulates the down-slope transmission in a shallow-water wedge formed by a sloping bottom. The main arrivals are the direct arrival and the sequence of reflected ray or image arrivals. On referring to Fig. 11.8.3, one can see that groups of the same sign of image arrivals are expected—that is, a pair from above the free surface and a pair of negative images from locations beneath the rigid bottom. The next arrivals are pairs of positive images also from above and beneath the boundaries. The image arrivals exist as long as Equation 11.8.37 is satisfied. The last arrival is the diffraction from the intersecting line at the contact between the rigid bottom and the free surface (the beach). In real beachs, irregularities of the contact would cause the diffraction arrival to be very small.

The parameters for two examples of the waveforms of the diffracted components were chosen to match the experiments that are described later. The first example is for the interior wedge (Fig. 11.8.5). The diffraction component was computed using Equation 11.8.65 and a sampling interval of $t_0 = 10\ \mu s$. The diffraction pressure is positive, has a large value of $|p(t)|$ at τ_0, and has a tail that

decreases with time. The spectrum of the diffraction component is shown in Fig. 11.8.4b. Although they are not shown, the spectra of the direct arrival and the reflected ray paths (from the images) are constant as a function of frequency.

The simplified structure of a continent consists of a gently sloping bottom to the "shelf break," where the slope becomes much steeper. The sketch, shown in Fig. 11.8.5, is an exaggerated shelf model.

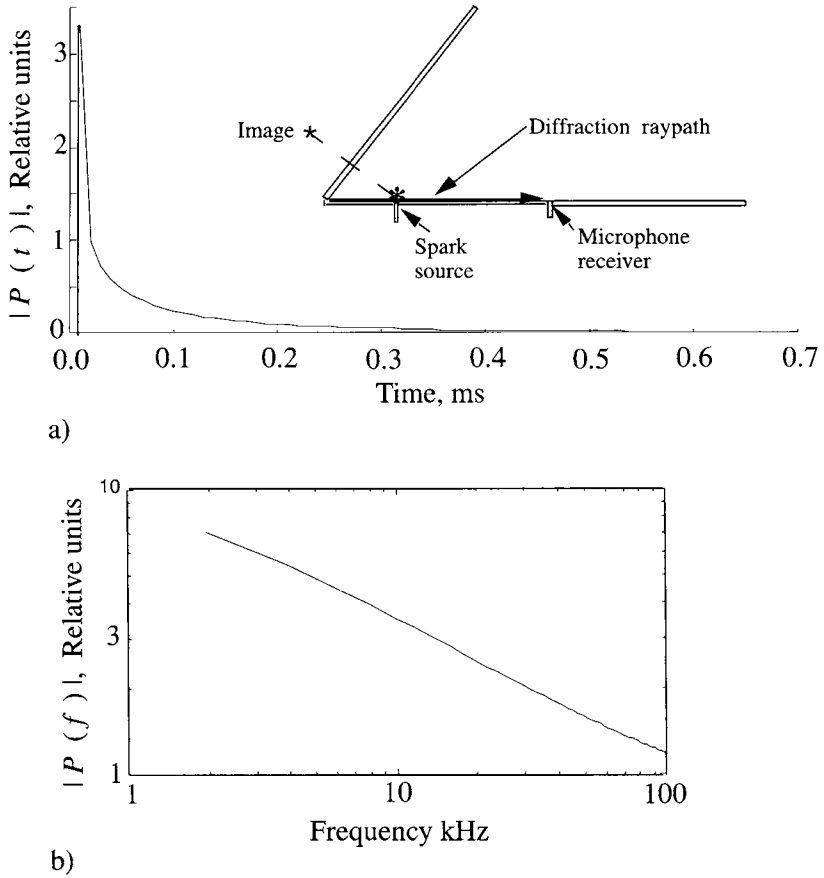

Figure 11.8.4 Numerical example of the diffraction arrival from a 52° rigid wedge line of intersecting planes. The rigid wedge walls and the locations of the source and receiver are $\theta_w = 52°$; $r_0 = 0.49\,\text{m}$; $\theta_0 = 0$, $r = 1.613\,\text{m}$; and $\theta = 0$. The source and receiver are flush-mounted in the boundary wall. The reference pressure is the image reflection at vertical incidence. a) The sound pressure $p(t)$. b) Fourier transformation $|P(f)|$ of $p(t)$.

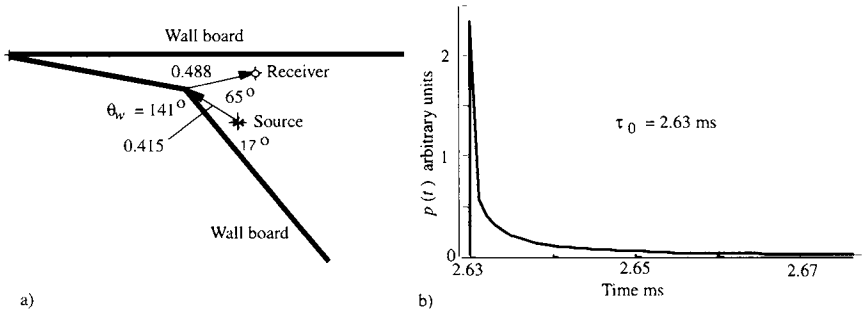

Figure 11.8.5 Diffraction from a model shelf break. a) Shelf model. b) The diffraction arrival from the wedge at a shelf break is shown. The amplitude units are arbitrary.

11.8.5 COMPARISONS OF THEORY AND EXPERIMENTS

Many aspects of the wedge theory have been verified in detail by experiments. Comparative tests in the frequency domain are summarized in section 12.3.1. At certain angles, the amplitudes of the Kirchhoff diffraction arrivals are found to be wrong by many decibels, but the Biot-Tolstoy diffraction predictions agree with experiment.

A series of laboratory experiments in air were made to test critical parts of the extensions in the time domain. A spark source was used for the transmissions because the arrivals were separated by time of arrival. Questions were: (1) What is the dependence of the waveforms of diffracted components on the wedge angle and quality of the wedge? (2) What are the amplitudes and waveforms of the components reflected by planes having finite dimensions? (3) What are the effects of finite facet widths, diffractions, and double diffractions on model simulations of a ridge feature on the sea floor? (See Li and Clay 1988; Clay, Chu, and Li 1993; and Li, Chu, and Clay 1994.)

We give some of the results of the time-domain research here. The impulse source was a spark in air, and the receiver was a small microphone. Figure 11.8.6 shows the transmission in free air from the spark to the small electret microphone, the filter, and the recording system. The free-air transmission was used as the reference source function for convolutions with the theoretical transmissions and comparisons with experiments.

Figure 11.8.7 shows a comparison of the theoretical arrivals and the data for a 12.07° wedge. For this rigid-rigid wedge transmission, all arrivals are positive. The first arrival is the direct path, and the last arrival is the diffraction arrival.

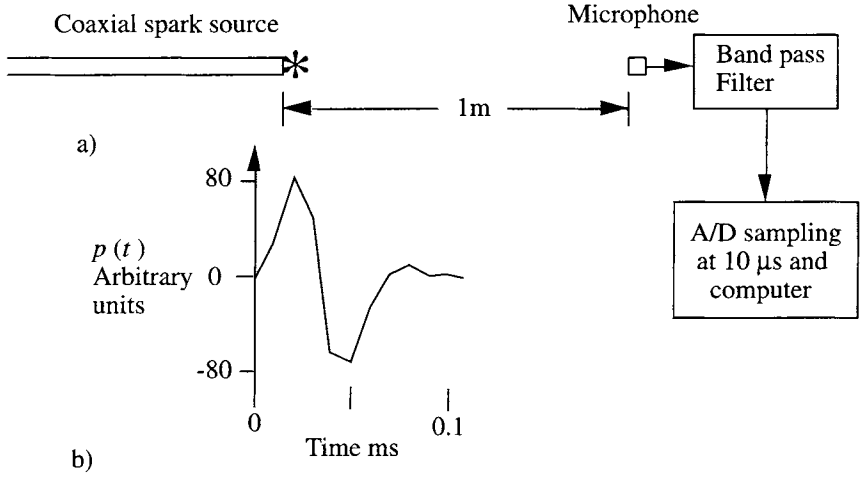

Figure 11.8.6 Pressure signal from a spark source. Reflecting surfaces such as the ceiling and floor were far enough away for the reference transmissions to be made in "free air." a) A coaxial spark was the source, and the receiving microphone was a 6 mm diameter electret microphone. After bandpass filtering, the pressure signal was sampled at a 100 kHz frequency and stored in the computer. b) $p(t)$ is an example of a typical transmission. (From Li, S., and C. S. Clay, "Sound transmission experiments from an impulsive source near rigid wedges," *J. Acoust. Soc. Am.* **84**, 2135–43, 1988.)

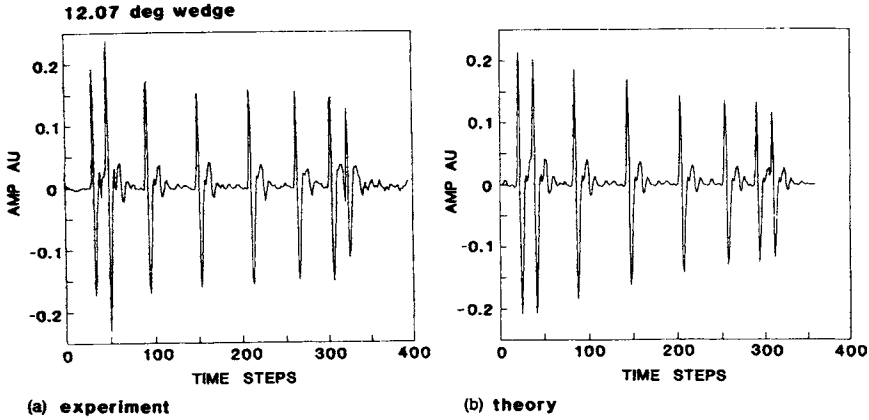

Figure 11.8.7 Sound transmission measurements in an acoustic wedge, $\theta_w = 12.15°$. The spark source and the microphone were mounted flush on the wedge wall. The distances from the line of intersection were $r_0 = 0.49$ m and $r = 1.613$ m. The direct transmission time (3.12 ms) is suppressed. (From Li, S., and C. S. Clay, "Sound transmission experiments from an impulsive source near rigid wedges," *J. Acoust. Soc. Am.* **84**, 2135–43, 1988.)

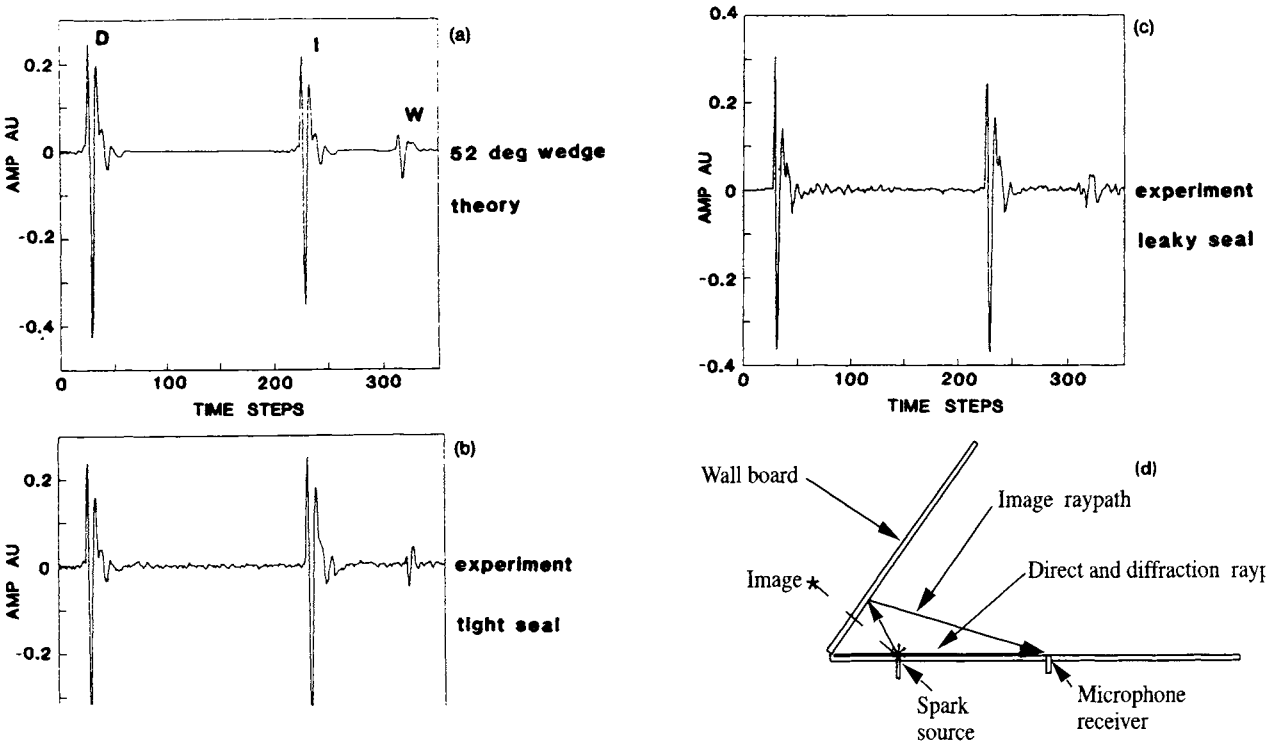

Figure 11.8.8 Transmissions at a 52° rigid wedge. The wedge is shown in the inset, and the parameters are in the caption of Fig. 11.8.4. The acoustic and signal processing systems are the same as was used for the "free-air" transmission shown in Fig. 11.6.5. The theoretical (unconvolved) diffraction pressure signal and its spectrum are shown in Fig. 11.8.4. The time steps are 0.01 ms, and part of the travel time along the direct path (3.12 ms) is suppressed. a) Theoretical transmission. Direct is "D"; image is "I"; diffraction is "W." b) Experiment with tight seal at the line of intersecting planes. c) Leaky seal. (From Li, S., and C. S. Clay, "Sound transmission experiments from an impulsive source near rigid wedges," *J. Acoust. Soc. Am.* **84**, 2135–43, 1988.)

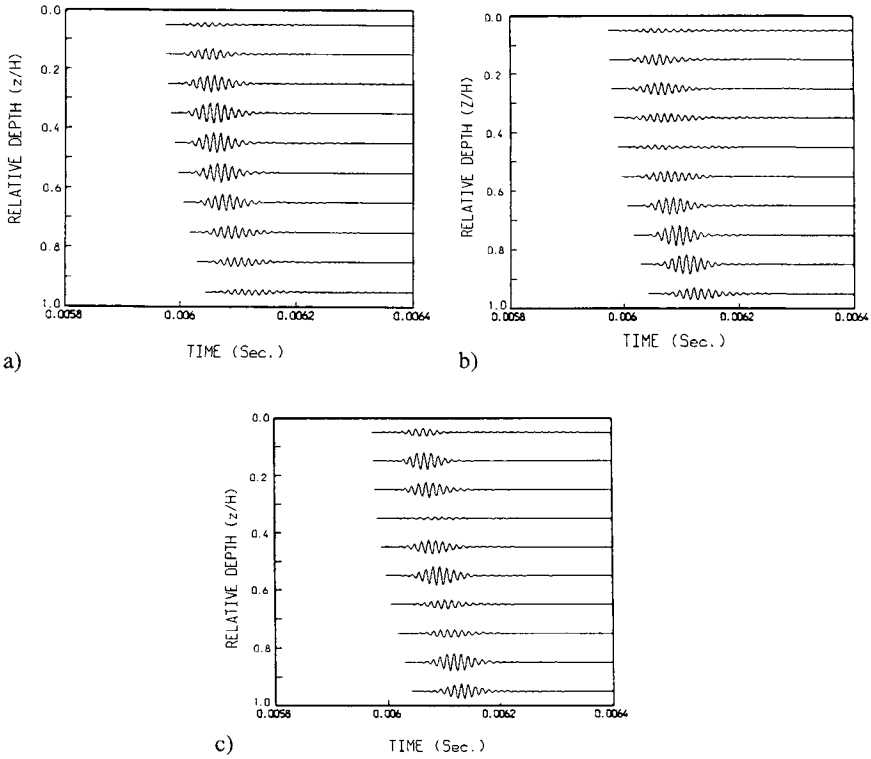

Figure 11.8.9 Simulated arrivals for single modes in the wedge waveguide. The wedge waveguide is shown in Fig. 11.6.1. The slope is 9°. As in the experiment, single modes were excited, and the pressures were observed at a set of depths. For comparison, the data are shown in Fig. 11.6.3b. (From Chu, D., "Exact solution for a density contrast shallow water wedge using normal coordiantes," *J. Acoust. Soc. Am.* **87**, 2442–50, 1990.)

The ray path for the direct arrival traveled from the flush-mounted source to the flush-mounted microphone, as sketched in Fig. 11.8.4a. The radiation from the spark was a little weaker along this direction, and the wall board probably absorbed a little energy. Thus, the amplitude of the direct arrival is relatively smaller than the early reflected paths and less than the theoretical amplitude. The image arrivals occur between the direct arrival and the diffraction arrival. The times of the theoretical and experimental direct, image, and diffraction arrivals agree. The waveforms are the same (ignoring the noise), and, except for the direct arrival, the relative amplitudes are the same within a few percent.

Comparisons of theory and experiment for the wide 52° wedge are shown on Fig. 11.8.8. These comparisons are interesting because they show the effect of

leakage/imperfections at the line of intersecting planes. Leakage reduces the amplitude of the diffraction arrival.

A simplified beach construction is sketched in Fig. 11.8.1d. Chu (1990) compared his contrast-density solution for the wedge waveguide under a half-space of air with the experimental results of Tindle et al. (1987) and section 11.6.2. For the simulation, the point sources were placed at positions of the transducers, shown in Fig. 11.6.1. The source excitations were chosen, as in Tindle et al., to excite single modes. Simulated time domain transmissions in the first three modes are shown in Fig. 11.8.9. The depth and mode dependence of these waveforms can be compared with the experimental waveform shown in Fig. 11.6.3b. The ray-path/image solution gives the same amplitude dependence of the arrivals on depth as in Fig. 11.6.3b.

Problems

The problems are identified by section number. In doing the calculations for sound pressures, determine the relative amplitudes and ignore the source power.

Section 11.1

11.1.1 Compare the exact values and the large κr approximation (Equation 11.1.10) for $H_0^{(2)}(\kappa r)$. Test the range of $0.2 < \kappa r < 5$.

11.1.2 Compute and plot the wave number components γ_m and κ_m for a waveguide that has free upper and lower interfaces. The waveguide is 10 m thick. Plot the first three modes as functions of frequency. If cut-off exists, explain why.

11.1.3 Use the waveguide parameters in Table 11.1 for this problem. For the modes 1 and 2, compute the penetration into medium 2 and sketch the pressure field beneath the bottom in Fig. 11.1.6.

11.1.4 Use the waveguide parameters in Table 11.1 and 150 Hz frequency for this problem. Use the concept of the ray reflection beyond the critical angle, section 2.6.4, to construct an equivalent waveguide for modes 1 and 2. Compute a simulated transmission run (as in Fig. 11.1.8) for the equivalent waveguide.

Section 11.2

11.2.1 Make a photocopied enlargement of Fig. 11.2.1 and do a group velocity analysis.

11.2.2 Draw the ray paths and compute the travel times for the model in Table 11.1. Let the source be at 1000 m range and 13 m depth. The receiver is at 7 m depth. a) Display the signal for an impulse source. Use the no-phase-shift approximation for the first calculation. b) Use the equivalent bottom interface (section 2.6.4) for a calculation and comparison.

Section 11.3

11.3.1 Use the free top and free bottom water waveguide for simplicity. The wave guide is 20 m thick, and the source and the receiving array are at 15 m depth. The source has the frequency of 200 Hz and is at 10000 m range. Horizontal arrays can be steered to locate the direction to a source. The line array is 750 m long and has 10 elements. The array processing includes time delays for digitally steering the beam to "look" in different directions. The steering directions are from 0° at normal to the line array to ±90°. a) How many modes are excited? b) Compute the array output *for each mode* as a function of steering angle for the source directions of 0° and end fire, 90° directions. c) Repeat b), except that all modes are received. For simplicity, ignore the mode interference terms.

Section 11.5

11.5.1 Use the matched filter/matched signal to compute the ambiguity function for a source location task. For simplicity, let the waveguide have 20 m depth of water over a free reflection bottom. The source for the simulation is at 10,000 m range and 13 m depth. Let the source transmit an impulse (i.e., explosive shot). a) Calculate and display the signal at the receiver, 13 m depth. b) Compute ambiguity functions for the bandpass filters at 100–200 Hz, 100–500 Hz, and 100–1000 Hz.

Section 11.6

11.6.1 Discuss the effects of water waves on sound transmissions. Read Clay, Wang, and Shang (1985). Compare their conclusions to those given in Tolstoy and Clay (1987, p. 232–36).

11.6.2 How would you expect the time dependence of a surface to affect the transmission in a waveguide? J. A. Scrimger describes an elegant experiment: "Signal Amplitude and Phase Fluctuations Induced by Surface Waves in Ducted Sound Propagation" (*J. Acoust. Soc. Am.* **33**, 239–74 1961). What are the most important regions for causing fluctuations of the sound transmissions?

Section 11.7

11.7.1 Use the wedge having rigid boundaries with the angle $\theta_w = 57°$, as in Fig. 11.8.7, the medium is air, $c = 346$ m/s. Determine the image positions for a source at $\theta_0 = 0°$ and $r_0 = 0.49$ m. Put the receiver at $r = 1.613$ m and $\theta = 0°$. a) Calculate the pressure response relative to the direct transmission for an impulse source. Let $t_0 = 0.01$ ms and $\delta = 0.00001$. b) Test the effects of leakage by letting $\delta = 1$, 0.1, 0.01, and so forth. b) What is the transmission for $\theta_w = 60°$? Explain any difference.

11.7.2 Assume a wedge having rigid boundaries and the angle $\theta_w = 57°$, as in Fig. 11.8.7. The medium is air, $c = 346$ m/s. Determine the image positions for a source at $\theta_0 = 11°$ and $r_0 = 0.49$ m. Put the receiver at $r = 1.613$ m and $\theta = 50°$. Calculate the pressure response relative to the direct transmission for an impulse source. Let $t_0 = 0.01$ ms. Test the effects of leakage by letting $\delta = 1$, 0.1, 0.01, and so on.

11.7.3 Assume the wedge has rigid boundaries and the angle $\theta_w = 57°$, as in Fig. 11.8.7. The medium is water, $c = 1500$ m/s. Determine the image positions for a source at $\theta_0 = 11°$ and $r_0 = 2.12$ m. Put the receiver at $r = 7.0$ m and $\theta = 50°$. Calculate the pressure response relative to the direct transmission for an impulse source. Let $t_0 = 0.01$ ms. Test the effects of leakage by letting $\delta = 1$, 0.1, 0.01, and so forth.

11.7.4 Repeat Problem 11.7.3 for a wedge that has free boundaries.

11.7.5 Repeat Problem 11.7.3 for a wedge that has a free upper boundary ($\theta_w = 57°$) and a rigid lower boundary.

Chapter 12 | Scattering at Elements of a Rough Surface

12.1 The Helmholtz–Kirchhoff Integral for Surface Scatter 542
12.2 Implementation of Biot–Tolstoy Theory of Impulse Scatter from Wedges and Plates 542
12.2.1 Theory for Infinite Wedges 542
12.2.2 Reflection and Diffraction in the Time Domain: Realizations and Verifications 546
12.2.3 Digital Implementation for Finite Wedges 551
12.2.4 Simplifications 554
12.3 Digital Calculations of Biot–Tolstoy Diffraction in the Frequency Domain 555
12.3.1 Comparison of Diffraction Backscatter-Predictions of HK and BT Theories 559
12.3.2 Double Diffraction 559
12.3.3 Forward Diffraction at a Seamount 562
12.3.4 The Finite Wedge Approximation to the Inifinite Wedge 565
12.3.5 Components of Reverberation from Rough Surfaces 568
12.4 BT Wedge Assemblage Techniques for Rough Surfaces 569
12.4.1 Parallel Wedges: Laboratory Test of a Sinusoidal Long-Crested Water Surface 569
12.4.2 Parallel Wedges: The Ocean as a Low-Frequency Diffraction Grating 570
12.4.3 Synthetic Seismic Profiles 573

Wedges are simple models of several naturally occuring roughness elements at sea, including sea swell, lineal rock outcroppings on the sea floor, keels (underwater ridges), and leads (ice separations) of the Arctic ice canopy. It is therefore fruitful to interpret the scatter from a statistically rough sea surface or rough sea bottom as being made up of scatter from a sequence of contiguous finite wedges. Even a large seamount has been effectively interpreted as being acoustically equivalent to two or three contiguous wedges fitted to the profile of the seamount.

For these reasons, we look at finite planes and wedges as *elements of scattering*, so that we can interpret the character of the sea floor and the sea surface when they are remotely sensed.

As stated in the simple qualitative description of the interaction of sound with a section of a plane in Chapter 2, both rigid body scattering and scattering from a fluid interface are made up of reflection and diffraction, and sometimes transmission as well. In this chapter we look, quantitatively, at these components of scatter from elements of a rough surface, in two ways. The exact Biot–Tolstoy wedge solution, which was developed in Chapter 11, is a firm foundation that can be extended to wedge geometries that are the elements of scattering from rough surfaces as varied as the ocean bottom, sea ice ridges, and seamounts. The

Helmholtz–Kirchhoff method is the best-known classical technique for some of these problems. The two methods are compared in some simple, fundamental cases.

12.1 The Helmholtz–Kirchhoff Integral for Surface Scatter

The Helmholtz–Kirchhoff (HK) technique, an attractive implementation of Huygens' Principle, gives one a "feel" for the problem. However, the solutions often turn out to be approximate rather than exact. The method was reviewed in Chapter 7 and applied to scattering from fish in Chapter 9. Detailed laboratory tests, to be described in this chapter, show that the HK theory yields good predictions for diffraction backscatter from a plate only when the sound incidence is nearly perpendicular to the surface and when the frequency is high. The general consequences of the approximations of the Helmholtz–Kirchhoff method, when used with the Kirchhoff approximation, have been evaluated, and some solutions have been substantially improved by several authors. Meecham (1956) was the first to show that additional terms can be neglected when the minimum radius of curvature of the surface is much greater than the acoustic wavelength. De Santo and Shisha (1974) gave a numerical solution that includes additional terms. Thorsos (1988) proved that, for a long-crested, randomly rough surface, it is the spatial correlation length that must be greater than the acoustic wavelength for the Kirchhoff approximation to yield accurate results. Many of these "corrections" to the HK theory are sometimes moot because the Biot–Tolstoy exact solution for scattering by a wedge (or plate) agrees with all experiments for several specific surface scattering elements such as plates and wedges, whereas the HK solution often does not.

12.2 Implementation of Biot–Tolstoy Theory of Impulse Scatter from Wedges and Plates

12.2.1 THEORY FOR INFINITE WEDGES

To provide a building block for rough surface scattering, we turn to a simplified but accurate interpretation (Medwin 1981) of the rigorous Biot–Tolstoy (1957) theory of diffraction by a rigid infinite wedge. As discussed in Chapter 11, Biot and Tolstoy used the "normal coordinate method" to solve the ideal rigid wedge problem in the time domain. The detailed derivation is in Chapter 3 and Appendix 5 of Tolstoy and Clay (1987). The complete solution describes two

components of the scatter: (1) a set of images (virtual sources that replace the reflecting surfaces), the number of which is a function of the wedge angle and the angles of incidence and scatter as described in Chapter 11; and (2) a true diffraction wave from the wedge crest. A big advantage of the BT solution is that it gives the *times* of the reflections and diffraction directly, as well as the time-varying *amplitudes*. The solution may then be transformed to the frequency domain as needed.

A principal interest in this chapter is the diffraction from the exterior wedge — that is, the body wedge, with $\theta_w > 180°$ as shown in Fig. 12.2.1. When the wedge angle is opened up to $\theta_w = 2\pi$, the ridge of the body wedge is the mating edge of the two semi-infinite plates.

For sound diffracted from a rigid wedge, Bremhorst (1978) and Medwin (1981) reinterpreted Equation 5.24 of Biot–Tolstoy (1957), which had concluded with the applied mathematical description of a "rate of change of the scalar potential function," rather than the experimentally verifiable "acoustic pressure." The trick was to replace the BT doublet source by a point source Dirac delta function of volume flow, $\dot{V}$, at $t = 0$. Section 4.1 shows that, at the instant when there is this injection of volume flow at a point, there is a spherical radiation of acoustic pressure given by

$$p = [(\rho_A \dot{V}/(4\pi R))][\delta(t - R/c)] \tag{12.2.1a}$$

Note: For digital implementation, one writes the impulse pressure field radiated into free space as

$$p = (P_0 R_0/R)(\Delta t)\delta_f(t - R/c) \tag{12.2.1b}$$

where δ_f is the source finite delta function Equation 3.1.1, which is defined in terms of impulse duration Δt.

$$\delta_f(t) = 1/\Delta t \quad \text{for} \quad 0 \le t \le \Delta t \quad \text{and} \quad \delta_f(t) = 0 \quad \text{otherwise} \tag{12.2.1c}$$

The introduction of Equation 12.2.1 into the BT theory (which has been called the BTM solution) permitted Biot–Tolstoy's Equation 5.24 to become the following simple expression for the diffracted pressure from a rigid wedge as a function of time, the rate of volume flow, and the source/receiver wedge geometry, which could readily be transformed to the frequency domain.

$$p(t) = \left(\frac{-\dot{V}\rho_A c}{4\pi\theta_w}\right)\left(\frac{\beta_+}{rr_0 \sinh \eta}\right) \exp(-\pi\eta/\theta_w), \quad t \ge \tau_0 \tag{12.2.2a}$$

$$p(t) = 0 \qquad t < \tau_0$$

where (see Fig. 12.2.1a) r_0 and r are perpendicular ranges from source or receiver to wedge crest, respectively; θ_0 and θ are angles from a wedge side to source or receiver, respectively; θ_w is the wedge angle measured in the fluid as shown; y is the separation of the range vectors at the wedge crest; τ_0 is the "least" (minimum) time from source to crest to receiver; ρ_A and c are the density and sound speed of the medium; and $\dot{V}$ is the source strength in m^3/s.

Note: Comparison with Equation 11.8.64, which was developed in terms of an impulse pressure P_0 of duration Δt at source range R_0, shows that

$$\dot{V} = \frac{4\pi P_0 R_0}{\rho_A} \Delta t \tag{12.2.2b}$$

Also, for a rigid wedge, as given in Equation 11.8.63,

$$\beta_+ = \sum \frac{\sin\left[(\pi/\theta_w)(\pi \pm \theta \pm \theta_0)\right]}{1 - 2\exp\left(-\pi\eta/\theta_w\right)\cos\left[(\pi/\theta_w)(\pi \pm \theta \pm \theta_0)\right] + \exp\left(-2\pi\eta/\theta_w\right)} \tag{12.2.3}$$

where, from Equations 11.8.24 and 11.8.27,

$$\eta = \operatorname{arc\,cosh}\left[c^2t^2 - (r^2 + r_0^2 + y^2)\right]/(2rr_0) \tag{12.2.4}$$

and the least-time, from Fig. 12.2.1, is

$$\tau_0 = \left[(r + r_0)^2 + y^2\right]^{1/2}/c \tag{12.2.5}$$

For diffraction, we are interested in the time, τ, after the least time, τ_0,

$$\tau = t - \tau_0 \tag{12.2.6}$$

In terms of τ and τ_0, we have

$$\eta = \operatorname{arc\,cosh}\left[\frac{c^2(2\tau_0\tau + \tau^2)}{2rr_0} + 1\right] \tag{12.2.7a}$$

or

$$(\sinh\eta)^{-1} = \left[\left(\frac{c^2\tau_0\tau}{rr_0} + \frac{c^2\tau^2}{2rr_0} + 1\right)^2 - 1\right]^{-1/2} \tag{12.2.7b}$$

As in Equation 11.8.63, we employ the Greek letter Σ in Equation 12.2.3 as an abbreviated symbol to designate the sum of the four terms obtained by using the four possible combinations of signs:

$$(\pi + \theta + \theta_0),\ (\pi + \theta - \theta_0),\ (\pi - \theta + \theta_0),\quad \text{and}\quad (\pi - \theta - \theta_0)$$

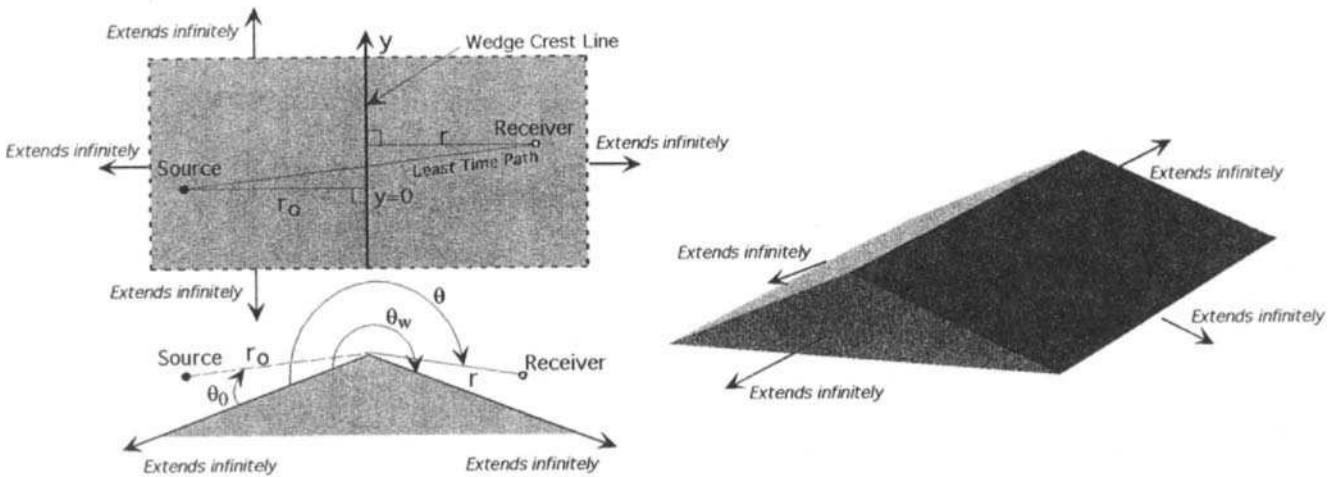

Figure 12.2.1 Wedge geometry and symbols for the BT solution, shown for a body wedge. The unfolded geometry and the least-time path are pictured.

The BT theory has been broadened substantially by Kinney et al. (1983), Chu (1990) and Davis and Scharstein (1997) to apply to wedge surfaces of different impedances. For example, for pressure-release situations, the zero pressure boundary condition is realized by reversing the signs of two of the terms so that $(\pi + \theta + \theta_0)$ becomes $-(\pi + \theta + \theta_0)$ and $(\pi - \theta - \theta_0)$ becomes $(-\pi + \theta + \theta_0)$. That form of Equation 12.2.3 is called β_-. The various forms of the solution were given in Equations 11.8.65 through 11.8.68.

The infinite wedge diffractions given by Equations 12.2.2 to 12.2.7 may be supplemented by reflections as described in Chapter 11 and as determined by the geometry. For the reflection amplitude, the R in Equation 12.2.1 is the total path length fom source to reflecting facet to receiver.

12.2.2 REFLECTION AND DIFFRACTION IN THE TIME DOMAIN: REALIZATIONS AND VERIFICATIONS

The theoretical prescription for scatter of a Dirac delta function pressure by an infinite rigid wedge has been effectively realized by several laboratory experiments in order to verify the predictions and to model scattering elements at sea. To represent the conditions of the theory, the following three techniques are used.

(1) *Dirac delta function sound source*: A short-duration, impulselike source is used, and the theory for a delta function source, section 12.2.1, is convolved with the experimental source wave form to produce the predicted wave form for the scatter. This is then compared with the laboratory experimental wave form.

(2) *Infinite wedge*: The experiment is concluded before receiving scatter from the ends of the finite wedge.

(3) *Rigid wedge*: The laboratory wedge material has a high acoustic impedance (ρc) relative to the surrounding medium. To maximize the contrast, usually the medium is air rather than water, and often the wedge material is plasterboard (also called sheetrock) which has a smooth surface, and which damps compressional and shear waves which are absent from the theory.

Right-Angle Wedge

Li and Clay (1988) studied reflected and diffracted components of forward scatter in the time domain by using a laboratory right-angle rigid wedge ($\theta_w = 270°$) as

shown at the left of Fig. 12.2.2. The source and receiver were on a line 79 cm above the wedge, and the theoretical BT solution for a delta function source was calculated for ten different displacements at the constant source to receiver separation 81 cm (right side of Fig. 12.2.2). The direct signal and theoretical reflection and diffraction components are calculated from Equation 12.2.2. The direct and reflected sound appear as sharply peaked curves which represent the Dirac δ function. The much weaker diffraction signal is negative when the midpoint of the source/receiver is over the horizontal surface (positive x displacements) and positive when it is beyond the edge (negative x values). The diffraction is stronger when the midpoint between source and receiver is closer to over the crest of the wedge. When the reflection point is at the edge, $x = 0$, there is a half-amplitude "reflection" from the corner.

The laboratory experiment uses a signal as shown in Fig. 12.2.3. The experimental result is at the left side of Fig. 12.2.4. The predicted scatter, at the right side of Fig. 12.2.4, is obtained by convolving the theoretical solution with the experimental signal shown in Fig. 12.2.3. Direct, reflected, and diffracted signals are all seen in Fig. 12.2.4. For positive values of x, there are reflections which dominate the total scattered signal; the delayed, negative diffraction is just evident. For negative values of x, the only scatter is the positive diffraction component.

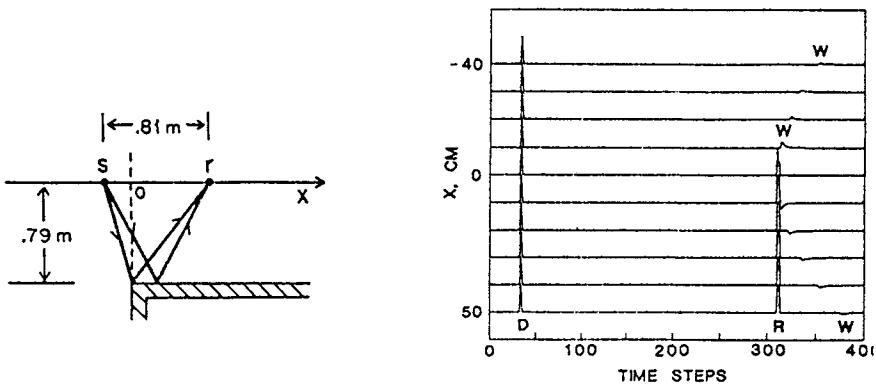

Figure 12.2.2 *Left*, geometry of the theoretical and experimental test of the theory. *Right*, the theoretical wedge solution for 10 positions of a delta function source/receiver at fixed separation on a line over the wedge. The direct signal is D, reflected is R, and wedge diffracted is W. The half-amplitude diffraction occurs at $x = 0$, the midpoint of the source/receiver over the crest of the wedges. (From Li, S., and C. S. Clay, "Sound transmission experiments from an impulsive source near rigid wedges," *J. Acoust. Soc. Am.* **84**, 2135–43, 1988.)

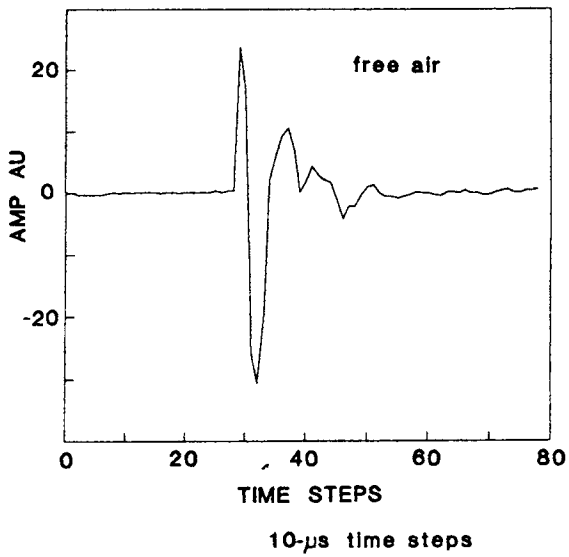

Figure 12.2.3 Free space reception of signal from a spark source. Receiver is a 0.6 cm electret microphone. Signal sampled at 10 μs intervals. (From Li, S., and C. S. Clay, "Sound transmission experiments from an impulsive source near rigid wedges," *J. Acoust. Soc. Am.* **84**, 2135–43, 1988.)

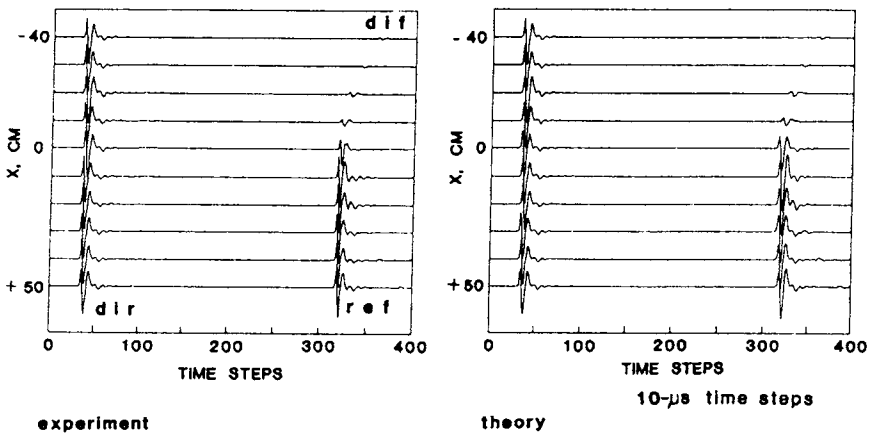

Figure 12.2.4 Experimental and theoretical signals of direct, reflected, and diffracted sound from the wedge-scattering experiment sketched in Fig. 12.2.2. The direct and reflected (when it exists) signals occur at constant time delays, independent of source/receiver positions. The diffraction timing, amplitude, and phase depend on the position of the source/receiver with respect to the wedge ridge. (From Li, S., and C. S. Clay, "Sound transmission experiments from an impulsive source near rigid wedges," *J. Acoust. Soc. Am.* **84**, 2135–43, 1988.)

Right-Angle Rigid Step

Chambers and Berthelot (1994) have used the BTM method — Equations 12.2.1 to 12.2.7 — to predict the contributions from the reflection and the two diffractions that occur in propagation over a step discontinuity (Fig. 12.2.5). Their extensive impulse measurements have confirmed that the theory provides accurate time-domain predictions for that geometry. They also show that the acoustic field scattered from the step is essentially unchanged if the step is smoothly curved with a radius less than the predominant wavelength of the sound. The experiment can be considered to be a representation of propagation over an escarpment at sea.

The geometry is at the left in Fig. 12.2.5 (not to scale). The source is a spark with peak-to-trough duration approximately 50 μs. In addition to the direct incident sound "i" (see Fig. 12.2.6), the step results in potential reflection from the top plate, "r1"; reflection from the bottom plate, "r2"; and diffraction from the top exterior corner at E "d1" and component "d2" which is diffracted at the top corner and then reflected at the bottom of the step. Multiple diffractions, which would be of lesser strength, are not considered.

Two, three, or four of the five signal components can be received in the five different zones shown at the right of Fig 12.2.5. A microphone in zone 1 receives i, r1, and d1; in zone 2, i, r1, d1, and d2; in zone 3, i, d1, and d2; in zone 4, i, r2, d1, and d2; in zone 5, d1 and d2. These expectations have been confirmed by moving a microphone at radius 34.3 cm over an arc that passes from zone 4

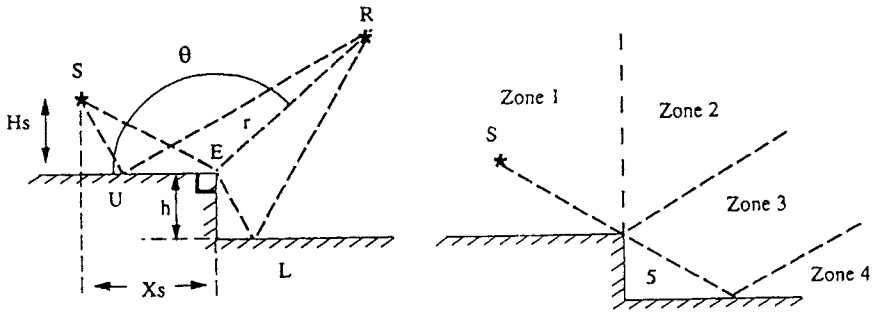

Figure 12.2.5 *Left*, the geometry of the step discontinuity experiment, $H_s = 19.3$ cm $X_s = 46.6$ cm and $h = 1.8$ cm (the height in the figure has been exaggerated). *Right*, the five zones of potential interference between the four principal components of incidence, reflection, and diffraction. (From Chambers, J. B., and Y. H. Berthelot, "Time domain experiments on the diffraction of sound by a step discontinuity," *J. Acoust. Soc. Am.* **96**, 1887–92, 1994.)

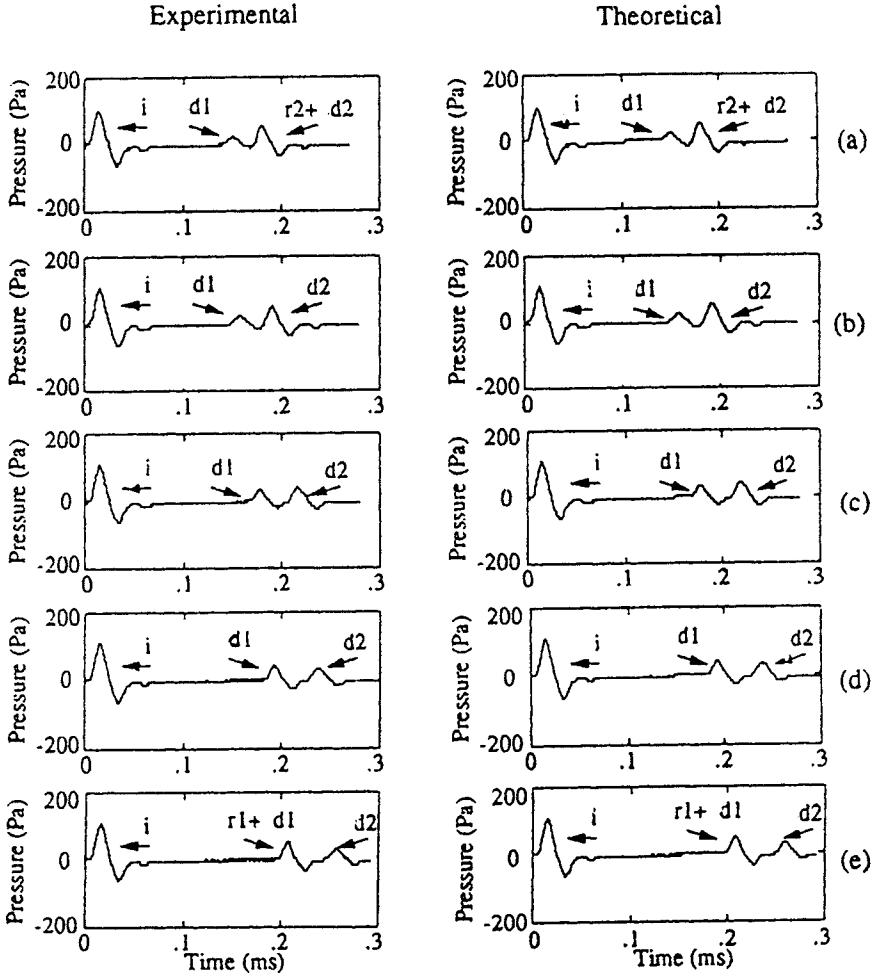

Figure 12.2.6 Experimental and theoretical reflections and diffractions within and near transition zones for a rigid step geometry. Receiver moves along arc 34.3 cm from corner E (see Fig. 12.2.5). (a) In zone 4 close to zone 3. (b) At edge of zone 3. (c) In middle of zone 3. (d) At edge of zone 3. (e) In zone 2, close to zone 3. (From Chambers, J. B., and Y. H. Berthelot, "Time domain experiments on the diffraction of sound by a step discontinuity," *J. Acoust. Soc. Am.* **96**, 1887–92, 1994.)

through zone 3 to zone 2. Note that in Fig. 12.2.6 the simple diffraction d2 moves in to replace the reflected diffraction r2 at the edge of zones 3 and 4, and the top plate reflection r1 comes in as one moves into zone 2. The experimental and theoretical oscillograms are virtually identical.

Right-Angle Rigid Wedge on a Rigid Plane

The geometry of a 90° triangular rigid wedge protruding above a rigid plane (Fig. 12.2.7) has been examined by Li et al. (1994). In this more complicated case, in addition to reflections and "single" diffractions, there are significant diffractions of the diffracted signals, which we call "double diffractions." The analysis of double diffraction is in section 12.3.2.

12.2.3 DIGITAL IMPLEMENTATION FOR FINITE WEDGES

The diffraction arrival in the time domain was discussed in section 11.8.3. One way to implement Equation 12.2.2 for digital calculations is to obtain the average $p(t)$ over each of many discrete intervals. This produces a series of impulses as shown in Fig. 12.2.8 from regions of the wedge as indicated in the inset of Fig. 12.2.8 and in Fig. 12.2.9. The integration may be performed by using the DCADRE routine (Digital Cautious Adaptive Romberg Extrapolation), which is listed in IMSL Library Edition 9.2 (1984). In fact, away from the shadow boundary and the reflection direction, the pressure is generally changing slowly enough to permit the mid-time instantaneous value to represent the average with only a small error. The time increment ΔT is selected to produce the minimum bandwidth BW (Min) $= (2\,\Delta T)^{-1}$ for the desired frequency spectral description.

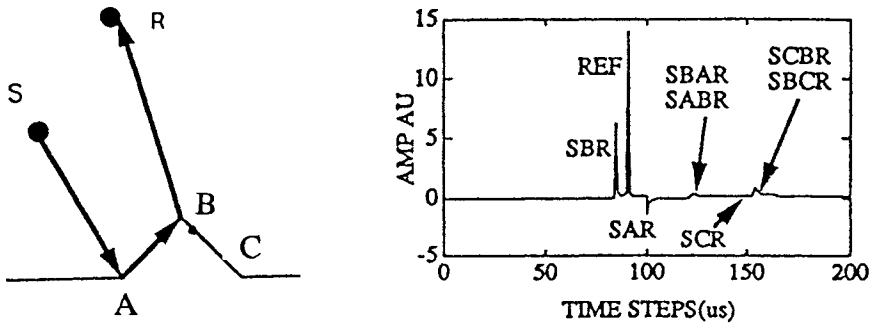

Figure 12.2.7 Geometry (*left*) and reflection and diffraction amplitudes (*right*) for a 90° rigid wedge on a rigid plane. The paths are indicated by the combination of letters, for instance, SBR is a single diffraction at B; REF is a simple reflection; SABR is a double diffraction of the signal that starts at S, is diffracted first at A and then at B, and then goes to the receiver. In (x, y, z) cm; the source is at $(20, -13.0)$, receiver is at $(20, +13,0)$, where y is the ridge direction. (From Li, S., D. Chu, and C. S. Clay, "Time domain reflections and diffractions from facet-wedge constructions: acoustic experiments including double diffractions," *J. Acoust. Soc. Am.* **96**, 3715–20, 1994.)

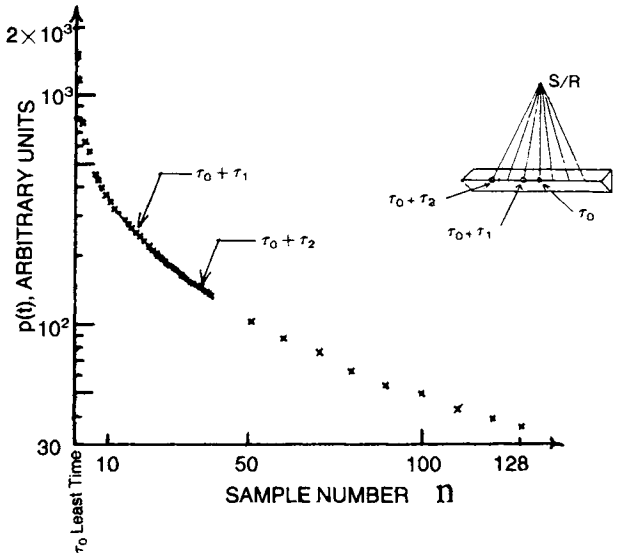

Figure 12.2.8 Some of the discrete values of impulse pressure for diffracted backscatter from a rigid right-angle wedge ($\theta_w = 270°$) in air, calculated from Equation 12.2.2. The impulse pressures are separated by $\Delta T = 1$ μs. The range is $r = r_0 = 50$ cm, and the angles of incidence and scatter are $\theta = \theta_0 = 146°$. (From Medwin, H., M. J. Browne, K. R. Johnson, and P. L. Denny, "Low frequency backscatter from Arctic leads," *J. Acoust. Soc. Am.* **83**, 1794–1803, 1988.)

Where the pressure is rapidly changing as a function of travel time, the integration for the singular least-time point may be unstable. Keiffer et al. (1994) replaced the original integration range, as shown in Fig 12.2.8, by a more robust integration with a different definition of the index $n = 0$. In Keiffer's method, the separation between adjacent points is still ΔT, but the integration is centered on $\tau = (\Delta T)/2, 3(\Delta T)/2, 5(\Delta T)/2$, and so forth:

$$\left\langle p\left(\tau_0 + \frac{\Delta T}{2}\right)\right\rangle = \frac{1}{\Delta T}\int_{\tau_0}^{\tau_0 + \Delta T} p(t)\, dt \qquad \textbf{(12.2.8a)}$$

In general,

$$\tau_n = \left(\frac{2n+1}{2}\right)\Delta T \qquad \textbf{(12.2.8b)}$$

with $n = 0, 1, 2$, and so forth.

Once the diffracted pressure given by Equations 12.2.2 and 12.2.3 has been

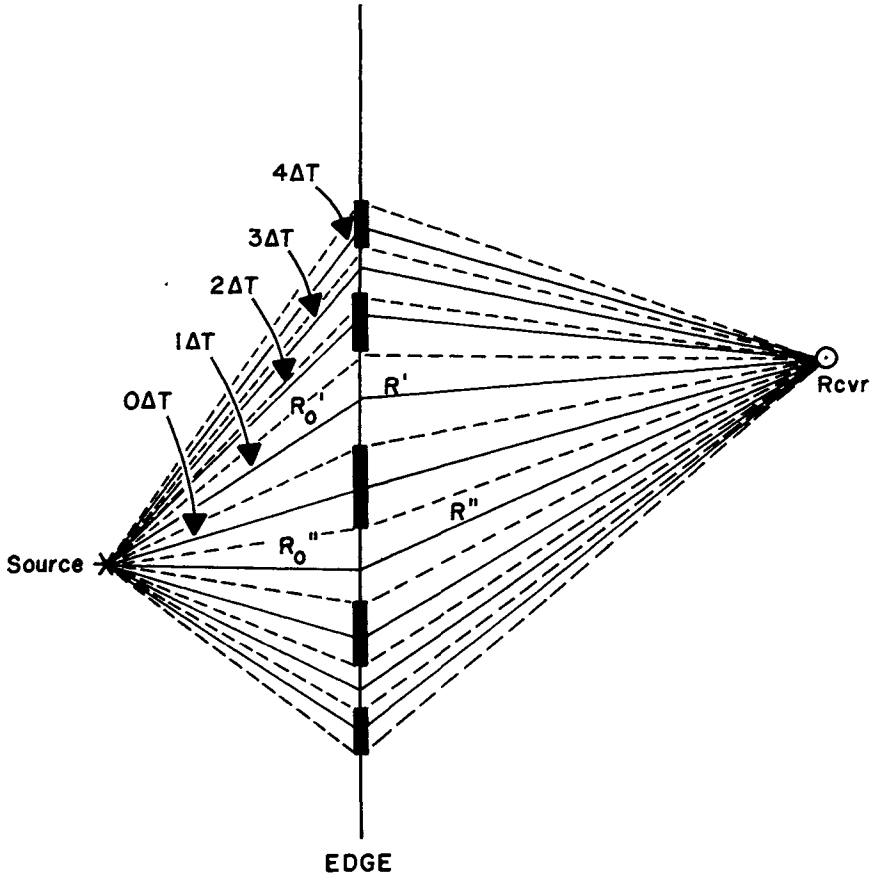

Figure 12.2.9 Unfolded geometry showing discrete paths (solid lines) and their boundaries at $n \pm (1/2)\,\Delta T$ (dashed lines) for the assumption that $n = 0$ is the least-time path. The blackened regions on the wedge crest are Huygens sources for even-ordered time lags. (From Medwin, H., E. Childs, and G. M. Jebsen, "Impulse studies of double diffraction: a discrete Huygens interpretation," *J. Acoust. Soc. Am.* **72**, 1005–13, 1982.)

digitized, the continuous diffracted signal may be interpreted as a series of contributions from Huygens wavelets that radiate sequentially from the wedge ridge, starting with the largest contributor from the intersection of the least-time path with the wedge. In this interpretation, the least-time impulse is the first and the strongest of the sequence; it is followed by pairs of wavelets of lesser strength from each side of the least-time intercept. Fig. 12.2.9 shows this interpretation.

12.2.4 SIMPLIFICATIONS

The largest diffraction contributions occur for incremental times that are small compared to the least-time, $\tau \ll \tau_0$. Then certain analytical simplifications can be calculated,

$$\lim_{\tau \to \tau_0} (r\, r_0 \sinh Y\ )^{-1} \to (2\tau_0\, \tau\, c^{\,2}\, r\, r_0)^{-1/2} \tag{12.2.9}$$

and, except near the geometrical shadow boundary or reflection direction, we have the appproximation

$$p(\tau) \simeq B\tau^{-1/2} \tag{12.2.10}$$

where

$$B = \left[\frac{\dot{V}\rho_A \beta}{4\pi\sqrt{2}(\tau_0 r r_0)^{1/2}\theta_w}\right]$$

and

$$\dot{V} = 4\pi P_0 R_0(\Delta t)/\rho_A$$

Under these conditions, except for the rapidly changing pressure at the least-time point $n = 0$, the discrete pressures at $n\ \Delta T$ are given simply by

$$\begin{aligned} \langle p\,(n\,\Delta T\ )\rangle_{n \geq 1} &= \frac{B}{\Delta T}\int_{(n-1/2)\Delta T}^{(n+1/2)\Delta T} \tau^{-1/2}\, d\tau \\ &= B\left(\frac{2}{\Delta T}\right)^{1/2}\left[(2n+1)^{1/2} - (2n-1)^{1/2}\right] \end{aligned} \tag{12.2.11}$$

The effect of being close to the geometrical shadow boundary has been evaluated (Medwin et al. 1982) by considering the small angular displacement, ε, away from the shadow boundary:

$$\theta = \theta_0 + \pi + \varepsilon \tag{12.2.12}$$

It is found that Equation 12.2.11 holds, provided that

$$\varepsilon >> \left|\frac{c\tau_0}{(r\, r_0)^{1/2}}\right|\left(\frac{\tau}{\tau_0}\right)^{1/2} \tag{12.2.13}$$

The spectral response is shown in Fig. 12.3.1.

12.3 Digital Calculations of Biot–Tolstoy Diffraction in the Frequency Domain

In considering the spectral response implied by the BT impulse theory, one notes first that, away from the shadow boundary or reflection direction, for times small compared with the least time, $\tau \ll \tau_0$, the Fourier transform of Equation 12.2.10 gives the frequency spectrum,

$$P(f) = (B/2)(1 + i)f^{-1/2} \tag{12.3.1}$$

where B is given in Equation 12.2.10.

The $f^{-1/2}$ dependence is an analytical statement that describes the commonly observed fact that high frequencies do not bend around corners as well as low frequencies do.

The common reference pressure is the "white noise" spectral description of a Dirac delta function free-field point source,

$$P_\delta(f) = \frac{\dot{V}\rho_A}{4\pi RN\Delta T} = \frac{P_0 R_0}{R}\left(\frac{\Delta t}{N\Delta T}\right) \tag{12.3.2}$$

where $N\,\Delta T$ is the total duration of the sequence of samples that has been Fourier-transformed, and is $\dot{V}$ the source strength, m^3/s. The time between samples, ΔT, is selected to yield the bandwidth, BW, that is ultimately desired, where $BW_{\text{Min}} = (2\,\Delta T)^{-1}$. Practically, one sets $BW = 4BW_{\text{Min}}$ This achieves the smaller values of ΔT that are desirable for the rapidly changing strong early arrivals.

It is convenient to form the ratio of Equations 12.3.1 to 12.3.2 and thereby obtain the relative diffracted pressure compared with the point source pressure for a given frequency. This quantity is independent of the source strength $\dot{V}$ or the source reference pressure P_0 and is a popular way to show the relative strength of the diffracted signal. Such a description is presented in Fig 12.3.1, where the spectrum is plotted as a function of penetration into the shadow region, ε. As ε approaches zero, the diffracted sound approaches one-half of the free-field pressure (−6 dB), independent of the frequency. The $f^{-1/2}$ asymptote is recognized as the slope for low frequencies at $\varepsilon = 10°$ in this case.

Detailed predictions of rigid wedge impulse theory (Equation 12.2.2) and its transform to the frequency domain (Equation 12.3.1) have been verified

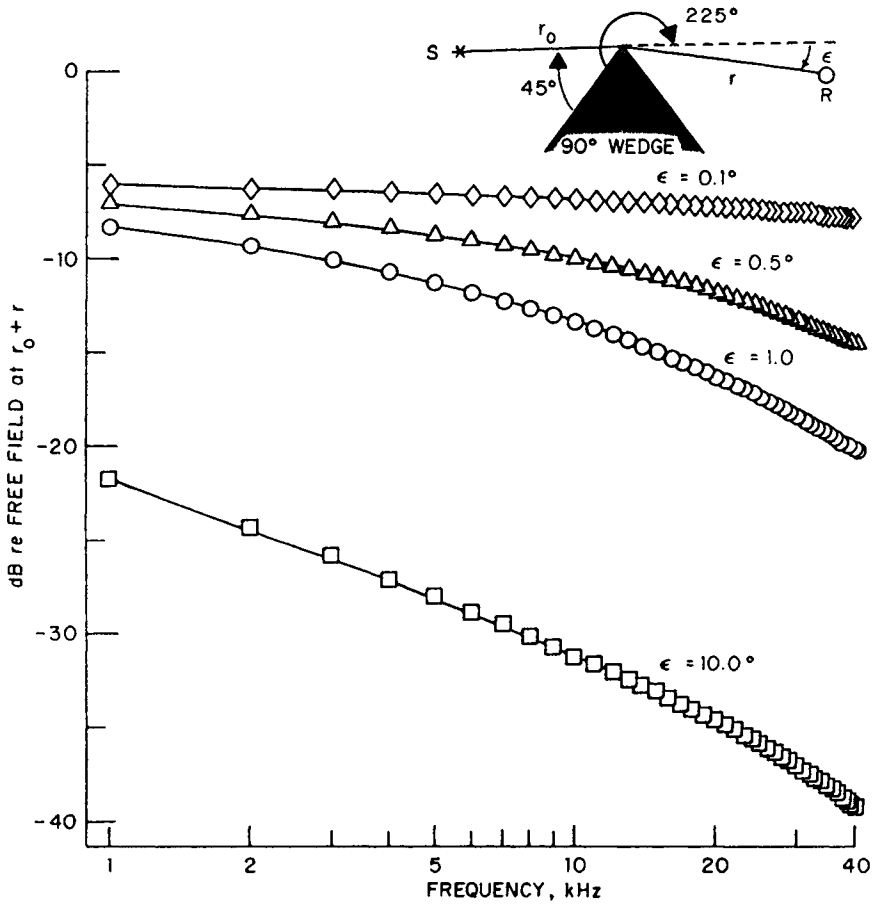

Figure 12.3.1 Spectra of relative diffracted pressure as a function of angle of penetration, ε, into the geometrical shadow region when $r = r_0 = 100\,\text{m}$, $\theta_0 = 45°$ for a right-angle wedge ($\theta_w = 270°$). (From Medwin, H., E. Childs, and G. M. Jebsen, "Impulse studies of double diffraction: a discrete Huygens interpretation," *J. Acoust. Soc. Am.* **72**, 1005–13, 1982.)

by several laboratory tests employing realistic rigid surfaces in air. In these validating experiments, solid wedges are used in air because a surface is more nearly "rigid" in air than in water, owing to the greater ρc mismatch. But also, since one must avoid extraneous scatter from the ends of a real wedge, the required size of the wedge can be one-fifth as great in air as in water.

The polar diagram of BT diffraction scatter for a right-angle wedge, Fig.12.3.2, gives an instant comprehension of the relative amplitude and

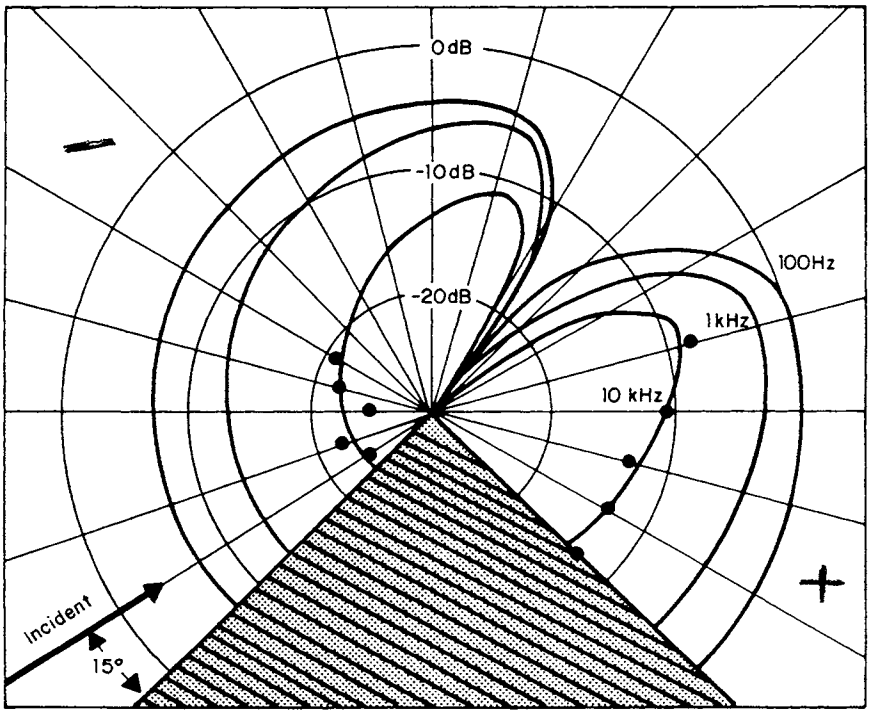

Figure 12.3.2 Polar diagram of diffraction loss compared with divergence loss for a free-field range $r + r_0$ for a right-angle rigid wedge, $\theta_w = 270°$ in air. The ranges are $r = r_0 = 25$ cm. The phase is positive for the right lobe and negative for the left lobe. Comparison with experimental data dots at 10 kHz is from Bremhorst (1978) and Bremhorst and Medwin (1978). (For details, see Medwin, H., "Shadowing by finite noise barriers," *J. Acoust. Soc. Am.* **69**, 1060–64, 1981.)

different phase of the scatter in diffferent directions. This calculation is a model of the backscatter and the forward diffraction into the "shadow" region of an escarpment at sea. This polar diagram, which shows diffraction loss (in dB relative to the level if the signal had diverged spherically from a point source to the total range $R = r + r_0$), when compared to experiment, was the first evidence of the effectiveness of the BT theory.

The frequency spectral response, such as in Fig. 12.3.2, is a quantitative measure of the excellent agreement of BT theory with experiment for certain prototype geometries. The limited realm of agreement of HK theory with experiment is demonstrated in the next section.

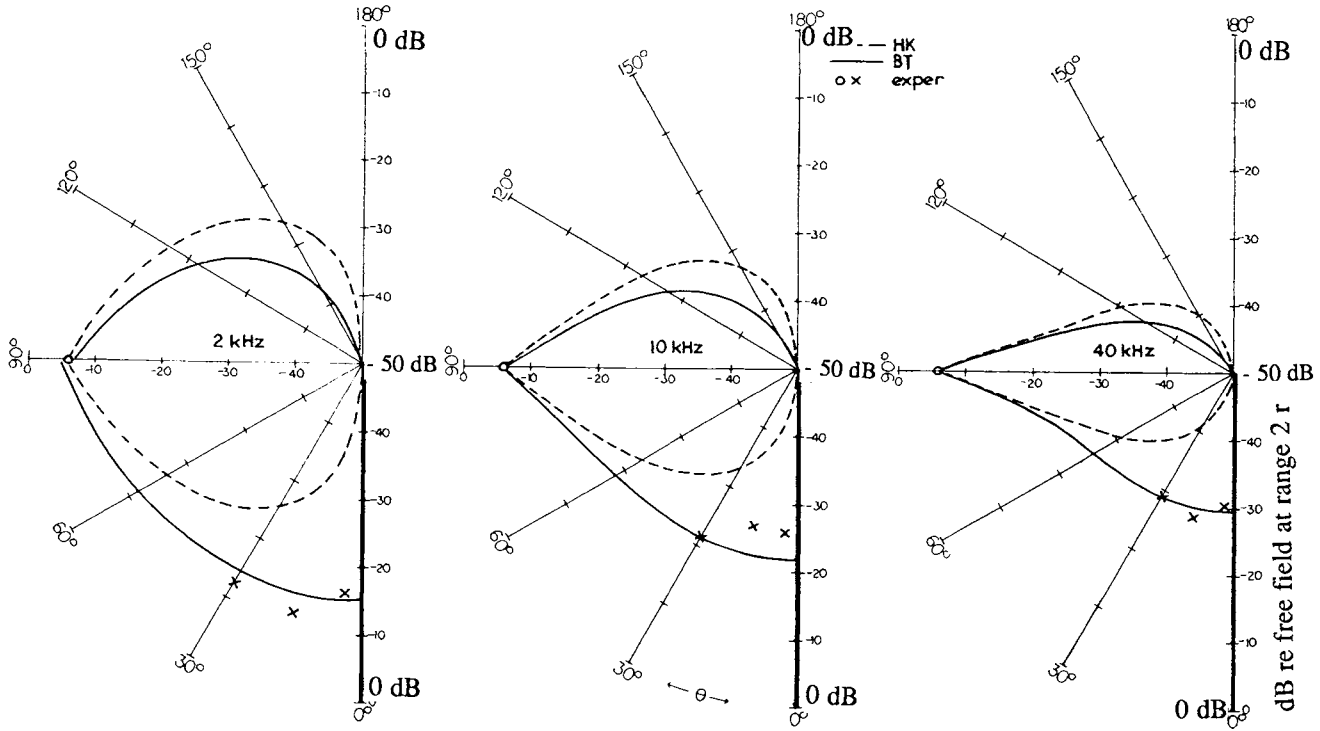

Figure 12.3.3 Angular dependence of diffraction backscatter from a rigid plate at 2, 10, and 40 kHz, predicted by HK (dashed line) and BT (solid line) theories, and measured at range 25 cm in air. (From Jebsen, G. M., and H. Medwin, "On the failure of the Kirchoff assumption in backscatter," *J. Acoust. Soc. Am.* **72**, 1607–11, 1982.)

12.3.1 COMPARISON OF DIFFRACTION BACKSCATTER PREDICTIONS OF HK AND BT THEORIES

To compare and test the HK and BT theories of diffraction backscatter, two experiments were conducted in air, with the source/receiver at a separation of 25 cm fom two different diffractors (Jebsen 1981). One diffractor was a rigid plate with one edge exposed, $\theta_w = 360°$, the other a rigid right-angle wedge, $\theta_w = 270°$. The more prominent reflections from the perpendicular surfaces were excluded from the analysis by gating the backscattered signal in the experiment.

Fig. 12.3.3 shows the results at three frequencies for the semi-infinite plate. The experiment agrees with the BT theory at all angles measured. It agrees wih the HK prediction only at (and presumably near) normal incidence to the diffracting plate. The HK prediction of zero acoustic pressure on the plate is far from the true behavior for low frequencies, although its discrepancy becomes smaller at higher frequencies.

The comparison of the two theories with laboratory experiment is shown for a right-angle rigid wedge in Fig. 12.3.4. Again the experiment agrees with BT theory. The error in the HK prediction has decreased from about 15 dB for $\theta = 15°$ to approximately 10 dB for $\theta = 30°$.

12.3.2 DOUBLE DIFFRACTION

The Huygens interpretation of the action at a diffracting edge, as shown in Fig. 12.2.9, is that the original source initiates reradiation from "secondary sources" on the diffracting edge. The pressure signal received at the field point is the accumulation of the radiation from delta function sources initiated at the proper times along that edge.

In many problems (for example, shadowing by a seamount or *guyot*) there is a second diffracting edge, between the first one and the receiver. Fig. 12.3.5 is an idealization of the geometry.

From the Huygens point of view, there will be an infinite number of sources on the first edge, each of which spawns an infinite number of sources on the second edge. Practically, because they are far stronger than the later arrivals, only the earliest arrivals need to be considered.

The "secondary source" contributions come in pairs from points on either side of the least-time crestal source, which is located at the point of intersection of the source-receiver axis and the first crestline. These secondary sources will have the source strengths $\dot{V}ssn$, which are necessary to produce the expected field after

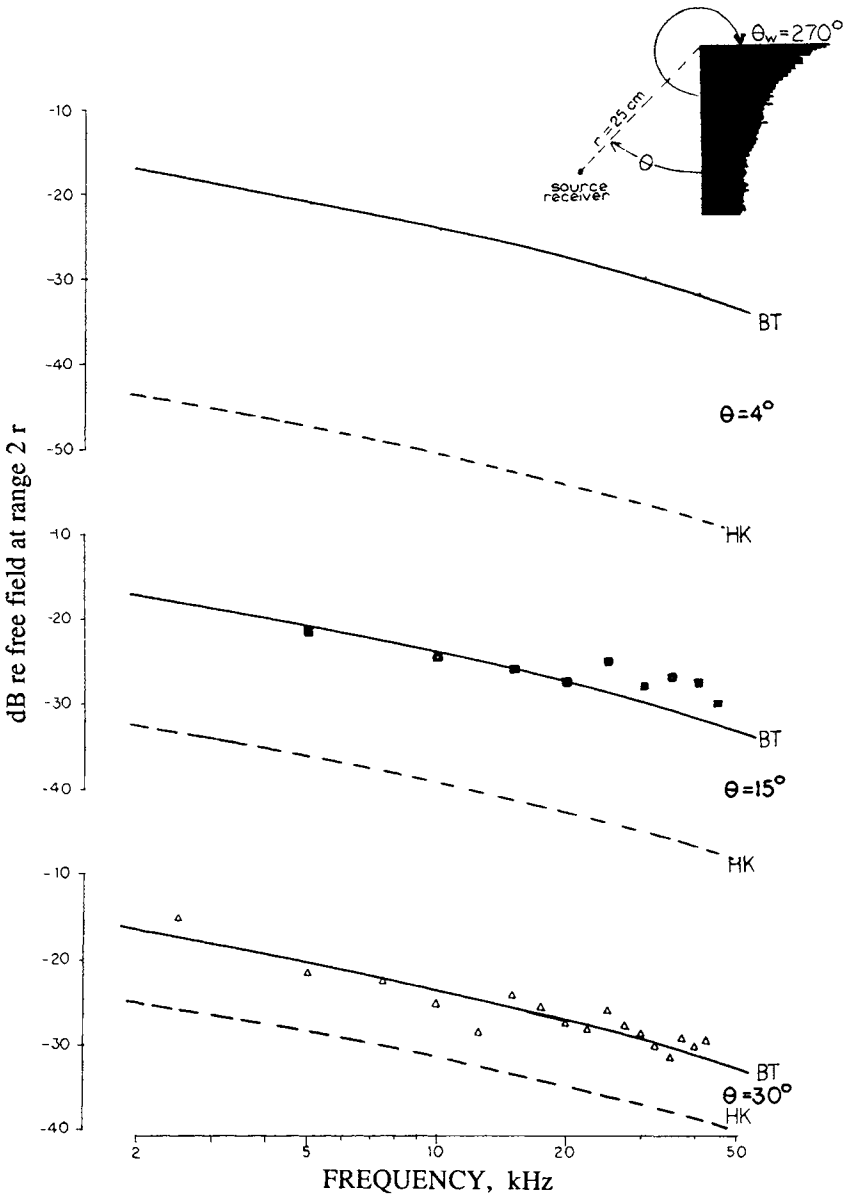

Figure 12.3.4 Backscatter diffraction from a right-angle wedge measured in air at range $r = r_0 = 25$ cm. Comparison between experiment, Biot–Tolstoy theory, and Helmholtz–Kirchhoff theory at three different angles with respect to the wedge face. (Data from Bremhorst, 1978; Theory from Jebsen, G. M., and H. Medwin, "On the failure of the Kirchoff assumption in backscatter," *J. Acoust. Soc. Am.* **72**, 1607–11, 1982.)

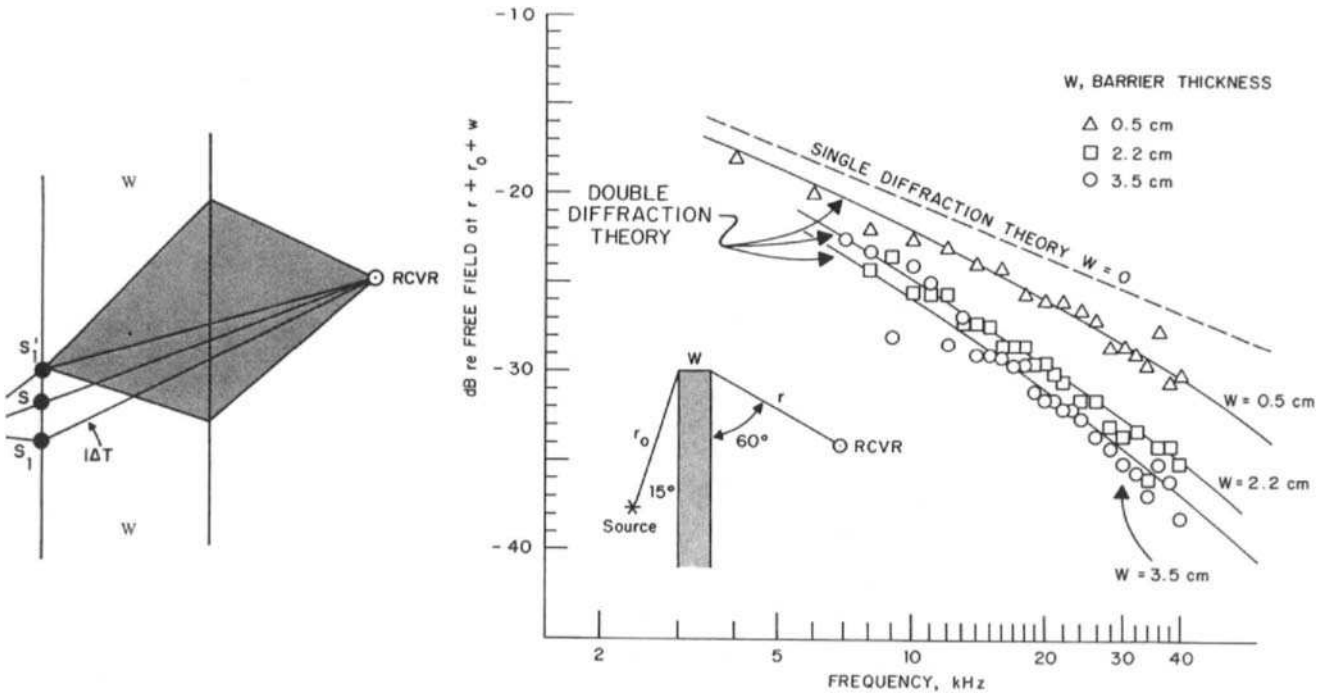

Figure 12.3.5 *Left*, double diffraction geometry for a barrier of thickness W. The general case is shown in the unfolded geometry with the least time contributor from S and the $n = 1$ contributors, S_1 and S_1', at 1 ΔT. One of the 1 ΔT contributors is shown as the source of a second line of diffractors from the second edge. *Right*, relative spectral loss calculated for three thick-plate barriers at range $r = r_0 = 25$ cm. The double-diffraction laboratory data points (Jebsen 1981; Medwin et al. 1982) compare well with the double-diffraction theory; the single-diffraction theory, dashed line, $w = 0$, does not describe the diffraction adequately. (From Medwin, H., E. Childs, and G. M. Jebsen, "Impulse studies of double diffraction: a discrete Huygens interpretation," *J. Acoust. Soc. Am.* **72**, 1005–13, 1982.)

traveling the range R from their crest positions to the field position. That is, for a symmetrical geometry, the n th secondary source has the strength

$$\dot{V}_{ssn} = \left(\frac{1}{2}\right) \frac{\langle p(n\Delta T)\rangle}{p_\delta} \dot{V} \tag{12.3.3a}$$

where

$$p_\delta = \frac{\dot{V}\rho_A}{4\pi R \Delta T} \tag{12.3.3b}$$

The calculation of the mean value < > follows the prescription of Equation 12.2.8. Calculations for nonsymmetrical contributions are considered in Medwin et al. (1982).

12.3.3 FORWARD DIFFRACTION AT A SEAMOUNT

Submerged mountains, "seamounts," can interrupt sound propagation and create a shadow zone behind the obstacle. This was conclusively demonstrated by Canadian experiments at Dickins seamount off the coast of British Columbia (Fig. 12.3.6). (The seamount was named for a respected scientist of the U.S. Coast and Geodetic Services, not the famous English author, Charles Dickens).

In the experiment at Dickins seamount, a CW shadowing loss of 15 dB at 230 Hz was first observed by Ebbeson and Turner (1983). Later, using an explosive source, a splitting of the signal was found by Chapman and Ebbeson (1983). The earlier arrival showed a frequency-dependent shadowing loss proportional to $f^{1/2}$; it was the only signal during high sea states.

The experimental results at sea have been explained by using a laboratory model to consider the two means by which sound may reach into the shadow. The later arrival, revealed by an impulse source, is due to multiple reflections between the insonified surface of the seamount and the ocean surface. This contribution, which repeatedly involves the ocean surface, cannot be found during high sea states because of losses by scattering at the rough ocean surface. The rough surface was modeled by a gravel-covered plate suspended over the laboratory seamount. The laboratory ratio of (wavelength)/(surface rms height) was the same as the ocean ratio λ/h for a Pierson-Moskovitz sea during the 35 knot wind, as calculated from Equation 13.1.12.

At this point we are more interested in the earlier arrival, which the model proved to be due to forward scatter along the rough insonified seamount face followed by diffraction over the crest of the seamount. Both at sea and in scale model experiments by Spaulding (1979) and Jordan (1981), this component was

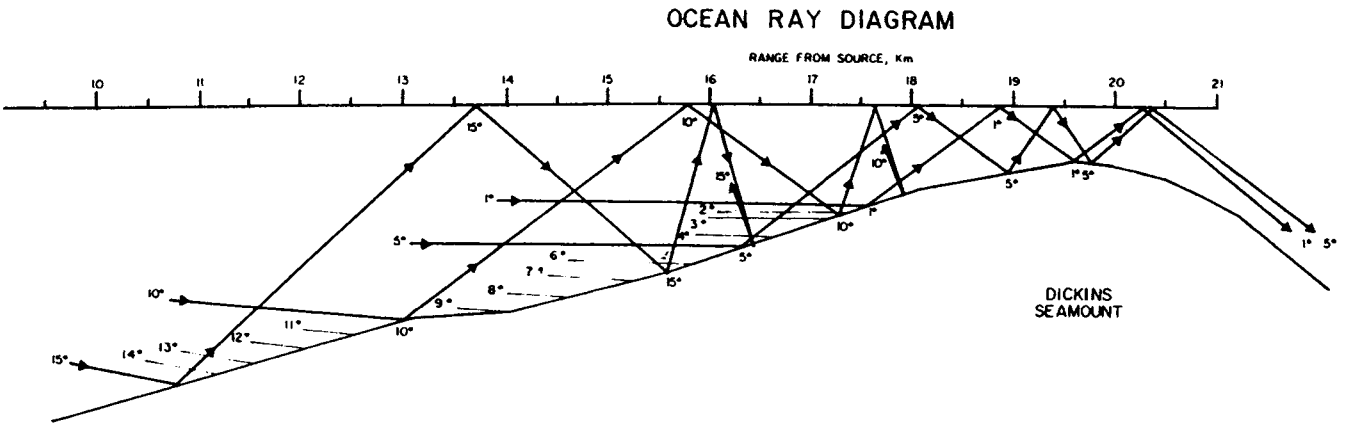

Figure 12.3.6 Reconstruction of sound wave interaction at upslope of Dickins seamount in experiments by Ebbeson and Turner (1983) and Chapman and Ebbeson (1983). The sound source is about 20 km to the left of the crest. The incoming rays are identified by their angles with the horizontal at the source. The 15° ray reflects on itself after 2 sea surface reflections and 3 interactions with the seamount; it does not go over the seamount. The 5° ray forward reflects from the seamount 3 times and from the ocean surface 3 times before it crosses over the seamount. The forward scattered wave at the rough seamount surface diffracts over the crest and arrives at the hydrophone sooner than the multiply reflected rays. However, it is weakened by scattering from the rough ocean surface, as well as from the seamount. (From Medwin, H., E. Childs, E. A. Jordan, and R. J. Spaulding, Jr., "Sound scatter and shadowing at a seamount: hybrid physical solutions in two and three dimensions," *J. Acoust. Soc. Am.* **75**, 1478–90, 1984.)

found to have the $f^{-1/2}$ dependence predicted by the simplified spectral version of the BT theory (Equation 12.3.1). The work is summarized in Medwin et al. (1984).

The diffraction component can be roughly estimated by assuming that the seamount is a simple exterior rigid wedge of upslope and downslope 14° with the horizontal ($\theta_w = 208°$), where we ignore all the bumps along the way. A more accurate prediction is obtained by using the double-diffraction technique described in the previous section. Equation 12.3.1 shows that there is a range dependence $r^{-1/2}$ and a frequency dependence $f^{-1/2}$ (or $\lambda^{+1/2}$). Therefore, in order to have the scaling independent of range and frequency, the magnitude of the *diffraction strength, DS*, is defined in terms of the diffracted spectral pressure, P_D,

$$DS = 20 \log \left(\frac{P_D r_0}{P_0 R_0} \right) \left(\frac{r}{\lambda} \right)^{1/2} \tag{12.3.4}$$

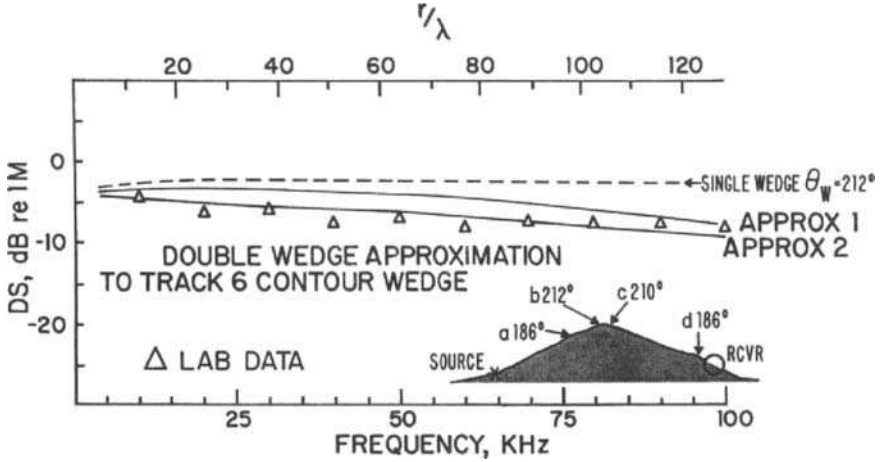

Figure 12.3.7 Comparison of laboratory diffraction strengths (data triangles, Δ) plotted versus r/λ (upper abscissa) with a theoretical calculation for a symmetrical single wedge of slope 14° and with two different freehand-drawn two-dimensional double-diffraction models of Dickins seamount shown in silhouette. The lower abscissa in kHz are the frequencies of the sound in the laboratory model where the range was several centimeters. In model approximation 1 it is assumed that the two wedges are $\theta_w = 186°$ and $\theta_w = 210°$ at crests a and c, respectively; in the second model it is assumed that the wedges have angles $\theta_w = 212°$ and $\theta_w = 186°$ at positions b and d. The wedges are assumed to have crest lines perpendicular to the sound track. The double-diffraction calculation for model approximation 2 agrees with experiment with less than 1 dB rms error. (From Medwin, H., E. Childs, E. A. Jordan, and R. J. Spaulding, Jr., "Sound scatter and shadowing at a seamount: hybrid physical solutions in two and three dimensions," *J. Acoust. Soc. Am.* **75**, 1478–90, 1984.)

where $P_D = P_D(\theta, \theta_0, \theta_w r, r_0, z)$ is the diffracted pressure given by, Equation 12.3.1, and P_0 is the reference pressure at the reference distance R_0 (=1 m).

This definition allows us to compare air laboratory experimental data at frequencies of tens of kilohertz and ranges of tens of centimeters on the same graph as ocean data at frequencies of the order of 100 Hz and at ranges of several kilometers. The definition permits theoretical wedge diffraction calculations to also be presented as a function of r/λ, as shown in Fig. 12.3.7.

12.3.4 THE FINITE WEDGE APPROXIMATION TO THE INFINITE WEDGE

The Biot–Tolstoy solution is for an infinite wedge. The crest length is infinite, and the two facets that comprise the wedge are semi-infinite planes joined at the crest line. To use the BT equations in the real world, one truncates the infinite time series of the diffracted pulse. The truncation is done either 1) when the remaining terms can offer no significant correction to the total diffraction amplitude; 2) at the time when the incident sound is beyond the end of the wedge; or 3) in order to obtain a desired frequency resolution (=1/duration of signal) after performing the Fourier transform.

Finite Crest Length

The scatter from a *finite* wedge, insonified by perpendicular incidence to the wedge crest at its midpoint, will lack the tail of the impulse response shown for the "infinite" wedge in Fig. 12.2.8. The spectral diffraction from such a real wedge is found by transforming the truncated BT impulse response to the frequency domain. It will be a function of the sound frequency, the wedge angle θ_w, the angles θ_0 and θ, and the ranges r_0 and r.

Greatest interest is in the case of backscatter, $\theta_0 = \theta$ and $r_0 = r$. For backscatter at a given range, shorter wedges cause shorter duration responses — that is, the impulse response of Fig. 12.2.8 becomes more truncated. For backscatter from a given length of the wedge crest, greater ranges cause the wedge impulse response to be of shorter duration; again the response is truncated.

Finite wedge backscatter for a point source shows the effect of a Fresnel zone–like interference that depends on the length of the wedge and the sound frequency (recall section 2.6.6 for point-source sound scattered by a finite plane surface). Also, the spectral diffracted pressure can be expected to decrease rapidly when the wedge crest length W is less than $(\lambda r)^{1/2}$, where λ is the wavelength in the transformed signal, and r is the range; the effect is reminiscent of Rayleigh scatter

of a plane wave by a sphere that is small compared with the wavelength (recall Fig. 7.5.4 for plane wave incidence).

Offset Wedge

An offset wedge will cause decreased basckscatter because the important pressure contributions at, and near, the least-time impulse component are missing. Some of the spectral effects have been analyzed in the context of low-frequency backscatter from Arctic leads in Medwin et al. (1988). Numerical tests

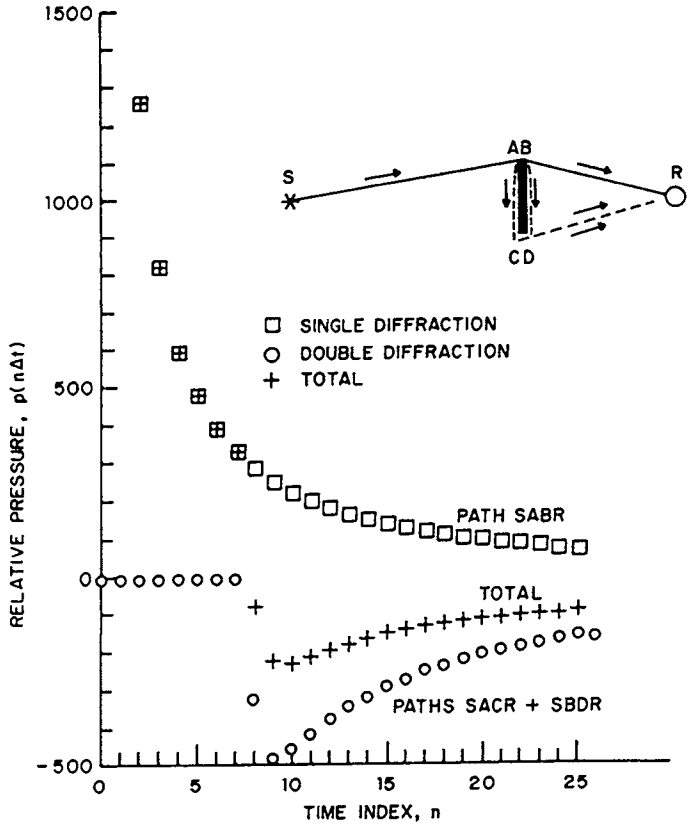

Figure 12.3.8 Numerical calculation of strip diffraction for the upper paths. The total pressure-time behavior is the sum of the single diffraction contribution by path SABR and those of opposite phase by double diffraction paths SACR and SBDR. The symmetrical lower paths such as SCDR are not shown. The BT impulse was sampled at 160 kHz. The strip width was 4 cm; source to strip range, 14.5 cm; strip to receiver, 9.5 cm. (From Medwin, H., E. Childs, and G. M. Jebsen, "Impulse studies of double diffraction: a discrete Huygens interpretation," *J. Acoust. Soc. Am.* **72**, 1005–13, 1982.)

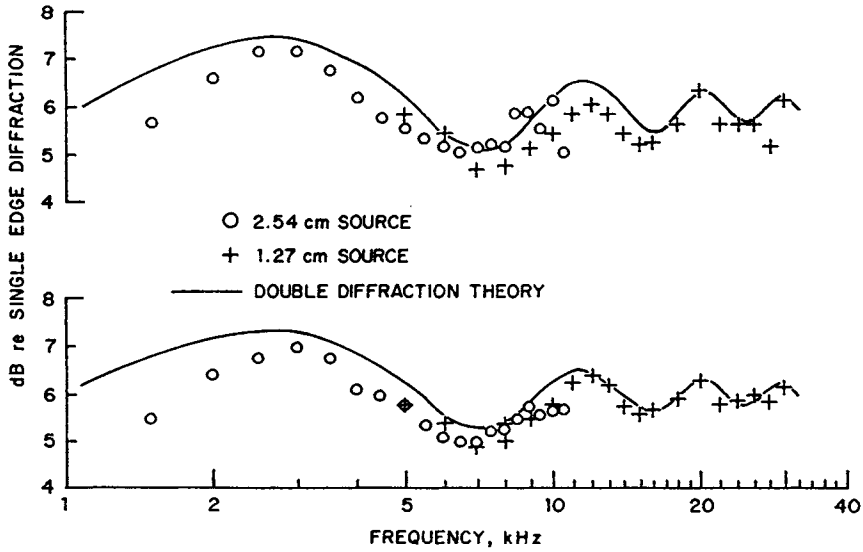

Figure 12.3.9 Spectra of diffracted pressures of a 4 cm strip relative to that of a single edge. The curve is the Fourier transform of the theoretical impulse response of the previous figure, which used double-diffraction theory. Data circles were obtained with a 2.54 cm diameter source, crosses with a 1.27 cm source in an anechoic chamber. The impulse was sampled at 160 kHz. The strip width was 4 cm; source to strip range, 14.5 cm; strip to receiver, 9.5 cm; the curve of the upper graph corresponds to the impulse in Fig. 12.3.8. The case of strip to receiver distance 23.2 cm is in the lower graph. The strip is within the first Fresnel zone of the source for frequencies less than 20 kHz. (From Medwin, H., E. Childs, and G. M. Jebsen, "Impulse studies of double diffraction: a discrete Huygens interpretation," *J. Acoust. Soc. Am.* **72**, 1005–13, 1982.)

by Denny and Johnson (1986) and Browne (1987) have shown that, when the series is converted to the frequency domain, the offset loss in backscattered spectral energy is greater for the higher frequencies and can be specified in terms of the order of the harmonic of the frequency in the transform. The higher frequencies are reduced more because they are more sensitive to the missing, rapidly decreasing, impulse-pressure contributions that occur immeditely after the least-time impulse component.

Finite Facet Width (Finite Wedge "Skirts")

The dependence of diffraction on facet width is revealed by the results of the thin "strip" experiment described in Figs. 12.3.8 and 12.3.9. The geometry of the forward scatter and the pressure-time behavior in the thin strip experiment are

sketched in Fig. 12.3.8. The sound from a point source follows three principal paths (and their symmetrical counterparts, which are not shown). The two sides of the thin plate are identified by points A and B at the top and C and D at the bottom. The principal paths are the single diffraction trajectory SABR and the double-diffraction paths SACR along the front face AC and SBDR along the shadowed face BD. The double diffraction is calculated by dividing the diffraction from the first wedge into several Huygens wavelet sources for the second wedge (section 12.3.2). Paths SACR and SBDR show the same amplitudes but opposite phase shifts at A and B and then reversed phase shifts at C and D, so that the pulse that propagates from CD to R is a *double* pulse that arrives at a delayed time relative to the single diffraction path SABR. That event, which determines the constructive and destructive interference peaks and troughs in the frequency domain, occurs at time index $n = 8$ in Fig. 12.3.8.

If the double-diffraction paths and the time-dependent interferences did not exist, the situation could be represented by the sum of the two single diffractions from edges of the semi-infinite plates at AB and CD. In that case, the diffraction field for the strip would be 6 dB greater than the field from a single semi-infinite plate. But the double-diffraction paths strongly perturb this simple addition with a periodicity that depends on the strip width. The theoretical and experimental spectra are presented in Fig. 12.3.9 for a 4 cm-wide strip. The periodicity of the interference effect is about 8 kHz, which is the reciprocal of the time required to traverse the strip.

The prediction of the double-diffraction treatment, using the BT formulation, is essentially correct, and shows an rms discrepancy of only about 0.5 dB compared with the experiment for frequencies over 2 kHz. The agreement with experiment begins to deteriorate for frequencies below about 2 kHz because of an inadequate number of samples in the sampling time of the experiment.

12.3.5 COMPONENTS OF REVERBERATION FROM ROUGH SURFACES

When a facet of a rough surface is perpendicular to the incident sound, dominating reflection will take place to a degree that depends on the size of the facet in terms of the Fresnel zone conditions (section 2.6.6). When there are no reflecting facets, the surface reverberation will be made up of ridge diffractions.

When the acoustic impedance and the detailed topography of a surface are known to the scale of the wavelength of the insonification, the reverberation can be calculated from the theory in this chapter.

12.4 BT Wedge Assemblage Techniques for Rough Surfaces

Knowledge of the impulse reflection and diffraction from a single wedge is the building block used to calculate the scatter from a complex, known surface. The wedge assemblage (WA) technique replaces the surface by several contiguous wedges. The BT theory described in section 12.2 is employed to calculate the scatter from each wedge element. These inpulse pressures are simply added to calculate the scatter from the assemblage; we call this the BT/WA method.

12.4.1 PARALLEL WEDGES: LABORATORY TEST OF A SINUSOIDAL LONG-CRESTED WATER SURFACE

Swell waves are long-crested waves from a distant storm. To model this, one can use a long-crested, sinusoidal water wave system for the test of the wedge assemblage method at an air/water interface. The laboratory wave system shown was driven by an oscillating plunger (Fig. 12.4.1). The cross-sectional displacement was given by

$$\zeta(x_s) = a \sin(2\pi x_s/\Lambda_s) \tag{12.4.1}$$

where a = surface wave amplitude = 0.305 cm; Λ_s = surface wavelength = 8.8 cm; x_s = distance along the surface; $\zeta(x_s)$ = water surface displacement.

For the purposes of the BT/WA calculations, several posssible wedge spacings were tried, as shown in Fig. 12.4.2. It turned out that there was little difference in

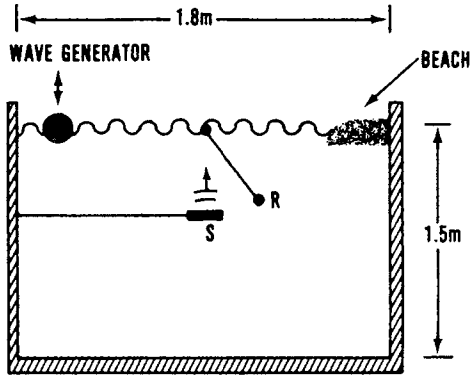

Figure 12.4.1 Water tank experiment to test the BT/WA technique. The source is S; the receiver is R. The wave generator was a rod that moved up and down. (From Kinney, W. A., C. S. Clay, and G. A. Sandness, "Scattering from a corrugated surface: comparison between experiment, Helmholtz–Kirchhoff theory, and the facet-ensemble method," *J. Acoust. Soc. Am.* **73**, 183–94, 1983.)

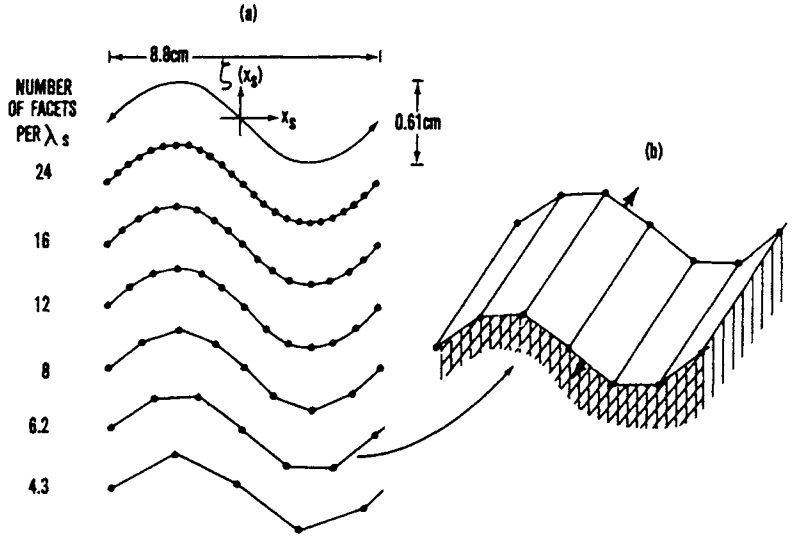

Figure 12.4.2 Wedge approximations to the experimental surface for application of the BT/WA method. (From Kinney, W. A., and C. S. Clay, "Insufficiency of surface spatial power spectrum for estimating scattering strength and coherence—numerical studies," *J. Acoust. Soc. Am.* **78**, 1777–84, 1985.)

the calculation of the field as long as there were more than 6 facets per surface wavelength.

The two theoretical results and the experimental scattered pressures are shown in Fig. 12.4.3. Either the BT/WA or HK solution fits the experiment (with differences of about 10 percent) for scattered angle less than 40°, which suggests that the HK method is not all that bad. But the results of section 12.3.1 and other critical tests advise us that, for larger angles, or steep waves, the HK solution would have been seriously in error.

12.4.2 PARALLEL WEDGES: THE OCEAN AS A LOW-FREQUENCY DIFFRACTION GRATING

When there is no local wind-driven sea, several theories have shown that the periodic, long-crested waves from a distant storm scatter underwater sound like a "diffraction grating." Because of their importance to science and technology, there have been several exact analytical solutions to the problem of electromagnetic "reflection" by a diffraction grating. These solutions provide a critical test of the wedge assemblage technique using BT elements (Novarini and Medwin 1985).

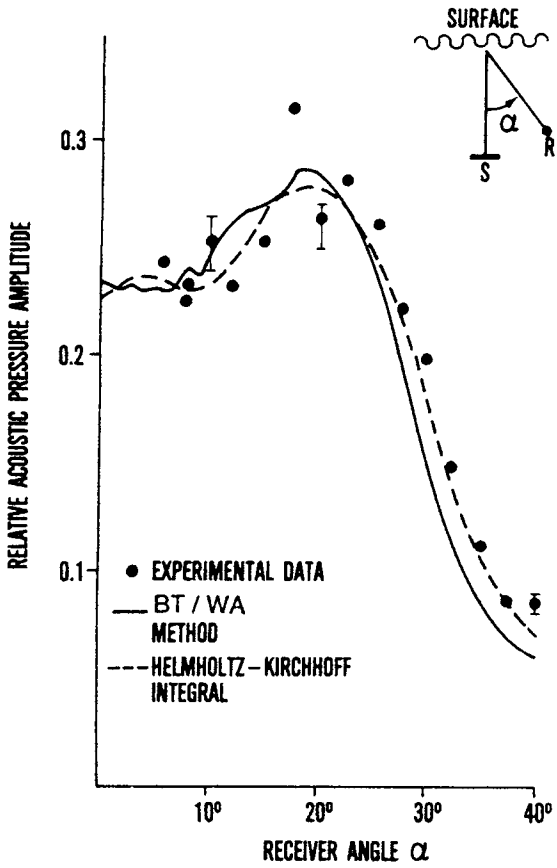

Figure 12.4.3 Comparison of experimental values with predictions of the BT wedge assemblage method and the HK method for the laboratory experiment described in Figs. 12.4.1 and 12.4.2. (From Kinney, W. A., C. S. Clay, and G. A. Sandness, "Scattering from a corrugated surface: comparison between experiment, Helmholtz-Kirchhoff theory, and the facet-ensemble method," *J. Acoust. Soc. Am.* **73**, 183–94, 1983.)

The "grating equation," which defines the scatter, is

$$\sin \theta_m = m\,(\lambda / D) + \sin \theta_i \tag{12.4.2}$$

where θ_m and θ_i are the angles of diffraction scatter and incidence, respectively, as measured from the normal to the plane of the grating (Fig. 12.4.4a). The integers $m = 0, +1, +2$, and so on are called the "orders" of the diffraction grating; the orders determine the angles at which wave reinforcement occurs because of integral wavelength path differences for the different wedges. The

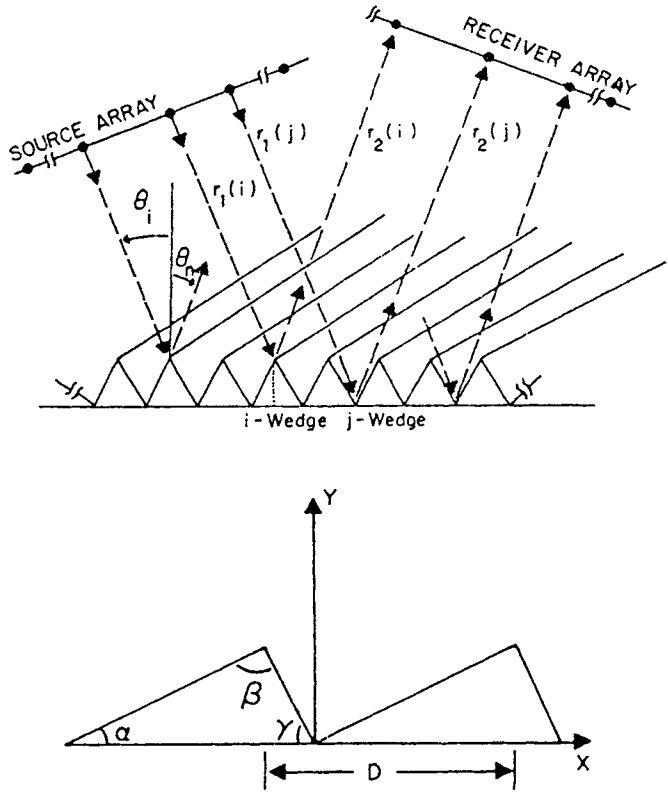

Figure 12.4.4 a) Geometry of the simulated experimental setup, used as a model for the BT wedge assemblage calculation of the scatter. b) Surface profile for the asymmetric (echelette) grating calculation. (From Novarini, J. C., and H. Medwin, "Computer modeling of resonant sound scattering from a periodic assemblage of wedges: comparison with theories of diffraction gratings," *J. Acoust. Soc. Am.* **77**, 1754–59, 1985.)

integer $m = 0$ corresponds to specular (mirror direction) scattering. The wedge separation is D. The geometry of an *echelette* (ladder) grating is sketched in Fig. 12.4.4b.

Two interpretations have to be made to compare the BT wedge asemblage calculation for acoustics with the analytical electromagnetic solutions. First, the BT/WA solution is for a point source, whereas the electromagnetic solutions are for plane waves. To achieve the equivalent of a plane wave, an array of point sources is assumed to represent the plane wave. A receiver array (whose outputs are to be summed) is proposed to collect the sound at the scattered angle of interest (Fig. 12.4.4a). The second change is to recognize that the boundary

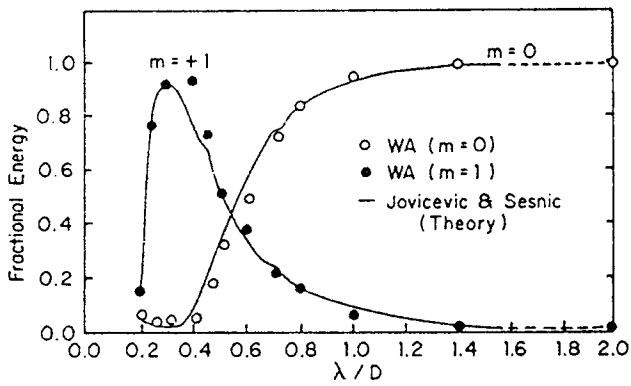

Figure 12.4.5 Fractional energy at two diffracted orders, $m = 0$ and $m = 1$, as a function of relative wavelength to wedge separation, for a pressure-release surface with an echelette shape, where $\alpha = 10°$ and $\beta = 90°$ in Fig. 12.4.4. The angle between the incident beam and the first-order diffracted beam is zero. Dots are BT/WA calculations; solid lines are theory by Jovicevic and Sesnic (1972); dashed lines are extrapolations. (From Novarini, J. C., and H. Medwin, "Computer modeling of resonant sound scattering from a periodic assemblage of wedges: comparison with theories of diffraction gratings," *J. Acoust. Soc. Am.* **77**, 1754–59, 1985.)

conditions for a pressure release acoustical wave are the same as for an electromagnetic $E \,||$ (parallel field) wave.

Since all the scattered energy concentrates into the various diffracted orders, the fractional energy in a given order is used to define its energy in Fig. 12.4.5 for orders $m = 0$ and $m = 1$. The BT wedge assemblage solutions are compared with electromagnetic theory as a function of λ/D, where D is the periodic wedge separation. This research shows that diffraction gratings (which are a model of parallel, equally spaced, long-crested waves in the oceanic world), operating wavelengths comparable to the crest separation, produce their scatter by diffraction, not by reflection. Computer model results of the type shown were achieved by the use of only 6 or 7 wedges, with a discrepancy of less than 10 percent.

12.4.3 SYNTHETIC SEISMIC PROFILES

For the seismic study, source and receiver are at the same location. Because of its accuracy, the BT solution has been proposed by Hutton (1987) as a reference for seismic diffraction modeling. Seismic wedge calculations can be performed on a much larger scale, as in the seamount problem (section 12.3.3) or in the seismic study by Daneshvar and Clay (1987). In the latter case, the bathymetry was

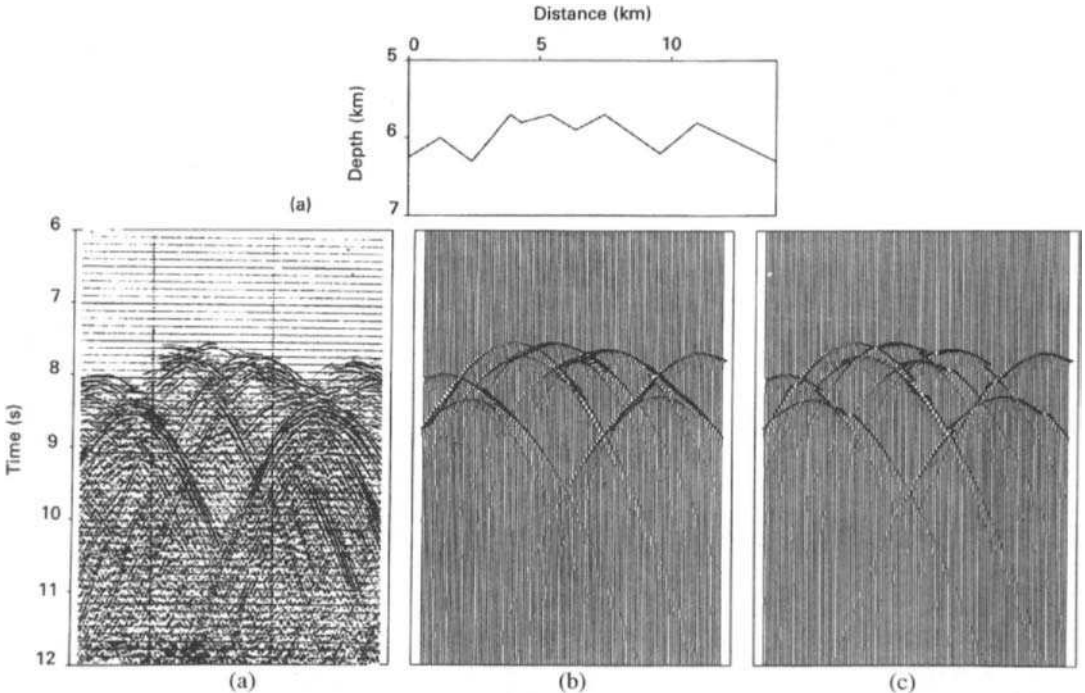

Figure 12.4.6 Comparison of a segment of seismic profile data and synthetic seismograms constructed by using the WA method. A facet and wedge bathymetric model of the sea floor is (a) above the seismograms. (b) Seismic profile obtained in the field; (c) synthetic seismogram, including reflections from plane facets as well as wedge diffractions; (d) synthetic seismogram showing diffraction arrivals only. (From Daneshvar, M. R., and C. S. Clay, "Imaging of rough surfaces for impulsive and continuously radiating sources," *J. Acoust. Soc. Am.* **82**, 360–69, 1987.)

known on a gross scale over a range of about 15 km (top of Fig. 12.4.6). The actual seismic profile (a) shows not only the scattering from the changes of slope (wedges crests) of the bathymetry, but scattering from under the surface as well. A synthetic seismogram (b) was constructed using only the bathymetry shown and including both the BT crest diffractions and facet reflections. It was initially assumed that the surface of the facet was rigid and smooth enough for facet reflections (b). In fact, when the reflections were omitted (c), an even better synthetic seismogram was obtained. The interpretation is that, for the frequencies being used, the facet surfaces were rough enough to cause diffuse scatter and thereby to eliminate the need for the reflection component of the BT solution. Only diffraction from the wedge crests was important.

Problems

Section 12.2

12.2.1 Write computer programs for Equations 12.2.1 through 12.2.7 so that you can solve the following problems.

12.2.2 Use your computer program of the BT theory to verify the graph of Fig. 12.3.2, which describes diffraction of 100 Hz, 1 kHz, and 10 kHz sound by a rigid wedge in air when the source and receiver ranges are 25 cm and $\theta_0 = \theta = 15°$.

12.2.3 Repeat the calculation of Problem 12.2.2 when the source and receiver are in air at a range of 100 m from the crest.

12.2.4 Repeat the calculation of Problem 12.2.2 when the source and receiver are at a range of 100 m from a right-angle ridge in the ocean. Repeat the calculation when the source and receiver are at a range of 1 km in the ocean (assume $c = 1500\,\text{m/s}$).

12.2.5 Repeat the calculation of Problem 12.2.4 when the source is at range 1 km; angle $\theta_0 = 30°, 45°, 60°$, and 85°; and receiver is at range 100 m, $\theta = 15°$.

Section 12.3

12.3.1 Use your computer program of the BT theory to verify the predictions for backscatter diffraction by a rigid plate in air as shown in Fig 12.3.3 for frequencies 2 kHz, 10 kHz, and 40 kHz at angles 0°, 30°, and 60°.

12.3.2 Calculate the forward diffraction loss (compared with spherical divergence over the same distance) for a range of frequencies for a symmetrical, wedgelike seamount of slope 14° on each side of the wedge ($\theta_w = 208°$).

Assume that the water is isothermal and ignore the effect of the water surface above the seamount. Assume that the ranges are $r = r_0 = 2\,\text{km}$, that the source is on the upslope of the seamount, and that the receiver is on the downslope.

12.3.3 How would your answer to the previous problem change if, instead of a downslope, there is a horizontal mesa ($\theta_w = 194°$) on the right side of the wedge?

12.3.4 How would your answer to Problem 12.3.3 change if there is a horizontal mesa that extends for 1 km at the top of the seamount (a *guyot*)?

12.3.5 (Advanced) a) Calculate the diffraction backscatter (relative to an infinite wedge) as a function of frequency for a finite, rigid-ridge outcropping that is 2 m high and 10 m long and has a crest wedge angle of $\theta_w = 270°$. Assume that the outcropping is insonified perpendicular to its 10 m length, at incidence $\theta_0 = \theta = \theta = 20°$ and a range $r = r_0 = 100\,\text{m}$. What minimum effective frequency would this suggest for detection of diffraction by a side-scan sonar? Note that there are two single diffracting "wedges" — the crest wedge of $\theta_w = 270°$ and the wedge of angle $\theta_w = 135°$ between the base of the outcropping and the horizontal sea floor. b) Compare the strength of the two diffracted signals with that from a 1 m^2 reflecting facet that happens to be on the rough outcropping. Comment.

12.3.6 (Advanced) Consider the previous problem. How does the minimum effective frequency of the crest diffraction depend on the range? How does this depend on the angle of incidence $\theta_0 = \theta$? How does this depend on the ridge wedge angle θ_w?

Chapter 13 | Scattering and Transmission at Statistically Rough Surfaces

13.1 Descriptions of Ocean Surfaces 578
13.1.1 The Wind-Blown Surface 578
13.1.2 The Rough Ocean Bottom 589
13.2 Forward Scatter in the Specular (Mirror) Direction: Simple Concepts 593
13.2.1 Mean Coherent Scattered Pressure in the Specular Direction, Acoustical Roughness 594
13.2.2 Inverting for the PDF of Heights 596
13.2.3 Statistics of Scatter in the Specular Direction 597
13.2.4 Intensity of Sound Scattered in the Specular Direction: Scale-Model Results 601
13.2.5 Other Specular Scatter Effects 605
13.3 Surface Scatter of Sound 606
13.3.1 Scatter of a Spherical Wave: Helmholtz–Kirchhoff–Fresnel Solution 607
13.3.2 Mean-Squared Scattered Pressure: Surface Scattering Strength 610
13.3.3 Dependence of Specular Scatter on the Parameters of the Experiment: Apparent Reflection Coefficient and Bottom Loss (dB) 613
13.3.4 Scale-Model Proofs of the Dependence of Scatter on Parameters of the Experiment 615
13.3.5 Computer Model of Point-Source Backscatter from an Ocean Surface 618
13.3.6 Scattering from a Two-Dimensional Rough Surface: Tri-Wedge Computer Assemblages 623
13.3.7 Effect of Bubbles below the Ocean Surface 625
13.4 Near Grazing Scatter at a Steep-Sloped, Rough Surface 627
13.5 Point-Source Transmission through a Rough Interface 632
13.5.1 Smooth Air-Sea Interface 632
13.5.2 Rough Air-Sea Interface 635

The real sea floor and the real sea surface are randomly rough. Sound signals are imperfectly reflected and partly scattered by rough surfaces. The statistics of the scattered sound pressure can be predicted after the statistics of the rough surface have been specified. The first pragmatic step in predicting sound scatter is to define the surface roughness in terms of those concepts developed by the physical oceanographer and geophysicist that fit the needs of the ocean acoustician. The two main, interconnected types of descriptors useful to the acoustician are: a) the statistical description such as the probability density function of the rough surface displacements (with respect to the mean surface) or slopes, and their statistical moments (e.g., the rms values); and b) the temporal and spatial spectra of the rough surface with their transforms, the correlation functions. The most efficient use of these variables depends on the surface as well as the desired acoustical

description — for example, the correlation of the acoustic scatter is most easily expressed in terms of the correlation of the scattering surface.

Conventional descriptions of the wind-blown surface are different from those of the rough ocean bottom. In section 13.1 we present surface statistical descriptions that are most effective in predicting sound scatter at the ocean surface and ocean bottom. Some of the most convincing laboratory scale models and simplified analyses of the coherent and incoherent components of scatter in the mirror direction are summarized in section 13.2. The general Helmholtz–Kirchhoff–Fresnel solution for scattering in any direction from a known surface is given in section 13.3. The special case of grazing incidence over steep-sloped rough surfaces is the topic of section 13.4. Theoretical and experimental transmissions through smooth and rough surfaces are considered in section 13.5.

13.1 Descriptions of Ocean Surfaces

13.1.1 THE WIND-BLOWN SURFACE

Phillips (1977) and Lighthill (1978) give lucid descriptions of surface gravity waves. Oceanographers commonly describe the ocean surface in terms of the probability density function (PDF) of the displacements of the rough surface, the frequency spectrum of the displacements, and the directional wave spectrum. As we see in the following sections, not only those quantities but also the PDF of the slopes of the surface and the correlation function of the surface displacements are closely related to the scattering of sound from the surface. We introduce these quantities briefly here, and present examples of data from real seas as well as laboratory "seas." Properly designed laboratory scale models are effective devices for controlled studies of sound scatter.

The PDF of displacements of a wind-blown sea is close to Gaussian, as seen, for example, in Fig. 13.1.1. The Gaussian PDF is given by,

$$w(\zeta) = \frac{1}{h\sqrt{2\pi}} \exp\left[-\frac{1}{2}\left(\frac{\zeta}{h}\right)^2\right] \tag{13.1.1}$$

where ζ is the displacement from the mean surface and h is the rms height of the displacements.

The first two moments are

$$m_1 = \langle \zeta \rangle = 0 \tag{13.1.2a}$$

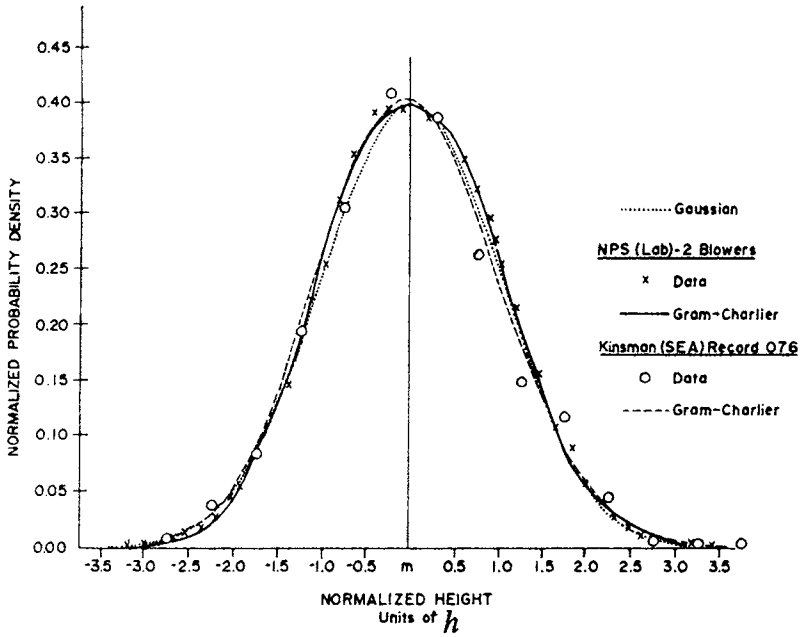

Figure 13.1.1 Normalized PDF of water surface displacements. Ocean data are circles; dashed line is a fitted curve using first four moments of the Gram-Charlier expansion with $h = 2.72$ cm, $m_3 = 0.092$, and $m_4 = 0.031$ for wind 6.75 m/s, measured 12.5 m above surface at sea, from Kinsman (1960). Crosses are data for a carefully designed laboratory "sea" with $h = 0.119$ cm, $m_3 = 0.086$, and $m_4 = 0.073$; solid line is laboratory four-moment fit. The Gaussian is the simple dotted curve. (From Medwin, H., and C. S. Clay, "Dependence of spatial and temporal correlation of forward scattered underwater sound on the surface statistics: part II—experiment." *J. Acoust. Soc. Am.* **47**, 1419–29, 1970.)

and

$$m_2 = \langle \zeta^2 \rangle = h^2 \tag{13.1.2b}$$

Modifications of the simple Gaussian are necessary for a more nearly correct specification of the ocean PDF. These are components of a Gram-Charlier series described by Longuet-Higgins (1963) in terms of the moments.

Two of the higher-order moments are the skewness,

$$m_3 = \langle \zeta^3 \rangle / (2\langle \zeta^2 \rangle^{3/2}) \tag{13.1.3}$$

and the kurtosis, (or "peakedness"),

$$m_4 = (\langle \zeta^4 \rangle - 3\langle \zeta^2 \rangle^2)/(2\langle \zeta^2 \rangle^2) \tag{13.1.4}$$

Extensive studies of scattering from an oceanlike surface have been performed in laboratory scale models. The laboratory "sea" is generated by a paddle, or fans in a water-wind tunnel. The scaling is accomplished by using higher laboratory sound frequencies, in order to reproduce the ratio h/λ of an acoustical scattering trial at sea. The higher-order moments m_3 and m_4 should be similar for the scaling to be appropriate for acoustical scattering studies. In Fig. 13.1.1 the laboratory m_3 and m_4 are within the range of sea values for wind speeds 4 to 9 m/s.

The PDF of sea slopes is also important in sound scatter from the sea surface. Fig. 13.1.2a presents the crosswind (subscript c) and windward (subscript w) behavior for a 10 m/s wind at sea (Cox and Munk 1954). The latter shows the skewness expected in the windward direction; both measurements show peakedness. The mean squared slopes for clean water were empirically given as

$$\begin{aligned} s_w^2 &= 0.000 + 3.16 \times 10^{-3} W \pm 0.004 \\ s_c^2 &= 0.003 + 1.92 \times 10^{-3} W \pm 0.002 \\ s^2 &= s_w^2 + s_c^2 = 0.003 + 5.12 \times 10^{-3} W \pm 0.004 \end{aligned} \tag{13.1.5}$$

where wind speed W is in m/s, measured at the traditional height 12.5 m above the surface at sea; s is the rms slope independent of direction. Oily water has lesser rms slopes. Slopes of a laboratory model are shown in Fig. 13.1.2b.

The temporal autocorrelation of heights $\zeta(t)$ is the temporal autocovariance divided by the mean squared height,

$$C(\tau) = (<\zeta(t)\,\zeta(t+\tau)>)/h^2 \tag{13.1.6}$$

where τ is the time lag.

A "typical" temporal correlation at sea is shown at the top of Fig. 13.1.3. It is typical in that it shows a periodicity that corresponds to the frequency of the most prominent wave component, and a correlation magnitude that decreases as the time lag increases. A very similar scaled version of the temporal correlation at sea can be achieved by the use of a programmed plunger or fans operating in a sufficiently long water tank with the result as shown at the bottom of Fig. 13.1.3.

To manipulate analytical expressions for the correlation of acoustical scatter as a function of the correlation of ocean surface displacement, a first step is to approximate the temporal surface correlation — for example, by writing it empirically as

$$C(\tau) = \exp\left[-(\tau/T)^2 \cos \Omega_m \tau\right] \tag{13.1.7}$$

a)

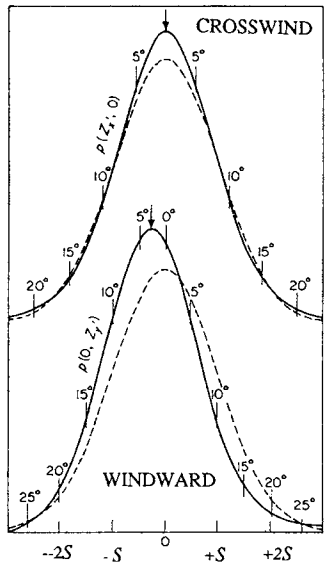

b)

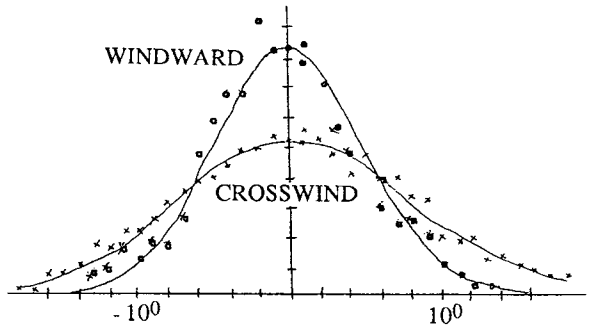

Figure 13.1.2 a) PDF of slopes measured optically during 10 m/s wind at sea. The solid lines are observed normalized distributions crosswind and windward; dashed lines are simple Gaussians of the same rms slope. (From Cox, C. S., and W. Munk, "Statistics of the sea surface derived from sun glitter," *J. Marine Res.* **13**, 198–227, 1954.) b) slope PDF for NPS laboratory 3 blower "sea" obtained by two-minute integrations of photocell output using a colocated point light source for various angles windward and crosswind. The lines are simple Gaussians of the same rms slope (windward, circles, $s_w = 7.8°$; crosswind, crosses $s_c = 4.9°$). (From Ball, E. C., and J. A. Carlson, "Acoustic backscatter from a random rough water surface," M.S. thesis, Naval Postgraduate School, Monterey, Calif., 1967.)

where T is the time lag for $C = e^{-1}$ and Ω_m is close to the angular frequency of the peak of the surface wave displacement spectrum (Fig. 13.1.3).

The general expression for the temporal autocovariance of the surface displacements is related to its spectral density, $\Phi(\Omega)$, [m^2/Hz] by the Wiener-

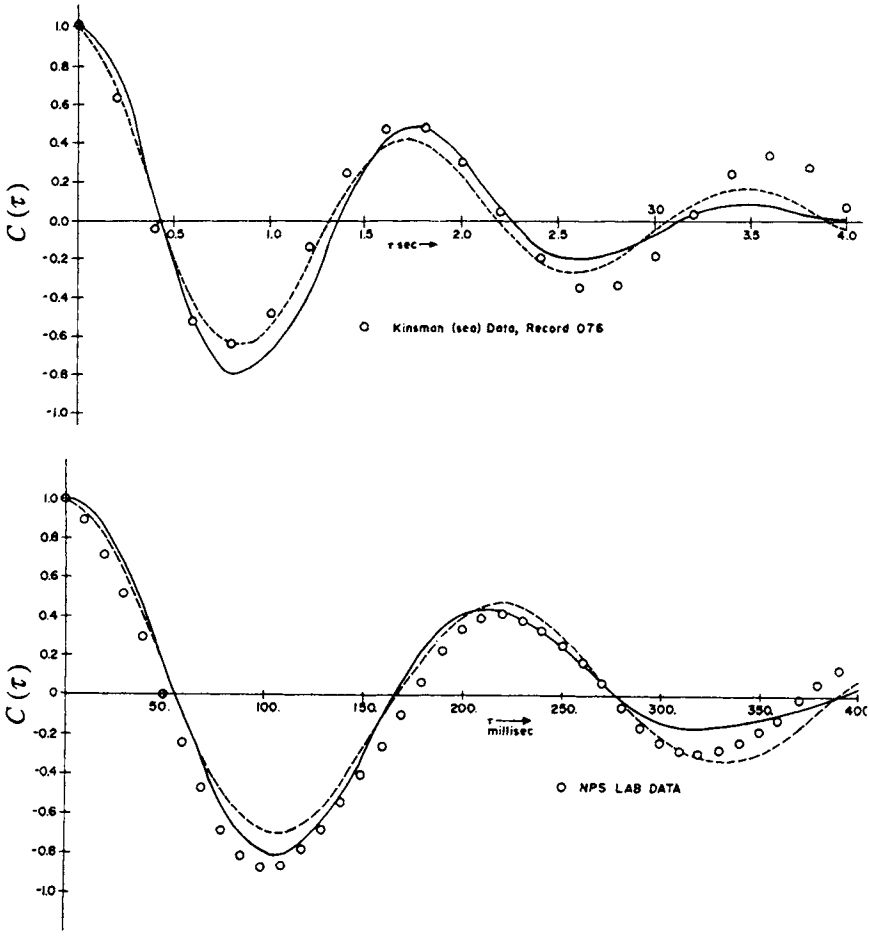

Figure 13.1.3 *Above*, a temporal correlation function at sea for a low wind speed case from Kinsman (1960). Circles are data points. Solid line is a fit to Equation 13.1.7 with $\Omega_m = (2\pi/1.78)\ \text{sec}^{-1}$ and $T = 2.0\,\text{sec}$. *Below*, a temporal correlation function in a water wind tunnel at the Naval Postgraduate School; the solid line is fitted to Equation 13.1.7. The NPS correlation constants are $\Omega_m = 9\pi\ \text{sec}^{-1}$ and $T = 0.24\,\text{sec}$. The scaling is $(\Omega_m)_{\text{Lab}}/(\Omega_m)_{\text{Sea}} = 8.1$ and $(T)_{\text{Sea}}/(T)\text{Lab} = 8.3$. Dashed lines are damped exponential fittings. (From Medwin, H., and C. S. Clay, "Dependence of spatial and temporal correlation of forward scattered underwater sound on the surface statistics: part II—experiment." *J. Acoust. Soc. Am.* **47**, 1419–29, 1970.)

Khinchine theorem, which gives the transforms (section 6.4). To compare with his graph, we follow the normalization of the transform relation as in Phillips (1977), Equation 4.1.16, but with our symbols:

$$\Phi(\Omega) = \frac{1}{2\pi}\int_{-\infty}^{\infty} h^2 C(\tau) e^{+i\Omega t}\, d\tau$$
$$C(\tau) = h^{-2}\int_{-\infty}^{\infty} \Phi(\Omega) e^{-i\Omega\tau}\, d\Omega \qquad \textbf{(13.1.8)}$$

where $\Omega = 2\pi F$ is the angular frequency of a component F ($\sec^{-1}$) of the surface waves.

The spectral density is the part of the total mean-squared height in a 1 hertz bandwidth. Therefore the mean-squared height, h^2, is the integral over all frequencies:

$$h^2 = \int_0^{\infty} \Phi(\Omega)\, d\Omega \qquad \textbf{(13.1.9)}$$

Similarly, the mean-squared slope, s^2, is obtained from the K^2-weighted spectrum, where $K = 2\pi/\Lambda$ is the wave number of the surface wave component of wavelength Λ. Using the expression for a gravity wave system, $\Omega^2 = Kg$, where g is the acceleration of gravity, 9.8 m/s^2, Cox and Munk (1954) show that the mean-squared slope is

$$s^2 = g^{-2}\int_0^{\infty} \Omega^4 \Phi(\Omega)\, d\Omega \qquad \textbf{(13.1.10)}$$

The frequency spectrum of ocean displacements has been measured many times. Fig. 13.1.4 shows several of these from Phillips (1970).

The Pierson-Moskowitz (1964) frequency spectrum is an empirical expression for the spectral density of ocean displacements due to wind-blown waves acting over an infinite fetch:

$$\Phi(\Omega, W) = \alpha g^2 \Omega^{-5} \exp\left[-\beta(\Omega_0/\Omega)^4\right] \qquad (\text{m}^2/\text{Hz}) \qquad \textbf{(13.1.11)}$$

where Ω, radians/sec, is the angular frequency of an ocean surface wave component; $\Omega_0 = g/W$ = nominal angular frequency of the peak of the spectrum; W = wind speed (m/s) at 19.5 m above sea surface; $\alpha = 8.1 \times 10^{-3}$; $\beta = 0.74$; $g = 9.8$ m/s^2.

The Pierson-Moskovitz spectrum is integrated over all frequencies to give the rms height in meters of such a surface, as a function of wind speed in m/s.

$$h = \int_0^{\infty} \Phi(\Omega)\, d\Omega = \left(\frac{\alpha}{\beta}\right)^{1/2}\left(\frac{W^2}{2g}\right) = 0.0053\, W^2 \qquad \textbf{(13.1.12)}$$

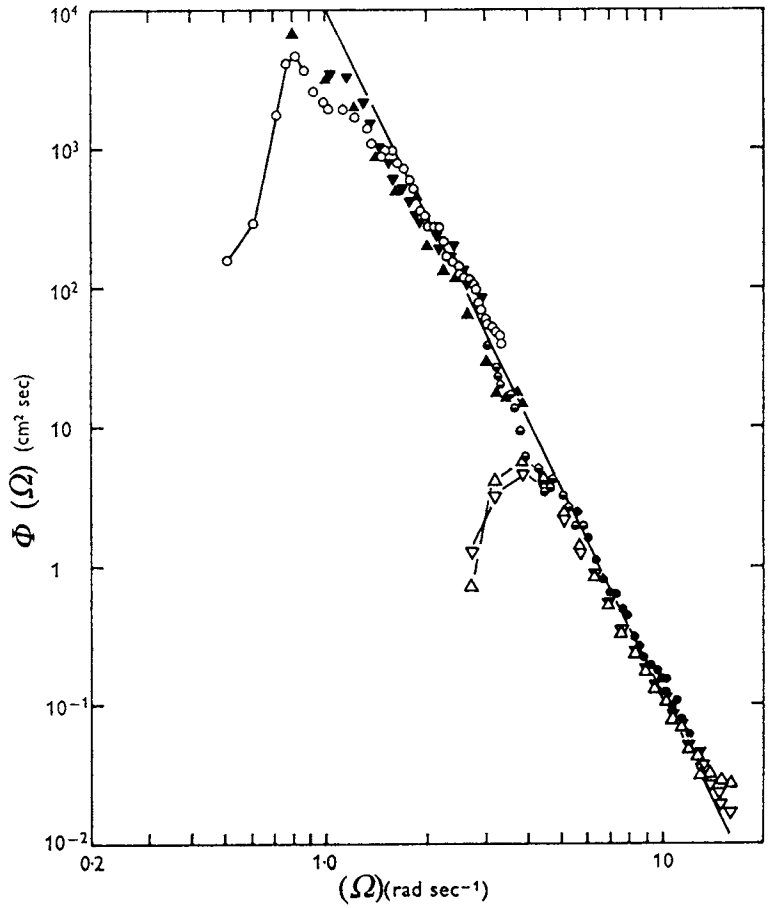

Figure 13.1.4 The equilibrium range of the frequency spectrum of wind-generated waves from seven experiments, including 52 spectra. The shape of the spectral peak is shown in only three cases. The straight line has the slope -5, as in Equation 13.1.11. (From Phillips, O. M., *The Dynamics of the Upper Ocean*, 2nd ed.; Cambridge University Press; New York, 1970.)

In general, there is no reason to assume that the ocean surface is isotropic. Consequently, sound scatter from the ocean surface is usually dependent on the direction of the sound beam with respect to the axial direction of the surface wave system. To take account of this anisotropic surface, the *directional* wave spectrum must be specified. Kuperman (1975) does this in a general way. One very simple approximate form employed by Fortuin and Boer (1971) and

Novarini et al. (1992) assumes that there is a $\cos^2\theta$ dependence of the spectral amplitude, where θ is the angle with respect to the wind direction. This gives simply

$$\Phi(\Omega, W, \theta) = \alpha g^2 \Omega^{-5} \exp\left[-\beta(\Omega_0/\Omega)^4\right]\cos^2\theta \qquad \textbf{(13.1.13)}$$

A more flexible description uses the two-dimensional spatial correlation function of spatial lags ξ and η for the x and y directions. This is the analog of the temporal correlation function. It may be Fourier-transformed to obtain the two-dimensional wave number spectrum of the surface. In the x direction, the transform pair is written in Phillips's (1977) way:

$$\Phi(\kappa_x) = \frac{1}{2\pi} \int_{-\infty}^{\infty} C(\xi) e^{-i\kappa_x \xi}\, d\xi \qquad \textbf{(13.1.14)}$$

$$C(\xi) = \int_{-\infty}^{\infty} \Phi(\kappa_x) e^{i\kappa_x \xi}\, d\kappa_x \qquad \textbf{(13.1.15)}$$

where K_x is a wave number component in the x direction.

Similar relations exist for the y direction, in which case η is a spatial lag and K_y is a wave number component in the y direction.

The character of the two-dimensional spatial correlation functions at sea can be seen from the ocean examples plotted at the top of Fig. 13.1.5, from the SWOP (Stereo Wave Observation Project) report (see Kinsman 1965). A scaled version of the ocean correlation functions, at the bottom of Fig. 13.1.5, was obtained by the use of a set of fans in a water wind tunnel designed to study sound scatter from an oceanlike surface.

A useful view of the windward surface spatial correlation function is that it can be approximated by the simple empirical expression

$$C(\xi) = \exp\left[-(\xi/L_x)^2\right]\cos K_{xm}\xi \qquad \text{Windward} \qquad \textbf{(13.1.16)}$$

where L_x is the correlation length in the x direction and K_{xm} is the wave number in spatial correlation space that corresponds to the most prominent surface wavelength in the x direction. Sometimes acoustician theorists set K_{xm} equal to zero and assume that the Gaussian form $\exp[-(\xi/L_x)^2]$ is an acceptable approximation.

The crosswind spatial correlation function does not oscillate with the spatial lag as does the windward (Equation 13.1.16). The function is sometimes approximated by either an exponential or a Gaussian form, depending on the particular sea. The Gaussian form is written as

$$C(\eta) = \exp\left[-(\eta/L_y)^2\right] \qquad \text{Crosswind} \qquad \textbf{(13.1.17)}$$

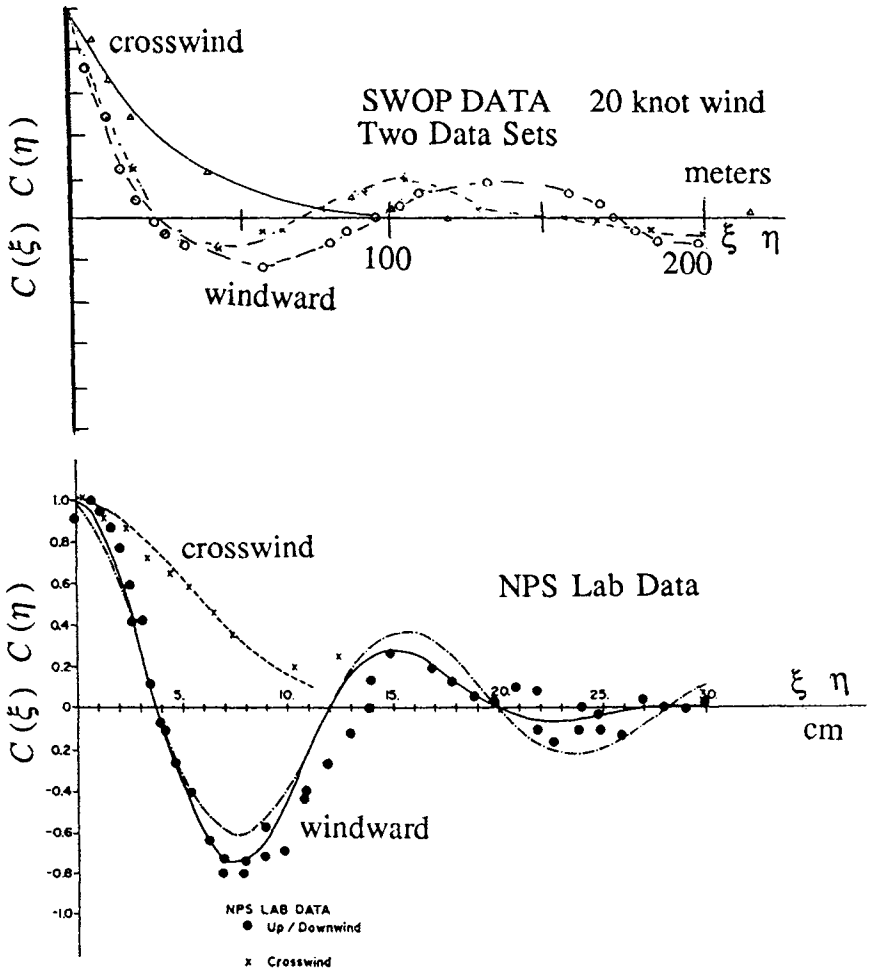

Figure 13.1.5 *Above*, spatial correlation functions measured at sea by the Stereo Wave Observation Project (SWOP) during 10 m/s winds. Triangles and solid line are crosswind; circles, crosses, and dashed lines are windward. (From Cole, L. J., et al., "The directional spectrum of a wind generated sea as determined from data obtained by the Stereo Wave Observation project, *Meteorol. Papers* (N.Y.U., Coll. of Eng.) **2**(6), 1960 and Kinsman, B. "Surface waves at short fetches and low wind speeds: a field study," *Chesapeake Bay Inst. Tech. Rep. 129*, Johns Hopkins, 1960.) *Below*, windward and cross-wind spatial correlation functions generated by fans in a water wind tunnel at the Naval Postgraduate School. When fitted to Equations 13.1.16 and 13.1.17, the constants for the laboratory sea are $L = 14.0$ cm, $K_{ym} = \pi/8$ cm^{-1}, and $L_y = 7.35$ cm. (From Medwin, H., and C. S. Clay, "Dependence of spatial and temporal correlation of forward scattered underwater sound on the surface statistics: part II—experiment." *J. Acoust. Soc. Am.* **47**, 1419–29, 1970.)

where L_y is the correlation lengths in the y direction. For long-crested waves, $L_y \gg L_x$.

Fig. 13.1.6 is a two-dimensional presentation of the surface correlation of displacements generated by fans in a laboratory "sea" to study the dependence of scattered sound correlation on surface correlation. The windward and crosswind components are shown in Fig. 13.1.5.

Although Equation 13.1.7 is a useful representation of the surface temporal correlation function, and Equations 13.1.16 and 13.1.17 represent the components of the spatial correlation functions, laboratory research (Medwin et al. 1970) has made it clear that the space-time correlation is *not* separable into its spatial and temporal components.

In the laboratory "sea" described by Fig. 13.1.7, the envelope of the crests moves at the group velocity of the waves,

$$u = L_x / T \tag{13.1.18}$$

while the individual crests move at the phase velocity,

$$v = \Omega_m / K_{xm} \tag{13.1.19}$$

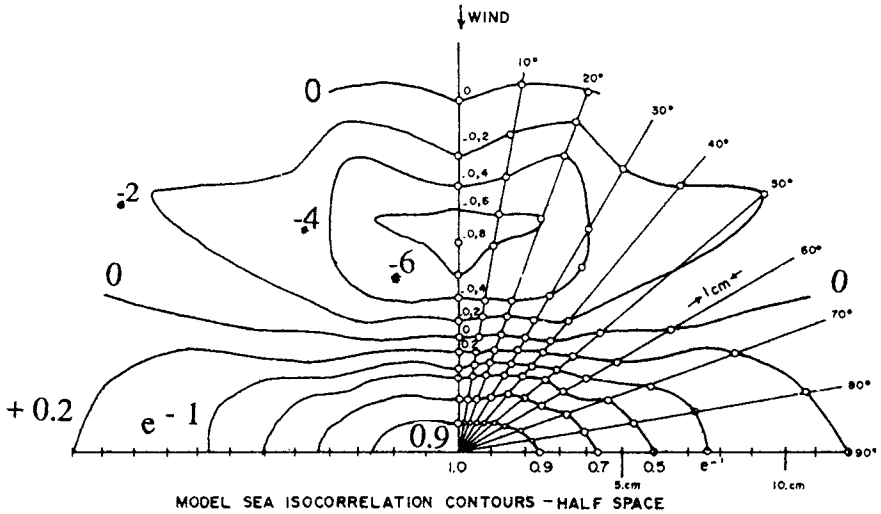

Figure 13.1.6 Two-dimensional spatial correlation of displacements in a laboratory sea generated by fans. The correlation lengths are spatial lags for the e^{-1} values. The data were collected by time averages for spatial lags in a fixed region, which is assumed by ergodicity to equal the data for those lags over many regions of a large surface area at an instant of time. The windward and crosswind components were shown in Fig. 13.1.5. (From Medwin, H., and C. S. Clay, "Dependence of spatial and temporal correlation of forward scattered underwater sound on the surface statistics: part II—experiment." *J. Acoust. Soc. Am.* **47**, 1419–29, 1970a. See also Clay and Medwin, part I—theory, 1970.)

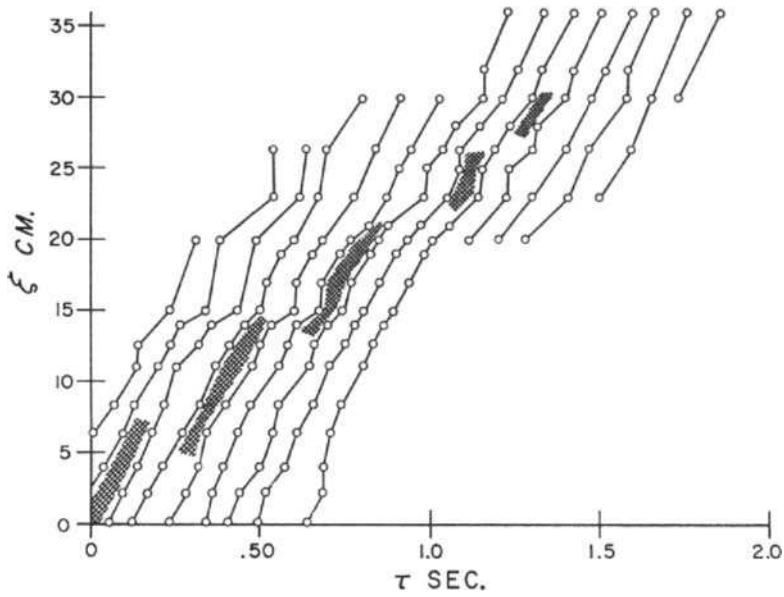

Figure 13.1.7 Map of the correlation function $C(\xi, \tau)$ of a wind-blown laboratory water surface. The circles are ξ, τ values that yield zero correlation. These are connected by lines whose slope gives the phase velocity of the correlation v, Equation 13.1.19. The shaded areas are correlations greater than 0.5. The correlation group velocity, u, Equation 13.1.18, is the slope of the maxima of the correlation. (From Medwin, H., C. S. Clay, J. M. Berkson, and D. L. Jaggard, "Traveling correlation function of the heights of windblown water waves," *J. Geophys. Res.* **75**, 4519–24, 1970.)

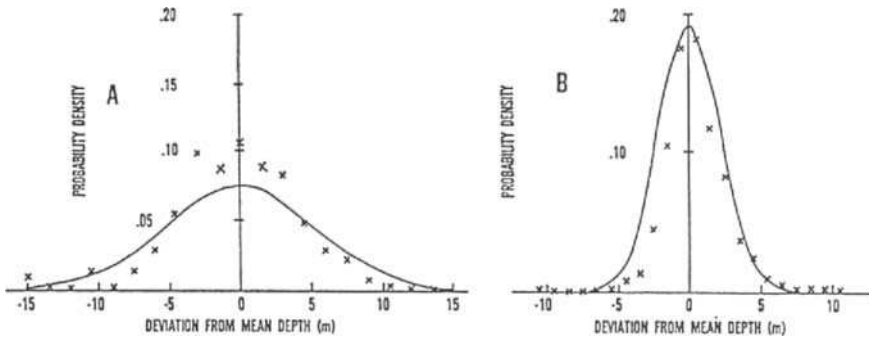

Figure 13.1.8 Two examples of the PDF of the ocean bottom displacements, at scales of the order of meters. The solid lines are the Gaussian PDF after filtering through a high-pass spatial filter of wave number $= 0.003\ \mathrm{m}^{-1}$. On the left a Norwegian sea basin; on the right a Norwegian sea marginal plateau. (From Berkson, J. M., and J. E. Mathews, "Statistical properties of seafloor roughness," in *Acoustics of the Sea-Bed*, ed. N. G. Psace, Bath University Press; Bath, England, pp. 215–23, 1983.)

An equation describing this "traveling correlation function" that reduces to the separate correlation functions — Equations 13.1.7, 13.1.16, and 13.1.17 — is

$$C(\xi, \eta, \tau) = \exp\left[-(\xi - u\tau)^2/L_x^2\right] \exp\left[-(\eta/L_y)^2\right] \cos\left(K_{xm}\xi - \Omega_m\tau\right) \quad \textbf{(13.1.20)}$$

A three-dimensional surface correlation function such as Equation 13.1.20 has been used to predict the correlation of sound scattered from the sea surface (Clay and Medwin 1970).

13.1.2 THE ROUGH OCEAN BOTTOM

PDF of Displacements and RMS Roughness

The ocean bottom roughness is sometimes defined in terms of its PDF of displacements above and below the mean, as in Fig. 13.1.8, or, more often, in terms of the rms deviation from the mean, h, which is called the "bottom roughness," as shown in Table 13.1.

Spatial Frequency Spectrum

A different presentation exploits the spatial transform relations of the previous section. In analogy to the Pierson-Moskovitz *temporal* frequency spectrum for water waves, one specifies a *spatial* frequency spectrum in terms of the wave number, K (radians per wave length) or, quite commonly, in terms of the cycles per unit distance, $\mathcal{K}$. A vast variability of spectra of ocean bottoms has been observed.

The framework adopted is to assume that the spatial "power" spectral density of the roughness follows the empirical law

$$\Phi(\mathcal{K}) \sim \mathcal{K}^{-b} \quad \textbf{(13.1.21)}$$

where Φ is the "power" spectral density in units of [m^2/(cycle/distance)], $\mathcal{K}$ is the spatial cycle frequency (e.g., cycles/m or cycles/km), and b is a constant that is fitted for the "province" of the bottom that is being described. The parameter b is often assumed to be 3, but values from less than 2 to 5 have been found, as shown in the following Table 13.1 from Berkson and Matthews (1983).

Sometimes the amplitude spectrum is specified rather than the "power" spectrum. Then, instead of Equation 13.1.21, the empirical equation is

$$\mathcal{A}(\mathcal{K}) \sim \mathcal{K}^{-b/2} \quad \textbf{(13.1.22)}$$

Table 13.1 **Roughnesses of Various Sea Bottoms**

Physiographic Province	*Ocean*	*Band-Limited h, RMS (Meters)*	*b*
Rise	Atlantic	3.7	3.2
Continental Slope	Atlantic	6.4	2.2
Seamount	Atlantic	3.6	2.1
Abyssal Plain	Atlantic	<1.3	—
Abyssal Plain	Atlantic	<1.5	—
Rise	Norwegian Sea	<1.1	—
Abyssal Hills	Pacific	3.4	4.9
Continental Shelf	Norwegian Sea	2.5	2.0
Marginal Plateau	Norwegian Sea	1.9	1.9
Abyssal Hills	Pacific	2.5	4.2
Continental Rise	Mediterranean	<1.4	—
Continental Rise	Norwegian Sea	<1.2	—
Marginal Plateau	Norwegian Sea	2.1	1.5
Abyssal Hills	Pacific	2.3	2.2
Continental Rise	Mediterranean	<1.0	—
Basin	Norwegian Sea	5.4	1.8
Basaltic Interface*	Atlantic (av. of 50)	259 ± 74	1.8 ± 0.4
Basaltic interface*	Pacific (av. of 50)	99 ± 36	1.6 ± 0.4

RMS displacement (roughness), h, and spectral slope parameter b, for various band-limited topographies as defined in Equation 13.1.21. Spatial wave number band pass is 0.003 to 0.03^{-1} for all cases except the basaltic interfaces (*), where the band pass is from 0.00006 to $0.003\ m^{-1}$. In cases where the RMS roughness is less than the resolution of the measuring system, the upper limit of RMS is given, and b is not estimated. Source: Berkson and Matthews (1983).

The appropriate spectral description of a backscattering patch of ocean bottom depends on the beam pattern "footprint" (that is, the insonified area) and the frequency of the sound. The description of the province is generally determined from echo soundings made from a ship on the ocean surface. Then the footprint is very large, and the returns are averaged, so that the scale of that spectral description is many meters or a fraction of a kilometer. On the other hand, a remotely operated undersea vehicle operating at higher frequencies at closer ranges will backscatter from a much smaller footprint. The spectral description and the rms roughness appropriate to such a usage is very different, and the predictions of backscatter will require a different value of b in Equation 13.1.21. At intermediate ranges, the backscattering is determined by the tilt of the surface as well as the local patch descriptors. Quantitative methods for performing such

an analysis have been described by Fox and Hayes (1985) for the large-scale problem. Goff and Jordan (1988) have demonstrated how Sea Beam backscatter data (see Chapter 14) from a track 100 to 200 km long can be inverted to provide a statistical description of the sea-floor morphology.

The power law relations and spectral regions of applicability depend on physiographic provinces (Malinverno 1989a, 1989b). Over limited dimensions on the sea floor and a limited spectral range, one can compute the root-mean-square roughness and spatial correlation functions from measurements of the displacements with respect to the mean level.

Circularly Symmetric Isotropic Correlation Function

A two-parameter isotropic surface correlation function can be written

$$C(r) = \exp\left[-\left|\frac{r}{L}\right|^n\right] \tag{13.1.23}$$

where L is the omnidirectional "correlation distance" and parameter n is a positive number. Examples of correlation functions and their spectra are shown in Fig. 13.1.9.

The function (Equation 13.1.23) is the exponential when $n = 1$ and the Gaussian when $n = 2$. The power of n in the correlation function is an indicator of the shape of the surface. When $n > 1$, the correlation function decays gradually for $r/L < 1$; this corresponds to a surface having large radii of curvature. When $n < 1$, the correlation decays very rapidly in the region $r/L < 1$; this corresponds to a surface having sharp angular features. The corresponding spectra and correlation functions for the exponents $0.5 \leq n \leq 2.0$ are shown in Fig. 13.1.9. The Fourier transformations were evaluated numerically.

Laboratory Model of a Rough Ocean Bottom

A laboratory scale model of an "isotropic" rough surface was constructed by a visually "uniform" distribution of #2 aquarium gravel (consisting of stones roughly 1/4″ in size) in order to scale-model the coupling between modes of propagation in a rough-surfaced waveguide (Kasputis and Hill 1984). The results of very careful measurements of the statistics of the "uniform," "isotropic" surface are a cautionary demonstration of how unlikely it is to find an isotropic correlation function in the real world. (Furthermore, turbidity currents in the ocean can cause significant anisotropy of the correlation function.) The rms height was 0.150 cm; the correlations were different in different directions (Fig. 13.1.10), with correlation lengths that ranged from 1.2 to approximately 2.0 mm

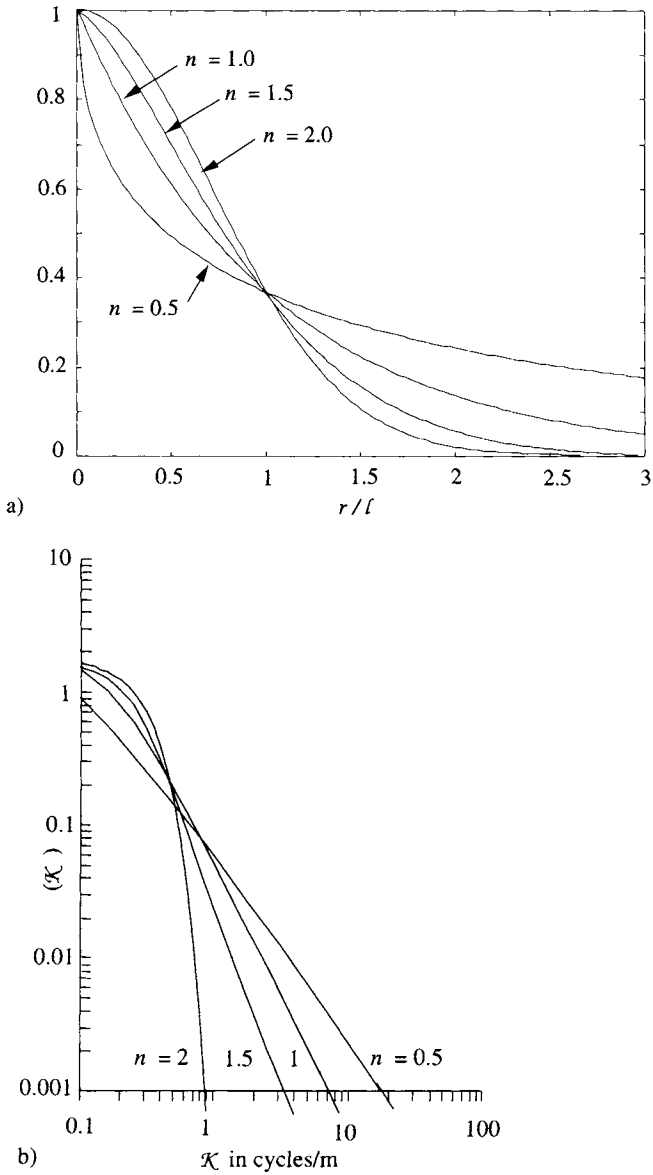

Figure 13.1.9 Examples of isotropic correlation functions a) described by Equation 13.1.23 for various values of n, and their spatial "power" spectra, $\Phi(\mathcal{K})$, which are Fourier transforms of the spatial correlation functions b). The Gaussian correlation function is the case $n = 2$.

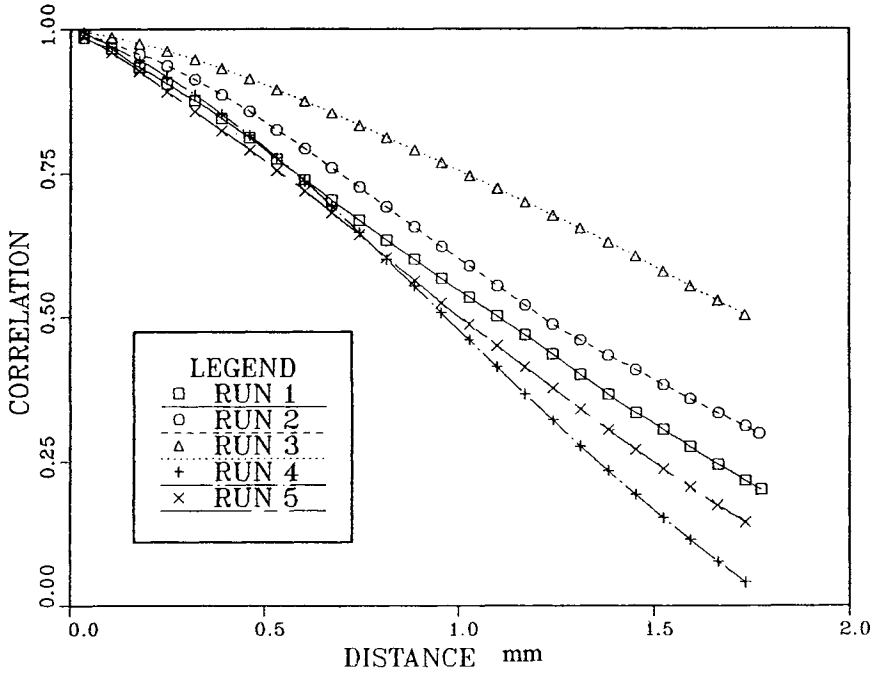

Figure 13.1.10 Variation of correlation function for different directions in a laboratory scale model that used "uniformly spread" nominal 1/4″ gravel. The Kasputis-designed micrometer measured heights in increments of 20 microns at spacing of 35 microns. (From Kasputis, S., and P. Hill, "Measurement of mode interaction due to waveguide surface roughness," MS thesis, Naval Postgraduate School, Monterey, CA, 1984.)

(depending on the direction), with an average value of 1.48 mm. Comparing with Fig. 13.1.9, we clearly see that the different values of n were all somewhat greater than unity.

13.2 Forward Scatter in the Specular (Mirror) Direction: Simple Concepts

Before we apply the general HKF theory to scatter from a rough surface (section 13.3), it is helpful to consider the important case of surface scatter in the mirror (specular) direction under simplifying assumptions. The results of this section provide guidance in the interpretation of the more general problem. "Specular scatter" is defined as scatter in the direction of mirror reflection (i.e., the angle of scatter equals the angle of incidence and is in the same plane of incidence). Our important conclusion will be that specular scatter consists of a coherent

component, which has a fixed-phase relation with respect to the incident sound, and an incoherent component. The coherent component will be found to depend on the rms height and the PDF of the surface roughness. The incoherent sound is a function of the two-dimensional statistics of the surface and the geometry of the experiment.

The special case of specular scatter at grazing incidence to a steep-sloped rough surface will be discussed in section 13.4.

13.2.1 MEAN COHERENT SCATTERED PRESSURE IN THE SPECULAR DIRECTION, ACOUSTICAL ROUGHNESS

Consider Fig. 13.2.1, in which a spherical wave front, which is approximated by a CW plane wave segment at (AA), is incident on a rough surface that has homogeneous, stationary statistics as described in section 13.1. Assume that all points of the interface have a reflection coefficient $\mathcal{R}_{12}$ due to the impedance change at the interface, and that $ka \gg 1$ where a is the local radius of curvature and k is the acoustic wave number. With this Kirchhoff assumption, each ray experiences a phase shift relative to the phase of reflection from the mean surface. The phase shift depends on k, the surface displacement, ζ, and the angle of incidence, θ. The specular scatter contributions come from insonified horizontal facets. For a facet with displacement ζ, the path difference to the plane wave position at BB is $2\zeta \cos \theta$ and the spatial phase difference equals

$$k\ (2\zeta \cos \theta\ ) \tag{13.2.1}$$

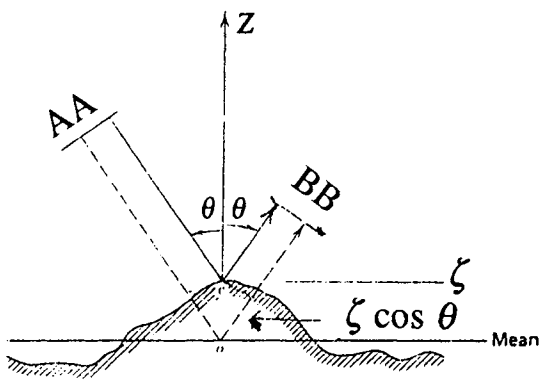

Figure 13.2.1 Path differences for specular scatter from a typical horizontal facet of a rough surface. In general, many such horizontal facets will be insonified by an incident beam.

In terms of the perfect mirror-reflected signal from the mid-surface, at any instant the real value of the pressure reflected at a facet of the rough surface will be

$$p_{rough} = \mathcal{R}_{12}\, p_{mir} \cos(2k\zeta \cos\theta) \tag{13.2.2}$$

We assume that during each ping the rough surface is "frozen" in time. The many horizontal facets of different elevations within an insonified surface result in many contributions to the total specularly scattered pressure at any instant of time. For a given surface configuration (a "realization"), the interfering sum of the contributing pressures produces a coherent pressure as represented by p_{rough}. Similarly, other surface realizations of the same statistics produce specularly scattered, phase-shifted signals.

The average pressure from these interfering reflections at a particular time depends on the statistics of the surface. For simplicity, assume that the PDF of the surface is Gaussian. To find the average relative pressure, calculate the product of the relative amplitude of each component—$\mathcal{R}_{12} \cos(2k\zeta \cos\theta)$ times the Gaussian PDF from Equation 13.1.1—and integrate over all ζ. The average of the ratio of the coherent, specularly scattered pressure to the mirror-reflected pressure from the mean surface is

$$\left\langle \frac{p_{rough}}{p_{mirror}} \right\rangle = \mathcal{R}_{12} \int_{-\infty}^{\infty} \{\cos(2k\zeta \cos\theta)\} \left\{ \frac{1}{h\sqrt{2\pi}} \exp\left[-\frac{1}{2} \left(\frac{\zeta}{h} \right)^2 \right] \right\} d\zeta \tag{13.2.3}$$

where h is the rms displacement of the surface. The integration yields the coherent reflection coefficient for a Gaussian rough surface,

$$\mathcal{R}_{coh} = \left\langle \frac{p_{rough}}{p_{mirror}} \right\rangle = \mathcal{R}_{12} e^{-(2kh\cos\theta)^2/2} \tag{13.2.4}$$

Note that, for CW, the stacking average over instantaneous values is equivalent to an average over the peak values $\mathcal{R}_{coh} = \langle P_{rough}/P_{mirror} \rangle$.

The rough surface coherent pressure reflection coefficient, $\mathcal{R}_{coh}$, which is often called $\langle \mathcal{R} \rangle$ in the literature, is the product of the coefficent due to a change of medium, $\mathcal{R}_{12}$ (section 2.6.11), and that fraction owing to mutual phase cancellations of the scatter contributions, $\exp[-(2kh\cos\theta)^2/2]$. When the rough surface is symmetrical—that is, when the skewness moment m_3 (Equation 13.1.3) of the displacements is zero—the contributing phase shifts from below and above the mean level cancel each other. Then, although the amplitude is reduced, the phase of the coherent mean pressure is the same as would occur for a mirror-reflected pressure from the mean surface. When there is peakedness or

kurtosis (Equation 13.1.4), more of the horizontal facets are at small or zero displacements from the mean surface, and the coherent component is enhanced.

The specularly scattered coherent intensity relative to the mirror-reflected intensity is

$$\mathcal{R}_{coh}^2 = \mathcal{R}_{12}^2 e^{-g_R} \tag{13.2.5a}$$

where

$$g_R, \text{ the ``acoustical roughness''} = (4k^2h^2 \cos^2 \theta) \tag{13.2.5b}$$

Sometimes the quantity $(g_R)^{1/2}$ is called the "Rayleigh Roughness Parameter," to honor the discoverer of the effect. Sometimes Equation 13.2.5b is written in terms of the grazing angle, in which case the sine of the grazing angle replaces the cosine of the angle with the normal to the surface. An "acoustically smooth" surface, $g_R \ll 1$, has stronger specularly scattered energy because it has an rms height much less than the acoustic wavelength or is nearer grazing, $\theta \to 90^0$. (But see section 13.4 for steep-sloped roughness elements.)

The predictions of Equation 13.2.5a have been carefully tested many times in laboratory wind-blown wave systems with a near-Gaussian PDF of heights. Mayo (1969) correlated the incident and scattered signals in the specular direction at 50 kHz and 100 kHz, at seven angles of incidence and several surface rms heights, 0.1 cm $< h <$ 0.45 cm (Fig. 13.2.2). The simple conclusion (Equation 13.2.5a) is confirmed up to $g_R \cong 1$. Data from these and additional experiments have been analyzed by Clay, Medwin, and Wright (1973), who found that small deviations from the Gaussian PDF, and shadowing, profoundly change the coherent scatter at large g_R. An early determination of bottom rms roughness by studying coherent specular scatter from the deep sea floor was that of Clay (1966).

13.2.2 INVERTING FOR THE PDF OF HEIGHTS

For a general PDF of heights, $w(\zeta)$, Equation 13.2.3 would be written

$$\left\langle \frac{p_{rough}}{p_{mirror}} \right\rangle = \mathcal{R}_{12} \int_{-\infty}^{\infty} w(\zeta) \{ e^{-2ik\zeta \cos\theta} \} \, d\zeta \tag{13.2.6a}$$

Note that the integral (13.2.6a) has the form of the Fourier integral transformation, with ω replaced by $2k \cos \theta$. Therefore one can calculate its inverse,

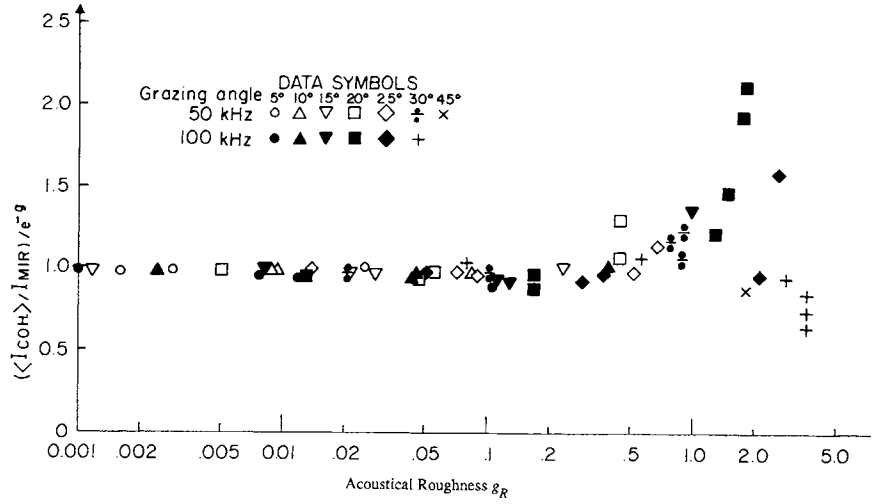

Figure 13.2.2 Ratio of rough-surface, specularly scattered coherent intensity ($I_{coherent}$) to smooth-surface reflection, I_{mirror}, relative to the simple theoretical prediction e^{-g_R}, for various values of roughness parameter, g_R. (From Mayo, N. H., "Near-grazing, specular scattering of underwater sound from sea and swell," M.S. thesis, U.S. Naval Postgraduate School, Monterey, Calif., 1969.)

which is the acoustical estimate, w_a, of the PDF of the surface displacements,

$$w_a(\zeta) = \frac{1}{\pi \mathcal{R}_{12}} \int_{-\infty}^{\infty} \mathcal{R}_{ss} \exp(2ik\zeta \cos\theta) d(k \cos\theta) \qquad \textbf{(13.2.6b)}$$

The good agreement between the observed specular scatter and that predicted from the wave height as well as the result of inversion are shown in Fig.13.2.3 for a laboratory experiment of Spindel and Schultheiss (1972).

13.2.3 STATISTICS OF SCATTER IN THE SPECULAR DIRECTION

Assume that we have a CW beam specularly scatttered from an ocean surface. As the ocean surface moves by a fixed sonar, or as a sound beam on a ship moves past a rough bottom surface, the scattered pressure amplitude $|P|$ will fluctuate. From statistics theory (see also section 9.4.2), it is known that the mean-squared value of a randomly varying quantity is equal to the square of its mean value plus the variance of the quantity. Therefore the total specularly scattered intensity, which is proportional to $\langle |P^2| \rangle$, can be determined from the sum of the coherent

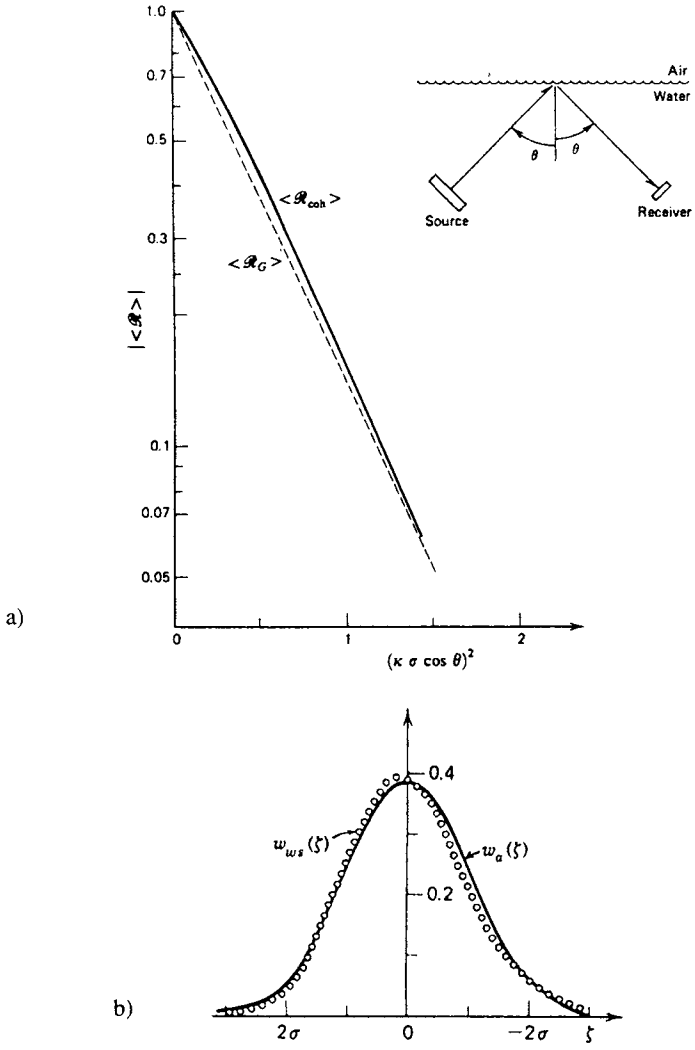

Figure 13.2.3 a) Coherent reflection coefficient for specular scatter, $\langle \mathcal{R}_{coh} \rangle$, measured in a laboratory, wind-driven sea compared with the value predicted from a Gaussian PDF of surface displacements $\langle \mathcal{R}_G \rangle$. b) The PDF inverted from acoustical measurements w_a (Equation 13.2.6) is compared with the wave staff measurements of the PDF, w_{ws}. (From Spindel, R. C., and P. M. Schultheiss, "Acoustic surface-reflection channel characterization through impulse response measurements," *J. Acoust. Soc. Am.* **51**, 1812, 1972.)

component described in the previous section, $\langle |P| \rangle^2$, and an incoherent component, the variance of $|P|$,

$$\langle |P^2| \rangle = \langle |P| \rangle^2 + \text{Var}\,|P| \tag{13.2.7}$$

Var $|P|$, a measure of the random phase and amplitude of the scattered sound that depends on the correlation of surface displacements, will be considered in the next section. The similarity between variability of the envelope of scattered sound and the statistics of noise added to a sinusoid in an electrical circuit allows the results developed by S. O. Rice (1954) to be adapted to sound scatter (see also section 9.4.2). Ricean statistics for sound scatter can be defined in terms of the relative coherence,

$$\gamma = (\text{coherent intensity})/(\text{incoherent intensity}) = \langle |P| \rangle^2 / \text{Var}\,|P| \tag{13.2.8}$$

For acoustically smooth surfaces, $g_R < 1$, $\gamma > 1$, there is a relatively large coherent component, and the specularly scattered pressure distribution is nearly Gaussian (Equation 13.1.1). At the other extreme, for acoustically rough surfaces, $g_R > 1, \gamma < 1$, the probability density function approaches the Rayleigh PDF for the sum of a large number of randomly phased, equal amplitude components,

$$w_{Rayl}(|P|) = \frac{|P|}{h^2} \exp\left(-\frac{|P|^2}{2h^2}\right) \tag{13.2.9a}$$

The distribution described by Equation 13.2.9a was derived by Lord Rayleigh (1894, 1896, 1945) for the specific problem of determining the sum of a large number of randomly phased, equal-amplitude wave components. It can be shown (e.g., Beckmann and Spizzichino 1963) that of all possible distributions of the amplitude of a field scattered by a symmetrically distributed rough surface, the Rayleigh distribution has the greatest variance; in terms of acoustic pressure during sound scatter, that value is

$$\text{Variance} = 0.212\langle (|P_{\text{scat}}|/|P_{\text{mir}}|)^2 \rangle \tag{13.2.9b}$$

where $|P_{\text{mir}}|$ is the amplitude of the pressure that would be reflected from a mirror-smooth surface.

Electrical engineers sometimes represent the magnitude and phase of a time-varying component by a "phasor." A phasor is drawn with a length proportional to the amplitude and at an angle that represents the relative phase of the component. Phasors add like vectors. From the phasor point of view, a near-Gaussian distribution is caused by the addition of a strong constant phasor (representing the mean value of the scattered sound) to much smaller, randomly distributed, time-variable phasors. On the other hand, the Rayleigh distribution is

approached for sound scatter when the constant phasor component, which represents the coherent signal, is very small compared with the variable, randomly phased contributions.

The change of the PDF of the scatter for surfaces of different acoustical roughnesses has been demonstrated by using a laboratory wind-driven sea. In the top panel of Fig. 13.2.4, at $g_R = 0.12$, $\gamma = 10$, the coherent intensity $\langle |P^2| \rangle$ is 10

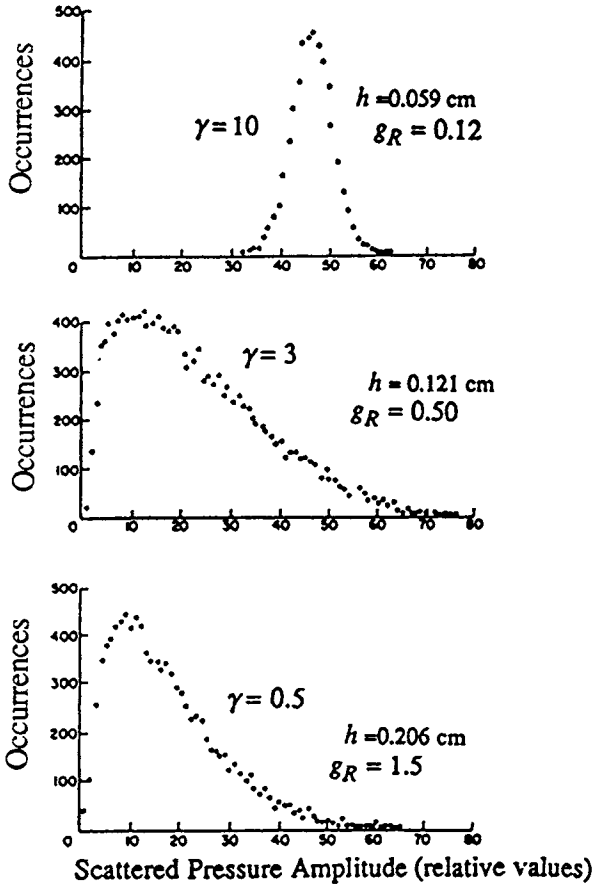

Figure 13.2.4 PDF of specularly scattered, normal-incidence sound amplitudes for three laboratory Gaussian water surfaces of rms heights, $h = 0.059$ cm, 0.121 cm, and 0.206 cm (*top to bottom*). The PDF of the pressure amplitude goes from Gaussian to Rayleigh as the acoustical roughness increases (*top to bottom*) from $g_R = 0.12$ to 0.50 to 1.5 and the relative coherence of the specularly scattered sound intensity, γ, decreases fom 10 to 3 to 0.5. The sound frequency was 70 kHz. (From Ball, E. C., and J. A. Carlson, "Acoustic backscatter from a random rough water surface," M.S. thesis, Naval Postgraduate School, Monterey, Calif., 1967.) See also Stephens (1970, Chap. 3).

times the incoherent Var P, and the PDF of the amplitude of the specular scatter is virtually Gaussian, with a large mean value of $|P|$. When $g_R = 1.5$, $\gamma = 0.5$ (bottom panel), and the coherent intensity is half the incoherent, the peak-scattered amplitude has been greatly reduced and has nearly a Rayleigh PDF.

13.2.4 *INTENSITY OF SOUND SCATTERED IN THE SPECULAR DIRECTION: SCALE-MODEL RESULTS*

The coherent component of intensity in the specular direction decreases with increasing acoustical roughness (Fig. 13.2.3a). Extensive theoretical research has shown that at roughness $g_R \gg 1$, the total scattered intensity will be dominated by the incoherent component. For plane-wave incidence at a surface with a Gaussian PDF and a Gaussian correlation function, the forms of the contributing components are shown in Fig. 13.2.5.

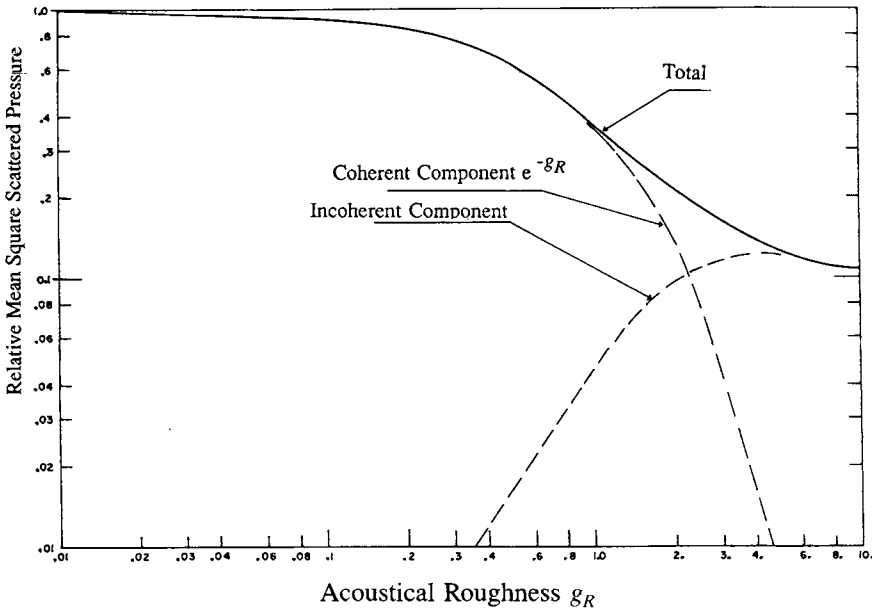

Typical Behavior of Coherent and Incoherent Components in Specular Scatter

Figure 13.2.5 Specularly scattered, mean-squared pressure relative to mirror reflection as a function of the surface acoustical roughness, g_R, showing the dominating coherent component at low roughness and the controlling incoherent component at larger acoustical roughness that depends on the surface correlation function and the area insonified. To get these theoretical results, an incident plane wave of cross section area A is assumed, as well as a Gaussian PDF of heights and a Gaussian spatial correlation function.

The incoherent scattering theory line of Fig. 13.2.5 has been calculated by assuming that the incident sound is a plane wave of cross section area A, that the surface roughness has a Gaussian PDF of heights and an isotropic Gaussian spatial correlation function of displacements. The asymptotic high-frequency value is then found to be proportional to the insonified area and inversely proportional to the mean-square slope, s^2. Eckart (1953), Beckmann and Spizzichino (1963), and Tolstoy and Clay (1966, 1987) also show that, for such a Gaussian surface, the rms slope, s, is simply related to the rms height, h, and the isotropic spatial correlation length, L.

The general relation is

$$\langle s^2 \rangle = -h^2 \frac{\partial^2 [C(\xi)]}{\partial \xi^2}\Big|_{\xi = 0} \tag{13.2.10a}$$

From Equation 13.1.17, for an isotropic Gaussian spatial correlation function of correlation length L,

$$C(\xi) = \exp[-(\xi/L)^2] \tag{13.2.10b}$$

After differentiating (13.2.10b) to insert into (13.2.10a),

$$s = \sqrt{2}h/L \tag{13.2.10c}$$

where s is the rms value of the isotropic slope. However, note that real surfaces such as in Figs. 13.1.5 and 13.1.10 generally do not have an isotropic Gaussian spatial correlation function.

Laboratory experiments by Ball and Carlson (1967) and Medwin (1967), observing multifrequency, normal-incidence scatter in a wind wave tunnel, have confirmed the form of Fig. 13.2.5. At the top of Fig. 13.2.6 is a sketch of one experimental setup to measure the specular scatter at normal incidence. The PDF of the slopes was determined by photographing ten cases of the glitter deflection at various positions below a string grid as shown typically at the bottom of Fig. 13.2.6. The rms slope s and ratio of the windward to the crosswind slopes, s_w/s_c, were similar to Fig. 13.1.2 and were found from Equation 13.1.5 to be equivalent to a wind 1.4 m/s at 12.5 m over an ocean surface. The rms slope has also been obtained by integration of the output of a photocell, using a colocated point source (see Fig. 13.1.2) in this early experiment.

To determine both h and s by specular scatter, eight sequential pings of frequencies from 21 to 194 kHz, total duration 2.2 ms, were radiated perpendicular to the surface, from a low Q Mylar transducer. The PDF of the specular scatter at 21 kHz was nearly Gaussian; therefore it was assumed that, at that frequency, the scatter was coherent, and Equation 13.2.5 was used to

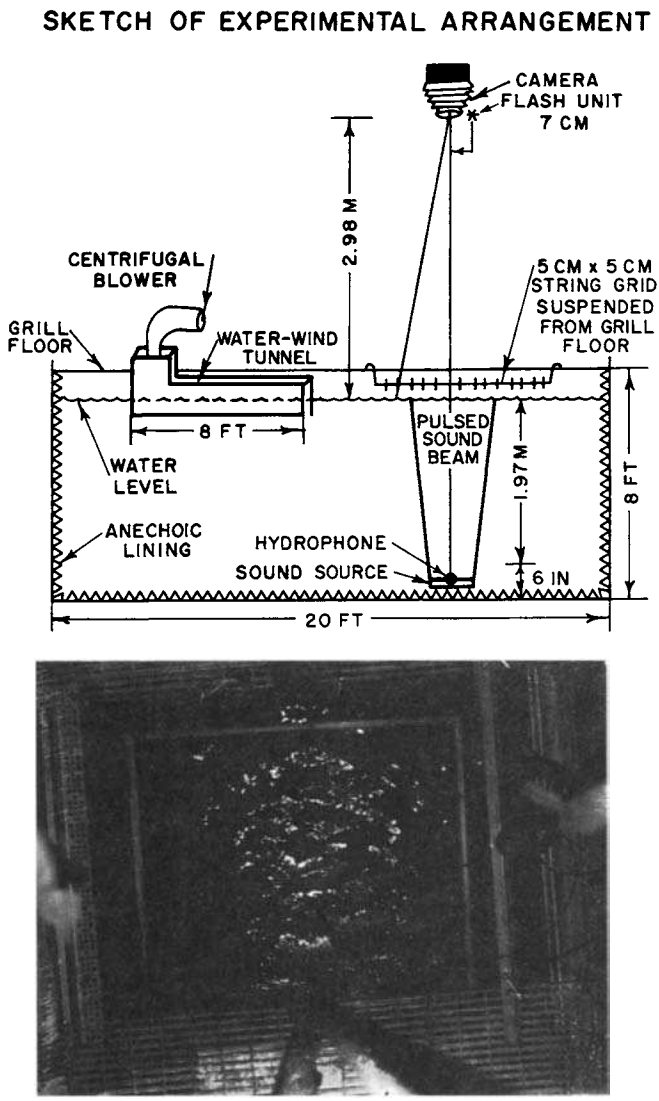

Figure 13.2.6 *Above*, sketch of experimental arrangement. The floating water wind tunnel was constructed of wood in the form of an inverted "U" in cross section. The 2.2 ms duration pulsed sound beam was a sequence of 12 to 29 cycles of each of eight frequencies from 21 to 194 kHz insonifying the surface in the transducer's near field. *Below*, a typical glitter pattern used to determine the PDF of slopes by the light deflection. (From Medwin, H., "Specular scattering of underwater sound from a wind-driven surface," *J. Acoust. Soc. Am.* **41**, 1485–95, 1967.)

calculate the rms height, h. This allowed the specification of the acoustical roughnesses $0.3 < g_R < 25$ for the range of frequencies of the experiment.

At $g_R = 10, 14, 19, 25$, the statistics of the scatter approached the Rayleigh PDF. Therefore, the specular scatter was assumed to be totally incoherent for these four asymptotic points (Fig. 13.2.7). The rms slope s was calculated from acoustics theory for $g_R \gg 1$ and found to be in satisfactory agreement with the optical value.

In summary, the value of the rms slope, obtained optically, or from formulas such as Equation 13.1.5 for the ocean surface, can be used to estimate the magnitude of the asymptotic (large g_R) incoherent component of specular scatter for a surface assumed to have a Gaussian PDF and a Gaussian correlation function. Inversely, the rms slope, s, can be estimated from measurements of specular scatter for large g_R values if the surface is Gaussian in height and correlation function (see section 13.3.3).

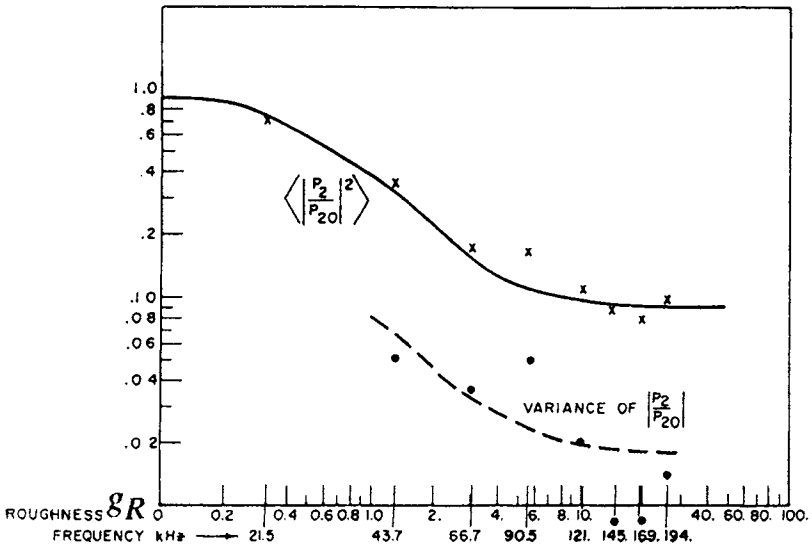

Figure 13.2.7 Experimental results showing the normal-incidence, mean-squared, specularly scattered pressure relative to mirror reflection for eight frequencies, using the wind wave laboratory arrangement shown in Fig. 13.2.6. The nearly plane-wave insonification of the surface was over an area approximately equal to the area of the source, a 24 cm diameter piston. For $g_R < 1$, the relative intensity goes as $\exp(-g_R)$. For $g_R > 10$, the relative intensity is independent of frequency and is proportional to the insonified area and inversely proportional to the mean-square slope. The theoretical variance for a Rayleigh PDF (Equation 13.2.9b) is shown by dashed line for the mostly incoherent specular scatter at $g_R > 1$. (From Medwin, H., "Specular scattering of underwater sound from a wind-driven surface," *J. Acoust. Soc. Am.* **41**, 1485–95, 1967.)

A much more extensive set of laboratory measurements (Thorne and Pace 1984) employed a parametric source (section 5.4) to get narrow beams with a wide range of frequencies. An underwater pressure-release surface was constructed of low-density polyurethane with Gaussian PDF of displacements and a simple "isotropic" Gaussian correlation function to represent an ocean surface. The phase-sensitive HKF scattering solution of section A10.5 of Clay and Medwin (1977) (see section 13.3.2 of this chapter) was used to predict the incoherent normal incidence surface scatter, and the inverse proportionality to the mean-square slope, s^2, was confirmed (for this Gaussian surface) to be independent of sound frequency for $g_R \geq 10$. The interrelation of s, h, and L (Equation 13.2.10c) was applied to calculate s.

Ocean Experiments

Clay (1966) showed that the bottom roughness is characteristic of sea bottom processes, and suggested ways to measure it. The methods were then used by Leong (1973) and Clay and Leong (1974) to consider a sea-floor area southwest of Spain. The 12 kHz echo-sounding profiles, the 3.5 kHz subbottom profiles, and the seismic profiles (25 to 100 Hz) were analyzed to estimate the sea-floor roughness periodograms in the four spatial wavelength ranges: less than 1 km, 0.6 to 3 km, 2 to 6 km, and 6 to 12 km. The histograms of the spectral estimates mapped consistently into small "provinces" on the sea floor.

T. K. Stanton (1984) has employed a technique similar to the experiment resulting in Fig. 13.2.7 to obtain the rms height h of ocean bottom "micro-roughness" at small values of g_R and has supplemented this by obtaining bottom correlation information from the Ricean statistics of the specularly scattered sound. A ship-mounted 3.5 kHz sonar was used at water depths of 20–30 m to identify ripples, beds of rocks, and nodules.

13.2.5 OTHER SPECULAR SCATTER EFFECTS

Non-Gaussian Surfaces

The several derivations that lead to the conclusions that rms height h can be obtained from the low roughness ($g_R \ll 1$) specular scatter, and rms slope s can be determined from the very high roughness data ($g_R \gg 1$), are based on surfaces defined by a Gaussian PDF of heights and Gaussian correlation function (simply, "Gaussian surfaces"). When the surface is not Gaussian, one may find several

arbitrary surface realizations that produce scattered pressures that deviate from the above conclusions (Kinney and Clay 1985).

Short-Term Signal Enhancements

The theoretical predictions of specular scatter, and the measurements that lead to statistical data such as displayed in Fig. 13.2.4, are based on long-term observations for a Gaussian surface. But a Gaussian surface will produce very different scatter for shorter periods of time. It may even cause acoustic pressures greater than for plane surface reflection, for shorter periods of time (Medwin 1967). For example, Perkins (1974) and Shields (1977) have used a laboratory wind-blown Gaussian surface to demonstrate signal enhancement (compared with average values) of the order of 3 to 5 dB for surfaces of roughness of $0.5 < g_R < 4$ during experiments that lasted for five "ocean" surface wave periods. At sea, this would correspond to specular scattering enhancements over many seconds to minutes for certain sound frequencies.

Long-Range Reverberation

Theoretically, it should be possible to use long-range reverberation to extract information about prominent underwater topographic features. Good progress has been made, so that it is now clear that major echoes in reverberation come from the faces of escarpments that are large enough and flat enough (compared to the acoustic wavelength) and properly oriented to coherently reflect the incident sound in a deterministic manner. A positive ocean-basin geomorphological identification has been made by use of 268 Hz sound traveling beyond two convergence zones over ranges of 100 km even in the presence of refraction, Lloyd's mirror interferences, and the cacophony caused by smaller diffractors at the western Mid-Atlantic Ridge (Makris et al. 1995).

13.3 Surface Scatter of Sound

The original theoretical research on scattering from rough surfaces dealt with incident plane waves and dates from the 1950s (Eckart 1953; Isakovitch 1952); the first book was by Beckmann and Spizzichino (1963).[1] A recent, excellent book gives a detailed treatment of surface scattering using incident plane waves

[1]Most of this electromagnetics reference deals with scalar waves that may be interpreted as acoustic waves.

with the Helmholtz-Kirchhoff integral to compute scattering at rough interfaces (Ogilvy 1992).

Direct applications to ocean acoustics requires the introduction of Fresnel corrections (Horton 1970). Horton pointed out that the incident-plane-wave assumption is equivalent to having a large planar transducer radiating to the scattering surface in the near field. In the incident-plane-wave assumption, the scattering surface is small compared with the first Fresnel zone. (This was the condition in the experiment described in Fig. 13.2.6.) However, common underwater field experiments have geometries with small transducers far from the scattering surface. Then, the incident wave fields are curved, and Fresnel effects and corrections are important. We call the theory that includes Fresnel effects the HKF theory.

The conditions for validity of the Kirchhoff and small-slope assumptions made in the original derivations (which we follow) is a field of active research. In general, one compares exact solutions for specific geometries with the various approximate theoretical approaches and looks for higher-speed methods of calculation. Thorsos (1988) points out that predictions based on the Kirchhoff approximation are generally acccurate for surfaces with a Gaussian PDF of heights and slopes, provided that the correlation length is greater than the sound wavelength, $L > \lambda$. Kaczkowski and Thorsos (1994) use the parameter *khs* (where k is the acoustic wave number, h is the Gaussian rms height, and s is the Gaussian rms slope) to evaluate an efficient "operator expansion method" of solution. Thorsos and Broschat (1995) have extended the Voronovitch (1985) small-slope approximation method to speed the accurate calculation of scattering from rough surfaces.

13.3.1 SCATTER OF A SPHERICAL WAVE: HELMHOLTZ–KIRCHHOFF–FRESNEL SOLUTION

Now we formally employ the HKF theorem developed in Section 7.2 to derive the scattering of a CW signal as a function of the sonar characteristics and the surface statistics. Assume the source projects a Gaussian beam pattern (section 4.2) that insonifies a small area of the rough surface (Fig. 13.3.1). The Gaussian insonification function is convenient because it can be integrated easily.

We will use the HKF integral (Equation 7.2.19) with the following assumptions:

(1) The source and receiver are far from the insonified area.

(2) The dimensions of the source are small compared with R_1 and R_2.

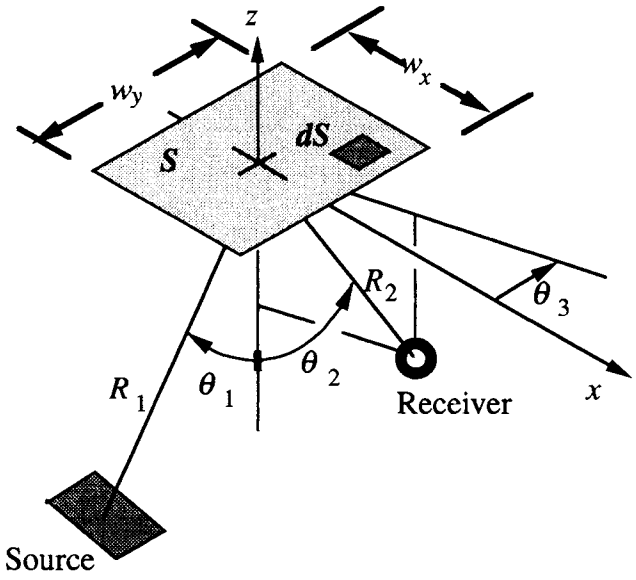

Figure 13.3.1 Scattering geometry. Differential area dS is at the position x, y and has height ζ with respect to the mean surface. The plane of the source is perpendicular to range R_1, which is in the x-z plane. The plane of the transducer x'-y' is normal to R_1.

(3) No surface shadowing occurs.

(4) The reflection coefficient, $\mathcal{R}_{12}$, is constant over the insonified area.

(5) The scatter diverges spherically from the insonified points.

The incident sound pressure is

$$p_{inc} = \frac{D_t P_0 R_0 \exp\ [\, i\,(\,\omega t - k R_s\,)\,]}{R_s} \tag{13.3.1}$$

where R_s is the range from source to surface element dS (Fig. 13.3.1); P_0 is the source pressure at range $R_0 = 1$ m; D_t is the Gaussian transmission function; W_g and L_g are the half-beam widths to $D_t = e^{-1}$, described by

$$\Delta\phi \cong \sin\phi = \frac{2}{kW_g} \tag{13.3.2a}$$

and

$$\Delta\chi \cong \sin\chi = \frac{2}{kL_g} \tag{13.3.2b}$$

At distance R_1, the transducer's insonification factor is

$$D_t = \exp\left(-\frac{x^2}{X^2} - \frac{y^2}{Y^2}\right) \tag{13.3.2c}$$

where

$$X \cong R_1 \frac{\Delta\chi}{\cos\theta_1} \quad \text{and} \quad Y \cong R_1 \Delta\phi \tag{13.3.2d}$$

The pressure scattered from a point at range R_2 to the receiver is

$$p \cong \frac{ip_0 R_0 \mathcal{R}_{12} k G(\theta) \exp[i\omega t - ik(R_1 + R_2)]}{2\pi R_1 R_2} \times \int\int_{-\infty}^{\infty} D_t \exp\left[-i\left(\frac{x^2}{x_f^2} + \frac{y^2}{y_f^2} + 2\alpha x + 2\beta y + 2\gamma\zeta\right)\right] dy\, dx \tag{13.3.3a}$$

where

$$x_f^{-2} \equiv \frac{k}{2}\left(\frac{\cos^2\theta_1}{R_1} + \frac{1 - \sin^2\theta_2 \cos^2\theta_3}{R_2}\right) \tag{13.3.3b}$$

$$y_f^{-2} \equiv \frac{k}{2}\left(\frac{1}{R_1} + \frac{1 - \sin^2\theta_2 \sin^2\theta_3}{R_2}\right) \tag{13.3.3c}$$

$$G(\theta) \cong \frac{\cos\theta_1 + \cos\theta_2}{2} \tag{13.3.4}$$

$$2\alpha \equiv k(\sin\theta_1 - \sin\theta_2 \cos\theta_3) \tag{13.3.5a}$$

$$2\beta \equiv -k(\sin\theta_2 \sin\theta_3) \tag{13.3.5b}$$

$$2\gamma \equiv k(\cos\theta_1 + \cos\theta_2) \tag{13.3.5c}$$

Equation 13.3.4 is the small slope form of $G(\theta)$. From Tolstoy and Clay (1987, p. 199) and Ogilvy (1992, p. 84), the larger slope correction form of Equation 13.3.4 is

$$G_{sc}(\theta) \approx \frac{1 + \cos\theta_1 \cos\theta_2 - \sin\theta_1 \sin\theta_2 \cos\theta_3}{\cos\theta_1 + \cos\theta_2} \tag{13.3.6}$$

This factor misbehaves as the θ_1 and θ_2 tend to 90° — that is, at grazing angles of incidence. We suggest using Equation 13.3.4 near grazing. (See also section 13.4 for grazing incidence at steep-sloped surfaces.)

Smooth Surface Image Reflection

When roughness $\zeta = 0$, the integation of the HKF integral (Equation 13.3.3a) over the infinite limits gives the reflection as describred by a virtual image behind the surface. For an example, we choose the vertically incident specular direction and evaluate the parameters as follows:

$$D_t = 1, G(\theta) = 1, \alpha = 0, \beta = 0, \gamma\zeta = 0, \quad \text{and}$$
$$x_f^{-2} = y_f^{-2} = \frac{k}{2}\left(\frac{1}{R_1} + \frac{1}{R_2}\right) = \frac{k(R_1 + R_2)}{2R_1R_2} \tag{13.3.7a}$$

The integral (Equation 13.3.3a) reduces to

$$p \cong \frac{ip_0R_0\mathcal{R}_{12}k\exp\left[i\omega t - ik(R_1 + R_2)\right]}{2\pi R_1R_2} \times \int\int_{-\infty}^{\infty} \exp\left[-ik(x^2 + y^2)\left(\frac{R_1 + R_2}{2R_1R_2}\right)\right] dy\,dx \tag{13.3.7b}$$

From mathematical handbooks, the infinite integral is

$$\int_{-\infty}^{\infty} e^{-a^2x^2} dx = \frac{\sqrt{\pi}}{a} \tag{13.3.8a}$$

where

$$a^2 = \frac{ik(R_1 + R_2)}{2R_1R_2} \tag{13.3.8b}$$

Therefore, the evaluation of the HKF integral for a smooth surface gives the reflected pressure as due to a virtual image at range $R_1 + R_2$,

$$p = \frac{p_0R_0\mathcal{R}_{12}\exp\left[i\omega t - ik(R_1 + R_2)\right]}{R_1 + R_2} \tag{13.3.8c}$$

The HKF integral converges to the image reflection because we kept the second-order terms in the integral.

13.3.2 MEAN-SQUARED SCATTERED PRESSURE: SURFACE SCATTERING STRENGTH

The scattered sound intensity depends on the rms height h and the correlation of the nearby surface displacements within the insonified area. We use Equation 13.3.8c to compute the covariance $\langle p^*p(\zeta, \eta, \tau)\rangle$. To do the operation

symbolically, let the complex conjugate p^* represent the contribution from area dS and $p(\xi, \eta, \tau)$, that from the nearby surface element dS':

$$p^* = \int_s P[x, y, \tau]^* \exp[2i\gamma\zeta]\, dS \tag{13.3.9}$$

$$p(\xi, \eta, \tau') = \int_s P[x', y', \tau'] \exp[-2i\gamma\zeta']\, dS' \tag{13.3.10}$$

The covariance of the scattered pressure is

$$\langle pp^* \rangle_{scat} = \int_{s'} \int_s P[x, y, \tau]^* P[x', y', \tau'] \langle \exp[2i\gamma(\zeta - \zeta')] \rangle\, dS\, dS' \tag{13.3.11}$$

The Rough Surface Term

The surface's effect on the incident wave is described by the expression within $\langle\ \rangle$, which is called *the characterisic function* $\mathcal{W}$:

$$\mathcal{W} = \langle \exp[2i\gamma(\zeta - \zeta')] \rangle = \int_{-\infty}^{\infty} \int_{-\infty}^{\infty} w_2 \exp[2i\gamma(\zeta - \zeta')\, d\zeta\, d\zeta' \tag{13.3.12}$$

where w_2 is the bivariate PDF, which depends on both the PDF at a point and the correlation of the surface heights, $C(\xi, \eta)$, between points.

$$w_2(x, y, x + \xi, y + \eta) \equiv [2\pi h^2 (1 - C^2)^{1/2}]^{-1} \exp\left\{ -\frac{\zeta_1^2 + \zeta_2^2 - 2\zeta_1 \zeta_2 C}{2h^2(1 - C^2)} \right\} \tag{13.3.13a}$$

where

$$C = \frac{\langle \zeta_1 \zeta_2 \rangle}{h^2} \tag{13.3.13b}$$

For a statistically stationary surface, the value of $\mathcal{W}$ depends on ζ and ζ' and is a function of the separation ξ and η.

Change variables to include an assumed dependence of $\mathcal{W}$ on ξ and η,

$$\begin{aligned} x &= x'' + \frac{\xi}{2}, \quad y = y'' + \frac{\eta}{2} \\ x' &= x'' - \frac{\xi}{2}, \quad y' = y'' - \frac{\eta}{2} \end{aligned} \tag{13.3.14}$$

The surface integrals become

$$\int ( )\, dS \int ( )\, dS' = \int\int_{-\infty}^{\infty} ( )\, dx''\, dy'' \int\int_{-\infty}^{\infty} ( )\, d\xi''\, d\eta'' \tag{13.3.15}$$

The Beam Geometry Term

This term is expressed as

$$\mathcal{G} \exp\left(+2i\alpha\xi + 2i\beta\eta\right) \tag{13.3.16a}$$

where

$$\mathcal{G} \equiv \exp\left(-a_\xi \xi^2 - a_\eta \eta^2\right) \tag{13.3.16b}$$

and

$$a_\xi = \frac{X^2}{2x_f^4} + \frac{1}{2X^2}, \quad a_\eta = \frac{Y^2}{2y_f^4} + \frac{1}{2Y^2} \tag{13.3.16c}$$

Therefore, the general expression for the mean-squared scattered pressure is

$$\langle p\, p^* \rangle = p_0^2 R_0^2 \frac{\mathcal{R}_{12}{}^2 k^2 G^2(\theta) A e^{i\omega\tau}}{8\pi^2 R_1^2 R_2^2} \int\int_{-\infty}^{\infty} \mathcal{G}\, \mathcal{W}\, e^{2i(\alpha\xi + \beta\eta)} d\xi\, d\eta \tag{13.3.17}$$

where $A = \pi XY$ is the insonified area.

One notes that, since the scatter is a function of the geometry through α and β, bistatic experiments are needed to characterize the surface correlation function. On the other hand, in the specular direction, where $\alpha = \beta = 0$, the rms height h can be determined as discussed in section 13.2.

Commonly, for surface-scattered sound, Equation 13.3.17 is written in the simpler form

$$\langle p\, p^* \rangle = p_0^2 R_0^2 \frac{A}{R_1^2 R_2^2} \mathcal{S} \tag{13.3.18}$$

where the scattering coefficient, $\mathcal{S}$, which includes all of the parameters that describe the experiment and the surface, is

$$\mathcal{S} = \frac{\mathcal{R}_{12}{}^2 k^2 G^2(\theta) e^{i\omega\tau}}{8\pi^2} \int\int_{-\infty}^{\infty} \mathcal{G}\, \mathcal{W}\, e^{2i(\alpha\xi + \beta\eta)} d\xi\, d\eta \tag{13.3.19}$$

If the assumptions of the derivation are correct, we can characterize a rough surface acoustically by performing an experiment to get the surface-scattering coefficient

$$\mathcal{S} = \frac{\langle p\, p^* \rangle}{P_0^2\, R_0^2} \frac{R_1^2\, R_2^2}{A} \tag{13.3.20a}$$

for CW or

$$\mathcal{S} = \frac{[tips]_s}{[tips]_0} \frac{R_1^2\, R_2^2}{R_0^2 A} \tag{13.3.20b}$$

for an impulse.

It is common to use the 10 times logarithm of $\mathcal{S}$, to obtain the *scattering strength of the surface* $\mathcal{SS}$, which is expressed in decibels:

$$\mathcal{SS} = 10 \log_{10} \mathcal{S}\ (\text{dB}) \tag{13.3.21}$$

In general, to characterize the surface acoustically, through $\mathcal{S}$, the complete Equation 13.3.17 must be integrated, using the surface correlation function and the particular beam pattern of the experiment. The solution is then best left to computer integration.

Since $\mathcal{S}$ has the form of a two-dimensional Fourier integral, in principle, measurements of $\mathcal{S}$ can be used to determine the roughness parameters.

13.3.3 *DEPENDENCE OF SPECULAR SCATTER ON THE PARAMETERS OF THE EXPERIMENT: APPARENT REFLECTION COEFFICIENT AND BOTTOM LOSS (dB)*

Some people like to look at the specularly scattered sound (mirror direction) as an apparent reflection, which is then simply called a "reflection with reduced amplitude." This permits the characterization of an ocean bottom surface interaction in terms of the simple concept of "bottom loss per bounce." To do this, the squared "apparent reflection coefficient," $\mathcal{R}_a^2$, is written in terms of a point source at range R_1 from the surface, and the receiver at range R_2 from the surface, and is defined in terms of the received intensity, assuming spherical divergence.

$$\langle p\, p^* \rangle = p_0^2\, R_0^2 \frac{\mathcal{R}_a^{\,2}}{(R_1 + R_2)^2} \tag{13.3.22}$$

One needs to look at the concept analytically to determine the implications of Equation 13.3.22. To evaluate $\mathcal{R}_a^2$ analytically, introduce $\langle pp^* \rangle / (p_0^2 R_0^2)$ from Equation 13.3.17. For specular scatter, $\alpha = \beta = 0$ and $G(\theta) = \cos\theta$. Also use

$A = \pi XY = \pi[R_1(\Delta\chi)/\cos\theta][R_1 \Delta\varphi]$ to get

$$\mathcal{R}_a^2 = \frac{\mathcal{R}_{12}^2 k^2 (\cos\theta)(\Delta\chi)(\Delta\varphi) e^{i\omega\tau}(R_1 + R_2)^2}{8\pi R_1^2 R_2^2} \int\int_{-\infty}^{\infty} \mathcal{G}\, \mathcal{W} d\xi\, d\eta \qquad \textbf{(13.3.23a)}$$

Clearly, this squared apparent reflection coefficient not only depends on the ranges R_1 and R_2 but also is a function of the frequency, the geometry, the beam pattern, and the correlation function of the surface (through $\mathcal{W}$). Equation 13.3.22 is therefore a superficially simple representation of the complex specular scattering process. Some of the real consequences of specular scatter were described from the point of view of laboratory experiments in section 13.2.4.

When the apparent reflection coefficient is used, one expresses the bottom loss as

$$BL\,(\text{dB}) = 10 \log_{10} (\mathcal{R}_a^2) \qquad \textbf{(13.3.23b)}$$

When the bottom is smooth, the problems due to incoherent scattering components disappear, and the bottom loss is simply

$$BL\,(\text{dB}) = 10 \log_{10} (\mathcal{R}_{12}^2) \qquad \textbf{(13.3.23c)}$$

for a smooth bottom.

Dependence on Surface Correlation Function

When the PDF of surface displacements is approximately Gaussian, one estimates the characteristic function $\mathcal{W}$ by using the bivariate Gaussian PDF, w_2 of Equation 13.3.13a in Equation 13.3.12, to obtain

$$\mathcal{W} = \exp[-4\gamma^2 h^2 (1 - C(\xi, \eta))] \qquad \textbf{(13.3.24)}$$

The specular scattering direction is particularly simple. In order to evaluate $\langle pp^* \rangle$, we first obtain 2γ from Equation 13.3.5c,

$$2\gamma = 2k \cos\theta \qquad (\text{specular}, \theta_1 = \theta_2, \theta_3 = 0) \qquad \textbf{(13.3.25)}$$

The characteristic function is then given in terms of the acoustical roughness parameter, g_R (see Equation 13.2.5b), and the correlation function

$$\mathcal{W}_{\text{spec}} = \exp[-g_R (1 - C(\xi, \eta))] \qquad \textbf{(13.3.26)}$$

where $g_R = 4k^2 h^2 \cos^2\theta$.

Incoherent scatter depends on the form of the spatial correlation function. Gently curving surfaces have spatial correlation functions that may be described by

$$C = 1 - a_2\xi^2 - b_2\eta^2 \tag{13.3.27}$$

where ξ and η are the orthogonal spatial lags. These are, in fact, the first three terms of the expansion of the two-dimensional Gaussian correlation functions given in Equations 13.1.16 and 13.1.17.

Surfaces with sharply peaked corners may be describable by an exponential function or by a linear approximation to the exponential correlation function,

$$C = 1 - a_1|\xi| - b_1|\eta| \tag{13.3.28}$$

In either case

$$C = 0 \quad \text{for} \quad \eta > \eta_1 \quad \text{and} \quad \xi > \xi_1 \tag{13.3.29}$$

Clay and Leong (1974) and Clay and Medwin (1977, pp. 520–22), give algebraic expresions for the evaluation of S, assuming the correlation function is described by Equation 13.3.27 or 13.3.28.

13.3.4 SCALE-MODEL PROOFS OF THE DEPENDENCE OF SCATTER ON PARAMETERS OF THE EXPERIMENT

Dependence on Angle of Incidence

The dependence on angle of incidence of a spherical wave is revealed in Fig. 13.3.2. Seven cycles of frequency 200 kHz were normally incident at a wind-blown surface, and the display was intensity-modulated to show the fluctuations of the sound amplitude. When $g_R < 1$, the first return (from directly over the source) is virtually unaffected by the rough surface, but contributions from farther off-axis are increasingly incoherent. When $g_R > 1$, not only the off-axis scatter but also the normal scatter varies strongly with time. There is a demonstrable dependence on the beam pattern.

Dependence on Beam Width

To show the dependence of the surface-scattering coefficient $\mathcal{S}$ on the beam width of an incident spherical wave, Clay and Sandness (1971) evaluated the theoretical expression for $\mathcal{S}$ (Equation 13.3.19) by first using their measurements of the surface correlation function and the geometry of the sound beam to determine $\mathcal{G}$

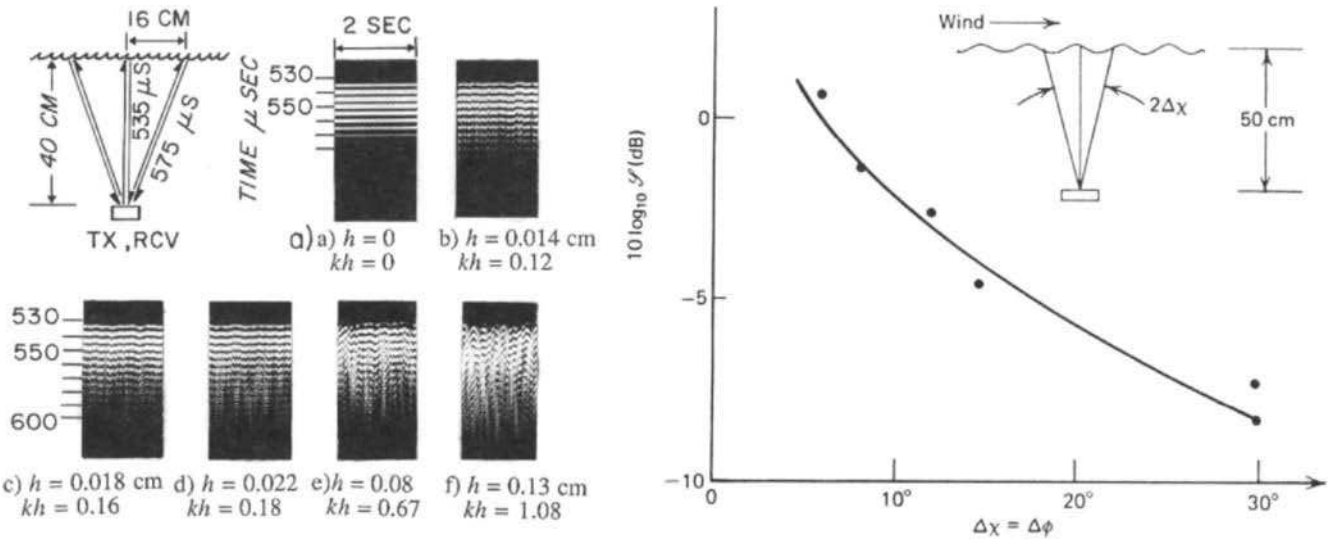

Figure 13.3.2 *Left*, intensity-modulated signals, specularly backscattered at normal incidence from a laboratory wind-blown surface. The white areas are positive phases of the signals. Signal frequency 200 kHz; ping length 7 cycles; 35 μs duration. *Right*, dependence of S on beam width of the transducer. Points are experimental values of S for six transducers of different beam widths at the same range. Curve is theoretical and is based on experimental measurements of the laboratory sea surface and the sonar beam characteristics. Rms height $h = 0.14$ cm, $g_R = 5.5$. From Clay and Sandness (1971). See also Clay and Medwin (1977, Figs. 10.5.5 and 10.5.6) for the correlation functions and their approximations.

and $\mathcal{W}$ for a normal-incidence laboratory experiment. The predicted curve of $\mathcal{S}$ is shown in Fig. 13.3.2. It agreed with the experimental values of $\mathcal{S}$, obtained with six transducers of different beam width. Both determinations confirmed that, for a given rough surface, $\mathcal{S}$ *depends on the beam width.* Experimental determinations of $\mathcal{S}$ are system- and geometry-dependent, rather than solely rough-surface–dependent.

Dependence on Range

Thorne and Pace (1984) and Pace et al. (1985) have specialized the HKF solution (section A10.5 of Clay and Medwin [1977] or Equation 13.3.19 of the previous section) to large acoustical roughness ($g_R \geq 10$) at normal incidence. This is the realm dominated by incoherent scatter, as indicated in Figs. 13.2.5 and 13.2.7. To simplify the calculation and the experiment, they evaluated the specular scatter of a Gaussian beam incident at right angles to a rough surface of pressure reflection coefficient $\mathcal{R}_{12}$ that has a Gaussian PDF of displacements and a Gaussian correlation function. The purpose of this model was to determine how $\mathcal{S}$ depends on range, and therefore to check on the region of applicability of the common Equation (13.3.20a).

The experiment showed that the surface-scattering coefficient increases from low values in "near-field scattering" to stable values that can be used to define a rough surface in "far-field scattering." The increase in $\mathcal{S}$ for an increasing range, and the transition from near-field to far-field incoherent scatter, was verified by extensive laboratory experiments using manufactured polyurethane ("pressure-release") and gravel ("rigid") Gaussian surfaces. One of their figures for a pressure-release surface is Fig. 13.3.3.

Equation 13.2.10c was invoked to convert from the measured correlation length to the desired dependence on slope. The far-field scattering region, within which the frequency-independent incoherent scatter can be used to characterize an isotropic Gaussian surface, is then given by

$$R_2 \geq R_1/[(2s/\theta_0) - 1] \tag{13.3.30}$$

where s is the rms slope of the surface, and θ_0 is the e^{-1} pressure half-beam angle of the transducer.

For source and receiver at the same range, $R_2 = R_1$, the far-field region is simply

$$\theta_0 \leq s \tag{13.3.31}$$

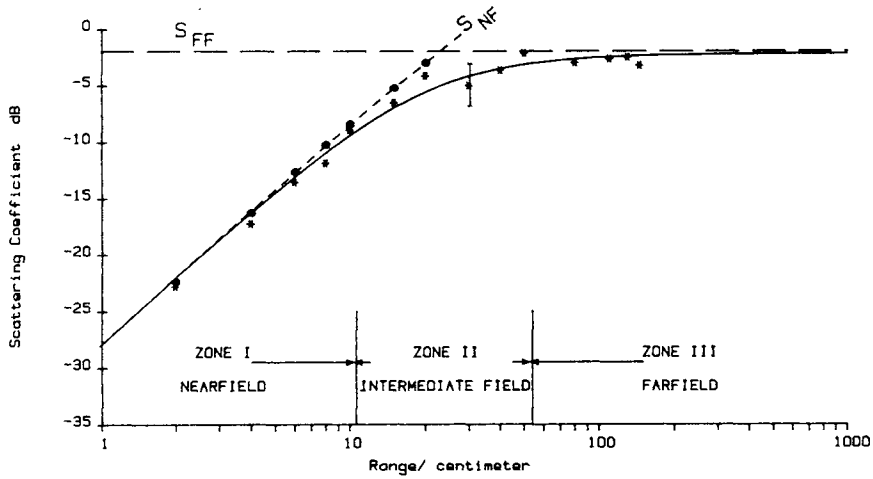

Figure 13.3.3 Scattering strength as a function of range for a manufactured Gaussian pressure-release surface insonified at normal incidence by frequency 250 kHz ($g_R = 15$). The dots are experimental. The curved line is theoretical. $\mathcal{S}_{FF}$ is the far-field asymptote that occurs at $\theta_0 \leq s$, where θ_0 is the beam angle and s is the surface rms slope. (From Pace, N. G., Z. K. S. Al-Hamdani, and P. D. Thorne, "The range dependence of normal incidence acoustic backscatter from a rough surface," *J. Acoust. Soc. Am.* **77**, 101–12, 1985.)

It is shown that under these special conditions, within the far-field region, the scattering coefficient of the acoustically very rough interface, $g_R \geq 10$, has the constant value, independent of frequency,

$$\mathcal{S} = \mathcal{R}_{12}^2/(16\pi s^2) \tag{13.3.32}$$

where $\mathcal{R}_{12}$ is the pressure reflection coefficient at the interface.

Under these conditions, the rms slope could be determined from Equation 13.3.32 and the isotropic Gaussian correlation function could be calculated from Equation 13.2.10c.

13.3.5 COMPUTER MODEL OF POINT-SOURCE BACKSCATTER FROM AN OCEAN SURFACE

Generally a surface is studied by monostatic backscatter. The concept of "surface backscattering strength," *BSS*, has been used to characterize the backscatter from a surface that consists of point scatterers. From Equation 13.3.20a,

$$BSS = 10 \log_{10}\left(\frac{I_{BS}}{I_0}\frac{R^4}{R_0^2 A}\right) \tag{13.3.33}$$

where I_{BS} = backscattered intensity measured at the source/receiver; I_0 = source intensity at 1 m; R = range (meters) fom source/receiver to scattering surface; R_0 = reference range at source = 1 m; A = scattering area (m^2).

The derivation that led to the concept of a scattering coefficient S in Equation 13.3.18 assumes that the point scatterers will cause the far-field intensity range dependence to vary as R^{-2} from the surface. But is it correct that scattering from the ocean surface is point scattering? One notes that if the ocean surface is smooth, for a point source the relative scattered (reflected) intensity varies as R^{-2}, not R^{-4}. If the ocean is wedgelike, the relative scattered intensity varies as R^{-3}. In either case, it is clear that the definition of *BSS* is critically dependent on the type of scatterer at the ocean surface.

We have selected the wedge as a flexible element that can accomodate the various behaviors of a real rough surface. The flexibility derives from the fact that a wedge is comprised of reflecting facets and a diffracting edge. Furthermore, at long range, a finite wedge looks like a point scatterer, particularly if the incident sound has a wavelength that is large compared with the wedge extent.

The theory for single wedges is given in sections 11.8 and 12.2. A computer model based on single wedge scattering was exercised by Medwin and Novarini (1981) to determine the backscatter from an ocean surface made up of finite wedge elements. First a model ocean surface was generated, as in Fig. 13.3.4. The surface has a Gaussian PDF of displacements selected to produce an rms height appropriate to the wind (Equation 13.1.12) and with wedge spacing in the windward direction to produce an appropriate surface-displacement correlation function (see section 13.1.1). The extent of the wedge was set by the correlation length in the crosswind direction. For a 5 m/s wind speed, the model rms wave height was Gaussian, ranging from $h = 0.139$ m to 0.15 m compared with a theoretical value of 0.14 m. The windward correlation length was 2.7 m compared with the theoretical value 3.3 m. The rms slope was 6.3°, compared with 7.1° ± 0.9° for a Cox and Munk type of calculation from Equation 13.1.5.

Fifteen surfaces were defined, each containing 9 wedges (10 facets). The equations in section 12.2.1 for a pressure-release wedge were used to calculate the impulse response. Fig. 13.3.5, which is a typical response curve, shows 9 wedge diffractions and one case of a reflection from a facet. The magnitudes and phases of the wedge diffractions depend on the angle of incidence as noted for single wedges, in section 12.2.1.

Some of the results of the computer simulation are shown in Fig. 13.3.6. The left figure demonstrates that the grazing angle (30°) backscatter may fall between R^{-3} and R^{-4}, depending on the frequency. This grazing angle was selected because it is more than three times the rms slope; therefore, reflections are

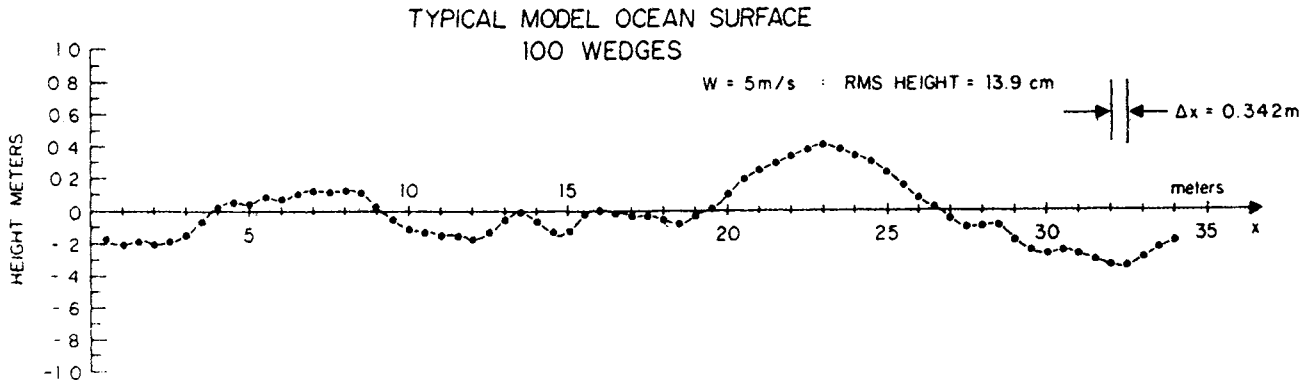

Figure 13.3.4 Model ocean surface with 100 wedges, appropriate to a wind speed of 5 m/s. Spacing between wedges, 0.342 m; rms height, 0.139 m; spatial correlation length, 2.7 m; surface rms slope, 6.3°. (From Medwin, H., and J. C. Novarini, "Backscattering strength and the range dependence of sound scattered from the ocean surface," *J. Acoust. Soc. Am.* **69**, 108–11, 1981b.)

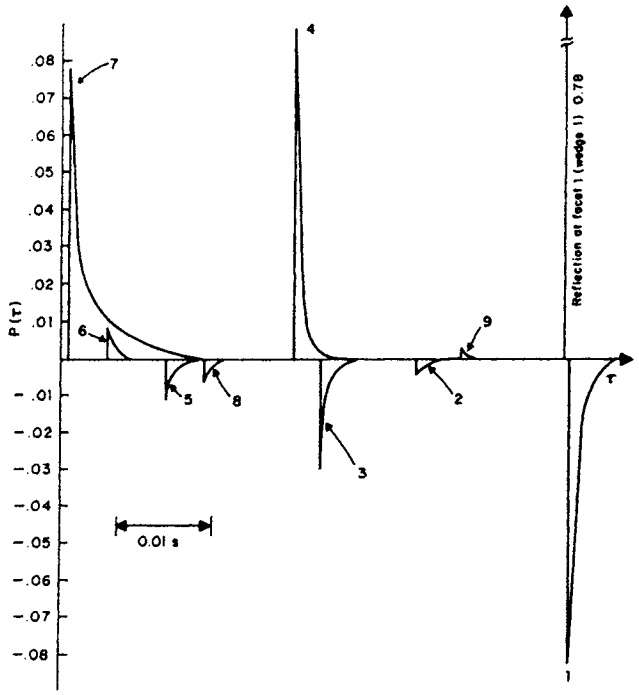

Figure 13.3.5 Impulse response for one nine-wedge surface. The order of the wedge numbering was sequential along the surface; it differs from the time of arrival of the reflection and diffractions because of the range differences. For this case, wind speed is 20 m/s; range, 500 m. (From Medwin, H., and J. C. Novarini, "Backscattering strength and the range dependence of sound scattered from the ocean surface," *J. Acoust. Soc. Am.* **69**, 108–11, 1981.)

virtually absent, and we are looking at only the diffraction effect. The range dependence is R^{-4} (point scattering) for the low frequencies only, that is when the acoustic wavelength is comparable to, or larger than, the surface correlation lengths. For 8000 and 16,000 Hz, however, the acoustic wavelengths are less than one-tenth the correlation lengths. Then the scatterers are wedgelike, and the backscattered intensity follows the R^{-3} law to about 200 m. At greater ranges, interference between the wedge scatter causes the transition to the R^{-4} behavior.

The backscatter is large when a facet *reflects*; for example, it is large near vertical incidence because horizontal facets are then very common (see Fig. 13.1.2). Backscatter decreases to very small values for incidence angles nearer to grazing because it is asssumed that there are no vertical facets. The *diffracted* sound is the *only* significant component of intensity during backscatter at angles of incidence very much greater than the rms slope. For example, from Fig. 13.1.2

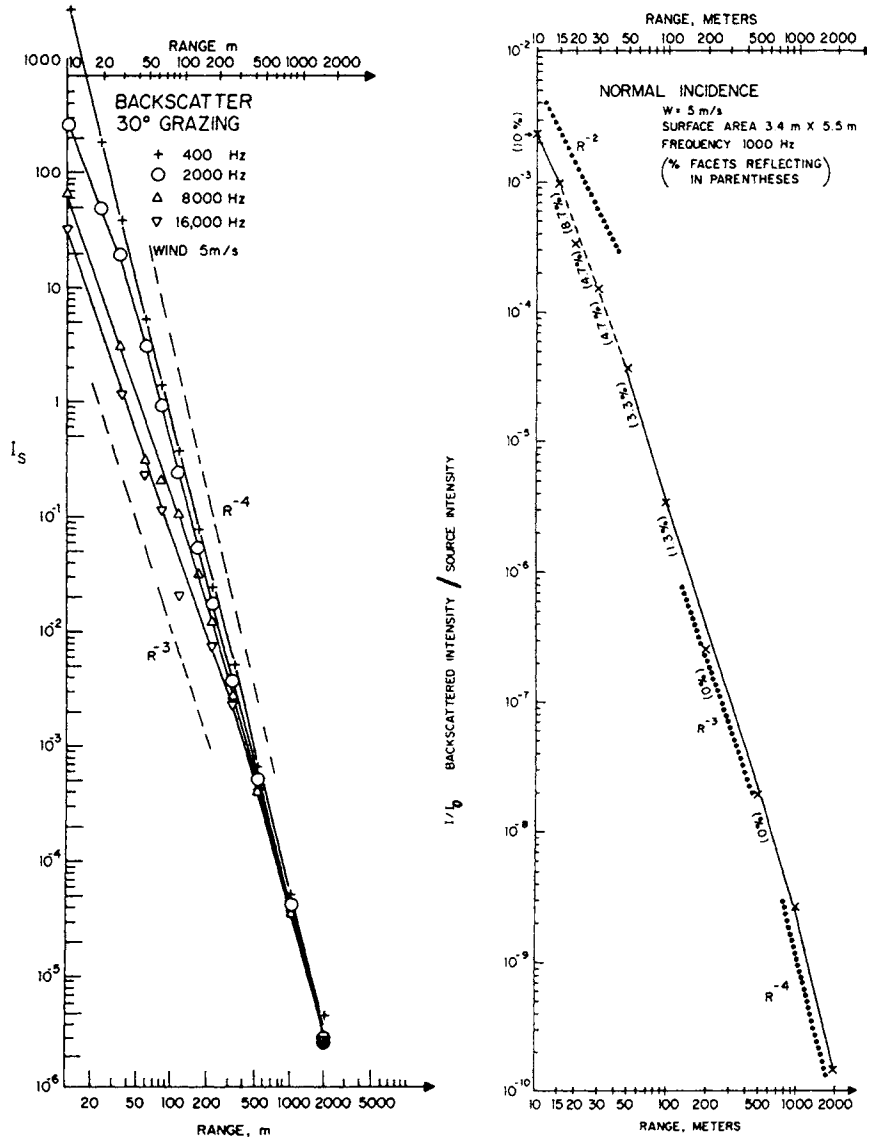

Figure 13.3.6 *Left*, backscattered intensity as a function of range for a fixed area of surface defined by one spatial correlation length in each direction (3.4 m upwind × 5.5 m crosswind). Four frequencies shown for 5 m/s wind, 30° grazing angle. The dashed lines bounding the calculated scattered intensities are theoretical slopes for wedge scattering (R^{-3}) and point scattering (R^{-4}). *Right*, relative backscattered intensity for normal-incidence backscatter at frequency 1000 Hz. The dotted lines show the idealized slopes for facet reflection, wedge scatter, and point scatter. (From Medwin, H., and J. C. Novarini, "Backscattering strength and the range dependence of sound scattered from the ocean surface," *J. Acoust. Soc. Am.* **69**, 108–11, 1981.)

and tables of areas under the Gaussian PDF, at an angle of incidence greater than twice the rms slope, only 5 percent of the facets will be perpendicular to the incoming rays and thereby reflect. In that case the major part of the backscatter will come from diffraction and will depend sensitively on the correlation function of the surface.

The graph at the right of Fig. 13.3.6 shows the effect of horizontal facet reflections that occurs with a high probability at normal incidence and that will be found more often at shorter ranges than at long ranges. Within about 10 m of the surface, about 9 percent of the facets are effectively reflecting; from 10 to 30 m, about 4 percent of the facets produce reflections, and these dominate and give the appearance of a reflecting surface, rather than a scattering surface, and determine the R^{-2} behavior. Beyond 50 m, less than 1 percent of the facets are oriented to cause reflection and, because of the dominating interference of the diffractions from the wedges, the net result appears like point scattering and varies as R^{-4}.

This exercise has shown us that scattering from the ocean surface is *not* always point scattering. This suspicion had been growing for two decades, (e.g., Mikeska and McKinney 1978).

In all cases, it would be prudent to verify that the range dependence is R^{-4} before one assumes that the measurement is of far-field point scattering from ocean surfaces or bottoms, and before one applies Equation 13.3.20a or 13.3.21 to characterize the surface scatter.

13.3.6 SCATTERING FROM A TWO-DIMENSIONAL ROUGH SURFACE: TRI-WEDGE COMPUTER ASSEMBLAGES

The approach described in the previous section has been extended by Keiffer and Novarini (1990) to the complete problem of a two-dimensional rough surface. The surface is divided into triangular elements that can be tilted in any direction. The terminology "virtual wedge" is used for the infinitely long wedge crest that would be obtained if a side of a triangle is extended to include the least-time, perpendicular location. The BT solution for the virtual wedge is truncated on both sides to correspond to the times during which that edge of the triangle is insonified for a given source and receiver position (Fig. 13.3.7). This limited impulse component, which represents the "physical wedge," is then combined at the proper times with the impulses from all the other edges of the insonified triangles that describe the surface.

The "tri-wedge assemblage" technique has been validated by solving and comparing with exact solutions of the classical scattering from a hard or soft disk (see Fig. 13.3.8 and Keiffer et al. 1994). The computer time needed for the

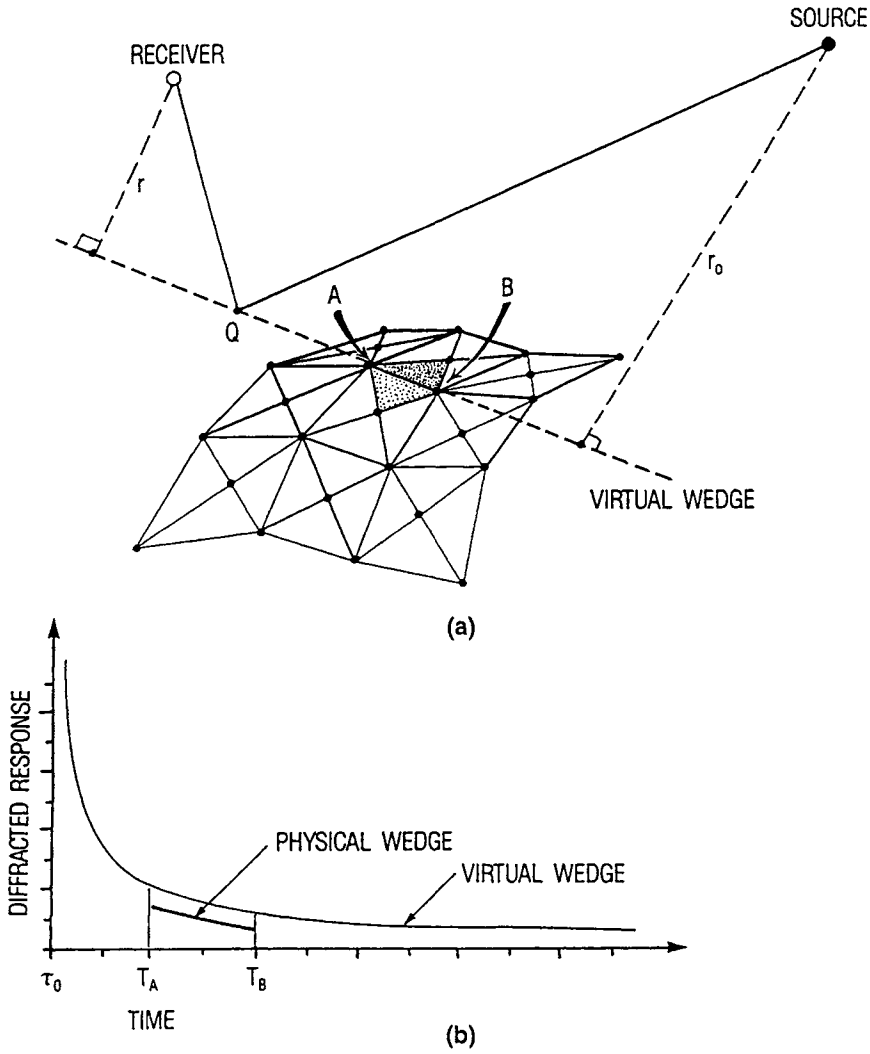

Figure 13.3.7 (a) Scattering geometry for the two-dimensional ocean surface and (b) impulse response for a truncated facet. From Keiffer and Novarini (1990).

tri-wedge assemblage technique was only 1/3600 of that required for an exact solution in this case.

The two-dimensional rough ocean surface is generated by starting with a series of random numbers that, when normalized for the particular wind speed, represent the displacement above or below the mean level of the water. Realizations of sea surfaces having a desired spectrum are achieved by specifying

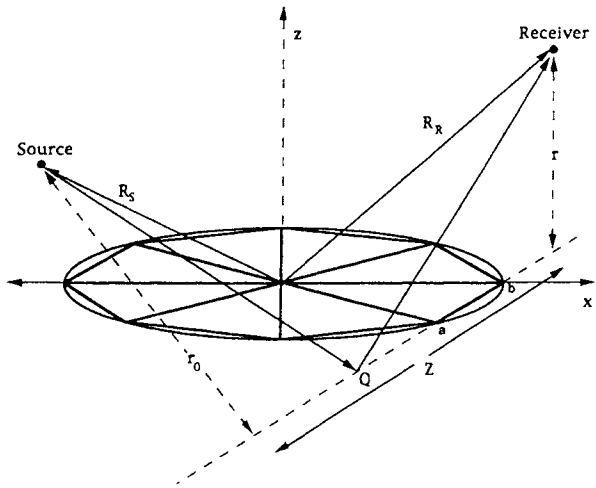

Figure 13.3.8 Tri-wedge assemblage for the test case of scattering from a circular disk. (From Keiffer, R. S., J. C. Novarini, and G. V. Norton, "The impulse response of an aperture: numerical calculations within the framework of the wedge assemblage method," *J. Acoust. Soc. Am.* **95**, 3–12, 1994.)

the appropriate rms height, rms slopes in the x and y directions, and spatial correlation functions in the x (windward) and y (crosswind) directions as a function of wind speed and fetch (see section 13.1.1).

Comparisons of the tri-wedge assemblage impulse solution (transformed to the frequency domain) are shown in Fig. 13.3.9 for single-surface realizations for the difficult case of backscatter at 60° for each of two wind speeds. The complete solution for the scatter from a time-varying ocean surface would be obtained by calculating the scatter for many realizations and then calculating the statistics of sound scatter due to the time-varying ocean condition.

13.3.7 EFFECT OF BUBBLES BELOW THE OCEAN SURFACE

From Chapter 8 it is clear that both the sound attenuation and speed are functions of bubbles under the surface, and that the bubble density is a non-uniform function of depth and location. There are several consequences:

(1) Significant energy loss can occur as sound approaches the surface; this excess attenuation is a function of the sound frequency and the local bubble distribution.

(2) Sound approaching the surface is refracted due to the generally greater bubble density nearer the surface; for low-frequency sound

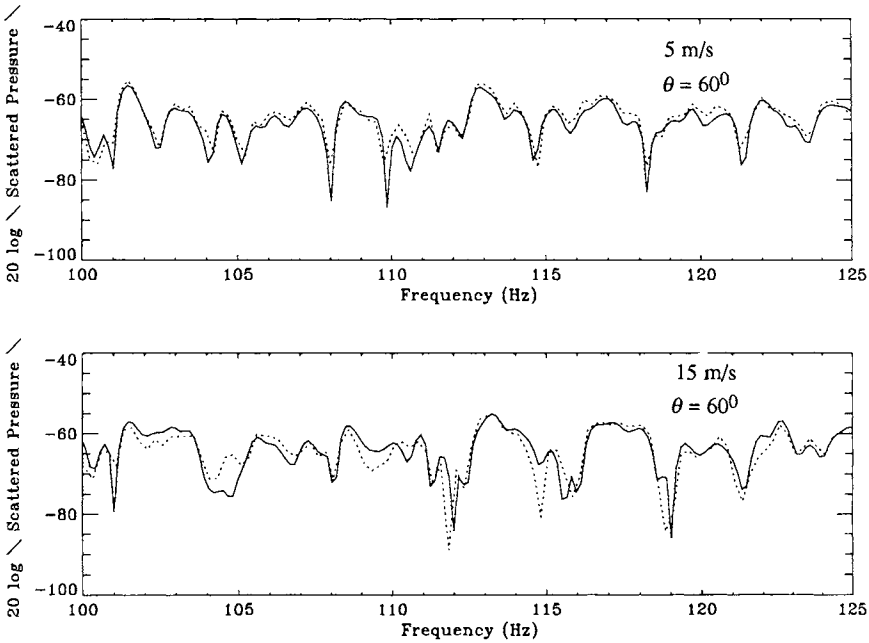

Figure 13.3.9 Comparison of a highly accurate solution (dotted line) with tri-wedge assemblage solution (solid line) for single realizations of a directional Pierson–Moskowitz sea, at 60° angle of incidence, for wind speeds 5 and 15 m/s, rms height 0.15 and 1.4 m, respectively. The grid size was 2048 × 2048 points covering 3 km at intervals of 1.5 m. Source and receiver range 50 km. (From Keiffer, R. S., and J. C. Novarini, "A versatile time domain model for acoustic scattering from 2-D ocean surfaces," *J. Acoust. Soc. Am.*, in preparation, 1997.)

(<10 kHz), the sound speed is less than the bubble-free speed, and the angle of ray incidence becomes more nearly normal at the rough surface.

(3) Bubble resonance frequencies fluctuate as a function of the fluctuating ambient pressure at depth (Equation 8.2.13 and Fig. 8.4.7). Therefore, sound that interacts with the bubbly region fluctuates in amplitude and phase as a function of time and position (Medwin et al. 1975).

The historical Fig. 13.3.10 shows the first quantitative explanation of the potential effect of adding the omnidirectional scatter of postulated bubble densities to directional rough surface backscatter calculated from the Beckmann and Spizzichino theory (1963). The paper was written in the days before there were data of ambient bubble densities at sea. The combination of the two scattering processes produces large backscatter that is strongly dependent on angle of incidence near the normal and less, essentially constant, backscatter for

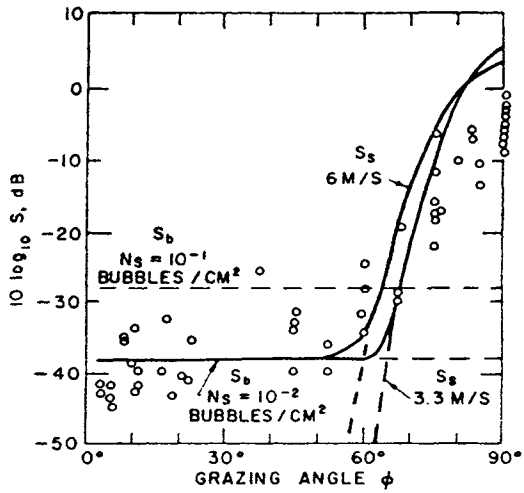

Figure 13.3.10 Backscatter from a rough surface for two wind speeds and backscatter from two postulated below-surface unresolved column-resonant bubble densities (horizontal lines). The circles are experimental data of Urick and Hoover (1956) at 60 kHz during 4–5 m/s winds. (From Clay, C. S., and H. Medwin, "High-frequency acoustical reverberation from a rough sea surface," *J. Acoust. Soc. Am.* **36**, 2131–34, 1964a.)

grazing angles $\theta_g < 60°$, owing to unresolvable bubbles below the surface. The calculation was done for the frequency of 60 kHz to compare with the acoustic data available.

13.4 Near Grazing Scatter at a Steep-Sloped, Rough Surface

One would expect that sound *specularly scattered* from a rough, rigid surface is always weaker than when it is *reflected* from a smooth rigid surface. However, when the scattering elements are steep, there is an important exception to that expectation that has been tested in a laboratory model of a rough sea bottom.

Consider "low-frequency" scatter, $kd < 1$, where d is the separation between roughness elements, and "low-roughness" surfaces, $kh < 1$, where h is the height of the roughness elements. A specialized low-frequency theory by I. Tolstoy (1979) takes into account secondary scatter and shadowing and shows that there is a strong *boundary wave* at near grazing incidence under those conditions. The theory does not require the roughness elements to have small slopes, as in most theories. In fact, steep-sloped elements are essential to the existence of the effect. (See also a more general series of papers by V. Twersky and colleagues dating from the 1950s—for instance, R. Lucas and V. Twersky [1986].)

There is a simple qualitative explanation of the phenomenon. Recall Rayleigh scatter from a single sphere ($ka < 1$), where a is the sphere radius (subsections 7.5.2 and 7.5.5). There is a significant component radiated in the forward direction. When $kd \ll 1$, forward scattering from adjacent spheres is nearly in phase and adds coherently. The result is a large net forward component of scatter in the grazing, specular direction.

In the Tolstoy (1985) derivations, the roughness scattering elements are replaced by a continuous surface distribution of monopole and dipole sources (as identified in section 7.5). These pseudo-sources represent the primary scattering, multiple scattering, and shadowing at the elements. This low-frequency, near-grazing specialization leads to a simple expression for a large, coherently scattered boundary wave which propagates outward from a point source in a thin layer of the fluid adjacent to the steep-sloped roughness elements.

Because the low-frequency scattering is predominantly in the forward direction, a point source near the rough surface generates a cylindrical boundary wave which has its greatest amplitude at the rough interface and smaller values away from that surface. At large ranges, the cylindrically diverging boundary wave amplitude exceeds the spherically diverging direct wave amplitude. For a rigid hemispherical approximation to the roughness elements, at $kr \gg 1$ and near grazing incidence, the normalized spectrum is predicted to be a function of a *scattering parameter* ε, the range r, the wave number k.

We consider only the special case of grazing incidence ($\theta = 90°$). For this condition, the scattered wave is a maximum and becomes the boundary wave with amplitude,

$$P_B = \varepsilon(2\pi r)^{-1/2} k^{3/2} \tag{13.4.1}$$

The critical *scattering parameter*, ε, with units of length, is proportional to the volume of the protuberances per unit area. It is a function of the shape and packing density of the roughness elements. For close-packed hemispheres, Tolstoy gives the value

$$\varepsilon = 4.44 \times 10^{-2} d \tag{13.4.2}$$

where d is the separation.

To compare with the direct wave, the normalized spectral amplitude for the delta function source in the half-space is

$$P_D = (2\pi r)^{-1} \tag{13.4.3}$$

Therefore, at grazing incidence,

$$P_B/P_D = \varepsilon(2\pi r)^{1/2}k^{3/2} \tag{13.4.4}$$

The boundary wave is also predicted to be dispersive. Tolstoy's theoretical dispersion of the grazing, specularly scattered sound over a spherical bosslike surface is

$$(c - v)/c \simeq 1 - (k_S/k_R) = A\varepsilon^2k^2 \tag{13.4.5}$$

where k_R and k_S are propagation constants over the rough and smooth surfaces; c is the speed in free space; v is the phase velocity over the rough surface; and $A = 0.5$ for hemisphere theory.

The grazing propagation of a low-frequency wave over a low-roughness surface is describable in terms of

$$p_{rough} = p_{smooth} + p_{boundary} \tag{13.4.6}$$

where $p_{smooth} = P_D \exp[i(\omega t - k_S r)]$; $p_{boundary} = P_B \exp[i(\omega t - k_B r)]$; $k_S = \omega/c$ is the propagation constant at the smooth surface; and k_B is the propagation constant for the boundary wave.

Laboratory experiments at grazing incidence over gravel have been used to extend the theory to "real world" surfaces. In the case of a randomly rough surface, the scattering parameter ε is empirically determined from the slope of the relative boundary wave amplitude, and the dispersion constant A comes from the slope of the relative speed curve (Fig. 13.4.1). The experimental technique involves computer subtraction of an impulse signal propagated over the smooth surface (the direct wave) from the signal for the rough surface; the difference yields the boundary wave due to the surface scatter.

The laboratory experiments have gone beyond the Tolstoy theory to reveal that the growth phase of the boundary wave is limited at the higher frequencies. This happens not only because of the condition $kd < 1$ but also because two other factors are important: the boundary wave is partly scattered outside of the vicinity of the rough surface; the increasingly lagging phase shifts become self-destructive at greater ranges. In the original theory the ratio P_B/P_D could be predicted for any range when the rms slope, h, and parameter, ε, are known. However, extensive laboratory studies lead to the conclusion that the peak value is generally given by

$$(P_B/P_D)_{\max} = 2.7 \tag{13.4.7}$$

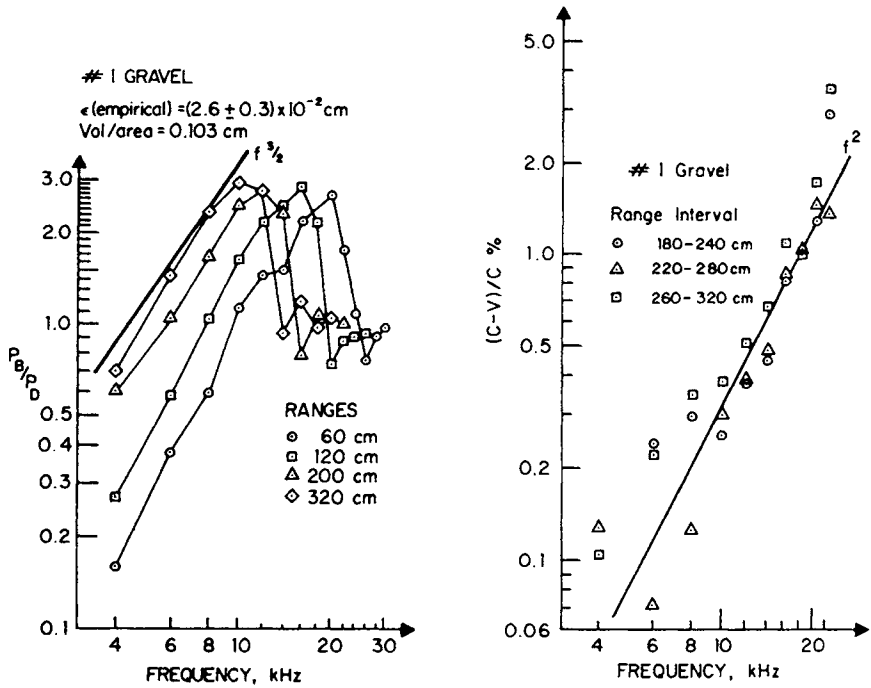

Figure 13.4.1 Laboratory boundary wave propagation over a randomly rough surface constructed of #1 aquarium gravel of volume/area 0.103 cm. *Left*, boundary wave amplitude P_B for grazing incidence over a randomly rough surface, normalized with respect to the smooth surface (direct) amplitude P_D. The relative amplitudes agree with theoretical (straight line) slope $f^{3/2}$ until a peak amplitude is reached. From the curve, the empirical value of the scattering parameter, ε, is $2.6 \pm 0.3 \times 10^{-2}$ cm for the gravel. *Right*, frequency dependence of the phase velocity of the rough surface wave with relative speed varying as f^2, in agreement with theory. The straight-line fit gives a dispersion constant $A = 1.35$ for the gravel. (From Medwin, H., and G. L. D'Spain, "Near-grazing, low-frequency propagation over randomly rough, rigid surfaces," *J. Acoust. Soc. Am.* **79**, 657–65, 1986a.)

One consequence of the grazing boundary wave scatter is the prediction of a gradient of velocity near a rough, hard ocean bottom (Medwin and Novarini 1984). This would mean that grazing sound rays would be displaced relative to the smooth bottom ray behavior. Inverting the problem, knowledge of the beam displacement as shown in Fig. 3.3.3 observed, say, at the ocean surface could yield an estimate of the roughness of the unseen rigid bottom.

A second consequence occurs in waveguide propagation. The boundary wave phenomenon alters both the amplitudes and the phase speeds of modes of a waveguide when one of the surfaces is rough. Fig. 13.4.2 presents laboratory

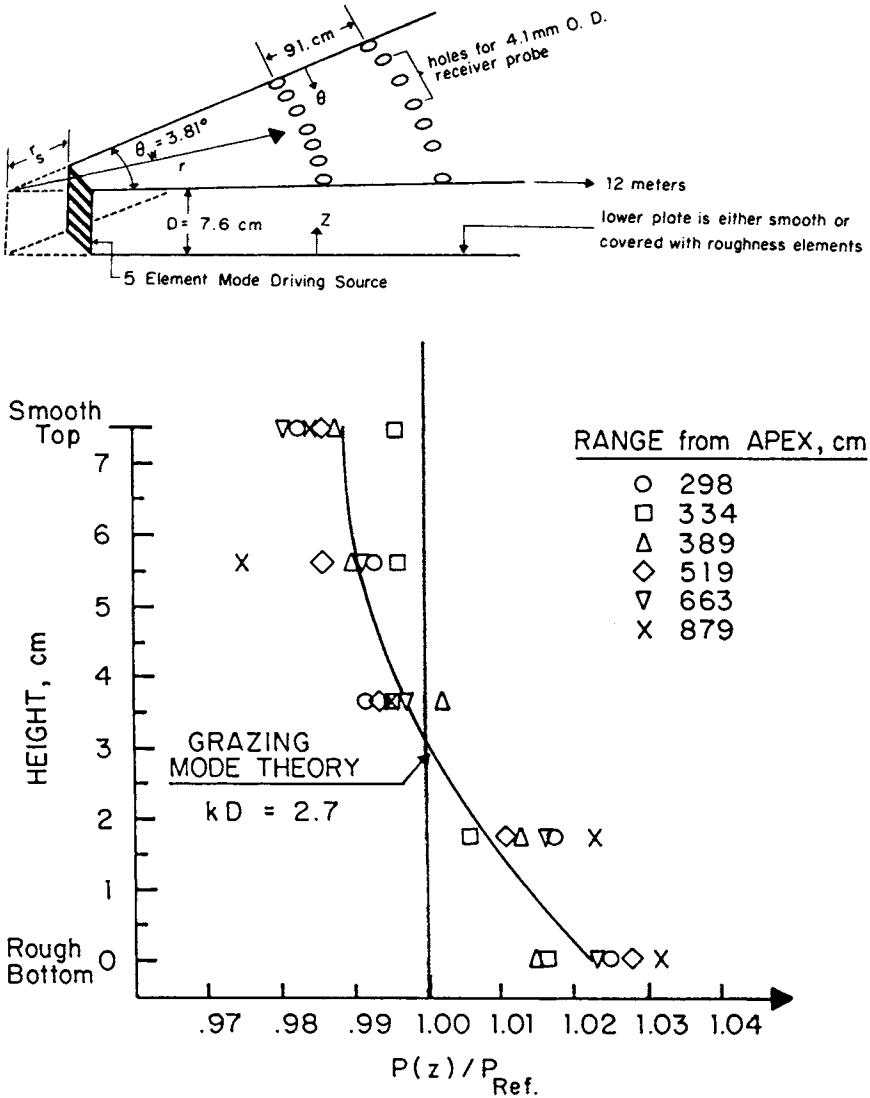

Figure 13.4.2 Propagation in an air-filled, rigid-walled wedge sectoral waveguide with the bottom covered with gravel. Wave number $k = 0.366\,\text{cm}^{-1}$, waveguide height, $D = 7.6\,\text{cm}$. The pressure is greater near the rough surface than at the smooth surface. Solid line is theory. (From Medwin, H., K. J. Reitzel, and G. L. D'Spain, "Normal modes in a rough waveguide: theory and experiment," *J. Acoust. Soc. Am.* **80**, 1507–14, 1986.)

experimental results compared with theory for the grazing mode in a rough, rigid-walled waveguide. In a smooth $m = 0$ cylindrical mode (see also Chapter 11), the acoustic pressure has the same value across the rigid-walled waveguide; in the rough-surfaced waveguide the pressure at the rough surface is greater than at the smooth surface. The effect is well predicted by theory (Medwin et al. 1986). This variation from a uniform pressure amplitude becomes very much greater as the sound approaches cut-off. The variation in the pressure distribution is accompanied by a decrease in the phase velocity of the grazing mode.

A third observation (Medwin et al. 1984) is that the boundary wave diffracts over the crest of a ridge in the same manner as for a typical wave as described in Chapter 12.

13.5 Point-Source Transmission through a Rough Interface

13.5.1 SMOOTH AIR-SEA INTERFACE

Plane Wave

From section 2.6, a plane wave going from a fluid medium described by $\rho_1 c_1$ through a smooth interface into a medium described by $\rho_2 c_2$ is described by the pressure transmission coefficient,

$$\mathcal{T}_{12} = \frac{2\rho_2 c_2 \cos\theta_1}{\rho_2 c_2 \cos\theta_1 + \rho_1 c_1 \cos\theta_2} \qquad \textbf{(2.6.11b)}$$

The ray direction is described by Snell's Law,

$$\theta_2 = \arcsin\left(\frac{c_2}{c_1}\sin\theta_1\right) \qquad \textbf{(2.6.12)}$$

where θ_1 is the angle of incidence measured to the normal of the interface, and θ_2 is the angle of transmission measured to the normal.

For sound going from air to water, $\rho_2 c_2 \cong (1000\ \text{kg/m}^3)\ (1500\ \text{m/s}) \gg \rho_1 c_1 \cong (1\ \text{kg/m}^3)\ (330\ \text{m/s})$; therefore for a plane wave $\tau_{12} \cong 2$, the pressure is doubled at the surface.

For a plane wave from air to water, there is a critical angle of incidence (Equation 2.6.13),

$$\theta_1 = \theta_c = \arcsin(c_1/c_2) \cong \arcsin(330/1500) \cong 13^\circ \qquad \textbf{(13.5.1)}$$

Plane-wave theory shows that for $\theta_1 > 13^\circ$, there is an evanescent wave in the water (section 2.6.1).

Point Source

Invoking the Kirchhoff assumption one can argue that, for a point source, the plane-wave transmission coefficient given by Equation 2.6.11 may be used at all incident points on the surface. Consequently, only a cone of energy with incident angles less than 13° would penetrate into the smooth sea. To determine the dependence on source height, H, and receiver depth, D, we calculate the effect of a ray spreading at a smooth interface (Fig. 13.5.1). This is done by comparing the incident intensity passing through a conical shell at angle θ_1 and incremental width $d\theta_1$ with the transmitted intensity at angle θ_2 and incremental width $d\theta_1$ at the surface.

At the surface, where the surface pressures in media 1 and 2 are p_{1s} and p_{2s}, the incident and transmitted powers through a ring of area A are

$$\Pi_1 = \left(\frac{p_{1s}^2 A \cos\theta_1}{\rho_1 c_1}\right) \tag{13.5.2a}$$

$$\Pi_2 = \left(\frac{p_{2s}^2 A \cos\theta_2}{\rho_2 c_2}\right) \tag{13.5.2b}$$

For a source at height H (see Fig. 13.5.1), the incident intensity at the surface is

$$I_{1s} = \frac{\Pi_1 \cos^2\theta_1}{2\pi H^2 \sin\theta_1 \, d\theta_1} \tag{13.5.3}$$

The transmitted intensity received at depth D is

$$I_2 = \frac{\Pi_2}{2\pi(H\tan\theta_1 + D\tan\theta_2)\left(\dfrac{H\tan\theta_1}{\sin\theta_2} + \dfrac{D}{\cos\theta_2}\right)d\theta_2} \tag{13.5.4}$$

The ratio of the transmitted to the incident pressure at the surface is given by Equation 2.6.11b. Finally, after significant algebraic manipulation, Hagy (1970) shows that the change in sound pressure for a mirrorlike surface is given by

$$TC = 20\log\frac{P_2}{P_{1s}} = -20\log\left[\left(1 + \frac{c_2 D\cos\theta_1}{c_1 H\cos\theta_2}\right)(2\cos\theta_1\cos\theta_2)^{-1}\right] \tag{13.5.5a}$$

The transmission change to "ground zero," immediately below the source, is

$$TC_Z = TC - 20\log_{10}(\cos\theta_1) \tag{13.5.5b}$$

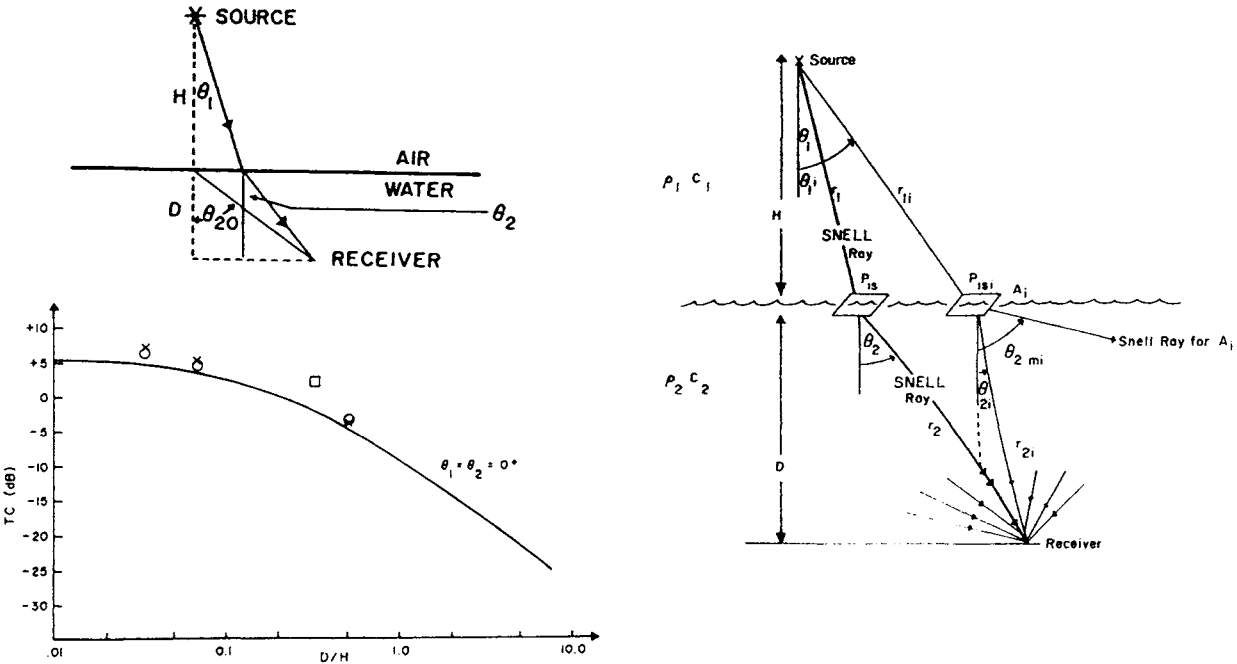

Figure 13.5.1 *Top left*, geometry of transmission into smooth water from a point source in air. *Bottom left*, pressure transmission change, TC, as a function of the depth to height ratio, D/H, for sound at normal incidence through a low-roughness ocean surface. Solid line is the theoretical prediction; data are low-roughness experimental values for $0.04 < g_l < 0.15$; circles for a helicopter sound source, crosses and squares for flyovers by a P3 aircraft. *Right*, geometry for a rough ocean surface. (From Medwin, H., R. A. Helbig, and J. D. Hagy, Jr., "Spectral characteristics of sound transmission through the rough sea surface," *J. Acoust. Soc. Am.* **54**, 99–109, 1973.)

where TC is the transmission change in dB across the smooth interface for the geometry shown in Fig. 13.5.1. At normal incidence, when $H \gg D$, the pressure in the water will be twice as high as the incident pressure ($TC = +6$ dB), whereas when $D \gg H$, the pressure in the water decreases proportional to the depth — that is, 6 dB per double distance. The smooth-surface theory (Equation 13.5.5a) has been verified in an anechoic tank and then at sea (Fig. 13.5.1). In the ocean experiment, the sound source was a hovering helicopter or fly-by aircraft. The "almost smooth surface" for the ocean analysis was in the frequency band 100 to 200 Hz, so that, with the sea $h = 14.5$ cm, the acoustical roughnesss for transmission was $0.04 < g_t < 0.15$, where g_t is given by (Equation 13.5.6b).

13.5.2 ROUGH AIR-SEA INTERFACE

The acoustical roughness parameter for transmission, g_t, depends on the in-water and in-air phase shifts relative to the interface. It is different from that for reflection, g_R, by virtue of the different sound speeds and refraction in the second medium. It was derived by Hagy (1970) and may be calculated from Equation A10.7.3 of Clay and Medwin (1977),

$$(g_t)^{1/2} = h(k_1 \cos\theta_1 - k_2 \cos\theta_2) \qquad \textbf{(13.5.6a)}$$

or

$$(g_t)^{1/2} = k_1 h[\cos\theta_1 - (c_1/c_2)\cos\theta_2] \qquad \textbf{(13.5.6b)}$$

where h is the rms height of the surface; θ_1 is the angle of incidence in the first medium, where the sound speed is c_1; and θ_2 and c_2 are for the second medium.

For transmission from air to water, $c_2 > c_1$ and $\theta_2 > \theta_1$, so that the first term dominates.

For large acoustical roughness of the surface, energy that would not have penetrated beyond the critical angle for a smooth surface *is* transmitted through the angled facets of the rough surface. These incoherent components may be calculated by applying the theory of the previous section to transmission as shown by Hagy (1970) and in section A10.7 of Clay and Medwin (1977).

The ratio (P_2/P_{1s}) was measured in extensive at-sea experiments using the Floating Instrument Platform FLIP of Scripps Institution of Oceanography as a base of operations. The 100 to 1000 Hz band noise of hovering U.S. Navy helicopters and fly-by P3C aircraft were the sound sources at height 180 m. The sound receivers were sonobuoy hydrophones at 6 m and 90 m depth.

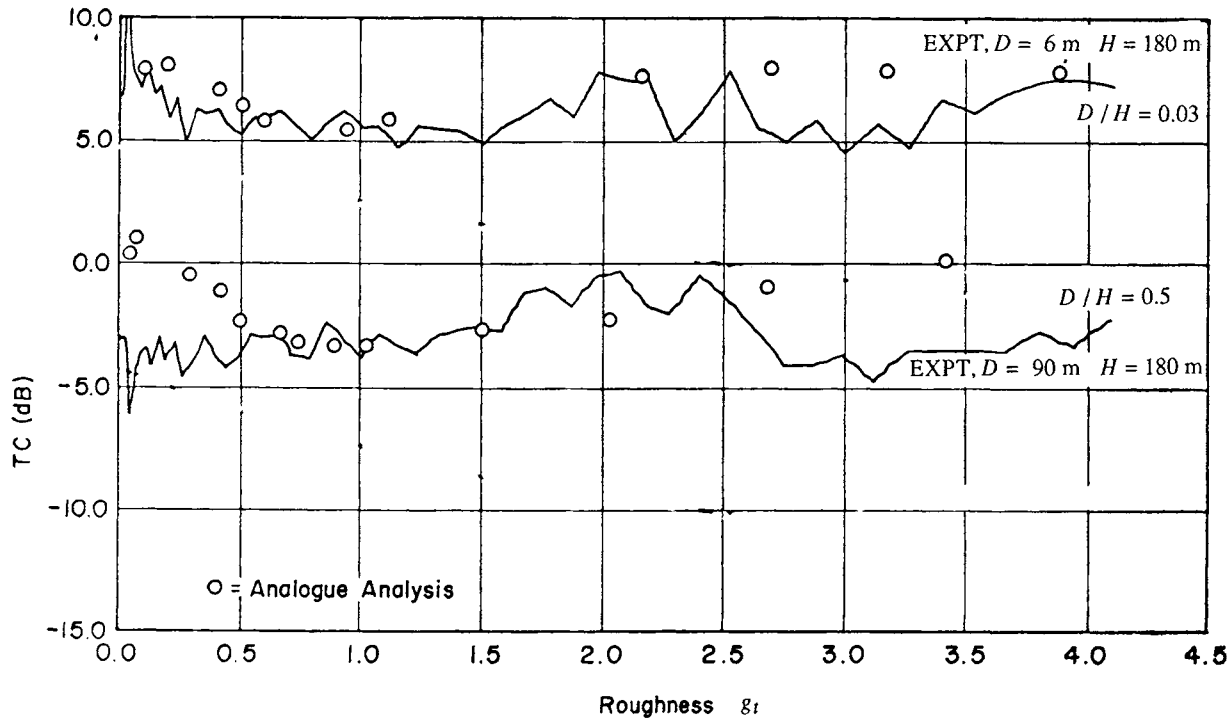

Figure 13.5.2 Pressure transmission change as a function of surface acoustical roughness for transmission, g_t, for a point source at $H = 180$ m above the sea. The receivers were at depth $D = 6$ m and 90 m, directly under the source. The surface rms height was $h = 13$ cm; correlation lengh was $L \cong 150$ cm. The source was a hovering helicopter. Solid line is digital analysis with 2 Hz frequency resolution for the noise in the 100 Hz to 1000 Hz band. The circles are spectral levels derived from analog band filtering. From Helbig (1970). (See Medwin, H., R. A. Helbig, and J. D. Hagy, Jr., "Spectral characteristics of sound transmission through the rough sea surface," *J. Acoust. Soc. Am.* **54**, 99–109, 1973.)

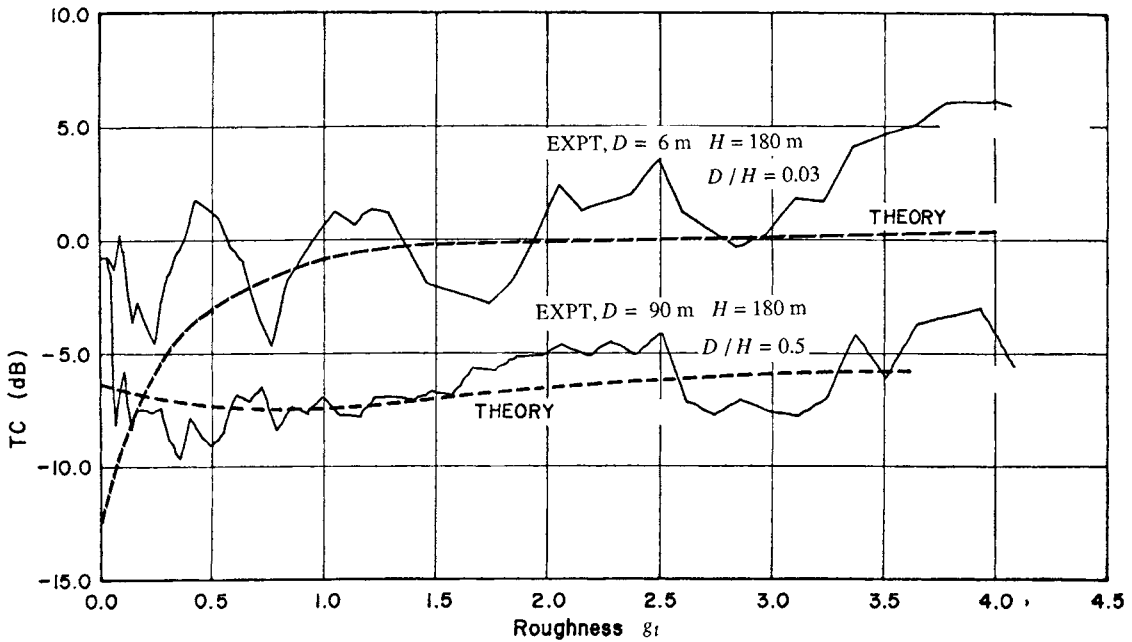

Figure 13.5.3 Pressure transmission change as a function of surface acoustical roughness for transmission, g_1, for a point source at $H = 180$ m above a sea of rms height $h = 13$ cm. The receivers at depth $D = 6$ m and 90 m are offset by 75 m from the ground-zero point under the source. The offset angles are 85° for the 6 m hydrophone and 40° for the 90 m hydrophone. Solid line is digital analysis from 100 Hz to 1000 Hz with 2 Hz frequency resolution. From Helbig (1970). Dashed line is HK thoeretical solution by Hagy (1970). (For theory, see also Medwin, H., and J. D. Hagy, Jr., "Helmholz–Kirchhoff Theory for Sound Transmission Through a Statistically Rough Plane Interface Between Dissimilar Fluids," *J. Acoust. Soc. Am.* **51**, 1083, 1972; for experimental details, see Medwin, H., R. A. Helbig, and J. D. Hagy, Jr., "Spectral characteristics of sound transmission through the rough sea surface," *J. Acoust. Soc. Am.* **54**, 99–109, 1973.)

When the source was over the shallow hydrophone ($\theta_1 = \theta_2 = 0°$) and $D/H = 0.03$, the transmission change was $+6 \pm 1$ dB not only at low roughness but also at higher frequencies, where $g_t = 4.2$. (See Fig. 13.5.2.) This was due to the incoherent contributions that came in from other positions beyond the normal-incidence direction. For the hydrophone at depth 90 m, where $D/H = 0.5$, there is a similar effect. Off-axis transmission contributions through a rough surface provide a TC that shows more energy than the theoretical loss 4.1 dB as predicted for smooth surfaces by Equation 13.5.5a.

When the 180 m high-sound source is offset from the hydrophones, so that the Snell angles in the water are 85° for the 6 m depth hydrophone, and 40° for the 90 m hydrophone, there are incoherent contributions from insonified regions beyond the transmission cone. Significantly, much more sound is received at larger surface roughness, especially by the shallow hydrophone, in general agreement with the theoretical solution (Fig. 13.5.3).

Problems

Section 13.1

13.1.1 Integrate the Pierson-Moskovitz spectrum over all frequencies to obtain the rms height, h.

13.1.2 Use the two graphs in Fig. 13.1.5 to give analytical equations — such as Equations 13.1.16 and 13.1.17 — for the SWOP correlations. Plot those equations and compare with the actual data in Fig. 13.1.5.

13.1.3 Derive the PDF of a swell wave, $\zeta = a \sin K_x x$. Answer $w(\zeta) = \pi^{-1}(a^2 - \zeta^2)^{-1/2}$ for $\zeta < a$.

Section 13.2

13.2.1 A 38 kHz sound beam is specularly scattered from a sea surface of rms height $h = 2$ cm. Determine the angles at which the relative coherent intensity $\mathcal{R}_{\text{coh}} > 0.7$.

13.2.2 Use the data on coastal bubble densities, resonant at 60 kHz (Chapter 8), to calculate the proper position of the horizontal bubble backscattering line in Fig. 13.2.6.

Section 13.3

13.3.1 Use "reasonable" values to describe a rough sea surface and calculate the backscatter of a "reasonable" sonar as a function of angle of incidence.

13.3.2 Repeat the calculation of the previous problem to determine forward scatter as a function of the grazing angle of incidence.

Section 13.4

13.4.1 Using the laboratory experiments as a guide, and "reasonable" assumptions, calculate the low-frequency, grazing-incidence, relative boundary wave amplitude for propagation over a bed of manganese nodules of reasonable diameter.

13.4.2 Using the laboratory experiments as a guide, and "reasonable" assumptions, calculate the phase velocity of grazing sound over a rock-strewn bottom, assuming close-packed boulders of diameter about 1 m, and correlation functions as shown in Fig. 13.1.10.

Section 13.5

13.5.1 Derive Equation 13.5.4 for the transmitted intensity across a smooth interface between two media.

13.5.2 Verify Equation 13.5.5a.

Chapter 14 | Mapping the Sea Floor

14.1 Bathymetric and Seismic Profiles: Geophysics 640
14.2 Deep-Tow Side-Scan Sonar Mapping of the Sea Floor 641
14.3 Swath Mapping from Surface Vessels 644
14.3.1 Acoustic Survey: Laurentian Fan 646
14.3.2 Swath-Mapping System 647
14.3.3 Data Reduction 649
14.3.4 Theoretical Backscattered Sound Pressures 650
14.4 Analytical and Numerical Evaluations of the Scattering Coefficients 653
14.4.1 Cylindrically Symmetric Correlation Function 653
14.5 An Analysis of the Backscattered Data in Two Areas: Spatial Correlations 654
14.5.1 Assumptions 656
14.6 An Analysis of the Backscattered Data in Two Areas: Spatial Spectra 659

The topography and structure of the sea floor are enormously varied. One cannot use one sonar system and one method of data analysis for the whole ocean. We suggest four guiding principles: 1) as the spatial and temporal resolution of sonar systems improve, more and more small features are displayed; 2) as the frequency of a sonar goes lower, the sea floor appears to become smoother; 3) there are always unresolved features; and 4) global positioning systems and accurate navigation are absolutely essential.

14.1 Bathymetric and Seismic Profiles: Geophysics

Vertical echo sounders (Section 10.1.1) are the workhorses of marine geology and geophysics. The 12 kHz echo sounder frequency is low enough to obtain usable reflections from the deepest parts of the ocean—for example, the 10,830 m depth of the Challenger Deep in the Mariana Trench. Over very smooth sediment deposits, *subbottom* reflections from interfaces at several meters depth can be observed for signal frequencies as high as 12 kHz. Another standard echo sounder has a 3.5 kHz carrier frequency. This echo sounder can penetrate the subbottom structure to a 100 or so meters. Both the 12 kHz and the 3.5 kHz echo sounders can be mounted on the hulls of oceanographic survey vessels. For deep penetration to kilometers of depth, oceanographic geophysicists use seismic profiling systems. Commonly used seismic sources are "air guns," sparks, and explosives. The receiver is an array of hydrophones. As sketched in Fig. 14.1.1,

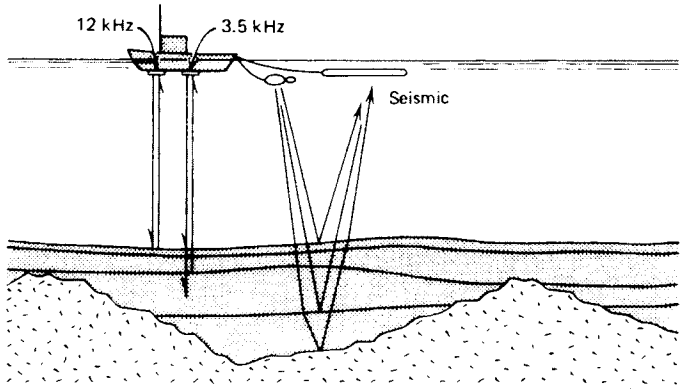

Figure 14.1.1 Seismic profiling system. Many kinds of towing configurations are used.

the source and receiving array are towed behind the survey vessel. The frequency ranges for seismic profiling systems are usually 100 Hz and lower.

Comparisons of the acoustic profiles for three systems and two examples of sea floors are shown in Fig. 14.1.2. The increase of subbottom penetration as the frequency decreases is apparent. *The Sea* (vol. 3, ed. M. N. Hill, 1963) gives broad discussions of early applications of geophysical, geological, and acoustical methods for exploring the sea floor. *The Physics of Sound in Marine Sediments* (ed. Hampton, 1974) gives a 10-year progress report in describing the acoustic properties of sea-floor sediments. Compressional wave attenuations are in Hamilton (1987) and Kibblewhite (1989). Bowles (1997) gives an extensive review and tables of shear-wave velocities and attenuation in fine-grained marine sediments. Many symposium volumes and monographs have been published (*Oceanographic Atlas of the North Atlantic* 1965; Kuperman and Jensen 1980; Akal and Berkson 1986; Vogt and Tucholk 1986).

14.2 Deep-Tow Side-Scan Sonar Mapping of the Sea Floor

Bottom-scanning sonar technology has gone from a simple echo sounder pointed sideways to instruments that have carefully designed beam patterns, very sophisticated time-varying gains, and image processing. One of the early deep tow surveys was made during the search for the lost submarine *Thresher* (April 10, 1963). The image of a wreck on the sea floor (Fig. 1.3.5) shows what a high-resolution sonar can do. Side-scanning sonars are towed at approximately 0.2 times the maximum range above the bottom to give a map of the locations of

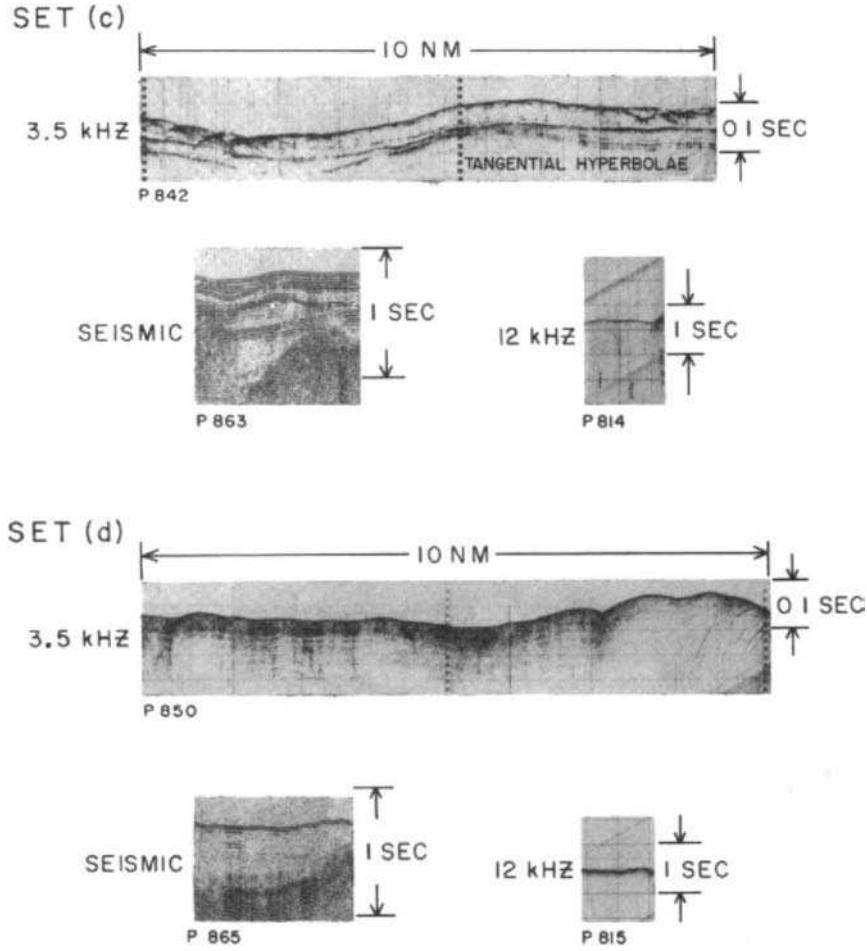

Figure 14.1.2 Acoustic profiles from the *Kane9, 1968 cruise*. The profiles within each set were taken from the same rough area. (From Lowrie, A., and E. Escowitz, *Kane 9. Global Ocean Floor Analysis and Research Data Series*. U.S. Naval Oceanographic Office, 1969.)

scatterers on the sea floor. Even in the deep ocean, side-scan sonars that have a range of 500 m are towed about 100 m above the bottom. The maximum tow speeds are a few km/hr. The area is on the continental shelf and has extremely varied morphology (Clay, Ess, and Weisman 1964). All of the data were recorded on a paper graphic recorder, and the image processing was done photographically. Examples of side-scan records are shown in Fig. 14.2.1. Black is a strong return and a large-surface (back) scattering coefficient. The white area

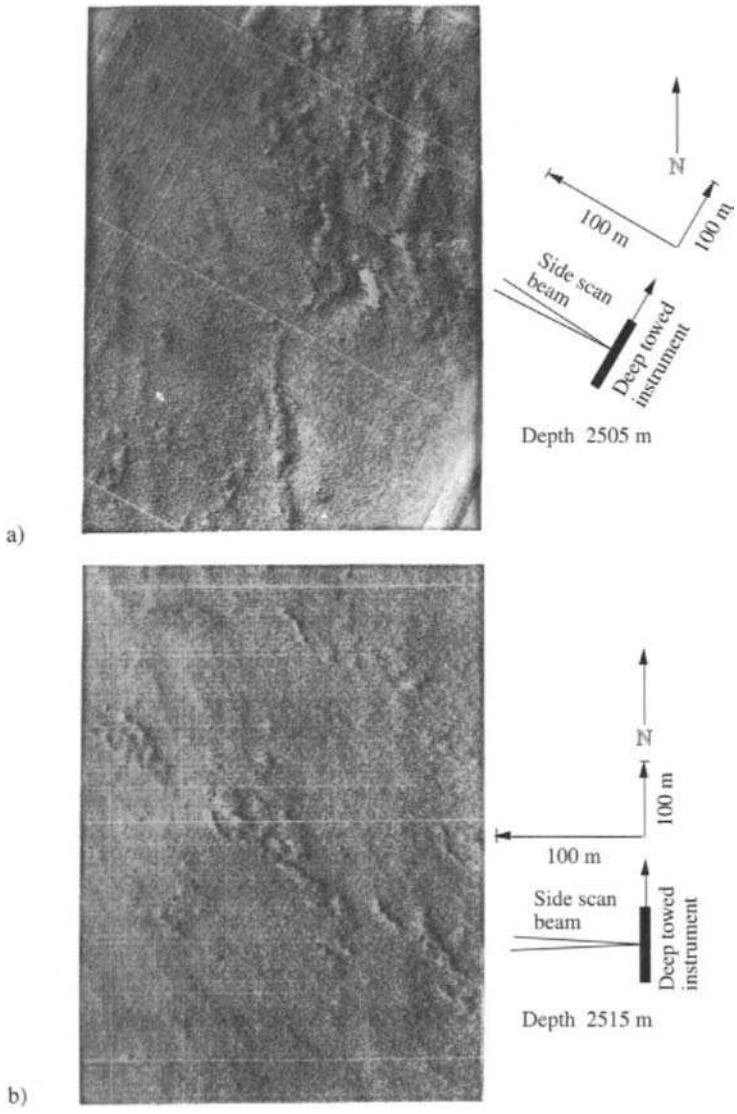

Figure 14.2.1 Deep-tow side-scan images of the sea floor. Side-scan images are from the areas #1 and #6 as indicated in the tracing of features shown in Fig. 14.2.2. The carrier frequencies were 215 and 225 kHz. The ping duration was 1 ms. The peak input power to the transducers was about 300 watts. The beam widths were 70° vertical and 0.3° horizontal. The swath was 375 m to port and 375 m starboard. The instrument was towed about 60 m above the bottom. (From Clay, C. S., J. Ess, and I. Weisman, "Lateral echo sounding of the ocean bottom on the continental rise," *J. Geophys. Res.* **69**, 3823–35, 1964b.)

indicates small return and a shadow or a depression. The side-scan image shows features that give stronger surface (back) scattering than the background. For an optical analogy, put a few objects on a cloth-covered table and illuminate them with a flash light at grazing angles to the table top and then look down on the objects and their shadows.

Side-scanning sonars record the backscatter from features on the bottom at very small grazing angles. Here the intensity of backscatter is very sensitive to the spatial correlation function. Numerical studies of the backscattering coefficients have shown that the backscatter is easily observed when the correlation coefficients have a $|\xi|$ dependence at small $|\xi/L|$ and $kh > 1$. Commonly, sand waves and gravel interfaces have this $|\xi|$ dependence and give strong backscatter. The correlation coefficients, for smoothly undulating interfaces, have the ξ^2 dependence at small $(\xi/L)^2$ (see section 13.1). The backscatter is very small at shallow grazing angles.

The graphic records were assembled into a mosaic image of the sea floor. After reduction to page size, the mosaic is not suitable for reproduction. The features on the mosaic were traced and superimposed onto a bathymetric chart of the area (Fig. 14.2.2).

The bottom has smooth sediments, gravel, wavelike features, and just plain puzzling features. This research shows that smooth-sediment-covered areas have very small uniform surface scattering coefficients. Ridges, gravel beds, sand waves, grooves, and so forth show as dark and light features. It takes much geological imagination to guess what the images represent.

Deep-tow side-scan surveys are extremely expensive and difficult to do. During the summer of 1963, the oceanographic vessel USNS *Gibbs* and 25 scientists were at sea for two months and only mapped 20 km^2 of sea floor. A team of scientists spent nine months on the data analysis, preparation of the figures, and writing the manuscript (Clay, Ess, and Weisman 1964). Tyce et al. (1980) describe the later, more efficient developments in deep-tow technology.

14.3 Swath Mapping from Surface Vessels

As is evident in Fig. 14.2.2, bathymetry and side-scan images are complementary. Bathymetry shows the water depths and general structure of the sea floor. Side-scan images give a measure of the surface (back) scattering coefficient. But a month or two of ship time is far too expensive to map only 20 km^2 of sea floor. Multibeam sonar or swath-mapping techniques have greatly improved the efficiency of sea charting because normal surveying speeds of 12 km/hr are used. Although the spatial resolution obtained from surface vessels is not as good as from deep-towed instruments, the side-scan images display the surface-

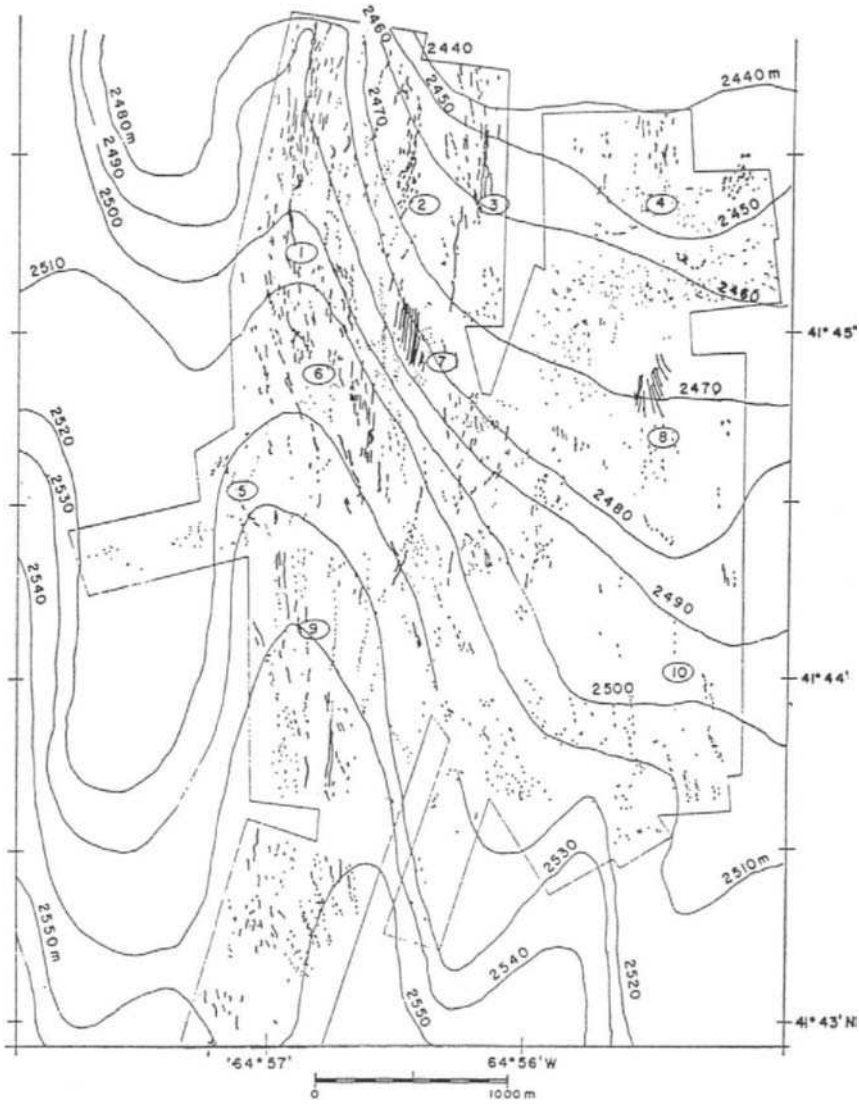

Figure 14.2.2 Tracing of features on a mosaic of side-scan records. The area is at the bottom of the continental rise at 41°50′N and 64°57′W. The features are superimposed on bathymetric contours. The sounding velocity is 1500 m/s. The circled numbers are drawn beneath the sonar images. Only #1 and #6 are included here. (From Clay, C. S., J. Ess, and I. Weisman, "Lateral echo sounding of the ocean bottom on the continental rise," *J. Geophys. Res.* **69**, 3823–35, 1964b.)

scattering coefficients and give another dimension in remote sensing of the sea floor.

An introduction to a special section on sea-floor mapping is in Detrick (1986). Tyce (1986) reviews deep-sea-floor mapping systems.

14.3.1 ACOUSTIC SURVEY: LAURENTIAN FAN

The area is located approximately 100 to 125 km south of the 1929 earthquake epicenter on the Grand Banks off Newfoundland. It caused immense slumping. The bathymetric map and ship track lines are shown in Fig. 14.3.1. The resulting turbidity currents broke submarine cables in a number of places (Heezen and Hollister 1971). The fan has a complex geomorphology owing to the presence of strong turbidity current activity. The turbidity currents primarily distribute thick sands and gravels on the channel floor. Most of the acoustic survey, Fig. 13.4.1, was made within the relatively flat channel floor, where the gradient is only 0.5 degrees (Talukdar, Tyce, and Clay 1995).

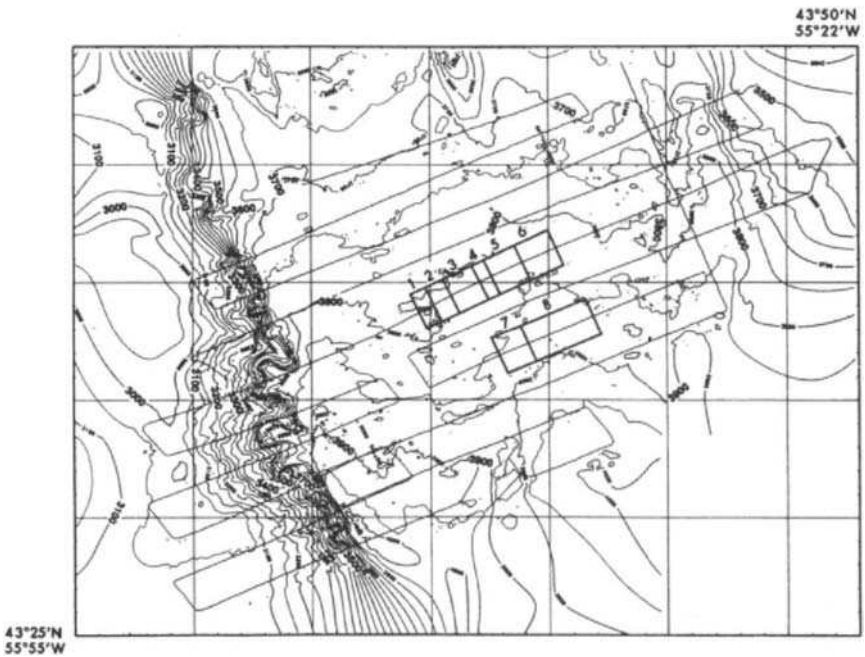

Figure 14.3.1 Bathymetric map of the survey area and locations of backscatter analysis sites (contour intervals are in meters). Type A areas are 1, 3, 5, and 7. Type B areas are 2, 4, 6, and 8. (From Talukdar, K. K., R. C. Tyce, and C. S. Clay, "Interpretation of sea beam backscatter data collected at the Laurentian Fan off Nova Scotia using acoustic backscatter theory," *J. Acoust. Soc.* **97**, 1545–58, 1995.)

14.3.2 SWATH-MAPPING SYSTEM

The 1986 version of the Sea Beam system is a hull-mounted, multi-narrow-beam sonar. It was designed to obtain high-resolution bathymetry for a swath width of about 75 percent of the water depth. As shown in Fig. 14.3.2, it has one fan-shaped transmit beam oriented across track and 16 fan-shaped receiver beams

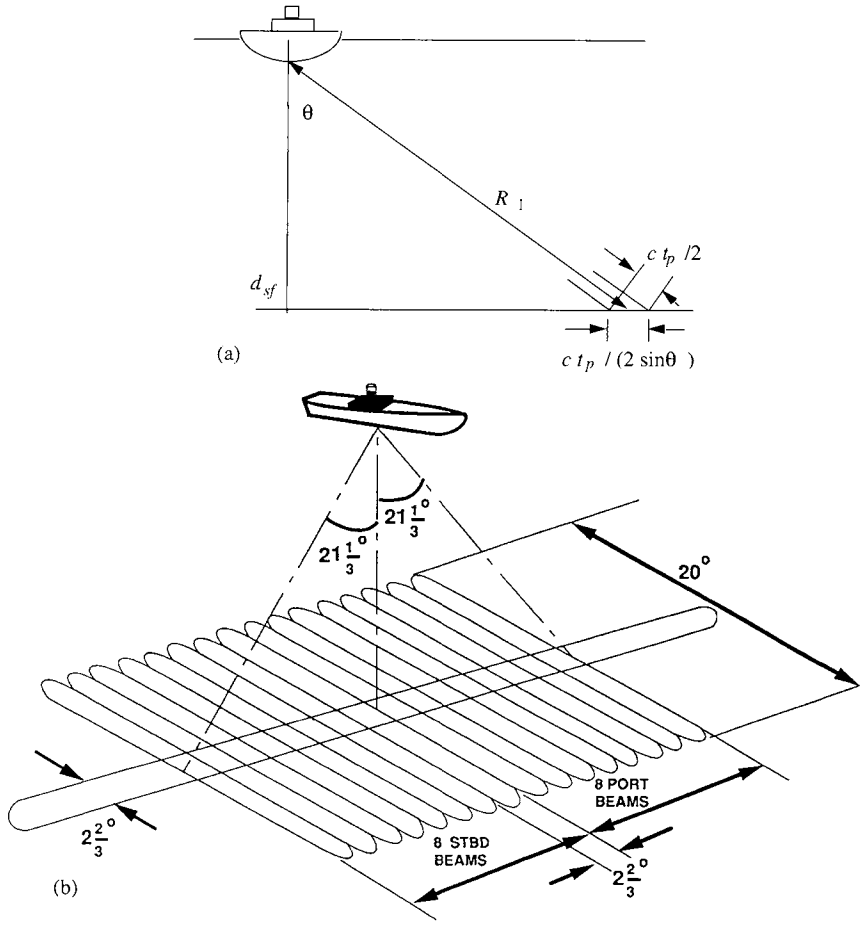

Figure 14.3.2 Transmit and receive geometry of the 1986 Sea Beam system. Transmission beam is fanlike and normal to the track. The reception beams are fans along the track. The intersections are the "footprints." The travel times to a footprint and its beam angle are used to compute the depth of the footprint. The frequency of the pings is 12.158 kHz, and the ping duration is 7-ms. (From Talukdar, K. K., R. C. Tyce, and C. S. Clay, "Interpretation of sea beam backscatter data collected at the Laurentian Fan off Nova Scotia using acoustic backscatter theory," *J. Acoust. Soc.* **97**, 1545–58, 1995.)

oriented perpendicular to the transmit beam. The directions of the receiver beams are evenly spaced at (8/3)° to form effectively 8 port and 8 starboard beams.

In the system's normal mode of operation, the backscattered echoes are compensated for roll and refraction and then integrated to determine a single range and angle to the bottom for the center of that beam. The actual beam angles are determined dynamically for every ping. A maximum of 16 depths and their cross-track positions are determined for each transmission. The envelopes of the rectified return signals or backscattered data are recorded on magnetic tape for acoustic research.

The intensity-modulated side-scan images of sound scattered at the sea floor add another dimension to the data. The resolution of features on the sea floor, as given by the Sea Beam "footprint," is about 170 × 170 m at 3800 m depth. In backscatter, the lateral width Δx of the bottom insonified by the sonar ping is

$$\Delta x \approx t_p c / (2 \sin\theta_1) \tag{14.3.1}$$

where t_p is the duration of the sonar ping and θ_1 is the angle of incidence at the bottom. Values of Δx for incident angles of 5° and 20° are 60 and 16 m. Except for vertical incidence, the lateral resolution is better in side-scan modes than the resolution is in beam-forming modes.

The footprint is the spatial resolution of the insonification on the sea floor (Fig. 14.3.2). The depth of the footprint gives the resolved bathymetry, and this is the "deterministic" part. The unresolved features within the footprint are defined as being "random."

For practical necessity, one makes assumptions about the sea floor within a footprint: 1) the PDF of the roughness relative to a mean surface in a footprint is Gaussian; 2) the roughness and the spatial correlation functions are the same everywhere in a footprint; 3) the roughness, h, and spatial correlation functions, $C(L)$, remain the same for usable distances along the track; and 4) the slope of a mean surface in a footprint can be got from bathymetric data. Details are given by de Moustier and Alexandrou (1991).

Side-scan images are constructed by combining the beams on the port side to produce a single, time-dependent record for each ping. The same process is applied to the starboard beams. Fig. 14.3.3 shows the side-scan image of the Laurentian fan. The side-scan images were studied to choose areas where these simplifying assumptions could be satisfied. The chosen areas, 1–8 as shown on the bathymetric chart, are along the ship track and on a relatively flat area on the fan. The side-scan display (Fig. 14.3.3) shows relatively uniform backscatter from patches on each side of the ship track.

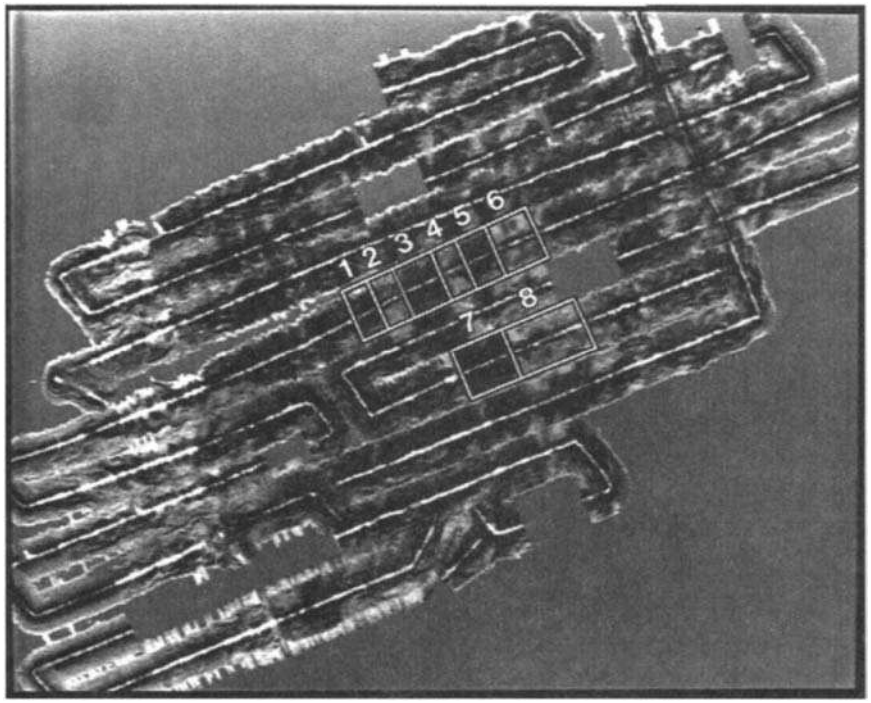

Figure 14.3.3 Side-scan image of the Laurentian fan. The image was constructed by combining the output of adjacent beams. Time was converted to distance along a flat bottom for construction of the mosaic. The backscattered returns are displayed on a logarithmic gray scale. Type A areas (1, 3, 5, and 7) are dark. Type B areas (2, 4, 6, and 8) are light. (From Talukdar, K. K., R. C. Tyce, and C. S. Clay, "Interpretation of sea beam backscatter data collected at the Laurentian Fan off Nova Scotia using acoustic backscatter theory," *J. Acoust. Soc.* **97**, 1545–58, 1995.)

The backscatter changes abruptly from "dark" or strong backscatter (type A: 1, 3, 5, 7) to "light" weak backscatter (type B: 2, 4, 6, 8) as one goes from area 1 to 2 and so on. These data were analyzed to estimate the roughness parameters and structure of the sea floor and to "explain" why the "A" areas have strong backscatter and the "B" areas have smaller backscattered sound.

14.3.3 DATA REDUCTION

Computations of the experimental scattering coefficients are the first steps in data reduction. The experimental scattering coefficient is computed by using the form

of Equation 13.3.20:

$$S_{\exp}(k, \theta_1, R_1, R_2, A) \equiv \frac{|pp^*| R_1^2 R_2^2}{|p_0 p_0^*| R_0^2 A} \tag{14.3.2}$$

where k is the wave number; θ_1 is the incident angle; $|pp^*|$ is the square of the envelope at the receiver; $|p_0 p_0^*|$ is the square of the source envelope at the reference distance R_0; R_1 is the distance to A from the transmitting transducer; R_2 is the distance from A to the receiving transducer; A is the insonified area. The Sea Beam system was not calibrated, so that measurements of $S_{\exp}$ are relative to the same arbitrary reference. The relative dependence of $S_{\exp}$ on θ_1 will be the basis of data analysis.

The dependence of $S_{\exp}(k, \theta_1, R_1, R_2, A)$, or just $S_{\exp}$ on surface roughness is implied. The distances R_1 and R_2 are large enough that the wavefront spreading is nearly spherical. The sound speed in water is c.

14.3.4 THEORETICAL BACKSCATTERED SOUND PRESSURES

In the backscattering mode, the scattering expressions in Equations 13.3.3 through 13.3.6 simplify as follows:

$$R_1 = R_2, \theta_1 = -\theta_2, \theta_3 = 0 \tag{14.3.3}$$

and the expressions for α, β, and γ (Equation 13.3.5) reduce to

$$\alpha = k \cos\theta_1, \quad \beta = 0, \text{ and } \gamma = k \cos\theta_1 \tag{14.3.4}$$

The "slope-corrected" form of G_{sc} (Equation 13.3.6) becomes

$$G_{sc}(\theta) \approx \frac{1}{\cos\theta_1} \tag{14.3.5}$$

$$R_1 = \frac{d_{sf}}{\cos\theta_1} \tag{14.3.6}$$

$$x_f^{-2} = \frac{k}{R_1} \cos^2\theta_1, \quad y_f^{-2} = \frac{k}{R_1} \tag{14.3.7}$$

where d_{sf} is the depth of the sea floor beneath the transducers. The theoretical backscattered pressure is

$$p = \frac{ip_0 R_0 \mathcal{R}_{12} k \exp(i\omega t - 2ikR_1)}{2\pi R_1^2 \cos(\theta_1)} \int_{-\infty}^{\infty} dx \int_{-\infty}^{\infty} D_t D_r \times \exp\left[-i\left(\frac{x^2}{x_f^2} + \frac{y^2}{y_f^2} + 2\alpha x - 2\gamma\zeta\right)\right] dy \tag{14.3.8}$$

where $\mathcal{R}_{12}$ is the pressure reflection coefficient at the interface; k is the wave number; D_r is the receiver directivity function; D_t is the transmitter directivity function; ζ is the surface height above a mean surface.

The effective beam pattern is the product of the transmitted beam and the received beams. At vertical incidence, the directivity function for the insonified area is

$$D_t D_r \approx \exp\left[-\left(\frac{x^2}{X_0^2} + \frac{y^2}{Y_0^2}\right)\right] \tag{14.3.9a}$$

and

$$X_0 \approx d_{sf} \Delta\varphi_t, \quad Y_0 \approx d_{sf} \Delta\varphi_r \quad \text{for} \quad \theta_1 = 0 \tag{14.3.9b}$$

where $\Delta\phi_t$ is the *half-beam* width of the transmit beam along track and $\Delta\phi_r$ is the *half-beam* width of the receiver beam normal to the track. The half-beam widths are equal and

$$\Delta\phi = \Delta\phi_t = \Delta\phi_r = (4/3)^\circ \tag{14.3.9c}$$

At angles larger than 0, we use the transmitted ping duration t_p and sound speed c to write X_0 and Y_0 as follows:

$$X_0 \approx \frac{c\, t_p}{4 \sin\theta_1}, \quad Y_0 \approx \frac{d_{sf}\, \Delta\phi}{\cos\theta_1} \quad \text{for} \quad \theta_1 \geq \frac{8^\circ}{3} \tag{14.3.10}$$

The mean absolute pressure squared is given in Equation 13.3.20. In backscatter, the theoretical mean squared pressure is

$$\langle p^2 \rangle \approx \frac{k^2 p_0^2 R_0^2 \mathcal{R}_{12}^2 X_0 Y_0}{8\pi R_1^4 \cos^2\theta_1} \int_{-\infty}^{\infty} \int_{-\infty}^{\infty} \mathcal{G}\mathcal{W} \exp(2i\alpha\xi) d\xi\, d\eta \tag{14.3.11}$$

where

$$\mathcal{G} \equiv \exp\left(-a_\xi \xi^2 - a_\eta \eta^2\right) \tag{14.3.12}$$

$$a_\xi \equiv \frac{1}{2X_0^2} + \frac{k^2 X_0^2 \cos^4\theta_1}{2R_1^2} \tag{14.3.13}$$

$$a_\eta \equiv \frac{1}{2Y_0^2} + \frac{k^2 Y_0^2}{2R_1^2} \tag{14.3.14}$$

$$C = 1 - a_1|\xi| - a_2\xi^2 - b_1|\eta| - b_2\eta^2 \tag{14.3.15}$$

and

$$\mathcal{W} \equiv \exp\left[-\gamma^2 h^2 (1 - C)\right] \tag{14.3.16}$$

The area is

$$A = \pi X_0 Y_0 \tag{14.3.17}$$

Since the the spatial correlation function is symmetric,

$$C(\xi, \eta) = C(-\xi, -\eta) \tag{14.3.18}$$

and $\mathcal{G}$ is even, the doubly infinite integrals for $\langle p^2 \rangle$ reduce to the following:

$$\langle p^2 \rangle \approx \frac{k^2 p_0^2 R_0^2 \mathcal{R}_{12}^2 X_0 Y_0}{2\pi R_1^4 \cos^2\theta_1} \int_0^\infty \int_0^\infty \mathcal{G}\mathcal{W} \cos(2\alpha\xi)\, d\xi\, d\eta \tag{14.3.19}$$

With these changes, the theoretical backscattering coefficient (Equation 13.3.20a) becomes

$$S(k, \theta_1, R_1, A) \approx \frac{k^2 \mathcal{R}_{12}^2}{2\pi^2 \cos^2\theta_1} \int_0^\infty \int_0^\infty \mathcal{G}\mathcal{W} \cos(2\alpha\xi)\, d\xi\, d\eta \tag{14.3.20}$$

where the function $\mathcal{G}$ includes the parameters k, θ_1, R_1, and A. The surface roughness, h, and the spatial correlation function, C, are contained in the function $\mathcal{W}$.

Except for a few special cases such as *incident plane waves and near-field measurements*, the geometric information in $\mathcal{G}$ cannot be moved out of the integral. Thus measurements of S_{exp} depend on the sonar system that was used to make the measurements. *As demonstrated in Chapter 13, the only parameters that don't depend on the sonar system are the bottom roughness, spatial correlation functions or spectral densities, and sound speeds.*

14.4 Analytical and Numerical Evaluations of the Scattering Coefficients

Approximate evaluations of the scattering integrals in Equation 14.3.20 are possible for the spatial correlation coefficients given in Equations 13.3.27 and 13.3.27 (Clay and Leong 1974; Clay and Medwin 1977 Appendix A10). Because $\mathcal{G}$ tends to 0 rapidly as ξ and η increase, numerical evaluations are practical.

14.4.1 CYLINDRICALLY SYMMETRIC CORRELATION FUNCTION

A two-parameter, cylindrically symmetric correlation function is

$$C\ (r\ ) = \exp\ [\ -\ |\frac{r}{L}\ |^{n}\ ] \tag{14.4.1}$$

where L is a "correlation distance" and n is a positive parameter. Examples of the correlation functions and their spectra are shown in Fig. 13.1.9.

Equation 14.4.1 becomes the exponential function for $n = 1$ and the Gaussian function for $n = 2$. The power of n in the correlation function is an indicator of the shape of the surface. Large n causes the correlation function to decay gradually for $r < 1$, and this corresponds to a surface having large radii of curvatures. Small n causes the correlation to decay very rapidly, and this corresponds to a surface having sharp angular features. The corresponding spectra for correlation functions having the exponents 0.5–2.0 are shown in Fig. 13.1.9b. The Fourier transformations were evaluated numerically.

Transformation of the scattering function from rectangular coordinates to the cylindrical coordinates r and ψ uses the transformations

$$\xi = r\ \cos\psi \quad \text{and} \quad \eta = r\ \sin\psi \tag{14.4.2}$$

The transformation of $(a_{\xi}x^2 + a_{\eta}\eta^2)$ to cylindrical coordinates is simplified by letting

$$a_r \approx a_{\xi} \approx a_{\eta} \quad \text{for} \quad \theta_1 < 25^{\circ} \tag{14.4.3}$$

and computing an average a_r using $a_r \approx (a_{\xi} + a_{\eta})/2$. With these approximations, the theoretical backscattering coefficient (Equation 13.3.19) becomes

$$\mathcal{S} \approx \frac{k^2 \mathcal{R}_{12}^2}{8\pi^2 \cos^2\theta_1} \int_0^{\infty} \int_0^{2\pi} \exp\left(-a_r r^2\right) \exp\left(i2kr \sin\theta_1 \cos\psi\right) \mathcal{W} r\, dr\, d\psi \tag{14.4.4}$$

and

$$\mathcal{W}\ \equiv \exp\ \{\ -\ \gamma^2 h^{\,2}\ [1\ -\ \exp\ (\ -\ |\frac{r}{L}\ |^{n}\ )\ ]\ \} \tag{14.4.5}$$

The evaluation of the integral over ψ gives

$$S \approx \frac{k^2 \mathcal{R}_{12}^2}{4\pi^2 \cos^2\theta_1} \int_0^\infty J_0(2kr \sin\theta_1) \exp(-a_r r^2) \mathcal{W} r\, dr \quad (14.4.6)$$

The integral is evaluated numerically. The backscattering strength in dB is

$$\text{Backscattering strength} = 10 \log_{10}(S)\,\text{dB} \quad (14.4.7)$$

14.5 An Analysis of the Backscattered Data in Two Areas: Spatial Correlations

The side-scan map (Fig. 14.3.3) shows areas of light and dark patches. These eight sites on the channel floor (Fig. 14.3.1) were selected for study. We assume that the sea-floor roughness and physical properties are statistically stationary within those areas.

The Sea Beam sonar system used was not calibrated for this effort—that is, the projector source level and the various gains applied to the return signals are not known—so the backscattering strengths are computed with reference to an arbitrary level. The choice of an arbitrary reference has the effect of translating the backscattering strength versus incident angle curves up or down from the true level, but the shapes of the curves remain unaltered. The plots of the backscattering strength versus angle for the type "A" areas are shown in Fig. 14.5.1. The backscattering strengths versus angle have gradual decreases as the incident angle decreases.

A nonlinear regression technique was used to estimate the roughness parameters and structure. Since the backscatter data is referenced arbitrarily, the source function, reflection coefficient, and so forth in Equation 14.4.5 are carried as a scaling factor, B_{sf}.

The best fits for the A-type areas of regions are shown in Fig. 14.5.1, and the corresponding parameters are summarized in Table 14.1. Generally, all of the type A areas have similar descriptions. We hypothesize that these areas are covered with gravel. Marine geologists define gravel as being the loose material that ranges in size from 2 to 256 mm (Gross 1972, Glossary).

Data from the B-type areas (Fig. 14.5.2) have an initial sharp drop followed by a gradual decrease. These scattering data could not be fitted by a single interface scattering model.

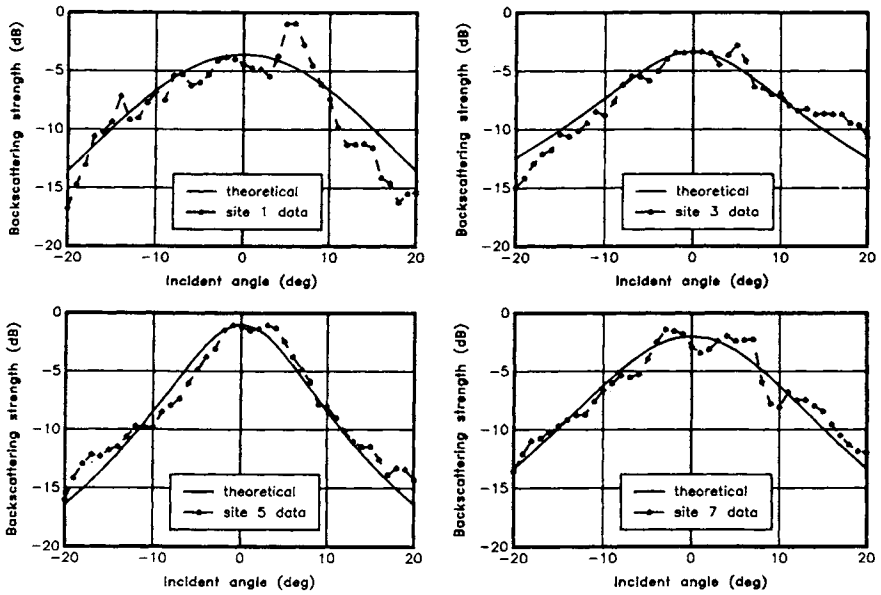

Figure 14.5.1 Backscattering strengths (dB) from the type A areas. The data points are the solid circles connected by short lines, and the solid lines are the theoretical scattering functions. The parameters are given in Table 14.1. The reference is arbitrary. (From Talukdar, K. K., R. C. Tyce, and C. S. Clay, "Interpretation of sea beam backscatter data collected at the Laurentian Fan off Nova Scotia using acoustic backscatter theory," *J. Acoust. Soc. Am.* **97**, 1545–58, 1995.)

Table 14.1 **Summary of the Estimated Parameters for Type A Areas**

Area	*Scale Factor* B_{sf}	*rms Height, m* h	*Exponent* n	*Correlation length, m* L
1	0.77	0.08	1.5	1.4
3	0.93	0.06	0.96	2.0
5	0.70	0.07	1.15	2.7
7	0.85	0.08	1.30	2.0
Avg	0.81	0.07	1.22	2.0

(From Talukdar, K. K., R. C. Tyce, and C. S. Clay, "Interpretation of sea beam backscatter data collected at the Laurentian Fan off Nova Scotia using acoustic backscatter theory," *J. Acoust. Soc. Am.* **97**, 1545–58, 1995.)

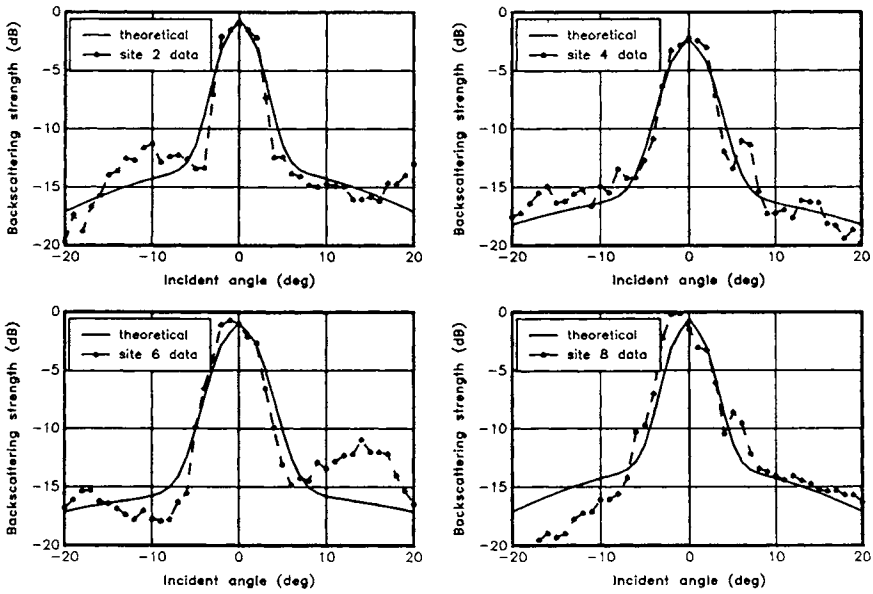

Figure 14.5.2 Backscattering strengths (dB) from the type B areas. The data points are the solid circles connected by short lines, and the solid lines are the theoretical scattering functions. The parameters are given in Table 14.2. The reference is arbitrary. (From Talukdar, K. K., R. C. Tyce, and C. S. Clay, "Interpretation of sea beam backscatter data collected at the Laurentian Fan off Nova Scotia using acoustic backscatter theory," *J. Acoust. Soc. Am.* **97**, 1545–58, 1995.)

Volume scattering from scatterers underneath the scattering surface has been proposed as a possible contributor to the total scattering process in shallower waters (Jackson et al. 1986; Matsumto et al. 1993). However, the channel floor is a region of strong turbidity current activity. Since turbidity currents deposit sediments in an orderly manner with distinct facies, scattering from subsurface layers seems more likely. Figure 14.5.3 shows deep-tow data that were taken over an area southwest of this survey.

Assuming that the structure shown in Fig. 14.5.3 commonly occurs in this geologic environment, the theory was modified to include scattering from a subbottom interface (Fig. 14.5.4).

14.5.1 ASSUMPTIONS

1) The surface and the subbottom scattering add incoherently as the square of sound pressures. 2) The scattered intensity from the subbottom layer is attenuated in the sediments. 3) If $\mathscr{S}_s$ and $\mathscr{S}_b$ are the backscattering coefficients from the

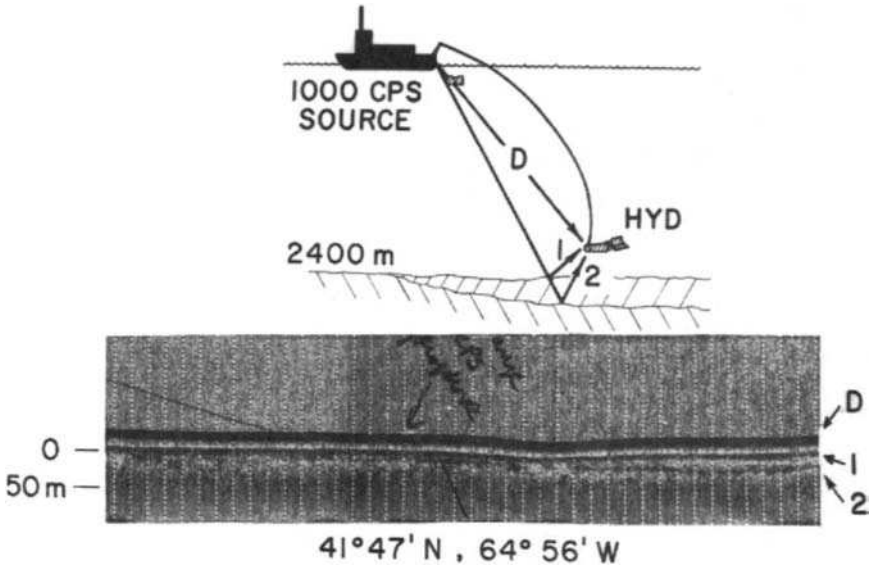

Figure 14.5.3 Deep-tow acoustic profile. The source was a 1000 Hz ping. D is the direct arrival, and the reflections scattering from interfaces 1 and 2 are indicated. The length of the profile is approximately 2.5 km. This profile was taken during the survey shown in Fig. 14.2.2. The poor quality of the reflection from interface 2 is typical of scattering from a rough interface. Interface 1 on the right side appears to be smoother. The short profile shows the transition from two layers to one layer.

surface and subbottom, respectively, then the total backscattering coefficients, $\mathcal{S}_T$, is equal to

$$\mathcal{S}_T = \mathcal{S}_S + \mathcal{S}_b 10^{-2\alpha_s d_s/10} \tag{14.5.1}$$

where α_s is the attenuation in sediment in dB/m, and d_s is the depth of layer. Assuming thin layers, both $\mathcal{S}_s$ and $\mathcal{S}_b$ were calculated using the scattering equation (13.4.22). The attenuation in the sediments can vary widely depending on the grain size, porosity, material type, and so on. From the literature, the

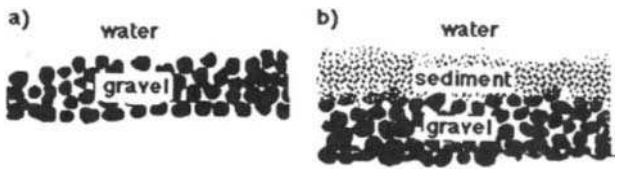

Figure 14.5.4 Cartoons of the interfaces at the type A and B areas. a) Type A is gravel. b) Type B has a thin layer of sediment over gravel. (From Talukdar, K. K., R. C. Tyce, and C. S. Clay, "Interpretation of sea beam backscatter data collected at the Laurentian Fan off Nova Scotia using acoustic backscatter theory," *J. Acoust. Soc. Am.* **97**, 1545–58, 1995.)

attenuation range for 12 kHz can be expected to be from as low as 0.7 dB/m to as high as 6 dB/m (Hamilton 1972). An estimate of 1 dB/m was selected for carrying out the best fit analysis.

The density and velocity of compressional waves in saturated, silty sand are estimated as 1320 kg/m^3 and 1540 m/s; correspondingly, a plane-wave pressure reflection coefficient is 0.14. The density and velocity of compressional waves in marine gravels is not readily available in the literature. Values of 2000 kg/m^3 for the density and 1800 m/s for the velocity yield a reflection coefficient of 0.28 (Hamilton 1972). The ratio of the two reflection coefficients is 0.5, which agrees with the averaged ratio 0.5 of (B_{sf1}/B_{sf2}), obtained from Tables 14.1 and 14.2, strengthening the possibility that the backscatter analysis indicates a primarily rough gravel surface sometimes covered with a lighter and smoother silty sand.

Table 14.2 **Summary of the Estimated Parameters for Type B Areas**

Top layer Interface 1 Area	*Scale Factor* B_{sf1}	*rms Height, m* h_1	*Exponent* n_1	*Correlation Length, m* L_1	*Sediment Depth, m* d_s
2	0.21	0.03	2.0	1.2	0.24
4	0.20	0.03	1.9	1.2	0.58
6	0.25	0.03	1.9	1.05	0.44
8	0.29	0.03	2.0	0.95	0.33
Avg	0.24	0.03	1.95	1.1	0.40
Bottom Layer Interface 2 Area	*Scale factor* B_{sf2}	*rms Height, m* h_2	*Exponent* n_2	*Correlation Length, m* L_2	
2	0.47	0.08	1.3	1.0	
4	0.45	0.1	1.4	1.0	
6	0.53	0.1	1.3	0.95	
8	0.44	0.08	1.2	1.1	
Avg	0.48	0.09	1.3	1.01	

(From Talukdar, K. K., R. C. Tyce, and C. S. Clay, "Interpretation of sea beam backscatter data collected at the Laurentian Fan off Nova Scotia using acoustic backscatter theory," *J. Acoust. Soc. Am.* **97**, 1545–58, 1995.)

The best fit procedures for type B areas involve nine parameters: B_{sf1}, h_1, n_1, and L_1 for the top layer; B_{sf2}, h_2, n_2, and L_2 for the bottom layer; and d_s, the sediment depth. The results of the analysis are the theoretical curves in Fig. 14.5.2. Considering the assumptions, the agreement between the data and the theory is good. The parameters are summarized in Table 14.2. The thickness of the assumed layer, estimated from regression analysis, varies from approximately 24 to 58 cm, which is too thin to show on conventional subbottom profilers.

It is evident that two distinct sets of parameters are present in Table 14.2. The subsurface layer has not only a higher rms roughness but a lower correlation length and exponent, indicating its coarse nature. Moreover, the parameters h, n, and L estimated for the subsurface are comparable to the parameters of Table 14.1 for the type A areas. The top-layer parameters of Table 14.2 exhibit lower rms height, higher correlation length, and exponents indicating a smoother surface. The spatial correlation function is nearly Gaussian. Although the material providing the rougher surface is more abundant on the sea floor, deposits on the order of tens of centimeters thick of a smoother material occur regularly. Since the channel floor mainly consists of coarse sands and gravels, the analysis indicates a scenario sketched in Fig. 14.5.4, where the scattering from the type A areas is only from the gravel water interface. At other places it is a combination of scattering from both the sediment-water and sediment-gravel interface. The validity of this hypothesis can only be tested by collecting cores and photographs from these areas.

14.6 An Analysis of the Backscattered Data in Two Areas: Spatial Spectra

The Wiener-Khinchine spectral transformations (Equations 6.4.8 and 13.1.23) were made on the average spatial correlation functions in Tables 14.1 and 14.2. The spectra are shown in Fig. 14.6.1. The spatial (power) spectrum for area A fits a power law, where $\mathcal{K}$ is reciprocal wavelength,

$$\Phi(\mathcal{K}) \approx [5.5 \times 10^{-5}]\, \mathcal{K}^{-2.25} \quad \text{for} \quad 0.2 < \mathcal{K} \tag{14.6.1}$$

over a wide range of spatial frequency (Fig. 14.6.1a). As shown in Fig. 14.6.1b, the top interface is approximately a Gaussian and does not fit a power law. The lower interface (Fig. 14.6.1c) appears to fit the power law

$$\Phi(\mathcal{K}) \approx [5 \times 10^{-5}]\, \mathcal{K}^{-2.36} \quad \text{for} \quad 0.4 < \mathcal{K} \tag{14.6.2}$$

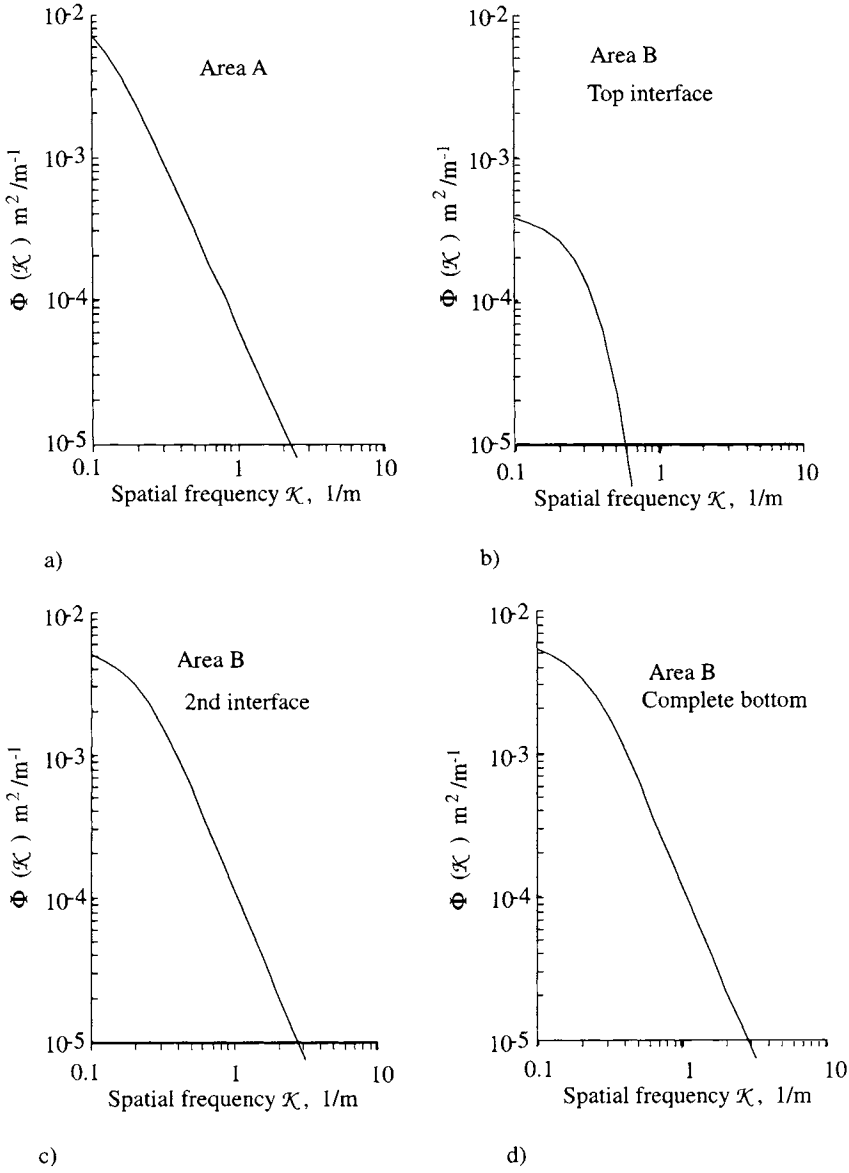

Figure 14.6.1 Spatial spectra of the areas A and B. These (power) spectra $\phi(\kappa)$ were computed by taking the cosine Fourier transformation of the spatial correlation functions. κ is the reciprocal wavelength or cycles per meter. (From Talukdar, K. K., R. C. Tyce, and C. S. Clay, "Interpretation of sea beam backscatter data collected at the Laurentian Fan off Nova Scotia using acoustic backscatter theory," *J. Acoust. Soc. Am.* **97**, 1545–58, 1995.)

Comparisons of the spectra for Fig. 14.6.1c and d show that the contribution from the top interface is buried in the spectra of the rougher lower interface. Malinverno (1989a, 1989b) describes tests of linear models of sea-floor topography and shows that a power spectrum of a random walk process varies as $\mathcal{K}^{-2}$. The exponents in Equations 14.6.1 and 14.6.2 are a little larger than 2, and these values are consistent with the spatial spectra of sea-floor topography.

References

See also the following section, Bibliography, for book references and books for supplementary study.

Note: Most of the references are to journals or books that are easily available. Other technical reports and theses may be obtained from the National Technical Information Service (NTIS), 5285 Port Royal Road, Springfield, VA 22161. Sales Desk (open 8:30 A.M. through 5:00 P.M. Eastern time, Monday through Friday): phone order, (703) 487-4650; or FAX (703) 487-4679.

Abegg, F.; A. Anderson; L. Buzi; A. P. Lyons; and T. H. Orsi, "Free methane concentration and bubble characteristics in Eckernfoerde Bay, Germany," *Proceedings of the Gassy Mud Workshop*, Kiel, Germany, 11–12 July 1994.

Abramowitz, M.; and I. A. Stegun, "Handbook of Mathematical Functions," *Natl. Bur. Stand.*, Applied Mathematical Series **55**. Government Printing Office; Washington, D.C. (1964).

Anderson, A. L.; and W. R. Bryant, "Gassy sediment occurrence and properties: Northern Gulf of Mexico," *Geo-Marine Letters* **10**, 209–20 (1990).

———, "Acoustic properties of shallow seafloor gas," *Offshore Technology Conference Proceedings* **5955** (1989).

Anderson, A. L.; and Loyd D. Hampton, "Acoustics of gas-bearing sediments I. Background," *J. Acoust. Soc. Am.* **67**, 1865–89 (1980a).

———, "Acoustics of gas-bearing sediments II. Measurements and Models," *J. Acoust. Soc. Am.* **67**, 1890–1903 (1980b).

Anderson, V. C., "Sound scattering from a fluid sphere," *J. Acoust. Soc. Am.* **22**, 426–431 (1950).

Andreeva, I. B., "Scattering of sound by air bladders of fish in deep sound scattering ocean layers," *Sov. Phys. Acoust.* **10**, 17–20 (1964).

Arnold, J. M.; and L. B. Felsen, "Intrinsic modes in a nonseparable ocean waveguide," *J. Acoust. Soc. Am.* **76**, 850–60 (1984).

Arnone, R. W.; R. W. Nero; J. M. Jech; I. De Palma, "Acoustic imaging of biological and physical processes within Gulf Stream meanders," *EOS* **71**, 982 (July 17, 1990).

Asaki, T. J.; and P. L. Marston, "Free decay of shape oscillations of bubbles acousticallly trapped in water and sea water," *J. Fluid Mech.* **300**, 149–67 (1995).

Au, W. W. L., *The Sonar of Dolphins*; Springer-Verlag, New York (1993).

Backus, M. M., "Water reverberations: Their nature and elimination," *Geophysics* **26**, 233–61 (1959).

Baker, B. B.; and E. T. Copson, *The Mathematical Theory of Huygens' Principle*, Oxford, 1950.

Baggeroer, A. B.; and W. A. Kuperman, "An overview of matched methods in ocean acoustics," *IEEE J. Ocean. Eng.* **18**, (4) 401–24 (1993).

Baggeroer, A. B.; W. A. Kuperman; and P. N. Mikhalevsky, "Matched field processing in ocean acoustics," in J. M. F. Moura and I. M. G. Lourtie (eds.), *Proceedings of the NATO Advanced Study Institute on Signal Processing for Ocean Exploration*. Kluwer, Dordrecht, Netherlands (1993).

Ball, E. C.; and J. A. Carlson, "Acoustic backscatter from a random rough water surface," M.S. thesis, Naval Postgraduate School, Monterey, Calif. (1967).

Barham, E. G., "Siphonophores and the deep scattering layer," *Science* **140**, 3568, 826–28 (1963).

Barnhouse, P. D. C.; M. J. Stoffel; and R. E. Zimdar, "Instrumentation to determine the presence and acoustic effect of microbubbles near the sea surface," M.S. Thesis, U.S. Naval Postgraduate School, Monterey, Calif. (1964).

Barraclough, W. E.; R. J. LeBrasseur; and O. D. Kennedy, "Shallow scattering layer in the subarctic Pacific Ocean: Detection by high-frequency echo sounder," *Science* **166**, 611–13 (1969).

Bary, B. McK.; and R. E. Peiper, "Sonic-scattering studies Saanich Inlet, British Columbia: A preliminary report," in *Proceedings of an International Symposium on Biological Sound Scattering in the Ocean*, G. B. Farquhar (ed.), pp. 601–11 (U.S. Government Printing Office, Washington, D.C., 1970).

Bass, A. H.; and R. Baker, "Sexual dimorphisms in the vocal control system of a teleost fish: Morphology of physiologically identified neurons," *J. Neurobiology* **21**, 1155–68 (1990).

Beckmann, P.; and A. Spizzichino, *The Scattering of Electromagnetic Waves from Rough Surfaces*; Macmillan; New York (1963).

Berkson, J. M.; and C. S. Clay, "Microphysiography and possible iceberg grooves on the floor of Western Lake Superior," *Geol. Soc. Bull.* **84**, 1315–28 (1973).

Berkson, J. M.; and J. E. Mathews, "Statistical properties of seafloor roughness," in *Acoustics of the Sea-Bed*, ed. N. G. Psace, Bath University Press; Bath, England, pp. 215–23 (1983).

Berktay, H. O., "Possible exploitation of non-linear acoustics in underwater transmitting applications," *J. Sound Vib.* **2**, 435–61 (1965).

Berktay, H. O.; and T. G. Muir, "Arrays of parametric receiving arrays," *J. Acoust. Soc. Am.* **53**, 1377–83 (1973).

Beyer, R. T., *Nonlinear Acoustics*, Naval Sea Systems Command, 1974; Government Printing Office; Washington, D.C., stock no. 0-596-215 (1975).

———, "Radiation pressure—the history of a mislabeled tensor," *J. Acoust. Soc. Am.* **63**, 1025–30 (1978).

Bies, D. A. J., "Attenuation in magnesium sulfate solutions," *Chem. Phys.* **23**, 428 (1955).

Biot, M. A.; and I. Tolstoy, "Formulation of wave propagation in infinite media by normal coordinates with an application to diffraction," *J. Acoust. Soc. Am.* **29**, 381–91 (1957).

Black, L. J., "Physical analysis of distortion produced by the nonlinearity of the medium," *J. Acoust. Soc. Am.* **12**, 266–67 (1940).

Blanchard, D. C.; and A. H. Woodcock, "Bubble formation and modification in the sea and its meteorological significance," *Tellus* **9**, 145–58 (1957).

Born, M.; and E. Wolf, *Principles of Optics*; Pergamon Press; Oxford (1965).

Bowles, F. A., "Observations on attenuation and shear-wave velocity in fine-grained, marine sediments," *J. Acoust. Soc. Am.* **101**, 3385–97 (1997).

Brandt, S. B., "Acoustic determination of fish abundance and distribution in Lake Michigan with special reference to temperature," M.S. thesis, University of Wisconsin (1975).

———, "Application of knowledge-based systems to fisheries management and acoustic abundance measures," in J. Palmer, ed., *NOAA Workshop on Knowledge-Based Systems and Marine Sciences*, Fairfax, Va., VSG 89-03, May 21–29, p. 93–117 (1989).

Brantley, R. K.; and A. H. Bass, "Alternative male spawning tactics and acoustic signals in the plainfin midshipman fish *Porichthys notatus* Girard (Teleostei, Batrachoididae)," *Ecology* **96**, 213–32 (1994).

Breitz, N. D.; and H. Medwin, "Instrumentation for *in-situ* acoustical measurements of bubble spectra under breaking waves," *J. Acoust. Soc. Am.* **86**, 739–43 (1989).

Brekhovskikh, L. M., *Waves in Layered Media*; Academic Press; New York (1980).

Bremhorst, J. H., "Impulse wave diffraction by rigid wedges and plates," M.S. thesis, Naval Postgraduate School, Monterey, Calif., (December 1978). See also abstract, same title, Bremshorst, J. H. and H. Medwin, *J. Acoust. Soc. Am.* **64**, S1, S64 (A) (1978).

Bridal, L. S.; K. D. Wallace; R. L. Trousil; S. A. Wickline; and J. G. Miller, "Frequency dependence of acoustic backscatter from 5 to 65 MHz of polystyrene beads in agarose," *J. Acoust. Soc. Am.* **100**, 1841–48 (1996).

Brillouin, L., "The scattering cross section of spheres for electromagnetic waves," *J. Applied Physics* **20**, 1110–25 (1949).

Brown, D. A., "Flextensional hydrophone," *J. Acoust. Soc. Am.* **96**, 3208 (1994).

Browne, M. J., "Underwater acoustic backscatter from a model of arctic ice open leads and pressure ridges," M.S. thesis, Naval Postgraduate School, Monterey, Calif., (Jun 1987).

Bucker, H. P., "Use of calculated sound fields and matched-field detection to locate sound sources in shallow water," *J. Acoust. Soc. Am.* **59**, 368–73 (1976).

Buckingham, M. J., "Theory of three-dimensional acoustic propagation in a wedgelike ocean with a penetrable bottom," *J. Acoust. Soc. Am.* **82**, 198–210 (1987).

Buckingham, M. J.; and A. Tolstoy, "An analytical solution for benchmark problem 1: The 'ideal' wedge," *J. Acoust. Soc. Am.* **87**, 1511–13 (1990). Wedge benchmark paper.

Buckingham, M. J.; B. V. Berkhout; and S. A. L. Glegg, "Imaging the ocean with ambient noise," *Nature* **356**, 327–29 (1992).

Buckingham, M. J.; and J. R. Potter, "Acoustic daylight imaging: vision in the ocean," *GSA Today* **4**, 99–102 (1994).

Busnel, R.-G.; and J. F. Fish, *Animal Sonar Systems*; Plenum Press; New York (1980).

Buxcey, S.; J. E. McNeil; and R. H. Marks, Jr., "Acoustic detection of microbubbles and particulate matter near the sea surface," M.S. thesis, Naval Postgraduate School, Monterey, Calif. (1965).

Carey, W. M.; and M. P. Bradley, "Low-frequency ocean surface noise sources," *J. Acoust. Soc. Am.* **78**(S1), S1–2(A) (1985).

Carstensen, E. L. "Self-reciprocity calibration of electroacoustic transducers," *J. Acoust. Soc. Am.* **19**, 702(L) (1947).

Cartmill, J. W.; and M.-Y. Su, "Bubble size distribution under saltwater and freshwater breaking waves," *Dynamics of Atmospheres and Oceans* **20**, 25–31 (1993).

Cerveny, V.; and R. Ravindra, *Theory of Seismic Head Waves*; University of Toronto Press; Toronto (1971).

Chambers, J. B.; and Y. H. Berthelot, "Time domain experiments on the diffraction of sound by a step discontinuity," *J. Acoust. Soc. Am.* **96**, 1887–92 (1994).

Chamuel, J. R.; and G. H. Brooke, "Transient Scholte wave transmission along rough liquid-solid interfaces," *J. Acoust. Soc. Am.* **83**, 1336–44 (1988a).

———, "Transient Rayleigh wave transmission along periodic and random grooved surfaces," *J. Acoust. Soc. Am.* **84**, 1363–72 (1988b).

———, "Shallow-water acoustic studies using an air-suspended water waveguide model," *J. Acoust. Soc. Am.* **84**, 1777–86 (1988c).

Chapman, N. R.; and G. R. Ebbeson, "Acoustic shadowing by an isolated seamount," *J. Acoust. Soc. Am.* **73**, 1979–84 (1983).

Chapman, N. R., "Source levels of shallow explosive charges," *J. Acoust. Soc. Am.* **84**, 697–702 (1988).

———, "Measurement of the waveform parameters of shallow explosive charges," *J. Acoust. Soc. Am.* **78**, 672–81 (1995).

Chiu, C.-S.; J. Lynch; and O. M. Johannessen, "Tomographic resolution of mesoscale eddies in the marginal ice zone: a preliminary study," *J. Geophys. Res.* **92**, C7, 6886–6902 (1987).

Chiu, C.-S.; J. H. Miller; W. W. Denner; and J. F. Lynch, "Forward modeling of the Barents Sea tomography: Vertical line array data and inversion highlights," in *Full-Field Inversion Methods in Ocean and Seismic Acoustics*, O. Diachok, A. Caiti, P. Gerstoft and H. Schmidt (eds.), Kluwer Academic Publishers, Dordrecht, Netherlands 237–42 (1995).

Chu, D., "Impulse response of density contrast wedge," Ph.D. thesis, University of Wisconsin, Madison (1989a).

———, "Impulse response of density contrast wedge using normal coordinates," *J. Acoust. Soc. Am.* **86**, 1883–96 (1989b).

———, "Exact solution for a density contrast shallow-water wedge using normal coordinates," *J. Acoust. Soc. Am.* **87**, 2442–50 (1990).

Chu, D.; T. K. Stanton; and P. H. Wiebe, "Frequency dependence of backscattering from live individual zooplankton," *ICES J. Mar. Sci.* **49**, 97–106 (1992).

Clark, C. W., "Application of US Navy underwater hydrophone arrays for scientific research on whales," *Rept. Int. Whal. Commission* **45**, 210–12 (1995).

Clay, C. S.; and H. Medwin, "High-frequency acoustical reverberation from a rough sea surface," *J. Acoust. Soc. Am.* **36**, 2131–34 (1964a).

Clay, C. S.; J. Ess; and I. Weisman, "Lateral echo sounding of the ocean bottom on the continental rise," *J. Geophys. Res.* **69**, 3823–35 (1964b).

Clay, C. S., "Effect of a slightly irregular boundary on the coherence of waveguide propagation," *J. Acoust. Soc. Am.* **36**, 833–37 (1964c).

Clay, C. S.; and P. A. Rona, "Studies of seismic reflections from thin layers on the ocean bottom in the Western Atlantic," *J. Geophys. Res.* **70**, 855–69 (1965).

Clay, C. S., "Use of arrays for acoustic transmission in a noisy ocean," *Rev. Geophys.* **4**, 475–507 (1966a).

———, "Coherent reflection of sound from the sea bottom," *J. Geophys. Res.* **71**, 2037–45 (1966b).

———, "Possible inertial period time dependence of signal transmission in the ocean," *J. Acoust. Soc. Am.* **41**, 524–25 (1967).

Clay, C. S.; and H. Medwin, "Dependence of spatial and temporal correlation of forward scattered underwater sound on the surface statistics: part I—theory," *J. Acoust. Soc. Am.* **47**, 1412–18 (1970). See also Medwin and Clay, part II experiment (1970).

Clay, C. S.; and G. A. Sandness, "Effect of beam width on acoustic signals scattered at a rough surface," Advisory Group for Aerospace Research and Development, *North Atlantic Treaty Organization Conference Proceedings* 21(90), 1–8 (1971).

Clay, C. S.; H. Medwin; and W. M. Wright, "Specularly scattered sound and the probability density function of a rough surface," *J. Acoust. Soc. Am.* **53**, 1677–82 (1973).

Clay, C. S.; and W. Leong, "Acoustic estimates of the topography and roughness spectrum of the seafloor southeast of the Iberian Peninsula," in *Physics of Sound in Marine Sediments*, ed. by L. Hampton; Plenum; New York, pp. 373–446 (1974).

Clay, C. S.; and H. Medwin, *Acoustical Oceanography*; John Wiley; New York (1977a).

Clay, C. S., "Deconvolution of the fish scattering PDF from the echo PDF for a single transducer sonar," *J. Acoust. Soc. Am.* **73**, 1989–94 (1983).

Clay, C. S.; and B. G. Heist, "Acoustic scattering by fish acoustic models and a two-parameter fit," *J. Acoust. Soc. Am.* **75**, 1077–83 (1984).

Clay, C. S.; Y. Y. Wang; and E. C. Shang, "Sound field fluctuations in a shallow water waveguide," *J. Acoust. Soc. Am.* **77**, 424–28 (1985).

Clay, C. S.; and W. A. Kinney, "Numerical computations of time-domain diffractions from wedges and reflections from facets," *J. Acoust. Soc. Am.* **83**, 2126–33 (1988).

Clay, C. S., "Optimum time domain signal transmission and source location in a waveguide," *J. Acoust. Soc. Am.* **81**, 660–64 (1987).

Clay, C. S.; and S. Li, "Time domain signal transmission and source location in a waveguide: Matched filter and deconvolution experiments," *J. Acoust. Soc. Am.* **83**, 1377–83 (1988).

Clay, C. S., "Low-resolution acoustic scattering models: Fluid-filled cylinders and fish with swimbladders," *J. Acoust. Soc. Am.* **89**, 2168–79 (1991).

Clay, C. S., "Composite ray-mode approximations for backscattered sound from gas-filled cylinders and swimbladders," *J. Acoust. Soc. Am.* **92**, 2173–80 (1992).

Clay, C. S.; D. Chu; and C. Li, "Specular reflection of transient pressures from finite width plane facet," *J. Acoust. Soc. Am.* **94**, 2279–86 (1993).

Clay, C. S.; and J. K. Horne, "Acoustic models of fish: the Atlantic cod (Gadus morhua)," *J. Acoust. Soc. Am.* **96**, 1661–68 (1994).

———, "Analysis of rather high-frequency sound echoes from ensembles of fish," *J. Acoust. Soc. Am.* **98**, 2881 (1995).

Cole, Robert H., *Underwater Explosions*; Princeton University Press; Princeton, N.J. (1948).

Colladon, J. D.; and J. K. F. Sturm, "The Compression of Liquids" (in French), *Ann. Chim. Phys.* Series **2**(36), part IV, "Speed of Sound in Liquids," 236–57 (1827).

Collins, M. D., "Benchmark calculations for higher-order parabolic equations," *J. Acoust. Soc. Am.* **87**, 1535–38 (1990). Wedge benchmark paper.

Commander, K.; and E. Moritz, "Off-resonance contributions to acoustical bubble spectra," *J. Acoust. Soc. Am.* **85**, 2665–69 (1989).

Commander, K.; and R. J. McDonald, "Finite-element solution of the inverse problem in bubble swarm acoustics," *J. Acoust. Soc. Am.* **89**, 592–97 (1991).

Cote, L. J., et al., "The directional spectrum of a wind generated sea as determined from data obtained by the Stereo Wave Observation Project, *Meteorol. Papers* (N.Y.U., Coll. of Eng.) **2**(6) (1960).

Cox, C. S.; and W. Munk, "Statistics of the sea surface derived from sun glitter," *J. Marine Res.* **13**, 198–227 (1954).

Cornuelle, B. D., et al., "Tomographic maps of the ocean mesoscale," *J. Phys. Oceanogr.* **15**, 133–52 (1985).

Craig, R. E.; and S. T. Forbes, "Design of a sonar for fish counting," *Fisk. Dir. Ser. Vav. Unders.* **15**, 210–19 (1969).

Crowther, P., "Bubble noise creation mechanisms," in *Sea Surface Sound*; Kluwer; Dordrecht, Netherlands, pp. 131–50 (1988).

Cummings, W. C.; and D. V. Holliday, "Sounds and source levels from bowhead whales off Pt. Barrow, Alaska," *J. Acoust. Soc. Am.* **82**, 814–21 (1987).

Daneshvar, M. R.; and C. S. Clay, "Imaging of rough surfaces for impulsive and continuously radiating sources," *J. Acoust. Soc. Am.* **82**, 360–69 (1987).

Daniel, A. C., Jr., "Bubble production by breaking waves," M.S. thesis, Naval Postgraduate School, Monterey, CA (1989).

Davis, A. M. J.; and R. W. Scharstein, "The complete extension of the Biot-Tolstoy solution to the density contrast wedge," *J. Acoust. Soc. Am.* **101**, 1821–35 (1997).

Del Grosso, V. A., "New equation for the speed of sound in natural waters (with comparisons to other equations)," *J. Acoust. Soc. Am.* **56**, 1084–91 (1974).

de Moustier, C., "Beyond bathymetry: mapping acoustic backscattering from the deep seafloor with Sea Beam," *J. Acoust. Soc. Am.* **79**, 316–31 (1986).

———, "State-of-the-art in swath bathymetry survey systems," *Inter. Hydro. Rev.* **65**, 25–54 (1988).

de Moustier, C.; and D. Alexandrou, "Angular dependence of 12 kHz seafloor acoustic backscatter," *J. Acoust. Soc. Am.* **90**, 522–31 (1991).

Denny, P. L.; and K. R. Johnson, "Underwater acoustic scatter from a model of the Arctic ice canopy," M.S. thesis, Naval Postgraduate School, Monterey, CA (1986).

DeSanto, J. A.; and O. Shisha, "Numerical solution of a singular integral equation in random rough surface scattering theory," *J. Comput. Phys.* **15**, 286–92 (1974).

DeSanto, J. A., "Relations between solutions of the Helmholtz and parabolic equation for sound propagation," *J. Acoust. Soc. Am.* **62**, 295–97 (1977).

Detrick, R. S., "Introduction to the seafloor mapping section," *J. Geophys Res.* **91**(B3), 3331–3520 (1984). The sequence of papers demonstrate the methods and applications of Sea Beam and deep-tow technologies.

Devin, Charles, Jr., "Survey of thermal, radiation and viscous damping of pulsating air bubbles in water," *J. Acoust. Soc. Am.* **31**, 1654–67 (1959).

Do, M. A.; and A. M. Surti, "Estimation of dorsal aspect target strength of deep-water fish using a simple model of swimbladder back scattering," *J. Acoust. Soc. Am.* **87**, 1588–96 (1990).

Ebbeson, G. R.; and R. G. Turner, "Sound propagation over Dickins Seamount," *J. Acoust. Soc. Am.* **73**, 143–52 (1983).

Eby, R. K.; A. O. Williams; R. P. Ryan; and P. Tarmarkin, "Study of acoustic propagation in a two-layered model," *J. Acoust. Soc. Am.* **32**, 88–99 (1960). Refers to an unpublished Technical Report 56-1 of the Research Analysis Group, Brown University (May 1956) in which the "adiabatic" approximation is postulated.

Eckart, C., "Vortices and streams caused by sound waves," *Phys. Rev.* **73**, 68–76 (1948).

———, "The scattering of sound from the sea surface," *J. Acoust. Soc. Am.* **25**, 566–70 (1953).

———, ed., *Principles and Applications of Underwater Sound*, Department of the Navy, NAVMAT P-9674; Government Printing Office; Washington, D.C. (1968).

Ehrenberg, J. E., "A method for extracting target strength distribution from acoustic echoes," in *Proc. IEEE Inter. Conf. on Engineering in the Ocean Envr.*, vol. 1; IEEE; New York, pp. 61–64 (1972).

———, The dual-beam system: a technique for making in situ measurements of the target strengths of fish. *Oceans '74: Proc. IEEE Inter. Conf. on Engineering in the Ocean Envr.*; IEEE; New York, pp. 152–55 (1974).

Elder, S. A., "Cavitation microstreaming," *J. Acoust. Soc. Am.* **31**, 54–64 (1959).

Eller, A. I., "Damping constants of pulsating bubbles," *J. Acoust. Soc. Am.* **47**, 1469–70 (1970).

Ewing, M.; and J. L. Worzel, "Long-range sound transmission," in *Propagation of Sound in the Ocean*, Memoir 27; Geological Society of America; New York, Fig. 5, p. 19 (1948).

Ewing, W. M.; W. S. Jardetzky; and F. Press, *Elastic Waves in Layered Media*; McGraw-Hill; New York (1962).

Faran, J. J., "Sound scattering by solid cylinders and spheres," *J. Acoust. Soc. Am.* **23**, 405–18 (1951).

Farmer, D.; and S. Vagle, "Waveguide propagation of ambient sound in the ocean surface bubble layer," *J. Acoust. Soc. Am.* **86**, 1897–1908 (1989).

Farquhar, G. Brooke, ed., *Proceedings of an International Symposium on Biological Sound Scattering in the Ocean*, Maury Center for Ocean Science, Department of the Navy, Washington, D.C.; Government Printing Office; Washington, D.C., stock no. 0851-0053 (1970).

Felsen, L. B., "Benchmarks: An option for quality assessment," *J. Acoust. Soc. Am.* **87**, 1497–98 (1990).

Feuillade, C.; D. R. Del Balzo; and W. A. Kinney, "Shallow-water matched-field localization," *J. Acoust. Soc. Am.* **88**, 423–33 (1990).

Feuillade, C.; and C. S. Clay, "Source imaging and sidelobe suppression using time-domain techniques in a shallow water waveguide," *J. Acoust. Soc. Am.* **92**, 2165–72 (1992).

Feuillade, C.; and M. Werby, "Resonances of deformed gas bubbles in liquids," *J. Acoust. Soc. Am.* **96**, 3684–92 (1994).

Feuillade, C., "Scattering from collective modes of air bubbles in water and the physical mechanism of superresonances," *J. Acoust. Soc. Am.* **98**, 1178–90 (1995).

———, "The collective acoustic properties of water containing resonating air bubbles, and its effect on the propagation of sound," *J. Acoust. Soc. Am.* **98**, 2937 (A) (1995b).

Feuillade, C.; and R. W. Nero, "Viscous and elastic swimbladder models for acoustical scattering from fish," **100**, 2806 (A) (1996).

Feuillade, C.; and R. W. Nero, "A viscous-elastic swimbladder model for describing enhanced-frequency resonance scattering from fish," *J. Acoust. Soc. Am.* **101**, in press (1997).

Fisher, F. H.; and S. A. Levison, "Dependence of the low frequency (1 kHz) relaxation in seawater on boron concentration," *J. Acoust. Soc. Am.* **54**, 291 (1973).

Fisher, F. H.; and V. P. Simmons, "Sound absorption in sea water," *J. Acoust. Soc. Am.* **62**, 558–64 (1977).

Fizell, R. G., "Application of high-resolution processing to range and depth estimation using ambiguity function methods," *J. Acoust. Soc. Am.* **82**, 606–13 (1987).

Flatte, S. M.; and R. B. Stoughton, "Theory of acoustic measurement of internal wave strength as a function of depth, horizontal position and time," *J. Geophys. Res.* **91** (C6), 7709–20 (1986).

Flynn, H. G., "Physics of acoustic cavitation in liquids," in W. P. Mason, ed., *Physical Acoustics,* vol. 1, part B; Academic Press; New York, pp. 57–172 (1964).

Foote, K. G., "Linearity of fisheries acoustics, with addition theorems," *J. Acoust. Soc. Am.* **73**, 1932–40 (1983).

———, "Rather-high-frequency sound scattered by swimbladdered fish," *J. Acoust. Soc. Am.* **78**, 688–700 (1985).

———, "Fish target strengths for use in echo integrator surveys," *J. Acoust. Soc. Am.* **82**, 981–87 (1987).

Foote, K. G.; and J. J. Traynor, "Comparison of walleye pollock target strength estimates determined from in situ measurements and calculations based on swimbladder form," *J. Acoust. Soc. Am.* **83**, 9–17 (1988).

Foote, K. G., "Speed of sound in *Euphausia superba*," *J. Acoust. Soc. Am.* **87**, 1404–8 (1990).

Forbes, S. T.; and O. Nakken, eds., *Manual of Methods for Fisheries Resource Survey and Appraisal*, part 2. *The Use of Acoustic Instruments for Fish Detection and Abundance Estimation*, Food and Agricultural Organization of the United Nations; FAO Manuals in Fisheries Science No. 5; Rome (1972).

Foreman, T. L., "An exact ray theoretical formulation of the Helmholtz equation," *J. Acoust. Soc. Am.* **86**, 234–46 (1989).

Fortuin, L., "Survey of literature on reflection and scattering of sound waves at the sea surface," *J. Acoust. Soc. Am.* **47**, 1209–28 (1970).

Fortuin, L.; and J. G. de Boer, "Spatial and temporal correlation of the sea surface," *J. Acoust. Soc. Am.* **49**, 1677(L) (1971).

Fox, F. E.; and K. F. Herzfeld, "On the forces producing the ultrasonic wind," *Phys. Rev.* **78**, 156–57 (1950).

———, "Gas bubbles with organic skin as cavitation nuclei," *J. Acoust. Soc. Am.* **26**, 984–89 (1954).

Fox, C. G.; and D. E. Hayes, "Quantitaive methods for analyzing the roughness of the seafloor," *Rev. Geophys. and Space Physics* **23**, 1–48 (1985).

François, R. E.; and G. R. Garrison, "Sound absorption based on ocean measurements. Part I: pure water and magnesium sulfate contributions," *J. Acoust. Soc. Am.* **72**, 896–907 (1982a).

———, "Sound absorption based on ocean measurements. Part II: boric acid contribution and equation for total absorption," *J. Acoust. Soc. Am.* **72**, 1879–90 (1982b).

Friedlander, F. G., "Simple progressive solutions of the wave equation," *Cambridge Philosophical Society* **42**, 360–73 (1946).

Frisk, G. V.; J. F. Lynch; and S. D. Rajan, "Determination of compressional wave speed profiles using modal inverse techniques in a range-dependent environment in Nantucket Sound," *J. Acoust. Soc. Am.* **86**, 1928–39 (1989).

Furusawa, M., "Prolate spheriodal models for predicting general trends of fish target strength," *J. Acoust. Soc. Japan* **9**, 13–24 (1988).

———, "Designing quantitative echo sounders," *J. Acoust. Soc. Am.* **90**, 26–36 (1991).

Gabor, D., "Theory of communications, Part 3," *J. Inst. Elect. Engrs.* **93**, 429–41 (1946).

Gagnon, G. J.; and C. W. Clark, "The use of US Navy IUSS passive sonar to monitor the movement of blue whales," Tenth Biennial Conference on the Biology of Marine Mammals; Galveston, Texas, Abstract, p. 50 (1993).

Gaunaurd, G. C., "Sonar cross sections of bodies partially insonified by finite sound beams," *IEEE J. Ocean Eng.*, **OE-10**, 213–30 (1986).

Gazanhes, C.; and J. L. Garnier, "Experiments on single mode excitation in shallow water propagation," *J. Acoust. Soc. Am.* **69**, 963–69 (1981).

Glotov, V. P., et al., "Investigation of the scattering of sound by bubbles generated by an artificial wind in seawater and the statistical distribution of bubble sizes," *Sov. Phys.—Acoust.* **7**, 341–45 (1962).

Goff, J. A.; and T. H. Jordon, "Stochastic modeling of seafloor morphology and inversion of sea beam data for second-order statistics," *J. Geophys. Res.* **93**, 13589–606 (1988).

Gray, L. M.; and D. S. Greeley, "Source level model for propellor blade rate radiation for the world's merchant fleet," *J. Acoust. Soc. Am.* **67**, 516–22 (1980).

Greenlaw, C. F., "Acoustical estimation of zooplankton populations," *Limnol. Oceanogr.* **24**, 226–42 (1979).

Greenlaw, C. F.; and R. K. Johnson, "Physical and acoustical properties of zooplankton," *J. Acoust. Soc. Am.* **72**, 1706–10 (1982).

Guthrie, A. N.; R. M. Fitzgerald; D. A. Nutile; and J. D. Shaffer, "Long-range low-frequency CW propagation in the deep ocean: Antigua–Newfoundland," *J. Acoust. Soc. Am.* **56**, 58–69 (1974).

Hagy, J. D., Jr., "Transmission of sound through a randomly rough air-sea interface," M.S. thesis, Naval Postgraduate School, Monterey, Calif. (1970).

Hall, M. V., "A comprehensive model of wind-generated bubbles in the ocean and predictions of the effects on sound propagation at frequencies up to 40 kHz," *J. Acoust. Soc. Am.* **86**, 1103–17 (1989).

Hamilton, E. L., "Sediment sound velocity measurements made *in situ* from the bathyscaphe *Trieste*," *J. Geophys. Res.* **68**, 5991–98 (1963).

———, *Sound Velocity, Elasticity, and Related Properties of Marine Sediments, North Pacific*; Naval Undersea Research and Development Center; San Diego, Calif., Technical Publication 143 (1969).

———, *Sound Velocity, Elasticity, and Related Properties of Marine Sediments, North Pacific*; Naval Undersea Research and Development Center; San Diego, Calif., Technical Publication 144 (1969). Also *J. Geophys. Res.* **75**, 4423–46 (1970).

———, "The elastic properties of marine sediments," *J. Geophys. Res.* **76**, 579–604 (1971a).

———, "Prediction of *in-situ* acoustic and elastic properties of marine sediments," *Geophysics* **36**, 266–84 (1971b).

———, "Compressional wave attenuation in marine sediments," *Geophysics* **37**, 620–46 (1972).

———, ed., *Physics of Sound in Marine Sediments*; Plenum Press; New York (1974).

———, "Sound velocity as a function of depth in marine sediments," *J. Acoust. Soc. Am.* **78**, 1384–55 (1985).

Hamilton, M. F., "Fundamentals and applications of nonlinear acoustics," in T. W. Wright, ed., Nonlinear Wave Propagation in Mechanics, AMD vol. 77, pp. 1–28 (1986).

Hardin, R. H.; and F. D. Tappert, "Applications of the split-step Fourier method to the numerical solution of nonlinear and variable coefficient wave equation," *SIAM Review* **16**, 243–60 (1973).

Haslett, R. W. G., "Determination of the acoustic scatter patterns and cross sections of fish models and ellipsoids," *Brit. J. Appl. Phys.* **13**, 611–20 (1962).

Helbig, R. A., "The effects of ocean surface roughness on the transmission of sound from an airborne source," M.S. thesis, Naval Postgraduate School, Monterey, Calif. (1970).

Hersey, J. B.; and R. H. Backus, "Sound scattering by marine organisms," in M. N. Hill, ed., *The Sea*, vol. 1; John Wiley & Sons; New York, pp. 499–507 (1962).

Hickling, R., "Frequency dependence of echoes from bodies of different shapes," *J. Acoust. Soc. Am.* **30**, 137–39 (1958).

Hill, M. N., ed., *The Sea*, vol. 3; Wiley-Interscience; New York (1963).

Hinich, M. J., "Maximum likelihood signal processing for a vertical array," *J. Acoust. Soc. Am.* **54**, 499–503 (1973).

Holliday, D. V., "Resonance structure in echoes from schooled pelagic fish," *J. Acoust. Soc. Am.* **51**, 1322–32 (1972).

Holliday, D. V.; and R. E. Pieper, "Volume scattering strengths and zooplankton distributions at acoustic frequencies between 0.5 and 3 MHz," *J. Acoust. Soc. Am.* **67**, 135–46 (1980).

Holliday, D. V.; R. E. Pieper; and G. S. Klepple, "Determination of zooplankton size and distribution with multifrequency acoustic technology," *J. Cons. Int. Explor. Mer.* **46**, 52–61 (1989).

———, "Bioacoustical oceanography at high frequencies," *ICES J. Mar. Sci.* **52**, 279–96 (1995).

Horton, C. W., Sr.; and D. R. Melton, "Importance of the Fresnel correction in scattering from a rough surface, II. Scattering coefficient," *J. Acoust. Soc. Am.* **47**, 299–303 (1970). See also Melton and Horton for part 1.

Howe, B. M.; P. F. Worcester; and R. C. Spindel, "Ocean acoustic tomography: mesoscale velocity," *J. Geophys. Res.* **92** (C4), 3785–3805 (1987).

Huang, K.; and C. S. Clay, "Backscatter cross section of live fish: PDF and aspect," *J. Acoust. Soc. Am.* **67**, 795–802 (1980).

Huffman, T. B.; and D. L. Zveare, "Sound speed dispersion, attenuation and inferred microbubbles in the upper ocean," M.S. thesis, Naval Postgraduate School, Monterey, Calif. (1974).

Hutton, G. D., "The perfectly reflecting wedge used as a control in seismic diffraction modelling," *Geophysical Prospecting* **35**, 681 (1987).

Isakovich, M. A., "The scattering of waves from a statistically rough surface," (in Russian). *Zhurn. Eksp. Teor. Fiz.* **23**, 305–14 (1952).

Jackson, D. R.; D. P. Winebrenner; and A. Ishimaru, "Application of the composite roughness model to high-frequency backscattering," *J. Acoust. Soc. Am.* **79**, 1410–22 (1986).

Jacobson, P. T.; C. S. Clay; and J. J. Magnuson, "Size, distribution, and abundance of pelagic fish by deconvolution of single beam acoustic data," *J. Cons. Int. Explor. Mer.* **189**, 404–11 (1990).

Jacobus, R. W., "Underwater sound radiation from large raindrops," M.S. thesis, Naval Postgraduate School, Monterey, Calif. (1991).

Jebsen, G. M., "Acoustic diffraction by a finite barrier: theories and experiment," M.S. thesis, Naval Postgraduate School, Monterey, Calif. (1981).

Jebsen, G. M., and H. Medwin, "On the failure of the Kirchhoff assumption in backscatter," *J. Acoust. Soc. Am.* **72**, 1607–11 (1982).

Jensen, F. B.; and C. M. Ferla, "Numerical solutions of range-dependent benchmark problems in ocean acoustics," *J. Acoust. Soc. Am.* **87**, 1499–1510 (1990). Wedge benchmark paper.

Johnson, B. D.; and R. C. Cook, "Bubble populations and spectra in coastal water: a photographic approach," *J. Geophys. Res.* **84**, 3761–66 (1979).

Johnson, R. K., "Sound scattering from a fluid sphere revisited," *J. Acoust. Soc. Am.* **61**, 375–77 (1977) and erratum ibid 63, 626 (E) (1978).

Jordan, E. A. "Acoustic boundary wave generation and shadowing at a seamount," M.S. thesis, Naval Postgraduate School, Monterey, Calif. (1981).

Jech, J. M.; D. M. Schael; and C. S. Clay, "Application of three sound scattering models to threadfin shad (*Dorosoma petenense*)," *J. Acoust. Soc. Am.* **98**, 2262–69 (1995).

Jesus, S. M., "Broadband matched-field processing of transient signals in shallow water," *J. Acoust. Soc. Am.* **93**, 1841–50 (1993).

Jovicevic, S.; and S. Sesnic, "Diffraction of a parallel and perpendicular polarized wave from an echelette grating," *J. Opt. Soc. Am.* **62**, 865–77 (1972).

Kaczkowski, P. J.; and E. I. Thorsos, "Application of the operator expansion method to scattering from one-dimensional, moderately rough Dirichlet random surfaces," *J. Acoust. Soc. Am.* **96**, 957–72 (1994).

Kasputis, S.; and P. Hill, "Measurement of mode interaction due to waveguide surface roughness," M.S. thesis, Naval Postgraduate School, Monterey, CA (December 1984).

Keiffer, R. S.; and J. C. Novarini, "A wedge assemblage method for 3-D acoustic scattering from sea surfaces: comparison with a Helmholtz-Kirchhoff method," in *Computational Acoustics,* vol. 1, ed. D. Lee, A. Cakmak, and R. Vichnevetsky; Elsevier North Holland; Amsterdam, 67–81 (1990).

Keiffer, R. S., J. C. Novarini; and G. V. Norton, "The impulse response of an aperture: numerical calculations within the framework of the wedge assemblage method," *J. Acoust. Soc. Am.* **95**, 3–12 (1994).

Keiffer, R. S.; and J. C. Novarini, "A versatile time domain model for acoustic scattering from 2-D ocean surfaces," *J. Acoust. Soc. Am.* (In preparation; 1997).

Kibblewhite, A. C., "Attenuation of sound in marine sediments: A review with emphasis on new low-frequency data," *J. Acoust. Soc. Am.* **86**, 716–38 (1989).

Kibblewhite, A. C.; and C. Y. Wu, "The theoretical description of wave-wave interactions as a noise source in the ocean," *J. Acoust. Soc. Am.* **89**, 2241–52 (1991).

Kinney, W. A.; C. S. Clay; and G. A. Sandness, "Scattering from a corrugated surface: comparison between experiment, Helmholtz-Kirchhoff theory, and the facet-ensemble method," *J. Acoust. Soc. Am.* **73**, 183–94 (1983).

Kinney, W. A.; and C. S. Clay, "Insufficiency of surface spatial power spectrum for estimating scattering strength and coherence—numerical studies," *J. Acoust. Soc. Am.* **78**, 1777–84 (1985).

Kinsman, B. "Surface waves at short fetches and low wind speeds: a field study," *Chesapeake Bay Inst. Tech. Rep. 129*, Johns Hopkins (1960).

———, *Wind Waves*; Prentice-Hall; Englewood Cliffs, N.J. (1965).

Knudsen, V. O.; R. S. Alford; and J. W. Emliing, "Underwater ambient noise," *J. Marine Res.* **7**, 410–29 (1948).

Kuperman, W. A., "Coherent component of specular reflection and transmission at a randomly rough, two-fluid interface," *J. Acoust. Soc. Am.* **58**, 365–70 (1975).

Kurgan, A., "Underwater sound radiated by impacts and bubbles created by raindrops," M.S. thesis, Naval Postgraduate School, Monterey, CA (1989).

LaFond, E. C.; and J. Dill, "Do invisible microbubbles exist in the sea?" Navy Electronics Lab., San Diego, CA (1957).

Lamarre, E.; and W. K. Melville, "Sound speed measurements near the sea surface," *J. Acoust. Soc. Am.* **95**, 1317–28 (1994).

Latham, M. W., "Side looking fish finder," U.S. Patent Number 5,260,912, November 9, 1993.

Lebedeva, L. P., "Measurement of the dynamic complex shear modulus of animal tissues," *Sov. Phys.-Acoust.* **11**, 163–65 (1965).

Lee, D., "The state-of-the-art parabolic equation approximation as applied to underwater acoustic propagation with discussions on intensive computations," *J. Acoust. Soc. Am.* **76**, (S1), S9(A) (1984).

Leonard, R. W., "The attenuation of ultrasonic waves in water," *J. Acoust. Soc. Am.* **20**, 224 (Abstract) (1948).

Leonard, R. W.; P. C. Combs; and L. R. Skidmore, "Attenuation of sound in sea water," *J. Acoust. Soc. Am.* **21**, 63 (1949).

Leong, W. L., "Use of acoustic scattering theory to interpret marine geophysical data," Ph.D. dissertation, University of Wisconsin, Madison (1973).

Leroy, C. C., "Sound propagation in the Mediterranean Sea," in *Underwater Acoustics, Vol. 2*, 203–41, V. M. Albers (Ed.) Plenum Press, New York (1967).

Levin, F. K., "The seismic properties of Lake Maracaibo," *Geophysics* **27**, 35–47 (1962).

Lhermitte, R. "Doppler sonar observations of tidal flow," *J. Geophys. Res.* **88**, 725–42 (1983).

Li, S.; and C. S. Clay, "Optimum time domain signal transmission and source location in a waveguide: Experiments in an ideal wedge waveguide," *J. Acoust. Soc. Am.* **82**, 1409–17 (1987).

Li, S.; and C. S. Clay, "Sound transmission experiments from an impulsive source near rigid wedges," *J. Acoust. Soc. Am.* **84**, 2135–43 (1988).

Li, S.; D. Chu; and C. S. Clay, "Time domain reflections and diffractions from facet-wedge constructions: acoustic experiments including double diffractions," *J. Acoust. Soc. Am.* **96**, 3715–20 (1994).

Liebermann, L. N., "Second viscosity of fluids," *Phys. Rev.* **75**, 1415–22 (1949).

———, "Analysis of rough surfaces by scattering," *J. Acoust. Soc. Am.* **35**, 932 (1963).

Lineback, J. A.; D. L. Gross; and R. P. Meyer, "Glacial tills under Lake Michigan," *Environmental Geology Notes*, no. 69, Illinois State Geological Survey, Urbana (July 1974).

Livingston, E.; and O. Diachok, "Estimation of average under-ice reflection amplitudes and phases using matched-field processing," *J. Acoust. Soc. Am.* **86**, 1909–19 (1989).

Lockwood, J. C.; and J. G. Willette, "High-speed method for computing the exact solution for the pressure variations in the near field of a baffled piston," *J. Acoust. Soc. Am.* **53**, 735–41 (1973).

Loewen, M. R.; and W. K. Melville, "A model of the sound generated by breaking waves," *J. Acoust. Soc. Am.* **90**, 2075–80 (1991).

Longuet-Higgins, M. S., "The statistical geometry of random surfaces," *Proc. Symp. Appl. Math.* **13**, American Mathematical Society (1962).

———, "The effect of non-linearities on the statistical distributions in the theory of sea waves," *J. Fluid Mech.* **17**, 459–80 (1963).

———, "Bubble noise spectra," *J. Acoust. Soc. Am.* **87**, 652–61 (1990).

———, "Non-linear damping of bubble oscillations by resonant interaction," *J. Acoust. Soc. Am.* **91**, 1414–22 (1992).

Lowrie, A.; and E. Escowitz, *Kane 9: Global Ocean Floor Analysis and Research Data Series*; U.S. Naval Oceanographic Office (1969).

Love, R. H., "Maximum side-aspect target strength of an individual fish," *J. Acoust. Soc. Am.* **46**, 746–60 (1969).

———, "Dorsal-aspect target strength of an individual fish," *J. Acoust. Soc. Am.* **49**, 816–23 (1971).

———, "Target strength of an individual fish at any aspect," *J. Acoust. Soc. Am.* **62**, 1397–1403 (1977).

———, "Resonant acoustic scattering by swimbladder-bearing fish," *J. Acoust. Soc. Am.* **64**, 571–80 (1978).

———, "A comparison of volume scattering strength data with model calculations based on quasisynoptically collected fishery data," *J. Acoust. Soc. Am.* **94**, 2255–68 (1993).

Løvik, A., "Acoustic measurement of the gas bubble spectrum in water" in *Cavitation and Inhomogeneities in Underwater Acoustics*, W. Lauterborn (ed.), Springer, Berlin (1980).

Lucas, R. J.; and V. Twersky, "Coherent response to a point source irradiating a rough plane," *J. Acoust. Soc. Am.* **76**, 1847–63 (1984).

———, "Inversion of data for near-grazing propagation over rough surfaces," *J. Acoust. Soc. Am.* **80**, 1459–72 (1986).

Lyons, A. P.; M. E. Duncan; A. L. Anderson; and J. A. Hawkins, "Predictions of the acoustic scattering response of free methane bubbles in muddy sediments," *J. Acoust. Soc. Am.* **99**, 163–72 (1996).

McCammon, D. F.; and S. T. McDaniel, "The influence of the physical properties of ice on reflectivity," *J. Acoust. Soc. Am.* **77**, 499–507 (1985).

McCartney, B. S.; and B. McK. Bary, "Echosounding on probable gas bubbles from the bottom of Saanich Inlet, British Columbia," *Deep-Sea Research* **123**, 285–94 (1965).

McCartney, B. S.; and A. R. Stubbs, "Measurement of the target strength of fish in dorsal aspect, including swimbladder resonance," in *Proceedings of an International Symposium on Biological Sound Scattering in the Ocean*, ed. G. B. Farquhar; U.S. Government Printing Office; Washington, D.C., pp. 180–211 (1970).

McDaniel, S. T., "Propagation of normal modes in parabolic approximation," *J. Acoust. Soc. Am.* **57**, 307–11 (1975a).

———, "Parabolic approximation for underwater sound propagation," *J. Acoust. Soc. Am.* **58**, 1178–85 (1975b).

———, "Mode coupling due to interaction with the sea bed," *J. Acoust. Soc. Am.* **72**, 916–23 (1982).

Mackenzie, K. V., "Nine-term equation for sound speed in the oceans," *J. Acoust. Soc. Am.* **70**, 807–12 (1981).

Makris, N. C.; R. Z. Avelino; and R. Menis, "Deterministic reverberation from ocean ridges," *J. Acoust. Soc. Am.* **97**, 3547–74 (1995).

Malinverno, A., "Segmentation of topographic profiles of the seafloor based on a self-affine model," *IEEE J. of Oce. Eng.* **14**, 348–59 (1989).

———, "Testing linear models of sea-floor topography," *Pageoph* **131**, 139–55 (1989).

———, "Inverse square-root dependence of mid-ocean-ridge flank roughness on spreading rate," *Nature* **352**, 58–60 (1991).

Marshall, N. B., "Swimbladder development and the life of deep-sea fish," in G. Brooke Farquhar, ed., *Proceedings of an International Symposium on Biological Sound Scattering in the Ocean*, Maury Center for Ocean Science; U.S. Government Printing Office; Washington, D.C., stock no. 0851-0053, pp. 69–78 (1970).

Martin, H. W., "Decibel—the name for the transmission unit," *The Bell System Technical Journal* **1**, 1–2 (1929). See ibid **3**, 400–08 (1924).

Matsumoto, H.; R. P. Dziak; and C. G. Fox, "Estimation of seafloor microtopographic roughness through modeling of acoustic backscatter data recorded by multibeam sonar systems," *J. Acoust. Soc. Am.* **94**, 2776–87 (1993).

Maynard, G. L.; G. H. Sutton; D. M. Hussong; and L. W. Kroenke, "The Seismic Wide Angle Reflection Method in the Study of Ocean Sediment Velocity Structure," in L. L. Hampton, ed., *Physics of Sound in Marine Sediments*; Plenum Press; New York, pp. 89–118 (1974).

Mayo, N. H., "Near-grazing, specular scattering of underwater sound from sea and swell," M.S. thesis, Naval Postgraduate School, Monterey, Calif. (1969).

McDaniel, S. T., "Vertical spatial coherence of backscatter from bubbles," *IEEE J. Oceanic Eng.* **12**, 349–56 (1987).

McNaught, D. C., "Developments in acoustic plankton sampling," *Proc. 12th Conf. Great Lakes Res.*, 76–84 (1968).

———, "Acoustical zooplankton distributions," *Proc. 11th Conf. Great Lakes Res.*, 61–68 (1969).

Medwin, H.; and I. Rudnick, "Surface and volume sources of vorticity in acoustic fields," *J. Acoust. Soc. Am.* **25**, 538–40 (1953).

Medwin, H.; "Acoustic streaming experiment in gases," *J. Acoust. Soc. Am.* **26**, 332–40 (1954).

———, "Specular scattering of underwater sound from a wind-driven surface," *J. Acoust. Soc. Am.* **41**, 1485–95 (1967).

———, "*In-situ* acoustic measurements of bubble populations in coastal waters," *J. Geophys. Res.* **75**, 599–611 (1970).

Medwin, H.; and C. S. Clay, "Dependence of spatial and temporal correlation of forward scattered underwater sound on the surface statistics: part II—experiment." *J. Acoust. Soc. Am.* **47**, 1419–29 (1970a). See also Clay and Medwin, part I—theory (1970).

Medwin, H.; C. S. Clay; J. M. Berkson; and D. L. Jaggard, "Traveling correlation function of the heights of windblown water waves," *J. Geophys. Res.* **75**, 4519–24 (1970b).

Medwin, H.; and J. D. Hagy, Jr., "Helmholtz–Kirchhoff theory for sound transmission through a statistically rough plane interface between dissimilar fluids," *J. Acoust. Soc. Am.* **51**, 1083 (1972).

Medwin, H.; R. A. Helbig; and J. D. Hagy, Jr., "Spectral characteristics of sound transmission through the rough sea surface," *J. Acoust. Soc. Am.* **54**, 99–109 (1973).

Medwin, H., "Acoustic fluctuations due to microbubbles in the near-surface ocean," *J. Acoust. Soc. Am.* **56**, 1100–04 (1974).

———, "Speed of sound in water: a simple equation for realistic parameters," *J. Acoust. Soc. Am.* **58**, 1318–19 (1975a).

Medwin, H.; J. Fitzgerald; and G. Rautmann, "Acoustic miniprobing for ocean microstructure and bubbles," *J. Geophys. Res.* **80**, 405–413 (1975b).

Medwin, H., "*In situ* measurements of microbubbles at sea," *J. Geophys. Res.* **82**, 971–76 (1977a).

———, "Acoustical determinations of bubble-size spectra," *J. Acoust. Soc. Am.* **62**, 1041–44 (1977b).

———, "Counting bubbles acoustically; a review," *Ultrasonics* **15**, 7–13 (1977c).

Medwin, H.; and J. C. Novarini, "Rough surface backscatter with secondary diffraction and without Kirchhoff approximation," *J. Acoust. Soc. Am.* **67** (S1) S67 (A) (1980).

Medwin, H., "Shadowing by finite noise barriers," *J. Acoust. Soc. Am.* **69**, 1060–64 (1981a).

Medwin, H.; and J. C. Novarini, "Backscattering strength and the range dependence of sound scattered from the ocean surface," *J. Acoust. Soc. Am.* **69**, 108–11 (1981b).

Medwin, H.; E. Childs; and G. M. Jebsen, "Impulse studies of double diffraction: a discrete Huygens interpretation," *J. Acoust. Soc. Am.* **72**, 1005–13 (1982).

Medwin, H.; E. Childs; E. A. Jordan; and R. J. Spaulding, Jr., "Sound scatter and shadowing at a seamount: hybrid physical solutions in two and three dimensions," *J. Acoust. Soc. Am.* **75**, 1478–90 (1984a).

Medwin, H.; G. L. D'Spain; E. Childs; and S. J. Hollis, "Low-frequency grazing propagation over periodic, steep-sloped, rigid roughness elements," *J. Acoust. Soc. Am.* **76**, 1774–90 (1984b).

Medwin, H.; and J. C. Novarini, "Modified sound refraction near a rough ocean bottom," *J. Acoust. Soc. Am.* **76**, 1791–96 (1984c).

Medwin, H.; and G. L. D'Spain, "Near-grazing, low-frequency propagation over randomly rough, rigid surfaces," *J. Acoust. Soc. Am.* **79**, 657–65 (1986a).

Medwin, H.; K. J. Reitzel; and G. L. D'Spain, "Normal modes in a rough waveguide: theory and experiment," *J. Acoust. Soc. Am.* **80**, 1507–14 (1986b).

Medwin, H.; K. J. Reitzel; and M. J. Browne, "Elements of Arctic surface scatter: Part III, the head wave," *J. Acoust. Soc. Am.* **82** (S1), S31 (A) (1987).

Medwin, H.; M. J. Browne; K. R. Johnson; and P. L. Denny, "Low frequency backscatter from Arctic leads," *J. Acoust. Soc. Am.* **83**, 1794–1803 (1988).

Medwin, H.; and N. D. Breitz, "Ambient and transient bubble spectral densities in quiescent seas and under spilling breakers," *J. Geophys. Res.* **94**, 12,751–12,759 (1989a).

Medwin, H.; and M. M. Beaky, "Bubble sources of the Knudsen sea noise spectra," *J. Acoust. Soc. Am.* **86**, 1124–30 (1989b).

Medwin, H.; and A. C. Daniel, Jr., "Acoustical measurements of bubble production by spilling breakers," *J. Acoust. Soc. Am.* **88**, 408–12 (1990).

Medwin, H.; A. Kurgen; and J. A. Nystuen, "Impact and bubble sound from raindrops at normal and oblique incidence," *J. Acoust. Soc. Am.* **88**, 413–18 (1990).

Medwin, H.; J. A. Nystuen; P. W. Jacobus; L. H. Ostwald; and D. E. Snyder, "The anatomy of underwater rain noise," *J. Acoust. Soc. Am.* **92**, 1613–23 (1992).

Meecham, W., "On the use of the Kirchhoff approximation for the solution of reflection problems," *J. Rational Mech. Anal.* **5**, 323–33 (1956).

Mellberg, L. E.; and O. M. Johannessen, "Layered oceanic microstructure—its effect on sound propagation," *J. Acoust. Soc. Am.* **53**, 571–80 (1973).

Mellen, R. H.; and D. G. Browning, "Variability of low-frequency sound absorption in the ocean: pH dependence," *J. Acoust. Soc. Am.* **61**, 704–06 (1977).

Mellen, R. H.; D. G. Browning; and V. P. Simmons, "Investigation of chemical sound absorption in sea water, Part IV," *J. Acoust. Soc. Am.* **74**, 987–93 (1983).

Melton, D. R.; and C. W. Horton, Sr., "Importance of Fresnel correction in scattering from a rough surface. I. Phase and amplitude fluctuations," *J. Acoust. Soc. Am.* **47**, 290–98 (1970). See also Horton and Melton, Part II (1970).

Messino, D.; D. Sette; and F. Wanderlingh, "Statistical approach to ultrasonic cavitation," *J. Acoust. Soc. Am.* **35**, 1575–83 (1963).

Mikeska, E. E.; and C. M. McKinney, "Range dependence of underwater echoes from randomly rough surfaces," *J. Acoust. Soc. Am.* **63**, 1375–80 (1978).

Miller, G. A., Sr., "Underwater sound radiation from single large raindrops at terminal velocity: The effects of a sloped water surface at impact," M.S. thesis, Naval Postgraduate School, Monterey, CA (1992).

Miller, J. H.; J. F. Lynch; and C.-S. Chiu, "Estimation of sea surface spectra using acoustic tomography," *J. Acoust. Soc. Am.* **86**, 326–45 (1989).

Millikan, R. A.; D. Roller; and E. C. Watson, *Mechanics, Molecular Physlcs, Heat, and Sound*; MIT Press; Cambridge, Mass. (1965).

Minnaert, M., "On musical air bubbles and the sounds of running water," *Phil. Mag.* (7) **16**, 235–48 (1933).

Mitson, R. B., "Underwater noise of research vessels," *Cooperative Research Report 209*; International Council for the Exploration of the Sea, Copenhagen, Denmark (May 1995).

Moffett, M. B.; P. J. Westervelt; and R. T. Beyer, "Large-amplitude pulse propagation—a transient effect," *J. Acoust. Soc. Am.* **47**, 1473–74 (1970).

Monahan, E., and I. G. O'Muircheartaigh, "Whitecaps and the passive remote sensing of the ocean surface," *Int. J. Remote Sensing* **7**, 627–42 (1986).

Muir, T. G., "Non-linear acoustics and its role in the sedimentary geophysics of the sea," in L. L. Hampton, ed., *Physics of Sound in Marine Sediments*; Plenum Press; New York, pp. 241–87 (1974).

Mulhearn, P. J., "Distribution of microbubbles in coastal waters," *J. Geophys. Res.* **86**, 6429–34 (July 1981).

Munk, W.; and C. Wunsch, "Ocean acoustic tomography: a scheme for large scale monitoring," *Deep-Sea Res.* **26A**, 123–61 (1979).

Munk, W., "Acoustic monitoring of ocean gyres," *J. Fluid Mech.* **173**, 43–53 (1986).

Nakken, O.; and K. Olsen, "Target strength measurements of fish," *Rapp. P.-V. Reun. Cons. Int. Explor. Mer.* **170**, 52–69 (1977).

Nero, R. W.; J. J. Magnuson; S. B. Brandt; T. K. Stanton; and J. M. Jech, "Finescale biological patchness of 70 kHz acoustic scattering at the edge of the Gulf Stream-EchoFront 85," *Deep-Sea Res.* **37**, 999–1016 (1990).

Neubauer, W. G.; and L. R. Dragonette, "Observation of waves radiated from circular cylinders caused by an incident pulse," *J. Acoust. Soc. Am.* **48**, 1135–49 (1970).

Nichols, R. H., "Infrasonic noise sources: Wind versus waves," *J. Acoust. Soc. Am.* **82**, 1395–402 (1987) and ibid **82**, 2150 (E) (1987).

Northrop, J.; and J. G. Colborn, "Sofar channel axial sound speed and depth in the Atlantic Ocean," *J. Geophys. Res.* **79**, 5633–41 (1974).

Novarini, J. C.; and H. Medwin, "Diffraction, reflection, and interference during near-grazing and near-normal ocean surface backscattering," *J. Acoust. Soc. Am.* **64**, 260–68 (1978).

———, "Computer modeling of resonant sound scattering from a periodic assemblage of wedges: comparison with theories of diffraction gratings," *J. Acoust. Soc. Am.* **77**, 1754–59 (1985).

Novarini, J. C.; R. S. Keiffer; and J. W. Caruthers, "Forward scattering from fetch-limited and swell-contaminated sea surfaces," *J. Acoust. Soc. Am.* **92**, 2099–2108 (1992).

Novarini, J. C.; and G. V. Norton, "Acoustic index of refraction in the background bubble layer of the ocean: an updated bubble spectrum and the computer program CBUBBLY," *Naval Research Lab Rept.*, NRL/FR/7181—93-9432 (March 10, 1994).

Nyborg, W., "Acoustic streaming," in W. P. Mason, ed., *Physical Acoustics*, vol. 2, part B; Academic Press, New York, pp. 265–331 (1965).

Nystuen, J. A.; L. H. Ostwald, Jr.; and H. Medwin, "The hydroacoustics of a raindrop impact," *J. Acoust. Soc. Am.* **92**, 1017–21 (1992).

———, "An explanation of the sound generated by light rain in the presence of wind" in *Natural Physical Sources of Underwater Sound*, ed. B. R. Kerman; Kluwer Press; Dordrecht, Netherlands, pp. 659–69 (1993).

———, "Acoustical rainfall analysis: rainfall drop size distribution using the underwater sound field," *J. Atmospheric and Oceanic Technology* **13**, 74–84 (1996).

O'Brien, P. N. S., "Model seismology: the critical refraction of elastic waves," *Geophysics*, **20**, 227–42 (1955).

Oguz, H. N.; and A. Prosperetti, "Bubble oscillations in the vicinity of a nearly plane-free surface," *J. Acoust. Soc. Am.* **87**, 2085–92 (1990).

O'Hern, T. J.; et al., "Comparison of holographic and Coulter Counter measurements of cavitation nuclei in the ocean," *J. Fluids Eng.* **110**, 200–07 (1988).

Orsi, T. H.; C. M. Edwards; and A. L. Anderson, "X-ray computed tomography: a nondestructive method for quantitative analysis of sediment cores," *J. Sedimentary Research* **A64**, 690–93 (1994).

Pace, N. G.; Z. K. S. Al-Hamdani; and P. D. Thorne, "The range dependence of normal incidence acoustic backscatter from a rough surface," *J. Acoust. Soc. Am.* **77**, 101–12 (1985).

Palmer, D. R., "Eikonal approximation and the parabolic equation," *J. Acoust. Soc. Am.* **60**, 343–54 (1976).

Parvulescu, A., "Signal detection in a multipath medium by MESS processing," *J. Acoust. Soc. Am.* **33**, 1674 (A) (1961).

Parvulescu, A.; and C. S. Clay, "Reproducibility of signal transmissions in the ocean," *Radio Eng. Electron.* **29**, 223–28 (1965).

Parvulescu A., "Matched-signal (MESS) processing by the ocean," *J. Acoust. Soc. Am.* **98**, 943–60 (1995).

Parsons, T. R.; and M. Takahashi, *Biological Oceanic Processes*; Pergamon Press; New York (1973).

Parsons, A. R.; R. H. Bourke; R. Muench; C.-S. Chiu; J. F. Lunch; J. H. Miller; A. J. Plueddemann; and R. Pawlowicz, "The Barents Sea polar front in summer," *J. Geophys. Res.* **101** (C6), 14201–21 (1996).

Pedersen, M. A., "Acoustic intensity anomalies introduced by constant sound velocity gradients," *J. Acoust. Soc. Am.* **33**, 465–74 (1961).

Pekeris, C. L., "Theory of propagation of explosive sound in shallow water," in *Propagation of Sound in the Oceans*, Geological Society of America Memoir 27, New York (1948).

Perkins, J. B. III, "Amplitude modulation of acoustic signals by ocean waves and the effect on signal detection," M.S. thesis, Naval Postgraduate School, Monterey, Calif. (1974).

Peterson, M. L.; C. S. Clay; and S. B. Brandt, "Acoustic estimates of fish density and scattering function," *J. Acoust. Soc. Am.* **60**, 618–22 (1976).

Phillips, O. M., *The Dynamics of the Upper Ocean*, 2nd ed.; Cambridge University Press; New York (1970).

Pierce, A. D., "Extension of the method of normal mode to sound propagation in an almost stratified medium," *J. Acoust. Soc. Am.* **37**, 19–27 (1965).

Pierson, W. J.; and L. Moskowitz, "A proposed spectral form for fully developed wind seas based on the similarity theory of S. A. Kitaigorodskii," *J. Geophys. Res.* **69**, 5181–90 (1964).

Pinkel, R.; A. Plueddemann; and R. Williams, "Internal wave observations from *FLIP* in MILDEX," *J. Phys. Oceanogr.* **17**, 1737–57 (1987).

Pinkel, R., "Doppler sonar measurements of ocean waves and currents," *Marine Tech. Soc. J.* **20**, 58–67 (1986).

Pinkel, R.; and J. A. Smith, "Open ocean surface wave measurements using Doppler sonar," *J. Geophys. Res.* **92**, 12967–73 (1987).

Porter, M. B., "Acoustic models and sonar systems," *IEEE J. Ocean. Eng.* **18** (4) 425–37 (1993).

Prosperetti, A., "Thermal effects and damping mechanisms in the forced radial oscillations of gas bubbles in liquids," *J. Acoust. Soc. Am.* **61**, 17–27 (1977).

Prosperetti, A., "Bubble-related ambient noise in the ocean," *J. Acoust. Soc. Am.* **84**, 1024–54 (1988).

Prosperetti, A.; N. Q. Lu; and H. S. Kim, "Active and passive acoustic behavior of bubble clouds at the ocean's surface," *J. Acoust. Soc. Am.* **93**, 3117–27 (1993).

Proud, J. M.; R. T. Beyer; and P. Tamarkin, "Reflection of sound from randomly rough surfaces," *J. Appl. Phys.* **31**, 543–52 (1960).

Pumphrey, H. C.; L. A. Crum; and L. Bjorno, "Underwater sound produced by individual drop impacts," *J. Acoust. Soc. Am.* **85**, 1518–26 (1989).

Rayleigh, Lord [J. W. Strutt], *The Theory of Sound*, vols. 1 and 2 (2d eds. 1894 and 1896); Dover; New York (1945).

Rhode, D. F.; T. G. Goldsberry; W. S. Olsen; and C. R. Reeves, "Band elimination processor for an experimental parametric receiving array," *J. Acoust. Soc. Am.* **66**, 484–87 (1979).

Rice, S. O., "Mathematical analysis of random noise," in *Selected Papers on Noise and Stochastic Processes*, ed. N. Wax; Dover; New York, pp. 133–294 (1954).

Robinson, B. J., "*In-situ* measurement of fish target strenght," *Proc. 1978 Inst. Acoustics Specialists Meeting on Acoustics in Fisheries*, Hull, U.K. (1978).

Roderick, W. I.; and B. F. Cron, "Frequency spectra of forward-scattered sound from the ocean surface," *J. Acoust. Soc. Am.* **48**, 759–66 (1970).

Rogers, P. H., "Weak-shock solution of underwater explosive shock waves," *J. Acoust. Soc. Am.* **62**, 1412–19 (1977).

Rudstam, L. G.; C. S. Clay; and J. J. Magnuson, "Density estimates and size of cisco, *Coregonus artedii*, using analysis of echo peak PDF from a single transducer sonar," *Can. J. Fish. Aquat. Sci.* **44**, 811–21 (1987).

Rusby, J. S. M., "The onset of sound wave distortion and cavitation in seawater," *J. Sound Vib.* **13**, 257–67 (1970).

Sand, O.; and A. D. Hawkins, "Acoustic properties of the cod swimbladder," *J. Experimental Biology* **58**, 797–820 (1973).

Sandness, G. A., "A numerical evaluation of the Helmholtz integral in acoustic scattering," Ph.D. dissertation, Department of Geology and Geophysics, University of Wisconsin, Madison (1973). Available through University Microfilms, Ann Arbor, Michigan.

Sarkar, K.; and A. Prosperetti, "Coherent and incoherent scattering by oceanic bubbles," *J. Acoust. Soc. Am.* **96**, 332–41 (1994).

Schiff, L. I., *Quantum Mechanics*; McGraw-Hill; New York, pp. 178–87 (1949).

Schulkin, M.; and H. W. Marsh, "Sound absorption in seawater," *J. Acoust. Soc. Am.* **35**, 864–65 (1962).

Scofield, C., "Oscillating microbubbles created by water drops falling on fresh and salt water: Amplitude, damping and the effects of temperature and salinity," M.S. thesis, Naval Postgraduate School, Monterey, CA (1992).

Scrimger, A., "Signal amplitude and phase fluctuations induced by surface waves in ducted sound propagation," *J. Acoust. Soc. Am.* **33**, 239–74 (1961).

Sheldon, R. W.; A. Prakash; and W. H. Sutiliffe, Jr., "The size distribution of particles in the ocean," *Limnol. Oceanogr.* **17**, 327–40 (1972).

Shields, R. B, Jr., "Signal enhancement of specularly scattered underwater sound," M.S. Thesis, Naval Postgraduate School, Monterey, Calif. (1977).

Shooter, J. A., et al., "Acoustic saturation of spherical waves in water," *J. Acoust. Soc. Am.* **55**, 54–62 (1974).

Simmons, V. P., "Investigation of the 1 kHz sound absorption in sea water," Ph.D. dissertation, University of California, San Diego, (1975).

Sims, C. C., "Bubble transducer for radiating high-power low-frequency sound in water," *J. Acoust. Soc. Am.* **32**, 1305 (1960).

Sinclair, D., "Light scattering by spherical particles," *J. Optical Soc. Am.* **37**, 473–81 (1947).

Skretting, A.; and C. C. Leroy, "Sound attenuation between 200 Hz and 10 kHz," *J. Acoust. Soc. Am.* **49**, 276–82 (1971).

Slifko, J. P., "Pressure pulse characteristics of deep explosions as functions of depth and range," *Naval Ordnance Laboratory NOTLR* **67–87** (21 September 1967).

Snyder, D. E., "Characteristics of sound radiation from large raindrops," M.S. thesis, Naval Postgraduate School, Monterey, Calif. (1990).

Spaulding, R. P., Jr., "Physical modeling of sound shadowing by seamounts," M.S. thesis, Naval Postgraduate School, Monterey, Calif. (1979).

Spiesberger, J. L.; E. Terray; and K. Prada, "Successful ray modeling of acoustic multipaths over a 3000-km section in the Pacific," *J. Acoust. Soc. Am.* **95**, 3654–57 (1994).

Spindel, R. C.; and P. M. Schultheiss, "Acoustic surface-reflection channel characterization through impulse response measurements," *J. Acoust. Soc. Am.* **51**, 1812 (1972).

———, "Two-dimensional probability structure of wind-driven waves," *J. Acoust. Soc. Am.* **52**, 1065–68 (1972).

Stanton, T. K., "Sonar estimates of seafloor microroughness," *J. Acoust. Soc. Am.* **75**, 809–18 (1984).

———, "Volume scatter: echo peak PDF," *J. Acoust Soc. Am.* **77**, 1358–1366 (1985a).

———, "Density estimates of biological sound scatters using sonar echo peak PDFs," *J. Acoust. Soc. Am.* **78**, 1868–73 (1985b).

Stanton, T. K.; and C. S. Clay, "Sonar echo statics as a remote-sensing tool: volume and seafloor," *IEEE J. Ocean. Eng.* **OE-11**(1) 79–96 (1986).

———, "Sound scattering by cylinders of finite length. I. Fluid cylinders," *J. Acoust. Soc. Am.* **83**, 55–63 (1988a).

———, "Sound scattering by cylinders of finite length. II. Elastic cylinders," *J. Acoust. Soc. Am.* **83**, 64–67 (1988b).

———, "Sound scattering by cylinders of finite length. III. Deformed cylinders," *J. Acoust. Soc. Am.* **86**, 691–705 (1988c).

———, "Simple approximate formulas for backscattering of sound by spherical and elongated objects," *J. Acoust. Soc. Am.* **86**, 1499–1510 (1989).

———, "Sound scattered by rough elongated elastic objects. I: means of scattered field," *J. Acoust. Soc. Am.* **92**, 1641–44 (1992a).

Stanton, T. K.; and D. Chu, "Sound scattering by rough elongated elastic objects. II: fluctuations of scattered field," *J. Acoust. Soc. Am.* **92**, 1665–78 (1992b).

Stanton, T. K.; C. S. Clay; and D. Chu, "Ray representation of sound scattering by weakly scattering deformed fluid cylinders: simple physics and applications to zooplankton," *J. Acoust. Soc. Am.* **94**, 3454–62 (1993).

Stanton, T. K.; P. H. Wiebe; D. Chu; and L. Goodman, "Acoustic characterization and discrimination of marine zooplankton and turbulence," *ICES, J. Mar. Sci.* **31**, 469–79 (1994).

Stanzial, D.; N. Prodi; and G Schiffrer, "Reactive acoustic intensity for general fields and energy polarization," *J. Acoust. Soc. Am.* **99**, 1868–76 (1996).

Starritt, H. C.; F. A. Duck; and V. F. Humphrey, "An experimental investigation of streaming in pulsed diagnostic ultrasound beams," *Ultrasound in Med. & Biol.* **15**, 363–73 (1989).

Stenzel, H., "On the disturbance of a sound field brought about by a rigid sphere," in German, *Elektr. Nachr. Tech.* **15**, 71–78 (1938). Transl. G. R. Barnard and C. W. Horton, Sr., and republished as *Technical Report No. 159*, Defense Research Laboratory, University of Texas, Austin (1959).

Stephen, R. A., "Solutions to range-dependent benchmark problems by the finite-difference method," *J. Acoust. Soc. Am.* **87**, 1527–34 (1990). Wedge benchmark paper.

Stephens, R. W. B., ed., *Underwater Acoustics*; Wiley; New York (1970). Chapter 3, "Scattering from the Sea Surface," by H. Medwin.

Stokes, G. G., "On the dynamical theory of diffraction," *Trans. Camb. Phil. Soc.* **9**, 1 (1849), reprinted in Stokes, *Mathematical and Physical Papers*, vol. 2, Cambridge University Press, Cambridge, 1883, pp. 243–328.

Stoll, R. D., "Acoustic waves in saturated sediments," in L. L. Hampton, ed., *Physics of Sound in Marine Sediments*; Plenum Press; New York, pp. 19–40 (1974).

Strasberg, M., "Pulsation frequency of non-spherical gas bubbles in liquids," *J. Acoust. Soc. Am.* **25**, 536 (1953).

———, "Gas bubbles as sources of sound in liquids," *J. Acoust. Soc. Am.* **28**, 20 (1956).

Stroud, J. S.; and P. L. Marston, "Transient bubble oscillations associated with the underwater noise of rain detected optically and some properties of light scattered by bubbles," in *Bubble Dynamics and Interface Phenomena*, ed. J. R. Blake et al.; Kluwer Academic Publishing; Amsterdam, pp. 161–69 (1994).

Strutt, J. W. [Lord Rayleigh], *The Theory of Sound*, vol. 2 (2d ed. 1896); Dover; New York, p. 89, 282 (1945).

Sun, Y.; R. Nash; and C. S. Clay, "Acoustic measurements of the anatomy of fish at 220 kHz," *J. Acoust. Soc. Am.* **78**, 1772–76 (1985).

Sun, Z.; G. Gimenez; and F. Denis, "Calculation of the impulse response of a rigid sphere using the physical optic method and modal method jointly," *J. Acoust. Soc. Am.* **89**, 10–18 (1991).

Talukdar, K. K.; R. C. Tyce; and C. S. Clay, "Interpretation of Sea Beam backscatter data collected at the Laurentian Fan off Nova Scotia using acoustic backscatter theory," *J. Acoust. Soc. Am.* **97**, 1545–58 (1995).

Tappert, F. D., "The parabolic equation approximation method in wave propagation and underwater acoustics," in J. B. Keller and J. S. Papadakis, *Lecture Notes in Physics*, Springer-Verlag, New York (1977).

Tappert, F. D.; and R. H. Hardin, "Computer simulation of long-range ocean acoustic propagation using the parabolic equation method," *Eighth International Congress on Acoustics*, 452 (1974).

Thorne, P. D.; and N. G. Pace, "Acoustic studies of broadband scattering from a model rough surface," *J. Acoust. Soc. Am.* **75**, 133–44 (1984).

Thorne, P. D.; N. G. Pace; and Z. K. S. Al-Hamdani, "Laboratory measurements of backscattering from marine sediments," *J. Acoust. Soc. Am.* **84**, 303–9 (1988).

Thorp, W. H., "Deep-ocean sound attenuation in the sub- and low-kilocycle-per sec region," *J. Acoust. Soc. Am.* **38**, 648–54 (1965).

Thorpe, S. A., "On the clouds of bubbles formed by breaking wind-waves in deep water, and their role in air-sea gas transfer," *Philos. Trans. R. Soc. London*, Ser. A, **304**, 155–210 (1982).

Thorsos, E. I., "The validity of the Kirchhoff approximation for rough surface scattering using a Gaussian roughness spectrum," *J. Acoust. Soc. Am.* **83**, 78–92 (1988).

Thorsos, E.I.; and D. R. Jackson, "The validity of a perturbation approximation for rough surface scattering using a Gaussian roughness spectrum," *J. Acoust. Soc. Am.* **86**, 261–77 (1989).

Thorsos, E. I., "Acoustic scattering from a Pierson-Moskowitz sea surface," *J. Acoust. Soc. Am.* **88**, 335–49 (1990).

Thorsos, E. I.; and S. L. Broschat, "An investigation of the small slope approximation for scattering from rough surfaces. Part I: theory," *J. Acoust. Soc. Am.* **97**, 2082–93 (1995).

Thompson, D. J., "Wide-angle parabolic equation solutions to two range-dependent benchmark problems," *J. Acoust. Soc. Am.* **87**, 1514–20 (1990). Wedge benchmark paper.

Tindle, C. T.; H. Hobaek; and T. G. Muir, "Downslope propagation of normal modes in a shallow water wedge," *J. Acoust. Soc. Am.* **81**, 275–86 (1987a).

———, "Normal modes filtering for downslope propagation in a shallow water wedge," *J. Acoust. Soc. Am.* **81**, 287–94 (1987b).

Tjøtta, S.; and J. N. Tjøtta, "Acoustic streaming in ultrasonic beams," *Proceedings of the 13th International Symposium on Non-linear Acoustics*, pp. 601–7 World Scientific, London (1993).

Tolstoy, I., *Wave Propagation*; McGraw-Hill; New York (1973).

———, "The scattering of spherical pulses by slightly rough surfaces," *J. Acoust. Soc. Am.* **66**, 1135–44 (1979).

———, "Rough surface boundary wave attenuation due to incoherent scatter," *J. Acoust. Soc. Am.* **77**, 482–88 (1985).

———, "Diffraction by a hard, truncated wedge and strip," *IEEE J. Ocean. Eng.* **14**, 4 (1989a).

———, "Exact, explicit solutions for diffractions by hard sound barriers and seamounts," *J. Acoust. Soc. Am.* **85**, 661 (1989b).

Tolstoy, I.; and C. S. Clay, *Ocean Acoustics*; McGraw-Hill; New York (1966). Reprinted by the Acoustical Society of America, Woodbury, N.Y. (1987).

Traynor, J. J.; and J. E. Ehrenberg, "Evaluation of the dual beam acoustic fish target strength estimation method," *J. Fish. Res. Board Can.* **36**, 1065–71 (1979).

———, "Fish and standard-sphere, target-strength measurements obtained with a dual-beam and split-beam echo-sounding system," *Rapp. P.-V. Reun. Cons. Int. Explor. Mer.* **189**, 325–35 (1990).

Trevorrow, M. V., "Multifrequency acoustic investigations of juvenile and adult fish in Lake Biwa, Japan," *J. Acoust. Soc. Am.* **100**, 3042–52 (1996).

Trorey, A. W., "A simple theory for seismic diffractions," *Geophysics* **35**, 762–84 (1970).

Tyce, R. C.; L. A. Mayer; and F. N. Spiess, "Near-bottom seismic profiling: high lateral variability, anomalous amplitudes, and estimates of attenuation," *J. Acoust. Soc. Am.* **68**, 1291–1402 (1980).

Tyce, R. C., "Deep seafloor mapping systems—a review," *Mar. Tech. J.* **20**, 4–16 (1986).

Updegtraff, G. E.; and V. C. Anderson, "Bubble noise and wavelet spills recorded 1 m below the ocean surface," *J. Acoust. Soc. Am.* **89**, 2264–79 (1991).

Urick, R. J.; and R. M. Hoover, "Backscattering of sound fom the sea surface: its measurement, causes and applications to the prediction of reverberation levels," *J. Acoust. Soc. Am.* **28**, 1038–42 (1956).

Vagel, S.; and D. M. Farmer, "The measurement of bubble-size distributions by acoustical backscatter," *J. Atmos. and Ocean Tech.* **9**, 630–44 (1992).

Van Vleck, J. H.; and D. Middleton, "A theoretical comparison of the visual, aural, and meter reception of pulsed signals in the presence of noise," *J. Appl. Phys.* **17**, 940–71 (1946).

Voronovich, A., "Small-slope approximation in wave scattering by rough surfaces," *Sov. Phys. JETP* **62**, 65–70 (1985).

Wagner, R. J., "Shadowing of randomly rough surfaces," *J. Acoust. Soc. Am.* **41**, 138–47 (1967).

Wang, P. C. C.; and H. Medwin, "Stochastic models of the scattering of sound by bubbles in the upper ocean," *Quart. J. of Appl. Math.* 411–25 (January 1975).

Wang, T.-C.; and E.-C. Shang, *Underwater Acoustics*, Science Press, China (1981).

Waterman, P. C., "New formulation of acoustic scattering," *J. Acoust. Soc. Am.* **45**, 1417–29 (1969).

Werth, G. C.; D. T. Liu; and A. W. Trorey, "Offshore singing-field experiments and theoretical interpretation," *Geophysics* **24**, 220–30 (1959).

Westervelt, P. J., "Parametric acoustic array," *J. Acoust. Soc. Am.* **35**, 535–37 (1963).

Weston, D. E., "A moirè fringe analog of sound propagation in shallow water," *J. Acoust. Soc. Am.* **32**, 647–54 (1960).

———, "Acoustic interaction effects in arrays of small spheres," *J. Acoust. Soc. Am.* **39**, 316–22 (1966).

———, "Sound Propagation in the Presence of Bladder Fish," in V. M. Albers, ed., *Underwater Acoustics*, vol. 2; Plenum Press; New York, pp. 55–88 (1967).

Westwood, E. K., "Ray model solutions to the benchmark wedge problems," *J. Acoust. Soc. Am.* **87**, 1539–45 (1990). Wedge benchmark paper.

Wiebe, P. H.; C. H. Greene; T. K. Stanton; and J. Burczynski, "Sound scattering by live zooplankton and micronekton: empirical studies with a dual-beam acoustical system," *J. Acoust. Soc. Am.* **88**, 2346–60 (1990).

Wildt, R., ed., "Acoustic properties of wakes," part 4 of *Physics of Sound in the Sea*, vol. 8; Summary Technical Report of Div. 6, National Defense Research Committee, Department of the Navy; Washington, D.C. (1946). Reissued by Naval Material Command, 1969.

Williams, A. O.; and M. N. Lewis, "Research Analysis Group (Brown University) Technical Report 56-1 (May 1956), unpublished.

Williams, R. E.; and H. F. Battestin, "Coherent recombination of acoustic multipath signals propagation in the deep ocean," *J. Acoust. Soc. Am.* **50**, 1433–42 (1971).

Wilson, O. B.; and R. W. Leonard, "Measurements of sound absorption in aqueous salt solutions by a resonator method," *J. Acoust. Soc. Am.* **26**, 223–26 (1954).

Wood, A. B., *A Textbook of Sound*; Macmillan; New York (1955).

Woodward, P. M., *Probability and Information Theory with Applications to Radar*, 2d ed.; Pergamon Press; New York (1964).

Worzel, J. L.; and M. Ewing, "Explosion sound in shallow water," in *Propagation of Sound in the Ocean*," Geological Society of America Memoir 27; New York (1948).

Yang, C. T., "Effectiveness of mode filtering: A comparison of matched-field and matched-mode processing," *J. Acoust. Soc. Am.* **87**, 2072–84 (1990).

———, "Broadband source localization and signature estimation," *J. Acoust. Soc. Am.* **93**, 1797–1806 (1993).

Ye, Z., "Low frequency acoustic scattering by gas-filled prolate spheroids in liquids," *J. Acoust. Soc. Am.* **101**, 1495–52 (1997).

———, "Acoustic dispersion and attenuation in many spherical scatterer systems and the Kramers–Kronig relations," *J. Acoust. Soc. Am.* **101**(6), 3299–305 (1997).

Yeager, E.; F. H. Fisher; J. Miceli; and R. Bressel, "Origin of the low-frequency sound absorption in seawater," *J. Acoust. Soc. Am.* **53**, 1705–07 (1973).

Zimdar, R. E.; P. D. Barnhouse; and M. J. Stoffel; "Instrumentation to determine the presence and acoustic effect of microbubbles near the sea surface," M.S. thesis, Naval Postgraduate School, Monterey, Calif. (1964).

Bibliography

Abramowitz, A.; and I. A. Stegun. *Handbook of Mathematical Functions*; U.S. Government Printing Office; Washington, D. C. (1964).

Akal, T.; and J. M. Berkson, eds. *Ocean Seismo-Acoustics Low Frequency Underwater Acoustics*; Plenum Press; New York (1986).

Aki, K.; and P. G. Richards, *Quantative Seismology Theory and Methods, Vols. 1 and 2*; W. H. Freeman and Company; San Francisco (1980).

Albers, V. M., ed. *Underwater Acoustics, Vol. 2*; Plenum Press; New York (1967).

———, ed. *Underwater Sound: Benchmark Papers in Acoustics*; Dowden, Hutchinson & Ross; Stroudsburg, Pa. (1972).

Au, W. W. L. *The Sonar of Dolphins*; Springer-Verlag; New York (1993).

Beckmann, P.; and A. Spizzichino. *The Scattering of Electromagnetic Waves from Rough Surfaces*; Pergamon Press; New York (1963).

Beyer, R. T. *Nonlinear Acoustics*; Naval Ship Systems Command, U.S. Navy; Washington, D.C. (1974).

Blackman, R. B.; and J. W. Tukey. *The Measurement of Power Spectra*; Dover; New York (1958).

Bobber, R. J. *Underwater Electroacoustic Measurements*; Naval Research Lab; Washington, D.C. (1970).

Born, M.; and E. Wolf. *Principles of Optics*; Pergamon Press; New York (1965).

Box, G. E. P.; and G. M. Jenkins. *Time Series Analysis, Forcasting, and Control*; Holden-Day; San Francisco (1970).

Brekhovskikh, L. M. *Waves in Layered Media*; Academic Press; New York (1980).

Brekhovskikh, L. M.; and O. A. Godin. *Acoustics of Layered Media 1*; Springer-Verlag; Berlin (1990).

Buckingham, M. J.; and J. R. Potter. *Sea Surface Sound '94*; World Scientific; Singapore (1995).

Busnel, R.-G.; and J. F. Fish. *Animal Sonar Systems*; Plenum Press; New York (1980).

Cerveny, V.; and R. Ravindra. *Theory of Seismic Headwaves*; University of Toronto Press; Toronto (1971).

Chernov, L. A. *Wave Propagation on a Random Medium*; McGraw-Hill; New York (1960).

Churchill, R. V.; and J. W. Brown. *Fourier Series and Boundary Value Problems*, 4th ed.; McGraw-Hill; New York (1978).

Claerbout, Jon. *Imaging the Earth's Interior*; Oxford; Blackwell (1985).

Clay, C. S. *Elementary Exploration Seismology*; Prentice-Hall; Englewood Cilffs, N.J. (1990).

Clay, C. S.; and H. Medwin. *Acoustical Oceanography*; Wiley; New York (1977).

Cole, R. H. *Underwater Explosives*; Princeton University Press; Princeton, N.J. (1948).

Eckart, C., ed. *Principles and Applications of Underwater Sound.* Originally issued 1946; reissued 1968. U.S. Department of the Navy, NAVMAT, P9674.

Erdelyi, A., ed. *Tables of Integral Transforms*; McGraw-Hill Book Company; New York (1954).

Ewing, M.; J. L. Worzel; and C. L. Pekeris. *Propagation of Sound in the Ocean, the Geological Society of America Memoir 27*; New York (1948).

Farquhar, G. B., ed. *Proceedings of an International Symposium on Biological Sound Scattering in the Ocean*; U.S. Government Printing Office; Washington, D.C. (1970).

Flatte, S. M., ed. *Sound Transmission through a Fluctuating Ocean*; Cambridge University Press; Cambridge (1979).

Friedlander, F. G. *Sound Pulses*; Cambridge University Press; Cambridge (1958).

Gradshteyn, I. S.; and I. M. Ryzhik. *Table of Integrals, Series, and Products*; Academic Press; New York (1980).

Gross, M. G. *Oceanography: A View of the Earth*; Prentice-Hall; Englewood Cliffs, N.J. (1972).

Hampton, L., ed. *Physics of Sound in Marine Sediments*; Plenum Press; New York (1974).

Heezen, B. C.; and C. D. Hollister. *The Face of the Deep*; Oxford University Press; New York (1971).

Herzfeld, K. Fl; and T. A. Litovitz. *Absorption and Dispersion of Ultrasonic Waves*; Academic Press; San Diego (1959).

Hubral, P.; and T. Krey. *Interval Velocities from Seismic Reflection Time Measurements*; Society of Exploration Geophysics; Tulsa (1980).

Jackson, J. D. *Classical Electrodynamics*; Wiley; New York (1962).

Kanasewich, E. R. *Time Sequence Analysis in Geophysics*, 3d ed.; University of Alberta Press; Edmonton (1981).

Kerman, B. R., ed. *Sea Surface Sound: Proceedings of the 1987 Conference on Natural Mechanisms of Surface Generated Noise in the Ocean*, Lerici, Italy; Kluwer; Dordrecht, Netherlands (1988).

———. *Natural Physical Sources of Underwater Sound; Sea Surface Sound 2; Proceedings of the 1990 Conference on Natural Mechanisms of Surface Generated Noise in the Ocean*, Lerici, Italy; Kluwer; Dordrecht, Netherlands (1993).

Kuperman, W. A.; and F. B. Jensen, eds. *Bottom-Interacting Ocean Acoustics*; Plenum Press; New York (1980).

Lauterborn, W., ed. *Cavitation and Inhomogeneities in Underwater Acoustics*; Springer-Verlag; Berlin (1980).

Landau, L. D.; and E. M. Lifshitz. *Fluid Mechanics,* English trans.; Addison-Wesley; Reading, Mass. (1959).

Lee, D.; R. L., Sternberg; and M. H. Shultz, eds. *Computational Acoustics. Volume 1: Wave Propagation; Volume 2: Algorithms and Applications.* North-Holland, New York (1988).

Lee, Y. W. *Statistical Theory of Communication*; John Wiley & Sons; New York (1960).

Lighthill, J. *Waves in Fluids*; Cambridge University Press; Cambridge (1978, 1979).

Lowrie, A.; and E. Escowitz. *Kane 9*; U.S. Naval Oceanographic Office, U.S. Government Printing Office; Washington, D.C. (1969)

MacLennan, D. N.; and E. J. Simmonds. *Fisheries Acoustics*; Van Nostrand-Reinhold; (1992).

Menke, W. *Geophysical Data Analysis: Discrete Inverse Theory*; Academic Press; New York (1984).

Monahan, E. C.; and Gearoid MacNiocaill, eds. *Oceanic Whitecaps and Their Role in Air-Sea Exchange Processes*; D. Reidel Publishing Co.; Dordrecht, Netherlands (1986).

Morse, P. M. *Vibration and Sound* (1948), 2d ed., Acoustical Society of America; Woodbury, N.Y. (1991).

Munk, W.; P. Worcester; and C. Wunsch. *Ocean Acoustic Tomography*; Cambridge University Press; New York (1995).

National Academy of Sciences. *Ocean Wave Spectra: Proceedings of a Conference*; Prentice-Hall; Englewood Cliffs, N.J. (1963).

Naugolnykh, S. A.; and L. A. Ostrovsky. *Non-Linear Wave Processes in Acoustics*; Cambridge University Press; New York (1997).

Neubauer, W. G. *Acoustic Reflections from Surfaces and Shapes*; Naval Research Laboratory; Washington D.C. (1986).

Novikov, B. K.; O. V. Rudenko; and V. I. Timoshenko. *Nonlinear Underwater Acoustics*; Acoustical Society of America; Woodbury, N.Y. (1987).

Oglivy, J. A. *Theory of Wave Scattering from Random Surfaces*; IOP Publishing Ltd; London (1992).

Olson, H. F. *Elements of Acoustical Engineering*, 2d ed.; D. Van Nostrand; New York (1947).

Oppenheim, A. V.; and R. W. Schafer. *Digital Signal Processing*; Prentice-Hall; Englewood Cliffs, N.J. (1975).

Pace, N. G., ed. *Acoustics and the Seabed*; Bath University Press; Bath, U.K. (1983).

Pekeris, C. L. "Theory of propagation of explosive sound in shallow water," in *The Geological Society of America Memoir 27*; Geological Society of America; New York (1948).

Phillips, O. M. *The Dynamics of the Upper Ocean* 2d ed.; Cambridge University Press; Cambridge (1980).

Pickard, G. L.; and W. J. Emery. *Descriptive Physical Oceanography*, 4th Edition; Pergamon Press; New York (1982).

Pierce, A. D. *Acoustics*; Acoustical Society of America; Woodbury, N.Y. (1991).

Potter, J.; and A. Warn-Varnas. *Ocean Variability and Acoustic Propagation*; Kluwer Academic Publishers; Boston (1991).

Rayleigh, Lord [J. W. Strutt]. *The Theory of Sound* (2nd ed. 1896); Dover Publications; New York (1945).

Robinson, E. A.; and S. Treitel. *Geophysical Signal Analysis*; Prentice-Hall; Englewood Cliffs, N.J. (1980).

Rona, P. A. *NOAA Atlas 3. The Central North Atlantic Ocean Basin and Continental Margins: Geology, Geophysics, Geochemistry, and Resources Including the Trans-Atlantic Geotraverese (TAG)*; U.S. Department of Commerce, National Oceanic and Atmospheric Administration, Environmental Research Laboratories, Miami (1980).

Ross, D. *Mechanics of Underwater Noise*; Peninsula Publishing; Los Altos, Calif. (1987).

Shiff, L. *Quantum Mechanics*; McGraw Hill; New York (1949).

Stoll, R. D. *Sediment Acoustics*; Springer-Verlag; New York (1989).

Tate, J. T.; and L. Spitzer, eds. *The Physics of Sound in the Sea: Summary Technical Report of Division 6*; U.S. Government Printing Office; Washington, D.C. (1946).

Tolstoy, I. *Wave Propagation*; McGraw-Hill; New York (1973).

Tucker, D. G.; and B. K. Gazey. *Applied Underwater Acoustics*; Pergamon Press; New York (1966).

Urick, R. J. *Principles of Underwater Sound*, 3d ed.; Peninsula Publishing; Los Altos, Calif. (1983).

v. Karman, T.; and M. A. Biot. *Mathematical Methods in Engineering*; McGraw-Hill Book Company; New York (1940).

Vogt, P. R.; and B. E. Tucholke, eds. *The Geology of North America: The Western North Atlantic Region*; Geological Society of America; New York (1986).

Wilson, O. B. *An Introduction to the Theory and Design of Sonar Transducers*; Peninsula Publishing; Los Altos, Calif. (1985).

Worzel, J. L.; and M. Ewing. "The propagation of sound in the ocean," in *The Geological Society of America Memoir 27*; Geological Society of America; New York (1948).

Ziomek, L. J. *Underwater Acoustics: A Linear Systems Theory Approach*; Academic Press; New York (1985).

Symbols

Different ocean acoustic specialties such as wave propagation, scattering by objects and rough surfaces, transducers, nonlinear propagation, oceanography, geophysics, and fishery acoustics use some of the same symbols in different contexts. Where possible, our expressions use symbols appropriate to the different technical areas; thus some of the same symbols and parameters appear in different contexts. We employ Italicized Times Roman, greek, and Zapf Chancery fonts for symbols. When the meaning is clear, and in order to simplify the notation, the functional dependence may be omitted. When the units of the quantity are not obvious, we specify them. The number in parentheses refers to the equation where the symbol is encountered first in this text. A&S refers to symbols and sections in Abramowitz and Stegun (1964).

a	radius of a sphere or cylinder
a	the ray parameter for refraction (3.3.3)
a_{ec}	radius of an equivalent volume cylinder (7.4.26)
a_{es}	radius of an equivalent volume sphere (7.4.27)
a_n	displacement amplitude of the nth transducer element (4.2.7)
A	dispersion constant for the boundary wave, dimensionless (13.2.16); insonified area (13.3.17)
A_m	amplitude of the mth cylindrical mode at the source (11.1.20)
A_s	amplitude factor proportional to source power in modal analysis (11.1.23)
A_n	amplitude of the sum of hydrophone signals (10.1.2)
A/D	analog to digital conversion
b	real component of the ratio of specific heats, γ, dimensionless (8.2.23); separation between adjacent elements of a line source (4.2.1)
b_n	gradient of sound speed,(m/s)/m (3.3.15)
B/A	parameter of nonlinearity, dimensionless (5.1.8)

BW	bandwidth, Hz
BSS	backscattering strength (13.3.33)
B	pressure amplitude for impulse diffraction, pascal $\sec^{1/2}$ (12.2.10)
c	sound speed or velocity; subscripts identify the medium or type of wave (1.2.1 and 3.3.2); c_R, Rayleigh wave; c_s, shear wave; c_p, compressional wave
$C(k)$	covariance of a random signal (6.4.1); C_{uk} unknown (sample) covariance matrix (11.5.2)
$C(\tau)$	autocorrelation of time varying surface (13.1.7)
$C(\xi)$	spatial correlation in the x direction of a rough surface (13.1.15)
$C_{xx}(\tau)$	autocovariance of a signal (6.4.7)
$C(x)$	Fresnel cosine integral; also see $S(x)$
d	a distance or separation (4.8.2); imaginary component of the complex ratio of specific heats, γ, dimensionless (8.2.23)
dB	decibel, 20 $\log_{10}$ of ratio of pressures, voltages, and so forth to appropriate reference values; 10 $\log_{10}$ of ratio of intensities, or powers to appropriate reference values; subscript $_{10}$ is often omitted
dS	element of area
DSL	deep scattering layer (biological) (section 9.3.4)
D	transducer and array directional responses; also with subscripts and functional dependence as in $D(\theta)$, D_t, and D_r directivity factors for transmitter and receiver, dimensionless (4.2.13); diffraction terms in the wedge solution (11.8.51); periodic separation of wedges (12.4.2)
$\mathcal{D}$	product of transmit and receive directivities (10.4.1)
DI_t, DI_r	directivity index for transmission, reception, dB, $10\log_{10}(D_t)$, and 10 $\log_{10}(D_r)$, (4.5.9 and 13.3.1)
DF	detection factor (11.5.4)
DS	diffraction strength, dB (11.5.4)

D_b	damping rate, $\sec^{-1}$ (8.2.43)
e	base of natural logrithms, 2.71828; error matrix for matrix inversion (10.6.2); ratio of bulk elasticities in two media; $e_n(t)$ amplitude of envelope of a ping (10.2.1 and 10.4.14)
e_G	amplitude of the envelope within "gate open" interval (9.4.10)
esr	equivalent spherical radius (Fig. 10.6.3)
E_m	message energy passing through an area in a given time, joules (3.1.11 and 6.6.3)
E_n	bulk modulus of elasticity of medium n (2.5.5 and 2.5.7)
$E_{xx}(f_j)$	energy spectral density at frequency f_j (6.2.44)
f	sound frequency, Hz (2.3.2)
f_m	frequency of the mth harmonic; subscripts give specific harmonic
f_c	carrier frequency, Hz (6.3.2); waveguide cut-off frequency (11.1.53)
$f(t), f(x)$	general functions of time or position
f_r	relaxation frequency of a molecular process (3.4.22)
f_b	simple bubble breathing frequency, Hz (8.2.13)
f_R	corrected bubble breathing frequency, Hz (8.2.27)
f_d	frequency of damped oscillation, $\sec^{-1}$ (8.2.50); heterodyne-shifted frequency (10.2.8)
f_H	heterodyning frequency (10.2.3)
$\boldsymbol{f}$	a generalized vector (7.2.1)
F	ratio of near-surface bubble frequency to free-space frequency (8.2.53); frequency of an ocean surface gravity wave, $\sec^{-1}$ (Fig. 8.4.6)
g	acceleration of gravity, m/s^2 (8.2.14); ratio of densities in two media
g_r	volume flow per unit length, m^2/s (7.4.16)
g_R	acoustical roughness for scatter from a randomly rough surface (13.2.5)

g_t	acoustical roughness for transmission through a randomly rough surface (13.5.6)
g_A	linear sonar receiver gain factor
$g(t)$	a function of time (3.1.3)
g_{rcvr}	gain of receiver (10.2.23)
g_{TVG}	time-varying gain function (10.2.24)
$g_2 = \pm[(c_2/c_1)^2 - 1]^{1/2}$	function for incident angles greater than critical (2.6.14 and 11.1.32)
G	sonar receiver gain in dB (10.2.23); pressure transmission function in a waveguide (11.1.29); scattering angular function (13.3.4)
$\mathcal{G}$	imaginary value for transmission (2.6.14); beam geometry term in rough-surface scatter (13.3.16)
$G^* = G + G'$	dynamic shear modulus, (newtons/m^2)/(m/s) (8.6.1)
h	ratio of sound speeds for two media (7.3.24); height (2.6.31); $h(t)$ filter response
$H_n^{(1)}(x)$ and $H_n^{(2)}(x)$	cylindrical Hankel functions (7.4.18) (A&S, chap. 9)
$i = \sqrt{-1}$	imaginary number; also a summation index
i or $i(t)$	instantaneous intensity: the energy passing through a perpendicular unit area in unit time, watts/m^2, a vector (2.1.2)
i, j, k	unit vectors along coordinates x, y, and z
I	time average intensity, watts/m^2 (2.5.16); current in transducer calibration, amperes (4.7.1); I (...) spectral intensity in 1 Hz band, (watts/m^2)/Hz
I_n	an integral in the wedge diffraction solution (11.8.18)
$\boldsymbol{j}$	unit vector along coordinate y
$j_n(x)$	spherical Bessel function of first kind and order n (A&S chap. 10); see $y_n(x)$ for companion function
$J_n(x)$	cylindrical Bessel function of first kind and order n (A&S chap. 9); see $Y_n(x)$ for companion function
J	transducer reciprocity factor, watts/Pa^2 (4.8.1)
k	wave number or propagation constant, m^{-1} (2.3.5b); subscripts give the medium; an integer in the image construction of the wedge problem (11.8.35)

k_0	a reference wave number (11.7.1)
k_R	grazing propagation constant over a rough surface (13.2.16)
k_S	grazing propagation constant over a smooth surface (13.2.16)
k_B	grazing propagation constant for boundary wave over a rough surface (13.2.17)
$\boldsymbol{k}$	unit vector along coordinate z
k_{LW}	empirical constant for fish weight, gm/cm^3 (9.5.24)
K	ocean surface wave number, radians/meter (13.1.13); compressibility, reciprocal of bulk elasticity, Kg s^{-2} m^{-1} (6.3.21)
$\mathcal{K}$	ocean bottom spatial cycle frequency, cycles/meter (13.1.21); thermal conductivity of a gas (8.2.28a); horizontal component of wave number in waveguide (11.1.7)
$K_{v/p}$	transducer voltage to pressure conversion factor, volts/μPa (4.5.3)
$K_{p/v}$	transducer pressure to voltage conversion factor, at a defined position, Pa/volt (4.6.1)
l	dipole separation (4.1.9)
L	length of a cylinder, or a rectangular transducer face, or a path (2.6.30); folding depth, distance to decrease to e^{-1} of reference value (8.4.2); spatial correlation length, where subscripts indicate direction (13.1.16)
L_{ec}	equivalent scattering length of a cylinder; subscripts *ebc* for equivalent bent cylinder; subscript x for projection on x axis and so on (9.6.1 and 9.6.3)
$\mathcal{L}(\theta, \phi, f)$	acoustic scattering length or amplitude (spectral) in θ, ϕ direction, meters (7.1.3); subscripts give particular case—for example, *blad* for bladder (9.5.1), *bod* for body (9.5.12), and K for Kirchhoff method
$\mathcal{L}_{bs}(f)$	acoustic backscattering length (7.1.9)
$\mathcal{L}_{gs}$	acoustic scattering length for geometrical scatter (7.5.6)

$\lvert\mathcal{L}_{bs}(L/\lambda)\rvert/L$	relative, or reduced, backscattering length (9.5.16)
ln	natural logrithm to base e
log, $\log_{10}$, log(.)	logarithm to base 10
m	lumped mass of an oscillating acoustical system (8.2.1); source mass injection/volume (4.1.5); statistical moment of a surface roughness, subscript indicates order (13.1.2); mode number in a waveguide (7.4.2 and 11.1.13); order of diffraction by a grating (12.4.2)
M	number of modes (7.4.24); mass per unit area per unit time (5.4.4)
$\mathcal{M}$	acoustical Mach number (2.5.11 and 5.1.14)
n	an integer (2.6.36); the number of sources (4.2.2); index of refraction (11.7.1)
$n(a)\,da$	number of bubbles of radius a, in increment da, per unit volume, m^{-3} (8.3.8)
$\boldsymbol{n}$	vector normal to an area, dS; matrix vector for density components of scatterers, m^{-3} (10.6.7)
n_b	number of scattering bodies per unit volume, m^{-3} (9.3.7 and 10.4.27); noise output voltage of an array (11.3.8)
$n_n(x)$ or $y_n(x)$	spherical Bessel function of order n (A&S chap. 10)
n_{cdf}	critical density of fish, number per unit volume, m^{-3} (10.3.7)
N	correction for spherical wave reflection (2.6.40); number of elements of a transducer (4.2.1)
N_m	bandpass-filtered noise voltage of the mth mode (11.3.8)
N_{it}	number of independent trials (6.4.11)
$N_n(x)$ or $Y_n(x)$	cylindrical Bessel function of order n (A&S chap. 9)
N_{pings}	number of pings (10.4.24)
$\mathcal{N}_{\text{em}}$	number of echoes in the mth amplitude bin per ping (10.4.24)

p	instantaneous acoustic pressures, pascals or micropascals (2.5.1a); subscripts give name—*inc* for incident, *s* or *scat* for scattered (7.1.1); p_d, acoustic pressure radiated by a dipole (4.1.10); p_0, instantaneous acoustic pressure at the reference distance R_0; p_A, ambient pressure, pascals or micropascals (7.4.25); p_T, total pressure (2.5.1a); p_{ns}, backscattered pressure with narrow-beam sonar (10.3.8); p_{ws}, backscattered pressure with wide-beam sonar (10.3.9); p_δ, impulse of pressure, pascal sec (12.3.4)
P	amplitude of acoustic pressures; P_0 at the reference distance R_0 (2.3.1); P_{ax}, axial acoustic pressure amplitude (4.5.5); P_2, pressure amplitude of second harmonic (5.1.12)
P_{RL}	Langevin radiation pressure, pascals (5.5.1)
$P(f)$	spectral acoustic pressure, pascals/Hz
$P(z)$	polynomial generating function of acoustic pressure
$[path]$	acoustic pressure and time history, dimensionless (3.2.3)
$[paf]$	path amplitude factor, dimensionless (3.2.4 and 3.4.36)
Pa	pascal, unit of pressure: 1 newton/m^2
$\mathcal{P}[x_n] = w(x_n)\Delta x$	probability of observing x_n in $x_n \pm \Delta x/2$, subscripts give specific functions
$\mathcal{P}_E(e_n)$	joint probability function (10.4.14)
$\mathcal{P}(\Delta V_G)$	probability of body being in gated volume (10.4.7)
PDF	probability density function
PSD	power spectral density, watts/Hz (6.6.5)
q_m	mode excitation, pascals (11.1.25)
q_n	normal coordinate in the wedge solution (11.8.7)
Q	quality of a resonant system, $Q = f_c/\Delta f$ or $Q = 1/\delta$
Q_t	directivity factor, subscript t for transmitter, r for receiver, dimensionless (4.5.7)

r	radial distance in polar and cylindrical coordinates, r, z, and ϕ; r_{uk}, unknown range (11.3.17); r_{tr}, trial range in matched filter (11.3.19); r_0, range source to diffracting wedge; r, range from diffracting wedge to receiver (Fig. 11.8.1 and Fig 12.2.1)
R	range in spherical coordinates, R, θ, and ϕ; R_s, range source to scatterer (13.3.1); R_0, reference range, usually 1 meter (2.1.2); R_c, "critical range" for far-field of transducer (2.4.16)
R_m	lumped mechanical resistance of an oscillating system, newtons/(m/s) (8.2.38)
$\mathcal{R}(R)$	radial function solution of the wave equation (2.7.37)
$\mathcal{R}_{12}$	plane wave pressure reflection coefficient at the 1-2 interface (2.6.8)
$\mathcal{R}_{ss}$	specular scatter, coherent reflection coefficient (13.2.4)
$\mathcal{R}_a$	apparent reflection coefficient (13.3.22)
s	lumped stiffness of an oscillating system, newton/m (8.2.1)
$s(t)$	sum of pressure or voltage signals of all receivers in a waveguide (11.3.1)
s	rms slope of a surface; s_w, rms slope in windward direction; s_c, rms slope in the cross wind direction (13.1.5)
$s_v(f)$	volume sattering coefficient, m^2/m^3
$\boldsymbol{s}$	matrix vector of volume scattering coefficients (10.6.6)
S_{bs}	backscattering cross section per unit volume, m^{-1} (8.3.8)
S_v	volume backscattering strength in dB (9.3.19)
S	transducer source response at a designated position, μPa/ampere (4.8.1)
$S(\omega)$	waveguide source function, Hz^{-1} (11.2.3)
$S(x)$	Fresnel sine integral (9.6.7); see also $C(x)$ in A&S chap. 7

S	salinity, parts per thousand (1.2.1); cross sectional area—for example, of a raytube (3.2.14)
S	surface scattering coefficient (13.3.32)
SL	source level, dB (3.4.43)
SPL	sound pressure level, dB (3.4.44)
t	time; subscripts give particular times
t_0	time between samples (section 6.2.1)
$t_n = nt_0$	the digital time of a sample (6.2.10)
t_p	actual ping duration (6.3.1)
t_d	effective ping duration (6.3.3)
t_{dir}	direct travel time from source to receiver (11.8.20)
τ_r	relaxation time of a molecular process (3.4.15)
$[tips]$	time integral of pressure squared; subscript $_{GV}$ for the gated volume (3.1.13 and 9.3.2)
$[ties]$	time integral of an echo squared (voltage^{2}sec or pressure^{2}sec) (9.4.12)
$[trans\ (r, f)]$	transmission fraction, dimensionless (3.4.39)
T	period of a periodic wave, sec
T	temperature, degreees centigrade (1.2.1)
$T(t)$	temporal function for propagation of acoustic pressure, dimensionless (2.7.20 and 11.1.2)
TL	transmission level, dB (3.4.45 and 3.4.53)
TC	transmission change of level, dB (13.5.5)
$\mathcal{T}_{12}$	plane wave pressure transmission coefficient at the 1-2 interface (2.6.8)
TS	target strength, dB re 1 m^2 (7.1.4)
TS_{re}	''reduced'' target strength, various references (9.6.6 and 9.6.9) (caption Fig. 9.5.7)
TVG	time-varying gain (Fig. 10.2.2)
u, v, w	rectangular components of particle velocity in x, y, and z directions, m/s (2.5.2 and 2.7.1)
u_R	radial particle velocity at range R (3.1.5)

$u(r, z)$	function of range and depth in waveguide propagation (11.7.2)
u	group velocity of ocean surface wave (13.1.18)
u_{gm}	group velocity of mth waveguide mode (11.2.8)
u_{gmm}	group velocity minimum of mth waveguide mode (11.2.8)
U_a	amplitude of radial particle velocity at $R = a$ (4.1.1)
U	void fraction, ratio of bubble volume to total volume (8.3.34)
$U(Q)$	scattered (spectral) acoustic field at a point Q
U_s	incident acoustic field at the surface, in scattering calculations
U_E	Laplace generating function (10.4.31)
U	a scalar solution of the wave equation (7.2.4)
$U(r)$	radial dependence of field in cylindrical coordinates, dimensionless (11.1.2)
U_s	propagation speed of a shock wave (5.4.4)
v	voltage at a transducer (4.6.3); v_n, voltage peak for narrow-beam receiver (10.3.13); v_w, voltage peak for wide-beam transducer
v	particle velocity in the y direction
v_{rm}	phase velocity of mth mode propagating in the r direction (11.2.2)
v	surface wave phase velocity (13.1.19)
$v(r)$	the range function in the parabolic equation (11.7.2)
V_0	transducer input voltage amplitude (4.6.1)
V_{AB}	a voltage during transducer calibration (4.7.1)
V	volume (8.2.4)
$\dot{V}$	rate of volume flow, m^3/s (4.1.4 and 12.2.2a)
Var	the statistical variance (9.4.3)
w	weight of explosive, kg (5.4.1)
w	particle velocity in the z direction, m/s

$w(x_n)$	probability density function, PDF; $w(x_n)\Delta x$ is the probability of observing a value of x_n between $x_n - \Delta x/2$ and $x_n + \Delta x/2$; w_{Rayl}, Rayleigh probability density function (13.2.9); w_E, PDF of an echo (10.4.16); w_F, PDF of fish scattering length (10.4.18)
W_f	fish weight, gm (9.5.24)
W	width, of a rectangular face
W_T, W_E, W_F	Laplace generating functions (10.4.30, 10.4.32 and 10.4.34)
$\mathcal{W}$	characteristic function for scatter from a two-dimensional rough surface (13.3.12)
x, y, z	rectangular coordinates in X, Y, Z system
x_{crit}	critical (minimum) distance for far-field approximation (5.2.4)
$x(n)$	the nth digital input amplitude (6.2.2)
$x(t)$	filter input source signal at time t (Table 6.1); a signal (10.2.1)
X	a distance (5.1.12)
$X(x)$	a function of coordinate x (2.7.20)
$X(f)$	input amplitude spectral density (6.2.36)
$X_{fft}(m)$	the mth spectral component in an FFT (6.2.1)
y	a rectangular coordinate
$y(t)$	filter output in time domain (Table 6.1)
$y_M(j)$	convolution of signals (6.5.1)
$Y(y)$	a function of coordinate y (2.7.20)
$Y_n(x)$	spherical Bessel function of order n (A&S chap 10)
$Y(f)$	output amplitude spectral density (6.2.36)
Y	non–shock wave energy in an explosion, joules (5.4.8)
Y	ratio, resonance frequency divided by insonification frequency (8.3.25)

z	a rectangular coordinate; depth m (1.2.1); z_{uk}, unknown depth (11.3.17); z_{tr}, trial depth for matched filter (11.3.19)
$Z(z)$	a function of coordinate z (2.7.20); $Z_m(z)$ eigenfunction of z dependence of mode m in cylindrical coordinates (11.1.15)
z_i	source depth vector matrix eigenfunction for waveguide (11.4.1)
z_j	receiver depth vector matrix eigenfunction for waveguide (11.4.1)
α_e	naperian logarithmic attenuation rate for plane waves, nepers/m (3.4.1)
α	attenuation rate for plane waves, dB/m (3.4.6)
α_b	plane wave logarithmic attenuation rate due to bubbles, dB/m (8.3.18)
α	a constant in the Pierson-Moskovitz wind wave spectrum, dimensionless (13.1.11)
α	function of angles in rough surface scatter (13.3.5a)
α	ratio, gate open duration/signal duration (9.4.13)
β	ratio of bubble interior pressure to ambient pressure (8.2.27)
β	a parameter in the equation of a parabolic bent cylinder (9.6.4)
β	a parameter in nonlinear propagation (5.1.11)
β	a constant in the Pierson-Moskovitz wind wave spectrum, dimensionless (13.1.11)
β	a function of angles in rough surface scatter (13.3.5b)
β_+	a parameter in wedge diffraction (11.8.63 and 12.2.3)
γ	a function of angles in rough surface scatter (13.3.5b)
γ	vertical component of wave number in cylindrical waveguide propagation (11.1.7)
γ_m	eigenvalue of mth mode in z direction (11.1.13)
γ	ratio of specific heats of a gas; $\gamma = 1.4$ for air, dimensionless (5.4.9)

$\gamma(f) = \sigma_c(f)/\sigma_d(f)$	ratio of coherent to incoherent components in Rician PDF (9.4.8); see also Fig. 13.2.4
Γ	exponential power in the adiabatic relation (5.1.2)
δ	an increment (2.1.1)
δ	an empirical damping constant for dissipation in wedge diffraction (11.8.48)
δ	total damping constant of a bubble, dimensionless (8.2.30)
δ_r	bubble damping constant due to reradiation (scattering), dimensionless (8.2.30)
δ_t	bubble damping constant due to thermal conductivity, dimensionless (8.2.30)
δ_v	bubble damping constant due to shear viscosity, dimensionless (8.2.30)
δ_R	total bubble damping constant at resonance, dimensionless (8.2.31)
δ_{Rr}	bubble damping constant due to reradiation at resonance, dimensionless (8.2.31)
δ_{Rt}	bubble damping constant due to thermal conductivity at resonance, dimensionless (8.2.31)
δ_{Rv}	bubble damping constant due to shear viscosity at resonance, dimensionless (8.2.31)
$\delta(t - t_n)$	Dirac delta function, everywhere 0 except infinite at $t = t_n$ (3.1.1)
$\delta(n - m)$	Kronecker delta function; value unity when $m = n$; otherwise zero (11.1.17)
δ_f	finite, discrete delta function (11.8.40 and 12.2.1a)
δ_m	attenuation rate of mth mode (11.1.27)
Δ	a finite increment, as in Δf for a narrow frequency band; ΔR for a range difference (2.4.15); Δz for virtual surface displacement (2.6.25); ΔE for energy passing through an incremental area ΔS (3.1.11); $\Delta\sigma_s$ for differential scattering cross section (7.1.5); Δt for digital duration of a delta function (3.1.1); Δt,

	duration of impulse source (11.8.11); Δt_{ww}, duration of "water wave" in a waveguide (11.5.11)
ΔT	time between impulses (12.2.8)
Δf	effective frequency bandwidth between half-power or half-intensity points (6.3.2)
$\Delta = kL \sin \chi$	a phase shift in scattering from cylinders (7.4.21)
∇	gradient operator (2.7.4, 2.7.10, and 2.7.15)
$\nabla\cdot$	divergence operator (2.7.7, 2.7.13, and 2.7.17)
∇^2	Laplacian operator (2.7.9, 2.7.14, and 2.7.18)
ε	a small quantity; as in length of sagitta of the arc (2.4.1)
ε	roughness parameter for boundary wave (13.2.12)
ε	angular displacement from diffraction shadow boundary (12.2.2)
ε_R	energy per unit area at range R (3.1.15)
ζ	surface displacement (12.4.1)
η	a phase shift (10.2.4)
η	a function of time and distance in wedge diffraction (11.8.26 and 12.2.7)
η	angle of incidence at a cylinder (7.3.15)
θ	polar coordinate in spherical coordinates; angle with the axis of radiation (4.2.2); angle with the normal to the surface in plane wave reflections (2.2.3, 3.3.3, and 11.1.8); angle between diffracting wedge face and receiver (Fig. 11.8.1); angle between sound beam axis and wind wave system direction (13.1.13)
θ_0	angle between diffracting wedge and source (Fig. 11.8.1)
θ_w	wedge angle; angle in fluid between sides of a diffracting wedge (Fig. 11.8.1)
θ_i	angle of incidence at a scatterer (7.5.1)
θ_s	angle of scatter at a body (7.5.4)
θ_c	critical angle for total reflection (2.6.13)

$\mathcal{K}$	thermal conductivity of a gas, cal/(cm s °C) (8.2.28a and 9.5.22)
$\mathcal{K}$	wave number of an ocean wave component (13.1.13); subscripts designate direction (13.1.14)
λ	acoustic wavelength (2.3.1)
λ_a	apparent acoustic wavelength in doppler shift (3.6.1)
λ_s	spatial distance between samples (section 6.1)
Λ	ocean wavelength
Λ	waveguide mode interference wavelength (11.1.55)
μ	dynamic coefficient of shear viscosity, pascal sec (3.4.10)
μ_b	dynamic coefficient of bulk viscosity, pascal sec (3.4.9)
μ_m	waveguide parameter that includes unknown source power, depth, and range (11.5.7)
ν	a parameter in the wedge diffraction solution (11.8.19)
ν_m	a quantity proportional to the energy flux in mode m (11.1.16)
ξ	a parameter in the wedge diffraction solution (11.8.24)
Π	power passing through an area, watts (3.1.16)
Π_{gs}	geometrically scattered power, watts (7.5.4)
Π_M	source message power, watts (6.6.1)
$\Pi_{xx}(f_m)$	spectral density (1 Hz band) of a source at frequency f_m, volt^2/Hz, or pascal^2/Hz (6.4.13 and 6.4.15)
ρ	acoustic density, kg/m^3; subscript numbers identify the medium (2.5.16)
ρ_A	ambient density of the medium, kg/m^3 (2.5.16)
ρ_T	total density of the medium, kg/m^3 (2.5.16)
σ_e	total extinction cross section of a body, m^2 (7.1.12)
σ_s	total scattering cross section of a body, m^2 (7.1.11)
σ_a	total absorption cross section of a body, m^2 (7.1.11)

$\sigma_{bs}(f)$	obsolete form of backscattering (differential) cross section (Clay and Medwin 1977) (7.1.8); see $\Delta\sigma_{bs}(f)$
$\sigma_c(f)$	concentrated (mean) component of the backscattering (differential) cross section (9.4.4)
$\sigma_d(f)$	distributed (variable) component of the backscattering (differential) cross section (9.4.5)
τ	a delay time (3.1.9); a decay time (5.4.2); surface tension (9.5.22); travel time excess beyond the least time in wedge diffraction (11.8.28 and 12.2.6)
τ_0	travel time from source to wedge crest to receiver (11.8.21)
τ_{12}	pressure transmission coefficient at 1-2 interface (2.6.11)
ϕ	azimuthal spherical coordinate
Φ	phase angle (2.4.17); phase shift (2.6.17)
$\Phi(\Omega)$	ocean wave spectral density, m^2/Hz (13.1.8)
χ	tilt angle of a cylinder (7.3.19)
ψ	empirical phase shift or amplitude adjustment (7.3.21 and 9.5.1); spatial part of the solution to the wave equation in cylindrical coordinates (11.8.2)
Ψ_D	integrated beam pattern (4.5.4 and 9.3.11)
ω	angular frequency, radians/sec (2.3.5a); subscript number is harmonic number (5.3.1); subscript letter is descriptive (5.3.6)
Ω	element of solid angle (3.1.11a)
Ω	angular frequency of a time-varying ocean surface displacement (13.1.8); Ω_m is the frequency of the maximum (13.1.7)

Subject Index

Absorption, 18, 104
Acoustic
  boundary layer, 180
  daylight, 411
  density, 36
  equation of state, 154
  particle velocity, 65
  power, 76, 143
  pressure, 37, 65
  radiation pressure, 177
  streaming, 178
Acoustical oceanography, 1
  active, 8
  passive, 15
Adiabatic
  approximation, 509
  gas relation, 154
Algorithms, 225
  Biot-Tolstoy wedge, 530
  deconvolution for fish data, 445
  MATLAB signal processing, 225
Approximations
  adiabatic, 509
  far field, 31
  Fraunhofer, 29
  Fresnel, 29
  plane wave, 28
Array
  cosine, 13
  Gaussian, 135
  line, 135
  triangular, 135
  uniform, 135
  waveguide, 4
Attenuation, 103
  decibels, 104
  formulas, 109
  nepers, 103

Backscattering length
  bubble, 290
  fish, 352
Bandshifting, 418
Beam width, 146
Bioacoustic pyramid, 349
Biological pyramid, 4
Biot-Tolstoy exact wedge theory, 519
Bottom loss, 613
Boundary
  hard, 44
  soft, 44
Boundary wave
  dispersion, 630
  propagation, 627
  wave guide, 631

Breaking wave, 334
Bubble, 287
  backscattering length, 290
  corrections, 307
  cross sections, 302, 305
  damped motion, 304, 306, 310
  damping, 299
  lumped constant, technique, 292
  modal solution, 289
  non-spherical, 308
  oscillating mass of, 293
  resonance frequency of, 294
  scatter directivity, 290
  sediments, 341
  stiffness of, 293
Bubbly water
  attenuation, 314
  dispersion, 317
  scatter, 311

Caustics, 94
Cavitation, 158
Channel axis, 7
Characteristic equation for waveguide, 477
Coherent reflection coefficient, 595
  inversion for PDF of heights, 596
Condensation, 19
Conservation
  energy, 82
  mass, 37
Convolution, 195. See also *Deconvolution*
  for echo PDF, 443
Coordinates
  cylindrical, 61
  Eulerian, 36
  Lagrangean, 36
  spherical, 61
Correlation
  auto, 209
  cross, 421
Critical angle, 41
Critical fish density, 431
Critical reflection, 50, 476
Cross section. See also *Bubble*
  absorption, 238
  extinction, 238
  scattering, 238
Cylinder scatter
  finite, 262
  finite fluid, 255, 257
  infinite, 259
  modal solution, 258
  penetrable, 252
  tilted, 256, 263

Decibels, 104
Deconvolution, 445, 449
Deep scattering layer (DSL), 361
Delta function
  Dirac, 72
  Kronecker, 473
Density
  acoustic, 36
  ambient, 36
  total, 36
Differential scattering cross section. See also *Scattering, cross section*
  and scattering length, 237
  and target strength, 240
Diffraction, 18
  double, 559
  edge, 23
  plate, 558
  thick-plate, 561
  wedge, 552, 557
Directional response, 147
Directivity, 134
  factor, 145
  index, 146
Dispersion, 18
  bubbly water, 317
  wave guide, 486
Doppler shift, 119
  navigation, 124
  particle motion, 120
  sea surface, 122
Dual-beam transducer sonars, 432

Echo sounder, 407, 422
Eigenfunction, 472
Eigenvalue, 472
Energy
  conservation, 18
  density, 76
  message, 75
Ensemble of fish
  PDF of echoes–random fish tilts, etc., 451
  volume scattering coefficient, 361
Equivalence of source/receiver directivity, 146

Far field, 66
Filter, 184, 188, 197
  matched, 209
Finite wedge scattering, 543
  for impulse, 552
  for Huygens sources in, 553
  in frequency domain, 564
  for shadow penetration, 556
  for wedge spectra, 557
  for finite crest length, 563
  for offset wedge, 563
  for strip, 566
Fish
  acoustical parameters, 376
  body scatter, 378
  critical density, 432
  ensembles, 450
  models, 372, 381, 386, 396
  patchiness, Plate 5
  structure, 363
  swimbladder parameters, 389
  swimbladder resonance, 384
  swimbladder scatter, 374
  target strength, 383
  tilts, 454
  whole scatter, 379
Fluctuations of sound transmissions
  due to bubbles, 319
  long-range transmission, 501
  shallow water waveguide, 486
Fourier
  integrals, 191
  series, 191, 192
Fraunhofer region, 25
Frequency, 26
  angular, 26
Fresnel zones, 55, 351
  approximation, 246

Gas globe, 174
Gated signal, 199
Gauss theorem, 241
Geometrical dispersion, 486
  group velocity, 487
  phase velocity, 486
Global warming, 8
Green's function, 475
  transmission, 375
Green's theorem, 242

Harmonic distortion, 156
Helmholtz-Kirchhoff (HK) methods
  and experiment, 557–560
  for fish body, 373, 378
  for fish swimbladder, 373
  for fluid cylinders, 252
  for rectangular plane facet, 249
  for wedges, 542
  for zooplankton, 392
  Fresnel approximation, 246
  Kirchhoff approximation, 244
Hilbert transformation
  at caustic, 97
Homogeneous medium, 18
Hooke's Law, 38
Huygens' Principle, 19

Images
  Biot-Tolstoy wedge, 524
  construction with reflections, 78
  Huygens' construction, 21
Imaging
  ocean bottom, 10
  ocean surface, 12
  ocean volume, 12
Impedance
  specific acoustic, 39
Impulse, 72

Impulse reflection
  by fluid cylinder, 396
  by live decapod shrimp, 397
Integrated beam pattern, 144
Intensity
  average, 41
  instantaneous, 40, 74
Interference, 18
  at an interface, 33
  Lloyd's mirror, 34
  Inverse solution for multiple frequencies, 461
Isotropic medium, 18

Kirchhoff approximation, 244. See also *Helmholtz-Kirchhoff methods*

Laplace generating function, 445
  z-transform, 445
Laplacian, 60

Mach number, 40, 158
Matched
  field processing, 502
  filter processing, 209
  waveguide, 497
  field, 502
  signal, 501, 506
Mode. See also *Waveguide*, 469
  characterisic equation, 477
  excitation, 474
  orthogonality of, 473
  processing, 505
  transmission function, 475
Mode filters, 493
  by arrays, 493, 497
  by matched array, 498
  for noise, 496
Mode interferences, 484
Molecular relaxation, 105
  boric acid, 109
  magnesium sulfate, 108
Monopole, 128
Multiple arrivals by raypaths, 80

Near field, 142
Non-linearity, 155
Normal coordinates, 519. See also *Wedge impulse scatter*
  diffraction, 527
  generalized force and source, 519
  images, 524
  theory and experiment, 534
Normal modes. See also *Mode*
  fluid cylinder, 258
  fluid sphere, 267
  plane-layered media, 469

Obliquity factor, 20
Ocean bottom
  backscatter, 650
  correlation function, 591
  deep tow side-scan images, 643
  mosaic of deep tow, 645
  spatial correlation functions, 589, 591, 651, 653
  spatial frequency spectra, 588–591, 659
  spatial spectrum, 589
Ocean surface
  frequency spectrum, 583
  moments, 579
  PDF of displacements, 578
  PDF of slopes, 580
  space-time correlation, 588
  spatial correlation, 585
  temporal correlation, 580
Ocean volume
  biological and physical realms, 2, 3
  physical characteristics, 2

Parabolic equation (PE), 514
Parametric receiver, 168
  directivity, 169
Parametric source, 162
  directivity, 167
Particle velocity, 37, 74
PDF. See *Statistics*
Period, 26
Phase
  shift of caustic, 91
  spatial, 26
  temporal, 26
  velocity, 486
Plane wave approximation, 58, 78, 235, 350
Plankton
  bubble-carrying, 401
  zooplankton, 401
Power, radiated, 76
Pressure
  acoustic, 37
  ambient, 37
  impulse, 74
  pulse timing, 8
  ray tube, 83
  reference, 113
  release, 44
  total, 37

Rainfall, 337
Rankine-Hugoniot equations, 173
Rarefaction, 19
Ray
  caustics, 94
  crossing, 94
  multiple paths, 80
  parameter, 85
  paths, 71, 89
  tracing, 85
Ray path
  amplitude factor [*paf*], 77
  time, 77
Reflection, 18
  along ray paths, 78
  coefficient, 43
  from a disk, 57
  layers, 46
  multiple layers, 69, 477
  plane wave, 22

sediment, 45
wedge wall, 524
Reflector
virtual, 50
Refraction, 18
plane wave, 22, 85
Reverberation
bodies, 353
bubble, 311
Reynolds stress tensor, 129

Sampling
Nyquist, 184
spatial, 185
temporal, 185
Saturation, 159
Scale model
boundary wave, 627
head wave, 53
rough waveguide, 631
seamount, 563
surface scatter, 603
transmission, 632, 635
Scattering, 24, 110
cross section, differential, 227
cross section, total, 238
length, 237
modal solution, 258
plane facet, 249
specular, 249
Sea beam swath mapping, 647
backscatter. See *Ocean bottom*
Seamount diffraction, 563
computer model, 564
scale model, 563
Shock wave
growth, 153
repeated, 156
single, 170
theory, 173
Side scan, 11. See also *Sonar*
Signal
CW, 24
impulse, 72
ping, 236
random, 204
Sine function, 137
Single transducer sonars, 437
Smokers, 12, Plate 3
Snell's Law, 22, 85
Sofar, 71
Sonar, 10, 16
calibration, 427
Doppler, 409
dual beam, 432
equations, 111, 113
multibeam, 408
side scan, 408
single transducer technique, 437
split beam, 435
system specifications, 424
Sound
biological, 215
channel, 469
Knudsen sea noise, 214
physical, 213
rainfall, 214
sea surface, 214
ship, 219
Sound speed
in bubbly region, 155
variation with T, s, z, 3, 26
Sound speed profiles
Arctic ocean, 90
Mediterranean Sea, 98
North Atlantic, 91
Source
array, 133
demodulation, 170
dipole, 130
directivity, 134
Gaussian, 135
location, 501, 502, 506
materials, 132
monopole, 128
piston, 138
weighting, 135
Spectral
dependence, 208
smoothing, 206
Spectrum
random signal, 200
relation to correlation, 203
Specular scatter, 594
coherent component, 594
image reflection, 610
incoherent component, 601
scale model of, 603
signal enhancement, 606
statistics of, 594, 599
Speed of sound, 3, 85
profile, 87
Sphere scatter
equivalent, 265
fluid, 284
geometrical, 268
mode solution, 276
Rayleigh, 271
rigid, 281
scattering cross section, 280
Split-beam transducer sonars, 435
State, equation of, 38
Statistics
beam pattern, 439
echo PDF, 441
extremal, 370
Rayleigh, 370
Rician, 369
Surface roughness
acoustical, 596
coherent scatter, 596
Rayleigh parameter, 595
statistics, 578
Surface scatter
apparent reflection, 614

Surface scatter, (continued)
beam width dependence, 614
bubble effect on, 625
computer model of, 618
grazing incidence, 627
incident angle dependence, 615
range dependence, 617
scattering parameter, 628
spherical wave, HKF theory, 607
two-dimensional, 623
Swath mapping, 10, Plate 2
Swimbladder examples
brook trout, 450
cod, 365
pollack, 364
shad, 384
Swimbladder sound scattering
high-frequency, 374
low-frequency, 386

Target strength, 240
of fish, 383, 430
reduced, 390
Thermocline, 5
Time integral pressure squared [*tips*], 76
for many scatterers, 357
processing, 426
Time reversed transmissions, 501
matched signals, 209, 506
Tomography, 8, 116, Plate 1
Total reflection. See also *Critical reflection*
in waveguide, 477
Transducer
calibration, 15, 149
directional beam pattern, 138
fish survey, 447
intergrated beam pattern, 144
line source, 135
orientation, 351
PDF, 440
piston, 138
power, 143
Transformation, finite Fourier, 188
Transmission
anomaly, 35
fraction, 111
layer, 46
loss, 114
plane wave coefficient, 43
rough interface spherical wave, 635
smooth interface spherical wave, 632
Transmission function, waveguide, 475

Velocity
group, 487
phase, 486
Viscosity
bulk, 104
shear, 104
Volume backscatter
coefficient, 360
strength, 361
Volume flow, 128
point source, 543
Volume reverberation equations, 460

Water waves, 122
Wave
compressional, 18
equation, 38, 55
head, 51
impulse, 19
internal, 15
number, 26
rectangular coordinates, 62
spherical coordinates, 64
standing, 33
traveling, 27
Waveguide, 469
boundary, 476
cut-off frequencies, 480
eigenfunction, 471
matched filter, 498
noise, 496
optimum filter, 497
transmission, 499
wedge, 510, 516
Wavelength, 24
Wedge impulse scatter, 522, 546, 549, 552
BT theory, 516
BTM technique, 543
different boundaries, 531
diffractions, 527, 544
digital implementation, 543, 551
experiments, 533
Huygens' sources, 533
offset wedge, 563
reflections, 524
strip, 566
synthetic seismic profile, 573
waveguide, 516
Wedge spectral scatter, 554
double diffraction, 559
parallel wedges, 568, 572
plate, 557, 566
right-angle bump, 551
right-angle step, 549
right-angle wedge, 547, 556
seamount, 562
shadow penetration, 556
strip, 567
Whale tracking, 16

Zooplankton. See also *Plankton*
allometric descriptions, 393
backscattered sound, 391
distribution profile, 463, Plate 4
HK models, 392
multifrequency inversion, 461
physical properties, 394, 395
reverberation, 458, 460
shrimp backscatter, 378
target strength, 400

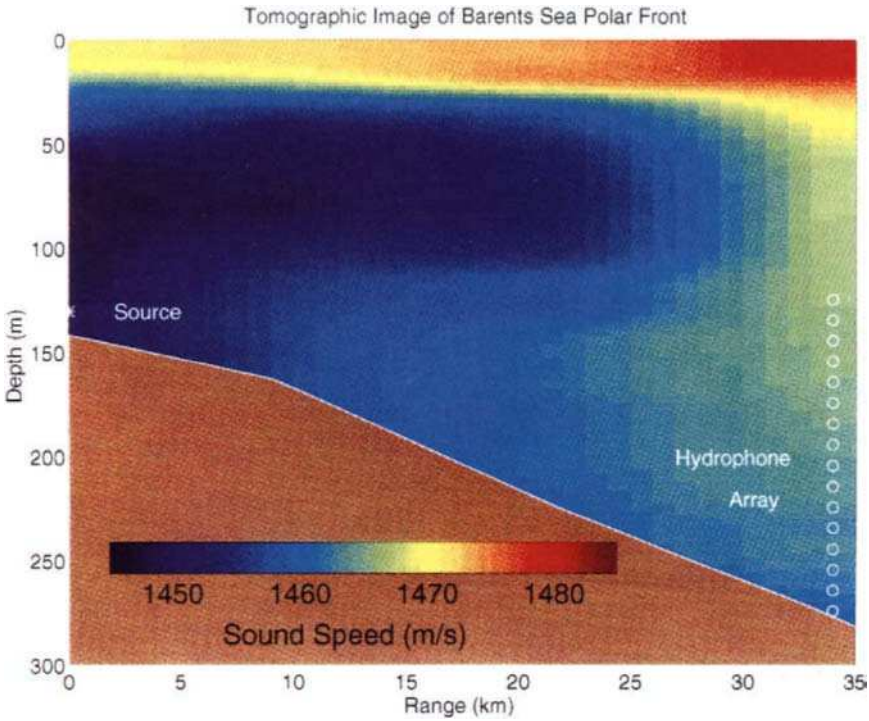

Plate 1 A tomographic image of the sound speed at a polar front in the coastal water of the Barents Sea. A single source of frequency 224 Hz was precisely timed to the 16 receiving elements in the vertical array to provide the input for the inversion which yielded sound speeds from time-of-arrival differences. The temperatures can be calculated from sound speeds by using an equation such as Equation 1.3.1 with an assumption about the salinity. (Chiu, C.-S., J. H. Miller, W. W. Denner, and J. P. Lynch, "Forward modeling of Barents Sea tomography: Vertical line array data and inversion highlights." in *Full-Field Inversion Methods in Ocean and Seismic Acoustics*, O. Diachok, A. Caiti, P. Gerstoft, and H. Schmidt [eds.], Kluwer Academic Publishers, Dordrecht, Netherlands, 237-242, 1995; Parsons, A. R., R. H. Bourke, R. Muench, C.-S. Chiu, J. F. Lynch, J. H. Miller, A. J. Plueddemann, and R. Pawlowicz, "The Barents Sea polar front in summer," *J. Geophys. Res.* **101** [C6], 14201-21 [1996]).

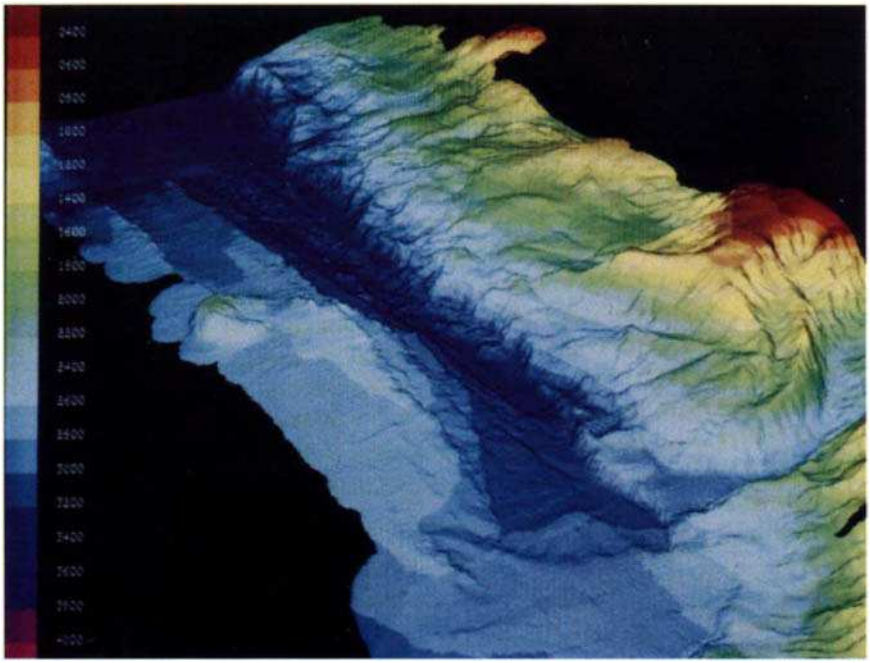

Plate 2 Computer-generated image showing a spreading section of the Chilean Ridge (*left*) colliding with the continental margin of Chile (*right*). The Chilean Trench (*left*) is being overridden by the South American plate. The dark blue trough running from upper left toward the center is the rift valley floor, marked by a line of small volcanic centers. The color code to the left is in meters depth. Bathymetric data were acquired with the SEABEAM swath-mapping system operating at 12 kHz from the R/V Conrad of the Lamont-Doherty Geological Observatory in January 1988. Analysis and color image by Robert C. Tyce, Joyce Miller, and Scott Fergusson, Department of Ocean Engineering, University of Rhode Island.

Plate 3 Three-dimensional reconstruction of two hydrothermal plumes emanating from black smoker-type sea-floor hot springs. Data obtained at sound frequency 330 kHz. (P. A. Rona et al, "Acoustic imaging of hydrothermal plumes," *Geophy. Res. Ltrs.* **18** [12], 2233–36 [1991]).

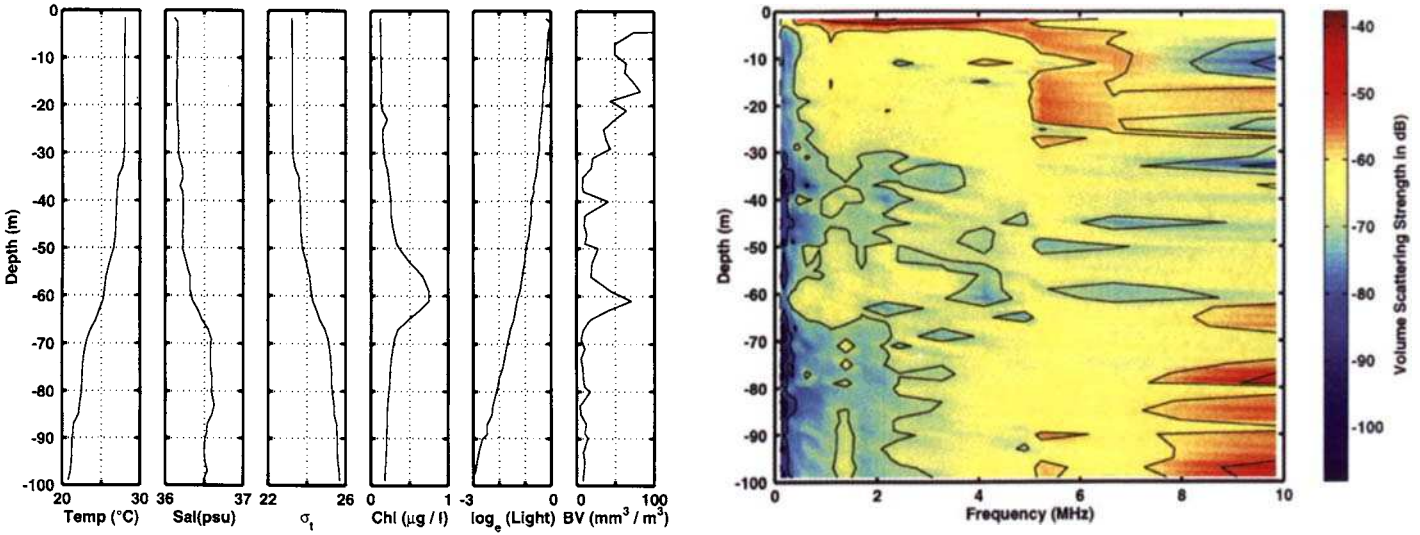

Plate 4a Volume scattering strength from small zooplankton (equivalent spherical radii 0.1 to 4 mm) obtained by backscatter of 21 discrete frequencies 100 kHz to 10 MHz. Simultaneous recording of temperature, salinity, excess density (sigma), and chlorophyll permits one to deduce the ecological conditions required by different size organisms. Data from a station at the northwest wall of the Gulf Stream off Cape Hatteras, North Carolina (35°20′N 74°35′W). These data were collected at 11:35 local time on 12 August 1995. (D. V. Holliday et al., "Determination of zooplankton size and distribution with multifrequency acoustic technology," *J. Cons. Int. Explor. Met.* **46**, 52-61 [1989]).

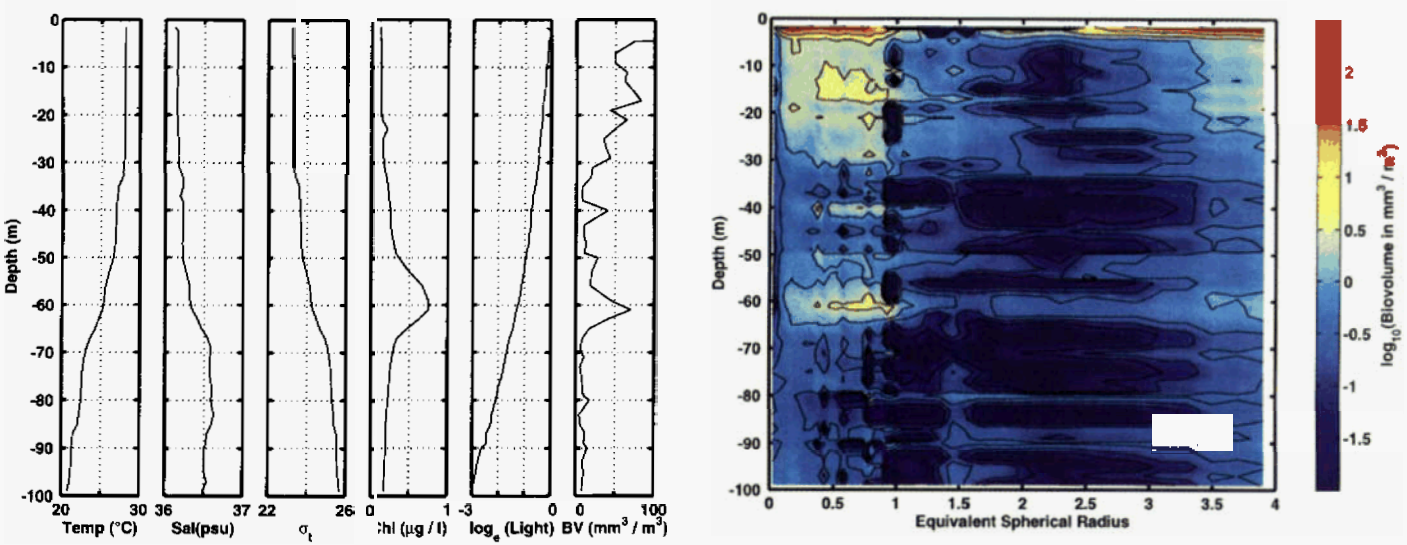

Plate 4b Biovolume of populations of small zooplankton (equivalent spherical radii 0.1 to 4 mm) obtained by backscatter of 21 discrete frequencies 100 kHz to 10 MHz. See plate 4A. Simultaneous recording of temperature, salinity, excess density (sigma), and chlorophyll permits one to deduce the ecological conditions required by different size organisms. (D. V. Holliday et al., "Determination of zooplankton size and distribution with multifrequency acoustic technology," *J. Cons. Int. Explor. Met.* **46**, 52-61 [1989]).

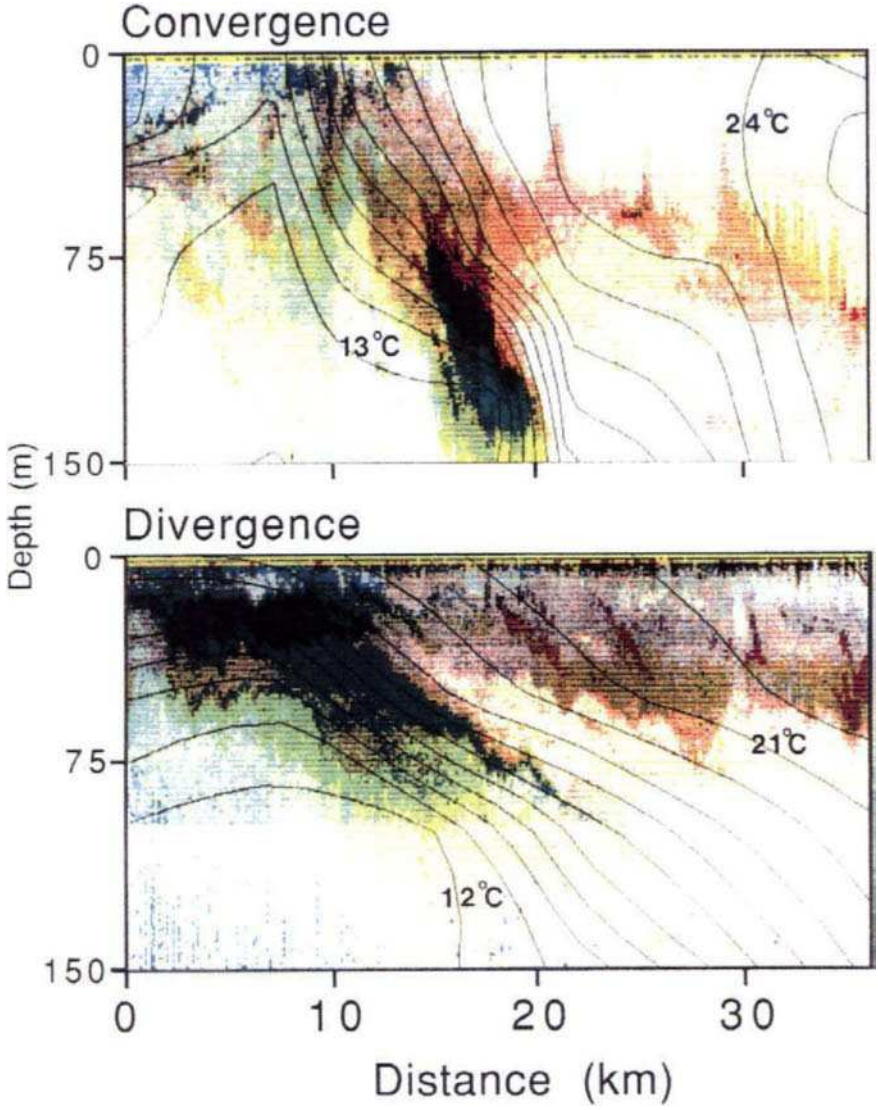

Plate 5 Multifrequency acoustical imagery which describes nekton behavior at convergent (downwelling) and divergent (upwelling) sections of a Gulf Stream meander. Each figure combines three colors–red, yellow, and blue–to represent backscatter of frequencies 38, 70, and 200 kHz, respectively. The color intensity is proportional to the volume backscattering strength. Approximate animal sizes (estimated from concepts such as in Chapters 7, 8, and 9) were 40 mm (red), 20 mm (yellow), and 10 mm (blue). (Arnone, R. W., R. W. Nero, J. M. Jech, I. De Palma, "Acoustic imaging of biological and physical processes within Gulf Stream meanders," *EOS* **71**, 982 [July 17, 1990]).